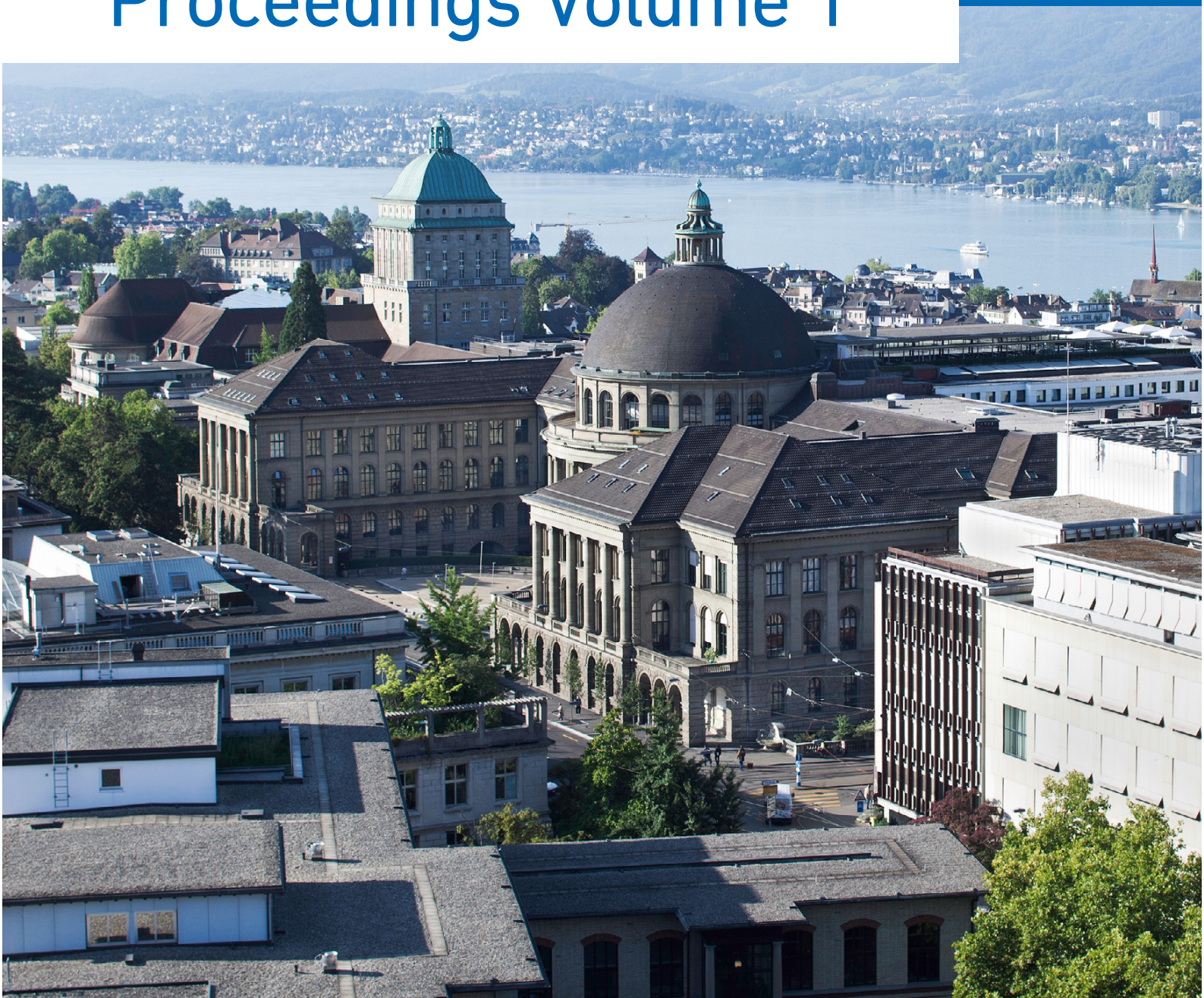




17th Biennial SGA Meeting
ETH Zurich, Switzerland
August 28 – September 1

Proceedings Volume 1



ISBN 978-2-8399-4044-3



The theme for this 17th edition is “Mineral Resources in a Changing World”

Suggested citation for the entire proceedings:

Proceedings of the 17th SGA Biennial Meeting, 28 August – 1 September 2023, Zurich, Switzerland, 1182 pages.

Suggested citation for an individual paper:

Carcamo-Valencia IC, Torró L, Proenza JA, Ramírez-Briones JS, Ayala L, Viveen W, Aiglsperger T, Baby P (2023) Cobalt-rich manganese nodules in Pliocene marine deposits of the onshore forearc Pisco Basin, Peru. In: Proceedings of the 17th SGA Biennial Meeting, 28 August – 1 September 2023, 2:280–283.

Volume 1

Porphyry-type and skarn deposits

Geothermal systems and epithermal ore deposits

Hydrothermal mineralization associated with highly fractionated magmas (e.g., Li, Be, Sn, W, Nb, Ta)

IOCG and magnetite-apatite deposits

Volume 2

VMS and seafloor mineralization

Gold: a journey from sources to precipitation sites and processes

Metallogenesis in sedimentary basins

Supergene ore forming processes

Volume 3

Critical minerals and geo-inspired technologies for a carbon-neutral future

Mineral deposits related to mafic-ultramafic intrusions

Ore genesis associated with alkaline-carbonatite systems

Advances in analytical techniques applied for ore deposits research and mineral exploration

New sensing instruments and processing methods in mineral exploration

Machine learning, data mining and new target generation in mineral exploration

This publication cannot be reproduced in whole or in part without the permission of The Society for Geology Applied to Mineral Deposits (SGA).

A digital version of this Proceedings is available from the SGA website www.e-sga.org

Welcome to SGA2023,

Welcome to Zürich,

Mineral Resources in a Changing World. In the context of an undeniable and threatening climate change, a suite of financial crisis, global sanitary challenges, and geopolitical tensions have stamped in a snowball effect the start of the XXIst century. Yet, we contend that an optimistic and united approach to lead the “Green New Deal” is possible. Thus, we have prepared a conference program comprising (1) the presentation of the latest findings in ore deposit and critical material research, (2) invited talks by plenary speakers to bring concrete insights and inspiring solutions for the challenges our economies need to face and solve in our acute awareness of climate change mitigation, and a reasoned exploitation of resources with optimal management of the environment, and (3) lively and enthusiastic scientific and social exchange between all participants from early-career researchers and students to high-ranking industry delegates and government agency representatives.

We wish you an instructive and rewarding 17th Biennial Meeting of the SGA.

Your Local Organizing Committee

Conference Chairs	Cyril Chelle-Michou (ETH Zurich, Switzerland) Nicolas J. Saintilan (ETH Zurich, Switzerland)
Scientific Program Chairs	Massimo Chiaradia (University of Geneva, Switzerland) Zoltán Zajacz (University of Geneva, Switzerland)
Field trip Chairs	David Dolejš (University of Freiburg, Germany) Jochen Kolb (Karlsruhe Institute of Technology, Germany)
Short Course Chair	Kalin Kouzmanov (University of Geneva, Switzerland)

ETH zürich



**UNIVERSITÉ
DE GENÈVE**



Preface

With its load of unexplored mineral deposits, Switzerland has no metal mining activity. Yet, it is a country at the heart of the mineral resource industry. Indeed, Switzerland focuses a third of the world metal trading and two thirds of the world gold refinement. It is also in Switzerland that the SGA was legally incorporated back in 1971. Fifty-two years later, the SGA was back in Switzerland with the first SGA Biennial meeting of the post-COVID era, hosted at ETH Zurich between August 28 and September 1 2023. The world SGA community, with over 430 international delegates from 58 countries, gathered in Zurich to share knowledge and understanding of how mineral resources formed in Earth history, and how they may be discovered and exploited in a virtuous manner towards the environment and local communities. Our delegates include students (40%), academics (37%), industry (18%), and government (5%) representative from all regions of the planet.

The conference featured a four-day program with five plenary sessions, up to four concurrent technical sessions and one poster session on display over three full days. The scientific program comprised 21 keynote presentations, 169 regular oral presentations (including 72 students) and 135 posters (including 55 students). The important student contribution was and will remain a highlight of the 17th SGA Biennial meeting. It shows how dynamic our community is with a clear vision into the future of the world supply of metal and study of mineral deposits in a context of unprecedented challenges, yet riddled with what should also be seen as optimistic opportunities to be grasped.

SGA Zurich 2023 would not have been possible without the dedication of the local organizing committee, the ETH event team, Symporg and the strong support from our local and international sponsors. We are deeply indebted to the presenters and their co-authors for their contributions, and the session convenors for organizing and running their session, and for reviewing their session papers.

We are delighted to present you the Proceedings of the 17th SGA Biennial Meeting. With this edition, the SGA council decided to come back exclusively to the 4-page-long peer-reviewed short papers, which has been the distinct signature of the SGA meetings. The Proceedings is made up of three volumes totaling almost 1200 pages and includes 309 short papers.

Cyril Chelle-Michou
Nicolas Saintilan
Conference Chairs

Sponsors

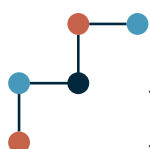
Patron Sponsor

The BHP logo consists of the letters "BHP" in a bold, orange, sans-serif font.

Student Patron Sponsor

The Glencore logo features the word "GLEN" in a black, serif font, followed by "CORE" in a black, sans-serif font.

Gold Sponsor



**Swiss National
Science Foundation**

**Zürich,
Switzerland.**

Silver Sponsor

The Boliden logo features the word "BOLIDEN" in a bold, blue, sans-serif font, with a small "NMM" logo to its left.

PAN AMERICAN
— SILVER —

The Teck logo, featuring the word "Teck" in a bold, blue, sans-serif font.

Bronze Sponsor

The RoyalRoad logo, featuring a stylized blue and orange "R" above the word "RoyalRoad" in a blue and orange sans-serif font.

FIRST QUANTUM
MINERALS LTD.

We thank all convenors of SGA 2023

Session 1a. Porphyry-type and skarn deposits

Andreas Audétat, Bayerisches Geoinstitut, Germany
Bertrand Rottier, Université Laval, Canada

Session 1b. Geothermal systems and epithermal ore deposits

Isabelle Chambefort, GNS Science, New Zealand
Thomas Driesner, ETH Zurich, Switzerland

Session 1c. Hydrothermal mineralization associated with highly fractionated magmas (e.g., Li, Be, Sn, W, Nb, Ta)

Matthieu Harlaux, BRGM, France
Hélène Legros, University of Alberta, Canada
Mathias Burisch, Colorado School of Mines, USA
Celestine Mercer, USGS, USA

Session 1d. IOCG and magnetite-apatite deposits

Adam Simon, University of Michigan, USA
Tobias Schlegel, CSIRO Mineral Resources, Australia
Irene del Real, Universidad Austral de Chile, Chile

Session 2. VMS and seafloor mineralization

Clifford Patten, Karlsruhe Institute of Technology, Germany
Ana Patrícia Jesus, Universidade de Lisboa, Portugal
Rémi Coltat, Instituto Andaluz De Ciencias De La Tierra, Spain
Melissa Anderson, University of Toronto, Canada

Session 3. Gold: a journey from sources to precipitation sites and processes

Georges Beaudoin, Université Laval, Canada
Steffen Hagemann, CET - University of Western Australia, Australia
Crystal LaFlamme, Université Laval, Canada

Session 4a. Metallogenesis in sedimentary basins

Philippe Muchez, KU Leuven, Belgium
Garth Graham, USGS, USA
Sam Spinks, Teck Resources, Australia

Session 4b. Supergene ore forming processes

Nicola Mondillo, Università degli Studi di Napoli Federico II, Italy
Cristina Villanova-de-Benavent, Universitat De Barcelona, Spain

Session 5. Critical minerals and geo-inspired technologies for a carbon-neutral future

Alexander Gysi, New Mexico Institute of Mining and Technology, USA
Katharina Pfaff, Colorado School of Mines, USA
Daniel Harlov, Deutsches GeoForschungsZentrum GFZ, Germany

Session 6a. Mineral deposits related to mafic-ultramafic intrusions

Eduardo Mansur, Geological Survey of Norway, Norway
Giada Iacono-Marziano, CNRS-ISTO, France
William Smith, Carleton University, Canada

Session 6b. Ore genesis associated with alkaline-carbonatite systems

Sophie Decrée, Royal Belgian Institute of Natural Sciences, Belgium
Francesco Stoppa, Università Gabriele d'Annunzio, Italy
Benjamin Walter, Karlsruhe Institute of Technology, Germany

Session 7a. Advances in analytical techniques applied for ore deposits research and mineral exploration

Marco Fiorentini, CET - University of Western Australia, Australia
Amanda Stoltze, Ivanhoe Mines Exploration, DRC

Session 7b. New sensing instruments and processing methods in mineral exploration

Doug Schouten, Ideon Technologies, Inc., Canada
Glenn Chubak, Dias Geophysical, Canada
Thibaut Astic, KoBold Metals, Canada

Session 7c. Machine learning, data mining and new target generation in mineral exploration

Daniel Gregory, University of Toronto, Canada
Chetan Nathwani, ETH Zurich, Switzerland
Francisca Maepa, BHP, Canada

Porphyry-type and skarn deposits

Copper Creek, Arizona: Laramide Early Halo Style Porphyry, Breccia and Massive Sulphide Mineralization	1
T. Bissig, D. Padilla, M. Sánchez, P. Harbidge	
The role of magmatic sulphide saturation in the formation of the supergiant porphyry copper deposits from Central Chile.....	5
Y. Cajal, I. Campbell, C. Carrasco-Godoy	
Metallogenic model of the Eocene Zn-Pb(-Ag) Santa María and Antares bodies of the Velardeña skarn district (Durango, Mexico).....	9
N. Cano, A. Camprubí, E. González-Partida, P. Alfonso, D. P. Miggins, E. Fuentes- Guzmán, E. Cienfuegos-Alvarado, A. K. González-Ambrocio, V. Colas	
Tracking deep crustal evolution in porphyry copper systems: preliminary results from the Tres Cerrillos Cu-Mo prospect, Western Cordillera of Ecuador.....	13
H. Carrasco, M. Chiaradia, F. Del Rio, A. Aguilar, S. Cubelli, C. Rodríguez, C. Urrutia	
State-of-the-art garnet petrochronology in the Yerington district: What does it tell us about Cu skarn formation?.....	17
M. P. Castellanos Melendez, D. Rubatto, F. Piccoli, J. Allaz, M. Guillong, O. Bachmann	
Hydrothermal alteration chemistry and mineralogy of the Maricunga-style Vendaval Central Cu-Au porphyry.....	20
F. Cernuschi, S. Gigola, W. Brownscombe, T. Ireland, J. Banyard, D. Arribasplata, J. Schorr, P. Gonnet, P. Sosa, M. Duran	
Magmatic evolution of the Archean Upper Beaver Intrusive Complex and its implications for Au-Cu mineralization	24
M. Cloutier, B. Rottier, R. Sherlock, G. Beaudoin, J. Sutton, O. Côté-Mantha, J. Davies, M. Perrot	
Volatiles in zircon-hosted apatite from the Escondida porphyry copper district, northern Chile.....	28
G. Consuma, A. I.S. Kemp, L. Martin, S. Hagemann, M. L. Fiorentini, B. Tattitch	
White mica alteration in the Gaby porphyry copper district, Northern Chile.....	32
A. Cugerone, K. Kouzmanov, L. Fontboté, L. Krampert, C. Rodriguez, S. Pichott Henríquez, R.Pardo	
Mineralogical and compositional evidence of a district-scale Sn-W skarn system in SW Sardinia: a review	36
M. Luca Deidda, A. Idini, D. Fancello, L. Tavazzani, F. Bégué, K. Kouzmanov, G. De Giudici, M. Moroni, S. Naitza	
Trace element and sulphur isotope composition of selected minerals from the W-Mo porphyry deposit Ochťiná-Rochovce	40
D. Delgado Yáñez, P. Koděra ¹ , M. Keith, F. Börner, F. Bakos	
Hydrothermal alteration zonation and Au-Cu footprint of the New York breccia pipe, Ok Tedi, Papua New Guinea.....	44
J. Dunga, S. Hagemann, P. Pollard, M. Fiorentini	
Redox state, sulphur and chalcophile element budgets during magma differentiation in thick continental arcs: case study at the Parinacota volcano.....	48
I. Mateo Espinel Pachón, Z. Zajacz, C. González Rodríguez, M. Schirra, W. Li, M. Miranda	

Fluid evolution and Re enrichment in the Maronia Cu-Mo±Au porphyry, NE Greece. Insights from mineral microanalysis and fluid inclusions constraints	52
J. J. Falkenberg, V. Melfos, M. Keith, M. Hohl, K. M. Haase, P. Voudouris, A. Höss, J. Wenske, R. Klemd, C. Beier, M. Kutzschbach, H. Strauss	
Evidence for a High-Level Porphyritic Intrusion Below the Sunnyside Epithermal Vein Deposit, Colorado	56
M. Guzman, T. Monecke, T. J. Reynolds, T. Casadevall	
Switch in magma source linked to an evolving geodynaminc environment in the Farallon Negro Volcanic Complex, NW Argentina	60
M. Ince, S. Hagemann, M. Fiorentini, T. Kemp, N. Rubinstein	
Unravelling Hypogene to Supergene Processes in a Concealed Porphyry: Insights from the Santa Cruz Copper Deposit, Arizona, USA	64
S.Kocher, B. M Frieman, T. Monecke, H. J Stein, C. J Seligman, H. Hanneman, S. Vandekerkhove	
Texture, composition, alteration styles in the Permo-Triassic granodiorite and the Eocene tonalite porphyry at the Gaby porphyry copper deposit, Chile	67
L. Krampert, K. Kouzmanov, A. Cugerone, L. Fontboté, C. Rodríguez, R. Pardo, S. Pichott Henriquez	
Genesis of Mineralized Skarns: reanalysis of decarbonation reactions, decarbonatization, and carbonate melting during infiltrative contact metasomatism.....	71
D. Lentz	
Oxidation and hydration states of porphyry-copper ore-forming magmas recorded by trace elements in zircon	74
R. Loucks, M. Fiorentini	
Early zircon saturation and low Zr content of PCD-forming magmatic differentiation series: a guide for exploration targeting.....	78
R. Loucks, M. Fiorentini	
Pyrite as a porphyry Cu indicator mineral: new insights from the Myszków Mo-Cu-W deposit (Poland) and future perspectives	82
B. Naglik, M. Dumańska-Słowik, R. Habryn, T. Toboła, A. Sosnal	
Cold arc magma differentiation linked to porphyry copper deposit formation?.....	86
C. Nathwani, S. Large, J. Blundy, M. Loader, Y. Buret, J. J. Wilkinson, K. McCann, C. Chelle-Michou	
LA-ICP-MS trace element analysis of pyrite from the Bakoudou gold deposit, South Gabon: Implications for ore genesis.....	90
N. Nzaou Mabika, A. Wafik, A. Boushaba, D. Gaboury, L. Maacha, M. Gharrabi, B. Maamar	
Sulfur and chalcophile metal transfer via sulfide-volatile compound drops during magma mixing: evidence from the Christiana-Santorini-Kolumbo volcanic field	93
C. Patten, S. Hector, S. Kilias, M. Ulrich, A. Peillod, A. Beranoaguirre, P. Nomikou, E. Eiche, J. Kolb	
Fluid inclusion study in quartz of the Rudnik Pb-Zn-Cu-Ag skarn deposit, Serbia	97
S. Petrović, R. Bakker, V. Cvetković, R. Jelenković	
El Chichón volcano, Mexico: A window into an active Porphyry-Cu-Mo-Au system	100
M. F. Reyes Gonzalez, J. Roberge, C. N. Mercer, A. A. Camacho Pérez, G. Arrieta García, S. Suresh Babu, P. Eliseo Carbajal Martínez	

Probing sulfur behavior in arc magmas with immiscible magmatic sulfides and apatite: Complementary data sets to assess ore-forming potential	104
H. Rezeau, Y. Buret, B. Klein, O. Jagoutz, S. Ono	
New experimental data on potassic vs. albitic alteration	108
T. Roodpeyma, T. Driesner	
Evolution of the Skouries porphyry Cu-Au system by trace element variations	112
A. Höss, R. Klemm, M. Keith, K. Haase, V. Melfos, L. Gerlach, F. Pelloth, J. Falkenberg, P. Voudouris	
U-Pb ages and trace elements of zircons from Loei and Truong Son fold belts, Laos: Implication for porphyry deposit fertility.....	116
P. Sritangsirikul, S. Meffre, K. Zaw, I. Belousov, Y. Jen Lai, A. Richards, P. Charusiri	
The apparent decoupling of magmatic and hydrothermal activities in the Chuquicamata District	120
A. Virmond, D. Selby, D. Szymanowski, J-F Wotzlav, C. Chelle-Michou	
Sulfide resorption contributes to porphyry deposit formation in collisional settings.....	124
W-J Xia, R. Wang, F. Jenner	
Can post-subduction porphyry Cu magmas form by partial melting of typical lower crustal amphibole-rich cumulates?	128
J. Zhang, Jia Chang, R. Wang, A. Audétat	

Geothermal systems and epithermal ore deposits

Hydrodynamics of crustal detachments and syn-kinematic granites: numerical exploration and implication on uranium mobilities.....	132
K. Bock, Y. Branquet, P. Boulvais, T. Duretz	
Las Minas newly recognized epithermal deposit and its relationship with Tatatila Las Minas Skarn, Veracruz, Mexico.....	136
P. Carbajal, J. Castro Mora, J. Roberge, G. Arrieta, G. Paulson Pitchaimani, C. N. Mercer	
Melt inclusions types within related processes in the Dănești - Piatra Roșie realm (Maramureș County, Romania).....	139
I. Pinteă, G. Dincă, S. S. Udubașa, M. Munteanu	
Thermodynamic modeling of hydrothermal equilibria: a critical assessment using mineral solubility and aqueous speciation.....	143
D. Dolejs, F. Salomone	
Complex genetic model of the shear-zone hosted epithermal Au-Ag-Pb-Zn-Cu deposit Banská Hodruša at the Rozália mine, Slovakia.....	147
P. Koděra, J. Lexa, M. Chovan, R. Vojtko, A. Kubač, B. Rottier, M. Rybárik, J. Průch	
Numerical simulations of pulsed epithermal ore-forming events in geothermal systems with incrementally growing magma reservoirs.....	151
M. Korges, P. Weis	

Coupling structural evolution and fluid flow in metallogenic and geothermal systems	155
P. Ledru, G. Chi, G. Milesi, J. Mercadier	
Trace element variations and sulphur isotopic ratios of enargite and alunite from the quartz-pyrite-gold orebodies, Mankayan District, Philippines	159
P. Manalo, R. Mine, R. Takahashi, A. Imai, A. Agangi, G. Alburo, L. Subang, R. R. Parcon-Calamohoy, M. de los Santos	
In-situ trace element analyses of pyrite from the Pefka epithermal Cu-Au-Te-In-Se deposit, Rhodope, Northern Greece	163
M. Melfou, P. Voudouris, R. Klemm, M. Keith, V. Melfos, L. Papadopoulou, N. Kantiranis	
Fault Permeability and Active Hydrothermal Systems: A Key to Infer the Formation of Unconformity-Related Uranium Deposits from Athabasca Basin (Canada)	167
G. Milesi, P. Ledru, P. Marchal, M. Bourges, C. Perrière, J. Scibek, A. Le Beux, J. Mercadier	
Study of Hydrothermally Altered Zones within the Gujarat-Khachkovi Ore Field Using Terra ASTER Multispectral Satellite Data. Georgia	171
G. Mindiashvili	
Mineralogy, Pb isotopes in galena, and Nd isotopes in associated dykes from Ag-Hg Imiter deposit, Anti-Atlas, Morocco: implications for metal sources	174
M. Ousbih, B. Cousens, Y. Geraud, A. Favier, H. El bilali, M. Ezzghoudy, F. Askkour, S. El Mouden, A. Gaouzi, H. Oubaassine, R. Ernst, M. Ikenne	
Vanadium and Indium enrichment in La Luz epithermal system, Patagonia, Argentina	177
M. Pagola, S. M. Jovic, D. Palma, D. Guido, D. Hughes	
Using PHREEQC for mineral prospecting in waters related to geothermal systems in Wyoming: possible precipitation of hydroxyapatite enriched with REEs	180
J. D. Palma Montealegre, T. Heinrich Cramer	
3D lithological and structural model and prospectivity of the Late Cretaceous Sakdrisi Gold-Copper Epithermal deposit, Bolnisi district, Lesser Caucasus, Georgia	184
N. Popkhadze, B. Gogia, S. Tagviashvili, G. Ugrekheldze, M. Natsvlishvili, J. Shubitidze, Ş. Utku Sönmez, R. Moritz	
A Comparative Study of VMS and Epithermal Deposit Settings in the Eastern Pontides, NE Turkey: Insights from Geochronology and Lithogeochemistry	188
Ş. Utku Sönmez, R. Moritz, S. Keskin, F. Turlin, A. Ulianov, Ü. Aydın	
Pb-containing aluminium phosphate-sulphate mineralization from the advanced argillic alteration in the Chelopech epithermal high-sulphidation Cu-Au deposit.....	192
S. Georgieva, E. Stefanova, A. Hikov, M. Kadiyski, S. Georgiev, M. Trifonova	
Metal Endowment of Magmatic Brines from Active Geothermal Reservoirs	196
B. Tattitch, J. Blundy, O. Laurent	
Numerical constraints on the hydrothermal fluid evolution forming the Pirquitas Sn-Ag-Pb-Zn deposit in NW Argentina	200
M. Stoltnow, P. Weis, M. Korges	
Ore Mineral Textures of the Midas Low-Sulfidation Epithermal Deposit: Implications for Ore-Forming Processes.....	204
L. Zeeck, T. Monecke, T. J. Reynolds, K. Pfaff, N. M. Kelly	

Hydrothermal mineralization associated with highly fractionated magmas (e.g., Li, Be, Sn, W, Nb, Ta)

Spodumene textural variations in a deformed LCT-type pegmatite. A case study from the Musha-Ntunga area, Rwanda.....	208
J. Acke, D. Kwizera, A. Goodship, S. Dewaele, R. Barros, C. Burlet, S. Nachtergaele, A. Borst	
Magmatic-Hydrothermal Mineral Formation Systems: A Geological Study.....	212
J. U. Aparicio Abadía	
Diachronous tin mineralization in the Iberian Pyrite Belt.....	214
I. Borrajo, F. Tornos, C. Conde, G. Ares, J. Hanchar, M. Wälle, R-Q Zhang, J. Royal, T. Moody	
Magmatic-hydrothermal stratabound W-(Sn) mineralization in the Iberian Variscan Massif: The Barxa deposit.....	218
I. Borrajo, F. Tornos, J. Hanchar, J. Fuenlabrada, T. Bauer	
The role of micas in the origin of granite-related Sn-W-Nb-Ta mineralization.....	222
K. Breiter, M. Vašinová Galiová, M. Hložková	
Fluid evolution in the San Rafael Sn-Cu lode deposit, Peru: Constraints from fluid inclusion analyses and chlorite geochemistry.....	226
M. C. Martínez, K. Kouzmanov, A. Tsay, Z. Zajacz, F. Bégué, M. Harlaux, M. Kalinaj, L. Fontboté	
Multi-phase tungsten mineralisation at the world class Hemerdon deposit, south-west England .	230
E. Deady, K. Moore, R. Shail, K. Goodenough, S. Chenery	
U-Pb columbite-tantalite ages from NW-Amazonian Craton, Colombia.....	233
J. A. Franco, A. Von Quadt, A. Bonilla, A. Piraquive, T. Cramer, Z. Amaya	
Rare-earth element mineralization in altered pegmatites from the Djurkovo Pb-Zn deposit, Central Rhodopes	238
S. Georgieva, R. Vassileva, G. Milenkov, J. Cempírek, R. Škoda	
Pegmatite REE-mineral association from the Kroushev Dol base metal deposit (south Bulgaria): mineral replacements and timing of formation.....	242
R. Vassileva, S. Georgieva, G. Milenkov, J. Cempírek, R. Škoda, E. Stefanova, V. Grozdev, I. Peytcheva	
Comparison of the Beauvoir and Cínovec rare metal granite/greisen systems: Role of muscovitization on Li-Sn-W-Ta hydrothermal remobilization	246
M. Harlaux, O. Blein, B. Gourcerol	
Dating and trace-element characterisation of Sn-W skarn-, greisen- and metamorphic vein-type occurrences from East-Greenland.....	250
N. Keulen, B. Heredia, S. Malkki, T. B. Thomsen, D.R.N. Rosa, D. Whitehead	
Magmatic Silica Caps associated with Intrusion-related ore deposits.....	254
D. Kirwin, R. Seltmann	
Fluids involved in W-Be skarns from the Canadian Cordillera: example from the Cantung and Lened deposits, NWT, Canada	258
H. Legros, V. Elongo, O. Laurent, E. Adlakha, H. Falck, C. Chelle-Michou, P. Lecumberri-Sanchez	

Metallogeny of tin: From rocks to ore	261
B. Lehmann	
Tin Deposition from Cooling Magmatic Fluids Revealed by Ion Probe Cassiterite Oxygen Isotope Analysis	262
Y. Li, O. Bachmann, X-H Li	
In situ LA-ICP-MS U-Pb age of cassiterite from Auxiliadora Sn-W vein type deposit, northwestern Spain	266
I. Losada, I. Borrajo, J. E. Ruiz-Mora, L. M Rodriguez-Terente, F. Tornos, J. Hanchar	
U-Pb Zircon Geochronology of the San Rafael Sn(-Cu) Deposit San Rafael (Peru): Sources of Magmas and Magmatic Evolution	270
S. Markovic, L. Tavazzani, D. Szymanowski, K. Kouzmanov, C. Chelle-Michou	
Critical minerals in Climax-type magmatic-hydrothermal systems	274
C. Mercer, M. Guzman, A. Hofstra, J. Rosera	
Comparative study of pegmatites from the Central Rhodopean Pb-Zn deposits (Bulgaria).....	278
G. Milenkov, R. Vassileva, S. Georgieva, K. Kouzmanov, J. Cempírek, Y. Georgieva	
Regional rock geochemistry of granites and elvans in SW England: delineation of composite intrusions and Sn-Li potential	282
C. Moon, B. Simons, N. Harper, F. Jackson, R. Shail, C. Yeomans	
Scheelite in the Panasqueira tungsten deposit. An example of host rock control in tungstate composition	286
F. Noronha, F. Pinto, J. Ferreira	
Ore-forming events at the W-rich Santa Comba deposit, NW Spain.....	290
C. Pita, F. Tornos, I. Borrajo, L. Boixet, E. Crespo	
Major and trace element composition of the Lithium-rich Tuff from the Macusani Volcanic Field, Puno, Peru.....	295
J. Ramirez, L. Torró, L. Tavazzani, L. Monnier, O. Laurent, M. Segovia-More, M. Sanandres-Flores, J. Vallance, C. Chelle-Michou, S. Salvi, P. Baby	
High-temperature meteoric water incursion in the Beauvoir rare-metal granite: insights from apatite	299
O. Rocher, J. Mercadier, A. Richard, C. Ballouard, L. Monnier, O. Laurent, N. Bouden, J. Villeneuve, P. Fullenwarth	
High-resolution mineralogy of Lithium-rich Tuff from the Macusani Volcanic Field, Puno, Peru...	303
M. Segovia-More, L. Torró, C. Villanova-de-Benavent, J. Ramírez-Briones, J. Vallance, L. Monnier, O. Laurent, S. Salvi, P. Baby, J. Proenza, F. Nieto	
Characteristics of productive and barren Jecheon adakitic intrusions in the Hwanggangri mineralized district, Republic of Korea.....	307
J. Seo, S. G. Choi, G. E. Shin, Y. J. Lee	
Structural features tied to mineral deposits deformed by shear zones.....	311
S. Jacko, R. Farkašovský, J. Kondela, A. Thiessen	
Tourmaline composition records fluid-rock interaction: implications for cassiterite precipitation in the Triassic Chacaltaya district, Bolivia	315
L. Torró, M. Harlaux, A. Castro-Morante, J. Vallance, L. Tavazzani, A-S Bouvier, T. Bovay, C. Chelle-Michou, T. Sempere, J. Carles Melgarejo	

Lithium-bearing micas in the 'Lithium-rich Tuff' from the Macusani Volcanic Field, Puno, Peru ...	319
L. Torró, C. Villanova-de-Benavent, L. Monnier, O. Laurent, M. K Segovia-More, M. K Sanandres-Flores, J. S Ramírez-Briones, J. Vallance, S. Salvi, P. Baby, J. A Proenza, F. Nieto	
Fluid exsolution in the outer zones of the Emmons Pegmatite (Maine, USA)	323
L. van der Does, N. Hulsbosch, J. Elsen, P. Muchez, M-L Sirbescu	
Large-scale HFSE and REE mobility linked to the formation of vein-type U-deposits in the Moldanubian Zone of the Bohemian Massif	327
M. Kubeš, V. Wertich, J. Leichtmann, M. Holá, J. Mercadier, M. Cuney	
Preliminary results of U-Pb dating and trace element analysis of cassiterites from the Western Sudetes, SW Poland	331
W. Zygo, K. Foltyn, T. Thomsen, B. Heredia, A. Piestrzynski	
Genthelvite from the world-class beryllium-polymetallic deposit - Perga, Ukraine	335
A. Piestrzynski, B. Zygo, W. Zygo, J. Pieczonka, A. Berezovsky	

IOCG and magnetite-apatite deposits

Assessing REE-phosphate mineral chemistry for ISCG exploration	339
T. Batch, C. Tiddy, A. Brotodewo, D. Giles	
Alteration Footprints of Metasomatic Iron and Alkali-Calcic Systems in the Northern Norrbotten, Sweden.....	343
O. Blein, M. Harlaux, L. Corriveau, E. P. Lynch, T. Niiranen, V. Lisitsin, K. Ehrig, J-F Montreuil, B. Gourcerol	
Similarities, yet differences: Olympic Dam, Oak Dam West, Wirrda Well, Island Dam and Acropolis IOCG deposits, Olympic Cu-Au Province, South Australia	347
K. Ehrig, C. L. Ciobanu, N. J. Cook, V. S. Kamenetsky, M. Kamenetsky, J. McPhie	
Apatite and REE in iron oxide-apatite (IOA) deposits.....	351
D. Harlov	
Fe-O isotope systematics and magnetite chemistry of the Malmberget iron-oxide apatite deposit, Sweden.....	354
J. Henriksson, V. R. Troll, E. Kooijman, I. Blindeman	
Variations in Trace Element Chemistry of Pyrite from the Starra IOCG deposit, Queensland, Australia as proxy for Cu-Au Mineralization	358
M. Hohl, J. Steadman, J. Cloutier, S. Barker, D. Cooke	
Hydrothermal origin of bladed titanomagnetite during early alteration stages at the Starra IOCG deposits, Queensland, Australia	362
M. Hohl, J. Steadman, J. Cloutier, K. Goemann	
A geological update on the Viscaria Cu-Fe deposit, Kiruna district, Northern Sweden.....	363
M. Imaña, R. Armstrong, D. Sandoval, M. Jez, E. Nkioh, M. Krockert	
The Formation of the Pilot Knob Iron Ore Cluster in Southeast Missouri, USA: Implication for the Exploration for Iron Oxide Apatite Deposits.....	367

M. Locmelis, B. Tunnell, B. Sullivan, C. Seeger, S. Dare, R. Mathur

Assessing silicate-liquid immiscibility using trace element in titanomagnetite and ilmenite in the Raftsund intrusion, Lofoten-Vesteraalen AMCG suite, Northern Norway..... 370
N. Coint, E. Mansur, J. Keiding

Genesis of iron ore deposit at Ga-Nchabeleng area 373
J. Mapula Maponya, H. R. Mundalamo, J. S. Ogola

Insights into IOA and IOCG deposit genesis from comparative isotopic analysis of Fe and Cu isotope compositions in magnetite and ores 377
R. Mathur, M. Di Maio, L. Godfrey, A. C. Simon, C. Emproto, V. Lisitsin, C. Dhnaram, I. Sanislav, I. del Real

Controls on iron oxide-Cu-Au mineralisation: dogma versus data 378
T. Schlegel, W. Liu, H. McFarlane, R. Birchall, J. Austin

Characterization of the Kiskamavaara IOCG-(Co) deposit, northern Norrbotten, Sweden 382
I. Van Der Werf, J. Andersson, T. Bauer, T. Kearney

Copper Creek, Arizona: Laramide Early Halo Style Porphyry, Breccia and Massive Sulphide Mineralization

Thomas Bissig¹, Dante Padilla¹, Matias Sanchez², Paul Harbidge¹

¹Faraday Copper Corp. 250-200 Burrard St. Vancouver, BC, Canada

²Faultrocks Inc. Victoria, BC, Canada

Abstract. Copper Creek is an unusual porphyry Cu-Mo district characterized by early halo style veining and magmatic cupola style mineralization overprinted by abundant hydrothermal breccias. The latter commonly contain high-grade mineralization. Massive sulphide bodies interpreted as silica-replacive intermediate sulphidation mineralization occur locally as well. Breccias are dominantly crackle or jigsaw fit breccias with sulphide cement and sericite +/- kaolinite alteration. They probably didn't breach the surface during emplacement.

The mineralization is largely hosted by the 62 Ma Copper Creek batholith and 63 Ma Glory Hole volcanics emplaced in a NW trending Laramide thrust fault system, later reactivated during Basin and Range extension. While breccias and porphyry intrusions followed this principal NW orientation, a prominent array of steeply dipping E to ENE oriented as well as shallowly west dipping extensional veins controlled early halo style porphyry mineralization.

Mineralization styles and cross-cutting relationships suggest that early halo-style porphyry mineralization took place at approximately 5-6 km crustal depth followed by rapid exhumation which facilitated the emplacement of hydrothermal breccias. Thus, the mineral system was emplaced at a time of an important tectonic transition.

1 Introduction

Copper Creek in Arizona is one of the largest undeveloped copper deposits in the prolific Laramide copper province of Southwestern US and northern Mexico, with 422 million tons of 0.48% Cu equivalent measured and indicated resource (Fig. 1: Faraday Copper news release May 3rd 2022).

Mineralization styles differ from those in other deposits in the region and from the classic porphyry model. Early halo style porphyry veins (e.g., Proffett, 2009), are dominant whereas A and B-type veins are comparatively rare. In addition, the district is known for widespread breccia hosted mineralization, with recently identified massive sulphide mineralized zones consisting of chalcopyrite, bornite and pyrite. This paper summarizes the current understanding of the geology and mineralization of this district.



Figure 1. Location of Copper Creek, relative to other major porphyry copper deposits and prospects in southern Arizona.

1.1. Exploration and Mining History

Small scale mining in the district occurred intermittently between 1861 and 1982 with approximately 300,000 t of ore produced from the Old Reliable and Childs-Aldwinkle mines in the early 20th century.

More than 200 km of drilling was carried out in the district, the bulk of it between the mid-1990s and 2015. Exploration including drilling resumed after 7 years of minimal activity in late 2021 when the new Management of Faraday Copper Corp. took over the project.

2. Geology of Copper Creek

The Copper Creek deposit is in the Galiuro mountains in southern Arizona, approximately 20 km NE of the historic San Manuel mine at the intersection of two major trends of porphyry copper deposits (Fig. 1).

Mineralization at Copper Creek is largely hosted by the Palaeocene (~62 Ma) Copper Creek batholith which intruded Palaeocene Glory Hole volcanics (~63 Ma) and Proterozoic to Palaeozoic sedimentary rocks (Fig. 2). The Copper Creek batholith is compositionally zoned and contains a shallowly west dipping monzogranite domain at depth and a dioritic border phase (Fig. 3), with the bulk being of granodioritic composition. Four main types of granodiorite to quartz diorite porphyry dykes and plugs have been recognized; these largely intruded before and during mineralisation (cf., Riedell et al. 2013).

Hydrothermal breccias crosscut both the batholith and Glory Hole volcanics. The Oligocene Galiuro

volcanics cover the Copper Creek batholith and Glory Hole volcanics.

The Copper Creek batholith, porphyries and breccias were emplaced in the hanging wall of the NW trending Holy Joe thrust fault (Favorito and Sedorff, 2018) and parallel, related structures.

Over 400 mapped breccias form two prominent NW-aligned trends: the Western and Eastern breccia trends, the latter containing the bulk of the resource (Fig. 2) but only 17 of the mapped breccias have been sufficiently drilled to be included in the current mineral resource estimate.

The Western breccia trend is characterized by widespread argillic and locally advanced argillic alteration and widespread occurrence of tourmaline, whereas alteration in the Eastern breccia trend is more confined and dominated by quartz-sericite +/- kaolinite.

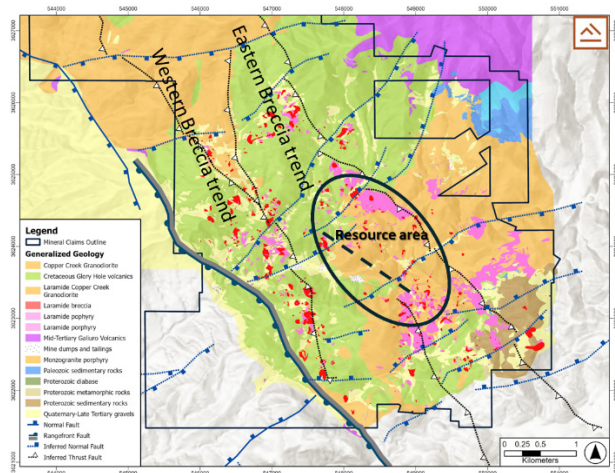


Figure 2: Geology, structural architecture, and distribution of breccias in the copper Creek district. Dashed line in the resource area indicates approximate section trace for Figure 3.

The thrust faults were variably reactivated as extensional faults during Miocene Basin and Range extension leading to more exhumation in the Eastern, compared to the Western breccia trend, which also explains the more mature stage of exploration in the eastern trend with ~90% of the historic drilling focused there.

3. Alteration and Mineralization

The mineralization can be subdivided into an early porphyry stage overprinted by breccia-hosted mineralization. Supergene oxidation and secondary sulphide enrichment are relatively minor but occurred within the uppermost 10-40 m.

The bulk of the porphyry stage mineralization is hosted by early halo veins in the American Eagle zone (Fig. 3, 4) above the monzogranite domain, i.e., 500 to 1100 m below present surface. Two dominant vein orientations are recognized: steeply dipping E to NE striking extensional veins crosscut shallowly west to southwest dipping extensional veins. Sulphides are vertically zoned from

pyrite>chalcopyrite to chalcopyrite to bornite-chalcopyrite. Mineralization hosted by miarolitic cavities and coarse quartz +/- K-feldspar veins, interpreted as a variation of unidirectional solidification textures (UST's) is important in some areas such as in the Keel zone.

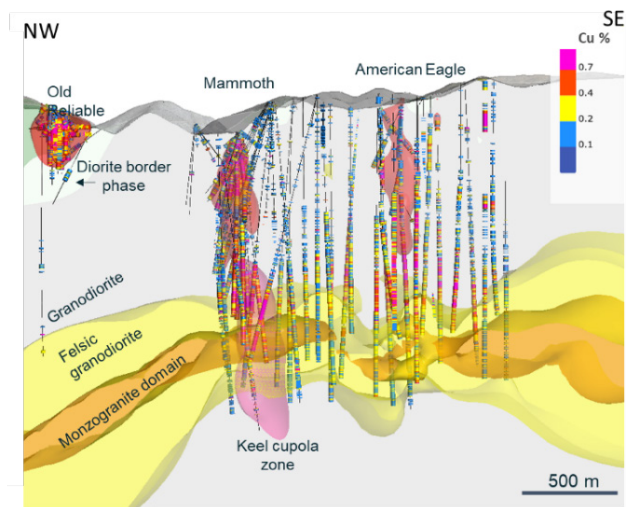


Figure 3: Long section through the American Eagle and Keel zone, showing the batholith zonation and copper mineralization concentrated above the monzogranite domain.

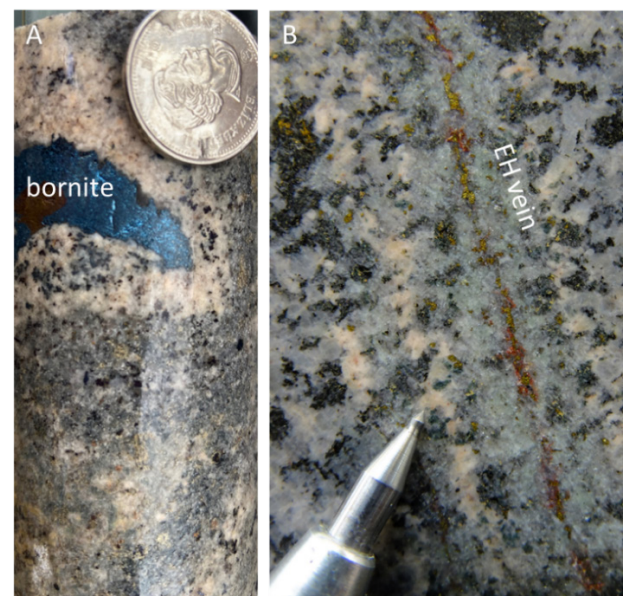


Figure 4: Examples of early-stage mineralization styles: A) miarolitic cavity with central bornite infill surrounded by K-feldspar: Keel cupola zone; B) Early halo vein cutting granodiorite with finely disseminated chalcopyrite with muscovite-biotite and K-feldspar alteration in halo: American Eagle zone.

Alteration is overall subtle during the first stage of mineralization and is characterized by biotite, muscovite and K-feldspar in the early halo veins with localized zones of K-feldspar flooding as well as secondary biotite.

Breccia-hosted mineralization occurs dominantly as sulphide cement to crackle and jigsaw fit breccias without appreciable clastic matrix (Fig. 5). The breccias have not experienced significant clast rounding or milling and are not thought to have breached the surface at the time of formation.



Figure 5: Examples of late-stage mineralization styles: A) Glory Hole breccia with pyrite-chalcopyrite cementing angular, sericite-kaolinite altered clasts. B) Massive chalcopyrite-bornite-pyrite mineralization from Copper Prince. The overall zone has 10.83% Cu over 15 m.

Alteration associated with mineralized breccias is quartz-sericite +/- kaolinite. Breccias can be vertically extensive with up to 1430 m of known vertical extent in the Keel-Mammoth zone (see also Andersson et al. 2009) but are only few 100 m across. The Mammoth breccia is the largest known breccia body. It reaches within 30 m of present-day surface but does not crop out (Andersson et al. 2009) and recent drilling suggests that it overprints earlier cupola style mineralization in the Keel zone over 1000 m below surface.

During Faraday's phase II drilling program, a zone of massive sulphide mineralization (15 m @ 10.83% Cu, 55.6 g/t Ag and 1.65 g/t Au; Fig. 5) was discovered approximately 200 m below surface near the Copper Prince breccia. Sulphides in this zone are dominantly chalcopyrite with variable amounts of pyrite and bornite and are spatially associated with highly crystalline kaolinite and sericite alteration. This zone contains the highest gold grades known from the Copper Creek district.

3.1 Mine plan

Approximately one third of the measured and indicated resource is hosted in high-grade breccias and occurs near the surface, whereas the remainder occurs as porphyry style and magmatic cupola style mineralization 500-1100 m below surface. This distribution of the mineralized resource lends itself to an initial open pit mine plan followed by the development of an underground block caving operation.

4. Discussion and Conclusions

Mineralization at Copper Creek was emplaced immediately after Laramide orogeny and was controlled by a significant NW striking thrust fault. This setting is consistent with porphyry deposits elsewhere, including the Central Andes (e.g., Mpodozis and Cornejo, 2012). Both, the distribution of breccias and vein orientations can be explained by this setting, with early subhorizontal veining forming during thrusting and E to NE oriented steeply dipping extensional veins explained by extension normal to the orogen following compressional deformation. Breccias were emplaced in the hanging wall of the orogen parallel thrust faults.

Reactivation of thrust faults as normal faults during Neogene basin and range extension led to the preservation of shallow portions of the mineral system, including epithermal alteration assemblages in the Western- compared to the Eastern Breccia trend.

Early halo vein hosted mineralization is interpreted to reflect relatively deep crustal emplacement of porphyry mineralization at approximately 5-6 km crustal depth (e.g., Proffett, 2009). Conversely, hydrothermal brecciation occurs above magmatic cupolas where fluid pressure is sufficient to overcome confining lithostatic pressure which would be facilitated at shallower crustal depths. However, there is no evidence that any of these breccias breached the surface at the time of emplacement. Nevertheless, the cross-cutting relationships suggest that the Copper Creek mineral system experienced a period of rapid exhumation accompanied by breccia emplacement following the emplacement of Early Halo vein hosted mineralization. This interpretation is also consistent with the structural observations from the district which suggest that mineralization was emplaced following Laramide orogeny during a time of tectonic relaxation.

The processes forming massive sulphide zones at Copper Prince are interpreted to be somewhat similar to some of those described from Bor, Serbia (Klimentyeva et al. 2021). There, they have been explained as silicate-replacive orebodies resulting from a high-sulphidation overprint on earlier porphyry Cu-Au mineralization. Due to their limited size, such massive sulphide zones can be challenging to explore for, but the exceptional grades make them a worthwhile exploration objective at Copper Creek.

Acknowledgements

This paper is the outcome of exploration by Faraday Copper since Nov. 2021. It builds on a wealth of data and knowledge from preceding companies (see also Riedell et al. 2013). The contributions of the entire geology team at San Manuel Arizona are acknowledged.

References

- Anderson ED, Atkinson WW, Marsh T, Iriondo A (2009) Geology and geochemistry of the Mammoth breccia pipe, Copper Creek mining district, southeastern Arizona: evidence for a magmatic–hydrothermal origin. *Mineralium Deposita* 44:151-170.
- Favorito DA, Seedorff E (2018) Discovery of major basement-cored uplifts in the northern Galiuro Mountains, Southeastern Arizona: Implications for regional Laramide deformation style and structural evolution. *Tectonics* 37:3916-3940.
- Klimentyeva D, Driesner T, von Quadt A, Tončić T, and Heinrich C (2021) Silicate-replacive high sulfidation massive sulfide orebodies in a porphyry Cu-Au system: Bor, Serbia. *Mineralium Deposita* 56:1423-1448.
- Mpodozis C, Cornejo P (2012) Cenozoic tectonics and porphyry copper systems of the Chilean Andes. *Society of Economic Geologists Special Publication Number 16*:329-360.
- Proffett JM (2009) High Cu grades in porphyry Cu deposits and their relationship to emplacement depth of magmatic sources. *Geology* 37:675-678.
- Riedell KB, Sandberg RJ, Guthrie JO, Gorecki AD, Lambiotte MJ, Reynolds SJ, Proffett JM, Ybarra SJ, Poulter JE (2013) Early Halo Type Porphyry and Breccia Cu-Mo Mineralization at Copper Creek, Pinal County, Arizona. Extended Abstract SEG 2013 conference, Whistler, BC, Canada, 9 p.

The role of magmatic sulphide saturation in the formation of the supergiant porphyry copper deposits from Central Chile

Yamila Cajal^{1,2}, Ian H. Campbell¹, Carlos I. Carrasco-Godoy¹

¹Research School of Earth Sciences, The Australian National University

²Centre for Ore Deposit and Earth Sciences, University of Tasmania

Abstract. Porphyry copper deposits have been widely studied; however, it is still unclear why some systems are fertile while others are not. This work explores this question by studying igneous rocks associated with the world's largest and third largest copper deposits, the Rio Blanco and El Teniente Cu deposits, located in Central Chile, with special emphasis on the role that sulphide saturation plays in magma fertility. We provide new whole-rock, major and trace elements data, including platinum group elements from intrusions related to these deposits. The results show that the Rio Blanco and El Teniente magmatic systems reached sulphide saturation early in their evolution. This depleted the magma in Au, relative to Cu, leading to the formation of Cu-dominated deposits. It is concluded that the timing of sulphide saturation did not play a key role in the formation of these deposits because early sulphide saturation did not prevent their formation. Instead, we argue that other factors such as the small amount of sulphide melt to precipitate from the magma and the enormous size of the magma chamber, were responsible for the formation of these supergiant deposits.

1 Introduction

There are several factors that affect the ability of magmas to form a porphyry deposit, such as: the tectonic setting; the depth of magma emplacement; the duration of the magmatic activity; the metal and water content and oxidation state of the magma; among others (e.g. Richards 2003, 2013; Cooke et al. 2005; Audétat and Simon 2012; Wilkinson 2013). Although it is usually the combination and optimization of all these processes that lead to the formation of economic porphyries (Richards, 2003, 2013), this study focuses on the role that the timing of sulphide saturation plays in magma fertility.

Previous studies (e.g. Park et al. 2013, 2019; Cocker et al. 2015; Hao et al. 2017; Lowczak et al. 2018) have shown that the Platinum Group Elements (PGE) can be used to identify the onset of sulphide saturation because they have a strong affinity for immiscible sulphide melts during magmatic differentiation. It has been suggested that if sulphide saturation occurs early in the magmatic evolution, chalcophile elements, including Cu and Au, will be trapped in the magma chamber and, therefore, will not be available to enter the fluid phase when volatile exsolution occurs, which will prevent the formation of an economic deposit (Hamlyn et al. 1985; Park et al. 2013; Cocker et al. 2015; Hao et al. 2017).

This study evaluates the role that the timing of sulphide saturation plays in copper-gold magma fertility in the Andes of Central Chile, where the

world's largest copper reserves are found. For this, we have studied igneous rocks associated with the Rio Blanco and El Teniente porphyry copper deposits. We present new whole-rock geochemistry for the intrusions from these deposits, including whole-rock major and trace elements concentrations, with an emphasis on the PGE.

2 Geological setting

The Rio Blanco and El Teniente porphyry copper deposits are located in the Main Cordillera of the Andes of central Chile (Fig. 1). They contain the largest and third largest known concentration of copper in the world, each of them containing more than 100 Mt of this metal (Mudd and Jowitt 2018). Molybdenum is an important by-product.

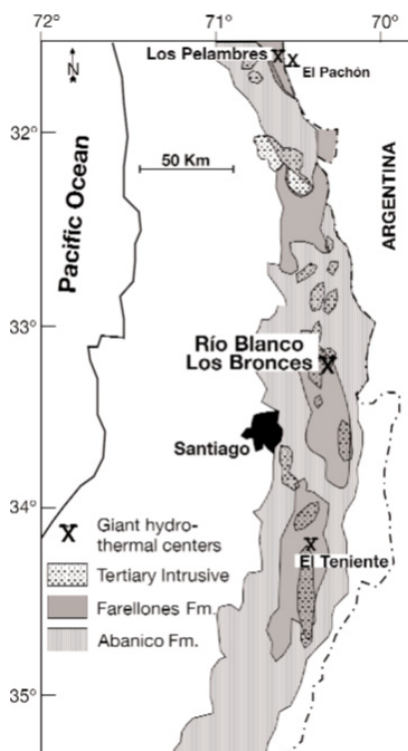


Figure 1. Simplified regional geologic map of the Late Tertiary magmatic belt of Central Chile (Serrano et al. 1996 in Deckart et al. 2005).

These deposits are part of the Miocene-Pliocene metallogenic belt of Central Chile (Maksaev et al. 2004). This belt coincides with the position of the Miocene volcanic centres (Fig. 1), which comprises volcanic and volcanoclastic rocks of the Farellones and Abanico formations (Maksaev et al. 2004). Both

units are intruded by late Miocene to early Pliocene plutons (Fig. 1), the late stages of which are temporally and spatially related to the Cu-Mo mineralization (Cannell et al. 2005; Stern et al. 2011; Mpodozis and Cornejo 2012).

At the Rio Blanco-Los Bronces District, the San Francisco Batholith was emplaced between 16.4 ± 0.2 and 8.16 ± 0.45 Ma (Warnaars et al. 1985; Deckart et al. 2005; Toro et al. 2012). The Cu-Mo endowment is hosted in porphyry stocks and breccia pipes that formed between 8.36 ± 0.06 Ma and 4.87 ± 0.02 Ma (Toro et al. 2012; Deckart et al. 2014). The magmatic activity ended with the emplacement of the post-mineralization La Copa Volcanic Complex at 4.92 ± 0.1 to 4.31 ± 0.05 Ma (Warnaars et al. 1985; Deckart et al. 2005; Toro et al. 2012).

The magmatism at El Teniente includes a large pre-mineral intrusive complex that includes the El Teniente Mafic Complex, emplaced at 8.9 ± 1.4 Ma (Stern et al. 2011), and the Sewell Tonalite, which formed between 7.4 ± 1.5 Ma and 6.15 ± 0.08 Ma (Cuadra 1986; Maksaev et al. 2004). Several felsic intrusions, linked to the mineralization were emplaced between 6.46 and 4.82 Ma (Mpodozis and Cornejo 2012). The formation of post-mineralization lamprophyre dikes at 3.85 ± 0.18 Ma (Maksaev et al. 2004) mark the last magmatic pulse in the district (Cuadra 1986).

This long magmatic history and wide range of compositions make these deposits ideal cases to study the role of the timing of sulphide saturation in the formation of porphyry copper deposits.

3 Samples and methods

A total of fifty-eight drill-core samples from both deposits were collected with the support of the Andina and El Teniente divisions of CODELCO, and Exploraciones Mineras Andinas (EMSA). The samples were selected to cover the widest possible range of compositions and to avoid areas with strong hydrothermal alteration. They include the different lithologies recognized in the pre-mineralization and ore-related porphyritic intrusions. In addition, three samples of hydrothermal veins from Rio Blanco were also studied.

The samples were prepared for chemical analyses at the Research School of Earth Sciences (RSES) of the Australian National University (ANU). Approximately 1 kg of sample was crushed and ~200g was milled to the consistency of flour. Major elements were measured by XRF with sample digestion by lithium tetraborate fusion at Intertek Laboratories (Perth, Australia). Trace elements were analysed on lithium tetraborate fused samples and quantified by Laser Ablation Inductively Coupled Plasma Mass Spectrometry (LA-ICP-MS) at RSES-ANU.

The concentrations of PGE, Re and Au were determined using the Ni-sulphide fire assay, isotope dilution method (NiS-FA-ID) described by Park et al. (2012), which allows the determination of PGE at ultra-low concentrations (pg/g levels). For the

measurements, two quadrupole ICP-MS systems were used: An Agilent 7700x and a ThermoFisher iCap RQ, both at RSES-ANU. Duplicate analyses, procedural blanks and the reference material TDB-1 (CANMET diabase) were analysed in each analytical session to assess heterogeneity, contamination, accuracy and precision. The method detection limits (MDL) were calculated as half the difference between the highest and lowest values of the laboratory historical procedural blanks.

4 Results and discussions

4.1 Major and trace element geochemistry

The samples have different degrees of differentiation with compositions that range from basalt to rhyolite. The MgO contents in the samples range from 2.83 to 0.42 wt.% for Rio Blanco and from 5.63 to 0.62 wt.% for El Teniente.

The general coherence between the geochemical data and particularly, the sub-parallel rare earth elements (REE) and multi-incompatible elements patterns, indicate that the pre-mineralization and the porphyritic intrusions are co-genetic for each deposit. Although there is considerable scatter in the data, the concentrations of most of the major and trace elements vary continuously with decreasing MgO wt.%, which suggests that fractional crystallization dominated the observed variations.

4.2 PGE, Re and Au geochemistry

Most of the Ir, Rh and Ru contents of the samples are close to or below detection limits (b.d.l.) and for this reason, will not be discussed further. The Pd and Pt abundances in the Rio Blanco samples do not show any clear trend with decreasing MgO until ~1.4 wt.%, when the Pd and Pt values fall with decreasing MgO. Rhenium and Au concentrations in these samples are scattered, and they do not exhibit a clear trend. Although some scatter, at El Teniente District there is an overall decrease in the concentrations of Pt, Pd, Re and Au with decreasing MgO in the high MgO pre-mineralization intrusions, which suggests that sulphide saturation occurred early in the El Teniente magmatic system.

Figure 2 compares the variations in Pd and Pt in the Rio Blanco and El Teniente samples as a function of MgO with samples from Pual-Ridge and Niuatahi-Motutahi oceanic arc lavas (Park et al. 2013, 2015); the intrusions related to El Abra (Cocker et al. 2015) and Escondida (Hao et al. 2019) porphyry copper deposits and the Sanim and Sanyo-Ryoke barren suites (Park et al. 2019). The Rio Blanco and El Teniente intrusions show Pd and Pt concentrations that are about one order of magnitude lower than pre-sulphide saturation samples from Pual-Ridge and Niuatahi-Motutahi lavas but are similar to the post-sulphide saturation samples from the same locations. We interpret this to indicate that sulphide saturation occurred early in the Rio Blanco and El

Teniente magmatic systems, which caused an overall decrease in the PGE content of the magma.

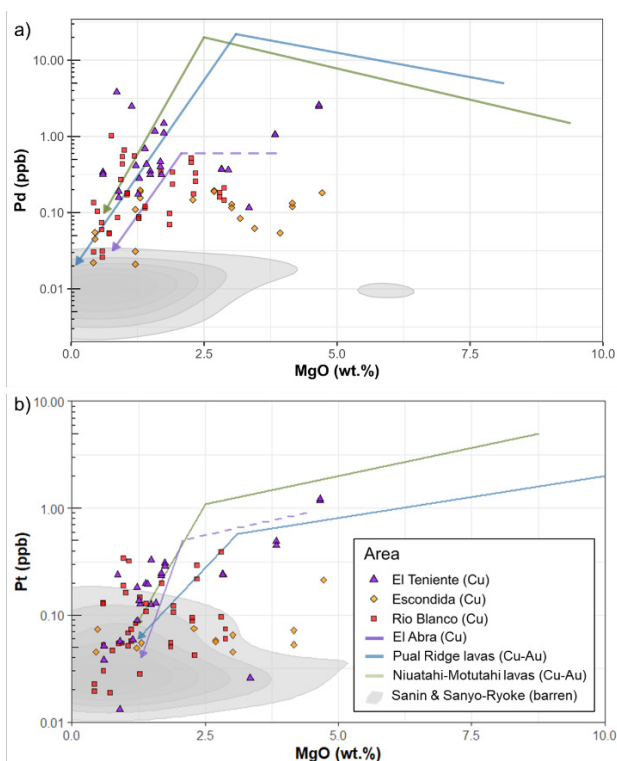


Figure 2. (a) Pd and (b) Pt versus MgO for the Rio Blanco and El Teniente intrusions (this study) compared to Escondida, (Hao et al. 2019) and El Abra (Cocker et al. 2015) porphyry copper deposits; the Pual Ridge and Niuatahi-Motutahi (Park et al. 2013, 2015) Cu-Au lavas; and the Sanin and Sanyo-Ryoke barren suites (Park et al. 2019). The Pd-Pt line trends are from the cited authors.

Sulphides cumulates also sequester Au and Cu, but their partition coefficients into sulphide melts are about one and two orders of magnitude lower than Pd and Pt (Mungall and Brenan 2014), respectively. Elements with lower partition coefficients will enter the immiscible sulphide melt at a lower rate. We suggest that the low Au content of the Rio Blanco and El Teniente ores are due to this element being sequestered by cumulus sulphides in a putative lower magma chamber. Here, Au remains trapped, and inaccessible to the ore-fluids that exsolve from upper crustal magma systems.

4.3 Implications for ore-forming processes

Previous studies have suggested that the timing of sulphide saturation relative to volatile exsolution, together with the amount of sulphide that separates from the melt, can play a critical role in determining the fertility of felsic magma systems (Park et al. 2015, 2019; Cocker et al. 2015; Hao et al. 2017; Lowczak et al. 2018). Here we have interpreted the Rio Blanco and El Teniente magmatic systems to have reached early sulphide saturation, before the MgO content of the magma had fallen to 3 and 6 wt.% MgO, respectively, in a deep, unexposed lower magma chamber. Although the Rio Blanco and El Teniente magmatic system experienced early

sulphide saturation, which must have resulted in a large fraction of the Cu being locked in the cumulates of the lower crustal magma chamber, this has not prevented the formation of two of world's largest copper deposits.

One possibility is that the amount of sulphide to precipitate from the melt was small, so it had little effect on the concentration of copper in the melt, due to its low partition coefficient in sulphide melts compared to Pd and Au. We suggest that early sulphide saturation caused an important depletion in the Pd and Au content of the residual melt, but it did not cause an important decrease in the Cu content due to its lower partition coefficient into immiscible sulphide melts compared to Pd and Au (Mungall and Brenan 2014; Cocker et al. 2015). Then, by the time that the evolving melt reached volatile exsolution, the magma still contained enough Cu to form a porphyry deposit. Furthermore, the significant decrease in the Au content of the magma compared to Cu is likely to have been responsible for the formation of a Cu-dominated porphyry deposit, rather than a Cu-Au one.

Although several factors may have contributed to the formation of these supergiant porphyry copper deposits, we suggest that the size of the magma chamber and its long duration were the most important. Assuming a magma that contains 50 ppm of Cu, a minimum of 1,400 km³ and 761 km³ are required to produce the ~184 and 100 Mt of Cu in the Rio Blanco and El Teniente deposits, respectively. However, this back-of-the-envelope calculation assumes that Cu was extracted with 100% efficiency, which is highly unlikely. A more realistic minimum volume is ten times this or 14,000 and 7,610 km³ respectively for each of the ore systems. Although we cannot calculate the exact size of the magma chamber that produced these deposits, it is clear that it was enormous.

5 Conclusions

The results from this study show that the magmas that produced the pre-mineralization and ore-related porphyries at the Rio Blanco and El Teniente deposits are co-magmatic. The overall low concentrations of PGE show that the Rio Blanco and El Teniente magmatic systems reached sulphide saturation at an early stage of their evolution, before their MgO content fell to 2.8 and 5.7 wt.% MgO, respectively. We interpret this to have occurred in a deep and unexposed lower magma chamber, where the sulphide cumulates trapped a significant proportion of the PGE, Au and Cu content in the magma. Gold was more affected than Cu due to its higher partition coefficient in sulphide melts, which explains why the Rio Blanco and El Teniente are Cu-dominant deposits with little Au.

The results from our study show that early sulphide saturation did not prevent the formation of the Rio Blanco and El Teniente deposits and therefore, we conclude that the timing of sulphide saturation did not play a key role in the formation of the supergiant

porphyry copper deposits in Central Chile. We propose that there are other factors controlled the formation of these deposits, including the small amount of sulphide melt that formed, the large size of the magma chamber and the long duration of the magmatic activity.

Acknowledgements

This study was financed by Australian Research Council Discovery Project [DP170103140] to Ian Campbell and Andrew Berry and by the 2020 SEG Student Research Grant from the Hugh McKinstry Fund to Yamila Cajal. The authors would like to acknowledge the Andina and El Teniente divisions of CODELCO and the Exploraciones Mineras Andinas for providing the samples for this study.

References

- Audétat A, Simon AC (2012) Magmatic controls on porphyry copper genesis. In: Hedenquist JW, Harris M, Camus F (eds) *Geology and genesis of major copper deposits and districts of the world: a tribute to Richard H. Sillitoe*. Society of Economic Geologists, Special Publication, pp 553–572
- Cannell J, Cooke DR, Walshe JL (2005) *Geology, Mineralization, Alteration, and Structural Evolution of the El Teniente Porphyry Cu-Mo Deposit*. Economic Geology 100:979–1003
- Cocker HA, Valente DL, Park J-W, Campbell IH (2015) Using platinum group elements to identify sulfide saturation in a porphyry Cu system: the El Abra porphyry Cu deposit, Northern Chile. *J Petrology* 56:2491–2514. <https://doi.org/10.1093/petrology/egv076>
- Cooke DR, Hollings P, Walshe JL (2005) Giant porphyry deposits: characteristics, distribution, and tectonic controls. *Economic Geology* 100:801–818
- Cuadra P (1986) Geocronología K-Ar del Yacimiento El Teniente y áreas adyacentes. *Revista Geologica de Chile* 27:3–26
- Deckart K, Clark AH, Aguilar CA, et al (2005) Magmatic and hydrothermal chronology of the giant Río Blanco porphyry copper deposit, Central Chile: implications of an integrated U-Pb and 40Ar/39Ar database. *Economic Geology* 905–934
- Deckart K, Silva W, Spröhnle C, Vela I (2014) Timing and duration of hydrothermal activity at the Los Bronces porphyry cluster: an update. *Miner Deposita* 49:535–546. <https://doi.org/10.1007/s00126-014-0512-9>
- Hamlyn PR, Keays RR, Cameron WE, et al (1985) Precious metals in magnesian low-Ti lavas: implications for metallogenesis and sulfur saturation in primary magmas. *Geochimica et Cosmochimica Acta* 49:1797–1811. [https://doi.org/10.1016/0016-7037\(85\)90150-4](https://doi.org/10.1016/0016-7037(85)90150-4)
- Hao H, Campbell IH, Park J-W, Cooke DR (2017) Platinum-group element geochemistry used to determine Cu and Au fertility in the Northparkes igneous suites, New South Wales, Australia. *Geochimica et Cosmochimica Acta* 216:372–392. <https://doi.org/10.1016/j.gca.2017.05.009>
- Hao H, Campbell IH, Richards JP, et al (2019) Platinum-group element geochemistry of the Escondida Igneous Suites, Northern Chile: implications for ore formation. *J Petrology* 60:487–514. <https://doi.org/10.1093/petrology/egz004>
- Lowczak JN, Campbell IH, Cocker H, et al (2018) Platinum-group element geochemistry of the Forest Reef Volcanics, southeastern Australia: Implications for porphyry Au-Cu mineralisation. *Geochimica et Cosmochimica Acta* 220:385–406. <https://doi.org/10.1016/j.gca.2017.09.052>
- Maksaev V, Munizaga F, McWilliams M, et al (2004) New Chronology for El Teniente, Chilean Andes, from U-Pb, 40Ar/39Ar, Re-Os, and Fission-Track Dating: Implications for the Evolution of a Supergiant Porphyry Cu-Mo Deposit. In: *Economic Geology*. Society of Economic Geologists, Special Publication, pp 15–54
- Mpodozis C, Cornejo P (2012) Cenozoic tectonics and porphyry copper systems of the Chilean Andes. In: Hedenquist JW, Harris M, Camus F (eds) *Geology and genesis of major copper deposits and districts of the world: a tribute to Richard H. Sillitoe*. Society of Economic Geologists, Special Publication, p 32
- Mudd GM, Jowitt SM (2018) Growing Global Copper Resources, Reserves and Production: Discovery Is Not the Only Control on Supply. *Economic Geology* 113:1235–1267. <https://doi.org/10.5382/econgeo.2018.4590>
- Mungall JE, Brenan JM (2014) Partitioning of platinum-group elements and Au between sulfide liquid and basalt and the origins of mantle-crust fractionation of the chalcophile elements. *Geochimica et Cosmochimica Acta* 125:265–289. <https://doi.org/10.1016/j.gca.2013.10.002>
- Park J-W, Campbell IH, Arculus RJ (2013) Platinum-alloy and sulfur saturation in an arc-related basalt to rhyolite suite: Evidence from the Pual Ridge lavas, the Eastern Manus Basin. *Geochimica et Cosmochimica Acta* 101:76–95. <https://doi.org/10.1016/j.gca.2012.10.001>
- Park J-W, Campbell IH, Kim J, Moon J-W (2015) The role of late sulfide saturation in the formation of a Cu- and Au-rich magma: insights from the platinum group element geochemistry of Niutahi-Motutahi Lavas, Tonga Rear Arc. *Journal of Petrology* 56:59–81. <https://doi.org/10.1093/petrology/egv071>
- Park J-W, Campbell IH, Malaviarachchi SPK, et al (2019) Chalcophile element fertility and the formation of porphyry Cu ± Au deposits. *Miner Deposita* 54:657–670. <https://doi.org/10.1007/s00126-018-0834-0>
- Richards JP (2003) Tectono-magmatic precursors for porphyry Cu-(Mo-Au) deposit formation. *Economic Geology* 98:1515–1533
- Richards JP (2013) Giant ore deposits formed by optimal alignments and combinations of geological processes. *Nature Geosci* 6:911–916. <https://doi.org/10.1038/ngeo1920>
- Serrano L, Vargas R, Stambuk V, et al (1996) The late Miocene to early Pliocene Río Blanco-Los Bronces Cu Deposit, Central Chilean Andes. In: Camus F, Sillitoe RH, Petersen R (eds) *Andean copper deposits: new discoveries, mineralization, styles and metallogeny*. Society of Economic Geology Special Publication
- Stern CR, Skewes MA, Arévalo A (2011) Magmatic Evolution of the Giant El Teniente Cu-Mo Deposit, Central Chile. *Journal of Petrology* 52:1591–1617. <https://doi.org/10.1093/petrology/egq029>
- Toro JC, Ortúzar J, Zamorano J, et al (2012) Protracted magmatic-hydrothermal history of the Río Blanco-Los Bronces District, Central Chile: development of world's greatest known concentration of copper. In: *Geology and genesis of major copper deposits and districts of the world: a tribute to Richard H. Sillitoe*. Society of Economic Geologists, Special Publication, pp 105–126
- Warnaars FW, Holmgren D. C, Barassi F. S (1985) Porphyry copper and tourmaline breccias at Los Bronces-Río Blanco, Chile. *Economic Geology* 80:1544–1565. <https://doi.org/10.2113/gsecongeo.80.6.1544>
- Wilkinson JJ (2013) Triggers for the formation of porphyry ore deposits in magmatic arcs. *Nature Geosci* 6:917–925. <https://doi.org/10.1038/ngeo1940>

Metallogenic model of the Eocene Zn-Pb(-Ag) Santa María and Antares bodies of the Velardeña skarn district (Durango, Mexico)

Néstor Cano¹, Antoni Camprubí², Eduardo González-Partida³, Pura Alfonso⁴, Daniel P. Miggins⁵, Edith Fuentes-Guzmán^{1,2,6}, Edith Cienfuegos-Alvarado^{2,6}, Ana K. González-Ambrocio¹, and Vanessa Colas¹

¹Posgrado en Ciencias de la Tierra, Universidad Nacional Autónoma de México. Mexico City, Mexico.

²Instituto de Geología, Universidad Nacional Autónoma de México. Juriquilla, Mexico.

³Centro de Geociencias, Universidad Nacional Autónoma de México. Mexico City, Mexico.

⁴Departament d'Enginyeria Minera, Industrial i TIC, Universitat Politècnica de Catalunya. Manresa, Catalonia, Spain.

⁵College of Earth, Ocean, and Atmospheric Sciences, Oregon State University. Corvallis, United States.

⁶Laboratorio Nacional de Geoquímica y Mineralogía. Mexico City, Mexico.

Abstract. The Santa María and Antares Zn-Pb skarn deposits from the Velardeña mining district are located in central-NW Mexico. They lie 470 m apart from each other along the contact between Oligocene felsic bodies and Cretaceous limestones. The prograde stage in these systems was promoted by fluids at ~600 °C and 15 wt. % NaCl equiv., and was dominated by garnet-wollastonite±vesuvianite±clinopyroxene and biotite±K-feldspar±magnetite assemblages. The retrograde stage formed by fluids around 400 °C and ~20-50 wt. % NaCl equiv., is characterized by chlorite-amphibole-epidote-calcite-quartz-sericite-adularia-fluorite-muscovite along with sphalerite-pyrite-galena-pyrrhotite-arsenopyrite-chalcocopyrite±fahlore±Bi-Sb-sulfosalts assemblages. $\delta^{18}\text{O}_{\text{calcite}}$ data between 15 and 20 ‰ in Santa María, and between 10 and 15 ‰ in Antares show a less-modified magmatic affinity for the latter. $\delta^{13}\text{C}_{\text{calcite}}$ values between 0 and -9 ‰ register recycling processes of sedimentary C. Moreover, $\delta^{34}\text{S}_{\text{VCDT}}$ values between -3 and 2 ‰ revealed a magmatic source for S. Altogether, these data suggest that, in Santa María, magmatic-derived fluids actively interacted with the wall rocks, which did not occur at Antares. In both bodies, ore deposition was triggered by cooling and neutralization of the magmatic derived fluids. The $^{40}\text{Ar}/^{39}\text{Ar}$ ages for adularia at ~37.5 Ma place the deposits within the Eocene-early Miocene metallogenetic epoch of central-NW Mexico.

1 Introduction

Skarn deposits are governed by diverse variables that control the evolution and type of mineralization —i.e., temperature and depth of formation, nature of wall rocks, $f\text{O}_2 - f\text{S}_2$ of involved fluids, and proximity to the heat/fluids source (Meinert et al. 2005). Sulfide-rich skarn deposits are common in central-NW Mexico, where silicic flare-ups during the Eocene-Oligocene intercepted carbonates units of the “Sector Transversal de Parras” (STP; Camprubí 2013).

The Zn-Pb±Ag Velardeña Mining District is located in Durango state and encompasses the Santa María and San Lorenzo ranges (Figure 1A). Skarn systems in the Santa María range are present along the contact between Cretaceous limestones (Cuesta del Cura Formation) and felsic intrusions from the Velardeña Intrusive Complex (Figure 1B). The combined resource of the Santa María and Antares deposits is 8 Mt, grading at 25 g/t Ag, 0.3-0.6 wt. % Pb, and 5-6 wt. % Zn.

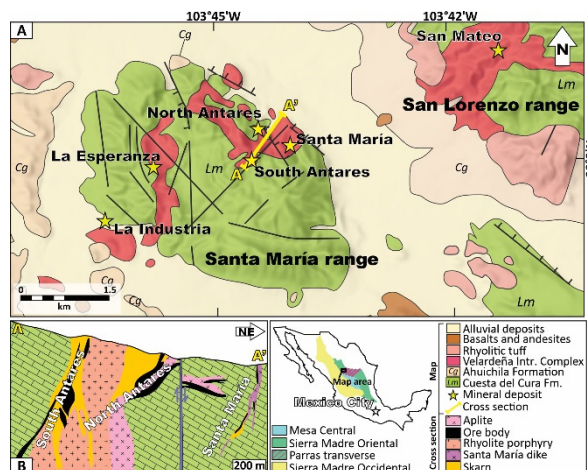


Figure 1. Geological map (A) and cross section (B) depicting the Antares and Santa María skarn deposits.

In the present study, we analyzed drill-core sample suites from the Antares and Santa María bodies through petrography, fluid inclusion studies, EPMA mineral chemistries, stable isotope analyses, and $^{40}\text{Ar}/^{39}\text{Ar}$ geochronology. Our results underpin the first comprehensive genetic model for the deposits. In addition, these data shed new light on the processes involved into the development of a Zn-Pb skarn system consisting of orebodies with distinct features. The orebodies at Antares are associated with a “typical” stock, whereas those at Santa María are the result of a smaller “satellite” intrusive (Figure 1B). This allows to assess, by comparison, two mineralization endmembers whose mineralizing fluids show variably modified magmatic signals due to interaction with the host limestones. Additionally, detailed studies on fluid evolution and mineral assemblages revealed peculiarities regarding physicochemical conditions of the fluids during ore precipitation (e.g., moderate-high temperature and salinity) —when compared to “traditional” Zn-Pb skarns (Chang et al. 2019).

2 Methodology

A total of 15 drill holes across the Santa María and Antares orebodies were provided by Industrias Peñoles. Quantitative mineral chemistry analyses were performed with a JEOL JXA-8900R electron probe micro-analyzer at the Laboratorio de Geoquímica y Mineralogía (LANGEM) with as

analytical condition: 20KeV, 20nA beam current, and 40s acquisition time.

Carbon and oxygen stable isotopes were analyzed in 82 samples of calcite from the wall-rocks and skarn system. Measurements were carried out at the LANGEM using a Thermo Finnigan MAT 253 mass spectrometer coupled with a Gas Bench II.

Sulfur isotopes were carried out in 61 pure sulfide separates from massive ores and mineralized veins. Analyses were performed at the Centres Científics i Tecnològics (Universitat de Barcelona) with a Delta Plus XP Thermo Fisher mass spectrometer coupled with a TC-EA pyrolyzer and a Carlo Erba 1108 elemental analyzer.

Fluid inclusion studies were carried out in 23 samples using a microscope coupled with a Linkam THMSG 600 stage, available at the LANGEM. Salinities were calculated using ice melting temperature or, when present, halite dissolution temperature following Bodnar (1993).

Two samples of adularia from the ore stage at Santa María were collected for $^{40}\text{Ar}/^{39}\text{Ar}$ dating. The analyses were performed at the Geochronology Laboratory of Oregon State University (OSU) on samples that had been previously irradiated at a TRIGA CLICIT nuclear reactor available at the Radiation Center of the OSU. A FCT-NM (28.201 ± 0.023 Ma) neutron fluence monitor was employed. The ages were obtained using an ARGUS-VI multi-collector mass spectrometer. Irradiated samples were placed in a high-vacuum sample chamber and incrementally heated by a 25 W Synrad CO_2 laser.

3 Results and discussion

3.1 Ore and gangue assemblages

Santa María

-Exoskarn: The prograde mineralogy consists of grossular-andradite, wollastonite, and vesuvianite, plus lesser calcite and quartz (Figure 2). The retrograde stage obliterates prograde minerals in most cases and consist of the following mineral assemblages: 1) garnet, tremolite, and calcite; 2) sericite, chlorite, calcite, quartz, tremolite, and lesser biotite, epidote, and muscovite; 3) actinolite, sphalerite, quartz, and pyrite; and 4) sulfides and sulfosalts accompanied by chlorite, fluorite, quartz, calcite, epidote, tremolite, and muscovite.

-Endoskarn: The prograde stage consists only of local biotitic alteration. In contrast, the retrograde stage consists of 1) actinolite, quartz, pyrite, and lesser scapolite, followed by 2) pseudorhombohedral adularia, fluorite, quartz, muscovite, and calcite. The latter assemblage is conspicuous and tightly related to ore deposition.

-Mineralization: Sulfides and sulfosalts formed massive replacement zones that obliterate any remaining sedimentary or igneous textures. Pyrite and sphalerite dominate the ore assemblages and coexist with variable amounts of galena, arsenopyrite, pyrrhotite, chalcopyrite, tetrahedrite-

hakite-freibergite, lillianite-gustavite, and heyrovskýite-eskimoite (Figure 3B-C, E). Fahlore and arsenopyrite geothermometry yielded 170-300 °C and 350-490 °C, respectively (Figure 3D, F).

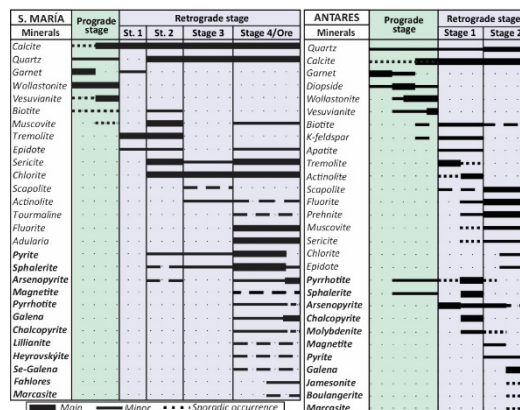


Figure 2. Paragenetic sequences for both orebodies.

Antares

-Exoskarn: Prograde assemblages are dominated by garnet, clinopyroxene, wollastonite, and vesuvianite. In some cases, pyrrhotite and sphalerite crystallized during garnet formation, and are observed as tiny solid inclusions, rims, or intercrystalline fillings. The retrograde event consists of actinolite, tremolite, quartz, calcite, epidote, and chlorite that accompany the most economically important mineralization in the orebody.

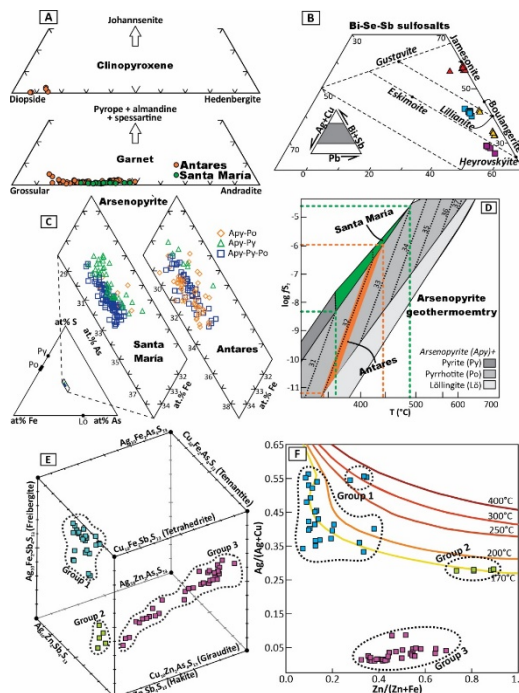


Figure 3. Diagrams for garnet-clinopyroxene (A), Bi-Se-Sb sulfosalts (B), arsenopyrite (C), and fahlores (E). Arsenopyrite (D) and fahlore (F) geothermometry.

-Endoskarn: Prograde minerals are grossular-andradite and diopside with locally pyrrhotite, arsenopyrite, and Fe-rich sphalerite. Further, biotite and K-feldspar alteration was produced at the end of the prograde stage and became more widespread during the retrograde stage, which is marked by 1) tremolite-actinolite, fluorite, and

apatite, and 2) muscovite, sericite, prehnite, scapolite, and pyrite assemblages.

-Mineralization: Massive sulfides and minor sulfosalts crystallized during two substages: 1) pyrrhotite, arsenopyrite, Fe-rich sphalerite, chalcopyrite, molybdenite, and 2) arsenopyrite, pyrite, galena, and minor pyrrhotite, molybdenite, jamesonite, boulangerite, and marcasite (Figure 1B-C). Arsenopyrite geothermometry yielded 350-450 °C (Figure 1D).

3.2 Fluid inclusion studies

Santa María

-Prograde stage: Secondary L + V fluid inclusions hosted in garnet exhibit ice melting temperatures (T_{mi}) averaging -28.9 °C (28.1 wt.% NaCl equiv.). The average homogenization temperature (T_h) to liquid is 437 °C (Figure 4A).

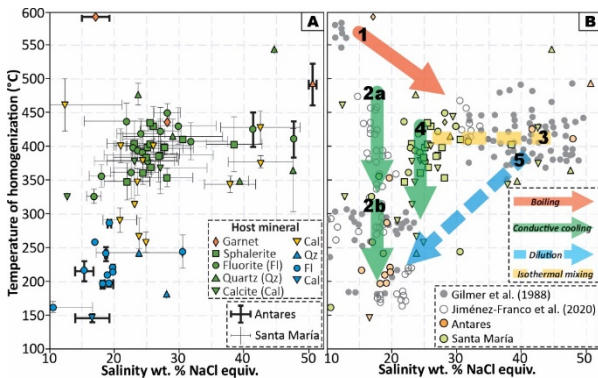


Figure 4. T_h vs. salinity plots with evolutionary trends (B).

-Ore stage: primary and pseudosecondary L + V fluid inclusion assemblages (FIAs) hosted in sphalerite, calcite, quartz, and fluorite from the ore stage have eutectic temperatures (T_e) between -120 and -90 °C, suggesting the occurrence of methane (confirmed through FT-IR spectroscopy analyses). The average T_{mi} are -19.2 ± 9.4 °C (1 σ) in FIAs hosted in calcite, -26.5 ± 5.3 °C in sphalerite, -22.8 ± 5.8 °C in fluorite, and -38.1 ± 11.9 °C in quartz, equivalent to salinities of 21.0 ± 7.5 , 26.6 ± 3.7 , 24.0 ± 4.1 , and 36.8 ± 10.2 wt. % NaCl equiv., respectively. The very low T_{mi} suggests abundant CaCl_2 in the salt assemblage, which is also revealed by hydrohalite melting temperatures around -50 °C approaching the H_2O -NaCl- CaCl_2 eutectic point (-51.0 °C). This could also explain the obtained high salinities in the absence of daughter halite crystals. Homogenization to liquid occurred at 374 ± 7 °C in FIAs hosted in calcite, 392 ± 23 °C in sphalerite, 399 ± 36 °C in fluorite, and 431 ± 81 °C in quartz.

Antares

-Prograde stage: FIAs enclosed in garnet display T_e around -40.0 °C, thus indicating the occurrence of bivalent cation chlorides (i.e., FeCl_2 or MgCl_2). The T_{mi} range between -16.7 and -11.4 °C (15.4 and 20.0 wt. % NaCl equiv.), and T_h varies between 595 and 598 °C. However, several fluid inclusions remained biphasic at 600 °C.

-Ore stage: Primary and pseudosecondary FIAs in fluorite from the massive ores contain daughter halite, sylvite, and two unidentified solids. The T_e at ~ -38.4 °C and -100.0 °C suggest the presence of MgCl_2 or FeCl_2 plus NaCl, KCl, and, perhaps, CH_4 . The average T_{mi} and T_h are -16.3 ± 0.2 °C and 416 ± 10 °C, respectively. Halite dissolution occurs at ~ 379 °C and sylvite between 195 and 299 °C, equivalent to salinities of 45.5 wt. % NaCl equiv.

3.3 C, O, and S stable isotopes

Santa María

Limestones display $\delta^{18}\text{O}_{\text{VSMOW}}$ from 18.5 to 19.5 ‰, and $\delta^{13}\text{C}_{\text{VPDB}}$ from -3.4 to 0.7 ‰. Calcite from the exoskarns has $\delta^{18}\text{O}_{\text{VSMOW}}$ between 14.8 and 18.1 ‰, and $\delta^{13}\text{C}_{\text{VPDB}}$ between -6.9 and -3.3 ‰, plotting near or within the magmatic fluids box. Marbles show $\delta^{18}\text{O}_{\text{VSMOW}}$ between 14.6 and 21.3 ‰, and $\delta^{13}\text{C}_{\text{VPDB}}$ between -8.0 and -0.5 ‰—i.e., mixed signatures between limestones and magmatic fluids—similar to calcite from massive sulfides ($\delta^{18}\text{O}_{\text{VSMOW}}$ from 14.6 to 21.1 ‰, and $\delta^{13}\text{C}_{\text{VPDB}}$ from -2.6 to -0.2 ‰).

$\delta^{34}\text{S}_{\text{VCDT}}$ values range between -3.2 and 1.7 ‰, matching those of magmatic S (~ 0 ‰; Hoefs, 2009). The $\delta^{34}\text{S}_{\text{VCDT}}$ values in arsenopyrite range between -2.6 and -0.3 ‰, between -2.8 and 0.5 ‰ in pyrite, between -0.7 and -0.2 ‰ in pyrrhotite, between -3.2 and 1.2 ‰ in sphalerite, at -1.4 ‰ in galena, and at -0.4 ‰ in marcasite.

Antares

Limestones display average $\delta^{13}\text{C}_{\text{VPDB}}$ values at 14.1 ‰ and $\delta^{18}\text{O}_{\text{VSMOW}}$ at -0.3 ‰. Calcite from prograde skarns yielded $\delta^{18}\text{O}_{\text{VSMOW}}$ between 9.4 and 15.4 ‰, and $\delta^{13}\text{C}_{\text{VPDB}}$ between -7.0 and -0.6 ‰—that is, within the fields of magmatic fluids. Similarly, calcite from marble yielded consistent $\delta^{18}\text{O}_{\text{VSMOW}}$ at ~ 13.1 ‰ and $\delta^{13}\text{C}_{\text{VPDB}}$ between -5.6 and -0.1 ‰, partly overlapping the magmatic fluids box. Moreover, calcite from massive sulfides yielded $\delta^{18}\text{O}_{\text{VSMOW}}$ between 12.2 and 20.1 ‰, and $\delta^{13}\text{C}_{\text{VPDB}}$ between -8.1 and 0.4 ‰, similar to magmatic fluid signatures. Overall, calcites from Antares show lower isotopic values than at Santa María, revealing less modified magmatic signals.

$\delta^{34}\text{S}_{\text{VCDT}}$ data range between -2.8 and 1.7 ‰ (magmatic S; Hoefs, 2009). $\delta^{34}\text{S}_{\text{VCDT}}$ values in arsenopyrite range between -1.5 and -0.6 ‰, between -1.4 and 1.2 ‰ in chalcopyrite, between -0.9 and 1.7 ‰ in galena, between -2.8 and 0.4 ‰ in pyrrhotite, between 0.0 and 0.4 ‰ in pyrite, between -1.9 and 1.5 ‰ in sphalerite, at -0.4 ‰ in marcasite, and at 0.8 ‰ in molybdenite.

3.4 $^{39}\text{Ar}/^{40}\text{Ar}$ geochronology

Two samples of pseudorhomboidal adularia from the ore stage at Santa María yielded plateau ages at 37.48 ± 0.09 , 37.62 ± 0.09 and 37.58 ± 0.09 Ma, and inverse isochron ages at 37.47 ± 0.13 and 37.64 ± 0.1 Ma. This reveals that the ore event at Santa María occurred during the latest Eocene.

4 Evolution of the skarn deposits

The Santa María and Antares Zn-Pb±Ag skarn deposits developed during the intrusion of felsic subalkaline-alkaline magmas into hypabyssal Cretaceous carbonates of the Sector Transversal de Parras (STP) during the Eocene-Oligocene. The age dates presented in this study are similar to other polymetallic skarn deposits along the STP (e.g., Concepción del Oro, Mazapil, and Mapimí; see references in Camprubí 2013).

The intrusion of igneous bodies into carbonate rocks generated extensive marble aureoles and was followed by metasomatism. Metasomatic pulses were produced by deep magmatic-exsolved fluids that flowed upwards along lithological contacts and reacted with limestones and, to a lesser extent, felsic rocks, producing high-temperature calcsilicate assemblages (Figures 2, 5). This process was promoted by single-phase fluids with moderate salinities. Albeit sulfides are normally scarce during the prograde stage in skarns, early pyrrhotite and sphalerite were partly coeval with garnet at Antares.

The ore event occurred during the retrograde stage, as is usually observed in skarn deposits elsewhere (Meinert et al. 2005). Ore stages at Antares and Santa María were produced by cyclic fluid pulses at intermediate temperatures (360–430 °C). These temperatures for the ore-stage are atypically high compared to what have been found in many Zn-Pb skarn deposits worldwide (e.g., Shu et al. 2021). Nevertheless, other relatively “high”-temperature deposits have been documented (e.g., El Mochito, Honduras; Samson et al. 2008).

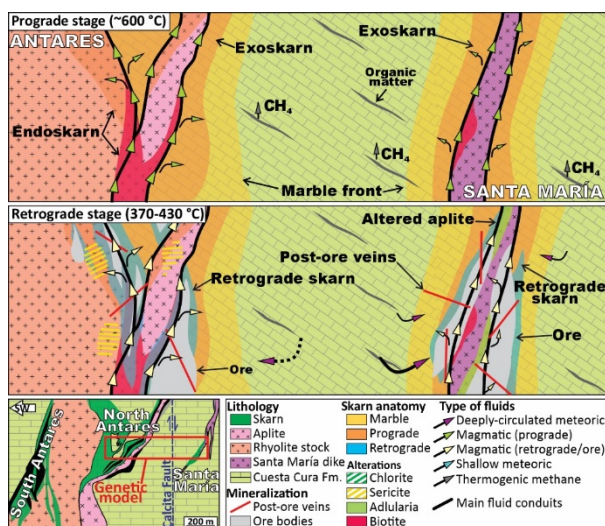


Figure 5. Genetic model for Antares and Santa María.

Hypogene ores consisting of sphalerite (either Fe-rich or Fe-poor) – pyrite – arsenopyrite ± fahlores at Santa María and pyrrhotite – Fe-rich sphalerite – arsenopyrite at Antares, suggest that, during the ore stage, the Antares body evolved along a low sulfidation trend, whereas Santa María records a transition from low- to intermediate-sulfidation as the system cooled (Einaudi et al. 2003).

The evolution of the fluids in each ore body behaved differently. At Antares, magmatic-derived

fluids evolved along deep boiling (arrow 1 in Figure 4B) and cooling paths (arrow 2a-2b). Later, boiled-off fluids experienced dilution with meteoric waters (arrow 5 in Figure 4B). Magmatic waters at Santa María followed a boiling path (arrow 1) that led to isothermal mixing with deeply-circulated meteoric fluids (arrow 3). Afterwards, cooling processes became dominant (arrow 4). In both ore bodies, ore deposition was mostly triggered by cooling and neutralization of the mineralizing fluids.

5 Conclusions

The Santa María and Antares ore bodies are Zn-Pb±Ag skarn deposits spatially linked to aplite dikes and rhyolitic stocks related to the initial silicic flare-ups of the Sierra Madre Occidental. Both deposits were formed in two major stages: prograde and retrograde/ore. The prograde stage was promoted by magmatic fluids that generated high-temperature alterations, which later evolved into cooler fluids that produced the retrograde and ore stages. Carbon-O isotopic data denote a magmatic signature in calcite from Antares, contrasting with trends at Santa María that are greatly influenced by the host limestones. Sulfur isotopes indicate a magmatic source for S.

Acknowledgements

CONACyT supported N.C. with a grant during his M.Sc. research, which was focused on this investigation. The study was supported by means of personal allocations to UNAM academicians. UNAM academics: María Colín, Alexander Iriondo, Carlos Linares, and Juan Vázquez are acknowledged for their kind assistance in sample preparation and laboratory analyses. We thank Industrias Peñoles for their help during the visit at mine's facilities.

References

- Bodnar R (1993) Revised equation and table for determining the freezing point depression of H₂O-NaCl solutions. *Geochim Cosmochim Acta*, 57(3):683–684.
- Camprubí A (2013) Tectonic and metallogenic history of Mexico. *Soc Econ Geol Spec Pub*, 17:201–243.
- Chang Z, Shu Q, Meinert, L (2019) Skarn deposits of China; *Soc Econ Geol Spec Pub*, 22:189–234.
- Einaudi M, Hedenquist J, Inan E (2003) Sulfidation state of fluids in active and extinct hydrothermal systems: transitions from porphyry to epithermal environments. *Soc Econ Geol Spec Pub*, 10: 1–51.
- Hoefs J (2009) Stable isotope geochemistry Sixth edition. Springer, Berlin Heidelberg.
- Meinert L, Dipple G, Nicolescu S (2005) World skarn deposits. *Econ Geol*, 100th Anniversary Volume:299–336.
- Samson I, Williams-Jones A, Ault K, Gagnon J, Fryer, B (2008) Source of fluids forming distal Zn-Pb-Ag skarns: Evidence from laser ablation-inductively coupled plasma-mass spectrometry analysis of fluid inclusions from El Mochito, Honduras. *Geology*, 36:947–950.
- Shu Q, Chang Z, Mavrogenes J (2021) Fluid compositions reveal fluid nature, metal deposition mechanisms, and mineralization potential: An example at the Haobugao Zn-Pb skarn, China. *Geology*, 49:473–477.

Tracking deep crustal evolution in porphyry copper systems: preliminary results from whole rock geochemistry and zircon trace elements in the Tres Cerrillos Cu-Mo prospect, Western Cordillera of Ecuador

Hugo Carrasco¹, Massimo Chiaradia¹, Francesca del Rio¹, Angelo Aguilar², Sergio Cubelli², Carolina Rodríguez², Carlos Urrutia².

¹Department of Earth Sciences, University of Geneva, rue des Maraîchers 13, 1205, Geneva, Switzerland.

²Corporación Nacional del Cobre de Chile (CODELCO), Huérfanos 1270, Santiago, Chile.

Abstract. The Tres Cerrillos prospect is a Miocene porphyry copper system located in the Western Cordillera of Ecuador, which is under an exploration program by EMSAEC (Codelco). Preliminary results from whole rock geochemistry and zircon trace elements of this magmatic-hydrothermal system show that porphyritic and precursor intrusions underwent a deep crustal evolution with suppression of plagioclase, and possibly involving some garnet fractionation in addition to amphibole. Whole rock geochemical proxies (Sr/Y, La/Y, V/Sc and Sr/Zr) and zircon trace elements suggest a fertile magmatic suite for this prospect. Future work will consist of placing mineral chemistry (e.g., zircon and apatite) within the frame of high precision CA-ID-TIMS U-Pb zircon geochronology to refine fertility indicators that can potentially be used as a proxy for metal endowments.

1 Introduction

Magmatism in thick convergent margins is a major process in the development of porphyry copper deposits (PCD) and large eruptions. Both require large magma volumes accumulated at upper crustal levels from magmas that have previously evolved in mid- to lower crustal zones (Chiaradia and Caricchi 2022). From the economic point of view, understanding the temporal evolution of fertile magmatic systems associated with supergiant PCD (>10 Mt Cu), from precursor intrusions (barren batholiths) to pre-, syn-, and post- mineralization porphyritic events, is crucial for developing toolkits for exploration and understanding what controls the different orders of magnitude of PCD. Here, we present preliminary results from whole rock geochemistry and zircon trace elements from precursor and syn-mineral porphyritic intrusions of the Tres Cerrillos prospect of the Western Cordillera of Ecuador assessing magma fertility for PCD and an early deep crustal evolution of their magmas.

The Tres Cerrillos prospect is a Cu-Mo porphyry system that is being explored by geologists of the EMSAEC team (Codelco) in the northernmost part of the Western Cordillera of Ecuador, approximately 120 km northeast from Quito (Figure 1). The basement rocks of the prospect mainly consist of allochthonous oceanic and island arc terranes (and associated sedimentary units), part of the Caribbean Large Igneous Province that collided and accreted to the continental margin of South America during the

Late Cretaceous (Vallejo et al. 2019). Subsequently, intermittent subduction has produced Cenozoic plutonic and volcanic arc units that intrude and overlie the basement rocks and are sites of ongoing exploration for porphyry copper systems (Figure 1). In fact, the northernmost part of the Western Cordillera is of high economic interest due to the recent discovery of the Cascabel porphyry Cu-Au deposit which is associated with Eocene rocks and the Llurimagua porphyry Cu-Mo of Miocene age, both defining two different metallogenic belts.

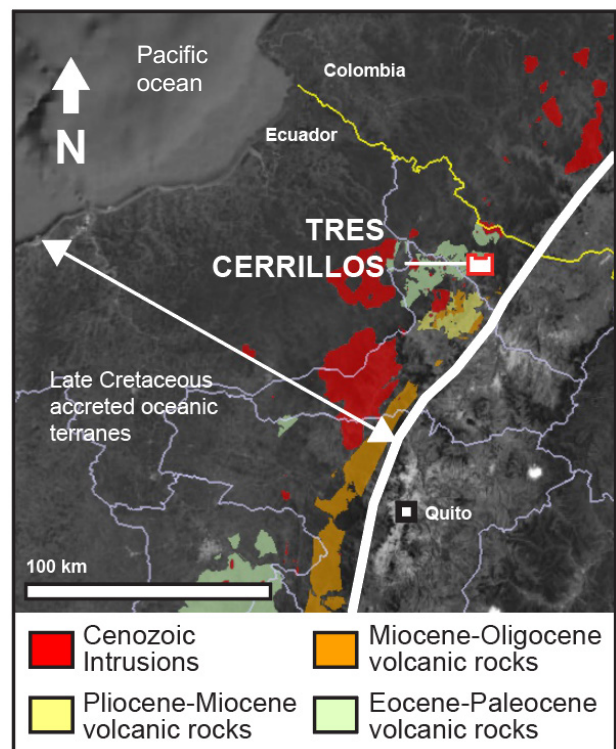


Figure 1. Location of the Tres Cerrillos prospect and simplified geology of the northwestern Ecuador.

The Tres Cerrillos project is centered on Miocene multiphase porphyritic intrusions of dacitic, quartzdioritic and dioritic compositions (Figure 2a), which are emplaced either into equigranular, granodioritic to dioritic intrusions (precursor intrusions that can be as old as Eocene, Figure 2b), or into the local basement. Various degrees of potassic (biotite-K-feldspar) and sericitic (quartz-

sericite) alteration develop extensively throughout the porphyry intrusions, where pyrite \pm chalcopyrite \pm molybdenite occur in stockwork veinlets. U-Pb zircon crystallization ages of the porphyritic intrusions reveals they are syn-mineralization, overlapping the range of Re-Os molybdenite dates that bracket the duration of the ore deposition (dates from CODELCO). The youngest mineralization age from Tres Cerrillos is similar to previous Re-Os molybdenite dates from the Chaucha Cu-Mo porphyry district located further south (i.e., 9.54 ± 0.05 Ma; Schütte 2012). Late andesitic dykes crosscut the system.

Future work will consist of placing mineral chemistry (e.g., zircon and apatite) within the frame of high precision CA-ID-TIMS U-Pb zircon geochronology to refine fertility indicators that can potentially be used as a proxy for metal endowments.

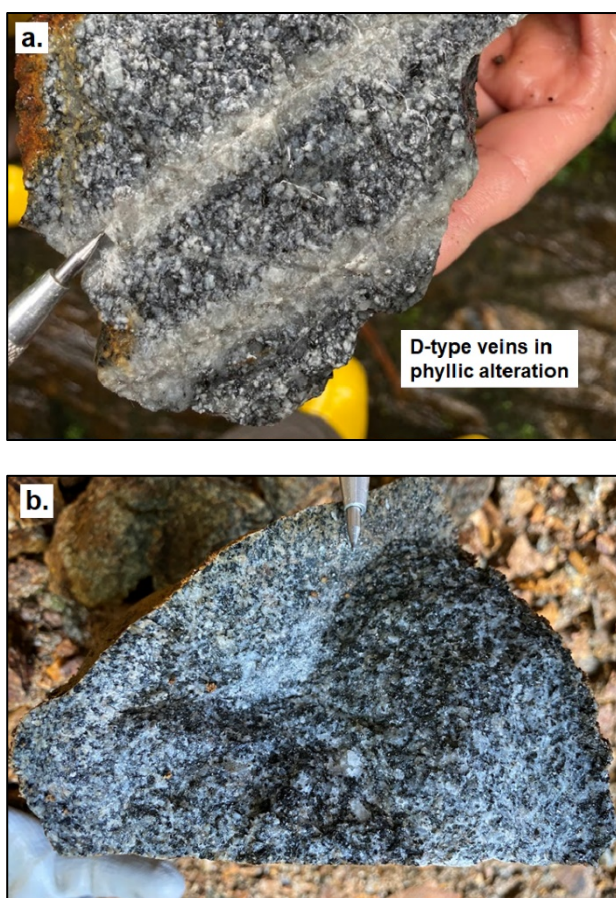


Figure 2. Main intrusions in the Tres Cerrillos prospect. **a.** Syn-mineralization, quartzdioritic porphyritic intrusion, showing sericitic alteration with D-type veins. **b.** Unaltered, equigranular, phaneritic granodiorite (precursor intrusion).

2 Whole rock geochemistry

The SiO_2 content from precursor and porphyry intrusions ranges between 57.8–72 wt%, while MgO content spans between 0.71–5.88 wt%. The volatile content (LOI) ranges mainly between 0.38–6.43 wt% which is high for igneous rocks in arc settings and indicates alteration. These intrusive rocks have a broad calc-alkaline signature that show

intermediate andesitic compositions when compared with incompatible elements (Nb/Y versus Zr/TiO₂ classification diagram, Figure 3a). The investigated rocks are the least altered ones as seen in the alteration box plot that compare major oxides (Figure 3b). However, they can be misleadingly classified as more felsic, due to the presence of quartz veinlets (Figure 2a).

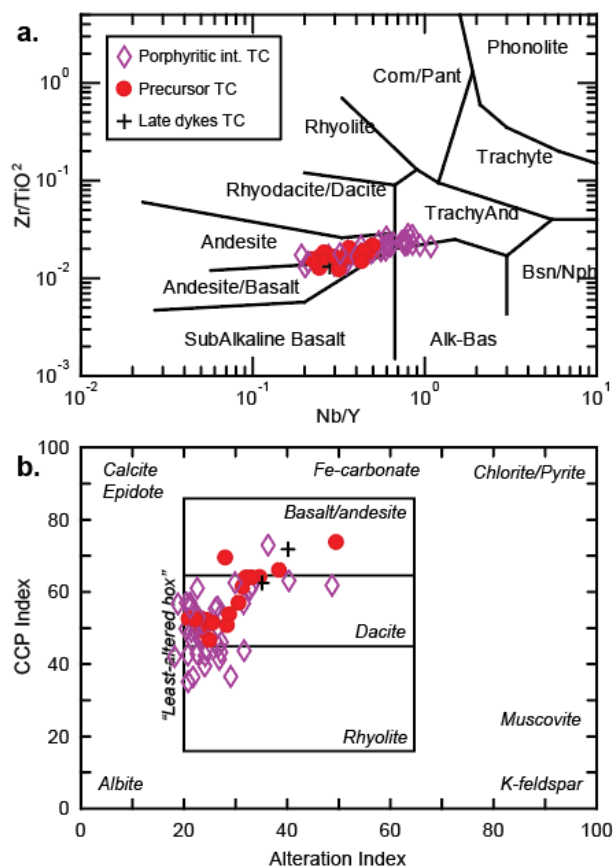


Figure 3. **a.** Nb/Y versus Zr/TiO₂ plot (Winchester and Floyd 1977). **b.** Alteration Box Plot (Large et al. 2001) that compares the Ishikawa Alteration Index versus Chlorite-carbonate-Pyrite index (CCPI).

Precursor intrusions, intra-mineral porphyries and late dykes (Figure 4a), show a strong enrichment of LREE compared to MREE and HREE, and a common lack of Eu anomaly in chondrite-normalized plots. Additionally, intra-mineral porphyritic intrusions display a clear depletion of MREE and HREE compared with precursor intrusions and late andesitic dykes. This MREE and HREE depletion could be due to amphibole \pm garnet \pm titanite fractionation. The systematic increase of Dy/Yb and Sm_(N)/Yb_(N) with differentiation proxies (i.e., MgO and SiO₂; Figure 4b, c) also support garnet \pm zircon fractionation, and therefore a possible deep crustal evolution of these magmas prior reaching shallow levels in the thick crust of the Western Cordillera of Ecuador (>35 km).

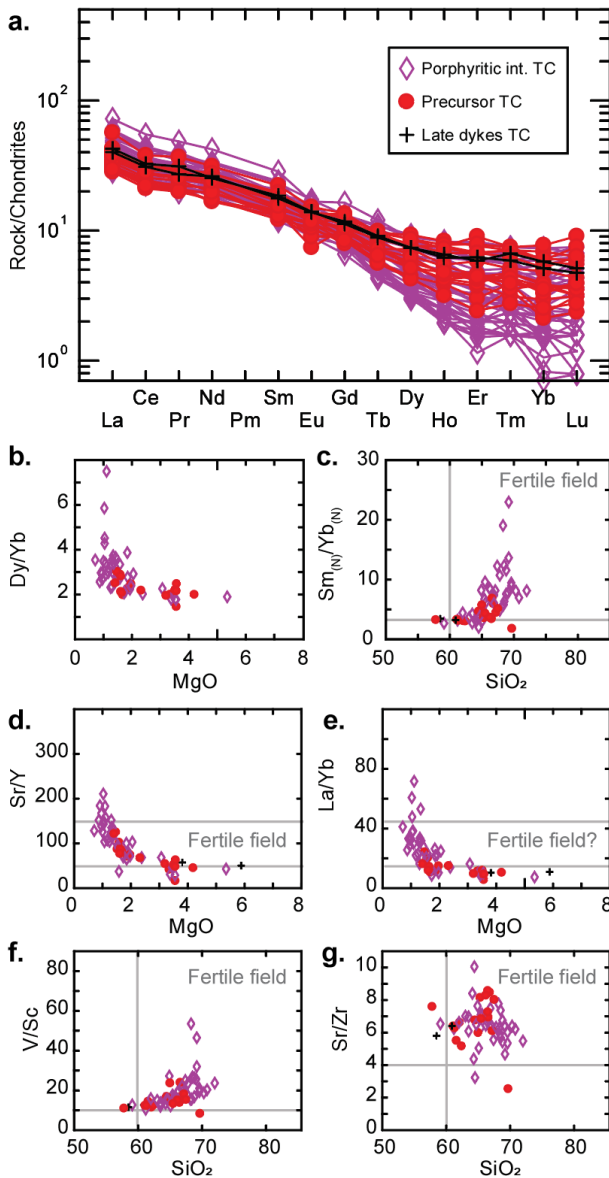


Figure 4. Whole rock geochemistry plots **a.** REE concentrations normalized to Chondrites. **b-g.** Geochemical proxies of magma fertility for porphyry copper systems.

Protracted magma storage at deep crustal level suppresses plagioclase fractionation (where Sr and Eu are compatible), whereas high pressure and H₂O content stabilize amphibole ± garnet (where Y, MREE and HREE are compatible) (Richards 2011; Chiaradia and Caricchi 2017). Therefore, assessing Sr/Y is of high importance as a magma fertility proxy. In the Tres Cerrillos prospect, Sr/Y ratios from the intra-mineral porphyritic intrusions have values that overlap the range of fertility (50-150), whereas precursor bodies and late dykes have lower values (Figure 4d). This probably reflects a different magmatic evolution for the two series. Likewise, the Sr/Y ratio decreases as the chemical composition of the magma is more primitive. This pattern is also shown by the La/Yb proxy when compared with MgO (Figure 4e). Other magma fertility proxies such as V/Sc and Sr/Zr also define a fertile behavior for the Tres Cerrillos magmatic suite (Figure 4f, g).

3 Zircon trace elements

Zircon trace elements proxies based on plots of Eu/Eu* (and also (Eu/Eu*)/Y) against Ce/Nd, Dy/Yb and (Ce/Nd)/Y (Lu et al. 2016) do not clearly discriminate between pre- and syn-mineralization samples from the same mineralized system. However, when comparing Dy/Yb versus Eu/Eu*, a distinction between the intra-mineral porphyritic intrusions of Tres Cerrillos and Eocene to Oligocene intrusion (old intrusions) becomes evident (Figure 5a), with the intra-mineral rocks presenting higher Dy/Yb values (~>0.3).

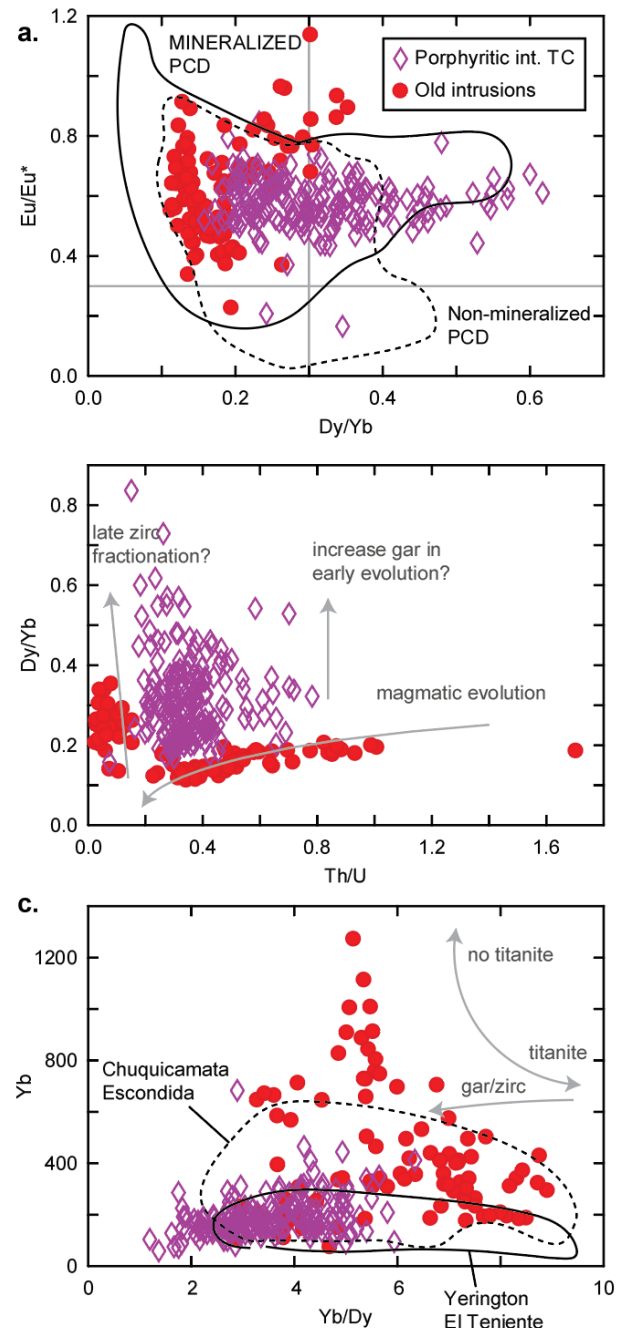


Figure 5. Zircon trace element plots **a.** Dy/Yb against Eu/Eu* (Lu et al. 2016), **b.** Th/U against Yb/Gd. **c.** Yb/Dy against Yb.

On the other hand, zircon trace elements can be used to assess the magmatic evolution of the fertile/barren rocks. Th/U is a ratio commonly used to track the crystallization from increasingly evolved magmas, with zircons having lower Th/U values being crystallized from more differentiated magmas. In the Th/U versus Dy/Yb plot (Figure 5b), the intra-mineral intrusions of the Tres Cerrillos prospect show higher Dy/Yb ratio at similar Th/U values, suggesting garnet fractionation at similar degrees of relatively early evolution, consistent with whole rock geochemistry results. In contrast, the old intrusion suite seems to have evolved at shallower levels following a differentiation trend with decreasing Dy/Yb as Th/U decreases, and a late zircon fractionation explaining the drastic increase in Dy/Yb values. These different magmatic evolution of barren versus fertile suites may provide regional geochemical tools to discriminate and fertile systems. In Figure 5c, a comparison between Yb/Dy versus Yb, where garnet fractionation is addressed with by low Yb and Yb/Dy ratio, shows that the Tres Cerrillos intra-mineral porphyritic intrusions possibly underwent a magmatic evolution similar to that of giant copper porphyry systems such as Chuquicamata, Escondida and El Teniente.

4 Conclusions

Syn-mineralization porphyritic intrusion of the Tres Cerrillos Cu-Mo prospect show evidence for a deeper crustal evolution compared with their precursor intrusions. In fact, both whole rock geochemistry and zircon trace elements suggest that these magmas could have experienced early garnet fractionation in addition to amphibole at lower crustal levels, a typical feature of fertile magmatic suites associated with PCD. Zircon geochemistry of Tres Cerrillos rocks shares similar geochemical characteristics as those of supergiant porphyry copper systems, making this prospect potentially important in terms of Cu endowment.

Acknowledgements

We are grateful with CODELCO for funding this project. Fieldwork benefited from the assistance of Hugo Narvaez and Yorki Patiño, exploration geologist of EMSAEC.

References

- Chiaradia M, Caricchi L (2017) Stochastic modelling of deep magmatic controls on porphyry copper deposit endowment. *Sci Rep* 7, 44523. <https://doi.org/10.1038/srep44523>
- Chiaradia M, Caricchi L (2022) Supergiant porphyry copper deposits are failed large eruptions. *Commun Earth Environ* 3, 107. <https://doi.org/10.1038/s43247-022-00440-7>
- Large RR, Gemmell JB, Paulick H, Huston DL (2001) The alteration box plot: A simple approach to understanding the relationship between alteration mineralogy and lithogeochemistry associated with volcanic-hosted massive sulfide deposits. *Economic geology*, 96(5), 957-971. <https://doi.org/10.2113/gsecongeo.96.5.957>
- Lu YJ, Loucks RR, Fiorentini M, McCuaig TC, Evans NJ, Yang ZM, et al (2016) Zircon Compositions as a pathfinder for Porphyry Cu±Mo±Au Deposits. *Soc. Econ. Geologists. Special Publ. Series* 19, 329-347. <https://doi.org/10.5382/SP.19.13>
- Richards JP (2011) High Sr/Y arc magmas and porphyry Cu±Mo±Au deposits: Just add water. *Economic Geology*, 106(7), 1075-1081. <https://doi.org/10.2113/econgeo.106.7.1075>
- Schütte P, Chiaradia M, Barra F, Villagómez D, & Beate B (2012) Metallogenic features of Miocene porphyry Cu and porphyry-related mineral deposits in Ecuador revealed by Re-Os, 40 Ar/39 Ar, and U-Pb geochronology. *Mineralium Deposita*, 47, 383-410. <https://doi.org/10.1007/s00126-011-0378-z>
- Vallejo C, Spikings RA, Horton BK, Luzieux L, Romero C, Winkler W, Thomsen TB (2019) Late Cretaceous to Miocene stratigraphy and provenance of the coastal forearc and Western Cordillera of Ecuador: Evidence for accretion of a single oceanic plateau fragment. In *Andean tectonics* (pp. 209-236). Elsevier. <https://doi.org/10.1016/B978-0-12-816009-1.00010-1>
- Winchester JA, Floyd PA (1977) Geochemical discrimination of different magma series and their differentiation products using immobile elements. *Chemical geology*, 20, 325-343. [https://doi.org/10.1016/0009-2541\(77\)90057-2](https://doi.org/10.1016/0009-2541(77)90057-2)

State-of-the-art garnet petrochronology in the Yerington district: What does it tell us about Cu skarn formation?

Maria Paula Castellanos Melendez¹; Daniela Rubatto²; Francesca Piccoli²; Julien Allaz¹; Marcel Guillong¹ and Olivier Bachmann¹

¹ETH Zürich, Institute of Geochemistry and Petrology, Zürich, Switzerland

²University of Bern, Institute of Geological Sciences, Bern, Switzerland

Abstract. The interaction between magmatic-hydrothermal fluids sourced from the Jurassic Yerington batholith and the carbonate-rich middle Triassic – early Jurassic basement produced several generations of metasomatic garnet-pyroxene skarn that locally contain Cu mineralization (Einaudi, 1977). The Cu-skarn is assumed to be genetically linked to the porphyry Cu deposits found in the Yerington district (Einaudi, 1977; Harris and Einaudi, 1982). However, state-of-the-art petrographic, geochemical, and geochronological evidence for a genetic link between porphyry-style and skarn mineralization is still lacking. Four different garnet textures have been identified throughout the Yerington skarn: (a) cm-sized coarse-grained oscillatory zoned garnet, (b) fine-grained matrix garnet associated with pyroxene, carbonate, and oxides, (c) breccia-filling garnet, and (d) vein garnet in non-brecciated settings. In this study we provide the first in-situ geochemical characterization of the different garnet textures that constitute the garnet-pyroxene Cu-skarn. Geochemical differences between garnet generations possibly document the origin and evolution of the metasomatizing fluids. Moreover, preliminary in situ LA-ICP-MS U-Pb dating of garnet further helps constraining a 4D skarn evolution and indicate at least two main events of garnet formation.

1 The Yerington Cu-Skarn

Skarn horizons or lenses are common within porphyry systems and economically important as they can host high-grade Cu (proximal) or base metal (distal) mineralization (e.g., Ok Tedi, Van Dongen et al. 2013; Bingham Canyon, Schlögl, 2018). At Yerington, at least two skarn generations formed by sequential magmatic activity: a skarnoid stage followed by a metasomatic stage (Harris and Einaudi, 1982). Several garnet generations have been petrographically and geochemically distinguished (Einaudi, 1977; Harris and Einaudi, 1982). Grossular-andradite garnet is characteristic of the skarnoid stage while the later metasomatic event produced more andraditic garnet. A later stage veined the skarn types with grossular-andradite garnet (Harris and Einaudi, 1982). Copper mineralization has been linked to coarse-grained andraditic garnet and is assumed to be genetically linked to the ore-forming fluids of the porphyry environment (Einaudi, 1977), although no clear evidence for this association exists. In this study we provide preliminary results of in situ petrochronology analyses on different garnet types throughout the Yerington skarn and aim at providing important insights into its formation and the so far assumed genetic link between the porphyry and the skarn environment in the district.

2 Materials and methods

Samples were collected in a field campaign in the vicinities of the Casting Copper Skarn and the Douglas Hill Mine in the Yerington district, Nevada, USA. Polished thin sections were studied by conventional transmitted light petrography and back-scattered electron (BSE) imaging with a JEOL JSM-6390LA scanning electron microscope.

Representative ca. 1x1 mm areas of the different garnet textural variations were selected for quantitative elemental mapping using a JEOL JXA 8230 electron microprobe at ETH Zurich. Major oxide maps were quantified and exported as wt% SiO₂, Al₂O₃, FeO_{total}, MgO, CaO, MnO and TiO₂ (Donovan et al., 2021). Trace element mapping was performed over areas for which major element maps were obtained using a Resonetics RESOLUTIONSE 193nm excimer laser system coupled to an Agilent 7900 quadrupole ICP-MS instrument at the University of Bern. Additionally, U-Pb in-situ garnet dating was done using an ASI RESOLUTION excimer ArF (193 nm) laser ablation system coupled to a Thermo Fisher Element XR sector field ICP-MS at ETH Zurich.

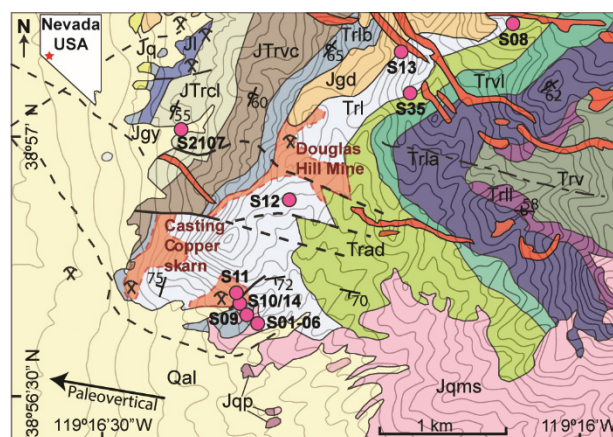


Figure 1. Geological map of the garnet-pyroxene Cu-skarn exposures in the Yerington district, Nevada, USA. Sample locations in fuchsia circles. Geological units: Jqms-quartz monzonite; Jqp-granite porphyry; Jq-quartzite; Jgy-gypsum; JLi-Ludwig limestone; JTrcl-argillite limestone felsite; JTrvc-rhyolitic siltstone; Trlb-argillaceous limestone; Trl-massive limestone; Trad-andesitic-dacitic tuff and sandstone; Trvl-rhyolitic sandstone and limestone; Trla-black calcareous argillite; Trll-dolomitic limestone; Trv-volcanic rocks; Qal-Quaternary alluvium. Modified after Barkoff et al. (2017).

3 Results and Discussion

3.1 Garnet textures

Throughout the skarn exposures garnet occurs in various textural positions as (a) cm-size coarse-grained oscillatory zoned crystals in garnetite, (b) fine-grained zoned or unzoned crystals in fine-grained domains associated with pyroxene, calcite, oxides and \pm apatite, (c) cement of brecciated coarse-grained crystals in hornfels, (d) overgrowths with or without oscillatory zoning that crosscut the coarse-grained zoned crystals, and (e) vein fillings (Fig. 2). BSE images reveal compositional differences between the different textural

occurrences of garnet. Generally, crosscutting overgrowths, breccia cement and vein fillings show distinctive darker BSE images matching Fe-poor domains. Similarly darker rims and intermediate bands are found in the brighter crystals and correlate with anisotropic domains under cross-polarized light microscopy. Such anisotropy, typical of grossular-andradite garnet (Cesare et al. 2019) could be the result of the incorporation of OH- in the garnet structure (Antao et al. 2017), lattice strains after garnet growth (Allen and Buseck, 1988) or initial growth with tetragonal symmetry (Cesare et al. 2019).

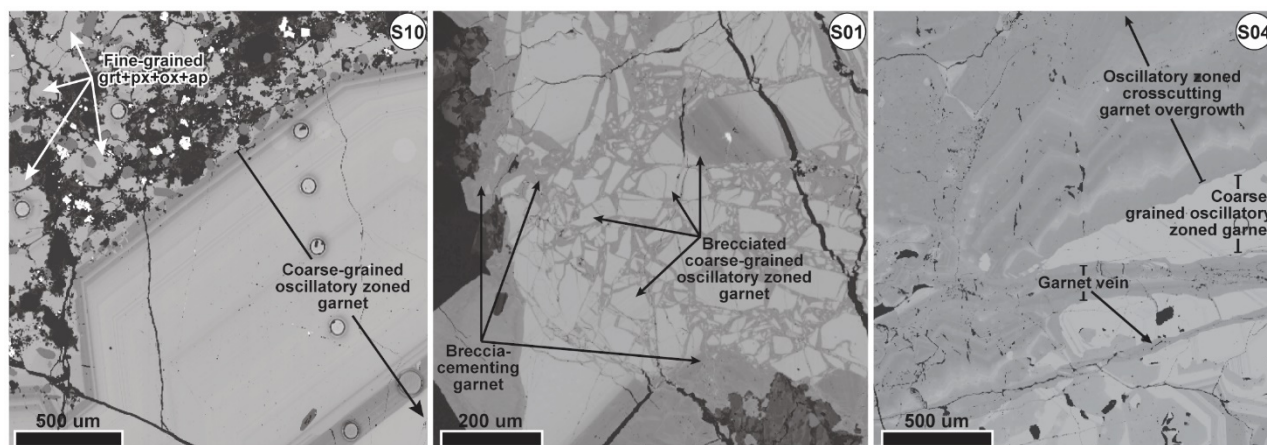


Figure 2. BSE images of the different textures of garnet in the Yerington skarn. Sample number is indicated at the top-right corner. Garnet occurs as coarse-grained oscillatory zoned crystals and fine-grained crystals in association with pyroxene, oxides, apatite, and carbonates (S10). Oscillatory zoned overgrowths and garnet veins also occur crosscutting the coarse-grained garnet (S04). Additionally, coarse garnet blobs occur with brecciated margins within hornfels where garnet cements the brecciated particles (S01).

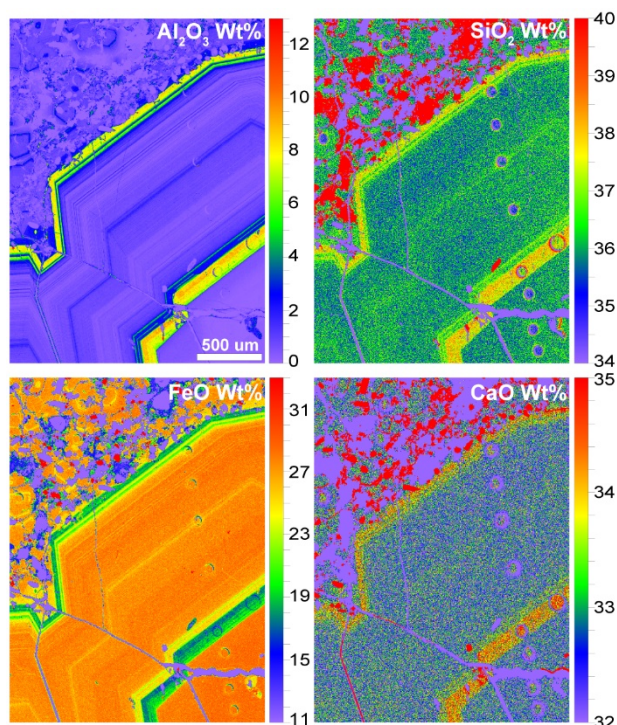


Figure 3. Quantitative element mapping of Al_2O_3 , SiO_2 , $\text{FeO}_{(\text{total})}$ and CaO wt% in garnet from sample S10. The maps highlight the coarse-grained oscillatory zoned garnet in association with a fine-

grained garnet + pyroxene + apatite + calcite domain.

3.2 Garnet geochemistry

Chemical variations suggested by BSE images are documented by quantitative electron microprobe mapping. Two main garnet compositions represent all textural variations throughout the district. Coarse-grained garnet is generally Fe-rich (And_{93-96}), with no MgO or MnO components. Narrow anisotropic intermediate bands and rims in this garnet type are Fe-poor and Al-rich (Gross_{24-36} , And_{58-69}) with SiO_2 and CaO enrichment (Fig. 3), and low MnO contents (up to 0.2 wt%). MgO is absent in all garnet types, while TiO_2 occurs sporadically in low contents (up to 1 wt%) correlated with Al-rich domains. Fine-grained garnet is generally Fe-rich (And_{91}) with or without Al-rich rims. Conversely, garnet overgrowths, breccia cement and vein fillings are generally Al-rich Fe-poor (Gross_{36-41} , And_{52-61}), except for S12 in the vicinities of the Douglas Hill mine, where coarse-grained garnet is generally Al-rich (Gross_{56} , And_{36}) with Fe-rich overgrowths and crosscutting veins (And_{77} , Gross_{19}).

Preliminary trace element mapping in S10 indicates that Fe-rich domains host variable but generally high U contents (up to 20 ppm), while U is depleted in the Al-rich zones. Other traces such as

Sc, V, Cr, Y and the HREE (from Gd to Lu) are also positively correlated with Al contents in the garnet rim while La, Ce, Pr and Nd are enriched in the Fe-rich core. These variable trace element compositions could be the result of significant variations in fluid chemistry during garnet formation. However, the scale and rate at which such variations occur is yet to be defined with further geochemical analyses on other samples throughout the district.

3.3 Garnet in-situ geochronology

Skarn garnet in situ U-Pb dating has been successfully achieved due to their variable U contents (e.g., Seman et al. 2017; Gevedon et al. 2018). High U contents in the studied garnet allowed for preliminary U-Pb in situ dating by LA-ICP-MS and we provide here the first garnet ages for the Yerington skarn. In general, Fe-rich garnet domains yield concordant Middle Jurassic U-Pb dates with negligible initial Pb contents. On the contrary, U-Pb dates in Al-rich rims are discordant with variable amounts of common Pb allowing for the construction of a well-defined Discordia line with Upper Jurassic lower intercept.

The definition of at least two resolvable ages, with no overlapping analytical uncertainties, of garnet formation in the Yerington skarn questions the genetic link between at least one of these events and the Middle Jurassic porphyry Cu formation (ca. 167.4 Ma; Carter et al. 2022). Additionally, the correlation between age and different garnet geochemical signatures might provide important insights into the characteristics of fertile fluids for Cu deposition. Undergoing further in-situ dating of the geochemically and texturally different garnet types will allow for a robust definition of a 4D garnet evolution in the Yerington skarn and the role of fluid chemistry in ore formation.

Acknowledgements

The authors would like to express their gratitude towards John Dilles and Richard Tosdal for their guidance in the field and insightful views on the formation of the Yerington Cu skarn.

References

- Allen, F. M., & Buseck, P. R. (1988). XRD, FTIR, and TEM studies of optically anisotropic grossular garnets. *American Mineralogist*, 73(5-6), 568-584.
- Antao, S. M., & Cruickshank, L. A. (2018). Crystal structure refinements of tetragonal (OH, F)-rich spessartine and henritermierite garnets. *Acta Crystallographica Section B: Structural Science, Crystal Engineering and Materials*, 74(1), 104-114.
- Barkoff, D. W., Ashley, K. T., & Steele-MacInnis, M. (2017). Pressures of skarn mineralization at Casting Copper, Nevada, USA, based on apatite inclusions in garnet. *Geology*, 45(10), 947-950.
- Carter, L. C., Tapster, S. R., Williamson, B. J., Buret, Y., Selby, D., Rollinson, G. K., ... & Parvaz, D. B. (2022). A rapid change in magma plumbing taps porphyry copper deposit-forming magmas. *Scientific Reports*, 12(1), 17272.
- Cesare, B., Nestola, F., Johnson, T., Mugnaioli, E., Della Ventura, G., Peruzzo, L., ... & Erickson, T. (2019). Garnet, the archetypal cubic mineral, grows tetragonal. *Scientific reports*, 9(1), 1-13.
- Donovan, J. J., Allaz, J. M., von der Handt, A., Seward, G. G. E., Neill, O., Goemann, K., Chouinard, J. & Carpenter, P. K. (2021). Quantitative WDS compositional mapping using the electron microprobe. *American Mineralogist* 106, 1717–1735.
- Einaudi, M. T. (1977). Petrogenesis of the copper-bearing skarn at the Mason Valley Mine, Yerington District, Nevada. *Economic Geology*, 72(5), 769-795.
- Gevedon, M., Seman, S., Barnes, J. D., Lackey, J. S., & Stockli, D. F. (2018). Unraveling histories of hydrothermal systems via U–Pb laser ablation dating of skarn garnet. *Earth and Planetary Science Letters*, 498, 237-246.
- Harris, N. B., & Einaudi, M. T. (1982). Skarn deposits in the Yerington District, Nevada; metasomatic skarn evolution near Ludwig. *Economic Geology*, 77(4), 877-898.
- Schlöglöva, K. (2018). Fluid Inclusion Analysis of other Host Minerals besides Quartz: Application to Granite-Related Quartz-Topaz Veins and Garnet Skarns in Porphyry Copper-Gold Ore Systems (Doctoral dissertation, ETH Zurich).
- Seman, S., Stockli, D. F., & McLean, N. M. (2017). U-Pb geochronology of grossular-andradite garnet. *Chemical Geology*, 460, 106-116.
- Van Dongen, M., Weinberg, R. F., & Tomkins, A. G. (2013). Grade distribution of the giant Ok Tedi Cu-Au deposit, Papua New Guinea. *Economic Geology*, 108(7), 1773-1781.

Hydrothermal alteration chemistry and mineralogy of the Maricunga-style Vendaval Central Cu-Au porphyry

Federico Cernuschi ^{1,2}, Santiago Gigola ^{3,2}, William Brownscombe ⁴, Tim Ireland ², James Banyard ², David Arribasplata ², Jaime Schorr ², Paula Gonnet ², Paula Sosa ², Mauricio Duran ²

¹Eclectic Rock, Punta del Este, Uruguay

²First Quantum Minerals, Salta, Argentina

³Independent Consultant, Mendoza, Argentina

⁴Natural History Museum, London, UK

Abstract. The hydrothermal alteration at the Vendaval Central Cu-Au Middle Miocene porphyry project (Salta, Argentina) was studied using drill-hole core logging, whole-rock compositions, and mineral phase maps acquired using a Tescan Integrated Mineral Analyser (TIMA) system. The central part of the prospect experienced four alteration stages: 1) calcic alteration with pyroxene and garnet, 2) K-silicate alteration with K-feldspar, biotite, magnetite, A quartz veins, and banded Maricunga quartz veins, 3) albitization and 4) intermediate argillic alteration overprint with smectites, hydrobiotite, calcite, and less chlorite. Shallow peripheral illitic alteration with pyrite and shallower remnants of advanced argillic alteration with deep and narrow breccias are also observed. The superimposition of these alteration stages results in whole rock compositions with high Na/Al and low K/Al. Nonetheless, Cu-Au mineralization is associated with K-silicate alteration, A veins, and banded Maricunga veins. Hydrothermal alteration at Maricunga porphyries like Vendaval is somewhat reminiscent of silica-saturated alkaline porphyry deposits elsewhere: early calcic alteration and late albitization with respect to K-silicate alteration and absent sericitic alteration. Similarly, the hypogene intermediate argillic overprint may be a common feature of Au-rich porphyries. The calcic alteration and albitization are not associated with a sedimentary wall-rock composition and are likely magmatic-hydrothermal in origin.

1 Introduction

Vendaval Central is a porphyry copper-gold project of Middle Miocene age located in Argentina next to the border with Chile at least 200 km N-NE of the northernmost gold-rich porphyry in the Maricunga Belt (Vila and Sillitoe 1991). The gold-bearing copper mineralization, type of quartz veinlets, age, and interpreted shallow emplacement depth suggest that Vendaval Central is part of the northern extension of this belt.



Figure 1. Schematic location map of Vendaval Central showing the Maricunga belt and its possible northern extension (modified from Muntean and Einaudi 2000).

The copper-gold mineralization (~1:1) is hosted by a series of at least five different quartz dioritic to dacitic porphyries (early to late-mineral) and the immediately adjacent andesitic volcanic flows and volcanic breccia. K-Ar dating indicates that the age of the volcanic host rocks is early to middle Miocene (Ramirez *et al.* 1991). The successive porphyry phases control quartz vein density and hypogene grades, as is normally found in A-vein-type porphyries (Proffett 2009).

The central parts of the system are characterized by a high density of sheeted quartz veinlets (>20-30 veins/meter) hosted in early mineral porphyry and immediately adjacent andesitic wall rock with strong K-silicate alteration (~850 x 350 m). These quartz veins display a banded Maricunga-style texture over the highest parts of the deposit and transition at depth into typical, granular A-type quartz-chalcopyrite-magnetite veinlets. Quartz vein truncations, quartz vein xenoliths, and sharp changes in hypogene grades are common at contacts between different porphyry phases.

2 Methodology

Two-meter-long split core samples (n=12.300) were obtained throughout the drill holes and assayed by inductively coupled plasma-atomic emission spectroscopy (ICP-AES) and inductively coupled plasma-mass spectroscopy (ICP-MS) following four-acid digestion (MEMS61 at ALS). Short wave infrared (SWIR) spot data was obtained on coarse rejects for each compositional sample (ALS) and processed using The Spectral Geologist. Compositional and spectral data were integrated and studied using ioGASTM in reference to geologic observations and cross-sections. Lithogeochemical units were inferred using immobile trace elements (e.g. Th, Zr, Nb, Sc). Hydrothermal alteration types were inferred by studying major element gains and losses (Ca, Na, K, Mg) and supported by SWIR mineralogy (see Halley 2020).

Twenty hand samples of key hydrothermal alteration types were obtained to produce polished thin sections and 25 mm polished blocks. Mineral phase maps were obtained on these samples using a Tescan Integrated Mineral Analyser (TIMA) system at the Natural History Museum, London. The analytical conditions were 25 kV accelerating voltage, 14 nA current, and a working distance of 15 mm. Standard instrument calibration was performed

prior to analysis. A pixel size of 5 microns was used for both backscatter electron imaging (BSE) and energy dispersive spectroscopy (EDS) modal analysis, and phase classifications were based on spectra chosen and identified from these analyses.

3 Hydrothermal alteration

Elemental gains and losses were studied independently for each magmatic lithogeochemical unit. Pre-alteration major element compositions were estimated from immobile trace elements concentrations. Some magmatic units are mildly alkaline, have slightly elevated Nb (>10 ppm) compared to sub-alkaline units, and may have more magmatic pyroxene than amphibole. The original magmatic compositions were likely slightly elevated in alkalis. The expected least altered compositions may be shifted to higher K/Al and/or Na/Al than typical sub-alkaline Andean magmas (Figure 2).

Most samples experienced multiple intense and overprinting alteration events that caused opposing effects on the gains and losses of major elements (Figures 2 & 3). Therefore, apparent least altered compositions may be, in reality, very altered samples. For this interpretation, we assumed that there are no completely preserved magmatic compositions and color-coded the samples according to the dominant alteration type inferred. Core logging observations, SWIR mineralogy, and TIMA mineral phase maps informed this interpretation.

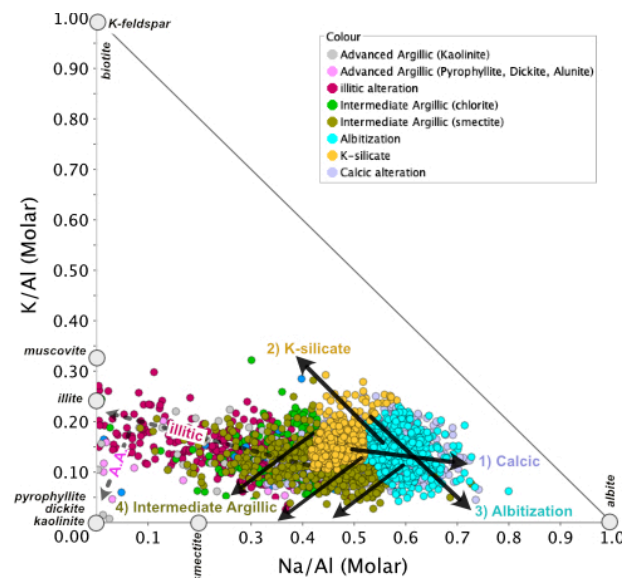


Figure 2. K/Al vs Na/Al gains and losses diagram showing a subset of samples of andesitic composition (wall-rock) and mineral compositions of relevant alteration minerals. Timing of illitic and advanced argillic alteration (A.A.) is not resolved.

Large areas within the central part of the system experienced four overlapping alteration stages (Figures 2 & 3) that in temporal order are: 1) calcic alteration, 2) K-silicate alteration, 3) albitization, and 4) intermediate argillic alteration.

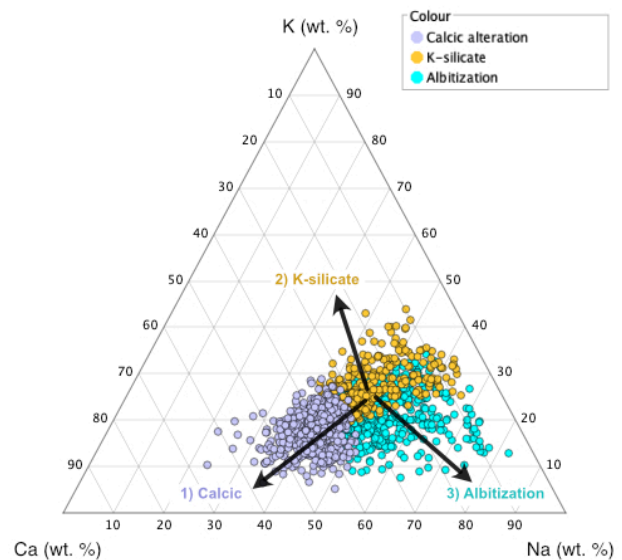


Figure 3. K-Ca-Na gains and losses diagram showing a subset of the samples from Figure 2 that are inferred as dominantly altered to K-silicate, calcic, or albitization.

3.1 Calcic alteration

The volcanic wall-rock and associated sub-volcanic units experienced an early stage of calcic alteration at the intermediate and deep zones of the system. This alteration gained Ca at the expense of K and Na (Figures 2 & 3), predates the bulk of Fe-Cu-sulfides and the intrusion of porphyry dikes. However, the calcic alteration is most intense near the dikes. It is observed as thin and irregular pyroxene veinlets of up to 2 mm thick and locally abundant garnet-pyroxene patches. The thin pyroxene veinlets are challenging to recognize in hand samples but are readily observed in TIMA images, where pyroxene is identified as augite (Figure 4 & 5). The patches are identified during logging, and the TIMA mineralogy indicates that pyroxene composition is hedenbergite, garnet is andradite, and both replace magmatic plagioclase (Anorthite 40, Figure 4).

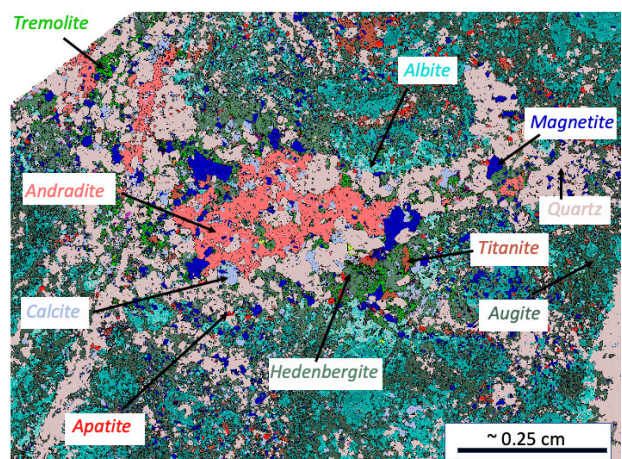


Figure 4. Garnet-pyroxene patches, pyroxene veinlets, and quartz veinlets with magnetite.

Pyroxene rims are commonly replaced by tremolite and other amphiboles (Figures 4 & 5). This hydration (uralitization) event may have started at the end of the Ca-alteration and continued during later stages of hydrothermal alteration.

3.2 K-silicate alteration

Within the Calcic alteration zone, a central area experienced K-silicate alteration where K was gained at the expense of Ca and Na. Therefore, in some cases, K-gains are overprinted to older Ca-gains (Figures 2 & 3). K-silicate alteration comprises hydrothermal K-feldspar, shreddy biotite, and magnetite that replaces magmatic plagioclase, pyroxene, and amphibole (Figure 5).

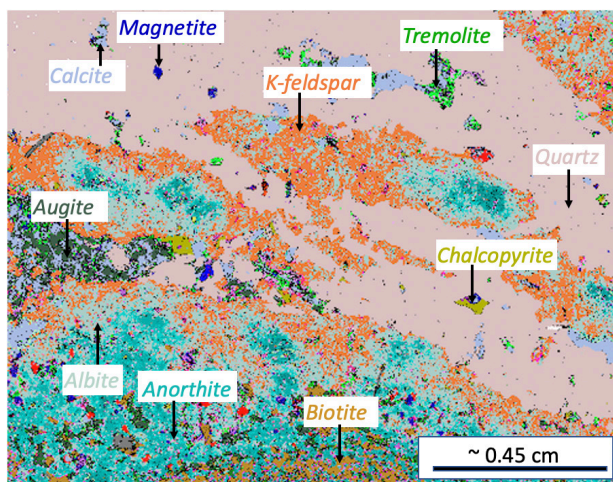


Figure 5. Quartz A veins with chalcopyrite and K-feldspar halos truncate augite veinlets. Albite rims magmatic anorthite and replaces hydrothermal K-feldspar. Thin biotite veinlets and shreddy biotite after pyroxene are also present.

Cross-cutting observations indicate that hydrothermal K-feldspar and biotite post-date pyroxene and garnet. Albite is observed in some cases in contact with K-feldspar, but not always. Some hydrothermal albite may have formed during K-silicate alteration by leftover Na after K-feldspar replaces magmatic anorthite. However, cross-cutting relationships in TIMA images suggest that most of the observed albite post-dates K-silicate alteration (see section 3.3).

K-feldspar and biotite form narrow but continuous selvages to A veins, banded Maricunga veins, and thin alkali seams with little quartz (Figure 5). Both quartz vein types crosscut the older pyroxene veins. K-feldspar is, in some cases, observed as younger outer selvages to the older pyroxene veins (Figure 5). To a lesser degree, K-feldspar and biotite are also observed as pervasive replacements of phenocrysts and groundmass.

A veins and banded Maricunga veins and associated K-feldspar and biotite outer selvages and patches contain chalcopyrite, pyrite, traces of bornite, and magnetite. Cu-Au bearing intercepts are rich in these vein types (Figure 5).

3.3 Albitization

The system's central part and periphery has hydrothermal albite that resulted from the gain of Na at the expense of Ca and K (Figure 2 & 3). This alteration is difficult to observe in a hand sample due to the minimal change in texture and color where magmatic anorthite is replaced by albite. Nonetheless, albite is readily observed in TIMA imaging (Figure 4 & 5) and inferred through gains and losses (Figure 2 & 3).

In TIMA images, albite can be observed in contact with older pyroxene veins, garnet patches, and K-feldspar/biotite (Figure 4 & 5). It is also observed as a pervasive replacement where magmatic anorthite and older hydrothermal K-feldspar are only locally preserved. At the system's periphery, albite is observed as the only hydrothermal mineral in samples that do not have evidence of previous calcic and K-silicate alteration. Therefore, albitization is considered younger than Calcic and K-silicate alteration and has been superimposed on both alteration types in some of the central areas of the system (Figures 2 & 3). Here, we choose the name albitization to avoid confusion with other types of Na- and Na-Ca-gains, where albite is also formed (see discussion).

Albitization does not remobilize older Fe-Cu sulfides, as its presence does not affect the Cu-Au grade. In heavily overprinted samples, albite can be observed containing Fe-Cu-sulphides and pyrite. However, traces of preserved hydrothermal K-feldspar, biotite, and A-veins indicate that albite overprints older K-silicate alteration. In these cases, the whole rock composition of a sample will plot at high Na/Al and low K/Al ratio despite having experienced an older stage of K-silicate alteration (Figure 2 & 3).

3.4 Intermediate argillic alteration

The central part of the system has experienced hypogene intermediate argillic alteration except on the very deep parts. This alteration particularly overprints K-silicate alteration, in some cases pervasively, and results in the loss of K and Na. The intermediate argillic alteration gives the rock a pale, light brown to orange color in hand sample. Different types of smectites and calcite are observed replacing magmatic anorthite, pyroxene, amphibole and hydrothermal pyroxene, K-feldspar, albite, magnetite, and biotite. Chlorite is also present; however, smectites are much more abundant (Figure 6). Hydrothermal and magmatic biotite are partially replaced by vermiculite, resulting in hydrobiotite (interlayered vermiculite-biotite, Cornejo 2021). The intense replacement of "shreddy" biotite by hydrobiotite, smectite and calcite results in samples with low K/Al and Na/Al (Figures 2 & 6). The intermediate argillic alteration has no associated pyrite and does not remobilize older Cu-Fe-sulphides nor introduce Au.

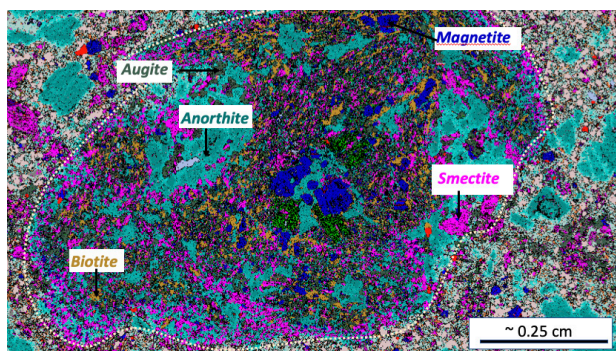


Figure 6. A pyroxene-anorthite oikocryst was replaced by biotite-magnetite (K-silicate alteration). Biotite and anorthite were then replaced by smectites (I.A.A.).

3.5 Illitic alteration and advanced argillic alteration

Advanced argillic (kaolinite, alunite, pyrophyllite, and dickite; Figure 2) in narrow polymictic phreatic breccias penetrate deeply (~500 m) on the south side of the deposit but are volumetrically restricted. Erosional remnants of the advanced argillic altered lithocap are preserved around Vendaval Central's higher ridges.

Sericitic alteration (muscovite) and D-type veins are absent. However, the barren shallow periphery surrounding Vendaval is altered to illite and has hair-like pyrite veinlets (lower K/Al than muscovite, Figure 2). We name this alteration "illitic" to differentiate it from intermediate argillic and sericitic alteration.

4 Discussion

At Vendaval Central, the K-silicate alteration is associated with Cu-Au bearing Fe-sulfide in quartz A veins, as in A-vein-type porphyries elsewhere (Proffett 2009). A-veins transition to banded Maricunga quartz veins with shallowing depth, as in other Maricunga deposits. This is likely a feature of the very shallow emplacement and rapid cooling (Muntean and Einaudi, 2000).

Other hydrothermal features at Vendaval Central may be comparable to those observed in silica-saturated alkaline deposits elsewhere. This may be related to the mildly alkaline nature of some of Vendaval's magmatic units. The early calcic alteration occurs at similar timing in other Maricunga deposits, and it is not related to Ca-rich wall-rock as in skarns associated with porphyry deposits elsewhere (Muntean and Einaudi 2000). Calcic alteration in Maricunga deposits appears to be magmatic-hydrothermal in origin, as proposed for some alkaline porphyries in BC, Canada (Lang *et al.* 1995). Similarly, albitization, as previously proposed by Muntean and Einaudi (2000), is not comparable to heating basin fluid-related sodic-calcic (e.g. Yerington, Nevada, Dilles and Einaudi 1992). Similar albitization that post-dates K-silicate alteration has also been observed in some alkaline porphyry

deposits in the Lachlan fold belt in SE Australia (Wilson *et al.* 2003), and also appears to be magmatic-hydrothermal in nature.

In both Maricunga and alkaline porphyries, typical sericitic alteration, as observed in calc-alkaline porphyries, is virtually absent. At Vendaval, the shallow peripheral illitic alteration with pyrite veins may be a temporal and spatial equivalent.

The widespread hypogene intermediate argillic alteration overprint of K-silicate alteration is a characteristic of Au-rich porphyries in the Maricunga belt. This overprint has also been described in other Andean Au-rich porphyries (Esperanza, Perelló *et al.* 2004) and is likely comparable to sericite-chlorite-clay (SCC) alteration in Au-rich porphyries in the SW Pacific (Sillitoe and Gappe, 1984), where chlorite-clay may overlap in space with older muscovite.

Acknowledgments

We thank First Quantum Minerals, Markku Lappalainen, and Steve Andersson for supporting this research and encouraging this publication.

References

- Cornejo, P (2021) Petrographic report of Vendaval samples. Internal to FQM.
- Dilles, J H and Einaudi, M T (1992) Wall-rock alteration and hydrothermal flow paths about the Ann-Mason porphyry copper deposit, Nevada: A 6-km vertical reconstruction: *Economic Geology*, v. 87, p. 1963–2001.
- Halley, S (2020) Mapping Magmatic and Hydrothermal Processes from Routine Exploration Geochemical Analyses. *Economic Geology*, 115 (3): 489–503. doi: <https://doi.org/10.5382/econgeo.4722>
- Lang, J R, Stanley, C R, Thompson, J F H and Dunne, K P E (1995) Na-K-Ca magmatic-hydrothermal alteration in alkalic porphyry Cu-Au deposits, British Columbia: Mineralogical Association of Canada Short Course, v. 23, p. 339–366.
- Muntean, J L and Einaudi, M T (2000) Porphyry Gold Deposits of the Refugio District, Maricunga Belt, Northern Chile. *Economic Geology*, 95(7), 1445.
- Perelló, J, Brockway, H, and Martini, R (2004) Discovery and geology of the Esperanza porphyry copper-gold deposit, Antofagasta Region, northern Chile: *Society of Economic Geologists Special Publication* 11, p. 167–186.
- Proffett, J M (2009) High Cu grades in porphyry Cu deposits and their relationship to emplacement depth of magmatic sources: *Geology*, v. 37, p. 675–678, doi:10.1130/G30072A.1
- Ramirez, C A, Gardeweg, M, Davidson, J and Pino, H (1991) Mapa Geológico del área de los volcanes Socompa y Pular: Región Antofagasta. Servicio Nacional de Geología y Minería, Chile.
- Sillitoe, R H, and Gappe, I M (1984) Philippine porphyry copper deposits Geologic setting and characteristics: United Nations Development Program, Coordinating Committee for Geosciences Programmes in East and Southeast Asia, Technical Publication 14, 89 p.
- Vila, T, Sillitoe, R H (1991) Gold-rich porphyry systems in the Maricunga Belt, northern Chile. *Economic Geology*, 86 (6): 1238–1260. doi: <https://doi.org/10.2113/gsecongeo.86.6.1238>
- Wilson, A J, Cooke, D R and Harper, B L (2003) The Ridgeway Gold-Copper Deposit: A High-Grade Alkalic Porphyry Deposit in the Lachlan Fold Belt, New South Wales, Australia. *Economic Geology* 2003; 98 (8): 1637–1666. doi: <https://doi.org/10.2113/gsecongeo.98.8.1637>

Magmatic evolution of the Archean Upper Beaver Intrusive Complex and its implications for Au-Cu mineralization

Michael Cloutier^{1,2}, Bertrand Rottier^{1,2}, Ross Sherlock³, Georges Beaudoin^{1,2}, Jonathan Sutton^{3,4}, Olivier Côté-Mantha⁴, Joshua Davies⁵, Morgann Perrot⁵

¹Département de Géologie et Génie Géologique, Université Laval, Québec, Canada

²Centre de recherche sur la géologie et l'ingénierie des ressources minérales (E4m), Québec, Canada

³Harquail School of Earth Sciences, Mineral Exploration Research Center, Laurentian University, Canada

⁴Agnico Eagle Mines Ltd, Exploration Canada

⁵Département des sciences de la Terre et de l'atmosphère/GEOTOP, Université du Québec à Montréal

Abstract. The Upper Beaver intrusion-related Au-Cu deposit is associated with the Archean Upper Beaver Intrusive Complex (UBIC). The UBIC is a polyphase intrusive complex with pre-, syn-, and post-mineralization phases. Whole-rock geochemistry is consistent with the UBIC having formed through magma mixing between a mafic to intermediate mantle-derived sanukitoid magma and an intermediate to felsic, basaltic-crust derived TTG magma. Phases of the UBIC that are associated with Au-Cu (+/- Mo) mineralization have a TTG magmatic affinity. LA-ICP-MS zircon geochronology shows that all phases of the UBIC were emplaced within error of ca. 2680 Ma which is consistent with previous Re-Os and U-Pb geochronology of molybdenite and zircon, respectively. Amphibole oxybarometry indicates that the UBIC was oxidized with fO_2 values between ΔNNO 0 and +1.6 which are similar to values from Phanerozoic arc magmas. Apatite geochemistry reveals a bimodal distribution in S content of the UBIC with the more felsic, mineralization-associated, TTG phases having lower S content than the more mafic sanukitoid phases. Additionally, negative Eu anomalies and low Sr content in apatite from the TTG phases are indicative of early plagioclase crystallization. This suggests that high magmatic H_2O content may not be a key factor for magmatic-hydrothermal Au-Cu mineralization in Archean systems.

1 Introduction

Magmatic-hydrothermal deposits are rare in the Archean compared to the Phanerozoic (Groves et al. 2005). This relative scarcity has been variably attributed to poor preservation, differences in geodynamic setting, and/or differences in physiochemical conditions (e.g., pressure, temperature, fO_2 , fS_2 , duration of the magmatic system) (Groves et al. 2005; Richards and Mumin 2013). In addition, the relative scarcity of these deposits in the Archean has resulted in a poor understanding on the processes controlling their fertility.

This study examines the magmatic evolution of the Archean Upper Beaver intrusive complex (UBIC) and its possible controls on mineralization in the related Au-Cu intrusion-related deposit.

2 The Upper Beaver Au-Cu Deposit

The Upper Beaver Au-Cu deposit (probable mineral reserves of ~1.4 Moz Au at 5.43 g/t and 20.0 kt Cu at 0.25%; indicated resources of ~0.4 Moz Au at 3.45 g/t and ~5.1 kt Cu at 0.14%; inferred resources of ~1.4 Moz Au at 5.07 g/t and ~17.3 kt Cu at 0.20%; Agnico Eagle Mines Ltd. 2023) comprises two temporally and mineralogically distinct Au-Cu(±Mo) intrusion-related mineralization events including 1) an early Ep+Adr skarnoid with replacement style Cp+Py+Mag+Au mineralization that is concordant to Blake River group mafic volcanics and volcanoclastics, and 2) later discordant Qz+Mag+Cc+Cp+Py+Hem+Au+Mol veins. Both mineralization events are spatially and temporally related to the UBIC which is subdivided into seven phases that are pre- syn- and post-mineralization (Figs. 1, 2). The earliest phase of the UBIC is a hypabyssal Amp-phyric diorite porphyry. The second phase of the UBIC is a Pl-Hbl glomerophyric diorite porphyry (GP). The GP is pre- to syn- the first Au-Cu mineralization event and is affected by the skarnoid alteration. The phases that post-date the first mineralization event are divided into two distinct groups (Fig. 2). The earlier of the two groups comprises three distinct dioritic to quartz-diorite phases that are defined by the presence of Amp±Pl phenocrysts. The latter of the two groups consists of Pl±Amp±Qz phyric monzodiorite to quartz-monzonite dykes (Fsp-porphyry) that crosscut all earlier phases. The Fsp-porphyry dykes have been divided based on their quartz content. However, it is not clear if they represent two distinct phases or a slight variation of mineralogy of the Pl+Amp±Qz porphyry. Finally, a post-mineralization Pl+Hbl phyric diorite dyke has been dated at 2678.7 ± 0.7 Ma (McNicol, unpublished) marking the end of the magmatic-hydrothermal system.

The first Au-Cu skarnoid mineralization event is spatially associated with and hosted within the early GP as well as being concordant to the host mafic Blake River volcanic and volcanoclastic rocks. The skarnoid and its host rocks are crosscut by the diorite to quartz diorite phases.

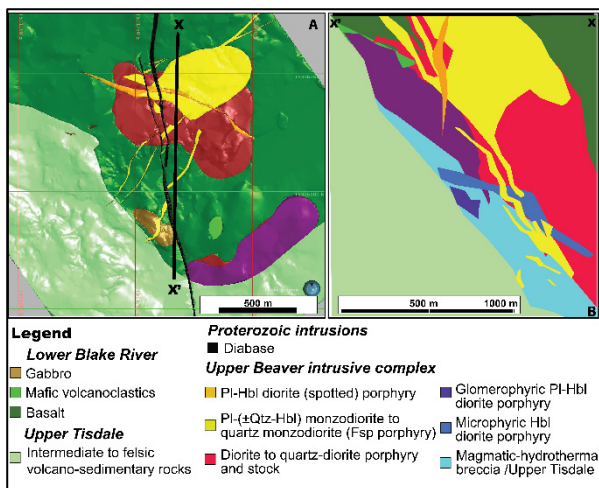


Figure 1. A) Simplified geological map of the Upper Beaver deposit. B) Cross section of the Upper Beaver deposit looking west (modified from Sutton and Côté-Mantha 2022)

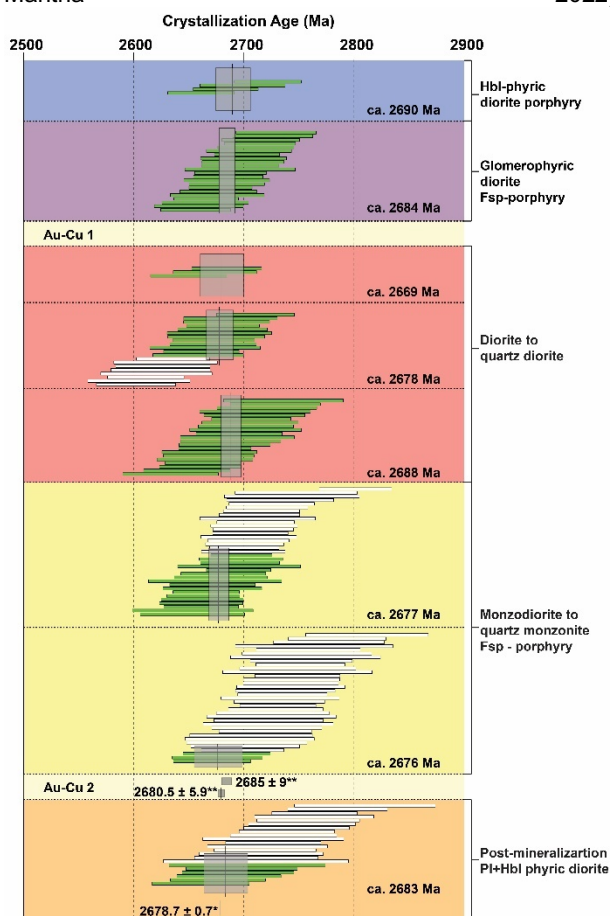


Figure 2. Relative timing and weighted mean zircon $^{207}\text{Pb}/^{206}\text{Pb}$ crystallization ages of the individual phases of the UBIC with the top being the earliest and bottom being the latest based on cross-cutting relationships. *Zircon U-Pb upper intercept crystallization age of 2678.7 ± 0.7 Ma (McNicoll, Unpublished). **Molybdenite Re-Os ages of 2685 ± 9 Ma and 2680.5 ± 5.9 Ma (Kontak et al. 2013; Mercier-Langevin et al. 2021, respectively).

The second mineralization event is responsible for most of the Au-Cu endowment of the Upper Beaver deposit and displays a spatio-temporal relationship with the Fsp-porphyry dykes. This event has been previously dated by Re-Os geochronology in molybdenite with ages of 2685 ± 9 Ma and 2680.5

± 5.9 Ma (Fig. 2; Kontak et al. 2013; Mercier-Langevin et al. 2021 respectively) which are consistent with the crystallization age for the late post-mineralization PI+Hbl phyrlic dyke.

3 U-Pb geochronology

New crystallization ages for each of the individual intrusive phases of the UBIC were determined using U-Pb methods in zircon by laser-ablation inductively coupled mass-spectrometry (LA-ICP-MS). Cathodoluminescence (CL) imaging of the zircons from the UBIC shows oscillatory and sector zoning with no evidence of inherited cores. Ages were calculated as a weighted mean of the $^{207}\text{Pb}/^{206}\text{Pb}$ ages for the youngest zircons in the samples. The number of zircons used for each age calculation was constrained using the maximum number of analyses for which the MSWD is consistent with a single population (Spencer et al. 2016). The second diorite to quartz diorite phase (Fig. 2) is an exception to this as the $^{207}\text{Pb}/^{206}\text{Pb}$ zircon ages for this sample form two populations with the younger population yielding a weighted mean $^{207}\text{Pb}/^{206}\text{Pb}$ age of ca. 2619 Ma. This age is significantly younger than the calculated ages for the Fsp-porphyry phases that crosscut this unit. Because this younger age is incompatible with observed field relationships, the older population was used in the age calculation.

All phases of the UBIC have crystallization ages within error of ca. 2680 Ma which is consistent with the previous U-Pb and Re-Os ages (Fig. 2; Kontak et al. 2013; Mercier-Langevin et al. 2021). A distinct difference is noted in the spread of $^{207}\text{Pb}/^{206}\text{Pb}$ ages in zircon from the UBIC, as the later Fsp-porphyry phases and post-mineralization PI+Hbl phyrlic diorite dyke have an abundance of inherited zircon, in contrast to the earlier phases that have minimal inheritance.

4 Geochemistry

Whole-rock geochemistry of the UBIC, using only the least altered samples based on optical petrography, micro-XRF maps, and geochemistry, shows that the intrusive complex is calc-alkaline to slightly alkaline and metaluminous. Compositionally the samples range from monzodiorite to quartz monzonite when plotted on a TAS diagram (Middlemost 1994). While the total alkali content ($\text{K}_2\text{O} + \text{Na}_2\text{O}$) of the UBIC is elevated across the range of SiO_2 , K_2O shows a negative correlation whereas Na_2O shows a positive correlation. General trace-elements signatures for the UBIC exhibit moderately to strongly fractionated REE patterns with minor Eu anomalies, elevated Sr/Y values, negative correlation between Dy/Yb and SiO_2 , and primitive mantle normalized patterns (enriched LILE and depleted Nb and Ta). These signatures are consistent with a hydrated source for the UBIC with fractionation being driven by amphibole and minimal plagioclase. The GP phase is an exception to these patterns having a less fractionated REE signature

(due to both relatively low La and high Yb concentrations) with an unfractionated HREE signature which suggests that amphibole and/or garnet were not fractionating phases for this unit (Fig. 3). On the A/CNK, Na₂O, FMSB discriminant diagram of Laurent et al. (2014), samples from the more mafic diorite to quartz-diorite phases plot within the sanukitoid-type field while the more felsic monzonite to quartz monzonite GP and Fsp-porphyry phases plot within the TTG-type field (Fig. 3).

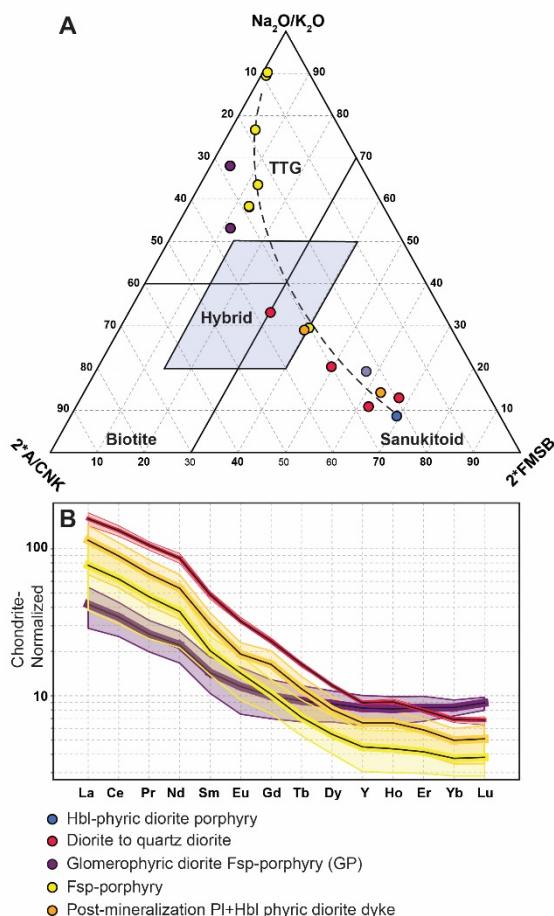


Figure 3. A) *A/CNK (molar Al/[Ca+Na+K]) vs Na₂O/K₂O vs 2*FMSB ([FeO + MgO]wt.% * [Sr + Ba]wt.%) ternary plot of Laurent et al. (2014) showing magmatic affinity of the UBIC. The dashed line is the calculated mixing line between the sanukitoid and TTG end-members. B) Chondrite normalized (Sun and McDonough, 1989) REE+Y spider diagram. Coloured outlines show the range of concentrations for the respective intrusive phases. Coloured lines with black centers are the average values for the intrusive phases.

5 Mineral Chemistry

Physiochemical conditions of the UBIC were constrained through the use of amphibole and apatite chemistry.

The Al-in-amphibole geothermometer (Putirka 2016) for the earlier diorite to quartz diorite phase indicates an emplacement temperature of 885°C - 935°C (±30°C). Amphibole from the later Fsp-porphyry indicates a lower emplacement temperature of 770°C - 840°C (±30°C). Amphibole oxybarometry (Ridolfi et al. 2010) for the dioritic to

quartz dioritic phase indicates fO_2 values between ΔNNO 0 and +1. The Fsp-porphyry are more oxidized with fO_2 values ΔNNO +0.5 and +1.6.

Apatite was analysed for major and trace elements for each of the phases of the UBIC. Sulfur content of apatite from the UBIC has a bimodal distribution and is comparable to the S content of apatite from Phanerozoic arc magmas (Meng et al. 2021a). Apatite from the main diorite to quartz diorite phases have the highest S content ranging from 0.15 – 0.35 wt.% while all other phases, including those associated with mineralization, typically have lower S content (0 – 0.175 wt.%). Manganese concentrations in apatite, which have been shown track melt evolution (Bromiley 2021), are positively correlated with Cl. This may suggest that the apatite crystallized prior to fluid exsolution and that S concentrations are reflective of the magma content. Apatite from the phases associated with mineralization (GP and Fsp-porphyry) have lower Sr concentrations and negative Eu anomalies compared to the other phases which is indicative of early plagioclase crystallization for these phases.

6 Discussion

6.1 Formation of the UBIC by magma mixing

The whole rock geochemical signatures are consistent with the UBIC having been derived from a hydrated source (Laurent et al. 2014). The sanukitoid-type signature of the more mafic dioritic and dioritic phases are suggestive of a predominately metasomatized mantle source. The TTG signature of the more felsic GP and Fsp-porphyry phases are suggestive of derivation from a hydrated low-K basaltic crust (Laurent et al. 2014). The negative K₂O vs SiO₂ correlation supports the UBIC having formed through mixing between melts derived from these two sources instead of fractional crystallization. The LA-ICP-MS U-Pb data from zircon are also consistent with two distinct sources as the phases that have a more “TTG-like” geochemical signature also have an abundance of inherited zircons. This abundance of inherited zircons is consistent with derivation from a crustal source.

6.2 Mineralization associated with low S, low H₂O magmas

Mineralization at the Upper Beaver deposit is spatially and temporally related to both GP and Fsp-porphyry phases. The relatively low S content of these phases as recorded by apatite indicates that high S content may not be a requirement for mineralization. Apatite from both the GP and Fsp-porphyry have negative Eu anomalies and low Sr concentrations consistent with plagioclase crystallization pre- to syn- apatite crystallization. Apatite is typically a near-liquidus phase in magmatic systems (Webster and Piccoli 2015), in agreement with our petrographic observations, which suggests that plagioclase was also a near-liquidus phase. The early crystallization of

plagioclase in turn suggests a relative low H₂O content for the GP and Fsp-porphyry phases as high H₂O has been shown to delay plagioclase crystallization (Loucks, 2014). This is in contrast to the causative magmas in Phanerozoic magmatic-hydrothermal systems which are typically more hydrous (Sillitoe, 2010; Richards, 2011; Loucks 2014). Relatively dry conditions are also reported for the other Archean mineralization-associated intrusions at the Archean (e.g., the Côté Gold Au±Cu deposit; Meng et al. 2021b). Evidence for these mineralization-associated magmas being relatively dry suggests that high magmatic H₂O content may not be a key factor in magmatic-hydrothermal Au±Cu mineralization for Archean systems.

7 Conclusions

The UBIC formed through mixing of at least two distinct magma derived from metasomatized mantle and basaltic crustal sources. U-Pb geochronology demonstrates that all phases of the intrusive complex were emplaced at ca. 2680 Ma and within the resolution of the LA-ICP-MS analysis. Amphibole and apatite chemistry shows that the physiochemical conditions (temperature, *f*O₂, S content) for emplacement of the UBIC are similar to conditions observed in Phanerozoic arc magmas. However, evidence of early plagioclase crystallization in the intrusive phases associated with mineralization suggest that they were relatively dry.

LASS-ICP-MS trace element and Lu-Hf isotopic analysis of previously analysed zircons to better constrain the physiochemical conditions and the degree of crustal contamination of the UBIC is in progress. High-precision dating of previously analysed zircons is currently in progress using CA-ID-TIMS to accurately constrain the total duration of the Upper Beaver magmatic-hydrothermal system.

Acknowledgements

This research is funded through a NSERC-Agnico Eagle Industrial Research Chair. The authors are grateful to Agnico Eagle Mines Ltd. for logistical support.

References

- Agnico Eagle Mines Limited (2023) Kirkland Lake Regional. <https://www.agnicoeagle.com/English/exploration/exploration-projects/Kirkland-Lake-project/default.aspx>
- Bromiley GD (2021) Do concentrations of Mn, Eu and Ce in apatite reliably record oxygen fugacity in magmas? *Lithos* 384–385:105900. <https://doi.org/10.1016/j.lithos.2020.105900>
- Groves DI, Vielreicher RM, Goldfarb RJ, Condie KC (2005) Controls on the heterogeneous distribution of mineral deposits through time. *SP* 248:71–101. <https://doi.org/10.1144/GSL.SP.2005.248.01.04>
- Kontak DJ, Dubé B, McNicoll V, et al (2013) The Upper Beaver Au-Cu deposit, Kirkland Lake, Ontario, Canada: An Archean IOCG analogue or just an intrusion-related iron oxide copper-gold deposit? *Geol. Assoc. Canada - Mineral. Assoc. Canada Conf*, May 21–24, Winnipeg, MB, Abstr. Vol. 36, p. 122
- Laurent O, Martin H, Moyen JF, Doucelance R (2014) The diversity and evolution of late-Archean granitoids: Evidence for the onset of “modern-style” plate tectonics between 3.0 and 2.5Ga. *Lithos* 205:208–235. <https://doi.org/10.1016/j.lithos.2014.06.012>
- Meng X, Kleinsasser JM, Richards JP, et al (2021a) Oxidized sulfur-rich arc magmas formed porphyry Cu deposits by 1.88 Ga. *Nat Commun* 12:2189. <https://doi.org/10.1038/s41467-021-22349-z>
- Meng X, Richards JP, Kontak DJ, et al (2021b) Variable Modes of Formation for Tonalite–Trondhjemite–Granodiorite–Diorite (TTG)-related Porphyry-type Cu ± Au Deposits in the Neoproterozoic Southern Abitibi Subprovince (Canada): Evidence from Petrochronology and Oxybarometry. *Journal of Petrology* 62: egab079. <https://doi.org/10.1093/petrology/egab079>
- Mercier-Langevin P, Creaser R, Dube B, et al (2021) Molybdenite Re-Os ages of a gold-rich vein, Porphyry zone, Upper Beaver deposit, Abitibi greenstone belt, Ontario. *Geological Survey of Canada Open File* 8789:13
- Middlemost EAK (1994) Naming materials in the magma/igneous rock system. *Earth-Science Reviews* 37:215–224. [https://doi.org/10.1016/0012-8252\(94\)90029-9](https://doi.org/10.1016/0012-8252(94)90029-9)
- Putirka K (2016) Amphibole thermometers and barometers for igneous systems and some implications for eruption mechanisms of felsic magmas at arc volcanoes. *American Mineralogist* 101:841–858. <https://doi.org/10.2138/am-2016-5506>
- Richards JP, Mumin AH (2013) Magmatic-hydrothermal processes within an evolving Earth: Iron oxide-copper-gold and porphyry Cu Mo Au deposits. *Geology* 41:767–770. <https://doi.org/10.1130/G34275.1>
- Ridolfi F, Renzulli A, Puerini M (2010) Stability and chemical equilibrium of amphibole in calc-alkaline magmas: an overview, new thermobarometric formulations and application to subduction-related volcanoes. *Contrib Mineral Petrol* 160:45–66. <https://doi.org/10.1007/s00410-009-0465-7>
- Spencer CJ, Kirkland CL, Taylor RJM (2016) Strategies towards statistically robust interpretations of in situ U–Pb zircon geochronology. *Geoscience Frontiers* 7:581–589. <https://doi.org/10.1016/j.gsf.2015.11.006>
- Sutton J, Côté-Mantha O (2022) Geology of the Archean Upper Beaver oxidised intrusion-related Au-Cu deposit (Kirkland Lake, Ontario). *Quebec Mineral Exploration Association XPLOR*, Oct 3–6, Montreal QC.
- Webster JD, Piccoli PM (2015) Magmatic Apatite: A Powerful, Yet Deceptive, Mineral. *Elements* 11:177–182. <https://doi.org/10.2113/gselements.11.3.177>

Volatiles in zircon-hosted apatite from the Escondida porphyry copper district, northern Chile

Giulia Consuma¹, Anthony I. S¹, Kemp, Laure Martin², Steffen Hagemann¹, Marco L. Fiorentini¹, Brian Tattitch¹

¹ Centre for Exploration Targeting, The University of Western Australia, Perth, Western Australia, Australia.

² Centre for Microscopy, Characterisation and Analysis, The University of Western Australia, Perth, WA 6009, Australia

Abstract. Apatite inclusions armoured in zircon are ideal candidates to fingerprint the original volatile component (S, Cl, F, OH) of ore-forming magmas. A thorough investigation of such inclusions, together with matrix apatite, is hereby used to elucidate the volatiles sources and pathways throughout the magmatic-hydrothermal stages of individual porphyry Cu deposits at Escondida, northern Chile. We selected a suit of least-altered samples, mineralised and barren, to resolve the physico-chemical conditions of the melt/fluid responsible for the Cu-Mo±Au mineralisation in Escondida during the long-lasting late Eocene-Oligocene (44-33 Ma) arc magmatic activity. SEM-BSE-CL imaging, together with measurements of halogens and sulfur concentrations with electron microprobe allowed us to build a comprehensive insight into the volatile content and geochemical signature of apatite. We also measured high precision $\delta^{34}\text{S}$ values in apatite via SIMS to elucidate the S isotope signature of apatite inclusions and matrix apatite. Our preliminary data show that detailed mineral chemistry, microtextural studies, and sulfur isotope measurements applied to apatite inclusions in zircon and matrix apatite provide a unique insight into the geochemical behaviour of sulfur and halogens in ore-forming magmas.

1 Introduction

Different volatile-rich species exsolve from silicate magmas at variable P-T conditions. In addition to water, chlorine (as a metal complexing agent) and sulfur (to sequester metals as sulfide minerals) are essential components for the generation of ore-porphyry magmas (i.e., Grondahl and Zajacz 2022; Tattitch et al. 2021). However, direct studies of the magmatic volatile components are hindered by degassing processes and by the limited suitability of inclusions for analyses. For this reason, the volatile budget and isotopic signature of the initial melt, together with constraints on the volatile sources in porphyry copper environments remain unresolved. To address this, we examine the budget of S, Cl, and other volatile species from the Escondida porphyry Cu-Mo±Au district by investigating apatite enclosed in zircon.

Apatite, $\text{Ca}_5(\text{PO}_4)_3(\text{F,Cl,OH})$, is a well-known repository of volatile species (H_2O , CO_2 , S, halogens) in addition to numerous trace elements, making it an excellent mineral to study the volatile budget of a magma (Piccoli and Candela 2002). Once encapsulated in zircon, apatite inclusions are able to preserve a unique record of the abundance of volatile ore-forming constituents, eliminating diffusion effects associated with late-stage melts and/or fluids (Kendall-Langley et al. 2021).

We use a multi-microanalytical approach (petrography, cathodoluminescence imaging, SEM-

BSE, EPMA and SIMS) in apatite enclosed in zircon and zoned matrix apatite to ultimately understand the role volatiles into the formation of high-grade copper deposits at Escondida.

2 Escondida porphyry Cu-Mo±Au district

The Escondida porphyry copper district is developed along the regional Domeyko Faut system in the Atacama Desert of Chile, ca. 170 km southeast of the port city of Antofagasta at an elevation of 3,050m above the sea level. The entire district comprises the Escondida cluster (namely, Escondida-Escondida-Este, Pampa Escondida, Baker, Pinta Verde, Escondida Norte-Zaldívar) and 15km north-west, the Chimborazo deposit (Figure 1). The ore-forming magmatism took place in the framework of the long-lasting late Eocene-Oligocene (44-33 Ma) arc magmatic activity (Hervé et al 2012 and references therein), favouring the emplacement of multiphase porphyry stocks (early, inter-, late). The Escondida stock intrudes a series of Paleocene andesites, corresponding to the *Augusta Victoria Formation*, which are interbedded by sedimentary units and are mostly exposed in the western and southern part of the district (Quiroz 2003 Unpubl MSc thesis). Magmatic-hydrothermal breccias of intermineral timing formed in all the deposits of the Escondida district, including Chimborazo, and host significant hypogene mineralisation (Hervé et al. 2012).

For this study, we sampled a suit of mineralised porphyries from the Escondida cluster and unmineralized volcanic and intrusive rocks that are spatially and temporally related to the Cu-Mo±Au mineralisation.

3 Analytical methods

3.1 SEM-CL analyses

The mineralogical and textural characterisation of apatite and zircon was carried out with an optical microscope and a Tescan VEGA3 scanning electron microscopy-energy dispersive spectroscopy (SEM-EDS) system. Mineral inclusions within the zircon crystals were analysed by EDS, allowing the identification of apatite inclusions. High contrast back scattered electron (BSE) and cathodoluminescence (CL) imaging was carried out on epoxy mounted zircon and apatite crystals to identify crystal growth structures and the presence of core domains that may represent older (pre-magmatic) components. Further apatite crystals

were characterised in thin sections, allowing a detailed microtextural investigation.

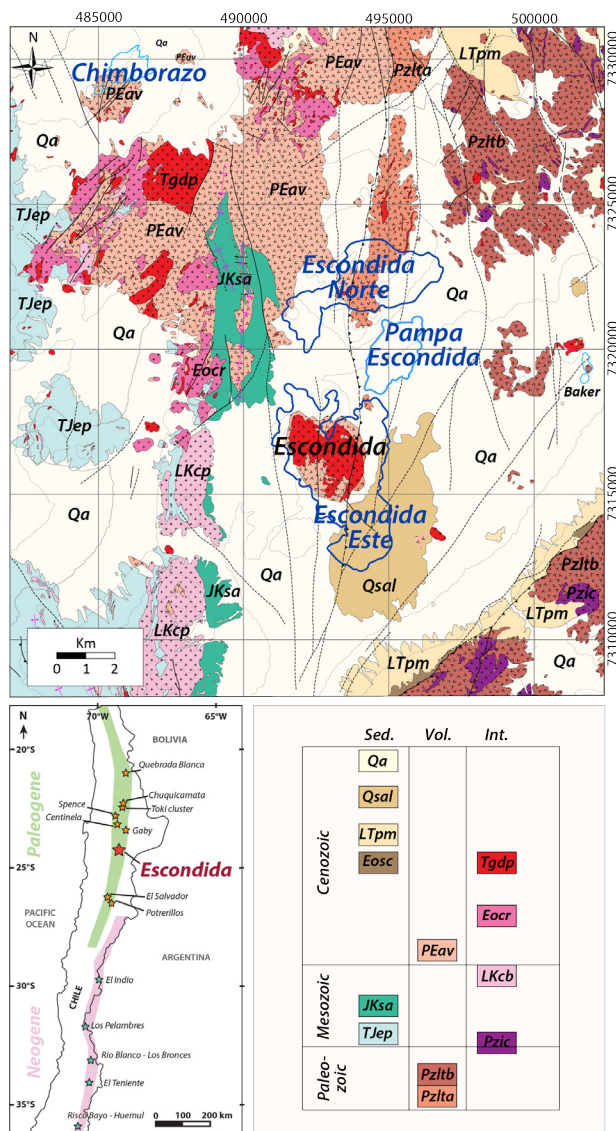


Figure 1. Geology of the Escondida district adapted and slightly modified from Gibson 2018 (published PhD Thesis) whose figure was originally based on mapping by Hervé et al. (2012) and Urzúa (2009). Map of the central and northern Chile showing the Paleogene and Neogene metallogenic belts is modified after Piquer et al. (2021).

3.2 EPMA – Apatite volatile contents

Major and minor elements of targeted groundmass apatite and apatite inclusions were measured with a JEOL 8350F field emission electron micro-analyser (EPMA) at the Centre for Microscopy, Characterisation, and analyses (CMCA) of the University of Western Australia. Elements F, Cl, Ca, P, Sr, S, Mn, Mg, Si, Na, La, Ce, and Nd were measured in apatite inclusions in zircon using a 15nA electron beam current, 15 kV accelerating voltage and a spot size of 5 µm. The EPMA spots were set to be perpendicular to the c-axis of apatite to avoid the disturbance from the orientation of apatite grains. The accuracy of the analyses relative to standards was the following: major elements (Ca

and P) < 1%; F and Cl < 2-3%; minor elements (S, Si, Ce, Na, Mn, Fe, Nd) <10%.

The F, Cl, OH concentrations of apatite inclusions were determined stoichiometrically following the approach of Ketcham (2015), assuming a full X-site.

3.3 SIMS – S isotope of apatite

In situ sulfur isotope (^{32}S and ^{34}S) analyses of apatite inclusions and matrix apatite were conducted using a CAMECA IMS1280 at the Centre for Microscopy, Characterisation, and analyses (CMCA) of the University of Western Australia. Zircon and apatite grains were mounted in epoxy resin and carefully polished. Epoxy resin mounts were therefore coated with 20nm-thick gold. Big1 grains were used as standard material, and the reader is referred to the work of Hammerli et al. (2021) for the analytical procedure. For matrix apatite, the sample surface was sputtered over a 15 x 15 µm area with a 10 kb, Gaussian Cs+ beam with intensity of ca. 1-3 nA and total impact energy of 20 keV. For apatite inclusions, the beam size was reduced to a 5 x 5 µm area.

4 Zircon and apatite microstructure

Zircon grains containing apatite inclusions were retrieved from mineral separation procedures and handpicked under a binocular microscope, mounted into epoxy mounts with zircon and apatite reference materials and polished to expose the mid-sections. BSE and CL imaging of zircon was carried out to detect zircon growth textures and zoning, in addition to identifying the mineral inclusion cargoes. Zircon grains in the mineralised samples range between 100 – 300 µm in length, with the majority around 200 µm in length and aspect ratios of 1:2 to 1:4. Most zircon grains contain mineral inclusions, with apatite as the most abundant followed by k-feldspar and quartz. Zircon grains from the barren intrusions show a larger size compared to those found in the mineralised samples, ranging between 100 to 500 µm in length and with the majority of the crystals around 300 µm. Spherical and lobate inclusions identified as melt inclusions are common in zircon from the unmineralized andesite host rock and other barren rocks. Zircon crystals display a range of internal textures revealed by CL (Figure 2). Secondary dissolution/reabsorption features are present in some grains and are most visible where they interrupt zoning. The reabsorption may just affect one CL band or affect a whole section of the zircon. The most common texture is oscillatory zoning, which exhibits bands ranging in CL intensity from a bright CL response to near black.

Apatite inclusions have a grain size ranging between 5 to 20 µm in the mineralised samples and reaching up to 40 µm in size in the associated unmineralized igneous rocks. The inclusions occur at the proximity of the zircon rims, with a few examples observed close to the zircon core. Thin sections observations show apatite crystals interstitial to silicates and inclusions of apatite within

other primary igneous minerals, such as plagioclase phenocrysts and amphibole. In the mineralised samples, anhedral apatite locally forms veins and veinlets in equilibrium with anhydrite. Euhedral crystals of apatite are also commonly found as inclusions in anhydrite. Matrix apatite often intergrows with hydrothermal minerals, such as rutile, ilmenite, anhydrite, pyrite, and chalcopyrite. Apatite crystals elongated on the c-axis commonly show inclusions of monazite, carbonates, anhydrite, K-feldspar, quartz, and zircon.

CL imaging reveals that the majority of apatite crystals parallel to the c-axis are chemically zoned. These apatite crystals usually show gradational zoning from near black cores to lighter rims under CL. However, irregular CL patches and homogenous CL colors are also observed in matrix apatite.

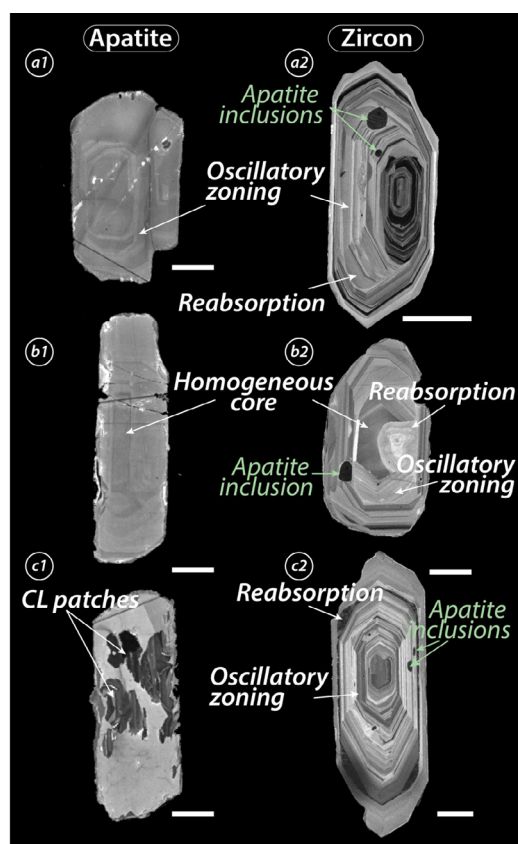


Figure 2. Cathodoluminescence images of apatite (a1, b1, c1) and zircon (a2, b2, c2) grains from mineralised samples showing examples of the most common internal textures and zoning. A 50µm-scale is shown for each grain.

5 Halogens, S content and S isotope of apatite inclusions

The barren samples exhibit variable F-Cl-OH and S compositions. Apatite inclusions from the biotite andesite porphyry show F concentrations of 1.18 to 2.58 wt%, Cl concentrations of 1.85 to 3.92 wt%, and OH concentrations of near zero to 0.83 wt%. Apatite from the quartz monzodiorite exhibits F concentration of 1.67 to 3.20 wt%, Cl concentration

of 1.14 to 3.06 wt%, and OH concentrations of 0.19 to 1.16 wt%. The few spots analyses of apatite inclusions from the fine-grained pyroxene-bearing monzodiorite and from the andesitic host rock show F values of 1.03-1.27 wt% and 1.76 wt%, Cl values of 1.88-2.16 and 1.32 wt%, and OH values of 1.25-1.31 and 1.27 wt%, respectively. Apatite inclusions across the regional samples always reveal S concentrations above the detection limit, ranging between 0.13 to 0.75 wt% SO₃. Further future SIMS measurements of apatite inclusions from the unmineralized samples will be carried out for comparison with the barren intrusions.

In the samples hosting the mineralisation, apatite inclusions record variable, but lower Cl concentrations compared to the unmineralized samples (Figure 3), with values spanning from 0.41 to 1.50 wt% Cl and few outliers. On the other hand, in the mineralized porphyries, apatite inclusions record SO₃ concentrations ranging between values below detection limit and 0.73 wt%, thus not showing significant distinctions with the apatite inclusions from the unmineralized samples.

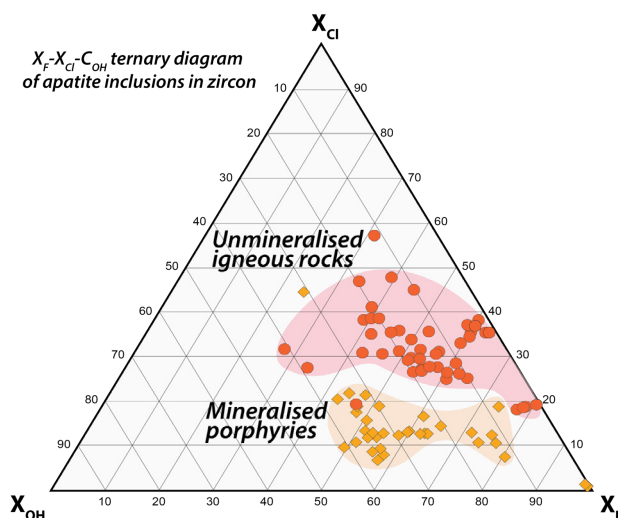


Figure 3. X_F-X_{Cl}-X_{OH} ternary diagram showing the compositional ranges of apatite inclusions in zircon from the studied mineralised and unmineralized samples. Mole fractions of F and Cl in apatite are calculated using the method of Piccoli and Candela (2002).

Apatite inclusions exhibit fairly homogeneous, positive, δ³⁴S values (δ³⁴S > 0‰), irrespective of the mineralisation stage recorded in the rock sample (i.e., early porphyry, late porphyry). Matrix apatite shows a strong zoning in cathodoluminescence (CL). The dark core under CL of matrix apatite shows positive δ³⁴S values, similar to those measured in the inclusions. The CL-lighter rims, instead, record δ³⁴S values trending toward lighter, negative values.

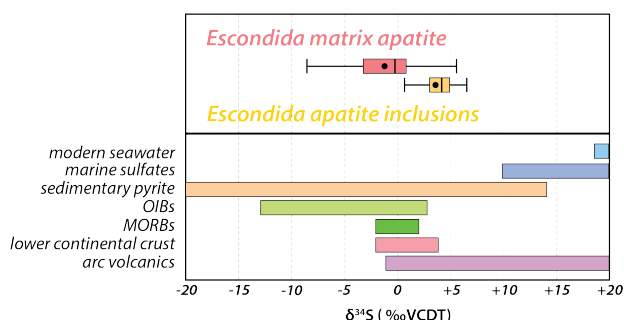


Figure 4. S isotope signature of the investigated apatite inclusions and matrix apatite from the mineralized samples. S isotopic compositions from different reservoirs are reported for comparison. The reader is referred to Hammerli et al. (2021) and reference therein for the full explanation.

6 Discussion and conclusion

The new microanalytical approach for studying the volatile component of apatite inclusions and matrix apatite from the Escondida porphyry Cu district involves a combination of microtextural studies, mineral chemistry and in-situ isotopic investigations. Further analytical measurements and experimental constraints are required to fully understand the physico-chemical conditions that favoured the mineralisation at Escondida. However, our preliminary data identified the potential to discriminate different pathways of halogens and S among different mineralised and barren samples. The grain size of the zircon separates is the first-order observation that differentiates between the mineralised and the barren rocks in Escondida. Specifically, the smaller size of the zircon grains (and associated apatite inclusions) from the mineralised samples compared to those from the barren intrusions could be attributed to a number of factors, including differences in magma ascent rates, depth of crystallization, and water availability. For example, it is possible that the ore-forming magma was emplaced at a shallower depth and cooled rapidly compared to the infertile-magma, resulting in smaller zircon and apatite crystals.

We identified a significant distinction in the Cl concentration of apatite inclusions from the Cl-poor mineralised porphyries and Cl-enriched barren rocks. One possible explanation is that the ore-forming magma lost Cl prior to the crystallization of apatite and its entrapment in the zircon. This loss of Cl may have occurred due to the partitioning of Cl into exsolving aqueous fluids during magma ascent. If this is the case, it would suggest that the Cu-Mo±Au porphyry bearing magma was originally richer in Cl than the apatite inclusions suggest. It is therefore essential to take into consideration the volatile composition of the source component that contributed to the melt as well as the involvement of other processes, such as magma mixing or crustal assimilation. Further constraints on the temperature of zircon crystallisation and apatite entrapment will

be applied to fully resolve the original halogens content of the ore-forming magma.

The S concentrations of the apatite inclusions are variably similar between mineralised and unmineralized samples. In the mineralised samples, the S concentrations and isotopic measurements indicate that matrix apatite records a complex magmatic-hydrothermal evolution, which trends toward lighter (and negative) $\delta^{34}\text{S}$ values and contrasts with the positive S isotopic signature of the zircon-hosted apatite. This may be attributed to S isotopic fractionation during low-T open-system processes, to the presence of anhydrite in the rock sample, or to the involvement of sulfur from different reservoirs.

Our preliminary data suggest that apatite inclusions in zircon are valuable tools for studying the volatile signature and behaviour of ore-forming and infertile-magmas in the Escondida district. Further research will be needed to fully understand the source of volatiles and their contribution to the Cu-Mo±Au mineralisation in Escondida.

Acknowledgements

BHP is thanked for providing the funds to conduct the field work in Escondida and the analytical work on apatite. Matvei Aleshin is thanked for assisting during the SIMS measurements at CMCA, UWA.

References

- Gibbson J (2018) Magmatic-hydrothermal evolution of the pampa Escondida porphyry copper deposit, Northern Chile. Publ. PhD Thesis, The University of Arizona.
- Grondahl C, Zajacz Z (2022) Sulfur and chlorine budgets control the ore fertility of arc magmas. *Nat Commun* 13, 4218. <https://doi.org/10.1038/s41467-022-31894-0>
- Hammerli J, Greber ND, Martin L et al (2021) Tracing sulfur sources in the crust via SIMS measurements of sulfur isotopes in apatite. *Chem Geol*, 579. <https://doi.org/10.1016/j.chemgeo.2021.120242>
- Hervé M, Sillitoe RH, Wong C, Fernández P, Crignola F, Ipinza M, Urzúa F (2012) Geologic Overview of the Escondida Porphyry Copper District, Northern Chile, in: *Geology and Genesis of Major Copper Deposits and Districts of the World. Tribute to Richard H. Sillitoe*. Society of Economic Geologists, Special Publication 16, 55-78.
- Kendall-Langley LA, Kemp AIS, Hawkesworth CJ, Craven J, Talavera C., Hinton R., Roberts MP, EIMF (2021) Quantifying F and Cl concentrations in granitic melts from apatite inclusions in zircon. *Contrib Mineral Petrol* 176, 58. <https://doi.org/10.1007/s00410-021-01813-5>
- Piccoli PM, Candela PA (2002) Apatite in Igneous Systems. *Reviews in Mineralogy and Geochemistry* 4. <https://doi.org/10.2138/rmg.2002.48.6>
- Piquer J, Sanchez-Alfaro P, Pérez-Flores P (2021) A new model for the optimal structural context for giant porphyry copper deposit formation. *Geology* 49, 597-601. <https://doi.org/10.1130/G48287.1>
- Tattitch B, Chelle-Michou C, Blundy J, Loucks RR (2021) Chemical feedbacks during magma degassing control chlorine partitioning and metal extraction in volcanic arcs. *Nat Commun* 12, 1774. <https://doi.org/10.1038/s41467-021-21887-w>

White mica alteration in the Gaby porphyry copper district, Northern Chile

Alexandre Cugerone¹, Kalin Kouzmanov¹, Lluís Fontboté¹, Luis Krampert¹, Carolina Rodríguez², Rubén Pardo², Sergio Pichott Henríquez²

¹Department of Earth Sciences, University of Geneva, 1205 Geneva, Switzerland

²CODELCO, Santiago, Chile

Abstract. White mica alteration in porphyry systems is often directly associated with economic mineralization. White mica chemistry may record the evolution of the hydrothermal system and could represent an important vectoring tool for Cu-Mo mineralization. However, in such setting, macro to microscale variations in white mica chemistry are still poorly understood. Here, we focus on the white mica alteration in the Gaby porphyry copper district (Northern Chile), using automated mineralogy (QEMSCAN), short-wave infrared (SWIR), and electron microprobe (EMPA) analyses. The Gaby district consists of Late Carboniferous-Early Permian volcano-sedimentary rocks, the Permo-Triassic Pampa Elvira plutonic complex, and Eocene tonalite porphyries. Two main types of white mica alteration are identified: i) Early green Fe-Mg-rich sericite is observed in veins, halos, and as pervasive alteration, frequently intergrown with chalcopyrite-bornite and low amounts of pyrite; ii) Late grey Fe-Mg-poor sericite is found disseminated, locally as secondary alteration on green sericite, and in halos of pyrite-rich veins. In these veins, green sericite is also present as infill, as well as in their outermost zone. Correlation between portable SWIR (TerraSpec) analyses and variations of white mica composition at micrometer scale as determined with QEMSCAN and EMPA demonstrates the strengths and limitations of the SWIR spectroscopy in exploration for porphyry systems.

1 Introduction

White mica alteration zones commonly host high-grade ore in porphyry systems (Reed et al. 2013; Uribe-Mogollon and Maher 2018; Alva-Jimenez et al. 2020). During the evolution of a porphyry system, white mica composition changes due to variations in fluid temperature and composition and is also influenced by the primary composition of the mineral replaced (e.g., plagioclase, biotite). Two general types of white mica/sericite alteration are recognized in porphyry systems (Uribe-Mogollon and Maher 2018; Skarmeta 2021): deep early green sericite alteration is typically associated with chlorite, whereas shallow late grey sericite alteration is not associated with chlorite.

Vectoring using white micas is commonly based on short-wave infrared (SWIR) spectroscopy, which records specific spectral characteristics such as the Al-OH peak position and depth (Chang and Yang 2012; Calder et al. 2022). The spectral signature of white mica is chemically influenced by the Tschermak substitution: $Al^{3+}_{tet} + Al^{3+}_{oct} \leftrightarrow Si^{4+}_{tet} + Mg^{2+}_{oct}$ or Fe^{2+}_{oct} (Guo et al. 2019; Cloutier et al. 2021). A recent study demonstrates the potential of using trace elements in white mica as a vectoring tool in porphyry systems (Uribe-Mogollon and Maher 2020).

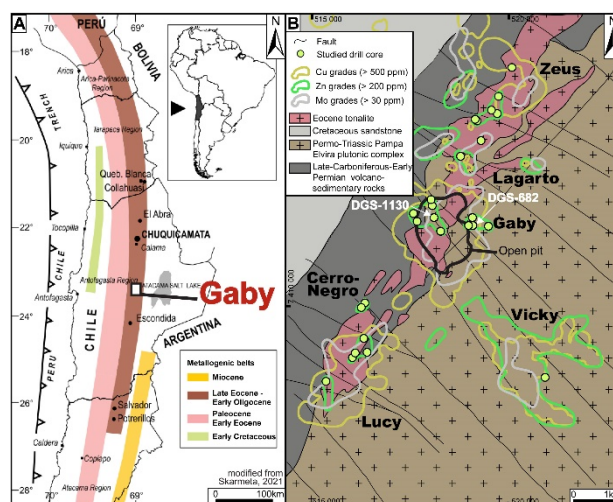


Figure 1. A. Location of the Gaby district within the Upper Eocene-lower Oligocene metallogenic belt in Chile (modified from Skarmeta 2021). B. Schematic geological map of the Gaby district with the reported grades for Cu, Zn and Mo and location of the two drill holes studied (DGS1130 and DGS682).

In porphyry deposits, stockwork veining is commonly a polyphase process, and frequently shows reopening textures with superimposed alteration halos (Rusk et al. 2008; Sillitoe 2010). Consequently, chemistry of white micas can be significantly affected by overprinting of multiple alteration/mineralization events.

In this contribution, we focus on the Gaby porphyry Cu-Mo deposit in Northern Chile. Based on petrographic observations, automated mineralogy (QEMSCAN), short-wave infrared (SWIR), and electron microprobe (EMPA) analyses, we discriminate a large variety of white mica textures and compositions, related to multiple mineralizing events, overprinting each-other in space and time.

2 Geology of the Gaby district

The Gaby district is located in the Late Eocene to Early Oligocene metallogenic belt, in Northern Chile (Figure 1A). The district includes the Gaby deposit, currently in operation, and numerous prospects such as Lucy, Cerro Negro, Vicky, Lagarto, and Zeus (Figure 1B). Mineralization is hosted in Eocene tonalite porphyritic intrusions, emplaced in the large composite Permo-Triassic Pampa Elvira plutonic complex, and locally in Late Carboniferous-Early Permian volcano-sedimentary rocks of the La Tabla Formation. The Eocene tonalite intrusions follow a

general N 040-50E trend, along the contact between the Pampa Elvira plutonic complex and the La Tabla Formation. The Permo-Triassic plutonic complex and most of the Eocene porphyries are similar in terms of texture and geochemistry, whereby the Pampa Elvira plutonic complex shows higher proportion of K-feldspar. Potassic alteration is observed all along strike of the Eocene porphyritic intrusions, as well as in the host Permo-Triassic plutonic complex.

Multiple sets of faults are noticed: NE-SW normal faults, and N-S to NW-SE reverse faults. The NW-SE normal faults show post-mineralization displacement that modifies the architecture of the district. The northern part (Zeus-Lagarto) is structurally deeper than the southern part (Lucy-Cerro Negro prospects; Figure 1B).

Porphyry-style mineralization is mainly disseminated and in veinlets; stockwork mineralization is not common (Figure 2). Chalcopyrite and bornite are the main copper minerals, frequently associated with molybdenite and quartz. Pyrite is typically associated with late D-veins. Supergene chalcocite, atacamite and chrysocolla can be observed at up to ~ 200-250 m below surface.

Late polymetallic veinlets have been noticed so far mainly in the southern part of the district, in the Cerro Negro, Lucy and Vicky prospects (Figure 1B), partly as reopening of pre-existing porphyry-style veinlets (Figure 3A). Sphalerite, galena, tennantite-tetrahedrite, pyrite and chalcopyrite occur together with quartz and/or multiple generations of carbonates including rhodochrosite, siderite, ankerite, siderite, and calcite, in part Fe and/or Mn-bearing.

3 Methods

One hundred thirteen samples were collected approximately every 5 meters from two drill holes in the Gaby open pit (Figure 1B). The studied interval of hole DGS1130 mostly intersects the Eocene tonalite porphyry (Figure 2) and the one of DGS682, the Pampa Elvira plutonic complex.

SWIR measurements were obtained using an ASD TerraSpec Halo Mineral Identifier. Three analyses were performed on each rock slice from which a thin section was also obtained. Acquisition time was 10s and the standard beam size - 1 cm. Absorption features (Al-OH, Mg-OH, Illite crystallinity) determined by the TerraSpec Halo internal software and The Spectral Geologist (TSG) software were compared. The results are generally similar (~ 0.1 nm). Based on the two mineralogical databases (TerraSpec halo and TSG), a last check of each Hull-quotient-transformed spectrum was completed.

Automated mineral analysis and textural imaging were performed using an FEI QEMSCAN Quanta 650F facility at the University of Geneva. The QEMSCAN system is equipped with two Bruker

QUANTAX light-element EDS detectors. White mica varieties were discriminated based on their Fe and Mg content and Al/Si ratio, while chlorite varieties - based on their Mg/Fe ratio and Mn content.

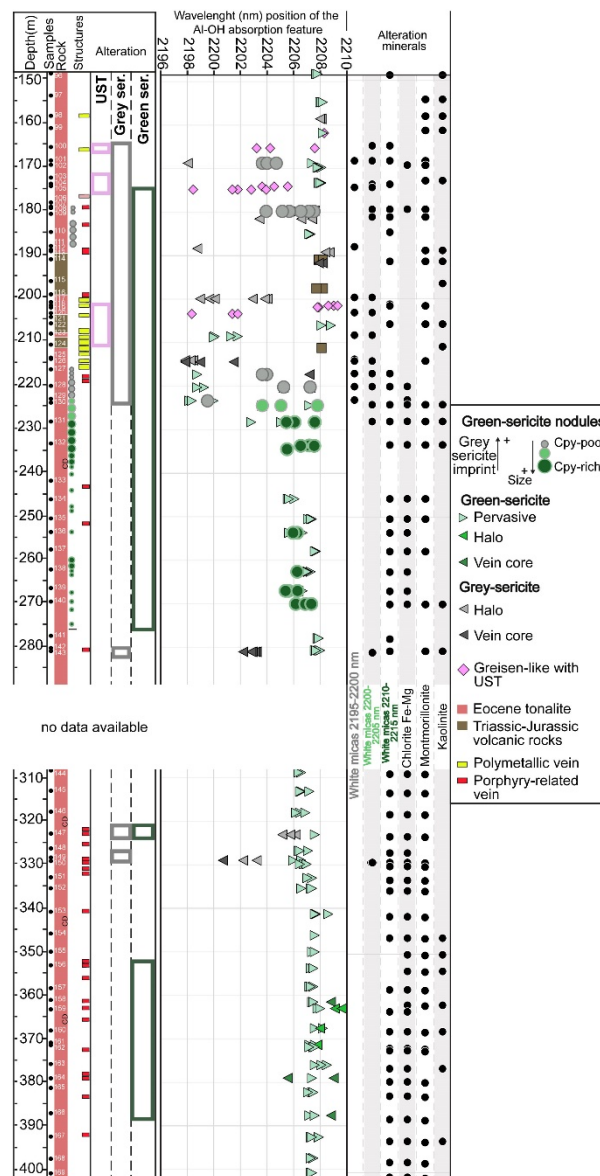


Figure 2. Log of drill hole DGS1130 reporting the type of host rock, the main mineralized structures, the type of alteration, and the Al-OH absorption feature and alteration minerals identified with SWIR.

Major and minor element compositions of white micas were determined by electron microprobe analysis (EMPA) using a JEOL JXA-8200 Superprobe microanalyzer equipped with five wavelength dispersive X-ray spectrometers (WDS) at the University of Geneva. Measured elements include Si, Ti, Al, Cr, Fe, Mn, Mg, Ca, Na, K, Ba and Cl. The acceleration voltage and beam current were 15 kV and 15 nA, and beam diameter used 5 µm.

4 Texture, chemistry, and SWIR signature of green and grey sericite

4.1 Green sericite

Green sericite is mostly observed in the deeper parts of the tonalite porphyries (from ~200 to ~400 m depth; Figure 2) but is also identified at shallow levels in the Pampa Elvira plutonic complex (~50 m in hole DGS682). Green sericite mostly consists of phengite, generally with grain size lower than 1mm. It occurs with chlorite that locally is enriched in Mn (up to 2-3 wt% Mn). Green sericite occurs as: (i) replacing pluri-centimetric magmatic nodules in the tonalite, only located in an interval from 170 to 270 m depth, that show frequently chalcopyrite along their borders; ii) as pervasive alteration; iii) in veinlets; iv) in alteration halos, preferentially in veinlets at around 300-400 m depth (Figures 2 and 3).

Microprobe analyses of green sericite yield relatively high Mg and Fe contents, ranging 0.15-0.35 apfu and 0.10-0.25 apfu, respectively, and low Na and Al contents, 0.01-0.55 and 2.45-2.70 apfu, respectively. Green sericite is frequently intergrown with chalcopyrite and low amounts of bornite (Figure 3).

4.2 Grey sericite

Grey sericite is composed of phengite, generally coarse-grained (up to few millimetres), and postdates the green sericite alteration. Grey sericite is mostly observed in the upper part of the drill hole (around 200 m; Figure 2) and frequently obliterates previous textures, especially green sericite in magmatic nodules. Two types of textures/structures are observed: i) grey sericite in the halos of pyrite-rich D-veins, with local occurrence of K-Fe-Mg-depleted illite close to pyrite (Figure 3 and 4); ii) pervasive alteration overprinting also green sericite alteration in magmatic nodules.

Microprobe data show generally low Fe and Mg contents, ranging 0.02-0.07 and 0.02-0.12 apfu, respectively (Figure 4). Sodium and Al contents in grey sericite reach 0.05-0.06 and 2.73-2.82 apfu, respectively.

Figure 4a illustrates variations of K, Mg and Fe along a transect across grey sericite halo of a pyrite-rich D-vein. Grains replacing former magmatic "book" biotite and occurring close to pyrite grains show the lowest K content. This is attributed to the presence of illite (typically depleted in K; Alva-Jimenez et al. 2020). No change in K content is observed between green and grey sericite. Iron and Mg are depleted in grey sericite compared to green sericite (Figure 4A), Al and Ti have similar content, and Si is higher in grey sericite. Si/(Fe+Mg) ratio (Figure 4B) is above 15 for grey sericite and lower than 15 for green sericite.

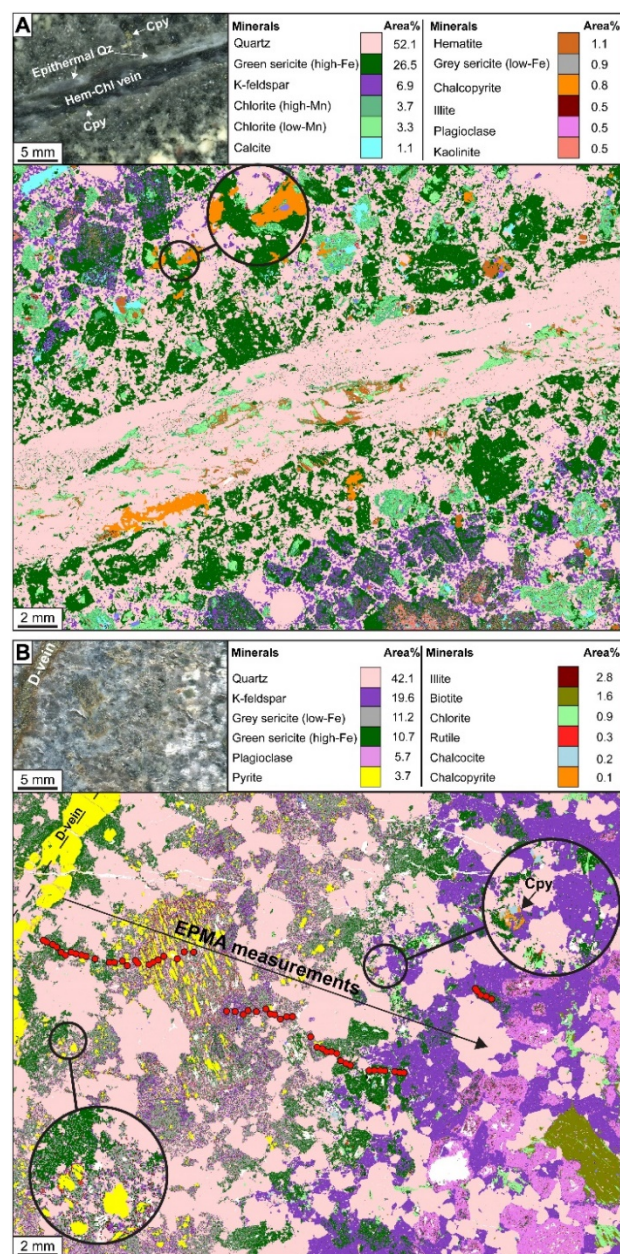


Figure 3. Two QEMSCAN maps of green and grey sericite alteration. A. Quartz-chalcopyrite vein reopened by chlorite-hematite-green sericite vein, subsequently reopened by a quartz-polymetallic vein. The halo of green sericite occurs along the chlorite-hematite vein. B. Pyrite-rich D-vein with halo composed of Fe-rich and Fe-poor sericite. Close to the vein and in the outermost halo, green sericite is observed but most of the halo is composed of grey sericite. K feldspar is intergrown with green sericite in the outer zone. Abbreviations - Chl: chlorite; Cpy: chalcopyrite; Hem: hematite; Qz: quartz)

4.3 Relationship between chemistry of green-grey sericite and SWIR absorption features

Generally, a good discrimination between grey and green sericite is obtained when comparing SWIR analyses (Al-OH absorption feature) and EMPA results (Figure 4C). A threshold around 2203.5 nm could be used to discriminate green sericite (higher Al-OH absorption features of 2203.5-2208 nm) and

grey sericite (< 2203.5 nm). However, some analyses corresponding to green sericite inner/outer halo or vein infill fall in the grey sericite field (below 2203.5 nm); they are interpreted as artefacts caused by mixtures of grey and green sericite.

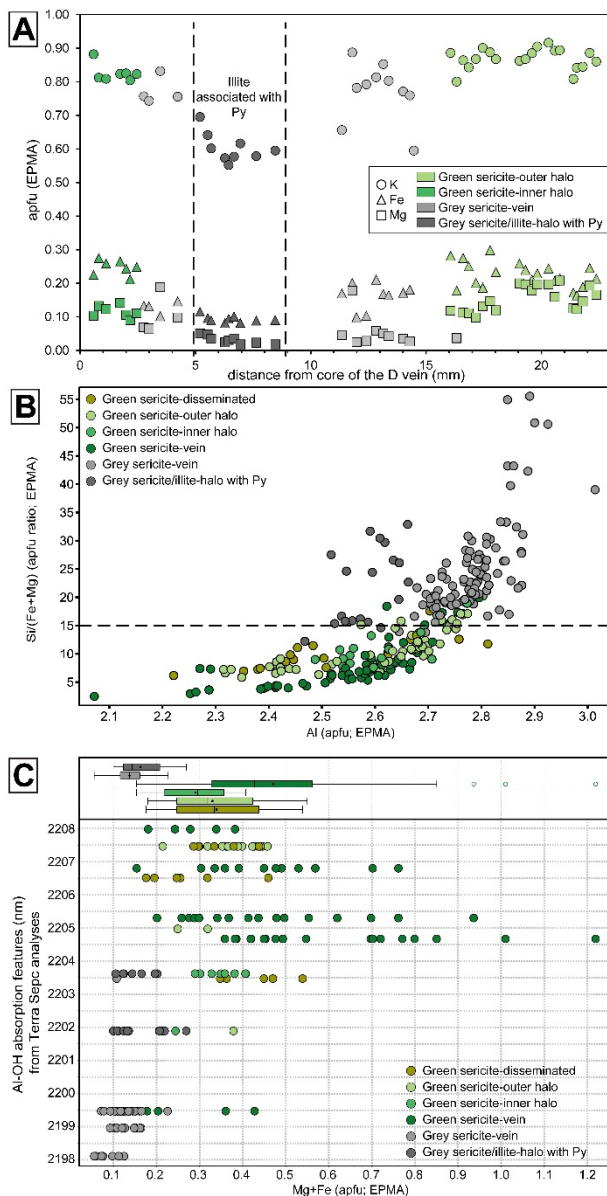


Figure 4. EMPA results on white micas. Green and grey sericite are discriminated. A. Potassium, Fe and Mg content (apfu) in a transect perpendicular to the alteration halo of a D-vein (location shown in Figure 3B). B. Si/(Fe+Mg) ratio vs Al_{tot} plot. C. Comparison between TerraSpec Al-OH absorption features and (Mg+Fe) content (apfu).

5 Conclusion

At Gaby, white mica alteration shows large textural diversity and in general a bimodal chemistry with green (Fe-Mg rich; Na-Al poor) and grey sericite (Fe-Mg poor; Na-Al rich). QEMSCAN mapping can be

used to discriminate green and grey sericite alteration successfully. In both, the Eocene tonalite and in the Permo-Triassic Pampa Elvira plutonic complex, a 40 m-thick interval around 200 m below present day surface is enriched in grey sericite alteration that overprints earlier green sericite alteration. This interval can be easily detected with TerraSpec analyses using the Al-OH absorption feature of white micas. Nonetheless, precise detection of the type of sericite is difficult when, at pluri-millimetric scale, a mixture of green and grey sericite exists, especially in D-vein halos.

Acknowledgements

The authors thank Codelco and Exploraciones Mineras S.A (EMSA) for the logistic and financial support, fruitful discussions, and access to the field area.

References

- Alva-Jimenez T, Tosdal RM, Dilles JH, Dipple G, Kent AJR, Halley S (2020) Chemical Variations in Hydrothermal White Mica across the Highland Valley Porphyry Cu-Mo District, British Columbia, Canada. *Econ Geol* 115:903–926.
- Calder MF, Chang Z, Arribas A, Gaibor A, Dunkley P, Pastoral J, Kouzmanov K, Spandler C, Hedenquist JW (2022) High-Grade Copper and Gold Deposited During Postpotassic Chlorite-White Mica-Albite Stage in the Far Southeast Porphyry Deposit, Philippines. *Econ Geol* 117:1573–1596.
- Chang Z, Yang Z (2012) Evaluation of inter-instrument variations among short wavelength infrared (SWIR) devices. *Econ Geol* 107:1479–1488.
- Cloutier J, Piercey SJ, Huntington J (2021) Mineralogy, mineral chemistry and SWIR spectral reflectance of chlorite and white mica. *Minerals* 11.
- Guo N, Thomas C, Tang J, Tong Q (2019) Mapping white mica alteration associated with the Jiama porphyry-skarn Cu deposit, central Tibet using field SWIR spectrometry. *Ore Geol Rev* 108:147–157.
- Reed M, Rusk B, Palandri J (2013) The Butte magmatic-hydrothermal system: One fluid yields all alteration and veins. *Econ Geol* 108:1379–1396.
- Rusk BG, Reed MH, Dilles JH (2008) Fluid inclusion evidence for magmatic-hydrothermal fluid evolution in the porphyry copper-molybdenum deposit at Butte, Montana. *Econ Geol* 103:307–334.
- Sillitoe RH (2010) Porphyry copper systems. *Econ Geol* 105:3–41.
- Skarmeta J (2021) Structural controls on alteration stages at the Chuquicamata Copper-Molybdenum deposit, Northern Chile. *Econ Geol* 116:1–28.
- Uribe-Mogollon C, Maher K (2018) White mica geochemistry of the copper cliff porphyry cu deposit: Insights from a vectoring tool applied to exploration. *Econ Geol* 113:1269–1295.
- Uribe-Mogollon C, Maher K (2020) White mica geochemistry: Discriminating between barren and mineralized porphyry systems. *Econ Geol* 115:325–354.

Mineralogical and compositional evidence of a district-scale Sn-W skarn system in SW Sardinia: a review

Matteo L. Deidda¹, Alfredo Idini¹, Dario Fancello¹, Lorenzo Tavazzani², Florence Bégué³, Kalin Kouzmanov³, Giovanni De Giudici¹, Marilena Moroni⁴, Stefano Naitza¹

¹Department of Chemical and Geological Sciences, University of Cagliari, Italy

²Institute of Geochemistry and Petrology, ETH Zürich, Switzerland

³Department of Earth Sciences, University of Geneva, Switzerland

⁴Department of Earth Sciences, University of Milan, Italy

Abstract. We studied three representative skarn orebodies of SW Sardinia (Perda Niedda, Monte Tamara and Rosas), related to ilmenite-series ferroan granites to assess their Sn-W and other Critical Raw Materials (CRM) metallogenic potential. The Perda Niedda skarn hosts magnetite, fluorite, cassiterite and minor sulfides in a garnet- (clinopyroxene)-amphibole-chlorite association at contact with granites. At Monte Tamara, scheelite-bearing hydrothermal veins and clinopyroxene-garnet skarns occur with minor cassiterite-stannite-molybdenite and Bi-sulfosalts. Base-metal sulfides with subordinate magnetite-cassiterite-fluorite veinlets prevail at Rosas. Clinopyroxene, garnet and epidote mineral chemistry from the three locations allows a detailed reconstruction of the mineralised systems, in terms of proximity to causative intrusion, compositional variations of ores and Sn-W and CRM enrichment. Overall, the highlighted common features of the three skarns indicate that they may be framed within a single, district-scale Sn-W skarn system. Overall, their different mineralogy and geochemical fingerprint reflect formation mechanisms controlled by their distance from the causative intrusion.

1 Introduction

Skarns are one of the most common classes of deposits for high-grade Sn and W mineralisation. Due to their industrial applications and supply risk, Sn is considered a “medium-scale” critical metal (Lehman 2021), whereas W is included in the Critical Raw Materials (CRM) list for Europe. In fact, Europe accounts only for the 7% of Sn and 4% of W global production, whereas China, Russia, SE Asia and S America, together, produce 78% of Sn and 91% of W. Therefore, re-evaluation of the CRM potential of old mining districts in Europe is now considered necessary by the EU Commission to keep up with these trends.

The Sulcis-Iglesiente (SW Sardinia) is an old mining district hosting numerous skarn orebodies (at least 50 documented occurrences) that were in part exploited for their Zn-Pb sulfide and/or Fe oxide ores. In this study, three representative skarns from the Sulcis-Iglesiente district (Perda Niedda, Monte Tamara and Rosas mines) have been investigated to evaluate the presence of Sn, W and other associated CRM (e.g., Bi, Mo, In) in the ores and, thus, to test the potential of SW Sardinia for Sn-W and CRM mineral exploration.

2 Geological setting

The SW portion of Sardinia (Sulcis-Iglesiente and Arburese regions) represents the External Zone of

the Variscan Chain in the region. The area includes a low-grade and mildly deformed Palaeozoic succession of Lower Cambrian sandstones, massive limestones and dolostones, nodular silty limestones, slates, and Middle-Upper Ordovician conglomerates and sandstones. These rocks were intruded at 289 ± 1 Ma (Boni et al. 2003) by F-bearing, ferroan, reduced (ilmenite-series) and slightly peraluminous monzogranites and leucogranites (GS1 suite: Conte et al. 2017) that were emplaced at less than 2 kbar. Based on these features, common among “tin-granites” (Lehmann 2021), the GS1 suite has been recognized as the metallogenic source for the numerous Sn-Mo-W ores of SW Sardinia (Naitza et al. 2017).

3 Analytical Methods

Field surveys and samplings were performed in the Perda Niedda, Monte Tamara and Rosas old mining areas. Petrographic, SEM-EDS, EPMA and LA-ICP-MS analyses took place at the University of Cagliari, University of Milan and University of Geneva and ETH Zürich.

4 Skarn and ore mineralogy

The Perda Niedda skarn ore consists of large magnetite-fluorite bodies at the exposed contact between Lower Cambrian carbonates and the GS1 Orida pluton. Sulfides are subordinate, except for sulfide-rich zones containing In-rich sphalerite, arsenopyrite, löllingite, pyrrhotite, native Bi and late-stage pyrite disseminations. The skarn consists of abundant green garnet; clinopyroxene and axinite occur at distal position from the granite contact. Garnet forms large idiomorphic, birefringent and concentrically zoned crystals frequently pervasively altered (chlorite, amphibole, phlogopite, quartz) and associated with fluorite, magnetite and cassiterite. Cassiterite is found (Figure 1a-b): a) as micro-inclusions in the altered garnet rims with magnetite; and b) in magnetite-cassiterite-sphalerite fine layers in a quartz-fluorite-chlorite mass (“wrigglite” textures; Kwak and Askins 1981).

The Monte Tamara skarn occurs at the contact between Lower Cambrian limestones and sandstones at 3 km from the nearest exposure of the GS1 granites. Carbonate-hosted scheelite-arsenopyrite-sphalerite hydrothermal veins are

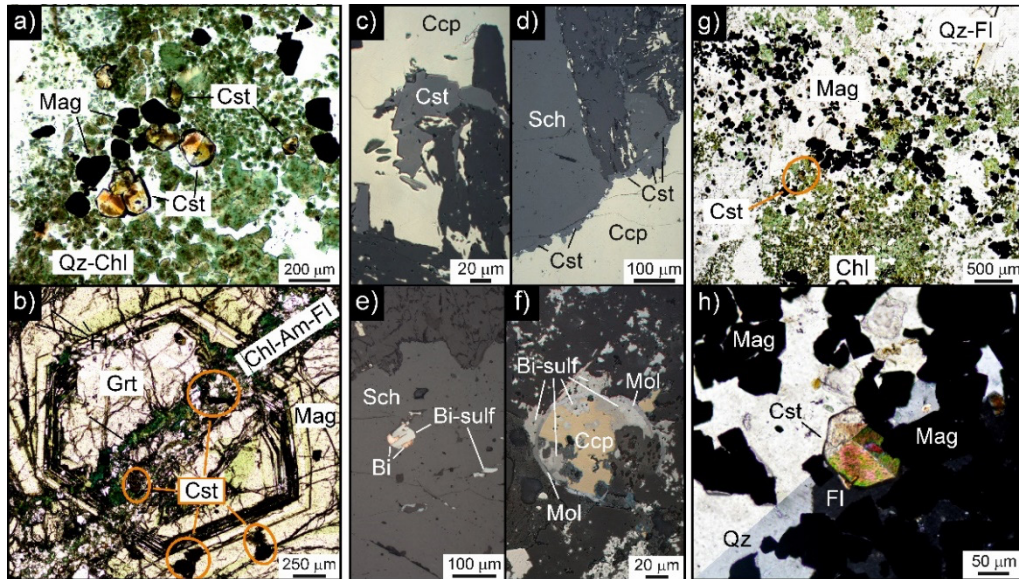


Figure 1. Photomicrographs of the W-Sn and Mo-Bi minerals of the Perda Niedda (a-b), Monte Tamara (c-f) and Rosas (g-h) skarns: a) “wrigglite”-type magnetite-cassiterite in a quartz-chlorite-fluorite gangue (Perda Niedda); b) cassiterite-magnetite enclosed in garnet altered to in chlorite-amphibole-fluorite (Perda Niedda); c) cassiterite associated with chalcopyrite and d) scheelite (Monte Tamara); e-f) Bi-sulfosalts with scheelite, chalcopyrite and molybdenite (Monte Tamara); g-h) “wrigglite”-type magnetite-cassiterite association (Rosas). Am = amphibole; Bi = native Bi; Bi-sulf = Bi-sulfosalts; Ccp = chalcopyrite; Chl = chlorite; Cst = cassiterite; FI = fluorite; Grt = garnet; Mag = magnetite; Mol = molybdenite; Sch = scheelite.

found in a distal position (Sinibidraixu; Deidda et al. 2023). The skarn consists of clinopyroxene and slightly subordinate garnet. Hydrothermal alteration of diopside and garnet produces actinolite, epidote, chlorite, calcite and quartz (Deidda et al. 2023). The ore includes variable proportions of scheelite, cassiterite, stannite, molybdenite, native Bi and Bi-sulfosalts as well as hematite, chalcopyrite, sphalerite, arsenopyrite, galena, pyrrhotite, pyrite and marcasite (Figure 1c-f).

Finally, the Rosas mine area is located on a regional-scale shear zone with numerous skarn orebodies along tectonic slices of Lower Cambrian limestones (Cocco et al. 2022). The nearest GS1 granite exposure is at 5 km distance from the ores, in the SE of the Monte Tamara area. A representative skarn occurrence (Barisonis sector) displays abundant clinopyroxene and minor garnet. Sphalerite, chalcopyrite and galena are the prevailing ore minerals. Cassiterite (Figure 1g-h) occurs with magnetite in “wrigglite”-like quartz-fluorite-chlorite assemblage (Cocco et al. 2022). Secondary phases include Ag-minerals, while some gold grains were observed in quartz.

5 Major and trace elements in silicates

5.1 Clinopyroxene

Clinopyroxene from Perda Niedda mostly belongs to the diopside endmember, with minor hedenbergite and johannsenite components (avg. $\text{Di}_{70.9}\text{Hed}_{6.5}\text{Jo}_{7.5}$; Figure 2). Clinopyroxene from Monte Tamara is diopsidic with moderate hedenbergite and low johannsenite percentages ($\text{Di}_{77.8}\text{Hed}_{19.6}\text{Jo}_{2.6}$). Conversely, clinopyroxene from

Rosas is markedly higher in the hedenbergite and johannsenite components (avg. $\text{Di}_{17.1}\text{Hed}_{64}\text{Jo}_{18.9}$). Tin content is usually low at Rosas (< 1 ppm) and Perda Niedda (3-26 ppm); occasionally high values were detected at Monte Tamara (171-4367 ppm). Tungsten does not exceed 1 ppm in all deposits.

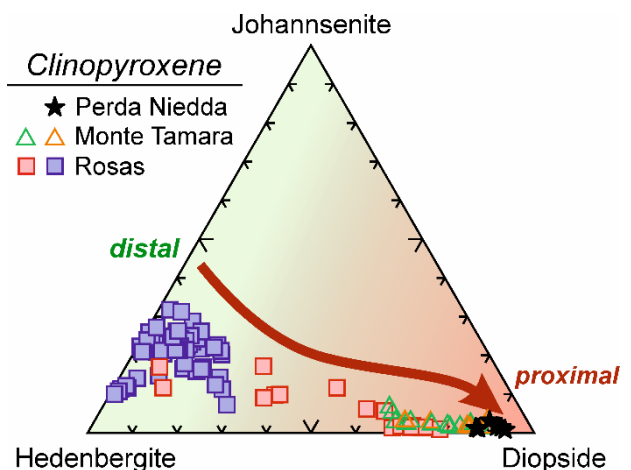


Figure 2. Relative proportions of diopside, hedenbergite and johannsenite endmembers in clinopyroxene from the Perda Niedda, Monte Tamara and Rosas skarn bodies. Higher hedenbergite and johannsenite contents correspond to distal skarns, whereas diopside correlates with proximal skarns (Meinert et al. 2005; Chang and Meinert 2008; Chang et al. 2019)

5.2 Garnet

The composition of garnet from Perda Niedda is andraditic (avg. $\text{Adr}_{96.9}\text{Grs}_{3.1}$), with sporadic

grossular enrichments ($\text{Adr}_{100-40.5}\text{Grs}_{0.00-59.5}$). Similarly, garnet from Monte Tamara is mostly andradite (avg. $\text{Adr}_{93.1}\text{Grs}_{6.9}$), but grossular may attain 63.2% (Deidda et al. 2023). Garnet from Rosas is variably enriched in grossular ($\text{Adr}_{100-25.5}\text{Grs}_{25.5-74.5}$). Tin is remarkably high in green, unaltered garnet from Perda Niedda and Monte Tamara, both with average contents of 1.5 wt% Sn. At Perda Niedda, Sn ranges from 0.2 to around 4 wt%. Tin is lower in garnet cores (avg. 9956 ppm Sn) and becomes moderately higher towards mantle (avg. 2.1 wt% Sn) and rims (avg. of 1.5 wt% Sn; Figure 3a). At Monte Tamara Sn in garnet is in the range 0.02-6 wt%. Similarly, Sn contents increase from cores (avg. 362 ppm Sn) to mantle (1 wt% Sn) and rims (2 wt% Sn; Figure 3b). Garnet from Rosas has markedly lower Sn contents (avg. of 6 ppm and up to 25 ppm).

The average W contents in the three deposits are comparable (113 ppm at Perda Niedda; 491 ppm at Monte Tamara; 82 ppm at Rosas). Garnet from the scheelite-bearing skarn of Monte Tamara attains the highest values of 2800 ppm. Aside from Monte Tamara garnet, tungsten contents tend to be higher in the cores (avg. 132 ppm at Perda Niedda; 9 ppm at Monte Tamara; 161 ppm at Rosas) and to decrease towards mantles (avg. 201 ppm at Perda Niedda; 626 ppm at Monte Tamara; 28 ppm at Rosas) and rims (avg. 71 ppm at Perda Niedda; 515 ppm at Monte Tamara; 37 ppm at Rosas). Indium is within the range 11-126 ppm at Perda Niedda (avg. 57 ppm), 2-110 ppm at Monte Tamara (avg. 31 ppm) and negligible at Rosas (< 1 ppm).

5.3 Epidote

In all studied samples, minerals of the epidote group mainly belong to the epidote ($\text{Ca}_2(\text{Fe}^{3+}, \text{Al})_3(\text{SiO}_4)_3(\text{OH})$) endmember, whereas clinozoisite ($\text{Ca}_2\text{Al}_3(\text{SiO}_4)_3(\text{OH})$) and piemontite ($\text{Ca}_2(\text{Al}, \text{Mn}^{2+}, \text{Fe}^{2+})_3(\text{SiO}_4)_3(\text{OH})$) are subordinate. Average compositions are comparable between Monte Tamara ($\text{Ep}_{77.9}\text{Czo}_{21.6}\text{Pmt}_{0.5}$) and Rosas ($\text{Ep}_{79.1}\text{Czo}_{20.1}\text{Pmt}_{0.9}$). Tin concentrations are remarkably higher at Monte Tamara (339-6688 ppm; avg. 2571 ppm) with respect to the Sn-poor epidote from Rosas (5-552 ppm; avg. 35 ppm). Indium is generally low in both deposits, though more often below the detection limit at Rosas (up to 1 ppm). Moderately higher In values were detected at Monte Tamara (1-42 ppm; avg. 8 ppm). Tungsten occasionally reaches maximum concentrations of 7 ppm at Monte Tamara.

6 Zoning of the Sn-W skarn system

The distance from the causative intrusion is a key-factor in controlling the features of skarn deposits. Typical features of distal skarns include higher proportions of clinopyroxene over garnet, Mn- and Fe-rich clinopyroxene, enrichment in Zn-Pb sulfides (Meinert 1997; Meinert et al. 2005). Conversely, exoskarn formation from F-rich greisen-related

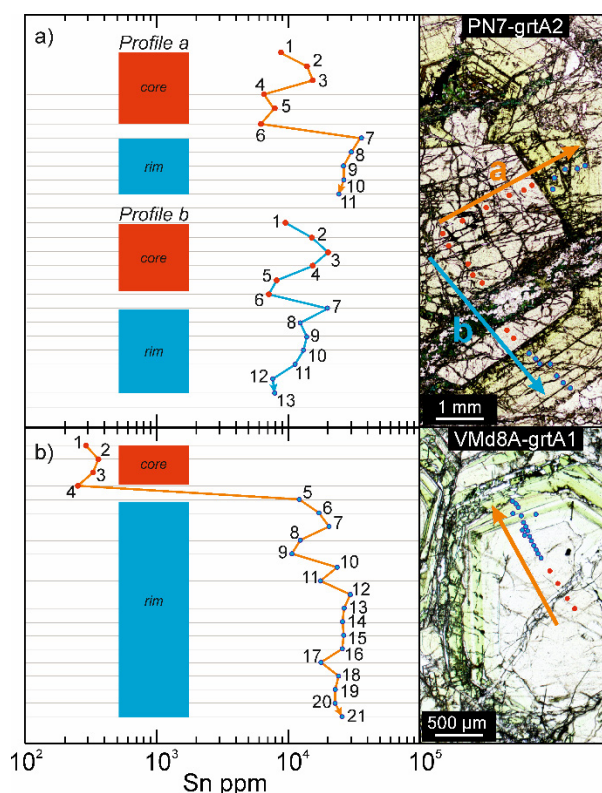


Figure 3. LA-ICP-MS compositional profiles in garnet from Perda Niedda (a) and Monte Tamara (b), showing progressive Sn enrichment from core (red dots) to rim (blue dots).

hydrothermal fluids (Štemprok 1987; Chang and Meinert 2004), abundance of cassiterite (Lehmann 2021) and molybdenite (Chang et al. 2019), the LREE-rich signature of scheelite (Yuan et al. 2019; Deidda et al. 2023) and the Sn-enrichments in garnet and epidote could be indicators for more proximal skarn mineralisation.

The Perda Niedda, Monte Tamara and Rosas represent different parts of a district-scale Sn-W skarn system. Each orebody, though, displays some peculiar features reflecting their formation at different relative distances from the intrusive source. In this view:

1. The Perda Niedda skarn represents the most proximal orebody in the system, as demonstrated by: (a) the exposed contact with GS1 granites; (b) greisen-like/endoskarn alteration accompanied by high fluorine activity; (c) the higher proportion of garnet versus clinopyroxene; (d) Sn and In enrichment in garnet; (e) abundant cassiterite associated with magnetite-fluorite, after garnet alteration; (f) diopsidic clinopyroxene.

2. The Monte Tamara skarn features are between proximal and distal, as indicated by: (a) no clear contact with GS1 granites; (b) scheelite prevails over cassiterite and other Sn-Mo-Bi minerals are found (stannite, molybdenite, native Bi and Bi-sulfosalts); (c) abundant Zn-Pb sulfides; (d) clinopyroxene (diopsidic) more abundant than garnet (f) Sn-rich garnet; (e) high Sn and In epidote.

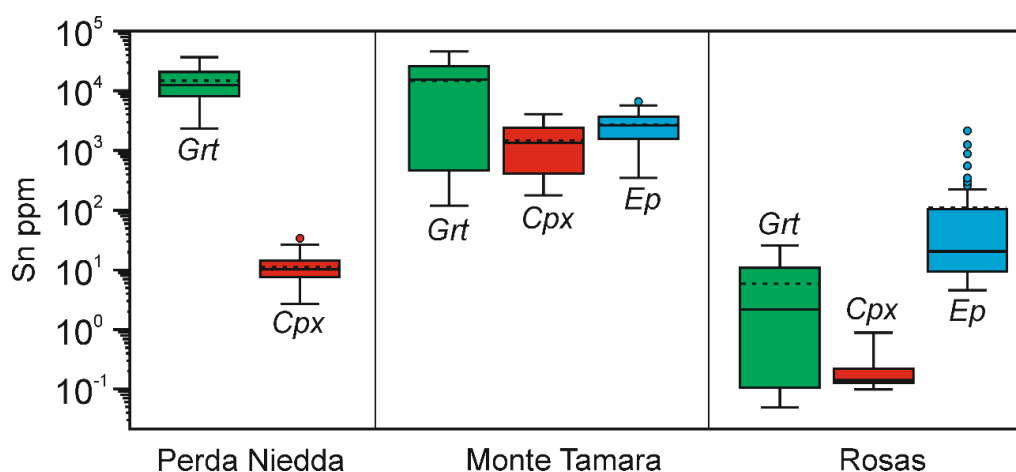


Figure 4. Statistical distribution of Sn in garnet (Grt), clinopyroxene (Cpx) and epidote (Ep) from the Perda Niedda, Monte Tamara and Rosas skarns. Calc-silicates from proximal skarns (Perda Niedda, Monte Tamara) are enriched in Sn if compared to distal skarns (Rosas).

3. Lastly, the Rosas skarn features are indicative of a distal deposit, as suggested by: (a) structural control, favouring extensive infiltration of fluids at larger distance; (b) rare cassiterite, scheelite, Bi-phases and no molybdenite; (c) abundant Zn-Pb sulfides and traces of Ag and Mn sulfides; (d) clinopyroxene more abundant than garnet; (e) hedenbergitic-johannsenitic clinopyroxene; (f) Sn-poor garnet and epidote.

7 Conclusion

All field, mineralogical and compositional evidence highlight the close relationship between the Perda Niedda, Monte Tamara and Rosas skarns and point out the existence of a district-scale Sn-W skarn system in SW Sardinia, strongly related with the GS1 granite intrusive unit. This is supported by the common presence in the orebodies of marker minerals such as cassiterite and, more occasionally, scheelite, Bi-phases, molybdenite and stannite.

Moreover, this work points out that Sn-rich garnet and, to a lesser extent, Sn-rich epidote are important markers for Sn-W mineralisation in skarns of SW Sardinia, similarly to other Sn-W skarn provinces worldwide (e.g., Huangshaping, Erzgebirge, French Massif Central).

In conclusion, our assessment of a zoned, district-scale Sn-W skarn system may have important implications for further and more accurate Sn-W and CRM mineral explorations in the several skarn occurrences in the SW Sardinia district.

Acknowledgements

MLD acknowledges RAS/FdS grant “Sustainable land management: the tools of geology for the environment” (F72F16003080002) and CeSAR (Centro Servizi d’Ateneo per la Ricerca; University of Cagliari).

References

- Boni M, Stein HJ, Zimmerman A, Villa IM (2003) Re-Os age for molybdenite from SW Sardinia (Italy): A comparison with $^{40}\text{Ar}/^{39}\text{Ar}$ dating of Variscan granitoids. *Miner Explor Sustain Dev* 247–250.
- Chang Z, Meinert LD (2004) The magmatic-hydrothermal transition - Evidence from quartz phenocryst textures and endoskarn abundance in Cu-Zn skarns at the Empire Mine, Idaho, USA. *Chem Geol* 210:149–171.
- Chang Z, Shu Q, Meinert LD (2019) Skarn Deposits of China. *SEG Spec Publ* 22:189–234.
- Cocco F, Attardi A, Deidda ML, et al (2022) Passive Structural Control on Skarn Mineralization Localization: A Case Study from the Variscan Rosas Shear Zone (SW Sardinia, Italy). *Minerals* 12:.
- Conte AM, Cuccuru S, D’Antonio M, et al (2017) The post-collisional late Variscan ferroan granites of southern Sardinia (Italy): Inferences for inhomogeneity of lower crust. *Lithos* 294–295:263–282.
- Deidda ML, Naitza S, Moroni M, et al (2023) Mineralogy of the scheelite-bearing ores of Monte Tamara, SW Sardinia: insights for the evolution of a Late Variscan W–Sn skarn system. *Mineral Mag* 87: 86–108.
- Kwak TAP, Askins PW (1981) The nomenclature of carbonate replacement deposits, with emphasis on Sn-F(-Be-Zn) “wrigglite” skarns. *J Geol Soc Aust* 28:123–136.
- Lehmann B (2021) Formation of tin ore deposits: A reassessment. *Lithos* 402–403:105756.
- Meinert LD (1997) Application of skarn deposit zonation models to mineral exploration. *Explor. Min. Geol.* 6:185–208.
- Meinert LD, Dipple GM, Nicolescu S (2005) World Skarn Deposits. *Economic Geology One Hundredth Anniv Vol* 299–336.
- Naitza S, Conte AM, Cuccuru S, et al (2017) A Late Variscan tin province associated to the ilmenite-series granites of the Sardinian Batholith (Italy): The Sn and Mo mineralisation around the Monte Linas ferroan granite. *Ore Geol Rev* 80:1259–1278.
- Paton C, Hellstrom J, Paul B, et al (2011) Iolite: Freeware for the visualisation and processing of mass spectrometric data. *J Anal At Spectrom* 26:2508–2518.
- Štemprok M (1987) Greisenization (a review). *Geol Rundschau* 76:169–175.
- Yuan L, Chi G, Wang M, et al (2019) Characteristics of REEs and trace elements in scheelite from the Zhuxi W deposit, South China: Implications for the ore-forming conditions and processes. *Ore Geol Rev* 109:585–597.

Trace element and sulphur isotope composition of selected minerals from the W-Mo porphyry deposit Ochtiná-Rochovce

Diego Delgado Yáñez¹, Peter Koděra¹, Manuel Keith², Frederik Börner², František Bakos³

¹ Department of Mineralogy, Petrology and Economic Geology, Comenius University in Bratislava, Ilkovičova 6, 84104 Bratislava, Slovak Republic,

² GeoZentrum Nordbayern, Friedrich-Alexander-Universität Erlangen-Nürnberg (FAU), Schlossgarten 5, 91054 Erlangen, Germany

³ Green View, s.r.o., Rigeleho 1, 811 02 Bratislava, Slovakia

Abstract. Porphyry W-Mo deposits are rare occurrences in the Earth crust and Ochtiná-Rochovce is the only one of its kind in the Western Carpathians. Lithological, mineralogical and veinlet descriptions, complemented by LA-ICP-MS trace element analysis and S isotope measurements of sulphide separates are indicative for a shift from reduced to oxidized conditions during the system evolution. Low Se and Te contents in both molybdenite and pyrite are related to the formation of these minerals at high temperatures, while decreasing Co in pyrite from early to late formed veinlets is related to decreasing temperature. High Nb contents in scheelite, wolframite and rutile reflect more oxidized conditions, while high contents of W, V, Nb and Cr in rutile suggest its hydrothermal origin. The S isotope composition of both molybdenite and pyrite of different generations suggests magmatic-hydrothermal origin of the fluids.

1 Introduction

The W-Mo deposit at Ochtiná-Rochovce (Slovakia) hosts a porphyry-type mineralisation, associated with a Late Cretaceous granite complex emplaced in the Lubeník-Margecany suture line (Bakos *et al.* 2016, Kohút *et al.* 2013). Bakos *et al.* (2016) estimated the resources at 5.0 Mt W ore and 2.4 Mt Mo ore at grades of 0.2% for both metals.

The deposit is hosted in a set of metasedimentary and metabasic rocks such as metasandstones, micaschists, phyllites and metabasalts, belonging to the Ochtiná, Rimava and Slatvina Formations, ranging from Lower Carboniferous to Permian age (Vozárová and Vozár 1988). The mineralisation is divided into a lower molybdenite zone and an upper wolframite-scheelite zone, other ore minerals found in the deposit are pyrite, chalcopyrite, pyrrhotite, among others (Lörincz *et al.* 1993; Bakos *et al.* 2016). The hydrothermal alteration has been described as concentric, including K-alteration, silicification, sericitisation, chloritisation and late carbonatisation.

Delgado *et al.* (2021) recognize pyrite with inclusions of chalcopyrite, pyrrhotite and galena, hosted in quartz-molybdenite, quartz-wolframite-scheelite and quartz veinlets, as well as veinlets purely formed by pyrite. The related EMPA-WDS results on pyrite from different generations did not show any compositional differences. The same study showed that scheelite commonly replaces wolframite, where the latter contains up to 7 wt. %

MgO; similar values were found by Ferenc and Uher (2006). Previous studies (e.g., Bendel, 2017; Ebel, 2021) showed that this mineral contains zones enriched in WO₃ reaching ~17 wt. % with average of 0.5-1 wt. % WO₃.

This work aims to provide an updated lithological, mineralogical, and geochemical characterisation and provides new insights into genetical characterisation of the mineralising fluids by trace element and sulphur isotope data of selected ore minerals.

2 Methodology

Approximately 40 drill core samples were described both macro- and microscopically to classify them by lithology, alteration, and veinlet types. A total of 16 selected samples with variable degrees of alteration, were analysed by whole rock X-ray diffraction (XRD) at the Earth Institute of the Slovak Academy of Sciences in Bratislava. Mineral abundances were quantified by the RockJock 11 software.

The major element composition of selected ore minerals was determined by a JEOL JXA-82000 superprobe at GeoZentrum Nordbayern and followed by in-situ laser ablation inductively coupled plasma mass spectrometry (LA-ICP-MS) for trace elements.

The trace element composition of selected minerals was determined by LA-ICP-MS analyses of minerals by a Teledyne Analyte Excite 193 nm laser attached to an 7500c quadrupole ICP-MS. The measurements were performed in spot mode using 35 microns. Smaller beam diameters were occasional used for smaller minerals. For molybdenite and pyrite the external standards MASS-1 (USGS), Po724 B2 SRM, (Fe, Ni)_{1-x}S and UQAC-FeS-1 were used. The wolframite, scheelite and rutile measurements were standardized by NIST SRM 610 and GSE-1G. Previous EMPA-WDS results on the same spots were used as internal standards: S for sulphides, Ca for scheelite, Fe for wolframite, Ti for rutile. Statistical parameters such as geometrical mean (GM) and its corresponding standard deviation (GSD) were calculated. The ranges shown in these results are based on both parameters and represent where 2/3 of the values

fall. Anomalous analyses related to micro-inclusions were discarded.

Sulphur isotope analyses of molybdenite and pyrite separates were performed using a Finnigan MAT 253 IR-MS at the Earth Institute of the Slovak Academy of Sciences in Banks Bystrica, with analytical errors between 0.15-0.20 ‰. This was complemented with data from Lőrincz *et al.* (1993) and unpublished results done by the Slovak State Geological Institute Dionýz Štúr. The median (mdn.) was calculated, and the ranges limits shown correspond to the first and third quartile.

3 Lithologies and their alterations

The main lithology in the study area corresponds to a well-foliated micaschist affiliated to the Ochtiná Formation, that includes muscovite intercalated with quartz-plagioclase bands. According to whole rock XRD analyses, the least altered samples contain 35-65 wt. % quartz, 20-50 wt. % muscovite and plagioclase <10 wt. %. The early potassic alteration is manifested by biotite (<30 wt. %) replacing muscovite and K-feldspar (<5 wt. %) altering plagioclase, while silicification lead to high quartz content of up to 70 wt. %. Chloritisation with up to 25 wt. % chlorite accompanied by minor epidote replaces plagioclase and secondary biotite. Argillitisation dominated by illite is found close to major quartz veinlets, rarely reaching clay abundances of up to 15 wt. %.

The previously reported 'metabasalts' are indeed amphibolite, locally accompanied by peridotite, intercalated in the micaschist of the Ochtiná Formation. Amphibolite contains 30-40 wt. % actinolite, ~30 wt. % plagioclase, and <10 wt. % pyroxene. It is affected by the same alteration styles, as described above for the micaschist, including K-alteration dominated by biotite (up to 20 wt. %), slight silicification and chloritisation ± epidote (up to 10 wt. %), replacing both earlier-formed amphibole and biotite. Previous alterations are overprinted by argillitisation dominated by smectite with total clays abundances of up to 10 wt. %. Peridotite was not analysed by XRD, but the microscopical description allows to estimate the olivine and pyroxene contents between 20-40 wt. vol % for each mineral, that occur in association with magnetite (< 20 vol. %), possibly derived from olivine decomposition, and undifferentiated serpentines (< 10 vol. %). Pyroxene and olivine are strongly altered to serpentine and chlorite.

The deepest parts of the system consist of an early foliated metasandstone of the Rimava Formation, which is characterised by quartz (60-75 wt. %) that is associated with feldspar and muscovite summing 25-40 wt. %. Low to moderated argillitisation dominated by illite (< 10 wt. %), as well as minor biotite and chlorite (both < 2 wt. %) was determined.

4 Veinlets

The main mineralisation at the deposit is hosted by at least 4 different types of veinlets: quartz-molybdenite±pyrite (1), pyrite±quartz (2), pyrite-scheelite (3) and quartz-wolframite-scheelite-pyrite (4). The early molybdenite-containing veinlets are associated with two quartz generations, namely coarse-grained (0.3-10 mm length) and fine-grained (<0.2 mm length) quartz. Molybdenite is observed as disseminated flakes of 0.3-0.5 mm length in the centre of the veinlets and as finer grained crystals (~0.2 mm length) following cracks in orientation, which is related to the second generation of quartz. This veinlet type locally also contains disseminated pyrite (up to 20 mm) and is accompanied by K-alteration and silicification hosted by micaschist and metasandstone.

Later pyrite-dominated veinlet type is filled by later fine-grained quartz (reaching up to 30 vol. %), are hosted by amphibolite and rarely also micaschist. This veinlet type contains traces of chalcopyrite and pyrrhotite and is accompanied by K-alteration halos, marked by K-feldspar and biotite. No crosscutting relationships were observed between the molybdenite and pyrite veinlets.

The main W-mineralisation is hosted by two types of veinlets. The first one is a pyrite-dominated type hosted by amphibolite, which contains rounded scheelite crystals up to 5 mm in length, rare chalcopyrite and bismuthinite inclusions, and minor quartz. Its alteration halo includes secondary biotite, and late chloritisation and argillitisation. The second group of W-bearing veinlets is characterised by scheelite replacing elongated disseminated wolframite crystals (up to 30 mm long), hosted by micaschist and crosscutting the pyrite±quartz veinlets. Disseminated pyrite inclusions in wolframite are frequent, and this veinlet type also rarely contains molybdenite and muscovite. Bimodal quartz was observed in these veinlets: coarse-grained quartz at the veinlet centres and a finer quartz precipitating at the veinlet margins.

5 Trace elements in selected minerals

Two samples containing molybdenite were analysed by LA-ICPMS: one from a quartz-molybdenite-pyrite veinlet (pyrite in this sample was also analysed) while the other one from the same veinlet type but lacking pyrite and hosted in micaschist.

The LA-ICPMS results indicate that the main trace elements in molybdenite are Fe, Pb, As and Sb. Iron has apparently different contents in the two analysed samples: 84-1043 ppm Fe (GM=297) in the first sample, and 25-82 ppm Fe (GM=45) in the other sample. For all analysed spots, Fe strongly correlates with As ($r=0.92$) and Sb ($r=0.74$). Bismuth and nickel are also highly correlated in molybdenite ($r=0.84$); while if plotted versus Fe+As+Sb to enables to distinguish molybdenite according to its trace element composition (Fig. 1A). Besides Fe, molybdenite in the quartz-molybdenite-pyrite veinlet is also richer in As (2-324 ppm, GM=27) compared to the other sample (2-6 ppm, GM=3) in the quartz-

molybdenite veinlet. Complementary, Re, Se and Te do not exceed 40, 87 and 5 ppm in molybdenite, respectively.

Pyrite from the quartz-molybdenite-pyrite (Py1), pyrite (Py2), pyrite-scheelite (Py3) and quartz-wolframite-scheelite (Py4) veinlets were analysed. Manganese, Co and Ni are generally the most abundant trace elements in pyrite (Fig. 1B). Py2 contains 38-1240 ppm Co+As (GM=216), while the other generation ranges 12-202 ppm Co+As (GM=49). Pyrite 2 is also enriched in Ni (45-475 ppm, GM=145) compared to the other pyrite generation (4-164 ppm, GM=27). Additionally, both As and Se are usually below 55 ppm in all pyrite generations.

Scheelite replacing wolframite shows high concentrations of Mn and Fe (up to 2 wt. % Fe+Mn), and it is easily differentiated from scheelite occurring in the pyrite veinlets, where Fe+Mn do not exceed 0.02 wt. %. The two scheelite generations can be distinguished by their LREE, HREE, Nb and Sr contents (Fig. 2). Scheelite in the pyrite veinlets is particularly enriched in both LREE (737-3495 ppm, GM=1605) and HREE (352-1407 ppm, GM=704) compared to scheelite replacing wolframite (LREE: 55-1420 ppm, GM=279; HREE: 2-420 ppm, GM=116).

Wolframite is not particularly enriched in any trace element. Ti and Nb have geometrical means close to 30 ppm, while HREE GM=20 ppm (Fig. 2).

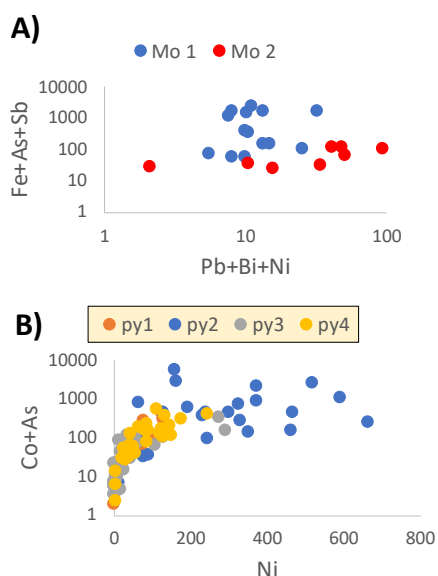


Figure 1. Graphs to discriminate different generations of sulphides by trace elements (in ppm). **A)** Pb+Bi+Ni vs. Fe discriminating Fe-rich molybdenite in quartz-pyrite veins (Mo1) and molybdenite in pyrite-free quartz veins (Mo 2). **B)** Ni vs. Co+As showing the difference among Co-Ni rich pyrite in pyrite veinlets (Py2) and other pyrite generations related to molybdenite (Py1), scheelite (Py3) and wolframite-scheelite (Py4), which are depleted in all those elements.

EMPA-WDS analyses of rutile showed high concentrations of V (0.45-0.9 wt. complement that other important trace elements are Nb, Cr and W. These elements are not correlated and range

between 692-2283 ppm Nb, 1789-4600 ppm W, and 142-1460 ppm Cr. Other important trace elements in rutile are Sn (GM=645 ppm), Zr (GM=93 ppm) and Ta (GM=72 ppm). LREE in rutile tend to be higher than HREE, but do not exceed 60 ppm in general. % GM=0.7), while LA-ICPMS results for the same mineral

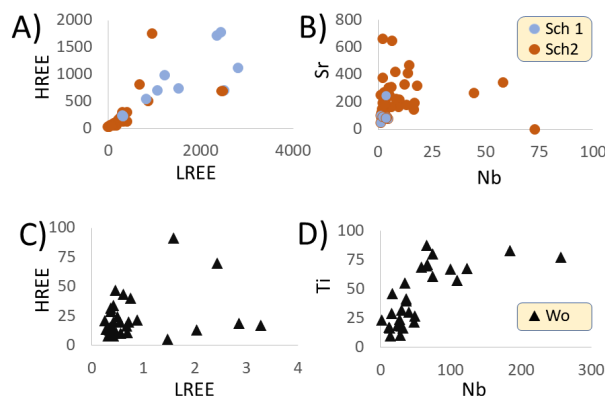


Figure 2. Selected trace elements compositions (all in ppm) of scheelite (Sch) and wolframite (Wo). **A)** LREE vs. HREE for scheelite, showing enrichment in both scheelite replacing wolframite (Sch 2) and scheelite in pyrite veinlets (Sch 1). **B)** Nb vs. Sr differentiates both scheelite generations. **C)** LREE vs. HREE in wolframite, displaying their low contents. **D)** Nb vs. Ti in wolframite, showing a positive correlation.

6 Sulphur isotopic composition

The S isotope values of molybdenite range between -1.0 to -0.4 ‰ (mdn, -0.6 ‰), which distribution is shown in Fig. 3. The $\delta^{34}\text{S}$ values in pyrite do not show a significant difference among the veinlet types, as all pyrite generations have most of values in the range 0 ± 0.4 ‰. Exceptions are one outlier with $\delta^{34}\text{S}$ 3.2‰ was found in a deep sample representing a quartz-molybdenite-pyrite veinlet hosted by parental granite at ca. 500 m depth and two vales (1.5 and 1.9 ‰) related to quartz-wolframite-scheelite-pyrite veinlets closer to surface.

7 Discussion and conclusions

As pyrite and pyrite-scheelite veinlets mainly occur in amphibolite hosted by muscovite-micaschist it is probable that this rock-type be related to the ore mineralisation. Amphibolite has likely released Ca^{2+} during the potassic alteration to generate scheelite in the pyrite-scheelite veinlets.

Textural evidence of quartz in molybdenite-bearing veinlets and the contrasting Fe concentrations in molybdenite suggest that it was formed in two stages, with the later one affected by enrichment of fluids in Fe, precipitating molybdenite in cracks with up to 1500 ppm of Fe, and fine-grained quartz. The abundance of Pb, As, Sb in molybdenite in contrast to Re, Se, Te could be related to increased fluid temperatures (> 300 °C) as suggested by Pašava *et al.* (2016). The lack of W in

molybdenite can be linked to reduced conditions of this mineralisation stage, according to the same authors. Wang *et al.* (2021) relate increasing Co in pyrite with increasing fluid temperatures, thus the pyrite veinlets could have been formed at higher temperatures than pyrite in the molybdenite- and W-bearing veinlets. Studied pyrites from 4 different generations of veinlets show lower Se and Te contents compared to a similar porphyry Mo-Cu-W deposit Myszków in Poland (Naglik *et al.* 2022), which can indicate relatively higher temperatures (> 400 °C) and dominantly reduced fluid (Keith *et al.* 2018). Both scheelite and wolframite are enriched in Nb, which can reflect a shift from reduced conditions related to earlier sulphide-rich veinlets to more oxidised conditions linked to W precipitation (Damian *et al.* 2006). In scheelite, Nb⁵⁺ and REE³⁺ can be incorporated by coupled substitution replacing Ca²⁺ and W⁶⁺ (Song *et al.* 2019).

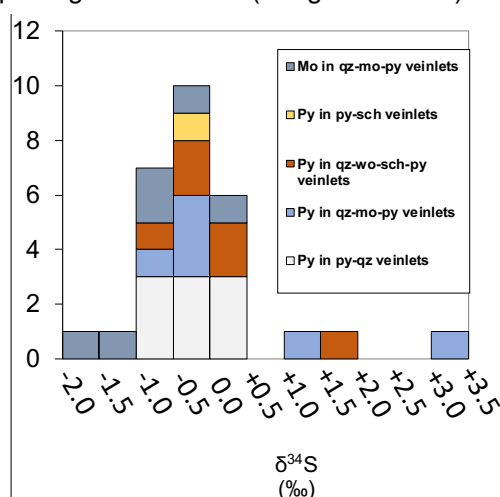


Figure 3. Histogram of sulphur isotopic composition of molybdenite and pyrite. Most of the values do not show significant variation among different veinlet generations.

The presence of high W and Nb contents in rutile, occurring close to W-bearing veinlets, indicate a genetic link to the tungsten mineralisation. The lower LREE content in rutile compared to scheelite can be explained by preferential incorporation of LREE in scheelite by substitution of Ca²⁺.

The S isotope data are indicative of mostly well-homogenised fluids of magmatic-hydrothermal origin, typical for porphyry type of deposits (Shanks 2014) that enriched in δ³⁴S towards the surface due to increasing water-rock interaction Wilson *et al.* 2006).

Acknowledgements

This work was supported by the Comenius University Grant for Doctoral Students UK/107/2021 and an Erasmus+ short stay scholarship at the GeoZentrum Nordbayern Erlangen in Germany. Special thanks to Dr. Helene Brätz for guiding the LA ICPMS work and its data reduction.

References

- Bakos, F., Jánošík, M. and Sýkora, M. (2016): Final report with reserves calculations - Ochtiná W, Mo, Re mineralisation. GreenView report: 38 p (in Slovak)
- Bendel, M. (2017): Mineralogical and technological description of the tungsten ore of Ochtiná, Slovakia (MSc thesis, Friedrich Schiller University Jena, Germany): 88 p.
- Damian, G., Damian, F., Konečný, P., and Kollárová, V. (2016). A new occurrence of wolframite-ferberite in Romania; *Romanian Journal of Mineral Deposits*, v. 89, p.49-54.
- Delgado, D., Koděra, P., and Bakos, F. (2021): Advances in lithological, mineralogical, and geochemical characterization of the W-Mo porphyry deposit Ochtiná-Rochovce. In: *Proceeding from the conference Geochémia 2021*, p. 131-135.
- Ebel, H. (2021). Mineralisation of the Kyslá Au-W and Ochtiná W-Mo deposits, Central Western Carpathians, Slovakia (MSc thesis, Eberhard Karls University Tuebingen, Germany), 69 p.
- Ferenc, S., and Uher, P. (2006): Magnesian wolframite from hydrothermal quartz veins in the Rochovce granite exocontact, Ochtiná, Western Carpathians, Slovakia. *Neues Jahrbuch für Mineralogie-Abhandlungen*, v. 183(2), p. 165-172.
- Hoefs J. (2009). *Stable isotope geochemistry*. Springer-Verlag, Berlin Heidelberg, 285 p.
- Keith, M., Smith, D. J., Jenkin, G. R., Holwell, D. A., and Dye, M. D. (2018): A review of Te and Se systematics in hydrothermal pyrite from precious metal deposits: Insights into ore-forming processes. *Ore Geology Reviews*, v. 96, p. 269-282.
- Kohút, M., Stein, H., Uher, P., Aimmerman, A., and Hraško, L. U. (2013): Re-Os and U-Th-Pb dating of the Rochovce granite and its mineralisation (Western Carpathians, Slovakia). *Geologica Carpathica*, v. 64(1), p. 71-79.
- Lörincz, L., Švantnerová, E., and Bachňák, M. (1993): Final report: Ochtiná-Rochovce Mo, W, exploration survey, status at 30.9.1993. MS, archive Geofond, Bratislava, 79365, 225 pp (in Slovak).
- Naglik, B., Toboła, T., Dumanska-Słowik, M., Dimitrova, D., Derkowski, P., Zielinski, G., Habryn, R. & Nadlonek, W. (2022). Multi-stage ore forming history of the Variscan porphyry Mo-Cu-W Myszków deposit (Poland): evidence from trace elements of pyrite. *Ore Geology Reviews*, 105185.
- Pašava, J., Svojtka, M., Veselovský, F., Ďurišová, J., Ackerman, L., Pour, O., Dábek, M., Halodová, P. and Haluzová, E. (2016): Laser ablation ICPMS study of trace element chemistry in molybdenite coupled with scanning electron microscopy (SEM) - an important tool for identification of different types of mineralization. *Ore Geology Reviews*, v. 72, p. 874-895.
- Shanks, W. (2014): *Stable Isotope Geochemistry of Mineral Deposits. Treatise on Geochemistry (Second edition)*, Elsevier Ltd.: Amsterdam, The Netherlands, pp 59-82.
- Song, G., Cook, N. J., Li, G., Qin, K., Ciobanu, C. L., Yang, Y., and Xu, Y. (2019): Scheelite geochemistry in porphyry-skarn W-Mo systems: A case study from the Gaojiabang Deposit, East China. *Ore Geology Reviews*, v. 113, 103084.
- Vozárová, A., and Vozár, J. (1988): Late Paleozoic in Western Carpathians. *Slovak Geological Survey, Bratislava*: 314 pp.
- Wang, K., Zhai, D., Liu, J., and Wu, H. (2021): LA-ICP-MS trace element analysis of pyrite from the Dafang gold deposit, South China: Implications for ore genesis. *Ore Geology Reviews*, v. 139, 104507.
- Wilson, A. J., Cooke, D. R., Harper, B. J., & Deyell, C. L. (2007). Sulfur isotopic zonation in the Cadia district, southeastern Australia: exploration significance and implications for the genesis of alkalic porphyry gold-copper deposits. *Mineralium Deposita*, 42, 465-487.

Hydrothermal alteration zonation and Au-Cu footprint of the New York breccia pipe, Ok Tedi, PNG

Jerry Dunga¹, Steffen G. Hagemann¹, Peter J. Pollard² and Marco L. Fiorentini¹

¹Centre for Exploration Targeting, School of Earth Sciences, University of Western Australia, CRAWLEY, WA, 6009, Australia.

²Pollard Geological Services Pty Ltd. Brisbane, Queensland, 4061, Australia.

Abstract. Preliminary findings from field mapping, core logging, assaying, and petrographic analysis of the large (400m by 1500m), deep seated (>1500m) New York breccia pipe adjacent to the Ok Tedi porphyry/skarn deposit indicate that: 1) the breccia itself and gold mineralisation display a significant vertical extension (>1500m); 2) early igneous breccias are overprinted by hydrothermal breccias, which are characterised by abundant hydrothermal infill and late brecciation affecting previously formed breccias (i.e. evidence of multiple brecciation events); 3) there is a strong vertical zonation, which is reflected in the presence of shallow base metal rich sulphides (galena-sphalerite) and gold with crosscutting epithermal-style quartz-rhodochrosite veins, and deep chalcopyrite-magnetite-pyrrhotite mineralisation in veins and breccias with carbonate-adularia alteration; 4) there is a distinct zonation in sulphide and oxide mineral assemblages, which is reflected in the occurrence of shallow pyrite-marcasite-hematite assemblages compared to pyrrhotite-magnetite at depth; and 5) there is evidence for long distance transportation of brecciated clasts, reflected in the presence of fragments of a mapped sandstone formation that underlies a thick (1.5-2.0km) siltstone unit which hosts the breccia. The hydrothermally zoned breccia pipe at New York, Ok Tedi, could represent the continuation of deeper porphyry mineralisation into epithermal environments.

1 Introduction

Breccia-hosted Au±Cu mineralisation in porphyry systems are discovered globally, represent extremely valuable targets, but have so far been poorly documented in terms of their morphologies and internal metallogenic structures. These breccias generally occur as steep, pipe-like bodies that are formed at the top of intrusions; they are often associated with high grade Cu-Au mineralisation (>1.5 %Cu, and > 2g/t Au¹) and show distinct zonation in ore mineralogy, hydrothermal alteration and brecciation style, displaying different fragment forms, both laterally and vertically.

Porphyry-related breccias are also delineated at Ok Tedi, a world-class porphyry/skarn Cu-Au deposit in Papua New Guinea. Although these breccias constitute a key host rock to mineralisation, they are seldom documented. Arnold and Fitzgerald (1977) first noted that brecciated rocks surrounding the Fubilan Quartz Monzonite Porphyry make up 10 to 20 % of the rocks in the Mt. Fubilan area. Few workers (e.g., Weinberg and van Dongen, unpublished report) briefly described them. Pollard (2014) appreciated the importance of breccias and noted how they control Cu-Au grade distribution at Ok Tedi. In their geochemical and geochronological

studies, Large et al. (2018) indicated that brecciation at Ok Tedi is late, and presumably, not ore-bearing, despite Pollard's (2014) observations of the strongly mineralised nature of brecciated rocks within the Fubilan Quartz Monzonite Porphyry.

The New York breccia pipe constitutes a recently discovered (2017) large breccia pipe (400m by >1500m) within 2km of the world-class Ok Tedi porphyry/skarn Cu-Au deposit (Erceg and Pollard 2020). This breccia pipe contains significant gold mineralisation, displays hydrothermal alteration zonation, and indicates evidence of shallow epithermal to deeper porphyry-style mineralisation. The relative and absolute timing, hydrothermal alteration, Cu-Au footprint and the breccia's genetic relationship to the Ok Tedi deposit remain unknown.

In this research, we make a significant contribution to the understanding of mineralised breccia pipes by studying in detail the New York breccia pipe that not only contains significant gold mineralisation, but also shows a close spatial relationship to the world-class porphyry Cu-Au and skarn deposit at Ok Tedi, Papua New Guinea.

2 Geological Setting

The Ok Tedi/Mt. Fubilan porphyry Cu-Au deposit, by comparison to other similar major deposits globally, is an exceptionally young system (1.1-1.3 Ma; Page and McDougal 1975, Large et al. 2018; Pollard et al. 2021). The deposit is located towards the far west of mainland New Guinea (Fig. 1). It lies between the north-west trending Papuan Fold and Thrust Belt (part of the Australian Craton) and the New Guinea Orogenic Belt (part of the oceanic island arc of the Pacific Plate). Regions between the belts are intruded by small but prospective Miocene to Pleistocene intrusions that are responsible for Cu-Au mineralisation in areas including Ok Tedi, Frieda River, Yanderra, Kainantu and the Wafi-Golpu deposits. Magmatism responsible for these intrusions is interpreted to be localised in zones of low stress, as a result of movement of the Pacific and Australian plates (Bamford 1972).

The Mt. Fubilan deposit is located within Tertiary (Oligocene to Mid-Miocene) medium- to fine-grained clastic sedimentary rocks that are up to 1000m in thickness in areas near the Mt. Fubilan deposit (Fig. 1). They have been subdivided into three rock groups based on lithology and regional stratigraphy (Bamford 1972). The first group includes the lower unit of intercalated siltstones and

sandstones, a second, middle unit of relatively pure limestone, and a third, upper unit of siltstones and sandstones, corresponding to the Ieru Formation, the Dari Limestone, and the Pnyang Formation, respectively.

The Ieru Formation is part of the Feing Group; it is of Jurassic to Late Cretaceous age (Arnold and Griffin 1978) but may be as young as Paleocene or early Eocene in places (Davies and Norvick 1974). It is composed of gray or gray-green, fine-grained sandstones, siltstones, and mudstones. The Toro Sandstone is also part of the Feing Group. It is the older of the two and consists of clean, partly glauconitic sandstones.

The Darai Limestone consists of massive to thick-bedded carbonates. It is late Eocene to middle Miocene in age. The formation varies from 500 to 1300m in thickness but is significantly thinner (about 240m) in the Mt. Fubilan area (Davies and Norvick 1974).

The Pnyang Formation consists of soft gray calcareous mudstones and siltstones with minor limestone interbeds (Davies and Norvick 1974). It is middle Miocene in age (Hill, 1989). The Pnyang Formation is locally about 1000m in thickness but increases to the west of the Ok Tedi mine area (Fookes et al. 1991).

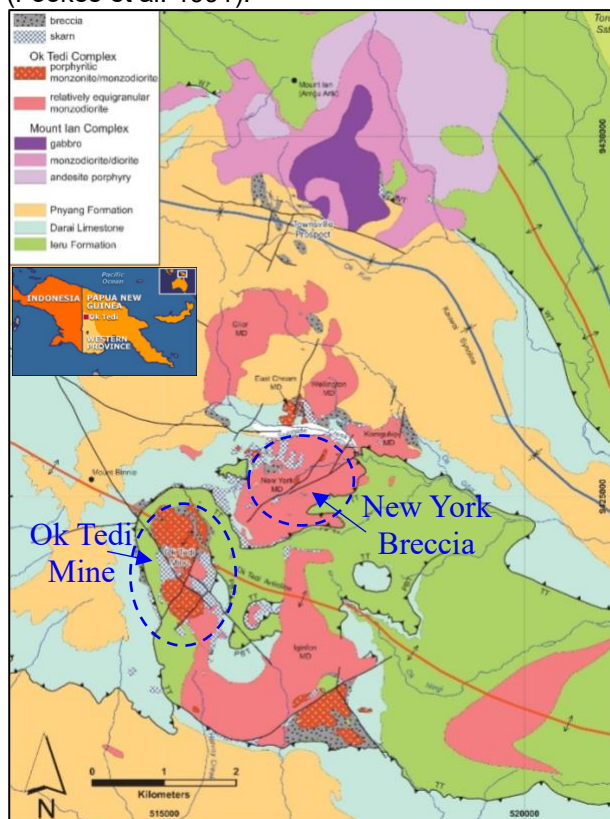


Figure 1. Geological map of the Ok Tedi district with circles indicating the location of the Ok Tedi deposit and the New York breccia pipe. The inset shows the location of the Ok Tedi Mine (Figure adapted and modified from Pollard et al. 2021).

Most of the sedimentary rocks are folded, faulted and intruded by numerous Pliocene to Pleistocene intrusive rocks that are distributed along the flanks of the fold belt. Most of these intrusions are small

(several square kilometres outcrop) and are of quartz-dioritic to monzonitic in composition. Two of these intrusions host significant high-grade copper, gold and silver ores that define the Mt. Fubilan deposit. These are the Fubilan Monzonite Porphyry, located in the northern part of the pit, and the Sydney Monzodiorite located to the south. Most of the Cu-Au ore occurs as disseminated mineralisation within the intrusions, adjacent sedimentary rocks, and as massive magnetite-sulphide skarns located at the contacts of the intrusions and limestone units (Fig. 1).

The Ok Tedi deposit is closely associated with two N-dipping thrust faults; the Parrots Beak thrust, and the Taranaki thrust. Both are suggested to have caused a vertical repetition of Darai Limestone and Ieru Siltstone and to have experienced pre- and post-mineralisation movements (Mason 1997; Van Dongen et al. 2013).

3 Breccia characteristics and hydrothermal alteration zonation

3.1 Stages of brecciation at the New York breccia pipe

The New York breccia pipe is a large (400m by >1500m), deep-seated (>1500m) breccia body that contains significant Au-Cu mineralisation. Field mapping, core logging and detailed petrographic analysis reveal two main stages of brecciation at the New York breccia pipe. The earliest (stage 1) is characterised by well-rounded to sub-angular, polymictic monzodioritic and porphyritic dike clasts cemented by igneous quartz and plagioclase matrix. The clast sizes range from mm-scale to 20cm fragments with predominantly matrix support (Fig. 2A, 2B). Rock flour is locally present.

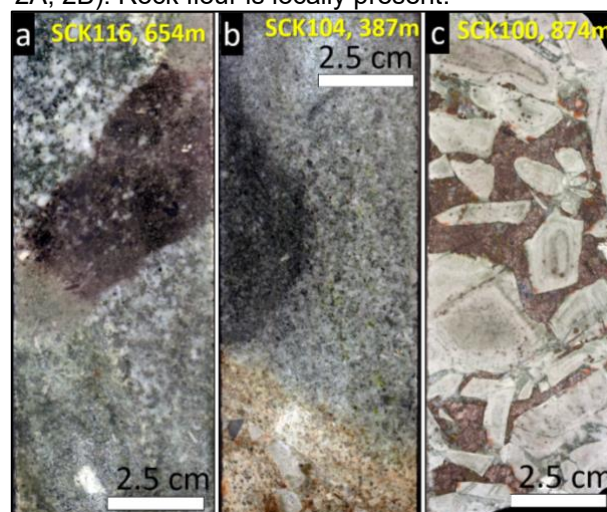


Figure 2. Photographs showing breccia stages within the New York breccia pipe. **a:** Igneous breccia. **b:** Igneous breccia (mafic clast) overprinted by hydrothermal breccia (brownish discolouration at the bottom). **c:** Hydrothermal breccia dominated by siltstone clasts and cemented by pyrrhotite matrix.

The second breccia stage is characterised by hydrothermal matrix (chlorite, calcite, quartz,

adularia, pyrite, pyrrhotite and magnetite) and clasts that are predominantly monomictic. They comprise either siltstone or monzodiorite. Locally, the presence of sandstone clasts, which are stratigraphically 1.5 to 2km beneath the siltstone units, are observed within the breccia. Fragments are angular to sub-rounded, ranging in sizes from mm-scale to 10cm and cemented by rock flour and hydrothermal matrix (Fig. 2B, 2C).

3.2 Vertical zonation of the New York breccia pipe

The New York breccia pipe shows distinct vertical zonation in breccia morphology, ore mineralogy, and hydrothermal alteration mineral assemblages.

Hydrothermal breccia dominates the upper 1000m of the breccia pipe, followed by igneous breccia at depth. At shallow depth (<400m), the hydrothermal breccia is dominated by angular, clast-supported fragments, which gradually become tabular, sub-rounded to well-rounded at depth. Clast composition also changes from monomictic, clast-supported siltstone fragments at shallow regions (<800m) to polymictic (siltstone, felsic dikes, mafic porphyritic dikes and monzodiorite), clast to matrix supported fragments below 800m depth (Fig. 3).

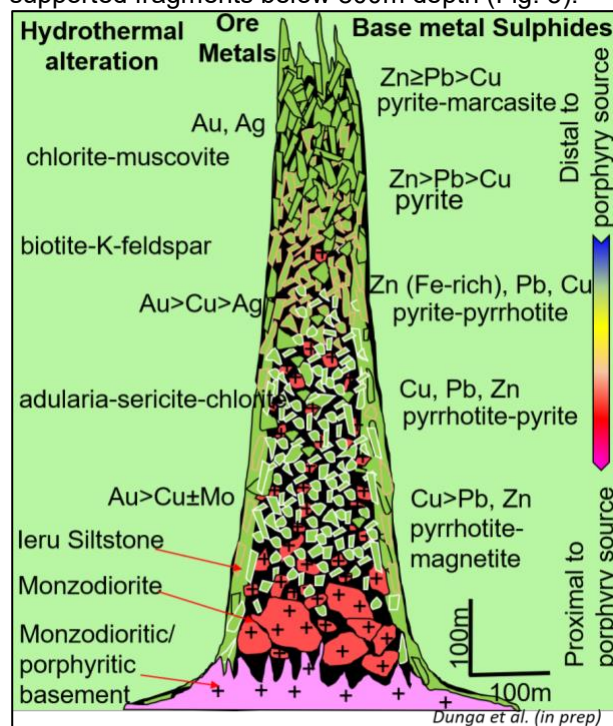


Figure 3. Schematic vertical section through the New York breccia pipe showing vertical hydrothermal alteration zonation, assemblages and metal distribution (drawn using insights from Kirwin 2018).

Clasts of igneous breccias within the hydrothermal breccias are dominant below 800m depth of the breccia pipe. In this zone, sub-rounded to well-rounded fragments of mafic intrusive rocks, felsic dikes and monzodiorite clasts are cemented by quartz and plagioclase matrix. This igneous breccia is then overprinted by hydrothermal breccias (Fig. 2B, 2C). The bottom of the igneous breccia is not

intersected by any of the deep (1400m) diamond drill holes yet. However, the extent of the mineralised hydrothermal breccia, even below the 1400m depth, reflects the significant depth of the New York breccia pipe.

The New York breccia pipe also shows strong vertical zonation in ore minerals indicated by shallow, base metal-rich sulphides (galena-sphalerite) and gold-silver with crosscutting epithermal quartz-rhodochrosite veins, and deep magnetite-pyrrhotite-chalcopyrite mineralisation with carbonate-adularia-quartz-chlorite infill (Fig. 2). There is also a distinct zonation in sulphide and oxide mineral assemblages reflected by shallow pyrite-marcasite-hematite compared to pyrrhotite-magnetite assemblages at depth. Hydrothermal alteration zonation ranges from chlorite-muscovite at shallow depth (<300m) to biotite-K-feldspar (between 300 – 400m depth), followed by adularia-chlorite-sericite below 500m depth (Fig. 3).

3.3 Stages of hydrothermal alteration and gold mineralisation

Three main stages of Cu-Au mineralisation are distinguished at the New York breccia pipe. Stages 1 and 2 are related to hydrothermal breccia mineralisation, whereas the final stage is related to thrust-controlled skarn mineralisation.

The first stage is defined by disseminated pyrite-magnetite within wall-rocks to massive and vein-filling pyrrhotite-pyrite-magnetite mineralisation as breccia infills and in thick (5-10cm) veins. Fibrous chlorite, quartz, calcite and ankerite define the gangue minerals (Fig. 4A, 4B). Hydrothermal alteration zonation is defined by chlorite-epidote-calcite, K-feldspar-biotite-sericite-chlorite, and adularia-sericite-chlorite-carbonate assemblages in distal, intermediate and proximal alteration zones, respectively.

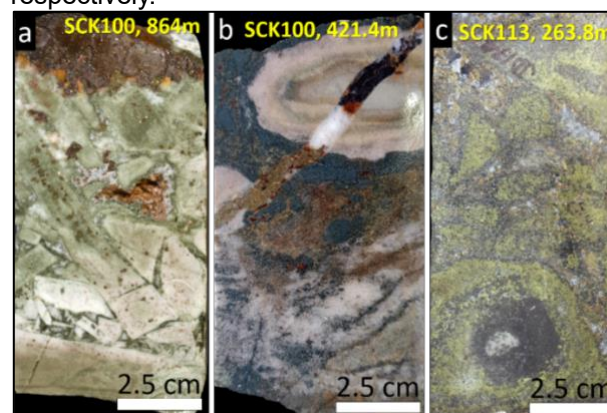


Figure 4. Photographs showing hydrothermal alteration and gold mineralisation stages within the New York breccia pipe. **a:** Stage 1 pyrrhotite-pyrite-galena-sphalerite-gold mineralisation related to the hydrothermal breccia within the Ieru Siltstone unit. **b:** Chlorite-altered Stage 1 breccia mineralisation cut by stage 2 related quartz-carbonate-galena-sphalerite vein. **c:** Skarn-related stage 3 clinopyroxene-actinolite alteration overprinting stage 1 chlorite altered breccia.

The second stage is defined by massive and vein-filling galena-sphalerite-chalcopryrite-pyrite mineralisation, accompanied by chlorite, quartz, calcite and dolomite as gangue minerals. Hydrothermal alteration zonation is similar to stage 1 mineralisation. However, the clear cross-cutting relationships, as displayed in Figure 4B, differentiates both stages.

The third stage is composed of massive magnetite skarn defined by magnetite-pyrite-hematite-galena-sphalerite-pyrrhotite mineralisation, associated with the Taranaki thrust. Quartz, calcite and dolomite constitute the major gangue minerals. Hydrothermal alteration zonation in stage 3 comprises chlorite-epidote-calcite, chlorite-actinolite-clinopyroxene-calcite-dolomite and magnetite-garnet-clinopyroxene-dolomite-phlogopite-actinolite in distal, intermediate and proximal alteration zones, respectively (Fig. 4C).

The different hydrothermal alteration and sulphide-rich mineralisation stages are shown in the paragenetic sequence diagram below (Fig. 5).

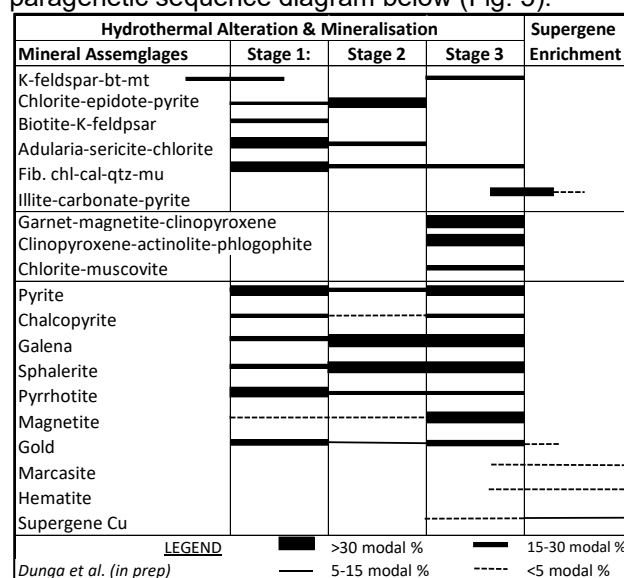


Figure 5. Paragenetic sequence diagram showing the main stages of hydrothermal alteration and gold mineralisation. Abbreviations: cal=calcite, chl=chlorite, Fib.=fibrous, mu=muscovite, qtz=quartz.

5 Conclusion

The New York breccia pipe is strongly mineralogically zoned, is pyrite-rich at the top, and at deeper levels, it displays increasing abundances of pyrrhotite±magnetite. The hydrothermal alteration zonation is characterised by crosscutting epithermal style quartz-rhodochrosite-sphalerite-galena-pyrite-pyrrhotite-chalcopryrite-calcite veins. Note that this hydrothermal alteration assemblage is not observed at Ok Tedi. The breccia fragments include different rock types with variable degrees of hydrothermal alteration and rounding which indicates significant fragment transport. There are abundant hydrothermal infill minerals (matrix), which form several overprinting stages. These observations suggest that there may be more than one magmatic, hydrothermal and brecciation event. Ongoing

studies may lead to the identification of new prospective high-grade areas that may be targeted in the future.

Acknowledgements

The Ok Tedi Mining Ltd is thanked for sponsoring this research project through a project grant. The University of Western Australia is also acknowledged for providing a research scholarship for the first author.

References

- Arnold, G. and Fitzgerald, F. (1977) Igneous rock types and their alteration, Mt. Fubilan porphyry copper deposit: Geological Survey of Papua New Guinea, Report 77/5, 10 p.
- Arnold, G.O. and Griffin, T.J. (1978) Intrusions and porphyry copper prospects of the Star Mountains, Papua New Guinea, *Econ. Geol.* v. 73, pp. 785-795.
- Bamford, R.W. (1972) The Mount Fubilan (Ok Tedi) porphyry copper deposit, territory of Papua and New Guinea, *Econ. Geol.* Vol. 67, pp.1019-1033.
- Davies, H.L. and Norvick, M. (1974) Blucher Range, Papua New Guinea: Australian Bureau of Min. Res., Geology and Geophysics. 1:250 000 Geological Map Series, Explanatory Notes.
- Erceg, M and Pollard, J.P. (2020) The discovery and geology of the New York Breccia and associated gold and base-metal mineralisation. *Australian Inst. of Geos., Bulletin* 70, p. 248-255.
- Fookes, P.G., Dale, S.G., Land, J.M. (1991) Some observations on a comparative aerial photography interpretation of a landslipped area: *Quarterly Journ. of Engin. Geol.* 24, p. 249-265.
- Hill, K.C. (1989) The Muller Anticline, Papua New Guinea; basement-cored, inverted extensional fault structures with opposite vergence: *Tectonophysics*, v. 158, p. 227-245.
- Kirwin, D.J. (2018) Characteristics of intrusion-related copper-bearing tourmaline breccia pipes. *Metals, Minerals, and Society. Society of Economic Geologists. Keystone, Colorado, USA. September 22-25, 2018.* http://www.segabstracts.org/abstract_summary.php?mode=public&abs_id=1033.
- Large, S.J.E., von Quadt, A., Wotzlaw, J-F., Guillong, M., and Heinrich, C.A. (2018) Magma evolution leading to porphyry Au-Cu mineralisation at the Ok Tedi deposit, Papua New Guinea: Trace element geochemistry and high-precision geochronology of igneous zircon: *Econ. Geol.*, v. 113, p. 39–61.
- Mason, R. (1997) Structure of the Alice anticline, Papua New Guinea: Serial balanced cross sections and their restoration: *Journal of Struct. Geol.*, v. 19, p. 719–734.
- Page, R.W. and McDougall, I. (1972) Ages of mineralisation of gold and porphyry copper deposits in the New Guinea Highlands: *Econ Geol.*, v. 67, p.1034-1048.
- Pollard, P.J. (2014) Grade distribution of the giant Ok Tedi Cu-Au deposit, Papua New Guinea – A Discussion, *Econ. Geol.*, v. 109, p 1489-1494.
- Pollard, P.J., Jongens, R., Stein, H., Fannings, C.M., Smillie, R (2021) Rapid Formation of Porphyry and Skarn Copper-Gold Mineralisation in a Postsubduction Environment: Re-Os and U-Pb Geochronology of the Ok Tedi Mine, Papua New Guinea: *Econ. Geol.* v. 116, No. 3. p. 533-558.
- van Dongen, M., Weinberg, R.F. and Tomkins, A.G. (2013) Grade distribution of the giant Ok Tedi Cu-Au deposit, Papua New Guinea: *Econ. Geol.*, v. 108, p. 1773-1781.

¹ These average grade values were derived from a literature search of 35 breccia pipe hosting porphyry Cu-Au deposits worldwide.

Redox state, sulphur and chalcophile element budgets during magma differentiation in thick continental arcs: case study at the Parinacota volcano

Iván Mateo Espinel Pachón¹, Zoltan Zajacz¹, Cristóbal González Rodríguez², Michael Schirra¹, Weikai Li¹ and Mara Miranda¹

¹University of Geneva, Switzerland

²Millenium Institute on Volcanic Risk Research- Ckelar Volcanoes, Chile

Abstract. Porphyry copper deposits are genetically linked to arc magmatism. Magma fertility for porphyry ore genesis is dependent on volatile element and ore metal budgets and the variation of redox conditions during magma differentiation. In this project, we analysed silicate melt inclusions from several eruptive events of the Parinacota volcano in northern Chile. Major and trace element data reveal the existence of a complex plumbing system with at least three different melts emplaced at different depths within the crust. Furthermore, the most primitive, highest Sr/Y melts show rather high sulphur contents (up to 6000 ppm) and high oxidation state ($\log fO_2 = FMQ+2.1$). This indicates that the initial oxidation of the magma occurs at the source or during the earliest stages of magma differentiation, and that high-Sr/Y, high-S signature can be introduced at the source.

1 Introduction

Arc magmas are most commonly thought to form by partial melting of a mantle source in which accessory sulphides are present, and therefore it is expected that early sulphide saturation takes place during the differentiation of these magmas at greater crustal depths (Matjuschkin et al. 2016; Chiaradia 2022). This may have a negative effect on the ore-forming potential of the magmas because the sulphides may sequester a significant part of the initial chalcophile metal budget of the magma if they are effectively fractionated. The amount of sulphide precipitated during magma differentiation in the crust will be dependent on how the redox state of the magma varies, starting from partial melting in the mantle through crustal magma differentiation, and also on the pressure (P) - temperature (T) - melt composition (X) – dependent shift in the fO_2 range of the sulphide to sulphate transition. Neither of these are fully understood at the moment (Jugo et al. 1999; Jugo 2009; Botcharnikov et al. 2011; Klimm et al. 2012; Matjuschkin et al. 2016; Nash et al. 2019).

Sulphur is also critically important to facilitate the precipitation of porphyry ore. It is most favourable to release S from the magma reservoir in the form of SO_2 , which in turn disproportionates to H_2SO_4 and H_2S over a narrow temperature range below 400 °C, leading to spatially focused ore metal sulphide precipitation. Thus, the redox state of the magma at the fluid exsolution state is also critically important. Overall, to understand magma fertility for porphyry ore genesis, it is important to constrain how the redox state of magmas evolve from partial melting in the mantle to the final stages of crystallization at

shallow crustal levels, and the interplay between this and S and chalcophile element budgets.

Many previous studies focused on the process of metal sequestration and fluid release from magmas in upper crustal magma reservoirs, whereas the role of deep crustal processes in regulating ore fertility have just started receiving rapidly increasing attention over the past 1-2 decades (Audétat and Pettke 2006; Audétat 2010, 2015; Zajacz et al. 2012; Li et al. 2015; Matjuschkin et al. 2016; Chiaradia and Caricchi 2017, 2022; Grondahl and Zajacz 2017, 2022; Rottier et al. 2020a, b; Chiaradia 2022).

This study aims to investigate volcanic systems on thick continental crust in the fertile Andean arc to study the interplay between magma redox, volatile element and ore metal concentrations during the differentiation of magmas emplaced at different crustal depths and magma fluxes. This presentation focuses on the Parinacota volcano.

The Parinacota volcano is located in northern Chile, near the Bolivian border (Figure 1). It is a stratovolcano that erupted rocks with a broad range of compositions from rhyolites to basaltic-andesites generated by magma differentiation at different levels within one of the thickest continental crust on earth (around 70 km crustal thickness) (Banaszak 2014; Ginibre and Davidson 2014a). The oldest units in the area, the Chungará andesites (CA) (163-116 ka) and the Old cone (oc) (52-20 ka), consist of amphibole-bearing andesites with additional clinopyroxene and plagioclase phenocrysts. Between 20-10 ka, an edifice collapse generated a debris avalanche towards the west. After this event, a new edifice started building up generating the young cone (yc) (8 ka-recent) amphibole-free andesites with clinopyroxene and plagioclase phenocrysts. Simultaneously with the build-up of the main edifice, some flank eruptions produced basaltic andesites that form the Ajatas flows (a1, a2, a3 and a4).

Parinacota represents a dynamic system that, with time, shows increasing magma flux rates (mafic recharge), leading to magma differentiation at shallower depths and less variable, in general more mafic magmas being erupted (Ginibre et al. 2005; Hora et al. 2007; Wörner et al. 2018). All these characteristics make it an excellent study area for our purposes.

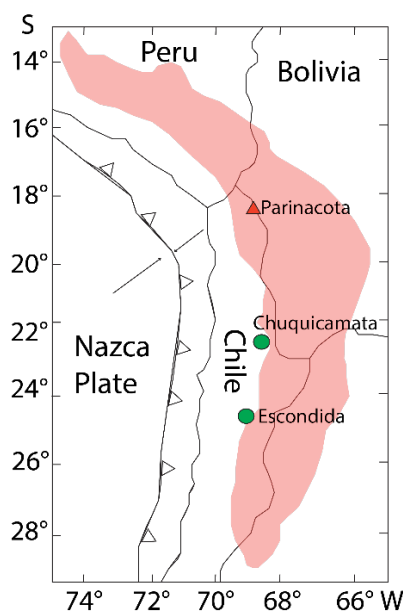


Figure 1. Map of the central volcanic zone of the Andes (red). Green circles are some of the giant porphyry deposits associated with Miocene subduction. Parínacota volcano is represented by the red triangle.

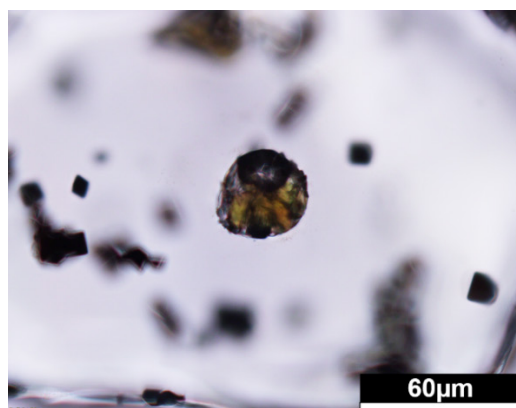


Figure 2. Recrystallized silicate melt inclusion trapped in an olivine phenocryst from Parínacota Volcano (a4 lavas). The olivine also contains Cr-spinel inclusions testifying for the primitive nature of the host magma.

2 Methodology

Volcanic rocks are final products of often complex magma evolution, which may for example involve mixing. Furthermore, their volatile budget is unrepresentative for the original magma due to pre- and syn-eruptive degassing. Therefore, we chose silicate melt inclusions (SMI) in magmatic phenocrysts as our primary source of information, which is complemented by mineral and whole-rock chemistry.

Major and minor element compositions of olivine and pyroxene were determined by using a JEOL 8200 superprobe electron microprobe, equipped with 5 Wavelength Dispersive X-ray Spectroscopy (WDS) detectors at the University of Geneva.

Silicate melt inclusions were analyzed by Laser Ablation Inductively Coupled Plasma Mass Spectrometry (LA-ICPMS) using the methodology of (Halter et al. 2002), which relies on the analysis of

the entire inclusion along with its host mineral and subsequent deconvolution of the inclusion and host signals (Figure 2). Important advantages are that the inclusion can be analysed without reheating, and that S and Cl concentrations can be determined simultaneously with major and trace elements without the risk of unrepresentative sampling due to missing volatiles that may have partitioned into the vapor bubble (Venugopal et al. 2020; Grondahl and Zajacz 2022). Analyses were done using an NWR 193 HE laser ablation system coupled with an Agilent 8900 triple quadrupole ICP-MS at the University of Geneva. We used a custom-built ablation cell and gas purification system to facilitate accurate determination of S and Cl concentrations along with a broad set of major and trace elements.

3 Petrography

Traditional petrography of the samples selected for melt inclusions studies allowed us to identify the following differences between the pre- (Chungará andesite (ca) and old cone (oc)) and post-collapse (young cone (yc) and Ajatas flows (a1-a2-a3-a4)) units (Fig.2): i) There is a change from amphibole-bearing to amphibole-free eruptive products. ii) Plagioclase phenocrysts in the pre-collapse lavas show more roundish borders and dissolution textures, which is not observed in post-collapse units. iii) Crystals in the post-collapse lavas are generally smaller iv) In the post-collapse units, except for yc, olivine is present but not as abundant as plagioclase or clinopyroxene.

Magmatic sulphides were not observed, indicating that sulphide saturation might have not taken place. Magnetite is the main oxide present in all the units as small inclusions within phenocrysts (olivine and clinopyroxene) or as an accessory mineral within the matrix, suggesting that it was one of the first phases to crystallize.

Olivine- and clinopyroxene-hosted SMIs are abundant in the yc lavas and the Ajata flows. Their sizes range from 5 to 100 μm. Contrarily, SMIs in the oc and ca are scarce, small (<20 μm) and are typically hosted in clinopyroxene. These latter are yet to be studied.

4 Mineral chemistry and thermobarometry

Diopside is the main clinopyroxene. High chromium oxide concentrations (up to 0.7%) and magnesium numbers (up to 85) in clinopyroxene cores suggest that a2 and a3 were generated from more primitive melts than a2, a4 and yc. Geothermobarometric estimations calculated by using the cpx-only Putirka (2008) thermobarometer yielded temperatures between 1050-1100°C for a2 and a3 and 1000-1050°C for a1, a4, yc and ca. Pressure estimations are less precise and range between 1-7 kbar displaying no systematic variations between the units.

Olivine is a mineral phase present in Ajata flows (a1, a2, a3 and a4). It usually hosts Cr-rich spinel

inclusions. In a2 and a3 lava flows, olivine occurs as euhedral phenocrysts in equilibrium with the matrix and have a magnesium number (Mg#) of 79-81 with Ni contents ranging between 400-1100 ppm, whereas olivines in a1 and a4 have Mg# of 74-79 and similar Ni values. Texturally, these more evolved olivines show clear disequilibrium indicated by the presence of orthopyroxene-magnetite symplectite, which have overgrown the olivine.

5 Silicate melt inclusion compositions

Melt inclusion compositions largely overlap with whole rock data but show more variability, in some rocks, suggesting mixing between different magma batches.

N-MORB - normalized trace element plots (Sun et al. 1989) show a depletion in fluid-immobile and an enrichment in fluid-mobile elements, typical of arc magmatism (Figure 3). Trace elements allow to identify two different components within a4: the first component (c1) has high Ba/Th, low Th/Nb and overall lower incompatible trace element concentrations compared to the other units. The second component (c2) has high Th/Nb, low Ba/Th ratios and has higher concentrations of fluid mobile elements. The most primitive melts (a2 and a3) show high Sr values ranging from 1000 up to 2000 ppm while in a1, a4 and yc the maximum value is around 950 ppm.

SMIs display Cl concentrations in the range of 1500-3000 ppm, which is on the high end of the typical range for arc magmas (Wallace 2005). On the other hand, S concentrations vary broadly and reach very high values (up to about 6000 ppm). S concentration positively correlate with the Sr/Y ratio, which can be as high as 100.

Oxygen fugacity was calculated using the partition coefficient of vanadium between olivine and silicate melt (D_V^{Ol-M}) following the method of Shishkina et al. (2018). Analysis of 47 olivine-melt pairs yielded a fO_2 of $\Delta QFM + 2.1 \pm 0.5$ for the Ajata flows.

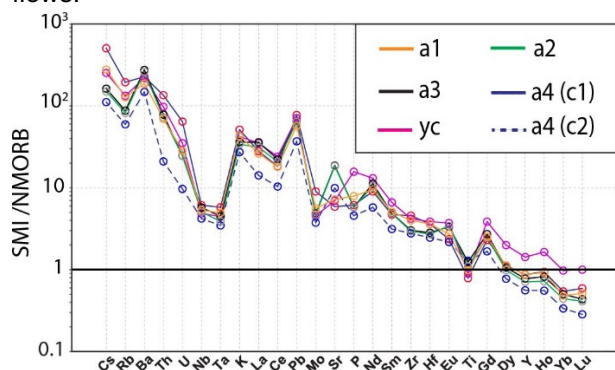


Figure 3. N-MORB normalized trace element variation diagram based on silicate melt inclusion compositions (median values shown for each unit).

6 Magmatic evolution and ore forming potential

We propose that the erupted rocks present in Parinacota are the result of the interaction of at least three different melts: i) A melt that generated a4-c1 with low Ba, Cs, Pb, Th/Nb, La/Yb, Th/U and high Ba/Th. These characteristics may be attributed to the input of slab-derived aqueous fluids to the mantle source of the magma combined with higher degree of melting ii) A high Sr/Y, Ba, Pb, Th/U and La/Yb, medium Th/Nb melt that yielded units a2 and a3, suggesting the additional influence of a subducted sediment component. iii) A low Sr/Y, Ba/Th, Nb/Ta, Sr and high Cs, Pb and Th/Nb melt that generate a4c2 and yc, suggesting a different mantle source with both sediment and aqueous fluid input. Overall, the high Th/U indicate that the metasomatic fluids derived from the slab or associated sediments were rich in silicate components. The high Ba/Th observed in some melts indicates a cooler slab fluid component, while high Th/Nb points towards a deep sediment melt component.

The high Sr/Y (80-100) component also correspond to high S values (3000-6000 ppm) well above the typical range of arc magmas. As this is a fairly primitive mantle melt, the enrichment cannot be a result of AFC processes at deep crustal level as originally proposed for other systems by Loucks (2014). Therefore, it appears the incorporation of high-Sr, high-S components in the mantle source may be an alternative way to generate positive correlation between Sr/Y ratio and S concentration, and at the same time, also to increase ore fertility. Based on the relatively high Th/Nb ratio and previously published isotope data (Ginibre and Davidson 2014b), we hypothesize that this component is subducted sediment, but further investigation is warranted.

Most Cu and Mo concentrations fall between 25-100 ppm and 1-3 ppm, respectively, which represent typical concentrations of the Andean Southern Volcanic Zone (33–40 °S) (Grondahl and Zajacz 2022) and arc magmas in general. They are consistent with minor to moderate sulphide fractionation at deeper crustal levels.

The nearly identical fO_2 estimates for all studied units at Parinacota, including the near-primitive mantle melts from a2, suggest that oxidation does not occur during early magma differentiation and that the oxidized nature of the Parinacota magmas is rather produced at the source. However, we do not discard the possibility that further changes in magma redox state can occur during differentiation, which will be revealed by the investigation of the more differentiated units (yc, oc and ca), which is currently in progress. Concentrations of Au and Pt will be also determined in large SMI, and will be used along with the concentrations of Cu and S to assess the amount and type of magmatic sulphides involved in the genesis of the various Parinacota magmas at greater crustal and mantle depths.

Acknowledgements

The European Research Council is thanked for the ERC Consolidator Grant funding to project OXYGEN.

References

- Audétat A (2010) Source and evolution of molybdenum in the porphyry Mo(-Nb) deposit at Cave Peak, Texas. *Journal of Petrology* 51:1739–1760. <https://doi.org/10.1093/petrology/egq037>
- Audétat A (2015) Compositional evolution and formation conditions of magmas and fluids related to porphyry molybdenization at Climax, Colorado. *Journal of Petrology* 56:1519–1546. <https://doi.org/10.1093/petrology/egv044>
- Audétat A, Pettke T (2006) Evolution of a porphyry-Cu mineralized magma system at Santa Rita, New Mexico (USA). *Journal of Petrology* 47:2021–2046. <https://doi.org/10.1093/petrology/egl035>
- Banaszak M (2014) Differentiation regimes in the Central Andean magma systems: case studies of Taapaca and Paríacota volcanoes, Northern Chile. Universität Göttingen
- Botcharnikov RE, Linnen RL, Wilke M, et al (2011) High gold concentrations in sulphide-bearing magma under oxidizing conditions. *Nat Geosci* 4:112–115. <https://doi.org/10.1038/ngeo1042>
- Chiaradia M (2022) Distinct magma evolution processes control the formation of porphyry Cu–Au deposits in thin and thick arcs. *Earth Planet Sci Lett* 599. <https://doi.org/10.1016/j.epsl.2022.117864>
- Chiaradia M, Caricchi L (2017) Stochastic modelling of deep magmatic controls on porphyry copper deposit endowment. *Sci Rep* 7:1–11. <https://doi.org/10.1038/srep44523>
- Chiaradia M, Caricchi L (2022) Supergiant porphyry copper deposits are failed large eruptions. *Commun Earth Environ* 3. <https://doi.org/10.1038/s43247-022-00440-7>
- Ginibre C, Davidson JP (2014a) Sr isotope zoning in plagioclase from paríacota volcano (Northern Chile): Quantifying magma mixing and crustal contamination. *Journal of Petrology* 55:1203–1238. <https://doi.org/10.1093/petrology/egu023>
- Ginibre C, Davidson JP (2014b) Sr Isotope Zoning in Plagioclase from Paríacota Volcano (Northern Chile): Quantifying Magma Mixing and Crustal Contamination. 55:1203–1238. <https://doi.org/10.1093/petrology/egu023>
- Ginibre C, Davidson JP, Wörner G (2005) Lower crustal influence on CVZ magmas: Insights from chemical and isotopic zoning in plagioclase at Paríacota volcano, North Chile. In: 6th International Symposium on Andean Geodynamics. pp 323–326
- Grondahl C, Zajacz Z (2022) Sulfur and chlorine budgets control the ore fertility of arc magmas. *Nat Commun* 13. <https://doi.org/10.1038/s41467-022-31894-0>
- Grondahl C, Zajacz Z (2017) Magmatic controls on the genesis of porphyry Cu–Mo–Au deposits: The Bingham Canyon example. *Earth Planet Sci Lett* 480:53–65. <https://doi.org/10.1016/j.epsl.2017.09.036>
- Halter WE, Pettke T, Heinrich CA, Rothen-rutishauser B (2002) Major to trace element analysis of melt inclusions by laser-ablation ICP-MS: methods of quantification. 183:63–86
- Hora JM, Singer BS, Wörner G (2007) Volcano evolution and eruptive flux on the thick crust of the Andean Central Volcanic Zone: 40Ar/39Ar constraints from Volcán Paríacota, Chile. *Bulletin of the Geological Society of America* 119:343–362. <https://doi.org/10.1130/B25954.1>
- Jugo PJ (2009) Sulfur content at sulfide saturation in oxidized magmas. *Geology* 37:415–418. <https://doi.org/10.1130/G25527A.1>
- Jugo PJ, Candela PA, Piccoli PM (1999) Magmatic sulfides and Au:Cu ratios in porphyry deposits: an experimental study of copper and gold partitioning at 850°C, 100 MPa in a haplogranitic melt-pyrrhotite-intermediate solid solution-gold metal assemblage, at gas saturation
- Klimm K, Kohn SC, Botcharnikov RE (2012) The dissolution mechanism of sulphur in hydrous silicate melts. II: Solubility and speciation of sulphur in hydrous silicate melts as a function of fO₂. *Chem Geol* 322–323:250–267. <https://doi.org/10.1016/j.chemgeo.2012.04.028>
- Li W, Audétat A, Zhang J (2015) The role of evaporites in the formation of magnetite-apatite deposits along the Middle and Lower Yangtze River, China: Evidence from LA-ICP-MS analysis of fluid inclusions. *Ore Geol Rev* 67:264–278. <https://doi.org/10.1016/j.oregeorev.2014.12.003>
- Loucks RR (2014) Distinctive composition of copper-ore-forming arc magmas. *Australian Journal of Earth Sciences* 61:5–16. <https://doi.org/10.1080/08120099.2013.865676>
- Matjuschkin V, Blundy JD, Brooker RA (2016) The effect of pressure on sulphur speciation in mid- to deep-crustal arc magmas and implications for the formation of porphyry copper deposits. *Contributions to Mineralogy and Petrology* 171. <https://doi.org/10.1007/s00410-016-1274-4>
- Nash WM, Smythe DJ, Wood BJ (2019) Compositional and temperature effects on sulfur speciation and solubility in silicate melts. *Earth Planet Sci Lett* 507:187–198. <https://doi.org/10.1016/j.epsl.2018.12.006>
- Rottier B, Audétat A, Koděra P, Lexa J (2020a) Magmatic evolution of the mineralized Štiavnica volcano (Central Slovakia): Evidence from thermobarometry, melt inclusions, and sulfide inclusions. *Journal of Volcanology and Geothermal Research* 401. <https://doi.org/10.1016/j.jvolgeores.2020.106967>
- Rottier B, Audétat A, Koděra P, Lexa J (2020b) Magmatic evolution of the mineralized Štiavnica volcano (Central Slovakia): Evidence from thermobarometry, melt inclusions, and sulfide inclusions. *Journal of Volcanology and Geothermal Research* 401. <https://doi.org/10.1016/j.jvolgeores.2020.106967>
- Shishkina TA, Portnyagin M V., Botcharnikov RE, et al (2018) Experimental calibration and implications of olivine-melt vanadium oxybarometry for hydrous basaltic arc magmas. *American Mineralogist* 103:369–383. <https://doi.org/10.2138/am-2018-6210>
- Sun S, McDonough WF, Sun S, McDonough WF (1989) Chemical and isotopic systematics of oceanic basalts: implications for mantle composition and processes. Geological Society, London, Special Publications 1989, 42:313–345. <https://doi.org/10.1144/GSL.SP.1989.042.01.19>
- Venugopal S, Schiavi F, Moune S, et al (2020) Melt inclusion vapour bubbles: the hidden reservoir for major and volatile elements. *Sci Rep* 10. <https://doi.org/10.1038/s41598-020-65226-3>
- Wallace PJ (2005) Volatiles in subduction zone magmas: Concentrations and fluxes based on melt inclusion and volcanic gas data. *Journal of Volcanology and Geothermal Research* 140:217–240. <https://doi.org/10.1016/j.jvolgeores.2004.07.023>
- Wörner G, Mamani M, Blum-Oeste M (2018) Magmatism in the central andes. *Elements* 14:237–244. <https://doi.org/10.2138/gselements.14.4.237>
- Zajacz Z, Candela PA, Piccoli PM, et al (2012) Gold and copper in volatile saturated mafic to intermediate magmas: Solubilities, partitioning, and implications for ore deposit formation. *Geochim Cosmochim Acta* 91:140–159. <https://doi.org/10.1016/j.gca.2012.05.033>

Fluid evolution and Re enrichment in the Maronia Cu-Mo±Au porphyry, NE Greece. Insights from mineral microanalysis and fluid inclusions constraints

Jan J. Falkenberg¹, Manuel Keith¹, Vasilios Melfos², Max Hohl³, Karsten M. Haase¹, Panagiotis Voudouris⁴, Alica Höss¹, Julia Wenske¹, Reiner Klemd¹, Christoph Beier⁵, Martin Kutzschbach⁶, Harald Strauss⁷

¹Friedrich-Alexander-Universität (FAU) Erlangen-Nürnberg, GeoZentrum Nordbayern, Germany

²Aristotle University Thessaloniki, Faculty of Geology, Thessaloniki, Greece

³University of Tasmania, CODES, Australia

⁴National and Kapodistrian University of Athens, Faculty of Geology & Geoenvironment, Athens, Greece

⁵Department of Geosciences and Geography, University of Helsinki, Helsinki, Finland

⁶Technische Universität Berlin, Chair of Applied Geochemistry, Berlin, Germany

⁷Westfälische-Wilhelms-Universität Münster, Institut für Geologie und Paläontologie, Münster, Germany

Abstract. Maronia is an exceptional Re-rich Cu-Mo ± Au porphyry systems in Thrace, NE Greece. Here, we present a micro-analytical, S isotope, and fluid inclusion approach in order to reveal the hydrothermal prerequisites required for the extreme Re enrichment which are poorly constrained up to date. Based on petrography, trace element chemistry of hydrothermal quartz (e.g., Al/Ti, Ge/Ti), and fluid inclusion microthermometry of consecutive vein generations, we establish the spatial and temporal fluid evolution. The fluid inclusions give evidence for systematic fluid cooling and continuous phase separation which is the main ore-forming process during the porphyry stages. The later epithermal stage formed by vapor condensation into meteoric water. This is consistent with salinity-sensitive (Co/As, As/Sb), temperature-sensitive (Se/Tl) and fluid source-sensitive (Se/Ge) pyrite trace element ratios. $\delta^{34}\text{S}$ values in pyrite vary in response to SO_2 disproportionation, phase separation, host rock buffering and fluid $f\text{O}_2$. Early extremely Re-rich molybdenite (6631 ± 4308 ppm) is related to higher temperatures and $f\text{O}_2$ compared to later molybdenite generations with lower Re (1746 ± 1184 ppm) contents. We conclude, that fluid cooling below 400 – 350°C and decreasing $f\text{O}_2$ are the main control on the Re precipitation efficiency in the potassic alteration on the deposit-scale.

1 Introduction

Porphyry Cu-Mo ± Au ± Re deposits are one of the most important global sources for base (Cu, Mo), precious, critical and rare (Se, Ag, Te, Re, Au, PGE) metals (Tabelin et al. 2021), which are essential for various high-tech applications, such as semiconductors, catalysts for petroleum refining, high temperature superalloys and photovoltaic production. However, their scarcity and poorly constrained enrichment processes, will likely lead to a supply risk in the near future (Grandell et al. 2016).

The Maronia Cu-Mo ± Au porphyry system is host to rare rheniite (ReS_2) and exceptional Re-rich molybdenite (up to 13800 ppm). It is associated to a high-K calc-alkaline to shoshonitic monzonite-monzogabbro intrusion into the metamorphic basement at 29.6 to 29.8 Ma in NE Greece (Fig. 1A, B) (Schaarschmidt et al. 2021). The pluton was subsequently intruded by a microgranite porphyry. It is associated with concentric zones of pervasive

potassic, sodic-calcic, propylitic, sericitic, and argillic alteration that host the Re-rich quartz-sulfide vein networks (Fig. 1C) (Melfos et al. 2020). The mineralized vein samples represent a lateral profile along the coastline of the Maronia porphyry (Fig. 1) and the hydrothermal stockworks are associated with qz-py-cpy-po A- and qz-py-mbl-rhn B-type veins in the potassic alteration, with qz-py-mbl D-type veins in the sericitic alteration and with qz-cc-py-ss E1, and qz-py-mcr-asp-ss E2-type veins in the argillic alteration.

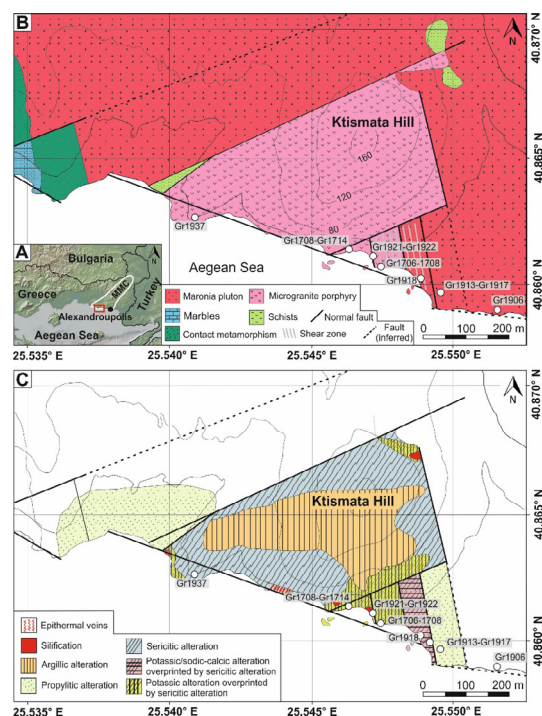


Figure 1. (A) Regional overview, (B) geological and (C) alteration map of the Maronia porphyry-epithermal system. Modified after Melfos et al. 2020

The trace element and S isotope composition of hydrothermal sulfides (e.g., pyrite, molybdenite) and hydrothermal quartz from consecutive porphyry-epithermal vein generations can provide valuable spatial and temporal information about the evolution

of the ore-forming fluids (Hutchison et al. 2020; Rottier and Casanova 2021; Keith et al. 2022). Quartz-hosted fluid inclusions give information on the temperature, salinity, and entrapment pressure of hydrothermal fluids and can record processes related to fluid phase separation (Bodnar et al. 2014).

Molybdenite commonly hosts most of the Re in porphyry deposits and its trace element composition can provide insights into the ore-forming processes. However, based on experimental studies (Xiong et al. 2006) and natural observation (Barton et al. 2020) Re shows a complex behaviour with respect to varying physicochemical fluid parameters (e.g., temperature, fO_2) and thus the major control on Re enrichment is enigmatic.

Here, we combine a multi-method trace element, S isotope and fluid inclusion approach in spatial and temporal consecutive vein generations allowing us to fingerprint the fluid evolution and establish the hydrothermal prerequisites favourable for extreme Re enrichment in distinct paragenetic stages.

2 Methodology

2.1 Microanalytical techniques

BSE and CL imaging by SEM was used to identify different mineral phases and to avoid microinclusions during subsequent LA-ICP-MS analysis. The trace element composition of pyrite, molybdenite, and arsenopyrite were measured by LA-ICP-MS at the GeoZentrum Nordbayern using a Teledyne Analyte Excite 193nm laser coupled with an Agilent 7500c ICP-MS. MASS-1 and FeNiS1 were used as primary and UQAC-FeS1 as secondary standards.

In-situ LA-ICP-MS trace element measurements of hydrothermal quartz were carried out at HelLabs, Department of Geosciences and Geography, University Helsinki using a coherent GeoLas MV 193 nm laser coupled with an Agilent 7900s ICP-MS. NIST SRM 612 was used as primary and NIST 610, BHVO-2G, and BCR-2G were used as secondary standards.

2.2 Fluid inclusion microthermometry

Following the CL imaging to distinguish different quartz generations, fluid inclusion microthermometry was carried out with a LINKAM THM-600/MS 90 heating-freezing stage, at the Department of Mineralogy, Petrology and Economic Geology at the Aristotle University of Thessaloniki, Greece.

2.3 $\delta^{34}\text{S}$ of pyrite, molybdenite and arsenopyrite

Sulfide powders (pyrite, molybdenite, arsenopyrite) were extracted and homogenized by a diamond microdrill from the vein matrix and analysed for their S isotopic composition by a Flash EA IsoLink elemental analyser interfaced to a ThermoScientific

Delta V Advantage isotope ratio mass spectrometer (EA-IRMS) at the Westfälische Wilhelms-Universität, Münster.

The in-situ S isotope values of pyrite have been determined at the MAGMA Lab TU Berlin using an Agilent8900 ICP-MS/MS (oxygen reaction gas) coupled to a Teledyne Analyte Excite 193 nm excimer laser. Mass fractionation was corrected using PPP-1 pyrite (Gilbert et al. 2014) as primary standard. Accuracy was verified on Balmat pyrite (Crowe and Vaughan 1996).

3 Results

3.1 Trace element composition of hydrothermal quartz, pyrite, molybdenite and arsenopyrite

Titanium contents in hydrothermal quartz systematically decrease during the porphyry-epithermal evolution and correlate with the CL intensity. Quartz trace element ratios of Al/Ti and Ge/Ti from the different vein types are consistent with quartz from other porphyry-style deposits (Fig. 2) and confirm the vein classification (Rottier and Casanova 2021). Based on an unpaired two-tailed t-test the mean Re content in molybdenite in earlier B-type (6631 ± 4308 ppm) and in later D-type (1746 ± 1184 ppm) is considered significantly ($p < 0.01$) different (Fig. 3). Pyrite compositions show a systematic increase of trace elements such as Au, Te, Ag, Pb, Tl, and As from the porphyry to the epithermal stages and porphyry pyrite is related to high Se/Ti, Co/As and Se/Ge but low As/Sb ratios where epithermal pyrite shows the opposite (Fig. 4).

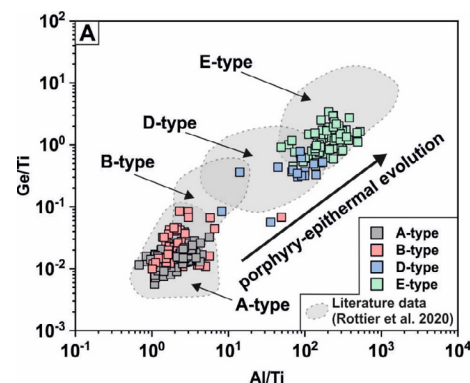


Figure 2. Quartz trace element ratios (Ge/Ti, Al/Ti) classify different vein types (Rottier and Casanova 2021).

3.3 $\delta^{34}\text{S}$ of pyrite, molybdenite and arsenopyrite

$\delta^{34}\text{S}$ values of sulfide separates (pyrite, molybdenite and arsenopyrite) range from 2.6 to 4.6 ‰, with the epithermal veins showing the highest and the porphyry veins yielding lower values. The $\delta^{34}\text{S}$ of molybdenite from B- (~3.2 ‰) and D-type (~3.3 ‰) veins are comparable (Fig. 5).

The in-situ $\delta^{34}\text{S}$ values of pyrite show a larger variation than pyrite separates and vary between -4.1 and 14.8 ‰ with multiple negative values in A- and B-type veins as well as large intra-grain variations (up to $\Delta\delta^{34}\text{S} = 9.5\text{‰}$). Based on an

unpaired two-tailed t-test the lower average $\delta^{34}\text{S}$ observed in the B-type veins ($\sim 2.9\text{‰}$) is significantly ($p = <0.01$) different than the similar $\delta^{34}\text{S}$ of A-, D- and E1- veins ($\sim 5.0\text{‰}$) (Fig. 5).

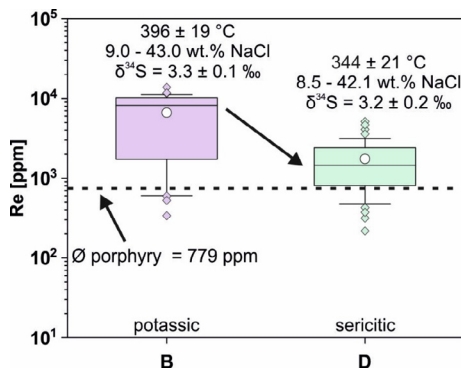


Figure 3. Rhenium content in molybdenite from B- and D-type veins at Maronia. The average Re content from porphyry molybdenite is adapted from Barton et al. 2020.

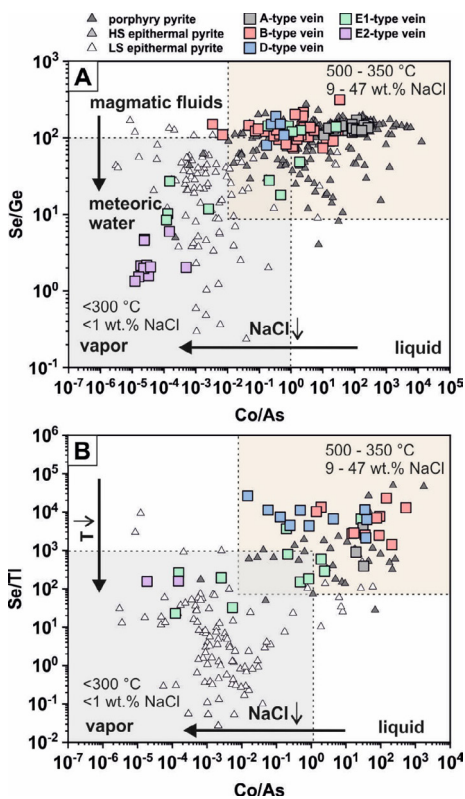


Figure 4. Fluid mixing-sensitive (Se/Ge), temperature-sensitive (Se/Ti) and salinity-sensitive (Co/As) pyrite trace element ratios.

3.4 Fluid microthermometry

Homogenization temperatures of quartz-hosted fluid inclusion decrease from early porphyry ($\sim 500^\circ\text{C}$) to later epithermal ($\sim 280^\circ\text{C}$) veins. Porphyry veins are associated with coexisting hypersaline (47.2 – 34.5 wt. % NaCl equiv.) and intermediate saline (20.4 – 8.5 wt. % NaCl equiv.) vapor-rich fluids. By contrast, epithermal veins are characterized by low saline (<0.7 wt. % NaCl) liquid-rich fluids (Fig. 6).

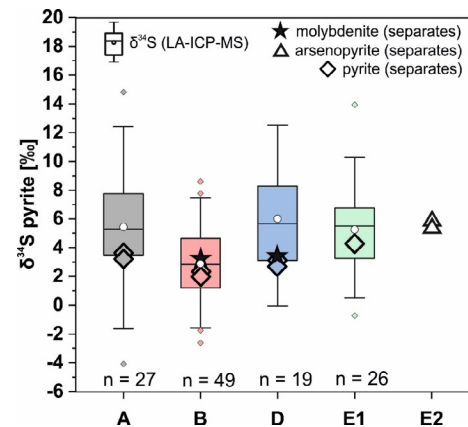


Figure 5. $\delta^{34}\text{S}$ of sulfide separates (pyrite, arsenopyrite, molybdenite) and in-situ $\delta^{34}\text{S}$ LA-ICP-MS of pyrite.

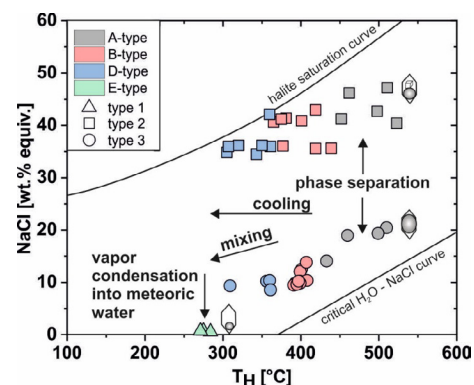


Figure 6. Homogenization temperature vs. salinity diagram of the different hydrothermal veins.

4 Discussion

4.1 Spatial and temporal fluid evolution

The combined use of quartz trace elements, alteration assemblages and fluid inclusion constraints reveal a systematic fluid evolution from neutral high temperature ($\sim 500^\circ\text{C}$) to moderate acidic low temperature ($\sim 280^\circ\text{C}$) conditions during the porphyry-epithermal transition (Fig. 2 – 6). During the formation of A-, B-, and D-type veins, phase separation was the main ore-forming process, whereas the E-type veins formed from the condensation and mixing of a vapor-rich fluid into meteoric waters (Fig. 6).

4.2 Effect of phase separation and fluid evolution on pyrite chemistry

Enrichment of trace elements like Au, Te, Ag, Pb, Tl, and As in epithermal stages is consistent with the formation at lower temperatures as revealed by fluid inclusion microthermometry and Ti-in-quartz thermometry. Similarly, temperature-sensitive trace element ratios of e.g., Se/Ti record the systematic cooling history of the fluid at Maronia. Co/As <1 in epithermal pyrite from Maronia is consistent with the formation from low salinity vapors whereas Co/As >1 (Fig. 4) is rather indicative for precipitation from hypersaline liquids due to the different vapor-

liquid partitioning of Co and As (Pokrovski et al. 2013). High Se/Ge of ~100 in porphyry pyrite is consistent with the pyrite precipitation from magmatic fluids, whereas Se/Ge <100 (Fig. 4A) observed in the epithermal pyrite suggests a contribution of meteoric waters (Keith et al. 2022) as also revealed by fluid inclusion constraints at Maronia (Fig. 6). High intra-grain $\delta^{34}\text{S}$ variation of pyrite can be related to S isotope fractionation during phase separation due to preferential partitioning of ^{34}S into SO_4^{2-} during the oxidation of H_2S to SO_4^{2-} (Börner et al. 2022).

4.3 Magmatic-hydrothermal controls on Re enrichment

The extremely high Re content (Fig. 3) and the occurrence of distinct ReS_2 phases suggest an anomalous high Re budget for the magmatic-hydrothermal fluids at Maronia. This may be linked to the subduction of Re-rich sediments, such as phosphorites or shales, in the Oligocene in NE Greece. As Re is essentially insoluble in reduced fluids (Xiong et al. 2006) systematic decrease of $f\text{O}_2$ is a strong process inducing Re precipitation and saturation from the ore-forming fluids. The decrease in $f\text{O}_2$ at Maronia is visible by the change from magnetite-bearing to magnetite-free mineral assemblages from the potassic to the sericitic alteration zone, decreasing of W contents in molybdenite, and lower $\delta^{34}\text{S}$ in B-type veins induced by high $\text{SO}_4/\text{H}_2\text{S}$ ratios of the fluids (Hutchison et al. 2020). The observed fluid temperatures suggest a possible Re solubility threshold between 350 to 400°C favouring formation of Re-rich molybdenite at temperature of ~400°C in B-type veins of the potassic alteration.

5 Conclusion

Vein and alteration mineralogy, trace element chemistry of hydrothermal quartz and pyrite as well as fluid inclusion microthermometry define the systematic fluid evolution and porphyry-epithermal transition at the exceptional Re-rich Maronia Cu-Mo ± Au porphyry-epithermal system. The Re enrichment in molybdenite in different paragenetic stages is favoured by high temperature (~400°C), oxidized fluids of the potassic alteration, whereas cooler (~350°C) fluids of the sericitic alteration result in lower Re contents. The rare occurrence of rheniite and the high Re content at Maronia compared to molybdenite from other porphyry systems globally suggest an exceptional high Re budget, which might be related to an enriched magmatic source induced by extensive sediment subduction in the Aegean region during the Oligocene.

Acknowledgements

This study was funded by project KE2395/21 (Priority Program DOME SPP 2238) of the Deutsche Forschungsgemeinschaft (DFG).

References

- Barton, I.F.; Rathkopf, C.A.; Barton, M.D. (2020): Rhenium in molybdenite: a database approach to identifying geochemical controls on the distribution of a critical element. *Mining, Metallurgy & Exploration* 37, 21–37.
- Bodnar, R.J.; Lecumberri-Sanchez, P.; Moncada, D.; Steele-MacInnis, M. (2014): 13.5–Fluid inclusions in hydrothermal ore deposits. *Treatise on geochemistry*. 2nd edn. Elsevier, Oxford 119, p. 142.
- Börner, F.; Keith, M.; Buecker, J.L.; Voudouris, P.; Klemd, R.; Haase, K.M. et al. (2022): In-situ trace element and S isotope systematics in pyrite from three porphyry-epithermal prospects, Limnos Island, Greece. *Frontiers in Earth Science*, p. 1637.
- Crowe, D.E.; Vaughan, R.G. (1996): Characterization and use of isotopically homogeneous standards for in situ laser microprobe analysis of 34 S/ 32 S ratios. *American Mineralogist* 81, 187–193.
- Gilbert, S.E.; Danyushevsky, L.V.; Rodemann, T.; Shimizu, N.; Gurenko, A.; Meffre, S. et al. (2014): Optimisation of laser parameters for the analysis of sulphur isotopes in sulphide minerals by laser ablation ICP-MS. *Journal of Analytical Atomic Spectrometry* 29, 1042–1051.
- Grandell, L.; Lehtilä, A.; Kivinen, M.; Koljonen, T.; Kihlman, S.; Lauri, L.S. (2016): Role of critical metals in the future markets of clean energy technologies. *Renewable Energy* 95, 53–62.
- Hutchison, W.; Finch, A.A.; Boyce, A.J. (2020): The sulfur isotope evolution of magmatic-hydrothermal fluids: insights into ore-forming processes. *Geochimica et Cosmochimica Acta* 288, 176–198.
- Keith, M.; Haase, K.M.; Chivas, A.R.; Klemd, R. (2022): Phase separation and fluid mixing revealed by trace element signatures in pyrite from porphyry systems. *Geochimica et Cosmochimica Acta*.
- Melfos, V.; Voudouris, P.; Melfou, M.; Sánchez, M.G.; Papadopoulou, L.; Filippidis, A. et al. (2020): Mineralogical Constraints on the Potassic and Sodic-Calcic Hydrothermal Alteration and Vein-Type Mineralization of the Maronia Porphyry Cu-Mo±Re±Au Deposit in NE Greece. *Minerals* 10, p. 182.
- Pokrovski, G.S.; Borisova, A.Y.; Bychkov, A.Y. (2013): Speciation and transport of metals and metalloids in geological vapors. *Reviews in mineralogy and geochemistry* 76, 165–218.
- Rottier, B.; Casanova, V. (2021): Trace element composition of quartz from porphyry systems: a tracer of the mineralizing fluid evolution. *Mineralium Deposita* 56, 843–862.
- Schaarschmidt, A.; Klemd, R.; Regelous, M.; Voudouris, P.C.; Melfos, V.; Haase, K.M. (2021): The formation of shoshonitic magma and its relationship to porphyry-type mineralisation: the Maronia pluton in NE Greece. *Lithos* 380, p. 105911.
- Tabelin, C.B.; Park, I.; Phengsaart, T.; Jeon, S.; Villacorte-Tabelin, M.; Alonzo, D. et al. (2021): Copper and critical metals production from porphyry ores and E-wastes: A review of resource availability, processing/recycling challenges, socio-environmental aspects, and sustainability issues. *Resources, Conservation and Recycling* 170, p. 105610.
- Xiong, Y.; Wood, S.; Kruszewski, J. (2006): Hydrothermal transport and deposition of rhenium under subcritical conditions revisited. *Economic Geology* 101, 471–478.

Evidence for a High-Level Porphyritic Intrusion Below the Sunnyside Epithermal Vein Deposit, Colorado

Mario Guzman^{1,2}, Thomas Monecke², T. James Reynolds^{2,3}, Thomas Casadevall¹

¹Department of Geology and Geological Engineering, Colorado School of Mines, Golden, Colorado, USA

²United States Geological Survey, Denver Federal Center, Denver, Colorado, USA

³FLUID INC., 1401 Wewatta Street #PH3, Denver, Colorado, USA

Abstract. High-temperature quartz veins were identified in drill core at ~600 m below the Sunnyside epithermal base and precious metal deposit in southwestern Colorado. The veins consist of early anhedral quartz that shows a bluish cathodoluminescence emission and hosts heterogeneous silicate melt inclusions. The early quartz is overgrown by a later generation of quartz that exhibits euhedral terminations with oscillatory growth zones showing a bright pink to purple cathodoluminescence emission. Both types of quartz are crosscut by ubiquitous planes of vapor-rich inclusions and some hypersaline liquid inclusions. In addition, secondary planes of intermediate-density inclusions occur. The petrographic characteristics of the two quartz types are similar to those in 'A' and 'B' veins encountered in shallow- and intermediate-depth porphyry deposits. The relationships at Sunnyside imply that these high-temperature veins formed from magmatic-hydrothermal fluids derived from an intrusion located not far below the lowest level of drilling. Sunnyside appears to be a rare example of an epithermal deposit that is directly connected to a high-level porphyritic intrusion.

1 Introduction

The Miocene Sunnyside intermediate-sulfidation epithermal deposit in the Eureka mining district in southwest Colorado comprises a set of near-vertical precious and base metal veins. Between 1902 and 1987, underground mining at Sunnyside yielded 800,000 ounces of gold and 14 million ounces of silver, making it one of the most prolific precious metal producers in Colorado (Bartos 1993).

Previous studies of the Sunnyside deposit largely focused on the epithermal mineralization occurring at 3,250–3,840 m above sea-level (Casadevall and Ohmoto 1977). However, exploration drill hole B-1 collared from the American Tunnel to a depth of 2,670 m above sea-level provides a unique opportunity to study the nature of veining up to ~600 m below the base of known epithermal mineralization.

This study is based on a petrographic and fluid inclusion study of the earliest quartz veins occurring at depth in the B-1 drill hole. The results demonstrate that early quartz veins formed from high-temperature magmatic-hydrothermal fluids, which suggests that the formation of the epithermal veins at Sunnyside deposit can be linked to a high-level porphyritic intrusion. This revises the earlier model by Casadevall and Ohmoto (1977), which inferred that the deposit formed from a hydrothermal system dominated by meteoric waters.

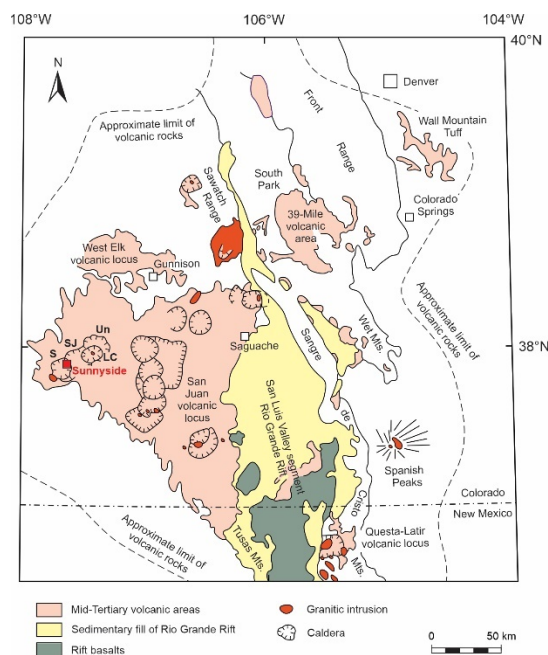


Figure 1. Geologic map of the Eocene to Oligocene Southern Rocky Mountain volcanic field in southwestern Colorado. The map also shows the locations of the Sunnyside deposit and major ignimbrite calderas. Un = Uncompahgre, LC = Lake City, SJ = San Juan, S = Silverton (modified from Lipman 2007).

2 Regional geology

The Sunnyside deposit is located within the San Juan Mountains of southwestern Colorado, an erosional remnant of the late Eocene to Oligocene Southern Rocky Mountain volcanic field that originally covered an area exceeding 100,000 km² stretching from southern Colorado to northern New Mexico (Fig. 1). Ignimbrite flareup-style continental arc volcanism developed on thick continental crust as the subducting Farallon oceanic plate rolled back from a flat configuration to a steeper dip (Lipman 2007).

The Sunnyside intermediate-sulfidation deposit is part of the Eureka mining district. The epithermal vein deposits in the district formed during and after the formation of the 28.35 Ma San Juan-Uncompahgre calderas and the younger, nested 27.6 Ma Silverton caldera (Lipman 2007). Mineralization at Sunnyside occurs within a dilatant zone between the Ross Basin and Sunnyside faults that crosscut the ring fractures produced during the collapse of the Silverton caldera.

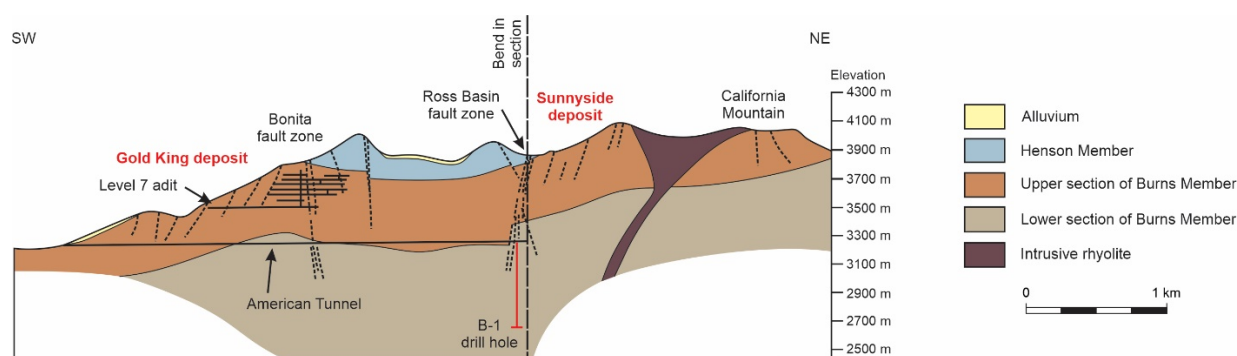


Figure 2. Cross section through the volcanic succession hosting the Sunnyside deposit (modified from Burbank and Luedke 1969).

At Sunnyside, porphyritic dark-grey or dark-green andesite or rhyodacite from the lower section of the Burns Member is recognized in deep drilling and exposures in the American Tunnel (Fig. 2). They are overlain by quartz latite lavas with minor intercalated tuffaceous deposits and flow breccias that comprise the upper section of the Burns Member, which is the main host of epithermal veins at Sunnyside (Casadevall and Ohmoto 1977). The volcanic rocks of the Burns Member are overlain by pyroxenephritic andesite lavas of the ~28.3 Ma Henson Member (Fig. 2). These lavas outcrop extensively on the surface (Casadevall and Ohmoto 1977).

The lower part of the volcanic succession hosting the Sunnyside deposit has been affected by pervasive quartz-sericite alteration. The quartz-sericite alteration gradually changes into a propylitic alteration assemblage upwards (Casadevall and Ohmoto 1977).

3 Materials and methods

Representative vein samples were collected from drill core B-1 (Fig. 2), which is now located at the Core Research Center of the U.S. Geological Survey. Doubly polished 80- μm -thick sections were prepared. These were studied in transmitted and reflected light to document vein textures and paragenetic relationships. Optical cathodoluminescence (CL) microscopy was performed on the thick sections using an HC5-LM hot-cathode CL microscope by Lumic Special Microscopes, Germany. The instrument was operated at 14 kV with a current density of ~10 $\mu\text{A mm}^{-2}$. Colour images were acquired using a high-sensitivity, Teledyne Lumenera Infinity 5-5 digital camera.

As fluid inclusions in quartz formed in the porphyry environment can be subjected to post-entrapment modification (Sun et al. 2021; Audétat 2022), microthermometry was conducted only on secondary assemblages of intermediate-density fluid inclusions that showed consistent liquid to vapor ratios. A procedure outlined in Goldstein and Reynolds (1994) was employed to identify the inclusion assemblage with the highest homogenization temperature (bracketed to a 5°C interval) in a given sample, which involved making a measurement and then scanning the sample identifying other

assemblages where bubbles had not yet homogenized until finally no other higher homogenization temperatures were measured. The microthermometric investigations were performed using a FLUID INC.-adapted U.S. Geological Survey gas-flow heating and freezing stage.

4 Petrography of deep veins

Drill core B-1 contains abundant narrow veinlets composed of vitreous, white or light grey quartz at depths of 510–585 m below the Sunnyside deposit (Fig. 3a). Microscopically, most of the quartz in these veins is anhedral, with individual grains ranging up to 200 μm in size (Fig. 3b). The quartz exhibits a dark blue CL emission (Fig. 3c). Locally, the anhedral quartz grains are overgrown by quartz forming euhedral crystal terminations. These later quartz overgrowths exhibit oscillatory growth zoning and are characterized by a bright pink or purple CL emission (Fig. 3c). Chalcopyrite and pyrite are paragenetically late forming ribbons or coatings along late fractures that crosscut the quartz. Contacts between the sulphides and both types of quartz are irregular or scalloped at the microscale (Fig. 3b, c).

The early anhedral quartz in the deep veins has unique fluid inclusion characteristics. The quartz contains abundant secondary fluid inclusions forming trails having a wispy appearance but lacks primary fluid inclusions defining growth zones (Fig. 3d). The fluid inclusion assemblages are dominated by vapor-rich fluid inclusions although hypersaline liquid inclusions also occur. Many fluid inclusions in the quartz have been affected by post-entrapment modification. These fluid inclusions have irregular shapes and exhibit variations in the vapor to liquid volumetric proportions within individual assemblages. In many cases, microcracks or planar arrays of neonate inclusions radiate outward from the inclusions (Fig. 3e). The early anhedral quartz also contains heterogeneous silicate melt inclusions. These typically consist of vapor bubbles deformed by unknown minerals filling the inclusions (Fig. 3f).

The euhedral quartz overgrowths on the earlier anhedral quartz grains are largely devoid of fluid inclusions (Fig. 4a). Secondary assemblages of intermediate-density fluid inclusions (Fig. 4b), hypersaline liquid inclusions (Fig. 4c), and vapor-rich

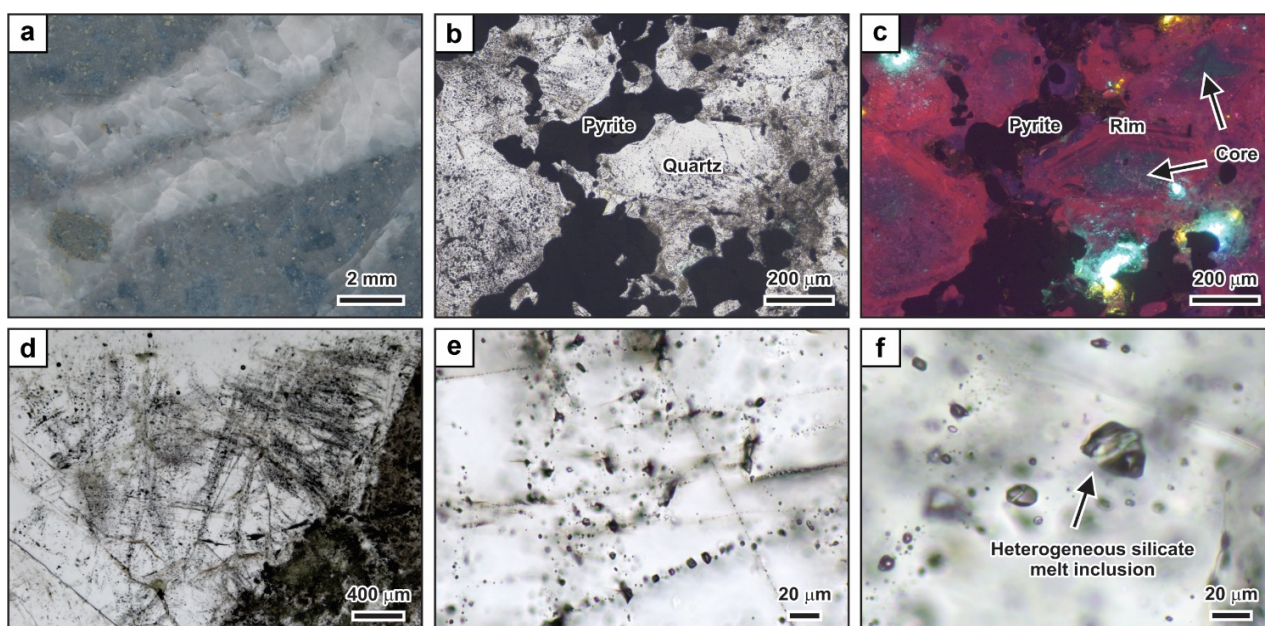


Figure 3. Microtextures and fluid inclusion inventory of high-temperature quartz from a deep drill hole at the Sunnyside deposit, Colorado. **a** Light grey quartz vein hosted by quartz latite. Sample V244-1674 (drill hole depth of 510 m). **b** Anhedral and granular quartz in a light grey quartz vein. Sample V244-1919 (drill hole depth of 585 m) **c** Corresponding optical cathodoluminescence image. The cores of the grains show a dark blue cathodoluminescence colour whereas the outer growth zones are banded and dark pink and purple. **d** Anhedral quartz grain containing ubiquitous healed microfractures defined by secondary inclusions. Sample V244-1674 (drill hole depth of 510 m). **e** Arrays of fluid inclusions that have been affected by post-entrapment modification. The fluid inclusions are highly irregular in shape, commonly with microcracks extending outward from the dark inclusions. Sample V244-1674 (drill hole depth of 510 m). **f** Heterogeneous silicate melt inclusion in an anhedral quartz grain. Sample V244-1674 (drill hole depth of 510 m).

inclusions (Fig. 4a-c) that show no visual evidence of post-entrapment modification locally cross-cut both quartz types. Heterogeneous silicate melt inclusions are not present in the clear quartz overgrowths. The highest homogenization temperature (380–385°C) for an intermediate-density, secondary fluid inclusion assemblage was measured in sample V244-1674 at a drill hole depth of 513 m. The assemblage has a salinity of 2.4 wt% NaCl equiv.

5 Discussion and conclusions

The petrographic evidence suggests that the quartz veins deep in the B-1 exploration drill hole below the Sunnyside deposit are similar to high-temperature ‘A’ veins in shallow- to intermediate-depth porphyry Cu deposits (Monecke et al. 2018). Quartz precipitation occurred in the two-phase field of the H₂O–NaCl system as the early quartz contains abundant vapor-rich fluid inclusions in addition to some hypersaline liquid inclusions, as originally noted by Casadevall and Ohmoto (1977). The presence of heterogeneous silicate melt inclusions suggests that the quartz could have formed at temperatures as high as $\geq 600^{\circ}\text{C}$ (cf. Rottier et al. 2016). Formation of the deep veins from such high-temperature magmatic-hydrothermal fluids implies the presence of a high-level porphyritic intrusion below Sunnyside.

Quartz formation at high temperatures in the deep veins at Sunnyside took place at lithostatic conditions as the volcanic wall rocks were likely heated within the contact metamorphic aureole of the

inferred high-level porphyritic intrusion. The ductile nature of the host rocks at these temperatures would have prevented the formation of a fracture network connected to the surface and the establishment of hydrostatic pressure conditions. However, after the formation of the anhedral quartz containing the heterogeneous silicate melt inclusions, the isotherms surrounding the high-level porphyritic intrusion must have retracted to depth. The fluid inclusion inventory of the anhedral quartz in the high-temperature veins was affected by post-entrapment modification due to the significant pressure differential (cf. Sterner and Bodnar 1989) caused by the change from lithostatic to hydrostatic conditions. Secondary fluid inclusion assemblages crosscutting the euhedral quartz overgrowths, which is equivalent to quartz in ‘B’ veins in porphyry deposits (cf. Monecke et al. 2018), have not been affected by post-entrapment modification. These inclusion assemblages containing vapor-rich and hypersaline liquid inclusions must, therefore, have been entrapped at hydrostatic conditions and likely never experienced significant pressure fluctuations after their formation. Quartz in ‘B’ veins in porphyry deposits forms close to the ductile-brittle transition at temperatures as low as $\sim 400^{\circ}\text{C}$, which allows establishment of through-going fracture networks to surface (Monecke et al. 2018). Intermediate-density fluid inclusions hosted by the ‘B’ vein quartz were entrapped at a minimum temperature of 380–385°C and a minimum pressure of ~ 240 bar, which

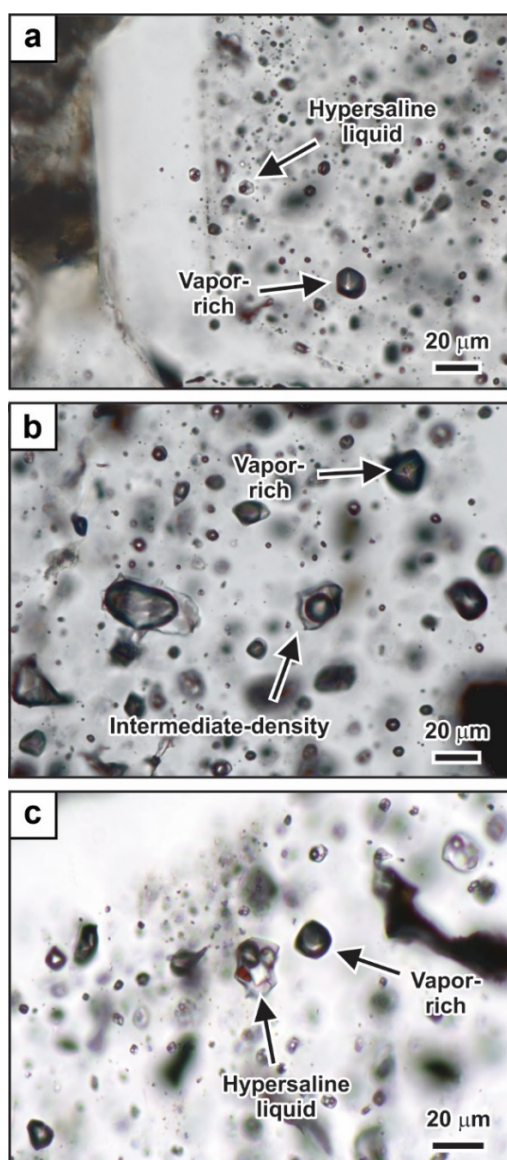


Figure 4. Fluid inclusion inventory of high-temperature quartz from a deep drill hole at the Sunnyside deposit, Colorado. **a** Euhedral quartz crystal with a clearer outer growth zone. The core contains abundant unmodified fluid inclusions, including hypersaline liquid and vapor-rich inclusions. **b** Intermediate-density and vapor-rich inclusions. **c** Hypersaline liquid and vapor-rich inclusions in the core of a euhedral quartz crystal. All images from sample V244-1684 (drill hole depth of 513 m).

corresponds to a minimum depth of ~2400 m below the paleosurface at hydrostatic conditions.

It is envisaged here that the epithermal veins at Sunnyside are an integral part of the evolution of a magmatic-hydrothermal system driven by a high-level porphyritic intrusion. Intermediate-density fluids released from the intrusion ascended along major faults forming the epithermal veins at Sunnyside. As the magmatic-hydrothermal system waned, minor base metal veins similar to those found at the Sunnyside deposit telescoped onto the earlier high-temperature veins in the deep part of the B-1 drill core.

The deep drilling at Sunnyside provides important constraints on the depth of the porphyritic intrusion. The exploration drill hole B-1 extends to a depth of

~600 m below the Sunnyside deposit. The presence of the high-temperature veins suggests that a high-level intrusion is in close proximity. The situation at Sunnyside contrasts with other epithermal deposits in the San Juan Mountains. For instance, Creede is located above, and laterally offset from, a deeply seated intrusion that is located several kilometres below the base of the epithermal mineralization (Barton et al. 2000).

Acknowledgements

This research was supported by the U.S. Geological Survey Mineral Resources Program and the Society of Economic Geologist Hugh McKinstry Student Research Grant. E. Anderson and D. Yager of the USGS assisted with sampling and provided helpful insights on the mine geology. Any use of trade, firm, or product names is for descriptive purposes only and does not imply endorsement by the U.S. Government.

References

- Audétat A (2022) A plea for more skepticism toward fluid inclusions: Part II. Homogenization via halite dissolution in brine inclusions from magmatic-hydrothermal systems is commonly the result of postentrapment modifications. *Econ Geol*, doi: 10.5382/econgeo.4974
- Barton PB, Rye RO, Bethke PM (2000) Evolution of the Creede caldera and its relation to mineralization in the Creede mining district, Colorado. *Geol Soc Amer Spec Pap* 346:301–326
- Bartos PJ (1993) Comparison of gold-rich and gold-poor quartz-base metal veins – Western San Juan Mountains, Colorado: The Mineral Point area as an example. *SEG Newsl* 15:1,6–11
- Burbank WS, Luedke RG (1969) Geology and ore deposits of the Eureka and adjoining districts, San Juan Mountains, Colorado. *US Geol Surv Prof Pap* 535, 73 p.
- Casadevall T, Ohmoto H (1977) Sunnyside mine, Eureka mining district, San Juan County, Colorado: Geochemistry of gold and base metal ore deposition in a volcanic environment. *Econ Geol* 72:1285–1320
- Lipman PW (2007) Incremental assembly and prolonged consolidation of Cordilleran magma chambers: Evidence from the Southern Rocky Mountain volcanic field. *Geosphere* 3:42–70
- Monecke T, Monecke J, Reynolds TJ, Tsuruoka S, Bennett MM, Skewes WB, Palin RM (2018) Quartz solubility in the H₂O–NaCl system: A framework for understanding vein formation in porphyry copper deposits. *Econ Geol* 113:1007–1046
- Rottier B, Kouzmanov K, Bouvier AS, Baumgartner LP, Wälle M, Rezeau H, Bendezú R, Fontboté L (2016) Heterogeneous melt and hypersaline liquid inclusions in shallow porphyry type mineralization as markers of the magmatic-hydrothermal transition (Cerró de Pasco district, Peru). *Chem Geol* 447:93–116
- Sterner SM, Bodnar RJ (1989) Synthetic fluid inclusions—VII. Re-equilibration of fluid inclusions in quartz during laboratory simulated metamorphic burial and uplift. *J metamorph Geol* 7:243–260
- Sun M, Monecke T, Reynolds TJ, Yang Z (2021) Understanding the evolution of magmatic-hydrothermal systems based on microtextural relationships, fluid inclusion petrography, and quartz solubility constraints: Insights into the formation of the Yulong Cu–Mo porphyry deposit, eastern Tibetan Plateau, China. *Mineral Deposita* 56:823–842

Switch in magma source linked to an evolving geodynamic environment in the Farallon Negro Volcanic Complex, NW Argentina

Madeleine Ince¹, Steffen Hagemann¹, Marco Fiorentini¹, Tony Kemp¹, Nora Rubinstein²

¹Centre for Exploration Targeting, School of Earth Sciences, University of Western Australia, Perth, Australia

²IGEBa, Departamento de Ciencias Geológicas, Facultad de Ciencias Exactas y Naturales, Buenos Aires, Argentina

Abstract. Constraining the source and processes contributing to porphyry Cu-Au formation on a district scale is fundamental for understanding the formation of Cu-Au mineralisation. The Farallon Negro Volcanic Complex contains the world-class Bajo de la Alumbrera porphyry Cu-Au deposit with weakly mineralised and barren porphyry intrusions, including El Durazno, San Lucas and Las Pampitas. Zircon trace element and isotope systematics are used to track the magmatic evolution of the Farallon Negro Volcanic Complex. The intrusions can be grouped into several stages. Stage 1 includes the El Durazno Au-Cu deposit (8.0 ± 0.3 Ma). El Durazno, whose emplacement was facilitated by localised extension, is from an enriched mantle-derived source (zircon $\delta^{18}\text{O} = 5.7 \pm 0.3\text{‰}$; zircon $\epsilon_{\text{Hf}} = -0.3 \pm 1.8$) with minor crustal assimilation. Stage 2 encompasses San Lucas (7.4 ± 0.1 to 7.3 ± 0.1 Ma), Las Pampitas (7.2 ± 0.2 to 7.0 ± 0.1 Ma) and Bajo de la Alumbrera (6.9 ± 0.1 to 6.8 ± 0.2 Ma). These display a mixed mantle-derived and supracrustal source (zircon $\delta^{18}\text{O} > 6.7\text{‰}$, zircon $\epsilon_{\text{Hf}} = < -2.2 \pm 1.0$) that homogenised in a lower-crustal MASH zone facilitated by regional compression. The combination of an enriched mantle source and accumulation in a lower-crustal MASH zone was favourable for Cu-Au mineralisation.

1 Introduction

Constraining the magma source is fundamental for understanding the petrogenetic processes leading to the genesis of giant porphyry Cu-Au deposits, especially in a gold-rich system (Park et al. 2021). The natural laboratory investigated here is the Farallon Negro Volcanic Complex (FNVC), which is a pre-eminent Cu-Au district in the Sierras Pampeanas of northwest Argentina (Fig. 1). It is a back-arc volcanic complex that hosts Cu-Au porphyry (Bajo de la Alumbrera, El Durazno, Agua Rica) and epithermal (Farallon Negro) deposits within an andesitic to dacitic volcanic complex (Proffett 2003). The FNVC contains other porphyritic intrusions that are of similar age and composition, but are significantly less mineralised, such as the San Lucas and Las Pampitas intrusions (Halter et al. 2004). Through comparison of zircon trace element and isotopic data from the Bajo de la Alumbrera porphyry intrusions to the San Lucas, Las Pampitas and El Durazno deposits, we assess the relationship between magma source and/or magma evolution and Cu-Au mineralisation.

2 Geological background

2.1 Geodynamic environment

The FNVC is located in the Sierras Pampeanas, which is in the northern part of the Pampean flat-slab segment (~ 27 to 33°S ; Fig. 1), a section where the Nazca plate has been subducting under the South American plate at a dip of ~ 5 – 10° since 9 Ma (Kay and Mpodozis 2002). The shallow subduction angle can be attributed to the combination of coeval trench-ward motion of thick cratonic lithosphere and trench retreat during subduction of the Juan Fernandez Ridge (JFR; Fig. 1), as discussed in Manea et al (2012) and Yáñez et al (2001). This process caused thinning of the continental lithospheric mantle and reduction of the asthenospheric wedge, causing cessation of volcanism and hydration of the lithosphere (Kay et al. 1999).

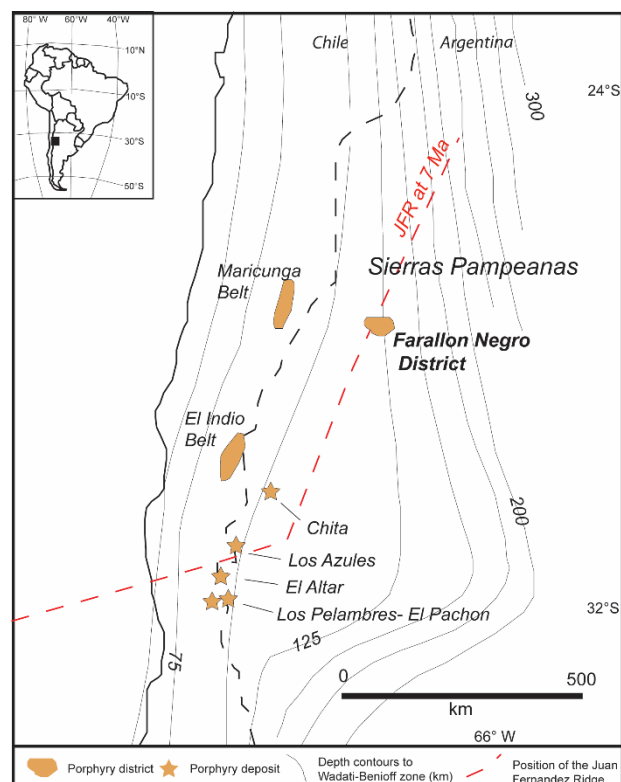


Figure 1. Location of the Farallon Negro Volcanic Complex and Miocene porphyry deposits. Light grey lines indicate depth to the Wadati-Benioff zone (Ramos et al. 2002) and the red dashed line indicates the position of the Juan Fernandez Ridge at 7 Ma (Yáñez et al. 2001).

2.2 Local geology and sample selection

Magmatism in the FNVC occurred from ~9.7 to 6 Ma (Ar-Ar hornblende and U-Pb zircon dating), broadly shifting from andesitic to dacitic in nature (Halter et al. 2004; Buret et al. 2016). The El Durazno porphyry intrusion was emplaced during the early stage of magmatism, and the Bajo de la Alumbreira, Las Pampitas and San Lucas systems later, from 7.3 to 6.0 Ma (Buret et al. 2016). The Bajo de la Alumbreira system comprises a stock of dacitic porphyries (intrusions P2, EP3, LP3, P4) intruding the surrounding basaltic andesite and andesite units (Fig. 3A). The main mineralizing event associated with dacitic porphyries P2 and EP3 has been previously dated between 7.22 ± 0.02 and 7.13 ± 0.02 Ma (zircon U-Pb CA-ID-TIMS; Buret et al. 2016). The grade of this deposit is 767 Mt @ 0.51% Cu and 0.64 g/t Au (Rubinstein et al. 2021).

The San Lucas porphyry is located ~6 km to the southeast of the Bajo de la Alumbreira deposit and largely comprises a rhyodacitic porphyry stock intruding a diorite (Fig. 3b) (Alderete 1999). The highest grade is 0.26% Cu, 0.35 g/t Au and 1.9 g/t Ag in the potassic alteration zone; however, mineralisation is considered uneconomic (Alderete 1999). Two samples were selected from San Lucas: a quartz andesite porphyry and a rhyodacite porphyry.

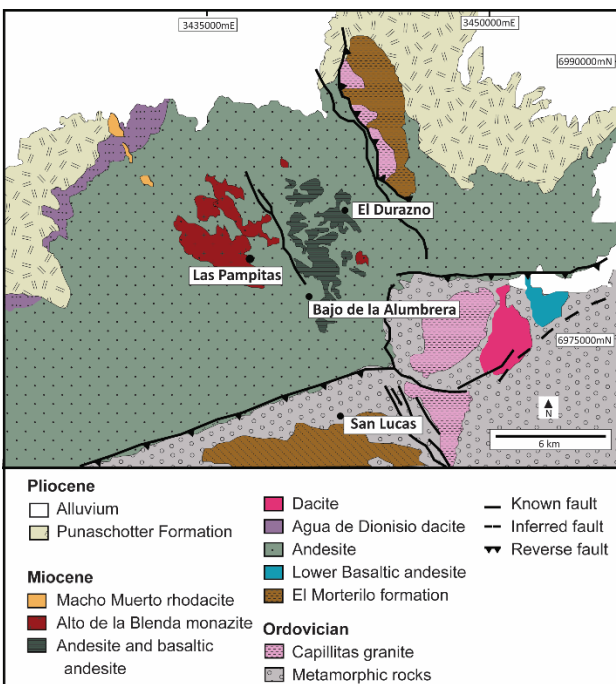


Figure 2. Geological map of the Farallon Negro Volcanic Complex showing those intrusions that were investigated in detail in this study. After Proffett (2003).

The Las Pampitas prospect is located ~4 km to the northwest of Bajo de la Alumbreira (Fig. 2) and has grades up to 0.13% Cu, 0.006% Mo and up to 1.06 g/t Au (average 0.07 g/t Au), and is considered uneconomic (Gutiérrez et al. 2006; Rubinstein et al. 2021). Three samples were analysed from Las Pampitas: a finer grained dacite porphyry, a coarser grained dacitic porphyry and a quartz andesite porphyry.

The El Durazno deposit is considered economically viable and contains 93 Mt at 0.15% Cu, 0.41 g/t Au (Glencore 2017). It was emplaced during the earlier stages of volcanism (Halter et al. 2004), with mineralisation hosted in a basaltic andesite porphyry (Fig. 2), which was analysed in this study.

3 Zircon U-Pb geochronology

The SHRIMP U-Pb ages generated in this study cannot resolve the within-deposit intrusive ages but can resolve the difference in ages between deposits. The El Durazno andesite porphyry is markedly older than the other intrusions, with an age of 8.0 ± 0.3 Ma ($n=10$, MSWD=1.3, 95% confidence). The San Lucas andesite porphyry and rhyodacite porphyries are ~0.4 my younger with ages of 7.4 ± 0.1 Ma ($n=10$, MSWD=1.0, 95% confidence) and 7.3 ± 0.1 Ma ($n=10$, MSWD=1.0, 95% confidence), respectively. The Las Pampitas dacitic porphyry intrusions have zircon U-Pb ages of 7.3 ± 0.1 Ma ($n=10$; MSWD=1.5, 95% confidence) and 7.0 ± 0.1 Ma ($n=10$, MSWD=2.1, 95% confidence), respectively. The quartz andesite porphyry has a zircon U-Pb age of 7.2 ± 0.2 Ma ($n=9$, MSWD=2.6, 95% confidence). The Bajo de la Alumbreira P2 and EP3 intrusions have the same zircon U-Pb age of 6.9 ± 0.2 Ma (P2: $n=13$, MSWD=1.8; EP3: $n=11$, MSWD=1.8, 95% confidence). LP3 also has the same age with a smaller uncertainty of 6.9 ± 0.1 Ma ($n=13$, MSWD=0.6, 95% confidence). P4 is the youngest intrusion, with a zircon U-Pb age of 6.8 ± 0.2 Ma ($n=10$, MSWD=0.6, 95% confidence).

These data can be combined with U-Pb ages of Halter et al. (2004), Borba et al. (2016) and Buret et al. (2016) to define three key stages of magmatism in the FNVC: (1) 9.5 to 8.0 Ma, (2) 7.5 to 6.5 Ma, and (3) 6.5 to 5 Ma (Fig. 3).

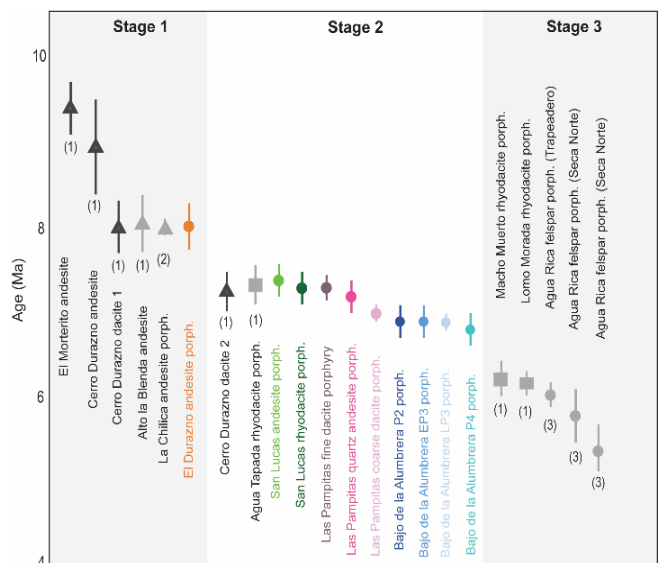


Figure 3. Summary of geochronological data from this study and the literature. Error bars are plotted at 95% confidence. Circles indicate ^{238}U - ^{206}Pb ages, triangles ^{40}Ar - ^{39}Ar biotite ages and squares $^{40}\text{Ar}/^{39}\text{Ar}$ hornblende

ages. Sources: (1) Halter et al. (2004), (2) Sasso (1997), and (3) Borba et al. (2020). Coloured points are from this study.

4 Magma source linked to geodynamic environment

4.1 Stage 1 magmatism (9.5 – 8.0 Ma)

The first stage of magmatism was primarily extrusive, basaltic to andesitic, and occurred during a period of localised extension (Halter et al. 2004).

The El Durazno intrusion formed at the end of stage 1 magmatism and was preceded by andesitic and basaltic lava flows and intrusions (Fig. 2). These units are hydrous (Halter et al. 2004). There is no trend towards a silicic composition over time as would be expected during fractional crystallisation, so therefore it is interpreted that a long-lived magma chamber was not established during this stage (Halter et al. 2005). Emplacement of El Durazno was facilitated by localised extension (Halter et al. 2004). The El Durazno porphyry has a zircon $\delta^{18}\text{O}$ signature of $5.7 \pm 0.1\text{‰}$ and ϵHf value of -0.3 ± 0.6 (2 SD, Fig. 4). The $\delta^{18}\text{O}$ value is consistent with a mantle-derived source (Valley et al. 2005). The ϵHf value is lower than those of ocean island basalt and mid ocean ridge basalts, which are generally above $\epsilon\text{Hf} = +5$ (Janney et al. 2005), indicating the presence of a crustal component in the El Durazno magma. Contamination of magma source in the mantle can decrease the $^{176}\text{Hf}/^{177}\text{Hf}$ ratio, but may not shift the O isotope signature (Roberts et al. 2013). Based on the subduction-zone tectonic setting, the source was likely to be mantle wedge that was recently contaminated by subducted crust and sediments (Chauvel et al. 2009). This may also include a contribution from sub-continental lithospheric mantle and/or minor assimilation of continental crust during the ascent of the magma.

4.2 Stages 2 and 3 magmatism (7.5 to 5 Ma)

The second stage of magmatism was mostly intrusive and is defined by intermediate to felsic magmatism. This period encompasses the San Lucas, Las Pampitas and Bajo de la Alumbrera intrusions (Fig. 3). Zircon crystals from all intrusions have an initial ϵHf of < -2.2 and $\delta^{18}\text{O}$ of $> 6.7\text{‰}$ (Fig. 4), indicative of an older supracrustal component in the source melt (Hawkesworth and Kemp 2006). Because of the distinctly elevated $\delta^{18}\text{O}$ values, it is likely that this supracrustal component was introduced in the crust rather than in the metasomatized mantle (Hawkesworth and Kemp 2006), perhaps in a lower crustal MASH zone (Hildreth and Moor bath 1988). The Agua Rica porphyry intrusions (stage 3 magmatism), to the south-east of Bajo de la Alumbrera, are interpreted as having the same source as Bajo de la Alumbrera, with a greater degree of crustal contamination (Borba et al. 2016).

Stages 2 and 3 of magmatism are likely a mix of stage 1 magmatism (mantle-derived) and a supracrustal component incorporated due to stalling of the magmas in the lower crust. The onset of regional transpression, linked to the peak of flat slab subduction at ~ 8 Ma (Kay and Mpodozis 2002), likely stalled the ascent of the mantle-derived magma, resulting in pooling in a lower crustal MASH zone, and mixing with felsic crust. It is suggested that this process in the lower-crustal MASH zone facilitated the build-up of volatiles and metals (Cu).

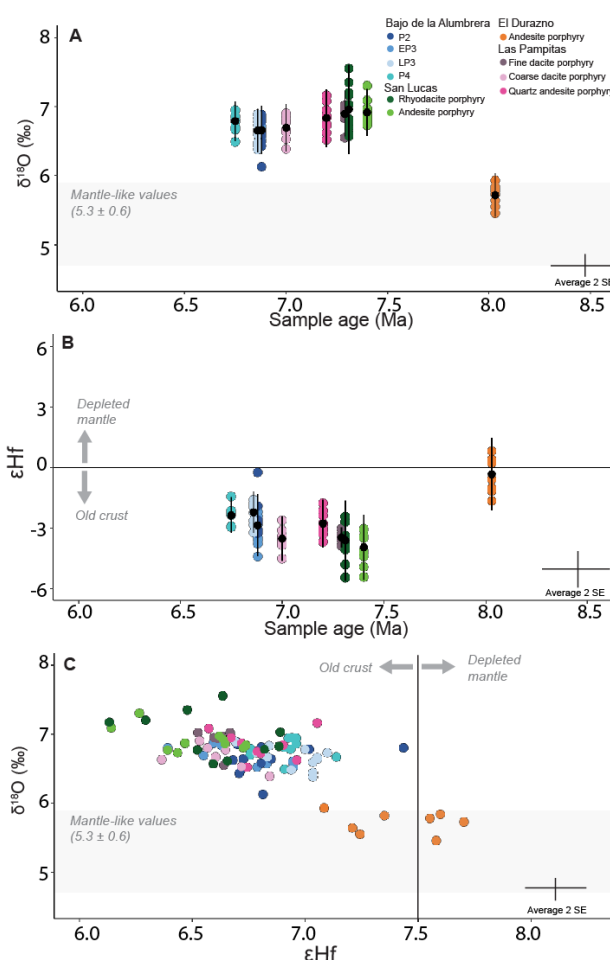


Figure 4. A: Zircon ϵHf vs sample age. Black bars indicate mean and 2 standard deviations. **B:** Zircon $\delta^{18}\text{O}$ vs ϵHf . Mantle-like oxygen value is after Valley et al. (2005). Average error bars are 2 standard errors (2 SE) of each spot.

5 Conclusion

Zircon Lu-Hf and O isotopic data record a switch in magma source between stage 1 and stage 2. The earlier magmatism of the FNVC, represented by the El Durazno porphyry, has a mantle source with minor crustal input, with magma ascent facilitated by localised extension (Halter et al. 2004). The early Cu-Au mineralisation of El Durazno indicates a mantle component with enrichment in Cu and Au. After ~ 8 Ma, the stalling of this magma in a lower crustal MASH zone and mixing with supracrustal material led to the accumulation of S, Cu and volatiles in the magma, with eventual sulfur

saturation and exsolution of volatiles leading to porphyry Cu-Au mineralisation at higher crustal levels. The combination of an enriched magma and favourable tectonic environment likely led to Cu-Au mineralisation at Bajo de la Alumbrera.

Acknowledgements

The authors would like to acknowledge the Centre for Microscopy, Characterisation and Analysis (CMCA) at UWA, where O isotope analysis and SEM CL imaging were undertaken and the John de Laeter Centre, Curtin University, where U-Pb zircon analyses were undertaken. We would like to acknowledge staff at Minera Alumbrera and YMAD for field support and technical support in collecting samples.

References

- Alderete MC (1999) Bajo de San Lucas, Catamarca In: Zappettini EO (ed) Recursos Minerales de la Republica Argentina. Instituto de Geologia y Recursos Minerales SEGEMAR, Buenos Aires, pp 1471-1473.
- Borba ML, Chemale F, Kawashita K, Takehara L, Babinski M, Bruckman M (2016) The Bajo de la Alumbrera and Agua Rica Cu–Au (Mo) porphyry deposits of Argentina: Genetic constraints on ore formation and sources based on isotope signatures. *Ore Geology Reviews* 75:116-124. doi: <https://doi.org/10.1016/j.oregeorev.2015.12.010>.
- Borba ML, Tassinari CCG, Kirk J, Ruiz J (2020) Ages and isotope evolution of the Agua Rica Cu-Au porphyry-epithermal deposit, NW Argentina. *Ore Geology Reviews* 119:103395. doi: <https://doi.org/10.1016/j.oregeorev.2020.103395>.
- Buret Y, von Quadt A, Heinrich C, Selby D, Wälle M, Peytcheva I (2016) From a long-lived upper-crustal magma chamber to rapid porphyry copper emplacement: Reading the geochemistry of zircon crystals at Bajo de la Alumbrera (NW Argentina). *Earth and Planetary Science Letters* 450:120-131. doi: <https://doi.org/10.1016/j.epsl.2016.06.017>.
- Glencore (2017) Resources and reserves as at 31 December 2017.
- Gutiérrez AA, Chong GD, Espinoza SR (2006) Exposures levels of the deposits of the Agua de Dionisio (YMAD) mining district, Catamarca. *Revista de la Asociacion Geologica Argentina* 61:269-278.
- Halter W, Bain N, Becker K, Heinrich C, Landtwing M, VonQuadt A, Clark A, Sasso A, Bissig T, Tosdal R (2004) From andesitic volcanism to the formation of a porphyry Cu-Au mineralizing magma chamber: The Farallón Negro Volcanic Complex, northwestern Argentina. *Journal of Volcanology and Geothermal Research* 136:1-30. doi: [10.1016/j.jvolgeores.2004.03.007](https://doi.org/10.1016/j.jvolgeores.2004.03.007).
- Halter WE, Heinrich CA, Pettke T (2005) Magma evolution and the formation of porphyry Cu–Au ore fluids: evidence from silicate and sulfide melt inclusions. *Mineralium Deposita* 39:845-863. doi: [10.1007/s00126-004-0457-5](https://doi.org/10.1007/s00126-004-0457-5).
- Hawkesworth CJ, Kemp AIS (2006) Using hafnium and oxygen isotopes in zircons to unravel the record of crustal evolution. *Chemical Geology* 226:144-162.
- Hildreth W, Moorbath S (1988) Crustal contributions to arc magmatism in the Andes of Central Chile. *Contributions to Mineralogy and Petrology* 98:455-489. doi: [10.1007/BF00372365](https://doi.org/10.1007/BF00372365).
- Janney PE, Le Roex AP, Carlson RW (2005) Hafnium Isotope and Trace Element Constraints on the Nature of Mantle Heterogeneity beneath the Central Southwest Indian Ridge (13°E to 47°E). *Journal of Petrology* 46:2427-2464. doi: [10.1093/ptrology/egi060](https://doi.org/10.1093/ptrology/egi060).
- Kay S, Mpodozis C (2002) Magmatism as a probe of Neogene shallowing of the Nazca Plate beneath the modern Chilean flat-slab. *Journal of South American Earth Sciences* 15:39-57. doi: [10.1016/S0895-9811\(02\)00005-6](https://doi.org/10.1016/S0895-9811(02)00005-6).
- Kay SM, Mpodozis C, Coira B (1999) Neogene Magmatism, Tectonism, and Mineral Deposits of the Central Andes (22° to 33° S Latitude) In: Skinner BJ (ed) *Geology and Ore Deposits of the Central Andes*. Society of Economic Geologists, pp 0.
- Manea vc, Perez-Gussinye M, Manea M (2012) Chilean flat slab subduction controlled by overriding plate thickness and trench rollback. *Geology* 40:35-38. doi: [10.1130/G32543.1](https://doi.org/10.1130/G32543.1).
- Park J-W, Campbell IH, Chiaradia M, Hao H, Lee C-T (2021) Crustal magmatic controls on the formation of porphyry copper deposits. *Nature Reviews Earth & Environment* 2:542-557. doi: [10.1038/s43017-021-00182-8](https://doi.org/10.1038/s43017-021-00182-8).
- Proffett J (2003) Geology of the Bajo de la Alumbrera Porphyry Copper-Gold Deposit, Argentina. *Economic Geology* 98:1535-1574. doi: [10.2113/98.8.1535](https://doi.org/10.2113/98.8.1535).
- Ramos V, Cristallini E, Perez D (2002) The Pampean flat-slab of the Central Andes. *Journal of South American Earth Sciences* 15:59-78. doi: [10.1016/S0895-9811\(02\)00006-8](https://doi.org/10.1016/S0895-9811(02)00006-8).
- Rubinstein NA, Zappettini EO, Gómez ALR (2021) Porphyry CU deposits in the Central Andes of Argentina: An overview. *Journal of South American Earth Sciences* 112:103543. doi: <https://doi.org/10.1016/j.jsames.2021.103543>.
- Sasso A (1997) Geological evolution and metallogenetic relationships of the Farallon Negro Volcanic Complex, NW Argentina. . Queen's University, Kingston pp 842.
- Valley JW, Lackey JS, Cavosie AJ, Clechenko CC, Spicuzza MJ, Basei MAS, Bindeman IN, Ferreira VP, Sial AN, King EM, Peck WH, Sinha AK, Wei CS (2005) 4.4 billion years of crustal maturation: oxygen isotope ratios of magmatic zircon Contributions to Mineralogy and Petrology. doi: [10.1007/s00410-005-0025-8](https://doi.org/10.1007/s00410-005-0025-8).
- Yáñez GA, Ranero CR, von Huene R, Díaz J (2001) Magnetic anomaly interpretation across the southern central Andes (32°–34°S): The role of the Juan Fernández Ridge in the late Tertiary evolution of the margin. *Journal of Geophysical Research: Solid Earth* 106:6325-6345. doi: <https://doi.org/10.1029/2000JB900337>.

Unravelling Hypogene to Supergene Processes in a Concealed Porphyry: Insights from the Santa Cruz Copper Deposit, Arizona, USA

Simon Kocher¹, Ben M. Frieman¹, Thomas Monecke¹, Holly J. Stein^{2,3}, Christopher J. Seligman⁴, Harry Hanneman⁴, Shawn Vandekerkhove⁴

¹Center to Advance the Science of Exploration to Reclamation in Mining, Department of Geology and Geological Engineering, Colorado School of Mines, Golden, CO, USA

²AIRIE, Applied Isotope Research for Industry and the Environment, Fort Collins, CO, USA

³Department of Geosciences, University of Oslo, Oslo, Norway

⁴Ivanhoe Electric, Casa Grande, AZ, USA

Abstract. An increasing demand for copper and lack of deposits exposed at surface force exploration to focus on targets at increasing depth or under deep cover. Recent exploration drilling at the Santa Cruz deposit in the southern Basin and Range Province has provided an opportunity to study a well-preserved example of a Laramide-aged hypogene deposit with a supergene enriched domain under up to 1000 m of post-mineral sedimentary cover. Paragenetic investigations are combined with Re-Os dating of molybdenite samples that establish new perspectives on emplacement and enrichment processes of the deposit. These results are compared to regional Re-Os data to establish a distinct Laramide-aged spatial trend in the distribution of deposits in the southern Arizona copper porphyry district. This comparison defines favourable temporal windows for deposit formation at ~75–70 Ma, ~65 Ma, and 60–55 Ma that likely relate to overriding tectonic controls.

1 Introduction

Porphyry deposits are the primary source of copper for the global economy. The discovery and development of deeper and/or concealed porphyry deposits will be critical to support green energy infrastructure in the 21st century and beyond. These deposits are typically associated with intermediate to felsic subvolcanic intrusions located in magmatic arc settings (Sillitoe 2010). Hypogene mineralisation in porphyry deposits comprises stockwork-hosted and disseminated sulphides that form large volumes of low-grade ore. However, supergene enrichment processes can lead to a significant increase in relative ore grade (Sillitoe 2005).

The Santa Cruz deposit is located 11 km west of Casa Grande, and approximately 9 km southwest of the previously mined Sacaton deposit in southern Arizona (Fig. 1). It was discovered in 1974 but not put into production due to low copper prices at the time.

The Santa Cruz deposit is primarily hosted by the ~1450–1350 Ma Oracle Granite (Tosdal and Wooden 2015) and minor diabase sills and dykes that are ~1100 Ma (Banks et al. 1972). Hypogene mineralisation is associated with Laramide aged quartz monzonite porphyry intrusions (Schmidt 1971; Vikre et al. 2014). Subsequently, the deposit underwent an extended period of erosion and oxidation, leading to the formation of a supergene enrichment blanket (Cook 1994; Kreis 1995). Basin and Range extension is marked by basaltic

magmatism forming diatreme-like structures and volcanic deposits (Vikre et al. 2014). Further extension and normal faulting dismembered the deposit into a series of fault blocks and led to the deposition of up to 1000 m of post-mineral sedimentary cover (Fig. 1). Based on recent estimates, the Santa Cruz deposit and related satellite zones contain 2.8 and 1.8 Mt total contained copper in indicated and inferred mineral resources, respectively (Nordmin Engineering 2023). Despite hosting significant resources, the age, structural framework, and a detailed understanding of the hypogene and supergene mineralisation are poorly constrained. This study includes paragenetic and geochronological results that further understanding of the emplacement and supergene enrichment processes recorded in the Santa Cruz deposit and establish when the deposit formed within the broader Arizona copper porphyry province.

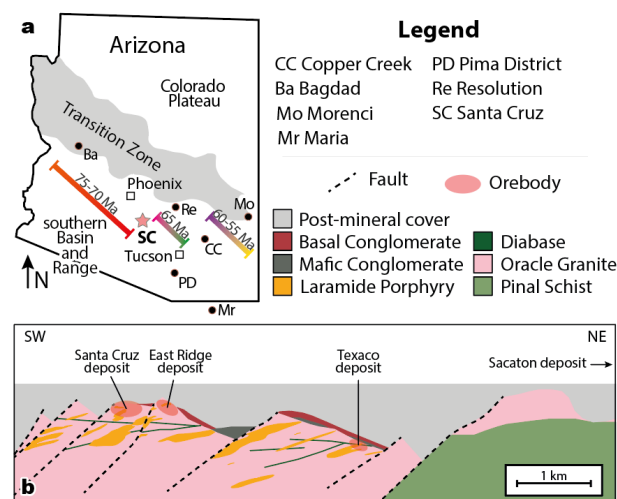


Figure 1. (a) Simplified regional map of Arizona showing the location of Santa Cruz and other major porphyry deposits discussed in the text. Age trends are derived from Re-Os dating (modified after Enders et al. 2006). (b) Schematic cross section through the Santa Cruz deposit (modified from Nordmin Engineering 2023).

2 Methodology

2.1 Optical petrography

Representative samples were collected of variably mineralised hypogene and supergene samples. From these, ~50 thin sections and polished resin blocks were

prepared and examined in transmitted and reflected light, prior to scanning electron microscopy.

2.2 Geochronology

Four vein samples containing visible molybdenite were selected from the Santa Cruz and Texaco deposits for Re-Os geochronology at the newly re-established Applied Isotope Research for Industry and the Environment (AIRIE) laboratory following the procedures of Stein et al. (2001). Molybdenite was carefully separated, and the separates were equilibrated with a mixed Re-double Os spike using inverse *aqua regia* for sample digestion in a Carius tube. Isotopic ratios were measured by NTIMS (negative thermal ionisation mass spectrometry) on a Triton instrument.

3 Results

3.1 Hypogene and supergene mineralogy

Petrographic observations suggest the presence of at least three individual porphyry phases, based on mineralogical and textural characteristics. These are referred to as granodiorite porphyry, quartz latite porphyry, and latite porphyry.

Typical porphyry-style veins in the form of A, B, C, and D veins (Gustafson and Hunt 1975) are present in the porphyry dykes and to a much lesser extent in the Oracle Granite. Veins frequently show signs of reopening. Potassic alteration is observed in association with A and B veins, resulting in secondary, shreddy biotite, often replacing other mafic minerals, and minor K-feldspar. C veins are accompanied by chlorite alteration, primarily affecting earlier biotite. Sericite alteration is most strongly developed in halos surrounding D veins.

The hypogene assemblage consists of chalcopyrite and minor bornite hosted in C and reopened B veins as well as in disseminations associated with vein halos. The occurrence of molybdenite is limited to the margins of B veins where it forms coarser aggregates intergrown with quartz and/or fine-grained smears. Pyrite is primarily associated with D veins, forming discrete sulphide-filled fractures and disseminations. Supergene mineralisation at Santa Cruz forms three distinct zones. The deepest zone is characterised by the replacement of hypogene chalcopyrite by covellite, bornite, and multiple other copper sulphide phases. At shallower depths the supergene assemblage comprises chalcocite and minor hematite partially or completely replacing pyrite. In the upper parts of the supergene enrichment blanket, the mineralogy is dominated by oxidised copper species, including abundant atacamite and chrysocolla.

3.2 Re-Os dating of molybdenite

The four molybdenite samples analysed yield highly precise dates that indicate molybdenite deposition at ~72–71 Ma. These analyses define a model age of 71.3 ± 1.4 Ma with an initial Os ratio of 0.2 (Fig. 2a). A

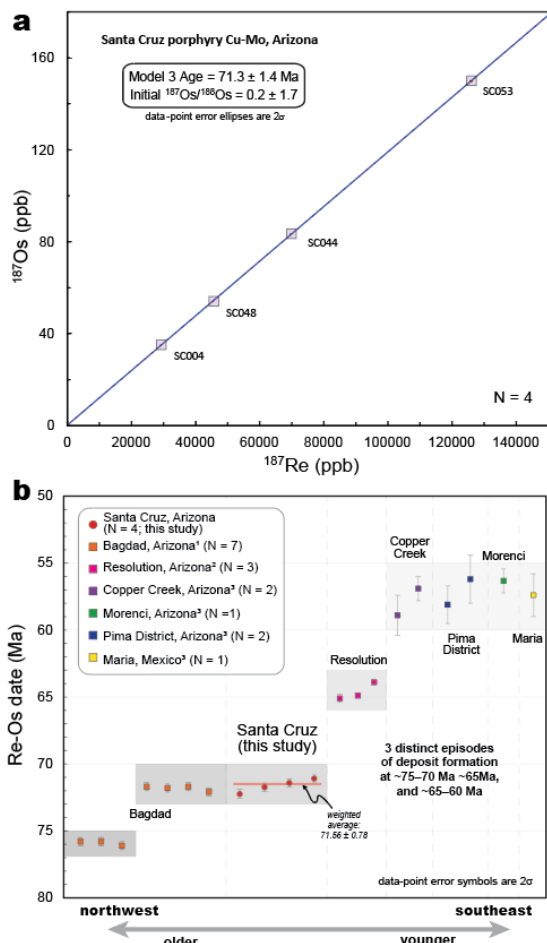
weighted average for these four analyses yields a similar date of 71.6 ± 0.8 Ma (Fig. 2b).

In order to compare, the Santa Cruz Re-Os results are plotted with published molybdenite results for Arizona and northern Mexico, including the Bagdad, Resolution, Copper Creek, Pima District, Morenci, and Maria deposits (Figs. 1 and 2). Together these results define three temporally distinct episodes of hypogene porphyry copper mineralisation in the region. The Santa Cruz results are comparable to the Bagdad porphyry, which gives Re-Os dates of ~76 Ma and ~72 Ma (Barra et al. 2003). To the east, Re-Os dates for molybdenite from the Resolution porphyry deposit yield younger ages that cluster around ~65 Ma (Hehnke et al. 2012). Deposits in southeastern Arizona and along the US-Mexico border have relatively young Re-Os ages of ~60–55 Ma (McCandless and Ruiz 1993).

4 Discussion and preliminary synthesis

Paragenetic studies conducted on the hypogene mineralisation preserved within deeper portions of the Santa Cruz deposit indicate the presence of A, B, C, and D veins. Molybdenite is associated with early B veins formed at high temperatures whereas chalcopyrite and bornite are present in C veins and reopened earlier veins. The pyrite-rich D veins are consistently late and associated with pervasive sericite alteration. Supergene processes have resulted in significant enhancement of copper grades.

Re-Os dating indicates that the hypogene mineralisation at Santa Cruz was emplaced at ~71.5 Ma (Fig. 2). This date is similar to molybdenite deposition ages in the Bagdad deposit (Barra et al. 2003; Figs. 1 and 2), suggesting broadly contemporaneous formation of these deposits. However, these Re-Os dates are relatively old when compared to porphyry deposits to the east and southeast of Santa Cruz. For example, Re-Os dates for the Resolution deposit are ~65 Ma (Hehnke et al. 2012), while all other deposits to the southeast (Copper Creek, Morenci, Pima District, and Maria) yield younger dates of ~60–55 Ma (Figs. 1 and 2). This west-northwest to east-southeast trend was recognised by McCandless and Ruiz (1993), who suggested that differences in the age and thickness of Precambrian crust of Arizona may have controlled the timing of mineralisation, wherein older (>1700 Ma) crust was spatially associated with the 75–70 Ma deposits while younger (<1700 Ma) Precambrian



Figure

2. (a) Re-Os results for the Santa Cruz molybdenite samples shown as an isochron age for the four samples analysed. (b) Re-Os dates for molybdenite samples from Santa Cruz compared to Re-Os dates from other copper deposits in Arizona (1 = Barra et al. 2003; 2 = Hehnke et al. 2012; 3 = McCandless and Ruiz 1993).

basement is host to the younger deposits. However, the Santa Cruz deposit is hosted by the 1450–1350 Ma Oracle Granite, indicating that <1700 Ma Precambrian basement can also host ~75–70 Ma porphyry deposits. This observation, when combined with an intermediate age for the Resolution deposit of ~65 Ma (Hehnke et al. 2012), may indicate that subduction-related porphyry copper deposits migrated progressively to the southeast (present-day distribution) and the major episodes of mineralisation occurred at distinct temporal intervals of ~75–70 Ma, ~65 Ma, and 60–55 Ma (Fig. 2) that may broadly coincide with changes in the overriding plate kinematics such as a transition to flat-slab subduction, ridge-subduction and/or oceanic plateau subduction (Cooke et al. 2005). Constraining Laramide-aged spatial and temporal trends in the formation of porphyry copper deposits is hampered by extensive, Tertiary-aged structural dismemberment within the Basin and Range Province. While this history complicates the interpretation of primary tectonic trends it also served to exhume and enrich many Arizona deposits through supergene

processes. Understanding Tertiary modification of Laramide hypogene mineralisation is critical to assess the economic potential of these deposits, particularly in concealed deposits like Santa Cruz where the supergene enriched zone is well-preserved and is host to a large proportion of known resources.

Acknowledgements

This work was supported by the National Science Foundation and conducted within CASERM, a joint industry-university collaborative research centre between the Colorado School of Mines and Virginia Tech under award numbers 1822146 and 1822108.

References

- Banks NG, Cornwall HR, Silberman ML, Creasey SC, Marvin RF (1972) Chronology of intrusion and ore deposition at Ray, Arizona: Part I, K-Ar ages. *Econ Geol* 67:864–878
- Barra F, Ruiz J, Mathur R, Titley S (2003) A Re-Os study of sulfide minerals from the Bagdad porphyry Cu-Mo deposit, northern Arizona, USA. *Mineral Deposita* 38:585–596
- Cook SS III (1994) The geologic history of supergene enrichment in the porphyry copper deposits of southwestern North America. PhD thesis, University of Arizona
- Cooke DR, Hollings P, Walshe JL (2005) Giant porphyry deposits: Characteristics, distribution, and tectonic controls. *Econ Geol* 100:801–818
- Enders MS, Knickerbocker C, Titley SR, Southam G (2006) The role of bacteria in the supergene environment of the Morenci porphyry copper deposit, Greenlee County, Arizona. *Econ Geol* 101:59–70
- Gustafson LB, Hunt JP (1975) The porphyry copper deposit at El Salvador, Chile. *Econ Geol* 70:857–912
- Hehnke C, Ballantyne G, Martin H, Hart W, Schwarz A, Stein H (2012) Geology and exploration progress at the Resolution porphyry Cu-Mo deposits, Arizona. *SEG Spec Publ* 16:147–166
- Kreis HG (1995) Geology of the Santa Cruz porphyry copper deposit. *Ariz Geol Soc Dig* 20:364–365
- McCandless TE, Ruiz J (1993) Rhenium-osmium evidence for regional mineralization in southwestern North America. *Science* 261:1282–1286
- Nordmin Engineering (2023) Mineral resource estimate update and S-K 1300 technical report summary for the Santa Cruz, Texaco and East Ridge deposits, Arizona, USA. Internal report to Ivanhoe Electric Inc., 230 p. <https://rb.gy/uzbjtg>
- Schmidt EH (1971) Belts of Laramide-age intrusive rocks and fissure veins in south central Arizona. *Ariz Geol Soc Dig* 9:61–69
- Sillitoe RH (2005) Supergene oxidized and enriched porphyry copper and related deposits. In: Hedenquist JW, Thompson JFH, Goldfarb RJ, Richards JP (eds) *Economic Geology 100th Anniversary Volume*. Society of Economic Geologists, Littleton, pp 723–768
- Sillitoe RH (2010) Porphyry copper systems. *Econ Geol* 105:3–41
- Stein HJ, Markey RJ, Morgan JW, Hannah JL, Scherstén A (2001) The remarkable Re-Os chronometer in molybdenite: How and why it works. *Terra Nova* 13:479–486
- Tosdal RM, Wooden JL (2015) Construction of the Jurassic magmatic arc, southeast California and southwest Arizona. *Geol Soc Amer Spec Pap* 513:189–221
- Vikre PG, Graybeal FT, Koutz FR (2014) Concealed basalt-matrix diatremes with Cu-Au-Ag-(Mo)-mineralized xenoliths, Santa Cruz porphyry Cu-(Mo) system, Pinal County, Arizona. *Econ Geol* 109:1271–1289

Texture, composition, alteration styles in the Permo-Triassic Pampa Elvira plutonic complex and the Eocene tonalite porphyry at the Gaby porphyry copper deposit, Chile

Luis Krampert¹, Kalin Kouzmanov¹, Alexandre Cugerone¹, Lluís Fontboté¹, Carolina Rodríguez², Rubén Pardo², Sergio Pichott Henríquez²

¹Department of Earth Sciences, University of Geneva, 1205 Geneva, Switzerland

²CODELCO, Santiago, Chile

Abstract. In some porphyry copper deposits, the similarity between pre-, syn- and post-mineral intrusions in terms of texture and geochemistry is a known issue. This is also the case at the Gaby porphyry Cu deposit in Northern Chile. This study aims to find features to discriminate between the Permo-Triassic Pampa Elvira plutonic complex (PEPC) which is volumetrically the main host rock of the deposit, and the ore-related Eocene tonalite porphyry (TP). Various field and analytical methods have been applied to a drill hole in the district's center to properly characterize the two lithologies. Fieldwork (core logging, magnetic susceptibility), automated mineralogy (QEMSCAN), whole rock geochemistry, and electron microprobe are techniques used so far. They reveal important variations in texture, grain size distribution, mineralogy, and chemistry. Relative proportions between the major rock-forming minerals plagioclase, alkali feldspar, quartz, and biotite are contrasting between the magmatic units. The Eu anomaly and element ratios (especially Sr/Y and Zr/Hf) strongly differ between the two magmatic suites and in combination, these features allow discrimination. Chemical features of alteration minerals such as white mica, chlorite, and biotite (Fe enrichment in chlorite) do show significant variations between the units but need complementation with trace element data by LA-ICP-MS.

1 Introduction

Northern Chile is recognized for hosting numerous small to very large porphyry copper deposits (Zappettini et al. 2001). One of the giant deposits is Chuquicamata. Zentilli et al. (2018) reported that one fundamental challenge during the exploration of the deposit was the discrimination between "ore-carrying Eocene porphyries" and a Triassic granodiorite with similar textural and geochemical characteristics.

Despite the extended research that was carried out on the Chuquicamata cluster, only recently Zentilli et al. (2018) attempted to solve this issue with whole-rock analyses and presented geochemical tools to distinguish the Triassic granodiorite from the Eocene porphyry stocks in the area. Standard geochemical characterization methods for trace elements (e.g., Winchester and Floyd 1977) did not yield a clear separation. The only consistent geochemical difference found by Zentilli et al. (2018) was that the main Eocene–Oligocene porphyries carry relatively less Fe and Ni than the Triassic granodiorite.

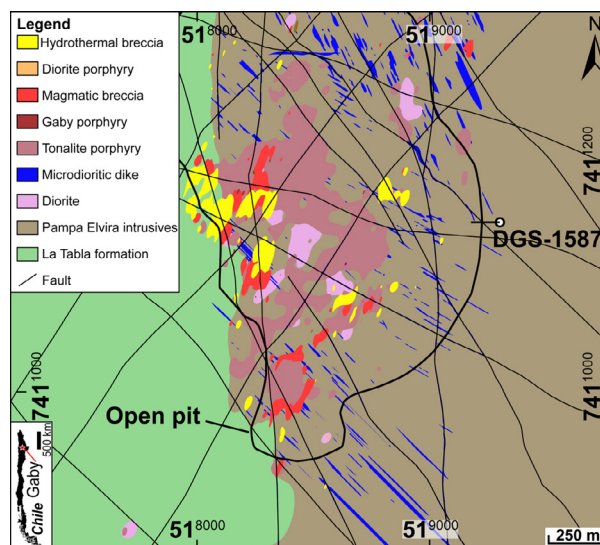


Figure 1. Simplified geological map of the Gaby district at an elevation of 2540 m.a.s.l. with an outline of the open pit. The location and trace of the drill hole DGS-1587 are marked (modified after Reygadas et al. 2023).

This study addresses a similar problem at the Gaby porphyry deposit, located around 120 km south of the Chuquicamata district. Here, the Permo-Triassic Pampa Elvira plutonic complex (PEPC) is one of the hosts for copper mineralization generated by Eocene porphyry intrusions (Dilles et al. 2000). The dominant composition found in the PEPC is granodiorite. Both lithologies are similar in texture and chemistry and have not yet been exhaustively investigated. This study uses magnetic susceptibility, bulk and mineral chemistry, and alteration styles to define criteria for differentiation and describe similarities between the PEPC and the tonalite porphyry (TP). The research focuses on part of a drill hole located in the center of the district (Figure 1), intercepting the contact between the two lithologies.

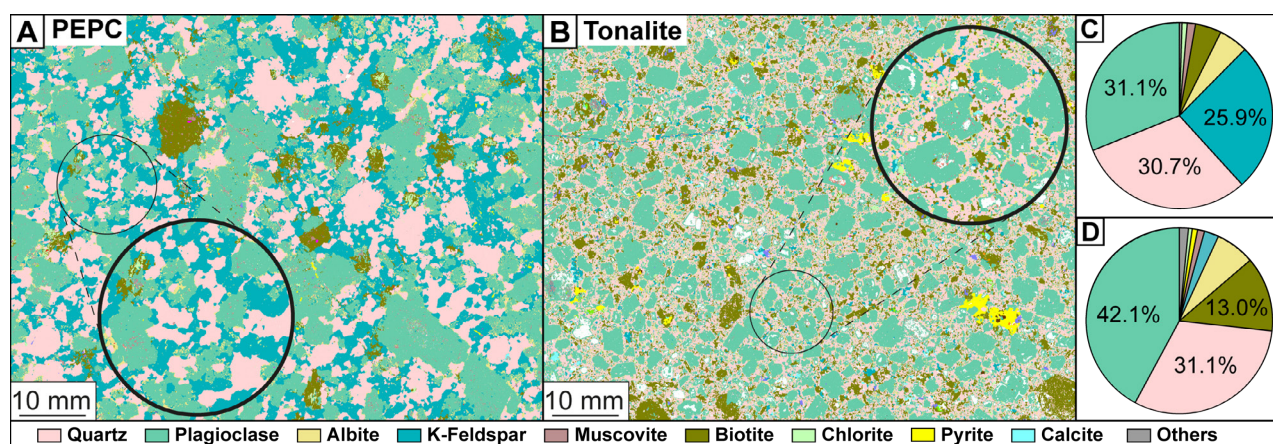


Figure 2. QEMSCAN maps of the two lithologies. **A** Non-mineralized sample of the PEPC. **B** Non-mineralized sample of the TP. **C** and **D** Pie charts of the area % of the selected samples in the PEPC (**A**) and in the TP (**B**). The low amount of alkali feldspar is demonstrated.

2 Methods

The analyzed samples (n=44) are mainly from a single drill hole (DGS-1587) in the center of the district intersecting the two main host lithologies, the PEPC and the TP. Geochemical and electron microprobe (EPMA) data are complemented with measurements from other drill holes in the vicinity of the Gaby open pit (Figure 1; Cugerone et al., this volume).

The magnetic susceptibility (MS) was recorded over the length of the drill core with a handheld magnetic susceptibility meter (KT-10). Measurements were taken in 50 cm intervals to increase the accuracy of the dataset.

Scanning electron microscopy-based automated mineralogy analysis (QEMSCAN) followed petrographic observations on thin sections. This method was used to generate mineral and elemental maps and define the relative mineral proportions on a thin-section scale.

Whole rock analyses of major and trace elements were performed by inductively coupled plasma atomic emission spectroscopy (ICP-AES) and by inductively coupled plasma mass spectroscopy (ICP-MS), respectively. As, Bi, Hg, In, Re, Sb, Se, Te, and Tl were measured with ICP-MS on an aqua regia solution and base metals by four acid digestion followed by ICP-AES. The results were filtered before using them in discrimination diagrams and strongly altered and mineralized samples were left out for these tasks.

White mica, chlorite, and biotite chemistry were studied with a JEOL JXA8200 SuperProbe EPMA at the University of Geneva. The following elements were measured: Si, Al, Ti, Fe, Ca, Mg, Na, K, Mn, Cr, Ba, and Cl. The results were normalized to 11 oxygen atoms per formula unit (apfu) for white mica and 28 apfu for chlorite.

Besides, X-ray diffraction analysis combined with short-wave infrared light spectroscopy was applied to target alteration minerals. LA-ICP-MS will be used to supplement the EPMA data.

3 Geology of the deposit

Porphyry copper deposits in northern Chile including the Gaby deposit formed during the Andean cycle of magmatism in the area. The largest deposits were developed in a relatively short period of around 10 m.y. during the Eocene-Oligocene (Maksaev and Zentilli 1988), forming the Paleogene metallogenic belt (e.g., Piquer et al. 2021). An essential factor for the formation of large deposits is the Domeyko fault zone. Structures belonging to the latter are also present at Gaby, where they preferentially align the intrusive bodies NE-SW (Piquer et al. 2021).

The major host rocks at Gaby are the Permo-Triassic Pampa Elvira plutonic complex consisting mainly of the granodiorite (GD), intruded by the Eocene TP, and the Late Carboniferous–Early Permian (Gardeweg et al. 1994 in Niemeyer et al. 2008) volcano-sedimentary La Tabla formation to the west (Camus 2003). There are multiple Eocene porphyry intrusions recognized in the area, but the TP is volumetrically the most abundant (Dilles et al. 2000). All units show internal heterogeneity in texture and degree of alteration.

The focus herein lies on a comparison of the distinctive texture, alteration, and mineralization styles of the PEPC and the TP near the Gaby open pit.

4 Texture, mineralogy, and geochemistry of the PEPC and the TP

The Pampa Elvira intrusive body can be described as a light grey phaneritic and moderately porphyritic rock consisting of quartz, alkali feldspar, altered plagioclase, and biotite. The magnetic susceptibility (MS) is relatively low and strongly dependent on vein distribution and alteration styles. At the district and drill hole scale, the PEPC can be relatively heterogeneous. Plagioclase and alkali feldspar commonly present sodic alteration (albite). QEMSCAN analyses suggest that roughly twice as much albite is present in the PEPC than in the TP (Figure 2). Albite is present as a product of pervasive alteration and as vein alteration halos.

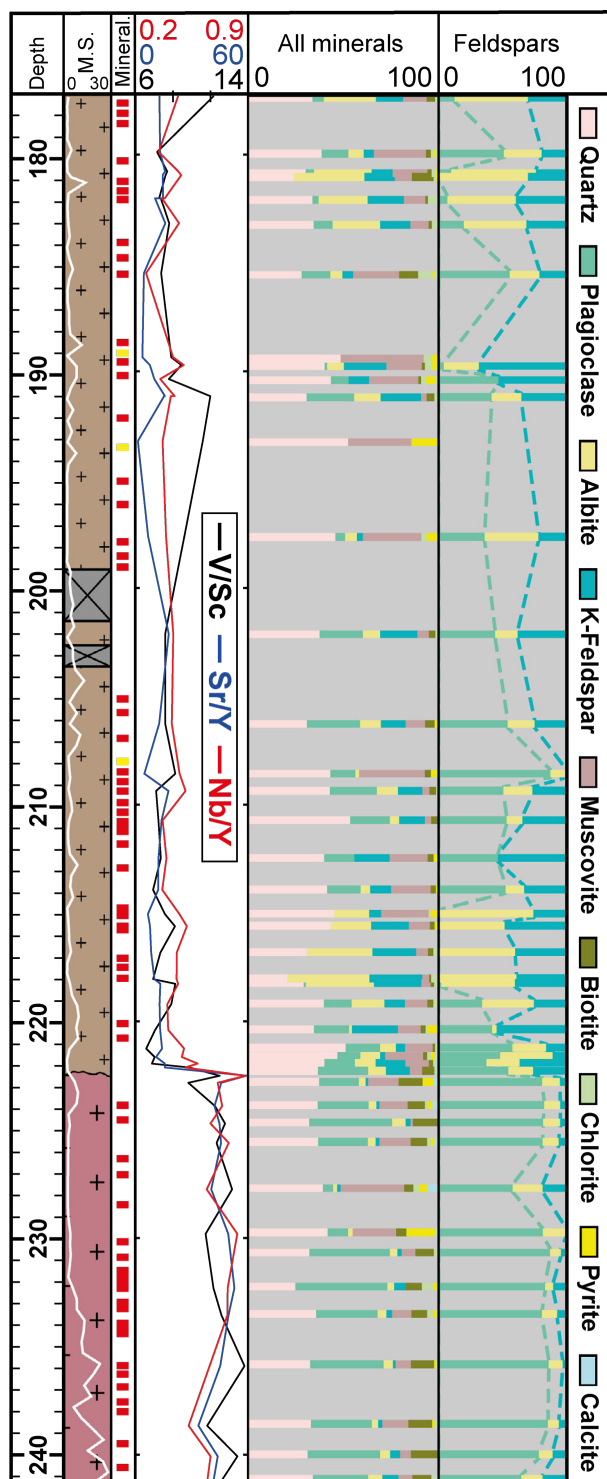


Figure 3. Drill log of DGS-1587 combining core logging with magnetic susceptibility data (MS in 10^{-3} SI) over depth, elemental ratios, and QEMSCAN mineral fractions (area %). The second column of QEMSCAN results presents the variation in feldspar content. Mineralization (Mineral.) type is presented as porphyry-style (red) and polymetallic (yellow) veins. Lithology color codes as in Figure 1.

Potassic alteration is observed overprinting the sodic alteration. Like albitization, it exists both along veins and as a background alteration in the host rock. The mineralization style does not vary

between the PEPC and the TP and cannot be used to differentiate these lithologies. However, several geochemical parameters can be used to separate the two igneous lithologies. The Eu anomaly is the tool with the best potential to easily discriminate the two units. The PEPC has an average negative Eu anomaly of 0.69. Variations of element ratios such as V/Sc, Sr/Y, Zr/Hf, and Nb/Y are strongly dependent on major magmatic processes and can also be used to differentiate the igneous units (Winchester and Floyd 1977; Halley 2020). Figure 3 shows their good correlation over depth and sharp increase at the igneous contact with the TP. The most consistent here appear to be Sr/Y (depending on plagioclase fractionation and the water content of the magma; Richards et al. 2012) and Zr/Hf (related to the fractional crystallization of zircons; Lowery Claiborne et al. 2006). The PEPC has an average Zr/Hf ratio of 34.6.

The TP is a dark grey porphyritic rock with an aphanitic groundmass. Its MS signal is higher in the deeper part of the core which is related to stronger potassic alteration. The rock consists mainly of large plagioclase phenocrysts in a fine-grained groundmass of quartz, alkali feldspar, and biotite. The amount of biotite is higher than in the PEPC (Figure 2). As aforementioned, the alteration is fundamentally different in the TP. Like in the PEPC, albitization is also present, but here it occurs as a weak background sodic alteration. Potassic alteration is characterized by an increase in hydrothermal biotite associated with minor alkali feldspar and magnetite. The TP has an average Eu anomaly of 0.95. This means that the anomaly is close to neutrality and therefore could be successfully used to discriminate the porphyritic intrusion from the host PEPC. Additionally, the Zr/Hf ratio is around 39.9 (compared to 34.6 in the PEPC). QEMSCAN was used to quantify the mineral proportions for each sample according to their depth in Figure 3. The increase in plagioclase and drop in alkali feldspar and albite contents are demonstrated.

5 Alteration mineral chemistry

White mica alteration does not vary significantly between the two lithologies. The white mica composition corresponds to muscovite–phengitic muscovite (Tischendorf et al. 2004). The compositional trends in white mica chemistry are presented in Figure 4A, showing higher variability in white mica chemistry in the PEPC.

Changes in chlorite chemistry between the PEPC and TP are also noticeable. All the chlorite grains analyzed can be described as trioctahedral Mg- and Fe-chlorites (Figure 4B). In the PEPC, the Fe and partly Al contents are higher than in the TP.

The magmatic and hydrothermal biotite chemistry reveals variation between the targeted grains but is inconclusive at this stage.

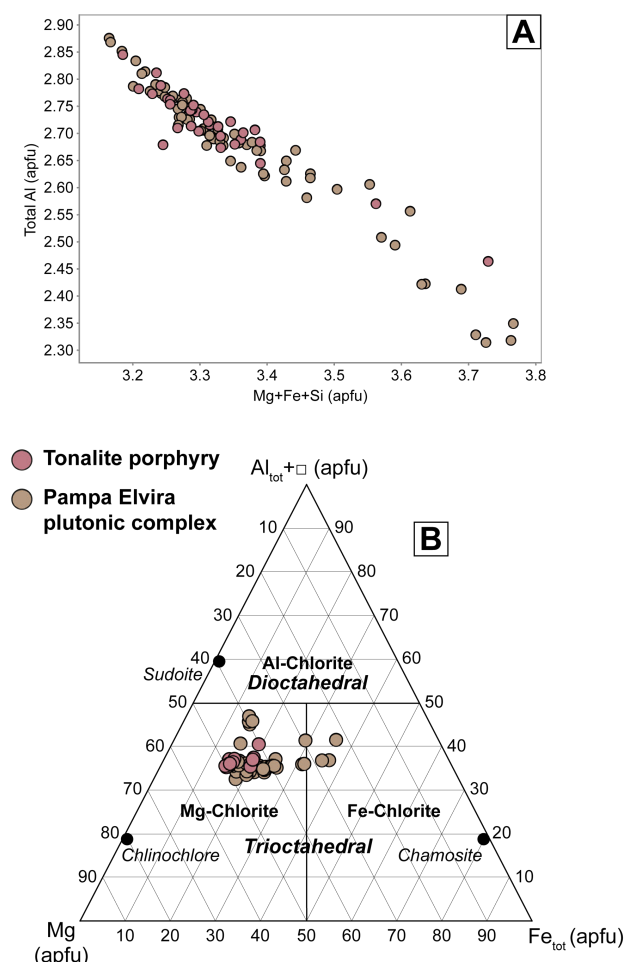


Figure 4. **A** Mg-Fe-Si versus total Al plot demonstrating the similarity in white mica chemistry. **B** Chlorite Total Al + octahedral vacancy-Mg-Fe compositional diagram, showing a range of Mg- to Fe-rich chlorite in the GD (after Zane and Weiss 1998).

6 Discussion and conclusions

While the PEPC and TP at the Gaby porphyry copper deposit cannot always be differentiated macroscopically, dominant alteration styles and some geochemical characteristics prove to be good vectors to discriminate them. The proportions of feldspars are largely controlled by lithology. The Eu anomaly, as well as Sr/Y and Zr/Hf ratios also yield good results. It is demonstrated that these methods can be applied on a single drill core or district scale and present a powerful tool for correct discrimination between macroscopically similar-looking lithologies.

White mica, chlorite, and biotite compositions revealed by EPMA indicate distinct trends in chemistry (e.g., chlorite depleted in Fe in TP), but require additional verification with trace element analysis by LA-ICP-MS technique.

Acknowledgements

The authors thank Codelco and Exploraciones Mineras S.A. (EMSA) for funding this project,

granting access to their facilities, and for continued support.

References

- Camus F (2003) Geología de los sistemas porfíricos en los Andes de Chile. Servicio Nacional de Geología y Minería. Cugerone A, Kouzmanov K, Fontboté L, Krampert L, Rodríguez C, Pardo R, Pichott Henríquez S (this volume) White mica alteration in the Gaby porphyry copper district, Northern Chile.
- Dilles JH, Winkler M, Essman J, Duncan R (2000) Petrologic and Geochemical Studies of the Gaby Sur Porphyry Copper Deposit, Northern Chile. Internal Report.
- Gardeweg M, Pino H, Ramirez CF, Davidson J (1994) Mapa geológico del área de Imilac y Sierra de Almeida, Región de Antofagasta. Servicio Nacional de Geología y Minería, Documentos de Trabajo No. 7, Escala 1:100.000. Santiago, Chile.
- Halley S (2020) Mapping magmatic and hydrothermal processes from routine exploration geochemical analyses. *Econ Geol* 115: 489–503.
- Lowery Claiborne L, Miller CF, Walker BA, et al (2006) Tracking magmatic processes through Zr/Hf ratios in rocks and Hf and Ti zoning in zircons: An example from the Spirit Mountain batholith, Nevada. *Mineral Mag* 70: 517–543.
- Maksaev V, Zentilli M (1988) Marco metalogénico regional de los megadepósitos de tipo porfido cuprífero del norte grande de Chile. *Congreso Geológico Chileno* 1: 181–212.
- Niemeyer H, Zavattieri AM, Ballent S, Zamuner A, Gallego O (2008) Triassic age of the continental Pular Formation, Sierra de Almeida, Antofagasta, northern Chile. *Revista Geológica de Chile*, 35(1), 147–161.
- Piquer J, Sanchez-Alfaro P, Pérez-Flores P (2021) A new model for the optimal structural context for giant porphyry copper deposit formation. *Geology* 49:597–601.
- Reygadas W, Chepillo J, Pardo R (2023) Programa Exploración. Mapa Litología-Estructuras, 1:20,000. Distrito Garbiela Mistral. Internal Report.
- Richards JP, Spell T, Rameh E, et al (2012) High Sr/Y magmas reflect arc maturity, high magmatic water content, and porphyry Cu ± Mo ± Au potential: Examples from the Tethyan arcs of central and eastern Iran and western Pakistan. *Econ Geol* 107: 295–332.
- Tischendorf G, Rieder M, Förster H-J, et al (2004) A new graphical presentation and subdivision of potassium micas. *Mineral Mag* 68: 649–667.
- Winchester JA, Floyd PA (1977) Geochemical discrimination of different magma series and their differentiation products using immobile elements. *Chem Geol* 20: 325–343.
- Zane A, Weiss Z (1998) A procedure for classifying rock-forming chlorites based on microprobe data. *Rend Lincei Sci Fis Nat* 9: 51–55.
- Zappettini E, Miranda-Angles V, Rodríguez C, et al (2001) Mapa metalogénico de la región fronteriza entre Argentina, Bolivia, Chile y Perú (14oS–28oS). Publicación Geológica Multinacional 2.
- Zentilli M, Maksaev V, Boric R, Wilson J (2018) Spatial coincidence and similar geochemistry of late Triassic and Eocene–Oligocene magmatism in the Andes of northern Chile: evidence from the MMH porphyry type Cu–Mo deposit, Chuquibambilla district. *International Journal of Earth Sciences* 107: 1097–1126.

Genesis of Mineralized Skarns: reanalysis of decarbonation reactions, decarbonatization, and carbonate melting during infiltrative contact metasomatism

David R Lentz¹

¹Dept. of Earth Sciences, University of New Brunswick, Fredericton, NB Canada

Abstract. The integration of silica activities (solubilities) in analysis of infiltrative metasomatic calc-silicate formation in limestones-marbles helps to reconcile available mineral-fluid phase modelling, fluid inclusion, and stable isotopic evidence. Very low $X(\text{CO}_2)$ (<0.01) is consistent with these volatiles, very high F/R, and the general absence of residual carbonates in prograde skarns. H_2CO_3 in this reaction, with low pH volatiles enhance carbonate solubilities, but also enhance carbonate melting, and mobilization. Mass-balance calculations consistently reveal substantial Ca-Mg carbonate loss from the system, beyond decarbonation. Carbonate-rich “veins” within and around contact metasomatic skarn systems, are generally devoid of silica, and variably mineralized in sulphides and sulfates, so maybe carbonate dykes consistent with their textures and mineral-chemical equilibria. Carbonate, salt, sulfate, and phosphatic melts are ionic liquids of very low viscosity and have different solution properties for many components, including mineralizing components introduced in the fluid infiltration process.

1 Introduction

Skarn deposits are some of the richest deposit systems in terms of grade, but also overall metal endowment. The prograde development of skarns has long been at issue as the traditional interpretation of calc-silicate forming reactions lead to erroneous interpretation of the $X(\text{CO}_2)$ of these fluids. Virtually all fluid inclusion studies of mineralized skarns do not exhibit CO_2 even with Raman or evidence of boiling, which had been advocated for these systems. Lentz and Suzuki (2000) showed that using silica activities (not 1 for quartz) applied to the T-P- $X(\text{CO}_2)$ result in calc-silicate assemblages and zonation consistent with observations, i.e. $X(\text{CO}_2) < 0.01$. Lentz (2005a) described extensive loss of carbonate (~ 50%) from selected skarn systems using mass-balance techniques consistent with these those findings. In addition, silica mass balancing supports extremely high fluid-rock ratio (F/R) associated with all infiltrative skarns. Lentz (2005b) further elaborated on this to demonstrate that this was not simple dissolution of carbonates that were stripped from skarns, but in fact carbonate melts were formed; these ideas were built off of Lentz (1999) were evidence was presented showing that this equilibria was consistent with the eutectic in the carbonate melt system (> 600°C) with a maximum of carbonic acid formed, so I postulated that some carbonatitic systems might be from either volatile fluxing and (or) syntectic reactions (Lentz 1998; Lentz 2005a).

Many of these complex reactions between limestones-marbles and a wide range of silicate melts were described by the infamous Reginald Daly over a century ago (see Lentz 2017).

2 Infiltrative metasomatism and decarbonation

Lentz and Suzuki (2000) used existing interpolations of silica solubility and their activities to show how the interpreted calc-silicate assemblages form at very low $X(\text{CO}_2)$ showing the consistency of silica solubility induced metasomatism with interpreted low CO_2 (< 1 %) in the H_2O infiltrating the skarn system (Fig. 1).

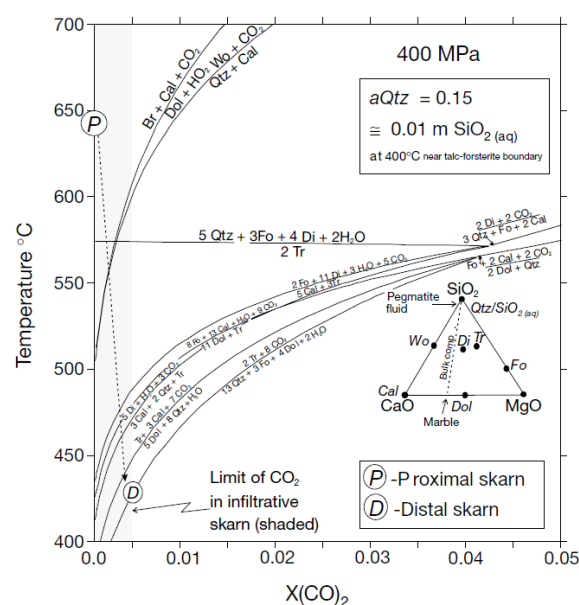


Figure 1. Temperature vs. $X(\text{CO}_2)$ in the Ca-Mg-Si-C-O-H system (400 MPa), illustrating the estimated stability of calc-silicate assemblages (CaCO_3 , MgCO_3 , SiO_2 projection) (modified after Lentz and Suzuki 2000).

Key is these mixed volatile equilibria and zoning relationships are valid over a huge range of P-T conditions to very low temperatures (T), consistent with critically low CO_2 contents of fluid inclusions, as well in all skarn-related magmatic hydrothermal systems. All prograde decarbonation is driven by infiltrating silica forming calc-silicates, so is limited by its solubility in water, so the system naturally stays very low in CO_2 ; therefore there is no need to invoke

CO₂-H₂O immiscibility and no reason to expect high CO₂ (>1 %) in fluid inclusions.

3 Decarbonization

Most skarns have minimal evidence for residual carbonates in the system, especially in prograde skarns. Lentz (2005a) noted that greater than 50% mass decrease occurred with skarnification, i.e. the carbonates were mobilized from the system. Although exsolving magmatic fluids are commonly invoked as the culprits in contact metasomatic skarns and they are known to be acidic, the amount of acidic fluids is considerable and beyond the capability of the infiltrative fluid. Carbonates have a retrograde solubility so at prograde infiltrative temperatures carbonates are typically negligibly soluble. Lentz (1998, 1999) reposed from the much earlier literature that carbonates could easily be melted at the P-T conditions of typical prograde skarn formation (see Fig. 2); there was never an intention to infer all carbonate melts were derived by these volatile fluxing or syntectic reactions with limestones, but rather help develop a realization that magmas could react in complex ways with limestones and marbles that helped explain some phenomena in and around skarn systems.

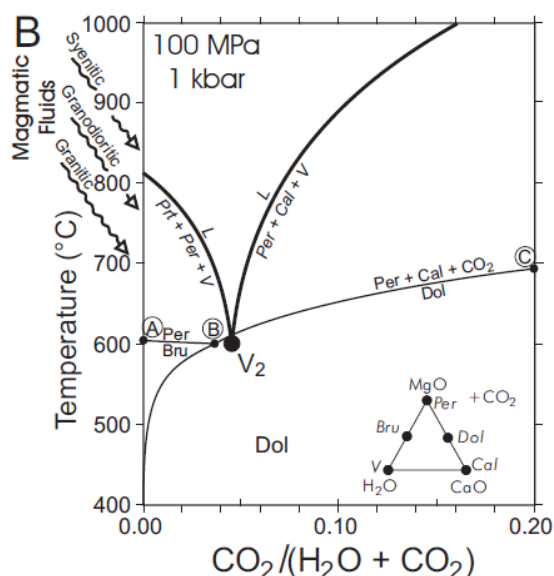


Figure 2. Temperature vs. $X(\text{CO}_2)$ diagram illustrating decarbonation reaction dolomite \leftrightarrow periclase (or brucite) + calcite + CO_2 [at a $X(\text{CO}_2) = 0.05$ relative to portlandite-calcite-periclase-vapor-liquid (melt) eutectic (MgO - CaO - CO_2 - H_2O system) (modified after Lentz 1999).

The substantial loss of carbonate during calc-silicate generation is probably a combination of dissolution by acidic volatiles and at advanced prograde stages by volatile-induced melting of carbonates during infiltration as described by Lentz (2005b).

3.1 Carbonate melt inclusions

Crystallized carbonate melt inclusions (cMIs) have been recognized in many magmatic systems including some related to skarns including vesuvianite skarn clasts erupted from Vesuvius (see Veksler and Lentz 2006). Trapping of melt inclusions is a natural consequence of calc-silicate formation, although the highly reactive and ephemeral nature of carbonates in continually reacted skarns makes them elusive in many systems. Saline brines to salt melts have a continuum with sparingly soluble carbonates or high T molten carbonate. Carbonates readily crystallize, and melt inclusions formed would immediately crystallize as well in the presence of the water-rich fluid; carbonate melts have as much dissolved volatiles as a silicate melt, so volatile fluxed carbonates easily have up to 10% H_2O in any pressurized system. Water and salts and sulfates, sulfides, and oxides associated with the original infiltrating volatiles are known to coexist with varieties of cMIs in skarn systems (Xu et al. 2023), as well as iron oxide (apatite) systems (cf. Lentz 2018, Bain et al. 2020).

4 Carbonate dykes with skarn association

Although rarely described, there are numerous carbonate vein and (or) dike-like features around contact metasomatic skarns. These features have commonly been considered veins, but many have dike like features. Chemically and isotopically they are consistent with a skarn derivation. Numerous researchers have referred to crustal carbonatites, some with and others without an obvious relation to skarns, although they are quite distinctive to any mantle carbonatitic system. Around large porphyry-related skarns, including iron skarns, they have been considered as veins, and even have magnetite-sulfides, as well as apatite, but rarely quartz. Carbonatitic to salt melts are ionic melts, so have extremely low viscosity, and depressurization during buoyant ascent-emplacement readily yields (exsolves) volatiles that enhances ascent beyond the distal skarn environment. Textures are wide ranging, but pseudo-aplitic to pegmatitic textures are evident reflecting the role of water-rich volatiles differentially exsolving and reacting with these ionic melts as quenching-crystallization occurs; it is easy to see how these could be interpreted as veins, and in the past many have referred to similar things descriptively as vein-dykes (see Lentz 1998).

5 Conclusions

This brief review highlights the intimate role silica-bearing magmatic volatiles have with formation of infiltrative (contact metasomatic) skarns that are mineralized. The silica solubilities are a controlling factor in decarbonation equilibria, which are consistent with observed $X(\text{CO}_2)$ and fluid inclusions. These very low $X(\text{CO}_2)$ are coincident with carbonate melting at $T_s > 600^\circ\text{C}$ and the maximum in the formation of carbonic acid that acts as a flux with H_2O . The extremely high F/R inferred

from silica mass balance constraints and the considerable loss of carbonates (decarbonatization) from the system suggest that carbonate melting in addition to carbonate dissolution by acidic magmatic volatiles are responsible. Crystallized carbonate melt inclusions are not uncommon, and have generally been overlooked for the most part in skarns and complex carbonate dykes that originated from skarns; these typically have evidence of association with saline brines or salt melts, as well as sulfates, sulphides, oxides, and magnetite with some calc-silicates to name a few as they are highly fluid ionic melts. Geochemically and isotopically these have been described as crustal carbonatites as they crystallize distal to most contact metasomatic skarn systems. Further work is needed to examine these carbonate-rich systems to ascertain if they are indeed veins or dykes, using cMIs to aid in that analysis.

Acknowledgements

I was financially supported as IAGOD Distinguished Lecturer (2020-2023).

References

- Bain, W.M., Steele-MacInnis, M., Li, K., Li, L., Mazdab, F.K. and Marsh, E. (2020): A fundamental role of carbonate-sulfate melts in formation of iron oxide-apatite deposits; *Nature Geoscience*, v. 13, p. 751–757, <https://doi.org/10.1038/s41561-020-0635-9>.
- Lentz, D.R. (1998): Late-tectonic U-Th-Mo-REE skarn and carbonatitic vein-dike systems in the southwestern Grenville Province: a Pegmatite-Related Pneumatolytic Model linked to Marble Melting (limestone syntexis); *In* *Mineralized Intrusion-Related Skarn Systems* (D.R. Lentz ed.). Mineralogical Association of Canada Short Course Volume 26, p. 519-657.
- Lentz, D.R. (1999): Carbonatite Genesis: a reexamination of the role of intrusion-related pneumatolytic skarn processes in limestone melting; *Geology*, v. 27, p. 335-338.
- Lentz, D.R. (2005a): Mass-balance Analysis of Mineralized Skarn Systems: Implications for Replacement Processes, Carbonate Mobility, and Permeability Evolution; *SGA 2005, Mineral Deposit Research, Meeting the Global Challenge*, Beijing, v. 1, p. 421-424.
- Lentz, D.R. (2005b): Reinterpretation of infiltrative skarn phase equilibria: implications for fluid phase composition and behaviour; *ECROFI VIII Conference*, Abstract volume.
- Lentz, D.R. (2017): Syntectic Reactions involving Limestones and Limestone-Derived Carbonatitic Melts in the Generation of some Peralkalic Magmas: Reflections on Reginald Daly's Insights 100 Years Later; *American Geophysical Union*.
- Lentz, D.R. (2018): Iron Oxide Copper-Gold (IOCG) Systems: examination of end-member models, physiochemical processes, and possible modern analogies. *IAGOD Salta, Argentina*.
- Lentz, D.R. and Suzuki, K. (2000): A low-F, pegmatitic granite-related Mo skarn from the southwestern Grenville Province, Ontario, Canada: petrology to phase equilibria implications; *Economic Geology*, v. 95, p. 1319-1337.
- Veksler, I.V. and Lentz, D.R. (2006): Parental magmas of plutonic carbonatites, carbonate-silicate immiscibility and decarbonation reactions: evidence from melt and fluid inclusions; *In* *Melt inclusions in Plutonic Rocks*, Edited by J. Webster. Mineralogical Association of Canada, Short Course volume 36, p. 123-150.
- Xu, X., Szemihelsky, M., Yan, J., Xie, Q. and Steele-MacInnis, M. (2023): Melt inclusion evidence for limestone assimilation, calc-silicate melts, and "magmatic skarn". *Geology* <https://doi.org/10.1130/G50893.1>

Oxidation and hydration states of porphyry-copper ore-forming magmas recorded by trace elements in zircon

Robert R. Loucks^{1,2}, Marco L. Fiorentini^{1,2}

¹Centre for Exploration Targeting, School of Earth Sciences, University of Western Australia, 35 Stirling Highway, Crawley WA 6009, Australia

²ARC Centre of Excellence for Core to Crust Fluid Systems, University of Western Australia, 35 Stirling Highway, Crawley WA 6009, Australia

Abstract. Trace elements in magmatic zircon preserve a record of the hydration state as well as oxidation state of the ore-forming silicate melts. The zircon trace-element ratio $(\text{Eu}/\text{Eu}^*)/\text{Yb}_\text{N}$ is formulated as an indicator of silicate melt hydration state and is empirically validated by comparison with hygrometry and geobarometry on coexisting hornblende phenocrysts. Zircon records tandem rise of oxidation state and hydration state of arc magmas during fluid-undersaturated magmatic differentiation at lower-crustal depths. Zircon records dehydration and further oxidation of ascending silicate melts as exsolving hydrothermal fluid segregates at lower-to upper-crustal depths. Porphyry-copper ore-forming melts have distinctive values and trends on zircon oxybarometer vs hygrometer plots. Our zircon oxybarometer and hygrometer are applicable to detrital zircons, permitting identification of watersheds that contain a copper-fertile igneous complex (exploration target) upstream from the sediment sampling site.

1 Zircon $(\text{Eu}/\text{Eu}^*)/\text{Yb}_\text{N}$ indicator of silicate melt hydration state

Arc magmas parental to porphyry copper deposits (PCDs) typically have high whole-rock Sr/Y and Eu/Yb ratios and $\text{H}_\text{O}/\text{Yb}_\text{N} < 1$ that indicate suppressed plagioclase and enhanced hornblende production over most of the course of mafic-to-felsic magmatic differentiation. Al-in-hornblende geobarometry and hygrometry on phenocrysts and experimental petrology indicate that those features are attributable to unusually high hydration state of the magmas over most of the course of mafic-to-felsic differentiation at Moho-vicinity pressures. Zircon inherits the $(\text{Eu}/\text{Eu}^*)/\text{Yb}_\text{N}$ feature of its parent melt, warped by zircon/melt partition coefficients. We formulate and empirically validate the trace-element ratio $(\text{Eu}/\text{Eu}^*)/\text{Yb}_\text{N}$ in zircon as an indicator of relative hydration states of silicate melts, including ones parental to PCDs.

2 Zircon $\text{Ce}/\sqrt{(\text{U}\times\text{Ti})}$ oxybarometer

Magmas parental to porphyry copper deposits commonly have igneous anhydrite and/or sulphate-rich apatite phenocrysts that indicate higher oxidation state than ordinary granitoid arc magmas (Hutchinson and Dilles, 2019). The ratio $\text{Ce}/\sqrt{(\text{U}\times\text{Ti})}$ in zircon has been formulated and calibrated by Loucks et al. (2020) as a quantitative measure of the parent melt's oxidation state, $\Delta\text{FMQ} = \log f\text{O}_2^{\text{sample}} - \log f\text{O}_2^{\text{FMQ}}$ wherein FMQ represents

the reference buffer fayalite + magnetite + quartz, and U_i represents radioactive-decay-corrected initial U content at the time that dated zircons crystallised. Empirical calibration using 1042 analysed zircons in 85 natural populations having independently constrained $\log f\text{O}_2$ in the range FMQ–4.9 to FMQ+2.9 retrieves the calibration data with a standard error of ± 0.6 log unit $f\text{O}_2$. We deploy it here to monitor the evolving oxidation state of melts during trans-crustal ascent and decompression-induced fluid exsolution at many igneous complexes.

3 Observed co-variation trends of magmatic hydration and oxidation states

Geobarometry, hygrometry, and oxybarometry on cores and rims of hornblende phenocrysts yield trends that corroborate our zircon-based indicators of silicate melt hydration state and oxidation state in the same igneous units, providing “proof of concept”, as shown in Figure 1. The hornblende data indicate continuous exsolution of H_2O -rich C-O-H-S-Cl fluid from ~700–800 MPa (~26–30 km depth) to subvolcanic, ore-forming depths, with concomitant oxidation of residual melt. Zircon records the same trends of melt oxidation during melt dehydration.

Figure 2 shows zircon hygrometry and oxybarometry trends in a succession of epizonal intrusions in the 35–21 Ma Meghri-Ordubad igneous complex in Armenia and in the 67–55 Ma Yarabamba-Quellaveco complex in southern Peru. Zircons in early intrusions form arrays of positive slope, with rising oxidation state as hydration state rises. Zircons in later intrusions, including ore-forming ones, define arrays having negative slopes, with further rise in oxidation state accompanying melt dehydration.

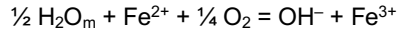
4 How PCD magmas become oxidised

4.1 Oxidation as dissolved H_2O increases in melts

Magmas stored in hot country rock near the Moho tend to last long enough to experience intermittent replenishments by hydrous basaltic melt from the mantle. Over successive cycles of replenishment and fractional crystallization, hybrid melts can accumulate high concentrations of inherited chemical components that are largely excluded from ultramafic cumulates— H_2O , CO_2 , Cl, Eu^{2+} , Fe^{3+} , etc.

In Figure 2, segments having steep positive slope are at least partially attributable to selective

sequestering of Fe^{2+} relative to Fe^{3+} by cumulus olivine, clinopyroxene and hornblende in ultramafic cumulates all of which have lower $\text{Fe}^{3+}/\text{Fe}^{2+}$ ratios than equilibrated silicate melt. However, the principal mechanism of melt oxidation is likely to be a rising ratio of molecular H_2O to hydroxyl as total dissolved H_2O accumulates in the melt during crystallisation:



(1a)

wherein H_2O_m represents molecular water dissolved in the melt, and OH^- replaces a bridging oxygen linking Al and Si in the tetrahedral framework. Activities of these species in the melt are related to the equilibrium constant K_1 by

$$\log [\text{Fe}^{3+}/\text{Fe}^{2+}] = \log K_1 + \log [\text{H}_2\text{O}_m^{1/2}/\text{OH}^-] + \frac{1}{4} \log f\text{O}_2 \quad (1b)$$

wherein brackets denote activities. Equation 1b shows that at a specified T and P (constant K_1) and specified $f\text{O}_2$, a rising ratio of $\text{H}_2\text{O}_m/\text{OH}^-$ in the melt requires a tandem rise

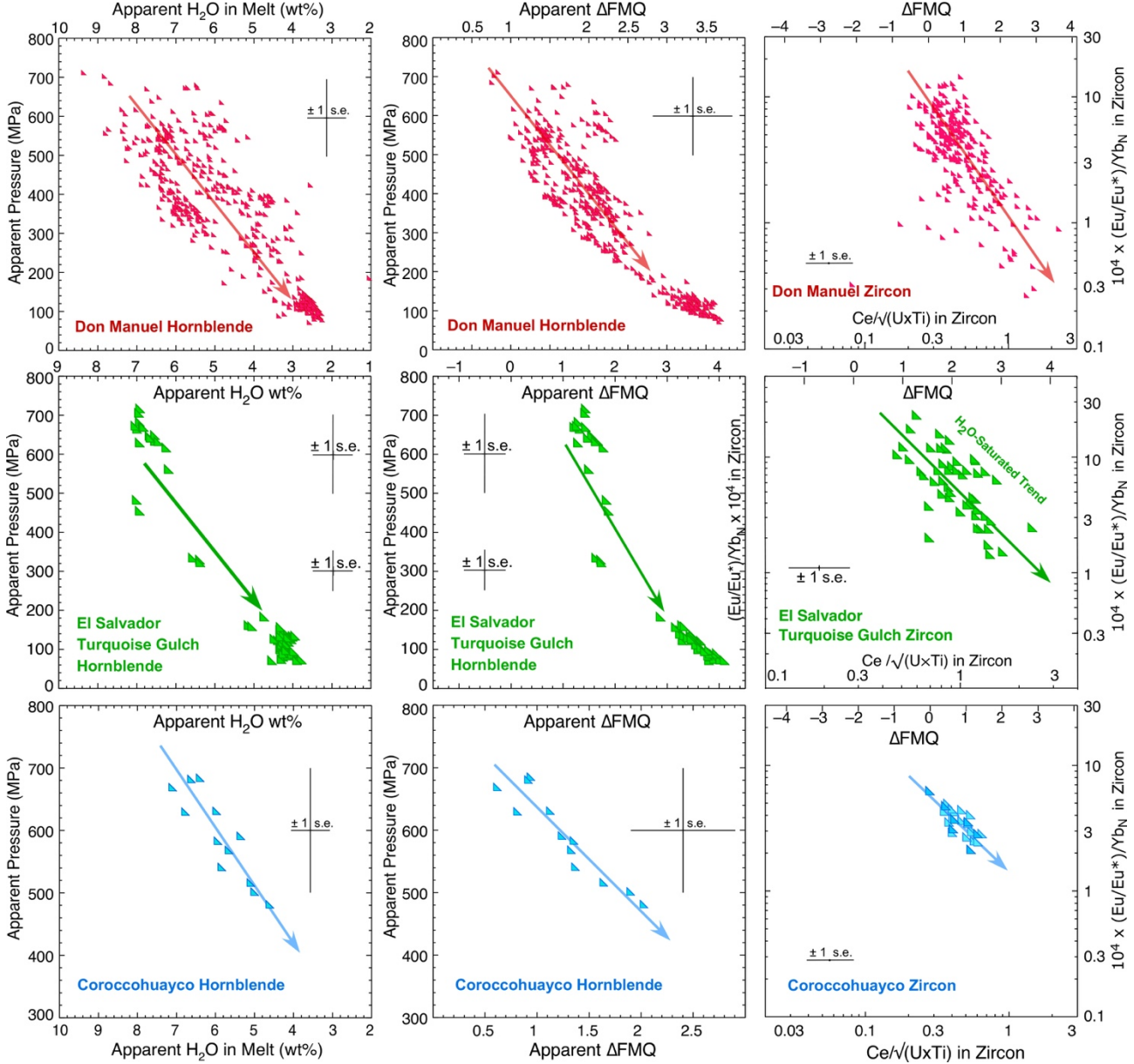


Figure 1. Proof of concept. Hornblende geobarometry-hygrometry-oxybarometry corroborates trends in zircon indicators of parent melt hydration state and oxidation state during trans-crustal ascent. Al-in-hornblende barometry on phenocryst cores and rims by the calibration of Mutch et al (2016) are plotted against apparent ΔFMQ and wt % H_2O dissolved in the melt according to the calibrations by Ridolfi et al (2010). Arrows show trends during decompression of ascending magmas and concomitant exsolution of hydrothermal fluid and oxidation of dehydrating melt. Panels on the right illustrate applications of our zircon composition parameters in the same igneous units. Hornblende and zircon analyses in the Don Manuel PCD and related intrusions, central Chile, are from Gilmer et al (2018); All analyses from host intrusions except xenoliths and mafic enclaves are plotted. Hornblende phenocryst compositions in the Cu(-Mo)-ore-forming L Porphyry stock in the Turquoise Gulch intrusive complex, El Salvador, Chile, were reported by Lee (2008). Zircon compositions in the L Porphyry were reported by Lee et al (2017). Amphibole compositions in Corocochuayco Hornblende Porphyry intrusion, central Peru, were reported by Chelle-Michou et al (2015). Zircon compositions in Hornblende Porphyry and Hornblende-Biotite Porphyry dacitic intrusions were reported by Chelle-Michou and Chiaradia (2014).

of its $\text{Fe}^{3+}/\text{Fe}^{2+}$ activity ratio, as theoretically predicted by Moretti (2005) and experimentally

demonstrated by Gaillard et al (2003) and by Schuessler et al (2008).

4.2 Melt oxidation as hydrothermal fluid segregates

H₂O solubility in granitic melts decreases ~4-fold during magma ascent from 800 MPa to 100 MPa (Holtz et al 1995). Al-in-hornblende barometry and hornblende hygrometry in Figure 1 indicate onset of fluid segregation at 700–800 MPa in response to decompression of ascending magma. A transition from fluid movement by intergranular filtration to channelling via propagating conduits tends to

occur at greater depth and lower vesicularity in moving magma than in stagnant magma, which facilitates gravitational segregation of exsolving volatiles to the top of the ascending magma column. To the degree that channelling and collection of segregated fluid remove it from effective diffusive communication with its parent melt, the residual melt's chemical evolution may be regarded as fractional distillation in a chemically open system.

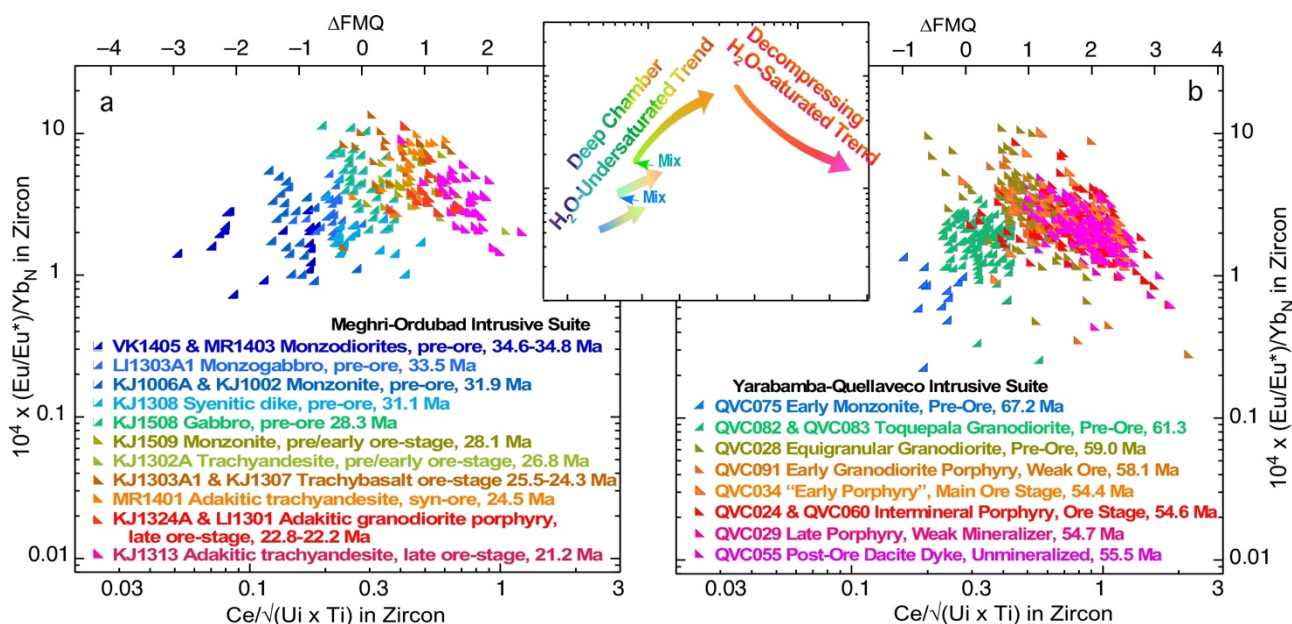


Figure 2. Co-evolution of melt oxidation and hydration states according to our indicators during magmatic differentiation. **(a)** LA-ICPMS analyses of zircons in successive pre-mineralisation and copper-mineralising intrusions in the Meghri-Ordubad intrusive complex, Armenia, showing sample number, lithologic unit and U-Pb age as reported by Rezeau et al (2019); **(b)** zircon analyses in successive pre-mineralisation and copper-mineralising intrusions and a post-ore intrusion in the Yarabamba-Quellaveco intrusive complex, southern Peru as reported by Nathwani et al (2021). Arrows in the inset panel schematically represent rising hydration state and oxidation state of melts through successive cycles of fluid-undersaturated magmatic differentiation and chamber replenishment (positive slope), followed by melt dehydration and further oxidation during fluid-saturated magma ascent (negative slope).

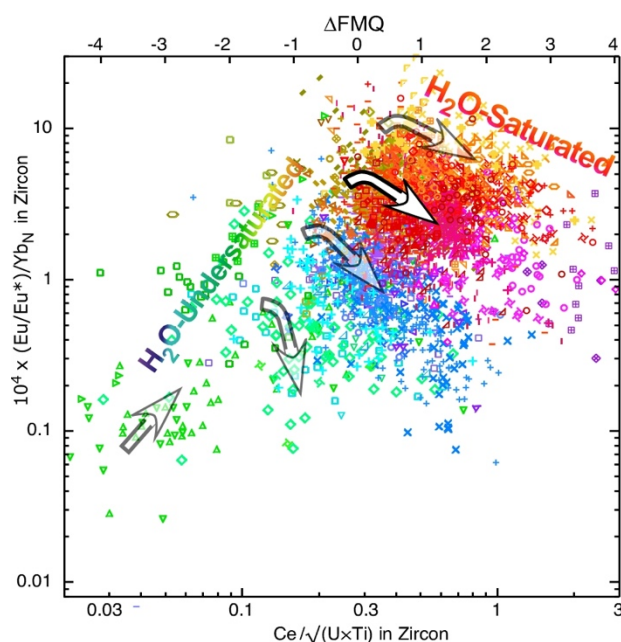


Figure 3. Zircons from PCD-forming intrusions in 37 districts are shown as red and orange symbols. Brown symbols represent zircons in pre-ore and post-ore intrusions in ore-hosting igneous complexes. Green, turquoise, blue, and purple symbols represent barren arc igneous suites. Arrows schematically represent the turn in trajectory at the transition from fluid-undersaturated melt (positive slope) to fluid-saturated evolution (negative slope) in granitoid melts of varied volatile content at the onset of fluid saturation.

Reduced members of the principal redox couples in the granitoid melts—H₂-H₂O, S⁴⁺-S⁶⁺, and Fe²⁺-Fe³⁺—partition into exsolving hydrothermal fluid more strongly than oxidised members, so segregation of exsolving fluid leaves a more oxidised residual melt (Humphreys et al, 2015; Scaillet et al, 1998; Bell and Simon, 2011). The 1982 eruption of El Chichón volcano (Mexico) and the 1991 eruption of Mt. Pinatubo (Philippines) released vastly more SO₂ than could have been dissolved in the erupted mass of melt, which implies that most of the erupted

sulphur was in hydrothermal fluid that had accumulated at the top of the pre-eruption magma column (Luhr et al., 1984; Gerlach et al., 1994). The El Chichón eruption included lithic fragments of porphyry-copper-style mineralisation (Luhr, 1983). The Pinatubo stratocone hosts the Dizon porphyry Cu-Au ore deposit and several Cu-Au prospects (Hattori and Keith, 2001).

Figure 3 is a plot of 5777 zircon compositions compiled from our own and other publications. The dataset includes 2220 zircons from intrusions inferred by the respective authors to have exsolved ore-forming magmatic-hydrothermal fluids in 37 major magmatic-hydrothermal Cu-rich ore deposits of Phanerozoic age worldwide. Those are compared to 3557 zircons from non-ore-forming magmas at Phanerozoic convergent plate margins. It is evident that these composition parameters in zircon effectively discriminate metallogenically fertile arc magmas from infertile ones.

5 CONCLUSION

Trace-element features of zircons that are diagnostic of unusually high hydration and oxidation states of their parent magma effectively discriminate Cu-ore-forming igneous complexes from ordinary, unmineralised arc igneous suites. Our discriminants of porphyry copper fertility are applicable to detrital zircons. The watershed-scale “footprint” of this diagnostic tool is much larger than the detection range of conventional geochemical sampling techniques and is applicable to paleo-watersheds. In application to paleo-drainages, it may identify fertile igneous complexes that formerly were exposed to erosion but are now buried under younger volcanic or sedimentary cover.

Acknowledgements

We thank Paul Agnew of Rio Tinto Exploration and Cam McCuaig and Natalie Caciagli of BHP Exploration for encouragement and helpful discussions. This study was supported in part by Rio Tinto Exploration. Additional financial support was provided by the Australian Research Council Centre of Excellence for Core to Crust Fluid Systems grant CE110001017.

References

Bell AS, Simon A. (2011) Experimental evidence for the alteration of the $\text{Fe}^{3+}/\Sigma\text{Fe}$ of silicate melt caused by the degassing of chlorine-bearing aqueous volatiles. *Geology* 39:499–502.

Chelle-Michou C, Chiaradia M, Béguelin P, Ulianov R (2015) Petrological evolution of the magmatic suite associated with the Corocochuayco Cu(-Au-Fe) porphyry-skarn deposit, Peru. *J Petrol* 56:1829–1862

Chelle-Michou C, Chiaradia M, Ovtcharova M, Ulianov A, Wotzlaw J-F (2014) Zircon petrochronology reveals the temporal link between porphyry systems and the magmatic evolution of their hidden plutonic roots (the Eocene Corocochuayco deposit, Peru). *Lithos* 198–199:129–140.

Gaillard, F, Pichavant, M, Scaillet, B (2003) Experimental determination of activities of FeO and Fe_2O_3 components

in hydrous silicic melts under oxidising conditions. *Geochim Cosmochim Acta* 67:4389–4409.

Gerlach TM, Westrich HR, Symonds RB. (1996) Pre-eruption vapor in magma of the climactic Mount Pinatubo eruption: source of the giant stratospheric sulfur dioxide cloud. In: Newhall CG, Punongbayan RS (Eds.), *Fire and Mud: Eruptions and Lahars of Mount Pinatubo*. University of Washington Press, Seattle, WA; Quezon City: Philippine Institute of Volcanology and Seismology, pp. 415–434.

Gilmer AK, Sparks RSJ, Blundy JD, Rust AC, Hauff F, Hoernle K, Spencer CJ, Tapster S (2018) Petrogenesis and assembly of the Don Manuel igneous complex, Miocene-Pliocene porphyry copper belt, central Chile. *J Petrol* 59: 1067–1108.

Hattori K., Keith JD (2001) Contribution of mafic melt to porphyry copper mineralization: evidence from Mount Pinatubo, Philippines, and Bingham Canyon, Utah, USA. *Mineral Deposita* 36:799–806.

Holtz F, Behrens H, Dingwell DB, Johannes W (1995) H_2O solubility in haplogranitic melts: Compositional, pressure, and temperature dependence. *Am Mineral* 80:94–108.

Humphreys MCS, Brooker RA, Fraser DG, Burgisser A, Mangan MT, McCammon C (2015) Coupled interactions between volatile activity and Fe oxidation state during arc crustal processes. *J Petrol* 56:795–814.

Hutchinson MC, Dilles JH (2019) Evidence for magmatic anhydrite in porphyry copper intrusions. *Econ Geol* 114:143–152.

Lee RG (2008) Genesis of the El Salvador porphyry copper deposit, Chile and distribution of epithermal alteration at Lassen Peak, California. PhD thesis, Corvallis, OR, Oregon State University, 344 p.

Lee RG, Dilles JH, Tosdal RM, Wooden JL, Mazdab FK (2017) Magmatic evolution of granodiorite intrusions at the El Salvador porphyry copper deposit, Chile, based on trace element composition and U/Pb age of zircons. *Econ Geol* 112:245–273.

Loucks RR, Fiorentini ML, Henriquez G, (2020) New magmatic oxybarometer using trace elements in zircon. *J Petrol* 61: egaa034.

Luhr JF (1983) The 1982 eruptions of El Chichón and the relationship to mineralized magmatic-hydrothermal systems [abs.]: *Geol. Soc. Am., Abs. w Prog.* 15:632.

Moretti R (2005) Polymerisation, basicity, oxidation state and their role in ionic modelling of silicate melts. *Annals Geophys.* 48:583–608.

Mutch, EJF, Blundy JD, Tattitch, BC, Cooper FJ, Brooker RA (2016) An experimental study of amphibole stability in low-pressure granitic magmas and a revised Al-in-hornblende geobarometer. *Contrib Mineral Petrol* 171: 85.

Nathwani CL, Simmons AT, Large SJE, Wilkinson JJ, Buret Y, Ihlenfeld C (2021) From long-lived batholith construction to giant porphyry copper deposit formation: petrological and zircon chemical evolution of the Quellaveco District, Southern Peru. *Contrib Mineral Petrol* 176:12.

Rezeau H, Moritz R, Wotzlaw J-F, Hovakimyan S, Tayan R (2019) Zircon petrochronology of the Meghri-Ordubad pluton, Lesser Caucasus: fingerprinting igneous processes and implications for the exploration of porphyry Cu-Mo deposits. *Econ. Geol.* 114:1365–1388.

Ridolfi F, Renzulli A, Puerini M (2010) Stability and chemical equilibrium of amphibole in calc-alkaline magmas: an overview, new thermobarometric formulations and application to subduction-related volcanoes. *Contrib Mineral Petrol* 160:45–66.

Scaillet B, Clemente B, Evans B, Pichavant M (1998) Redox control of sulfur degassing in silicic magmas. *J Geophys Res* 103:23937–23949.

Schuessler JA, Botcharnikov RE, Behrens H, Misiti V, Freda C (2008) Oxidation state of iron in hydrous phono-tephritic melts. *Am Mineral* 93:1493–1504.

Early zircon saturation and low Zr content of PCD-forming magmatic differentiation series: a guide for exploration targeting

Robert R. Loucks^{1,2}, Marco L. Fiorentini^{1,2}

¹Centre for Exploration Targeting, School of Earth Sciences, University of Western Australia, 35 Stirling Highway, Crawley WA 6009, Australia

²ARC Centre of Excellence for Core to Crust Fluid Systems, University of Western Australia, 35 Stirling Highway, Crawley WA 6009, Australia

Abstract. In orogenically deforming segments of convergent plate margins, horizontal compressive stress provides resistance to opening of tensile dike fractures and promotes entrapment of mantle-derived basaltic melts in magma chambers embedded in hot country rock at Moho-vicinity depths, where magmas cool slowly, and residual melts tend to last long enough to experience intermittent chamber replenishment by basaltic melts from the deeper mantle. Over several cycles of replenishment and fractional crystallisation, residual melts acquire high concentrations of inherited chemical components that were largely excluded from cumulus minerals—H₂O, Cl, CO₂, SO₃, etc. Accumulating H₂O re-orders the high-pressure crystallisation sequence of igneous minerals in successive cycles and leads to zircon saturation in mafic melts (basaltic andesite to mafic andesite compositions) of later cycles. Porphyry copper deposit (PCD) ore-forming magmas are chemically distinguished from ordinary arc granitoids by low Zr at zircon saturation, as well as by “adakitic” high Sr/Y and Eu/Yb that indicate unusually high dissolved H₂O in residual melts over most of the course of magmatic differentiation. Whole-rock Sr/Zr in rock samples retaining igneous plagioclase is a useful discriminant of Cu-fertile intrusive complexes.

1 Introduction

Lateral variations of tectonic stress along convergent plate margins have profound effects on the chemical course of magmatic differentiation of mantle-derived basaltic magmas. In non-compressive to weakly compressive stress settings, arc magmas follow a tholeiitic trend; in moderately compressive settings, a calc-alkalic trend is typical; in highly compressive, orogenically deforming arc segments, an adakitic differentiation trend is typical (Loucks, 2021).

2 Early to late zircon saturation in compressive to non-compressive arc segments

We illustrate the contrasting behaviour of Zr during magmatic differentiation in four magmatic arcs featuring adjacent compressive and non-compressive stress settings above the same subduction zone, and in which compression is induced by different tectonic mechanisms. Three of these case studies have major magmatic-hydrothermal Cu(-Au) ore deposits in the compressive segments.

2.1 Behaviour of Zr in adakites at the type locality on Adak Island

Figure 1 shows alternating compressive and non-compressive intervals due to rotation of block

segments in response to tangential shear by oblique subduction. There is a correlative alternation of volcanic edifices that are large shields of mainly basaltic composition at the eastern ends of the rotating blocks, but small stratocones of mainly andesitic and dacitic composition in the compressional western ends of the rotating blocks (Kay et al., 1982). Figure 1b shows trends of whole-rock ppm Zr versus wt% SiO₂. Semisopchnoi is the next major magmatic centre west of Adak that is erupting primitive basalts. In the Semisopchnoi suite (and other centres in non-compressive settings in the Aleutians), the ppm Zr trend rises steeply until zircon saturates at around 70% SiO₂. In the Adak suite (and other compressive segments), the Zr v SiO₂ trend is flatter. In Figure 1c, the Sr/Zr ratio shows divergent differentiation trends from initially similar mafic parent magmas. Evidence that andesitic lavas on Adak and nearby Kanaga evolved at high pressure is in their abundant xenoliths of tectonised spinel peridotite and cognate xenoliths of ultramafic cumulates and hornblende gabbro for which mineral barometry gives pressures in the 28–22 km depth range, where basaltic magmas pond just beneath the base of the crust and fractionally crystallise to residual melts of adakitic andesitic-dacitic compositions (DeBari et al., 1987; Conrad and Kay, 1984).

2.2 Early and late zircon saturation in other compressive and non-compressive pairs

Trends of whole-rock ppm Zr versus wt% SiO₂ in differentiation series parental to major porphyry-type Cu(±Mo±Au) deposits (El Teniente and Batu Hijau) and a high-sulphidation-epithermal-type Au-Cu deposit (Chinkuashih) are compared in Figure 2 with contemporaneous suites lacking significant Cu mineralisation in adjacent arc segments overlying the same subduction zone. In all three cases, the compressive intervals are over-riding buoyant features in the subducting plate. In all three panels, the data trends represent rising accumulation of Zr in residual melt as SiO₂ increases until the melt attains zircon saturation, followed by declining Zr content of residual melt as zircon segregates with other cumulus minerals. The Cu(-Au-Mo)-ore-forming magmatic differentiation trends (red) reach zircon saturation at an earlier stage of magmatic differentiation than do Cu-infertile suites (green).

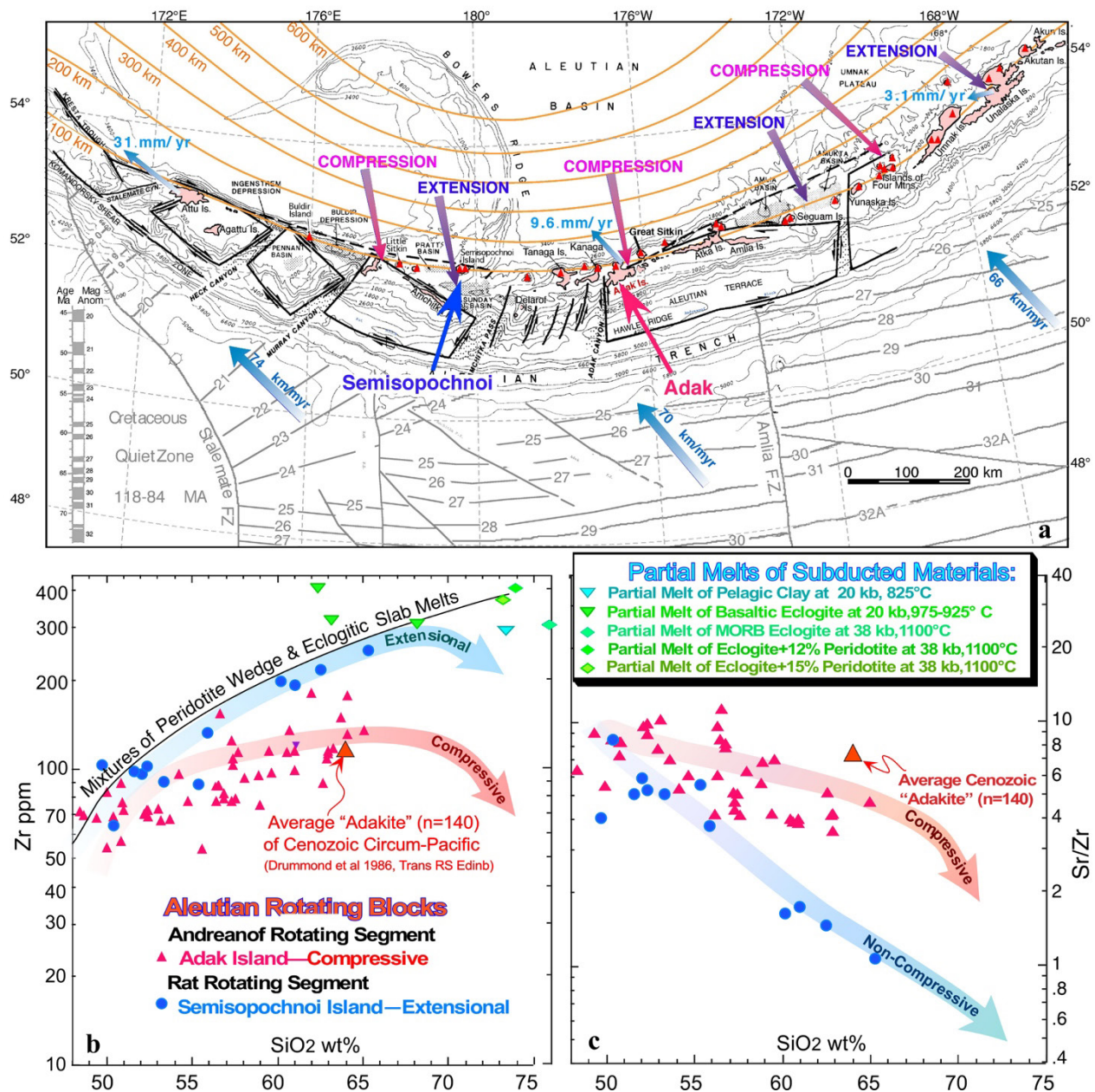


Figure 1. (a). In the eastern Aleutians, the plate convergence is nearly orthogonal to the trench, but westward along the Aleutians the convergence becomes increasingly oblique. Increasing tangential shear in the central and western Aleutians has caused the arc to break up into a lateral succession of block segments rotating clockwise (Geist et al., 1988). Seismically active transverse faults and coincident submarine canyons define the ends of the rotating blocks. Clockwise rotation of the eastern ends of the blocks away from the North American plate has produced extensional "summit basins" along the crest of the arc. Orange contours labelled "100 km" to "600 km" are depths to the top of the subducting slab, determined by local seismicity on the Wadati-Benioff zone at shallow depths ≤ 270 km, and determined by teleseismic tomographic imaging in aseismic portions of the slab at greater depths (Boyd and Creager, 1991). Locations of the calc-alkalic-adakitic Adak magmatic centre at the western end of the rotating Andreanof Block and of the tholeiitic Semisopchnoi magmatic centre at the eastern end of the rotating Rat Block are identified. **(b)** All available published whole-rock analyses of Quaternary samples are shown on this plot of ppm Zr in compiled analyses of samples from the Adak and Semisopchnoi magmatic centres. In Aleutian extensional settings, the trend of Zr vs SiO₂ rises steeply until zircon saturates at around 70% SiO₂. In the Adak suite and volcanoes in other compressive segments, the Zr vs SiO₂ trend is flatter. Adak magmas apparently attain zircon saturation at a mafic stage of magmatic differentiation. These trends are compared with Zr contents of compiled experimental partial melts of subducted materials (green symbols; data from Johnson and Plank, 1999; Rapp et al, 1999; Xiong, 2006). Plainly, the Adak series does not lie along a mixing line between slab melts and melts of asthenospheric mantle wedge, which invalidates the hypothesis by Defant and Drummond (1990) that adakites at Adak and other circum-Pacific localities were produced by partial melting of subducted materials. The composition of "average Cenozoic circum-Pacific adakite" is taken from the compilation by Drummond et al (1996). The Zr-SiO₂ plot effectively discriminates actual melts of subducted materials from "adakites", which are widely misinterpreted to be partial melts of subducted materials. **(c)** Contrasting trends of whole-rock Sr/Zr ratio in the compiled volcanic samples from Adak and Semisopchnoi. The Sr/Zr ratio shows divergent differentiation trends from initially similar mafic parent magmas, with a sub-horizontal trend in the compressive segments, and a steep, steady decline in the extensional settings.

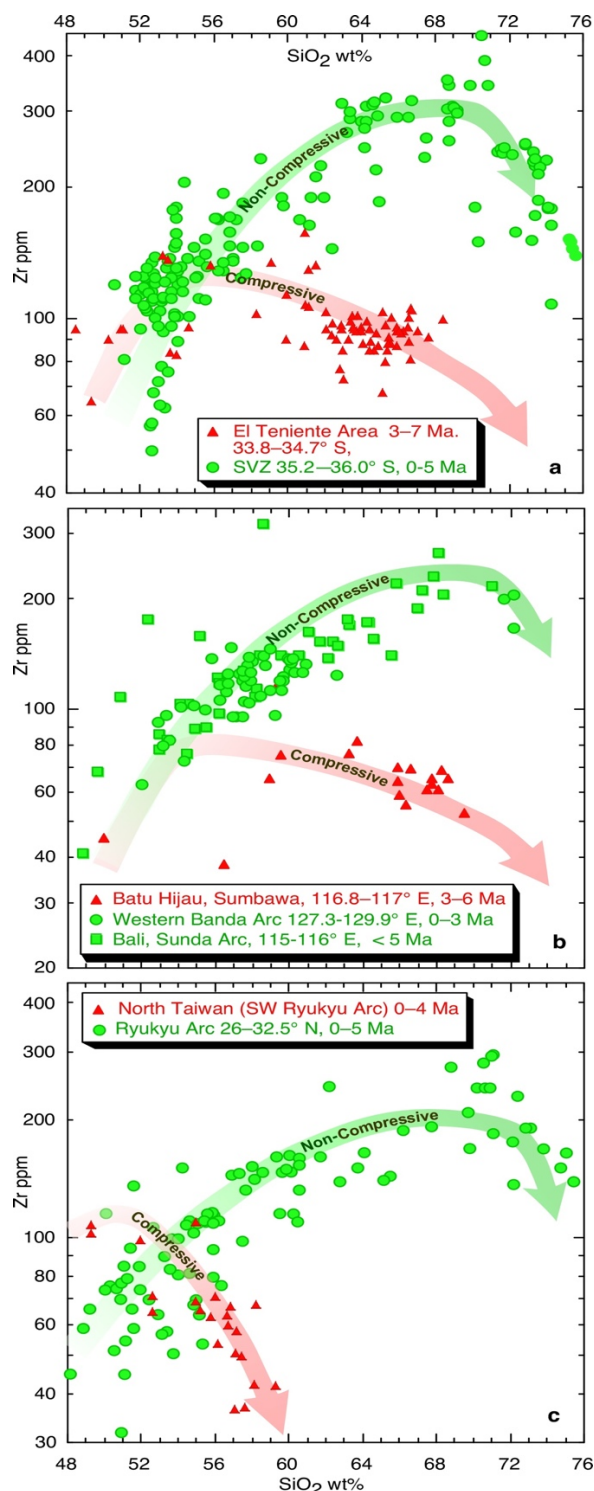


Figure 2(a,b,c). Compilation all available whole rock analyses (<http://www.earthchem.org/portal>) representing mafic-to-felsic differentiation series parental to major porphyry-type (El Teniente, Chile, and Batu Hijau, Indonesia) and high-sulfidation-epithermal-type (Chinkuashih, Taiwan) Cu(±Au±Mo) deposits, compared with contemporaneous suites in adjacent, unmineralized arc segments overlying the same subduction zone. In all three panels, the data trends represent rising accumulation of Zr in residual melt as SiO₂ increases until the melt attains zircon saturation, followed by declining Zr content of the residual melt as zircon segregates along with other cumulus minerals. The Cu(-Au-Mo)-ore-forming magmatic differentiation trends (red) reach zircon saturation at an earlier stage of magmatic differentiation than do Cu-infertile suites (green).

In Figure 2a, red symbols represent all available analyses of fresh or little-altered samples in the orogenically deforming region above the subducting Juan Fernandez aseismic ridge and encompassing the early Pliocene El Teniente porphyry Cu(-Mo) deposit. Green dots represent samples from the Southern Volcanic Zone (SVZ) compiled from many sources. The ore-related suite at Batu Hijau is from Fiorentini and Garwin (2009). Other Sunda and Banda arc samples are compiled from many sources. Ryukyu arc data in Figure 2c are compiled from many sources.

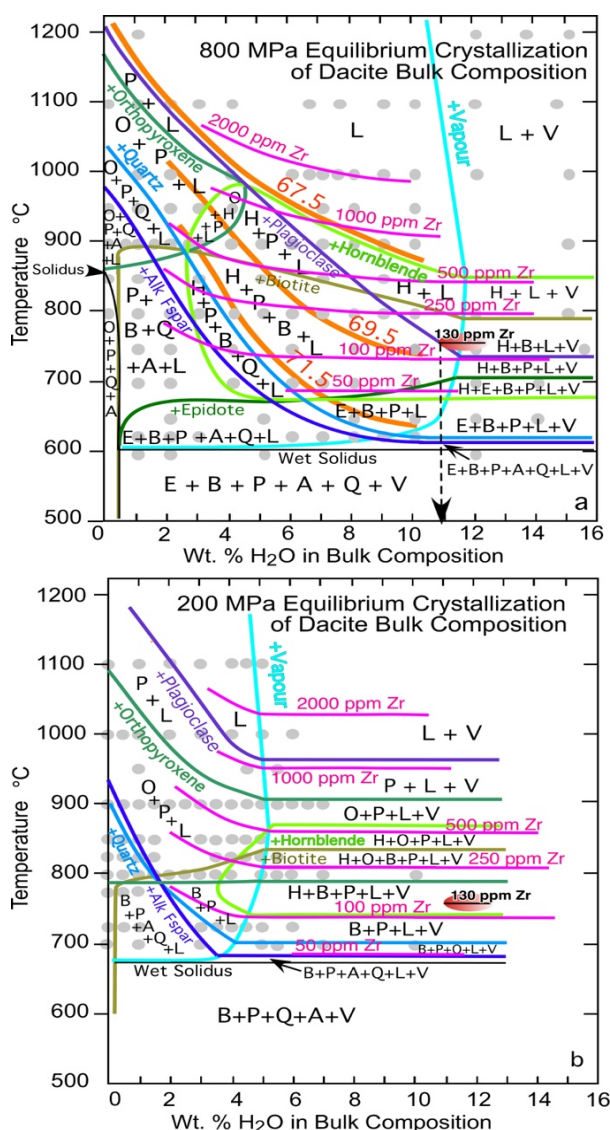


Figure 3(a,b). Stable phase assemblages at 800 MPa (a) and 200 MPa (b) in a dacitic bulk composition of varied H₂O content and temperature (grey dots; Naney, 1983). Orange contours show wt% SiO₂ in the melt (anhydrous basis). Pink contours show zircon solubility (ppm Zr) as calibrated by Crisp and Berry (2022). Phase labels: L = liquid (hydrous silicate melt), V = hydrothermal fluid, P = plagioclase, Q = quartz, A = alkali feldspar, B = biotite, H = hornblende, O = orthopyroxene, E = epidote. Crystallisation paths are vertical lines of constant bulk composition. At 800 MPa, hornblende saturates before plagioclase in bulk compositions having ≥4.5 wt% H₂O, yielding adakitic high Sr/Y and Eu/Yb in residual melts. The average 130 ppm Zr in PCD-forming melts plots at the edge of the 800 MPa plag-undersaturated, hbl-d-saturated adakitic field.

3 Cause of low Zr in PCD-forming magmas

Al-in-hornblende evidence compiled by Loucks (2021, his Fig. 7) shows that PCD-forming magmas undergo magmatic differentiation mainly at Moho-velocity pressures near 700-1100 MPa. Figure 3 shows experimentally determined phase relations in a granodiorite bulk composition at 800 and 200 MPa. At 800 MPa, as H₂O dissolved in the melt increases, saturation temperatures of anhydrous minerals are depressed more than the saturation temperature of zircon (subhorizontal contours), so in more hydrous melts, zircon advances in the saturation sequence of igneous minerals to precede plagioclase.

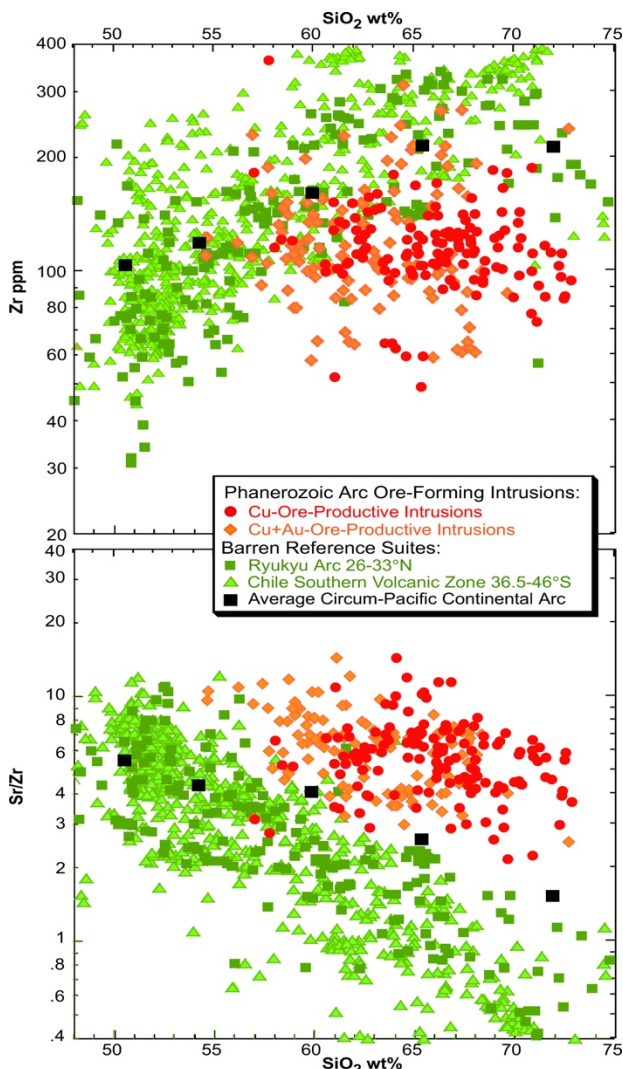


Figure 4(a). Zr contents of least-altered samples of intrusions directly parental to 120 major porphyry Cu(-Au-Mo) and high-sulphidation epithermal Cu-Au deposits of Phanerozoic age worldwide (compilation by Loucks, unpub) are represented by red and orange symbols. The Zr contents of these ore-stage magmas are compared to the Cu-infertile mafic-to-felsic differentiation series along the volcanic front of the continent-margin Ryukyu arc in the latitude interval 26–33°N. Black squares represent the Zr contents of average circum-Pacific continental-arc basalt, basaltic andesite, andesite, dacite, and rhyolite (from global compilations by R. Loucks, unpub).

(b) Cu-ore-forming calc-alkalic arc magmas have high Sr and low Zr contents, so the whole-rock Sr/Zr ratio is an effective discriminant of Cu-fertile intrusions having >57wt% SiO₂.

Very hydrous differentiation series reach plagioclase saturation and dacitic residual melt compositions at low temperatures, often <750°C. At such low temperatures, the Zr content of zircon-saturated melt is low. At 200 MPa, no crystallisation path (vertical) produces hornblende before plagioclase, so high-Sr/Y adakitic melts cannot develop at low pressures.

4 Application to mineral exploration

Figure 4 illustrates the effectiveness of whole-rock Zr and Sr/Zr ratios as discriminants of Cu-fertile magmas at convergent plate margins. The Sr/Zr ratio is applicable to samples retaining fresh or nearly fresh plagioclase.

Acknowledgements

This study was supported in part by the Australian Research Council Centre of Excellence for Core to Crust Fluid Systems grant CE110001017

References

- Boyd TM, Creager KC (1991) The geometry of Aleutian subduction: three-dimensional seismic imaging. *J Geophys Res* 96: 2267-2291.
- Conrad WK, Kay RW (1984) Ultramafic and mafic inclusions from Adak Island: crystallization history, and implications for the nature of primary magmas and crustal evolution in the Aleutian arc. *J Petrol* 25: 88-125.
- Crisp LJ, Berry AJ (2022) A new model for zircon saturation in silicate melts. *Contrib. Mineral. Petrol.* 177, 71.
- DeBari S, Kay SM, Kay RW (1987) Ultramafic xenoliths from Adagdak volcano, Adak, Aleutian Islands, Alaska: deformed igneous cumulates from the Moho of an island arc. *Jour Geol* 9: 329-341.
- Defant MJ, Drummond MS (1990) Derivation of some modern arc magmas by melting of young subducted lithosphere. *Nature* 347: 662-665.
- Drummond MS, Defant MJ, Kepezhinskas PK (1996) Petrogenesis of slab-derived trondhjemite-tonalite-dacite/adakite magmas. *Trans Roy Soc Edinburgh, Earth Sci* 87: 205-215.
- Fiorentini, ML and Garwin, SL (2010) Evidence of a mantle contribution in the genesis of magmatic rocks from the Neogene Batu Hijau district in the Sunda Arc, southwestern Sumbawa, Indonesia: *Contrib Mineral and Petrol* 159: 819-837
- Geist EL, Childs JR, Scholl DW (1988) The origin of summit basins of the Aleutian Ridge: implications for block rotation of an arc massif. *Tectonics* 7:327-341.
- Johnson, MC., Plank, T (1999) Dehydration and melting experiments constrain the fate of subducted sediments. *Geochim Geophys Geosyst* 1: 1999GC000014
- Kay SM, Kay RW, Citron GP. (1982) Tectonic controls on tholeiitic and calc-alkalic magmatism in the Aleutian arc. *J Geophys Res* 87: 4051-4072.
- Loucks, RR (2021) Deep entrapment of buoyant magmas by orogenic tectonic stress: its role in producing continental crust, adakites, and porphyry copper deposits. *Earth Sci. Rev.* 220: 103744.
- Naney MT (1983) Phase equilibria of rock-forming ferromagnesian silicates in granitic systems. *Am. J. Sci.* 283: 993-1033.
- Rapp, RP, Shimizu N, Norman MD, Applegate GS (1999) Reaction between slab-derived melts and peridotite in the mantle wedge: experimental constraints at 3.8 GPa. *Chem Geol* 160:335-356.
- Xiong X-L (2006) Trace element evidence for growth of early continental crust by melting of rutile-bearing hydrous eclogite. *Geology* 34: 945-948.

Pyrite as a porphyry Cu indicator mineral: new insights from the Myszków Mo-Cu-W deposit (Poland) and future perspectives

Beata Naglik¹, Magdalena Dumańska-Słowik², Ryszard Habryn¹, Tomasz Toboła², Artur Sosna¹

¹Polish Geological Institute-National Research Institute, Upper Silesian Branch, Sosnowiec, Poland

²AGH University of Science and Technology, Krakow, Poland

Abstract. Due to rapid technological progress and copper's growing importance as a green metal for renewable energy solutions, the demand for this metal increases annually. Hence, there is a strong need to develop new exploration tools, which will be helpful to discover new, deep-seated, and possibly smaller deposits with high-grade ore mineralization. Nowadays, geochemical prospecting seems to show a big potential to vector concealed ore bodies as a good alternative to deep drilling, and what is more important it might be implemented ahead of time at relatively lower costs. Several geochemical proxies for tracking pathways of metal precipitation have been established (e.g. chlorite, epidote, alunite proximators). While the potential of pyrite appears not to have been fully exploited yet to predict the likely direction of mineralized ore centers. In this work, we conclude on the typomorphic characteristics, microtexture, solid inclusions, and major and trace composition of various generations of pyrite from the Myszków Mo-Cu-W deposit (Poland) to confirm its ability to preserve petrogenetic information on different ore-grade mineralized events. A pilot study of sulphur isotope composition in pyrite from this deposit seems to be a promising tool for detecting proximity to mineralized centres.

1 Introduction

The low-carbon future of our societies relies on access to numerous mineral raw materials, the majority of which are closely linked to renewable energy sources (e.g. the production of solar panels, wind turbines, and energy-efficient lighting) and sustainable mobility (e.g. electric vehicles), in which the strategic metals are currently irreplaceable. Increasing demand for strategic elements cannot be met solely by recycling; so primary resources mining will be still crucial in the near future. The most important world's primary source of mineral raw materials for modern industry such as Cu and Mo as well as important contents of critical and precious metals such as Au, Ag, W, and Re are porphyry Cu deposits (PCDs) and related epithermal Au deposits. They are intrusion-centered ore bodies, in which metal-bearing minerals precipitated from hydrothermal fluids within an intrusive host and surrounding country rocks. Porphyry ore deposits typically occur within an alteration halo with characteristic mineralogical and chemical zoning patterns (e.g. Sillitoe 2010).

If one takes into account the exploration degree of the geological structure of the European Union countries, the discovery of new deposits with outcrops on the surface seems unlikely. To meet future demand for the strategic metals (e.g. copper,

tungsten), deep drilling and costly geophysical surveys are needed to discover deeper and possibly smaller deposits, including porphyry-Cu deposits, which are usually emplaced several kilometers below the Earth's surface. To assist porphyry exploration, the development of new pathfinders to target high-grade mineralization at reduced environmental and economic risk is therefore of significant interest.

Geochemical exploration seems to provide the response to these ongoing challenges. To date, significant research efforts have been made to develop effective geochemical vectoring tools, mostly based on whole rock geochemistry, e.g. Hf concentration, the Sr/Y, V/Sc, and Th/U ratios (Richards 2011; Loucks 2014). However, these proxies have limited applicability, since the hydrothermal fluids associated with ore deposits commonly obliterate the primary minerals and alter the whole-rock geochemical composition (e.g. Seedorff et al. 2005).

Quite recently, an alternative approach has been proposed that uses the compositions of individual magmatic and hydrothermal minerals to predict the likely direction and distance to mineralized centers, and the potential metal endowment of a research area, i.e. Ti-in chlorite proximator. (Wilkinson et al. 2015). However; the utility of mineral indices depends on the question of whether they are reproducible enough to be applicable in any porphyry-style system worldwide or maybe they are useful only in some specific terranes. The development of appropriate geochemical tools for exploration under cover is therefore a very challenging task and requires many validation studies in different geological settings to make them mature tools for tracing fluid flow pathways.

Pyrite is one of the indicator mineral that shows chemical and structural variations in response to a changeable ore-forming environment. In addition to being an important carrier of metalloids (As), precious (Au), and base (Cu) metals, pyrite also could be considered as a proxy indicator of physico-chemical conditions of its crystals growth (pH, temperature, redox, fluid-wall interactions, the composition of host rocks, phase separation and/or boiling). However; it is still a matter of debate if this robust mineral could be also used as an exploratory guide. Up to date, most studies have been focused on pyrite geochemistry as a tool for distinguishing different deposit types, mostly based on the Co/Ni ratio. The recent advances in LA-ICP-MS have

stimulated debates regarding the possibility to use pyrite geochemistry as a proxy for the mineralization centre in some hydrothermal ore deposits (e.g. Genna and Gaboury, 2015).

Hence, different generations of pyrite from the Myszków Mo-Cu-W deposit (the Kraków-Lubliniec Fault Zone - KLFZ, Central Poland) were comprehensively studied by mineralogical and geochemical techniques (Naglik et al. 2021; Naglik et al. 2022) and this paper concludes with an outlook to the future of the pyrite potential for further mineral prospecting in the porphyry Cu environment. The special interest given to the Myszków Mo-Cu-W deposit comes from the fact, that it has been recognized in detail through several dozen deep boreholes, and thus gives a unique opportunity to study systematic variations of pyrite characteristics with high resolution. It also remains the only European porphyry-style deposit of the Variscan age, and undergoing active exploration (Sutphin et al. 2013).

2 Geological settings

Porphyry copper mineralization of the Myszków Mo-Cu-W deposit is located at the contact zone between two distinctive tectonic units: (1) the Upper Silesian Block (USB) and (2) the Małopolska Block (MB), which have been considered as terranes of Gondwana and Baltica affinity, respectively. The most recent zircon U–Pb dating by SHRIMP (Jarmolowicz-Szulc 2020; Mikulski et al. 2019) together with Re–Os data of molybdenites (Stein et al. 2005) indicate Late Carboniferous to Early Permian age of magma generation and related mineralization events. Since most Variscan igneous rocks are either deeply eroded or petrochemically unsuitable for porphyry copper association, the Myszków Mo-Cu-W deposit provides an unusual example of porphyry copper mineralization with no analogue in Europe.

Despite the different age of the Myszków Mo-Cu-W deposit, the overall geochemical characteristics, mineralogy, and vein morphology are typical of calc-alkaline porphyry copper deposits elsewhere. The ore mineralization resulted here from both contact metamorphism (early, skarn type mineralization) and post-magmatic hydrothermal activity (main hydrothermal mineralization). Generally, three periods of mineralization have been defined at the Myszków deposit: (1) early, skarn-forming (period I), (2) main, hydrothermal (period II), and (3) late, post-ore (period III) (Ślósarz 2001, 1985). Period I is represented by magnetite-sulfide mineralization found in hornfelses, skarns, and metasomatites. Within period II, different stages of ore deposition have been distinguished: (1) feldspar-molybdenite veins with biotite, (2) quartz-feldspathic, pegmatitic veins, (3) quartz veins with molybdenite and scheelite (stockwork system), (4) black quartz veins with molybdenite, and (5) quartz-polymetallic veins (without molybdenite). Finally, period III produced mainly ankerite and barite-fluorite mineralization.

3 Typomorphic of porphyry-style pyrite in different mineralization stages

Four various generations of pyrite from the Myszków Mo-Cu-W deposit were analyzed by Naglik et al. (2021; 2022): (1) the I-type pyrite from the early, skarn-forming stage of mineralization; (2) the II-type pyrite coming from quartz-feldspathic pegmatitic veins; (3) the III-type pyrite from quartz veins with coexisting molybdenite and scheelite; and (4) the IV-type pyrite representing quartz-polymetallic assemblage.

The I-type pyrite, representing the early, skarn-forming stage of mineralization forms anhedral, fractured grains, often intergrown with biotite and magnetite. Generally, the I-type pyrite is characterized by a porous texture with clustered pores and abundant mineral inclusions, interpreted as a result of vigorous boiling (Naglik et al. 2021). Py-I shows relatively high average amount of Ni (~740 ppm) and Co (~640 ppm); however concentration of those elements exhibits a heterogenous, non-concentric mode. Such non-uniform trace elements distribution in pyrite was interpreted as another evidence of boiling. Elevated concentrations of Ni and Co in Py-I may point to the origin of mineralizing fluids with some mafic affinity (Naglik et al. 2022). The I-type pyrite probably crystallized over a wide range of temperatures. Some pyrite grains occur in close spatial association with biotite and magnetite and also host inclusions of these minerals. Hydrothermal biotite and magnetite are stable at a temperature higher than 450°C and such conditions probably also reflect the crystallization environment of I-type pyrite. However, the crystallization of pyrite continued until the fluids became much cooler, as evidenced by the presence of grains containing inclusions of Bi-minerals (e.g. bismuthinite).

The II-type pyrite comes from quartz-feldspathic pegmatitic veins. It contains numerous voids that can be relics of fluid inclusions. This generation of pyrite was probably formed under boiling conditions as evidenced by e.g. its co-existence with bladed-like calcite (Naglik et al. 2021). The most distinctive geochemical feature of Py-II is the relatively high Se/Te ratio, calculated at 28.30. It goes beyond the overall trend for the Myszków deposit according to which the Se/Te ratio decreases with a temperature of vein formation. Subtle differences between Py-II from central and more distal parts of the deposit were captured, including an increase of Co and Ni content toward the mineralization centre.

The III-type pyrite occurs in stockwork veins filled with quartz, molybdenite and scheelite. It formed under gentle to non-boiling conditions, and is characterized by a relatively diversified set of inclusions but their number within the single grain is relatively low. The III-type pyrite was probably precipitated from fluids of low oxygen fugacity (f_{O2}) which is suggested by the Te enrichment and the occurrence of cassiterite inclusions (Naglik et al. 2021).

2022). It was formed from fluids of moderate temperature, locally exceeding 400°C (primary inclusions of rutile). In contrast, associated quartz crystallized from oxidized fluids with tracers of boiling, at a temperature ranging from 360–240°C (Ślósarz 2001). Interestingly, the solid inclusions assemblages hosted in stockwork pyrite vary laterally and thus reflect the decreasing temperature outward from a central heat source.

The IV-type pyrite represents the final stage of main hydrothermal activity in the system. Pyrite forms euhedral to subhedral grains with cataclastic texture and numerous microfractures filled with galena and sphalerite. It shows scarcity of solid inclusions as being deposited under stable physicochemical conditions. Py-IV is rather depleted in trace elements; however, it contains the significant traces of As that correspond to the detectable content of structurally-bonded Au and Sb (Naglik et al. 2022). It bears, therefore, a quasi-epithermal signature. In addition, the association of As and Sb in Py-IV could be considered as a characteristic feature of fluids that underwent boiling at depth. The IV-type pyrite probably crystallized at a lower temperature range, as manifested by the presence of pyrite-hosted inclusions of aikinite-group minerals, which form at about 300°C. In this case, pyrite-hosted solid inclusions provided quite a good approximation to microthermometric results from co-existing gangue phases, according to which ores were formed from fluids at a temperature ranging from 298°C to 275°C (Ślósarz 2001).

4 The outlook

The critical economic value of PCDs caused the long-lasting research interest given to their origin and zonality patterns. However, still more research data is needed to be provided to broaden our knowledge about the metallogeny of this type of deposit. Some of the most challenging issues in that field include: (1) the tectonic regime of mineralization (i.e. a relation of porphyry deposits to large-scale tectonic events); (2) the physicochemical properties of mineralizing fluids (i.e. mechanisms of sulfides transport and their deposition, the origin of fluids salinity essential for mobilizing large quantities of the base metals, direct temperature-pressure conditions); (3) life span of magmatic/post magmatic activity; (4) the variation of fluids composition along with time and their impact on the ore minerals distribution; and (5) the influence of mafic magmas inputs on the deposit formation.

Another aspect is related to mineral prospecting. New mineral deposits are becoming more and more difficult to find and hence, further new proxies toward mineralization centre are very welcome to aid exploration wherever bulk or mineral indices are ineffective.

A new way of detecting proximity to the mineralized porphyry systems could be obtained with isotope geochemistry, including sulphur isotope composition of pyrite. To provide significant added

value and novelty for prospecting, further new geochemical indices should provide more precise information than can be obtained from bulk or mineral proxies, which hopefully will be more reproducible, i.e. enable to successfully localize centre of high-grade mineralization irrespective of the deposit geotectonic settings, the composition of the host intrusive, nature of the wall rocks, age of mineralization, erosion level, and size of the ore body. It is believed that the isotopic-based approach meets these criteria as probably being sensitive to the widespread boiling phenomena. Commonly, extensive boiling of hydrothermal fluids accompanies deposition of ore and gangue minerals, and thus, boiling horizons are considered a key-guides for exploration (e.g. Ham 1978). Hence, isotopic proxies provide vectors directly to the zones of the economic-grade mineralization, not to the source of heat, as do the mineral indices, i.e. Ti-in chlorite proximator (Cook et al. 2020). Sulphides precipitate in response to the temperature decrease and therefore, the center of thermal anomaly is not the center of high-grade mineralization (Cook et al. 2020).

A pilot study related to the isotopic signature of pyrite from the Myszków Mo-Cu-W deposit has already started at PGI-NRI. A small systematic variation of the S isotopic composition of pyrite is being recognized *via* SHRIMP. If some lateral zoning in the S composition of pyrite does exist in the porphyry Cu system, this new mineral indice might be utilized in the other perspectives areas at the Kraków-Lubliniec Fault Zone – one of the most promising tectonic unit for discovering new concealed Cu deposits of porphyry-type in Central Europe. It must be stated that systematic variations in sulphur isotope composition of pyrite were previously recognized in alkalic porphyry deposits of British Columbia (Pass 2010) and in the Cadia district, Australia (Wilson et al. 2007).

Moreover, as being formed under vigorous *via* gentle to non-boiling conditions (Naglik et al. 2021), pyrite and associated quartz from the KLFZ make this system a natural laboratory to investigate the geochemical behaviour of trace elements during boiling phenomena. The combination of microthermometry and geochemistry of pyrite- and quartz-hosted fluid inclusions (FIs) offers a unique opportunity to explore the vapour-liquid partitioning of metals over the wide range of temperature, pressure, and salinity of fluids. The boiling-induced effects on the distribution of elements in the studied area is not well-understood. This question becomes more intriguing when one takes into account the different geochemical behaviour of ore-forming components in various hydrothermal systems. For example, Au could be either preferentially partitioned into the brine (e.g. Keith et al. 2020) or the vapour (e.g. Heinrich et al. 1999) during boiling, and thus, redeposited at different distances from causative porphyry (or dispersed in country rocks).

5 Summary

Pyrite from the Myszków porphyry Mo-Cu-W deposit (the Kraków-Lubliniec Fault Zone, Poland) possesses several distinctive features with respect to spatial and temporal system evolution. It shows a diversified set of solid inclusions that reflect geobarometric and geothermometric information as well as represent the fluid conditions reached before their entrapment by the host mineral. Variations in compositional features of pyrite from different mineralization stages point to the changes in ore-forming processes along with time. Some geochemical differences between pyrites formed under boiling to non-boiling events were also found (e.g. Co, As, Sb and Au distribution). Our results confirm therefore that pyrite retains typomorphic characteristics of its ore and bears key-petrogenetic information, i.e. fingerprints of boiling.

Further studies of pyrite are therefore required and should include near-infrared microthermometric measurements and geochemical analysis *via* LA-ICP-MS of pyrite-hosted fluid inclusions.

However, when considering geochemical and morphological features of pyrite as a function of the proximity to high-grade mineralization the differences between specimens of main-stage pyrite are rather subtle and include changes in solid inclusions assemblages and small variations in geochemical composition, e.g. Co and Ni content. However, the isotopic characterization of pyrite might bring new solutions in this regard.

Acknowledgements

The final editorial work was financially supported by the Polish Geological Institute-National Research Institute statutory funds (Project No. 62.9012.2317.00.0 for B.N.) and the AGH University of Science and Technology (Project No. 16.16.140.315).

References

Cooke D. R., Wilkinson J.J., Baker M., Agnew P., Phillips J., Chang Z., Chen H., Wilkinson C.C., Inglis S., Hollings P., Zhang L., Gemmell J.B., White N.C., Danyushevsky L., Martin H. (2020) Using mineral chemistry to aid exploration: A case study from the Resolution porphyry Cu-Mo deposit, Arizona. *Econ. Geol.* 115(4): 813-840.

Genna D., Gaboury, D. (2015) Deciphering the hydrothermal evolution of a VMS system by LA-ICP-MS using trace elements in pyrite: an example from the Bracemac-McLeod deposits, Abitibi, Canada, and implications for exploration. *Econ. Geol.* 110(8): 2087-2108.

Ham C.G.C. (1978) Pressure gradients and boiling as mechanisms for localizing ore in porphyry systems. *US Department of the Interior*, 6(6): 745-754.

Heinrich C.A., Gunther D., Audétat A., Ulrich T., Frischknecht R. (1999) Metal fractionation between magmatic brine and vapor, determined by microanalysis of fluid inclusions. *Geology*, 27(8): 755-758.

Jarmołowicz-Szulc K. (2020) A reappraisal of K-Ar and new U-Pb age data for felsic rocks in the vicinity of the Kraków-Lubliniec fault zone (Southern Poland). *Geol. Q.* 64: 754-765. <https://doi.org/10.7306/gq.1549>.

Keith M., Smith D.J., Doyle K., Holwell D.A., Jenkin G.R., Barry T.L., Becker J., Rampe J. (2020) Pyrite chemistry: A new window into Au-Te ore-forming processes in alkaline

epithermal districts, Cripple Creek, Colorado. *Geochim. Cosmochim. Acta*, 274: 172-191.

Loucks R.R. (2014) Distinctive composition of copper-ore-forming arc magmas. *Austral. J. Earth Sci.* 61(1): 5-16.

Mikulski S.Z., Williams I.S., Markowiak M. (2019) Carboniferous-Permian magmatism and Mo-Cu (W) mineralization in the contact zone between the Małopolska and Upper Silesia Blocks (south Poland): An echo of the Baltica-Gondwana collision. *Int. J. Earth Sci.* 108(5): 1467-1492.

Naglik B., Dumańska-Słowik M., Toboła T., Derkowski P., Habryn R., Markowiak M. (2021) Diversity of Pyrite-Hosted Solid Inclusions and Their Metallogenic Implications — A Case Study from the Myszków Mo-Cu-W porphyry deposit (the Kraków-Lubliniec Fault Zone, Poland). *Minerals* 11: 1426.

Naglik B., Toboła T., Dumanska-Słowik M., Dimitrova D., Derkowski P., Zielinski G., Habryn R., Nadlonek, W. (2022) Multi-stage ore forming history of the Variscan porphyry Mo-Cu-W Myszków deposit (Poland): evidence from trace elements of pyrite. *Ore Geol. Rev.* 105185.

Pass H.E. (2010) Breccia-hosted chemical and mineralogical zonation patterns of the Northeast Zone, Mt. Polley Cu-Ag-Au alkalic porphyry deposit, British Columbia, Canada. Dissertation, University of Tasmania.

Richards J.P. (2011) High Sr/Y arc magmas and porphyry Cu±Mo±Au deposits: just add water. *Econ. Geol.* 106(7): 1075-1081.

Seedorff E., Dilles J.H., Proffett J.M., Einaudi M.T., Zurcher L., Stavast W.J., Johnson D.A., Barton M.D. (2005) Porphyry deposits: Characteristics and origin of hypogene features. *Society of Economic Geologists*.

Sillitoe R.H. (2010) Porphyry Copper Systems. *Econ. Geol.* 105: 3-41. <https://doi.org/10.2113/gsecongeo.105.1.3>.

Stein H., Markowiak M., Mikulski S.Z. (2005) Metamorphic to magmatic transition captured at the Myszków Mo-W deposit, southern Poland. In: Mao J., Bierlein F.P. (eds) *Mineral Deposit Research: Meeting the Global Challenge*. Springer Berlin Heidelberg, Berlin, pp. 833-836.

Sutphin D.M., Hammarstrom J.M., Drew L.J., Large D.E., Berger B.R., Dicken C., DeMarr M.W. (2013) Porphyry Copper Assessment of Europe, Exclusive of the Fennoscandian Shield, In: *Global Mineral Resource Assessment* (No. 2010-5090-K), US Geological Survey.

Ślósarz J. (2001) Mineralogical characteristics of the mineralization. In: Podemski M. (ed) *Palaeozoic Porphyry Molybdenum-Ungsten Deposit in the Myszków Area, Southern Poland*. Polish Geological Institute, Special papers, Warsaw, pp. 43-53.

Wilkinson J.J., Chang Z., Cooke D.R., Baker M.J., Wilkinson C.C., Inglis S., Chen H., Gemmell, J.B. (2015) The chlorite proximeter: A new tool for detecting porphyry ore deposits. *J. Geochem. Explor.* 152: 10-26.

Wilson A.J., Cooke D.R., Harper B.J., Deyell C.L. (2007) Sulfur isotopic zonation in the Cadia district, southeastern Australia: exploration significance and implications for the genesis of alkalic porphyry gold-copper deposits. *Miner. Depos.* 42: 465-487.

Cold arc magma differentiation linked to porphyry copper deposit formation?

Chetan Nathwani^{1,2,3}, Simon Large¹, Jon Blundy⁴, Matthew Loader¹, Yannick Buret¹, Jamie J. Wilkinson^{1,2}, Katie McCann^{1,2}, Cyril Chelle-Michou³

¹London Centre for Ore Deposits and Exploration (LODE), Natural History Museum, London, United Kingdom

²Department of Earth Science and Engineering, Imperial College London, United Kingdom

³Institute of Geochemistry and Petrology, Department of Earth Sciences, ETH Zürich, Switzerland

⁴Department of Earth Sciences, University of Oxford, United Kingdom

Abstract. The key processes responsible for the genesis of world-class porphyry copper deposits remain ambiguous. A high water content of parental magmas evolved in the deep crust is posited to be one key control on their formation, yet remains controversial. Here, we report trace element compositions of whole-rocks and zircons that pre-, syn- and post-date mineralisation from several major porphyry copper districts. We find clear temporal trends of decreasing zircon Ti and whole-rock Zr. Across all studied deposits and literature data, we find low zircon Ti and whole-rock Zr concentrations are inherent to intrusive rocks associated with porphyry Cu deposits. According to the Ti-in-zircon thermometer and zircon solubility models, these concentrations are consistent with porphyry Cu-related magmas being cold relative to other intermediate-felsic magmas (<800°C). We perform thermodynamic modelling to demonstrate that such low temperature magma differentiation can be readily explained by elevated water concentrations (>6 wt.%) of porphyry Cu magmas at depth which displaces the liquidus to lower temperatures. By integrating this with the latest zircon solubility models, we show that wet magma differentiation leads to zircon appearing as a relatively early crystallising phase at low temperature. Our study therefore provides new evidence that magmas related to porphyry Cu deposits contain characteristically high water contents (>6 wt.%).

1 Introduction

Porphyry copper deposits account for the majority of global copper and molybdenum production. Many of these systems are associated with syn-subduction magmatism and form during periods of strong compression and crustal thickening (Sillitoe 2010). The key magmatic processes responsible for the formation of an economic porphyry copper deposit, as opposed to a barren or subeconomic intrusion remain debated. Some have suggested that high magmatic water contents may be important, where differentiation of magmas at high pressure allows significant water to accumulate in derivative melts. This can subsequently enhance the ability of a magma to generate large volumes of copper-charged fluid (Richards 2011, Chiaradia and Caricchi 2017).

However, it has been argued that particularly wet arc magmas will rarely reach upper crustal levels, because they water saturate at depth leading to crystallisation and stalling (Chiaradia 2020). Other authors have argued that alternative processes may be more important including: high magmatic oxidation state, chalcophile fertility, large volumes of magma accumulation and rates of magma flux (Wilkinson 2013, Chelle-Michou and Rottier 2021).

Here we report whole-rock and zircon trace element compositions for rocks which overlap with batholith assembly and porphyry copper mineralisation in several porphyry copper districts. We focus in particular on the Los Bronces district, Central Chile, which is hosted by the San Francisco Batholith that records up to ~10 Myr of barren pluton assembly. We focus on temporal changes in whole-rock Zr and zircon Ti concentrations, and their ability to track changes in melt temperature and water content which reach minima and maxima, respectively, during porphyry Cu mineralisation.

2 Methodology

2.1 Sampling

Samples were collected from the Los Bronces porphyry Cu-Mo district (Fig. 1). Rocks were sampled from several discrete phases of the San Francisco Batholith and pre-mineralisation, sub-economic porphyry intrusions from across the district, in order to span the period leading up to porphyry Cu mineralisation. Samples of intrusions at Los Bronces interpreted to be coeval with porphyry mineralisation were collected from drillcore.

Samples were also collected from a range of other porphyry systems including Los Pelambres (Central Chile), Corcapunta (Peru), Chipispaya (Southern Peru) and Cerro Colorado (Northern Chile). Data were also compiled from a range of literature sources which report zircon trace element compositions in porphyry copper districts.

2.2 Whole-rock geochemistry

Rocks were crushed and pulverised to pulps and were analysed by inductively-coupled plasma atomic emission spectrometry for major elements and inductively-coupled plasma mass spectrometry for trace elements.

2.3 Zircon trace element geochemistry

and Analysis Centre at the Natural History Museum, London.

2.3 Modelling of zircon saturation

The effect of melt water content on melt temperatures was modelled using rhyolite-MELTS (Ghiorso and Gualda 2015). Equilibration of a starting andesite-dacite was carried out over a range of temperatures, water

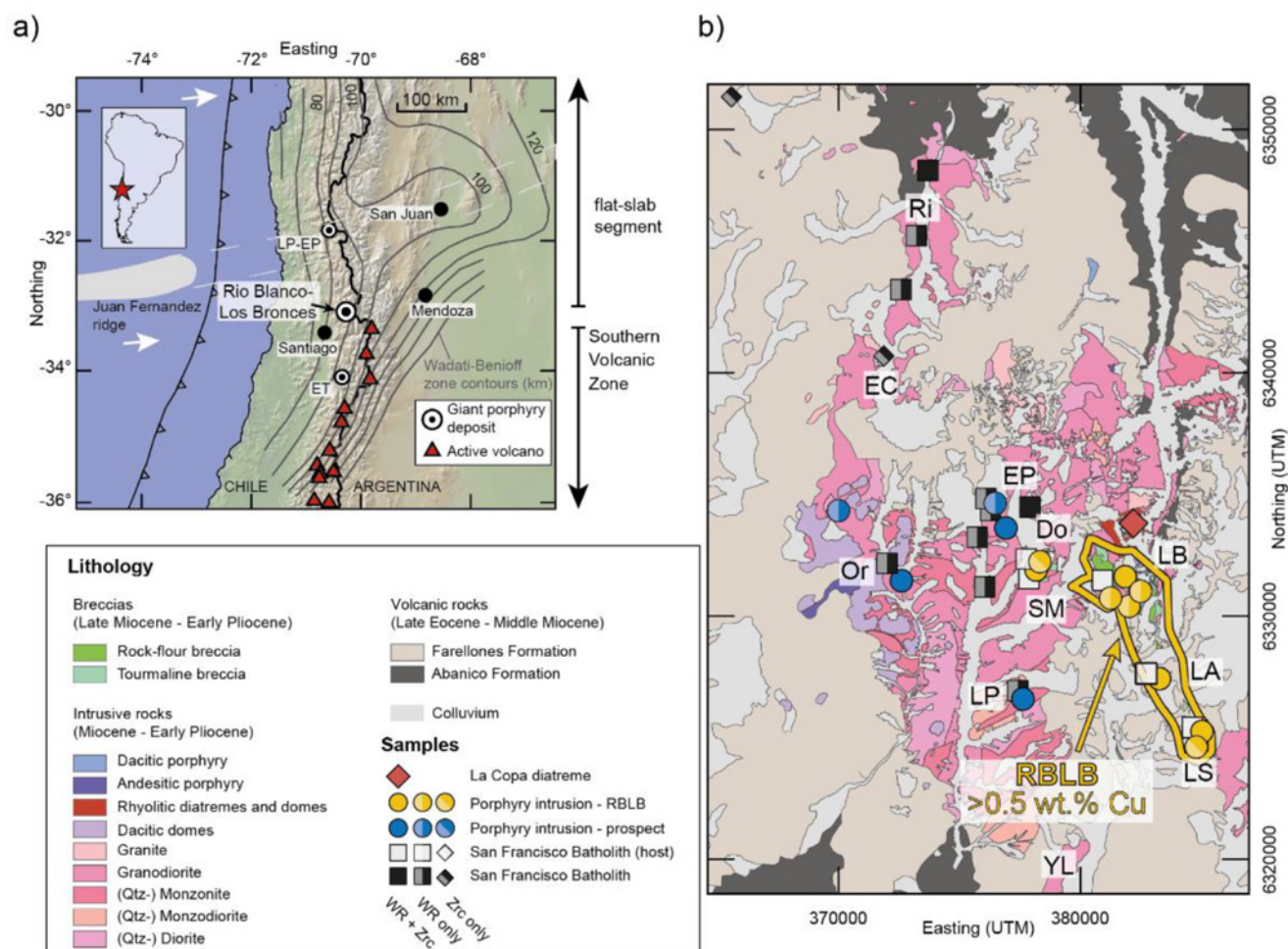


Figure 1. Geological map and setting of the San Francisco Batholith (SFB) and Rio Blanco-Los Bronces (RBLB) porphyry deposit cluster. A) Regional topographic map of Central Chile highlighting location of RBLB and neighbouring giant porphyry Cu cluster (Los Pelambres-El Pachón – LP-EP and El Teniente – ET). B) District-scale geological map of RBLB deposit cluster (modified after Piquer 2015). Sample localities are shown together with the surface expression of the domain containing >0.5 wt.% Cu (yellow line). District deposits/prospects are also shown: Do: Quebrada Dolores, EC: El Cruce, LA: La Agustina, LB: Los Bronces, LP: Los Piches, LS: Los Sulfatos, Or: Ortiga, Ri: Riecillos, SM: San Manuel, YL: Yerba Loca.

Zircons were separated from a subset of sampled rocks using conventional mineral separation techniques. They were first imaged using scanning electron microscope cathodoluminescence, and then analysed for trace element compositions using laser ablation inductively-coupled plasma mass spectrometry (LA-ICP-MS) synchronously with the isotopes required for U-Pb geochronology. All analyses were performed in the Imaging

contents and pressures. Zircon solubility was also integrated into this model using the latest empirical models (Crisp and Berry 2022).

3 Zr systematics and zircon Ti concentrations

Whole-rock Zr concentrations decrease over time in the Los Bronces district, from 200-300 ppm to ca. 100 ppm Zr. Zircon Ti decreases over the same time period, with the pre-

mineralisation zircons predominantly having concentrations between 20 and 5 ppm, whereas zircons from the porphyry intrusions associated with peak Cu mineralisation have < 5 ppm Ti.

In other porphyry systems studied here and reported from literature data, whole-rock Zr and zircon Ti generally decrease over time. Low whole-rock Zr (<150 ppm) and low zircon Ti (<7 ppm) are observed in all rocks associated with porphyry Cu mineralisation.

4 Do low temperatures and high water contents characterise porphyry magmas?

Crystallisation temperatures were calculated for zircon based on Ti concentrations using the experimental calibration of Ferry and Watson (2007) and implementing a pressure correction (Loucks et al. 2020). Assuming an activity of titania (a_{TiO_2}) of 0.6, an activity of silica of 1.0 (a_{SiO_2}) and a pressure of 400 MPa, porphyry zircons yield temperatures of 850-750°C. Based on an evaluation of the influence of variable a_{TiO_2} and pressure on zircon Ti concentrations we suggest that these parameters cannot fully account for the inherently low Ti in porphyry-related zircons.

We also attempted to calculate temperatures from whole-rock Zr in porphyry rocks, assuming porphyry rocks represent crystallised liquids and implementing Zr saturation thermometry. This approach yielded crystallisation temperatures of 700-740 °C.

The low temperatures inferred for porphyry magmas from the zircon record may be related to the timing of zircon saturation in such magmas and/or intrinsically lower magma temperatures. One key control on this may be melt water content, since previous work has suggested that magmas forming porphyry Cu deposits may have elevated water contents relative to typical arc magmas. In wet magmas, the liquidus is displaced to lower temperatures. Such low temperatures would thus be recorded upon zircon saturation.

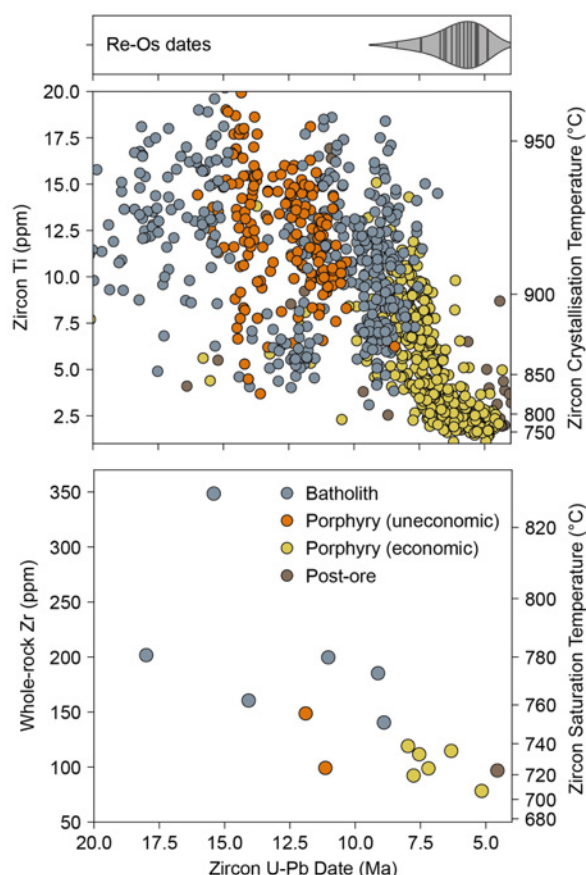


Figure 2. Zircon Ti and whole-rock Zr concentrations in the Los Bronces district over time. For zircon Ti concentrations, the U-Pb dates are single grain LA-ICP-MS analyses, whereas for whole-rock Zr these are weighted mean U-Pb dates. Temperature axes are given to show approximate temperature ranges according to Ti-in-zircon thermometry (Ferry and Watson 2007) and zircon saturation thermometry (Crisp and Berry 2022). Density distribution of molybdenite Re-Os mineralization dates is derived from data in Toro et al. (2012).

In order to test this, we used rhyolite-MELTS to model the influence of increasing water contents on the liquidus temperature and thermal trajectory of magmas during their storage and crystallisation. We also monitored the timing of zircon saturation in these models. We find that increasing initial melt H_2O from 2 to 6 wt.% can decrease the temperature of zircon saturation by ~100°C and that the initial Zr concentration of the magma strongly influences the temperature of zircon saturation. Decreasing initial Zr from 200 to 100 ppm leads to a ~70°C decrease in the temperature of zircon saturation.

Our results suggest that porphyry-related magmas contain elevated concentrations of water (>6 wt.%) and that zircons in these magmas crystallised at low temperatures at mid-crustal depths (>400 MPa), where, in intermediate to felsic melts,

such water solubility is possible. This finding is in accordance with studies linking porphyry copper deposit formation to wet, high-pressure arc magma differentiation.

5 Conclusions

Low whole-rock Zr and low zircon Ti are characteristic signatures of intrusive rocks associated with porphyry copper mineralisation. Distinct trends of decreasing whole-rock Zr and decreasing zircon Ti over multi-Myr durations in porphyry Cu districts track decreasing temperatures of magmas over time. We interpret these lower temperatures to reflect increasing melt water contents, which displaces the liquidus to lower temperatures. High water contents lead to zircon appearing as a relatively early crystallising phase at low

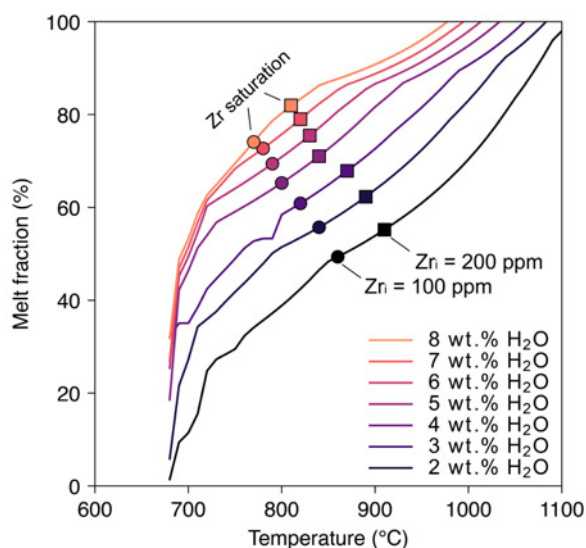


Figure 3. Results of rhyolite-MELTS modelling showing the temperature versus melt fraction of a cooling magma for different water contents between 2 and 8 wt.% H₂O. Symbols indicate the point of zircon saturation in each model given an initial Zr concentration (Zr_i) of 100 ppm (circles) and 200 ppm (squares).

temperatures. We suggest that zircons in porphyry Cu deposits record a history of deep, hydrous arc magma differentiation. Our study highlights that elevated melt water contents (>6 wt.%) are a key feature of magmas associated with porphyry Cu deposit formation.

Acknowledgements

This study was funded by NERC grant NE/P017452/1 “From Arc Magmas to Ore Systems” (FAMOS). CN also acknowledges funding from an ETH Zürich postdoctoral research fellowship. We are grateful to Anglo American, BHP and Antofagasta Minerals for providing access to samples and sampling

localities for this project, and on-site geologists and staff for their support.

References

- Chelle-Michou C, Rottier B (2021) Transcrustal magmatic controls on the size of porphyry Cu systems—State of knowledge and open questions. *Society of Economic Geologists Special Publication 1*: <https://doi.org/doi:10.5382/SP.24.06>
- Chiaradia M (2020) How Much Water in Basaltic Melts Parental to Porphyry Copper Deposits? *Frontiers in Earth Science* 0: <https://doi.org/10.3389/feart.2020.00138>
- Chiaradia M, Caricchi L (2017) Stochastic modelling of deep magmatic controls on porphyry copper deposit endowment. *Scientific Reports* 7:44523. <https://doi.org/10.1038/srep44523>
- Crisp LJ, Berry AJ (2022) A new model for zircon saturation in silicate melts. *Contrib Mineral Petrol* 177:71. <https://doi.org/10.1007/s00410-022-01925-6>
- Ferry JM, Watson EB (2007) New thermodynamic models and revised calibrations for the Ti-in-zircon and Zr-in-rutile thermometers. *Contributions to Mineralogy and Petrology* 154:429–437. <https://doi.org/10.1007/s00410-007-0201-0>
- Ghiorso MS, Gualda GAR (2015) An H₂O–CO₂ mixed fluid saturation model compatible with rhyolite-MELTS. *Contributions to Mineralogy and Petrology* 169:53. <https://doi.org/10.1007/s00410-015-1141-8>
- Loucks RR, Fiorentini ML, Henríquez GJ (2020) New Magmatic Oxybarometer Using Trace Elements in Zircon. *Journal of Petrology* 61: <https://doi.org/10.1093/petrology/egaa034>
- Richards JP (2011) High Sr/Y arc magmas and porphyry Cu ± Mo ± Au deposits: just add water. *Economic Geology* 106:1075–1081. <https://doi.org/10.2113/econgeo.106.7.1075>
- Sillitoe RH (2010) Porphyry Copper Systems. *Economic Geology* 105:3–41. <https://doi.org/10.2113/gsecongeo.105.1.3>
- Toro JC, Ortúzar J, Zamorano J, et al (2012) Protracted magmatic-hydrothermal history of the Río Blanco-Los Bronces district, Central Chile: Development of world’s greatest known concentration of copper. *Society of Economic Geologists Special Publication* 16:105–126
- Wilkinson JJ (2013) Triggers for the formation of porphyry ore deposits in magmatic arcs. *Nature Geoscience* 6:917–925. <https://doi.org/10.1038/ngeo1940>

LA-ICP-MS trace element analysis of pyrite from the Bakoudou gold deposit, South Gabon: Implications for ore genesis

Nazaire Nzaou Mabika¹, Amina Wafik¹, Abdellah Boushaba², Damien Gaboury³, Lhou Maacha⁴, Gharrabi Mohamed⁴, Benyounes Maamar⁴

¹ Cadi Ayyad University, Marrakech, Morocco

² Sidi Mohamed Ben Abdellah University, Fes, Morocco

³ Université du Québec à Chicoutimi, Chicoutimi, Canada

⁴ Managem Mining Company (SA), Casablanca, Morocco

Abstract. The Bakoudou gold deposit, southern Gabon, is hosted in the Archean basement granitoids of the Chaillu Massif. The orebody of the Bakoudou gold deposit occurs as quartz veins hosted in shear zones crosscutting TTG intrusive rocks. Quartz is the main gangue mineral, with minor sulfides such as pyrite and chalcopyrite. Gold is present in solid solution (Au^{+1}) and as nanoparticles of native gold (Au^0) in pyrite and mostly as free gold. Pyrite samples analysed by laser ablation inductively coupled plasma mass spectrometry (LA-ICP-MS) show high Ni (3.24–3600 ppm) and Co (4.68–4140 ppm) and low As (<34.50 ppm) and Au concentrations (<2.90 ppm) compared to Cu, which has rather high concentration of <3570 ppm. Moreover, the Au–As relationships of pyrites show a porphyry–epithermal transitional signature. Therefore, the Bakoudou gold deposit can be considered an example of Archean porphyry–epithermal transitional gold system, formed from magmatic fluids originating from a hidden porphyry system at depth. The disseminated free gold grains in the quartz veins may have originated from boiling of the mineralizing fluid (phase separation) and/or from remobilization of invisible gold in pyrite by later tectonic events and surficial weathering.

1 Introduction

The Precambrian basement of western Central Africa is represented by the Congo Craton, which covers the Gabon-Democratic Republic of Congo border and extends to the Cameroon-Gabon border (Nédélec et al. 1990). This basement is composed of Archean cratons welded together by Meso- and Paleoproterozoic belts (De Wit and Linol 2015) and is mainly represented on the Gabonese territory by the Chaillu Massif and the North Gabon Massif (Thiéblemont et al. 2009) (Figure 1). Gold mineralizations are common in the Archean basement of Gabon, and many placers have been exploited by artisans (Thiéblemont et al. 2009). However, primary gold mineralizations are rare, and the main representative example is the Bakoudou gold deposit (Thiéblemont et al. 2009). It is located in southeastern Gabon, in Haut-Ogooué Province, more precisely on the edge of the Chaillu Massif, approximately 100 km southwest of the Franceville basin (Thiéblemont et al. 2009, Figure 1). The gold mineralization occurs as quartz veins hosted in the gray granitoids of the Chaillu Massif (Thiéblemont et al. 2009). In this abstract, we provide and interpret trace element data from pyrite to constrain the origin and typology of the Bakoudou gold mineralization.

2 Methodology

Trace element concentrations from 23 pyrite grains were acquired by laser ablation inductively coupled plasma mass spectrometry (LA-ICP-MS) on polished thin sections of quartz vein samples. The analyses were performed at LabMaTer at the University of Quebec at Chicoutimi (UQAC), Canada, using an Excimer 193 nm Resonetics Resolution M-50 laser ablation system coupled with an Agilent 7700x mass spectrometer. The following isotopes were measured: 28Si, 33S, 34S, 51V, 52Cr, 55Mn, 57Fe, 59Co, 60Ni, 65Cu, 66Zn, 71Ga, 72Ge, 75As, 82Se, 107Ag, 111Cd, 115In, 118Sn, 121Sb, 126Te, 197Au, 205Tl, 208Pb and 209Bi. Analyses were performed using lines and rare spots, depending on the pyrite size, with laser beam diameters from 25 to 43 μm , a range of stage movement speeds from 2.5 to 5 $\mu\text{m/s}$, laser frequencies from 10 to 15 Hz and power from 4 to 5 mJ/pulse.

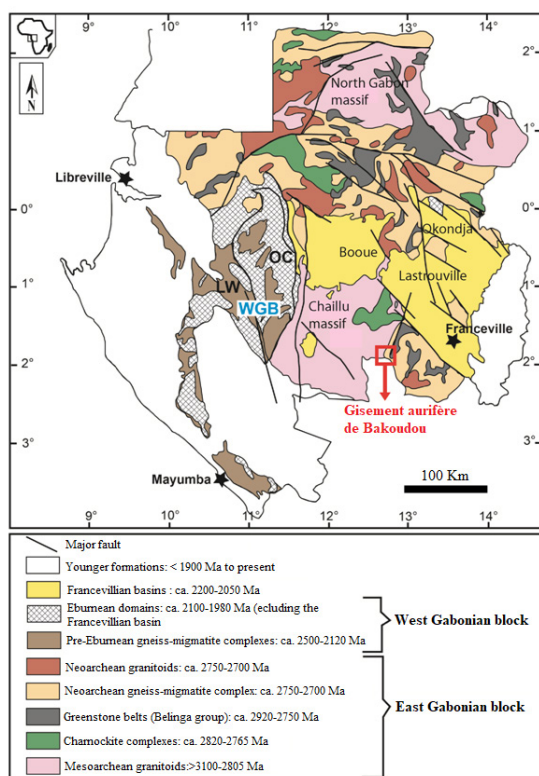


Figure 2. Geological map of the Gabonese Republic, modified from Thiéblemont et al. (2009)

3 Trace element geochemistry of pyrite

Pyrite is the predominant sulfide mineral in the orebody. It occurs as medium to coarse idiomorphic crystals, fractured and disseminated in the quartz veins (Figure 2). Some pyrites have chalcopryite inclusions (Figure 2). Pyrites have high Co (4.68–4140 ppm) and Ni (3.24–3600 ppm) contents, with Co/Ni ratios between 0.02 and 15.54 (average = 3.33 for 23 analyses). The concentrations of invisible gold and silver vary up to 2.90 ppm and 58 ppm, respectively. These pyrites are As-poor (≤ 34.50) but show high Cu (≤ 3570 ppm) contents. Antimony contents are very low (average = 0.03 ppm) and generally below the limit of detection in the majority of samples. However, Te values are above the detection limit and up to 136 ppm.

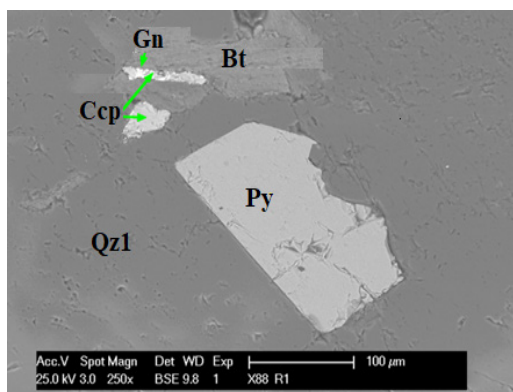


Figure 3. SEM images showing pyrite and chalcopryite enclosed in quartz, with galena inclusions in chalcopryite

4 Typology of the deposit

It has been shown that pyrite can record valuable information about the chemical evolution of the fluids from which it precipitated (e.g. Augustin and Gaboury 2019; Gaboury and Ore Sanchez 2020). In the Bakoundou gold deposit, pyrite represents the dominant sulfide mineral that formed during the main stage of mineralization. Therefore, trace element data for these pyrites can provide valuable information regarding the typology of this deposit (e.g. Deditius et al. 2014 and Le Mignot et al. 2017), as well as the origin of the potential mineralizing fluids (e.g. Large et al. 2013; Hu et al. 2016; Augustin and Gaboury 2019).

The pyrite trace element budget in this study shows that concentrations of invisible Au are low and vary from <0.01 to 2.90 ppm. Pyrite crystals are enriched in Cu (up to 3570 ppm) and poor in As (< 34.50 ppm). In the Cu–Ni + Co–As ternary diagram of Deditius et al. (2014) (Figure 3), all pyrite samples plot within the field of porphyry-related pyrites. On the As (mol%) vs. Au (mol%) diagram of Deditius et al. (2014) (Figure 4), the pyrite samples plot within the porphyry and transitional porphyry-epithermal fields. Furthermore, the presence of high Co (up to 4140 ppm) and Ni (up to 3600 ppm) concentrations in the pyrites of quartz veins, yielding Co/Ni ratios between 0.02 and 15.54 (average = 3.33), is consistent with a magmatic-hydrothermal origin (e.g. Zhang et al. 2014; Yu et al. 2018). This is supported by the As/Ag vs. Sb/Bi discriminant diagram of Augustin and Gaboury (2019), where our pyrite samples plot within the magmatic field for the mineralizing fluid source (Figure 5). Therefore, the Bakoundou gold deposit is considered to represent a porphyry–epithermal transitional gold system that shows a magmatic-hydrothermal signature.

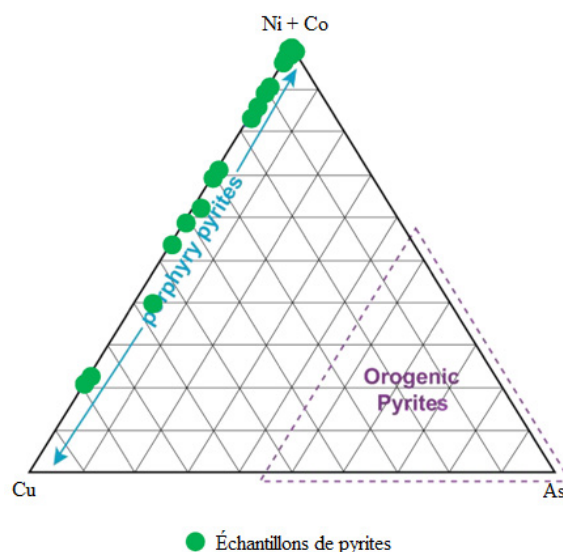


Figure 4. Cu–As–(Ni+Co) ternary diagram of Deditius et al. (2014) showing the porphyry character of the pyrites from the Bakoundou gold deposit.

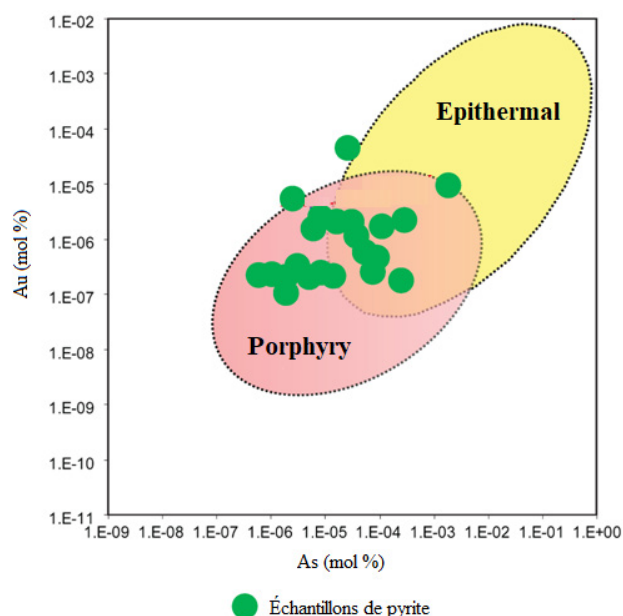


Figure 6. Au vs. As diagram (in mol%) of Deditius et al. (2014) showing the epithermal-porphyry character of the pyrites from the Bakoudou gold deposit.

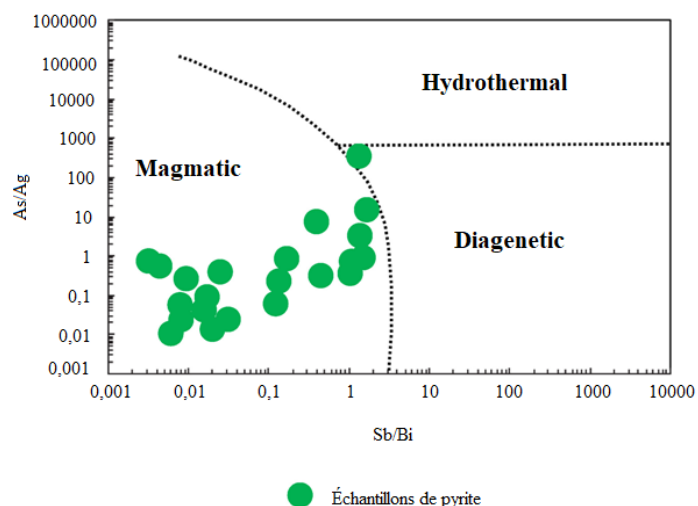


Figure 5. As/Ag vs. Sb/Bi diagram of Augustin and Gaboury (2019) indicating a magmatic fluid source for the pyrites from the Bakoudou gold deposit.

The Bakoudou gold deposit is hosted in shear zones. The orebody occurs as quartz veins, where quartz is the main gangue mineral. Minor sulfides, such as pyrite and chalcopyrite, occur within the deposit. Trace element data for pyrites from the quartz veins indicate that the Bakoudou gold deposit is a porphyry–epithermal transitional gold system that formed from magmatic fluids. Gold mineralization in quartz vein occurs as invisible gold in pyrite, but mostly as free gold. Free gold is interpreted to be a second event, resulting from phase separation of the mineralizing fluids or remobilization of invisible gold from pyrite grains by later tectonic events and/or pyrite oxidation in the upper part of the deposit.

Acknowledgements

This work was supported by the Managem Mining Company and the DLGR Laboratory (Department of

Geology, Faculty of Sciences Semlalia, Cadi Ayyad University, Marrakech, Morocco). LAMEQ of Université du Québec à Chicoutimi (UQAC) are thanked for the use of their LA-ICP-MS which enabled to measure trace element concentrations some pyrite grains.

References

- Augustin, J. and Gaboury, D. (2019): Multi-stage and multi-sourced fluid and gold in the formation of orogenic gold deposits in the world-class Mana district of Burkina Faso Revealed by LA-ICP-MS analysis of pyrites and arsenopyrites. *Ore Geology Reviews* 104, 495–521.
- De Wit, M.J. and Linol, B. (2015): Precambrian Basement of the Congo Basin and its Flanking Terrains. *Geology and Resource Potential of the Congo Basin*. pp. 19–37.
- Deditius, A., Reich, M., Kesler, S.E., Utsunomiya, S., Chrysoulis, S., Walshe, J.L., Hough, R., Ewing, R.C. (2014): The coupled geochemistry of Au and as in pyrite from hydrothermal ore deposits. *Geochem. Cosmochim. Acta* 140, 644–670.
- Gaboury, D. and Ore Sanchez, C. (2020): Electrochemical gold precipitation to explain extensive vertical and lateral mineralization in the world-class Poderosa-Pataz district, Peru. *Terra Nova* 32, 97–107.
- Hu, S.Y., Evans, K., Fisher, L., Rempel, K., Craw, D., Evans, N.J., Cumberland, S., Robert, A., Grice, K. (2016): Associations between sulfides, carbonaceous material, gold and other trace elements in polyframboids: implications for the source of orogenic gold deposits, Otago Schist, New Zealand. *Geochem. Cosmochim. Acta* 180, 197–213.
- Large, R.R., Meffre, S., Burnett, R., Guy, B., Bull, S., Gilbert, S., Goemann, K., Danyushevsky, L. (2013): Evidence for an intrabasinal source and multiple concentration processes in the formation of the carbon leader reef, Witwatersrand supergroup, South Africa. *Economic Geology* 108, 1215–1241.
- Le Mignot, E., Siebenaller, I., Beziat, D., Andre-Mayer, A.S., Reisberg, L., Salvi, S., Velasquez, G., Zimmermann, C., Nare, A. (2017): The Paleoproterozoic copper-gold deposits of the Gaoua district, Burkina Faso: superposition of orogenic gold on a porphyry copper occurrence? *Economic Geology* 112, 99–122.
- Vedelec, A., Nsifa, E.N., Martin, H. (1990): Major and trace element geochemistry of the Archaean Ntem plutonic complex (South Cameroon): petrogenesis and crustal evolution. *Precambrian Research* 47, 35–50.
- Thieblemont, D., Castaing, C., Billa, M., Bouton, P., Preat, A. (2009): Notice explicative de la Carte géologique et des Ressources minérales de la République Gabonaise à 1/1000000: Editions DGMG - Ministère des Mines, du Pétrole, des Hydrocarbures. pp. 384p Libreville.
- Yu, B., Zeng, Q., Frimmel, H.E., Wang, Y., Guo, W., Sun, G., Zhou, T., Li, J. (2018): Genesis of the Wulong gold deposit, northeastern North China Craton: constraints from fluid inclusions, H-O-S-Pb isotopes, and pyrite trace element concentrations. *Ore Geology Reviews* 102, 313–337.
- Zhang, J., Deng, J., Chen, H.Y., Yang, L.Q., Cooke, D., Danyushevsky, L., Gong, Q.J., 2014. LA-ICP-MS trace element analysis of pyrite from the Chang'an gold deposit, Sanjiang region, China: implication for ore-forming process. *Gondwana Research* 26, 557–575

Sulfur and chalcophile metal transfer via sulfide-volatile compound drops during magma mixing: evidence from the Christiana-Santorini-Kolumbo volcanic field

C.G.C. Patten¹, S. Hector¹, S. P. Kiliass², M. Ulrich³, A. Peillod¹, A. Beranoaguirre¹, P. Nomikou², E. Eiche¹, J. Kolb¹

¹*Chair of Geochemistry and Economic Geology, Institute of Applied Geosciences, Karlsruhe Institute of Technology, Germany*

²*Department of Geology and Geoenvironment, National and Kapodistrian University of Athens, Greece*

³*Institut Terre et Environnement de Strasbourg, Université de Strasbourg, CNRS, Strasbourg, France*

Abstract. Efficient transfer of S and chalcophile metals through the Earth's crust in arc magmatic-hydrothermal systems is paramount for the formation of large magmatic-hydrothermal ore deposits. Formation of sulfide-volatile compound drops in magmatic systems has been recognized as a potential key mechanism for such transfer but their behavior and evolution during dynamic arc magmatism remain cryptic. In this study, we report evidence of compound drops preserved in the active Christiana-Santorini-Kolumbo volcanic field. Two sulfide populations are defined: 1) micrometric sulfide blebs associated with vesicles and trapped within mafic enclave phenocrysts and 2) larger millimetric sulfide ovoids present at the margins between mafic enclaves and felsic host rocks. The sulfide ovoids form by accumulation and coalescence of compound drops and are eventually oxidized to magnetite during sulfide-volatile interaction. In-situ mineral analysis allows for the evaluation of metal mobility during oxidation with Bi, Cd, Cu, Ag, Tl, Te and Au showing high mobility into the volatile phase. Formation, coalescence, accumulation and oxidation of compound drops during magma mixing is a particularly efficient mechanism for transferring S and chalcophile metals in magmatic-hydrothermal arc systems.

1 Introduction

Effective fluxes of S and chalcophile metals (e.g. Cu, Au, Ag, Tl, Te, Bi) in the Earth's crust at arc settings are key for the formation of large hydrothermal ore deposits (porphyry, epithermal, volcanogenic massive sulfide, skarns; Richards 2011). The processes controlling such fluxes, however, are complex, with competitive effects during arc magmatic-hydrothermal evolution. Sulfur and chalcophile metals can be trapped in the lower crust via sulfide segregation or can be released in the upper crust via magmatic volatile degassing. The relative timing between such processes is critical in determining the fate of S and chalcophile metals. The formation of sulfide-volatile compound drops (i.e., droplets of sulfide melt attached to magmatic volatile phases) during magmatic evolution appears as an alternative and efficient mechanism for the transport of both S and chalcophile metals to the shallow crust (Mungall et al. 2015). Although such compound drops have been shown experimentally (Mungall et al. 2015) and identified in magmatic ultramafic systems (Le Vaillant et al. 2017), their preservation in complex magmatic-hydrothermal arc environments is scarce (Nadeau et al. 2010). Magmatism in arc

environments is dynamic, involving mixing and/or mingling of variably evolved melts. Injection of mafic melt into differentiated magmatic chambers appears as a key process for transferring S and chalcophile metals to shallower magmatic-hydrothermal systems (Wallace and Edmonds 2011). The fate of the compound drops in such dynamic environments is, however, poorly known and their role in the formation of arc-related hydrothermal ore deposits, although stipulated, remains cryptic.

In this study, we document the presence of compound drop remnants in the active magmatic-hydrothermal system of the Christiana-Santorini-Kolumbo (CSK) volcanic field, Greece. Based on detailed petrography, high-resolution X-ray fluorescence mapping and in-situ mineral chemistry analysis we highlight the complex mineral reactions and elemental transfers which occur in compound drops during complex magmatic evolution. The findings have important implications for S and chalcophile metals fluxes in arc-related shallow magmatic-hydrothermal systems.

2 Methods

Micro-XRF measurements were done using a Micro X-Ray Fluorescence (μ -XRF) Brucker M4 Tornado at the Institut Terre et Environnement de Strasbourg. μ -XRF chemical mappings were acquired with a 30 μ m step interval and a dwell time of 700 ms/pixel. Phase maps were calculated using the calculation procedure developed in house.

In-situ analyses of sulfide and oxide phases were carried out by Electron Micro Probe Analysis (EMPA) and by Laser Ablation-Inductively Coupled Plasma-Mass Spectrometry (LA-ICP-MS). EMPA analyses were carried out at the Institute of Geological Sciences from the University of Bern using a JEOL JXA-8200 Superprobe. LA-ICP-MS analysis were carried out at the Laboratory of Environment and Raw materials Analysis (LERA), Karlsruhe Institute of Technology, using a Teledyne 193 nm Excimer Laser coupled to an ICP-MS (Element XR ThermoFisher). Calibration and data quality checking was done using the sulfide pressed pellets Fe-S1, Fe-S4 and PTC1b from UQAC University for sulfide analyses and basaltic glasses BHVO-2, BCR-2 and BIR-1 from the USGS for oxide analysis

3 Evidence for sulfide-volatile compound drop remnants in the CSK volcanic field

The CSK volcanic field is an active and complex magmatic-hydrothermal system (Nomikou et al. 2019) showing evidence of magma mixing and mingling at the Nea Kameni and Kolumbo volcanoes.

Two sulfide populations related to volatile phases have been observed Nea Kameni and Kolumbo volcanoes (Fig. 1). The first population is defined by micrometric sulfide blebs related to micrometric vesicles hosted by pyroxene phenocrysts from andesitic enclaves in porous dacite from Nea Kameni (Fig. 1c). The sulfide blebs are mainly spherical and contain pyrrhotite and chalcopyrite with minor magnetite (Fig. 1c), characteristic of magmatic sulfide blebs. The vesicle associated with the sulfides varies from few microns up to tens of microns (Fig. 1c). They are either directly in contact with or closely related to the sulfides. The sulfide-vesicle pairs have similar shapes, sizes and mineralogy as those observed at the Merapi volcano (Nadeau et al. 2010), analogous to compound drops (Mungall et al. 2015) and, hence, are interpreted as well as compound drop remnants.

The second sulfide population observed is characterized by variably oxidized sulfide ovoids up to a few millimeters in diameter. They have a spherical to elongated ellipsoidal shape, are associated with large millimetric vesicles (Fig. 1a,b,d), and occur mainly at the interface between andesitic enclaves and dacitic host rocks. The sulfide

ovoids are either embayed in, in contact with or disconnected from the vesicles; the latter ranging in size range from several hundreds of microns to few millimeters (Fig. 1a). The sulfide ovoids are constituted mainly of pyrrhotite and pyrite with minor pentlandite, chalcocopyrite and covellite. Pyrrhotite appears as large grains (up to few mm) with discrete exsolution of pentlandite. Pyrite occurs as a replacement of pyrrhotite generally along fractures filled with magnetite; additionally, pyrite proportion increases towards magnetite-rich zones (Fig. 1d). Chalcocopyrite is scarce and has been observed in partly oxidized areas (Fig. 1d). It is often replaced by covellite associated with pyrite. Sulfides are replaced by fine-grained micrometric subhedral magnetite with discrete sulfide grains preserved in between (Fig. 1a,d). Sulfide replacement by magnetite ranges from limited, with discrete magnetite along fractures and at vesicle margins, to extensive, with almost magnetite-pure aggregates with discrete sulfides and porosity between the grains (Fig. 1 d).

4 Sulfide and oxide mineral compositions

In-situ analysis of sulfide and oxide phases from the sulfide blebs and ovoids allows the characterization of their origin and a better understanding of metal behavior during compound drop evolution.

Unaltered sulfide blebs of compound drops in silicate phenocrysts show a distinctive magmatic signature characterized by relatively high chalcophile element concentrations (Ni, Co, Cu, Ag

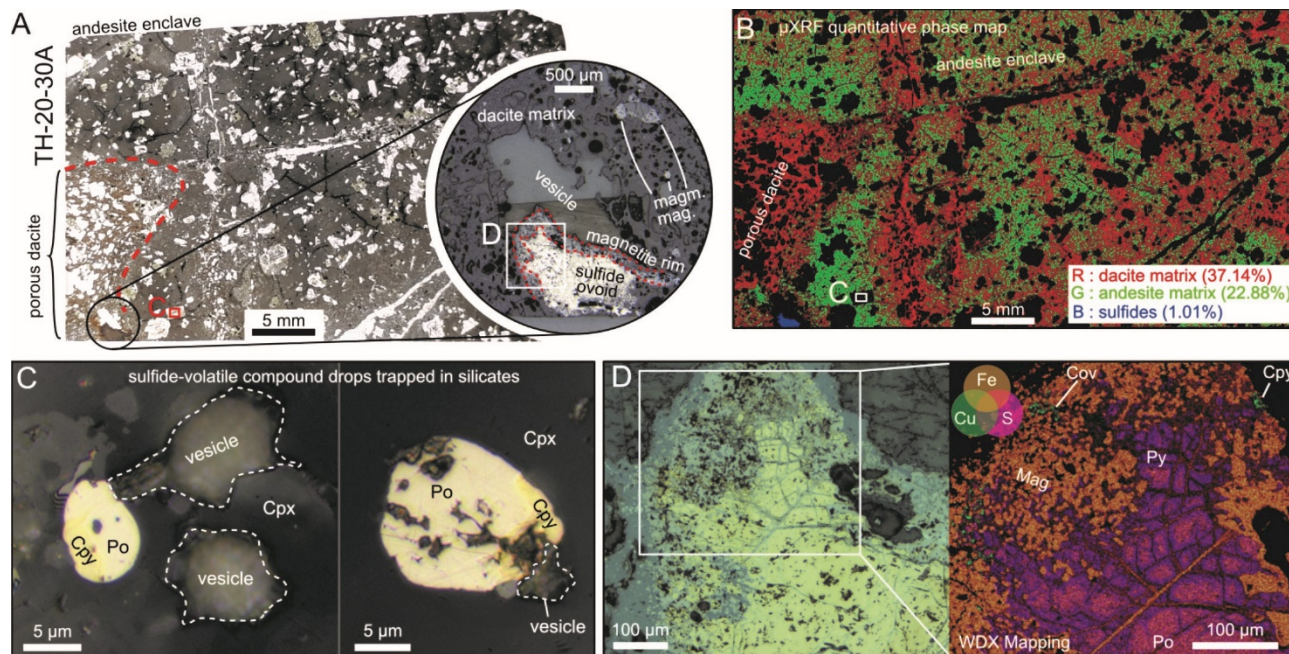


Figure 1. Petrology of sulfide and oxide phases related to sulfide-volatile compound drops at Nea Kameni volcano. A) Thin section of an andesite enclave in contact with porous dacite host rock. Sulfide ovoid associated with large vesicle at andesite/dacite margin (insert). B) micro-XRF quantitative phase map of A) showing the proportion of dacite matrix, andesitic matrix and sulfide phases (pyrrhotite and chalcopyrite). Mineral proportions are calculated from elemental micro-XRF mapping. Black zones represent porosity and silicate phenocrysts. C) Sulfide blebs and associated vesicles in pyroxene phenocryst. Sulfide blebs contain pyrrhotite (Po) and chalcopyrite (Cpy). D) Ovoid-shaped, partly oxidized sulfide melt occurring at the dacite/andesite interface in A). The sulfide ovoid is characterized by pyrrhotite (Po) in the core, pyrite (Py), chalcopyrite (Cpy), covellite (Cov) and magnetite (mag) in the rim. A' shows WDX scanning electron microscopy elemental mapping of S, Fe and Cu.

and Au; Fig. 2a) and an overall similar metal enrichment to compound drops from the Merapi volcano (Nadeau et al. 2010), and to mid-ocean ridge basalt (MORB) sulfide droplets (Patten et al. 2013). These similarities imply that the sulfide blebs formed from a sulfide-saturated melt. The sulfide blebs from the CSK volcanic field are more enriched in weakly chalcophile elements (Pb, Zn, As, Sn, Sb, Fig. 2a) compared to MORB sulfide droplets, which are enriched in strongly chalcophile elements (Au, Te, Ni), supporting that sulfide saturation occurred in an andesitic melt, slightly more evolved than a MORB.

Pyrrhotite, pyrite and partly oxidized chalcopyrite from the sulfide ovoids show comparable metal enrichment to the sulfide blebs (Fig. 2b). The partly oxidized chalcopyrite phases show marked enrichment in Ti, Au, Ag, Bi, Pb and As relative to pyrrhotite and pyrite, while the latter are enriched in Ni, Co and Mo (Fig. 2b). Such metal fractionation is akin to metal distribution during magmatic sulfide crystallization into monosulfide solid solution (MSS) and intermediate solid solution (ISS; Patten et al. 2013) supporting that the sulfide ovoids are well-differentiated magmatic sulfides overprinted by oxidation reactions.

The magnetite present within the sulfide ovoids has low concentrations in Ti, V, Mn, Zn, Co and Ni, which are usually enriched in magmatic magnetite crystallizing from a silicate melt (Dare et al. 2014). Hence, the analyzed magnetite did not form through magmatic process but rather by oxidation and replacement of the magmatic sulfides, as supported by petrographic observations

4 Sulfide and magmatic volatile fates during magmatic evolution at the Nea Kameni and Kolumbo volcanoes

Despite their spatial proximity, the Nea Kameni and Kolumbo volcanoes share distinct and complex magmatic plumbing systems. However, they are both characterized by shallow magmatic chambers (~4 and ~5 km deep, respectively) fed by mafic melts from deeper sources. The presence of magmatic sulfide blebs within the andesitic enclaves as well as the high S concentrations in andesite-hosted melt inclusions from Nea Kameni (~900-1000 ppm; Michaud et al. 2000) imply that the andesitic melt was sulfide-saturated upon injection into the shallow magmatic chamber. Additionally, the presence of trapped fluid inclusions in olivine and pyroxene in andesitic enclaves at Nea Kameni (Rizzo et al. 2015) suggests that magmatic volatile exsolution occurred within a similar timeframe to sulfide saturation; allowing bubble nucleation on magmatic sulfide droplets and formation of sulfide-volatile compound drops.

The similar mineralogy and composition, the spatial proximity as well as the close association with vesicles imply a genetic link between the magmatic sulfide blebs and the larger sulfide ovoids. The formation of the sulfide ovoids is likely

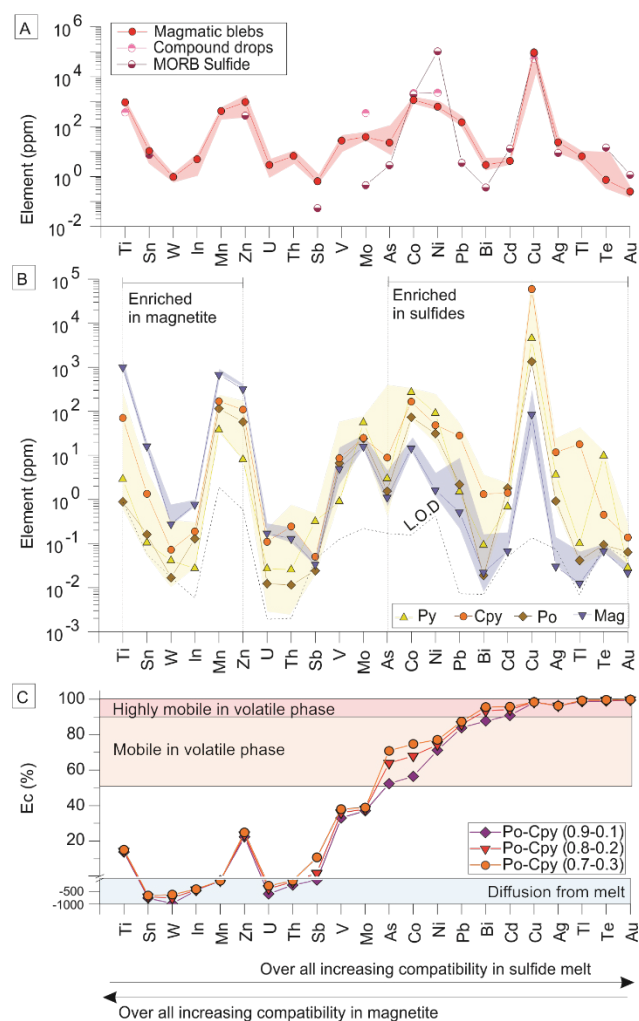


Figure 2. Trace metal content in sulfides and magnetite related to compound drops and magmatic volatile-sulfide emission coefficients. A) Median metal concentrations in magmatic sulfide bleb. Shaded area corresponds to the upper and lower quartiles. B) Median metal concentrations in pyrrhotite (Po), pyrite (Py), partly replaced chalcopyrite (Cpy) and magnetite (Mag) of ovoids. The yellow and blues shaded areas correspond to the upper and lower quartiles of all sulfides and magnetite, respectively. L.O.D. = limit of detection. C) Calculated magmatic volatile-sulfide emission coefficients with various fractions pyrrhotite and chalcopyrite. Negative values are due to element diffusion from the melt to the magnetite during oxidation as the compound drops are not closed systems.

to have occurred during magma mixing. Repeated injections of volatile-rich mafic (andesitic/basaltic) melts at Nea Kameni and Kolumbo result in their accumulation at the bottom of the magmatic chambers without extensive mixing with the felsic/intermediate melts. Continuous volatile exsolution from the mafic melts can lead to the formation of an intermediate hybrid layer between the mafic and felsic melts (Plail et al. 2018) as revealed by μ XRF mineral mapping (Fig. 1b) where the interface between the enclave and host rock is not sharp but rather diffuse. The interface between an underplating mafic melt and an overlying felsic melt is often a place where volatile bubbles, which have exsolved from the mafic melt, accumulate (Plail et al. 2018). Hence, it is inferred that compound

drops formed within the mafic melt rise toward the interface with the felsic melt where they stagnate and accumulate due to differences in physico-chemical conditions. During migration, stagnation and accumulation, the compound drops then coalesce (Iacono-Marziano et al. 2022) resulting in the formation of the larger sulfide ovoids.

During compound drops coalescence into sulfide ovoids, the temperature difference between the basaltic/andesitic and dacitic/rhyolitic melts (~1000–1200 °C and 750–900 °C, respectively) allows the sulfide liquid to crystallize as monosulfide solution (MSS, ~1050–1100 °C) and intermediate solid solution (ISS, ~850 °C) accounting for the differentiated pyrrhotite and chalcopyrite texture preserved in partly oxidized sulfide ovoids (Fig. 1). Sulfide differentiation is shortly followed by oxidation of the sulfides by the magmatic volatiles leading to progressive replacement of the MSS and ISS into pyrite and covellite and ultimately into magnetite.

The variably oxidized ovoids are either embayed into, partially associated with vesicles, or disconnected from vesicles (Fig. 1). This diversity of sulfide/oxide ovoid-vesicle textures suggests that the coalesced compound drop might eventually become unstable. The magmatic volatile phase, once disconnected with the oxide/sulfide phase will rise within the magmatic chambers as plume, through volatile pathways or from cracks in the magma crystal framework directly feeding shallower hydrothermal systems which can be involved ore deposit formation.

5 Element mobility during compound drop oxidation

Sulfide oxidation by magmatic fluids has been recognized as a key process for mobilizing S and metals to the shallow parts of arc magmatic-hydrothermal systems (Edmonds et al. 2018). The efficiency, however, for metal transfer from the sulfide to the magmatic volatiles remains unknown. Metal concentrations of the sulfide ovoids and associated magnetite are used as proxies for calculating emanation coefficients (Edmonds et al. 2018) defined as:

$$Ec_i = \left(\frac{C_{i\text{ sulf}}}{d_{i\text{ sulf}}} - \frac{C_{i\text{ mag}}}{d_{i\text{ mag}}} \right) / \left(\frac{C_{i\text{ sulf}}}{d_{i\text{ sulf}}} \right) * 100$$

with $C_{i\text{ sulf}}$ and $C_{i\text{ mag}}$ the concentration of a given element in the sulfide phases and in the magnetite, respectively and $d_{i\text{ sulf}}$ and $d_{i\text{ mag}}$ the density of the sulfide phases and magnetite respectively. During oxidation Ti, Sn, W, In, Mn, Zn, U and Th are incompatible and remain in the magnetite while Te, As, Au, Co, Ni, Pb, Bi, Cd, Ag, Cu and Tl are efficiently transferred into the magmatic volatiles (Fig. 2).

6 Conclusion

Study of the sulfide population at the Kameni and Kolumbo volcanoes reveal that sulfide-volatile

compound drops can form and evolve during the complex magmatic evolution of arc systems. Magma mingling between a mafic sulfide and volatile saturated melt with a felsic melt can lead to compound drops accumulation and coalescence at the melts' interface. The sulfide melt is eventually differentiated and then oxidize to magnetite due to the interaction with the volatile phase. During oxidation, trace elements present within the sulfide phases are variably released into the volatile phase with Bi, Cd, Cu, Ag, Tl, Te and Au being highly mobile. The volatile phase is eventually separated from the sulfide/oxide phases and is transported to the shallower part of the magmatic-hydrothermal system, possibly feeding magmatic-hydrothermal ore deposits.

References

- Edmonds M, Mather TA, Liu EJ (2018) A distinct metal fingerprint in arc volcanic emissions. *Nat Geosci* 11:790–794 . doi: <https://doi.org/10.1038/s41561-018-0214-5>
- Iacono-Marziano G, Le Vaillant M, Godel BM, et al (2022) The critical role of magma degassing in sulphide melt mobility and metal enrichment. *Nat Commun* 13:1–10 . doi: <https://doi.org/10.1038/s41467-022-30107-y>
- Le Vaillant M, Barnes SJ, Mungall JE, Mungall EL (2017) Role of degassing of the Noril'sk nickel deposits in the Permian–Triassic mass extinction event. *Proc Natl Acad Sci* 114:2485–2490 . doi: <https://doi.org/10.1073/pnas.1611086114>
- Michaud V, Clocchiatti R, Sbrana S (2000) The Minoan and post-Minoan eruptions, Santorini (Greece), in the light of melt inclusions: chlorine and sulphur behaviour. *J Volcanol Geotherm Res* 99:195–214
- Mungall JE, Brenan JM, Godel B, et al (2015) Transport of metals and sulphur in magmas by flotation of sulphide melt on vapour bubbles. *Nat Geosci* 8:216–219 . doi: [10.1038/ngeo2373](https://doi.org/10.1038/ngeo2373)
- Nadeau O, Williams-Jones AE, Stix J (2010) Sulphide magma as a source of metals in arc-related magmatic hydrothermal ore fluids. *Nat Geosci* 3:501–505 . doi: <https://doi.org/10.1038/ngeo899>
- Nomikou P, Hübscher C, Carey S (2019) The Christiana–Santorini–Kolumbo Volcanic Field. *Elem An Int Mag Mineral Geochemistry, Petrol* 15:171–176 . doi: <https://doi.org/10.2138/gselements.15.3.171>
- Patten CGC, Barnes S-J, Mathez EA, Jenner FE (2013) Partition coefficients of chalcophile elements between sulfide and silicate melts and the early crystallization history of sulfide liquid: LA-ICP-MS analysis of MORB sulfide droplets. *Chem Geol* 358: . doi: [10.1016/j.chemgeo.2013.08.040](https://doi.org/10.1016/j.chemgeo.2013.08.040)
- Plail M, Edmonds M, Woods AW, et al (2018) Mafic enclaves record syn-eruptive basalt intrusion and mixing. *Earth Planet Sci Lett* 484:30–40 . doi: <https://doi.org/10.1016/j.epsl.2017.11.033>
- Richards JP (2011) Magmatic to hydrothermal metal fluxes in convergent and collided margins. *Ore Geol Rev* 40:1–26 . doi: <https://doi.org/10.1016/j.oregeorev.2011.05.006>
- Rizzo AL, Barberi F, Carapezza ML, et al (2015) New mafic magma refilling a quiescent volcano: Evidence from He–Ne–Ar isotopes during the 2011–2012 unrest at Santorini, Greece. *Geochemistry, Geophys Geosystems* 16:798–814
- Wallace PJ, Edmonds M (2011) The Sulfur Budget in Magmas: Evidence from Melt Inclusions, Submarine Glasses, and Volcanic Gas Emissions. *Rev Mineral Geochemistry* 73:215–246 . doi: [10.2138/rmg.2011.73.8](https://doi.org/10.2138/rmg.2011.73.8)
- Meinert LD, Dipple GM, Nicolescu S (2005) World skarn deposits. *Econ Geol* 100th Anni:299–336.

Fluid inclusion study in quartz of the Rudnik Pb-Zn-Cu-Ag skarn deposit, Serbia

Stefan Petrović¹, Ronald J. Bakker², Vladica Cvetković¹, Rade Jelenković¹

¹University of Belgrade, Faculty of Mining and Geology, Serbia

²Montanuniversität Leoben, Department of Applied Geosciences and Geophysics, Austria

Abstract. Six types of fluid inclusions were identified in three growth zones of hydrothermal quartz from the Rudnik skarn deposit. In the core zone, primary two-phase fluid inclusions of high (type 1) and moderate salinity (type 2) homogenized to liquid between 350–430 °C and 340–420 °C, respectively. Raman analysis revealed that the vapour phases are a CO₂-CH₄ gas mixture, with a predominance of CO₂. The core contains and dispersed vapour-rich fluid inclusions of low salinity (type 3) composed of CO₂-CH₄-H₂S gas mixture with significant amounts of H₂S, as well as liquid-rich fluid inclusions (type 4) predominantly composed of pure water and small vapour phase with lower homogenization temperatures between 174–284 °C. In the transition zone, primary fluid inclusions arranged perpendicular to the growth zone (type 5) homogenize over a wide range of temperatures between 235–401 °C. The vapour phase is a CO₂-CH₄ gas mixture additionally enriched in CH₄ compared to the other types. Fluid inclusions in paths of the rim zone of the quartz (type 6) have a homogenization temperature between 259–385 °C. The vapour phase is a CO₂-CH₄ mixture with reduced CH₄ content, while the liquid phase has a low salinity.

1 Introduction

The Rudnik deposit is located in central Serbia and present one of the most significant polymetallic skarn deposits in the Serbo-Macedonian metallogenic province (Figure 1). Over 13 Mt of polymetallic ore (Pb-Zn-Cu-Ag) was found in the Rudnik deposit so far. Ore bodies are hosted in the complex of contact-metasomatically altered areas of the Upper Cretaceous flysch units (Djoković 2013) (Figure 2). Genesis of the ore deposit is temporally associated with the formation of the Oligocene-Miocene volcanic-intrusive complex and results of subsequent hydrothermal activities (Cvetković et al. 2016).

Quartz is commonly associated with the ore mineralization in the deposit. According to field and petrographic observations, we can distinguish two generations of quartz. The first, syn-ore generation of quartz is characterised by well-developed prismatic crystals intergrowth with ore minerals. This generation of quartz commonly has well-developed oscillatory growth zoning. The second generation is primarily represented by anhedral or, less extent, small idiomorphic quartz crystals which are coevally with calcite filling the voids between ore mineralization.

Until now, there are only preliminary studies on the presence of fluid inclusions (Blečić 1974). The primary task of the study is to determine the characteristics of fluid inclusions hosted in syn-ore quartz and to provide a contribution to define the

multiple events in the magmatic-hydrothermal system that led to the formation of the deposit.

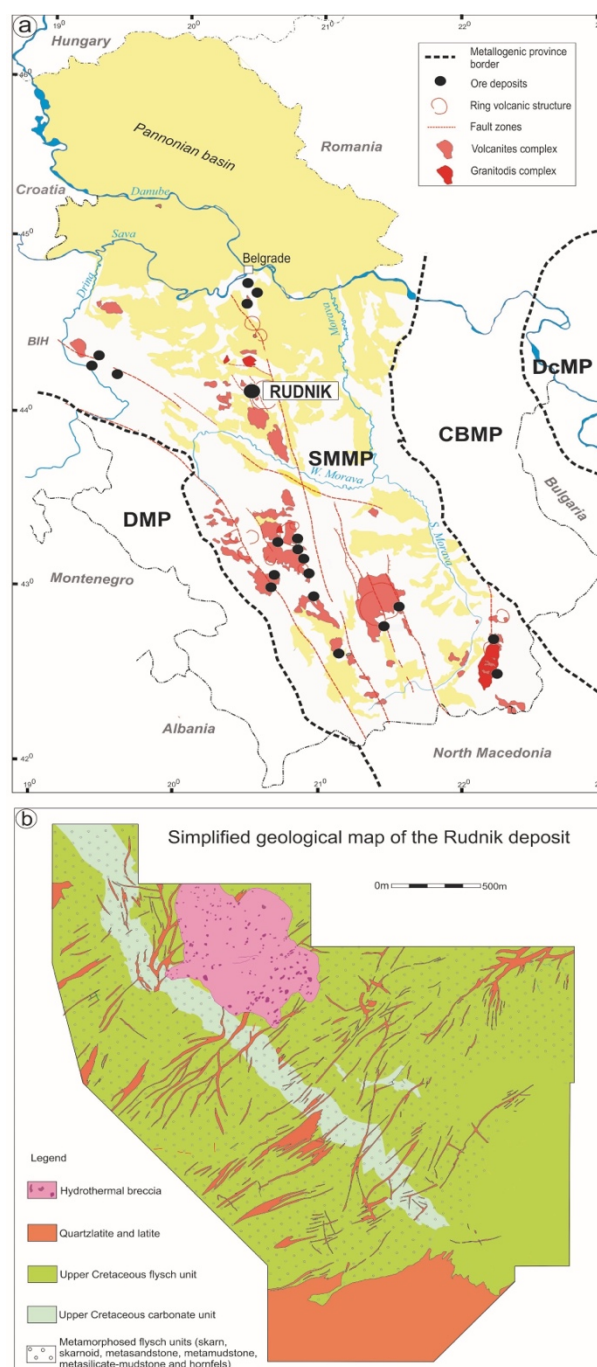


Figure 1. **a** Location of the Rudnik ore deposit in Serbo-Macedonian metallogenic province (adapted from Jelenkovic et al. 2008). **b** Simplified geological map of the Rudnik deposit (adapted from Djoković 2013)).

2 Methodology

Preparation of thick section was performed at the University of Belgrade, Faculty of Mining and Geology at the Department of Mineralogy, Crystallography, Petrology and Geochemistry and at the Department of Economic Geology. Fluid inclusions were studied from doubly polished thick sections of thickness ~150 µm.

Microthermometry of fluid inclusions was conducted at the Department of Applied Geosciences and Geophysics, chair of Resource Mineralogy at the University of Leoben in Austria and Fluid inclusion Laboratory at the Faculty of Mining and Geology at the University of Belgrade.

Microthermometry was carried out using a Linkam MDS 600 stage mounted on an Olympus BX 60 optical microscope in Leoben. Calibration of the Linkam stage was performed using synthetic fluid inclusion standards (pure H₂O, CO₂-H₂O mixtures) for the melting temperatures of CO₂ at -56.6 °C, of H₂O at 0.0 °C and the critical homogenisation temperature of H₂O at 374.0 °C. Microthermometry measurements at the Faculty of Mining and Geology in Belgrade were carried out on a THMSG600 heating stage connected to an Olympus BX51 microscope. The primary CO₂ standard WRECT-006160 was used for calibration. The reproducibility is ±0.1 °C between -60 °C and +100 °C and ±0.3 °C at higher temperatures.

Calculations of microthermometric parameters were performed using AqSo_NaCl software (Bakker 2018).

Raman spectroscopy was performed with a LabRAM (Department of Applied Geosciences and Geophysics, chair of Resource Mineralogy, Leoben) instrument, from the company Horiba Scientific, Jobin Yvon Technology. The LabRAM is operated with an Olympus microscope, and an LMPlanFI 100x/0.80 numerical aperture objective lens. A frequency-doubled 100 mW Nd-YAG laser with an excitation wavelength of 532.068 nm is used, with a laser power of about 1 to 2 mW at the sample surface. The scattered light is dispersed by 1800 grooves/mm gratings. The detector is an air-cooled (Peltier) CCD-3000 (1024 x 256 pixels) operating at -60 °C. Spectra are collected using multiple spectral windows between 100 to 3000 cm⁻¹, corresponding to a pixel resolution of about 1.64 cm⁻¹ at relative low wave numbers, and 1.35 cm⁻¹ at relative high wave numbers. A 100 µm slit combined with a 1000 µm confocal hole aperture is used to obtain the best resolved spectra.

3 Petrography

Colourless and transparent syn-ore quartz, in the form of idiomorphic crystals, has three visible crystal growth zones with fluid inclusions (Figure 2).

The core zone contains four types of fluid inclusions: 1) semi-irregular shaped fluid inclusions, up to 25 µm that occur in small groups. The volume fraction of the vapour phase varies between 20-30 vol. %.

2) fluid inclusions in trails that reflected partly healed cracks and internal growth zones. They have a regular locally negative-crystal shape, usually sizes up to 20 µm, and the volume fraction of the vapour phase varies between 50-60 vol. %. 3) regular, locally negative crystal shaped fluid inclusions, length up to 10 µm and extremely rich in vapour phase 90 vol. %. 4) elongated irregular shaped fluid inclusions liquid-rich to all-liquid, up to 40 µm in length, in trails (healed cracks) in the core.

The transition zone contains abundant fluid inclusions of irregular shape that are mainly elongated in an orientation perpendicular to growth-zone traces. These fluid inclusions have a length of 50-300 µm and the volume fraction of the vapour phase varies between 10-20 vol. %.

The rim contains traces of growth zones with fluid inclusions of regular shape, with an average length of 30 µm, and volume of the vapour phase varies between 20-30 vol. %.

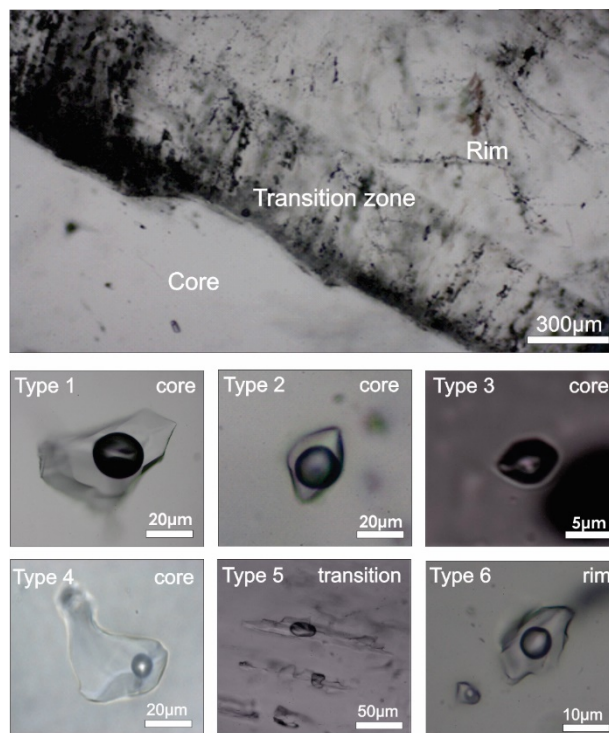


Figure 2. Photomicrograph of a piece of a quartz crystal with three visible growth zones and fluid inclusions. Below are the photomicrographs of single fluid inclusion types.

4 Raman spectroscopy

In the core, type 1 inclusions are characterised by a relatively high salinity of the liquid phase. The vapour phase is a gas mixture of CO₂-CH₄, with a predominance of CO₂. The relative low intensity of the CO₂ and CH₄ Raman spectra implies a low density of the vapour phase and high salinity.

Type 2 inclusions have an H₂O spectrum which corresponds to a moderate salinity, and the vapour phase is slightly enriched in CH₄ compared to type 1, but remains a CO₂-rich gas mixture. Some inclusions reveal minor amounts of additional H₂S.

Type 1 and 2 contain occasionally solid phases, i.e., accidentally trapped small crystals of calcite and mica.

Type 3 inclusions have a vapour phase consisting of a CO₂-CH₄-H₂S gas mixture that is enriched in CH₄ and with significant amounts of H₂S. The H₂O spectrum of the liquid phase reveals a relatively high shoulder at about 3200 cm⁻¹, which corresponds to low salinity.

Raman spectra of Type 4, liquid-rich to all-liquid fluid inclusions, reveal nearly pure CO₂ vapour and a H₂O liquid phase.

In the transitional zone, type 5 inclusions have a vapour phase that is relatively enriched in CH₄ in a mixture with CO₂. The Raman band of the liquid phase corresponds to a low salinity aqueous solution, similar to type 3.

Fluid inclusions in the rim zone, type 6, have a CO₂-enriched vapour phase with minor CH₄. The Raman spectrum of the liquid phase resembles a low salinity aqueous solution.

5 Microthermometry

Type 1 inclusions have a temperature of homogenization in the range of 350-430 °C with a mode at 380-390 °C. Ice melting temperatures are from -6 to -23 °C, corresponding to a calculated salinity between 9 and 24 wt.% NaCl eq., with a mode in the 12 to 16 wt.% NaCl eq..

Type 2 inclusions have relatively similar homogenization temperatures that range between 340 and 420 °C as type 1 inclusions and a slightly lower mode at 370-380 °C. Ice melting temperatures are in the range of -2 to -9 °C while salinity is from 4 to 12 wt.% NaCl eq. with a mode at 6-7 wt.% NaCl eq..

The low density of the vapour phase in type 3 does not allow any microthermometric analyses, i.e. homogenization or melting of CO₂ is not observed. Locally, the final ice melting temperature of the frozen aqueous phase occurs at temperatures of -1.0 to -4.0 °C, corresponding to a salinity of 1 to 6 wt.% NaCl eq..

Homogenization temperatures of type 4 inclusions are significantly lower than the previous types and are in the range of 148 to 245 °C. Ice melting temperatures occur from -0.7 to -4.9 °C while the salinity of this type varies between 1 and 8 wt.% NaCl eq..

Inclusion in the transition zone homogenize at a mode of 360 to 380 °C similar to type 2, but a wider range of 235-401 °C has been measured. Dissolution of ice occurs between -1 and -6 °C corresponding to a salinity of 2 to 8 wt.% NaCl eq.. Inclusions in the rim of quartz have homogenization temperatures between 259 and 385 °C with a mode at 340-360 °C. These temperatures are significantly lower than type 5 and higher than type 4. The melting

temperature of ice ranges from -2 to -3 °C, which corresponds to a low salinity of 2 to 5 wt.% NaCl eq..

6 Conclusion

The different fluid inclusions from the quartz growth zones reveal that deposition of the ore mineralization was the result of a multiphase evolution of the hydrothermal ore-forming fluid, similar to skarn deposits worldwide (Kwak, 1986; Meinert et al., 2003).

These events are preserved in distinguished types of fluid inclusions and reflected through their varying temperature of homogenization, salinity, and fluid composition.

The study shows that the examination of fluid inclusions from quartz can considerably contribute to tracing the evolution of hydrothermal ore-bearing fluid, which is associated with the genesis of the Rudnik skarn deposit.

Acknowledgements

Gratitude to Company Rudnik and flotation Rudnik for the sampling permit and helpful internal documentation material for the study.

The study was carried out within the Central European Exchange Program for University Studies-CEEPUS (Network: RS-0038-17-2122).

References

- Bakker RJ (2018) AqSo_NaCl: Computer program to calculate pTVx properties in the H₂O-NaCl fluid system applied to fluid inclusion research and pore fluid calculation. *Computers & geosciences*, 115, 122-133. <https://doi.org/10.1016/j.cageo.2018.03.003>
- Blečić N (1974) Tečno-gasne inkluzije i njihova primena pri istraživanju pojedinih jugoslovenskih ležišta mineralnih sirovina [Fluid inclusions and their application in the exploration of certain Yugoslav deposits of mineral raw materials. Master's thesis-in Serbian] Faculty of Mining and Geology, Belgrade.
- Cvetković V, Šarić K, Pécskay Z, & Gerdes A (2016) The Rudnik Mts. volcano-intrusive complex (central Serbia): An example of how magmatism controls metallogeny. *Geologia Croatica*, v. 69 (1), p. 89-99. <https://doi.org/10.4154/GC.2016.08>
- Djoković I (2013) Izveštaj o strukturno-geološkim karakteristikama ležišta Rudnik. [Report of structural and geological features of the Rudnik deposit-in Serbian]. Fund of internal documents of the Rudnik mine company, Rudnik.
- Jelenković R, Kostić A, Životić D, & Ercegovac M (2008) Mineral resources of Serbia. *Geologica carpathica*, 59(4), 345-361.
- Kwak TAP (1986) Fluid inclusions in skarns (carbonate replacement deposits). *Journal of Metamorphic Geology*, 4(4), 363-384.
- Meinert LD, Dipple GM, Nicolescu S (2005) World skarn deposits. *Econ Geol* 100th Anni:299-336.

El Chichón volcano, Mexico: A window into an active Porphyry-Cu-Mo-Au system.

María F. Reyes Gonzalez¹, Julie Roberge¹, Celestine N. Mercer², Angelica Adriana Camacho Pérez¹, Gerardo Arrieta Garcia³, Sujitha Suresh Babu¹, Pablo E. Carbajal Martínez¹

¹Posgrado ESIA Ticomán, Instituto Politécnico Nacional, CDMX, Mexico

²U.S. Geological Survey, Geology, Geophysics and Geochemistry Science Center, Denver, CO.

³Laboratorio Universitario de Geoquímica Isotópica (LUGIS), Instituto de Geofísica, Universidad Nacional Autónoma de México (UNAM), CDMX, Mexico

Abstract. The 1982 eruption of El Chichón volcano, Mexico, left an acid crater lake with energetic fumaroles and thermal spring activity. El Chichón displays mineralogical and geochemical characteristics that are unique with respect to typical arc volcanoes and other volcanic centers within the Chiapas belt, including mineralized lithic fragments. Several decade-old published research studies have alluded to the possible connection between El Chichón magmatism and porphyry Cu mineralization. We aim to summarize these observations, and along with new hornblende mineral thermobarometry demonstrate that they complement current models for the genesis of fertile parental magmas and the development of Porphyry Cu-Mo-Au Systems. We suggest that while the 1982 plinian eruption revealed the epithermal portion of the magmatic-hydrothermal system, the altered lithic fragments found in pyroclastic deposits likely represent a mineralized zone from an actively developing porphyry deposit at depth.

1 Introduction

The powerful 1982 eruption of El Chichón volcano in Mexico is recognized as the largest disaster in modern Mexican history, destroying villages and killing over 2,000 people analogous to Pompeii. The El Chichón plinian eruption of high-sulfur, anhydrite-bearing magma destroyed the summit lava dome exposing the shallow epithermal portion of an actively mineralizing magmatic-hydrothermal system. Although deposits in the Chiapas region may never see development due to its status as a Natural Reserve, El Chichón offers a spectacular natural laboratory to investigate active geologic processes important to the development of mineralization in Porphyry-Cu-Mo-Cu Systems.

2 Complex tectonic setting

El Chichón is an active stratovolcano located in the state of Chiapas, southeast of Mexico City. It is the only active volcano in the Chiapanecan Volcanic Arc (CVC), which is a short arc segment that extends along the state of Chiapas in a NW-SE direction (Damon and Montesinos 1978).

The tectonic setting at El Chichón is complex. It is located near the intersection of three plates: the Cocos, American, and Caribbean plates. To the SW, the Cocos plate subducts beneath the North American plate, while to the SE the North American plate borders the Caribbean plate by the Motagua-Polochic fault (Fig. 1). Seismicity is intense along the offshore trench and is deep-seated beneath Chiapas

inland (Damon and Montesinos 1978). The Chiapanecan Volcanic Arc aligned with the NE trending Tehuantepec fracture zone (Fig. 1), which has been interpreted as a torn segment of the Cocos plate that facilitates the ascent of hot asthenospheric mantle in the region (de Ignacio et al. 2003). The Tehuantepec fracture zone is associated with a drastic change in subduction angle of the Cocos plate, transitioning from 10° west of the ridge to 30° east of the ridge. This complex geometry may prime the Chiapas region for high heat flow, high influx of S-rich magma, and high permeability to magmas and hydrothermal fluids.

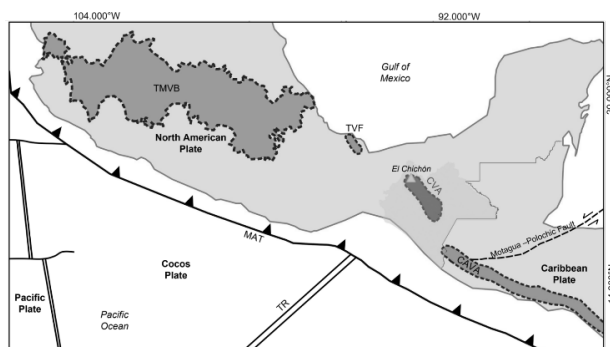


Figure 1. Location of the El Chichón volcano within the tectonic framework of Mexico (CVA=Chiapanecan Volcanic Arc; MAT= Middle America Trench; TR=Tehuantepec Ridge; TMVB=Trans-Mexican Volcanic Belt; TVF=Tuxtla Volcanic Field; CAVA=Central America Volcanic Arc).

3 El Chichón eruptive and petrogenetic history

The El Chichón volcanic complex has had eleven eruptive events in the last 8,000 years (Espíndola et al. 2000), but the construction of the actual edifice probably started during the Middle Pleistocene (Layer et al. 2009). Cathedral volcano, 4 km NW of the present edifice (Fig. 2), is the remnant of the oldest volcanic activity in the area (~1.64 Ma; Macias et al. 2010). The most recent eruptive event occurred between March 28 and April 4, 1982. The eruption began with the destruction of the previous dome, built after the 550 B.P. eruption, and gave rise to a crater lake that currently has numerous active fumaroles and thermal springs (Fig. 3).

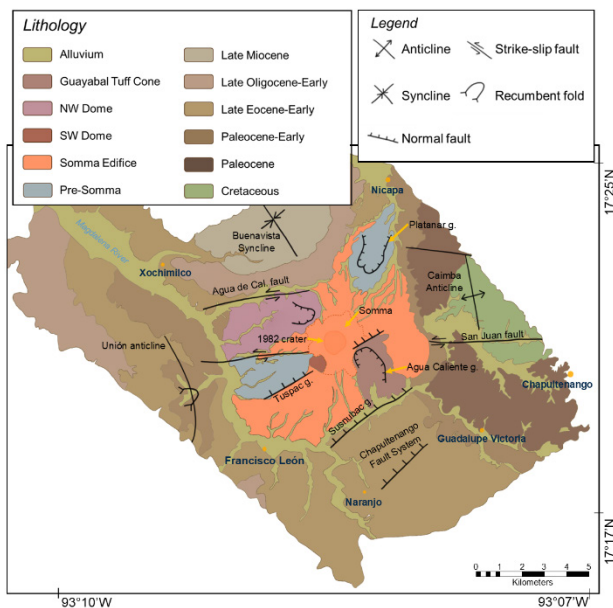


Figure 2. Geological map of El Chichón volcanic complex from Layer et al. (2009).

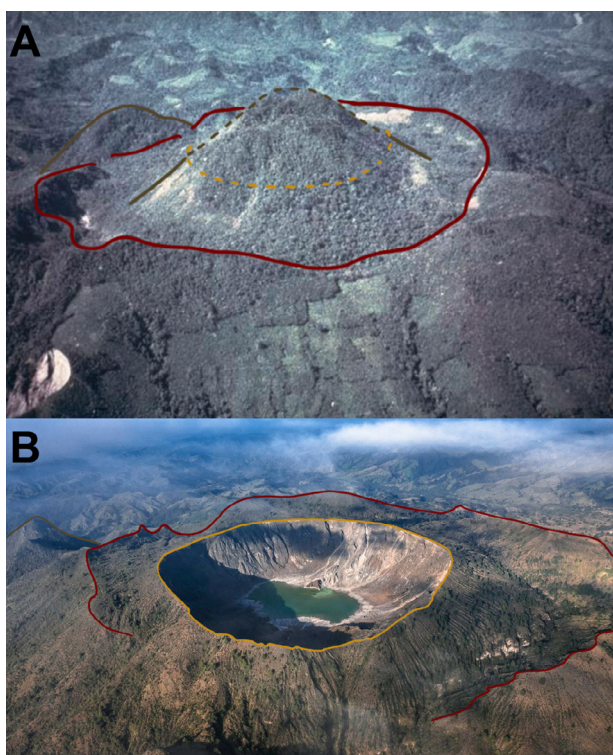


Figure 3. Photograph of El Chichón volcano before (A) and after (B) the 1982 eruption. The red outline represent the Somma Crater produced 279-209 ka while the yellow outline is the crater formed by the 1982 eruption.

More than 7 million tons of SO_2 was released into the atmosphere during the eruption and 9 surrounding towns were devastated, punctuated by the death of nearly 2,000 people (Sigurdsson et al. 1984).

Whole rock geochemical analysis of El Chichón eruptive products show a transitional calc-alkaline to adakite composition. Trachybasalt enclaves have been identified and there is a clear cogenetic relationship between all of the El Chichón eruptive products (Fig. 4).

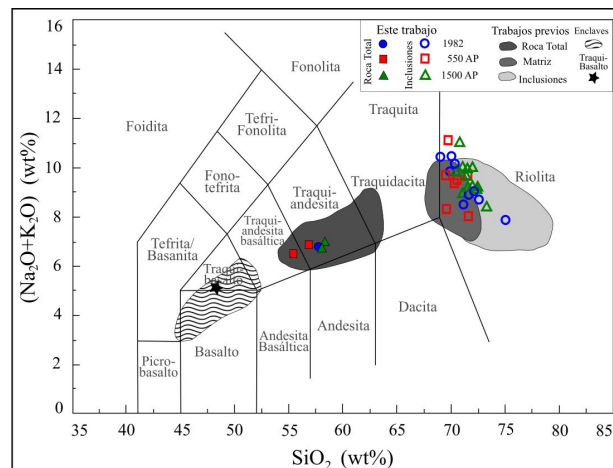


Figure 4. Total alkali versus silica diagram (LeBas et al. 1986) for El Chichón product. Colored symbols are from this work and shaded areas are from Luhr et al. (1984), Rose et al. (1984), Varekamp et al. (1984), Espindola et al. (2000) and García-Palomo et al. (2004).

4 Late Neogene and Quaternary metallogenesis in the Chiapanecan Volcanic Arc

Mineralization identified in the Chiapas region is part of a larger Au-Ag belt (Fig. 5). It includes several Miocene deposits that have been proposed as IOCG-clan deposits (Cerro Colorado, 18 Ma; El Carmen, 13-12 Ma; Cerro Colorado - Cerro Bustillo, <12.7 Ma) and the Toliman porphyry Cu deposit (5.75Ma; Camprubi 2009, and references therein). The most recent mineral deposits in the region include the porphyry Au-Ag, Cu-Au-Mo, and low sulfidation Au epithermal deposits of Ixhuatan (2.8 Ma) and the "Santa Fe" Cu-Au skarn deposit (2.29-2.24 Ma).



Figure 5. Distribution of mineral deposit belts throughout Mexico (map credit: Mexican Geological Survey).

Several observations indicate that active porphyry deposit mineralization is likely occurring within El Chichón. El Chichón eruptive products display mineralogical and geochemical characteristics that are unique with respect to typical arc volcanoes and other volcanic centers within the Chiapas belt. Pervasive magmatic anhydrite and titanite indicate a notably oxidized ($>\text{NNO}+0.5$) and sulfur-rich system. Our recent hornblende analyses

demonstrate magmas to be water rich (4-7 wt% H₂O) and evolving at great depths (200-700 MPa; 8-20 km depth) and at high temperatures (900-1000°C; Fig. 6). These data are in agreement with the CO₂ and He³/He⁴ data from El Chichón fumaroles that also suggest a greater depth of magma generation than is typical for arc volcanoes (Mazot et al. 2011).

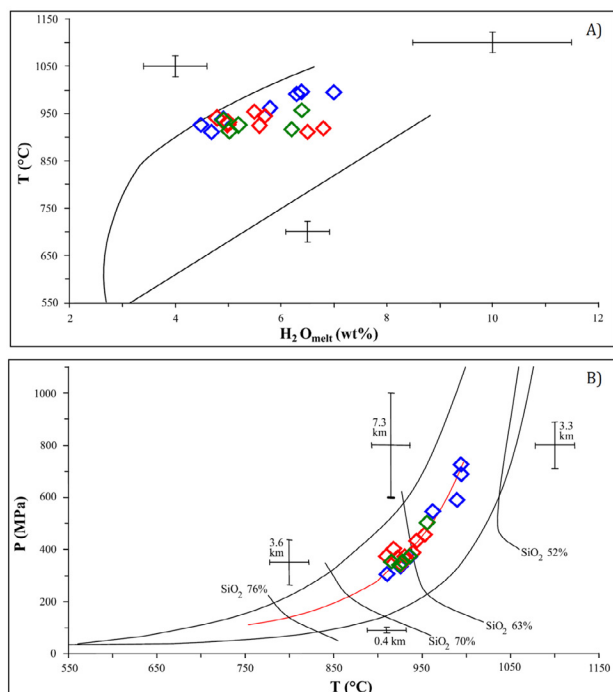


Figure 6. Application of the Ridolfi et al. (2010) geo-barohydrometer with newly acquired hornblende compositions.

Additionally, magmas are characterized by high Sr/Y values (~45; de Ignacio et al. 2003) coupled with moderate to low Y (<25 ppm). While this has been interpreted as adakite generation by direct melting of the subducting oceanic plate (Yogodzinski et al. 2001), an alternative or additional interpretation is that these “adakite-like” magmas have undergone deep-crustal evolution conducive to high magma fertility with respect to porphyry Cu-Mo-Au systems (e.g., Richards 2011). Given the unique tectonic setting and evidence for high water and sulfur contents, both of these processes could be at play. Modeling by Chiaradia and Carrichi (2017) also suggest that deep crustal magma processing >500 MPa may be key in generating fertile magmas with potential to produce economic ore deposits.

Magmatism at El Chichón has been relatively long-lived (1.6 Ma), which has also been shown to promote the development of large mineralized porphyry Cu-Mo-Au systems (Chiaradia et al. 2022). Analysis of ⁸⁷Sr/⁸⁶Sr isotopic zoning profiles in plagioclase by Tepley et al. (2000) demonstrated that the El Chichón system was repeatedly recharged by high temperature mafic magma, consistent with observations of mafic enclaves. This process is also conducive to keeping the magmatic system mobile and long-lived.

Finally, Luhr (2009) and Damon and Montesinos (1978) noted mineralized lithic fragments collected from pyroclastic deposits that appear to contain alteration indicative of deeper porphyry-style mineralization. These fragments contain host rock similar to the 1982 dome rock, but overprinted with mineralization including potassic alteration with abundant Mg-rich biotite with veinlets of anhydrite, reminiscent of early potassic, high temperature porphyry-style alteration (Reed 2013).

We suggest that while the 1982 plinian eruption revealed the epithermal portion of the magmatic-hydrothermal system, the altered lithic fragments likely represent a mineralized zone from an actively developing porphyry deposit at depth (Fig. 7; Sillitoe 2010; John et al. 2010; Hofstra et al. 2021).

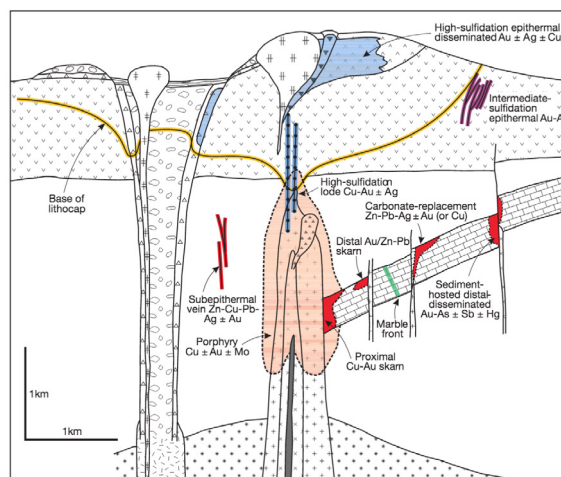


Figure 7. Anatomy of a Porphyry Cu-Mo-Au System showing the variety of ore deposit types that may develop within the system (Sillitoe 2010).

Acknowledgements

This project is funded by the individual project SIP-IPN (Secretaria de Investigación y Posgrado – Instituto Politécnico Nacional) no. 20221913. We thank Frank Tepley and Carlos Linares Lopez for their help with microprobes analysis. We also thank Alain Miron Velazquez, Nayeli Martinez Torres, Jorge Ivan Zuñiga Bautista and Jesús Guadarrama Garrido for field assistance.

References

- Camprubí, A. (2009). Major metallogenic provinces and epochs of Mexico: SGA News, 25, 1-21.
- Chiaradia, M. & Caricchi, L. (2022). Supergiant porphyry copper deposits are failed larged eruptions. *Commun Earth Environ* 3, 107. <https://doi.org/10.1038/s43247-022-00440-7>
- Damon, P., & Montesinos, E. (1978). Late Cenozoic volcanism and metallogenesis over an active Benioff zone in Chiapas, Mexico. *AGS-Dig.*, 11, 155-168.
- De Ignacio, C., Castañeiras, P., Márquez, Á., Oyarzun, R., Lillo, J., & López, I. (2003). El Chichon volcano (Chiapas volcanic belt, Mexico) transitional calc-alkaline to adakitic-like magmatism: petrologic and tectonic implications. *Int. Geol. Rev.*, 45(11), 1020-1028. <https://doi.org/10.2747/0020-6814.45.11.1020>
- Espíndola, J.M., Macías, J.L., Tilling, R.I., Sheridan, M.F. (2000). Volcanic history of El Chichón Volcano (Chiapas,

- Mexico) during the Holocene, and its impact on human activity. *Bull. Volcanol.* 62, 90–104. <https://doi.org/10.1007/s004459900064>
- García-Palomo, A. G., Macías, J. L., & Espíndola, J. M. (2004). Strike-slip faults and K-alkaline volcanism at El Chichón volcano, southeastern Mexico. *J. Volcanol. and Geotherm. Res.*, 136(3-4), 247–268. <https://doi.org/10.1016/j.jvolgeores.2004.04.001>
- Hofstra, A., Lisitsin, V., Corriveau, L., Paradis, S., Peter, J., Lauzière, K., Lawley, C., Gadd, M., Pilote, J., Honsberger, I., Bastrakov, E., Champion, D., Czarnota, K., Doublier, M., Huston, D., Raymond, O., VanDerWielen, S., Emsbo, P., Granitto, M., and Kreiner, D. (2021). Deposit classification scheme for the Critical Minerals Mapping Initiative Global Geochemical Database: U.S. Geological Survey Open-File Report 2021–1049, 60 p., <https://doi.org/10.3133/ofr20211049>.
- John, D.A., Ayuso, R.A., Barton, M.D., Blakely, R.J., Bodnar, R.J., Dilles, J.H., Gray, Floyd, Graybeal, F.T., Mars, J.C., McPhee, D.K., Seal, R.R., Taylor, R.D., and Vikre, P.G., (2010). Porphyry copper deposit model, chap. B of Mineral deposit models for resource assessment: U.S.G.S Sci. Investig. Rep. 5070–B, 169 p.
- Layer, P. W., García-Palomo, A., Jones, D., Macías, J. L., Arce, J. L., & Mora, J. C. (2009). El Chichón volcanic complex, Chiapas, México: Stages of evolution based on field mapping and $^{40}\text{Ar}/^{39}\text{Ar}$ geochronology. *Geophys. Int.*, 48(1), 33–54. <https://doi.org/10.22201/igeof.00167169p.2009.48.1.98>
- Luhr, J. F. (2008). Primary igneous anhydrite: Progress since its recognition in the 1982 El Chichón trachyandesite. *J. of Volcanol. and Geotherm. Res.*, 175(4), 394–407. <https://doi.org/10.1016/j.jvolgeores.2008.02.016>
- Macías JL, Arce JL, Garduño-Monroy VH, Rouwet D, Taran Y, Layer P, Jiménez A, Álvarez R (2010): Estudio de prospección geotérmica para evaluar el potencial del volcán Chichonal, Chiapas. Unpublished Report no. 9400047770 IGF-UNAM-CFE
- Mazot, A., Rouwet, D., Taran, Y., Inguaggiato, S. & Varley, N. (2011). CO₂ and He degassing at El Chichón volcano, Chiapas, Mexico: gas flux, origin and relationship with local and regional tectonics. *B Volcanol* 73, 423–441. <https://doi.org/10.1007/s00445-010-0443-y>
- Reed, M., Rusk, B. & Palandri, J. (2013). The Butte Magmatic-Hydrothermal System: One Fluid Yields All Alteration and Veins. *Econ Geol* 108, 1379–1396
- Richards, J. P. (2011). High Sr/Y arc magmas and porphyry Cu ± Mo ± Au deposits: just add water. *Econ Geol* 106, 1075–1081. <https://doi.org/10.2113/econgeo.106.7.1075>
- Sigurdsson, H., Carey, S. N., Espíndola J. M. (1984). The 1982 eruptions of El Chichón Volcano, Mexico (2): stratigraphy of pyroclastic deposits. *J Volcanol. Geotherm. Res.* 23. 11–37. [https://doi.org/10.1016/0377-0273\(84\)90055-6](https://doi.org/10.1016/0377-0273(84)90055-6)
- Sillitoe, R. H. (2010). Porphyry copper systems. *Econ. Geol.* 105(1), 3–41. <https://doi.org/10.2113/gsecongeo.105.1.3>
- Tepley III, F. J., Davidson, J. P., Tilling, R. I., & Arth, J. G. (2000). Magma mixing, recharge and eruption histories recorded in plagioclase phenocrysts from El Chichon Volcano, Mexico. *J. of Petrol.*, 41(9), 1397–1411. <https://doi.org/10.1093/petrology/41.9.1397>
- Varekamp, J. C., Luhr, J. F., & Prestegard, K. L. (1984). The 1982 eruptions of El Chichón Volcano (Chiapas, Mexico): character of the eruptions, ash-fall deposits, and gasphase. *J Volcanol. Geotherm. Res.* 23(1-2), 39–68. [https://doi.org/10.1016/0377-0273\(84\)90056-8](https://doi.org/10.1016/0377-0273(84)90056-8)
- Yogodzinski, G. M., Lees, J. M., Churikova, T. G., Dorendorf, F., Wöerner, G., & Volynets, O. N. (2001). Geochemical evidence for the melting of subducting oceanic lithosphere at plate edges. *Nature*, 409(6819), 500–504. <https://doi.org/10.1038/35054039>

Probing sulfur behavior in arc magmas with immiscible magmatic sulfides and apatite: Complementary data sets to assess ore-forming potential

Hervé Rezeau¹, Yannick Buret², Benjamin Z. Klein³, Oliver Jagoutz⁴, Shuhei Ono⁴

¹Department of Geosciences, University of Arizona, Tucson, USA

²Imaging and Analysis Centre, Natural History Museum, London, United Kingdom

³Institute of Earth Sciences, University of Lausanne, Bâtiment Géopolis, Lausanne, Switzerland

⁴Department of Earth, Atmospheric, and Planetary Sciences, Massachusetts Institute of Technology, Cambridge, USA

Abstract. Sulfur is one of the most abundant volatiles in subduction zones. Sulfur displays a complex behavior in arc magmas arising from its ability to partition between various phases (solid, immiscible liquid, gas and dissolved ions) and from its redox-dependent speciation (S^{2-} to S^{6+}). As a result, sulfur plays a critical role in the mobilization and transport of economically essential chalcophile elements (e.g., Cu, Au) during melt differentiation and fluid saturation and exsolution.

Herein, we first present whole rock sulfur isotope data in two crustal arc sections - the Early–Middle Jurassic Talkeetna Arc in south-central Alaska, and the Late Cretaceous Bear Valley Intrusive Suite (BVIS) in southern Sierra Nevada. These results reveal that melt differentiation is characterized by a $\delta^{34}S$ increase in the Talkeetna Arc and a $\delta^{34}S$ decrease in the BVIS. These opposing trends are explained by the crystallization of immiscible magmatic sulfides, and possibly upper crustal magma degassing, in the presence of dissolved oxidized and reduced sulfur species, respectively. Then, we examine the distribution of sulfur concentrations in magmatic apatites using high-resolution laser ablation mapping in two ore-related upper crustal magmatic systems namely the Meghri-Ordubad pluton in southern Armenia and Bajo de la Alumbrera in Argentina. This approach reveals a variety of textures including primary sulfur zoning highlighting episodes of sulfur-rich rejuvenation and sulfur degassing.

Collectively, our results argue that sulfur is an insightful geochemical tracer of redox conditions and crustal processes, which should be considered to assess ore-forming potential of arc magmas.

1 Introduction

Porphyry copper systems are primarily associated with oxidized, sulfur-rich and hydrous arc magmas (Richards 2022). Oxygen fugacity (fO_2) strongly controls sulfur speciation (sulfide, S^{2-} ; sulfate, S^{6+}), sulfur solubility, and hence the budget of chalcophile elements in arc magmas (Jugo et al. 2010). While Cu (and other economically important chalcophile elements) concentrations in melt may not represent a limiting factor for the formation of porphyry copper deposits, melt Cu concentrations certainly play a role to modulate the available mass of Cu that partition into the exsolving fluid phases and followed by Cu precipitation in porphyry copper systems (e.g., Rezeau and Jagoutz 2020). Thus, determining the evolution of sulfur speciation and sulfur concentrations during arc magmatic processes may help evaluate the ore-forming potential of arc magmas.

While some studies have shown that sulfur isotope (expressed as $\delta^{34}S$) represent useful tracers of sulfur speciation in arc magmas and thus fO_2 (Sasaki and Ishihara 1979; de Moor et al. 2022), others have used sulfur concentrations in apatite - a common accessory mineral in arc magmas - to monitor the evolution of sulfur and fO_2 in arc magmas (Streck and Dilles 1998; Chelle-Michou and Chiaradia 2017). Here, we first present whole rock sulfur isotope data for two exposed crustal arc sections to track sulfur isotope compositions during transcrustal magmatic processes. Then, we examine the distribution of sulfur concentrations in magmatic apatites using high-resolution laser ablation mapping to evaluate the evolution of sulfur concentrations in upper crustal magmatic systems associated with porphyry copper systems.

Our results show that whole rock sulfur isotopes can accurately identify intrusions that crystallized under oxidized and reduced conditions, while sulfur concentration maps in apatite reveal primary igneous sulfur zoning allowing us to track episodes of sulfur-rich rejuvenation and sulfur degassing. Combined, these complementary data sets could help identifying these geochemical features, and hence may provide insightful tools to assess the ore-forming potential of arc igneous rocks.

2 Sulfur isotope fractionation during crystallization-differentiation processes

2.1 Study areas

Two well-studied exposed crustal arc sections are investigated to evaluate sulfur isotope systematics during crustal magmatic differentiation processes.

The Early–Middle Jurassic intra-oceanic Talkeetna Arc section exposed in the Chugach Mountains, south-central Alaska, represents a faulted crustal arc section (Burns 1985). It exposes ultramafic units formed at ~ 0.9 – 1.2 GPa (~ 30 – 35 km-depth), basal gabbros formed at ~ 0.5 – 1 GPa (~ 15 – 30 km-depth), middle to upper crustal mafic to felsic intrusions formed at ~ 0.2 – 0.5 GPa (~ 5 – 15 km-depth), and basalt to rhyolite volcanic rocks capping underlying intrusions (Burns 1985; Debari and Coleman 1989; Greene et al. 2006). Furthermore, the juvenile radiogenic isotopic compositions ($\epsilon_{Nd(t)} = -6.7.8$; $^{87}Sr/^{86}Sr = 0.703379$ – 0.703951) argue for limited

crustal assimilation (e.g., Greene et al 2006; Rioux et al. 2007).

The Late Cretaceous Bear Valley Intrusive Suite (BVIS) exposes a 30 km-depth continuous crustal arc section emplaced within 1.39 ± 0.06 Ma in the southern Sierra Nevada (Klein et al. 2021; Klein and Jagoutz 2021). The deepest portion of the BVIS exposes mafic igneous cumulates formed at ~ 0.8 – 0.9 GPa (~ 25 – 30 km-depth), whereas shallower units consist of tonalites formed between ~ 0.7 GPa and ~ 0.2 GPa (~ 5 – 20 km-depth). Isotopic studies indicate that these rocks are characterized by ~ 5 – 20% of crustal assimilation (Klein et al. 2021).

In Talkeetna and BVIS, petrogenetic models suggest that SiO_2 -rich intrusions represent derivative melts from deep crustal crystallization-differentiation of a parental mafic melt (Greene et al. 2006; Klein and Jagoutz 2021; Rezeau et al. 2021, 2023). Importantly, both arc sections are characterized by ultramafic-mafic cumulates and felsic intrusions containing primary magmatic sulfides offering opportunities to track the evolution of sulfur isotopes ($\delta^{34}\text{S}$) during transcrustal magmatic processes.

2.2 Results and Interpretations

For each crustal section, we analyzed whole rock sulfur isotopes for samples representative of the entire compositional range and depths.

In Talkeetna, whole rock $\delta^{34}\text{S}$ values for 25 samples indicate a clear sulfur isotope fractionation during melt differentiation characterized by a $\delta^{34}\text{S}$ increase from -1.28 to $+5.61\text{‰}$ (Figure 1). Combined with a quantitative petrological model that constrains the liquid line of descent and sulfide saturation as a function of sulfur content, oxygen fugacity, pressure, and temperature, we demonstrate that saturation of immiscible magmatic sulfides is capable of generating such sulfur isotope fractionation in the presence of dissolved oxidized sulfur species (Rezeau et al 2023). The most positive $\delta^{34}\text{S}$ values observed for upper crustal felsic intrusions reflect enhanced sulfur fractionation due to fluid degassing. Therefore, we suggest that sulfide immiscibility and magma degassing are not mutually exclusive and represent complementary processes that combine to explain the observed range of positive $\delta^{34}\text{S}$ compositions in Talkeetna. Any influences by crustal assimilation of pre-existing oceanic crust containing seawater sulfate is unlikely. In the BVIS, whole rock $\delta^{34}\text{S}$ for 21 samples range from -5.1 to -1.2‰ , where $\delta^{34}\text{S}$ values for lower crustal mafic cumulates overlap with those of shallower tonalites (Figure 1). Additional whole rock $\delta^{34}\text{S}$ for six metasedimentary rock pendants reveal that deeper metasediments (~ 0.7 – 0.9 GPa) yield lighter $\delta^{34}\text{S}$ (-11.5 and -4.1‰) compared to shallower metasediments (~ 0.4 – 0.6 GPa) yielding heavier $\delta^{34}\text{S}$ (-0.7 to $+6.4\text{‰}$). The lack of correlation between $\delta^{34}\text{S}$ and the composition of mafic cumulates indicates heterogeneous crustal assimilation (~ 5 – 20%) of deep metasediments in the lower crust. In contrast, whole rock $\delta^{34}\text{S}$ values for tonalites are negatively

correlated with SiO_2 content or depths (Figure 1). This can be explained by saturation of immiscible magmatic sulfides and/or fluid degassing in the presence of dissolved reduced sulfur species, as opposed to crustal assimilation. In the BVIS, we suggest that primary arc melts ($\delta^{34}\text{S} \sim 0\text{‰}$) assimilate graphite-bearing metasediments in the deep crust promoting reduced conditions and saturation of immiscible magmatic sulfides characterized by negative $\delta^{34}\text{S}$. Then, reduced derivative tonalitic melts are produced and ascend to shallower crustal levels, where melt differentiation is accompanied by saturation of immiscible magmatic sulfides and/or fluid saturation leading progressive negative $\delta^{34}\text{S}$.

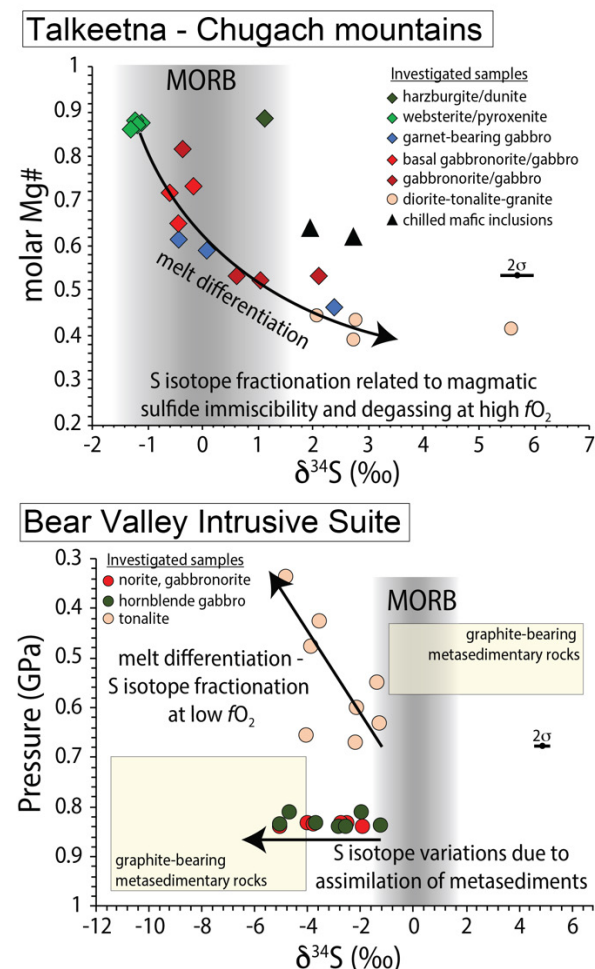


Figure 1. Evolution of sulfur isotope (expressed as $\delta^{34}\text{S}$) in rocks formed in the Talkeetna and Bear Valley Intrusion Suite arc sections. Top: whole rock S isotope compositions versus Mg# in Talkeetna rocks. Bottom: whole rock S isotope compositions versus pressure of crystallization in the Bear Valley Intrusive Suite rocks.

2.3 Implications for ore-forming potential

Our findings demonstrate that $\delta^{34}\text{S}$ is a faithful tracer of $f\text{O}_2$ during arc magma differentiation. For instance, both Talkeetna and BVIS consist of SiO_2 -rich upper crustal intrusions characterized by similar whole rock geochemistry, yet they yield contrasting $\delta^{34}\text{S}$ values indicating different evolution of $f\text{O}_2$ during melt differentiation between the two locations. Knowing that high $f\text{O}_2$ represent favourable

conditions for the formation of porphyry copper systems (Richards 2021), upper crustal intrusions with positive $\delta^{34}\text{S}$ should represent better exploration targets higher with respect to those with negative $\delta^{34}\text{S}$.

While our results are consistent with the pioneering work of Sasaki and Shinohara (1979), we argue that positive $\delta^{34}\text{S}$ values in arc magmas are unlikely to reflect the mantle source region and may, instead, fingerprint the combination of early magmatic sulfide immiscibility and later magma degassing. Both processes may increase the ore-forming potential as immiscible sulfides represent temporary metal carriers that can be remobilized if melt reaches fluid saturation and degassing (e.g., Nadeau et al. 2010; Heinrich and Connolly 2022). Overall, sulfur isotope compositions in arc magmas should provide valuable information to evaluate the relative ore-forming potential between sets of intrusions in a given regional district.

3 High-resolution laser ablation mapping of sulfur concentration in apatite

3.1 Methodology

Traditionally, apatite is not analysed by laser ablation inductively coupled plasma mass spectrometry (LA-ICP-MS) due to high background levels from $^{16}\text{O}^{16}\text{O}$, $^{16}\text{O}^{17}\text{O}$ and $^{16}\text{O}^{18}\text{O}$ species. However, the ability to reduce these interferences using reaction gases (O_2) has made it possible to measure the major sulfur isotope (^{32}S) as a reaction product ($^{32}\text{S}^{16}\text{O}$) therefore opening new avenues for sulfur analysis by ICP-MS (e.g., Nakano 2018). Furthermore, the new generation of laser ablation systems have ultra-fast signal washouts, permitting rapid elemental mapping at high repetition rates, thereby boosting sensitivity to permit smaller spot sizes. Here, we present LA-ICP-MS mapping of apatite crystals using the 193 nm Teledyne Iridia laser ablation system combined with an Agilent 8900 ICP-QQQ-MS. The full width of a single pulse at 10% of the maximum peak intensity was optimised at <5 ms in order to increase sensitivity and decrease imaging time. Individual maps (<100 x 100 μm to 300 x 100 μm) take between 1 and 5 minutes. Image processing and quantification was carried out using HDIP (v. 1.6). Routine analysis of Durango apatite reveals accuracy within the published range of sulfur concentrations. Our sulfur concentrations obtained from LA-ICP-MS maps are consistent with previously determined EMPA concentrations.

3.2 Results and interpretations

We use this approach to track the evolution of sulfur concentrations in the formation of magmatic hosted porphyry copper deposits in two well-studied case study areas: Bajo de la Alumbrera in Argentina and the Meghri-Ordubad pluton in southern Armenia. High-resolution concentration maps of apatite grains reveal a variety of textures including

primary igneous zoning, multi-phase growth, alteration and sulfide inclusions (Figure 2).

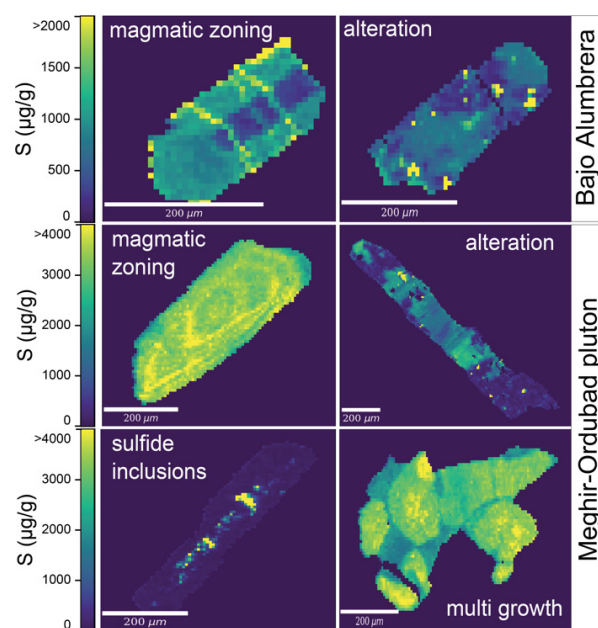


Figure 2. Representative high-resolution sulfur maps of apatite grains hosted in ore-related intrusions at Bajo de la Alumbrera and Meghri-Ordubad pluton.

In Bajo de la Alumbrera, apatite grains hosted in syn-mineralization altered intrusions reveal patchy sulfur zoning which show evidence for hydrothermal remobilization. In contrast, apatite from syn-mineralization volcanism display well-defined reverse sulfur zoning. These features are consistent with co-crystallizing plagioclase reverse zoning that is interpreted as rejuvenation of upper crustal reservoirs (Buret et al., 2017). In this case, it provides evidence for sulfur-rich mafic recharge.

In the Meghri-Ordubad pluton, we analyzed apatite grains hosted in shoshonitic intrusions that pre-date and that are contemporaneous to the formation of the large Kadjaran porphyry copper-molybdenum deposits (Rezeau et al 2016). Apatite grains hosted in syn-mineralization altered intrusions also reveal patchy sulfur zoning indicative of hydrothermal remobilization. In pre-mineralization intrusive rocks, primary sulfur zoning is interpreted as episodes of sulfur-rich mafic magma rejuvenation, whereas sulfur-poor zones may reflect sulfur degassing and/or saturation of co-existing magmatic anhydrite (Streck and Dilles 1998). The presence of sulfur-poor apatite with sulfide micro-inclusions suggests co-crystallization of apatite and magmatic sulfide at fairly reduced conditions where dissolved S^{2-} prevails with respect to S^{6+} in the melt. The multi-phase apatite growth is characterized by an early growth of euhedral sulfur-rich apatite grains that are cemented by late interstitial sulfur-poor anhedral apatite. While these textural features may either reflect two generations of magmatic apatites or an early generation of magmatic apatites that are resorbed during late deuteric or hydrothermal fluids, its origin remains elusive, and it requires further investigations.

3.3 Implications for ore-forming potential

We demonstrate the ability to generate fast and accurate high-resolution laser ablation mapping of sulfur concentration on apatite. This approach can reveal precious information on the sulfur distribution in apatite grains helping to monitor sulfur behavior during crustal magmatic processes. As sulfur-rich mafic rejuvenation of upper crustal felsic reservoirs is an important trigger for the formation of porphyry copper systems (Hattori and Keith 2001; Wilkinson 2013), revealing primary sulfur zoning in apatite would help identifying episodes of sulfur rejuvenation and degassing. As a result, this approach provides opportunities for the rapid assessment of sulfur concentrations in apatites and may provide insightful tools to evaluate the ore-forming potential of arc-related igneous rocks during mineral exploration.

Acknowledgements

This work was supported by the Swiss National Foundation postdoc mobility grant P400P2_194421 to Hervé Rezeau and by the National Science Foundation NSF EAR-1902179 and NSF EAR-1925863 to Oliver Jagoutz. The authors acknowledge Patrick Beaudry and Gareth Izon for collaboration on acquiring sulfur isotope data and for stimulating scientific discussions. Peter Kelemen is also acknowledged for sharing Talkeetna samples and key scientific inputs.

References

- Buret, Y., Wotzlaw, J. F., Roozen, S., Guillong, M., von Quadt, A., & Heinrich, C. A. (2017): Zircon petrochronological evidence for a plutonic-volcanic connection in porphyry copper deposits; *Geology*, v. 45(7), p. 623-626.
- Burns, L. E. (1985): The Border Ranges ultramafic and mafic complex, south-central Alaska: cumulate fractionates of island-arc volcanics; *Canadian Journal of Earth Sciences*, v. 22(7), p. 1020-1038.
- Chelle-Michou, C., and Chiaradia, M. (2017): Amphibole and apatite insights into the evolution and mass balance of Cl and S in magmas associated with porphyry copper deposits; *Contributions to Mineralogy and Petrology*, v. 172(11-12), p. 105.
- DeBari, S. M., and Coleman, R. G. (1989): Examination of the deep levels of an island arc: Evidence from the Tonsina ultramafic-mafic assemblage, Tonsina, Alaska; *Journal of Geophysical Research: Solid Earth*, v. 94, p.4373-4391.
- De Hoog, J. C. M., Mason, P. R. D., and Van Bergen, M. J. M. (2001): Sulfur and chalcophile elements in subduction zones: constraints from a laser ablation ICP-MS study of melt inclusions from Galunggung Volcano, Indonesia; *Geochimica et Cosmochimica Acta*, v.65, p.3147-3164.
- de Moor, J. M., Fischer, T. P., and Plank, T. (2022): Constraints on the sulfur subduction cycle in Central America from sulfur isotope compositions of volcanic gases; *Chemical Geology*, v. 588, 120627.
- Greene, A. R., DeBari, S. M., Kelemen, P. B., Blusztajn, J., and Clift, P. D. (2006): A detailed geochemical study of island arc crust: the Talkeetna arc section, south-central Alaska; *Journal of Petrology*, v. 47(6), p. 1051-1093.
- Hattori, K. H., and Keith, J. D. (2001): Contribution of mafic melt to porphyry copper mineralization: evidence from Mount Pinatubo, Philippines, and Bingham Canyon, Utah, USA; *Mineralium Deposita*, v. 36, p. 799-806.
- Heinrich, C. A., and Connolly, J. A. (2022): Physical transport of magmatic sulfides promotes copper enrichment in hydrothermal ore fluids; *Geology*, v. 50(10), p. 1101-1105.
- Jugo, P. J., Wilke, M., and Botcharnikov, R. E. (2010): Sulfur K-edge XANES analysis of natural and synthetic basaltic glasses: Implications for S speciation and S content as function of oxygen fugacity; *Geochimica et Cosmochimica Acta*, v. 74(20), p. 5926-5938.
- Klein, B. Z., and Jagoutz, O. (2021): Construction of a trans-crustal magma system: building the Bear Valley Intrusive Suite, southern Sierra Nevada, California; *Earth and Planetary Science Letters*, v. 553, 116624.
- Klein, B. Z., Jagoutz, O., and Ramezani, J. (2021): High-precision geochronology requires that ultrafast mantle-derived magmatic fluxes built the transcrustal Bear Valley Intrusive Suite, Sierra Nevada, California, USA; *Geology*, v. 49(1), p.106-110.
- Nadeau, O., Williams-Jones, A. E., and Stix, J. (2010): Sulphide magma as a source of metals in arc-related magmatic hydrothermal ore fluids; *Nature Geoscience*, v. 3(7), p.501-505.
- Nakano, K., (2018): Agilent Application Note, 5991-3520EN
- Rezeau, H., Jagoutz, O., Beaudry, P., Izon, G., Kelemen, P., and Ono, S. (2023): The role of immiscible sulfides for sulfur isotope fractionation in arc magmas: Insights from the Talkeetna Island arc crustal section, south-central Alaska; *Chemical Geology*, 121325.
- Rezeau, H., Klein, B. Z., and Jagoutz, O. (2021): Mixing dry and wet magmas in the lower crust of a continental arc: new petrological insights from the Bear Valley Intrusive Suite, southern Sierra Nevada, California; *Contributions to Mineralogy and Petrology*, v. 176(9), 73.
- Rezeau, H. and Jagoutz, O. (2020): The importance of H₂O in arc magmas for the formation of porphyry Cu deposits; *Ore Geology Reviews* 126, 103744.
- Rezeau, H., Moritz, R., Wotzlaw, J. F., Tayan, R., Melkonyan, R., Ulianov, A., Selby, D., d'Abzac, F.-X., and Stern, R. A. (2016): Temporal and genetic link between incremental pluton assembly and pulsed porphyry Cu-Mo formation in accretionary orogens; *Geology*, v. 44(8), p. 627-630.
- Richards, J. P. (2022): Porphyry copper deposit formation in arcs: What are the odds?; *Geosphere*, v. 18, p.130-155.
- Rioux, M., Hacker, B., Mattinson, J., Kelemen, P., Blusztajn, J., and Gehrels, G. (2007): Magmatic development of an intra-oceanic arc: High-precision U-Pb zircon and whole-rock isotopic analyses from the accreted Talkeetna arc, south-central Alaska; *Geological Society of America Bulletin*, v. 119(9-10), p. 1168-1184.
- Sasaki, A., and Ishihara, S. (1979): Sulfur isotopic composition of the magnetite-series and ilmenite-series granitoids in Japan; *Contributions to Mineralogy and Petrology*, v. 68, p. 107-115.
- Streck, M. J., and Dilles, J. H. (1998): Sulfur evolution of oxidized arc magmas as recorded in apatite from a porphyry copper batholith; *Geology*, v. 26, p. 523-526.
- Wilkinson, J. J. (2013): Triggers for the formation of porphyry ore deposits in magmatic arcs; *Nature Geoscience*, v. 6(11), p. 917-925.

New experimental data on potassic vs. albitic alteration

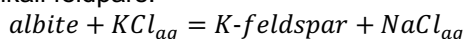
Taraneh Roodpeyma¹, Thomas Driesner¹

¹Department of Earth Sciences, ETH University, Zurich, Switzerland

Abstract. Porphyry copper deposits display different alteration types among which potassic alteration of plagioclase and amphiboles is the most prominent one as it typically overlaps with ore mineralization. However, in some Au-enriched porphyry deposits (e.g., Batu Hijau, Indonesia, and Bolcana, Romania), potassic feldspar alteration seems to be largely absent and albitic alteration is observed instead. K-Na exchange between fluid and alkali feldspars in reverse direction could be a plausible mechanism for albitic vs. potassic feldspar alteration but published experimental data seem to preclude this possibility of albitic alteration. As the published data bear significant problems we performed new experiments at 400 and 450°C and at different pressures over wide ranges of chloride concentrations. Results reveal that at low chloride concentrations and rather low pressures, cooling may potentially lead to albitic instead of potassic alteration. However, relationships are non-trivial if the full dependence on temperature, pressure and salinity is taken into account.

1 Introduction

Mapping of porphyry copper deposits revealed global similarities in terms of alteration patterns and vein sequences (e.g. Lowell and Guilbert 1970; Gustafson and Hunt 1975). Potassic alteration of plagioclase to K-feldspar and/or amphiboles to biotite has received particular interest as it is often correlated with the main ore zones (e.g., Seedorf et al. 2005). However, there are exceptions, the causes of which have remained elusive. For example, in some Au-enriched porphyry Cu deposits such as Batu Hijau, Indonesia (Schirra et al. 2022), and Bolcana, Romania (Blannin et al. 2019), potassic feldspar alteration is largely absent while biotite alteration of amphiboles is present and albitic feldspar alteration is observed instead. Although albitic alteration may simply reflect Ca-loss from plagioclase (e.g., Henley et al. 2022) or could belong to a post-potassic stage (e.g., Calder et al. 2023, and references therein), the question remains why no potassic feldspar alteration occurred. The exchange reaction of K and Na between fluid and alkali feldspars:



governs potassic feldspar alteration and implies a leading role of the fluid's K/Na concentration ratio for determining the direction of reaction, i.e., albite/sodic alteration may be possible by the reaction proceeding to the left. Previous experimental studies, however, are largely inconclusive whether sodic alteration of K-feldspar could be achieved: since the fluid's K/Na concentration ratio in equilibrium with albite and K-feldspar decreases with decreasing temperature (e.g. Orville 1963), heating of fluid would be required to achieve albitic alteration, or the fluid has to have a K/Na concentration ratio below the equilibrium

value, which is difficult to realize as long as plagioclase is present in the host rock. Furthermore, an in-depth analysis (Roodpeyma and Driesner 2020) of the existing experimental data revealed that the most relevant study (Lagache and Weisbrod 1977) is based on data that were obtained in the two phase liquid+vapor fluid field, which obscured the derivation of the correct equilibrium values.

In order to obtain improved data on equilibrium K/Na exchange between alkali feldspars and hydrothermal fluids, we performed new experiments at 400°C and 450°C, both at pressures equivalent to pure water densities of about 0.3 and 0.5 g cm⁻³, and for total aqueous concentrations ranging from 10⁻⁴ to 13 molal chloride. The comprehensive data set allows us to assess the effect of temperature, pressure, and total aqueous chloride molality at conditions relevant to porphyry deposit formation.

2 Experimental

The temperature, pressure, and chloride concentration range of the experiments were designed to close the existing gap of available data points (Roodpeyma et al. 2022). In order to be able to compare equilibrium K/Na molal ratios in the fluid, irrespective of the effect of (unknown) activity coefficients at finite concentrations, the experimental bulk concentration range starts from very dilute, close to infinite dilution, where the K/Na concentration ratio can be regarded as the equilibrium activity ratio (activity coefficients = 1). Following Lagache and Weisbrod (1977), we call the K/Na molal concentration ratio C , with C^∞ denoting the value at infinite dilution. Figure 1 illustrates the measured C for all types of used initial aqueous solutions (pure KCl solution, pure NaCl solution, mixture) in reaction with alkali feldspars under various total chloride concentrations. The equilibrium state is confidently achieved through reversed experiments over all concentrated regions. Some deviating data points at high concentration reflect an inadequate choice of reactant ratios, i.e., lacking a sufficient mole amount of alkalis in solid or fluid phases, not allowing the reaction to proceed to completion.

3 Results

3.1 Temperature effect

Arguably the biggest deviation from the previous state of knowledge is that C^∞ decreases with temperature at pressures equivalent to constant pure water density, at least for the studied temperature interval. At the given water density of 0.3 g cm⁻³, the present study shows that C^∞ value,

depicted in Fig. 1, decreases from 0.056 to 0.04 as temperature increases from 400 to 450°C. At elevated concentrations, the C ratio is around 0.2 and shows little change from 400 to 450°C (Fig. 2A,C); if any, then a minor increase in C may occur with increasing temperature. C values at higher concentrations are typically higher than the ones reported by Lagache and Weisbrod (1977). A similar trend is seen for experimental results at pressures equivalent to 0.5 g cm⁻³ pure water density (Fig. 2B,D).

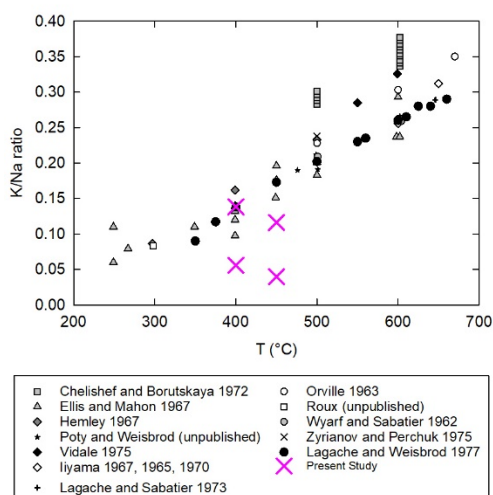


Figure 1. Effect of T on the K/Na molal ratio. New data compared to existing literature data

3.2 Pressure effect

At 400°C with increasing pressure equivalent to 0.3 g cm⁻³ (288 bar) to 0.5 g cm⁻³ (372 bar) pure water density, C^o increases significantly from 0.056 to 0.138 (Fig. 2C). This finding is qualitatively consistent with the data points of C versus total chloride molalities plotted by Lagache and Weisbrod (1977).

While Lagache and Weisbrod (1977) showed a recognizable pressure dependence on C values at 500°C and low concentrations, this finding apparently did not enter their derivation of equilibrium constants and has largely been ignored in the literature. Our results at 400°C as well as the data at 450°C show a much more pronounced pressure effect than indicated by the plots of Lagache and Weisbrod (1977).

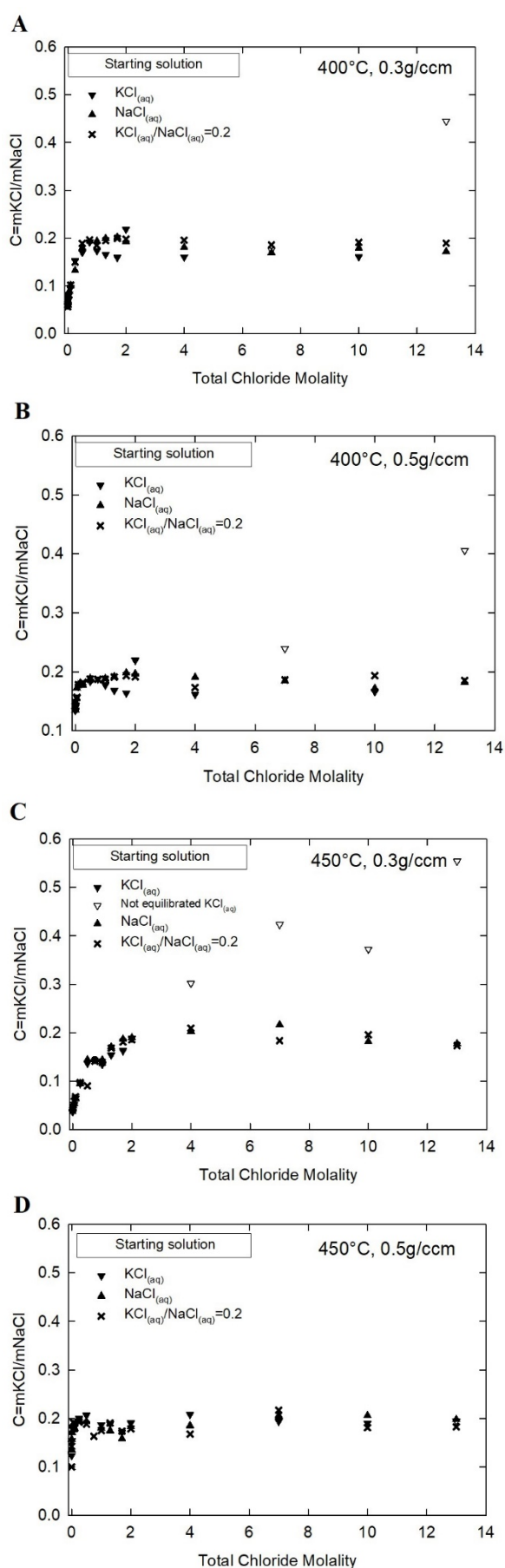


Figure 2. Experimental values of K/Na molal ratio at isotherms of 400 (A) and 450°C (C) and water density of 0.3 g cm⁻³ and at isotherms of 400 (B) and 450°C (D) and water density of 0.5 g cm⁻³

3.3 Concentration effect

C changes significantly as a function of concentration (Figures 2). However, it should be noted that all these C values represent equilibrium values at the given temperature and pressure and the concentration dependence is an expression of how activity coefficients for KCl and NaCl in the solution change differently with increasing concentration. There is evidence of liquid-vapor immiscibility at 450°C / 0.3 g cm⁻³ water density between ca. 0.1 and 2 m chloride concentration (however, with significant uncertainties).

4 Discussion

The new results imply that albitic instead of K-feldspar alteration may be possible for certain temperature-pressure-concentration paths of fluid in a porphyry-forming system. Namely – and contrary to previous thinking – a temperature decrease can induce albitic alteration, provided that the fluid is of low concentration and follows a temperature-pressure path of constant low or increasing density. This may be an explanation for its occurrence in gold-rich porphyries for which generally shallower depth of formation (and, therefore, lower pressure; Murakami et al. 2010) have been inferred.

(Near)-isothermal pressure decrease, on the contrary, would induce, at least at low concentrations, K-feldspar alteration. Our current data set does not yet allow to quantitatively assess which cooling paths and temperature-pressure-concentration window(s) would equally promote K-feldspar alteration. Given its widespread occurrence, however, such windows must be common in typical porphyry copper-forming systems.

The curved concentration dependence of the equilibrium K/Na ratio implies that mixing high- and low-concentration fluids may be an alternative way for inducing albitic alteration as the mixtures' C value would fall below the equilibrium curve in Figures 2. However, it is rather difficult to imagine how such fluids would follow independent flow paths prior to mixing.

5 Conclusion

Although the alteration pattern widely shows similarities among porphyry copper deposits, occasional sodic instead of potassic alteration of feldspar appears to violate the general sequence in some cases. As the role of cooling and depressurization during the fluid evolution paths has been widely emphasized, we presented new experimental data set studying the compositional state of the alkali feldspars-KCl-NaCl-H₂O system. Focusing on the K/Na molal ratio of fluid phase under influence of temperature, pressure, and concentration it is shown that temperature and pressure can have opposite effect on the equilibrated K/Na ratio, depending on the path. For example, decreasing temperature at a given density

leads to the increase of K/Na ratio in the fluid phase, that is, the chemical reaction proceeds towards albitic precipitation while a decrease in pressure at a given temperature decreases the K/Na equilibrium ratio, which drives the reaction towards potassic alteration. Moreover, the curved trend of the equilibrium fluid K/Na molal ratio versus concentration shows the advent of new equilibrium K/Na implies that mixing of low- and high-salinity fluid phases leads to homogenization at K/Na concentration ratios below the equilibrium curve. We conclude that the new experimental insights contribute to further understanding of porphyry deposits through closing experimental and conceptual gaps that have led to potentially erroneous assumptions about potassic vs. sodic feldspar alteration.

6 References

- Blannin R, Tusa L, Birtel S, Gutzmer J, Gilbricht S, Ivascanu P (2019) Metal deportment and ore variability of the Bolcana porphyry Au-Cu system (Apuseni Mts, Romania) - Implications for ore processing. 15th Biennial Meeting of the Society for Geology Applied to Mineral Deposits At: Glasgow. https://www.researchgate.net/publication/349523731_Metal_deportment_and_ore_variability_of_the_Bolcana_porphyry_Au-Cu_system_Apuseni_Mts_Romania_-_Implications_for_ore_processing
- Calder MF, Chang Z, Arribas A, Gaibor A, Dunkley P, Pastoral J, Kouzmanov K, Spandler C, Hedenquist JW (2022) High-Grade Copper and Gold Deposited During Postpotassic Chlorite-White Mica-Albite Stage in the Far Southeast Porphyry Deposit, Philippines. *Economic Geology* 117:1573-1596. <https://doi.org/10.5382/econgeo.4940>
- Fekete S, Weis P, Driesner T, Bouvier A (2016) Contrasting hydrological processes of meteoric water incursion during magmatic-hydrothermal ore deposition: An oxygen isotope study by ion microprobe. *Earth and Planetary Science Letters* 451:263-271. <https://doi.org/10.1016/j.epsl.2016.07.009>
- Gustafson LB, Hunt JP (1975) The porphyry copper deposit at El Salvador, Chile. *Economic Geology* 70:857-912.
- Henley R, Mernagh T, Leys C, Troitzsch U, Beviitt J, Brink F, Gardner J, Knuefing L, Wheeler J, Limaye A, Turner M, Zhang Y (2022) Potassium silicate alteration in porphyry copper-gold deposits: a case study at the giant maar-diatreme hosted Grasberg deposit, Indonesia. *Journal of Volcanology and Geothermal Research* 432. <https://doi.org/10.1016/j.jvolgeores.2022.107710>
- Lowell JD, Guilbert, JM (1970) Lateral and vertical alteration-mineralization zoning in porphyry ore deposits. *Economic Geology* 65:373-408.
- Lagache M, Weisbrod A (1977) The System: Two Alkali Feldspars-KCl-NaCl-H₂O at Moderate to High Temperatures and Low Pressures. *Contrib. Mineral. Petrol.* 62:77-101.
- Murakami H, Seo JH, Heinrich C (2010) The relation between Cu/Au ratio and formation depth of porphyry-style Cu-Au ± Mo deposits. *Miner Deposita* 45:11-21. <https://doi.org/10.1007/s00126-009-0255-1>
- Orville PM (1963) ALKALI ION EXCHANGE BETWEEN VAPOR AND FELDSPAR PHASES. *AMERICAN JOURNAL OF SCIENCE* 261:201-237.
- Parsons I (2012) Feldspars and their Reactions. Springer Dordrecht. <https://doi.org/10.1007/978-94-011-1106-5>
- Roodpeyma T, Driesner T (2020) A re-assessment of the equilibrium constant and aqueous activity ratios for the Albite – K-Feldspar – NaCl(aq) – KCl(aq). 18th Swiss Geoscience Meeting. https://geoscience-meeting.ch/sgm2020/wp-content/uploads/abstracts/Roodpeyma_Taraneh_08-21-20-04-09-14.pdf
- Roodpeyma T, Driesner T, Kost O (2022) Experimental study of thermodynamic behavior of NaCl-KCl electrolytes in reaction with alkali feldspars under supercritical condition of water.

- Goldschmidt Hawai'i 2022.
<https://conf.goldschmidt.info/goldschmidt/2022/meetingapp.cgi/Paper/10609>
- Schirra M, Laurent O, Zwyer T, Driesner T, Heinrich C (2022) Fluid Evolution at the Batu Hijau Porphyry Cu-Au Deposit, Indonesia: Hypogene Sulfide Precipitation from a Single-Phase Aqueous Magmatic Fluid During Chlorite–White-Mica Alteration. *Economic Geology* 117: 979-1012. <https://doi.org/10.5382/econgeo.4921>
- Seedorff E, Dilles JH, Proffett JM, Einaudi MT (2005) Porphyry deposits: Characteristics and origin of hypogene features. In: *Economic Geology, One Hundredth Anniversary Volume*. pp 251-298. <https://doi.org/10.5382/AV100.10>

Evolution of the Skouries porphyry Cu-Au system by trace element variations

Alica Höss¹, Reiner Klemd¹, Manuel Keith¹, Karsten M. Haase¹, Vasilios Melfos², Lisa Gerlach¹, Fabian Pelloth¹, Jan Falkenberg¹, Panagiotis Voudouris³

¹GeoZentrum Nordbayern, Friedrich-Alexander Universität (FAU) Erlangen-Nürnberg, 91054 Erlangen, Germany

²Aristotle University of Thessaloniki, Faculty of Geology, 54124 Thessaloniki, Greece

³National and Kapodistrian University of Athens, Faculty of Geology & Geoenvironment, 15784 Athens, Greece

Abstract. The Skouries deposit is a platinum-group element enriched Cu-Au porphyry system in NE Greece. The monzonite-syenite intrusions host a porphyry stockwork consisting of A- and B-type veins associated with potassic alteration, which is partly overprinted by C-type and D-type veins and related chlorite-sericite to sericitic alteration. The Cu-Au mineralization is dominated by pyrite, chalcopyrite, bornite, magnetite and additional native Au, telluride inclusions and platinum-group minerals. Incompatible trace element ratios of the host rocks (ICP-MS) were used to track the impact of alteration, while in-situ mineral chemistry (LA-ICP-MS) resolves changes in the fluid conditions. Trace element ratios of host rocks show that potassic alteration can change the composition of incompatible element ratios commonly used as tracers for magmatic signatures, such as (La/Sm)_N. Ti-in-quartz thermometry yields temperatures of 600°C ± 50° for the A-type veins, 610 ± 60°C for the early B-type veins and 545 ± 45°C for late B-type veins. Furthermore, the pyrite mineralization is characterized by systematic variations in trace element contents (e.g., As, Ag, Au) and ratios (e.g., Sb/As, Ag/As) that trace temperature variations of the hydrothermal fluid and implicate phase separation. Phase separation is further suggested to cause the precipitation of native gold during potassic alteration.

1 Introduction

Magmatic fluids play a key role in the Cu-Au enrichment in porphyry intrusions which can form enormous ore deposits with relatively low-grade metal contents. Porphyry Cu-Au mineralization forms in vein stockworks hosted by pervasive alteration halos surrounding the porphyry intrusion. The Serbo-Macedonian metallogenic belt extends from Serbia to northern Greece and is characterized by numerous porphyry deposits, either enriched in Cu, Cu-Au or Cu-Mo. The Skouries Cu-Au porphyry on the Chalkidiki peninsula contains ~289 Mt of ore at 0.43 % Cu and 0.58 g/t Au (Siron et al. 2018). The monzonite and syenite porphyry intrusions are of early Miocene age (20.56±0.48 Ma, Hahn 2014), and intruded into the Kerdilion and Vertiskos Unit (Siron et al. 2018). The Vertiskos Unit, which hosts the Skouries deposit, is mainly composed of schists, greenschist-facies gneisses, and a metamorphic sequence comprising thin interlayers of calcareous schist, marble and amphibolite (McFall et al. 2018). Additional micaceous schists of the Neoproterozoic to Ordovician age are present in close proximity to the Skouries porphyry (Siron et al. 2018). The Skouries Cu-Au deposit expands over an area of ~200m in diameter and >900m in depth and is characterized by monzonitic to porphyritic syenite

stocks and dykes with an associated porphyry stockwork (Figure 1). At least four intrusive stages, namely early monzonite, porphyritic syenite and melasyenite, and post-mineralization barren syenite were identified, which show extensive potassic and minor sericitic alteration (McFall et al. 2018). The Cu-Au mineralization is mainly hosted by pyrite, chalcopyrite, bornite, and accessories such as native gold, tellurides and PGE minerals in the vein system. The stockwork is dominated by A-type (qz+mt+cpy±bn), early B1- (reopening A-type veins, qz+mt+cp+py) and late B2-type (qz+cp+py±mt) veins. Late-stage massive pyrite-chalcopyrite veins (C-type and D-type) crosscut the main stage veining at depth, overprinting the potassic alteration with sericitic alteration (telescoping).

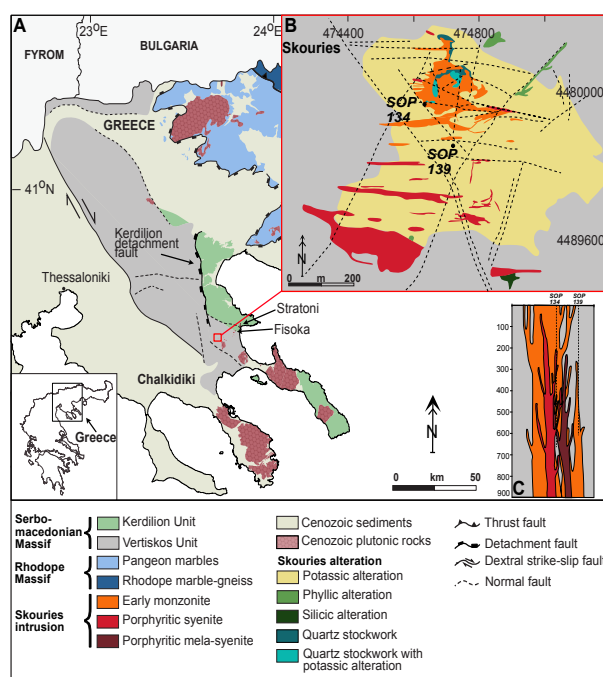


Figure 1. a) Geological map of the Greek part of the Serbo-Macedonian metallogenic belt (modified after Siron et al. 2018). b) Geological map the Skouries Porphyry and c) a schematic sketch of a section through the main ore body (modified after McFall et al. 2018).

2 Methodology

2.1 Micro-analytical techniques

The LA-ICP-MS study was conducted on sulfides and quartz with respect to the previously defined vein-types. A Teledyne Analyte Excite 193 nm laser coupled with an Agilent 7500c quadrupole ICP-MS, operating at a frequency of 20Hz, a fluence of 2.6 to 3.5 J/cm³, a plasma power of 1270W and a beam size of 35 µm was used at the GeoZentrum Nordbayern. For the quartz measurements, the operating setting was changed to a frequency of 10Hz, plasma power of 1280W, a fluence of 8.59 J/cm³ and a beam diameter of 65 µm.

2.2 Composition of the host rocks

The host rock samples were analyzed by XRD analyses on rock powder to quantify the type and degree of alteration due mineral abundances. The trace element measurements were performed by a Thermo Scientific X-Series 2 quadrupole ICP-MS at the GeoZentrum Nordbayern.

3 Results

3.1 Composition of the host rocks

The host rocks are dominated by potassic alteration, which is characterized by hydrothermal formation of orthoclase, biotite and magnetite, but can be overprinted by sericite and chlorite. The degree of alteration can therefore be quantified by the amount of orthoclase in each sample, determined by XRD and related whole rock major element data. The samples from the drill core SOP134 refer to the main ore body and vary considerably in their major and trace element composition, which refers to relatively minor and strong potassic alteration of monzonite and porphyry syenite. Trace element ratios of relatively fresh samples show (La/Sm)_N of 4 to 5, no Eu anomaly and chondritic Nb/Ta values of 20. In contrast, altered samples contain decreasing (La/Sm)_N between 5.8 and 7.6 with decreasing Yb, Eu/Eu* of 2 to 11, decreasing REE contents and Nb/Ta values (Figure 2). Altered samples with low Yb additionally have variable (La/Sm)_N ratios. The trace element concentration of hydrothermally altered samples from Skouries show systematic differences from fresh magmatic rocks of the area even for elements that are commonly suggested to be immobile (Figure 2).

3.2 Trace element composition of quartz and sulfides

The trace element composition of quartz was only determined for A- and B-type veins due to the lack of quartz in the later vein types. Quartz from A-type and early B-type veins (B1) contains the highest Ti content (43-145; 24-183 ppm), followed by quartz from the late B-type veins (B2) (28-86 ppm). Aluminum (103-1840 ppm), Sb (<1.3 ppm) and As (<12 ppm) display similar concentrations in quartz irrespective of their vein type, while Ge (0.7-1.7 ppm)

decreases in quartz from the A-type to the B-type veins.

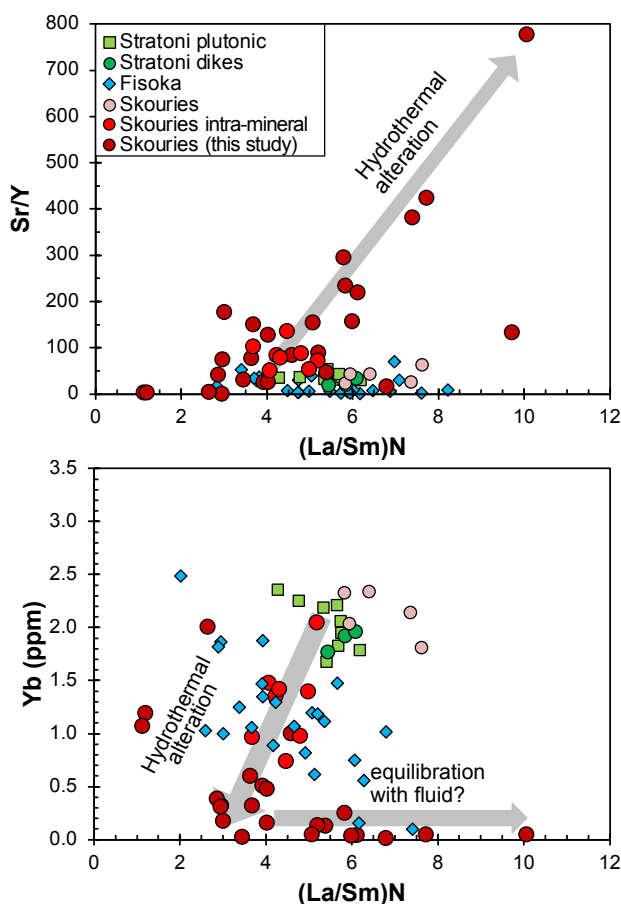


Figure 2. Trace element composition of host rocks (Drill core SOP134) from Skouries showing correlating Sr/Y and (La/Sm)_N with increasing potassic alteration, as well as decreasing (La/Sm)_N with decreasing Yb and increasing alteration. Literature data from Skouries and intrusions close to the deposit are added for comparison (Siron et al. 2018).

Bornite, chalcopyrite and pyrite were analyzed for their trace element content. Bornite is the major carrier of Te, Pb, Bi, Se, Ge and Ag, while Zn, Ga and In are highest in chalcopyrite and Co, Ni, As, Sb, Au and Tl are hosted by pyrite (Figure 3). Interestingly, bornite and chalcopyrite show relatively homogeneous trace element contents between different vein generations, while pyrite displays significant compositional variations.

Trace elements in pyrite vary systematically between the different vein generations and show increasing Sb, Au, Ag, Zn and Pb contents from the early B-type to the C-type veins, while As, Te are enriched in C-type veins. Furthermore, pyrite from D-type veins is generally depleted in most trace elements (e.g., Sb, Pb, Bi, Au, Ag, Zn) relative to the other vein types. Lastly, pyrite from early B-type veins is characterized by low trace element ratios (Sb/As < 0.01, Co/As < ~1), while later B-, C- and D-type veins show higher trace element ratios (Sb/As = 0.01 to 1, Co/As = 0.1 to 100).

4 Fingerprinting hydrothermal processes on the deposit scale

4.1 Chemical alteration of the host rock

The replacement of plagioclase by K-feldspar and of pyroxene, amphibole and magmatic biotite by hydrothermal biotite is typical for the potassic alteration of monzonites and syenites in porphyry Cu-Au systems (Sillitoe 2010). The extreme REE and HFSE depletion and decreasing light REE relative to middle REE with increasing alteration, resulting in lower $(La/Sm)_N$ values, indicate the mobilization of light REE by a high temperature fluid capable of transporting such incompatible elements (Figure 2).

However, the rocks with strongest alteration have elevated $(La/Sm)_N$ and Eu anomalies, thus probably indicating the equilibration of the highly altered rocks with the fluids. Consequently, we suggest that the typical high Sr/Y and La/Yb ratios of the host rocks observed in other porphyry systems (Loucks 2014) may also result from alteration processes and not always preserve the primary magmatic signature.

4.2 Constraints on the fluid evolution

The Ti-in-Quartz thermometer was applied (Ti activity = 1, equilibrium with rutile, $p_A=0.5$ kbar, $p_{B1,B2}=0.4$ kbar to calculate the temperatures of quartz precipitation (Huang and Audétat 2012). Calculated temperatures yielded within error similar temperatures for A-type veins ($600^\circ\text{C} \pm 48^\circ\text{C}$) and early B-type veins ($610 \pm 60^\circ\text{C}$) and lower temperatures for the late B-type veins ($545 \pm 45^\circ\text{C}$) (Figure 3).

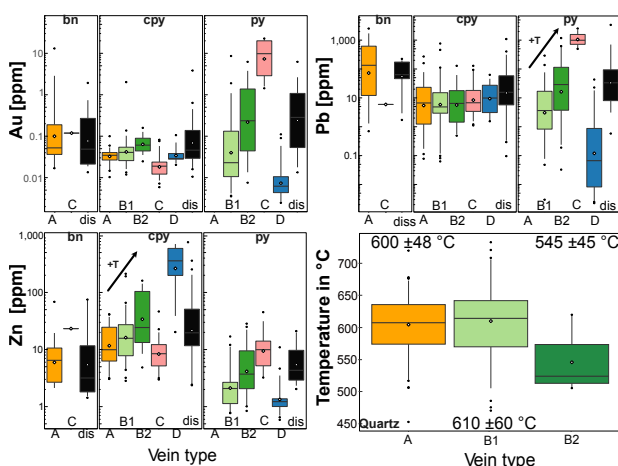


Figure 3. Boxplots of Au, Pb and Zn in bornite (bn), chalcopyrite (cpy) and pyrite (py) from the different vein generations and calculated temperatures for quartz from A-, B1-, and B2-type veins using the Ti-in-quartz thermometer (Huang and Audétat 2012).

Preliminary fluid inclusion results, which show a complex composition including NaCl and KCl, with minor CaCl_2 , FeCl_2 , and CO_2 , are within range of quartz temperatures for A-type veins. Homogenization temperatures range from 516 to

$>600^\circ\text{C}$ (salinities: 49-61 wt.% equiv. NaCl) for liquid-rich brine inclusions and from 523 to $>600^\circ\text{C}$ (salinities: 11-13 wt.% equiv. NaCl) for vapor-rich inclusions. B2-type veins show homogenization temperatures from 446 to 484°C for liquid-rich brine inclusions (salinities: 48-54 wt.% equiv. NaCl) and from 451 to 496°C (salinities: 7.3-6.9 wt.% equiv. NaCl) for vapor-rich inclusions.

Trace elements, such as Ag, Sb, Zn and Pb are enriched in pyrite that precipitated from lower temperature fluids (Franchini et al. 2015). Indeed, these elements increase from early B-type veins towards later C-type veins (Figure 3). Correspondingly, chalcopyrite displays decreasing Cd/Zn ratios from A-type to late B-type veins, which is also known as a temperature proxy (George et al. 2018). These trace element variations combined with the quartz thermometry and preliminary fluid inclusion results therefore indicate decreasing fluid temperatures between the vein generations.

In contrast to the temperature-dependent variations in the sulfide chemistry from A- to C-type veins, the pyrite in the D-type veins is depleted in most trace elements (e.g., Pb, Au, As). Phase separation forms a high-Cl liquid phase and a low-Cl vapor phase causing fractionation between volatile (e.g., As, Sb) and less-volatile (e.g., Pb) elements (Keith et al. 2022). Based on the temperature-independent low As/Sb and high Ti/Pb ratios of pyrite from D-type veins, we conclude that the D-type veins formed from a Cl-rich liquid after phase separation ("boiled liquid"), which lost its As content to the respective vapor, while Pb precipitated from the liquid phase (Figure 4). The low As/Sb and Co/As ratios in pyrite from early B-type veins may further imply repeated vapor fractionation of the early fluid. The coexistence of vapor- and liquid-rich inclusions observed in the preliminary fluid inclusion data supports phase separation.

5 Occurrence of Au in the Skouries deposit

The Skouries deposit is enriched in Au, which can either occur as native Au inclusions in the vein stockwork or precipitated in solid solution in sulfide minerals.

Micro-scale native gold inclusions, which are primary based on petrological observations, are mainly present in chalcopyrite from A- and early B-type veins. The Au-As ratio in pyrite further indicates nano-scale inclusions in pyrite from late B-type veins that could not be detected by LA-ICP-MS (Figure 4). Native gold usually precipitates from an Au-oversaturated fluid, which can be achieved by reducing the stability of Au complexes due to a change in temperature, pressure or availability of S. Gold saturation during potassic alteration is typically controlled by the sulfur budget rather than the temperature, and especially phase separation can effectively decrease the availability of S, which lowers the solubility of Au complexes (Pokrovski et al. 2014). Furthermore, Au in solid solution mainly occurs in pyrite related to B- and C-type veins while

chalcopyrite in general and pyrite from the late-stage D-type veins are depleted in Au (Figure 3, 4). This suggests variable gold precipitation and enrichment processes during the different paragenetic stages.

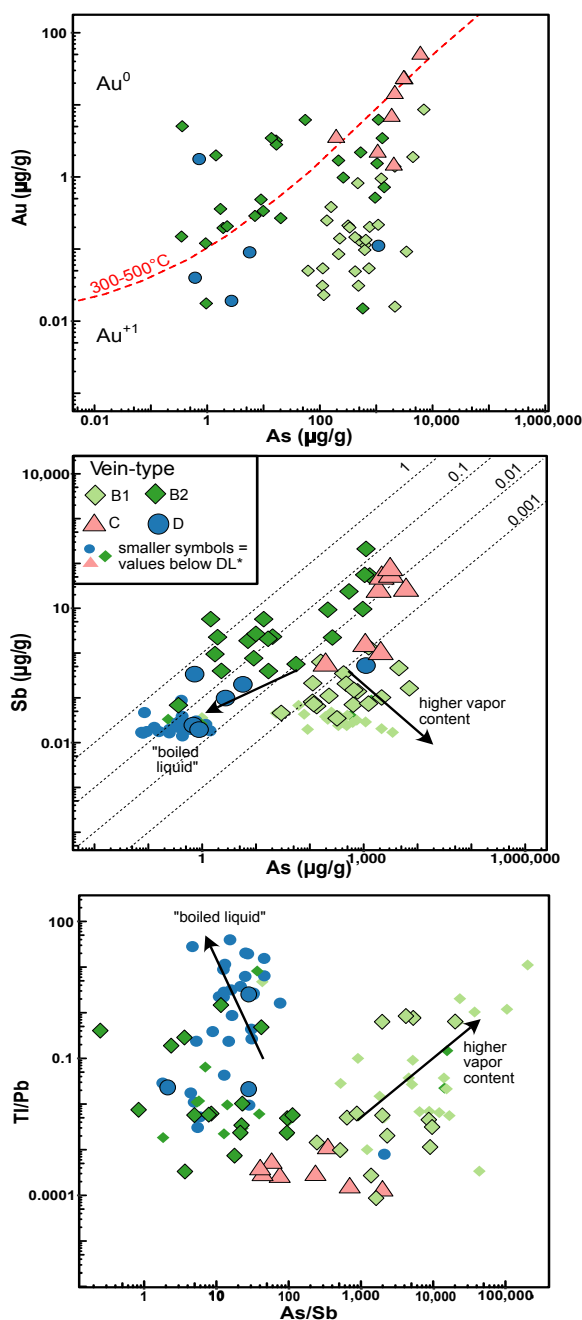


Figure 4. Trace elements and trace element ratios (As/Sb, TI/Pb) in pyrite from different vein generations indicative for phase separation and the vapor content in the fluid. The As-Au ratio gives the occurrence of Au in solid solution and as native inclusions based on the solubility limit of Au (Deditius et al. 2014). Values below detection as $DL/\sqrt{2}$.

6 Conclusion

We conclude that hydrothermal alteration changes incompatible trace element ratios like La/Yb and Sr/Y, believed to be typical signatures of magmatic

processes amongst others related to porphyry formation. Thus, host rocks need careful selection with respect to alteration before the interpretation of magmatic processes. The mineral composition suggests a decrease in temperature with the progressive evolution of the fluids and early phase separation observed in B-type vein sulfides. The fluid reached Au saturation during potassic alteration, probably caused by the early phase separation. This process effectively decreases the S availability in the fluid leading to Au oversaturation and hence precipitation of native gold and Au-rich sulfides. The residual liquid then precipitated sulfides with relatively low contents of As, Au and other trace elements in D-type veins.

Acknowledgements

Tim Baker is thanked for providing drill core samples and Helene Brätz for the support during the LA-ICP-MS analyses.

References

- Deditius AP, Reich M, Kesler SE, et al (2014) The coupled geochemistry of Au and As in pyrite from hydrothermal ore deposits. *Geochimica et Cosmochimica Acta* 140:644–670.
- Franchini M, McFarlane C, Maydagán L, et al (2015) Trace metals in pyrite and marcasite from the Agua Rica porphyry-high sulfidation epithermal deposit, Catamarca, Argentina: Textural features and metal zoning at the porphyry to epithermal transition. *Ore Geology Reviews* 66:366–387.
- George LL, Cook NJ, Crowe BBP, Ciobanu CL (2018) Trace elements in hydrothermal chalcopyrite. *Mineral mag* 82:59–88.
- Hahn A (2014) Nature, timing and geodynamic context of polymetallic mineralisation in the Kassandra mining district. Kingston University
- Huang R, Audétat A (2012) The titanium-in-quartz (TitaniQ) thermobarometer: A critical examination and re-calibration. *Geochimica et Cosmochimica Acta* 84:75–89.
- Keith M, Haase KM, Chivas AR, Klemd R (2022) Phase separation and fluid mixing revealed by trace element signatures in pyrite from porphyry systems. *Geochimica et Cosmochimica Acta* 329:185–205.
- Loucks RR (2014) Distinctive composition of copper-ore-forming arc magmas. *Australian Journal of Earth Sciences* 61:5–16.
- McFall KA, Naden J, Roberts S, et al (2018) Platinum-group minerals in the Skouries Cu-Au (Pd, Pt, Te) porphyry deposit. *Ore Geology Reviews* 99:344–364.
- Pokrovski GS, Akinfiev NN, Borisova AY, et al (2014) Gold speciation and transport in geological fluids: insights from experiments and physical-chemical modelling. *SP* 402:9–70.
- Sillitoe RH (2010) Porphyry Copper System. *Economic Geology* 105:3–41
- Siron CR, Rhys D, Thompson JFH, et al (2018) Structural Controls on Porphyry Au-Cu and Au-Rich Polymetallic Carbonate-Hosted Replacement Deposits of the Kassandra Mining District, Northern Greece. *Economic Geology* 113:309–345.

U-Pb ages and trace elements of zircons from Loei and Truong Son fold belts, northern Laos: Implication for porphyry deposit fertility

Peerapong Sritangsirikul¹, Sebastien Meffre¹, Khin Zaw¹, Ivan Belousov¹, Yi-Jen Lai², Alex Richards³, Punya Charusiri⁴

¹CODES Centre of Ore Deposit and Earth Sciences, University of Tasmania, Hobart, Tasmania 7001, Australia

²Macquarie GeoAnalytic, the Macquarie Analytical and Fabrication Facility (MAFF), Macquarie University, Sydney, New South Wales 2109, Australia

³Rio Tinto Exploration, Brisbane, Queensland 4001, Australia

⁴Morphology of Earth Surface and Advance Geohazards in Southeast Asia Research Unit (MESA RU), Department of Geology, Faculty of Science, Chulalongkorn University, Bangkok 10400, Thailand

Abstract. The Loei and Truong Son Fold Belts are well known as highly mineralized magmatic arc-related terranes in Southeast Asia. Zircon LA-ICP-MS studies provide U-Pb ages and magmatic fertility using trace elements of felsic to intermediate volcanic and plutonic rocks from ten prospects in the Loei and Truong Son fold belts, NW Laos region. The geochemical and geochronological analyses suggest at least three episodes of magmatism occurred in the region: Silurian-Devonian (434-411 Ma), Early to Middle Permian (299-277 Ma), and Late Permian to Middle Triassic (253-243 Ma). Key trace elements and ratios together with oxygen fugacity of magmas (e.g., Eu/Eu*, Dy/Yb, Ce/Nd, Δ FMQ) imply that the Phu Kham and the West of Vientiane area along the Mekong River are likely to be fertile for porphyry copper deposits. In contrast, the Pha Gnai and the other suites are less fertile. Therefore, zircon as a fertility indicator is a valuable tool to distinguish fertile magmatic suites from the barren suites in this area.

1 Introduction

The Loei (Loei-Phetchabun) Fold Belt (LFB) and the Truong Son Fold Belt (TSFB) are the most critical, highly mineralized volcano-magmatic arcs in mainland Southeast Asia. The NW-SE trending TSFB and the N-S trending LFB lies to the north of Khorat Plateau and the east of the Sukhothai Fold Belt and the Nan-Uttaradit Suture at the western margin of the Indochina terrane respectively (Figure 1A). The LFB consists of 1) Devonian-Carboniferous sedimentary rocks including claystones, shales, and sandstones with minor carbonates; 2) Carboniferous-Permian limestones and sandstones; 3) Triassic volcanoclastic rocks with minor claystones and limestones. 4) Late Paleozoic to Middle Triassic granitic rocks (Burrett et al. 2021; Khin Zaw et al. 2014; Shi et al. 2021). The TSFB consists of middle to upper Paleozoic volcano-sedimentary rocks along with late Paleozoic granitic rocks (Cromie et al. 2018; Zhang et al. 2020). Silurian granites and limestones also occur as the basement rocks in this terrane (Cromie et al. 2018).

The LFB hosts several major porphyry-related, copper-gold skarns and epithermal gold deposits such as Chatree deposit in Thailand (Salam et al. 2014). The porphyry-related skarn-type Cu-Au deposits (Puthep; PUT1 and PUT2, Phu Thap Fah, Phu Lon, French Mine) characterized by veins

typically centered on dioritic to granodioritic intrusions (Kamvong et al. 2014; Khin Zaw et al. 2014). Recently orogenic gold deposits are recorded (e.g., Phabon gold deposit, Guo et al. 2019) and stratabound Cu-Pb-Ag deposits (e.g., Ban Kiouchep, Zhang et al. 2020) were also reported.

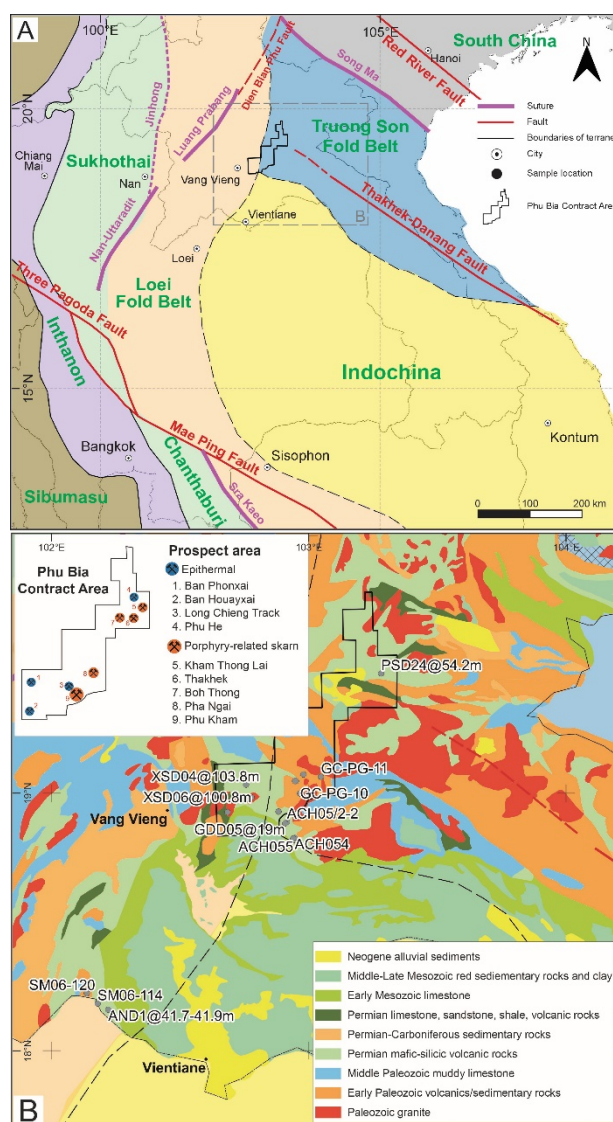


Figure 1. A Mainland Southeast Asia regional tectonic map **B** Simplified geological map of the Northwest Laos region.

Similar to the LFB, the TSFB contains major world-class porphyry-related skarn-type Cu-Au deposits (e.g., Phu Kham, Kamvong et al. 2014), epithermal Au deposits (e.g., Ban Houayxai, Manaka et al. 2014), sub-volcanic mesothermal Au deposits (e.g., Long Chieng Track, Leaman et al. 2019), sediment-hosted Au deposits (e.g., Sepon, Cromie et al. 2018) and orogenic gold deposits (Bounliyong et al. 2021). The geochemistry of zircons from volcanic and intrusive rocks using laser ablation inductively coupled plasma-mass spectrometry (LA-ICP-MS) has been used in mineralized fold belts worldwide to discriminate mineralized fertile magmas from pre-mineralization magmas and provides insights into complex petrogenesis that ended in a low-temperature, hydrous and oxidized fertile magma composition (e.g. Dilles et al. 2015; Leslie et al. 2022; Loucks et al. 2020; Lu et al. 2016). These techniques provide detailed geochemical information to investigate the petrogenesis of mineralized intrusive and volcanic rocks mainly in northern Laos by documenting the key trace element ratios (e.g., Eu/Eu*, (Ce/Nd)/Yb, Gd/Yb, and Hf) in zircons. These data are compared to discriminate the evolution of mineralized versus barren magmas highlighting the importance of zircon trace elements data and mineral fertility studies.

2 Methodology

2.1 Zircon LA-ICP-MS

The twenty-one selected zircon mounts are prepared from several Cu-Au and Au deposit and prospect sites in Laos (Figure 1B); 1) West of Vientiane along Mekong (porphyry skarn Cu \pm Au), 2) Ang Noi intrusion-related Au Prospect, 3) Ban Nape intrusion-related Prospect, 4) Ban Houayxai epithermal Au-Ag Deposit, 5) Long Chieng Track (LCT) low-S epithermal Au-Ag-Cu Deposit, 6) Phu Kham porphyry-related skarn Cu (-Au) Deposit, 7) Ban Phonxai epithermal Au Deposit, 8) Nhon Nhang sediment-hosted Cu-Au Prospect, 9) Phu He low-S epithermal Au-Ag Prospect, and 10) Pha Gnai porphyry-related skarn Cu \pm Au Prospect. The zircons were analyzed using an Agilent 7900 quadrupole ICPMS at CODES, the University of Tasmania, coupled to COMPex Pro 110 excimer laser operating at 193 nm wavelength and equipped with an ASI S155 laser ablation cell capable of holding 20 1-inch size grain mounts. The analysis was performed at least 1 hour after the ignition of the mass spectrometer to stabilize the machine. The primary and secondary standards zircons were analyzed at the beginning, at the end, and throughout the analytical run. The downhole fractionation, instrument drift, and mass bias correction factors for Pb/U ratios on zircons were calculated using analyses on the primary standard (91500) and checked on secondary standards (Temora), and Plešovice). The $^{207}\text{Pb}/^{206}\text{Pb}$ ratio was calibrated using analyses on NIST610. The zircons were analyzed with a laser beam at 29 μm spots at

5 Hz and approximately 2 J/cm² laser fluence. The 30-second gas blank was analyzed at the beginning of each measurement and followed by 30 seconds of ablation. The ablation was performed in He atmosphere flowing at 0.35 L/min and mixed with Ar straight after ablation flowing at 1.05 L/min. Each element was measured successively every 0.253 seconds and recorded for data reduction. Isotopic masses collected were ^{31}P , ^{49}Ti , ^{56}Fe , ^{89}Y , ^{91}Zr , ^{93}Nb , ^{139}La , ^{140}Ce , ^{141}Pr , ^{146}Nd , ^{147}Sm , ^{153}Eu , ^{157}Gd , ^{159}Tb , ^{163}Dy , ^{165}Ho , ^{166}Er , ^{169}Tm , ^{172}Yb , ^{175}Lu , ^{178}Hf , ^{181}Ta , ^{202}Hg , ^{204}Pb , ^{206}Pb , ^{207}Pb , ^{208}Pb , ^{232}Th , ^{235}U and ^{238}U . The U/Pb geochronology data reduction was conducted using the LADR software program. Cathodoluminescence (CL) imaging techniques were obtained and employed to document zircon grain structure at Central Science Laboratory at the University of Tasmania, using a FEI MLA650 scanning electron microscope (SEM). The CL images were the basis for locating and determining the options for LA-ICP-MS and Hf isotope analytical sites.

3 Zircon ages and trace elements

3.1 U-Pb ages

In Figure 2, U-Pb analyses from the zircons suggest that at least three episodes of magmatism occurred in the LFB and TSFB: Silurian-Devonian (434-411 Ma), Early to Middle Permian (299-277 Ma), and Late Permian to Middle Triassic (253-243 Ma). The Devonian-Carboniferous magmatic episode (ca 370-310 Ma) previously reported (Khin Zaw et al. 2014; Salam et al. 2014; Shi et al. 2021) was not observed in this study and probably occur in different locations. The results show that Early to Late Permian (299-250 Ma) magmatism is the dominant magmatic activity associated with epithermal and porphyry mineralization consistent with previous geochronology results (Khin Zaw et al., 2014; Kamvong et al., 2014; Shi et al., 2021).

3.2 Porphyry fertility

Zircon chondrite normalized REE shows light rare earth elements (LREE) depletion relative to the heavy rare earth elements (HREE) with positive Ce anomalies. This pattern is typical of zircons worldwide. Most analyzed zircons have similar REE patterns. However, samples from the Phu Kham porphyry-related skarn Cu (-Au) Deposits (GDD05@19m), Long Chieng Track (LCT) low-S epithermal Au-Ag-Cu Deposits (ACH067 and LSD9@50.9m), and West of Vientiane site (SM06-114) have anomalously high Ce with either a relatively small or no negative Eu anomaly. High oxidation state, magmatic water content, high S content, and a high degree of fractionation are key features of magmas fertile for porphyry Cu mineralization. The geochemistry of zircon is a robust, helpful tool for evaluating the mineralization

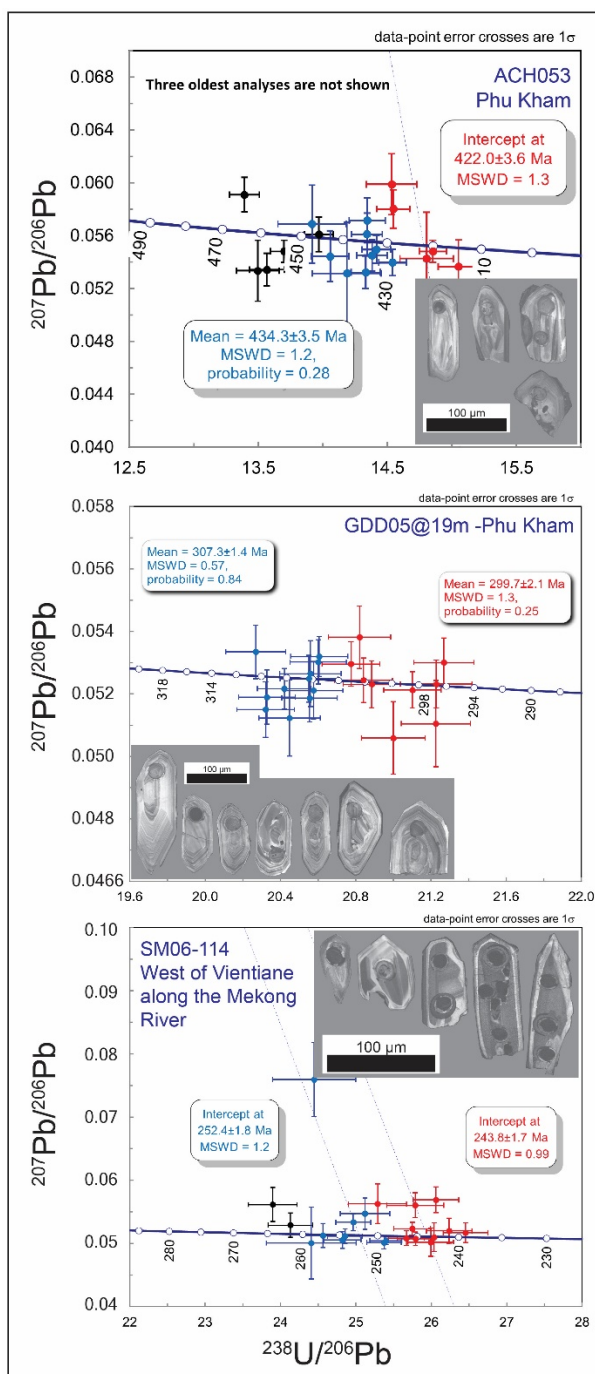


Figure 2. U-Pb Concordia isotopic age data for representative samples from the magmatic rocks along with their representative cathodoluminescence (CL) images from zircons.

potential in the porphyry environment (e.g., Lee et al., 2021; Loucks et al. 2020; Lu et al. 2016) and geochemical composition of zircon and ratios such as Eu/Eu^* , $(\text{Ce}/\text{Nd})/\text{Y}$, $104^*(\text{Eu}/\text{Eu}^*)/\text{Y}$, Hf (ppm), Dy/Yb , have been widely used as fertility indicators to discriminate those fertile magmas from barren magmas (e.g., Lu et al. 2016). Chondrite-normalized rare earth element pattern of zircon from the dacite porphyry from Phu Kham (GDD05@19m) demonstrates typically low abundances of LREE and relatively high HREE with positive Ce and negative Eu anomalies that are consistent with the signature

of oxidized and hydrous melts. Likewise, zircons from a quartz diorite from the West of Vientiane along the Mekong River (SM06-114), rhyolite porphyry (ACH067), and dacite (LSD09@50m) from the Long Chieng Track (LCT) also show large positive Ce anomaly with the small Eu anomaly that is typical of magmas fertile for porphyry Cu deposits. This contrasts with the other intrusive suites that display smaller positive Ce and more negative Eu anomalies. To further investigate the oxidation state of the magmas, the ΔFMQ values were calculated (fayalite-magnetite-quartz fO_2 buffer: calculated using oxybarometer method using Ce, U, and Ti in zircon from Loucks et al. 2020). The data clusters in three distinct groups of analyses with Permian and Triassic zircons from Phu Kham and Triassic zircons from West of Vientiane are from strongly oxidized magmas and Silurian zircons from the Phu Kham and LCT are from strongly reduced magmas (Figure 3). Several different thresholds have been used to discriminate intrusions that are fertile and non-fertile for porphyry deposits, (e.g., $\text{Eu}/\text{Eu}^* > 0.4$, Ballard et al. 2002; Dilles et al. 2015; $\text{Eu}/\text{Eu}^* > 0.3$, $10,000^*(\text{Eu}/\text{Eu}^*)/\text{Y} > 1$, $(\text{Ce}/\text{Nd})/\text{Y} > 0.01$ and lower $\text{Dy}/\text{Yb} < 0.3$, Lu et al. 2016). The dacite porphyry from the Phu Kham and quartz diorite from the West of Vientiane have the high Eu/Eu^* (> 0.5), and low Dy/Yb (< 0.2) are typical of hydrous magmas characterized by early amphibole and clinopyroxene crystallization and suppression of plagioclase crystallization. In contrast, most of the zircons from other magmatic rocks in Laos have a lower Eu/Eu^* (< 0.5). Zircons from some of the Long Chieng Track and Pha Gnai samples also had high values of Eu/Eu^* but show lower ΔFMQ values and are therefore considered less prospective. These analyses are also much more scattered on many of the trace element plots.

4 Conclusions

The Permo-Triassic magmatic suites from this study are identified to be more fertile than the Silurian-Devonian suites based on their zircon trace element compositions. The Phu Kham and the West of Vientiane area along the Mekong River are likely fertile for porphyry Cu deposits, whereas the Pha Gnai and the other suites are less fertile. Some of the Long Chieng Track samples are fertile, and further work is warranted in the area. This study suggests that zircon as a fertility indicator is a useful tool to distinguish fertile magmatic suites from the barren ones in this area.

Acknowledgments

This study has been financially supported by the Royal Thai Scholarship, Chulalongkorn University, Department of Mineral Resources (DMR), and Rio Tinto Exploration for the analytical costs.

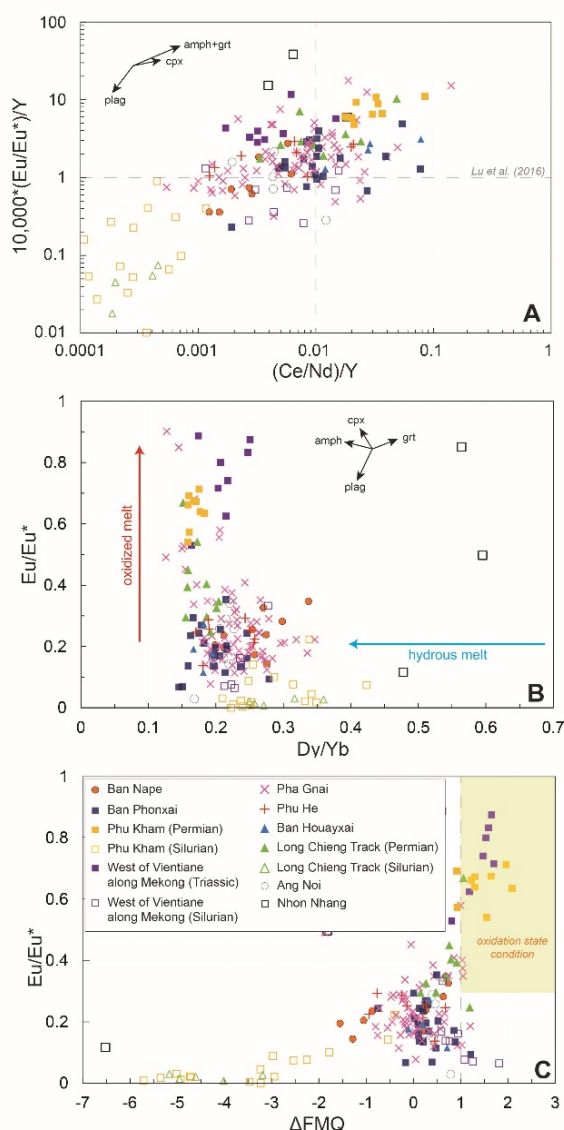


Figure 3. Zircon trace elements **A** $10,000 \cdot (\text{Eu}/\text{Eu}^*)/\text{Y}$ vs $(\text{Ce}/\text{Nd})/\text{Y}$ **B** Eu/Eu^* vs Dy/Yb **C** Eu/Eu^* vs ΔFMQ , differentiated based on trace element compositions in zircon related to oxidation and hydrous conditions.

References

- Bounliyong, P, Arribas, A, Watanabe, Y, Echigo, T, Wong, H, and Gold, K (2021). A new orogenic gold belt in Southeast Asia: Geology, mineralogy and genesis of the Vangtat gold deposit, Southeastern Laos. *Resource Geology*, 72(1).
- Burrett, C, Udachon, M, and Thassanapak, H (2021). The Truong Son, Loei-Phetchabun, and Kontum Terranes in Indochina: Provenance, Rifting, and Collisions. *Frontiers in Earth Science*, 9, 289.
- Cromie, PW, Makoundi, C, Zaw Khin, Cooke, DR, White, N, and Ryan, C (2018). Geochemistry of Au-bearing pyrite from the Sepon Mineral District, Laos DPR, Southeast Asia: Implications for ore genesis. *Journal of Asian Earth Sciences*, 164, p. 194–218.
- Dilles, JH, Kent, AJR, Wooden, JL, Tosdal, RM, Koleszar, A, Lee, RG, and Farmer, LP (2015). Zircon compositional evidence for sulfur-degassing from ore-forming arc magmas. *Economic Geology*, 110(1), p. 241–251.
- Guo, L, Liu, S, Hou, L, Wang, J, Shi, M, Zhang, Q, Nie, F, Yang, Y, and Peng, Z (2019). Fluid Inclusion and H-O Isotope Geochemistry of the Phapon Gold Deposit, NW Laos: Implications for Fluid Source and Ore Genesis. *Journal of Earth Science* 2019 30:1, 30(1), p. 80–94.
- Kamvong, T., Khin Zaw, Meffre, S, Maas, R, Stein, H, and Lai, CK (2014). Adakites in the Truong Son and Loei fold belts, Thailand and Laos: Genesis and implications for geodynamics and metallogeny. *Gondwana Research*, 26(1), p. 165–184.
- Khin Zaw, Meffre, S, Lai, CK, Burrett, C., Santosh, M., Graham, I., Manaka, T., Salam, A., Kamvong, T., and Cromie, P (2014). Tectonics and metallogeny of mainland Southeast Asia — A review and contribution. *Gondwana Research*, 26(1), p. 5–30.
- Leaman, P, Manaka, T, Jarical, K, Villar, M, and Libao, JB (2019). The geology and mineralization of the Long Chieng Track (LCT) subvolcanic Au-Ag-Cu-Pb-Zn deposit, Lao PDR. *Ore Geology Reviews*, 106, p. 387–402.
- Lee, RG, Byrne, K, D'Angelo, M, Hart, CJR, Hollings, P, Gleeson, SA, and Alfaro, M (2021). Using zircon trace element composition to assess porphyry copper potential of the Guichon Creek batholith and Highland Valley Copper deposit, south-central British Columbia. *Mineralium Deposita*, 56(2), p. 215–238.
- Leslie, C, Meffre, S, Cooke, DR, Thompson, J, Howard, N, and Barker, A (2021). Complex Petrogenesis of Porphyry-Related Magmas in the Cowal District, Australia: Insights from LA ICP-MS Zircon Imaging. In *Tectonomagmatic Influences on Metallogeny and Hydrothermal Ore Deposits: A Tribute to Jeremy P. Richards v.2*, p. 159–180.
- Loucks, RR, Fiorentini, ML, and Henriquez, GJ (2020). New magmatic oxybarometer using trace elements in zircon. *Journal of Petrology*, 61(3).
- Lu, YJ, Loucks, RR, Fiorentini, M, Campbell MT, Evans, NJ, Yang, ZM, Hou, ZQ, Kirkland, CL, Parra-Avila, LA, and Kobussen, A (2016). Zircon Compositions as a Pathfinder for Porphyry Cu ± Mo ± Au Deposits*. *Society of Economic Geologists*, 19 (February 2019), p. 329–347.
- Manaka, T, Khin Zaw, Meffre, S, Vasconcelos, PM, and Golding, SD (2014). The Ban Houayxai epithermal Au-Ag deposit in the Northern Lao PDR: Mineralization related to the Early Permian arc magmatism of the Truong Son Fold Belt. *Gondwana Research*, 26(1), p. 185–197.
- Salam, A, Khin Zaw, Meffre, S, McPhie, J, and Lai, CK (2014). Geochemistry and geochronology of the Chatree epithermal gold–silver deposit: Implications for the tectonic setting of the Loei Fold Belt, central Thailand. *Gondwana Research*, 26(1), p. 198–217.
- Shi, M, Khin Zaw, Liu, S, Xu, B, Meffre, S, Cong, F, Nie, F, Peng, Z, and Wu, Z (2021). Geochronology and petrogenesis of Carboniferous and Triassic volcanic rocks in NW Laos: Implications for the tectonic evolution of the Loei Fold Belt. *Journal of Asian Earth Sciences*, 208, 104661.
- Zhang, Z, Shu, Q, Wu, C, Zaw, Khin, Cromie, P, Von Dollen, M, Xu, J, and Li, X (2020). The endogenetic metallogeny of northern Laos and its relation to the intermediate-felsic magmatism at different stages of the Paleotethyan tectonics: A review and synthesis. *Ore Geology Reviews*, 123p,

The apparent decoupling of magmatic and hydrothermal activities in the Chuquicamata District

Adrianna L. Virmond¹, David Selby², Dawid Szymanowski¹, Jörn-Frederik Wotzlaw¹, Cyril Chelle-Michou¹

¹Department of Earth Sciences, ETH Zurich

²Department of Earth Sciences, Durham University

Abstract. Understanding the primary controls on the formation of mineral deposits is fundamental to assist exploration geologists in finding more resources in an ever growing high-demand world. Even though Porphyry Copper Systems have been extensively researched, the primary controls on the tonnage of deposits are still poorly quantified. Recent studies suggest the timescales and physical parameters involved in the formation of such deposits might be the missing key control. Here we investigate the behemothian deposits of the Chuquicamata District in northern Chile and show that prolonged magmatic and hydrothermal activities were involved in their formation. Our high precision geochronology results point to the occurrence of multiple magmatic-hydrothermal events, separated in space and time. An unexposed intrusion could explain the temporal gap between hydrothermal and magmatic activities in the Chuquicamata District. A long lived magmatic history with pulsed hydrothermal events in the same area seem to favour the formation of oversized deposits without triggering eruptions.

1 Introduction

The development of new technologies and consequent pursuit of alternative greener sources of energy will increase significantly the demand for metals in the coming decades. Porphyry copper deposits are the main source of copper and other base metals that will continue to play a key role in future. Thus, these systems have been thoroughly studied and many important ore-forming processes are well understood. However, one remaining question regarding porphyry copper systems (PCS) addresses the size distribution of such deposits, which varies over 5 orders of magnitude (Singer et al. 2008).

Since some of the processes involved are common to those that occur in most magmas in arc settings, it has been suggested that giant PCS are simply the result of the “perfect alignment” of processes and conditions (Richards 2013). Recent studies applied numerical simulations and suggested physical parameters could be the primary controls on the size of the deposits (e.g. Chelle-Michou et al. 2017; Chiaradia & Caricchi 2022). Such simulations show that the volume and duration of magmatic activity have a key control over the total endowment of a deposit and that magma volumes necessary to generate some of the largest deposits are comparable to those required to produce super eruptions (Chelle-Michou et al. 2017; Chelle-Michou & Rottier 2021; Chiaradia & Caricchi 2022). The relative timing of hydrothermal and magmatic activities in the Chuquicamata porphyry system, a

behemothian deposit located in northern Chile, is investigated here.

2 Geological Background

The Eocene-Oligocene metallogenic belt of northern Chile hosts many of the country's most important copper deposits, including the behemothian Chuquicamata, one of the biggest deposits in the world, with more than 100 Mt of copper and a mining history of over a century (Ossandón et al. 2001; Rivera et al. 2012; Figure 1). The Chuquicamata Intrusive Complex (CIC; Tomlinson et al. 2018) comprises the intrusive rocks associated with the Cu-Mo mineralization at the Chuquicamata and Radomiro Tomic deposits. It occurs as a NNE 14 km-long, 0.7–2 km-wide west-dipping subvertical dike that outcrops mostly within the mines, extending from Chuquicamata to north of the Radomiro Tomic mine (Rivera et al. 2012). In Chuquicamata, the unit presents, to the east, both intrusive and fault contacts with the Triassic East and Elena Granodiorites and Jurassic metasedimentary rocks of the Caracoles Group (Tomlinson et al. 2018). To the west, it is truncated by the West Fissure, which juxtaposes the complex against the Eocene Fortuna Complex (Ossandón et al. 2001; Rivera et al. 2012; Tomlinson et al. 2018). Towards the north, within the Radomiro Tomic mine, the complex presents intrusive contacts with the Elena Granodiorite to the east and to the west (Rivera et al. 2012).

The CIC is composed of three main units. The Este porphyry is the most abundant lithology, comprising most of the CIC. It is a granodiorite with “crowded” texture, abundant phenocrysts (plagioclase, biotite, deformed quartz, titanite and hornblende) in a fine-to coarse- groundmass composed of quartz and K-feldspar (Ossandón et al. 2001; Arnot 2003). Smaller bodies of texturally different porphyries intrude the Este porphyry: (1) the Banco porphyry, with bimodal size distribution of plagioclase phenocrysts, aphanitic groundmass (Arnot, 2003), often described as “more porphyritic” than Este porphyry (Ossandón et al. 2001; Rivera et al. 2012, Tomlinson et al. 2018); and (2) the Oeste porphyry, which presents a finer, aplitic groundmass, and lower crystallinity (Ossandón et al. 2001, Arnot 2003, Rivera et al 2012). A fourth variety of porphyry, the Fino porphyry, is reported only in the Radomiro Tomic mine. It differs from the Este porphyry mainly by presenting smaller biotite in the groundmass (Cabrera 2011; Tomlinson et al. 2018).

Previous work in the CIC reported that sharp intrusive contacts are observed only between Este and Banco porphyries, whereas the contact between Oeste and Este is diffuse and often gradational (Ossandón et al. 2001). The Fino porphyry is intruded by the Oeste Porphyry in the Radomiro Tomic mine (Tomlinson et al. 2018).

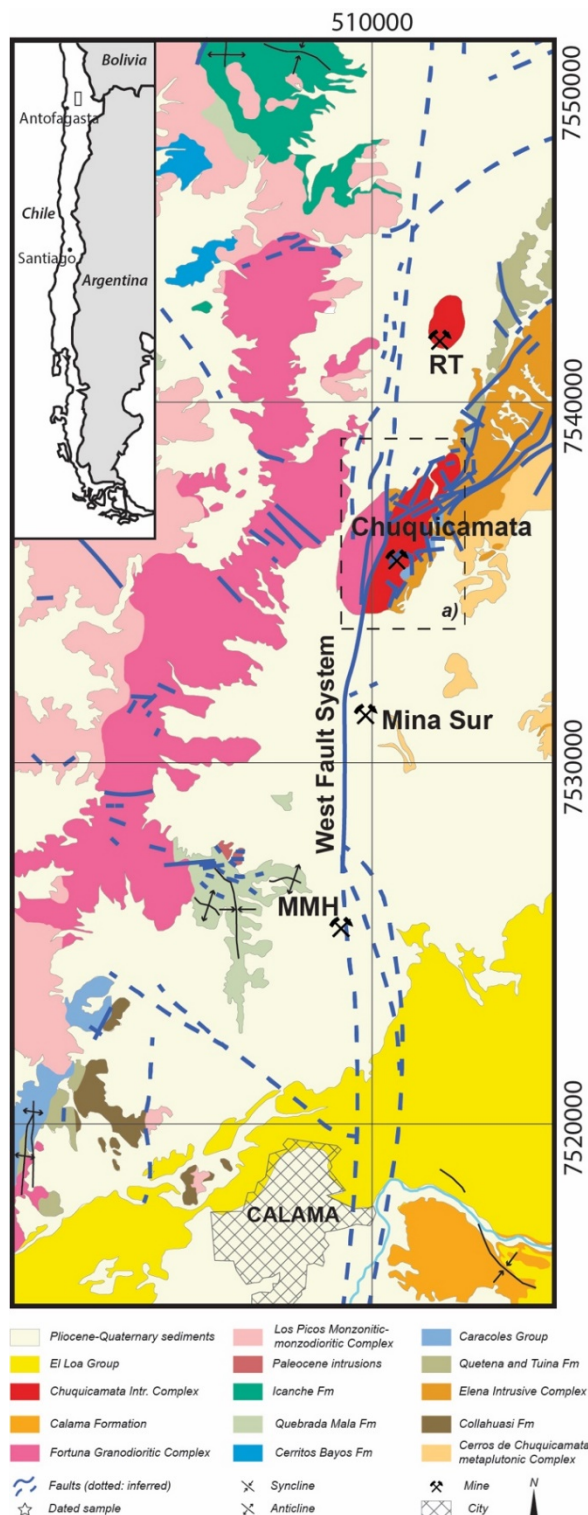


Figure 7 – Simplified geological map of the Chuquicamata District, modified after Rivera et al 2012.

Previous geochronological studies on the Chuquicamata District identified two ages of porphyry intrusion. The Este Porphyry yields zircon

U-Pb SHRIMP age of 35.2 ± 0.4 Ma (Ballard et al. 2001; Campbell et al. 2006) whereas the Oeste and Banco Porphyries yield younger and identical crystallization ages (34.0 ± 0.3 and 34.1 ± 0.3 Ma, respectively, Ballard et al. 2001; Campbell et al. 2006). Recent Re-Os molybdenite dates for the Chuquicamata mine, constrain the mineralization between 32.9 ± 0.2 and 31.9 ± 0.2 Ma (Barra et al. 2013). The long-lived protracted magmatic-hydrothermal history of Chuquicamata led authors to suggest superimposed events that ultimately produced the giant deposit (e.g. Ballard et al. 2001).

3 Materials and methods

3.1 Sample summary

Our geochronological investigation covers all lithologies found in the CIC, including a north - south spatial coverage of Este porphyry, the most abundant unit. Molybdenite occurring both in sheeted “blue veins” and small B-type veins were sampled.

3.2 Zircon U-Pb Geochronology

Zircon separates were obtained by conventional techniques (crushing, panning, sieving and density separation using a heavy liquid). After picking, the grains were annealed (900°C furnace for 48-60 h) and mounted in epoxy mounts. Preliminary U-Pb dating and trace element compositions of the outer rims of the crystals were obtained using LA-ICP-MS, in order to characterize the last magma from which the zircons crystallized. Afterwards, the grains are polished and cathodoluminescence (CL) images are obtained for textural characterization. A second LA-ICP-MS session was conducted on the cores and rims of the same grains to obtain dates and trace element compositions.

After data reduction, around 10 to 15 zircon crystals from each sample were selected for high precision geochronology using Chemical Abrasion Isotope Dilution Thermal Ionization Mass Spectrometry (CA-ID-TIMS). Grains were selected based on absence of inclusions and inheritance and homogeneity of the grain.

All LA-ICP-MS work was conducted in the Institute of Geochemistry and Petrology at ETH Zurich, using a 193-nm Resolution (S155) ArF excimer laser coupled to an Element SF-ICP-MS. CA-ID-TIMS analyses were conducted in the same institute and the samples were measured with a TRITON Plus thermal ionization mass spectrometer using protocols modified from von Quadts et al. (2016) and Wotzlaw et al. (2017).

3.3 Molybdenite Re-Os Geochronology

Molybdenite separates were prepared by handpicking under a binocular from samples that underwent crushing in the hydraulic press, dry sieving (fraction $<300\mu\text{m}$ and $>63\mu\text{m}$), magnetic

separation and density concentration by heavy liquid. Some samples were handpicked from fractions prepared following the HF dissolution protocol of Lawley and Selby (2012), more suitable for fine-grained molybdenite enclosed in quartz. Re-Os analyses were performed in the Source Rock and Sulphide Geochronology and Geochemistry Laboratory in Durham University.

4 Relative timing of magmatic and hydrothermal activities in Chuquicamata

Zircon U-Pb high precision geochronology shows the porphyry units present broad distribution of ages, lasting up to 1 Myr at the hand-sample scale. Within the Este porphyry, individual zircon dates tend to be older in the northern part of the CIC. Towards south, the zircon distribution tends to be much narrower (Figure 2).

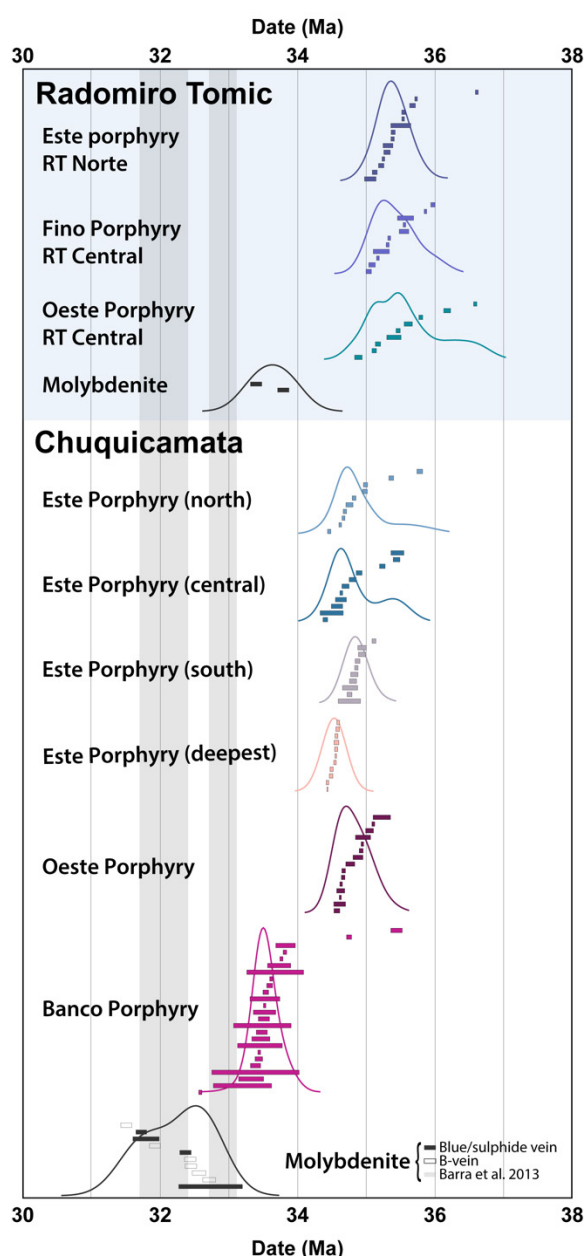


Figure 8 – Geochronological summary of the Chuquicamata Intrusive Complex. Each bar is an

individual date with its associated 2σ and the curves represent KDE for each sample. For the porphyries, the zircon U-Pb TIMS date is presented while for molybdenite, the Re-Os date is shown.

We interpret the youngest zircon dates as the emplacement ages for each sample. In Radomiro Tomic, emplacement ages are very similar between different porphyries, and up to 500 kyr older than in Chuquicamata. The Oeste porphyry in Radomiro Tomic has a slightly younger emplacement age, consistent with crosscutting relationships (e.g. Cabrera 2011).

In the Chuquicamata mine, the Este porphyry mostly presents similar emplacement ages (within uncertainty) regardless of spatial location. The Oeste porphyry presents indistinguishable zircon date distribution compared to the Este porphyry. Despite being considered up to 1 Myr younger (e.g. Ballard et al 2001; Campbell et al. 2006) our preliminary data suggest the Oeste porphyry is closely associated with Este porphyry and possibly reflects a local textural variant of the same unit. High precision zircon dating of the Banco porphyry confirm it is a younger intrusion in the system, emplaced up to 2 Myrs after the Este Porphyry.

The preferential occurrence of older zircon grains only in the northern part of the CIC (including Radomiro Tomic and the north of Chuquicamata) is coincident with samples topographically higher. This suggests older parts of the underlying magma reservoir are preferentially sampled in the northern part of the deposit, which appears to be further away from the feeding zone. The southernmost samples also come from deeper parts of the deposit (Figure 3), where the more homogeneous distribution of zircon dates occur. This could suggest either that this zone is fed by a more homogeneous section in the underlying pluton, or potentially that it's closer the feeder zone of the megadyke.

Molybdenite Re-Os geochronology results suggest a pulsed behaviour on hydrothermal activity in the CIC (Figure 2) and a clear correlation between vein type and molybdenite age. The oldest molybdenite ages are obtained in the Radomiro Tomic deposit, separated by a few ten of thousands of years from the hydrothermal activity within the Chuquicamata mine. There, molybdenite crystallized for over 1 Myr and the obtained dates suggest one continuous long-lived hydrothermal event. Alternatively, our data reflect a pulsed behaviour for molybdenite crystallization within the Chuquicamata mine that was unresolvable with high-precision Re-Os geochronology. In Chuquicamata the older set of molybdenite dates only marginally overlap with the Banco porphyry and may in fact be younger.

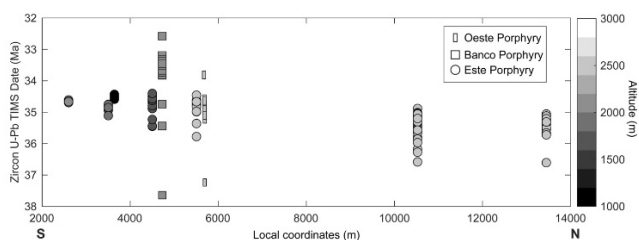


Figure 9 – Spatial distribution of zircon U-Pb dates for the CIC. Samples are color-coded according to the altitude they were taken from (true depth calculated with dip of drill cores).

5 Preliminary conclusions

We investigated the timescales of magmatic and hydrothermal activity in the Chuquicamata Intrusive Complex (CIC) using zircon and molybdenite high precision geochronology. Preliminary results suggest complex spatial distribution of dates, suggesting different parts of the underlying magma reservoir were preferentially sampled in different moments of time or crystallized zircons at different moments.

The apparent age gap between the emplacement of the porphyries and the hydrothermal activity observed in the Chuquicamata deposit raises an alert to assuming that the mineralized porphyries are necessarily genetically linked to the mineralization. In the CIC, it seems that the volumetrically minor Banco porphyry is the most temporally associated with the mineralization. However, the youngest molybdenite dates suggest there's potentially another unexposed intrusion, deep in the system and responsible for the mineralization, as previously suggested based on younger Ar-Ar and K-Ar dates obtained for the district (e.g. Ballard et al 2001; Rivera et al 2012).

Long lived magmatic systems with multiple episodes of intrusion and hydrothermal activity are also observed in other giant deposits, such as El Teniente (Spencer et al. 2015) and they seem to be favorable to forming behemothian deposits such as the Chuquicamata District.

Acknowledgements

We would like to acknowledge the help and support of the geologists from Codelco (distrito Norte), in special Elizabeth Demané, Rodrigo Rojas, Giorgio Realini and their teams.

References

Arnot, A.M. (2003): Evolution of the Hydrothermal Alteration at the Chuquicamata Porphyry Copper System, Northern Chile, PhD thesis, Dalhousie University, 450 p.

Ballard, J.R., Palin, J.M., Williams, I.S., Campbell, I.H., and Faunes A., A. (2001): Two ages of porphyry intrusion resolved for the super-giant Chuquicamata copper deposit of northern Chile by ELA-ICP-MS and SHRIMP: *Geology*, v. 29, no. 5, p. 383–386.

Barra, F., Alcota, H., Rivera, S., Valencia, V., Munizaga, F., and Maksaev, V. (2013): Timing and formation of porphyry Cu-Mo mineralization in the Chuquicamata district,

northern Chile: New constraints from the Toki cluster: *Mineralium Deposita*, v. 48, doi:10.1007/s00126-012-0452-1.

Cabrera, J.B. (2011): Estudio petrográfico y petroológico de los porfidos alimentadores del distrito mina Radomiro Tomic, II Region, Chile Memoria para optar al título de geólogo: Universidad de Concepcion, 179 p.

Campbell, I.H., Ballard, J.R., Palin, J.M., Allen, C., and Faunes, A. (2006): U-Pb Zircon Geochronology of Granitic Rocks from the Chuquicamata-El Abra Porphyry Copper Belt of Northern Chile: *Excimer Laser Ablation ICP-MS Analysis: Economic Geology*, v. 101, no. 7, p. 1327–1344, doi:10.2113/gsecongeo.101.7.1327

Chelle-Michou, C., Rottier, B., Caricchi, L., and Simpson, G. (2017): Tempo of magma degassing and the genesis of porphyry copper deposits: *Scientific Reports*, v. 7, no. 1, p. 40,566, doi:10.1038/srep40566

Chelle-Michou, C., Rottier, B. (2021): Transcrustal magmatic controls on the size of porphyry Cu systems: State of knowledge and open questions, *Society of Economic Geologists*, p. 87–100, doi: 10.5382/SP.24.06

Chiaradia, M., Caricchi, L. (2022): Supergiant porphyry copper deposits are failed large eruptions. *Commun Earth Environ* 3, 107. <https://doi.org/10.1038/s43247-022-00440-7>

Krogh, T. E. (1973): A low-contamination method for hydrothermal decomposition of zircon and extraction of U and Pb for isotopic age determinations, *Geochimica et Cosmochimica Acta*, v.37, pp 485–494.

Lawley, C.J.M., and Selby, D. (2012): Re-Os Geochronology of Quartz-enclosed ultrafine molybdenite: Implications for Ore Geochronology: *Economic Geology*, v. 107, no. 7, p. 1499–1505, doi:10.2113/econgeo.107.7.1499.

Ossandón, G., Fréaut C, R., Gustafson, L.B., Lindsay, D.D., and Zentilli, M. (2001): Geology of the Chuquicamata mine: A progress report: *Economic Geology*, v. 96, no. 2, p. 249–270, doi:10.2113/gsecongeo.96.2.249.

Richards, J.P. (2013): Giant ore deposits formed by optimal alignments and combinations of geological processes: *Nature Geoscience*, v. 6, no. 11, p. 911–916, doi:10.1038/ngeo1920.

Rivera, S.L., Alcota, H., Proffett, J., Díaz, J., Leiva, G., and Vergara, M. (2012): Update of the Geologic Setting and Porphyry Cu-Mo Deposits of the Chuquicamata District, Northern Chile, in *Geology and genesis of major copper deposits and districts of the world: Society of Economic Geologists*, p. 19–54, doi:10.5382/SP.16.02.

Singer, D., Berger, V., and Moring, B. (2008): Porphyry copper deposits of the world: Database and grade and tonnage models: Open File Report.

Spencer, E. T., Wilkinson, J. J., Creaser, R. A., Seguel, J. (2015): The Distribution and Timing of Molybdenite Mineralization at the El Teniente Cu-Mo Porphyry Deposit, Chile: *Economic Geology*, v. 110, p. 387–421.

Tomlinson, A., Blanco, N., Dilles, J., Maksaev, V., and Ladino, M. (2018): Carta Calama, región de Antofagasta, in *Carta Geológica de Chile, Serie Geología Básica*, v. No.199: Servicio Nacional de Geología y Minería, p. 199

von Quadt, A., Wotzlaw, J.F., Buret, Y., Large, S.J., Peytcheva, I., and Trinquier, A. (2016): High-precision zircon U/Pb geochronology by ID-TIMS using new 1013 ohm resistors: *Journal of Analytical Atomic Spectrometry*, v. 31, no. 3, p. 658–665, doi:10.1039/c5ja00457h.

Wotzlaw, J.F., Buret, Y., Large, S.J., Szymanowski, D., and von Quadt, A. (2017): ID-TIMS U-Pb geochronology at the 0.1‰ level using 1013 W resistors and simultaneous U and 18O/16O isotope ratio determination for accurate UO2 interference correction: *Journal of Analytical Atomic Spectrometry*, v. 32, no. 3, p. 579–586, doi:10.1039/c6ja00278a

Sulfide resorption contributes to porphyry deposit formation in collisional settings

Wen-jie Xia¹, Rui Wang^{1†}, and Frances Jenner²

¹State Key Laboratory of Geological Processes and Mineral Resources, and Institute of Earth Sciences, China University of Geosciences, Beijing 100083, China.

²School of Environment, Earth and Ecosystem Sciences, The Open University, Walton Hall, Milton Keynes, Buckinghamshire MK7 6AA, UK.

Abstract. Production of Cu-rich melts via melting of sulfide-bearing lower crustal cumulates is thought to contribute to porphyry Cu formation at the post-collisional Gangdese belt (Tibet). We present new whole rock platinum group elements (PGE) data for ore-causative granites (OCG), ore-related granites (ORG) and barren granites (BG) from the Gangdese belt. The OCG, ORG and BG show indistinguishable PGE and Cu/Ag at a given MgO during differentiation down to ~2 wt.% MgO. These systematics, together with the occurrence of sulfides, indicate that the propensity for some Gangdese magmas to be ore-associated is unrelated to the magma source or the magmatic evolution. The behavior of PGE and Cu during differentiation of the OCG, ORG and BG diverges when melts evolve past 2 wt.% MgO. The OCG and ORG rapidly reached fluid saturation and released their metals to the hydrothermal fluids or silicate melts as a result of sulfide resorption. In contrast, BG show the sharp decrease in Cu until ~1 wt. % MgO. Because the OCG are cogenetic with the ORG granitoids and contain textural evidence for focused fluid exsolution, we suggest that metals in the magma reservoir have been efficiently extracted when the magma body reach fluid saturation.

1 Introduction

A series of post-collisional (Miocene; 22-12Ma) porphyry copper deposits (PCDs) with Cu reserves of over 45 Mt have been discovered in the Gangdese magmatic belt in southern Tibet (Hou et al. 2009, 2015a; Yang and Cooke 2019). The ore-forming magmas are generally characterized by felsic composition, high-K calc-alkaline signature, high-Sr/Y and La/Yb ratios and are regarded as the products of melting of lower crustal mafic cumulates (Hou et al. 2015b; Wang et al. 2015, 2018). Previous studies have suggested that the ore-related magmas are more Cu-rich than the barren magmas because of melting of sulfides in the lower crust (Hou et al. 2015b) and/or secondary sulfides formed during hydrous metasomatism of the subcontinental lithospheric mantle (SCLM) (Zheng et al. 2019). However, numerous geochemical studies have suggested that magmas that are enriched in economic metals (e.g., Cu and Au) are not a requirement for porphyry Cu mineralization (Halter et al. 2005; Zhang and Audétat 2017; Du and Audétat 2020; Hao et al. 2021). Instead, several magmatic processes occurring in the upper to middle crust are regarded as contributing factors for the formation of PCDs, such as: (1) magmatic-sulfide fractionation happening before or after volatile exsolution (Jenner et al. 2010; Wilkinson 2013; Hao et al. 2019; Park et al. 2019); (2)

cannibalization of pre-existing magmatic sulfides in upper crustal magmatic mush systems (Halter et al. 2005; Nadeau et al. 2010); (3) the volume of magma with “normal” Cu concentrations; and (4) the timescales of magmatic activity (Chelle-Michou et al. 2017; Chiaradia and Caricchi 2017; Chelle-Michou and Rottier 2021).

In this study, we selected a series of Gangdese belt post-collisional granitoids from ore-causative (source porphyry stocks for porphyry mineralization), ore-related (precursor pluton or mafic dykes emplaced penecontemporaneously with porphyry stocks) and barren magmatic systems and use a combination of petrology, geochemistry and literature data to track the role of magmatic sulfides during ascent, differentiation, and degassing of Gangdese magmas.

2 Geological Settings

The Gangdese belt in southern Tibet preserves a continuous magmatic record from the Late Triassic to the middle Miocene, which includes Neo-Tethyan oceanic slab subduction from 210-60 Ma and the India-Asia collision from 60-55 Ma (Zhu et al. 2011; van Hinsbergen et al. 2012; Wang et al. 2018). The Miocene post-collisional extension-related magmatism is characterized by predominantly potassic-ultrapotassic (trachytic) volcanism west of ~89°E and by granitoids with high-Sr/Y ratios (also named high-Sr/Y granitoids) east of ~89°E (Wang et al., 2018). There are also sparse Oligocene high-Sr/Y granitoids at Zedang and Miocene diorite porphyries at Xigaze and in the ore fields (Fig. 1). Many of the Oligocene to Miocene granitic intrusions contain mafic magmatic enclaves (MME), which have been attributed to mixing between the high-Sr/Y granitic magmas and more mafic mantle-derived ultra-potassic magmas (Zheng et al. 2012; Lu et al. 2015). Alternatively, others attribute the occurrence of MME at other settings (e.g., Nisyros volcano, Aegean arc, Greece) to entrainment of clasts of mafic material (e.g., sulfide-bearing cumulates) from the lower crustal magmatic mush zones that lie beneath intrusions and volcanoes (e.g., hot crustal mush zones, see Annen et al. 2006) by melts that are filtering upwards through the mush zones (Georgatou et al. 2022 and references therein). Indeed, the MME associated with the Gangdese Miocene Qulong porphyry magmas (Yang 2008) show a range in Cu from 130 to 1287 ppm, which are consistent with the high Cu

concentrations expected for sulfide-bearing mushes (e.g., Chen et al. 2020; Guo et al. 2020).

Most of the porphyry Cu-Mo deposits in the Gangdese belt, including two giant deposits (Qulong, 2200 Mt @ 0.5% Cu; Jiama, 1055 Mt @ 0.44% Cu; Yang and Cooke 2019) and several smaller deposits, were formed in the Miocene, in response to rapid uplift and erosion of the Gangdese arc batholiths (Yang et al. 2009). These porphyry Cu(-Mo) systems are centered around granitic porphyritic stocks which intruded into and/or through composite precursor batholiths. The ore-causative stocks and other ore-bearing pre-mineralization and post-mineralization intrusions are commonly high-Sr/Y granitoids emplaced at 30-12 Ma. At some deposits the ore-causative stocks are associated with post-mineralization high-Mg diorites or lamprophyre dykes (Yang and Cooke, 2019). This study focuses on: (1) the ore-causative granitoids (OCG); (2) pre- and post-mineralization high-Sr/Y ore-related granitoids (ORG); and (3) high and low Sr/Y granitoids that are unrelated to any deposits, which are referred to here as barren granitoids (BG).

3 Results

3.1 Major and trace elements

On the total alkalis ($\text{Na}_2\text{O}+\text{K}_2\text{O}$) versus silica (TAS) diagram, the Gangdese samples show a range in compositions from monzodiorite to granite, with SiO_2 concentrations ranging from 50.2 wt. % to 75.5 wt. %. The OCG samples span to higher SiO_2 concentrations than the ORG and BG samples, whereas the BG samples span to lower SiO_2 concentrations compared to the other samples. All samples show a decrease in FeO_T with decreasing MgO. The least fractionated primitive (highest MgO) ORG samples are offset to lower FeO_T at a given MgO compared to the BG samples. However, all three groups of samples with ~2 wt.% MgO show an overlapping range in FeO_T . Collectively, the Gangdese samples show an initial increase in P_2O_5 with decreasing MgO and an inflection in the trend at ~3-5 wt.% MgO.

3.2 Chalcophile elements

The majority of the Gangdese samples analyzed for this study show a decrease in Cu concentrations with decreasing MgO from 361 ppm Cu in the most primitive MgO-rich sample, down to 15.2 ppm Cu in the most fractionated MgO-poor sample. The OCG, ORG and BG samples show an overlapping and very narrow range in Cu until at ~2wt.% MgO, then the OCG and ORG samples decrease of an order of magnitude. Exceptions include most of altered samples and two of the OCG samples and one of the ORG samples, which Cu contents are two orders of magnitude greater than the fresh OCG and ORG samples with the similar MgO concentrations. With the exceptions of one high Ag and Au BG sample, the altered samples also have relatively higher Ag

and Au contents than the fresh ones (Fig. 1). In contrast, the altered samples are indistinguishable from the other samples on plots of MgO versus FeO_T , P_2O_5 , Sr, Y and Sr/Y, Pd, Pt, Ir and Ru (Fig. 1). When compared to literature data for samples from the Gangdese with <2 wt.% MgO, it is notable that many other OCG and ORG samples also have extremely variable Cu at a given MgO compared to literature BG data. The BG samples show a moderate decrease in Cu with decreasing MgO and an inflection in the trend at ~1 wt.% MgO.

4 Chalcophile and siderophile element systematics of the Gangdese magmas

With the exception of three high Cu samples and altered samples, the majority of the sample analyses presented here show an overlapping and extremely narrow range in Cu concentrations. Notably, these Cu trends are defined by Gangdese samples from a range of different localities but mostly from Qulong. Similarly, with the exception for Pt, the other PGE, Au and Ag contents of ORG and OCG samples also are indistinguishable from the BG samples until ~2 wt.% MgO (Fig 1). Hence, the propensity for Gangdese magmas to fuel the formation of ore-deposits in the region appears to be unrelated to the initial Cu of the parental melt or the initial behavior of Cu during magma differentiation down to ~2 wt.% MgO. Hence, melting of lower-crustal sulfide-bearing cumulates (Hou et al. 2015b; Zheng et al. 2019) as a model to explain why only some of the magmas are ore-causative appears to be inconsistent with the chalcophile elements systematics of the Gangdese magmas. In particular, the <2 wt.% MgO samples that were analyzed for this study, together with literature data for <2 wt.% MgO samples (Fig. 1) show an extremely large range in chalcophile elements at a given MgO compared to samples with >2 wt.% MgO. Thus, it is important to assess the potential cause (s) of the inflection of these chalcophile elements trends and the difference between the ore-associated samples and barren ones.

The PGE and Cu show extremely various after ~2 wt.% MgO. Several previous studies (Nadeau et al., 2010; Reekie et al. 2019; Wieser et al. 2020; Georgatou et al., 2022) all show that the chalcophile elements contents have an instant change after sulfide resorption. Together with the texture evidence of fluid exsolution (e.g., miarolitic cavities and UST quartz) found in OCG porphyries (Yang et al. 2009), we suggest that the sulfides in magma reservoir may be resorbed after fluid exsolution.

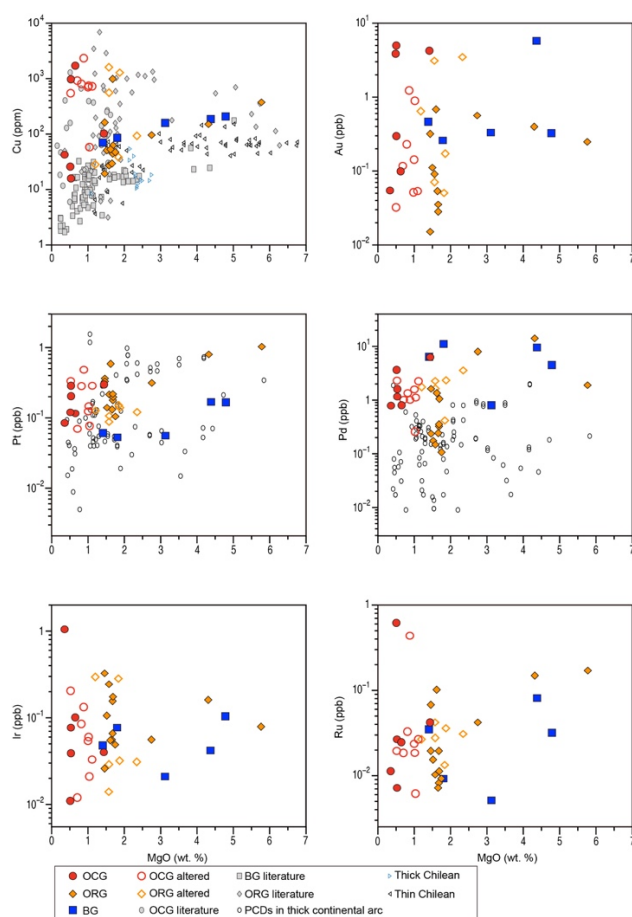


Figure 1. Plots of Cu, Au, Pt, Pd, Ir and Ru versus MgO for samples analyzed for this study, local previous study, and intrusions associated with porphyry deposits located in regions of thick ($\geq 55\text{km}$) Chilean crust.

Acknowledgements

This research was financially supported by the Chinese National Natural Science Foundation (42121002, 41973037 and 92162104) and the 111 Project (B18048). We thank Dr. Jian-feng Gao for support with analysis of PGEs.

References

- Annen C, Blundy JD, Sparks RSJ (2006) The Genesis of Intermediate and Silicic Magmas in Deep Crustal Hot Zones. *Journal of Petrology* 47:505–539. <https://doi.org/10.1093/petrology/egi084>
- Chelle-Michou C, Rottier B (2021) Transcrustal Magmatic Controls on the Size of Porphyry Cu Systems: State of Knowledge and Open Questions. In: *Tectonomagmatic Influences on Metallogeny and Hydrothermal Ore Deposits: A Tribute to Jeremy P. Richards (Volume I)*. Society of Economic Geologists, pp 87–100
- Chelle-Michou C, Rottier B, Caricchi L, Simpson G (2017) Tempo of magma degassing and the genesis of porphyry copper deposits. *Sci Rep* 7:40566. <https://doi.org/10.1038/srep40566>
- Chen K, Tang M, Lee C-TA, et al (2020) Sulfide-bearing cumulates in deep continental arcs: The missing copper reservoir. *Earth and Planetary Science Letters* 531:115971. <https://doi.org/10.1016/j.epsl.2019.115971>

- Chiaradia M, Caricchi L (2017) Stochastic modelling of deep magmatic controls on porphyry copper deposit endowment. *Sci Rep* 7:44523. <https://doi.org/10.1038/srep44523>
- Du J, Audétat A (2020) Early sulfide saturation is not detrimental to porphyry Cu-Au formation. *Geology* 48:519–524. <https://doi.org/10.1130/G47169.1>
- Georgatou A, Chiaradia M, Klaver M (2022) Deep to Shallow Sulfide Saturation at Nisyros Active Volcano. *Geochem Geophys Geosyst* 23:. <https://doi.org/10.1029/2021GC010161>
- Guo L, Jagoutz O, Shinevar WJ, Zhang H-F (2020) Formation and composition of the Late Cretaceous Gangdese arc lower crust in southern Tibet. *Contrib Mineral Petrol* 175:58. <https://doi.org/10.1007/s00410-020-01696-y>
- Halter WE, Heinrich CA, Pettke T (2005) Magma evolution and the formation of porphyry Cu-Au ore fluids: evidence from silicate and sulfide melt inclusions. *Miner Deposita* 39:845–863. <https://doi.org/10.1007/s00126-004-0457-5>
- Hao H, Campbell IH, Cooke DR, et al (2021) Geochronology, Petrogenesis and Oxidation State of the Northparkes Igneous Suite, New South Wales, Australia: Implications for Magma Fertility. *Economic Geology* 116:1161–1187. <https://doi.org/10.5382/econgeo.4825>
- Hao H, Campbell IH, Richards JP, et al (2019) Platinum-Group Element Geochemistry of the Escondida Igneous Suites, Northern Chile: Implications for Ore Formation. *Journal of Petrology* 60:487–514. <https://doi.org/10.1093/petrology/egz004>
- Hou Z, Duan L, Lu Y, et al (2015a) Lithospheric Architecture of the Lhasa Terrane and Its Control on Ore Deposits in the Himalayan-Tibetan Orogen. *Economic Geology* 110:1541–1575. <https://doi.org/10.2113/econgeo.110.6.1541>
- Hou Z, Yang Z, Lu Y, et al (2015b) A genetic linkage between subduction- and collision-related porphyry Cu deposits in continental collision zones. *Geology* 43:247–250. <https://doi.org/10.1130/G36362.1>
- Hou Z, Yang Z, Qu X, et al (2009) The Miocene Gangdese porphyry copper belt generated during post-collisional extension in the Tibetan Orogen. *Ore Geology Reviews* 36:25–51. <https://doi.org/10.1016/j.oregeorev.2008.09.006>
- Jenner FE, O'Neill HSTC, Arculus RJ, Mavrogenes JA (2010) The Magnetite Crisis in the Evolution of Arc-related Magmas and the Initial Concentration of Au, Ag and Cu. *Journal of Petrology* 51:2445–2464. <https://doi.org/10.1093/petrology/egq063>
- Lu Y-J, Loucks RR, Fiorentini ML, et al (2015) Fluid flux melting generated postcollisional high Sr/Y copper ore-forming water-rich magmas in Tibet. *Geology* 43:583–586. <https://doi.org/10.1130/G36734.1>
- Nadeau O, Williams-Jones AE, Stix J (2010) Sulfide magma as a source of metals in arc-related magmatic hydrothermal ore fluids. *Nature Geosci* 3:501–505. <https://doi.org/10.1038/ngeo899>
- Park J-W, Campbell IH, Malaviarachchi SPK, et al (2019) Chalcophile element fertility and the formation of porphyry Cu \pm Au deposits. *Miner Deposita* 54:657–670. <https://doi.org/10.1007/s00126-018-0834-0>
- Reekie CDJ, Jenner FE, Smythe DJ, et al (2019) Sulfide resorption during crustal ascent and degassing of oceanic plateau basalts. *Nat Commun* 10:82. <https://doi.org/10.1038/s41467-018-08001-3>
- van Hinsbergen DJJ, Lippert PC, Dupont-Nivet G, et al (2012) Greater India Basin hypothesis and a two-stage Cenozoic collision between India and Asia. *Proc Natl Acad Sci USA* 109:7659–7664. <https://doi.org/10.1073/pnas.1117262109>
- Wang R, Richards JP, Zhou L, et al (2015) The role of Indian

- and Tibetan lithosphere in spatial distribution of Cenozoic magmatism and porphyry Cu–Mo deposits in the Gangdese belt, southern Tibet. *Earth-Science Reviews* 150:68–94. <https://doi.org/10.1016/j.earscirev.2015.07.003>
- Wang R, Weinberg RF, Collins WJ, et al (2018) Origin of postcollisional magmas and formation of porphyry Cu deposits in southern Tibet. *Earth-Science Reviews* 181:122–143. <https://doi.org/10.1016/j.earscirev.2018.02.019>
- Wieser PE, Jenner F, Edmonds M, et al (2020) Chalcophile elements track the fate of sulfur at Kīlauea Volcano, Hawai‘i. *Geochimica et Cosmochimica Acta* 282:245–275. <https://doi.org/10.1016/j.gca.2020.05.018>
- Wilkinson JJ (2013) Triggers for the formation of porphyry ore deposits in magmatic arcs. *Nature Geosci* 6:917–925. <https://doi.org/10.1038/ngeo1940>
- Yang Z, Cooke DR (2019) Porphyry copper deposits in China. *Society of Economic Geologists Special Publication* 22: 133–1876
- Yang Z, Hou Z, White NC, et al (2009) Geology of the post-collisional porphyry copper–molybdenum deposit at Qulong, Tibet. *Ore Geology Reviews* 36:133–159. <https://doi.org/10.1016/j.oregeorev.2009.03.003>
- Zhang D, Audétat A (2017) What Caused the Formation of the Giant Bingham Canyon Porphyry Cu–Mo–Au Deposit? Insights from Melt Inclusions and Magmatic Sulfides. *Economic Geology* 112:221–244. <https://doi.org/10.2113/econgeo.112.2.221>
- Zheng Y-C, Hou Z-Q, Li W, et al (2012) Petrogenesis and Geological Implications of the Oligocene Chongmuda-Mingze Adakite-Like Intrusions and Their Mafic Enclaves, Southern Tibet. *The Journal of Geology* 120:647–669. <https://doi.org/10.1086/667812>
- Zheng Y-C, Liu S-A, Wu C-D, et al (2019) Cu isotopes reveal initial Cu enrichment in sources of giant porphyry deposits in a collisional setting. *Geology* 47:135–138. <https://doi.org/10.1130/G45362.1>
- Zhu D-C, Zhao Z-D, Niu Y, et al (2011) The Lhasa Terrane: Record of a microcontinent and its histories of drift and growth. *Earth and Planetary Science Letters* 301:241–255. <https://doi.org/10.1016/j.epsl.2010.11.005>

Can post-subduction porphyry Cu magmas form by partial melting of typical lower crustal amphibole-rich cumulates?

Jingbo Zhang^{1,2}, Jia Chang², Rui Wang¹, Andreas Audétat²

¹China University of Geosciences, Beijing, China

²University of Bayreuth, Bayreuth, Germany

Abstract. Lower crustal cumulates are considered a likely source for porphyry Cu-forming magmas in post-subduction settings. However, it remains controversial whether post-subduction porphyry Cu magmas can be produced by partial melting of lower crustal arc cumulates. Here we performed detailed petrographic and geochemical studies on exhumed lower to middle crustal cumulates from the Gangdese and Kohistan arc sections, and then conducted partial melting experiments at 1.5 GPa and 800–1150 °C using a piston cylinder press. Both the Gangdese and the Kohistan arc-root samples formed as cumulates in the lower to middle crust, but the Kohistan samples were subsequently brought into the garnet stability field during the India–Eurasia continental collision. Most of the Gangdese samples contain relatively high abundances of magmatic sulfides preserved in the form of monosulfide solid solution (MSS). In contrast, most of the Kohistan samples contain very low abundances of Cu-rich sulfides, probably due to metamorphic dehydration and up to 2 wt.% partial melting. Furthermore, the experimental partial melts contain much less K₂O, MgO, Cl and \pm S than typical post-subduction porphyry Cu-forming magmas. Hence, we conclude that the role of sulfide-rich arc cumulates in the formation of post-subduction porphyry Cu magmas has been severely overestimated.

1 Introduction

Porphyry Cu deposits are typically formed in subduction zones (Richards 2003; Sillitoe 2010). These subduction-related porphyry Cu magmas were produced by fractionation of mafic magmas derived from metasomatized asthenospheric mantle wedge, which provides the major source of metals (e.g., Cu and Au) and volatiles (e.g., H₂O, S and Cl) for the ore formation (Richards 2003, 2015b; Audétat and Simon 2012). However, large porphyry Cu deposits that are generally related to more potassium-rich magmas have been discovered in post-subduction settings (Hou et al. 2004; Richards 2009), particularly in the Alpine-Himalayan Tethyan orogen (Richards 2015a). Due to the absence of oceanic slab subduction during the formation of these deposits, the origin of the associated magmas has been a matter of debate. The most popular model proposes that post-subduction porphyry Cu magmas were produced by partial melting of lower crustal, amphibole-rich cumulates that were formed by earlier subduction-related magmatism, with or without minor contributions from lithospheric mantle-derived potassic to ultrapotassic mafic magmas (Hou et al. 2004; Yang et al. 2015; Wang et al. 2018). The lower crustal partial melting model suggests that dissolution of magmatic sulfides from amphibole-rich arc cumulates may have provided abundant Cu, Au

and S for post-subduction porphyry Cu magmas (Richards 2009; Hou et al. 2017; Chang and Audétat 2018; Hou and Wang 2019).

In this study, we first performed a detailed petrographic and geochemical study on two sets of exhumed amphibole (\pm garnet)-bearing lithologies at Lilong in the Tibetan Gangdese arc (SW China) and at Jijal in the Kohistan arc (NE Pakistan). Subsequently we conducted 14 piston-cylinder partial melting experiments on sulfide-rich hornblende and gabbro-norite from Gangdese at 1.5 GPa and 800–1150 °C. The results were used to reveal the petrogenesis of the Kohistan garnet-bearing lithologies and the behavior of magmatic sulfides during metamorphic and partial melting processes. Furthermore, the role of sulfide-rich, hydrous arc cumulates in the formation of post-subduction porphyry Cu magmas is discussed.

2 Results

2.1 Sulfide petrography and geochemistry

All the Gangdese arc-root samples contain magmatic sulfides in the form of sulfide inclusions within other minerals and in the form of interstitial sulfides. Well-preserved sulfide inclusions, consisting of pyrrhotite plus minor amounts of chalcopyrite and pentlandite (Figure 1a, b), are rather common in hornblende of hornblende samples. The hornblendites contain the most abundant magmatic sulfides (~0.4 vol.%). Sulfide inclusions in gabbroic rocks are hosted by both hornblende and plagioclase. Many sulfides (particularly the interstitial ones) are partially to completely altered to Fe oxide assemblages, in which tiny residual sulfides (pyrite or chalcopyrite) are often visible (Figure 1c). The sulfide inclusions consist dominantly of FeS, with 1.2–8.3 wt.% Cu, 0.1–1.5 wt.% Ni, and 0.2–0.4 wt.% Co.

In contrast, the Kohistan arc-root samples are generally very poor in magmatic sulfides. The olivine- and hornblende-clinopyroxene samples contain very rare sulfides that consist of pyrrhotite, pentlandite and chalcopyrite. No sulfides were found in the Kohistan garnet granulites. The modal abundance of sulfides in the garnet-bearing ultramafic samples (including the decomposed equivalents that can be identified) is highly variable from virtually none to ~1 vol.%. Hornblende or clinopyroxene in some samples contain a few well-preserved sulfide inclusions, all of which are

composed of pyrrhotite plus minor chalcopyrite \pm pentlandite/pyrite (Figure 1d). Garnets in some garnetites samples contain very Cu-rich sulfide inclusions that consist of either bornite plus chalcopyrite, pyrite \pm digenite (Figure 1e), or of chalcocite and digenite (Figure 1f). However, most sulfide inclusions and all intergranular sulfides in the garnet-bearing ultramafic samples were transformed into an intergrowth of greenschist-facies minerals (epidote + actinolite \pm albite \pm diopside), Cu-rich sulfides (chalcopyrite \pm bornite \pm digenite) and fine-grained hematite (Figure 1g, h). The Kohistan sulfide inclusions hosted in hornblende and clinopyroxene have similar compositions to the Gangdese MSS inclusions, but sulfide inclusions hosted in garnet show extremely variable Cu contents ranging from 12 to 80 wt.%.

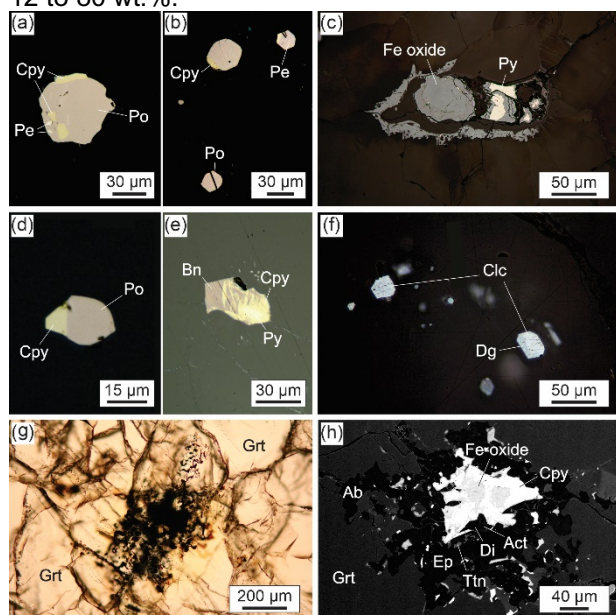
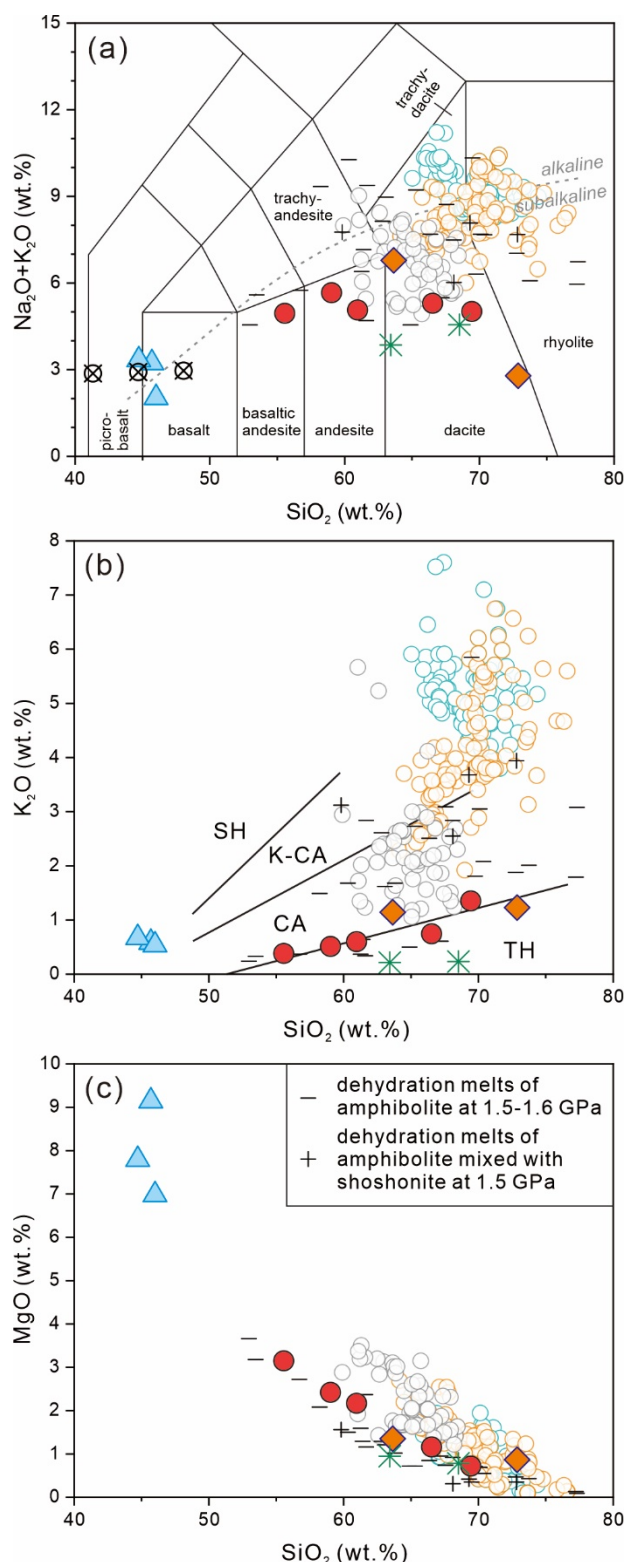


Figure 1 Photomicrographs and BSE image of sulfides from the Gangdese arc root (a-c) and the Kohistan arc root (d-h). Abbreviations: Bn – bornite; Cpy – chalcopyrite; Dg – digenite; Di – diopside; Pe – pentlandite; Po – pyrrhotite; Ab – albite; Act – actinolite; Ep – epidote; Grt – garnet; Ttn – titanite.

2.2 Experimental melt compositions

In the three runs using hornblende as starting material, the partial melts show basaltic compositions (38–41 wt.% SiO_2 normalized dry). By contrast, the partial melts in the other runs using gabbro-norite or the 1:1 mixture of gabbro-norite and hornblende as starting material show andesitic to rhyolitic compositions (56–73 wt.% SiO_2 normalized dry). In the latter runs, the SiO_2 contents of melts increase with the decrease of temperature, while the Al_2O_3 , MgO , FeO^T , CaO , and TiO_2 contents decrease with the decrease of temperature. The Na_2O contents of the melts vary from 1.5 to 5.6 wt.%, but most are in the range of 4.0–6.0 wt.%. Notably, all experimental melts show very low K_2O contents of ≤ 1.4 wt.% (Figure 2b).



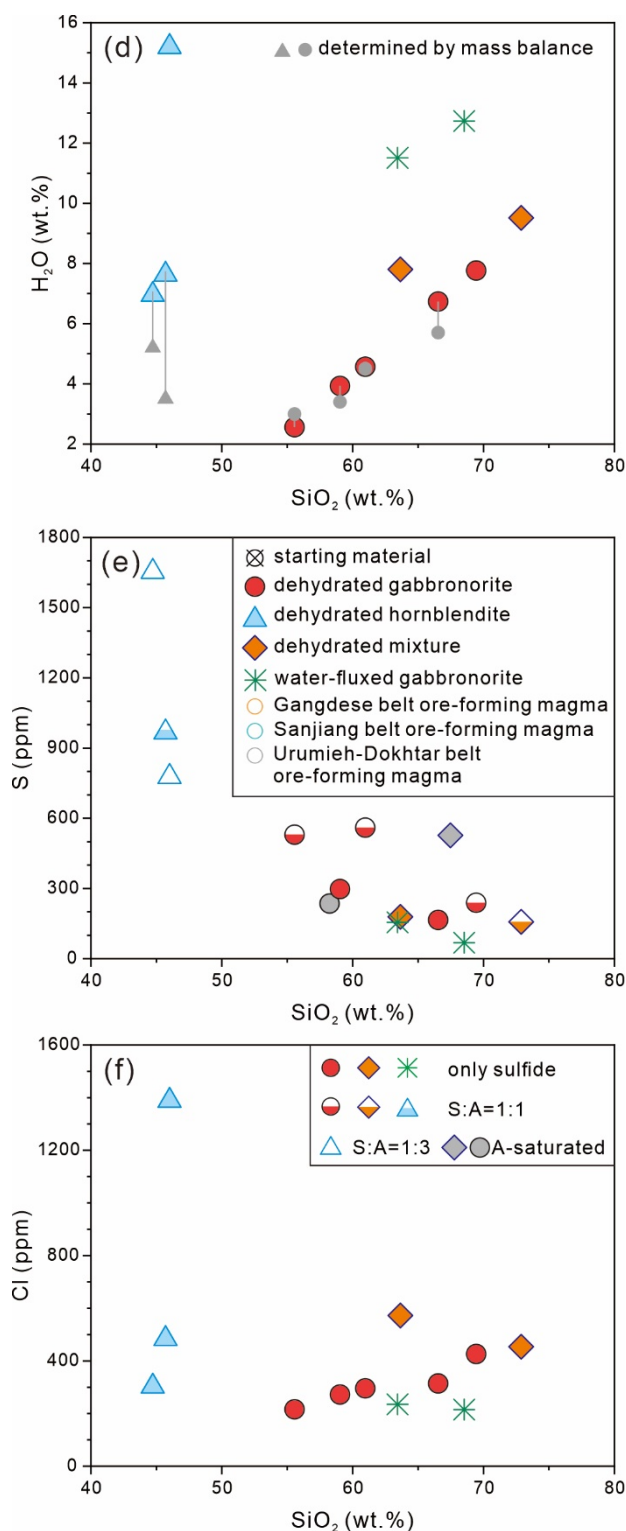


Figure 2 Diagrams showing the major and volatile element compositions of experimental melts produced in the present study (colored symbols) and in previous studies (minus and plus symbols), compared with the whole-rock compositions of post-subduction ore-forming magmas in the Tethyan Alpine-Himalaya orogenic belt. Abbreviations: CA – calc-alkaline series; K-CA – high-K calc-alkaline series; SH – shoshonite series; TH – tholeiite series; S – sulfide; A – anhydrite.

Water contents of partial melts were estimated by the difference of the EPMA totals to 100 wt.% and applying a correction based on the analysis of glasses with known H₂O contents (glasses #7, #13, #35 and #36 of Botcharnikov et al. 2011). For the runs that hornblende dehydration is the dominant reaction, the melt water content can be independently calculated by mass balance using an assumed 2 wt.% water in hornblende, and the EPMA-determined melt water contents are in good match with the results of mass balance calculations. For silicic melts (SiO₂ > 65 wt.%), the water content is greater than 6 wt.%. The melt water contents of the two water-fluxed runs are around 12 wt.%. Mafic melts of the hornblende melting experiments show relatively high S concentrations (779-1205 ppm by weight), whereas intermediate to felsic melts of all the other experiments contain ≤600 ppm S, even though two of the latter experiments were anhydrite-saturated. Both sulfide and anhydrite are stable, suggesting an oxygen fugacity between ΔFMQ+1.5 and ΔFMQ+2.5 (Parat et al. 2011). The intermediate to felsic melts also contain rather low Cl concentrations (≤600 ppm).

3 Implications for post-subduction porphyry Cu deposits

In contrast to "normal" porphyry Cu deposits, post-subduction porphyry Cu deposits formed when there was no ongoing subduction of oceanic slabs. The magmas associated with the latter type of ore deposits are characterized by relatively high potassium contents (≥3.0 wt.% K₂O; Figure 2b), high volatile contents (H₂O, S and Cl), and high oxidation state (Richard 2011, 2015b; Wang et al. 2018). In many studies it was proposed that these magmas were derived from re-melting of sulfide-bearing arc cumulates in the lower crust (e.g., Hou et al. 2017; Wang et al. 2018).

Consistent with several previous studies (Lee et al. 2012, Chiaradia 2014; Chang and Audétat 2018; Du and Audétat 2020), our study of arc-root samples suggests that sulfides indeed tend to be precipitated at the base of magmatic arcs, but abundant sulfides could have been removed by metamorphic dehydration prior to partial melting in the course of crustal thickening.

The presence of garnet in our partial melting experiments can lead to the generation of melts with high La/Yb and Sr/Y ratios, which are characteristic features of post-subduction porphyry magmas (e.g., Hou et al. 2004; Wang et al. 2019). However, both dehydration and water-fluxing partial melting experiments in our and most previous studies contain too little potassium (<3.0 wt.% K₂O including some runs with relatively high K₂O content in the starting materials; our experimental melts contain only 0.2-1.4 wt.% due to the relatively low K₂O content of the starting materials; Figure 2b). This is in strong contrast with the ≥3.0 wt.% K₂O of ore-forming magmas in the Gangdese and Sanjiang belts (Figure 2b). In addition, MgO contents of

partial melts in our and previous experiments are generally lower than those of the ore-forming magmas, particularly in the Urumieh-Dokhtar belt (Figure 2c).

High magmatic H₂O content is thought to be favorable for the formation of porphyry Cu deposits (Richards 2003), but the H₂O content of porphyry Cu magmas is poorly constrained. Our dehydration experiments show that the H₂O content of silicic partial melts (SiO₂ >65 wt.%) is more than 6 wt.% (Figure 2d), suggesting that breakdown of hornblende generates melts that may be hydrous enough to produce porphyry Cu deposits (Richards 2009). However, Lu et al. (2015) proposed that ore-forming magmas in post-subduction settings probably contained >10 wt.% H₂O. Apparently, more studies are needed to better understand the H₂O content of ore-forming magmas.

Two other volatile elements (S and Cl) are also crucial as ligands for the transportation and deposition of Cu (Richards 2003). Ore-forming magmas in subduction settings were estimated to contain up to 2500 ppm S (Grondahl and Zajacz 2022). The presence of abundant magmatic anhydrite in some subduction-related mineralizing porphyries suggests that the ore-forming magmas are relatively sulfur-rich (e.g., Audétat et al. 2004). Magmatic anhydrite was also found in the Qulong and Yulong post-subduction porphyry Cu deposits, suggesting that post-subduction porphyry Cu magmas may be also sulfur-rich. High sulfur contents of the Gangdese mineralizing magmas seem to be supported by high S contents of magmatic apatite (Tang et al. 2020). However, our experimental intermediate to felsic partial melts contain only 68-560 ppm S (Figure 2e). Typical intermediate to felsic arc magmas contain 500-2500 ppm Cl (Wallace 2005). The post-subduction porphyry Cu magmas at Bingham Canyon contain 1000-3000 ppm Cl (Grondahl and Zajacz 2017). However, Cl concentrations in our experimental intermediate to felsic partial melts are extremely low (210-570 ppm Cl; Figure 2f).

In summary, dehydration- or H₂O-fluxed partial melting of sulfide-rich, hydrous lower crustal arc cumulates does not produce magmas that match the relatively high K₂O, MgO, Cl and \pm S contents of post-subduction porphyry Cu magmas.

References

- Audétat A, Pettke T, Dolejš D (2004). Magmatic anhydrite and calcite in the ore-forming quartz-monzodiorite magma at Santa Rita, New Mexico (USA): genetic constraints on porphyry-Cu mineralization. *Lithos* 72:147-161
- Audétat A, Simon AC (2012). Magmatic controls on porphyry Cu genesis. *Society of Economic Geologists, Special Publications* 16:553-572
- Botcharnikov RE, Linnen RL, Wilke M, Holtz F, Jugo PJ, Berndt J (2011). High gold concentrations in sulphide-bearing magma under oxidizing conditions. *Nature Geoscience* 4:112-115
- Chang J, Audétat A (2018). Petrogenesis and metal content of hornblende-rich xenoliths from two Laramide-age magma systems in southwestern USA: Insights into the metal budget of arc magmas. *Journal of Petrology* 59:1869-1898
- Chiaradia M (2014). Copper enrichment in arc magmas controlled by overriding plate thickness. *Nature Geoscience* 7:43-46
- Du J, Audétat A (2020). Early sulfide saturation is not detrimental to porphyry Cu-Au formation. *Geology* 48:519-524
- Grondahl C, Zajacz Z (2017). Magmatic controls on the genesis of porphyry Cu-Mo-Au deposits: The Bingham Canyon example. *Earth and Planetary Science Letters* 480:53-65
- Grondahl C, Zajacz Z (2022). Sulfur and chlorine budgets control the ore fertility of arc magmas. *Nature Communications* 13:4218
- Hou ZQ, Gao YF, Qu XM, Rui ZY, Mo XX (2004). Origin of adakitic intrusives generated during mid-Miocene east-west extension in southern Tibet. *Earth and Planetary Science Letters* 220:139-155
- Hou ZQ, Wang R (2019). Fingerprinting metal transfer from mantle. *Nature Communications* 10:3150
- Hou ZQ, Zhou Y, Wang R, Zheng Y, He W, Zhao M, Evans NJ, Weinberg RF (2017). Recycling of metal-fertilized lower continental crust: Origin of non-arc Au-rich porphyry deposits at cratonic edges. *Geology* 45:563-566
- Lee CTA, Luffi P, Chin EJ, Bouchet R, Dasgupta R, Morton DM, Le Roux V, Yin QZ, Jin D (2012). Copper systematics in arc magmas and implications for crust-mantle differentiation. *Science* 336:64-68
- Lu YJ, Loucks RR, Fiorentini ML, Yang ZM, Hou ZQ (2015). Fluid flux melting generated postcollisional high Sr/Y copper ore-forming water-rich magmas in Tibet. *Geology* 43:583-586
- Parat F, Holtz F, Streck MJ (2011). Sulfur-bearing magmatic accessory minerals. *Reviews in Mineralogy & Geochemistry* 73:285-314
- Richards JP (2003). Tectono-magmatic precursors for porphyry Cu-(Mo-Au) deposit formation. *Economic Geology* 98:1515-1533
- Richards JP (2009). Postsubduction porphyry Cu-Au and epithermal Au deposits: Products of remelting of subduction-modified lithosphere. *Geology* 37:247-250
- Richards JP (2011). Magmatic to hydrothermal metal fluxes in convergent and collided margins. *Ore Geology Reviews* 40:1-26
- Richards JP (2015a). Tectonic, magmatic, and metallogenic evolution of the Tethyan orogen: From subduction to collision. *Ore Geology Reviews* 70:323-345
- Richards JP (2015b). The oxidation state, and sulfur and Cu contents of arc magmas: implication for metallogeny. *Lithos* 233:27-45
- Sillitoe RH (2010). Porphyry copper system. *Economic Geology* 105:3-41
- Tang M, Lee CTA, Ji WQ, Wang R, Costin G (2020). Crustal thickening and endogenic oxidation of magmatic sulfur. *Science Advances* 6
- Wallace PJ (2005). Volatiles in subduction zone magmas: concentrations and fluxes based on melt inclusion and volcanic gas data. *Journal of Volcanology and Geothermal Research* 140:217-240
- Wang R, Weinberg RF, Collins WJ, Richards JP, Zhu DC (2018). Origin of postcollisional magmas and formation of porphyry Cu deposits in southern Tibet. *Earth-Science Reviews* 181:122-143
- Wang X, Zhang JF, Rushmer T, Adam J, Turner S, Xu WC (2019). Adakite-like potassic magmatism and crust-mantle interaction in a postcollisional setting: An experimental study of melting beneath the Tibetan Plateau. *Journal of Geophysical Research: Solid Earth* 124:782-798
- Yang ZM, Lu YJ, Hou ZQ, Chang ZS (2015). High-Mg diorite from Qulong in southern Tibet: implications for the genesis of adakite-like intrusions and associated porphyry Cu deposits in collisional orogens. *Journal of Petrology* 56:227-254

Hydrodynamics of crustal detachments and syn-kinematic granites: numerical exploration and implication on uranium mobilities

Khaled Bock¹, Yannick Branquet^{1,2}, Philippe Boulvais¹, Thibault Duretz^{1,3}

¹ Univ Rennes, CNRS, Géosciences Rennes, UMR 6118, 35000 Rennes, France

² ISTO, UMR7327, Université d'Orléans, CNRS, BRGM, Orléans F-45071, France

³ Goethe Universität Frankfurt FB 11, Institut für Geowissenschaften Altenhöferallee 1, 60438 Frankfurt

Abstract. Detachment zones represent a meeting point between surface-derived fluids and rocks, potentially forming mineralized systems (e.g., uranium deposits). However, the hydrodynamics and solute transfer in these zones remain poorly understood, with limited knowledge of the role of plutons associated with detachments. To address these gaps, 2D hydrodynamic numerical models were developed. The study employed a strategy to constrain the numerical modelling set-up by considering the impact of topographical gradient and syntectonic magmatic activity. It also conducted a sensitivity analysis on permeability contrast between the detachment and crust domains and traced meteoric fluids into the detachment, discussing their implications on uranium mobility. The outcomes of the study demonstrate that downward fluid percolation from the surface into detachment zones occurs through two possible mechanisms: (1) an elevated topographic profile (≥ 3000 m) combined with high detachment permeability (i.e., 100 times higher than crust permeability), (2) the presence of a heat source like synkinematic pluton within the detachment. The latter mechanism was found to be more effective in facilitating the downward percolation of meteoric fluids that maintained their liquid state. Additionally, the study found that secondary faults in the hanging wall stabilize hydrodynamics by concentrating solute flows, creating areas favorable for mineralization.

1 Introduction

Detachments, also known as low-angle normal faults (LANF), are faults that occur on a sub-regional to regional scale with an initial shallow dip, likely less than 30 degrees. They are ductile-to-brittle normal faults that can be attributed to the evolution of shallow-dipping shear zones that hosted major crustal extensions, giving rise to metamorphic core complexes.

Detachment zones can host mineralization systems as they provide a pathway for fluids to interact with rocks (Bartley and Glazner 1985). In this regard, some detachments show per-ascensum hot fluid circulations (Famin and Nakashima 2005), and others show per-descensum meteoric fluid indicators (Morrison and Anderson 1998). Indeed, oxygen and hydrogen isotope signatures indicate that meteoric fluids can attain depths of about 4 to 10 km with a temperature of ca. 350°C (Morrison 1994).

Fluid flow in detachment zones is controlled primarily by buoyancy effects, topography, and permeability contrasts (Figure 1). Although pluton

emplacements can enhance buoyancy in the system, their influence on meteoric fluid circulations is yet unknown. It is uncertain whether they play a significant role in mineralized systems or prevent fluids from descending. Moreover, the hydrodynamics and solute transfer in these systems, with or without plutons, are insufficiently known in terms of the driving forces behind fluid flow, particularly topography, and are scarcely explored numerically or constrained by permeability (Person et al. 2007).

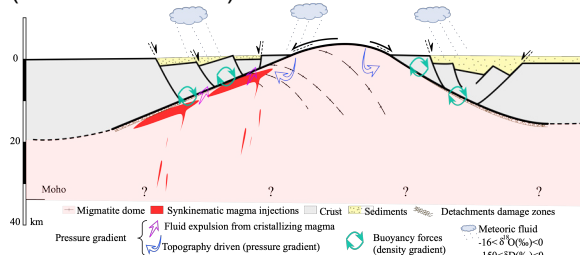


Figure 1. Major fluid driving forces within continental detachments.

Uranium deposits and mobilities in the southern Armorican detachment zones are linked to crustal detachments and syn-kinematic granitic plutons (Figure 2). The magmatic-hydrothermal history is multiphase, with the main mineralization occurring at ca. 300 Ma, soon after leucogranite emplacement.

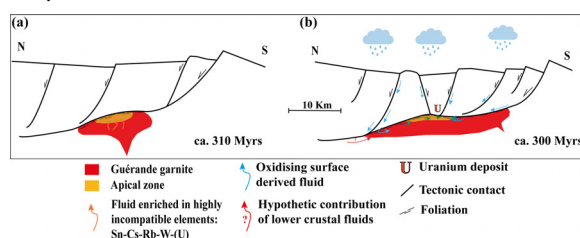


Figure 2. Conceptual model showing the main phases of the evolution of uranium mineralization in the Guérande leucogranite (Localized in the Armorican Massif). (a) Emplacement of the granitic pluton at ca. 310 Ma in an extensional deformation regime. (b) Brittle deformation at ca. 300 Ma allows the infiltration of meteoric fluids to leach the granite and transport the uraniferous species and precipitate them in the reducing zones. Modified after Ballouard et al. (2017)

The aim of this study is to improve our understanding of the meteoric fluid flow patterns in

detachment zones and their consequences for uranium species transport by building numerical hydrodynamic models based on the Guérande uranium mineralized system.

2 Numerical approach

2.1 Strategy

A series of numerical simulations using Comsol Multiphysics (finite element method) was performed. This numerical investigation has been categorized into three core parts, illustrated in Figure 3. Firstly, a 2D model was constructed to assess buoyancy without topography. Secondly, a model with two topographies (500 m and 3000 m) was tested with an additional driving force of pressure gradient. One topography model was chosen for the injection of a heat source represented by a pluton at two positions - shallow (≈ 4 km) and deep (≈ 10 km) - to understand the limits of the pluton's contribution to the hydrodynamic system. Following the first two steps, a sensitivity study was conducted on the tested permeability models.

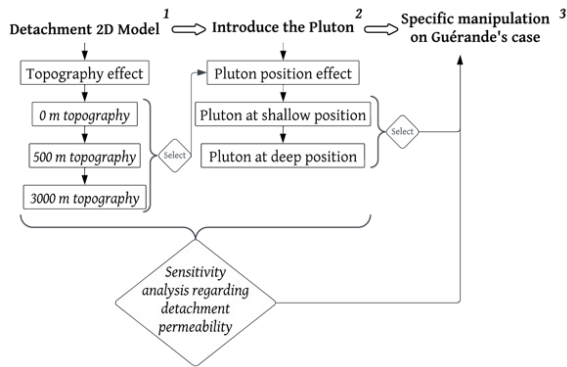


Figure 3. Flow chart of the main steps in the modelling process.

Subsequently, the third stage of the numerical investigation focused on the Guérande case with emphasis on the shallower pluton position. An initial 0-10 Ma calculation was performed without topography to establish a stable fluid flow period, followed by main models covering a time scale of 20 Ma with topographical gradient and pluton models. The detachment was active throughout the 20 Ma periods with the pluton activated between 10 and 11 Ma, using felsic magma temperature below 900 K.

2.2 Initial and boundary conditions

The initial and boundary conditions used for the simulations are shown in Figure 4. To improve accuracy, we increased the mesh resolution in the detachment region by using a maximum mesh size of 50 m and more meshed surfaces, as shown in Figure 4c.

The thickness of the detachment is an important factor since it determines the extent to which the

hydrodynamic system may arise. In detachment systems, the diffuse zone of strain can extend up to 1.5 km (Whitney et al. 2013). The damage zone is typically thicker in the hanging wall than in the footwall, and this asymmetry was incorporated into our model (Figure 4) with a detachment thickness ranging from 400 m at the surface to 1 km in depth.

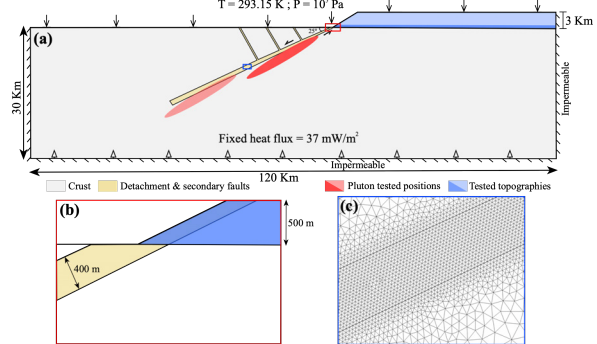


Figure 4. (a) The 2D geometry model displays the defined boundaries and initial conditions, along with the tested positions of the pluton and the topographical gradients. (b) A close-up showing the topography and the detachment thickness near the surface. (c) A zoomed-in view highlights the mesh resolution in the detachment domain. The model's both sides and bottom indicate no flow with thermal insulation on the left and right edges, at the top, the arrows denote the surface pressure, and surface temperature which varies according to the normal geothermal gradient. The arrows at the bottom indicate the heat flux.

2.3 Governing equations and physical parameters

Heat equations (Equation 1) and Darcy's law (Equation 2) were coupled in our models.

$$(\rho C_p)_{\text{eff}} \frac{\partial T}{\partial t} + \rho_f C_{p,f} u \cdot \nabla T + \nabla \cdot q = Q_t \quad (1)$$

$$q = -k_{\text{eff}} \nabla T$$

$$\frac{\partial}{\partial t} (\epsilon_p \rho_f) + \nabla \cdot (\rho_f u) = Q_m \quad (2)$$

$$u = -\frac{k}{\mu} (\nabla p + \rho_f g)$$

The permeability and the Peclet number (Pe) are both key parameters in our study, the former (described by Equations 3 and 4) guide the hydrodynamic system, whereas the latter (described by Equation 5) enables us to identify areas where thermal advection prevails over thermal conduction.

$$K_c = 5 \times 10^{-16} \times \exp\left(\frac{Y}{\delta}\right) \quad (3)$$

$$K_{d1} = K_c \times 10 ; K_{d2} = K_c \times 30 ;$$

$$K_{d3} = K_c \times 50 ; K_{d4} = K_c \times 100 \quad (4)$$

$$Pe = \frac{Lu}{\alpha} \quad \alpha = \frac{K}{(\rho C_p)} \quad (5)$$

3 Results and discussion

3.1 Topographic gradient effect

The relationship between topography gradient, detachment permeability (K_{d1} and K_{d4}), and fluid flow into the detachment zone through Peclet numbers (Pe) patterns are shown in Figure 5. The 500 m and 3000 m topography models with low detachment permeabilities exhibit Pe values exceeding 1, for which advection dominates over diffusion, in the superficial area due to gravity-driven downward fluid flow. With high detachment permeability, this flow extends deeper into the detachment, accompanied by a slight deformation of the isotherms in the 500 m model. The 3000 m topography model shows similar tendencies, with more pronounced and distinct isotherm deformation and higher Peclet number values. In contrast, apart from a small increase in the Pe values in the high detachment permeability, the topography-free model shows no significant disturbance to the horizontal isotherms.

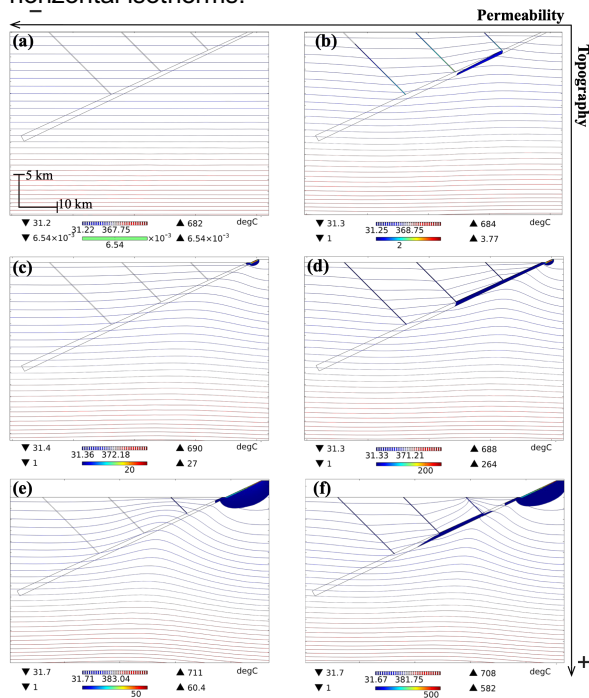


Figure 5. Topography models showing the Peclet number and isotherms within the detachment zone and its secondary faults. The two columns denoted (a) and (b) represent the permeability models K_{d1} and K_{d4} , respectively. The (a)-(b) line corresponds to the free topography model, while (c)-(d) and (e)-(f) represent the topography models of 500 m and 3000 m, respectively.

3.2 Pluton effect

For the sake of concision, only the nearest pluton position to the surface (Figure 6), which corresponds approximately to the position of the Guérande granite, will be presented. The K_{d3} model (Figure 6a) shows an increasing trend in the Peclet number during the activation of the pluton (10.5 Ma) and the cooling period (11.1 Ma). In both cases, we

observe the migration of the Peclet number values greater than 1 from the detachment zone to the hanging wall in the crust ahead of the pluton. Similar patterns are visible in the K_{d4} model (Figure 6b) with even higher Peclet number values, particularly during the pluton's active phase. Panels c and d in Figure 6 illustrate the Peclet number models by showing the direction of fluid flow in conjunction with the deformation of the isotherms. These visualizations demonstrate a downward fluid flow via two of the secondary faults along with the detachment, and an upward circulation towards the surface via the third secondary fault.

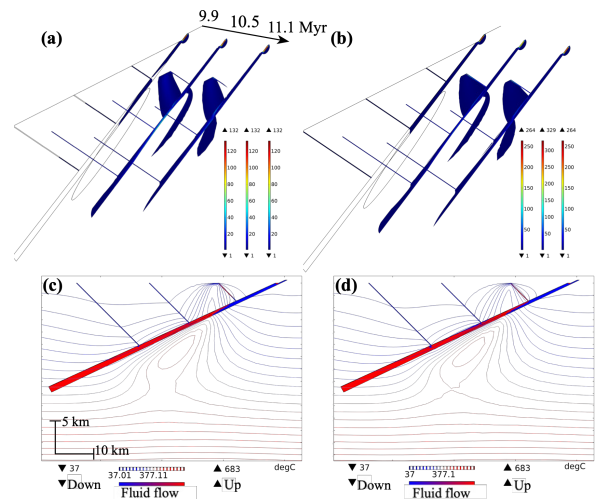


Figure 5. Evolution of the Peclet number in the detachment zone and associated secondary faults before, during, and after the pluton activity using two detachment permeability models K_{d3} and K_{d4} , correspondingly, for (a) and (b). In (c) and (d) Darcy velocities indicate fluid flow direction in detachment zones for both permeabilities K_{d3} and K_{d4} following pluton deactivation.

3.3 Detachment permeability sensitivity analysis

Figure 7 presents two cross-sections of the detachment and one of the three secondary faults, displaying the correlation between the Peclet numbers and the four tested detachment permeability laws (Equation 4). These models are limited to the first pluton position and the three topographic gradient models that were examined. In the detachment cross-section with no topography, all permeability models exhibit Peclet number values below one, whereas, in the detachment cross-section with a 3000 m topography setup, Peclet number values exceeding the thermal advection threshold are observed in three of the four detachment permeabilities (K_{d2} , K_{d3} , and K_{d4}). The Peclet numbers are relatively evenly distributed across all topography models in the high detachment permeability (K_{d4}) in the secondary fault cross-section, with all models indicating Peclet number values above 1. Hence, an increase in the Peclet number is evident with an increasing topographical gradient. The pluton model

cross-section panels (Figure 7d, e) exhibit a significant increase in Peclet number values during the activity of the pluton and cooling phases, particularly in the secondary fault.

In quantitative terms, the heat source underneath the detachment zone triggers significant surface-

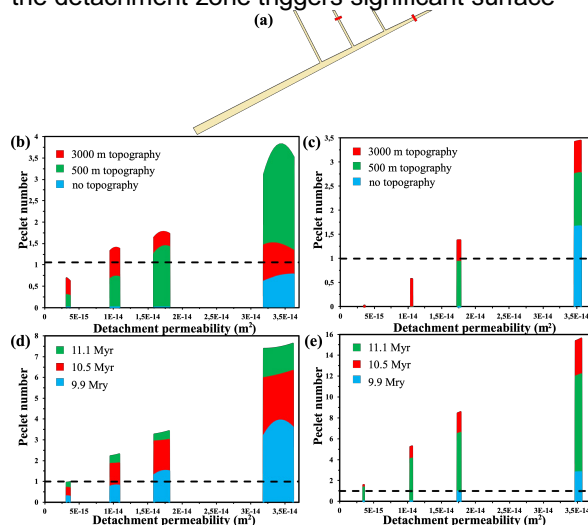


Figure 6. Peclet number as a function of detachment permeability models for two cross-sections from (a). Panels (b) and (c) respectively depict the detachment cross-section for the three tested topographies and the first pluton position at three different instants (before, during and after its activity). Similarly, panels (d) and (e) display the fault cut section.

derived fluid percolation, even in areas with low topographic gradients or permeability ratios. This is due to the temperature and permeability contrast between the pluton and its surrounding rocks (e.g., Eldursi et al. 2009; Launay et al. 2023). Fluid molecules from various surface locations (i.e., detachment and secondary faults), have been tracked deep into the detachment during the pluton's activation and cooling phases (10–12 Ma). The results of the tracking indicate that these fluids retained their liquid state and penetrated approximately to a depth ranging from 4 to 11 kilometers where they reaches the apex of the pluton.

4 Conclusions

The present investigation suggests that a hydrodynamic system featuring downward fluid flow patterns can arise through two models, knowing that forced convection and free convection play simultaneously in each. The first model involves a high topography gradient coupled with a high permeability ratio between the crust and the detachment zone, with the crust's permeability being at least $5 \times 10^{-16} \text{ m}^2$. The second model is associated with a magmatic activity represented by a syntectonic pluton emplacement that triggers advection and allows for rapid percolation ($\approx 2 \times 10^{-8} \text{ m} \cdot \text{s}^{-1}$) of surface-derived fluids into the detachment. The latter is deemed to be more

effective and more reliable of the two mechanisms. Leaching of the apical zones of the plutons, leading for instance to the leaching of uranium, as documented in the case of the Guérande granite (Ballouard et al. 2017).

The secondary faults in the hanging wall play a crucial role in stabilizing the hydrodynamics by concentrating solute flows and transporting meteoric fluids from the surface into the detachment zone. These findings shed light on the mechanisms of fluid migration in detachment zone systems, particularly in hydrothermal systems and uranium mineralization processes. Further research is needed, specifically through the integration of chemical components and the transport equation of uranium species, to investigate the influence of the outlined hydrodynamic mechanism on the precipitation and transport of uranium.

Acknowledgements

This study is granted by the NEEDS consortium through the URAMOD project.

References

- Ballouard, C., Poujol, M., Boulvais, P., Mercadier, J., Tartèse, R., Venneman, T., Deloule, E., Jolivet, M., Kéré, I., Cathelineau, M., & Cuney, M. (2017). Magmatic and hydrothermal behavior of uranium in syntectonic leucogranites: The uranium mineralization associated with the Hercynian Guérande granite (Armorican Massif, France). *Ore Geology Reviews*, 80, 309–331. <https://doi.org/10.1016/j.oregeorev.2016.06.034>
- Bartley, J. M., and Glazner, A. F. (1985). Hydrothermal systems and Tertiary low-angle normal faulting in the southwestern United States. *Geology*, 13(8), 562. [https://doi.org/10.1130/0091-7613\(1985\)13<562:HSATLN>2.0.CO;2](https://doi.org/10.1130/0091-7613(1985)13<562:HSATLN>2.0.CO;2)
- Bons PD, Gomez-Rivas E. Origin of Meteoric Fluids in Extensional Detachments. *Geofluids*. 2020; 2020:1-8. doi:10.1155/2020/7201545
- Eldursi K. Minéralisations et Circulations péri-granitiques: Modélisation numérique couplée 2D/3D, Applications au District minier de Tighza (Maroc-Central). Published online 2009:220.
- Famin, V., and Nakashima, S. (2005). Hydrothermal fluid venting along a seismogenic detachment fault in the Moresby rift (Woodlark basin, Papua New Guinea): HYDROTHERMAL FLUID VENTING. *Geochemistry, Geophysics, Geosystems*, 6(12), n/a-n/a. <https://doi.org/10.1029/2005GC001112>
- Launay G, Branquet Y, Sizaret S, Guillou-Frotier L, Gloaguen E. How greisenization could trigger the formation of large vein-and-greisen Sn-W deposits: A numerical investigation applied to the Panasqueira deposit. *Ore Geology Reviews*. 2023;153:105299. doi:10.1016/j.oregeorev.2023.105299
- Morrison, J., and Anderson, J. L. (1998). Footwall Refrigeration Along a Detachment Fault: Implications for the Thermal Evolution of Core Complexes. *Science*, 279(5347), 63–66. <https://doi.org/10.1126/science.279.5347.63>
- Morrison J. Meteoric water-rock interaction in the lower plate of the Whipple Mountain metamorphic core complex, California. *Journal of Metamorphic Geology*. 1994;12(6):827-840. doi:10.1111/j.1525-1314.1994.tb0062.x
- Person M, Mulch A, Teyssier C, Gao Y. Isotope transport and exchange within metamorphic core complexes. *American Journal of Science*. 2007;307(3):555-589. doi:10.2475/03.2007.01
- Whitney DL, Teyssier C, Rey P, Buck WR. Continental and oceanic core complexes. *Geological Society of America Bulletin*. 2013;125(3-4):273-298. doi:10.1130/B30754.1

Las Minas newly recognized epithermal deposit and its relationship with Tatatila-Las Minas Skarn, Veracruz, Mexico.

Pablo E. Carbajal¹, Jesús Castro Mora², Julie Roberge¹, Gerardo Arrieta³, Godwyn Paulson Pitchaimani¹, Celestine N. Mercer⁴.

¹Posgrado ESIA Ticomán, Instituto Politécnico Nacional, CDMX, Mexico

²Universidad Autónoma del Estado de Hidalgo, Mexico.

³Laboratorio Universitario de Geoquímica Isotópica (LUGIS), Instituto de Geofísica, Universidad Nacional Autónoma de México (UNAM), CDMX, Mexico

⁴U.S. Geological Survey, Geology, Geophysics and Geochemistry Science Center, Denver, CO.

Abstract. The Las Minas district, Veracruz, hosts the well-known Tatatila–Las Minas IOCG skarn deposits. Until now, the possibilities of other types of deposits in the area have been ignored because of the presence of this skarn, which has reported reserves of 719,000 oz Au eq. This work aims to show the existence of another type of mineral deposit overprinting the mineralized zone of the Tatatila–Las Minas skarn deposit. Regional geology shows a vast extension of dolomites and limestones of the Tamaulipas inferior formation which were intruded during the Miocene by three thermal events of granitic to granodioritic composition. As a result of the intrusions, a contact metamorphism zone was developed and led to the precipitation of skarn minerals rich in Cu–Fe–Au–Ag. Based on petrographic and mineralogical studies of skarn samples, evidence for hydrothermal fluid circulation and epithermal veins has been observed, suggesting the presence of an epithermal deposit overprinting large exposures of the skarn.

Linking the geological history of both deposits will help to understand if both mineralization events were cogenetic or originated from different geological events.

1 Introduction

The mining district of Las Minas (LM), Veracruz is within the youngest portion of the Trans Mexican Volcanic Belt (TMVB), in the east-central part of the state of Veracruz (Figure 1).

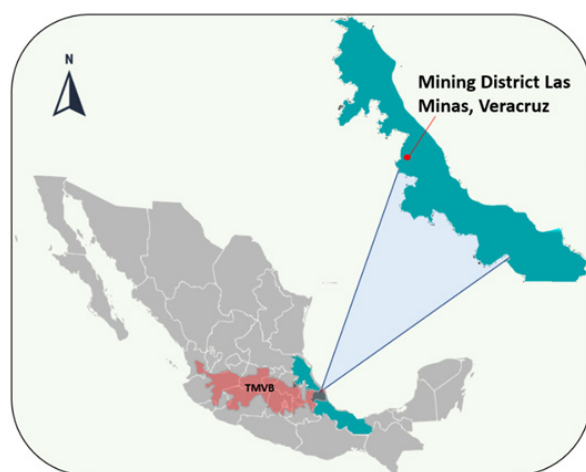


Figure 1: Location map of the studied area.

Attention in the mineralized zone of Las Minas is focused on the Tatatila–Las Minas IOCG skarn deposit that hosts Au, Ag and Cu that are currently

being exploited. However, we have discovered petrologic and mineralogic evidence indicating epithermal mineralisation overprinting the skarn. The aim of this study is to further characterize this newly identified mineralization.

The known mineralized zones in Las Minas consist of a Au–Cu–Ag–magnetite skarn and a Zn–Pb–Ag skarn (Fuentes-Guzmán et al. 2020). Metal values of the skarn deposit reported by the Mexican Gold Mining Corp (2023) show that concentrations vary from: Au 1 to 39.3 g/t, Ag 4.11 to 127 g/t and Cu 0.64% to 11.7%, with principal inferred reserves of 719,000 oz Au eq.

Exploration of the mineralized zones is challenging due to the topographic changes of mountains that are full of vegetation. But up to 1000 m of the stratigraphy of Las Minas is intermittently exposed in deep valleys cutting the high volcanic plains.

The skarn is largely exposed in the mining district (Figure 2) where large outcrops of carbonate rocks from the Tamaulipas Inferior formation outcrop. This is where the economic values of minerals of the skarn were found.

After a successful exploration, Mexican Gold Corporation has targeted exploitation of the skarn with open-pit methods.

The geologic and metallogenic framework of both the skarn and the possible epithermal deposit can help understand if the Tatatila–Las Minas IOCG skarn deposit is a part of a larger mineralized system that merits further exploration.

This study presents a digital elevation model with newly integrated observations of alteration zones, mineralogical, and petrographical information that we have collected. The map will also show previously published geologic and structural characteristics that will provide context to interpret our new observations. The map will help elucidate the paragenetic sequence of the skarn and the newly discovered epithermal deposit as well as the petrogenesis of the larger hydrothermal system.

Mining in Mexico is one of the main sources of employment (Azamar 2022). Therefore, the discovery of new mineralized zones in the municipality of Las Minas can help the state's economic growth and social welfare. It can be an important source of employment for both men and

women, promoting inclusion in mining and research.

2 Regional geologic context

The regional geology is summarized by the *Perote E14-B26* geological map (Fig. 2; Mexican Geological Service, 2007).

The north central part of the E14-B26 map is where the mining district of Las Minas is located (Figure 2). Early Cretaceous limestones and dolomites are intruded by three Miocene granite to granodiorite intrusive events. These middle Miocene (U-Pb 15.05 ± 0.94 Ma) and middle to late Miocene (U-Pb 15.27 ± 0.36 Ma and 14.33 ± 0.38 Ma) granitic and granodioritic rocks that are thought to be related to skarn genesis. These rocks were dated by $^{40}\text{Ar}/^{39}\text{Ar}$ methods using rare fuchsite, hornblende, K-feldspar and biotite (Fuentes-Guzman et al., 2020). They yielded two groups of ages: (A) late Oligocene to early Miocene (22.12 ± 0.74 Ma) and 19.04 ± 0.69 Ma and (B) middle to late Miocene with ages from 16.34 ± 0.20 Ma and 13.92 ± 0.22 Ma (Fuentes-Guzman et al., 2020). Thick sequences of rhyolite and andesite tuffs have been observed and are thought to be cogenetic with mineralizing granites, but they remain to be dated.

The Cretaceous and Miocene rocks have been covered by up to 200 m of pyroclastic flows which according to Olvera et al. (2020) came from the *Los Humeros* volcanic center, 20 km west and host to one of the biggest producing geothermal systems in Mexico.

There are two principal dextral faults that correspond with the alignment of two principal rivers: *Las Minas* and *La Trinidad*. The faults are oriented from NNE to SSW. Also, NNW to SSE faults are observed following some other rivers too.

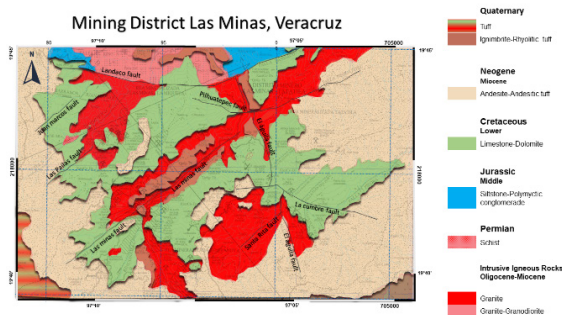


Figure 2: Geologic map of Las Minas mining district, Veracruz, Mexico.

3 Field observations

The proximal zone of the skarn is characterized by rocks with granoblastic texture and metallic IOCG mineralization with native copper, wollastonite, clinopyroxenes and garnet that vary from green to brown colors. Distal zone of the skarn is characterized by coarse to fine grain marble. There are calcite veins and coarse bladed calcite in outcrops indicating high temperature hydrothermal fluids, but their paragenesis is as yet unknown.

The skarn is cut by meter-wide granitic dykes that are mineralized, which in turn are cut by mafic dykes that are not mineralized or enriched in any precious metals. Although mineralization is not observed in mafic dykes, they help us to understand how the mining district was affected by regional thermal events that could affect future thermochronometry studies.

The zone that we hypothesize to be epithermal includes pervasive argillic alteration with coarse (3-4 cm) to fine (<1 cm) euhedral pyrite (Fig. 3).

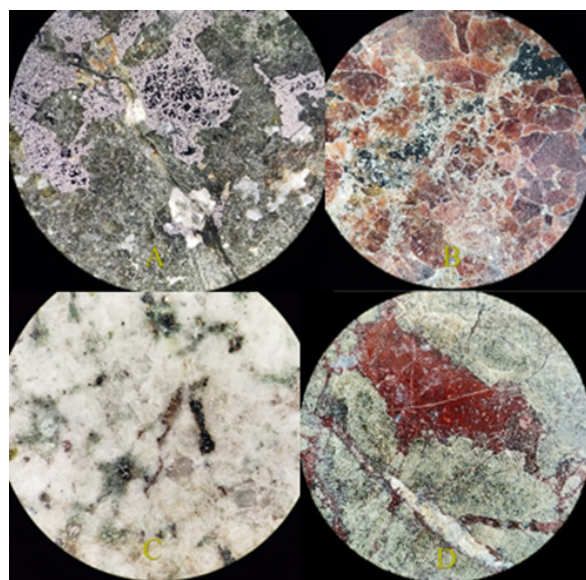


Figure 3: Microphotos of samples from the Tatatila-La Minas Skarn and epithermal (?) deposit.

4 Conclusions and future work

We propose the existence of an epithermal mineral deposit related to the Tatatila-Las Minas IOCG skarn deposit. We are currently synthesizing the digital elevation map with new geologic, alteration, and mineralogic observations in order to understand the temporal relationships and whether the epithermal deposit was formed contemporaneously with the skarn or if formed afterwards during another mineralising event. Future work will include Ar/Ar isotopic studies in order to constrain the paragenetic sequences of the proposed epithermal deposit relative to the skarn deposit.

Acknowledgements

We thank Diego Ibarra Garcia, Lizbeth Carillo Marrodan, Maria Fernanda Reyes Gonzalez and Regina Cuervo Morales for assistance in different parts of the project.

References

- Castro-Mora, J. C., Ortíz-Hernández, L. E., Escamilla-Casas, J. C., Cruz-Chávez, E., & Dorantes-Castro, C. G. (2016). Metalogénesis de la mineralización tipo IOCG relacionada al skarn del Distrito Minero Las Minas, Estado de Veracruz. *Tópicos de Investigación en*

- Ciencias de la Tierra y Materiales, 3, 128-143.
<https://doi.org/10.29057/aactm.v3i3.9617>
- Fuentes-Guzmán, E., Gonzales, E., Camprubí, A., Hernandez, G., Gabites, J., Iriondo, A., Ruggieri, G. and López, M. (2020): The Miocene Tatatila.Las Minas IOCG skarn deposits (Veracruz) as a result of adakitic magmatism in the Trans.Mexican Volcanic Belt; Boletín de la Sociedad Geológica Mexicana, v.72 (3), p 1-50.
- Olvera, E., Blanco, C., Monroy, V., Brogi, A., Liotta, D., Wheeler, W., Gómez, F., Najera, S., Jiménez, A., Guevara, J., Bastesen, E., Lepillier, B., Zucchi, M., Caggianelli, A. and Ruggieri Giovanni. (2020): Geology of Las Minas: an example of an exhumed geothermal system (Eastern Trans-Mexican Volcanic Belt); Journal of maps, v, 16:2, p. 918-926.
<https://doi.org/10.1080/17445647.2020.1842815>

Melt inclusions types within related processes in the Dănești - Piatra Roșie realm (Maramureș County, Romania)

Ioan Pinte¹, George Dincă¹, Sorin S. Udubașă², Marian Munteanu¹

¹ Geological Institute of Romania, Caransebes str., no 1, Bucharest, Romania

² Bucharest University, Nicolae Balcescu Blv., no1, Bucharest, Romania

Abstract. Globular sulfide/oxide, silicate melts, and hydrosaline melt inclusion are the main topic of this paper based upon petrography, microthermometry, Raman, and SEM/EDS analyses. Dănești-Piatra Roșie dacite complex is situated in the Gutâi volcanic zone between Baia Sprie and Căvnic epithermal Au-Ag-Pb-Zn-Cu-W-Sb-Te-As ore deposits. Volcanic lava domes are predominant and melt inclusions were studied in pyroxene, amphibole, plagioclase, quartz, and zircon, mainly as phenoclasts, collected from volcanic debris around Dănești village. Microtextural features and postentrapment modifications of the melt inclusions are suggestive for the magma mixing/mingling process in the shallow magma reservoirs. Homogenization temperature in selected silicate melt inclusions ranged between 715° and 1150°C of more than 200 measurements. The unique presence of hydrosaline melt inclusion trapped in mushy quartz as secondary (pseudosecondary) trails around 3.5 km depth suggesting brine lens formation around the volcanic conduit(s) and upper magma reservoir as in the active volcanism today worldwide, emphasized that this could be the main metal source for the epithermal ore deposits in the area. We noted the Cu- enrichment of the immiscible globular sulfide/oxide globules trapped in minerals and glass matrix as the main result of mafic mineral destruction during magma mixing and degassing.

1 Introduction

Immiscible (Fe-S-O), silicate-, and hydrosaline melt inclusions from pyroxene, amphibole, plagioclase, zircon, and quartz from Dănești-Piatra Roșie dacite complex (Figure 1) are representative for intrusive-extrusive volcanic products generated and accumulated in shallow magma reservoir(s) in a complex plumbing system as it was emphasized from thermobaric geochemistry data (Kovacs 2002; Grancea et al. 2003; Kovacs et al. 2021). Petrogenetic minerals were crystallized at various depth batches and suggest specific genetic processes such as magmatic immiscibility, magma mixing/mingling, decompression, and degassing, fluid phase separation, etc. Globular sulphide/oxide inclusions were found variously distributed in minerals as primary inclusions along the growth zones or randomly distributed in the groundmass, generally with a characteristic frothy microtexture (e.g. Laroque et al. 2000; Figure 4). Separate globular sulphide/oxide were also collected freely from volcanic debris and are the most complex ones composed of magnetite dendrites, globular pyrrhotite, Cu-rich sulphide globulae, monosulphide solid solution (mss), and intermediate solid solution (iss) within black silicate glass matrix (Pinte^{2008, 2015} - Figures 11 and

12). Silicate melt inclusion is monophasic, biphasic, and multiphasic with opaque and transparent daughter minerals. Their dimension is variable between less than (1-10) to (80-100) micrometres. Generally, they are primarily distributed along the primary growth zones, glassy and/or recrystallized in the internal sieve microtexture, frequently post-entrapment modified by partial remelting, cumulative aggregation, decrepitation, and stretching, because of the hot mafic magma input (e.g. Pinte²⁰¹⁵ - Figure 9). Former yellow-greenish transparent glassy solid inclusions (up to 150-200 micrometers) of silicate perilit-like globule could also be picked up under the binocular microscope (Pinte²⁰¹⁶ unpubl.). Hydrosaline melt inclusions containing halite, anhydrite(?), other salts, opaques, and other transparent daughter phases were described yet, only in one single quartz phenoclast from the outcrop of volcanic rocks around Dănești village.

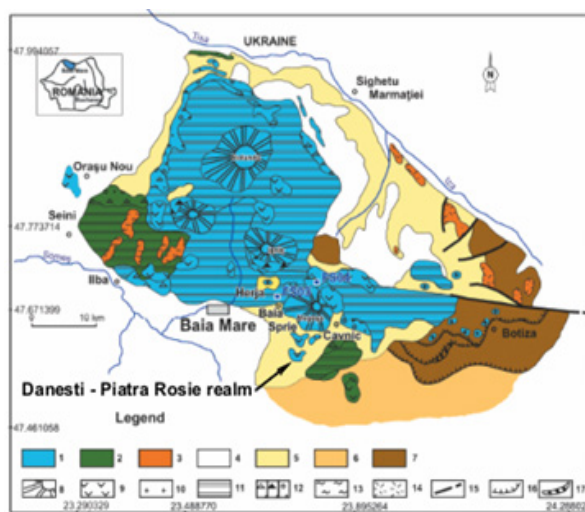


Figure 1. Dănești - Piatra Roșie realm on the simplified vulcanological map of the Gutâi Mts. (modified after Iancu and Kovacs eds. 2010). 1. Pannonian volcanics; 2. Sarmatian volcanics; 3. Badenian volcanics; 4. Quaternary; 5. Neogene sedimentary deposits; 6. Oligocene-Miocene sedimentary deposits; 7. Paleogene sedimentary deposits; 8. Effusive cones; 9. Extrusive domes; 10. Intrusives; 11. Volcano-tectonic depression filling; 12. Pyroclastic and epiclastic deposits; 13. Ignimbrites and associated volcanoclastics; 14. Primary and reworked tuffs; 15. Faults; 16. Overthrusts; 17. Pieniny Klippen Zone.

These are secondary or pseudosecondary in origin and the microthermometry results suggested

trapping at depths around 3.5 km. This is suggestive for brine lens formation in the upper part of the present-day volcanoes (Blundy et al. 2021) and is emphasized in this study that, together with the globular sulphide/oxide, these were the primary source of the epithermal mineralizations in the area (e.g. Baia Sprie, Cavnic, Dealul Crucii etc).

2 Methodology

Standard microthermometric measurements (e.g. Pintea 2014) were done in Linkam TS 1500 stage and a "self-built" microthermometric device, starting first at IMP-ETH Zurich (1994) and continued in 2005 and 2015 (Pintea 2006, 2015 – Figs. 78, 123, and Table 4; Pintea et al. 2016; Pintea et al. 2018 unpubl.), especially in unprepared washed grains picked up under a binocular microscope. SEM/EDS and Raman measurements were conducted at the Geological Institute of Romania. A Hitachi TM3030 SEM was used with acceleration voltage of 15 kV. Elemental analysis was done through Bruker's QUANTAX 70 EDS system. Micro-Raman spectra were obtained on polished samples using Renishaw InVia spectrometer with a Peltier cooled CCD detector, equipped with a Leica DM 2700M microscope and 20x, 50x objective lenses. Excitation was provided by a 532 nm laser (RL532C50, Renishaw) with 50 mW power, 10s exposure time, 1-5 accumulations and 1.5 cm⁻¹ spectral resolution.

3 Results

3.1 Microthermometry of the silicate melt inclusion

Generally, biphasic inclusions containing glass and vapour bubble(s) were used for microthermometry (Table 1). Frequently, the glass inclusions, mainly in quartz and plagioclase foaming during heating around T_g (glass melting temperature) suggested they were formed in a silicate magma layer saturated in vapour bubbles and the main cause of crystal fragmentation was the explosion of melt inclusions because of the hot magma injection in the magma reservoir (Pintea 2013). Reproducible final homogenization temperature of the trapped silicate foam was slightly variable because of specific foam rheology (Figure 2a).

3.2. Hydrosaline melt inclusion

This was found and described yet in one single quartz grain phenoclast, and consists of an assemblage of multiphasic brine inclusions (Pintea 2016) together with vapour rich ones, in refilled microfissures. Two deformed (remelted) silicate glass inclusions were found very close to each other in this grain (e.g. Figure 2b) and they have been homogenized around 837°-856°C. Brine inclusion contains halite, other salts, silicate, and

anhydrite(?) as transparent phases, and sulphide/oxide as opaque phases (Figure 2c). Microthermometric values of one replicated run calculated with *Sowat* (Driesner and Heinrich 2007) are written in Table 1. Despite the fact that there is just one measured assemblage in the mushy rhyolite quartz from Dănești-Piatra Roșie dacite complex, their significance is crucial because it is the first time that this kind of inclusions was found in magmatic quartz from the Gutâi Mountains, and their occurrence inside the lava dome at 3.5 km depth suggested the presence of a brine lens formed during volcanic activity comparable with

Table 1. Microthermometric data from biphasic glass inclusions in petrogenetic minerals from Dănești-Piatra Roșie dacite complex (modified from Pintea 2006, 2015, and 2016; Pintea et al. 2018 unpubl.), n= number of measurements.

Host mineral	Melt inclusion type	Homogenization temperature (Th) °C	Observations
Horn-blende	Biphasic (glass + vapor bubble) (n=1)	977	Host opacified at high temperature
Plagioclase	Biphasic (glass + vapor bubble(s)) (n=23)	811- 1150	Frequently foaming above 530°C
Quartz	Biphasic (glass + vapor bubble(s)) (n=176)	715-986	Almost all inclusions foaming around 530°C; Microsolid melted at 808°C and 844°C (n=2)
	Hydro-saline melt inclusion (n=1)	≥ 916-922	T _m halite= 555°C; Salinity= 67.7405wt% NaCl eq.; X _{NaCl} =0.40; P= 1332.55 bar, d= 1.0455 g/ccm; Single phase state. Replicated data T _m halite= 571°C; Salinity= 69.9075 wt% NaCl eq., X _{NaCl} = 0.41; P= 1265.04 bar; d= 1.06665 g/ccm; V+L phase state.

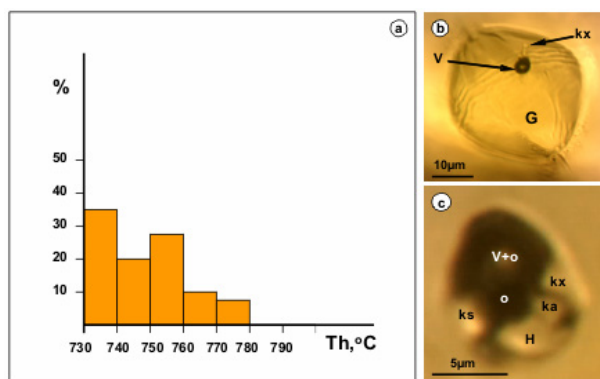


Figure 2. a. Reliability test in one single silicate foam glass inclusion showing variable homogenization temperature, in mushy quartz phenoclast from Dănești-Piatra Roșie dacite (data from Pintea 2006; $n=15$, median= 755°C); b. primary silicate foam glass inclusion; c. secondary (pseudosecondary) hydrosaline melt inclusion. Notations: Th- homogenization temperature, G- glass, V- vapor, kx- silicate solid, H- halite, Ks- other salt, ka- anhydrite(?), o- opaque.

present-day findings around the world (Blundy et al. 2021). Moreover, together with the globular sulphide/oxide immiscible melt (see below) were the main source of gold/base metal epithermal ore deposits from the area.

3.3 Raman and SEM/ EDS analyses of globular sulfide/oxide immiscible melt

They are comparable with common Fe-S-O immiscible melt described worldwide (e.g. Larocque et al. 2000; Georgatou et al. 2022; Heinrich and Connolly, 2022). There are two groups of inclusions studied in this paper: one is formed by separated black globules (Pintea 2008, 2015 - Figure 11) up to 1 mm diameter, composed of silicate glass, segregated sulphide, and oxide phases, mainly as pyrrhotite, monosulphide solid solution (mss), intermediate solid solution (iss), chalcopryite, dendritic magnetite, and possible pentlandite (Figure 3) the other one being represented by the frothy globular sulphide/oxide included in minerals and glass matrix. The Raman spectra suggested the presence (based on RRUFF database; e.g. Figure 4) of neighborite (NaMgF_3), yugawaralite ($\text{CaAl}_2\text{Si}_6\text{O}_{16.4}\text{H}_2\text{O}$), cotunnite (PbCl_2), and salammian (NH_4Cl) in the black matrix and digenite ($\text{Cu}_{1.8}\text{S}$), tenorite (CuO), bismuth (Bi), jamesonite ($\text{Pb}_4\text{FeSb}_6\text{S}_4$) in the white and yellow zones inside the sulphide globules.

4 Conclusions

Fe-S-O sulfide/oxide globule, silicate-, and hydrosaline melt inclusions from Dănești-Piatra Roșie rhyolite/dacite dome complex are representative for specific magmatic-hydrothermal processes evolved in a shallow magma chamber, around 3.5 km depth, before and during the

eruption, including immiscibility, magma mixing, crystallization, decompression, and degassing.

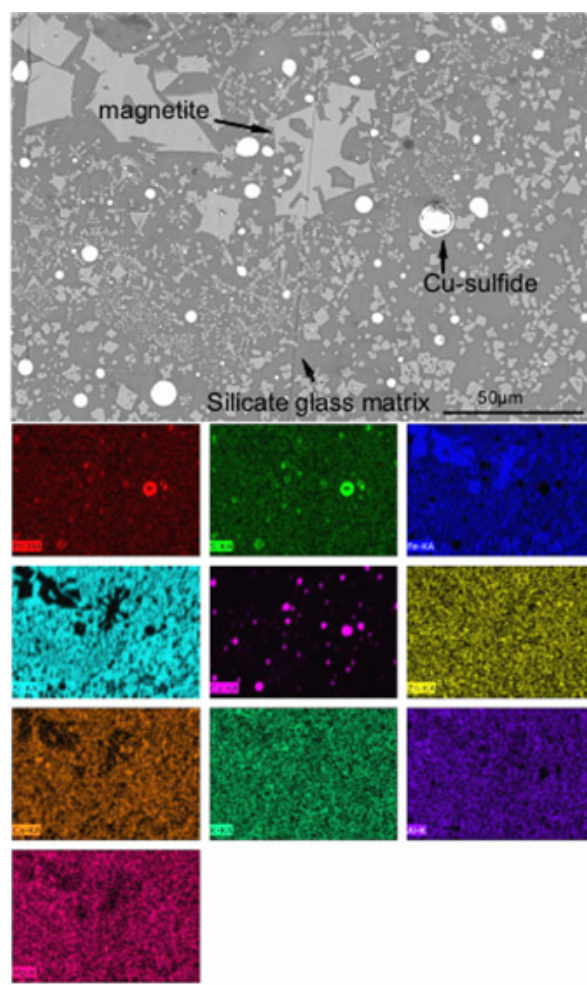


Figure 3. SEM/EDS mapped image within a separate Fe-S-O globule from Dănești-Piatra Roșie dacite debris near Dănești village (Maramures county) indicating composition of Pb, S, Fe, Si, Cu, Zn, Ca, K, Al, Mg.

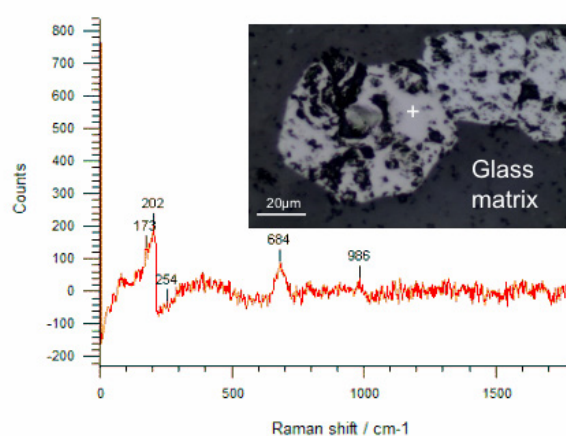


Figure 4. Raman spectra of a frothy Fe-S-O globule in silicate glass matrix from Dănești-Piatra Roșie dacite. RRUFF data base suggested the presence of Ca, Si, Al, Mg, Cu, Au, Pb, W, Sb, F, Cl, NH_4^+ , SO_4^{2-} , PO_4^{3-} in various mineral species.

Silicate melt inclusions in quartz, plagioclase, and amphibole indicated low temperature for the mushy rhyolite quartz at 715°C and up to 1150°C for the mafic magma input. During mixing/mingling processes, the mafic minerals were partially dissolved, releasing the Fe-S-O globular melts which concentrated Cu and other metallic elements in sulphide globule segregated from the basic silicate melt together with dendritic magnetite, and possible pentlandite exsolved during decompression and degassing. These were reworked by ultimate hydrosaline fluid and deposited in the upper part of the shallow magma reservoir and around the volcanic conduit(s). Raman and SEM/EDS preliminary analyses of the Fe-S-O globule indicate the presence of silicate, sulphides, oxide, fluoride, ammonium (NH_4^+), sulphate (SO_4^{2-}), phosphate (PO_4^{3-}), fluoride (F^-), and chloride (Cl^-) in mineral species containing Ca, Mg, K, Al, Si, Fe, Au, Cu, Pb, Zn, W, Bi, Sb, Ni, and probably more, representing the primary source of the ore elements in the convective hydrothermal systems from Baia Sprie, Căvnic, Dealul Crucii etc.

Acknowledgements

The authors acknowledge the financial support and access to SEM-EDS and Raman analysis, provided by the GeoEcoLab Laboratory (Geological Institute of Romania). The authors acknowledge the financial support by the national research project PN23-39-02-03.

References

- Blundy, J., Afanasyev, A., Tattich, B., Sparks, S., Melnik, O., Utkin, I., Rust, A. (2021): The economic potential of metalliferous sub-volcanic brines. *R. Soc. Open Sci.* 8 202192.
- Driesner, T. and Heinrich, C. (2007): The system H_2O -NaCl. Part I: Correlation formulae for phase relations in temperature pressure-composition space from 0 to 1000°C, 0 to 5000 bar, and 0 to 1 X_{NaCl} . *Geochimica et Cosmochimica Acta*, v. 71, p. 4880-4901.
- Georgatou, A., Chiaradia, M., Klaver, M. (2022): Deep to shallow sulfide saturation at Nisyros active volcano. *Geochemistry, Geophysics, Geosystems*, v. 23, issue 2, p. 1-21.
- Grancea, L., Fulop, A., Cuney, M., Leroy, J., Pironon, J. (2003): Magmatic evolution and ore-forming fluids in the origin of gold/base metals mineralization in the Baia Mare province, Romania. *Journal of Geochemical Exploration*, v.78 -79, p. 627-630.
- Heinrich C.A. and Connolly J.A.D. (2022): Physical transport of magmatic sulfides promotes copper enrichment in hydrothermal ore fluids. *Geology*, 50, p. 1101-1105.
- Iancu, O.G. and Kovacs, M., eds. (2010): Ore deposits and other classic localities in the Eastern Carpathians: From metamorphic to volcanics. *Acta Mineralogica - Petrographica*, Field guide series, Szeged, Hungary. V. 19, p.1-55.
- Kovacs, M., (2002): Petrogenesis of Subduction-Related Igneous Rocks from the Central Southeastern Area of the Gutâi Mts. Editura Dacia Cluj-Napoca. (in Romanian). 201 p.
- Kovacs, M., Fülöp, A., Seghedi, I., Pecskey, Z. (2021): Architecture of volcanic plumbing systems inferred from thermobarometry: A case study from the Miocene Gutâi volcanic zone in the Eastern Carpathians, Romania. *Lithos*, v. 396-397, 106191.
- Larocque, A.C.L., Stimac, J.A., Keith, J.D., Huminicki, M.A.E. (2000): Evidence for open-system behavior in immiscible Fe-S-O liquids in silicate magmas; implications for contributions of metals and sulfur to ore-forming fields. *Canadian Mineralogist*, v. 38, p. 1233-1250.
- Pintea, I., (2006): Melt inclusion texture and microthermometry in volcanic phenocrysts from the central neogene segment, East Carpathians, Romania. *An. Inst. Geol. of Romania, Bucharest*, v. 74, spec. issue, p.171-172.
- Pintea, I., (2008): Fluid and melt inclusion evidence for succession of magmatic and hydrothermal events from Neogene/Quaternary subduction zone in Carpathians. In *Pan-American Conference on research on Fluid Inclusions (PACROFI IX) - In memory of Edwin Roedder* (ed. H.E. Belkin), Program and Abstracts Reston, V.A, USA, p. 47.
- Pintea, I., (2013): Melt inclusions texture and thermal history in minerals from the Dej Tuff, Transylvania basin, Romania. *Romanian Jour. of Earth Sciences*, Bucharest, V. 87, issue 1-2, p.29-47.
- Pintea, I., (2014): The magmatic immiscibility between silicate-, brine-, and Fe-S-O melts from the porphyry (Cu-Au-Mo) deposits in the Carpathians (Romania): a review. *Romanian Jour. of Earth Sciences*, 87, issue 1-2, p. 1-33 (published 2023 at igr.ro).
- Pintea, I., (2015): Fluid in the earth crust and upper mantle: an atlas of the fluid and melt inclusions from Romania. *Romanian Jour. of Earth Sciences*, v. 87, issue 1-2, p. 35-250 (published 2023 at igr.ro).
- Pintea, I., (2016): A self-perspective research topic revealed during the elaboration of the Atlas "Fluid and Melt Inclusions from Romania". *Rom. J. Mineral Deposits*, v. 89, issue 1-2, p. 1-6.

Thermodynamic modeling of hydrothermal equilibria: a critical assessment using mineral solubility and aqueous speciation

David Dolejš¹, Federica Salomone¹

¹Institute of Earth and Environmental Sciences, University of Freiburg, Germany (david.dolejs@minpet.uni-freiburg.de)

Abstract. Ore formation in hydrothermal systems is commonly coupled to fluid-rock interaction and associated changes in acidity, redox and other system variables. These mechanisms are addressed by thermodynamic chemical equilibrium modelling, but the conventional electrostatic (Helgeson-Kirkham-Flowers, HKF) approach is inappropriate under high-temperature and low-pressure conditions relevant to shallow magmatic and epithermal systems. We explore available, alternative physico-chemical approaches to mineral solubility and aqueous speciation. Ten models for water dissociation accurately converge below 400 °C and increasingly diverge below 1.0 kbar at 600 °C. The ionization in low-density fluids is best captured by semicontinuum hydration or density models. Sixteen models for quartz solubility in water provide comparable and accurate performance up to 500-600 °C and reveal, for instance, the large sensitivity of the HKF model and its extrapolability to parameter calibration. The quartz solubility in low-density vapor is best reproduced by virial models or density approach with augmented functional form. We infer that for geochemical applications, the semi-empirical models using temperature, pressure and/or fluid density expansion (e.g., density models) are of superior quality to strictly physically based approaches. This provides basis for a new equation of state for aqueous species for simulating hydrothermal processes in high-temperature low-pressure settings.

1 Introduction

Mass transport by hydrothermal fluids is an essential mechanism for formation of diverse ore systems in magmatic-hydrothermal, orogenic, metamorphic and basinal settings (Yardley 2005, Williams-Jones and Heinrich 2005, Audétat 2019). Metal sequestration, transport and ore-mineral deposition are usually coupled to external factors (e.g., temperature and pressure gradients) or internal controls (e.g., acidity or redox changes during fluid-rock interaction; Reed 1997; Heinrich and Candela 2014). Our understanding of the fluid-mineral interaction inevitably relies on phase relations and chemical speciation in multicomponent systems and these equilibria are modeled by thermodynamic approaches (e.g., Reed 1998; Reed and Palandri 2006).

Since its introduction in 1980's, thermodynamic properties of aqueous solutes in hydrothermal fluids have been modelled with the Helgeson-Kirkham-Flowers equation of state and dataset (Tanger and Helgeson 1988; Shock et al. 1992). Despite of its attractiveness (extensive dataset, satisfactory performance in liquid-like fluids), the physical basis of this equation of state is not suitable for volatile constituents (e.g., CO₂, SO₂, H₂S, HCl, H₂) and for

use in low-density fluids (e.g., Akinfiev and Diamond 2003). This severely limits the chemical-equilibrium modeling of upper-crustal magmatic and subvolcanic systems including porphyry, skarn, greisen and epithermal systems.

However, chemical equilibria in hydrothermal systems can be approached by alternative physico-chemical approaches available in fluid engineering and supercritical fluid extraction (e.g., Palmer et al. 2004, Leusbrock et al. 2008). In this contribution we revisit the physico-chemical principles in high-temperature aqueous systems and illustrate development of a new thermodynamic model designed to predict speciation, solubility and fluid equilibria in hydrothermal systems, with emphasis on low-pressure and low-density settings.

2 Theory

Thermodynamic modelling of aqueous solutes in fluids over wide range of density represents a long-standing challenge in physical chemistry. At low fluid density, the species are variably hydrated (short-range interaction), but long-range interactions between solute and solvent molecules are negligible. At high fluid density, the solvent has flexible but finite structure, where long-range (electrostatic and volumetric) interactions dominate and they can only be described by field continuum approaches (Fig. 1). As a result, no continuous formulation for thermodynamic properties of aqueous species from low to high fluid density is available, and this is a major drawback for modeling and interpretation of fluid-mineral interaction in magmatic-hydrothermal and epithermal systems.

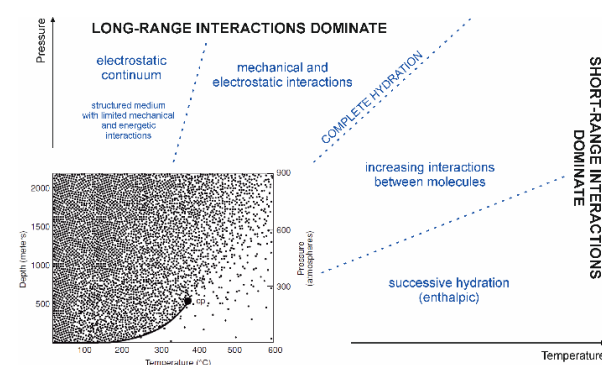


Figure 1. Schematic illustration of H₂O structure and solute-solvent interactions in the pressure-temperature space that define contributions to thermodynamic properties of aqueous species.

In low-density vapor, thermodynamic properties of the aqueous solute are conveniently modelled by introducing successively hydrated species in the gaseous standard state (hydration models). This approach is flexible and accurate at fluid density below ca. 0.1 g cm^{-3} . Its failure at greater densities indicates completion of the coordination sphere of water molecules around the solute species and the progressive onset of long-range interactions around the species. The fully hydrated state can be described: (1) empirically by correlating the thermodynamic properties with fluid density (density models) or, more simply, volume concentration of water (Mesmer et al. 1988, Marshall 2008). The functional form has been derived from several approximations to virial equation of state (Franck 1956, Akin'fiev and Plyasunov 2013, Plyasunov 2020), although the temperature or density dependence of interaction parameters is often complex and does not allow extrapolation to very high pressures. At high fluid densities, the interaction field around the solute species has been traditionally described by Born electrostatic theory (electrostatic models; Helgeson et al. 1981, Tanger and Helgeson 1988). These models are physical for charged species, but their performance for volatile solutes and at low fluid density is limited. Several attempts have been made to bridge the hydration and long-range continuum approaches (semi-continuum models; Tanger and Pitzer 1989; Bandura and Lvov 2006). We will evaluate available models from each group in several model systems.

3 Applications

3.1 Dissociation of water

Dissociation of water, $\text{H}_2\text{O} = \text{H}^+ + \text{OH}^-$, is a principal speciation equilibrium in aqueous systems. It has been extensively investigated by experiments (638 measurements; Arcis et al. 2020) and modelled by hydration, density, electrostatic and statistical-mechanical approaches (Figs. 2-3).

The experimental data extend to 800°C , but are essentially limited to fluid density between 0.4 and 0.9 g cm^{-3} . In practice, individual models remain fairly consistent up to 400°C (at $P = 500 \text{ bar}$), but remarkably diverge at higher temperatures (Fig. 2). At 800°C , the discrepancy reaches 15 orders of magnitude and it provides a cautionary illustration of essentially non-existent constraints on ionic-species equilibria at magmatic temperatures and intermediate to low fluid densities. With decreasing pressure, the decreasing fluid density promotes ionic association, thus leading to substantial decrease in H_2O dissociation constant. At $T = 600^\circ\text{C}$, the experimental trend is accurately reproduced by density and semi-continuum models, whereas the conventional electrostatic approach (HKF; Tanger and Helgeson 1988; Shock et al. 1992) tends to be inaccurate below 1.5 kbar and non-physical below 1.0 kbar .

The H_2O dissociation has been used as a proxy for other ionic equilibria in hydrothermal fluids (Ryzhenko et al. 1985). Our evaluation defines the limitations of the electrostatic model (HKF) and highlights the potential of semi-continuum hydration and density models for high-temperature and low-pressure hydrothermal conditions.

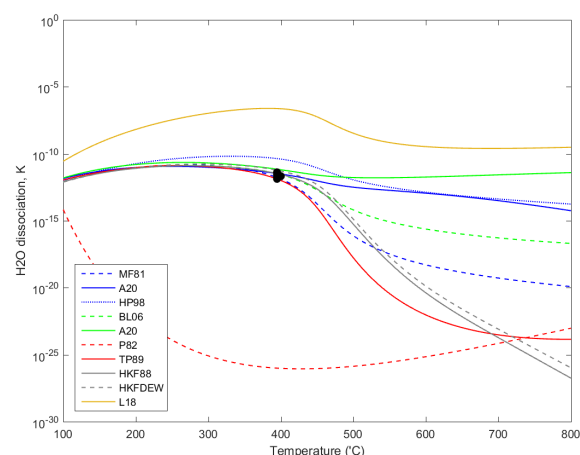


Figure 2. Variation of H_2O dissociation constant (K) with temperature at $P = 500 \text{ bar}$. Color scheme: blue – density models; green – empirical hydration models; red – successive hydration models; yellow – statistical-mechanical models. Point symbols are experimental data.

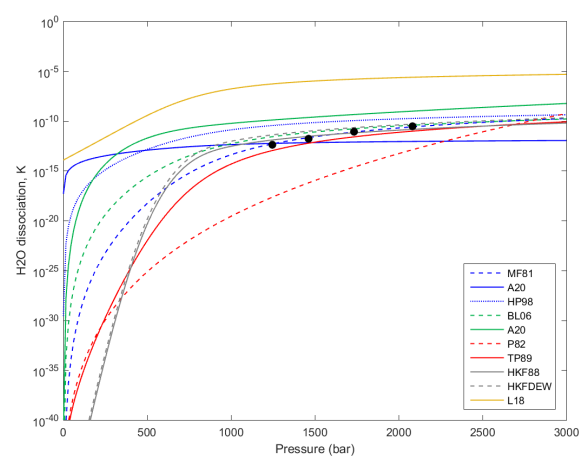


Figure 3. Variation of H_2O dissociation constant (K) with pressure at $T = 600^\circ\text{C}$. See Fig. 2 for symbol explanation.

3.2 Solubility of quartz

Solubility of quartz in aqueous fluid, expressed by generic equilibrium $\text{SiO}_2(\text{qz}) = \text{SiO}_2(\text{aq})$, provides a model system for mineral-fluid equilibria for the following reasons: (1) silica hydrate or silicic acid is a neutral species, stable over wide range of temperature, pressure and acidity; (2) solubility of quartz as a solid phase is low to moderate, hence solute-solute interaction effects remain negligible; (3) extensive coverage by experimental data (748 experiments; e.g., Dolejš and Manning 2010). In total, 16 thermodynamic models are available to predict the quartz solubility under hydrothermal conditions (Figs. 4-5).

The solubility of quartz in H_2O under moderate temperatures up to 500 °C (at $P = 500$ bar) is consistently and accurately reproduced by any of the thermodynamic approaches (Fig. 4). Above 500 °C, the electrostatic calibration by Sverjensky et al. (2014) and the density model by Holland & Powell (1998) start to deviate from experimental data, but other electrostatic (HKF) and density models maintain overall consistency up to 700 °C, as opposed to virial models (Fig. 4). The relative performance of individual physico-chemical approaches is best illustrated at subcritical conditions, where the differences in solubility in aqueous liquid vs. vapor are amplified (Fig. 5). At $T = 300$ °C, cannot be captured by miscellaneous, mainly advanced theoretical models. Likewise, the electrostatic (HKF) model does not approach the trend and magnitude of quartz solubility in steam. By contrast, the density models with augmented density dependence (Fournier and Potter 1982) or virial models offer accurate representation of experimental data.

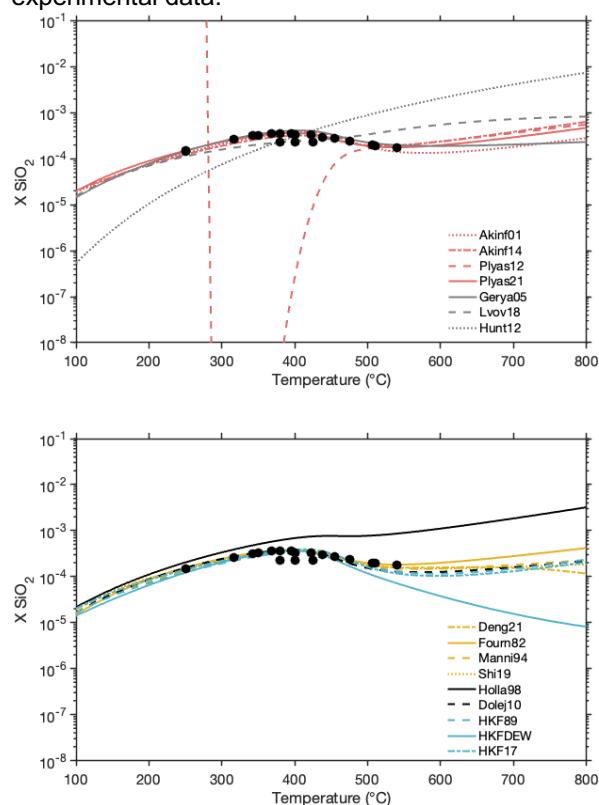


Figure 4. Variation of quartz solubility (expressed as mole fraction, X) with temperature at $P = 500$ bar. Legend: black – density models, blue – electrostatic models, gray – miscellaneous models, red – virial models, yellow – empirical density models. Point symbols are experimental data.

Overall, the quartz solubility data and models illustrate the limitations of the electrostatic (HKF) approach and emphasize the need for density-based or virial formulation for the thermodynamic properties of aqueous species in high-temperature and low-pressure (low-density) fluids.

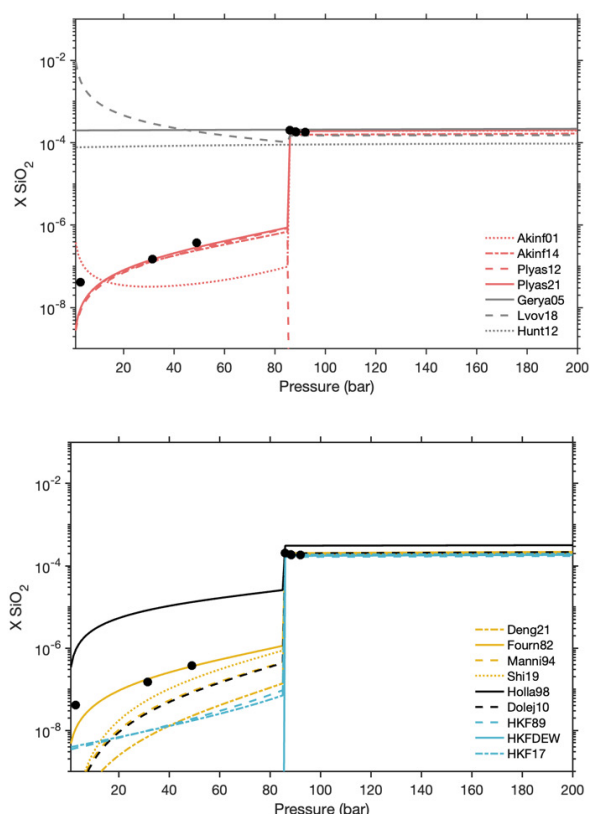


Figure 5. Variation of quartz solubility (expressed as mole fraction, X) with pressure at $T = 300$ °C. See Fig. 4 for symbol explanation.

4 Conclusions and outlook

This contribution illustrates the diversity of thermodynamic approaches to mineral solubility and aqueous speciation using several model systems. Equations of state for applications in geochemistry and ore formation are expected to provide reasonable extrapolation stability with respect to temperature, pressure or fluid density owing to limited experimental data and the need to cover complex, multicomponent systems. Statistical thermodynamics has offered several fundamental theories for model fluid systems (e.g., hard sphere fluid) and for solute-solvent interactions (e.g., scaled particle theory, fluctuation solution theory, mean spherical approximation). Despite their theoretical rigor, the pressure-temperature dependence of their parameters and leading terms is essentially unknown and difficult to constrain theoretically, unknown and this severely limits their application in geochemistry. In this sense, semi-theoretical or semi-empirical models that are primarily designed around temperature and pressure expansion of their thermodynamic functions are better suited for aqueous geochemistry and fluid-rock interaction.

Our approach is based on empirical comparison of a wide range of thermodynamic models with experimental data with (1) extensive coverage of the pressure-temperature space, and (2) constant and simple solute speciation. This includes solubility of oxide minerals (e.g., quartz) and speciation of

H₂O. Our critical assessment has revealed: (1) the conventional electrostatic (HKF) approach offers sufficient calibration flexibility to reproduce experimental data accurately, but not over a wide range of pressure-temperature conditions. The electrostatic approach cannot capture the trend and magnitude of solute properties in high-temperature and low-density fluids (below 1.0 kbar). (2) Models utilizing successive hydration offer large flexibility for speciation and solubility in low-density vapor, but their functional form is inappropriate and predictions meaningless when the full coordination by solvent has been achieved. (3) Density-based models appear to provide the best compromise between physically defined behaviour and limiting cases, extrapolation stability and accurate data reproducibility. Our intention is to formulate a new functional form for the thermodynamic properties of aqueous species that would extend to high temperatures and low pressures and thus open applications to ore formation in shallow magmatic, subvolcanic and epithermal systems.

Acknowledgements

This project has been financially supported by the German Research Council (DFG). We appreciate constructive editorial handling by Thomas Driesner.

References

- Akinfiev NN, Diamond LW (2003) Thermodynamic description of aqueous nonelectrolytes at infinite dilution over a wide range of state parameters. *Geochim Cosmochim Acta* 67: 613-627
- Akinfiev NN, Plyasunov AV (2013) Steam solubilities of solid MoO₃, ZnO and Cu₂O, calculated on a basis of a thermodynamic model. *Fluid Phase Equil* 338: 232-244
- Arcis H, Ferguson JP, Cox JS, Tremaine PR (2020) The ionization constant of water at elevated temperatures and pressures: New data from direct conductivity measurements and revised formulations from $T = 273$ K to 674 K and $p = 0.1$ MPa to 31 MPa. *J Phys Chem Ref Data* 49: 033103
- Audétat A (2019) The metal content of magmatic-hydrothermal fluids and its relationship to mineralization potential. *Econ Geol* 114: 1033-1056
- Bandura AV, Lvov SN (2006) The ionization constant of water over wide ranges of temperature and density. *J Phys Chem Ref Data* 35, 15-30
- Dolejš D (2013) Thermodynamics of aqueous species at high temperatures and pressures: equations of state and transport theory. *Rev Mineral Geoch* 76: 35-79
- Dolejš D, Manning CE (2010) Thermodynamic model for mineral solubility in aqueous fluids: theory, calibration and application to model fluid-flow systems. *Geofluids* 10: 20-40
- Fournier RO, Potter RW II (1982) An equation correlating the solubility of quartz in water from 25° to 900°C at pressures up to 10,000 bars. *Geochim Cosmochim Acta* 46: 1969-1973
- Franck EU (1956) Zur Löslichkeit fester Stoffe in verdichteten Gasen. *Z Phys Chemie NF* 6: 345-355
- Heinrich CA, Candela PA (2014) Fluids and ore formation in the Earth's crust. *Treatise Geochem* 13: 1-28.
- Helgeson HC, Kirkham D, Flowers GC (1981) Thermodynamic behavior of aqueous electrolytes at high pressures and temperatures. IV. Calculation of activity coefficients, osmotic coefficients, and apparent molal and standard and relative partial molal properties to 600°C and 5 kb. *Am J Sci* 281: 1249-1516
- Holland TJB, Powell R (1998) An internally consistent thermodynamic data set for phases of petrological interest. *J Metam Geol* 16: 309-343
- Leusbrock I, Metz SJ, Rexwinkel G, Versteeg GF (2008) Quantitative approaches for the description of solubilities of inorganic compounds in near-critical and supercritical water. *J Supercrit Fluids* 47: 117-127
- Marshall WL (2008) Aqueous electrolyte ionization over extreme ranges as simple fundamental relation with density and believed universal; sodium chloride ionization from 0° to 1000°C and to 1000 MPa (10000 Atm.). *Nat Prec* 2008 (DOI: 10.1038/npre.2008.2476.1)
- Mesmer RE, Marshall WL, Palmer DA, Simonson JM, Holmes HF (1988) Thermodynamics of aqueous association and ionization reactions at high temperatures and pressures. *J Solut Chem* 17: 699-718
- Palmer DA, Fernández-Prini RJ, Harvey AH (eds, 2004) Aqueous systems at elevated temperatures and pressures. *Physical chemistry in water, steam, and hydrothermal solutions*. Elsevier, Amsterdam, 753 p
- Plyasunov AV (2020) Predicting solubility of oxides of metals and metalloids in supercritical water. *Ind Eng Chem Res* 59: 970-980
- Reed MH (1997) Hydrothermal alteration and its relationship to ore fluid composition. In Barnes HL (ed) *Geochemistry of hydrothermal ore deposits* (3ed). Wiley, New York: 303-365
- Reed MH (1998) Calculation of simultaneous chemical equilibria in aqueous-mineral-gas systems and its application to modeling hydrothermal processes. *Rev Econ Geol* 10: 109-124
- Reed MH, Palandri J (2006) Sulfide mineral precipitation from hydrothermal fluids. *Rev Mineral Geochem* 61: 609-631
- Ryzhenko BN, Bryzgalin OV, Artamkina IY, Spassenykh MY, Shapkin AI (1985) An electrostatic model for the electrolytic dissociation of inorganic substances dissolved in water. *Geochem Internat* 22/9: 138-144
- Shock EL, Oelkers EH, Johnson JW, Sverjensky DA, Helgeson HC (1992) Calculation of the thermodynamic properties of aqueous species at high pressures and temperatures: effective electrostatic radii, dissociation constants and standard partial molal properties to 1000°C and 5 kbar. *J Chem Soc, Faraday Trans* 88: 803-826
- Sverjensky DA, Harrison B, Azzolini D (2014) Water in the deep Earth: The dielectric constant and the solubilities of quartz and corundum to 60 kb and 1200 °C. *Geochim Cosmochim Acta* 129: 125-145
- Tanger JC IV, Helgeson HC (1988) Calculation of the thermodynamic and transport properties of aqueous species at high pressures and temperatures: revised equations of state for the standard partial molal properties of ions and electrolytes. *Am J Sci* 288, 19-98
- Tanger JC IV, Pitzer KS (1989) Calculation of the thermodynamic properties of aqueous electrolytes to 1000 °C and 5000 bar from a semicontinuum model for ion hydration. *J Phys Chem* 93: 4941-4951
- Williams-Jones AE, Heinrich CA (2005) Vapor transport of metals and the formation of magmatic-hydrothermal deposits. *Econ Geol* 100: 1287-1312
- Yardley BWD (2005) Metal concentrations in crustal fluids and their relationship to ore formation. *Econ Geol* 100: 613-632

Complex genetic model of the shear-zone hosted epithermal Au-Ag-Pb-Zn-Cu deposit Banská Hodruša at the Rozália mine, Slovakia

Peter Koděra¹, Jaroslav Lexa², Martin Chovan¹, Rastislav Vojtko¹, Alexander Kubač³, Bertrand Rottier⁴, Matej Rybárik¹, Ján Prčuch⁵

¹Faculty of Natural Sciences, Comenius University, Bratislava, Slovakia

²Earth Science Institute, Slovak Academy of Sciences, Bratislava, Slovakia

³State Geological Institute of D. Štúr, Bratislava, Slovakia

⁴Département de Géologie et Génie Géologique, Université Laval, Québec, Canada

⁵Slovenská Banská, Ltd., Hodruša-Hámre, Slovakia

Abstract. Banská Hodruša intermediate sulfidation gold-rich deposit is hosted by a low-angle shear zone in the centre of the Neogene Štiavnica stratovolcano. It occurs on the historical Rozália mine, where base metal stockwork mineralisation and Cu-rich veins were mined in the past too. Geological evolution started with the emplacement of a granodiorite pluton, followed by its rapid exhumation and related sector collapse of the volcano at the base with the flat shear zone, later penetrated by quartz-diorite sills and final resurgent horst uplift related to accumulation of residual rhyolitic magma in the magma chamber. Tectonic events include cracking of the apical part of granodiorite on cooling and hydraulic fracturing, development of ring and subhorizontal structures above the granodiorite due to the relative subsidence of the central block into the chamber, two-stage formation of faults in the shear zone and final creation of steep faults related to the resurgent horst uplift. Hydrothermal events include exsolution of fluids from the granodiorite magma and their heterogenization, long-lasting fluid exsolution from the upper-crustal magma chamber and finally fluid exsolution from the residual rhyolitic magma. Supercritical fluids subsequently penetrated contraction cracks, andesite-granodiorite contact, shear zone, horst faults and they were variably affected by fluid mixing and boiling.

1 Introduction

The Au-Ag-Pb-Zn-Cu epithermal deposit Banská Hodruša of intermediate-sulphidation type is located in the central zone of Middle Miocene Štiavnica stratovolcano on the inner side of the Carpathian arc. It is the last active ore mine in Slovakia, with estimated total production ~10 t Au and 6 t Ag (Kubač et al. 2018). This deposit occurs at the historical Rozália mine 400–650 m below the current surface and it represents an unusual subhorizontal multi-stage vein system, hosted by a shear zone, corresponding to a low-angle normal fault zone (LANF). Epithermal Au-rich ore has been exploited here since 1992, but in the past this mine was also used to exploit steep Cu-Pb-Zn epithermal veins and a base-metal stockwork mineralization.

During the last decades, a considerable amount of geological, petrological, structural, mineralogical, geochemical and genetic data were obtained from this area (Table 1). This work presents a review of these data that are used to develop a complex genetic model of the deposit, including other spatially and genetically associated types of mineralisations present at the Rozália mine (Fig.1).

2 Mineralisations at the Rozália mine

The Au-Ag-Pb-Zn-Cu epithermal veins, hosted by the shear zone, occur in the pre-caldera andesites near the flat roof of a granodiorite pluton. The ore deposit developed in several stages (Kubač et al. 2018). The early stage consists of low-grade silicified breccia at the base of the deposit, occurring along E-W oriented subhorizontal structures dipping 20–30° to SE. The main ore mineralisation consists of stockwork of early steep veins (E-W, 40–60° to S) and a later system of veins inside the shear zone (NE-SW, ~45° to SE), accompanied by complementary detachment-hosted veins (<30°) in the roof of the shear zone. Veins consist of early quartz-rhodonite assemblage (incl. Mn-carbonates, chlorite) and later sulphide-gold assemblage (incl. sphalerite, galena, chalcopyrite, pyrite, rare Te-minerals and various gangue minerals). Mined ore contains 14 g/t Au, 17 g/t Ag, 0.6% Zn, 0.45% Pb, and 0.15% Cu in average. The shear zone was intruded by mostly post-mineralisation system of quartz-diorite porphyry sills. Post-ore veins include rare barren quartz veins of variable orientation mostly hosted by the porphyry. Major veins are accompanied by adularia, quartz and illite. Strong argillisation (illite ± quartz, pyrite) occurs in the roof of the shear zone (Koděra et al. 2017).

The stockwork mineralisation occurs some 1.5 km south of the Au-Ag deposit, mostly hosted by apical porphyritic part of the granodiorite pluton. It resembles a porphyry hydrothermal system including potassic alteration in the granodiorite, and advanced argillic alteration in overlying pre-caldera andesite (Koděra et al. 2004). Mined ores contained 2.5% Pb, 3.5% Zn, 0.4% Cu, 10 g/t Ag. Ore grades and intensity of potassium alteration decrease with depth.

The steep epithermal veins (50–70° to NE–SW) cut the base-metal stockwork, the gold-rich veins as well as quartz-diorite porphyry sills. They belong to an extensive system of veins in the central zone of the volcano with a zonal arrangement (Pb-Zn-Cu, Ag-Au, Au-Ag) and multi-stage filling (Kovalenker et al. 1991). At the Rozália mine the most important is the Rozália vein, mined for Cu-rich base metal ore (0.5–0.8% Cu, 0.2% Pb, 0.3% Zn, 10–20 g/t Ag, 0.1–0.2 g/t Au).

Stage	I		II	III	IV		V	VI
Age	13.6 Ma		13.6 – 13.5 Ma				13.5 – 13.0 Ma	12.2 – 11.4 Ma
Mineralisation / host rock	Fe-skarns / basement carbonates	Advanced argillic alteration / andesite	Pb-Zn-Cu stockwork / apical part of granodiorite & andesite	Silicite / subhorizont. structures in andesite in contact with granodiorite	Shear-zone hosted epithermal Au-Ag-Pb-Zn-Cu veins / andesite		Post-mineralisation Qtz veins / andesite & Qtz-diorite porphyry	Pb-Zn-Cu-Ag-Au horst veins / andesite & Qtz-diorite porphyry
					Qtz-Rdn vein filling	Sulf-Au vein filling		
Geological evolution	Emplacement of granodiorite pluton between prevolcanic basement and andesite, cooling, fluid exsolution during its crystallization		Fluid saturation in magma chamber, migration of fluid-saturated magma between subsiding basement and granodiorite pluton together with continuous granodiorite uplift and exhumation				Emplacement of most sill of Qtz-diorite porphyry	Final magma chamber cooling, cupola of fluid-saturated rhyolitic magma, horst uplift, fluid penetration into deep horst faults
			Penetration of fluids into contraction cracks	Penetration of fluid into andesite-granodiorite contact	Sectoral collapse of volcano at the base with argillites, fluids-filled structures, and basement carbonates; fluid penetration in the shear zone			
Tectonic evolution	Contraction cracking of granodiorite during cooling in subsolidus conditions		Fracturing due to relict contractional stress & hydraulic fracturing	Subhorizon. structures above the granodiorite & hydraulic fracturing	Initial N-S movement on shear zone	NW-SE reorientation of movement on shear zone	Ring and subhorizontal structures at sides and above granodiorite	Resurgent horst uplift in caldera centre, system of steep faults
Fluid evolution	Heterogenisation of fluids exsolved from granodiorite magma		Continued fluid exsolution from magma chamber, ascend in the form of supercritical fluids				No data	Ascend of supercritical fluids
	Brine cooling & mixing with meteoric water	Vapor condensation	Mixing of magmatic - meteoric fluids	Cooling of magmatic fluids	Boiling of magmatic fluid due to decompression			

Table 1. Summary of geological, tectonic and fluid evolution related to all major types of mineralisation in the Rozália mine in Banská Hodruša. Ages are based on data of Chernyshev et al. (2013) and Lexa et al. (2019).

3 Geological evolution

Stages of evolution related to mineralisation at the Rozália mine (Table 1, Fig. 1) are interpreted based on the structural and magmatic evolution of the Štiavnica stratovolcano (Chernyshev et al. 2013, Rottier et al. 2019) and dating of subvolcanic intrusions and caldera filling (Lexa et al. 2019). The most characteristic features of the volcano include an extensive caldera, a late-stage resurgent horst in the caldera centre and a large subvolcanic intrusive complex. Magmas associated with the hydrothermal mineralization were sourced from an upper crustal reservoir (1 to 3 kbar at 960 to 700 °C) that was active more than 3 million years. Ore deposits formed during periods of reservoir cooling when the residual melt reached fluid saturation.

The first evolutionary stage associated with mineralisations at the Rozália mine is related to the emplacement of the granodiorite magma between the prevolcanic basement and the pre-caldera andesite at a minimum depth of ~2 km (13.6 Ma). The intrusion has a relatively flat roof, probably as a consequence of a descent of the central block of basement rocks into the upper crustal magmatic reservoir, compensated by the displacement of magma above the block. On cooling and progress of crystallization, exsolution of fluid appeared, which was responsible for adjacent Fe-skarn mineralisation and advanced argillic alteration in the apical part of the pluton (Koděra et al. 2014).

During the next four evolutionary stages, cooling and possibly mixing of the magma in the reservoir, evidenced by thermobarometry and petrography, led to its saturation by fluids and their exsolution. This caused a decrease in magma density and its

migration and emplacement between the subsiding basement block and the granodiorite intrusion. Magma decompression in turn accelerated the fluid exsolution. These fluids migrated upwards using contraction cracks forming the base metal stockwork hydrothermal system (Stage 2) and later they penetrated the andesite-granodiorite contact forming barren silicites (Stage 3). The continuous emplacement of the fluid-saturated magma was also responsible for a rapid resurgent uplift and exhumation of the granodiorite pluton, finally leading to a sector collapse of the volcano, at the base with argillites, fluids-filled structures, and basement carbonates (Stage 4). Fluid penetration along a flat shear zone at the base of the collapse was responsible for the currently mined Au-rich veins. The accumulation of differentiated magma of lower density in the magmatic reservoir finally led to the emplacement of the post-mineralisation system of sill and dykes of quartz-diorite porphyry (13.5 – 13.0 Ma), especially using structures of the shear zone, and terminated the gold-forming hydrothermal activity in the area of the Rozália mine (Stage 5).

Subsequent geological evolution of the volcano did not directly affect mineralisation at the mine. It was represented by a caldera subsidence linked with extrusive activity of evolved andesites and post-caldera andesitic effusive activity. However, fluid saturation was not reached, as magma was relatively hot (up to 970 °C), probably due to large inputs of mafic magma into the upper-crustal reservoir.

The last evolutionary stage at the mine (Stage 6) is related to the final cooling of the magma chamber (<750 °C), when a cupola of fluid-saturated rhyolite magma developed in the chamber, representing

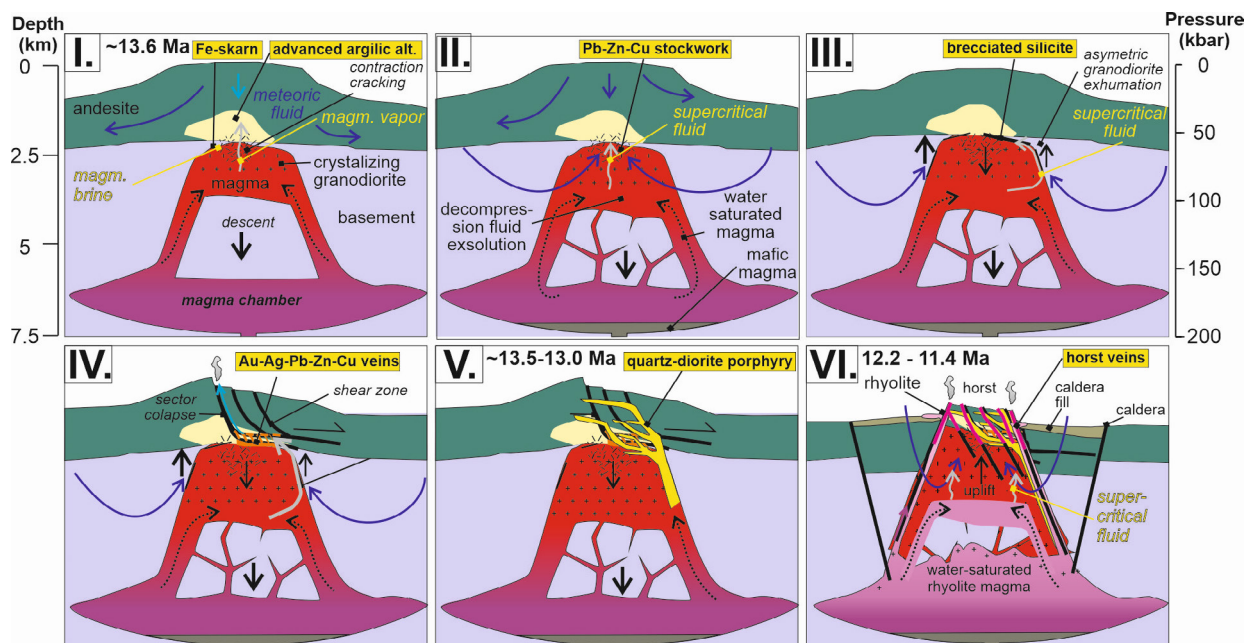


Figure 1. Stages and timing of geological evolution related to various mineralisation types at the Rozália mine, including corresponding tectonic and fluid evolution. See text and Table 1 for details.

interstitial melt segregated from the crystal mush. low density of the fluid saturated magma resulted in an uplift of the central zone of the volcano, forming a resurgent horst dome, and emplacement of rhyolite dikes and domes (12.2 - 11.4 Ma, outside the mine). Penetration of exsolved fluid into deep horst faults resulted in an extensive system of horst-related epithermal veins.

4 Tectonic evolution

Tectonic events and development of fractures were important for creation of fluid flow paths and the origin of various mineralisations at the Rozália mine. Tectonic evolution related to mineralisation is based on regional-scale and mine-scale structural analyses (Nemčok et al. 2000; Kubač et al. 2018).

The early base metal stockwork is related to a relict contractional stress in the granodiorite during cooling of the apical part of the intrusion, further enhanced by hydraulic fracturing. The resulting network of fractures enabled migration of fluids exsolving from the magma reservoir.

Silicites and silicified breccias of hydraulic fracturing on subhorizontal structures at the andesite-granodiorite contact are linked to the subsidence of the basement block into the upper-crustal magma chamber, including the solidified granodiorite pluton. Magmatic fluids released from the chamber penetrated the contact at a pressure close lithostatic.

Epithermal Au-Ag-Pb-Zn-Cu veins are related to the origin of the shear zone during the sector collapse of the volcano and the shear zone creation. The early movement on the shear zone was N-S oriented, forming an early stockwork of E-W oriented veins. Later movements on the shear zone were NW-SE oriented, forming a later system of

veins of NE-SW orientation. Post-ore emplacement of quartz-diorite porphyry magma was enabled by the same subhorizontal structures as the ore veins and fed from ring structures, both related to the reactivated underground cauldron subsidence of the central block.

Latest base metal epithermal veins are hosted by a complex system of steep NE-SW oriented faults related to the long-lasting resurgent horst uplift.

5 Fluid evolution

Evolution of fluids related to the various stages of mineralisation at the mine is interpreted from stable isotope, fluid inclusion and illite thermometry data from the skarn and base metal stockwork mineralisation (Koděra et al. 2004), from the gold-rich veins (Koděra et al. 2005; Kubač et al. 2018) and from the horst-related base metal veins (Kovalenker et al. 1991, Koděra et al. 2005), including recent LA ICMPS of fluid inclusions (Koděra et al. 2019, 2021).

Inclusions in quartz from the granodiorite showed that the magmatic fluid exsolved from the granodiorite magma experienced a phase separation into a hot (>600°C) hypersaline brine (up to 71 wt % NaCl eq.) and a vapor. Skarn mineralisation was produced from the brine mixed with meteoric water (215–370°C, up to 23 wt% NaCl eq.). Coeval advanced argillic alteration above the apical part of the granodiorite pluton originated from condensed magmatic vapor (191–367°C, up to 5 wt% NaCl eq.).

Base metal stockwork ore crystallised from fluids showing a positive correlation between salinity (5 - 0.5 wt.% NaCl eq.) and temperature (330 - 190 °C), indicative for mixing of magmatic and meteoric

fluids, also confirmed by combined O and H isotope data. The absence of boiling due to pressure constraints (granodiorite was still not sufficiently uplifted) could explain the absence of gold in ores.

Fluids associated with the gold-rich, shear-zone hosted veins had salinities (1-4 wt.% NaCl eq.) and temperatures (~250-310 °C) similar to the stockwork. Gold precipitation was mostly induced by boiling of decompressed fluids evolving from suprahydrostatic to hydrostatic conditions at a depth of ~550 m. Boiling in this subhorizontal system of veins was mostly related to opening of dilatational structures that enabled an active suction of fluids and their decompression. The main migration of paleofluids occurred along low-angle normal faults of the shear zone from S-SE to N-NW, as indicated by the geological setting of the quartz-diorite porphyry sills that intruded the shear zone at the end of the hydrothermal activity from S-SE. The main ore mineralisation is associated with areas with densely distributed dilatational structures, where both major boundaries of the shear zone were relatively close together, i.e. where the hanging-wall argillite was relatively close to foot-wall silicite. The strongly argillised upper boundary of the shear zone probably worked as a collector of hydrothermal fluids flowing along the shear zone, as well as a collector of vapour and gases escaping from boiling fluids throughout the entire thickness of the shear zone.

Fluids associated with the base metal horst-related veins have wide ranges of salinities (0.5 - 11.5 wt.% NaCl eq.) and temperatures (360 - 110 °C), related to their multistage filling, with evidence for boiling and mixing of fluids.

Magmatic fluids associated with the base metal stockwork and all epithermal mineralisations show increased B, As and Sb contents which indicates that these vapor-affiliated elements were not lost during fluid heterogenisation on ascent from the magma chamber. Thus, the fluid source was likely supercritical in nature, later contracted to liquid. The relatively constant composition of most inclusions (including metals) indicates a common long-lasting source of the fluids exsolved from the magma chamber. Furthermore, the composition of silicate melt inclusions from corresponding coeval magmatic rocks (Rottier et al. 2019) is in a good agreement with published fluid-melt fractionation factors.

6 Conclusions

The presented complex genetic model of the epithermal gold deposit and associated mineralisation types at the Rozália mine includes a sequence of events that started with the emplacement of a granodiorite pluton. Fe-skarns and advanced argillic alteration are related to heterogenisation of a fluid exsolved from the granodiorite magma. It follows fluid exsolution from the upper crustal magma chamber and penetration of supercritical fluids into contraction cracks in the

intrusion, resulting in the origin of Pb-Zn-Cu stockwork mineralization due to mixing with meteoric water. Gold-rich veins hosted by the shear zone are related to the rapid exhumation of the granodiorite, sector collapse of the volcano and penetration of the shear zone by supercritical fluids which were affected by boiling due to decompression. This hydrothermal activity was terminated by the emplacement of quartz-diorite porphyry sills in the shear zone. The latest base metal vein mineralisation at the mine is related to the development of a fluid-saturated residual magma in the magma chamber, resulting in a resurgent horst uplift and a system of steep faults, penetrated by supercritical fluids, later affected by boiling and mixing with meteoric water.

Acknowledgements

This work was supported by grants VEGA No. 1/0313/20 and APVV-15-0083.

References

- Chernyshev IV, Konečný V, Lexa J, Kovalenker VA, Jeleň S, Lebedev VA, Goltsman YuV (2013) K-Ar and Rb-Sr geochronology and evolution of the Štiavnica Stratovolcano, Central Slovakia. *Geol Carpath* 64:327-351.
- Koděra P, Lexa J, Rankin AH, Fallick AE (2004) Fluid evolution in a subvolcanic granodiorite pluton related to Fe and Pb-Zn mineralization, Banská Štiavnica ore district, Slovakia. *Econ Geol* 99:1745-1770.
- Koděra P, Lexa J, Rankin AH, Fallick AE (2005) Epithermal gold veins in a caldera setting: Banská Hodruša, Slovakia. *Miner Depos* 39:921-943.
- Koděra P, Kubač A, Uhlík P, Osacký M, Vojtko R, Chovan M, Lexa J, Žitňan P (2017) Hydrothermal alteration of a shallow-dipping epithermal Au-Ag-Pb-Zn-Cu deposit Banská Hodruša, Slovakia. *Proc 14th SGA Bien Meeting, Québec City, Canada, Vol 1: 159-162.*
- Koděra P, Kubač A, Uhlík P, Vojtko R, Chovan M, Lexa J, Milovský R, Laurent O, Fallick E.A., 2019: Fluid evolution and genesis of epithermal gold deposit hosted by a shear-zone: Banská Hodruša. *Proc 15th Biennial SGA Meeting*, 3, 1042 - 1045.
- Koděra P, Kubač A, Lexa J, Rottier, B., Laurent, O., 2021: External controls govern metal endowment and styles of ore mineralisation in andesite volcanoes – example from the Štiavnica stratovolcano, Slovakia. In *Proc 16th Biennial SGA Meeting*, 2, 96.
- Kovalenker, V.A., Jeleň, S., Levin, K.A., Naumov, V.B., Prokofjev, V.J., Rusinov, V.L., 1991: Mineral assemblages and physical-chemical model of the formation of gold-silver-polymetallic mineralisation on the deposit Banská Štiavnica (Central Slovakia). *Geol Carpath*, 42, 291 - 302.
- Kubač A, Chovan M, Koděra P, Kyle JR, Žitňan P, Lexa J, Vojtko R (2018) Mineralogy of the epithermal precious and base metal deposit Banská Hodruša at the Rozália mine (Slovakia). *Miner Petrol* 112:705–731.
- Lexa, J., Rottier, B., Yi, K., Audétat, A., Broska, I., Koděra, P., Kohút, M. 2019: Magmatic evolution of the Štiavnica volcano. *Proc. Geol Carpath 70 Internat. Conf.*, 5 pp.
- Nemčok M, Lexa O, Konečný P (2000) Calculations of tectonic, magmatic and residual stress in the Štiavnica Stratovolcano, Western Carpathians: implications for mineral precipitation paths. *Geol Carpath* 51: 19-36
- Rottier, B., Audétat, A., Koděra, P., Lexa, J., 2019: Magmatic evolution of the mineralized Štiavnica volcano (Central Slovakia): Evidence from thermobarometry, melt inclusions, and sulfide inclusions *J Volcan Geoth Res*, 401, 106967.

Numerical simulations of pulsed epithermal ore-forming events in geothermal systems with incrementally growing magma reservoirs

Maximilian Korges¹, Philipp Weis^{1,2}

¹*Institute of Earth and Environmental Science, University of Potsdam, Potsdam, Germany*

²*GFZ German Research Centre for Geosciences, Potsdam, Germany*

Abstract. Numerical models can provide unique insights into the temporal and spatial relationships of ore-forming processes. We use a model for magma reservoir growth to investigate the impact of sill injection rates on the hydrothermal system. The simulations with more episodic, low injection rates ($<1.3 \times 10^{-3} \text{ km}^3/\text{y}$) result in a highly variable fluid plume which allows almost pure magmatic fluids to migrate to shallower and cooler regions where they can phase separate and potentially form epithermal ore deposits. The modelling results point towards a relatively short time span of potential ore formation of a few thousands of years until the magmatic fluid plume retreats. Long-lived magma reservoirs which are forming at higher injection rates hamper the formation of high-grade epithermal deposits, but are more favourable for high-grade porphyry Cu deposits.

1 Introduction

Epithermal ore deposits are important resources for various precious (e.g. Au, Ag) and base (e.g. Cu, Pb, Zn) metals. They form within the uppermost 1.5 km of Earth's crust by circulation of hydrothermal fluids through fractured and porous rocks in geothermal and volcanic systems (Hedenquist & Arribas, 2022). The ore-forming fluids can be of pure meteoric or magmatic origin (potentially also including seawater), or variable mixtures of these end-members. Low-sulfidation epithermal deposits are characterized by low to moderate sulphur contents in the hydrothermal fluids, while high-sulfidation deposits have high sulphur contents, which is typically inferred to be related to a stronger influence of magmatic volatiles. High-sulfidation deposits can form at temperatures of 200-300°C (Hedenquist et al. 2000; Hedenquist & Arribas, 2022), which requires cooling of ascending magmatic (-dominated) fluids compared to volcanic fumaroles.

Many hydrothermal veins in epithermal deposits show evidence for pulsed ore formation with high metal contents limited to distinct growth zones. As a particularly efficient mechanism for metal enrichment to economic grades, transport and precipitation of precious metals has been proposed to occur by isochemical contraction of a single-phase magmatic vapor (which originated from an underlying magmatic-hydrothermal system where phase separation occurred) followed by a second phase-separation event of near-surface boiling (Heinrich et al. 2004). However, the timing and duration of epithermal mineralization as well as the evolution and state of the underlying, driving magmatic systems within the crust are still debated. The total time of ore precipitation has been

suggested to be less than 10 kyrs (e.g. Moncada et al. 2019), but the relationship to a magmatic system, which can be active for several hundreds of thousand years (Schöppa et al, 2017), remains unclear.

We used numerical models to investigate the connection of magma reservoir formation by incremental growth, fluid flow above a magmatic system and phase separation at shallow depths. The simulations are based on studies evaluating the formation of porphyry Cu deposits with connected distal epithermal mineralization (Korges et al. 2020). The numerical models focus on the physical hydrology by using non-linear fluid and rock properties, but so far cannot resolve the evolution of sulphur contents and other chemical fluid properties (e.g. pH, redox state). Nevertheless, they can give new insights into processes that are typically not exposed in active geothermal systems or preserved within the deposits.

2 Methods

Numerical simulations of magmatic-hydrothermal systems using CSMP++ have previously prescribed one large magmatic intrusion during model initialization (Weis et al., 2012). We have developed a new functionality that allows to resolve sill injection events as hot horizontal sheets of magma at variable intervals (Figure 1; Korges et al., 2020).

We assume that the simulated magma reservoirs grow from the top downwards by injecting the sills at a constant depth of 5 km and moving the mass and energy conserving variables of the control volumes within and below the sill location downwards. Sills are injected episodically after a specified time interval according to a time-integrated average magma flux. Every sill is represented by a selection of computational nodes spanning a total width of about 10 km and a thickness of 400 m.

All simulations start with an initial intrusion (3 sills in height) and are followed by 8 further intrusion events of single sills every 2.5, 15, or 30 thousand years of simulation time until the total volume of injected magma reaches approximately 210 km³ (11 sills). The different intervals correspond to average magma injection rates ranging from $7.5 \times 10^{-3} \text{ km}^3/\text{y}$ to $0.6 \times 10^{-3} \text{ km}^3/\text{y}$.

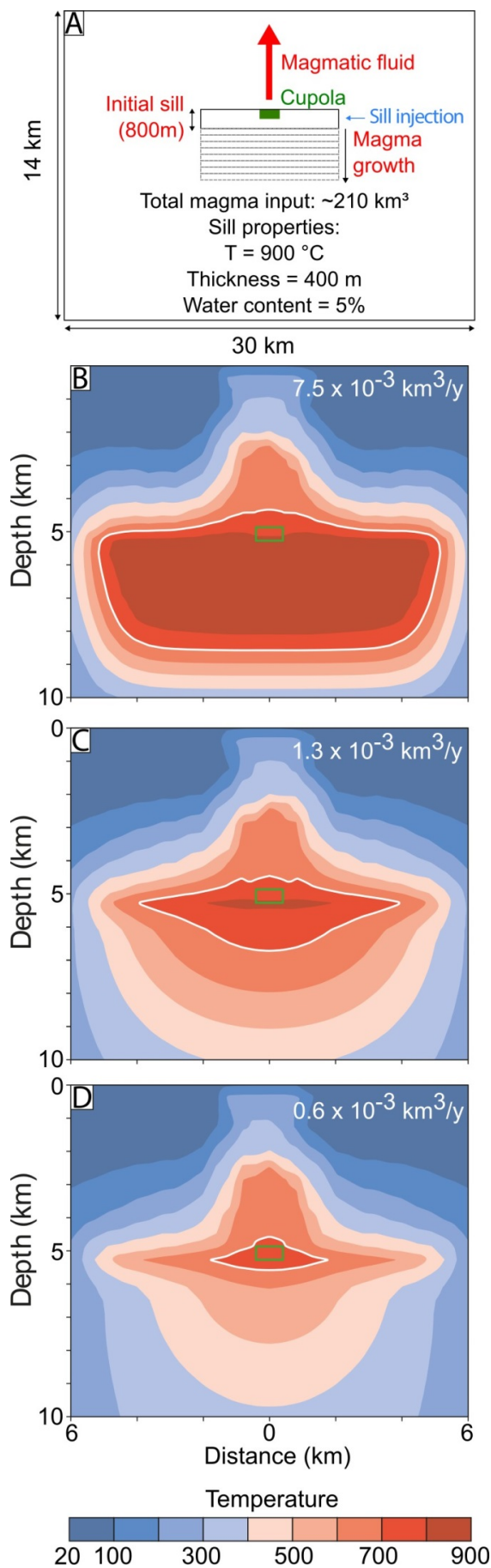


Figure 1. **A** Modelling setup and initial condition of the sills. The green box refers to the fluid injection location of the magma chamber (cupola). **B-D** Magma chamber dimensions after last sill injection with decreasing injection rate from B to D. All magma chambers show the state at 4 kyrs after the last sill. White lines correspond to the solidus temperature of 700°C. Adapted from Korges et al., 2020.

Saline magmatic fluids (10 wt% NaCl) are released through the central top part of the magma chamber, assuming a focussing mechanism within the magmatic system (e.g. Lamy-Chappuis et al., 2020) by processes unresolved in the simplified model used in this study. This “cupola” region is 800 m wide and has a fixed location. The spatial distribution of magmatic fluids during the evolution of the modelled system is monitored as a passive tracer. For the hydrothermal system, we apply a dynamic permeability model with depth-, temperature-, and pressure-dependent variations related to the brittle-ductile transition and hydraulic fracturing (Weis et al., 2012). The host rock is initially saturated with pure water to represent meteoric fluids.

3 Results

3.1 High magma-injection rate

High sill injection rates ($7.5 \times 10^{-3} \text{ km}^3/\text{y}$) result in rapid growth of a magma chamber with a vertical extent of 2-3 km while retaining the initial horizontal sill width (Figure 1B; Korges et al., 2020). During sill intrusion and after the last sill, the formed magma chamber contains regions with high melt contents and therefore also high amounts of fluid. The cooling rate of the magma reservoir thus leads to a continuous fluid release in which the event of the sill injection only has a minor influence on the extension of the fluid plume (Figure 2; videos of the fluid plumes are visualized in Korges et al. (2023)).

The magmatic water fraction in the near-surface epithermal domain is constant during the cooling of the system and only shows small variations over time with values of around 0.7 (referring to 70% of magmatic fluid and 30% of meteoric fluid). Due to the steady fluid release rate, the temperature distribution within the fluid plume is also stable over time (Figure 3). Figure 2 further displays the saturation of vapor within the fluid plume and at the surface, which is only slightly variable during the simulation.

3.2 Low magma-injection rate

Low sill injection rates of $1.3 \times 10^{-3} \text{ km}^3/\text{y}$ or $0.6 \times 10^{-3} \text{ km}^3/\text{y}$ result in a small magma chamber or complete crystallization between the sill emplacements, respectively (Figures 1C, D; Korges et al., 2020). Therefore, each new sill is injected in a cooler environment with (almost) no preserved melt, resulting in rapid cooling of the new intrusion and therefore high fluid release rates. The expelled magmatic fluid can reach the surface with magmatic

water fractions of 0.9 to 1 (almost pure magmatic fluid) for up to 1000 years after each pulse (Figure 3).

Due to the more dynamic fluid plume, the host rock at this region is cooler compared to fast-injection setups and, thus, even though the magmatic fluids dominate, the temperatures still first remain below 200°C due to thermal equilibration with the host rock. During the fluid release event, the host rock close to the surface gets heated to similar temperatures as in the high injection-rate setting (ca. 240°C). At these temperatures, the magmatic water fraction already starts to decrease because most fluids have left the magma reservoir due to its rapid cooling after sill injection. 3000 to 4000 years after the sill intrusion, the fluid plumes in the slow settings

decline, while the host rock at the surface keeps the elevated temperatures for several more thousands of years, again due to thermal buffering in the rock-dominated porous medium (Figure 3).

The occurrence of phase separation within the fluid plume in the simulation with lower injection rates is also more heterogeneous, with a decrease in the area of phase separation between pulses compared to the constant vapor region at higher rates (Figure 2). At the lowest simulated frequencies, phase separation at depth ceases before the next sill injection. In contrast, phase separation in the shallow epithermal regions persists over time in all settings. Larger regions with higher degrees of vapor saturation tend to form slightly after the magmatic fluid reaches the surface.

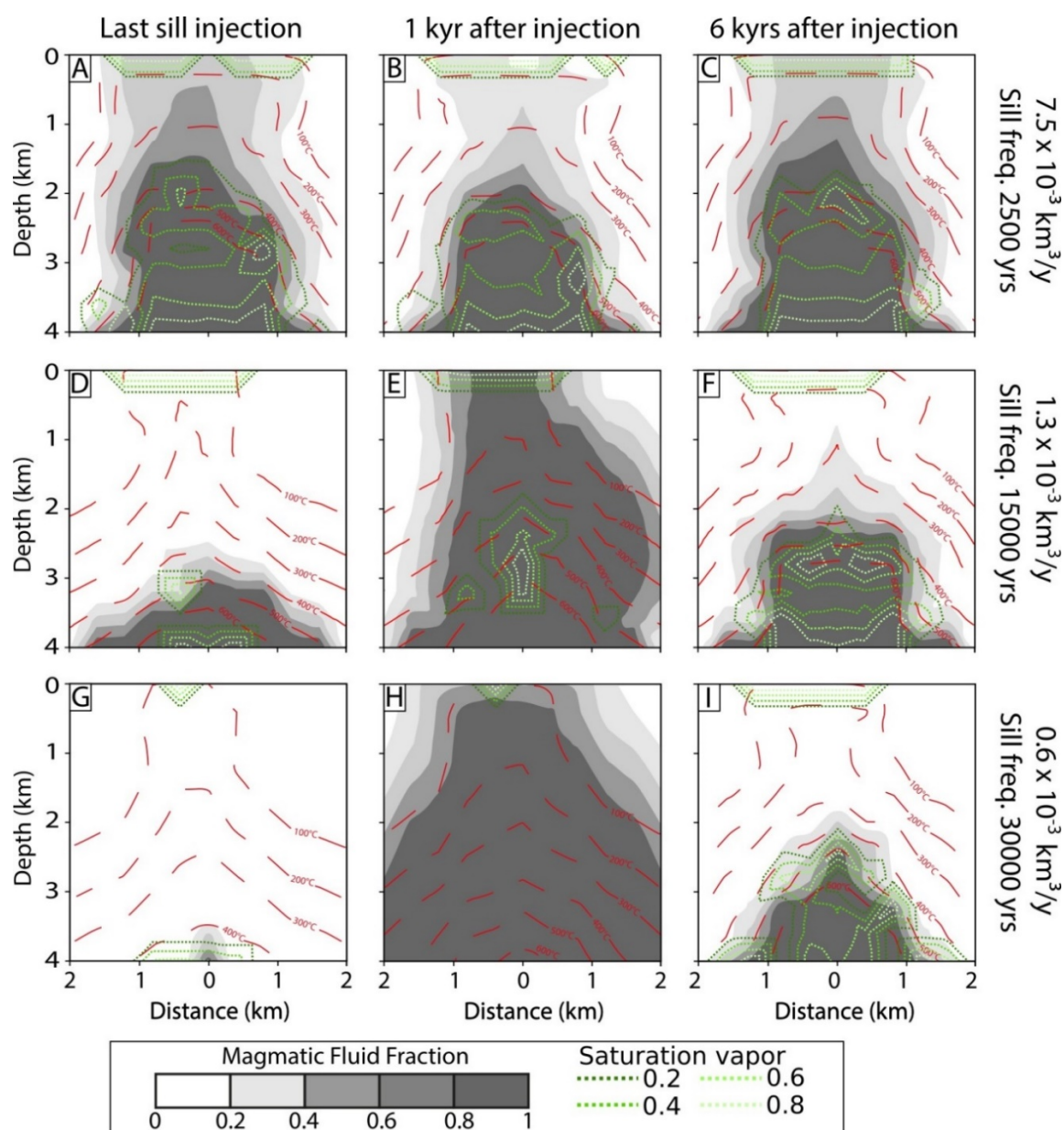


Figure 2. Fluid plumes above the cupola region of the magma reservoir (injection location at 5 km depth). **A-C:** High sill injection rates result in a steady fluid plume and little variations in fluid properties at the surface. **D-F:** Low injection rates result in a small magma chamber and a distinct impact of the sill injection on the fluid plume. **G-I:** The lowest used growth rate leads to a complete crystallization of the magma reservoir and a high impact of each sill injection on the fluid plume.

4 Discussion and Conclusions

The formation of high-sulfidation epithermal deposits requires large amounts of metal-enriched fluids at shallow depths. Our numerical simulations suggest that these conditions are more likely for a magmatic environment that produces distinct events of fluid exsolution and thus in settings with a rather low magmatic influx rate of $<1.3 \times 10^{-3} \text{ km}^3/\text{y}$. At these conditions, almost pure magmatic fluids can reach the epithermal domain, while the temperature regime is still dominated by the geothermal system that was prevalent before the fluid release event and agrees with high-sulfidation epithermal mineralization at 200-300°C (Hedenquist et al. 2000; Hedenquist & Arribas, 2022). Our simulations do not produce volcanic fumaroles at higher temperatures.

The simulations point toward the possibility of pure magmatic fluids at the surface which did not undergo previous phase separation at greater depth, although it only occurred for a short time period of less than 500 years. For most settings, two phase-separation events occur at different depths. Phase separation at depth can allow the fast-ascending vapor to contract and phase separate again at the surface. This process has been inferred as an efficient mechanism to preferentially transport precious metals with a vapor phase from deeper to shallower levels, where they get precipitated by the second phase separation event (Hedenquist et al. 2000, Heinrich et al 2004).

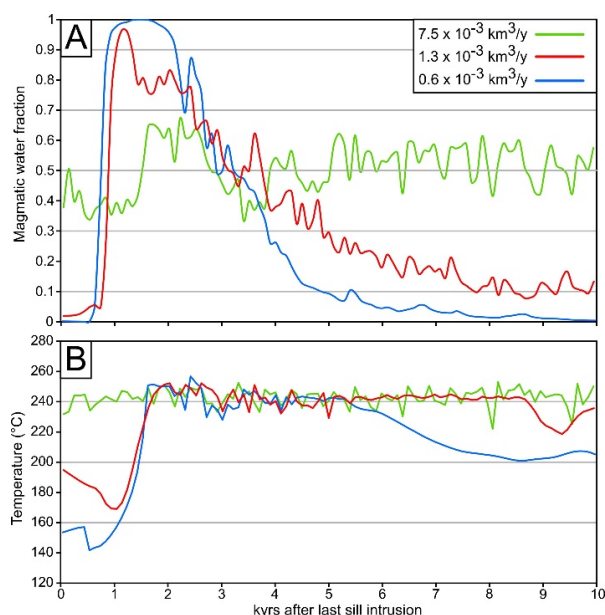


Figure 3. The evolution of the magmatic water fraction (A) and the temperature (B) in the center and 400 m below the surface of the simulation setup within 10000 years after the last sill intrusion.

The modelled ore-forming time span of several thousands of years is in line with recent fluid flow studies (Moncada et al., 2019). Our simulations suggest that rapid magma reservoir agglomerations hamper the formation of high-sulfidation epithermal

ore deposits, while at the same time are more likely to produce high-grade porphyry Cu deposits (Korges et al., 2020). Interestingly, our simplified simulations suggest that events of high-sulfidation mineralization with (almost) pure magmatic fluids are more likely to occur by sill injections into a long-lived geothermal system underlain by magma mush reservoirs, rather than systems with larger magma reservoirs with higher melt contents, which may be more characteristic for volcanic systems.

However, our generic simulations still rely on a large number of simplifications and assumptions, such as prescribed locations for sill injections and focused fluid release. Full reactive transport will be required to quantify the geochemical consequences of the physical hydrology. Future developments of the numerical model will provide more detailed insights into the interplay between porphyry and epithermal ore formation in geothermal and volcanic systems.

Acknowledgment

The authors thankfully acknowledge funding by the German Federal Ministry of Education and Research (BMBF; r4 program) and the German Research Foundation (DFG; DOME program).

References

- Hedenquist, J.W., Arribas, A., Gonzalez-Urien, E. (2000): Exploration for epithermal gold deposits. *Reviews in Economic Geology* 13, 45-77.
- Hedenquist, J.W. & Arribas, A. (2022): Exploration Implications of Multiple Formation Environments of Advanced Argillic Minerals. *Economic Geology* 117, 3, 609-643.
- Heinrich, C.A., Driesner, T., Stefánsson, A., Seward, T.M. (2004): Magmatic vapor contraction and the transport of gold from the porphyry environment to epithermal ore deposits, *Geology*, 32, 761-764.
- Korges, M., Weis, P., Andersen, C. (2020): The role of incremental magma chamber growth on ore formation in porphyry copper systems, *Earth and Planetary Science Letters*, Vol. 552, 116584.
- Korges, M., Weis, P., Andersen, C. (2023): Visualization of the incremental magma growth related to porphyry copper deposits obtained with numerical modeling, *GFZ Data Services*.
- Lamy-Chappuis, B., Heinrich, C.A., Driesner, T., Weis, P. (2020): Mechanisms and patterns of magmatic fluid transport in cooling hydrous intrusions. *Earth Planet. Sci. Lett.* 535, 116111.
- Moncada, D., Rimstidt, J.D., Bodnar, R.J (2019): How to form a giant epithermal precious metal deposit: Relationships between fluid flow rate, metal concentration of ore-forming fluids, duration of the ore-forming process, and ore grade and tonnage, *Ore Geology Reviews*, Volume 113, 103066.
- Schöpa, A., Annen, C., Dilles, J.H., Sparks, R.S.J., Blundy, J.D. (2017): Magma emplacement rates and porphyry copper deposits: thermal modeling of the Yerington Batholith, Nevada. *Econ. Geol.* 112, 1653–1672.
- Weis, P., Driesner, T., Heinrich, C. (2012): Porphyry-copper ore shells form at stable pressure-temperature fronts within dynamic fluid plumes, *Science* 338, 1613-1616.

Coupling structural evolution and fluid flow in metallogenic and geothermal systems

Patrick Ledru¹, Guoxiang Chi², Gaétan Milesi¹, Julien Mercadier¹

¹GeoRessources, CNRS, Université de Lorraine, Labcom CREGU, Vandœuvre-lès-Nancy, France

²University of Regina, Canada

Abstract. Understanding the structural framework of metallogenic provinces and identification of transient events during which fluid circulation and trapping of mineralization occur is a major challenge for exploration of mineral systems. Analogies between geothermal systems, orogenic gold and unconformity related deposits reveal the role of permeability enhancement during episodes marked by the coupling of tectonic activity and fluid flow. Thus, in the case of Unconformity-Related Uranium deposits of the Athabasca Basin (Saskatchewan, Canada), a new model can be proposed considering that the interplay between compressional fault reactivation and thermal convection is the main driver of this fluid flow system. Short-lived, deformation-driven fluid flow are recorded by the structural and mineralogical evolution of the reactivated basement-hosted fault system.

1. Introduction

The mineral system concept applied to Unconformity-Related Uranium (URU) deposits of the Athabasca Basin (Ledru 2019, Bruce et al. 2020, Ledru et al. 2023;) highlights the major role of crustal scale structures and of the geodynamic context in the onset and sustainability of the hydrothermal systems driving formation of the main orebodies. Within a structural framework defined by the geometry, kinematics and mechanical properties of the fault systems, the identification of transient pulses during which mineralizing fluids are circulating and trapped is critical for the reassessment and definition of exploration pathfinders and guides (McCuaig and Hronsky 2014).

Analogies between hydrothermal ore deposits formed at overpressured conditions during high fluid flux through fault zones and geothermal systems has been developed by Cox (2016). In the case of Enhanced Geothermal Systems, the overpressure induced by injection of fluids produces a stimulation of the permeability network of the drilled domain accompanied by seismic swarms that give a scanning of the fault system. Recent experiments in the Rhine graben have also demonstrated that following the early stages of stimulation, a geothermal reservoir hosted in the fault network has been revealed and can be considered as a self-organized hydrothermal system (Glass et al. 2021).

In the case of the Unconformity-Related Uranium deposits, recent studies have revealed common features with this configuration in which the coupling between structural evolution and fluid flow is critical to explain the formation of large deposits.

2. The architecture and the structural framework

The tectonic history of deeply rooted structures is critical to understand the natural processes at the origin of metallogenic provinces (McCuaig et al. 2010). These structures are responsible for crustal segmentation and are natural links between deep and shallow processes. They guided in many cases the intrusion of magma extracted from the mantle or generated during crustal melting and have recorded significant retrograde metamorphic evolution and hydrothermal alteration during the late orogenic evolution. By referring to geophysical imagery, Card (2020, Tschirhart et al. 2022) considers that protracted reactivation of deep-seated structures and their subsidiaries was a fundamental control on uranium mineralization in the southwestern Athabasca Basin. Based on the structural analysis and resulting cross sections (Ledru et al. 2023) and on numerical modelling (Poh et al. 2020), a similar interpretation is proposed for the Wollaston-Mudjatik transition zone that concentrates the main large to giant uranium deposits.

At the prospect and camp scale, the structural control for focusing mineralizing fluids and mineralization is well established as ore formation is spatially and temporally focused by the reactivation of the pre-Athabasca fault system (Jefferson et al. 2007). The general concept summarized in IAEA (2018) is that deposits were formed in fault zones and along the unconformity where reduced fluids from the basement and oxidized fluids from the basin were mixed. Structural traps opened during active faulting and were repeatedly brecciated (Hoeve and Quirt 1987; Kyser et al. 2000). In more detail, the alteration haloes considered to be related to the deposits are always developed in the vicinity of a fault system that crosscuts the unconformity. Most of these faults correspond to reactivated-inherited fault zones of the basement and have an associated reverse offset of the unconformity, up to several hundred meters along the Virgin River shear zone and below 100 m in the Wollaston-Mudjatik Transition Zone. These faults are often graphite-rich and cohesive to non-cohesive breccias are the most obvious expression of this reactivation.

At the camp scale, detailed structural and microstructural works reveal the polyphase history of these faults, rooted in the basement and propagating into the basin. Alteration paragenesis display a variety of association with microstructures that are often controlled by local faults and their

morphology (thickness and infilling of core and damage zones) and lithological contrast. The hydrothermal alteration within these deeply rooted faults, prior to the mineralization and presumably related to the pre-Athabasca exhumation, seems to have an efficient control on the further channeling of the mineralizing fluid, having deeply modified the original properties of the host rocks. Micro-brecciation and brittle fracturing associated with the polyphase history show how the permeability of these zones has been enhanced (Benedicto et al. 2021).

3. The transient effect

Recent findings and the comparison with their modern counterpart exploited as geothermal reservoirs, suggest that the lifetime of such hydrothermal systems might be much shorter and more dynamic than previously assumed (McCuaig and Hronsky. 2014; Cox 2016). Such pulsations could correspond to modifications of the crustal stress regime marked by highly localized deformation and enhancement of the permeability of the geological systems (Manga et al. 2012). Although no geochronological constraints exist on the time required to form the Athabasca deposits, first-order approximation from Raffensperger and Garven (1995) and Dargent et al. (2015) suggest that 0.1–1Myr is a viable estimate for the duration of the mineralizing event that could then correspond to transient events limited in time and space.

Based on regional geochrono-stratigraphic data, it has been proposed that the deposits were formed at depths of < 3 km (Chi et al. 2018). This mineralization depth estimation has important implications for the hydrodynamic regime and the geothermal gradient, both affecting the potential mechanisms of fluid flow related to U mineralization. A shallow burial environment, together with the sandstone-dominated nature of the basin sediments, favors a hydrostatic regime in the basin (Chi et al. 2013), instead of a lithostatic regime as assumed in the conventional model that considers a paleodepth of 5km. A hydrostatic regime facilitates establishment of fluid convection in the basin, which is further enhanced by elevated geothermal gradients as implied by high temperatures at shallow depths (Wang et al., 2021). This regime at the base of the basin in a shallow burial environment suggests that the unconformity surface is unlikely a hydraulic interface between hydrostatic and lithostatic regime; such an interface is likely located at greater depths in the basement. This hypothesis is supported by the study of graphite in basement faults hosting URU deposits (Song et al. 2022), which suggests that the faults may be reactivated due to the fault-valve mechanism ~5 km below the unconformity surface, whereas the upper tip of the faults may attracts fluids both from the basement and basin via the suction pump mechanism. Thus,

the formation of the URU deposits may be considered a result of coupled fault-valve and suction pump mechanism.

Dominantly C-O-H(-N) fluid inclusions trapped within ductile-brittle graphitic shear zones have been considered as associated to the retrograde metamorphism during the exhumation of the Trans-Hudson orogen (Martz et al. 2017). However, the temperature of the mineralizing fluids (150-250° C), suggested by the alteration mineral assemblages and fluid inclusion studies (Richard et al. 2016) and the revised paleodepth of the unconformity of <3km implies high geothermal gradient. The possible origin of such high geothermal gradient remains poorly constrained as no intrusion or volcanic activity has been so far identified within the basin. However, large wavelength anomalies related to mantle upwelling may have developed during the Nuna supercontinent breakup (Pehrsson et al. 2016). A bright band of reflectivity at about 8000m depth has been interpreted as a series of sub-horizontal sheet like diabase intrusions related to the Mackenzie igneous event at 1270 Ma (Jefferson et al. 2007) but nothing excludes that they could correspond to an earlier intrusion related to this Nuna breakup. Finally, modelling suggests that deeply rooted fault systems inherited from the pre-Athabasca orogens could operate as conduits to bring fluids and heat towards the upper parts of the crust, in particular during episodes of tectonic reactivation (Poh et al. 2022). In this case, the mineralized zones showing a high geothermal gradient could be “hot spots” situated at the intersection between this fault system and the unconformity. The discovery of carbonatite dykes within the fault system of the Patterson Lake corridor is another observation that supports such coupling between deep-seated and shallow processes (Johnstone et al. 2021).

In this context, possible deeply rooted basement fluids mixed with fluids originated from the basin lead to a major revision of the current model (Rabiei et al. 2021). Investigating gradients down-dip in the main reactivated shear zones recorded by mineralogy and fluid inclusions could be one way to test the hypothesis that brittle faults marking a significant offset of the unconformity could be rooted at depth and have a ductile equivalent enabling metamorphic fluids to be generated. Thus, the role of active faulting and shearing processes would be a trigger of the initiation of a self-organized hydrothermal system (Micklethwaite et al. 2010, Hronsky 2011) and the brittle-ductile transition could be considered as a threshold barrier.

Thermo-Hydraulic and Mechanic (THM) modelling evaluates different scenarios under which the fluid flow was controlled by faulting-related deformation and permeability enhancement. Modelling of simplified geometries of several deposits (Li et al. 2018, 2020; Eldursi et al. 2020), shows that basement faults generally promote fluid flow, fluids circulating downwards

from the basin within the basement (ingress flow) or upwards from basement reservoirs towards the basin (egress flow) both generated by either compressional deformation or fluid convection. The actual flow direction for a given basement fault is influenced by a combination of many factors, especially the dip angle and dip direction as well as spacing of neighbouring basement faults (Chi et al. 2013).

Understanding the geodynamic trigger of this reactivation is a major stake. Based on the dispersion of the U/Pb ages of the mineralization, many attempts of correlation with compressional far-field tectonic events have been done (Kyser and Cuney 2015). These correlations are based on geochronological data which are too much spread to be conclusive (Chi et al. 2018). Several structural observations can be advanced to constrain this trigger. Because of the unfavourable dip of these faults in the compressive stress field, their reactivation could only occur when fluid pressure exceeded the lithostatic load (Sibson et al. 1988; Sibson 2020). The presence of significant amount of graphite must also be underlined as a lubricant facilitating faulting and fluid flow that led to uranium mineralization (Song et al. 2022).

4. Discussion

The review of these different parameters highlights several critical elements that are compatible with other mineral systems (McCuaig and Hronsky 2014). A new model can be proposed considering that the interplay between compressional fault reactivation and thermal convection is the main driver of this fluid flow system (Li et al. 2020, Song et al. 2022). Short-lived, deformation-driven fluid flow are recorded by the structural and mineralogical evolution of the reactivated basement-hosted fault system. This tectonically active period may be associated with a far-field tectonic event and separated by long periods of quiescence. However, by analogy with enhanced or natural geothermal systems (Cox 2016), the possibility that these episodes are related to transient tectonic activity caused by fluid over-pressure should be also considered, interplay between compressional fault reactivation and thermal convection being still applicable. Thus, the formation of the giant deposits could happen during times when the prevailing geodynamic conditions impose strong threshold barriers to fluid flow, causing fluid-flux systems to become self-organized (Hronsky 2011). In this scenario, the presence of a basement hosted reservoir is suggested and the fluid expulsion occurred through transient exit pathways, faults acting like valve system (Sibson et al. 1988, Sibson 2020). In this framework, uranium may precipitate in structural traps as jogs and veins within the core and damage zones of the faults during inter seismic periods, graphite and sulphide being potential reducing agents facilitating the precipitation or reach the

unconformity and be trapped in the permeable sediments at the base of the basin if a clay or silicified cap is present.

5. Conclusion

Analogies between geothermal and mineral systems are applied to evaluate the processes at the origin of unconformity-related uranium deposits as known in the Athabasca Basin. Thus, the stimulation of inherited permeability networks and the role of structures in a given tectonic context appear as essential conditions in both systems to initiate, develop and sustainably operate high fluid fluxes within heat exchangers and chemicals that will lead to the formation of geothermal deposits or reservoirs. The recently conceptualized analogies between the induced seismicity of experiments in the development of improved geothermal reservoirs and the polyphase injection of hydrothermal fluids in the shear zones (Cox 2016) open new perspectives for the predictive targeting of reactivated and mineralized fossil zones in the deposits by comparison of the coupling between the deformation regimes and the circulation of fluids in the systems stimulated in a natural (deposits) and anthropogenic (improved geothermal) way.

Acknowledgements

The authors acknowledge the support of the French Agence Nationale de la Recherche (ANR), under grant ANR-21-CHIN-0006 (project Geomiln3D).

References

- Benedicto, A., Abdelrazek, M., Ledru, P., Mackay, C. (2021). Structural controls of uranium mineralization in the Athabasca Basin, Saskatchewan, Canada. *Geofluids*, 2021, Article ID 3853468, <https://doi.org/10.1155/2021/3853468>.
- Bruce, M., Kreuzer, O., Wilde, A., Buckingham, A., Butera, K., Bierlein, F. (2020). Unconformity-Type Uranium Systems: A Comparative Review and Predictive Modelling of Critical Genetic Factors. *Minerals*, 10, 738.
- Card, C. (2020). The Patterson Lake corridor of Saskatchewan, Canada: defining crystalline rocks in a deep-seated structure that hosts a giant, high-grade Proterozoic unconformity uranium system. *Geochem. Explor. Environ. Anal.*, 21, geochem2020-007. <https://doi.org/10.1144/geochem2020-007>
- Chi, G., Bosman, S., Card, C. (2013). Numerical modeling of fluid pressure regime in the Athabasca basin and implications for fluid flow models related to the unconformity-type uranium mineralization. *J. Geochem. Explor.*, 125, 8-19.
- Chi, G., Li, Z., Chu, H., Bethune, K.M., Quirt, D., Ledru, P., Normand, C., Card, C., Bosman, S., Davis, W.J., Potter, E.G. (2018). Shallow-burial mineralization system driven by magmatic heat sources at depth: a new perspective on factors controlling unconformity-related uranium deposits associated with Proterozoic basins. *Econ. Geol.*, 113(5), 1209-1217
- Chi G., Xu D., Xue C., Li Z., Ledru P., Deng T., Wang Y., Song H. (2022). Hydrodynamic Links between Shallow and Deep Mineralization Systems and Implications for Deep Mineral Exploration. *Acta Geologica Sinica (English Edition)*, 96(1): 1–25.
- Dargent, M., Truche, L., Dubessy, J., Bessaque, G., Marmier, H. (2015). Reduction kinetics of aqueous U(VI) in acidic chloride brines to uraninite by methane, hydrogen or C-graphite

- under hydrothermal conditions: Implications for the genesis of unconformity-related uranium ore deposits. *Geochim. Cosmochim. Acta*, 167, 11-26.
- Glaas, C., Patrier, P., Vidal, J., Beaufort, D., Genter, A. (2021). Clay Mineralogy. A Signature of Granitic Geothermal Reservoirs of the Central Upper Rhine Graben. *Minerals*, 11, 479. <https://doi.org/10.3390/min11050479>.
- Cox, S.F. (2016). Injection-driven swarm seismicity and permeability enhancement: implications for the dynamics of hydrothermal ore systems in high fluid-flux, overpressured faulting regimes - an invited paper. *Econ. Geol.*, 111, 559-587.
- Eldursi K., Chi, G., Bethune, K., Li, Z., Ledru, P., Quirt, D. (2020). New insights from 2- and 3-D numerical modelling on fluid flow mechanisms and geological factors responsible for the formation of the world-class Cigar Lake uranium deposit, eastern Athabasca Basin, Canada. *Miner. Deposita*, <https://doi.org/10.1007/s00126-020-00979-5>.
- Hoeve, J., Quirt, D. (1987) A stationary redox front as a critical factor in the formation of high-grade, unconformity-type uranium ores in the Athabasca Basin, Saskatchewan, Canada. *Bull. Mineral.*, 110, 157-171.
- Hronsky, J.M.A. (2011). Self-Organized Critical Systems and Ore Formation: The Key to Spatial Targeting? *SEG Newsletter*, 84, 14-16.
- IAEA (2018). Unconformity-related Uranium Deposits. *TECDOC*, 1857.
- Jefferson CW, Thomas DJ, Gandhi SS, Ramaekers P, Delaney G, Brisbin D, Cutts C, Portella P, Olson RA. (2007) Unconformity-associated uranium deposits of the Athabasca basin, Saskatchewan and Alberta. Geological Association of Canada, Mineral Deposits Division, Special Publication No. 5, pp. 273-305.
- Johnstone, D.D., Bethune, K.M., Card, C.D., Tschirhart, V. (2021). Structural evolution and related implications for uranium mineralization in the Patterson Lake corridor, southwestern Athabasca Basin, Saskatchewan, Canada. *Geochem. Explor. Environ. Anal.*, 21, geochem2020-030, <https://doi.org/10.1144/geochem2020-030>.
- Kyser, T.K., Hiatt, E., Renac, C., Durocher, K., Holk, G., Deckart, K. (2000). Diagenetic fluids in Paleo- and Mesoproterozoic sedimentary basins and their implications for long protracted fluid histories. In: *Fluids and Basin Evolution*, Kyser, T.K. (Ed.), *Min. Assoc. Can. Short Course*, 28, 225-262.
- Kyser, K., Cuney, M. (2015). Basins and uranium deposits. In: *Geology and Geochemistry of Uranium and Thorium Deposits*. Short course Series, 46, 224-250.
- Ledru, P. (2019). The Mineral System concept applied to unconformity-related uranium deposits of the Athabasca Basin (Canada). In: *Proceedings of the 15th SGA Biennial Meeting*, Glasgow, Scotland. 1179-1182.
- Ledru P., Benedicto A., Chi G., Khairallah C., Mercadier J., Poh J., Robbins J. (2023). The unconformity-related uranium mineral system of the Athabasca Basin (Canada). Wiley, *ISTE, Natural Resources: Applied Basic Research*, Chapter 3.
- Li, Z., Chi, G., Bethune, K.M., Eldursi, K., Thomas, D., Quirt, D., Ledru, P. (2018). Synchronous egress and ingress fluid flow related to compressional reactivation of basement faults: the Phoenix and Gryphon uranium deposits, SE Athabasca Basin, Saskatchewan, Canada. *Miner. Deposita*, [doi:10.1007/s00126-017-0737-5](https://doi.org/10.1007/s00126-017-0737-5).
- Li, Z., Chi, G., Bethune, K.M., Eldursi, K., Thomas, D., Quirt, D., Ledru, P., Thomas D. (2020). Interplay between thermal convection and compressional fault reactivation in the formation of unconformity-related uranium deposits. *Miner. Deposita*, [doi:10.1007/s00126-020-01011-6](https://doi.org/10.1007/s00126-020-01011-6).
- Manga, M., Beresnev, I., Brodsky, E.E., Elkhoury, J.E., Elsworth, D., Ingebritsen, S. E., Mays, D.C., Wang, C.Y. (2012). Changes in permeability caused by transient stresses: Field observations, experiments, and mechanisms. *Rev. Geophys.*, 50, RG2004, [doi:10.1029/2011RG000382](https://doi.org/10.1029/2011RG000382).
- Martz, P., Cathelineau, M., Mercadier, J., Boiron, M.C., Jaguin, J., Tarantola, A., Demacon, M., Gerbeaud, O., Quirt, D., Doney, A., Ledru, P. (2017). C-O-H-N fluids circulations and graphite precipitation in reactivated Hudsonian shear zones during basement uplift of the Wollaston-Mudjatik Transition Zone: Example of the Cigar Lake U deposit. *Lithos*, 222-245, [doi: 10.1016/j.lithos.2017.10.001](https://doi.org/10.1016/j.lithos.2017.10.001).
- McCuaig, T.C., Hronsky, J.M.A. (2014). The Mineral System Concept: The Key to Exploration Targeting. *Soc. Econ. Geol., Special Publication*, 18, 153-175.
- McCuaig, T.C., Beresford, S., Hronsky, J.M.A. (2010). Translating the mineral systems approach into an effective exploration targeting system. *Ore Geol. Rev.*, 38, 128-138.
- Micklethwaite, S., Sheldon, H.A., Baker, T. (2010). Active fault and shear processes and their implications for mineral deposit formation and discovery. *J. Struct. Geol.*, 32, 151-165.
- Pehrsson, S.J., Eglington, B.M., Evans, D.A.D., Huston, D., Reddy, S.M. (2016). Metallogeny and its link to orogenic style during the Nuna supercontinent cycle. In: *Supercontinent Cycles Through Earth History* Li, Z. X., Evans, D.A.D., Murphy, J. B. (eds), *Geol. Soc., London, Special Publications*, 424, 83-94.
- Poh, J., Yamato, P., Duretz, T., Gapais, D., Ledru, P. (2020). Precambrian deformation belts in compressive tectonic regimes: A numerical perspective. *Tectonophysics*, 777, doi.org/10.1016/j.tecto.2020.228350.
- Poh, J., Eldursi K., Ledru, Yamato, P., Chi G., Benedicto A. (2022). Role of Hydrothermal Circulation along and above Inherited Basement Structures Relating to Unconformity-Related Uranium Mineralization. *Geofluids Volume 2022*, Article ID 9131289, doi.org/10.1155/2022/9131289
- Rabiei, M., Chi, G., Potter, E.G., Tschirhart, V., MacKay, C., Frostad, S., McElroy, R., Ashley, R., McEwan, B. (2021). Fluid evolution along the Patterson Lake corridor in the SW Athabasca Basin: constraints from fluid inclusions and implications for unconformity-related uranium mineralization. *Geochem. Explor. Environ. Anal.*, 21, geochem2020-029, [/doi.org/10.1144/geochem2020-029](https://doi.org/10.1144/geochem2020-029).
- Raffensperger, J.P., Garven, G. (1995). The formation of unconformity-type uranium ore-deposits. Coupled groundwater-flow and heat transport modeling. *Am. J. Sci.*, 295, 581-636. doi.org/10.2475/ajs.295.5.581.
- Richard, A., Cathelineau, M., Boiron, M.-C., Mercadier, J., Banks, D.A., Cuney, M., 2016. Metal-rich fluid inclusions provide new insights into unconformity-related U deposits (Athabasca Basin and basement, Canada). *Mineral. Deposita*, 51, 249–270.
- Sibson, R.H. (2020). Preparation zones for large crustal earthquakes consequent on fault-valve action. *Earth Planets Space*, 72, 31, doi.org/10.1186/s40623-020-01153-x.
- Sibson, R.H., Robert, F., Poulsen, K.H. (1988). High angle reverse faults, fluid pressure cycling, and mesothermal gold-quartz deposits. *Geology*, 16, 551-555.
- Song, H., Chi, G., Wang, K., Li, Z., Bethune, K.M., Potter, E.G., Liu, Y. (2022). Raman spectroscopy as a tool to decipher the role of graphite in uranium mineralization – a case study of the world-class Phoenix uranium deposit in the Athabasca Basin, Canada. *Am. Mineral.*, 107, 2128–2142.
- Tschirhart, V., Potter, E. G., Powell, J. W., Roots, E. A., & Craven, J. A. (2022). Deep geological controls on formation of the highest-grade uranium deposits in the world: Magnetotelluric imaging of unconformity-related systems from the Athabasca Basin, Canada. *Geophysical Research Letters*, 49, e2022GL098208. <https://doi.org/10.1029/2022GL098208>
- Wang, K., Chi, G., Bethune, K.M., Li, Z., Blamey, N., Card, C., Potter, E.G., Liu, Y. (2018). Fluid P-T-X characteristics and evidence for boiling in the formation of the Phoenix uranium deposit (Athabasca Basin, Canada): implications for unconformity-related uranium mineralization mechanisms. *Ore Geol. Rev.*, 101, 122-142.

Trace element variations and sulphur isotopic ratios of enargite and alunite from the quartz-pyrite-gold orebodies, Mankayan District, Philippines

Pearlyn Manalo¹, Ryota Mine¹, Ryohei Takahashi¹, Akira Imai², Andrea Agangi¹, Glenn Alburo³, Leo Subang³, Rhyza Ruth Parcon-Calamohoy³, Mervin de los Santos³

¹Graduate School of International Resource Sciences, Akita University, Japan

²Department of Earth Resource Engineering, Kyushu University, Japan

³Lepanto Consolidated Mining Company, Inc., Philippines

Abstract. The quartz-pyrite-gold orebodies in the Mankayan District, Philippines is a high-sulfidation epithermal gold deposit that are hosted by Cretaceous metavolcanic basement rocks and Pliocene to Pleistocene dacitic porphyry and pyroclastics (Garcia 1991). This study focuses on two of the several quartz-pyrite-gold orebodies, namely the 1) Northwest orebody and 2) Florence East orebody. We investigate the variation of mineral chemistry of alunite and enargite, which are the dominant gangue and ore minerals, respectively. Compositional maps of alunite from the Northwest orebody show variation of K and Na contents within a single grain and across multiple grains. The element distribution of alunite crystals is either irregular or follows the crystal growth pattern. Meanwhile, the composition of alunite from the Florence East orebody is mostly homogeneous. Enargite shows variable degrees of As being locally substituted by Sb and Te through apparent oscillatory zones. Sulphur isotopic compositions of alunite range from -3.4 to +24.2 ‰, with the values from the Northwest orebody generally higher than those of the Florence East orebody. Meanwhile, the sulphur isotopic compositions of enargite in both orebodies are similar, ranging from -6.2 to -2.3 ‰. The trace element compositions and sulphur isotopic ratios of ore and gangue minerals reflect the varying conditions of the mineralizing environment.

1 Introduction

Alunite and enargite are the main gangue and ore minerals in high-sulfidation epithermal systems (Arribas, 1995; Deyell 2001). Previous studies proposed that the variation of alunite mineral chemistry reflects variations of several factors, such as temperature and composition of hydrothermal fluid (e.g. Deyell 2001). Relatively fewer studies have dwelled on the trace element composition of enargite (Deyell et al. 2011; Liu et al. 2019), focusing on different scales of element zoning. The factors that affect the trace element content of enargite are yet to be established.

The sulphur isotopic ratios of alunite have also been shown useful for the determination of the environment of formation (Rye 2005). Much less is known about the sulphur isotopic behaviour of enargite, as compared to the other ore minerals such as pyrite, galena, and sphalerite. The fractionation factor of enargite and H₂S is only assumed to be like that of sphalerite due to their similar structure (Hedenquist et al. 2017). Contributions of isotopic data from enargite would

further increase our understanding of how the values are affected by the environment of formation.

In high-sulfidation deposits, alunite and enargite usually coexist and are sometimes coeval (e.g. Manalo et al. 2018; 2020). The mineral chemistry of one mineral may affect the mineral chemistry of the other. Furthermore, the variations in the sulphur isotopic compositions of the two minerals have implications for the evolution of the bulk hydrothermal fluids. Understanding the variations in the mineral chemistry and isotopic compositions of coexisting ore and gangue minerals may lead to better understanding of the mineralizing system, in general. Thus, this study presents the preliminary results of a side-by-side comparison of the mineralogical and isotopic characteristics of alunite and enargite, in an attempt to see how fluid fluctuations are documented by the gangue and ore.

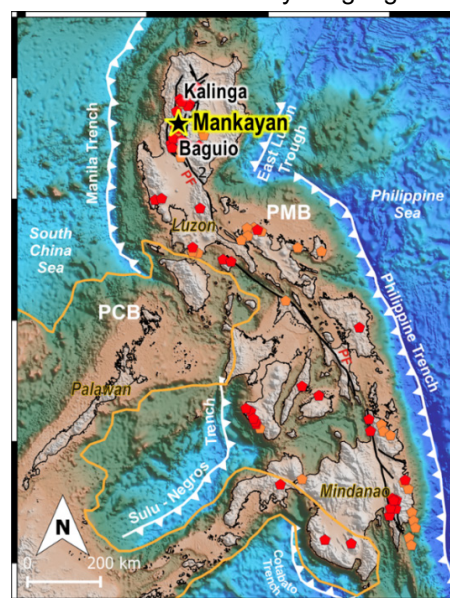


Figure 1. The Mankayan District is located in Luzon Island, Philippines. The area is affected by different tectonic elements, such as the subduction zone along the Manila Trench and the Philippine Fault Zone (Tsutsumi and Perez 2013). Several porphyry copper (red polygons) and epithermal gold (orange polygons) deposits are known throughout the archipelago (Jimenez 2002). Topography and bathymetry data is from Amante and Eakins (2011).

2 Geological Background

The Mankayan District is located within the Central Cordillera in western Luzon, Philippines (Figure 1). The oldest rocks in the district are the Cretaceous to Eocene Lepanto Metavolcanics (Figure 2; Garcia, 1991). These are unconformably overlain by volcanoclastic sequences of the Balili Formation and Apaoan Formation. Periods of magmatism in the district are recorded by the Middle Miocene Bagon Intrusives and the Plio-Pleistocene Imbanguila and Bato dacitic rocks, which occur as porphyry domes and pyroclastic deposits.

There are four types of mineralization in the Mankayan District. These comprise porphyry Cu-Au orebodies, carbonate Au-Ag-base metal veins, enargite-Au orebodies, and the quartz-pyrite-gold orebodies. The ages of the different types of deposits vary. The oldest reported age is 3.5 Ma of the Guinaoang porphyry deposit (Sillitoe and Angeles 1985), while the youngest age is 1.45 Ma of the Far Southeast porphyry deposit (Arribas et al. 1995). The ages of alunite related to the different high-sulfidation orebodies also vary. Arribas et al. (1995) reported K-Ar ages of alunite from the Lepanto Main enargite orebody ranging from 1.56 Ma to 1.17 Ma. Ar-Ar ages on alunite from the quartz-pyrite-gold veins in Northwest and Florence range from 3.0 Ma to 1.9 Ma (Manalo et al. 2018; 2020; Mine 2022).

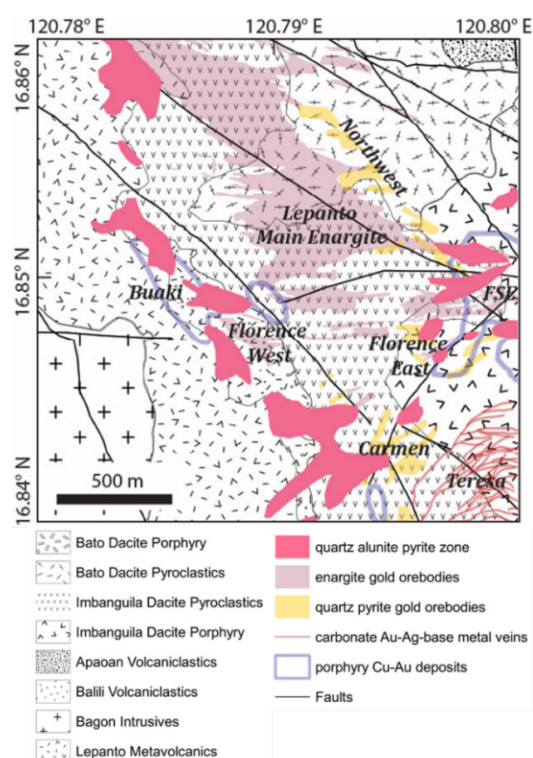


Figure 2. Location of the Northwest and Florence East Quartz-Pyrite-Gold orebodies in Lepanto, Mankayan, Philippines. The mineralization is mainly hosted by the Lepanto Metavolcanics and the Imbanguila Dacite Porphyry and Imbanguila Dacite Pyroclastics (modified from Garcia 1991).

3 Methods

Polished sections of rock samples collected from drill cores and underground tunnels of the Northwest and Florence orebodies were prepared. Descriptions of the samples have mostly been reported by Manalo et al. (2018, 2020). A Nikon Eclipse LV100N POL polarizing microscope was used for transmitted and reflected light petrography.

The chemical composition of alunite was analysed using a JEOL JXA-8230 electron probe microanalyzer in wavelength-dispersive mode. Potassium, Fe, Al, Na, P, Ba, S, Pb and Ca were analysed using a 15 kV acceleration voltage, 10 nA beam current and 15 μ m beam diameter, as suggested by Deyell 2001). The same instrument was used for the analysis of concentrations of As, Se, Fe, S, Sb, Te, Bi, Pb, Ag, Cu, Zn, Co, Ni, Au and Sn in enargite crystals. The measuring conditions are 20 kV acceleration voltage, 20 nA beam current and 5 μ m beam diameter. For alunite and enargite, standard specimens include the compounds KAlSi_3O_8 , $\text{NaAlSi}_2\text{O}_6$, Al_2O_3 , BaSO_4 , $\text{Ca}_5(\text{PO}_4)_3\text{F}$, FeS_2 , SnSe , GaAs , Sb_2S_3 , Bi_2S_3 , PbS , ZnS , and pure metals, Ag, Cu, Co, Ni, Au, and Te.

Crystals of alunite and enargite were carefully separated by handpicking using a binocular microscope. About 20 mg of enargite was decomposed using 20 mL 16N HNO_3 and 2 mL liquid Br_2 at 90 °C. The residue after overnight evaporation was redissolved using 10 mL 6N HCl and was subsequently diluted to 100 mL using distilled water. The solution was then filtered to remove the undissolved residue. The filtered solution was passed through a cation exchange column. Ten millilitres of 10% BaCl_2 was added to the 300 mL eluent to precipitate BaSO_4 crystals.

About 250 mg of alunite was dissolved using 0.5 M NaOH solution at 80 °C overnight. Undissolved materials were filtered. The solution passed through a cation-exchange column. The eluent was acidified using 10 mL 6N HCl and 10 mL of 10 % BaCl_2 solution was added to the solution to precipitate the BaSO_4 crystals.

The BaSO_4 precipitate was collected using a membrane filter and 50 mL syringe. After the precipitate dried, 0.4 to 0.5 mg of the BaSO_4 precipitate was packed with 2 to 3 mg V_2O_5 in a tin foil. The samples were combusted in a quartz tube at 1020 °C and the resulting SO_2 gas was isolated using a Thermo Fisher Scientific Flash 2000 Elemental Analyzer. The isotopic ratios were measured using Thermo Fisher Scientific Delta V Advantage isotope ratio mass spectrometer. Calibration curves were constructed using IAEA NBS-127, IAEA SO-5 and IAEA SO-6 standards. The sulphur isotopic ratios are presented relative to the sulphur isotopic ratio of the troilite of the Canon Diablo meteorite in per mil. The analytical uncertainty is ± 0.2 ‰.

4 Results

4.1 Sample description

The Northwest and Florence East orebodies display differences in the occurrence of enargite and alunite. In the Northwest orebody, alunite and enargite occur in distinct paragenetic sequences. Most of the alunite in the Northwest orebody is closely associated with abundant coarse-grained pyrite (Figure 3A), while enargite is more closely associated with quartz. The alunite deposited in an earlier stage than that of the enargite ore (Manalo et al. 2018). In contrast, enargite and alunite in the Florence East orebody are closely associated, and likely belong to the same stage (Figure 3B; Manalo et al. 2020).

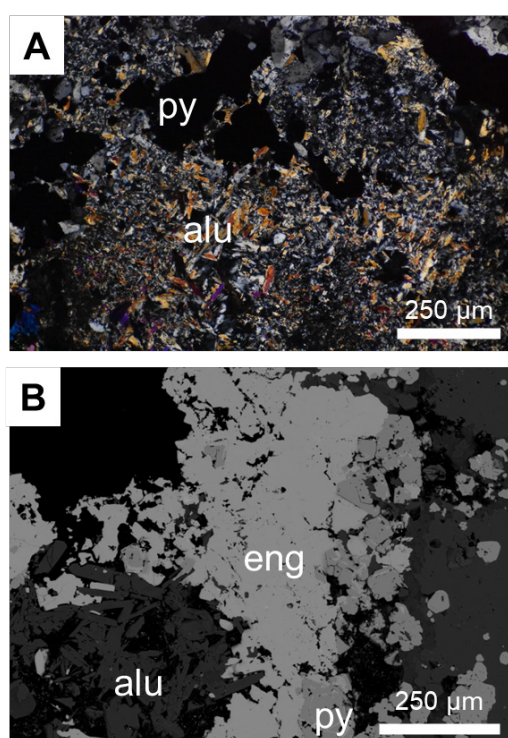


Figure 3. **A** A photomicrograph of a sample from the Northwest orebody showing alunite (alu) and pyrite (py) association. **B** A backscattered electron image of enargite (eng) coexisting with alunite in the Florence East orebody.

4.2 Mineral chemistry of alunite

In the Northwest orebody, coarse-grained tabular alunite commonly shows variation in K and Na contents, while Al and S contents are mostly uniform within a single grain and across multiple grains (Figure 4). There are apparent systematic variations in the concentrations of K and Na, which follow the crystal structure. Wide variations in the amount of Na substitution were observed in the samples from the Northwest orebody. However, some samples display irregular zonation. In the Florence East orebody, we observed relatively homogenous K-rich alunite.

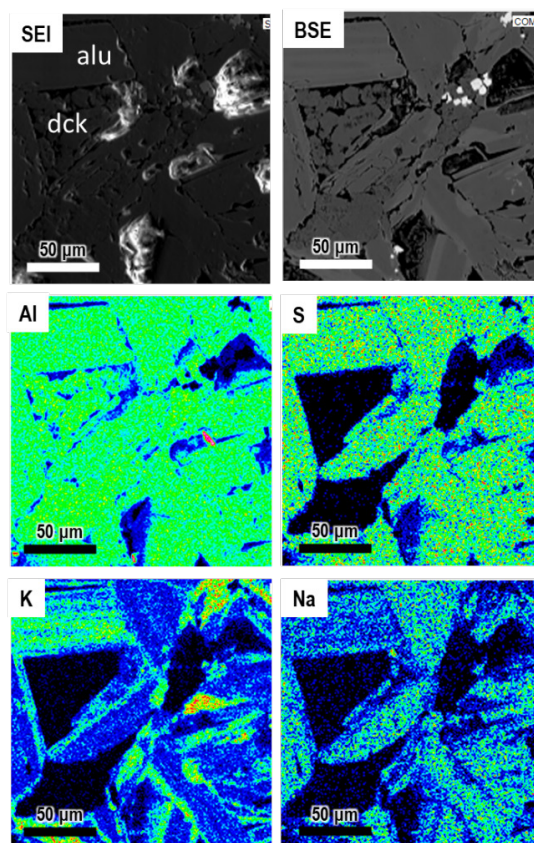


Figure 4. Elemental distribution maps of alunite from the Northwest orebody (alu – alunite; dck – dickite).

4.3 Mineral chemistry of enargite

The crystal habit of enargite in the Northwest and Florence East orebodies varies from being subhedral to anhedral. Luzonite commonly occurs with enargite. Antimony is the most abundant trace element in enargite, followed by Fe and Te. The average Sb content is 5000 ppm, with some values reaching 2 wt%. Tellurium concentration averages at 630 ppm, with several anomalous points reaching up to ~6000 ppm. The average concentration of Fe in enargite is 1840 ppm, with anomalous values reaching up to 1 wt%.

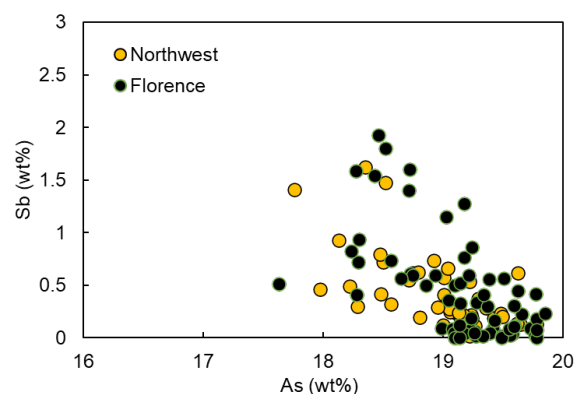


Figure 5. Bivariate plot comparing the As and Sb contents of enargite in the Northwest and Florence East orebodies.

Figure 6 shows oscillatory variations in Sb and Te contents of enargite that is limited only to a certain part of crystal. It also shows Fe enrichment in other parts of the enargite crystal.

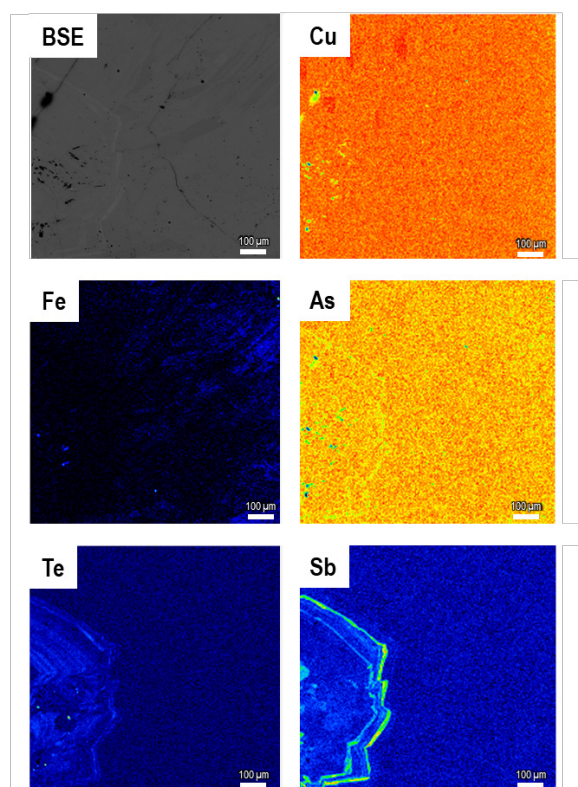


Figure 6. Elemental distribution maps of enargite from the Northwest orebody.

The concentration of Au in enargite is 250 ppm on average and 600 ppm maximum. Silver concentration varies from below the limit of detection (< 35 ppm) to 200 ppm. The concentration of Pb and Se were below the limits of detection in all the points analysed.

4.4 Sulphur isotopes

The sulphur isotope ratios of alunite show two distinct ranges. One group range from -3.4 ‰ to -1.7 ‰, while the other range is from +9.9 ‰ to +24.2 ‰. The sulphur isotope ratios of enargite range from -6.2 ‰ to -2.3 ‰ (Manalo et al. 2018; Mine 2022).

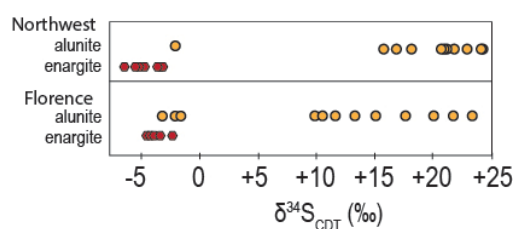


Figure 7. Variations of sulphur isotopic ratios of alunite and enargite in the Northwest and Florence East orebodies. Data of the Northwest orebody were from

Manalo et al. (2018), while those of the Florence orebody were from Manalo et al. (2020) and Mine (2022).

Figure 7 shows that the sulphur isotopic ratios of alunite from the Florence orebody have wider range than those of the Northwest orebody. On the other hand, the sulphur isotopic ratios of enargite from both orebodies overlap within a narrow range. Two samples of alunite from both orebodies have similar sulphur isotopic ratios to those of enargite, which may indicate that some alunite was formed in a supergene environment. Most of the alunite samples, however, have sulphur isotopic ratios that are within the typical range of magmatic-hydrothermal alunite and magmatic-steam alunite (Rye 2005).

Acknowledgements

We are grateful to Mr. Bryan Yap of the Lepanto Consolidated Mining Co., for permission to do research on the quartz-pyrite-gold veins. This research is funded by the Japan Society for the Promotion of Science (JSPS) Grant-in-Aid for Scientific Research 21K04960, 21KK0089 and 22K14633. Funding was also provided by the 2022 Dowa Holdings Inc., Young Researcher Grant.

References

- Amante, C., Eakins, B.W. (2009): ETOPO1 Arc-Minute Global Relief Model: Procedures, Data Sources and Analysis. NOAA Technical Memorandum NESDIS NGDC-24.
- Arribas, Jr., A., Hedenquist, J.W., Itaya, T., Okada, T., Concepcion, R.A., and Garcia, Jr., J.S. (1995): Contemporaneous formation of adjacent porphyry and epithermal Cu-Au deposits over 300 ka in northern Luzon, Philippines, *Geology*, v. 23, p. 337–340.
- Deyell, C.L. (2001): Alunite and High Sulfidation Gold-Silver-Copper Mineralization in the El Indio-Pascua Belt, Chile-Argentina. PhD Dissertation. University of British Columbia, Vancouver, Canada.
- Garcia, Jr., J.S. (1991): Geology and mineralization characteristics of the Mankayan mineral district, Benguet, Philippines: Geological Survey of Japan, Report 277, p. 21–30.
- Manalo, P.C., Imai, A., Subang, L., de los Santos, M., Yanagi, K., Takahashi, R., Blamey, R. (2018): Mineralization of the northwest quartz-pyrite-gold veins: Implications for multiple mineralization events at Lepanto, Mankayan Mineral District, northern Luzon, Philippines, *Economic Geology*, v. 113, p. 1609–1626.
- Manalo, P.C., Subang, L.L., Imai, A., de los Santos, M.C., Takahashi, R., Blamey, N.J.F. (2020): Geochemistry and fluid inclusions analysis of vein quartz in the multiple hydrothermal systems of the Mankayan Mineral District, Philippines, *Resource Geology*, v. 70, p. 1–27.
- Mine, R., Manalo, P., Takahashi, R., Agangi, A., Sato, H., Imai, A., Parcon-Calamohoy, R., Subang, L., de los Santos, M., Alburo, G. (2022): Characteristics of the Florence orebody, Lepanto Mine, Mankayan District, Philippines [abs.], The 71st Annual Meeting of the Society of Resource Geology, June 29 – July 1, Tokyo, Japan
- Rye, R.O., 2005, A review of the stable-isotope geochemistry of sulfate minerals in selected igneous environments and related hydrothermal systems: *Chemical Geology*, v. 215, p. 5–36.
- Sillitoe, R.H., Angeles, Jr., C.A., 1985, Geological characteristics and evolution of a gold rich porphyry copper deposit at Guinaoang, Luzon, Philippines [abs.]: Institute of Mining and Metallurgy, Asian Mining, London, 1985, Abstract Volume, p. 15–26.

In-situ trace element analyses of pyrite from the Pefka epithermal Cu-Au-Te-In-Se deposit, Rhodope, Northern Greece

Margarita Melfou¹, Panagiotis Voudouris², Reiner Klemm³, Manuel Keith³, Vasilios Melfos¹, Lambrini Papadopoulou¹, Nikolaos Kantiranis¹

¹ Faculty of Geology, Aristotle University of Thessaloniki, Greece

² Faculty of Geology and Geoenvironment, National and Kapodistrian University of Athens, Greece

³ GeoZentrum Nordbayern of Friedrich-Alexander-Universität (FAU) Erlangen-Nürnberg, Germany

Abstract The Pefka epithermal deposit is a high- to intermediate-sulfidation Cu-Au-Te-In-Se deposit located in the Rhodope metallogenic province of northern Greece, displaying complex ore mineralogy. Pyrite is ubiquitous in the different mineral assemblages. Pyrite grains are identified to be associated with early galena (py_{ga}), tennantite-(Cu) ($py_{tn-(Cu)}$), colusite (py_{col}), native-Au (py_{Au}) and late tellurides (py_{tel}). The crystal habit of the pyrite varies from euhedral to anhedral, and backscattered electron (BSE) imaging reveals at least two types of pyrite in the $py_{tn-(Cu)}$ association. Preliminary EPMA and LA-ICP-MS data allow the quantification of the critical and rare metal concentrations. The results show that the pyrite grains are particularly enriched in In, Se, Ag, Te, Hg and Bi. The Au and Te versus As concentrations in the pyrite are used to define some of the physicochemical conditions related to the deposition of these metals through the evolution of the system.

1 Introduction

The demand for critical, rare and base metals will increase in the following years as a result of the global energy transition towards low-carbon technologies (Grandell et al. 2016). Research in the enrichment processes of base, rare and critical metals is of high importance. Rhodope is a highly prosperous district in northern Greece for future research, exploration and exploitation of critical and rare metals associated with hydrothermal deposits. The Pefka deposit is a high- (HS) to intermediate- (IS) sulfidation epithermal deposit enriched in Cu-Au-Te-In-Se (Voudouris et al. 2022). Previous studies have identified the mineralogy and the main ore stages of the complex mineralization (Dimou et al. 1994; Repstock et al. 2015; Voudouris et al. 2022). However, the physicochemical conditions of each stage and the critical and rare metal distribution in the different sulfides and sulfosalts have not been studied in detail. This contribution aims to provide new preliminary data on the critical- and rare-metal enrichment of pyrite in the Pefka HS-IS epithermal mineralization and to constrain a part of the metallogenic evolution (HS and IS stages) of the mineralization based on these data.

2 Geological context

A highly prosperous district for epithermal mineralization hosted in Oligocene-Miocene volcanic rocks, is the Rhodope metallogenic province in Greece (Fig. 1a), located in the broader Western Tethyan metallogenic belt (Melfos and

Voudouris 2017; Voudouris et al. 2019). Rhodope is characterized by metamorphic core complexes exhumed during Late Cretaceous and Tertiary, by supra-detachment sedimentary basins, and by mafic to felsic magmatism of Late Eocene to Early Miocene age (Marchev et al. 2005; Voudouris et al. 2022). Intense hydrothermal alteration is associated with the magmatic rocks and thus the occurrence of numerous porphyry Cu-Mo-Au-Re and HS to IS epithermal mineralization is widespread (Voudouris et al. 2019, 2022).

The Pefka deposit belongs to the Pefka-Loutros area, part of the Rhodope, which hosts numerous HS and IS epithermal mineralization in hydrothermally altered volcanic rocks. Numerous precious and base-metal unexplored mineralizations occur in the area exhibiting complex alteration and mineral zonation patterns. The southern and western part of the Pefka-Loutros area exhibits silicic and advanced argillic altered outcrops associated with E-trending faults, which are rimmed outwards and downwards by sericitic and argillic alteration (Fig. 1b) (Voudouris et al. 2022).

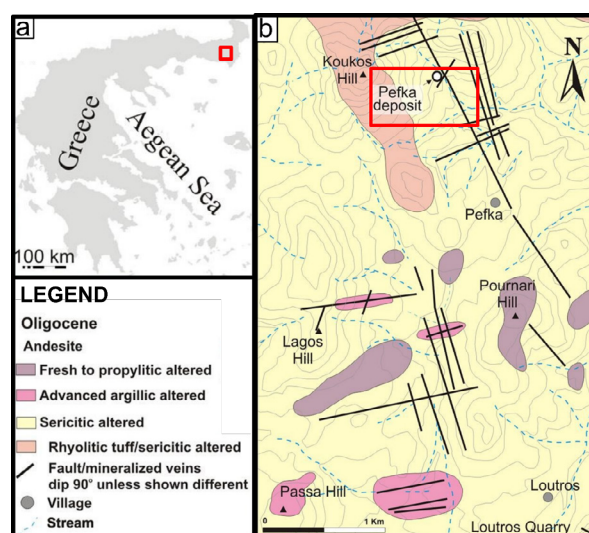


Figure 1. (a) Geological map of Greece. (b) Alteration map of the Pefka-Loutros area. Modified after Voudouris et al. (2022). The Pefka deposit is highlighted with the red rectangle in both images.

The Pefka deposit is hosted by altered andesites that are mainly related to intermediate argillic and sericitic to argillic alteration (Fig. 1b) (Voudouris 2006; Voudouris et al. 2022). It is

enriched in base, rare and critical metals (Cu, Fe, Au, Ag, Pb, Zn, Bi, Sn, Ge, Ga, In, Mo, V, As, Hg, Te and Se) displaying exceptional and rare ore mineralogy including numerous sulfides, sulfosalts, tellurides and native metals (Melfos and Voudouris 2012; Repstock et al. 2015; Voudouris et al. 2019, 2022). The deposit is characterized by at least three distinct mineralization styles. An early massive Se-rich galena vein has been identified crosscutting the altered host rocks. This early stage is followed by an NNW-trending HS vein system composed of quartz, enargite/luzonite, goldfieldite, watanabeite, colusite, chalcopryite, roquesite, tennantite-(Cu), and native gold (Repstock et al. 2015; Voudouris et al. 2022). In this HS stage, tennantite develops at the rims of the early galena grains and is extremely rich in In, up to 6.5 wt%, which is the highest concentration ever reported (Voudouris et al. 2022). Tennantite-(Cu) is part of the HS assemblage and also characterizes the transition from the HS stage to the IS stage (Voudouris et al. 2022). The late ore stage is characterized by a NE-trending, IS vein system that is composed primarily of carbonates, tellurides and tetrahedrite-(Zn) (Repstock et al. 2015; Voudouris et al. 2022).

3 Methods

Five representative samples of pyrite spatially associated with galena (py_{ga}), tennantite-(Cu) ($py_{tnt-(Cu)}$), colusite (py_{col}), native-Au (py_{Au}) and tellurides (py_{tel}) from the Pefka mineralization were collected from surface outcrops at the Pefka mine. Mineral identification and detailed imaging were conducted with scanning electron microscope - energy dispersive X-ray spectroscopy (SEM-EDS) and backscattered electrons (BSE), respectively, at the Faculty of Geology of the Aristotle University of Thessaloniki (AUTH). Further analyses for the major and trace elements in the pyrite grains of the Pefka mineralization were conducted with an electron probe micro-analyzer (EPMA) and laser ablation inductively coupled plasma mass spectrometry (LA-ICP-MS) at the GeoZentrum Nordbayern of Friedrich-Alexander-Universität (FAU) Erlangen-Nürnberg. The S content of the pyrite grains from the EPMA analyses was used as the internal standard for the quantification of the LA-ICP-MS data, with Glitter 4.4.4 software (Achterberg et al. 2001). The beam diameter was varied from 20 to 35 μm depending on the homogeneity and size of the targeted pyrite grains.

4 Results

4.1 Petrography of pyrite

Macroscopically, pyrite is associated with the galena (py_{ga}) (Fig. 2a), the quartz ($py_{tnt-(Cu)}$), py_{col} , py_{Au}) (Fig. 2b-c), and the carbonate (py_{tel}) (Fig. 2d) veins. It occurs as semi-massive veins or disseminations in quartz veins where it is

surrounded by sulfosalts (Fig. 2b) or is spatially related to barite grains (Fig. 2c). It also occurs in disseminations at the carbonate veins (Fig. 2d) and is associated with chalcopryite.

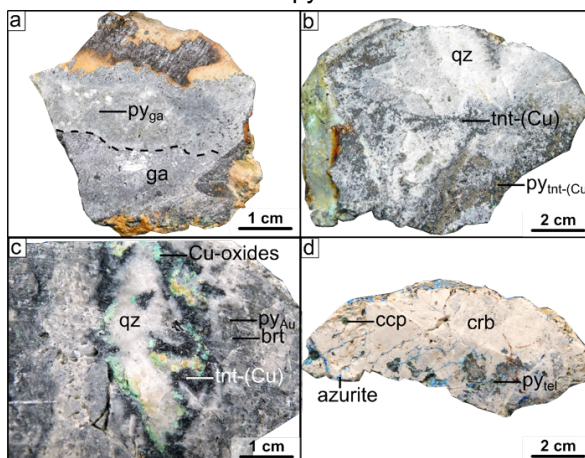


Figure 2. Images from the ore-related samples of Pefka mineralization with a focus on the relationships between alteration/ore mineralization and pyrite. (a) Galena vein in contact with altered rock with disseminated pyrite (py_{ga}). The dashed black line represents the border of the massive galena. (b) Massive quartz vein with pyrite ($py_{tnt-(Cu)}$) grains that are surrounded by tennantite-(Cu). (c) Quartz vein with tennantite-(Cu) and Cu-oxides. Pyrite (py_{Au}) occurs in disseminations in the quartz matrix closely associated with barite. (d) Carbonate vein with pyrite (py_{tel}), chalcopryite and azurite. Mineral abbreviations after Whitney and Evans (2010) and Au: native Au, tnt-(Cu): tennantite-(Cu), tel: tellurides.

Based on microscopy observations, pyrite occurs as euhedral or anhedral grains. Py_{ga} in spatial association with the early galena is usually euhedral and contains inclusions of rutile (Fig. 3a). Tennantite-tetrahedrite with small chalcopryite inclusions is found as mineral inclusions near the rims of the pyrite grains (Fig. 3a).

In samples from the NNW-trending HS vein system (Fig. 3b-d), $py_{tnt-(Cu)}$ is subhedral to anhedral and usually surrounded by massive or semi-massive tennantite-(Cu), (Fig. 3b-d) or supergene iron oxides (Fig. 3b-c). Py_{Au} grains are in proximity to native Au that is associated with tennantite-(Cu) usually near elongated barite grains (Fig. 3e). Late py_{tel} is euhedral and is related to chalcopryite and Zn-tetrahedrite (Fig. 3f). It usually hosts various mineral inclusions of the tetrahedrite-(Zn) and tellurides, e.g. coloradoite (HgTe). Back-scattered images show a slight zonation of the $py_{tnt-(Cu)}$ grains (Fig. 3a and d).

4.2 Trace element abundances in pyrite (EPMA and LA-ICP-MS)

Pyrite varies from As-poor (below detection limit) to As-rich (up to 1.5%) (Fig. 4a). Critical and rare metals are enriched in the pyrite grains, with up to 103 ppm In (Fig. 4b), up to 751 ppm Se (Fig. 4c), up to 1949 ppm Ag (Fig. 4d), up to 4977 ppm Te, up to 1110 ppm Hg and up to 760 ppm Bi. The measured

very high Se, Te, and Hg content of pyrite is possibly a result of the incorporation of mineral inclusions in the analytical volume. The presence of other metals has been also identified, with up to 61 ppm V, 4146 ppm Mn, 220 ppm Co, 161 ppm Ni, 3.5% Cu, 196 ppm Zn, 40 ppm Ga, 37 ppm Ge, 47 ppm Mo, 50 ppm Cd, 10 ppm Sn, 0.1% Sb, 4 ppm Au, 529 ppm TI, and 5% Pb.

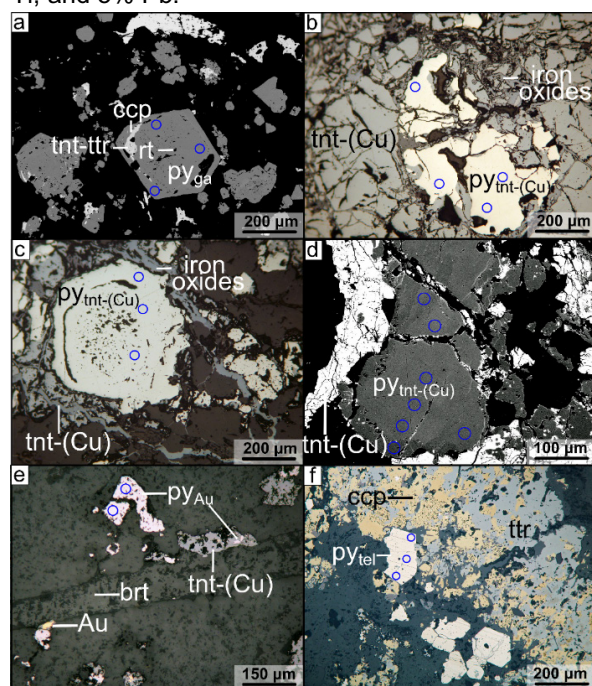


Figure 3. Microphotographs of sulfides-sulfosalts from the Pefka deposit with a focus on pyrite grains and their relationship to the other minerals, under reflected light (b, c, e and f) and on BSE images (a and d). The blue circles represent the LA-ICP-MS spots. (a) Euhedral py_{ga} grain spatially associated with the galena assemblage that encloses rutile and tennantite-tetrahedrite with small chalcopyrite grains. (b) $py_{tnt-(Cu)}$ surrounded by tennantite-(Cu). (c) Subhedral $py_{tnt-(Cu)}$ with porous core and clear rim. (d) $py_{tnt-(Cu)}$ with a brighter core and darker rim on the BSE image and in association with tennantite-(Cu). (e) py_{Au} in the proximity of a barite grain that is in contact with tennantite-(Cu) and native Au grains. (f) Subhedral py_{tel} in association with chalcopyrite and tetrahedrite. Mineral abbreviations after Whitney and Evans (2010) and Au: native Au, tnt-(Cu): tennantite-(Cu), tel: tellurides.

5 Discussion

5.1 Pyrite occurrence in the different ore stages

Py_{ga} is present as euhedral crystals in an altered volcanic rock in proximity to the early massive galena vein. However, it is not clear if it is contemporaneous and genetically related to the galena as intergrowths or crosscutting relationships have not been observed. Therefore, we chose to distinguish this sample and call it py_{ga} , as it shows different chemistry from the rest of the samples (Fig. 4), but its relation to galena remains controversial. The appearance of $py_{tnt-(Cu)}$, py_{col} , py_{Au} in the HS stage varies from subhedral to anhedral. The BSE imaging reveals that the dark rim of the $py_{tnt-(Cu)}$ in

Fig. 3d, hosts inclusions of tennantite-(Cu). This suggests that there are at least two types of pyrite in the HS stage. The first was probably pre-existing and the second was contemporaneous with the deposition of the sulfosalts. Py_{Au} of the HS stage is also interpreted to accompany the native Au deposition, as it is found as mineral inclusions in the sulfosalts that host the Au (Fig. 3e). Py_{tel} occurs at the late IS telluride-related stage accompanying the carbonates and the tetrahedrite-chalcopyrite assemblage. In this stage, py_{tel} is usually subhedral (Fig. 3f).

Therefore, combining these observations with the paragenetic sequence of Voudouris et al. (2022), the early IS galena is probably temporally related to the py_{ga} , the HS assemblage is accompanied by the $py_{tnt-(Cu)}$, the py_{Au} and the py_{col} , and the subsequent IS assemblage is accompanied by the py_{tel} .

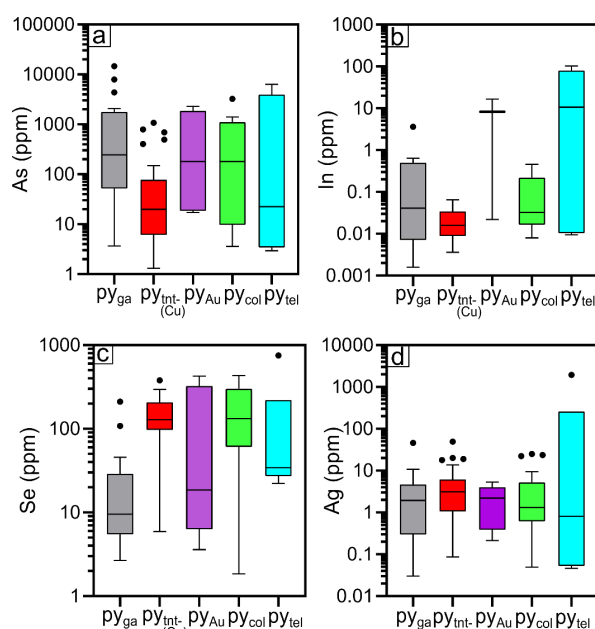


Figure 4. Tukey boxplots of As (a), In (b), Se (c) and Ag (d) variations of pyrite grains from the Pefka deposit for the different samples. Points represent outliers of the data and the horizontal line of each boxplot represents the median of the data. Mineral abbreviations after Whitney and Evans (2010) and Au: native Au, col: colusite, tnt-(Cu): tennantite-(Cu), and tel: tellurides.

5.2 Metallogenic implications through pyrite chemistry

Deditius et al. (2014) demonstrated that there is an increase in As and Au concentration in pyrite during the transition from the porphyry to the epithermal environment and showed that arsenian pyrite preserves the Au/As ratio of the parental fluids and thus can be used as a monitor for hydrothermal fluid evolution.

The results of Au and As concentration in pyrite from the Pefka deposit (Fig. 5a) from the different samples show that the Au/As ratio increases from the py_{ga} to the $py_{tnt-(Cu)}$, py_{col} and py_{Au} (HS stage)

and then again slightly decreases (but still remaining high) to the final py_{tel} (IS stage) (obvious from the blue dashed arrow of Fig. 5a). This indicates that the deposition of Au in the system mainly occurred during the HS and IS stage, which is consistent with the interpretation of Voudouris et al. (2022), and that the Au/As ratio of the fluids was higher during the HS stage.

The extreme enrichment of Te in Pefka is interpreted by Voudouris et al. (2022) to be related to extensive boiling processes. The increasing content of Te along with As concentration in the system from the HS to IS stage is evident from the increasing content of Te in pyrite from the early stages (py_{ga} , $py_{tnt-(Cu)}$, py_{Au} , py_{col}) to the IS stage with the deposition of tellurides (Fig. 5b). All the samples display several points that exceeds the solubility line of Te, that suggests that native Te inclusions are present in the pyrite. However, the py_{tel} displays Te as high as 4977 ppm (Fig. 5b), which is explained by the contemporaneous precipitation of tellurides of the IS stage. Keith et al. (2018) suggested that Te-rich pyrite precipitates from reduced fluids. Thus, an evolution from probably oxidized fluids of the HS stage towards reduced fluids of the IS stage may be assumed for the Pefka deposit.

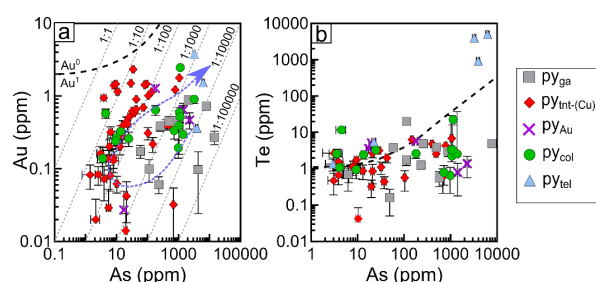


Figure 5. Concentrations and 1-sigma error ranges of Au (a) and Te (b) as a function of As in pyrite from the different samples of the Pefka deposit. The black dashed lines define the solubility limit of Au (a) and Te (b) below which Au and Te, respectively, are present in the structure of pyrite, while above is present as Au^0 and Te^0 inclusions in pyrite (after Reich et al. 2005; Keith et al. 2018). The blue dashed arrow in (a) represents the evolution of the average of the Au/As ratio of each sample compared to the paragenetic sequence. Mineral abbreviations after Whitney and Evans (2010) and Au: native Au, col: colusite, $tnt-(Cu)$: tennantite-(Cu), and tel: tellurides.

6 Conclusions

Pyrite grains from the Pefka deposit are spatially associated with galena (py_{ga}), tennantite-(Cu) ($py_{tnt-(Cu)}$), colusite (py_{col}), native-Au (py_{Au}) and tellurides (py_{tel}). The pyrite grains are particularly enriched in In, Se, Ag, Te, Hg and Bi. The Au and As concentrations of pyrite from the Pefka deposit suggest that the deposition of Au in the system occurred both in the HS and IS stages. The positive correlation of Te and As contents of the pyrite grains also suggests that at least the final IS assemblage was deposited from reduced fluids.

Acknowledgments

We gratefully acknowledge that part of this project is supported by the Society of the Economic Geologist (SEG) 2022 Student Research Grants (SRG 22-47) through the Hugh McKinstry Fund. Dr. Brätz is thanked for her assistance during the LA-ICP-MS analyses and data processing.

References

- Achterberg E, Ryan C, Jackson S, Griffin W (2001) Data reduction software for LA-ICP-MS. *Laser Ablation ICP-MS in the Earth Science* 29:239–243
- Deditius AP, Reich M, Kesler SE, Utsunomiya S, Chrysosoulis SL, Walshe J, Ewing RC (2014) The coupled geochemistry of Au and As in pyrite from hydrothermal ore deposits. *Geochimica et Cosmochimica Acta* 140:644–670. <https://doi.org/10.1016/j.gca.2014.05.045>
- Dimou E, Michael C, Serment R (1994) Mineralogical composition of epithermal polymetallic mineralization at Pefka, Rhodope. In: *Bull. Geol. Soc. Greece*. 30, 553–1550. pp 553–1550
- Grandell L, Lehtilä A, Kivinen M, Koljonen T, Kihlman S, Lauri LS (2016) Role of critical metals in the future markets of clean energy technologies. *Renewable Energy* 95:53–62. <https://doi.org/10.1016/j.renene.2016.03.102>
- Keith M, Smith DJ, Jenkin GRT, Holwell DA, Dye MD (2018) A review of Te and Se systematics in hydrothermal pyrite from precious metal deposits: Insights into ore-forming processes. *Ore Geology Reviews* 96:269–282. <https://doi.org/10.1016/j.oregeorev.2017.07.023>
- Marchev P, Kaiser-Rohrmeier M, Heinrich C, Ovtcharova M, von Quadt A, Raicheva R (2005) 2: Hydrothermal ore deposits related to post-orogenic extensional magmatism and core complex formation: The Rhodope Massif of Bulgaria and Greece. *Ore Geology Reviews* 27:53–89.
- Melfos V, Voudouris P (2017) Cenozoic metallogeny of Greece and potential for precious, critical and rare metals exploration. *Ore Geology Reviews* 89:1030–1057. <https://doi.org/10.1016/j.oregeorev.2017.05.029>
- Melfos V, Voudouris P (2012) Geological, Mineralogical and Geochemical Aspects for Critical and Rare Metals in Greece. *Minerals* 2:300–317. <https://doi.org/10.3390/min2040300>
- Reich M, Kesler SE, Utsunomiya S, Palenik CS, Chrysosoulis SL, Ewing RC (2005) Solubility of gold in arsenian pyrite. *Geochimica et Cosmochimica Acta* 69:2781–2796. <https://doi.org/10.1016/j.gca.2005.01.011>
- Repstock A, Voudouris P, Kolitsch U (2015) New occurrences of watanabeite, colusite, “arsenosulvanite” and “Cu-excess” tetrahedrite-tennantite at the Pefka high-sulfidation epithermal deposit, northeastern Greece. *njma* 192:135–149. <https://doi.org/10.1127/njma/2015/0276>
- Voudouris P (2006) A comparative mineralogical study of Te-rich magmatic-hydrothermal systems in northeastern Greece. *Mineralogy and Petrology* 87:241–275. <https://doi.org/10.1007/s00710-006-0131-y>
- Voudouris P, Mavrogenatos C, Spry PG, Baker T, Melfos V, Klemd R, Haase K, Repstock A, Djiba A, Bismayer U, Tarantola A, Scheffer C, Moritz R, Kouzmanov K, Alfieris D, Papavassiliou K, Schaarschmidt A, Galanopoulos E, Galanos E, Kołodziejczyk J, Stergiou C, Melfou M (2019) Porphyry and epithermal deposits in Greece: An overview, new discoveries, and mineralogical constraints on their genesis. *Ore Geology Reviews* 107:654–691. <https://doi.org/10.1016/j.oregeorev.2019.03.019>
- Voudouris P, Repstock A, Spry PG, Frenzel M, Mavrogenatos C, Keith M, Tarantola A, Melfos V, Tombros S, Zhai D, Cook NJ, Ciobanu CL, Schaarschmidt A, Rieck B, Kolitsch U, Falkenberg JJ (2022) Physicochemical constraints on indium-, tin-, germanium-, gallium-, gold-, and tellurium-bearing mineralizations in the Pefka and St Philippos polymetallic vein- and breccia-type deposits, Greece. *Ore Geology Reviews* 140:104348. <https://doi.org/10.1016/j.oregeorev.2021.104348>
- Whitney D, Evans B (2010) Abbreviations for Names of Rock-Forming Minerals. *American Mineralogist* 95:185–187.

Fault Permeability and Active Hydrothermal Systems: A Key to Infer the Formation of Unconformity-Related Uranium Deposits from Athabasca Basin (Canada)

Gaétan Milesi¹, Patrick Ledru¹, Paul Marchal¹, Matthieu Bourges¹, Clément Perrière¹, Jacek Scibek^{2,3}, Anthony Le Beux⁴, Julien Mercadier¹

¹GeoRessources, CNRS, Université de Lorraine, Labcom CREGU, France

²RWTH Aachen University, Germany

³Kyoto University, Japan

⁴ORANO, France

Abstract.

The Athabasca Basin region (Saskatchewan, Canada) hosts the highest grade and among the largest tonnage uranium deposits in the world. The formation of unconformity-related uranium (URU) deposits was essentially triggered by intense fluid circulations at the basin/basement interface that were channelized in a complex fault network. The development and the geometry of the fault systems had a first-order impact on the location and the size of uranium deposits. The intense fluid/rock interaction which affected that environment more than 1 Ga ago, however, strongly limits the characterization and quantification of these critical parameters. To overcome this problem, physical properties of fault systems and natural flow rates from active hydrothermal systems available in open databases have been used to define the possible range of values associated to fault permeability and fluid flow in the forming context (geometry/timing) of URU deposits.

1 Structural control on the formation of URU deposits of the Athabasca Basin

The Athabasca Proterozoic Basin region hosts some of the world's largest URU deposits (e.g. McArthur River, Cigar Lake) with uranium grading over 1% of up to 20% (Jefferson et al., 2007; Kyser and Cuney, 2015). These uranium deposits located at the interface between the basin and its crystalline basement were strongly controlled by a specific structural network marked by: i) the reactivation of basement-hosted faults and ii) the propagation of these fault and fracture networks through Athabasca Basin. The unconformity offset associated to fault reactivation is limited to 100s of meters and extends up to several kilometers along strike (Thomas et al., 2016; Ledru et al., 2022). Some of these fault systems channelized circulations of large volumes of uranium mineralizing fluids, the largest hydrothermal system being associated to the formation of "Giant" URU deposits. Such massive circulation of fluids, in addition to uranium deposition, is marked by large alteration haloes developed in both basement and basin (Kyser and Cuney, 2015; IAEA, 2018).

In this context, key elements for the formation of the URU deposits in the Athabasca Basin are questioned by Boiron et al. (2010), in particular: i) the origin and the composition of uranium mineralizing fluids, ii) fault fluid flows associated to mineralizing event and iii) timing and duration of the

paleo-fluid circulations. Concerning i), the fluids are marked by the highest content of uranium known so far in crustal fluids (Richard et al. 2012). The questions regarding the nature and conditions of fluid flow(s) and their timing/duration are, however, still open and have mainly been approached based on ore deposit models and footprints (Jefferson et al. 2017, IAEA, 2018) or numerical simulations (e.g. Li et al. 2018; Poh et al., 2022). In order to constrain these parameters and define criteria that favored the formation of "giant deposits" in such environment, we propose to compare the geological models resulting from exploration and mined deposits with active or fossil systems on which properties of the faults and fluid flow have been better constrained. Large new databases on fault permeability (Scibek, 2020) and natural thermal springs (Tamburello et al., 2022) allow to investigate: i) the range of possible fault permeability according to the displacement, and kinematics of the faults and ii) flow rates associated to active hydrothermal systems. These parameters cannot be precisely quantified on fossil hydrothermal systems, and we therefore propose an analogical approach to characterize them.

2 Fault zone permeability and fluid flow

2.1 Fault zone permeability

The petrophysical properties active faults can provide critical information (e.g. Faulkner et al., 2010). Fault zones are characterized by two main domains of deformation with different hydro-mechanical properties: i) Core Zone(s) (CZ) associated to fault rocks: breccias, cataclasites, gouges... These zones commonly act as a barrier for fluid circulation when the fault is not active (e.g. Sibson, 2000), ii) Damage zones (DZ) that are a fractured rock volume along fault core, characterized by an increase in fracture density compared to the surrounding host rocks (Caine et al., 1996). The damage due to the fault activity increases the permeability of the host rock by several orders of magnitude, thus allowing fluid circulation in fault zone (Mitchell and Faulkner, 2012). It is worth noting that the permeability can be increased significantly during the deformation, especially for high fluid flux hydrothermal systems (Cox, 2010). The fault permeability database of

Scibek (2020) allowed to discuss the range of permeability in fault zones considering fault displacement and kinematic (Fig. 1).

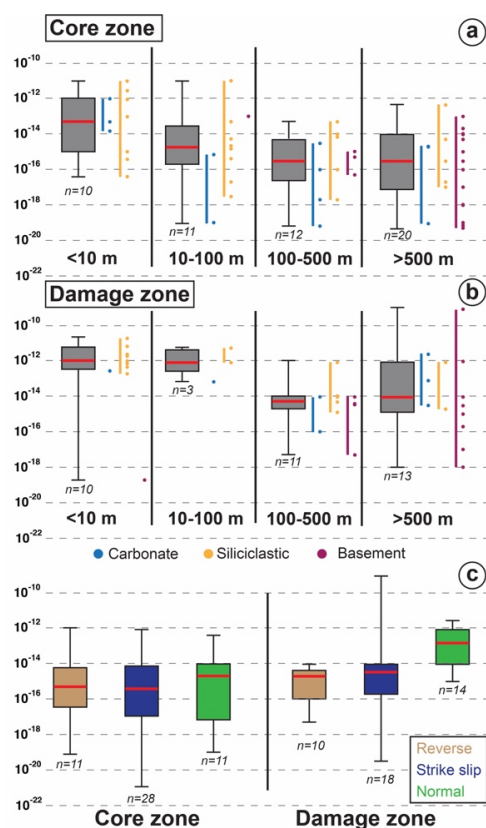


Figure 1. Box plots of CZ (a) and DZ (b) fault permeabilities according to different range of fault displacement, CZ and DZ permeabilities according to fault kinematic (c). The nature of host rocks is also considered. Database of Scibek (2020).

The CZ permeability (Fig. 1a) correlates to the fault displacement with median value $\sim 10^{-13}$ – 10^{-15} m² for displacement <100 m and $\sim 10^{-16}$ m² for fault with displacement >100 m. This significant decrease of permeability could be representative of fault rock evolution from breccias to gouges (Fischer and Knipe, 2001). In the basement, CZ permeabilities for fault displacement >500 m show a wide range of values from 10^{-13} to 10^{-19} m². The permeability values obtained for the DZ (Fig. 1b) are globally higher than for the CZ. For fault displacement <100 m, DZ permeability are $>10^{-13}$ m². The DZ permeability for fault displacement >100 m is lower with median value between 10^{-13} and 10^{-15} m². In the basement, DZ permeability for fault displacement >500 m shows a wide range of values from 10^{-12} to 10^{-18} m².

The apparent correlation between displacement and permeability must be interpreted with caution due to the lack of data for some fault displacement and results only for sedimentary photoliths for fault displacement <100 m. Basement faults with fault displacement >100 m are characterized by a wide range of permeability for CZ and DZ. Permeabilities in fault hosted in siliciclastics lithologies appear to be controlled by the fault displacement. It is

important to consider that the evolution of thickness of the DZ associated to the fault displacement (Mayolle et al., 2019 and references inside) and its heterogeneity is not considered here.

Median CZ permeability is similar for the different fault kinematics, while median DZ permeability is higher for normal kinematic ($\sim 10^{-13}$ m²) compared to reverse and strike-slip faults ($\sim 10^{-15}$ m², Fig. 1c). It is important to note a wide range of DZ permeability for strike-slip context. These values must be considered with caution because the fault length and initial protolith are not considered.

2.2 Water flow in active hydrothermal system

Tamburello et al. (2022) constitutes a database on $\sim 6,000$ worldwide thermal springs, including 1,483 flow rates. This synthesis shows a wide range of water flow values from 10^{-5} to ~ 5 m³.s⁻¹ that are associated to various hydrothermal contexts. This important database gives typical values on fluid flow of natural hydrothermal systems. Extreme values (10%) that could be representative of atypical hydrothermal systems (e.g. volcanic systems, deep sea vents) and potential bias in the database are not considered. 90% of the value are representative of natural hydrothermal flow, that represent fluid flow between 10^{-4} (0.1 l/s) and $4 \cdot 10^{-1}$ m³.s⁻¹ (400 l/s) with a median value of $3 \cdot 10^{-3}$ m³.s⁻¹ (3 l/s). The range obtained are consistent with values obtained on other natural fault hydrothermal systems (Milesi, 2020) or geothermal systems (Glaas et al., 2021).

3 Implications for URU deposits of the Athabasca Basin

3.1 Fault zone permeability and geometry of uranium deposits

The characterisation of alteration halo and mineralisation geometries is essential for assessing uranium reserves and/or alteration clay volumes. We investigate the impact of faults to better understand how permeability contrasts between fault structures and the protolith can affect fluid flow, using a simple flow model, based on a Fast Marching Method (scikit-fmm), which relies on a permeability-based velocity field, using the Eikonal equation with $F(x)$ the velocity field and $T(x)$ the arrival time field:

$$F(x) * \overrightarrow{\text{grad}} T(x) = 1$$

The models in Figure 2a reproduces the main geometry of the Athabasca Basin with a tabular sedimentary basin (S_0) overlying a sub-vertical metamorphic basement (S_1). We used the same fault zone geometry: DZ of ~ 60 m and CZ of ~ 1 m with a basement source of fluid in the different models. Given that we used geologically realistic values of permeability, we tested different contrasts between the protolith and of the damage zone. This contrast is varying between 10^2 and 10^6 (Fig. 2a). The shape of the front has been assimilated to a

limit of alteration or mineralisation to calculate the area affected for the different scenarios (Fig. 2b). These models are a first approach, as they only consider the permeability (k) as a control of the front propagation. According to Zhang et al (2016), other parameters like fluid compressibility and fluid dynamic viscosity should be considered.

The numerical modeling results obtained (Fig. 2a) highlight a significant control of the damage zone permeability on the development of fluid front, with a global increase of the alteration area consistent with the permeability contrast between DZ and protolith. The results between basin and basement show some differences (Fig. 2b). A global area increase is observed both for basement and basin. We can note a sharp increase for basement alteration area from 10^6 contrast of permeability. A significantly higher contrast of 10^{10} is needed to observe an alteration area increase in the basin.

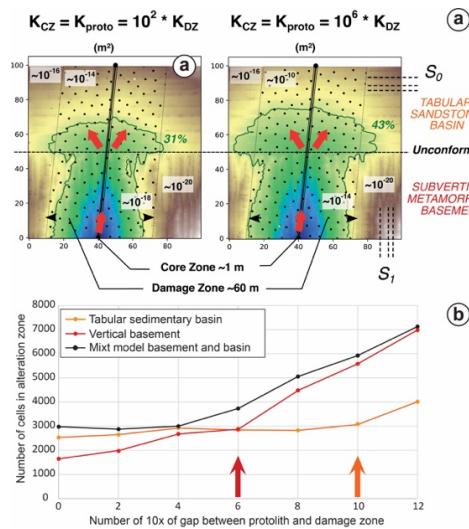


Figure 2. Front propagation model using fmm-scikit showing the effect of changing the permeability contrast on flow and altered areas.

3.2 Water flow implication for timing of formation of uranium deposits

Based on the database of Tamburello et al. (2022), we tested the minimum (0.1 l/s), maximum (400 l/s) and median value (3 l/s) for natural fluid flow using different uranium content in fluids: 0.1, 1 and 100 ppm to form a “giant deposit” of 100,000 tU. We considered 100%, 50% and 1% of uranium precipitation from fluids (Table 1).

The results obtained show that for the scenario of 100% of uranium precipitate from fluid all the fluid flow and uranium content in fluid can be generated from a range of time between 31.7 Myr and few years except for the lowest fluid flow and U content (317 Myr). For 50% of uranium precipitation efficiency, the results are between 63.4 Myr and ~1 kyr. Except for low uranium content in fluid (0.1 ppm) and fluid flow of 0.1 and 3 l/s, time to form U deposit are above 100 Myr. The last example, with only 1% of uranium precipitation efficiency from the

fluid show the need of fluid flow of 400 l/s and/or high U content (100 ppm) to form “giant deposit” in less than 100 Myr.

Table 1. Table of fluid circulation duration to formed “giant deposit” of 100,000 tonnes U, Values with no indication are in Myr, the red values are duration above 100 My.

100% of uranium content in fluid mineralized			
Fluid flow (l/s)	Fluid U content (ppm)		
	0.1	1	100
	0.1	317	31.7
	3	11	1.0
400	0.08	8 kyr	80 yr

50% of uranium content in fluid mineralized			
Fluid flow (l/s)	Fluid U content (ppm)		
	0.1	1	100
	0.1	634	63.4
	3	22	2.0
400	0.16	0.02	> 1 kyr

1% of uranium content in fluid mineralized			
Fluid flow (l/s)	Fluid U content (ppm)		
	0.1	1	100
	0.1	31700	3170
	3	1056	105
400	7.9	0.7	< 8 kyr

4 Implications for URU deposits of the Athabasca Basin

Numerical modelling results showed significant increase of the altered area for very high contrasts of permeability between the DZ and protolith, i.e., 10^{10} in the basin and 10^6 for the basement. Fluid circulation in the basin will be channelized both by fault and permeable layers of the basin (Fig. 2a). Considering, the important initial permeability of siliciclastic protolith compared to the basement lithologies (Fisher and Knipe, 2001), this very high contrast of permeability between fault DZ and basin protolith seems difficult to reach for faults with displacement ≤ 500 m (Fig. 1b). In Athabasca, the basement experienced several episodes of deformation (with different kinematics) that likely formed different generation of fractures and alteration. This tectonic superposition could have stimulated the permeability of these structures (e.g. Chauvet, 2019). The large range of values observed for DZ permeability (Fig. 1b) shows the potential of basement fault to localize high permeability contrast that can channelize large volume of mineralizing fluids until the unconformity.

The fluid flow associated to fault structures in the Athabasca Basin has been investigated using flow rates from active hydrothermal systems as analogy. The lifetime of hydrothermal circulation required for forming a giant U deposit is between 10 years and several hundred Myrs (Table 1) depending on the efficiency of redox, flow rates and U content in fluids. In the Athabasca Basin, Richard et al. (2012) proposed high U content in mineralizing fluids (>100 ppm) for the formation of “giant uranium deposits”. Several authors considered also efficient redox processes associated to the formation of uranium deposits in the Athabasca Basin (e.g. Richard et al., 2012; Dargent et al., 2015). For such conditions, the lifetime of mineralizing hydrothermal circulation required for the formation of a “giant

deposit” can be estimated as less than 3 Ma regardless of the flow rate (Table 1). The formation of URU deposits is rapid at the geological time scale. This does not allow one to decide between a DZ-scale sustained fluid convection or fluid pulses associated with deformation (Cox, 2016). Further investigations in weakly mineralized zones could provide new clues to better understand the key phenomena in the formation of “giant uranium deposits”.

5 Conclusions

Our results questioned the formation of URU deposits of the Athabasca Basin that could be also controlled by the contrast of permeability in basement fault zones. The location of uranium and alteration associated in the basin appear mainly controlled both by structural network and permeable layers. The flow rates do not constitute the only critical parameter for the formation of URU deposits. Considering the high U fluid content and efficient redox processes previously proposed in this area, a brief hydrothermal circulation from few years to ~3 Myr can form “Giant” URU deposits of the Athabasca Basin.

Acknowledgements

The authors acknowledge ANR funding, grant ANR-21-CHIN-0006 (project Geomin3D). T. Driesner for the abstract review.

References

- Boiron M-C, Cathelineau M, Richard A (2010) Fluid flows and metal deposition near basement /cover unconformity: lessons and analogies from Pb-Zn-F-Ba systems for the understanding of Proterozoic U deposits. *Geofluids*. <https://doi.org/10.1111/j.1468-8123.2010.00289.x>
- Caine JS, Evans JP, Forster CB (1996) Fault zone architecture and permeability structure. *Geol* 24:1025. [https://doi.org/10.1130/0091-7613\(1996\)024<1025:FZAAPS>2.3.CO;2](https://doi.org/10.1130/0091-7613(1996)024<1025:FZAAPS>2.3.CO;2)
- Chauvet A (2019) Structural Control of Ore Deposits: The Role of Pre-Existing Structures on the Formation of Mineralised Vein Systems. *Minerals* 9:56. <https://doi.org/10.3390/min9010056>
- Cox SF (2010) The application of failure mode diagrams for exploring the roles of fluid pressure and stress states in controlling styles of fracture-controlled permeability enhancement in faults and shear zones. *Geofluids*. <https://doi.org/10.1111/j.1468-8123.2010.00281.x>
- Dargent M, Truche L, Dubessy J, et al (2015) Reduction kinetics of aqueous U(VI) in acidic chloride brines to uraninite by methane, hydrogen or C-graphite under hydrothermal conditions: Implications for the genesis of unconformity-related uranium ore deposits. *Geochimica et Cosmochimica Acta* 167:11–26. <https://doi.org/10.1016/j.gca.2015.06.027>
- Faulkner DR, Jackson CAL, Lunn RJ, et al (2010) A review of recent developments concerning the structure, mechanics and fluid flow properties of fault zones. *Journal of Structural Geology* 32:1557–1575. <https://doi.org/10.1016/j.jsg.2010.06.009>
- Fisher Q J and Knipe R J (2001) The permeability of faults within siliciclastic petroleum reservoirs of the North Sea and Norwegian Continental Shelf. *Marine and Petroleum Geology*, 18(10), 1063-1081. [https://doi.org/10.1016/S0264-8172\(01\)00042-3](https://doi.org/10.1016/S0264-8172(01)00042-3)
- Glaas C, Vidal J, Genter A (2021) Structural characterization of naturally fractured geothermal reservoirs in the central Upper Rhine Graben. *Journal of Structural Geology* 148:104370. <https://doi.org/10.1016/j.jsg.2021.104370>
- IAEA (2018) Uranium 2018: Resources, Production and Demand, in: OECD (Ed.), Red Book. p. 550.
- Jefferson CW, Thomas DJ, Gandhi SS, et al (2007) Unconformity-associated uranium deposits of the Athabasca basin, Saskatchewan and Alberta. Geological Association of Canada, Mineral Deposits Division, Special Publication No. 5, pp. 273-305.
- Kyser K and Cuney M. (2015) Chapter 8: Basins and uranium deposits: Mineralogical Association of Canada. Mineralogical Association of Canada, Short Course Series, 46: 225–304.
- Ledru P, Benedicto A, Chi G et al (2022) The unconformity-related uranium mineral system of the Athabasca Basin (Canada). Dans *Ressources métalliques 2*, Decrée, S. (dir.). ISTE Editions, Londres
- Li Z, Chi G, Bethune KM et al. (2018) Numerical simulation of strain localization and its relationship to formation of the Sue unconformity-related uranium deposits, eastern Athabasca Basin, Canada. *Ore Geology Reviews*, vol. 101, pp. 17–31, 2018. <https://doi.org/10.1016/j.oregeorev.2018.07.004>
- Mayolle S, Soliva R, Caniven Y, et al (2019) Scaling of fault damage zones in carbonate rocks. *Journal of Structural Geology* 124:35–50. <https://doi.org/10.1016/j.jsg.2019.03.007>
- Mitchell TM, Faulkner DR (2009) The nature and origin of off-fault damage surrounding strike-slip fault zones with a wide range of displacements: A field study from the Atacama fault system, northern Chile. *Journal of Structural Geology* 31:802–816. <https://doi.org/10.1016/j.jsg.2009.05.002>
- Milesi G (2020). Analyse thermochronologique, géochimique et structurale du système hydrothermal de la faille de la Têt (Pyrénées, France): un nouvel outil d'exploration géothermique. Doctoral dissertation, University Montpellier. HAL Id: tel-0334031.
- Poh J, Eldursi K, Ledru et al (2022) Role of Hydrothermal Circulation along and above Inherited Basement Structures Relating to Unconformity-Related Uranium Mineralization. *Geofluids*. <https://doi.org/10.1155/2022/9131289>
- Richard A, Rozsypal C, Mercadier J, et al (2012) Giant uranium deposits formed from exceptionally uranium-rich acidic brines. *Nature Geosci* 5:142–146. <https://doi.org/10.1038/ngeo1338>
- Scibek J (2020) Multidisciplinary database of permeability of fault zones and surrounding protolith rocks at world-wide sites. *Sci Data* 7:95. <https://doi.org/10.1038/s41597-020-0435-5>
- Sibson RH (2000) Fluid involvement in normal faulting. *Journal of Geodynamics* 29:469–499. [https://doi.org/10.1016/S0264-3707\(99\)00042-3](https://doi.org/10.1016/S0264-3707(99)00042-3)
- Tamburello G, Chiodini G, Ciotoli G, et al (2022) Global thermal spring distribution and relationship to endogenous and exogenous factors. *Nat Commun* 13:6378. <https://doi.org/10.1038/s41467-022-34115-w>
- Thomas D, Aubin A., Zaluski G. (2016). What Does an Athabasca Basin Uranium Deposit Footprint Look Like? Empirical characteristics and the relevance to exploration. Saskatchewan Geological Society Luncheon, Nov. 2016.
- Zhang Y, Bansal N, Fujita Y et al (2016). From Streamlines to Fast Marching: Rapid Simulation and Performance Assessment of Shale-Gas Reservoirs by Use of Diffusive Time of Flight as a Spatial Coordinate. *SPE Journal*, 21(05), 1883-1898. <https://doi.org/10.2118/168997-PA>

Study of Hydrothermally Altered Zones within the Gujarat-Khachkovi Ore Field Using Terra ASTER Multispectral Satellite Data. Georgia.

Giorgi Mindiashvili

Ivane Javakhishvili Tbilisi State University. Faculty of Exact and Natural Sciences, Department of Geology.

Abstract. This work involves the interpretation of data obtained through remote sensing analyses and techniques to identify geological features and potential ore fields in the Gudjareti-Khachkovi area of South-East Georgia, utilizing ASTER Multispectral satellite data. The conducted research indicates the significant roles of magmatic processes and hydrothermally altered zones within the studied area, which are characterized by pyritized, oxidized, and clay-altered rocks. These rocks are frequently highly fractured and cemented by quartz, as well as quartz-gold veins of various sizes, shapes, and orientations. It is evident that hydrothermal alterations and mineralization types do not fully depict the current geological processes in the study area. However, the research demonstrates a genetic relationship between ore mineralization processes and the region's magmatic activities. We anticipate that our findings will contribute to the enhanced utilization of remote sensing methods and increase the efficiency of ore exploration in Georgia.

1 Introduction

The study area exhibits abundant vegetation, snow, and glaciers, and is frequently affected by cloud cover. Consequently, efforts were made to acquire the most suitable satellite data from the available ASTER images to accurately represent the area while minimizing snow and cloud coverage. The satellite data was collected on November 24, 2021. The ASTER image used in this study indicates approximately 2% cloud cover, 20% vegetation, and 35% snow cover across the entire region. Despite the dense vegetation in the area, various rock types have been identified and characterized through lithological descriptions, mineral mapping techniques, and geological feature analyses. To verify the observed anomalies, ground truth studies should be conducted in the licensed areas. However, due to the small size of the area, it was not feasible to carry out these studies. Therefore, all analyses were performed using the complete ASTER image to detect all available geological features in the region. The Adjara-Trialeti region was formed as a rift zone at the end of the Cretaceous period and underwent folding during the Paleogene era. It primarily consists of trachytic and trachytic-andesitic volcanogenic-sedimentary rocks, although plutonic rocks also play a significant role in the overall structure. Plutonic rocks in the area include syenite, monzonite, and gabbro. Modern research suggests that syenite-trachytic magmatic activity can occur in subduction zones,

mantle plume activity regions, post-collisional tectonic areas, and continental rift environments. In all cases, the formation of this type of magmatism is influenced by mantle magma on the lithosphere, followed by processes such as hybridism, assimilation, and metasomatism. The plutons within the Adjara-Trialeti folded zone form various types and sizes of bodies that intersect with igneous sedimentary rocks. Based on paleontological data, the volcanic-sedimentary formations are dated to the middle Eocene. Some researchers consider the plutonic bodies in the Adjara-Trialeti zone to be synchronous with volcanic activity, categorizing them as middle Eocene. Others identify multiple phases of intrusion. It is important to note that intensive hydrothermal ore mineralization processes often occur in the contact zones between igneous sedimentary rocks and plutonic bodies, leading to the formation of significant ore fields such as Merisi Vakijvari, Zoti, Garta-Dzama, Gudjareti-Khachkovi, and others. The focus of our research is the Gudjareti-Khachkovi ore field, which was investigated using remote sensing techniques. This research carries substantial scientific and practical importance.

2. Method of Study

Terra ASTER satellite data has been specifically developed for the purpose of detecting geological features on Earth. Depending on the objectives of the study, various data can be obtained through the analysis of the area. Consequently, the remote sensing method and analyses exhibit differences based on the specific objectives. A comprehensive examination of the entire ASTER image has been conducted, involving multiple analyses to determine lithological variations and perform the mineral mapping. Additionally, different algorithms have been employed to uncover details regarding structural elements and interpret the formation type. This study aims to explore the gold mine and associated geological features in the proposed Gudjareti-Khachkovi ore fields. The investigations conducted do not directly focus on analysing metallic minerals but rather aim to understand the formation environment of the considered mine deposit. Furthermore, methods have been applied to investigate alterations in mineralogy and the formation environment. ASTER data consists of three types of spectral bands: VNIR (visible near-infrared), SWIR (shortwave infrared), and TIR (thermal infrared). Initially, these spectral bands

were combined to create a comprehensive dataset. Subsequently, the ASTER data underwent atmospheric correction processing to eliminate moisture content and other atmospheric particles that could potentially impact the analysis negatively. The satellite image was georeferenced by incorporating the UTM (Universal Transverse Mercator) coordinate system and the WGS 84 datum in zone 38. Following the pre-processing stage, remote sensing analysis was conducted in accordance with internationally recognized standards and algorithms specifically developed for mine exploration. Due to the significant vegetation cover, snow, and wetlands present in the majority of the area, these regions were excluded from the image analysis and masked out. Thus, vegetation, snow, clouds, and wetlands were disregarded in the analysis. Only areas where rocks were observed in the images were selected for further image processing. Consequently, the investigation focused on examining the lithological and mineralogical features observed in very specific and narrow areas. In this process, regions, where these features exhibited continuity, were identified, and interpretations were made based on these specific areas. Therefore, not only the study area but the entire territory captured in the full image was thoroughly investigated.

2.1 Image analysis and results

It is important to note that the study in the study area was conducted for the first time using the remote sensing method. While it is evident that hydrothermal alterations and mineralization types may not fully depict the current geological processes of the study area, the conducted works have demonstrated a genetic relationship between ore mineralization processes and the magmatic activities in the region. The following analyses were carried out, and the results were obtained using ASTER data (Fig. 1). Through the remote sensing method, hydrothermally altered zones were identified, and the areas exhibiting geochemical anomalies were delineated (Fig. 2).

3. Conclusion

The conducted works have demonstrated that the data acquired through the remote sensing method accurately replicate the contours of the known mineral manifestations. This finding highlights the effectiveness of remote sensing in detecting and delineating existing mineralized zones. Additionally, the method has enabled the identification of several previously unknown and significant mineralization zones. These findings signify the potential for further exploration and prospecting activities within the study area. Based on the interpretation of the conducted studies, we emphasize the need for focused attention on the northern side of the research object. The presence of mineralization zones in this specific area warrants thorough

investigation and exploration efforts. It is crucial to allocate resources and conduct detailed geological surveys, including fieldwork and geophysical studies, to gain a comprehensive understanding of the potential mineral deposits in the region. In conclusion, the promising results obtained from the remote sensing analysis of the Gudjareti-Khachkovi ore field indicate the importance of conducting comprehensive geological works in the future. These investigations should involve a multidisciplinary approach, incorporating various geological and geophysical techniques to further delineate and assess the potential for the presence of economically viable mineral deposits. Such endeavours will contribute to the broader understanding of the region's geological characteristics and aid in the identification of industrial-grade mineral resources.

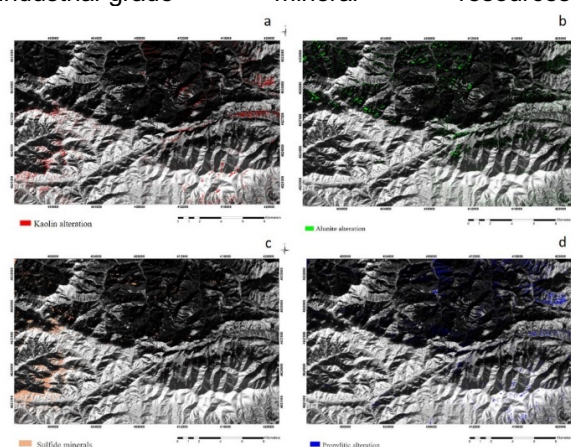


Figure 1. ASTER SWIR bands. Anomalies of mineralization zones

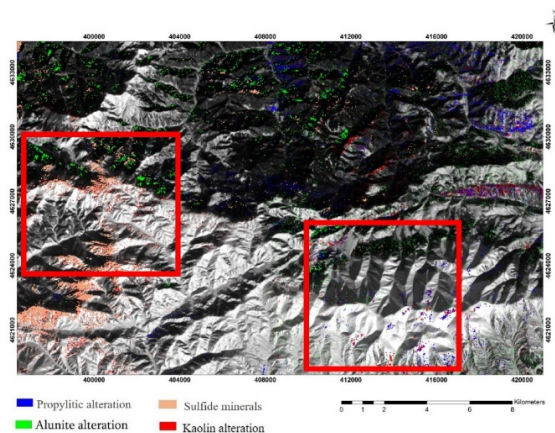


Figure 2. Complete picture of the survey conducted by the remote sensing method

Acknowledgements

This research [PHDF-21-179] has been supported by Shota Rustaveli National Science Foundation of Georgia (SRNSFG)

References

- Gamkrelidze I. (1986) Geodynamic evolution of the Caucasus and adjacent areas in Alpine time. *Tectonophysics*, 127: 261-277.
- Duggen S., Hoernle K., Bogaard P. et al. (2005) Post-collisional transition from subduction- to intraplate-type magmatism in the westernmost Mediterranean: evidence for continental-edge delamination of subcontinental lithosphere. *J. Petrology*, 46: 1155-1201.
- Ashwal L., Torsvik T., Horvath P., Harris C., et al. (2016) A mantle-derived origin for Mauritian trachytes. *J Petrology*, 57: 1645-1676.
- Chung S.-L., Chu M.-F., Zhang Y. et al. (2005) Tibetan tectonic evolution inferred from spatial and temporal variations in post-collisional magmatism. *Earth-Sci. Rev.*, 68: 173-196.
- Peccerillo A., Barberio M. R., Yirgu G. et al., (2003) Relationships between mafic and peralkaline silicic magmatism in continental rift settings: a petrological, geochemical and isotopic study of the Gedemsa volcano, central Ethiopian rift. *J. Petrol*, 44: 2003-2032.
- David Bluashvili, Ketil Benashvili, Giorgi Mindiashvili, David Makadze (2020) New Data on the Dzama-Gudjareti Ore Knot (Georgia), *Bulletin of the Georgian National Academy of Sciences*, vol. 14. No. 3.
- Jong S.M., Meer F.D., Clevers J.G. (2004) Basics of Remote Sensing. In: Jong S.M.D., Meer F.D.V. Remote Sensing Image Analysis: Including the Spatial Domain. Remote Sensing and Digital Image Processing, vol. 5. Springer, Dordrecht. https://doi.org/10.1007/978-1-4020-2560-0_1
- Yamaguchi, Y. & Naito, C. (2003) Spectral indices for lithological discrimination and mapping by using the ASTER SWIR bands. *International Journal of Remote Sensing*, 24, 4311- 432
- Van Der Meer, F. (2002) Basic physics of spectrometry. In: F.D. Van Der Meer & S.M. De Jong (Eds.), *Imaging Spectrometry. Basic Principles and Prospective Applications* (pp. 3- 16). Hingham (MA), USA: Kluwer Academic Publishers.
- Rowan, L., Hook, S., Abrams, M. & Mars, J. (2003) Mapping hydrothermally altered rocks at Cuprite, Nevada, using the advanced space borne thermal emission and reflection radiometer (ASTER), a new satellite-imaging system. *Economic Geology*, 98, 1019-1027.
- Alimohammadi M., Alirezaei S., Kontak D.J., 2015. Application of ASTER data for exploration of porphyry copper deposits: A case study of Daraloo–Sarmeshk area, southern part of the Kerman copper belt, Iran. *Ore Geology Reviews* 70, 290–304.
- Galley, A.G., Hannington, M.D., Jonasson, I.R., 2007. Volcanogenic massive sulphide deposits. In: GOODFELLOW W. D. ed. *Mineral deposits of Canada: a synthesis of major deposit-types, district metallogeny, the evolution of geological provinces, and exploration methods*. Geological Association of Canada, Mineral Deposits Division, Special Publication no. 5. St. John's, NL, Canada 141-161.
- Hosseini Zadeh, M., Tangestani. M.H., Roldan. F.V., Yusta. I., 2014a. Spectral characteristics of minerals in alteration zones associated with porphyry copper deposits in the middle part of Kerman copper belt, SE Iran. *Ore Geology Reviews* 62, 191–198.
- Mars, J.C., Rowan, L.C., 2006. Regional mapping of phyllic and argillic-altered rocks in the Zagros magmatic arc, Iran, using Advanced Spaceborne Thermal Emission and Reflection Radiometer (ASTER) data and logical operator algorithms. *Geosphere* 2, 161–186.

Mineralogy, Pb isotopes in galena, and Nd isotopes in associated dykes from the Ag-Hg Imiter deposit, Anti-Atlas, Morocco: implications for metal sources

Mehdi Ousbih¹, Brian Cousens², Yves Geraud³, Alexiane Favier³, Hafida El Bilali^{4,5}, Mohamed Ezzghoudy¹, Askkour Fatiha¹, Salim El Mouden⁶, Abdelaziz Gaouzi⁶, Oubaassine Hssane⁷, Richard Ernst^{4,5}, Moha Ikenne¹

¹Department of Geology, Faculty of Sciences, Ibn Zohr University, Agadir, Morocco.

²Isotope Geochemistry and Geochronology Research Centre, Department of Earth Sciences, Carleton University, Ottawa, Canada.

³University of Lorraine-CNRS-GeoRessources, Nancy, France.

⁴Department of Earth Sciences, Carleton University, Ottawa, Canada.

⁵Department of Geology and Geography, National Research Tomsk State University, Russian Federation.

⁶Managem Group, Casablanca, Morocco.

⁷Department of Geology, Faculty of Sciences, Cadi Ayyad University, Marrakech, Morocco.

Abstract. The Imiter deposit is a significant silver-rich base metal deposit. The deposit is primarily composed of sub-horizontal ore bodies that occur at the contact between the Sagro Group (630-604 Ma) shales and Ouarzazate Group (590-540 Ma) volcanics. The silver mineralisation occurs as steeply-dipping north-trending veins, low south-dipping veins and stockwork ore within conglomerates, tuffs and andesites. The ore mineralogy consists of Ag-Hg amalgam, argentite, polybasite, tetrahedrite-tennantite, proustite-pyrargyrite, acanthite, chalcopyrite, arsenopyrite, pyrite, sphalerite, and galena. The lead isotopic data of galena reveal two distinct groups, indicating two different origins for mineralizing fluids: one from the crust and the second from the mantle. The silver deposits are closely associated with a swarm of mafic to felsic dykes with different trends: NE to N70 in the Sagro Group and N-S to N10 in the OG. The first group is characterized by initial $^{143}\text{Nd}/^{144}\text{Nd}$ ratios ranging from 0.511787 to 0.511970, moderately negative ϵ_{Nd} values (-0.15 to -2.78), and older Nd model ages (1.3-1.7 Ga), suggesting a locally enriched mantle source or significant crustal contamination. The second group has initial $^{143}\text{Nd}/^{144}\text{Nd}$ ratios between 0.511885 and 0.512075, Nd model ages between 1.00 and 1.29 Ga, and positive ϵ_{Nd} values between 0.02 and 2.84, indicating a more juvenile source.

1 Introduction

The main primary Ag ore deposits are predominantly of hydrothermal origin and include various types such as epithermal (low-, intermediate- and high-sulfidation), volcanogenic massive sulphides (VMS), sedimentary-exhalative (SEDEX), sediment-hosted Ag-Cu, carbonate replacement and skarns, porphyry Cu, deeply formed mesothermal Ag-Pb-Zn, and Ag-Co-Ni-As veins (Kesler and Simon 2015). The Neoproterozoic-Cambrian transition period has significant implications for ore deposit metallogenesis and igneous crustal evolution in the northwest of the Western African Craton (Fig. 1). In Morocco, the known hydrothermal deposits are mostly associated with lithological units of the Anti-Atlas region. Important examples of such deposits include the Bou Azzer and the Imiter districts, which are currently being actively mined (Levresse et al. 2004; Ikenne et al. 2007, 2021).

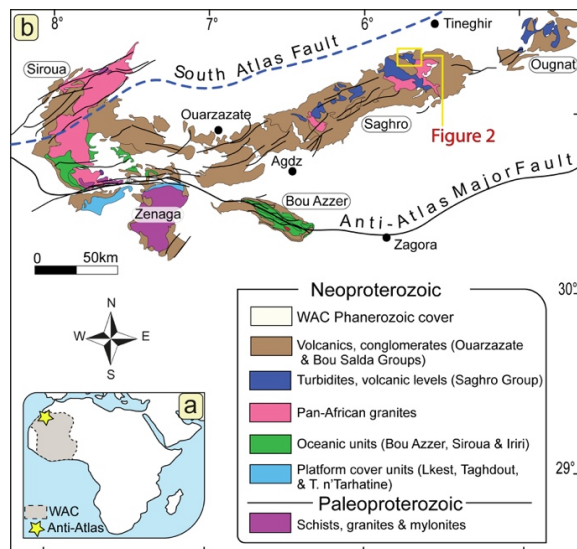


Figure 1. a. Location of the Anti-Atlas belt along the northwestern margin of the West African Craton. b. Simplified map of the eastern part of the Anti-Atlas belt, showing the main Precambrian inliers, with the location of the Imiter mine area labelled **Figure 2** (modified from Gasquet et al. 2005).

The Imiter Ag deposit (IAD), as the world's tenth-largest producer of Ag ores, has a long mining history dating back to the VIIIth century (Levresse et al. 2004). The ore bodies of the mine are controlled, and mainly distributed, along a major fault contact between lower Ediacaran turbiditic series and Late Ediacaran volcano-sedimentary, subvolcanic, and plutonic rocks (Fig. 2). The Ag mineralisation occurs also as steeply-dipping north-trending veins, south-dipping veins hosted within sandstones, all related to the major Imiter fault. Secondly, the mineralization is also present in the form of stockwork ore within conglomerates, tuffs and andesites. The IAD is comprised of four main mining sectors, namely Imiter I, Imiter II, Imiter South, and Igoudrane. The mineralization exhibits diverse textures such as brecciated, ribbon, and disseminated textures, and the gangue minerals are primarily quartz and carbonates. The ore body Ag mineralization is closely associated with

intermediate to mafic dykes that crosscut the Saghro Group basement as well as the Ouarzazate Group. The genesis of the IAD has been a challenging problem in the Anti-Atlas region in recent years. Despite multiple geochemical investigations, important aspects such as the origin(s) of the ore-forming fluids, sources of heat and metal components, mechanism(s) of ore deposition, and the age of mineralization remain elusive.

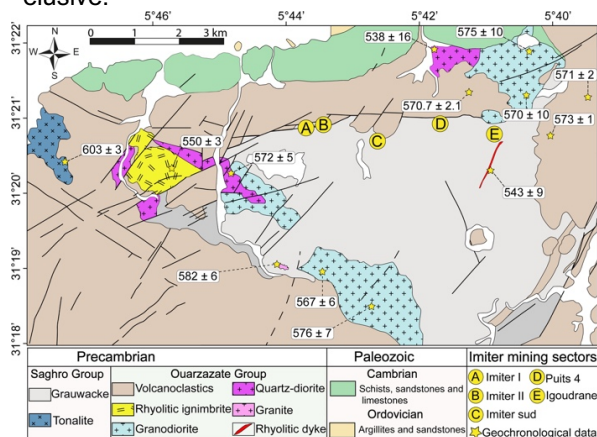


Figure 2. Geological map of the Imiter mine area showing the location of the mining sectors.

2 Methodology

Field mapping, core logging, outcrop sampling, and facies analysis were carried out during two field trips covering three cross-sections. Doubly polished thin sections were prepared for scanning electron microscopy (SEM), backscattered electron imaging (MEB), and electron probe microanalysis (EPMA). Additionally, twelve samples were selected for Pb isotope analyses based on criteria such as elevation, host rock, vein direction and orientation, mineralization texture, mineral assemblage, and Ag content. We collected twenty dykes and sills from the surface and underground workings around the mine for geochemistry and Nd isotopes. Based on their petrography, mineralogy, and texture, the dyke rocks are categorized into basalts, basaltic-andesites, andesites, quartz-microdiorites, and keratophyres.

3 Mineral chemistry

The main mineral phases associated with Ag have been analyzed in the Ag-Hg amalgam in sulfide and Ag stages (Baroudi 2002; Levresse et al. 2016): galena, pyrite, arsenopyrite, sphalerite, freibergite, and öllingite. The high Zn, Fe, Cu, and Sb contents in galena are associated with significant variations in Pb content. Hg was absent from the analyses, ruling out the possibility of micro- inclusions of Ag-Hg amalgam. However, microanalyses conducted on other coexisting base sulfides revealed the presence of Hg, indicating that the hydrothermal system is rich in Hg and possibly supersaturated. A sharp change in physicochemical conditions (temperature, pH, salinity) likely caused the galena

to incorporate higher amounts of Zn, Fe, Cu, and, to a lesser extent, Sb, Bi, and Mn, resulting in the absence of Hg (Baroudi et al. 2001; Levresse et al. 2004).

4 Pb isotope composition

The Pb isotope compositions of these samples were compared with other Anti-Atlas ores in conventional covariation diagrams, specifically the $^{207}\text{Pb}/^{204}\text{Pb}$ vs. $^{206}\text{Pb}/^{204}\text{Pb}$ and $^{208}\text{Pb}/^{204}\text{Pb}$ vs. $^{206}\text{Pb}/^{204}\text{Pb}$ diagrams. The data show a scattered distribution, but we identified two distinct groups (Fig. 3). The first group has $^{206}\text{Pb}/^{204}\text{Pb}$ values ranging from 18.172 to 18.540, observed in IGD-LN, R4, and SS1 structures. The Pb isotope values plot between the Stacey-Kramers (1975) curve and the Doe-Zartman (1979) orogene curve on the $^{208}\text{Pb}/^{204}\text{Pb}$ versus $^{206}\text{Pb}/^{204}\text{Pb}$ diagram, indicating a significant crustal component. The second group includes values ranging from 18.101 to 18.138, observed in the SS2, Igd-S, LN, N5, R6, F1S, SNN1, and F0 structures. These Pb isotope values plot significantly below both the Stacey-Kramers (1975) curve and the Doe-Zartman (1979) orogene curve on the $^{208}\text{Pb}/^{204}\text{Pb}$ versus $^{206}\text{Pb}/^{204}\text{Pb}$ diagram, consistent with a larger upper crust or mantle component.

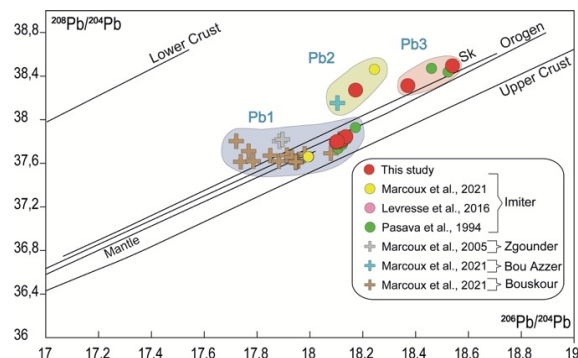


Figure 3. Plot of $^{208}\text{Pb}/^{204}\text{Pb}$ versus $^{206}\text{Pb}/^{204}\text{Pb}$ from Imiter mine and other Anti Atlas ores (Sk = Stacey-Kramers (1975); other curves from Zartman and Doe (1981)).

5 Nd isotopes of dykes

The OG cover, as well as the SG series are cross-cut by a swarm of dykes ranging in two main directions: NE to ENE in the SG series and N-S to NNE in the OG volcanoclastic series. The dykes are basalt, basaltic-andesite, dacite, microdiorite, and keratophyre. Based on the Nd isotope analyses, two distinct groups of IMD samples are identified (Fig. 4). The first group (IMD 1) displays initial $^{143}\text{Nd}/^{144}\text{Nd}$ ratios ranging from 0.511787 to 0.511970, moderately negative ϵNd values between -0.15 and -2.78, and older Nd model ages ranging from 1.3 to 1.7 Ga. In contrast, the second group (IMD 2) has initial $^{143}\text{Nd}/^{144}\text{Nd}$ ratios between 0.511885 and 0.512075, positive ϵNd values between 0.02 and 2.84, and model ages ranging from 1.00 to 1.29 Ga. Furthermore, the ϵNd values of the latter group (IMD 2) exhibit a negative correlation with SiO_2 .

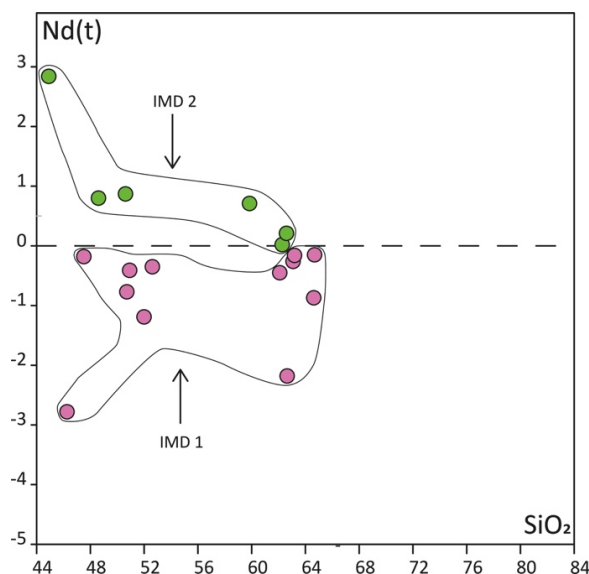


Figure 4. ϵ Nd values exhibit a negative correlation with SiO_2 for the IMD 2.

6 Conclusions

The observed absence of Hg in galena is likely a result of sharp physicochemical changes, leading to enhanced incorporation of Zn, Fe, Cu, and, to a lesser extent, Sb, Bi, and Mn. The Pb isotope values exhibit two distinct groups, with the first group indicating a prominent contribution from the crust. The second group is characterized by a composition consistent with a larger influence from the upper crust or mantle. The dyke swarms associated with the IAD, including diverse silicic, mafic, and

intermediate compositions, are classified into two groups based on distinctive Nd signatures.

References

- Ikenne M, Ennaciri A, Ouguir H, Cousens B, Ziyadi R, Mouhagir M, El-Gaouzi A (2007) Geochemical signature and geodynamic significance of an ag-hg mineralized dyke swarm in the neoproterozoic inlier of imiter - Anti-Atlas (Morocco). *Ophiolite* 32 (2): 109-18. <https://doi.org/10.4454/phiolite.v32i2.351>.
- Ikenne M, Souhassou M, Saintilan N. J, Karfal A, Hassani A. E, Moundi Y, Ousbih M, Ezzghoudi M, Zouhir M, Maacha L (2021) Cobalt–nickel–copper arsenide, sulfarsenide and sulfide mineralization in the Bou Azzer window, Anti-Atlas, Morocco: one century of multi-disciplinary and geological investigations, mineral exploration and mining. Geological Society, London, Special Publications 502(1): 45-66. <https://doi.org/10.1144/SP502-2019-132>.
- Levresse G, Cheilletz A, Gasquet D, Reisberg L, Deloule E, Marty B, Kyser K (2004) Osmium, sulphur, and helium isotopic results from the giant Neoproterozoic epithermal Imiter silver deposit, Morocco: evidence for a mantle source. *Chemical geology* 207(1-2): 59-79. <https://doi.org/10.1016/j.chemgeo.2004.02.004>.
- Kesler S, Simon (2015) Mineral Resources, Economics and the Environment (2nd ed.). Cambridge University Press, Cambridge <https://doi.org/10.1017/CBO9781139871426>.
- Stacey J.S, Kramers J.D (1975) Approximation of terrestrial lead isotope evolution by a two-stage model. *Earth Planet. Sci. Letters* 26:207–221. [https://doi.org/10.1016/0012-821X\(75\)90088-6](https://doi.org/10.1016/0012-821X(75)90088-6).
- Baroudi, Z., 2002. Le gisement Ag-Hg d'Imiter (Anti-Atlas Oriental) : minéralisation, fluides associés et condition de dépôt. Doctoral dissertation, Thèse Doct d'Etat, Univ. Hassan II Mohammedia, Casablanca (Maroc), 280 p.

Vanadium and Indium enrichment in La Luz epithermal system, Patagonia, Argentina

Morena L.S. Pagola^{1 2}, Sebastián M. Jovic^{1 2 3}, Diego S. Palma^{1 2}, Diego M. Guido^{1 2}, Daniel Hughes⁴

1. Instituto de Recursos Minerales, Facultad de Ciencias Naturales y Museo, Universidad Nacional de La Plata, Argentina.

2. Consejo Nacional de Investigaciones Científicas y Técnicas, Argentina.

3. Departamento de Geología, Universidad de Buenos Aires, Buenos Aires, Argentina.

4. Trendix Mining S.A.

Abstract.

Vanadium and Indium are considered critical raw materials because of their economic importance and supply risk. The sustainable supply of these elements is fundamental for the global electronics industry and its role in the transition to clean energy (steel production for wind turbines, vanadium-based redox flow batteries, solar photovoltaic panels, and nuclear power in electricity generation). The La Luz project is a poorly explored intermediate sulfidation epithermal deposit located in Patagonia, Argentina. It is enriched in Cu, Ag, Pb, Au, and Zn and with rare enrichment in V, In, and W and anomalies of Ga, Bi, Mo, Sb, and Te. Recent whole rock analyses of ore samples have shown high concentrations in these metals (up to 1455 ppm vanadium and 310 ppm indium). The presence of these metals, mainly V, is relatively rare in this type of deposit and represents a discovery in the region.

1 Introduction

The La Luz project is in the central part of Rio Negro province, Patagonia Argentina, 30 km northwest from the town of Los Menucos in the Los Menucos mining district (Fig. 1).

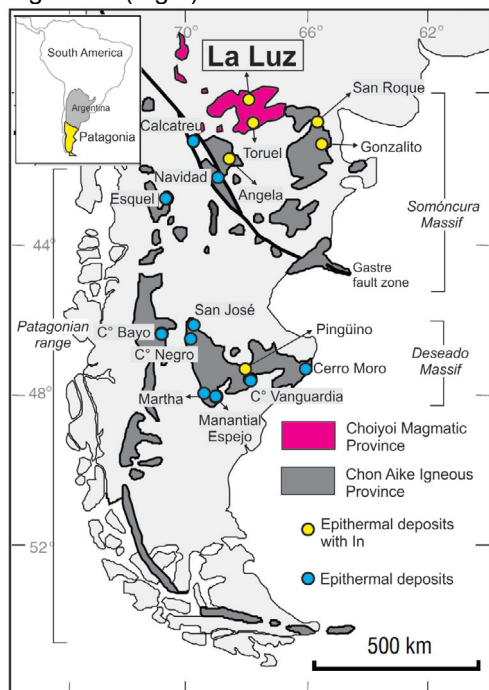


Figure 1. Map of the distribution of epithermal deposits in Argentine Patagonia, discriminating deposits where

anomalous indium contents are observed. Modified from Jovic et al. (2015).

2 Regional geology

The Los Menucos mining district is located in the Somoncú Massif, which is composed of an Early Paleozoic metamorphic complex (Pankhurst et al. 2006), overlain by marine clastic deposits (Silurian to Lower Devonian) of the Sierra Grande Formation (Camino 1999), intruded by Permian (La Esperanza Complex), and Triassic plutonic and volcano-sedimentary rocks (Los Menucos Complex), alternating with Upper Jurassic calc-alkaline and bimodal subaerial volcanism of the Chon Aike Silicic Large Igneous Province, a long-lived (>25 Ma) extensional volcanism (Pankhurst et al., 2000). Above are Jurassic sedimentary rocks. Large basaltic lava flows of the Oligocene age cover about 15,000 km² of this massif. There are two important Jurassic deposits at the Somoncú massif, Navidad (23,441.7 t Ag and 1.35 Mt Pb, world-class according to Singer, 1995) and Calcatreu (2.325 g/t AuEq) which are aligned along the same Gastre regional fault, an NW-SE cortical scale structure.

3 La Luz project

The system has been interpreted as an intermediate sulfidation epithermal deposit with gold, silver, indium, lead, copper, zinc, molybdenum, and vanadium anomalies associated with quartz and carbonate vein systems. Several vein systems have been recognized in the study area, but we will focus on those in which anomalous amounts of V and In have been detected; they are the La Luz *sensu stricto*, Gael, Esmeralda, and Mila I system. The main minerals identified are galena, sphalerite, malachite, chrysocolla, and native copper.

3.1 La Luz vein system

It is a system of sigmoidal quartz veins forming a structure 220 meters long and 60 meters wide. The mineralization consists of galena, chalcopryite, and sphalerite with high silver content and minor gold (Fig. 2 A). Recent whole rock analyses of ore samples have yielded indium values up to 310 ppm and vanadium up to 744 ppm (Table I).

3.2 Gael vein system

It is composed by 14 veins of variable width ranging between 0.30 and 1.10 meters. A saccharoidal quartz vein with abundant manganese oxide, arsenic oxide, malachite, and azurite is observed at surface (Fig. 2 B). Geochemistry showed high silver, copper, and vanadium values up to 699 ppm and indium up to 50 ppm (Table I).

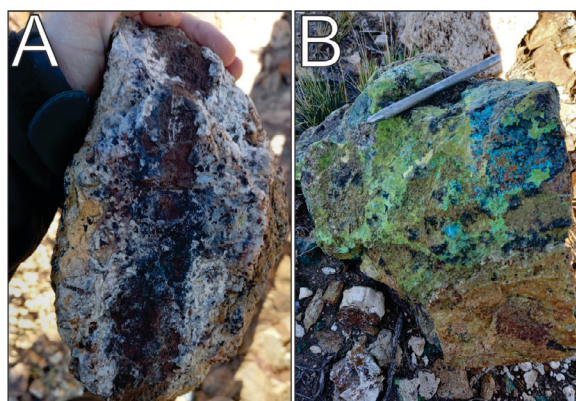


Figure 2. La Luz vein system (A) and Gael vein system (B) at the surface.

3.3 Esmeralda vein system

The vein is 40 cm thick and of unknown length. At the surface, it contains high amounts of manganese and arsenic oxides with galena, sphalerite, and covellite (Fig. 3 A). ICP analyses of ore samples showed high amounts of vanadium (up to 1455 ppm), 149 ppm gallium, and 175 ppm indium (Table I).

3.4 Mila vein system

It consists of three vein structures, with a visible strike length of 250 meters varying in width from 1.10 to 2.8 meters (Fig. 3 B). A brown saccharoidal quartz vein, with fine sphalerite, minor hematite and siderite, is observed at surface. Geochemistry showed high values of silver, gold, lead, zinc, and over 880 ppm vanadium (Table I).

	La Luz	Gael	Esmeralda	Mila I
Au	0.33	2.1	0.42	13.44
Ag	159	>100	340	2.154
Cu	>10000	>10000	7152	483
Pb	>10000	>10000	55366	5292
Zn	>10000	3350	9007	2141
In	310	50.3	175	13
V	744	699	1455	882
W	440	199	420	520

Table I. Whole rock analyses in ppm (www.trendixmining.com.ar).

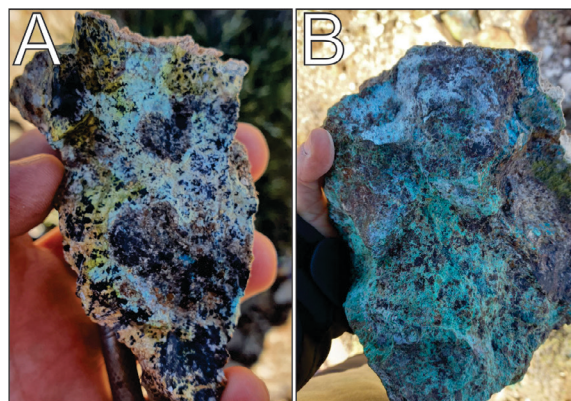


Figure 3. Esmeralda system vein (A) and Mila I vein at the surface (B).

4 Final considerations

A considerable anomaly of vanadium and indium, rare metals in this type of deposit, was found in surface samples. A positive correlation between Cu-In is observed and could reflect the coupled substitution of In and Cu in the sphalerite, for example, a coupled substitution of $2(\text{Zn}, \text{Fe})$ for Cu-In (Johan 1988, Ohta 1989, Sinclair et al. 2006). A positive correlation between Pb-V is also observed, which is likely related to the presence of some lead vanadate such as vanadinite. These metals, mainly V, are relatively rare in epithermal systems and represent a discovery in the region.

Regarding the vanadium source, V^{+3} replaces Fe^{+3} in iron-rich minerals such as amphibole, biotite, magnetite, and pyroxene; and Al^{+3} in the structure of secondary minerals such as clays (micas, smectites, illite, kaolinite, and chlorite), Fe-Mn hydrated oxides and organic-rich facies during diagenesis (Lipinski et al., 2003). Carbonaceous shales can contain up to $16,000 \text{ mg kg}^{-1}$ (Vine and Tourtelot, 1970) compared to non-carbonaceous shales that average 130 mg kg^{-1} V (Turekian and Wedepohl, 1961). Considering all this, we can think of two possible sources of V, 1) dioritic intrusions of the Los Menucos Complex or 2) sedimentary rocks (with shales and carbonaceous facies) of the Puesto Vera Formation (also belonging to the Los Menucos Complex).

The assemblage of these metals increases the mining potential and must be considered during future exploration duties.

References

- Caminos, R. (1999): Geología Argentina; Subsecretaría de Minería de la Nación, Servicio Geológico Minero Argentino, Instituto de Geología y Recursos Minerales, Anales N°29.
- Johan, Z. (1988): Indium and germanium in the structure of sphalerite: an example of coupled substitution with copper. *Mineral. Petrol.* 39, 211-229. <https://doi.org/10.1007/BF01163036>
- Jovic, S. M., López, L., Guido, D., Redigonda, J., Páez, G., Ruiz, R., Permuy Vidal, C. (2015): Presencia de indio en sistemas epitermales polimetálicos de Patagonia. *Rev Asoc Geol Argent* 71: 433-437.

- Ohta, E. (1989): Occurrence and chemistry of indium-containing minerals from the Toyoha mine, Hokkaido, Japan. *Mining Geol.* 39, 355-372. https://doi.org/10.11456/shigenchishitsu1951.39.218_355
- Rapela, C. W., Pankhurst, R. J., Fanning, C. M., y Herve, F. (2005): Pacific subduction coeval with the Karoo mantle plume: the early Jurassic subcordilleran belt of northwestern Patagonia. *Terrane Processes at the Margins of Gondwana*; Geological Society of London, Special Publications, 246:217–239. <https://doi.org/10.1144/GSL.SP.2005.246.01.0>
- Sinclair, W.D., Kooiman, G.J.A., Martin, D.A. & Kjarsgaard, I.M. (2006): Geology, geochemistry and mineralogy of indium resources at Mount Pleasant, New Brunswick, Canada. *Ore Geol. Rev.* 28, 123-145 <https://doi.org/10.1016/j.oregeorev.2003.03.001>
- Singer, D.A. (1995): World class base and preciousmetal deposit: A quantitative analysis. *EconomicGeology*, v.90,p.88-104. <https://doi.org/10.2113/gsecongeo.90.1.88>
- Turekian, K.K., Wedepohl, K.H. (1961): Distribution of the elements in some major units of the earth's crust. *Geol. Soc. Am. Bull.* 72 (2), 175–192.
- Vine, J.D., Tourtelo, E., (1970): Geochemistry of black shale deposits-a summary report. *Econ. Geol.* 65 (3), 253–272.

Using PHREEQC for mineral prospecting in waters related to geothermal systems in Wyoming: possible precipitation of hydroxyapatite enriched with REEs

Juan David Palma Montealegre¹, Thomas Heinrich Cramer¹

¹ Departamento de Geociencias, Universidad Nacional de Colombia – Sede Bogotá, Colombia.

Abstract. The increasing demand for REEs related to the transition to a green energy encourages their exploration using innovative methodologies. This project discusses the use of the PHREEQC software to get information about the minerals that may precipitate in waters related to geothermal systems, as function of the temperature ($T(^{\circ}\text{C})$), pH, and chemical composition of water, in a case study in Wyoming, USA. We have modelled the data of 46 different samples, with an array of 18 different minor and major chemical constituents. The results show the possible precipitation of 36 diverse mineral phases, highlighting, for some minerals, a trend to increased precipitation in warmer and more basic waters. The investigation focused on 9 locations with possible precipitations of hydroxyapatite, a mineral able to capture REEs in aqueous systems. These locations are related to the Wasatch Formation, which consists of sedimentary rocks with reports of frequent detrital monazite and apatite presence. The REEs were plotted in a spider diagram to argue the potential enrichment of REEs in the hydroxyapatites of each location. This project highlights an innovative methodology for REE-bearing mineral exploration, which can be improved and potentially used in other prospective areas.

1 Introduction

Geothermal systems are important for the economic development of humanity, not only as sources of geothermal energy, but also for the mobilization of various chemical elements and their subsequent precipitation in minerals. This chemical mobilization represents an opportunity for research on critical elements for Energy Transition, such as Li and REEs, using new methodologies and techniques.

The U.S. Department of Energy has carried out numerous studies about the concentration of REEs in geothermal fluids in the USA (Quillinan et al. 2018), resulting in the elaboration of hydrogeochemical datasets that can be used for modelling using PHREEQC Version 3 (Parkhurst 2013), which is a software package that allows performing geochemical calculations for aqueous systems. It can simulate the behaviour of aqueous solutions that contain multiple dissolved species, including ions, gases, and solids. PHREEQC uses a set of thermodynamic and kinetic data to calculate the equilibrium concentrations of the various species in solution. The data processing can provide important information about the water-rock interaction and consequently the origin of the fluid and the history of its passage through underground materials in shallow and deep reservoirs (Chidambaram et al. 2012).

This project uses PHREEQC for Saturation Index (SI) calculation, which is a measure of how close the solution is to being saturated with respect to a specific mineral. The SI is defined as the log ratio of the ion activity product of the mineral to its solubility product at a given $T(^{\circ}\text{C})$ and pressure, i.e., $\text{SI} = \log(\text{IAP}/\text{Ksp})$, where IAP is the ion activity product, divided by the mineral solubility product (Ksp) at a given $T(^{\circ}\text{C})$ and pressure. $\text{SI} > 0$ indicates supersaturation or tendency to precipitation of minerals, whereas $\text{SI} < 0$ means undersaturation or dissolution of minerals.

The use of PHREEQC as a tool for mineral prospecting consists in looking at the relationship of SI for different mineral phases, focusing on hydroxyapatite (Hyap), with $T(^{\circ}\text{C})$, pH, as well as the location of the water sample. This methodology was applied using a dataset called “REEs in Produced Waters in Wyoming” (Quillinan 2017) with chemical data from 46 water samples in Wyoming, USA, close to Jackson, Green River, Gillett, Riverton, and Cheyenne (Figure 1). From this dataset we retrieved information about $T(^{\circ}\text{C})$, pH, depth (samples from wells and from springs), concentrations of minor and major constituents (Al, Ba, Ca, Cl, F, K, Li, Mg, Na, SO_4 , B, Mn, P, Si, Br, Fe, NH_4 , Sr) in mg/L, and concentrations of REEs (Ce, Dy, Er, Eu, Gd, Ho, La, Lu, Nd, Pr, Sc, Sm, Tb, Tm, Yb) in ng/L.

The geothermal system of Wyoming is result of at least three different factors (Breckenridge 1978): for NW-Wyoming, the convection of hot fluids associated with the Yellowstone Plateau volcanic field, as well as heat conduction from the Yellowstone Hotspot (Christiansen et al. 2002); and for middle east Wyoming, the geothermal gradient increase due to the sediment load accumulated since the Cretaceous in the Western Interior Basin (Milliken 2007).

2 Results and discussion

2.1 Saturation Indices

Using the chemical composition of the 46 water samples at different $T(^{\circ}\text{C})$ and pH, PHREEQC calculated the SI for 36 different possible mineral phases. The SI variation is analysed as function of Temperature (Figure 2) and pH (Figure 3). The relationship between the calculated SI and $T(^{\circ}\text{C})$ shows the tendency of each mineral to precipitate in a temperature range from 5.3 to 63.1 $^{\circ}\text{C}$.

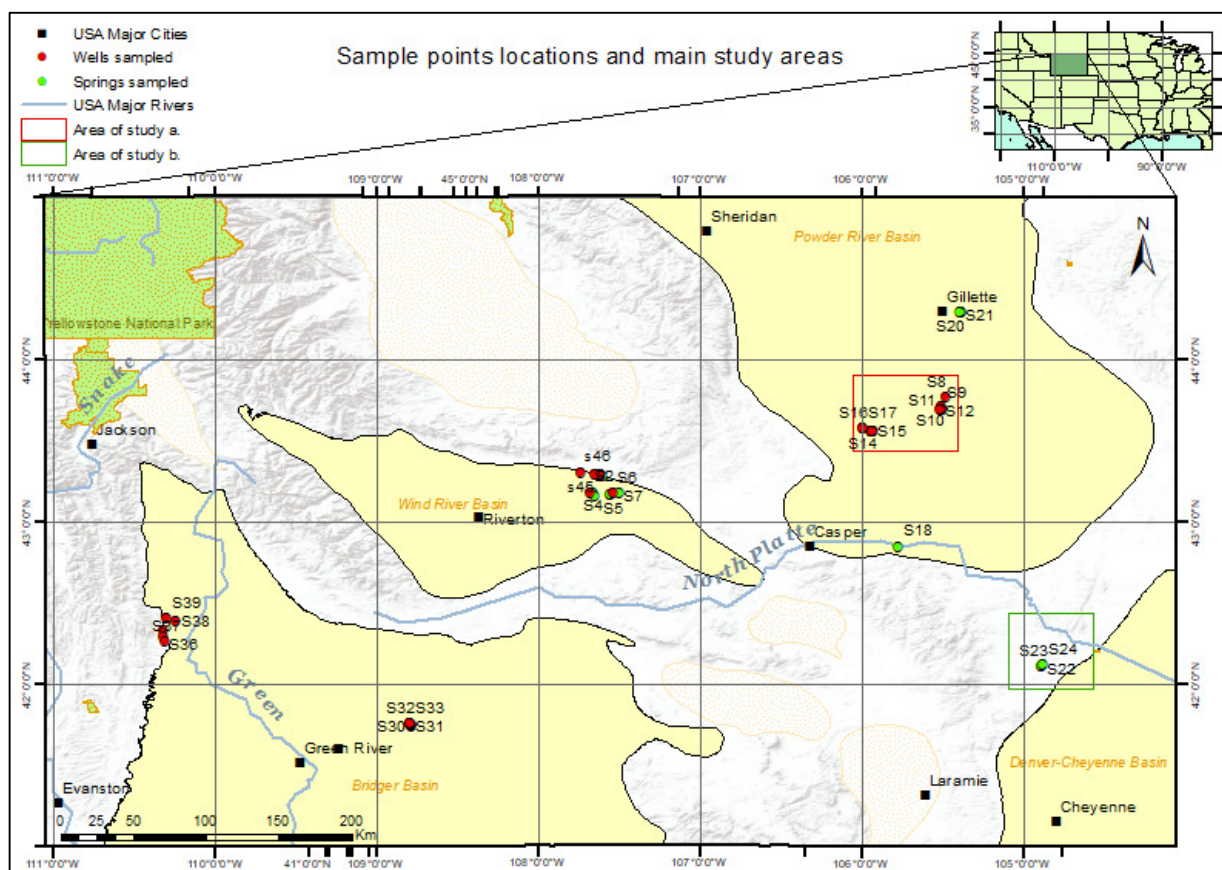


Figure 1. Map of the Wyoming state with the location of the 46 sampling points (labelled as SN (N=1-46)), and the polygons of two main study areas a) and b) discussed in Figure 5. Also shown are the principal basins, i.e., Powder River Basin, Wind River Basin, Bridger Basin, and the Denver-Cheyenne Basin

Although other variables like pH, pressure, and chemical constituent concentration must be considered, some minerals show a maximum SI value for $T \geq 45^\circ\text{C}$ (albite, anorthite, Ca-montmorillonite, hydroxyapatite, illite, K-feldspar, muscovite, kaolinite, and vivianite), while others for $T < 15^\circ\text{C}$ ($\text{Al}(\text{OH})_3$, alunite, anhydrite, celestite, chlorite, chrysotile, dolomite, $\text{Fe}(\text{OH})_3$, fluorite, gibbsite, goethite, gypsum, halite, hematite, jarosite-K, rhodochrosite, sepiolite, siderite, sylvite, talc, and witherite).

The SI relationship with pH shows additional interesting tendencies to investigate. In a pH-range from 6.53 to 10.01, most of the minerals reached maximum SI values in almost neutral waters (pH 7-8) with some exceptions which reached their maximum SI values in more basic waters (pH ≥ 8). These exceptions are $\text{Al}(\text{OH})_3$, alunite, anhydrite, celestite, chlorite, chrysotile, dolomite, $\text{Fe}(\text{OH})_3$, fluorite, gibbsite, goethite, gypsum, halite, hematite, sepiolite, sylvite, talc, and witherite; resulting in a typical behaviour of SI in the function

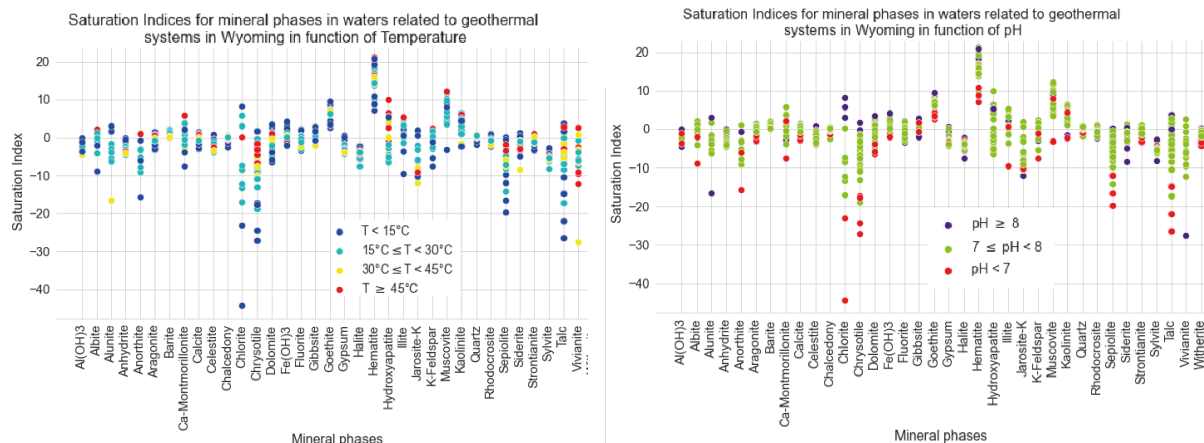


Figure 2. SI for the 36 mineral phases possibly formed in 46 water samples as function of Temperature.

of pH.

Figure 3. SI for the 36 mineral phases possibly formed in 46 water samples as function of pH.

Minerals with maximum SI-values in more basic waters are the same as those with maximum tendency to precipitate at $T < 15^{\circ}\text{C}$, except for jarosite-K, rhodochrosite, and siderite, showing that, for some species, the pH will likely be the prevalent saturation factor, not temperature. One of the conclusions here is a higher possibility of minerals to precipitate in the water samples at $T \geq 45^{\circ}\text{C}$ and/or $\text{pH} \geq 8$.

2.2 Hydroxyapatite: REE absorption potential

Hydroxyapatite (Hyap) can effectively sorb REEs from aqueous solutions (e.g., Granados-Correa 2012, Ignjatović et al. 2019). The mechanism behind this sorption is believed to be due to the ion-exchange properties of Hyap, where the positively charged REE ions are attracted to the negatively charged phosphate groups in the Hyap structure, and a certain occupation of the two Ca^{2+} -sites in the apatite structure. Additionally, the surface properties of Hyap, such as area and porosity, can also play a role in the sorption of REEs. Hyap nanoparticles, for example, have been shown to have a high surface area-to-volume ratio, which can increase their ability to sorb REE (Fleet 1999).

2.3 Hydroxyapatite: possible distribution and geological context

The section 2.1 demonstrates the tendency of Hyap to precipitate in some water samples at locations where waters have $T > 30^{\circ}\text{C}$ or $\text{pH} > 7.2$. This relationship is shown in Figure 4, which is also useful to represent graphically the tendency for some minerals to form in waters with $T \geq 45^{\circ}\text{C}$ or $\text{pH} \geq 8$, a statement of the end of 2.1 section.

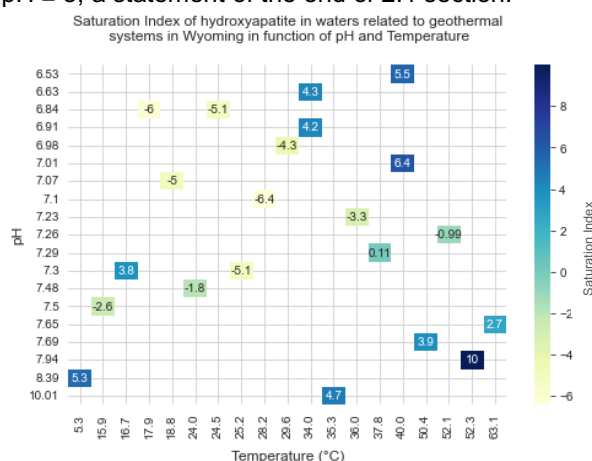


Figure 4. SI for hydroxyapatite in the function of pH and $T(^{\circ}\text{C})$.

The sample points labelled as SN (N=1-46), show a positive Hyap-SI for: S8, S10, S11, S12, S13, S14, S15, S16, and S23. All these water samples were taken from a well in the subsurface, excluding S23, which was sampled from a spring.

Their geographical distribution is shown in Figure 5, which is a map that also allows comparing the

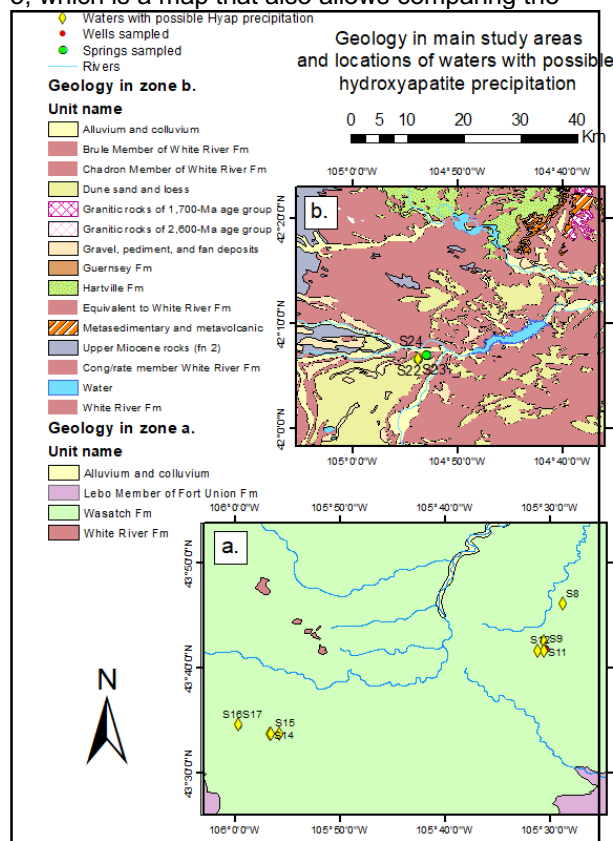


Figure 5. Geological map of the main study areas (a) and (b) with location of waters with possible hydroxyapatite precipitation.

geology of the area with the composition of the waters with positive Hyap-SI and shows the two different areas (a) and (b) from Figure 1. In zone (a) the main geological formation that can affect the composition of the water is the Wasatch Formation, which outcrops in the Powder River Basin and is made up of sedimentary rocks, including sandstone, shale, and siltstone, which were deposited during the Eocene. It contains also large amounts of coal formed from plants and trees in a lacustrine ambient (Divay 2016). This formation has also abundant detrital apatite and monazite (Pocknall 1987).

In zone (b) the principal geological formation is the White River Formation, which consists primarily of sandstone, siltstone, and mudstone, deposited in various environments such as rivers, lakes, and floodplains during the Eocene (Emry 1975).

This geology helps us explaining the presence of phosphorus and calcium to produce hydroxyapatite nowadays. In zone (a), the presence of detrital apatite and monazite can be also associated with the Bear Lodge Mountains, located in the northwest of Gillette, where an alkaline complex with REE mineralization from carbonatites outcrops which host fluorocarbonates (bastnäsite, parisite, and synchysite), ancylite, monazite, cerianite, burbankite, and carboxenite (Moore et al. 2015), but this relationship needs to be tested in future research. Zone (b), in comparison with zone (a), has no reports of detrital apatite or monazite on the White River Formation

yet. This geological difference may be the reason why zone (a) presents higher contents of P (Table 1), but more samples must be taken in zone (b) to make the comparison clearer.

To better understand the possible REEs-Hyap absorption in waters shown in Figure 5, the REEs concentrations were plotted in the spider diagram of Figure 6 following the methodology of Quillinan (2018).

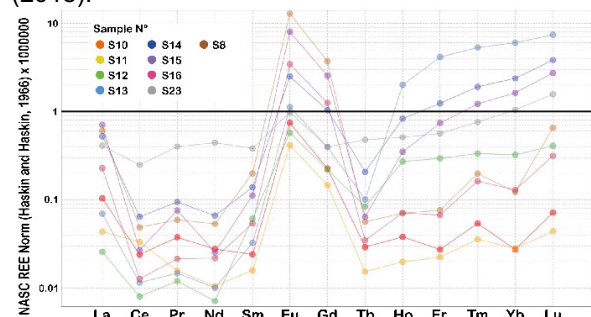


Figure 6. REE-concentration normalized to NASC in the water samples of areas (a) and (b) influenced by the clastic apatite-monazite, and carbon-rich sedimentary Wasatch Formation and the sediments of the White River Formation.

The most relevant concentrations and characteristics of the water samples with positive Hyap-SI are presented in Table 1. This work can motivate responsible REE extraction from geothermal systems as by-products using hydroxyapatite. For future research, other geothermal systems can be modelled to find correlations with this work or other possibilities for extraction of critical minerals to the development of society, like REEs themselves, lithium, and silica, among others.

Table 1. most relevant concentrations and characteristics of the water samples with positive Hyap-SI. N/A means "Not data available". Data from Quillinan (2017).

SampleN°	Location	P(mg/L)	Ca(mg/L)	T(°C)	pH	Hydroxyapatite SI	ΣREE (ng/L)
S5	Close to Riverton	4.9	3	35.3	10.01	4.72	11.27585558
S8	Zone (a)	0.8	734	16.7	7.3	3.78	68.42256417
S10	Zone (a)	19.2	83	52.3	7.94	9.99	9.546970852
S12	Zone (a)	1.6	60	50.4	7.69	3.92	10.20288777
S13	Zone (a)	1.8	1680	40	7.01	6.36	54.91360515
S14	Zone (a)	14.6	814	40	6.53	5.51	53.50249862
S15	Zone (a)	5.6	386	34	6.91	4.25	62.57984922
S16	Zone (a)	1.8	1770	34	6.63	4.3	22.25289777
S23	Zone (b)	0.5	198	5.3	8.39	5.33	68.66972272
S43	Close to Riverton	2.6	13	63.1	7.65	2.74	N/A
S44	Close to Riverton	1.9	22	37.8	7.29	0.11	N/A

3 Conclusions

Using PHREEQC as a tool for mineral prospecting is an innovative methodology with some limitations and uncertainties. The input data may be found in hydro-chemical databases and adjusted to the objective. For the studied waters from wells and springs close to Jackson, Green River, Gillett, Riverton, and Cheyenne in Wyoming, hydroxyapatite and absorbed REEs tend to precipitate in waters with $T \geq 45^{\circ}\text{C}$ or $\text{pH} \geq 8$.

Acknowledgments

This work was possible thanks to the support of the SGA Student Chapter, beginning with Anna Vymazalová, who encouraged the first author to

make the investigation, and all the SGA Student Chapter UNAL Bogotá family. Thanks to professors Ariel Cadena, Clemencia Gómez, Germán Prieto, and Daniel Hernández. Finally, thanks to Scott Quillinan et al. for letting their database open to use, and the Universidad Nacional de Colombia for their support in the knowledge applied in this work.

References

- Breckenridge R.M., Hinckley B.S. (1978): Thermal Springs of Wyoming. The Geological Survey of Wyoming bulletin, 60: 1-3.
- Chidambaram S., Anandhan P., Prasanna M.V., Ramanathan A.L., Srinivasamoorthy K., Kumar G.S. (2012): Hydrogeochemical Modelling for Groundwater in Neyveli Aquifer, Tamil Nadu, India, Using PHREEQC: A Case Study. *Nat Resour Res* 21(3):311–324.
- Christiansen R. L., Foulger G. R., & Evans J. R. (2002). Upper-mantle origin of the Yellowstone hotspot. *Geological Society of America Bulletin*, 114(10), 1245–1256.
- Divay J.D., Murray A.M. (2016): An early Eocene fish fauna from the Bitter Creek area of the Wasatch Formation of southwestern Wyoming, U.S.A. *J Vertebr Paleontol* 36(5):e1196211.
- Emry R.J. (1975): Revised Tertiary Stratigraphy and Paleontology of the Western Beaver Divide, Fremont County, Wyoming. *Smithson Contrib Paleobiol* 25:1–20.
- Fleet M.E., Liu X., Pan Y. (2000): Site Preference of Rare Earth Elements in Hydroxyapatite $[\text{Ca}_{10}(\text{PO}_4)_6(\text{OH})_2]$. *J Solid State Chem* 149(2):391–398.
- Granados-Correa F., Vilchis-Granados J., Jiménez-Reyes M., Quiroz-Granados L.A. (2013): Adsorption Behaviour of La(III) and Eu(III) Ions from Aqueous Solutions by Hydroxyapatite: Kinetic, Isotherm, and Thermodynamic Studies. *J Chem* 2013:751696.
- Ignjatović N.L., Mančić L., Vuković M., Stojanović Z., Nikolić M.G., Škapin S., Jovanović S., Veselinović L., Uskoković V., Lazić S., Marković S., Lazarević M.M., Uskoković D.P. (2019): Rare-earth (Gd³⁺, Yb³⁺/Tm³⁺, Eu³⁺) co-doped hydroxyapatite as magnetic, up-conversion and down-conversion materials for multimodal imaging. *Sci Rep* 9:16305.
- Milliken M. (2007). Geothermal resources at Naval petroleum reserve-3 (NPR-3), Wyoming. In *PROCEEDINGS of Thirty-Second Workshop on Geothermal Reservoir Engineering*, Stanford University.
- Moore M., Chakhmouradian A. R., Mariano A. N., & Sidhu R. (2015). Evolution of rare-earth mineralization in the Bear Lodge carbonatite, Wyoming: Mineralogical and isotopic evidence. *Ore Geology Reviews*, 64, 499–521.
- Parkhurst D.L., Appelo C.A.J. (2013): Description of input and examples for PHREEQC version 3: a computer program for speciation, batch-reaction, one-dimensional transport, and inverse geochemical calculations. Technical Report. U.S. Geological Survey.
- Quillinan S., Nye C., Neupane G., and McLing T. (2017): Rare Earth Element Concentrations in Wyoming's Produced Waters. United States. U.S. Geological Survey. Technical Report. University of Wyoming. Dataset obtained from the Geothermal Data Repository.
- Quillinan S., Nye C., Engle M., Bartos T.T., Neupane G., Brant J., Bagdonas D., McLing T., McLaughlin J.F., Phillips E., Hallberg L.L., Shahabadi M., Johnson M. (2018): Assessing rare earth element concentrations in geothermal and oil and gas produced waters: A potential domestic source of strategic mineral commodities. Technical Report. University of Wyoming.

3D lithological and structural model and prospectivity of the Late Cretaceous Sakdrisi Gold-Copper Epithermal deposit, Bolnisi district, Lesser Caucasus, Georgia

Nino Popkhadze¹, Badri Gogia², Shota Tagviashvili², Giga Ugrekhelidze², Malkhaz Natsvlishvili², Joni Shubititze², Safak Utku Sönmez³, Robert Moritz³

¹*Al. Janelidze Institute of Geology of Iv. Javakhishvili Tbilisi State University & RMG Rich Metals Group*

²*RMG Rich metals Group, Georgia*

³*Department of Earth Sciences, University of Geneva, Switzerland*

Abstract. The Bolnisi mining district is located at the north-eastern extremity of the Lesser Caucasus metallogenic belt and to the west it continues into the Eastern Pontides. The Late Cretaceous Sakdrisi epithermal deposit is one of the on-going exploration targets in the Bolnisi ore district. Detailed mapping, detailed lithological and the structural database for 3D modelling allowed us to discover new ore zones and promising resources for the future. The ore zones in the Sakdrisi deposit are related to a lower volcano-sedimentary (VS) complex, where an upper VS complex consists of barren welded ignimbrite and cross cutting dikes. The main ore bodies are controlled by central and southern faults and a meridian fault located between the Sakdrisi 4 and 5 open pits. Pumice-bearing rock types together with explosive breccia where channelways for the ore-forming fluids. Thus, the deposit is both lithologically and structurally controlled.

1 Introduction

The Sakdrisi gold-copper epithermal deposit of the Bolnisi district is located in a distinct zone within the eastern extension of the eastern Pontides in Turkey (Moritz et al 2020; Yilmaz et al 2000) (Fig.1A), and belongs to the Tethyan metallogenic belt, linking the Anatolian and Iranian tectonic zones. Numerous ore deposits and prospects are known in the Bolnisi district, where Late Cretaceous bimodal volcanism resulted in mafic and felsic rock types. The latter are a major host of ore deposits and prospects, and are locally known as the felsic Mashavera and Gasandami suites. Mineralization in Bolnisi district occurs in two different age groups: in Turonian to early Santonian host rocks (Madneuli deposit; Tsiteli Sopeli, Kvemo Bolnisi and Kazreti prospects) and in Campanian hosts (Sakdrisi and Beqtakari deposits; Darbazi, Imedi, Bnelikhevi and Samgreti prospects) (Gugushvili, et al. 2014) (Fig.1B).

2 Regional geology and stratigraphy

The Late Cretaceous Sakdrisi gold-copper deposit is one of the major deposits of Bolnisi district. The Bolnisi volcano-tectonic depression is a part of the Artvin-Bolnisi belt, which is characterized by an arc association formed mainly during the Liassic-Campanian interval and represents a distinct tectonic zone along the

Tethyan metallogenic belt. This favorable geotectonic location of the Late Cretaceous Bolnisi ore district between the Lesser Caucasus and the Eastern Pontides is reflected by its geological diversity and mineral deposit distribution.

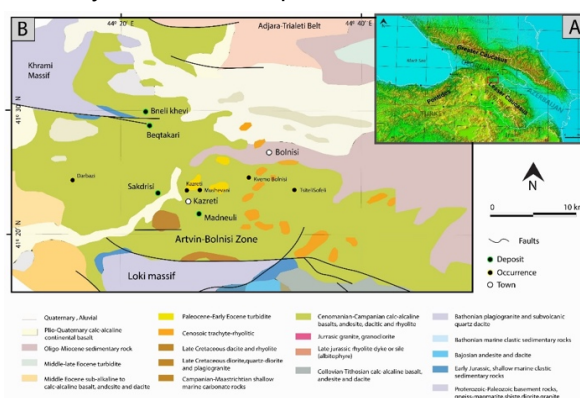


Figure 1. A) Location of the Bolnisi district, B) geological map of the Bolnisi mining district with ore deposits and occurrences.

The Artvin-Bolnisi zone comprises a Hercynian orogenetic basement, which consists of Precambrian and Paleozoic granite, gneiss and plagiogranite, cropping out in the Khrami and Loki massifs, overlain by Carboniferous volcano-sedimentary rocks (Fig.1B). Within the Artvin-Bolnisi zone, the 3000-4000 m thick Late Cretaceous section is dominated by calc-alkaline basalt, andesite, dacite and rhyolite (lava, and pyroclastic rocks) (Fig.1B). Volcanic rocks belong to shallow marine to subaerial settings. Predominant Late Cretaceous volcanic and volcano-sedimentary rocks in this region include rhyodacitic ignimbrite, ash fall and density current deposits with a phreatomagmatic origin (Popkhadze et al 2017; Popkhadze et al 2014). Based on lithological and paleontological data, Late Cretaceous sequences in this region are subdivided into six volcanogenic suites and correspond to Cenomanian and Maastrichtian in age (Apkhazava 1988). The bimodal character of Late Cretaceous volcanism is manifested by the alternation of mafic and felsic suites stratigraphically and geochemistry (Moritz et al

2020). The arc-related, calc-alkaline volcanic rocks include abundant pyroclastic rocks, lava, extrusive domes, and subvolcanic intrusions and dikes, with a predominantly rhyolitic, dacitic and andesitic composition, except one Santonian suite (Tanzia) and one late Campanian suite (Shorsholeti), which are dominantly basaltic and partly alkaline in composition (Gugushvili et al 2014; Popkhadze et al 2014). The Late Cretaceous volcanic rocks were deposited in a shallow-water environment (Adamia Sh et al 2011).

3 The geology of the Sakdrisi deposit

3.1 Host rock characteristics

The Sakdrisi deposit consists of a 2 km long cluster of five mineralized centers aligned along a NE-oriented thrust fault zone (Golay et al 2018). Two complexes have been recognized in the Sakdrisi deposit hosted by the Mashavera Group, including: the Lower Volcano-Sedimentary Complex (LVSC) and the Upper Volcano-Sedimentary Complex (UVSC) (Jelev et al. 2020; Popkhadze et al 2021), separated by a NE oriented thrust fault zone (Golay 2019; Golay et al 2018). The Lower volcano-sedimentary complex (LVSC) is composed of a thick (over 200m) sequence of alternating pumice tuff, massive and layered ash tuff, clastic rocks with different size of pumice rich horizons, locally transition from a pumice-rich part to fine-grained intervals, layered tuff with gypsum and ignimbrite-like tuff (Fig.2).

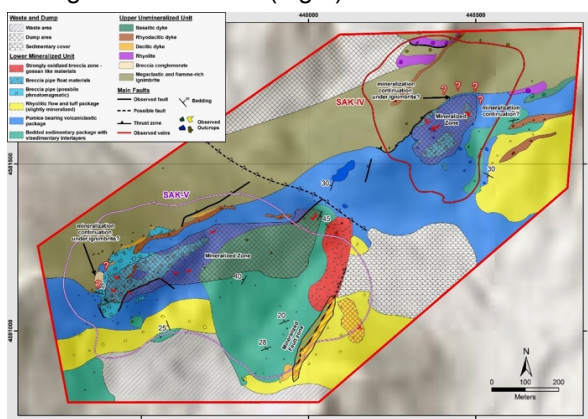


Figure 2. The geological map of the Sakdrisi 4 and 5 open pits.

The upper parts of this complex have been affected by intense silification and associated Au-Cu mineralization. The Upper volcano-sedimentary complex (UVSC) includes ignimbrite. Apart from typical vitroclastic (fiame) ignimbrite, this suite includes also bomb and block intervals, layers of pelitic ash tuff. UVSC is intruded by andesite-basaltic and rhyolite/rhyodacitic dikes (Popkhadze et al 2022; Popkhadze et al 2023). This sequence is non-mineralized, which overlaps the lower mineralized sequence, documented by the thrust ignimbrite pyroclastic flow.

3.2 3D geological model of the Sakdrisi deposit

A 3D lithological-structural and ore bodies model was constructed in Leapfrog Geo, using historical and new geological maps and the drill hole database recorded in an Excel sheet. In total, 200 drill holes were described and interpreted from the Sakdrisi 5 and 4 ore bodies (part from Sakdrisi 3 also) (Figs.3 and 4).

Based on drill hole description and mapping the following lithostratigraphic units have been identified in the UVSC:

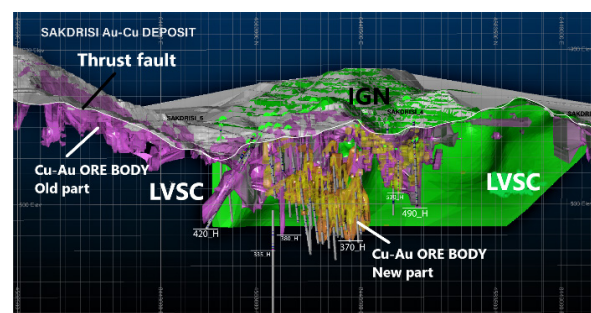


Figure 3. 3D Lithological-structural model of the Sakdrisi 4 and 5 ore bodies, with ore distribution zones.

welded ignimbrite, rhyodacitic and andesite-basaltic dikes and sedimentary formation (SF), which is the thrust fault zone with crushed and clay-altered black sedimentary rocks, in some places the so-called breccia - conglomerate and tuff. The lower LVSC consists of: pumice tuff, massive fine-grained tuff, pumice tuff with transition intervals to fine-grained, thin-bedded tuff/mudstone with gypsum veins and ignimbrite-like tuff. Explosive breccia crosscuts these lower lithological units at different levels and hosts gold-copper ore bodies. The upper mineralized lithological unit (pumice tuff) in some places is strongly oxidized and silicified. As these sequences are crosscut by mafic and felsic dikes. The non-mineralized upper (UVSC) and lower (LVSC) are separated by a thrust fault zone, including the sedimentary formation (SF), which is also non-mineralized.

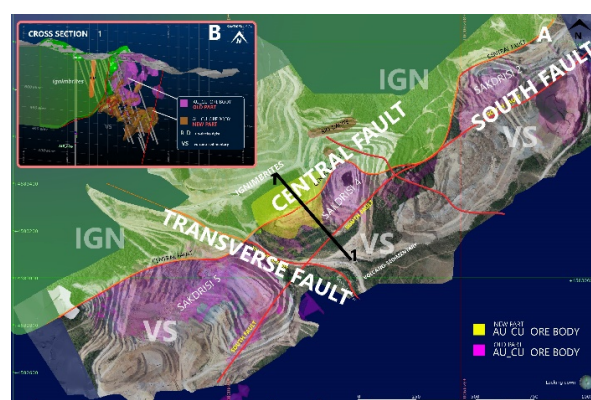


Figure 4. 3D regional model of the Sakdrisi deposit, with modelled faults, lithology and principal open pit locations.

Explosive breccia: explosive breccia outcrops in the Sakdrisi 5 and partly in the Sakdrisi 4 open pits. In Sakdrisi 5, it is possible to see the stratigraphic/sharp contact of the explosive breccia with different lithological units (Fig. 5): crosscutting the pumice tuff and bedded VS complex. The breccia consists of various sized, rounded and sharp rock fragments of pumice tuff, massive fine-grained tuff, black clayey tuff and locally bedded tuff (Fig. 6A). The breccia varies between clast-rich and matrix-rich varieties.



Figure 5. The lithological units and fault zones with a gossan-like supergene ore location in Sakdrisi 5.

Some of the rock fragments contain quartz sulphide veins with chalcopyrite also in the matrix, some places cross cutting with quartz/quartz sulphide veins/veinlets and stockworks. In Sakdrisi 5, it is still possible to observe the classical breccia pipe injected in oxidized clastic pumice tuff (Fig. 6B).

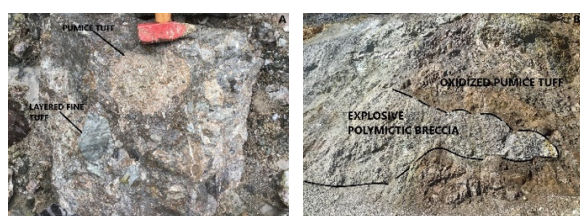


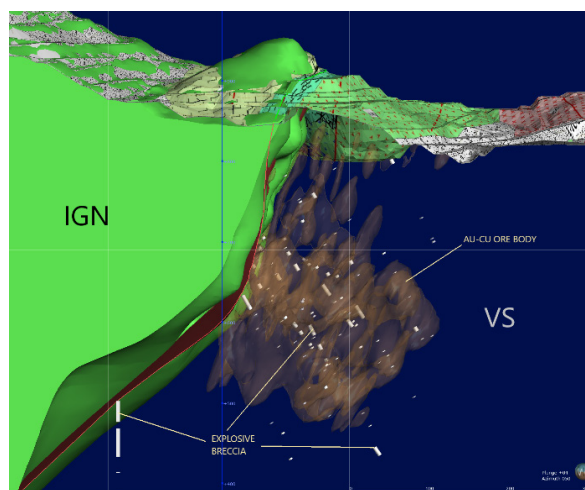
Figure 6. A. Explosive polymictic breccia with different rock fragments: bedded fine-grained tuff and pumice tuff. B. Polymictic breccia pipe injected in an oxidized pumice tuff.

In Figure 7, we have illustrated the preliminary 3D scheme of distribution of explosive breccia pipe from the Sakdrisi 4 ore body in the lower LVSC mineralized unit and correlation with ore bodies morphology (Fig. 7).

Structural modelling (Figs. 4 and 5): The central fault is represented by a thrust fault zone with upper barren ignimbrite, the South fault is very clear at the Sakdrisi 5 open pit, where it is a sharp contact of bedded grey/blueish bedded rocks (gypsum-bearing in some places) with strongly oxidized and silicified pumice tuff and fine-grained tuff units (Fig. 5). The northwest-oriented transverse fault is identified between the Sakdrisi 5 and Sakdrisi 4 ore bodies, also Sakdrisi 4 and Sakdrisi 3 and Sakdrisi 3 and Sakdrisi 2 (Fig. 4) (Migineishvili et al 2009).

Figure 7. 3D Lithological-structural model of the Sakdrisi 4 ore body with explosive breccia pipes and ore bodies.

4 Ore bodies: distribution and types



Veins: a vertical zoning of gold grades was observed in quartz/quartz barite and quartz/sulfide veins and low to medium grade in stockworks. Disseminated ore is present in permeable host rocks and in explosive breccia. Supergene mineralization: mostly the upper part of the LVSC (pumice tuff) is affected by surface weathering and supergene overprint is in located areas of the main (mostly consists gold mineralization and locally copper also). Thus, the mineralization is commonly hosted in high permeability zones (pumice tuff), either restricted to subvertical veins or explosive breccia or disseminated in intensively leached rocks. The gossan-like supergene ore with highest gold concentrations and less copper was recognized in Sakdrisi 5 (Fig. 5), where gossan horizon consists of alluvial heterolithic breccia consisting of eroded and transported gossans displaced possibly as far as several hundred meters away from their sources. The distribution of major minerals throughout the gossan profiles like goethite, hematite, quartz and jarosite and the statistical analyses distinguish three separate zones, which was well observed on the profile and was a gradual contact with roughly parallel to current topography. Possibly subsequent local uplift of the gossan-rich rocks by neotectonic movements facilitated the rejuvenation of the oxidation of the ores.

4 Conclusions and recommendations

Two major trends of faults are recognized in the Sakdrisi area: NE and NW directions and dikes also are oriented mostly to the NE direction. The central fault/thrust fault developed when ignimbrite pyroclastic flow was thrust and overlapped

already the mineralized zone. Thus, the Central fault represents the upper limit of mineralized zone. The south fault zone is represented by a sharp contact with strongly oxidized and silicified with the LVSC unit, which raises the doubt that this fault is later than mineralization, although it is still a subject of study. The transverse faults are very noticeable in this deposit at this stage.

The lower base of mineralization zone in Sakdrisi 4 is observed in some drill holes in layered tuff with gypsum veins and locally ignimbrite-like tuff. Recent data from 400–600 m deep drill cores indicate enriched mineralized zones, which is a new discovery for this deposit. To develop the similar drilling project will be increased the perspectivity of the Sakdrisi deposit.

It is possible to conclude, that in the Sakdrisi deposit there is both a structural and a lithological control: the fault system created the fractures along which mineralized quartz, quartz-barite and quartz-sulfide and sulfide veins have been emplaced. The explosive breccia is mostly mineralized, even non-mineralized explosive breccia pipe in the close system created very fractured/permeable zones for fluid migration. Clastic/pumice-bearing rocks from Sakdrisi deposit is a good permeable rock, which here is strongly oxidized and mostly gold-bearing.

In conclusion, the 3D modelling of the Sakdrisi deposit is critical in this study allowing to visualize and integrate different datasets (from old and new drillings) in a lithological, structural and stratigraphic interpretation connected with the ore bodies distribution. 3D modelling of ore bearing explosive breccia outlines the spatial circulation of hydrothermal fluids in the system.

Acknowledgements

The authors would like to thank the Rich Metal Group for access to open pits and prospects, and for logistical support. The research would not have been possible without constant support provided by SGA, SEG and IAVCEI organizations for attending many international conferences, where the works about the Bolnisi district has been presented.

References

- Adamia Sh, Zakariadze G, Chkhotua T, Sadradze N, Tsereteli N, Chabukiani A, Gventsadze A (2011) Geology of the Caucasus: A review. *Turkish Journal of Earth Sciences*, v.20: 489-544
- Apkhazava M (1988) Late Cretaceous volcanism and volcanic structures at Bolnisi volcano-tectonic depression (Doctoral dissertation). Tbilisi, Georgia; Caucasus Institute of Mineral resources; 0-304
- Gugushvili v, Bukia A, Goderdzishvili N, Javakhidze D, Zakaraia D, Muladze I, Shavishvili I, Shubitidze J, Tchokhonelidze M (2014) Bolnisi ore district: geological development and structure, genesis of mineralization, economic potential and perspectives. Caucasus Mining Group, Tbilisi. Ed. Natsvlishvili MP 55 p (in Russian)
- Golay T, Moritz R, Popkhadze N, Natsvlishvili M (2018) The Sakdrisi Au-Cu deposit, Bolnisi mining district, Georgia: providing a genetic model based on petrographic, geochemical, structural, and alteration studies. The 16th Swiss Geoscience Meeting, Bern, Switzerland, 30 November-1st December, pp. 104-105
- Golay T (2019) The Sakdrisi Au-Cu deposit, Bolnisi mining district, Georgia: providing a genetic model based on petrographic, geochemical, structural and alteration studies. MSc thesis, University of Geneva. pp.1-181
- Jelev V, Bitsadze N, Ananiashvili G, Aslanishvili G, Shavishvili I, Natsvlishvili M (2021) Litho-structural geological mapping of Sakdrisi and Madneuli deposits. Unpublished report for RMG. Tbilisi, Georgia. pp 0-31
- Migineishvili R, Gaxaria D, Natsvlishvili M (2009) Geological map of Sakdrisi deposit. Unpublished enclosure report for RMG (In English)
- Moritz R, Melkonyan R, Selby D, Popkhadze N, Gugushvili V, Tayan R, Ramazanov V (2016) Metallogeny of the Lesser Caucasus: From Arc Construction to Postcollision Evolution. *Society of Economic Geologists, Special Publication 19*, pp.157-192
- Moritz R, Popkhadze N, Hassig M, Golay T, Lavoie J, Gugushvili V, Ulianov A, Ovtcharova M, Grosjean M, Chiaradia M, Dumitrica P (2020). At the crossroads of the Lesser Caucasus and the Eastern Pontides: Late to Early Eocene magmatic and geodynamic evolution of the Bolnisi district, Georgia. *Lithos-105872*, Volumes 378-379
- Popkhadze N, Moritz R, Natsvlishvili M, Bitsadze N (2017) First evidence of phreatomagmatic breccia at the Madneuli Polymetallic Deposit, Bolnisi district, Lesser Caucasus, Georgia. In: *proceedings of the 14th SGA biennial meeting: Mineral resources to discovery*, 20-23 August, Quebec City, Canada; 1:323-326
- Popkhadze N, Moritz R, Gugushvili V (2014) Architecture of Upper Cretaceous rhyodacitic hyaloclastite at the polymetallic Madneuli deposit, Lesser Caucasus, Georgia. *Cent. Eur. J. Geosci 6(3)*:308-329
- Popkhadze N, Sonmez S, Moritz R, Natsvlishvili M, Bluashvili V, Gagnidze N (2022) The Late Cretaceous Sakdrisi epithermal deposit, Bolnisi district (Lesser Caucasus, Georgia): Geology and ore deposit setting. XXII International Congress of the CBGA, Plovdiv, Bulgaria, 7-11 September. pp.362
- Popkhadze N, Moritz R, Sonmez S, Lipartia T, Natsvlishvili M, Gogia B (2023) The Late Cretaceous volcanism in Bolnisi district: lithological, structural and stratigraphic control on ore deposits, Lesser Caucasus, Georgia. IAVCEI2023 Scientific Assembly, 30 June-3 February, Rotorua, New Zealand. P.855
- Popkhadze N, Somenz S, Bluashvili V, Natsvlishvili M (2021) The Geological map of Sakdrisi deposit. Unpublished report for RMG. Kazreti, Georgia
- Yilmaz A, Adamia Sh, Chabukiani T, Chkhotua T, Erdogan K, Tuzcu S, Karabilykogly M (2000) Structural correlation of the southern Transcaucasus (Georgia)-Eastern Pontides (Turkey)-Tectonics and magmatism in Turkey and the surrounding area. *Geological Society of London Special Publication*, 173:171-182

A Comparative Study of VMS and Epithermal Deposit Settings in the Eastern Pontides, NE Turkey: Insights from Geochronology and Lithogeochemistry

Şafak Utku Sönmez¹, Robert Moritz¹, Serdar Keskin², François Turlin¹, Alexey Ulianov³, Ümit Aydın²

¹Department of Earth Sciences, University of Geneva, Rue des Maraîchers 13, 1205 Geneva, Switzerland

²General Directorate of Mineral Research and Exploration of Turkey, Department of Mineral Research and Exploration, Ankara 06520, Turkey

³Institute of Earth Sciences, University of Lausanne, 1015 Lausanne, Switzerland

Abstract. The Eastern Pontides, Turkey host a diverse range of mineral deposits, including volcanogenic massive sulfide (VMS) and epithermal deposits. VMS deposits are predominantly hosted by the Late Cretaceous Kızılıkaya Formation, whereas epithermal deposits are hosted by the Tirebolu Formation. Favorable host rocks for VMS deposits include felsic volcanic rocks, particularly rhyodacite of tholeiitic to calc-alkaline composition, whereas epithermal deposits are typically hosted by calc-alkaline to shoshonitic rhyolitic-dacitic lava flows. The switch from VMS to epithermal deposit formation coincides with the transition from the older Kızılıkaya to the younger Tirebolu Formation (ca. 84-82Ma). The age of Late Cretaceous intrusive complexes hosting porphyry Cu-Mo deposits further coincides with the host rock age of epithermal deposits/occurrences. The switch in the orientation of Late Cretaceous dikes at the Yanıklı prospect documents a major rotation of the regional shortening axis at ~82Ma. The Eastern Pontides of Turkey are a significant metallogenic belt with a high potential for both VMS and epithermal deposits. Our new geochronological constraints provide fundamental insights about the formation and evolution of this metallogenic belt.

1 Introduction

The Eastern Pontides (EPs) orogenic belt is a remarkable segment of the Western Tethyan Metallogenic Belt, which hosts numerous mineral deposits, including porphyry Cu-Mo, precious metal epithermal, and volcanogenic massive sulfide (VMS) deposits. They occur in various regions within the EPs, including the Giresun, Ordu, and Artvin districts, and are associated with Late Cretaceous bimodal submarine magmatism (Aydın et al. 2020; Eyuboglu et al. 2014, 2021; Kandemir et al. 2019; Oğuz-Saka et al. 2023, Özdamar 2016). The boundaries between the different host rock formations are still uncertain within certain districts due to overlapping formation ages and variable geochemical signatures. Additionally, it is unclear which mineralization style is related to each formation, further contributing to the ongoing debate.

The aim of our study is to address the uncertainties related to mineral occurrences hosted by the Late Cretaceous bimodal submarine magmatic rocks in the Eastern Pontides. The current state of research on the mineral deposits of the region is presented in this study, along with a detailed description of the characteristics of the geological formations.

2 Late Cretaceous Magmatism in the Eastern Pontides

The Late Cretaceous volcanic rocks from the EPs are divided into four formations, which were formed during two different magmatic cycles (Aydın et al. 2020; Eyuboglu et al. 2021; Kandemir et al. 2019). Each cycle comprises a mafic and a felsic rock formation (Figure 1; Aydın et al. 2020; Eyuboglu et al. 2014, 2021; Kandemir et al. 2019; Oğuz-Saka et al. 2023). The lowermost formation of the first magmatic cycle is the Çatak Formation, which includes pillow basalt, basaltic-andesitic tuff and breccia, siltstone and marl alternations. ⁴⁰Ar/³⁹Ar dating of 92.1 Ma of the lower basaltic groundmass and planktonic foraminifera from pelagic limestone from the basal part of the Çatak Formation indicate an early/mid-Turonian–Santonian age (Kandemir et al. 2019). The overlying late Turonian to early Santonian Kızılıkaya Formation comprises dacitic and rhyodacitic domes and flows, along with intermediate andesitic stocks and dikes (Aydın et al. 2020; Eyuboglu et al. 2014, 2021; Kandemir et al. 2019). The mid-late Santonian–Campanian Çağlayan Formation of the second magmatic cycle, which consists of pillow basalt, basaltic-andesitic tuff and breccia, siltstone, and marl alternations, intrudes and overlays the Kızılıkaya Formation in certain areas. Lastly, the youngest volcanic and volcanoclastic unit of the Cretaceous EPs is the Çayırbağ Formation of the second magmatic cycle, also known as the Tirebolu Formation, which is dominated by felsic volcanism (Aydın et al. 2020; Eyuboglu et al. 2014, 2021; Kandemir et al. 2019).

3 Settings of VMS Systems Hosted by Felsic Magmatic Rocks of the First Magmatic Cycle

The Kızılıkaya Formation is composed of dacitic to rhyolitic rocks with varying tholeiitic to calc-alkaline compositions. The felsic rocks of the Kızılıkaya Formation are favourable host rocks of VMS deposits in various regions, including Artvin, Rize, Giresun, etc (Figure 2).

In the Artvin District, Murgul, Hod Maden, and Kılıçkaya are major VMS deposits-occurrences hosted by the Kızılıkaya Formation.

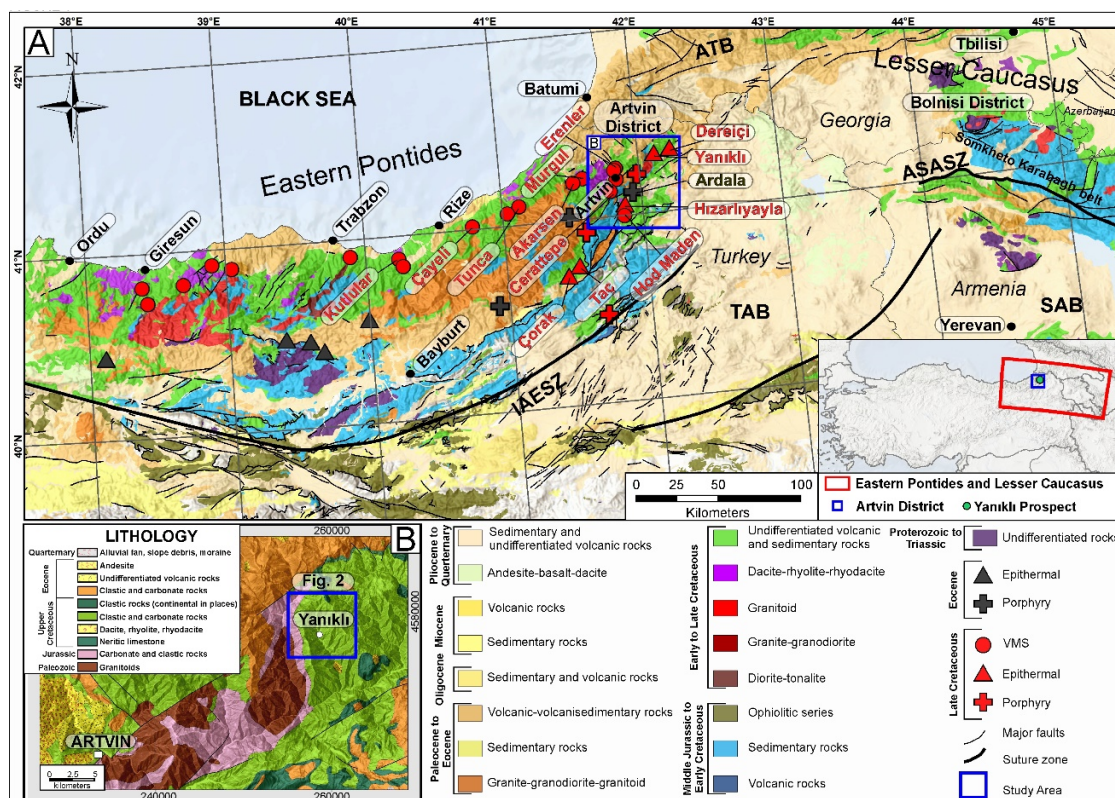


Figure 7. A) Simplified geology of northeastern Anatolia and the Lesser Caucasus (after Delibaş et al. 2016; Kandemir et al. 2019; Moritz et al. 2020). B) Geology of the Artvin District (simplified from the MTA 2002 1:500k geo map, Aydın et al. 2020). Abbreviations of tectonic zones and faults: ASASZ = Amasia-Sevan-Akera suture zone, ATB = Adjara-Trialeti belt, IAESZ = Izmir-Ankara-Erzincan suture, KB = Kapan block (Eurasian margin), SAB = South Armenian block, TAB Tauride-Anatolide block.

The felsic host rocks have been dated at 88.8 ± 0.9 Ma ($^{40}\text{Ar}/^{39}\text{Ar}$), and one unmineralized felsic rock has been dated at 86.51 ± 0.35 Ma (U-Pb) (Aydın et al. 2020; Bilir et al. 2022; Kandemir et al. 2019). Moreover, Rabayrol et al. (2023) reported an alteration age of the Taç prospect based on muscovite $^{40}\text{Ar}/^{39}\text{Ar}$ dating, which yielded an age of 86.3 ± 0.2 Ma.

The Tunca VMS occurrence located in the Rize region is hosted by a dacitic tuff breccia of the Kızılkaya Formation and U-Pb dating yielded an age of 88.1 ± 1.2 Ma (Revan et al. 2017). The Köprübaşı VMS occurrence related to the Kızılkaya Formation in the Giresun region is hosted by rocks dated at 91.1 ± 1.3 Ma and 82.6 ± 1 Ma (Eyuboglu et al. 2014). Furthermore, the host rocks of ore-bearing samples from the same region have yielded U-Pb concordia ages of 83.23 ± 0.21 Ma to 88.23 ± 0.37 Ma (Oğuz-Saka et al. 2023).

The ages of the host rocks of the VMS deposits indicate that they have been formed around 91-83 Ma. It is concluded that the Kızılkaya formation is a favourable host rock environment of the early magmatic cycle for VMS-style mineralization (Figure 2).

4 Late-stage Felsic Magmatic Rocks of the Second Magmatic Cycle As Hosts of Epithermal Polymetallic-Au Deposits and Occurrences

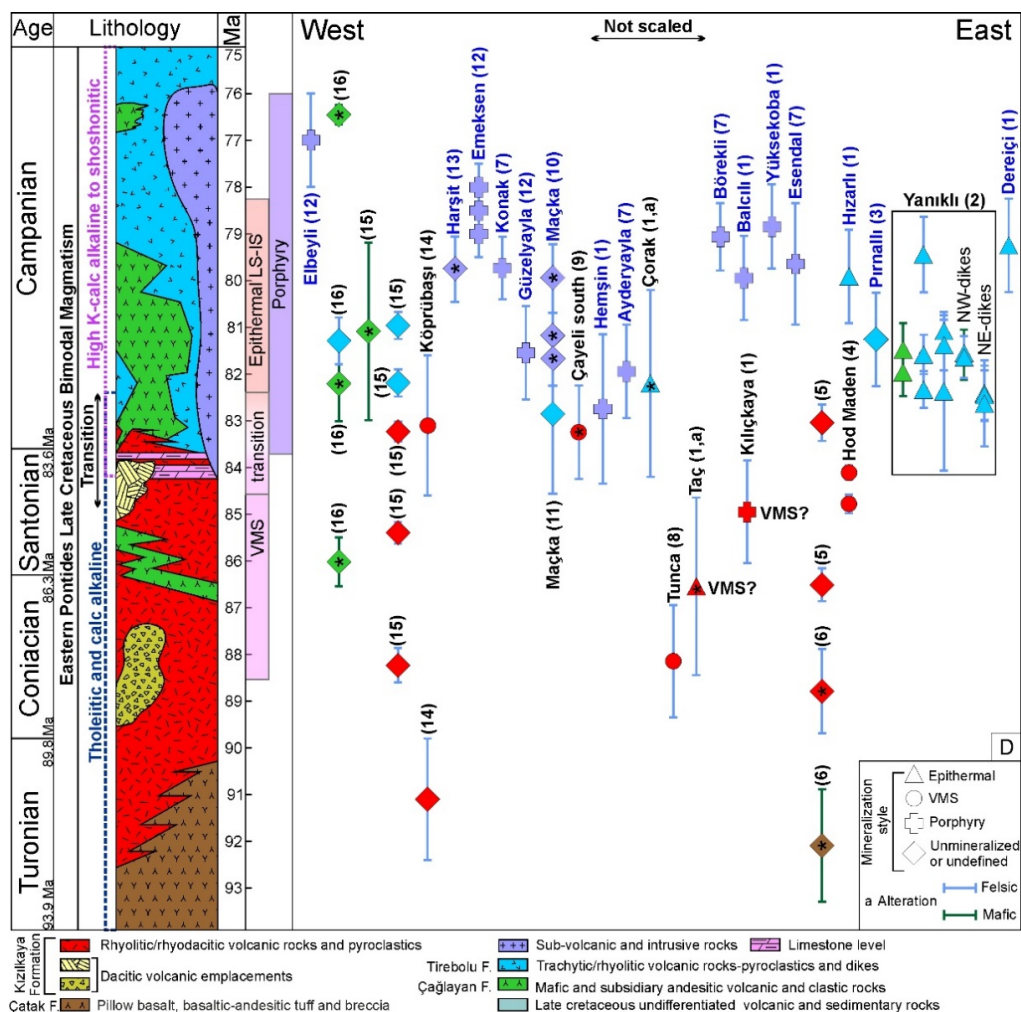
The Tirebolu Formation is the youngest event of felsic magmatism characterized by a calc-alkaline to shoshonitic composition. Within this formation, epithermal vein-type deposits are mainly associated with calc-alkaline rhyodacite volcanic rocks.

The Artvin District is a significant location for late epithermal ore formation, including Yanıklı (this study), Dereiçi (U-Pb; 79.2 ± 1 Ma), Hızarlı (U-Pb; 79.5 ± 1 Ma). The $^{40}\text{Ar}/^{39}\text{Ar}$ alteration age of the Çorak epithermal system from the Taç prospect is 82.2 ± 2 Ma (Rabayrol et al. 2023). Thus, Taç and Çorak are remarkable examples of epithermal deposits/occurrences that postdate the formation of VMS deposits (Figure 2).

The age interval of the Tirebolu Formation in the Giresun region has been defined by a U-Pb zircon concordia age of 82.19 ± 0.29 Ma and 80.96 ± 0.29 Ma (Oğuz-Saka et al. 2023). This geochemical and geochronological transition suggests a VMS-epithermal switch that coincides with the Kızılkaya and Tirebolu formation transition at ~ 84 -82 Ma.

The age of the host rocks of epithermal occurrences also corresponds to the age of Late Cretaceous intrusive complexes hosting porphyry Cu-Mo deposits in the Eastern Pontides (Figure 2; Delibaş et al. 2016; Kuşcu et al. 2019; Rabayrol et al. 2023).

5 Implications From the Yanıklı Prospect, Artvin District



crystallization ages, ranging from 82.41 ± 0.59 Ma to 82.63 ± 0.92 Ma. The younger generation of NW-trending dikes of the KDike-2 unit are predominantly composed of mafic rocks and have a weighted $^{206}\text{Pb}/^{238}\text{U}$ mean age of 81.64 ± 0.45 Ma. These distinct dike orientations indicate that the main shortening axis (σ_1) has rotated over time between the two dike generations. During the first generation of dike emplacement, the shortening orientation was NE-SW, and resulted in a NE-trending dike en-échelon pattern. The modification of the tectonic stress regime took place at ~ 82 Ma. The second dike generation was controlled by a NW-SE shortening axis and resulted in the emplacement of NW-oriented dikes.

6 Conclusions

The Eastern Pontides region is a major metallogenic belt, mainly characterized by VMS and epithermal systems. VMS deposits are mainly hosted by the Late Cretaceous Kızılkaya Formation, whereas the Tirebolu Formation hosts epithermal deposits. The ideal host rocks for VMS deposits are felsic volcanic rocks, particularly rhyodacite of tholeiitic to calc-alkaline composition, whereas epithermal deposits are typically hosted by calc-alkaline to shoshonitic rhyolitic-dacitic lava flows. The switch between the two distinct metallogenic regimes occurred concurrently with the transition from the older Kızılkaya to the younger Tirebolu Formation at ~ 84 - 82 Ma. This coincided with a rotation of the shortening axis from a NE-orientation to a NW-orientation, indicating a major change in the tectonic setting at the Yanıklı prospect.

Acknowledgements

The research was funded by the Swiss National Science Foundation through research grant 200021_188714. Additionally, Ş.U. Sönmez acknowledges the support of the Hugh McKinstry Fund, a student research grant program of the SEG Foundation of Canada. The authors would like to express their sincere gratitude to the General Directorate of Mineral Research and Exploration Turkey (MTA) for granting access to the Yanıklı prospect (project codes of 2019-2020-2021-32-13-06 and 2021-32-13-07), and to the exploration geologists of the MTA Eastern Black Sea District Office (S. Saka, C. Boysan, A. Ağan, and others) for their invaluable assistance and support throughout the project.

References

Alan İ, Balcı V, Keskin H, Altun İ et al (2019) Tectonostratigraphic characteristics of the area between Çayeli (Rize) and Ispir (Erzurum). *Bull. Miner. Res.*, 1-29.
 Aydin F (2014) Geochronology, geochemistry, and petrogenesis of the Maçka subvolcanic intrusions: implications for the Late Cretaceous magmatic and geodynamic evolution of the eastern part of the Sakarya Zone, northeastern Turkey. *Int Geol Rev* 1246–1275.

Aydin F, Oğuz-Saka S, Şen C et al (2020) Temporal, geochemical and geodynamic evolution of the Late Cretaceous subduction zone volcanism in the eastern Sakarya Zone, NE Turkey: Implications for mantle-crust interaction in an arc setting. *J Asian Earth Sci* doi:https://doi.org/10.1016/j.jseaes.2019.104217
 Bilir E, Kuşcu İ, Moritz R et al (2022) Hod Maden Deposit, Eastern Pontides, NE Turkey: A Cretaceous Au-rich VMS System - Geochemical and Isotopic Characterization of Hydrothermal Alteration and Mineralization. *Sustainable Mineral Resources Supply: Challenges for Future Generations*, (p. 5). Geneva.
 Delibaş O, Moritz R, Ulianov A et al (2016) Cretaceous subduction-related magmatism and associated porphyry-type Cu–Mo prospects in the Eastern Pontides, Turkey: New constraints from geochronology and geochemistry. *Lithos* 248-251:119–137.
 Eyuboglu Y, Dudás F, Zhu D et al (2021) Late Cretaceous alkaline magmas of the Eastern Pontides Orogenic Belt (NE Turkey): A review with new geological, geochemical and geochronological data. *Gondwana Res* 97:204–239.
 Eyuboglu Y, Santosh M, Yi K et al (2014) The Eastern Black Sea-type volcanogenic massive sulfide deposits: Geochemistry, zircon U–Pb geochronology and an overview of the geodynamics of ore genesis. *Ore Geol Rev* 59:29-54.
 Kandemir Ö, Akbayram K, Çobankaya M et al (2019) From arc evolution to arc-continent collision: Late Cretaceous–middle Eocene geology of the Eastern Pontides, northeastern Turkey. *GSA Bulletin* 131:1889-1906.
 Karsli O, Caran Ş, Dokuz A et al (2012) A-type granitoids from the Eastern Pontides, NE Turkey: Records for generation of hybrid A-type rocks in a subduction-related environment. *Tectonophysics* 530-531:208-224.
 Karsli O, Dokuz A, Uysal İ et al (2010) Relative contributions of crust and mantle to generation of Campanian high-K calc-alkaline I-type granitoids in a subduction setting, with special reference to the Harşit Pluton, Eastern Turkey. *Contrib to Mineral Petrol* 160:467–487.
 Kuscu , Tosdal R, Kuscu G (2019) Episodic porphyry Cu (-Mo-Au) formation and associated magmatic evolution in Turkish Tethyan collage. *Ore Geol Rev* 107: 119-154.
 Moritz R, Popkhadze N, Hässig et al (2020). At the crossroads of the Lesser Caucasus and the Eastern Pontides: Late Cretaceous to early Eocene magmatic and geodynamic evolution of the Bolnisi district, Georgia. *Lithos*, 378-379.
 Oğuz-Saka S, Aydin F, Karsli O et al (2023) Two-stage bimodal volcanism in a Late Cretaceous arc/back-arc setting, NE Turkey: constraints from volcano-stratigraphy, zircon U-Pb and $^{40}\text{Ar}/^{39}\text{Ar}$ geochronology and whole-rock elemental and Sr-Nd-Pb isotope geochemistry. *Lithos* 440-441:107018.
 Özdamar Ş (2016) Geochemistry and geochronology of late Mesozoic volcanic rocks in the northern part of the Eastern Pontide Orogenic Belt (NE Turkey): Implications for the closure of the Neotethys Ocean. *Lithos*, 240-256.
 Rabayrol F, Wainwright A, Lee R et al (2022) District-Scale VMS to Porphyry-Epithermal Transitions in Subduction to Postcollisional Tectonic Environments: The Artvin Au-Cu District and the Hod Gold Corridor, Eastern Pontides Belt, Turkey. *Econ Geol.* doi:https://doi.org/10.5382/econgeo.4983
 Revan M, Hisatani K, Miyamoto, H et al (2017) Geology, U-Pb geochronology, and stable isotope geochemistry of the Tunca semi-massive sulfide mineralization, Black Sea region, NE Turkey: Implications for ore genesis. *Ore Geol Rev* 89:369-389.
 Sönmez ŞU, Moritz R, Turlin F et al (2022) Age and composition of magmatic rocks, and hydrothermal alteration characteristics of the Yanıklı Prospect, Eastern Pontides, Turkey. *Sustainable Mineral Resources Supply: Challenges for Future Generations*, (p. 48). Geneva.

Pb-containing aluminium phosphate-sulphate mineralization from the advanced argillic alteration in the Chelopech epithermal high-sulphidation Cu-Au deposit

Sylvina Georgieva¹, Elitsa Stefanova¹, Atanas Hikov¹, Milen Kadiyski², Stoyan Georgiev¹, Mariana Trifonova³

¹ Geological Institute, Bulgarian Academy of Sciences, Sofia, Bulgaria

² Aurubis Bulgaria AD, Pirdop, Bulgaria

³ Dundee Precious Metals Chelopech EAD, Bulgaria

Abstract. The Chelopech epithermal high-sulphidation Cu-Au deposit is one of the significant and well described deposits in Europe. Its hydrothermal advanced-argillic alteration footprint extensively developed in depth is very suitable for exploring potential geochemical vectoring and indicators. Alunite and aluminium-phosphate-sulphate (APS) minerals are common in the advanced argillic alteration zone of the deposit. Although these minerals are formed along with similar mineral association (quartz, dickite/kaolinite, barite, ore mineralization) they reveal different geochemical properties across the altered rock volume and with distance to the ore bodies and the depth. The studied APS mineralization is established westwards from the ore block 151, level 400, westernmost part of the deposit. Its chemical composition refers to woodhouseite-svanbergite-hinsdalite solid solution with Ca- to Sr-rich and Pb-rich varieties without reaching pure end-member. The main peculiarity of the APS from the distal zones compared to the previous published data about APS from the deposit, found in the frame of the ore bodies and in depth (>1300 m) is the remarkable enrichment of Pb content up to 15 wt% PbO. The geochemical signatures of the APS as members of the alunite supergroup could have a potential to be used as directional indicators towards the orebody after careful consideration.

1 Introduction

The aluminium phosphate-sulphate minerals (APS) belong to the alunite supergroup that consists of three mineral groups. The supergroup contains more than 40 mineral species with general formula $DG_3(TO_4)_2(OH, H_2O)_6$, where D is a large cation (Na, K, Ag, NH₄, Pb, Ca, Ba, Sr, REE, U), G is occupied by Al, Fe, Cu or Zn in octahedral coordination, and T is dominated by P, S and As in tetrahedral coordination (Jambor 1999; Dill 2001). These minerals typically occur in advanced argillic style acidic and intermediate pyroclastic, volcanic and subvolcanic rocks related or not to ore mineralization. Such relations have been documented in a large number of epithermal high-sulphidation ore deposits. The geochemical peculiarities of alunite and APS minerals have recently become an object of interest for the exploration in terms to evaluate the distance to the intrusive centre or to distinguish mineralized from barren systems (e.g., Chang et al 2011). APS mineralization (svanbergite-woodhouseite, florencite and crandallite) are broadly established in the advanced argillic alteration of the Chelopech

deposit in close proximity to the ore bodies. The mineralization is developed down to a depth of >1300 m (Georgieva et al 2002; Georgieva and Velinova 2014). This report provides new data about Pb-containing APS minerals established in the advanced argillic alteration from the western part of the Chelopech deposit in drill-hole samples, traced westwards and distant from the economically outlined ore bodies.

2 Methodology

Materials used in this study are hydrothermally altered in advanced argillic alteration granodiorite samples from the EXT151-400-19 drill-core, mine level 400, western part of the Chelopech deposit. The drill-hole starts from the western peripheral part of the ore-block 151, and shifts outwards of the ore-block to the west. Prior to SEM-EDS chemical study, the mineral composition and relationships in the rocks were examined in thin sections using optical and scanning-electron microscopy.

A VEGA 3 XMU SEM by Tescan at Aurubis Bulgaria AD was used for BSE imaging and determination of major element composition of minerals with EDS. We used a 20 kV accelerating voltage; beam calibration was done using pure copper. The formulae units were calculated based on the assumption that P+S is 2 *apfu* (Jambor 1999).

3 Geological setting

The Chelopech high-sulphidation epithermal Cu-Au deposit is ranked among the most significant European Cu-Au deposits. As part of the Elatsite-Chelopech ore field, it is situated in the northern part of the Panagyurishte ore region within the central parts of the Srednogie tectonic zone. The Panagyurishte ore region is characterized with the presence of a cluster of porphyry Cu (e.g., Elatsite, Assarel, Medet) and epithermal Cu-Au (e.g., Chelopech, Elshitsa, Radka) deposits.

The ore mineralization of the Chelopech deposit is hosted in an Upper Cretaceous volcanic and volcano-sedimentary complex (Popov et al. 1983), transgressively overlying gneisses, amphibolites, schists and phyllites of Neoproterozoic to Paleozoic

age (Peytcheva and von Quadt 2004; Carrigan et al. 2006). The Upper Cretaceous volcanic complex consists mainly of intermediate-composition varieties (andesitic, trachydacitic to dacitic) of Turonian age (Stoykov et al. 2004). Recently, Marton et al (2016) proposed a new geological model with a shallow multiphase intrusive complex intersected by vertically extended, intrusion-related breccia bodies with at least one maar-diatreme eruptive centre. The diatreme is related to a granodiorite phase associated with: 1) porphyry Cu-Mo-Au stockwork in the Petrovden area; 2) distal base metal sulphide veins in the Petrovden and Vozdol areas; 3) high-sulphidation Cu-Au mineralization in the Chelopech and Sharlo Dere areas.

Larg parts of the rocks in the vicinity of the Chelopech deposit are overprinted by extensive hydrothermal alteration. The ore mineralization is generally associated with a vast zone of advanced argillic alteration surrounded by halos of quartz-sericitic and propylitic alteration (Georgieva 2017). The economic Cu-Au mineralization is most strongly developed in the volcanic breccia and/or along fractures and represents massive to stockwork bodies, veins and disseminations. Enargite, lusonite, tennantite, chalcopyrite and bornite are the main sulphides and sulphosalts in the ore mineralization along with abundant subordinate and sporadic minerals including tellurides and selenides (Terziev 1968; Petrunov 1995).

4 Results

The studied APS mineralization occurs in the advanced argillic altered granodiorites established westwards from the ore block 151, level 400, westernmost part of the deposit. Besides the intensive alteration, the granodiorites are cut by up to 1 cm wide pyrite veins and late enargite-tennantite nests and veinlets. Along with enargite and tennantite weak mineralization of chalcopyrite, bornite, goldfieldite, tetrahedrite, galena and clausthalite are established. As a gangue mineralization bladed sub- to euhedral barite crystals up to 3 mm occur. Commonly, the APS mineralization is developed as up to 200 µm sub- to euhedral crystals in association with abundant quartz, clay minerals (dickite/kaolinite), barite and disseminated pyrite. Generally, they intergrowth with barite and dickite/kaolinite. Euhedral crystals up to 100 µm can occur as inclusions in ore minerals including enargite and tennantite. The cores of certain APS grains and crystals are replaced by clay minerals (dickite/kaolinite). Clear chemical zoning in the majority of the studied crystals are observed in back-scattered electron (BSE) images (Fig. 1).

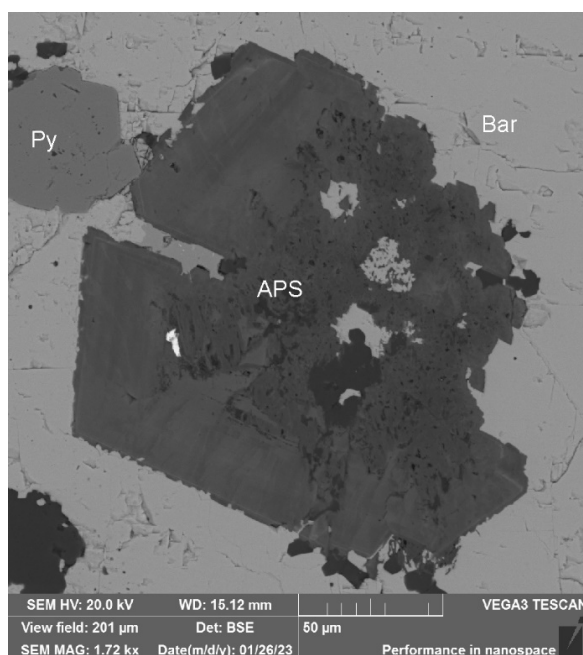


Figure 1. BSE image of zonal APS crystal in barite. Abbreviations: Py – pyrite; Bar - barite

The chemical SEM-EDS analyses reveal that the APS minerals belong mainly to the woodhouseite-svanbergite-hinsdalite solid solution series: $(\text{Ca}, \text{Sr}, \text{Pb})\text{Al}_3(\text{PO}_4, \text{SO}_4)_2(\text{OH}, \text{H}_2\text{O})_6$. Their composition ranges from Ca- to Sr-rich and Pb-rich phases without reaching the pure end-members (Fig. 2A). In addition, minor amounts of Ba (Fig. 2B) and LREE are also established. The chemical zoning observed in BSE images is mainly due to variations of Ca, Sr, Pb and Ba contents in *D* crystal structure site. The maximum CaO content is up to 10.3 wt%, SrO - up to 12.3 wt%, PbO – up to 15 wt%. Low contents of K₂O and Na₂O exist in some of the samples. The *G* site is mostly occupied by Al – up to 38.87 wt% Al₂O₃, small amount of Cu - up to 4.57 wt% CuO and Fe - up to 1.87 wt% Fe₂O₃. The phosphorus/sulphur molar ratio from *T* site is close to a 1:1 (Fig. 2C) in the predominant number of analyses. In some analytical points the ratio is more than 3:1. Regarding the Ca-rich varieties compositions close to woodhouseite (with P:S = 1:1) and crandallite (P:S > 3:1) are established.

Our preliminary observations show that the cores of APS crystals have higher Ca and P contents while the peripheries are enriched in Pb. The elevated Ca and P contents in the cores could be explained by apatite dissolution and replacement in acid environment of advanced argillic alteration (Stoffregen 1987; Georgieva and Velinova 2014).

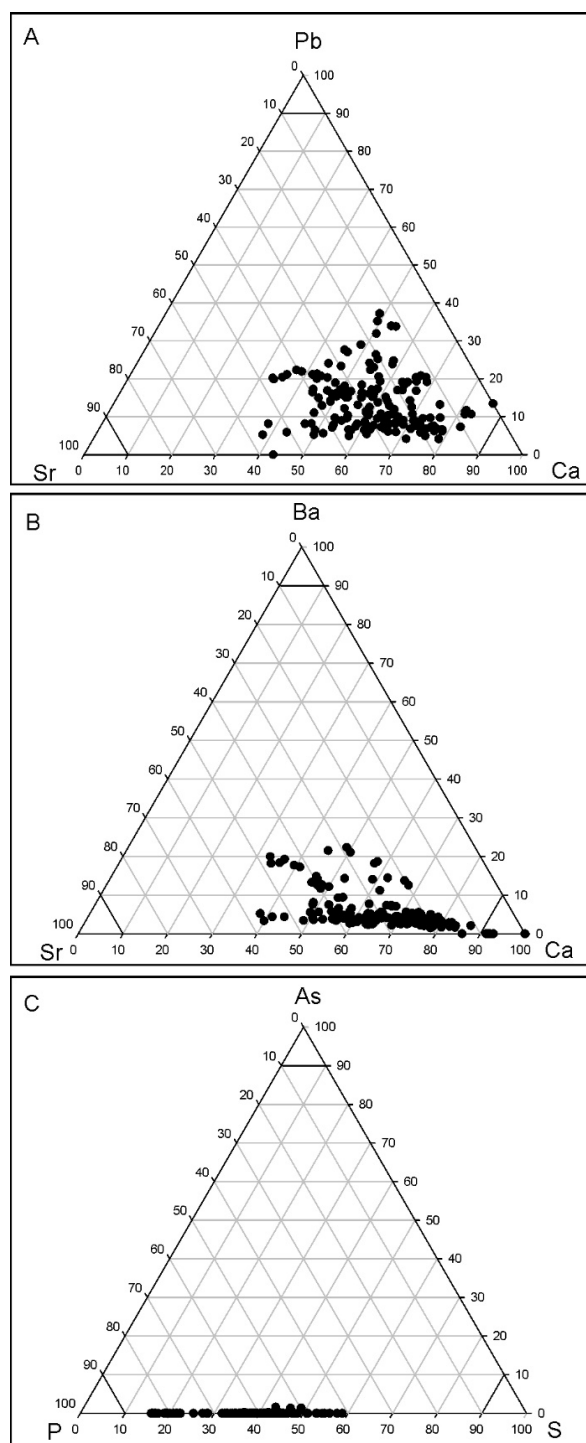


Figure 2. A, B) Cation compositions in the *D* sites of zonal APS; C) Anion composition in the *T* sites of APS

5 Discussion and concluding remarks

The studied APS mineralization is located in the westernmost part of the Chelopech Cu-Au deposit, i.e., in a distal position to the orebody. It has similar occurrence and mineral association compared to the previously studied APS mineralization from the ore blocks at level 405 and from the deep drill-holes 600 and 600a (>1300 m depth). The APS from

these localities belong to the svanbergite, woodhouseite, svanbergite-woodhouseite solid solution series from high Ca- to high Sr-varieties with minor amounts of Ba and K. Florencite $(\text{Ce,La,Nd})\text{Al}_3(\text{PO}_4)_2(\text{OH})_6$ and crandallite $(\text{CaAl}_3(\text{PO}_4)_2(\text{OH})_5 \cdot \text{H}_2\text{O})$ as end members are also established (Georgieva et al 2002; Georgieva and Velinova 2014). The main difference between APS minerals from the different localities is their chemistry. The APS mineralization located in a distal position to the orebodies are remarkably enriched in Pb. The chemical composition of the APS reveal Ca, Sr and Pb as main constituents along with less Ba, LREE, K, and Na. This Pb-containing APS mineralization refer to the alunite supergroup with woodhouseite- svanbergite-hinsdalite composition from Ca- to Sr-rich and Pb-rich varieties without reaching pure end-members.

Chang et al (2011) also determined variable Pb-content in alunite from the Mankayan mineral district, Philippines. According to the authors the Pb content in alunite increase with increasing distance from the intrusive center causing the ore mineralization. Our preliminary data are in agreement with the observation of Chang et al (2011) and show Pb-rich APS minerals in a distal parts of the deposit. This suggest that the increased Pb content in the APS could also be considered as a similar directional indicator though further examinations are needed.

Acknowledgements

The study is financially supported by the Bulgarian National Science Fund KP-06-N44/4, 12.2020 project.

References

- Carrigan C, Mukasa S, Haydutow I, Kolcheva K. (2006) Neoproterozoic magmatism and Carboniferous high-grade metamorphism in the Sredna Gora Zone, Bulgaria: An extension of the Gondwana-derived Avalonian-Cadomian belt?. *Precambrian Res* 147(3–4): 404–416. <https://doi.org/10.1016/j.precamres.2006.01.026>
- Chang Z, Hedenquist JW, White NC, Cooke DR, Roach M, Deyell CL, Garcia J, Gemmell JB, McKnight S, Cuison AL (2011) Exploration Tools for Linked Porphyry and Epithermal Deposits: Example from the Mankayan Intrusion-Centered Cu-Au District, Luzon, Philippines. *Econ Geol* 106(8): 1365–1398. <https://doi.org/10.2113/econgeo.106.8.1365>
- Dill HG (2001) The geology of aluminium phosphates and sulphates of the alunite group minerals: A review. *Earth Sci Rev* 53: 35–93.
- Georgieva S (2017) Mineral association and their distribution in hydrothermal alteration zones of the Chelopech high-sulphidation deposit, Bulgaria. *Geol Balc* 46(2): 11–16.
- Georgieva S, Velinova N (2014) Florencite-(Ce, La, Nd) and crandallite from the advanced argillic alteration in the Chelopech high-sulphidation epithermal Cu-Au deposit, Bulgaria. *Compt Rend Acad Bulg Sci* 67(12): 1669–1678.
- Georgieva S, Velinova N, Petrunov R, Moritz R, Chambefort I, (2002) Aluminium phosphate-sulphate minerals in the Chelopech Cu-Au deposit: spatial development, chemistry and genetic significance. *Geochem Miner Petr* 39: 39–53.

- Jambor JL (1999) Nomenclature of the alunite supergroup. *Canad Mineral* 37: 1323–1341.
- Marton I, Dintchev Y, Trifonova M, Hadzhieva N, Grigorova M et al (2016) A new geological model for the Chelopech Au-Cu deposit in Bulgaria: exploring a maar-diatreme system within an intrusive environment. In: SEG-MJD 2016 Conf. (electronic abstracts).
- Petrunov R (1995) Ore mineral paragenesis and zoning in the deposit of Chelopech. *Geochem Mineral Petrol* 30: 89–98 (in Bulgarian, with English abstract).
- Peytcheva I, von Quadt A (2004) The Palaeozoic protoliths of Central Srednogorie, Bulgaria: records in zircons from basement rocks and Cretaceous magmatites. *Proceedings of the Fifth International Symposium on the Eastern Mediterranean Geology*, 14–20 April 2004, Thessaloniki, Greece, 392–395.
- Popov P, Vladimirov V, Bakardjiev S (1983) Structural model of the polyformational Chelopech copper field (Bulgaria). *Geol Rud Mestorojd* 25(5): 3–11 (in Russian).
- Stoffregen RE, Alpers CN (1987) Woodhouseite and svanbergite in hydrothermal ore deposits: products of apatite destruction during advanced argillic alteration. *Canad Mineral* 25: 201–211.
- Stoykov S, Peytcheva I, von Quadt A, Moritz R, Frank M, Fontignie D (2004) Timing and magma evolution of the Chelopech volcanic complex (Bulgaria). *Schweiz Mineral Petrogr Mitt* 84: 101–117.
- Terziev G (1968) Mineral composition and genesis of the Chelopech ore deposit. *Bull Geol Inst, series Geochem Mineral Petrogr* 17: 123–187 (in Bulgarian, with English abstract)

Metal Endowment of Magmatic Brines from Active Geothermal Reservoirs

Brian Tattitch¹, Jon Blundy², Oscar Laurent^{3,4}

¹University of Western Australia, Perth, Australia

²University of Oxford, Oxford, United Kingdom

³CNRS-Géosciences Environnement Toulouse, France

⁴Institute of Geochemistry and Petrology, Department of Earth Sciences, ETH Zurich, Zurich, Switzerland

Abstract. Exploration for efficient clean geothermal power is targeting ever deeper “supercritical” geothermal reservoirs. Many supercritical reservoirs are accumulations of high-temperature magmatic fluids. Unlike heated meteoric water, these saline fluids and hypersaline brines contain significant endowments of critical elements. To quantify these endowments we examined brine inclusions from 3 active geothermal systems (Kakkonda, Japan; Larderello, Italy; Muara Laboh, Indonesia) and deep samples from 2 active volcanoes (Soufriere Hills Volcano, Montserrat; Ascension Island Volcano, mid-Atlantic). The brines recovered from these systems are extremely salty, (TDS > 50wt% NaCl_{eq}). The highest temperature inclusions show maximum trapping temperatures > 500°C. Maximum concentrations of selected elements are: 0.27% Sr and 3 ppm Au (Larderello); 2.7% Mn, 0.9% Zn, 0.7% Cu, 0.3% Pb (Kakkonda); 0.2wt% Cu (Muara Laboh); 0.5% B, 900 ppm Ba, 500 ppm Li and 90 ppm Ag (Montserrat); 0.19% Rb, 350 ppm Mo, 180 ppm W and 4 ppm Au (Ascension). We will show how these brines fit into a broader picture of ancient ore fluids, and modern geothermal systems. Our data also suggest that recovery of these critical elements could provide additional economic value to geothermal production and some systems could become a new versatile economic resource in their own right.

1 Introduction

It has been well established that the solubility of many critical metals relies on the presence of abundant carrier anions, or ligands to stabilize large, dissolved concentrations of metals at high temperature. In magmatic environments saline fluids are responsible for concentrating and transporting a huge range of ore metals from their parental magmas to the site of ore deposition (e.g. Candela and Holland 1984, Kouzmanov and Pokrovski 2012, Tattitch and Blundy 2017). There is strong evidence that these types of saline magmatic fluids were not unique to systems leading to ore deposition, but rather that many shallow evolved magmatic systems (e.g. granitic intrusions and arc volcanoes) commonly degas fluids rich in metals (e.g. Audetat et al. 2008, Edmonds et al. 2018).

However, the hypersaline metalliferous brines observed at depth in granites and ore deposits are not the same as the volcanic emissions observed at the surface today. Volcanic fumaroles do retain an imprint of the metal-rich nature of their generation, but only transport a tiny fraction of the metal endowment initially imparted when they were degassed from deep magma reservoirs. This is because when saline fluids ascend away from the

magmatic hearth, they cannot retain their entire metal-chloride load. As they ascend at high-temperature the decompression inescapably leads to the formation of metal-rich hypersaline brine as the metal-Cl solubility in the ascending vapor decreases. The textural association of these two fluids in magmatic systems (e.g. Fournier 1999) and more recent numerical modelling of magmatic degassing (Afanasyev et al. 2018) both show that the hypersaline brine formed during decompression is commonly left behind, accumulating at depth, while the low-density metal-poor vapor is released; it is this metal-poor vapor that feeds volcanic fumaroles in active volcanoes.

While there is abundant evidence from volcanic monitoring that magmatic vapors contain magmatic derived metals, this only provides a window into the modern geothermal brine reservoirs left behind at depth. To understand the endowment of modern brine reservoirs we need to examine them directly. Our early investigation of modern brine reservoirs (Blundy et al. 2021) revealed that these brines are significantly enriched in base metals (Cu, Zn, Pb) similar to brines associated with porphyry ore deposits. These data show that the base metal concentration in the cooling brines is likely limited by sulfide solubility, fractionating Cu from the more soluble Zn and Pb. Linking the brine trace data to models for brine lens generation shows that protracted periods of degassing and brine accumulation will lead to either a substantial soluble Cu reservoir, or substantial Cu-sulfide deposition dependant on the availability of reduced sulfur (Blundy et al. 2021). Nonetheless, drilling deep hot brine wells, maintaining well integrity and preventing unwanted scaling prior to metal recovery pose significant challenges for exploiting these brines for metals or energy. To overcome these challenges and evaluate the economic potential of these brines we need a more complete understanding of their composition and distribution.

Here we will present a greatly expanded modern brine dataset with all major salts and 14 key trace metals and trace elements. Our expanded dataset shows that hypersaline modern brines from around the world are commonly more enriched in critical metals than geothermal fluids or other brines utilized for metal production (e.g. Harto 2013) and more have an even larger and more versatile potential metal endowment than reported previously (Blundy et al. 2021).

2 Methods

Here we present evidence of the presence of metal-rich hypersaline magmatic brines in 3 active geothermal reservoirs (Kakkonda, Japan, Larderello, Italy, Muara Laboh, Indonesia) and 2 active volcanoes (Soufriere Hills Volcano,

Montserrat and Ascension Island Volcano, mid-Atlantic) (Figure 1). These sites were chosen because at each site there was already an indication of conductive saline fluids at depth (Rizzo et al. 2022, Uchida et al. 2000, Dyaksa et al. 2016, Ryan et al. 2013), or shallow magma in the case of Ascension Island (Chamberlain et al. 2016)

Figure 1: Map of Sample Locations for Active Hydrothermal Systems Containing Deep Hypersaline Brines

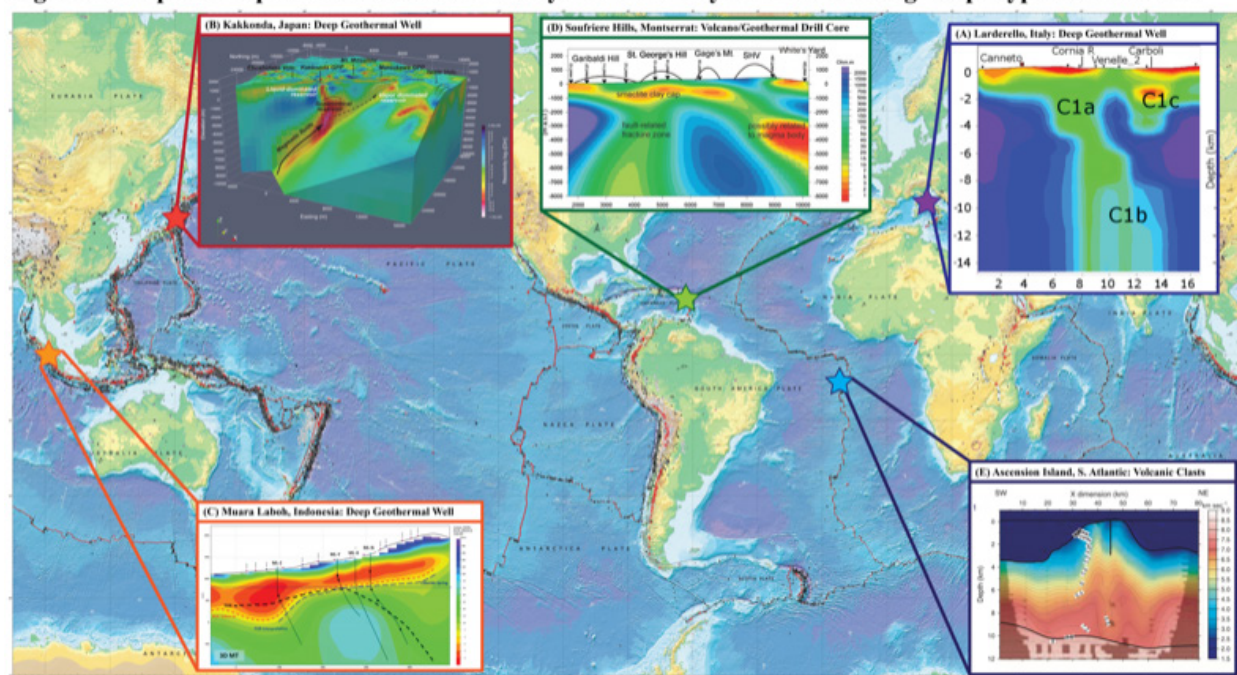


Figure 1. World map (Base map USGS I-2800) showing the sample locations of the 5 sites examined for evidence of metalliferous hypersaline brine in deep geothermal reservoirs. Electrical conductivity surveys, highlighting conductive fluids at depth are shown for sites (A) Larderello, (B) Kakkonda, (C) Muara Laboh, and (D) Montserrat, along with a seismic survey of site (E) Ascension Island, showing magma at depth.

2.1 Fluid inclusion Analyses

We obtained deep drill core samples from the 3 intrusive magmatic geothermal systems (Kakkonda-well WD-1a, Larderello- wells Travale-1s and Radicondoli-26, Muara Laboh- well H4) along with drill core samples from the exploratory well from Soufriere Hills Volcano (SVH) on Montserrat. From the geothermal sites we recovered several generations of quartz veins to search for hypersaline brine fluid inclusions. No quartz veins were present in the drill core from Montserrat. As a result, we recovered several “micro-miarolitic” cavities from the Montserrat drill core filled with hydrothermal quartz.

No drill core material is available from Ascension Island. However, volcanic clasts recovered from the island occasionally contain fragments of granitic material from the roots of the volcano. We extracted grains of magmatic quartz and sanidine from these granitic clasts to search for brine inclusions. Figure 2 shows photo-micrographs of typical brine fluid inclusions recovered from each of these 5 sites.

Each inclusion assemblage was examined using a Linkam XY1400 stage to determine the dissolution

temperature for the halite daughter minerals (T_m^{Halite}), as well as the contraction vapor bubble ($T_m^{\text{L-V}}$). Upon dissolution of both phases the inclusions were considered homogenized back to their original single brine liquid composition (T_h).

2.2 LA-ICPMS Analyses

Inclusion assemblages with a significant number of brine inclusions of sufficient size ($>15 \mu\text{m}$) were selected for ICPMS analysis using a quadrupole mass spectrometer and a custom 193 nm laser system at ETH Zurich. We examined both major (Na, K, Ca, Fe, Mn) and trace element (Li, Cu, Zn, As, Mo, Ag, Sb, W, Au, Pb, B, Rb, Sr, Ba) abundances in the inclusions standardized to a total salinity determined by microthermometry. Spot size in increased stepwise until ablating the entire inclusion. Transient signals from the ICPMS were integrated in SILLS (Guillong et al. 2008) to quantify the concentration of all the elements of interest for each inclusion. Brine compositions will then be reported as averages for each of the samples once inclusion signals are screened for any irregularities (missing salt signals, major elements below LOD).

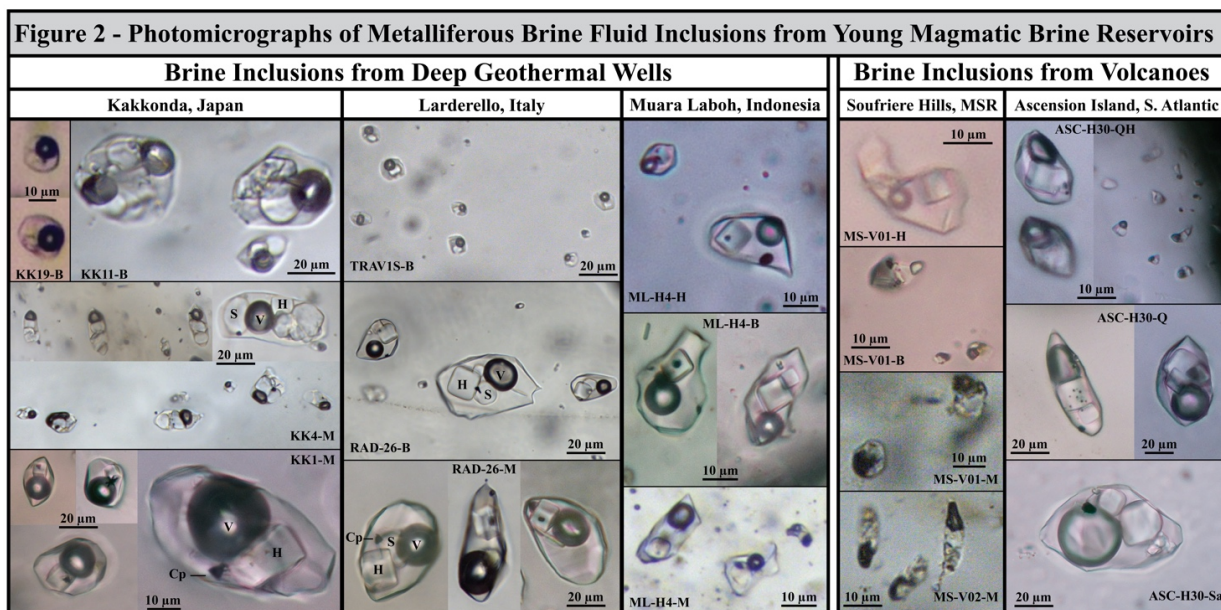


Figure 2. Photo-micrographs of brine fluid inclusions from each of the 5 geothermal/volcanic sites examined. Inclusions all show at least one halite daughter mineral along with a contraction vapor bubble formed on cooling to room temperature. Many of the inclusions also contain opaque daughter minerals formed from mixtures of oxide and sulfide, again formed upon cooling the metal-rich brine inclusions. Homogenization of these inclusions back to a single liquid phase was used to determine the salinity and trapping temperature of the inclusions.

3 Results

Histograms showing the ranges of T_m^{Halite} and $T_m^{\text{L-V}}$ for each of the samples examined from each of the 5 sites are shown in Figure 3. Microthermometry data shows that the brines in these systems are truly hypersaline and have a salinity in excess of >50wt% NaCl_{eq} for nearly all samples. The highest temperature brines also have trapping temperatures (preserved as T_h) in excess of 500°C. These high temperatures are consistent with the magmatic origin of the saline fluids that formed these brine reservoirs at depth.

We will present complete LA-ICPMS analyses of the entire brine sample suite at the SGA meeting. The highest concentrations for some selected elements include: 0.27% Sr and 3 ppm Au (Larderello); 2.7% Mn, 0.9% Zn, 0.7% Cu, 0.3% Pb (Kakkonda); 0.2wt% Cu (Muara Laboh); 0.5% B, 900 ppm Ba, 500 ppm Li and 90 ppm Ag (Montserrat); 0.19% Rb, 350 ppm Mo, 180 ppm W and 4 ppm Au (Ascension). This expanded dataset confirmed the previous observation that the modern magmatic brine reservoirs examined are well endowed with base metals (Blundy et al. 2021) similar to brines recovered from ore veins in arc magmatic-hydrothermal deposits (Kouzmanov and Pokrovski 2012). However, our data shows that these brines are endowed with much more than base metals.

The complete sample suite will also be compared to a database of analyses from ancient brine ore fluids and granite-hosted brine inclusions as well as deep geothermal brines and dilute geothermal waters. We will discuss how our data highlights that

modern brines are very similar to the ore fluids that formed ore deposits in the past. Characterizing these brines can provide valuable information about the nature of magmatic brines that can lead to ore formation without the challenges of resetting inclusions and overprinting that are common in ancient ore systems. They can provide information about high-temperature alteration, ore mineral solubility, and the extent of brine reservoirs above intrusions. All of these aspects of modern brine lenses can provide new insights into the nature of magmatic hydrothermal ore deposition.

Yet, understanding these high-temperature brines can also help with developing new models for supercritical geothermal wells, or developing new materials to allow for protracted exposure of wells to corrosive supercritical fluids near these brines, or perhaps exposure to the brines themselves. Yet, our data show that these brines are also much more endowed in critical metals and other valuable elements than any of the geothermal waters or brines currently exploited for metal recovery.

Finally, the large array of valuable elements dissolved in the brines represent a significant potential economic resource if they could be recovered. As such, deep magmatic brines could provide an entirely new way to secure some of these critical elements and magmatic brine reservoirs could become an economic resource in their own right. Each of these facets of the scientific and economic potential of brine lenses will also be discussed.

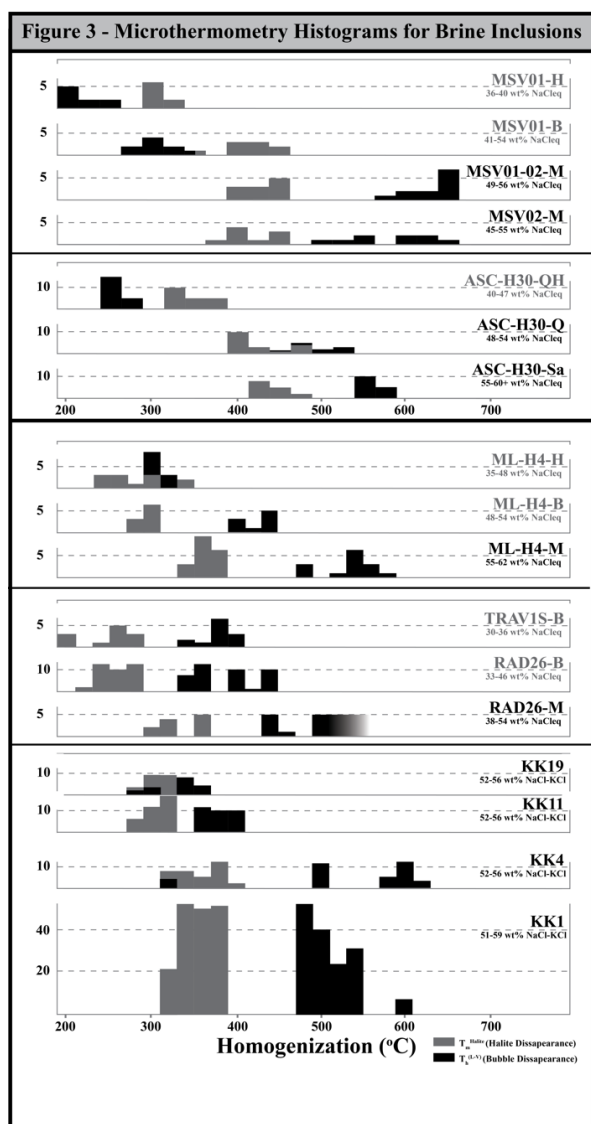


Figure 3. Histograms showing the ranges for T_{m}^{Halite} and T_{m}^{L-V} for each of the brine sample sets examined in this study. Halite dissolution temperatures were used to determine the salinity of the brine inclusions. Most inclusions homogenized by bubble disappearance after halite dissolution and T_{m}^{L-V} was then used to determine the trapping conditions for the brines.

Acknowledgements

We would like to acknowledge BHP for supporting this research project and ETH Zurich and Cyril Chelle-Michou for assistance with the LA-ICPMS analyses. We would also like to thank AIST and the Japanese Geologic Survey for providing access to the Kakkonda drill cores; Paolo Fulignati for drill core samples from Larderello; Jim Stimac for samples from Muara Laboh; The Montserrat Volcano Observatory, BGS and Adam Stinton for samples

from the SHV; and Chris Harris for samples from Ascension Island.

References

- Afanasyev A., Blundy J., Melnik O. and Sparks S. (2018) Formation of magmatic brine lenses via focussed fluid-flow beneath volcanoes. *Earth Planet. Sci. Lett.* **486**, 119–128.
- Audétat A., Pettke T., Heinrich C. A. and Bodnar R. J. (2008) Special Paper: The Composition of Magmatic-Hydrothermal Fluids in Barren and Mineralized Intrusions. *Econ. Geol.* **103**, 877–908.
- Blundy J., Afanasyev A., Tattitch B., Sparks S., Melnik O., Utkin I., and Rust A. (2021) The economic potential of metalliferous sub-volcanic brines. *R. Soc. open sci.* **8**
- Candela P. A. and Holland H. D. (1984) The partitioning of copper and molybdenum between silicate melts and aqueous fluids. *Geochim. Cosmochim. Ac.* **48**, 373–380.
- Chamberlain K.J., Barclay J., Preece K., Brown R.J., Davidson J.P., EIMF (2016) Origin and evolution of silicic magmas at ocean islands: Perspectives from a zoned fall deposit on Ascension Island, South Atlantic. *Journal of Volcanology And Geothermal Research*, V. 327, pp 349–360
- Harto, Christopher. *Argonne Geothermal Geochemical Database v2.0*. United States: N. p., 2013. Web. doi:10.15121/1149726.
- Dyaksa D.A., Ramadhan I., Ganefianto N. (2016) Magnetotelluric Reliability for Exploration Drilling Stage: Study Cases in Muara Laboh and Rantau Dedap Geothermal Project, Sumatera, Indonesia. *Proceedings, 41st Workshop on Geothermal Reservoir Engineering*. Feb. 22–24
- Edmonds M., Mather TA, Liu EJ. (2018) A distinct metal fingerprint in arc volcanic emissions. *Nat. Geosci.* **11**, 790.
- Fournier R. O. (1999) Hydrothermal processes related to movement of fluid from plastic into brittle rock in the magmatic-epithermal environment. *Econ. Geol.* **94**, 1193–1211.
- Kouzmanov K. and Pokrovski G. S. (2012) Hydrothermal controls on metal distribution in porphyry Cu (–Mo–Au) systems. *Soc. Econ. Geol. Spec. Publ.* **16**, 573–618.
- Guillong M., Meier D.L., Allan M.M., Heinrich C.A., and Yordley B.W.D. (2008) Appendix A6: SILLS: A Matlab-based program for the reduction of laser ablation ICP-MS data of homogeneous materials and inclusions. *MAC Short Course 40: Laser-Ablation-ICP-MS in Earth Sciences: Current practices and outstanding issues*.
- Rizzo E., Giampaolo V., Capozzoli L., De Martino G., Romano G., Santilano A., Manzella A. (2022) 3D deep geoelectrical exploration in the Larderello geothermal sites (Italy), *Physics of the Earth and Planetary Interiors*, V. 329–330
- Ryan G.A., Peacock J.R., Shalev E., and Rugis J. (2013), Montserrat geothermal system: A 3D conceptual model, *Geophys. Res. Lett.*, **40**, 2038–2043
- Tattitch B. C. and Blundy J. D. (2017) Cu-Mo partitioning between felsic melts and saline-aqueous fluids as a function of XNaCleq, fO_2 , and fS_2 . *Am. Mineral.* **102**, 1987–2006.
- Uchida, T., Ogawa, Y., Takakura, S. and Mitsuhashi, Y. (2000). Geoelectrical investigation of the Kakkonda geothermal field, northern Japan. In *proceedings world geothermal congress, Tohoku-Kyushu, Japan* pp. 1893–1898.

Numerical constraints on the hydrothermal fluid evolution forming the Pirquitas Sn-Ag-Pb-Zn deposit in NW Argentina

Malte Stoltznow^{1,2}, Philipp Weis^{1,2}, Maximilian Korges¹

¹*Institute of Earth and Environmental Science, University of Potsdam, Germany*

²*GFZ German Research Centre for Geosciences, Potsdam, Germany*

Abstract. The epithermal Pirquitas Sn-Ag-Pb-Zn mine in NW Argentina is hosted in a domain of metamorphosed sediments without geological evidence for volcanic activity within a distance of about 10 km from the deposit. However, recent geochemical studies of ore-stage fluid inclusions indicate a significant contribution of magmatic volatiles. We tested different formation models by applying an existing numerical process model for porphyry-epithermal systems with a magmatic intrusion located either at a distance of about 10 km underneath the nearest active volcano or hidden underneath the deposit. The results show that the migration of the ore fluid over a 10-km distance results in metal precipitation by cooling before the deposit site is reached. In contrast, simulations with a hidden magmatic intrusion beneath the Pirquitas deposit are in line with field observations, which include mineralized hydrothermal breccias in the deposit area.

1 Introduction

Magmatic-hydrothermal systems form a variety of ore deposits at different proximities to upper-crustal hydrous magma chambers, ranging from greisenization in the roof zone of the intrusion, porphyry mineralization at intermediate depths to epithermal vein deposits near the surface (e.g. Hedenquist and Lowenstern 1994; Sillitoe 2010). Base metal zoning can extend horizontally by distances of up to 8 km, typically containing a proximal Cu-rich core region surrounded by Pb-Zn-Ag mineralization at more distal settings (Lang and Eastoe 1988; Sillitoe 2010). The physical transport processes and chemical precipitation mechanisms vary between deposit types and are often still debated. For this study, we investigated the fluid evolution from proximal to distal settings at the epithermal Pirquitas Sn-Ag-Pb-Zn Mine in NW Argentina, where the origin of the mineralizing fluids is unclear.

The Pirquitas Mine is suggested to be the southernmost of the polymetallic epithermal deposits of the Central Andean Tin Belt (CATB; Fig. 1) (e.g., Paar et al. 2000; Passamani et al. 2020) and its formation is a topic of debate. While the Peruvian and Bolivian deposits of the CATB have a clear association with Miocene magmatism (e.g., Grant et al. 1979), Pirquitas lacks a direct connection to magmatic activity. However, there is evidence from noble gas isotopes for magmatic fluid contribution to the ore fluid, which formed the Pirquitas mineralization (Desanois et al. 2019), and the presence of the Cortaderas breccia, which is

suggested to be underlain by an inferred intrusion (Slater et al. 2021).

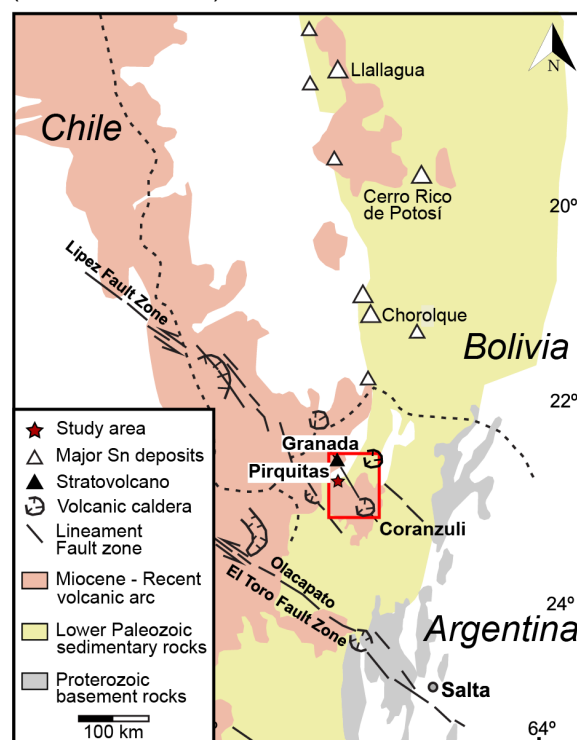


Figure 1. Map of the southern sector of the Central Andean Tin Belt with the location of the Pirquitas deposit in the southernmost part. Miocene porphyry and subvolcanic intrusions, caldera structures, major WNW-trending lineaments, and fault zones as well as the dominant host rock lithologies are shown (modified from Passamani et al. 2020).

Passamani et al. (2020) propose that a complex magmatic-hydrothermal fluid system could be fed from the nearby Granada volcano and the Coranzuli caldera, which are connected by the Lipez lineament over a distance of ~30 km (Fig. 1). This model suggests that the formation of the Pirquitas system may include ore fluids expelled from a magma reservoir underlying the Granada volcano, which would have travelled a distance of at least 8 km (Fig. 2a).

As an alternative explanation, the model infers a hidden intrusion located underneath the Pirquitas Mine (Fig. 2a). Such an intrusion would promote fluid temperatures of >500°C as suggested for the Bolivian deposits (e.g., Sugaki et al. 1988), which have, however, not been observed in Pirquitas yet,

where the maximum temperature estimate from fluid inclusion analyses is $<400^{\circ}\text{C}$ (Desanois et al. 2019).

Analyses of fluid inclusions hosted in hydrothermal vein quartz and ore minerals from the Pirquitas Mine indicate that the hydrothermal system was characterized by mixing of magmatic fluids and meteoric water (Desanois et al. 2019). This model also proposes that there might be a hidden high-grade Ag (\pm base metals) lens at depth, which may have served as a source region for later remobilization eventually forming the mineralization at Pirquitas. This interpretation is supported by noble gas analyses (Desanois et al. 2019) and the existence of hydrothermal breccias with mineralized clasts at locations near the open pit mine, which indicates that the hydrothermal system extends to greater depth and suggests that the fluid source may rather be located underneath the deposit.

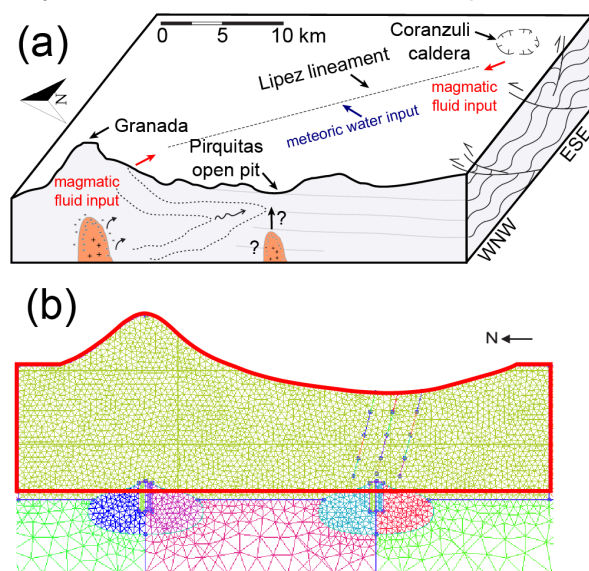


Figure 2. (a) Conceptual model showing the Lipez lineament connecting the Granada stratovolcano and the Coranzuli caldera, forming a complex magmatic-hydrothermal system with potential ore fluids either being related to the Granada volcano or to a hidden proximal intrusion at depth below the Pirquitas open-pit mine (modified from Passamani et al. 2020). (b) Excerpt of the modelling mesh approximating the geological setting including the two hypothesized magma reservoirs at about 5 km depth.

2 Methods

We use numerical simulations to test the different conceptual formation models. Based on the parametrization of Weis et al. (2012), we performed simulations testing the hydrology of mineral systems, where mineralization formed (i) at a distance of about 10 km and (ii) directly above a magmatic intrusion (Fig. 2b). Our approaches include a modelling setup with a total extension of 40×9 km. Both the stratovolcano, which rises 2 km above, and an assumed valley, which has incised to a maximum of 1 km below the ambient level, are exaggerating field observations to achieve broader

fluid transport by topography-driven groundwater flow. The geometry includes two magma reservoirs, which can be switched on and off in the model configurations for either distal (simulation 1, Fig. 3a) or proximal (simulation 2, Fig. 3b) settings.

The numerical model simulates the release of magmatic fluids from a cooling and crystallizing magma reservoir and its interaction with a dynamic permeability model for hydraulic fracturing that mimics the formation of stockwork veining, and the convection of meteoric fluids. Previous simulations have shown how the interplay of these processes self-organizes into a hydrological divide between a magmatic fluid plume at high temperatures and high pressures and a hydrothermal system with mixed magmatic-meteoric fluids at lower temperatures and pressures (for a detailed description see Weis et al. 2012).

3 Results and Interpretation

With the numerical modelling approach, we can test different formation models for the Pirquitas Deposit, which are based on geochemical (Desanois et al. 2019; Slater et al. 2021), geophysical (Soler et al. 2007) and structural geological (Passamani et al. 2020) studies. Figures 3a and b display the evolution of the hydrology after a simulation time of 15 kyrs, which represents the broadest migration of the temperature fronts.

3.1 Distal Setting

Simulation 1 includes a magma reservoir underlying a stratovolcano. The vertical extension of the stratovolcano promotes the flow of meteoric water towards greater depth suppressing the ascent of magmatic fluid, the accompanied temperature front, and the formation of domains with bulk salinities of >40 wt% NaCl eq. (Fig. 3a). Although fluids containing bulk salinities up to 20 wt% NaCl eq. can travel distances of up to 10 km and thus reach the site of the Pirquitas mineralization, fluid temperatures in this area are limited to $<100^{\circ}\text{C}$.

Based on simulation results from Stoltnow et al. (2023), which used base metal solubilities reported by Kouzmanov and Pokrovski (2012), this thermal evolution implies that the area in which base metals may accumulate to economic values is restricted to the domain directly overlying the injection point. In this domain, the pore fluid factor is below 0.7 (beginning of the hydrostatic pressure regime) and extends to the 200°C isotherm (Fig. 3a). Consequently, the simulation representing a distal source for the fluids and metals may rather produce an economic mineralization underneath the Granada volcano at a distance of some 10 km, but unlikely produced the primary mineralization at Pirquitas.

3.2 Proximal Setting

In contrast, simulation 2 tests the proximal setup with an inferred magma reservoir right beneath the open-pit mine of the Piriquitas Deposit (Fig. 3b). The vertical depression located above the magma chamber causes a strong inflow of meteoric fluids, which focuses ascending magmatic fluids and the accompanying temperature front. Although the domain right beyond the hydrological divide is characterized by bulk salinities >80 wt% NaCl eq. due the local and temporal saturation of the fluids in solid halite, the overall migration of saline fluids (>0 wt% NaCl eq.) is restricted to the focused region between the hydrological divide and the Piriquitas open pit (Fig. 3b).

Similarly, the area of potential economic metal enrichment is more focused (~2 km horizontal extension) compared to the distal setting (~4 km horizontal extension) and reaches shallower depths of ~2 km. Furthermore, higher bulk salinities along the outer part of the hydrological divide could support an overall higher metal enrichment potential (Stoltnow et al., 2023) and higher ore grades. The modelled depth level, temperature, salinity, and mixed origin (magmatic and meteoric) of hydrothermal ore formation are in agreement with recent findings (Desanois et al. 2019; Slater et al. 2021). In addition, the modelled transition from lithostatic to hydrostatic fluid pressures at the hydrological divide would be in line with the presence of a hydrothermal breccia below the Piriquitas Mine.

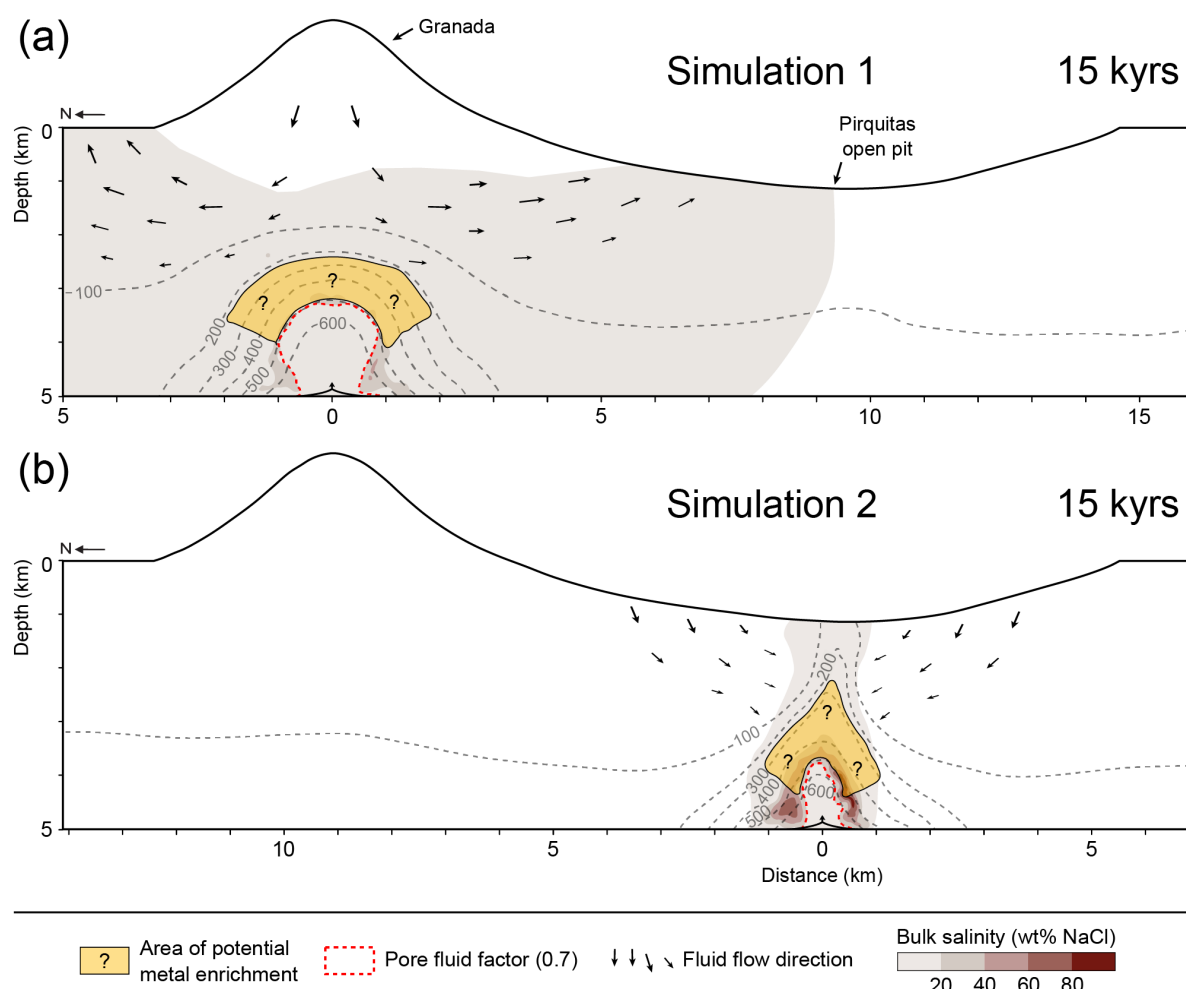


Figure 3. Bulk fluid salinity (colours) and isotherms (dashed lines) of the modelled Piriquitas hydrothermal system after 15 kyr with a magma reservoir beneath the Granada stratovolcano (a) and beneath the Piriquitas deposit (b). The extent of the areas with potential and economic metal enrichment is based on modelling results in Stoltnow et al. (2023). The pore fluid factor (fluid pressure divided by lithostatic pressure) of 0.7 indicates the transition from near-hydrostatic to near-lithostatic fluid pressures. Arrows at a depth of 5 km refer to the fluid injection location at the cupola region of the magma reservoir.

4 Discussion and Conclusions

Our modeling results show that fluids necessary to form Piriquitas-like mineralization may not be

transported farther than 2-3 km in both horizontal and vertical directions from the porphyry region of the magma reservoir (Fig. 3b). Later remobilization can lead to further transport and reprecipitation of

base metals at further distances (Stoltnow et al. 2023), but is unlikely to be permissive with the hypothesis of the Pirquitas mineralization being fed by a magma reservoir underneath the Granada stratovolcano (e.g. Passamani et al. 2020).

Instead, the simulations rather highlight the necessity of an intrusion underneath or in closer proximity to a Pirquitas-like mineralization, which has also been proposed previously (Desanois et al. 2019; Passamani et al. 2020; Slater et al. 2021). These findings are supported by the occurrence of hydrothermal breccias at both the Pirquitas Deposit and the Cortaderas Deposit some 500 m north of the Pirquitas open pit, which is proposed to be underlain by a hidden intrusion (Slater et al. 2021).

The simulations rely on a number of simplifications. In this reconnaissance study, we reduced the geological complexity to investigate first-order controls on the ore-forming hydrothermal system. To obtain a lateral transport by 10 km from the cupola region of the magma reservoir, the model required a significant topographic gradient from the volcano summit to the deposit location as a driving force for the convection of meteoric fluids. However, the same process also leads to strong cooling of the metal-bearing magmatic fluids. Further simulations could include more geological heterogeneity in the permeability structure, e.g., by including fault zones or low-permeability lithocaps, which may support lateral fluid migration with less cooling.

In general, the simulations show that the quantification of first-order controls on the physical hydrology at the porphyry-epithermal transition can be instrumental to understand the ore-forming system beyond the deposit scale.

Acknowledgements

This project is part of the international research training group StRATEGy at the University of Potsdam (Germany) and was funded jointly by the German Research Foundation (DFG) and the State of Brandenburg, Germany.

References

- Desanois L, Lüders V, Niedermann S, Trumbull RB (2019) Formation of epithermal Sn-Ag-(Zn) vein-type mineralization at the Pirquitas deposit, NW Argentina: Fluid inclusion and noble gas isotopic constraints. *Chem Geol* 508:78–91.
- Grant JN, Halls C, Avila Salinas W, Snelling NJ (1979) K-Ar ages of igneous rocks and mineralization in part of the Bolivian tin belt. *Econ Geol* 74:838–851. <https://doi.org/10.2113/gsecongeo.74.4.838>
- Hedenquist JW, Lowenstern JB (1994) The role of magmas in the formation of hydrothermal ore deposits. *Nature* 370: 519–527
- Kouzmanov K, Pokrovski G (2012) Hydrothermal Controls on Metal Distribution in Porphyry Cu (-Mo-Au) Systems. SEG Special Publication 16:573–618
- Lang JR, Eastoe CJ (1988) Relationships between a porphyry Cu-Mo deposit, base and precious metal veins and Laramide intrusions, Mineral Park, Arizona. *Econ Geol* 83:551–567. <https://doi.org/10.2113/gsecongeo.83.3.551>
- Paar WH, Miletich R, Topa D, et al (2000) Suredaite, PbSnS₃, a new mineral species, from the Pirquitas Ag-Sn deposit, NW-Argentina: mineralogy and crystal structure. *Am Miner* 85:1066–1075. <https://doi.org/doi:10.2138/am-2000-0723>
- Passamani FM, Bongiolo EM, Nepomuceno de Oliveira F, Neumann R (2020) Geology and structural controls of the Ag–Sn–Zn Pirquitas deposit, northwestern Argentina. *J South Am Earth Sci* 100:102537. <https://doi.org/https://doi.org/10.1016/j.jsames.2020.102537>
- Sillitoe RH (2010) Porphyry copper systems. *Econ Geol* 105: 3–41 <https://doi.org/10.2113/gsecongeo.105.1.3>
- Slater ET, Kontak DJ, McDonald AM, Fayek M (2021) Origin of a multi-stage epithermal Ag-Zn-Pb-Sn deposit: the Miocene Cortaderas breccia body, Pirquitas mine, NW Argentina. *Miner Depos* 56:381–406. <https://doi.org/10.1007/s00126-020-00976-8>
- Soler MM, Caffee PJ, Coira BL, et al (2007) Geology of the Vilama caldera: A new interpretation of a large-scale explosive event in the Central Andean plateau during the Upper Miocene. *J Volcanol Geotherm Res* 164:27–53. <https://doi.org/https://doi.org/10.1016/j.jvolgeores.2007.04.002>
- Stoltnow M, Weis P, Korges M (2023) Hydrological controls on base metal precipitation and zoning at the porphyry-epithermal transition constrained by numerical modeling. *Sci Rep* <https://doi.org/10.1038/s41598-023-30572-5>
- Sugaki A, Kojima S, Shimada N (1988) Fluid inclusion studies of the polymetallic hydrothermal ore deposits in bolivia. *Miner Depos* 23:9–15. <https://doi.org/10.1007/BF00204221>
- Weis P, Driesner T, Heinrich CA (2012) Porphyry-Copper Ore Shells Form at Stable Pressure-Temperature Fronts Within Dynamic Fluid Plumes. *Science* 338:1613–1616. <https://doi.org/10.1126/science.1225009>

Ore Mineral Textures of the Midas Low-Sulfidation Epithermal Deposit: Implications for Ore-Forming Processes

Lauren R. Zeeck¹, Thomas Monecke¹, T. James Reynolds^{1,2}, Katharina Pfaff¹, Nigel M. Kelly³

¹Department of Geology and Geological Engineering, Colorado School of Mines, Golden, CO, USA

²FLUID INC., 1401 Wewatta St. #PH3, Denver, Colorado 80202, USA

³Bruker Nano Analytics, 415 N Quay Street, Kennewick, WA 99336, USA

Abstract. Ore and gangue mineral textures of high-grade quartz vein material from the middle Miocene Midas Au-Ag deposit near Elko, Nevada, were studied to identify the processes that resulted in precious metal enrichment at this low-sulphidation epithermal deposit. Ore minerals in high-grade samples occur as dendritic aggregates within distinct ginguero bands. The delicate ore mineral dendrites are hosted by mosaic quartz that appears to have formed through recrystallisation of a microspherical silica precursor. Based on the comparison to modern geothermal systems, this microspherical silica precursor is interpreted to have been gel-like opal-A_G originally. The occurrence of ore mineral dendrites and microspherical opal-A_G suggests that mineral precipitation at Midas occurred at far-from-equilibrium conditions. The findings of this study are consistent with previous models linking high-grade precious metal enrichment in low-sulfidation epithermal deposits to episodic flash vaporisation of the hydrothermal liquids within hundreds of meters from the paleosurface.

1 Introduction

The Miocene Midas low-sulfidation epithermal deposit located along the Northern Nevada Rift (NNR) in the Battle Mountain-Eureka trend in northeast Nevada comprises a complex of high-grade Au-Ag veins. Previously known as the Ken Snyder mine, underground mining at Midas yielded over 2.2 million ounces of gold and 27.6 million ounces of silver from 1998 to 2017, making it the largest known producer in this region (Leavitt et al. 2004; Thompson 2017).

Previous studies on the ore mineralogy of the Midas deposit focus on the multiple stages of mineral deposition which formed the main veins, namely the Colorado Grande and Gold Crown veins. Ore minerals include naumannite, aguilarite, and electrum with minor amounts of native silver and fischerite, plus rare lead-, copper-, and iron-selenide minerals (Goldstrand and Schmidt 2000).

The present contribution reports on findings from the study of fourteen high-grade vein samples from the Colorado Grande, Gold Crown, Snow White, Discovery, and Sleeping Beauty veins. The results of this petrographic study demonstrate that ore minerals at Midas were deposited under chemical disequilibrium conditions established during flash vaporisation of the hydrothermal liquids and that these conditions propagated down to at least ~500 m depth below surface.

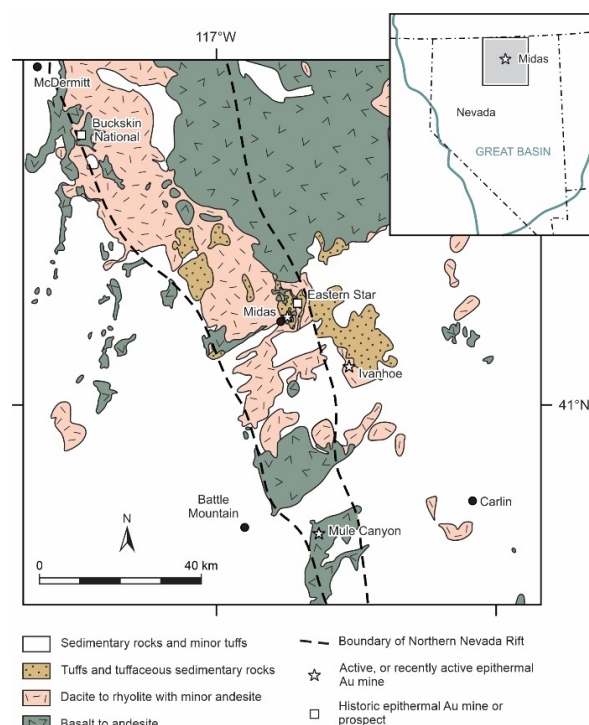


Figure 1. Regional geology and location of the Northern Nevada Rift. The map also highlights the locations of major low-sulfidation epithermal precious metal occurrences (modified from Leavitt et al. 2004).

2 Regional geology

The Midas deposit is located in the Midas mining district and occurs along the eastern margin of the NNR (Fig. 1). The NNR is a north-northwest trending lineament defined by a positive aeromagnetic anomaly that extends ~500 km from south-eastern Nevada to the Nevada-Oregon border (John et al. 2000). Formation of the NNR is related to regional extension and subsequent emplacement of mafic magmas related to the Yellowstone hot spot (John et al. 2000).

The Midas deposit is coeval with Miocene bimodal volcanism that occurred along the NNR from 16.5 to 14.7 Ma (Zoback et al. 1994; John et al. 2000; Leavitt et al. 2004). The Midas volcanic assemblage includes felsic ash-flow tuffs, flows, domes, and volcanoclastic sedimentary deposits, as well as mafic sills and dikes (Goldstrand and Schmidt 2000; Leavitt et al. 2004).

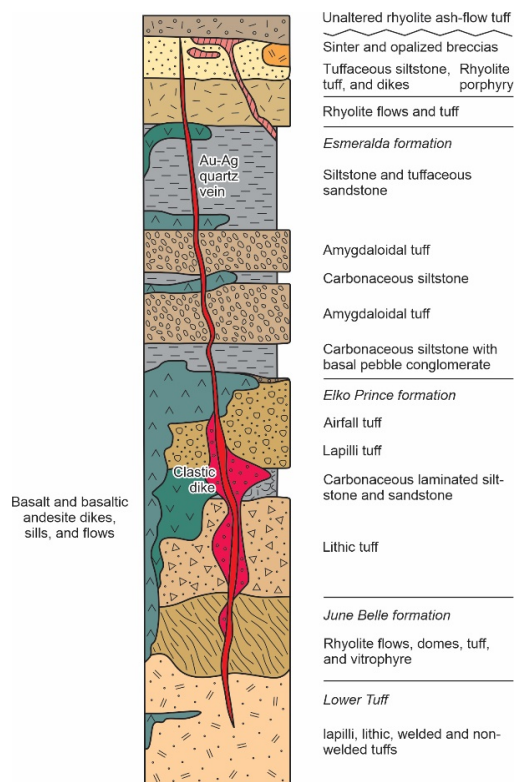


Figure 2. Generalized stratigraphic section of the Midas deposit. Ore is primarily confined to steeply dipping quartz veins (shown in red), which crosscut all units below the unaltered rhyolite ash-flow unit (modified from Goldstrand and Schmidt 2000; Leavitt et al. 2004).

Host rocks to the Midas deposit consist of four primary stratigraphic units, the Lower Tuff, June Belle, Elko Prince, and Esmeralda formations, that extend to a depth of ~1.5 km below the present-day surface (Leavitt et al. 2004). Mineralized quartz veins are steeply dipping and crosscut all principal stratigraphic units (Fig. 2). These are topped by an unaltered rhyolite ash-flow tuff.

3 Materials and methods

Representative vein samples were collected from twelve drill holes (C96-0008, C96-0011, MKC-0232, MKC-0244, MKC-0266, MKC-0267, MSC-0158, MSC-0165, MSC-0171, and RG-0038, RG-0096, and RG-0100) at Hecla's core storage near Elko, Nevada. Initially, the distribution of major and trace elements in cut hand specimens and billets was mapped using a bench-top Bruker M4 Tornado μ XRF. The spot size of acquisition was ~25 μ m. Element mapping was conducted at a line scan spacing of 50 μ m, and a data acquisition dwell time of 50 ms per pixel. Following data acquisition, X-ray peaks were checked manually.

Following μ XRF analysis, single-sided polished 80- μ m-thick sections were prepared. These were studied in transmitted and reflected light using an Olympus BX51 microscope to document ore and gangue mineral textures.

Following optical petrography, ore mineralogy was determined using automated scanning electron microscopy at the Colorado School of Mines. Samples were loaded into the TESCAN-VEGA-3 Model LMU VP-SEM platform, which is controlled by the TIMA3 software package. Four energy dispersive X-ray (EDX) spectrometers acquired spectra with a beam stepping interval of 25 μ m, an accelerating voltage of 20 keV, and a beam intensity of 17. Results output by the TIMA software allows a compositional map to be generated and composition assignments to be grouped appropriately. In addition to automated scanning electron microscopy, a TESCAN MIRA3 LMH Schottky field emission-scanning electron microscope equipped with a single-crystal YAG backscatter electron detector was used to study the ore mineralogy. Imaging was performed at a working distance of 10 mm and an accelerating voltage of 15 kV. Semiquantitative chemical analyses of minerals were performed by energy-dispersive X-ray spectroscopy using an attached Bruker XFlash 6|30 silicon drift detector.

4 Ore mineral petrography

Veins samples from the Midas low-sulphidation epithermal deposit are typically massive, crustiform, or brecciated. Bonanza-grade samples contain colloform bands of quartz of varying colour, texture, grain size, and thickness. Typically, quartz is white to translucent. Many vein samples contain adularia that is milky-white in colour and commonly is intergrown with quartz. Quartz pseudomorphs of calcite are common.

In the bonanza-grade vein samples from Midas, ore minerals primarily occur in specific colloform bands within the crustiform veins or are distributed irregularly between the clasts and matrix of brecciated samples. Ore minerals typically occur as dendritic aggregates (Fig. 3a). Element maps created by μ XRF show that elevated Ag concentrations typically correlate with Se-enrichment. Bands of high-grade Ag sometimes contain high Au concentrations. However, there is no direct correlation between Ag and Au at the microscale (Figs. 3b, c).

Au and Ag are present primarily as naumannite, aguilarite, and electrum in the samples investigated. Sulfoselenides are light grey, weakly anisotropic, and have a low reflectance with a metallic or adamantine lustre. The Ag sulfoselenides can be intergrown with minor electrum. Electrum aggregates range from 15 to 40 μ m in size. They are golden to whitish in reflected light.

The ore mineral dendrites are hosted by microcrystalline quartz (Fig. 3d). The microcrystalline quartz appears to have formed through recrystallisation of a silica precursor. In least-recrystallized areas, the quartz shows a mosaic texture in crossed-polarized light whereby individual quartz grains have irregular and inter-

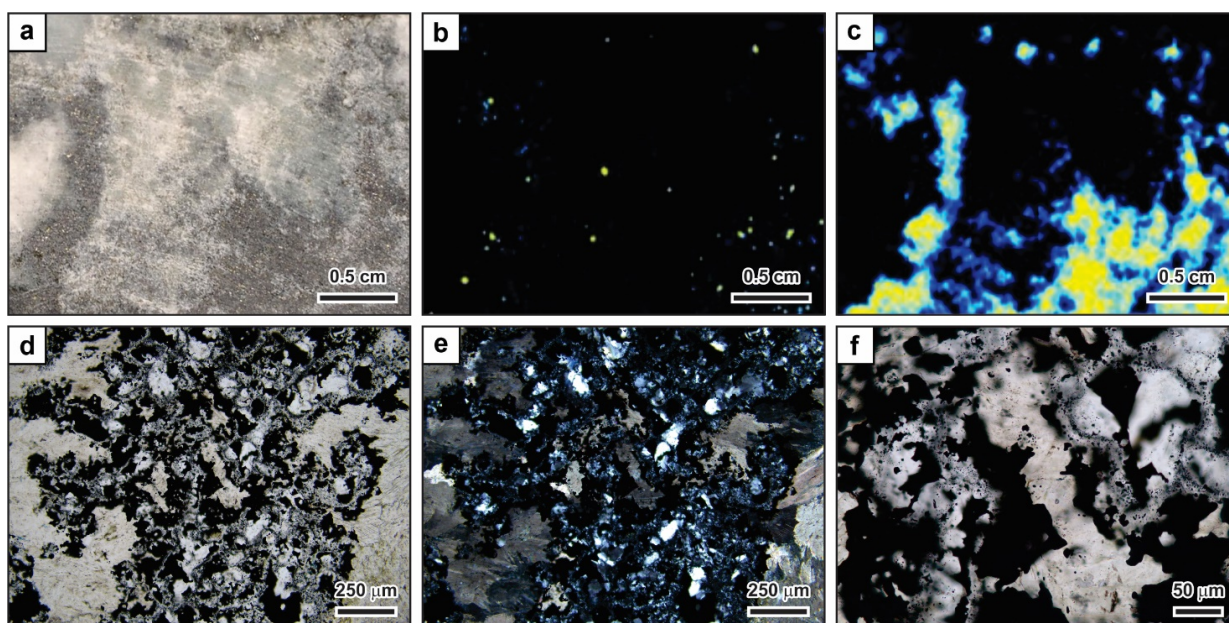


Figure 3. Microtextures and trace element maps of a representative quartz vein sample from drill hole MKC-0232 at the Midas deposit, Nevada. **a** RGB sample image of the scanned billet MKC-0232G (drill hole depth of 349 m). **b** μ XRF element map of Au count rates. Individual gold grains are scattered. **c** μ XRF element map of Ag count rates. Ag is present in higher quantities than Au and forms aggregates that are dendritic in nature. **d** Photomicrograph of ore mineral dendrite. Plane-polarized light. **e** Same field of view showing the mosaic texture of the quartz hosting the ore mineral dendrite. Crossed-polarized light. **f** High-magnification image of ore mineral grains in contact with the mosaic quartz. The recrystallisation of the silica matrix locally resulted in the formation of small euhedral quartz crystals.

penetrating grain boundaries and differ in orientation (Fig. 3e). Where intensely recrystallized, the quartz grains have polygonal shapes. At the microscale, the ore minerals are in contact with the recrystallized microcrystalline quartz. In some cases, the quartz forming the matrix is overgrown by small euhedral quartz crystals (Fig. 3f). Ore minerals also occur as encapsulated inclusions in the quartz (Fig. 3f).

5 Discussion and conclusions

The textural observations at Midas are similar to those in other low-sulphidation epithermal deposits. Previous research suggests that the mosaic quartz that is now present in the vein samples at Midas formed through recrystallisation of a noncrystalline silica precursor. This precursor phase was originally microspherical in nature, similar to opal-A_G, which forms a common scale in geothermal systems (Moncada et al. 2012; Taksavas et al. 2018; Tharalson et al. 2019; Zeeck et al. 2021; Monecke et al. 2023).

It has been proposed that ore mineral dendrites form in open spaces through colloidal metal transport (Saunders 1990). However, recent studies by Monecke et al. (2023) on the McLaughlin low-sulphidation epithermal deposit in California have shown that ore mineral dendrite formation took place within bands of noncrystalline silica gel. The gel provided a protective layer within which the ore mineral dendrites may grow through diffusion and advection processes (Monecke et al. 2023). The dendrites at Midas likely formed in the same manner. The delicate ore mineral dendrites are

encapsulated by the mosaic quartz that formed through recrystallisation of the microspherical silica precursor. The colloform silica bands appear to have formed first.

Previous workers have shown that deposition of the noncrystalline silica forming the matrix to the ore mineral dendrites required the hydrothermal liquids to periodically reach extreme supersaturation. Such high degrees of silica supersaturation were most likely achieved through vapor loss associated with catastrophic pressure drops accompanying hydrothermal eruptions on the surface. Following flash vaporisation of hydrothermal liquids, ore mineral dendrites grew within the newly deposited silica gel from the metal-laden hydrothermal liquids. Repetition of this process through time would explain that the colloform veins in low-sulphidation epithermal deposits contain multiple, discrete ginguero bands (Moncada et al. 2012; Taksavas et al. 2018; Tharalson et al. 2019; Zeeck et al. 2021; Monecke et al. 2023).

The samples from the Midas low-sulphidation epithermal deposit provide important context for understanding the formation of high-grade veins in the epithermal environment. Samples investigated containing ore mineral dendrites in ginguero bands were sampled at depths of up to ~500 m below the surface. This implies that flash vaporisation of the hydrothermal liquids along the controlling structures must have occurred to significant depths below the paleosurface. As such, bonanza-grade ore zones in low-sulphidation deposits formed through flash vaporisation may reach to greater depths than predicted by the generally accepted model of epithermal ore formation (Buchanan 1981).

Acknowledgments

John Marma and Hecla Mining Company are thanked for their help in procuring samples. High Mesa Petrographics conducted the thin section preparation. We thank Quinton Hennigh for his insights into the geology of epithermal deposits.

References

- Buchanan LJ (1981) Precious metal deposits associated with volcanic environments in the southwest Ariz Geol Soc Dig 14:237–262
- Goldstrand PM, Schmidt KW, (2000) Geology, mineralization, and ore controls at the Ken Snyder gold-silver mine, Elko County, Nevada. In: Cluer JK, Price JG, Struhsacker EM, Hardyman RF, Morris CL (eds) *Geology and Ore Deposits 2000: The Great Basin and Beyond*. Geol Soc Nev Symp Proc, pp 265–287
- John DA, Wallace AR, Ponce DA, Fleck RB, Conrad JE (2000) New perspectives on the geology and origin of the northern Nevada rift. In: Cluer JK, Price JG, Struhsacker EM, Hardyman RF, Morris CL (eds) *Geology and Ore Deposits 2000: The Great Basin and Beyond*. Geol Soc Nev Symp Proc, pp 127–154
- Leavitt ED, Spell TL, Goldstrand PM, Arehart GB (2004) Geochronology of the Midas low-sulfidation epithermal gold-silver deposit, Elko county, Nevada. *Econ Geol* 99:1665–1686
- Moncada D, Mutchler S, Nieto A, Reynolds TJ, Rimstidt JD, Bodnar RJ (2012) Mineral textures and fluid inclusion petrography of the epithermal Ag–Au deposits at Guanajuato, Mexico: Application to exploration. *J Geochem Explor* 114:20–35
- Monecke T, Reynolds TJ, Taksavasu T, Tharalson ER, Zeeck LR, Guzman M, Gissler G, Sherlock R (2023) Natural growth of gold dendrites within silica gels. *Geology* 51:189–192
- Saunders JA (1990) Colloidal transport of gold and silica in epithermal precious-metal systems: Evidence from the Sleeper deposit, Nevada. *Geology* 18:757–760
- Taksavasu T, Monecke T, Reynolds TJ (2018) Textural characteristics of noncrystalline silica in sinters and quartz veins: Implications for the formation of bonanza veins in low-sulfidation epithermal deposits. *Minerals* 8:331
- Tharalson ER, Monecke T, Reynolds TJ, Zeeck L, Pfaff K, Kelly NM (2019) The distribution of precious metals in high-grade banded quartz veins from low-sulfidation epithermal deposits: Constraints from μ XRF mapping. *Minerals* 9:740
- Thompson W (2017) Update of geology within the Midas Au/Ag mining district, Elko County, Nevada. *Geol Soc Nev Newsl* 33:3
- Zeeck LR, Monecke T, Reynolds JT, Tharalson ER, Pfaff K, Kelly NM, Hennigh QT (2021) Textural characteristics of barren and mineralized colloform quartz bands at the low-sulfidation epithermal deposits of the Omu Camp in Hokkaido, Japan: Implications for processes resulting in bonanza-grade precious metal enrichment. *Econ Geol* 116:407–425
- Zoback ML, McKee EH, Blakely RJ, Thompson GA (1994) The northern Nevada rift: Regional tectono-magmatic relations and middle Miocene stress direction. *Geol Soc Am Bull* 106:371–382

Spodumene textural variations in a deformed LCT-type pegmatite. A case study from the Musha-Ntungwa area, Rwanda

Jolan Acke^{1,4}, Daniel Kwizera³, Alastair Goodship³, Stijn Dewaele⁴, Renata Barros⁵, Christian Burlet⁵, Simon Nachtergaele⁶, Anouk Borst^{1,2}

¹ Department of Earth and Environmental Sciences, KU Leuven, Leuven-Heverlee, Belgium

² Geodynamics and mineral resources, Royal Museum for Central Africa, Tervuren, Belgium

³ PIRAN Rwanda Ltd, St Peters Port, Guernsey, UK

⁴ Mineralogy & Petrology Research Group, University of Ghent, Belgium

⁵ Geological Survey of Belgium, Brussels, Belgium, Royal Belgian Institute of Natural Sciences, Brussels, Belgium

⁶ Department of Urban and Environmental Engineering, University of Liège, Liège, Belgium

Abstract. Spodumene, the main lithium-bearing mineral of the Musha-Ntungwa LCT-type pegmatite deposit in Rwanda displays a variety of textures. Two distinct groups are identified based on grain size, habit, textural intergrowth features, optical properties and associated mineral assemblages. Contrary to the uniform euhedral primary group 1 spodumene with thin rims of symplectitic quartz-spodumene intergrowths (SQUI), group 2 spodumenes display a variety of textures which are linked to primary spodumene deformation, recrystallisation and alteration. Under shear stress, spodumene tends to deform in a brittle way causing large grains to break down along weak spots, such as cleavage planes. In addition, fluid influx along grain boundaries and cleavage planes can modify the spodumene composition and texture. LIBS analyses confirmed that lithium is leached from primary spodumene crystals along grain boundaries and cleavage planes. In this study, the interplay between both mechanisms is investigated to determine the (re)distribution of lithium.

1 Introduction

Granitic pegmatites are complex coarse-grained rocks that generally form from the last bits of a solidifying granitic melt (London 2018). In that process, different economically valuable metals such as lithium, tantalum, niobium and tin can be concentrated due to fractional crystallisation and hydrothermal processes (e.g. Hulsbosch et al. 2016). Understanding the genesis, emplacement and mineralisation style of these pegmatites is thus a crucial step in their potential exploitation.

Lithium-cesium-tantalum (LCT) pegmatites in the Karagwe-Ankole and Kibara Mesoproterozoic belts in Central Africa are typically associated with granitic magmatism during the early Neoproterozoic (Fernandez-Alonso et al. 2012). Here, we study LCT-type pegmatites from the Musha-Ntungwa area in Eastern Rwanda, an area that is currently exploited for coltan- and cassiterite-bearing kaolinised pegmatite and cassiterite-rich quartz veins through shallow (up to 50m) underground mining operations. A recent drilling campaign by the mining company discovered lithium enrichment in fresh to moderately weathered spodumene pegmatites at depths between 100-400m. These unique samples

provide a rare insight in the mineralisation, deformation and alteration style of spodumene pegmatites and the associated distribution of lithium within a potential high-grade deposit.

2 Methods

Samples were taken from fresh unweathered to medium weathered pegmatite drill core, from depths between 150 and 400m. A total of 40 thin sections and corresponding slabs were prepared. Microscopic examination consisted of petrographic microscopy and cold cathodoluminescence (CL) microscopy at KU Leuven. A Tescan field emission gun scanning electron microscope (FEG-SEM) was operated with a Tescan Back-scatter electron detector (BSE) and an Oxford Instruments energy-dispersive X-ray spectroscopy detector (EDX) at KU Leuven, to compose high-resolution BSE images and detailed elemental maps. Operating parameters to obtain the BSE images were a working distance of 10 mm, an accelerating voltage of 15 Kev and a beam current of 300 pA. Operating parameters to produce elemental maps were a working distance of 15 mm, an accelerating voltage of 20 Kev and a beam current of 10 nA. Laser Induced Breakdown Spectroscopy (LIBS) was carried out at the Geological Survey of Belgium to map the lithium distribution (Figure 4). The device is equipped with a compact pulsed diode-pumped Nd:YAG laser and 2 spectrometers: a 4-channel Avantes Avaspec EVO 4096CL with covering wavelength range of 200-572 nm and 0.07-0.09 nm spectral resolution, and a single channel Avantes Avaspec EVO 2048CL, with a covering wavelength range of 570-686 nm and 0.18 nm spectral resolution. Laser spot size is 100 µm. A collection of standards were measured to ensure peak intensities are within 0.1 nm of standard values (Kramida et al. 2019).

3 Spodumene textures

Based on petrographic observations, the spodumene from Musha-Ntungwa is subdivided in two major groups. The first group is characterised by large spodumene crystal with uniform grain size

(c-axis length ranges usually between 2-5 cm), an elongated, eu- to subhedral crystal habit, with a narrow rim of droplet-like quartz intergrowths on the margin of the crystal (Figure 1A). The crystals display characteristic simple twinning and two cleavages, with planes intersecting at an angle of approximately 90°.

The second group of spodumene crystals, which are much smaller in size, exhibit a variety of textures. On the contact with group 1 spodumene crystals, thin spodumene needles are sometimes observed and intergrown with quartz. This quartz-spodumene assemblage is almost exclusively observed in contact with feldspar, mostly albite, and to a lesser extent with microcline and sometimes muscovite. The needles are oriented more or less orthogonal to the group 1 spodumene grain boundary (Figure 1B, 2B). Solitary spodumene needles or clusters of needles also occur within the matrix, spatially separated from group 1 spodumene crystals. Secondly, subhedral spodumene grains, often with clearly visible cleavage planes, are observed as foliated ribbons, intergrown with fine quartz grains and interstitial anhedral apatite (Figure 1C). A third variety of group 2 spodumene occurs as irregular crystals with a variety of shapes, distinctly grouped together (Figure 2A). Intermediate textures of these three endmember groups are also observed. Figure 2 shows these different types of textures with cold CL microscopy.

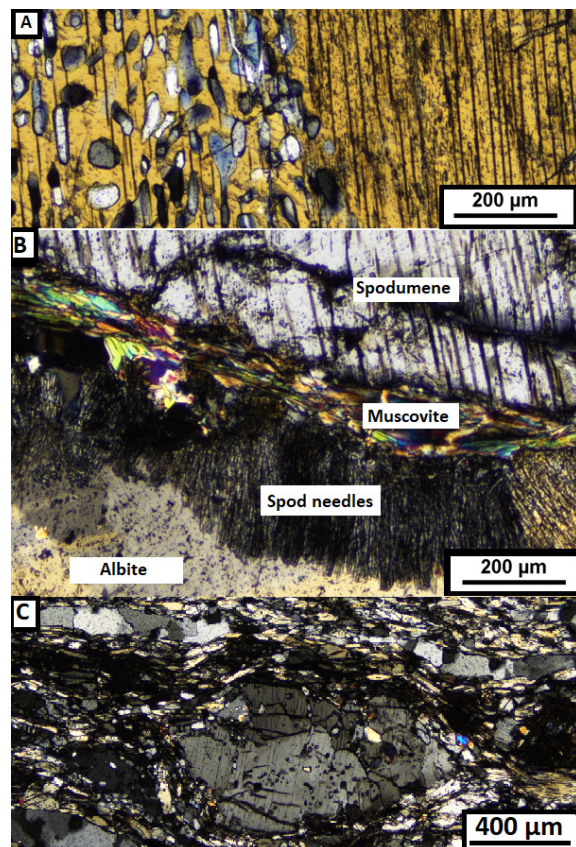


Figure 1. Overview of textural variations seen in association with large spodumene crystals. (A) Droplet symplectite of quartz-spodumene at the edge of the crystal. (B) Needle-like spodumene (spod needles) intergrown with quartz at spodumene border, surrounded by albite. (C) Spodumene fish surrounded by fine-grained foliated spodumene-quartz matrix, quartz ribbons and interstitial apatite.

4 Deformation structures

Different major minerals display typical deformation microstructures. Quartz grains within the matrix are often small and show traces of major ductile deformation, with pronounced lobate grain boundaries, indicative of elevated temperatures (Stipp et al. 2002). In addition, larger quartz grains show undulose and chessboard extinction. In the pegmatite zones with the highest degree of deformation observed, monomineralic quartz ribbons are present (Figure 1C, 3). Muscovite often defines the foliation in a sample, indicated by thin bands of stretched muscovite, with curved cleavage and 'mica fish'. Albite is mostly subhedral and displays intracrystalline deformation patterns, such as deformation twins and bookshelf sliding (Passchier and Trouw 2005).

Deformed spodumene crystals of both group 1 and group 2 can be observed. Large spodumene crystals behave in a more brittle way, as indicated by kinked spodumene twins and 'spodumene fish', with smaller group 2 spodumene grains in the strain cap area and recrystallised quartz in the strain shadow area (Figure 1C, 3). Similar to albite, large spodumene crystals display bookshelf sliding or micro-fracturing (Passchier and Trouw 2005). The mica fish, quartz ribbons, albite deformation twins and spodumene fish are all indicative of intense shear deformation, occurring during or shortly after pegmatite emplacement and crystallisation.

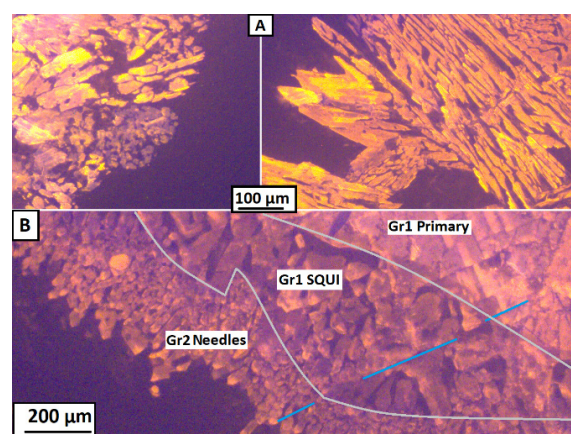


Figure 2. Cold cathodoluminescence microscopy images indicating textural variations of spodumene. (A) Group 2 spodumene textural variations. (B) Textural variation at the border of a large spodumene grain. Blue line indicates continuation of a cleavage plane from group 1 (primary crystal and SQUI) to group 2 spodumene (needles).

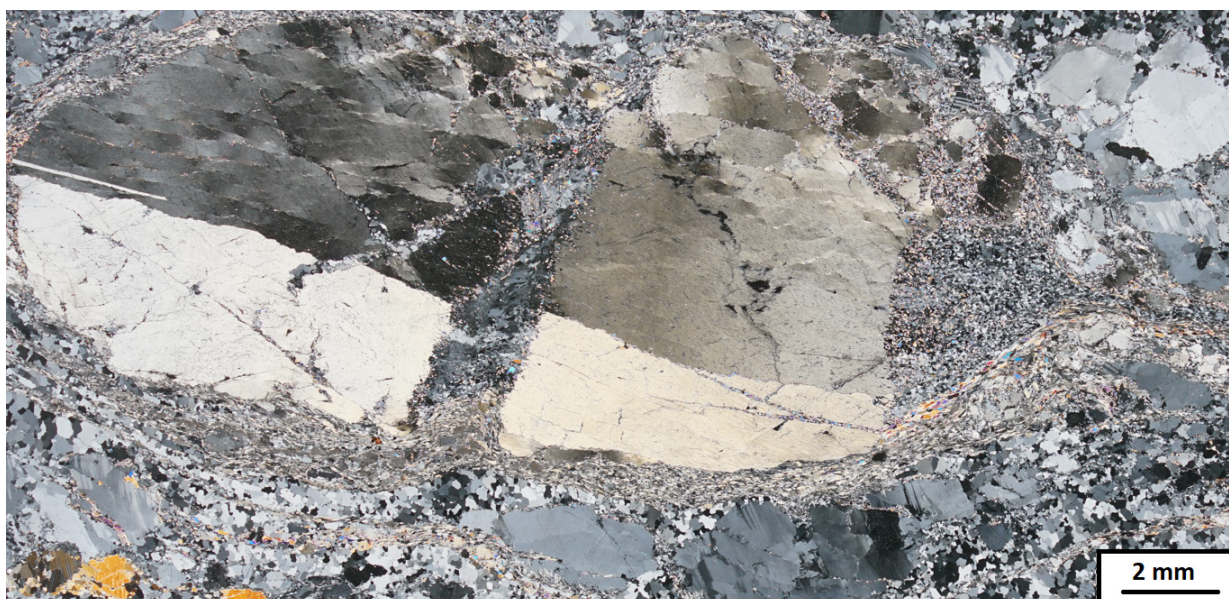


Figure 3. Overview of a thin section displaying a portion of a deformed pegmatite zone. The central spodumene 'fish' shows bookshelf sliding and is surrounded by a matrix of fine-grained spodumene, quartz and apatite. Primary albite grains show deformation twins.

5 Implications for lithium distribution

Using SEM-EDX analyses on the different textural varieties of spodumene, major elemental ratios of Si and Al appear to be identical, and no other major elements are detected. However, minor, trace- and major light elements cannot be measured using this technique. In order to map lithium distributions within the various spodumene textures, we carried out preliminary LIBS analyses. Figure 4 shows an overview map of a small core sample consisting of a moderately altered large, elongated spodumene grain, displayed as a lithium heat map. The spodumene grain is surrounded by albite and quartz. This heat map shows that lithium concentrations near cracks and cleavage planes are significantly lower (purple and dark blue colours) than in the center of the crystal (yellow-red colours). This suggests that lithium was partially leached from the crystal, whereby the cleavage planes, cracks and the external grain boundary provided fluid pathways for lithium to be disseminated. The leaching of lithium from spodumene is further evidenced by increased lithium concentrations in albitised zones near remnant spodumene grains.

6 Discussion

The largest spodumene crystals, belonging to group 1, occur in zones of the pegmatites showing the lowest degree of deformation. These large uniform crystals are considered to be of primary magmatic-hydrothermal origin. The quartz-spodumene boundary intergrowth that occurs on the boundary of group 1 spodumene crystals, as illustrated in Figure 1A and referred to as 'droplet symplectite SQUI', is also considered a primary growth feature. This is supported by the continuous

cleavage from the large spodumene crystal into the SQUI droplet symplectite (Figure 1A). Group 2 spodumene has clearly crystallised later, however still strongly spatially associated with the large group 1 spodumene crystals. This is evidenced by the continuation of cleavage planes from group 1 to group 2 spodumene crystals as shown in Figure 2B. The wide variety of textural variations in group 2 is proposed to be due to the interplay between deformation mechanisms and fluid-assisted recrystallisation and alteration or overgrowth of primary spodumene. Alongside secondary spodumene, observed replacement and overgrowing products include albite, muscovite and apatite. As such, group 2 spodumene-quartz needles are the result of intense recrystallisation of primary spodumene. In an early stage, displayed in Figure 1B, recrystallisation only affected the margins of the large spodumene crystals whereas in a more progressive stage, as visualised in Figure 2A, large spodumene grains are completely replaced by group 2 spodumene. Here, spodumene cleavages likely acted as fluid pathways inducing primary spodumene breakdown and replacement along these weaker zones. This is manifested in the precipitation of secondary albite and muscovite within opened spodumene cleavages.

In the most intensely sheared and deformed zones, small elongated spodumene grains presumably formed from larger grains deformed in a brittle way, breaking apart along their main c-axis cleavage planes. These small spodumene grains inherited features (remnant cleavage) from their 'ancestor' large spodumene grains.

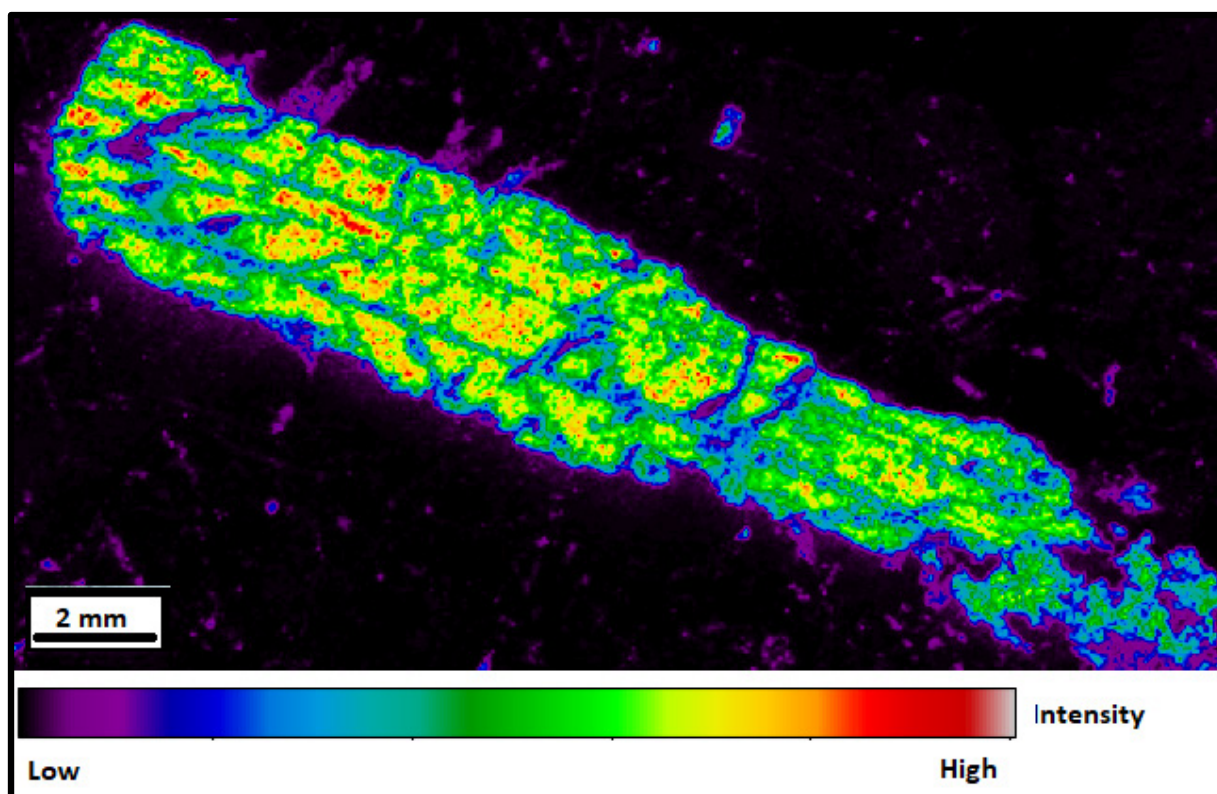


Figure 4. LIBS Lithium heat map of an elongated spodumene grain surrounded by albite.

7 Conclusions

The LCT-type pegmatite deposits in the Musha-Ntunga area in Rwanda offer a unique insight in the mineralisation, high temperature deformation and subsolidus alteration of a spodumene-rich pegmatite system. Based on grain size, two groups of spodumene are distinguished. Group 1 spodumene consists of large, euhedral and brittle deformed primary grains with droplet symplectite spodumene-quartz intergrowths (SQUI) along its rims, while group 2 represents a range of textural varieties of fine-grained secondary spodumene. The two main processes causing recrystallisation of primary spodumene are deformation (shear) and the presence of magmatic-hydrothermal fluids in the system. Although SEM-EDX analyses did not indicate a change of major elemental compositions between the different textural varieties, LIBS mapping shows that the concentration and distribution of lithium is strongly influenced by these two processes. Lithium is easily leached from the primary host and dispersed in the surrounding rock during the magmatic-hydrothermal stage.

Acknowledgements

Herman Nijs is thanked for thin section preparation. Lionel Sematuro and other colleagues from Piran Rwanda Ltd/TRINITY Metals Group are thanked for supplying the samples for this study.

References

- Fernandez-Alonso M, Cutten H, De Waele B, Tack L, Tahon A, Baudet D, Barritt SD (2012) The Mesoproterozoic Karagwe-Ankole Belt (formerly the NE Kibara Belt): The result of prolonged extensional intracratonic basin development punctuated by two short-lived far-field compressional events. *Precambrian Res.* 216–219, 63–86. <https://doi.org/10.1016/j.precamres.2012.06.007>.
- Hulsbosch N, Boiron M-C, Dewaele S, Muchez P (2016) Fluid fractionation of tungsten during granite–pegmatite differentiation and the metal source of peribatholithic W quartz veins: Evidence from the Karagwe-Ankole Belt (Rwanda). *Geochim. Cosmochim. Acta* 175, 299–318.
- Kramida A, Ralchenko Y, Reader J, NIST ASD Team (2019) NIST Atomic Spectra Database (ver. 5.7.1). National Institute of Standards and Technology, Gaithersburg, MD. <https://doi.org/10.18434/T4W30F>.
- London D (2018) Ore-forming processes within granitic pegmatites. *Ore Geology Reviews*, 101, 349–383. <https://doi.org/10.1016/j.oregeorev.2018.04.020>.
- Passchier C and Trouw R (2005) *Microtectonics* (2nd, Revised and Enlarged ed.). Berlin, Heidelberg: Springer Berlin / Heidelberg. <https://doi.org/10.1007/3-540-29359-0>.
- Stipp M, Stünitz H, Heilbronner R, Schmid S (2002) The eastern Tonale fault zone: A 'natural laboratory' for crystal plastic deformation of quartz over a temperature range from 250 to 700°C. *Journal of Structural Geology*, 24(12), 1861–1884. [https://doi.org/10.1016/S0191-8141\(02\)00035-4](https://doi.org/10.1016/S0191-8141(02)00035-4).

Magmatic-Hydrothermal Mineral Formation Systems: A Geological Study

Jhoshua U. Aparicio¹

¹UNAL, Bogotá D.C, Colombia

Abstract. In this paper we will talk about magmatic-hydrothermal deposits, their importance as a source of valuable metals and their different uses nowadays. In addition, we will also cover one of the most important advances in the study of magmatic-hydrothermal deposits, Laser Ablation Inductively Coupled Plasma Mass Spectrometry (LA-ICP-MS), and how this analytical technique has greatly improved our ability to study the geochemistry of magmatic-hydrothermal mineral-forming systems, allowing us to gain new insights into the processes that control the formation of these deposits.

1 Introduction

Magmatic-hydrothermal mineral-forming systems are created from the interaction of magma and hydrothermal fluids. It has been revealed that these deposits form in three main stages:

1. Magma intrusion: Magma intrudes into the earth's crust and cools, releasing volatile fluids.
2. Circulation of hydrothermal fluids: Hydrothermal fluids rise through the surrounding rocks and mix with magmatic fluids forming complex mineral deposits. In some cases, these fluids may also come from external sources such as groundwater.
3. Mineral deposition: Hydrothermal fluids are deposited in the surrounding rocks forming mineral deposits, which are deposited by changes in saturation, temperature and pressure drop or Ph variations. These deposits are important sources of sulfides, oxides, sulfosalts and/or native elements (Espinoza 2020).

Magmatic-hydrothermal mineral forming systems are found all over the world, but are especially common in subduction areas, where one tectonic plate is forced under another. In these regions, intense tectonic activity provides the heat and energy necessary for the formation of these deposits, which are commonly located in places such as (Figure 1):

The Pacific Ring of Fire, which includes countries such as Japan, Indonesia, the Philippines and Chile.

The Andes Mountains in South America, which crosses countries such as Chile, Argentina, Peru and Bolivia.

The Iberian Peninsula in Europe, where copper, lead and zinc deposits are found in places such as the Iberian pyritic belt.

The Rhine river basin in Europe, where there are zinc, lead and copper deposits.

The Ferriferous Quadrilateral in Brazil, where there are important iron deposits (Berger 1985).

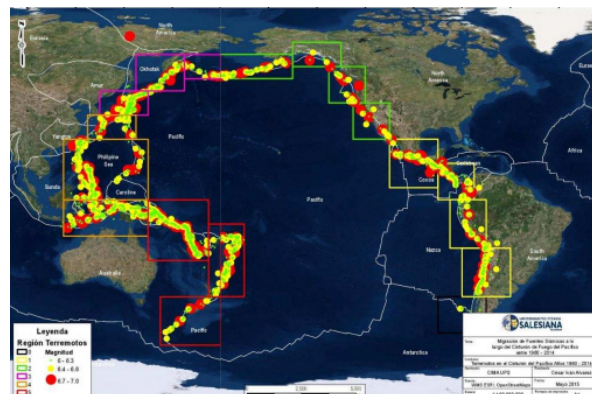


Figure 1. The geographic distribution of the fire belt is observed, where an ideal environment for finding magmatic-hydrothermal deposits is presented. López (2017).

These formation systems are important because they contain minerals of economic interest such as gold, silver, and copper, which are highly demanded in the industry.

It should be emphasized that the interest in this type of deposits is not merely economic, as exploration is necessary for the energy transition proposed in the Sustainable Development Goals (SDGs) developed by the UN in the last decade (Watari 2019).

One of the most widely used ways to study magmatic-hydrothermal deposits is Laser Ablation Inductively Coupled Plasma Mass Spectrometry (LA-ICP-MS) which will be discussed below.

2 Laser Ablation Inductively Coupled Plasma Mass Spectrometry (LA-ICP-MS)

The LA-ICP-MS analysis process can be divided into two main parts: sampling, which consists of laser ablation and ionization in a plasma, and mass spectrometry.

In inductively coupled plasma and laser ablation, the sample is vaporized using a high-energy pulsed laser beam, which is directed through the objective lens of the modified petrographic microscope. The sample surface is viewed with a charge-coupled device (CCD) camera mounted on the microscope, allowing precise laser spot location. Laser pulses cause energetic atoms, ions, molecules and solid particles to be ejected from the target. The removed aerosols are transported in argon or helium gas to the inductively coupled plasma. In the torch, which is heated by induction to approximately 10,000°C, the plasma formed provides a rich source of excited and ionized

atoms. The combination of ICP and MS technologies enables rapid quantitative elemental analysis with high precision and low detection limits (Adburiyim 2006).

In mass spectrometry, on the other hand, the device can analyse both chemical elements and small organic molecules. It requires the sample to be in a gaseous state, including solutions or solids. It measures the masses of elements or molecules of chemical compounds by separation of charged particles. The sample is ionized, and the ions are electrostatically directed to a mass analyser, where they are separated according to their m/z ratio and then sent to a detector, this is best understood by looking at Figure 2 (Adburiyim 2006).

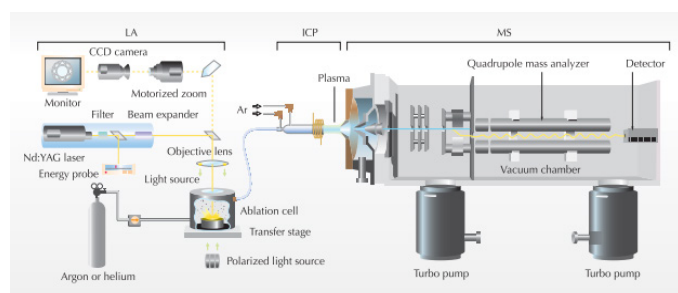


Figure 1. Graphical representation of how LA-ICP-MS is used. The sample is placed in the ablation cell and the laser beam is focused on the sample with the help of a CCD camera. The ablated material forms an aerosol, which is transported by an argon or helium carrier gas to the ICP-MS plasma. In the ICP, the laser-ablated particles are vaporized and ionized. The ions are extracted by the vacuum interface and guided to the mass analyser, where they are separated by their mass-to-charge ratio and finally detected. Adburiyim (2006).

Knowing how LA-ICP-MS data acquisition works, it is used in the search for magmatic-hydrothermal deposits to measure trace element concentrations in minerals and rocks. Briefly, the technique uses a laser to vaporize a small amount of sample, which is then ionized and fed into a mass spectrometer (Adburiyim 2006). The resulting signal provides us with information about the chemical composition of the sample.

2.1 LA-ICP-MS and its use for the study of magmatic-hydrothermal deposits.

One of the most important advances in the study of magmatic-hydrothermal deposits has been with LA-ICP-MS. This analytical technique has greatly improved our ability to study the geochemistry of magmatic-hydrothermal mineral-forming systems, allowing us to gain new insights into the processes that control the formation of these deposits.

LA-ICP-MS has been used to study the distribution of trace elements in magmatic-hydrothermal ore deposits. This has allowed us to identify the processes that control the mobility of

these elements, which in turn has improved our understanding of the genesis of mineral deposits.

3 Conclusions

In conclusion, the formation of magmatic-hydrothermal ore-forming systems and their related hydrothermal systems, as well as the formation of ores associated with highly fractionated silicic magmas, are important areas of research for geologists and mining professionals for our development as a society.

Understanding the geochemistry and geology of these systems is critical to identifying new deposits and optimizing mining methods in a responsible and sustainable manner. Recent advances in analytical techniques have improved our understanding of these systems, enabling more effective exploration and mining strategies.

Importantly, magmatic-hydrothermal deposits can be very valuable to the mining industry, as they may contain deposits of precious metals and other minerals of high economic value. However, their exploitation can have significant environmental impacts and it is important to manage these resources responsibly and sustainably.

Acknowledgements

We would like to thank the UNAL for its constant support in the search for information and significant contributions at the time of writing the document, as well as the SGA for allowing us to have the opportunity to write this scientific article.

References

- Abduriyim, A., and Kitawaki H (2006) APPLICATIONS OF LASER ABLATION-INDUCTIVELY COUPLED PLASMA-MASS SPECTROMETRY (LA-ICP-MS) TO GEMOLOGY <https://www.gia.edu/doc/SU06A1.pdf>
- Berger B, and Bethke P.M., (1985) Geology and Geochemistry of Epithermal Systems <https://pubs.geoscienceworld.org/segweb/books/book/1214/Geology-and-Geochemistry-of-Epithermal-Systems>
- Espinoza A.S., (2020) Apuntes de Yacimientos Magmático-Hidrotermales para el curso de Metalogenia de la Facultad de Ingeniería <http://www.ptolomeo.unam.mx:8080/xmlui/bitstream/handle/132.248.52.100/17342/Material%20did%C3%A1ctica.pdf?sequence=5&isAllowed=y>
- López A., Álvarez C.I., and Villarreal E (2017) MIGRACIÓN DE FUENTES SÍSMICAS A LO LARGO DEL CINTURÓN DE FUEGO DEL PACÍFICO <https://dialnet.unirioja.es/servlet/articulo?codigo=5969874>
- Watari T., McLellan B.C., Giurco D., Dominish E., Yamasue E., Nansai K., (2019) Total material requirement for the global energy transition to 2050: A focus on transport and electricity <https://reader.elsevier.com/reader/sd/pii/S0921344919302290?token=5740989F265371B64A6D43FF8C7C610D03C6CA71A37F6D6A69AB9F076C4D0951BE94F2132755096C42E92EDD352A9F46&originRegion=us-east-1&originCreation=20230304030728>

Diachronous tin mineralization in the Iberian Pyrite Belt

Iñigo Borrajo¹, Fernando Tornos^{1,2}, Carmen Conde¹, Gonzalo Ares¹, John M. Hanchar², Markus Wälle^{2,3}, Rong-Qing Zhang⁴, James Royal⁵, Tim Moody⁵

¹*Instituto de Geociencias (IGEO, CSIC-UCM), Spain*

²*Department of Earth Sciences, Memorial University of Newfoundland, Canada*

³*Swiss Gemmological Institute (SSEF), Switzerland*

⁴*School of Earth Sciences and Engineering, Nanjing University, China*

⁵*Pan Global Resources Inc, Canada*

Abstract. LA-ICP-MS U-Pb dates of cassiterite from two Sn-rich volcanogenic massive sulfide deposits in the Iberian Pyrite Belt (IPB) (La Romana and Neves Corvo), Spain and Portugal display an offset of ca. 17 Ma and suggest that major tin deposition took place coevally with the host massive sulfides at ca. 360 Ma but was later remobilized and reconcentrated along shear zones during the Variscan deformation and metamorphism around 336 Ma.

1 Introduction

The Iberian Pyrite Belt represents one of the most important metallogenic provinces in Europe. Here, volcanogenic massive sulfides (VMS) are interbedded with shale and felsic volcanic rocks and deposited at or close the seafloor; they generally include an underlying stockwork-like feeder zone (Barriga 1990; Tornos 2006 and references therein). One key feature of the Iberian Pyrite Belt is the abundance of Sn hosted by cassiterite or less commonly by stannite. However, only few deposits host high (up to economic) contents of Sn, like the Lagoa Salgada deposit (measured + indicated resources of 10.3 Mt @ 0.16% of Sn; www.ascendantresources.com; Oliveira et al. 2013), the recently discovered La Romana prospect with yet unconstrained resources (www.panglobalresources.com) or the outstanding Neves Corvo deposit with a total endowment of 300,000 metric tons of Sn metal (Relvas et al. 2006a).

The origin of Sn in the Pyrite Belt is poorly constrained and remains enigmatic. Relvas et al. (2006a) have proposed that it is associated with magmatic-hydrothermal fluids related with underlying intrusions of peraluminous granitoids. However, Relvas et al. (2001) and Tornos (2006) have proposed that tin mineralization was hydrothermally leached from underlying (meta)-sediments in this belt as proposed for the tin-rich sediment-hosted Sullivan deposit in the British Columbia (Slack et al. 2020).

In this study, we present new U-Pb dating of cassiterite that shows that there were at least two individual events of cassiterite formation.

2 Geological context

The Iberian Pyrite Belt is a wide belt in the northernmost part of the South Portuguese Zone, southwest Iberia. It is dominated by igneous (volcanic and intrusive) and sedimentary rocks in a relatively simple geological sequence that includes

form bottom to top (Fig. 1): Phyllite-Quartzite (PQ) Group, a monotonous detrital package of Late Devonian age; the Volcanic Sedimentary (VS) Complex, a heterogeneous unit of mafic-felsic volcanic rocks interbedded with shale, previously dated as late Famennian to middle Visean age, and that fills an intracontinental marine basin; and the Baixo Alentejo Flysch Group, a turbidite-like unit complex of early to Middle Carboniferous age.

The La Romana project is close to the Aznalcóllar-Los Frailes cluster, in the southeastern border of the IPB, partially covered by the sediments of the post-Miocene Guadalquivir Basin (Fig. 1). The mineralization occurs mostly as volcanic-hosted bodies located above a rhyodacite dome complex. Host rocks include coherent porphyritic dacite and rhyolite, different types of volcanoclastic rocks with monomictic and/or polymictic composition, and dark shale.

The Neves Corvo is located in the west part of the IPB in Portugal (Fig. 1). It is hosted by a sequence formed mainly of mudstone and felsic volcanic facies divided in three main sequences from bottom to top: rhyolite fiamme-rich facies, coherent porphyritic rhyolite interbedded with shale and volcanoclastic rocks, and a monomictic dacite breccia (Rosa et al., 2008). The mineralization is interbedded with shale or replaces permeable facies of the related coherent and volcanoclastic rocks.

Both, the La Romana and Neves Corvo deposits were affected by intense deformation during the different stages of the Variscan orogeny with widespread southward thrusting.

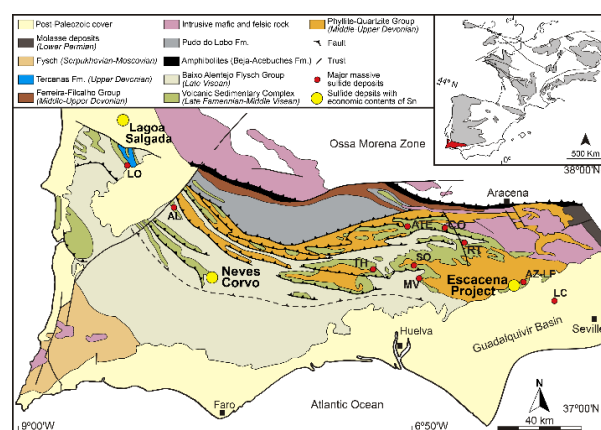


Figure 1. Geological map showing the location of the La Romana (Escacena) and Neves Corvo

deposits. LC: Las Cruces; LF: Los Frailes; Az: Aznalcollar; RT: Riotinto; SO: Sotiel; TH: Tharsis; ATE: Aguas Teñidas; CO: Concepcion; MV: Masa Valverde; AL: Aljustrel; LO: Lousal.

3 Mineralization at La Romana and Neves Corvo deposits

The mineralization at La Romana consists of stratabound massive sulfides replacing pervasively altered shale and probably formed by subseafloor replacement. It includes dominant pyrite with lesser amounts of chalcopyrite and traces of sphalerite and galena. The sphalerite includes micro-sized inclusions of cassiterite. However, the most prominent tin mineralization forms up to cm-sized masses of coarse-grained cassiterite with quartz, chalcopyrite and chlorite within shear bands that crosscut the massive sulfides (Fig 2A).

The Neves Corvo deposit encloses seven tectonically stacked massive sulfide orebodies, some of them including the originally underlying stockwork. The mineralization stands out for the high Cu and Zn, and locally very high Sn grades. The orebodies include different styles of mineralization: 1) massive sulfides, composed by Cu, Sn, Pb and Zn-rich ores; 2) stockwork, including Cu, Sn and Zn ores; and, 3) banded ore ("rubane") consisting in high grade Cu and Sn mineralization tectonically emplaced on the top of the massive sulfides. Cassiterite occurs as large, almost monomineral massive orebodies in the rubane ore (Fig. 2B) or within the stockwork as quartz-cassiterite-rich stringers. The Cu-rich massive sulfides also include minor fine grained cassiterite, stannite and complex Sn-bearing sulfosalts.

4 Methods

This research is focused on cassiterite from the rubane ore at Neves Corvo and that in shear zones at La Romana. Large (> 1 mm) grains of cassiterite were easily separated by handpicking and mounted in an epoxy disc and polished to expose the crystal centres. Areas free of cracks or inclusions were selected for U-Pb dating by using optical microscopy and BSE images.

LA-ICP-MS U-Pb dating of cassiterite was done at the Micro Analysis Facility (MAF) at Memorial University of Newfoundland, St. John's, Canada by using a Thermo Finnigan Element XR high-resolution single collector ICPMS interfaced to a Coherent GeoLas 193 nm Excimer laser. The U-Pb analysis were collected during a single session in December 2022. The conditions used were an energy density of 4 J/cm² and a pulse frequency of 10 Hz and a laser spot size diameter of 110 µm. Yankee and Cligga Head cassiterite was used as the primary standard and validation material (Carr et al. 2020; Tapster and Brighter 2020).

5 Results

Twenty-two spot analyses in the La Romana cassiterite sample yielded a lower intercept age on a Tera-Wasserburg diagram (Tera and Wasserburg, 1972) of 336.1 ± 4.0 Ma (2σ , MSWD = 3.1). Twenty-two analysis of the Neves Corvo cassiterite yielded an age of 360.6 ± 5 Ma (2σ , MSWD = 2.8). Approximate U and Th concentrations are 3.42 to 17.11 ppm and 0.18 to 3.86 ppm respectively in the sample from Neves Corvo and at La Romana U contents are between 6.66 and 62.50 ppm and Th contents between 0.06 and 25.80 ppm.

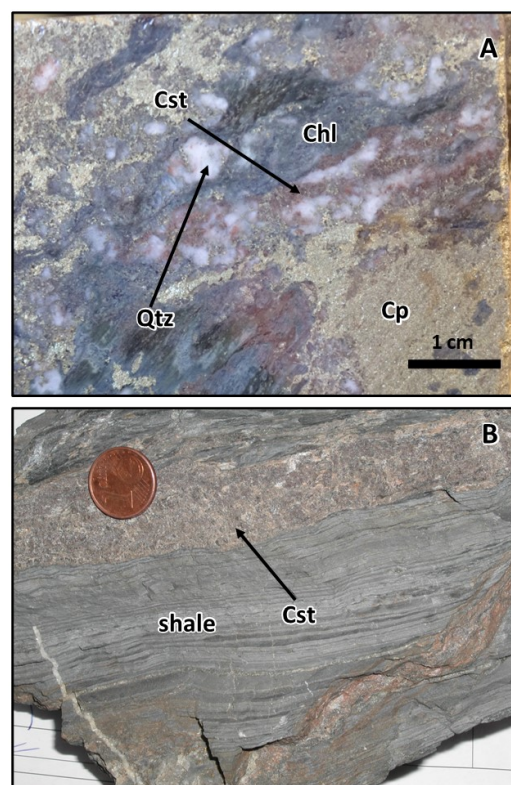


Figure 2. Textural relationships of cassiterite. **A** Late veins with quartz, chlorite, chalcopyrite and cassiterite at the La Romana. **B** Cassiterite interbedded with shale from the rubane ore at the Neves Corvo deposit. Cp: chalcopyrite; Qtz: quartz; Cst: cassiterite; Chl: chlorite.

Closure temperature of the U-Pb isotopic system in cassiterite has been estimated to be higher than 500 °C for grains of 1-µm radii (Zhang et al. 2011). Thus, the obtained dates in this study are interpreted as the crystallization age of the cassiterite mineralization.

6 Discussion

Palynostratigraphic studies (e.g. Pereira et al. 1996; Matos et al. 2011) along with U-Pb dating of the host volcanic rocks (Barrie et al. 2002; Paslawski et al. 2021; Pereira et al. 2021; Mello et al. 2022), between many others, have helped to constrain the timing of the mineralization in the IPB. However, direct absolute dating of VMS

deposits is still problematic because of the fine-grained size of the mineralization and the lack of good geochronometers. Mathur et al. (1999) obtained Re-Os dates in pyrite-rich ores for the giant Rio Tinto (346 ± 26 Ma) and Tharsis (353 ± 44 Ma) deposits, while Relvas et al. (2001) and Munhá et al. (2005) reported Re-Os (358 ± 29 Ma) and Rb-Sr (347 ± 25 Ma) dates for the massive and stockwork ores of the Neves Corvo deposit. All these dates display large analytical errors.

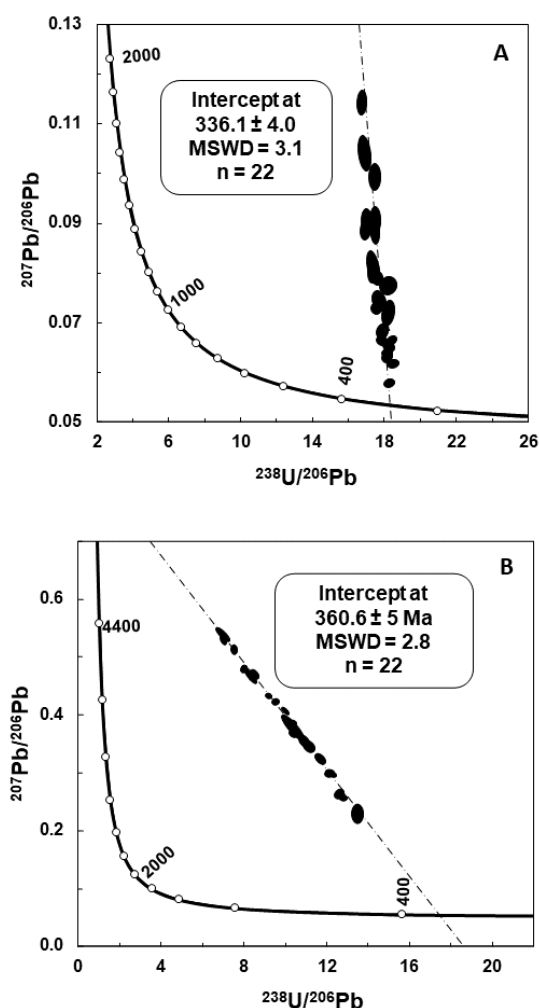


Figure 3. Tera-Wasserburg (Tera and Wasserbourg 1972) concordia diagrams of cassiterite from the IPB. **A** La Romana **B** Neves Corvo. Error envelopes are 2 sigma.

Recently, Li et al. (2019) reported U-Pb dates for cassiterite from the massive ore (364.4 ± 4.4), the fissural ore (367.5 ± 8.7) and the rubane ore (365.2 ± 5.3 and 363.4 ± 5.8) at Neves Corvo. All these dates overlap within errors with the result obtained in the present study. In the Neves Corvo area five different episodes of felsic volcanism between ca. 354 ± 2 Ma and 385 ± 2 Ma have been reported by Oliveira et al. (2013) by U-Pb dating of igneous zircon. Here, the main stage of massive sulphide deposition has been interpreted to have taken place during late Strunian time (ca. 360.0 -

361.5 Ma), associated with the black shales and rhyolites of the ca. 359 ± 3 Ma volcanic event (Pereira et al. 2021). This implies that the felsic volcanism, shale sedimentation and sulfide and cassiterite mineralization are essentially coeval.

At the La Romana deposit the absolute age of the associated igneous host rocks remains unknown.

Pereira et al. (1996) based on miospores collected from the black shales hosting the massive sulfides at the Los Frailes-Aznalcollar-La Romana orebodies suggested an uppermost Devonian age (Strunian: ca. 360.0-361.5 Ma). In contrast, Nesbitt et al. (1999) dated hydrothermal zircon in the stockwork zone of the Los Frailes deposit at 345.7 ± 4.7 Ma. This date is in good agreement with the U-Pb date in cassiterite from La Romana suggesting a late regional hydrothermal event in the area at ca. 343 Ma. This event is also broadly coeval with the late volcanism in the Riotinto area at ca. 340 Ma (e.g. Valenzuela et al. 2011; Mello et al. 2022) and several plutonic rocks in the Sierra Norte Batholith in the NE of the IPB (Paslawski et al. 2021; Fig. 1).

The geochronological data available do not constrain the sources of Sn but can provide important information when combined with field observations and other geochemical data. At Neves Corvo, the hydrogen, oxygen and Sr-Nd isotopic data of Relvas et al. (2001, 2006b) suggests that Sn was precipitated from hydrothermal fluids that were of different composition from those that formed the bulk of the massive sulfide mineralization. Tin-bearing fluids could be related to the upflow of magmatic-hydrothermal fluids related with a deep peraluminous granite (Relvas et al. 2006b; Marques et al. 2020). However, Tornos (2006) suggests that Sn is related to the same fluids forming the bulk of the VMS deposits and derived from the hydrothermal leaching of the siliciclastic sediments of the PQ Group or an underlying continental basement. The major problem of any magmatic-hydrothermal model is the lack of peraluminous magmatism in a magmatic arc with calc-alkaline felsic rocks. Collision-related peraluminous magmatism postdates the Sn mineralization at Neves Corvo by more than 30 Ma.

A further metal extraction from the basement reservoir or a remobilization of older mineralization during the polyphase Variscan deformation and metamorphism (Dallmayer et al. 1997) could have generated a second Sn-rich event at ca. 342 Ma at La Romana. This is consistent with the occurrence of cassiterite mineralization in syn-tectonic Variscan shear zones in this deposit.

This hypothesis agrees with the recent study of Romer et al. (2022) suggesting that in the Variscan Belt, Sn was remobilized during prograde metamorphism between 400 and 340 Ma.

Conclusions

U-Pb dating of cassiterite from La Romana and Neves Corvo in the Iberian Pyrite Belt reveals two events at ca. 336 ± 4.1 Ma and 360.6 ± 5 Ma of tin mineralization. The first one is coeval with the formation of the massive sulfides with Sn being leached from the underlying siliciclastic rocks. The second event is of Variscan age and probably related with syn-tectonic deformation.

Acknowledgements

Funded by an internal research grant of Memorial University of Newfoundland, the iTARG3T Project (EIT Raw Materials of the European Union's Horizon 2020 Grant No. 18036) and the EIS Project (Horizon Europe Grant No. 101057357). The authors thank Pan Global Resources for supporting the research.

References

- Barrie TC, Amelin Y, Pascual E (2002) U–Pb geochronology of VMS mineralization in the Iberian Pyrite Belt. *Miner Depos* 37:684–703. <https://doi.org/10.1007/s00126-002-0302-7>
- Barriga F (1990) Metallogenesis in the Iberian pyrite belt. In: Dallmeyer RD, Martinez Garcia E (eds) *Pre-Mesozoic geology of Iberia*. Springer-Verlag, Berlin Heidelberg New York, pp 369–379
- Carr P, Zink S, Bennett V, et al (2020) A new method for U-Pb geochronology of cassiterite by ID-TIMS applied to the Mole Granite polymetallic system, eastern Australia. *Chem Geol* 539:119539
- Dallmeyer RD, Catalán JRM, Arenas R, Ibarrauchi J, Gutiérrez G, Farias P, Bastida F, Aller, J (1997) Diachronous Variscan tectonothermal activity in the NW Iberian Massif: evidence from $^{40}\text{Ar}/^{39}\text{Ar}$ dating of regional fabrics. *Tectonophysics* 277:307–337.
- Li X, Zhao K, Jiang S, Palmer M (2019) In-situ U-Pb geochronology and sulfur isotopes constrain the metallogenesis of the giant Neves Corvo deposit, Iberian Pyrite Belt. *Ore Geol Rev* 105:223–235
- Marques AFA, Relvas JM, Scott SD, Rosa C, Guillong M (2020) Melt inclusions in quartz from felsic volcanic rocks of the Iberian Pyrite Belt: clues for magmatic ore metal transfer towards VMS-forming systems. *Ore Geol Rev* 126:103743.
- Mathur R, Ruiz J, Tornos F (1999) Age and sources of the ore at Tharsis and Rio Tinto, Iberian pyrite belt, from Re–Os isotopes. *Miner Depos* 34:790–793. <https://doi.org/10.1007/S001260050239>
- Matos JX, Pereira Z, Rosa CJP, et al (2011) Late Strunian age: a key time frame for VMS deposit exploration in the Iberian Pyrite Belt. In: 11th SGA Biennial Meeting: Let's Talk Ore Deposits
- Mello C de, Tornos F, Conde C, et al (2022) Geology, Geochemistry, and Geochronology of the Giant Rio Tinto VMS Deposit, Iberian Pyrite Belt, Spain. *Econ Geol* 117:1149–1177
- Munhá J, Relvas J, Barriga F, Conceição P (2005) Osmium isotope systematics in the Iberian Pyrite Belt. In: *Mineral Deposit Research: Meeting the Global Challenge: Proceedings of the Eighth Biennial SGA Meeting Beijing, China, 18–21 August 2005*. Springer Berlin Heidelberg, pp 663–666
- Nesbitt RW, Pascual E, Fanning CM, et al (1999) U-Pb dating of stockwork zircons from the eastern Iberian Pyrite Belt. *J Geol Soc London* 156:7–10. <https://doi.org/10.1144/GSJGS.156.1.0007>
- Oliveira D de, Matos J, Rosa C, et al (2011) The Lagoa Salgada orebody, Iberian Pyrite Belt, Portugal. *Econ Geol* 106:1111–1128
- Oliveira JT, Rosa CJP, Pereira Z, et al (2013) Geology of the Rosário-Neves Corvo antiform, Iberian Pyrite Belt, Portugal: New insights from physical volcanology, palynostratigraphy and isotope geochronology studies. *Miner Depos* 48:749–766. <https://doi.org/10.1007/S00126-012-0453-0>
- Paslawski LE, Braid JA, Quesada C, McFarlane CM (2021) Geochronology of the Iberian pyrite belt and the sierra norte batholith: Lower plate magmatism during supercontinent amalgamation? *Geol Soc Spec Publ* 503:589–617. <https://doi.org/10.1144/SP503-2020-5>
- Pereira Z, Matos JX, Rita Solá A, et al (2021) Geology of the recently discovered massive and stockwork sulphide mineralization at Semblana, Rosa Magra and Monte Branco, Neves–Corvo mine region, Iberian Pyrite Belt, Portugal. *Geol Mag* 158:1253–1268. <https://doi.org/10.1017/S0016756820001284>
- Pereira Z, Ramos RS, Pons J, Oliveira J (1996) Edad devónica (Strunianense) de las mineralizaciones de Aznalcóllar (Faja Pirítica Ibérica) en base a palinología. *Geogaceta* 20:1609–1612
- Relvas J, Barriga F, Ferreira A, et al (2006a) Hydrothermal alteration and mineralization in the Neves-Corvo volcanic-hosted massive sulfide deposit, Portugal. I. Geology, mineralogy, and geochemistry. *Econ Geol* 101:753–790
- Relvas J, Barriga F, Longstaffe F (2006b) Hydrothermal alteration and mineralization in the Neves-Corvo volcanic-hosted massive sulfide deposit, Portugal. II. Oxygen, hydrogen, and carbon isotopes. *Econ Geol* 101:797–804
- Relvas J, Tassinari C, Munhá J, Barriga F (2001) Multiple sources for ore-forming fluids in the Neves Corvo VHMS Deposit of the Iberian Pyrite Belt (Portugal): strontium, neodymium and lead isotope evidence. *Miner Depos* 36:416–427. <https://doi.org/10.1007/s001260100168>
- Romer R, Kroner U, Schmidt C, Legler C (2022) Mobilization of tin during continental subduction-accretion processes. *Geology* 50:1361–1365. <https://doi.org/10.1130/G50466.1>
- Rosa CJ, McPhie J, Relvas JM, Pereira Z, Oliveira T, Pacheco N (2008) Facies analyses and volcanic setting of the giant Neves Corvo massive sulfide deposit, Iberian Pyrite Belt, Portugal. *Miner Depos* 43:449–466.
- Slack JF, Neymark LA, Moscati RJ, Lowers HA, Ransom P, W, Hauser RL, Adams, DT (2020) Origin of tin mineralization in the Sullivan Pb–Zn–Ag deposit, British Columbia: Constraints from textures, geochemistry, and LA-ICP-MS U–Pb geochronology of cassiterite. *Econ Geol* 115:1699–1724.
- Tapster S, Bright JW (2020) High-precision ID-TIMS cassiterite U–Pb systematics using a low-contamination hydrothermal decomposition: implications for LA-ICP-MS and ore deposit geochronology. *GChron* 2:425–441.
- Tera F, Wasserburg GJ (1972) U–Th–Pb systematics in three Apollo 14 basalts and the problem of initial Pb in lunar rocks. *Earth and Planet Sci Lett* 14:281–304.
- Tornos F (2006) Environment of formation and styles of volcanogenic massive sulfides: The Iberian Pyrite Belt. *Ore Geol Rev* 28:259–307
- Valenzuela F, Donaire T, Pin C, et al (2011) Geochemistry and U–Pb dating of felsic volcanic rocks in the Riotinto–Nerva unit, Iberian Pyrite Belt, Spain: crustal thinning, progressive crustal melting and massive sulphide genesis. *J Geol Soc London* 168:717–731. <https://doi.org/10.1144/0016-76492010-081>
- Zhang DL, Peng JT, Hu RZ, et al (2011) The closure of U–Pb isotope system in cassiterite and its reliability for dating. *Geological Review* 57: <http://www.ascendantresources.com>. Accessed February 27, 2023
- <http://www.panglobalresources.com>. Accessed February 27, 2023

Magmatic-hydrothermal stratabound W-(Sn) mineralization in the Iberian Variscan Massif: The Barxa deposit

Iñigo Borrajo¹, Fernando Tornos¹, John M. Hanchar², Jose M. Fuenlabrada³, Tobias E. Bauer⁴

¹*Instituto de Geociencias (IGEO, CSIC-UCM), C/Severo Ochoa, 7, 28040 Madrid, Spain*

²*Department of Earth Sciences, Memorial University of Newfoundland, St. John's, NL, Canada A1C 5S7*

³*Unidad de Geocronología (CAI de Ciencias de la Tierra y Arqueometría), Universidad Complutense. 28040 Madrid, Spain*

⁴*Division of Geosciences and Environmental Engineering, Luleå University of Technology, Luleå SE-971 87, Sweden*

Abstract. Stratabound scheelite mineralization distal to granitic rocks represents a minor group of deposits within the framework of the W-Sn metallogenic province of the European Variscan Belt; however, this style of mineralization can have large tonnages and grades. The recently discovered Barxa and Valtreixal deposits in NW Spain are somewhat different to the other scheelite-rich stratabound deposits in Iberia. They display a lateral zonation from the crosscutting Sn-rich veins that acted as feeder zones and include a proximal greisen-like alteration and a distal alteration that consists of an Al-rich calcic skarn. The ϵNd_i values of the stratabound orebodies range between those of the granitic dikes distal to the mineralization (ϵNd_i between -6.5 and -5.5) and the host unaltered metapelites (ϵNd_i between -12 and -10.4). Mineralization in the skarn-like alteration shows values similar to those in the host metapelites, while the greisen-like assemblage has closer ϵNd_i values to those of the granitic dykes.

1 Introduction

Tungsten-(tin) mineralization worldwide usually occurs spatially associated with felsic intrusions giving rise to a wide spectra of magmatic-hydrothermal ore deposits including veins, skarns, pegmatites, disseminations in evolved granitic cupolas, porphyries, and breccia pipes (e.g. Derré 1982).

Perigranitic vein systems hosting high grade low tonnage W mineralization has been largely mined during the last centuries in the European Variscan Belt, where they represent the dominant mineralization style (e.g. Harlaux et al. 2018). Along with this classical mineralization, a short number of deposits are characterized by being related to stratabound scheelite-rich orebodies with an alteration somewhat similar to that of skarns. Many of these deposits show no obvious spatial relationship with Variscan granitoids (Schermerhorn 1981; Arribas 1983; Gaspar and Inverno 2000). The Mittersill deposit (Austria) belongs to this group and with more than 10 Mt @ > 0.4% WO_3 represents one of the largest tungsten deposits in Europe (Ordosch et al. 2019).

Two new stratabound scheelite deposits have been found in Western Iberia. They include the Valtreixal deposit with inferred resources of 10 Mt @ 0.28 WO_3 (www.almonty.com) and the Barxa deposit with unknown resources. The high tonnage and high and homogeneous W grades make them

an attractive target for mining and contrast with vein-like deposits being usually smaller in size and with more erratic ore grades.

In this study we present geological evidences and isotope geochemistry data of the Barxa deposit that support that, despite being unrelated to any magmatic intrusion, is a distal replacement of favourable rocks with a magmatic-hydrothermal origin.

2 Geological Context

The Barxa deposit is located in NW Iberia, close to the contact between the Central Iberian Zone (CIZ) and the Schist Domain of the Galicia-Tras-os-Montes Zone (GTMZ) (Martínez Catalán et al. 2004; Díez-Montes 2006). Within the studied region, the CIZ includes gneisses, metasediments and metavolcanic rocks, while the Schist Domain is mostly dominated by metapelitic rocks (Fig. 1). In detail, the rocks hosting the Barxa deposit consist of a monotonous succession of Late Cambrian to Silurian phyllites (Farias 1989; Farias et al. 2014) deformed and metamorphosed during the Variscan Orogeny and intruded by younger granitic suites ranging from early syn- tectonic and late syn-tectonic to post-tectonic (Díez-Montes 2006; Fig. 1).

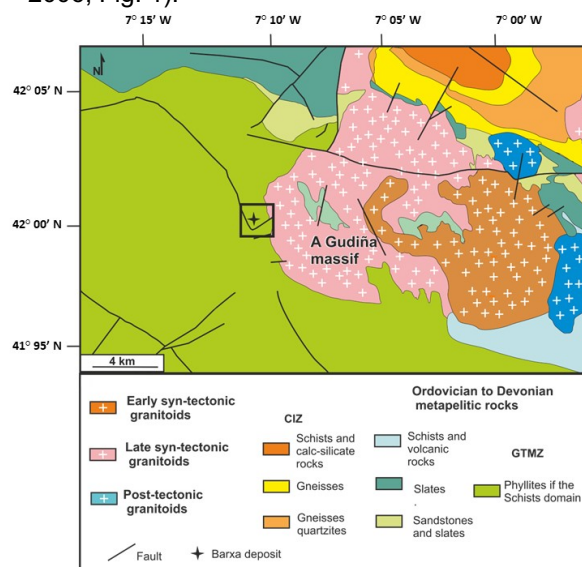


Figure 1 Regional geological map of the Barxa deposit area. Modified from Díez-Montes (2006).

The syn-tectonic A Gudiña granite is the closest intrusion to the Barxa deposit (Fig.1). It shows a clear intrusive contact with the host phyllites towards its SW border generating a contact metamorphic aureole. Here, there are several irregular granitic dykes with a pinch-and-swell morphology intruding parallel to the regional cleavage. Here, the granite displays a pervasive greisen-like hydrothermal alteration and host abundant Sn-rich quartz veins. One of these dykes with 3 m to 15 m thick and with a length of around 80 m is known as the Barxa granite.

3 The Barxa deposit

W-(Sn) mineralization is hosted by at least four stratabound calc-silicate bodies of decametric dimensions with a E-W trend and dipping 30-40° SW that are interbedded with the phyllites (Fig. 2). The mineralized bodies are adjacent to a NNE-SSW trending fault.

The orebodies are more competent than the host phyllite; they have a large-scale boudin morphology, edges are usually sheared and brecciated and are the preferential site for the formation of up to 2 m thick NE-SW-trending quartz and minor tourmaline veins (Fig. 2). When crosscutting the stratabound mineralization the veins have a well-developed selvage of quartz-muscovite-scheelite-cassiterite (greisen-like assemblage) that laterally prograde on a much larger zone of clinozoisite-quartz-scheelite (skarn-like assemblage).

Outside of these bodies there are little evidences of metasomatism. Locally, the phyllite enveloping the mineralization shows a muscovite-tourmaline-rich halo.

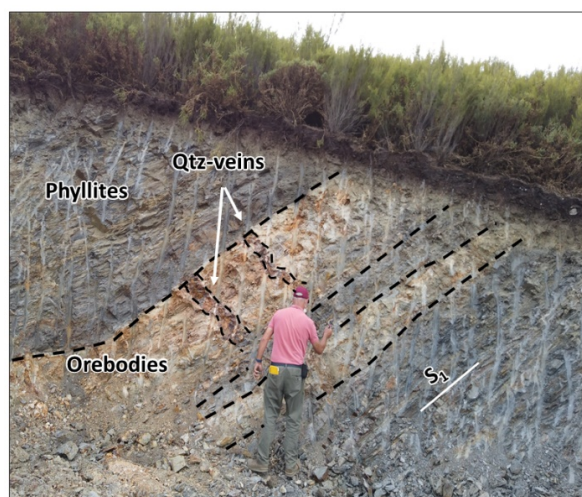


Figure 2 Outcrop of the Barxa stratabound orebodies that are subparallel to the layering of the host phyllites and are crosscut by NE-SW trending quartz veins which do not propagate throughout the host rock.

3 The stratabound orebodies

The mineralization includes two different metasomatic zones, a proximal greisen like-alteration and a distal, dominant skarn-like alteration. This latter is a coarse-grained massive brownish rock composed mostly of anhedral quartz crystals and large sub-euhedral unoriented and zoned clinozoisite crystals (Fig. 3A). Scheelite grains of up to 2 mm in size occur intergrown with clinozoisite and quartz (Fig. 3A). Only locally, this assemblage replaces a previous prograde calcic skarn made up aggregate of massive grossular with crystals of up to 0.7 cm in size and having a high intergranular permeability. This zonation is typical of iron-poor calcic skarns with the clinozoisite-quartz assemblage forming at temperatures below ca. 440°C for a fluid pressure close to 1 kb.

The garnet assemblage represents the oldest metasomatic rock but we have not found any evidences of the unreplaced protolith. This is probably caused by its complete replacement by the metasomatic assemblage, as reported in other scheelite-rich stratabound deposits in Iberia (Gaspar and Inverno 2000).

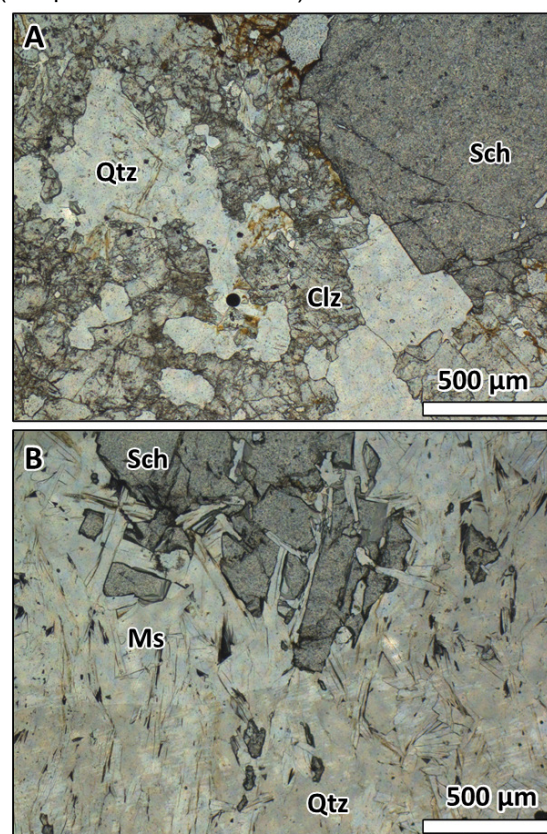


Figure 3 Plane-polarized transmitted light images showing mineralogical and textural features of scheelite from Barxa deposit. **A** Large scheelite (sch) grain intergrown with clinozoisite (Clz) and quartz (Qtz) in the skarn-like alteration. **B** Scheelite crystals intergrown with muscovite (Ms) in the greisen.

The greisen alteration progrades on the skarn-like assemblage. It includes two zones with contrasting W and Sn tenors. The W-rich greisen consists of medium-grained muscovite crystals of up to 500 μm in size, quartz, minor sub-millimetric apatite grains, scarce tourmaline and minor rutile, ilmenite and arsenopyrite. Scheelite aggregates of up to 1 mm in size are intergrown in this assemblage (Fig. 3B). Proximal to the quartz veins there is a Sn-rich greisen, with total thickness of less than 10 cm. It is dominated by large muscovite grains up to 1 mm in size (Fig. 4) and includes minor quartz and apatite. Cassiterite grains with sizes ranging between 15 μm and 500 μm occur intergrown with muscovite (Fig. 4).

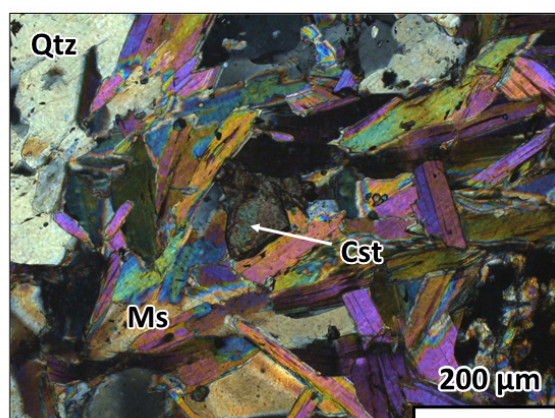


Figure 4 Cross polarized transmitted light image of a cassiterite (Cst) grain intergrown with coarse-grained muscovite (Ms) from the Sn-rich greisen of the Barxa deposit.

All the metasomatic rocks are locally crosscut by late mm-thick sulfide-rich veins with arsenopyrite, pyrite and minor chalcopyrite.

4 Fluid evolution and sources of Sr and Nd

The Rb, Sr, Sm and Nd concentrations and the $^{87}\text{Sr}/^{86}\text{Sr}$ and $^{147}\text{Nd}/^{144}\text{Nd}$ isotopic ratios of samples from the different metasomatic assemblages, the Barxa granite and the host unaltered phyllites were analyzed at the Centro de Geocronología y Geoquímica Isotópica (CAI de Ciencias de la Tierra y Arqueometría) of the Universidad Complutense de Madrid (UCM) using isotope dilution thermal ionization mass spectrometry (IDTIMS).

Syn-kinematic granites emplaced in the NW of the Iberian Variscan Massif between 325 and 310 Ma (Dias et al. 1998). Reported ages of other Sn-W deposits in the area range between 330 and 300 Ma (Melleton et al. 2011; Zhang et al. 2019). Therefore, initial isotopic ratios have been recalculated at an average age of 310 Ma.

The initial Sr isotope composition of the Barxa granite is homogeneous displaying strongly radiogenic $^{87}\text{Sr}/^{86}\text{Sr}_i$ ratios between 0.71825 and

0.71916. In contrast, the host phyllites show more heterogeneous values between 0.71458 and 0.72048. This isotopic heterogeneity is typical in the metasediments from the NW Iberia which sometimes show unexpected low $^{87}\text{Sr}/^{86}\text{Sr}$ values, interpreted as led by weathering and diagenetic processes due the high mobility of Rb and Sr (Villasca et al. 2014). The metasomatic rocks also display a wide range in the $^{87}\text{Sr}/^{86}\text{Sr}_i$ ratios that range between 0.70799 and 0.72475.

The high variability and overlapping in the granite and metapelites $^{87}\text{Sr}/^{86}\text{Sr}_i$ ratios made it difficult to interpret the obtained results.

In contrast, $\epsilon\text{Nd}_{310 \text{ Ma}}$ values in the phyllites and the Barxa granite lay in two contrasting and well-defined fields. The metapelites have ϵNd_i ratios that range between -12.0 and -10.4, consistent with a derivation from an old crustal reservoir; more juvenile $\epsilon\text{Nd}_{310 \text{ Ma}}$ values between -6.4 and -5.1 were obtained for the Barxa granite, which are similar to those of the dominant peraluminous syn-kinematic granitic suite in NW Iberia ranging between -9 and -5 (Dias et al. 2002; Villasca et al. 2009; Martins et al. 2013).

The stratabound mineralization has intermediate Nd isotopic compositions between the Barxa granite and the phyllites. This suggests that Nd mineralization is derived from the host sedimentary sequence and an external fluid in isotopic disequilibrium with the host rocks.

In detail, the $\square\text{Nd}_i$ values track a trend of progressive fluid-rock reaction. Samples proximal to the quartz veins (Sn-rich greisen, W-rich greisen and the quartz-tourmaline veins) have ϵNd_i values ranging between -9.6 and -8.4 and samples from the distal skarn-like alteration have more negative values between -10.4 and -9.6. This trend is consistent with the inflow of a fluid with higher $^{143}\text{Nd}/^{144}\text{Nd}$ values that circulated through the fluid channel ways now represented by the quartz veins. The most likely source for fluids is the Barxa granite, located ca. 2 km away, or any equivalent intrusion located beneath the stratabound mineralization. If that holds true, the magmatic-hydrothermal fluids exsolved from the granite during crystallization and that produced greisenization and Sn-rich mineralization are the same that formed the mineralization at Barxa W-Sn deposits.

4 Conclusions

The recently discovered Barxa deposit in NW Iberia includes at least four large scheelite-rich distal skarns dominated by quartz and clinozoisite formed at relatively low temperatures and replacing an unknown protolith. Nd isotope geochemistry suggests that the mineralization formed due to the reaction with the metasediments of fluids derived from a distal crystallizing granite and strongly suggest that in Fe-poor systems, W-rich fluids can travel far from the source till they

find a suitable lithology where to precipitate by fluid-rock interaction.

Acknowledgements

This research was conducted within the iTARG3T (Innovative targeting & processing of W-Sn-Ta-Li ores: towards EU's self-supply) project funded by the EIT Raw Materials of the European Union's Horizon 2020 (GA 18036) and Hugo Dummett Mineral Discovery Fund (SEG) grant to Iñigo Borrajo. Thanks to J. Ruiz, C. Rodríguez, I. Solaz, I. Losada, C. Casquet and E. Crespo for their constructive reviews and suggestions.

References

- Arribas A (1983) Geología y metalogenia del yacimiento «Virgen de la Encina», Ponferrada (León). *Tecniterrae* 56:36–75
- Derré C (1982) Caracteristiques de la Distribution des Gisements à Etain et Tungstène Dans L'Ouest de L'Europe. *Miner Depos* 17:55–77.
- Dias G, Leterrier J, Mendes A, et al (1998) U–Pb zircon and monazite geochronology of post-collisional Hercynian granitoids from the Central Iberian Zone (Northern Portugal). *Lithos* 45:349–369
- Dias G, Simões PP, Ferreira N, and Leterrier J (2002) Mantle and crustal sources in the genesis of late-Hercynian granitoids (NW Portugal): geochemical and Sr–Nd isotopic constraints. *Gondwana Res* 5:287–305
- Díez-Montes A (2006) La Geología del Dominio “Ollo de Sapo” en las comarcas de Sanabria y Terra do Bolo. Universidad de Salamanca
- Farias P (1989) La geología de la región del sinforme de Verín (Cordillera herciniana, NW de España). Universidad de Oviedo
- Farias P, Casado B, Marcos A, et al (2014) U–Pb zircon SHRIMP evidence for Cambrian volcanism in the Schistose Domain within the Galicia-Trás-os-Montes Zone (Variscan Orogen, NW Iberian Peninsula). *Geol Acta* 209–218
- Gaspar L, Inverno CM (2000) Mineralogy and metasomatic evolution of distal strata-bound scheelite skarns in the Riba de Alva Mine, Northeastern Portugal. *Econ Geol* 95:1259–1275
- Harlaux M, Mercadier J, Marignac C, et al (2018) Tracing metal sources in peribatholithic hydrothermal W deposits based on the chemical composition of wolframite: The example of the Variscan French Massif Central. *Chem Geol* 479:58–85
- Martínez Catalán JR, Martínez Poyatos D, Bea F (2004) Zona Centroibérica. In: Vera JA (ed) *Geología de España SGE-IGME. Sociedad Geológica de España-Instituto Geológico y Minero de España, Madrid*, pp 68–133
- Martins HC, Sant H, Noronha F (2013) Late-Variscan emplacement and genesis of the Vieira do Minho composite pluton, Central Iberian Zone: Constraints from U–Pb zircon geochronology, AMS data and Sr–Nd–O isotope geochemistry. *Lithos* 162:221–235
- Melleton J, Gloaguen E, Frei D, Lima A (2011) U–Pb dating of columbite-tantalite from Variscan rare-elements granites and pegmatites. In: *Goldschmidt*. p Vol. 75, No. 3, 1452
- Ordosch A, Raith JG, Schmidt S, Aupers K (2019) Polyphase scheelite and stanniferous silicates in a W–(Sn) skarn close to Felbertal tungsten mine, Eastern Alps. *Mineral Petrol* 113:703–725. <https://doi.org/10.1007/S00710-019-00675-X>
- Schermerhorn LJG (1981) Framework and evolution of Hercynian mineralization in the Iberian Meseta. *Leidse Geolo Meded* 52:23–56
- Villaseca C, Bellido F, Pérez-Soba C, Billström K (2009) Multiple crustal sources for post-tectonic I-type granites in the Hercynian Iberian Belt. *Mineral Petrol* 96:197–211
- Villaseca C, Merino E, Oyarzun R, Orejana D, Pérez-Soba C, and Chicharro E (2014) Contrasting chemical and isotopic signatures from Neoproterozoic metasedimentary rocks in the Central Iberian Zone (Spain) of pre-Variscan Europe: Implications for terrane analysis and Early Ordovician magmatic belts. *Precambrian Res* 245:131–145.
- Zhang R, Ramos V, Leal S, et al (2019) U–Pb geochronology of cassiterites from primary Sn mineralizations in Sn–W Variscan Metallogenic Province, Portugal. In: *Advances in Understanding Hydrothermal Processes, Life with Ore Deposits on Earth—15th SGA Biennial Meeting*. pp 357–360 <https://almonty.com> Almonty Industries - Leaders In Tungsten. Accessed February 27, 2023

The role of micas in the origin of granite-related Sn-W-Nb-Ta mineralization

Karel Breiter¹, Michaela Vašinová Galiová¹, Michaela Hložková¹

¹BIC, Purkyňova 648, 62100 Brno, Czech Republic

Abstract. About 3000 spot LA-ICP-MS analyses of micas from eight typical rare-metal granite plutons were evaluated to establish possible correlation among trace-element (Li, Nb, Sn, Ta, W) spectra of micas. Igneous and hydrothermal micas play a substantial role in rare metal accumulation and redistribution although behavior of rare metals during magmatic/hydrothermal evolution of granites is highly variable. Maximum contents of metals in granitic mica reach ca. 1200 ppm Sn, 350 ppm W, 2300 ppm Nb and 600 ppm Ta, while micas in greisens reached 1500 ppm Sn, 140 ppm W, 500 ppm Nb and 150 ppm Ta. With increasing granite fractionation, the contents of Li in mica increase, while the contents of rare metals usually decrease as a consequence of the crystallization of Li-mica after the crystallization of the rare metal-bearing accessories. In greisens, similar to granites, Li-poor micas (muscovite, annite) are relatively Sn, W, Nb, Ta-enriched, while Li-rich zinnwaldite tends to be Sn, W, Nb, Ta-poor. Among distinctly mineralized quartz–mica veins, intragranitic veins (+cassiterite, wolframite) at Čínovec contain HFSE-poor zinnwaldite, while exogranitic wolframite-bearing veins at Panasqueira contains W-rich muscovite.

1 Introduction

Micas are, besides quartz and feldspars, the most common rock-forming minerals in all prospectively fertile rare-metal granites (RMG). Among common minerals, micas are certainly the most important host of many trace elements, strategic metals (Sn, W, Nb, Ta) and rare alkalis (Li, Rb, Cs) in particular. A routine application of ICP-MS method coupled with laser ablation to geological material in the last two decades allowed to obtain a large amount of *in situ* trace elements data on micas from fertile granitoids and related mineralization (van Lichtenvelde et al. 2008; Xie et al. 2015; Legros et al. 2018; Launay et al. 2021; Monnier et al. 2022; Breiter et al. 2019, 2022, 2023). A comprehensive overview of the behavior of trace elements in micas during magmatic and hydrothermal processes is, however, still missing. We attempt to partly fill this gap targeting on the changes in Li, Sn, W, Nb and Ta in micas during a transition from the magmatic to hydrothermal stage of system evolution.

2 Studied granite plutons

Eight typical geologically well documented RMG plutons of different ages, geotectonic positions, geochemical types, and styles of mineralization were selected for this review (Figure 1):

1. Madeira metaaluminous to peralkaline pluton (1824–1818 Ma), Pitinga province, Brazil (Costi et al. 2009). The youngest subintrusion, peralkaline

albite (+riebeckite, annite, lepidolite) granite contains large cryolite bodies and disseminated Sn, Nb and Th-mineralization.

2. Wiborg batholith, Finland, (1.67–1.54 Ga) including a late Kimi Li-mica-bearing granite stock, represents the large Lower Proterozoic rapakivi-type plutons with small late RMG intrusions (Lukkari et al. 2009).

3. Orlovka, Transbaikalian region, Russia, sub- to peraluminous Jurassic pluton forms a layered body consisting of the (ascending order) biotite, muscovite, zinnwaldite and lepidolite facies with disseminated Ta-minerals (Badanina et al. 2004).

4. Čínovec/Zinnwald sub- to peraluminous late-Variscan granite pluton, Eastern Erzgebirge, Czech Republic/Germany intruded after a collapse of the Upper Carboniferous Teplice-Altenberg caldera. It is composed of lower biotite and upper zinnwaldite facies, the latter affected by pervasive zinnwaldite-dominant greisenization, and intersected by flat quartz-zinnwaldite veins with cassiterite and wolframite (Johan et al. 2012; Breiter et al. 2017).

5. Nejdek, late Variscan peraluminous pluton in the Western Erzgebirge, is composed of several facies of biotite granites and small late zinnwaldite granite stocks. It contains cupola-shaped quartz-Li-biotite greisen bodies with wolframite, and numerous steep zones of fissure-related quartz-muscovite greisen with cassiterite (Breiter 2012).

6. Beauvoir Li, P, F-rich lepidolite leucogranite (~310 Ma) is vertically fractionated and contains disseminated Sn and Ta mineralization (Raimbault et al. 1995). On the other side, the extent of muscovite bearing greisen is limited and the exo-

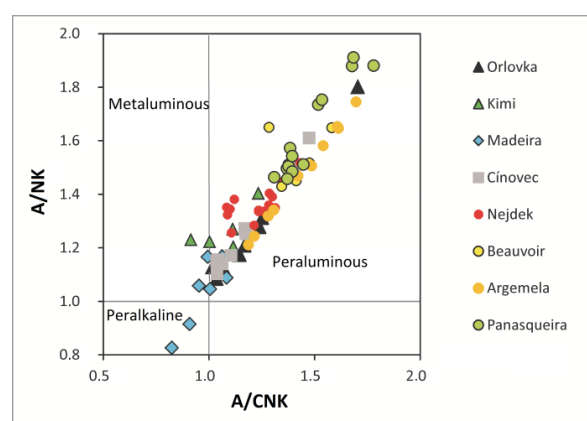


Figure 1. Classification of the studied granites according to their peraluminosity/alkalinity (Badanina et al. 2004; Costi et al. 2009; Lukkari et al. 2009; Raimbault et al. 1995; author's data).

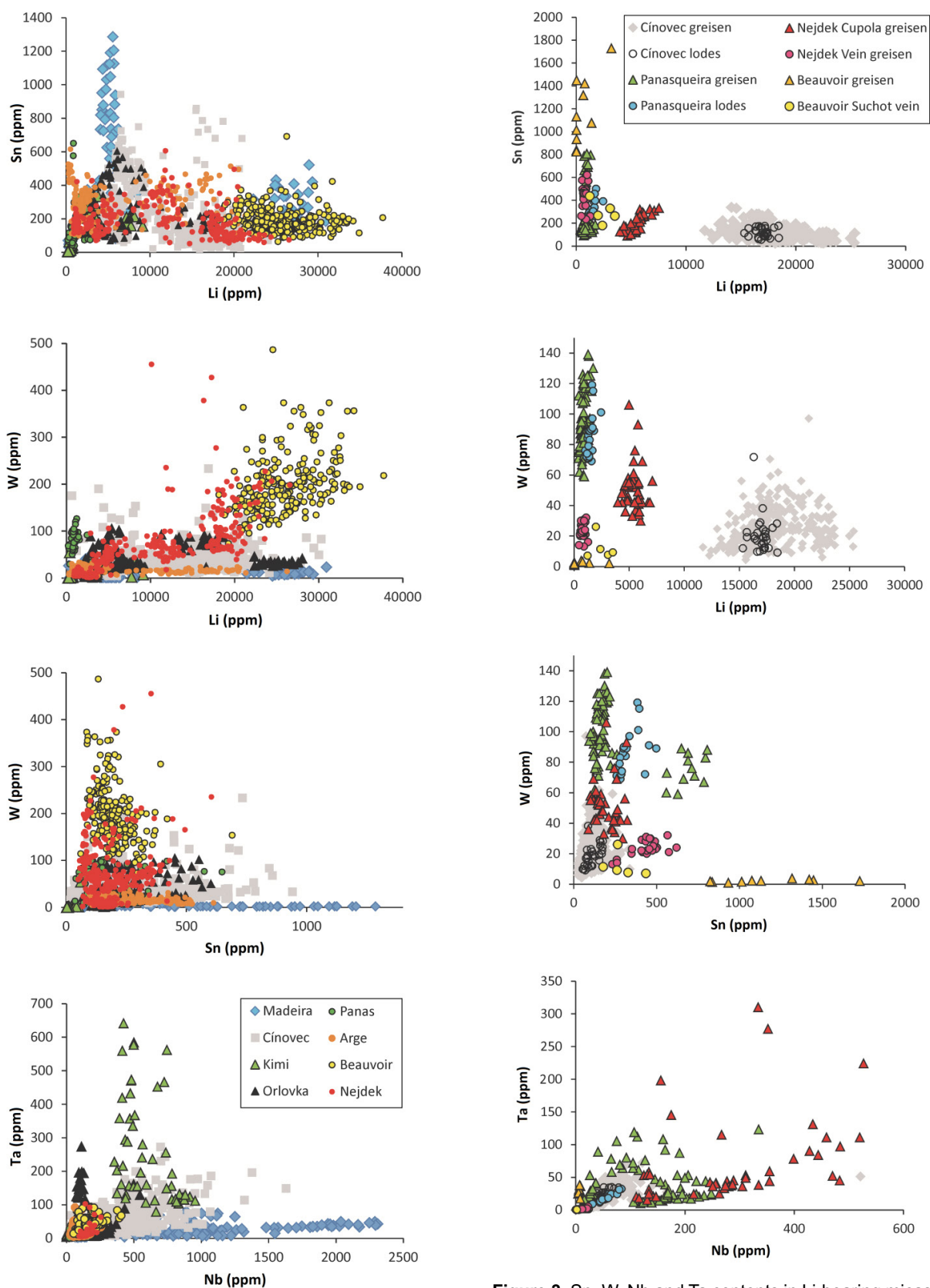


Figure 2. Sn, W, Nb and Ta contents in Li-bearing micas from fertile granitoids. Author's data.

Figure 3. Sn, W, Nb and Ta contents in Li-bearing micas from greisen and granite-related veins. Data from the Beauvoir greisen and the Suchot vein from Monnier et al. (2022), other author's data. Note the different scales in both figures.

contact aureole comprises only individual quartz veins (Monnier et al. 2022).

7. Panasqueira peraluminous pluton, Portugal, is composed of two-mica and muscovite facies, the later forming a greisenized cupola and a swarm of flat thick exocontact quartz-muscovite veins rich in wolframite (Marignac et al. 2020; Launay et al. 2021; Breiter et al. 2023).

8. Argemela stock, Portugal, is a small (<1 km²) two-phase leucogranite intrusion rich in Li, P, and F, with distinctly zoned mica phenocrysts (muscovite to lepidolite), with scarce thin intragranitic quartz-wolframite veinlets (Charoy and Noronha 1996; Michaud and Pichavant 2020; Breiter et al. 2022).

The Beauvoir, Argemela, Panasqueira and Nejdek plutons represent strongly peraluminous, P-rich (S-type) (late)-orogenic granites, while Kimi, Orlovka and Cínovec represent mostly subaluminous, P-poor, post-orogenic (A-type) granites. Madeira albite granite is an example of scarce mica-bearing peralkaline granites.

The Cínovec deposits is the best example of pervasive Li-rich greisenization with addition of some mineralized intragranitic quartz veins, while the Beauvoir, Orlovka and Madeira deposits contain dominantly disseminated magmatic mineralization. The Panasqueira deposit is a typical exocontact vein-type deposit. In all these mineralization types, micas play an important role.

3 Analytical methods

The contents of trace elements in mica from Cínovec and Nejdek were analyzed using solid-state Nd:YAG laser (UP 213, New Wave Research, Inc., Fremont, California, USA) coupled to quadrupole-based ICP mass spectrometer Agilent 7500ce (Agilent Technologies, Inc., Santa Clara, California, USA) installed in the Department of Chemistry, Masaryk University, Brno. Other samples were analyzed at Faculty of Chemistry, Brno University of Technology and BIC Brno. Here, an ArF* excimer 193 nm laser ablation system Analyte Excite+ (Teledyne CETAC Technologies, Omaha, Nebraska, USA) was connected to the Agilent 7900 quadrupole ICP mass spectrometer (Agilent Technologies, Inc., Santa Clara, California, USA). For more details see Breiter et al. (2023).

4 Contents of Sn, W, Nb and Ta in micas from fertile granites

Tin, W, Nb, and Ta are high-field-strength-elements (HFSE); in the magmatic stage they commonly enter the early crystallized Ti oxides, or tend to form disseminated cassiterite, columbite or pyrochlore groups of minerals later. Their contents in mica thus depend on the timing of crystallization of mica vs. accessory minerals. The content of Li in mica is a relevant indicator of geochemical evolution of magmatic systems. Thus, the results are presented as bivariate Li vs. metal diagrams (Figures 2, 3).

Tin is one of ubiquitous trace elements in mica starting from common calc-alkaline granites (up to 100 ppm); reaching 600 ppm in phengite from Orlovka and in zinnwaldite from Piaotang, China (Legros et al. 2018), 800 ppm in biotite and zinnwaldite from Cínovec, and 1300 ppm in annite from peralkaline granite of Madeira. The contents of W reached about 100 ppm in muscovite from Panasqueira and in phengite and zinnwaldite from Orlovka, 200 ppm in zinnwaldite from Nejdek, and 350 ppm in lepidolite from Beauvoir. The Sn/W values, (18 in C1 chondrites, McDonough and Sun 1995) vary from >100 in micas in peralkaline Madeira granite to 0.5 in Beauvoir and Nejdek and do not correlate with Sn or W fertility of the pluton.

Niobium is the most common trace element in micas among all discussed HFSE, reaching about 1000 ppm in biotite from Cínovec, 1500 ppm in Li-annite from Huangshan, China (Zhu et al. 2018), and 2400 ppm in annite from peralkaline granite from Madeira. The highest values of Ta, up to 200 ppm, were found in micas from Orlovka, Cínovec, Nejdek and from the Tanco pegmatite (Van Lichtenvelde et al. 2008). The Nb/Ta values in micas (Nb/Ta=17 in chondrite, McDonough and Sun 1995) are very variable: from ~50 in peralkaline granite of Madeira through ~5 in Beauvoir and Nejdek to 0.5 in zinnwaldite from Orlovka.

The contents of all HFSE in micas usually increase during initial stages of magmatic fractionation, while their behaviour in final stages of plutons evolution is very diverse. Generally, with increasing Li-contents, the contents of Sn, Nb and Ta decreased, while the contents of W increase or remain stable. An exception is the strong enrichment in Ta and Nb in late magmatic rims of lepidolite at Argemela (Breiter et al. 2022).

5 Micas from greisen and ore veins

The term “greisen” comprises a whole range of potentially ore-bearing quartz–mica dominated hydrothermal lithologies. The composition of greisen micas spans from muscovite across zinnwaldite to annite, whereas Li-enriched varieties are the most typical.

Pervasive greisens forming large pericontact bodies in granite cupolas are typical for shallow-level granite intrusions in the Erzgebirge: zinnwaldite-rich greisens in cupolas of strongly evolved granites usually contain cassiterite >> wolframite, while wolframite dominates in annite-bearing cupola-shaped greisens in less evolved granite facies. Lower-tempered fissure-related muscovite (phengite)-dominated greisens are usually cassiterite-bearing. In greisens, much like in granites, Li-poor micas (muscovite, annite) are Sn, W, Nb, Ta-enriched, while Li-rich zinnwaldite tends to be Sn, W, Nb, Ta-poor. Among distinctly mineralized quartz–mica veins, the intragranitic veins (+cassiterite and wolframite) at Cínovec contain HFSE-poor zinnwaldite, while the exogranitic wolframite-bearing veins at Panasqueira contain W-rich muscovite.

Lower contents of Sn and W in greisen micas at Cínovec compared to those in their magmatic precursors led Johan et al. (2012) to believe that magmatic annite was the main reservoir of Sn and W. During greisenization, the metals were, by the action of F-rich solutions, released forming cassiterite and wolframite in veins and greisen bodies. In contrast, Monnier et al. (2022) documented from Beauvoir, that, in this case a F-poor fluid destroyed magmatic cassiterite and W-enriched lepidolite; released tin was bound to newly formed Sn-rich (up to 1700 ppm) greisen muscovite, while W was transported away, forming exocontact vein-type wolframite mineralization.

6 Concluding remarks

Igneous and hydrothermal micas play a substantial role in HFSE accumulation and redistribution. The maximum contents reach ca. 1200 ppm Sn, 350 ppm W, 2300 ppm Nb and 200 ppm Ta.

With increasing fractionation of granite systems, demonstrated as vertical zoning (Cínovec, Orlovka, Beauvoir) or as a suite of subsequent intrusions (Madeira, Nejdek, Panasqueira), Li contents in mica increase, while the contents of HFSE usually decrease. Rather than the influence of the crystal structure, it is a consequence of the crystallization of Li-mica after the crystallization of the HFSE accessories. An exception is the Beauvoir granite with nearly identical contents of HFSE along the whole known vertical profile.

Micas from the peraluminous RMG are generally enriched in W, while micas from the subaluminous A-type granites are relatively enriched in Nb.

During greisenization, the share of mica in the HFSE budget usually strongly decreases and rutile, cassiterite and columbite become the main hosts of rare metals. However, an opposite example was recorded at Beauvoir. This illustrates the great variability in HFSE behavior during the magmatic/hydrothermal transition, which calls for further research.

Acknowledgements

This contribution was supported by the Czech Science Foundation, project EXPRO 19-29124X.

References

- Badanina EV, Veksler IV, Thomas R et al (2004) Magmatic evolution of Li-F rare-metal granites: a case study of melt inclusions in the Khangilay complex, Eastern Transbaikalia (Russia). *Chem Geol* 210: 113–133
- Breiter K (2012) Nearly contemporaneous evolution of the A- and S-type fractionated granites in the Krušné hory/Erzgebirge Mts., Central Europe. *Lithos* 151: 105–121
- Breiter K, Ďurišová J, Hrstka T et al (2017) Assessment of magmatic vs. metasomatic processes in rare-metal granites: a case study of the Cínovec-Zinnwald Sn–W–Li deposit, Central Europe. *Lithos* 292: 198–217
- Breiter K, Hložková M, Korblová Z, Vašíňová Galiová M (2019) Diversity of lithium mica compositions in mineralized granite–greisen system: Cínovec Li–Sn–W deposit, Erzgebirge. *Ore Geol Rev* 106: 12–27
- Breiter K, Ďurišová J, Korblová Z et al. (2022) Rock textures and mineral zoning – A clue to understanding rare-metal granite evolution: Argemela stock, Central-Eastern Portugal. *Lithos* 410–411: 106562
- Breiter K, Ďurišová J, Korblová Z et al. (2023) Granite Pluton at the Panasqueira Tungsten Deposit. *Minerals* 13, 163.
- Charoy B, Noronha F (1996) Multistage growth of a rare-element, volatile-rich microgranite at Argemela (Portugal). *J Petrol* 37: 73–94
- Costi HT, Dall'Agnol R, Pichavant M, Rämö OT (2009) The peralkaline tin-mineralized Madeira cryolite albite-rich granite of Pitinga, Amazonian craton, Brazil: petrography, mineralogy and crystallization processes. *Canad Mineral* 47: 1301–1327
- Johan Z, Strnad L, Johan V (2012) Evolution of the Cínovec (Zinnwald) granite cupola, Czech Republic: composition of feldspars and micas, a clue to the origin of W, Sn mineralization. *Canad Mineral* 50: 1131–1148
- Launay G, Sizaret S, Lach P et al (2021) Genetic relationship between greisenization and Sn–W mineralizations in vein and greisen deposits: insights from the Panasqueira deposit (Portugal). *BSGF Earth Sci Bull* 192: 2
- Legros H, Marignac C, Tabary T et al (2018) The ore-forming magmatic-hydrothermal system of the Piaotang W–Sn deposit (Jiangxi, China) as seen from Li–mica geochemistry. *Amer Mineral* 103: 39–54
- Lukkari S, Thomas R, Haapala I (2009) Crystallization of the Kymi topaz granite stock within the Wiborg rapakivi batholith, Finland: Evidence from melt inclusions. *Canad Mineral* 47: 1359–1374
- Marignac C, Cuney M, Cathelineau M et al (2020) The Panasqueira rare metal granite suites and their involvement in the genesis of the world-class Panasqueira W–Sn–Cu deposit: a petrographic, mineralogical, and geochemical study. *Minerals* 10: 562
- McDonough WF, Sun S (1995) The composition of the Earth. *Chem Geol* 120: 223–253
- Michaud JAS, Pichavant M (2020) Magmatic fractionation and the magmatic-hydrothermal transition in rare metal granites: evidence from Argemela (Central Portugal). *Geochim Cosmochim Acta* 289: 130–157
- Monnier L, Salvi S, Melleton J et al (2022) Mica trace-element signatures: highlighting superimposed W–Sn mineralizations and fluid sources. *Chem Geol* 600: 120866
- Raimbault L, Cuney M, Azencott C et al (1995) Geochemical evidence for a multistage magmatic genesis of Ta–Sn–Li mineralization in the granite at Beauvoir, French Massif Central. *Econ Geol* 90: 548–596
- Van Lichtenvelde M, Grégoire M, Linnen RL et al (2008) Trace element geochemistry by laser ablation ICP-MS of micas associated with Ta mineralization in the Tanco pegmatite, Manitoba, Canada. *Contrib Mineral Petrol* 155: 791–806
- Xie L, Wang RC, Groat LA et al (2015) A combined EMPA and LA-ICP-MS study of Li-bearing mica and Sn–Ti oxide minerals from the Qiguling topaz rhyolite (Qitianling district, China): the role of fluorine in origin of tin mineralization. *Ore Geol Rev* 65: 779–792
- Zhu Z, Wang R, Marignac C et al (2018) A new type of rare metal granite with Nb-rich mica: the early Cretaceous Huangshan rare-metal granite suite, northeast Jiangxi Province, China. *Amer Mineral* 103: 1530–1544

Fluid evolution in the San Rafael Sn-Cu lode deposit, Peru: Constraints from fluid inclusion analyses and chlorite geochemistry

Malena Cazorla Martínez^{1*}, Kalin Kouzmanov¹, Alexandra Tsay¹, Zoltán Zajacz¹, Florence Bégué¹, Matthieu Harlaux², Miroslav Kalinaj³, Lluís Fontboté¹

¹Department of Earth sciences, University of Geneva, Geneva, Switzerland

²BRGM – French Geological Survey, 45060 Orléans, France

³MINSUR S.A., Peru

*Present address: iCRAG, University College Dublin Belfield, Dublin 4, Ireland

Abstract. We have studied the evolution of mineralizing fluids in the world-class San Rafael Sn-Cu lode district, Peru, by investigating the major and trace element compositions of fluid inclusions and hydrothermal chlorite from four major mineralization stages of the deposit. Hypersaline liquid, vapor, and liquid-vapor fluid inclusion assemblages in quartz, fluorite, and cassiterite have been analyzed by microthermometry, Raman spectroscopy and LA-ICP-MS. Salinity and homogenization temperature decrease from stage I to stage IV. Most element concentrations in the fluid inclusions (e.g., Zn, Pb, Na) decrease progressively from stage I to stage IV, except for B. Fluid mixing at 350–250°C of a hypersaline, high-temperature, metal-bearing, magmatic fluid with a low-temperature and low-salinity fluid is proposed to explain the fluid dilution and the decrease in temperature and salinity. Widespread presence of CH₄ in fluid inclusions indicates the reduced character of the fluids. Constant B content throughout the four hydrothermal stages could result from the replacement of early-stage tourmaline by chlorite, bringing B into solution continuously. Copper, Zn, Pb, and Mn are enriched in chlorite belonging to stage IV. The Ti/Pb and Ni/Cu trace element ratios in chlorite correlate with fluid temperatures and could be used as proxies for temperature evolution at San Rafael.

1 Introduction

The Central Andean tin belt (CATB) of the South American Cordillera is a major metallogenic province that extends from southern Peru, through Bolivia, to northern Argentina (Lehmann et al. 1990). The CATB hosts numerous Sn-W±Ag-Cu deposits, including Mesozoic mesothermal Sn-W deposits in its northern sector, and Oligocene to Miocene polymetallic Sn-W deposits along the entire belt (Clark et al. 1990). The San Rafael Sn-Cu deposit, located in the northernmost tip of the CATB, is currently one of the largest hypogene Sn deposits worldwide (total past production + remaining resources of >1.5 Mt of Sn with an average grade of 3.7%; Harlaux et al. 2023). In 2020, Minsur S.A. has reported 195,300 t fine Sn in measured + indicated resources and 73,600 t fine Sn in inferred resources, while total reserves were estimated at 132,000 t fine Sn (Minsur S.A. 2021). The geological and structural setting, the paragenetic sequence, and the rock and mineral geochemistry of the San Rafael deposit have been extensively studied (e.g., Arenas 1980; Palma 1981; Kontak and Clark 2002; Mlynarczyk et al. 2003;

Mlynarczyk 2005; Mlynarczyk and Williams-Jones 2005, 2006; Wagner et al. 2009; Corthay 2014; Prado Flores 2015; Harlaux et al. 2020, 2021a, b). Fluid inclusion microthermometry data for San Rafael have been reported in some of the previous studies; however, no trace element data about the mineralizing fluids are available for this major Sn deposit.

In the present study, we report new fluid inclusion trace element analyses and chlorite mineral compositional data that provide new insights into the fluid evolution of the world-class San Rafael Sn-Cu lode deposit with emphasis on the origin of the mineralizing fluids and ore forming processes.

2 Geological setting

The San Rafael deposit is located in the Eastern Cordillera of southeast Peru. The San Rafael intrusive complex consists of several granitic bodies, which were emplaced during the Late Oligocene (ca. 24 Ma) into Carboniferous and Ordovician metasedimentary rocks, producing contact metamorphism (Kontak and Clark 2002; Harlaux et al. 2021a, 2023). The mineralization is hosted by NW-trending, quartz-cassiterite-sulfide veins and breccia bodies, both spatially associated with the granitic complex (Kontak and Clark 2002; Mlynarczyk et al. 2003), as well as late-stage polymetallic veins.

Four major mineralization stages have been identified at San Rafael (Arenas 1980; Palma 1981; Kontak and Clark 2002; Mlynarczyk et al. 2003; Wagner et al. 2009): (1) an early, pre-ore quartz-tourmaline stage I; (2) a main Sn ore stage II, occurring in quartz-chlorite-cassiterite veins and breccia bodies; (3) a sulfide-dominant stage III, associated to the major deposition of base metal sulfides (e.g., chalcopyrite, pyrrhotite, sphalerite, arsenopyrite, pyrite, and galena); and finally (4) a late, barren stage IV, consisting of banded silica, platy calcite, fluorite, adularia, with minor sulfides and carbonates.

3 Materials and methods

Thirty-two samples, both from surface outcrops and underground workings from the San Rafael mine

and the Quenamari prospect, representative of each of the mineralization stages have been selected. Mineralogy and textures were studied by optical microscopy, optical and SEM cathodoluminescence, BSE imaging, and QEMSCAN mapping at the Department of Earth sciences, University of Geneva.

Petrography of fluid inclusion assemblages (FIA) was followed by microthermometric measurements on a Linkam THMSG 600 stage mounted on a Leica DMLB microscope for transparent minerals, and a Linkam FTIR 600 stage mounted on an Olympus BH2 microscope for near-infrared microthermometry of opaque minerals. Raman spectroscopy analyses have been performed on the vapor, liquid, and solid phases in the FIs, using a LabRAM HR Evolution (HORIBA Scientific) Raman spectrometer. LA-ICP-MS analyses on individual FIs were conducted using a NWR 193 He Laser Ablation system coupled to an Agilent 8900 triple quadrupole mass spectrometer. Isotopes analyzed include ^7Li , ^{11}B , ^{23}Na , ^{29}Si , ^{34}S , ^{35}Cl , ^{39}K , ^{43}Ca , ^{55}Mn , ^{56}Fe , ^{65}Cu , ^{66}Zn , ^{75}As , ^{79}Br , ^{85}Rb , ^{88}Sr , ^{108}Ag , ^{118}Sn , ^{133}Cs , ^{137}Ba , ^{204}Tl , and ^{208}Pb .

Hydrothermal chlorites from 9 samples have been analyzed by EMPA for major and minor elements using a JEOL 8200 Superprobe and by LA-ICP-MS for trace elements using a NWR 193 He Laser Ablation system coupled to an Agilent 8900 triple quadrupole mass spectrometer.

4 Results

4.1 Fluid inclusion study

FIs from the four mineralization stages have been studied (Figure 1): secondary hypersaline liquid (L-V-NaCl; “brines”), high-density vapor (V), and aqueous liquid-vapor (L-V) FIAs in stage-I quartz and tourmaline; primary and pseudo-secondary L-V and low-density V FIAs in stage-II quartz; primary and pseudo-secondary L-V FIAs in stage-III quartz; and primary, pseudo-secondary, and secondary L-V, solid-liquid-vapor (L-V-S), and boiling (liquid+vapor) FIAs in stage IV quartz and fluorite. Average homogenization temperatures for stages I, II, III and IV are $402 \pm 27^\circ\text{C}$, $287 \pm 26^\circ\text{C}$, $291 \pm 47^\circ\text{C}$, and $244 \pm 35^\circ\text{C}$, respectively. Fluid salinity ranges between 48.0 ± 2.5 wt% NaCl eq. for L-V-NaCl FIs, and 15.6 ± 4.5 wt% NaCl eq. for L-V FIs in stage I. Average salinity in stage II is 7.5 ± 6.3 wt% NaCl eq., 5.3 ± 3.0 wt% NaCl eq. in stage III, 4.1 ± 3.3 wt% NaCl eq. in fluorite-hosted FIAs from stage IV, and 0.6 ± 0.6 wt% NaCl eq. in banded silica-hosted FIAs from stage IV.

Raman spectroscopy analyses allowed identification of CH_4 in FIs from all the stages, boric acid in FIs from stages II and IV, calcite crystals in FIs from stage IV, and Fe-bearing hydroxylchloride daughter crystals in brines from stage I (i.e., Fe-pyrosomalite $\text{Fe}_8\text{Si}_6\text{O}_{15}(\text{OH}, \text{Cl})_{10}$ and hibbingite $\gamma\text{-Fe}_2(\text{OH})_3\text{Cl}$).

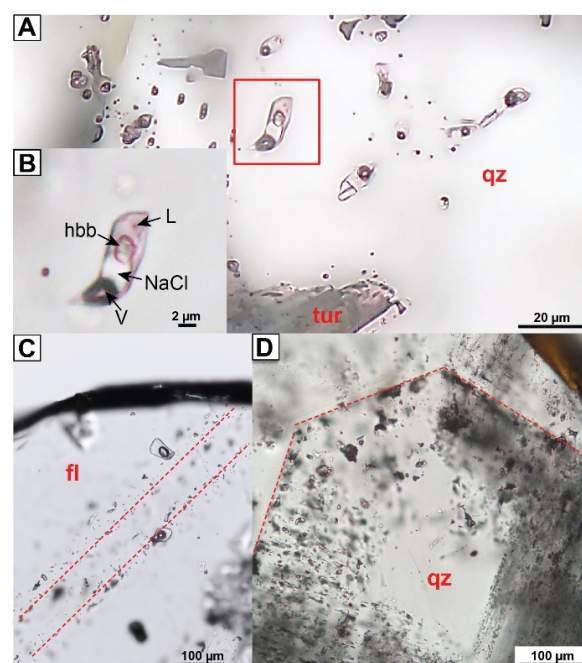


Figure 1. Fluid inclusion assemblages observed in studied samples from the San Rafael Sn-Cu deposit. A) Quartz-hosted L-V-NaCl FIs from stage I. B) Close up of the FI in A. C) Fluorite-hosted primary L-V FIAs from stage IV. D) Quartz-hosted primary L-V FIAs from stage IV. Dashed red lines represent primary growth banding. Abbreviations: fl - fluorite; hbb - hibbingite; L - liquid; qz - quartz; tur - tourmaline; V - vapor.

LA-ICP-MS analyses of FIAs show variations of up to 3 orders of magnitude for Na, K, Ca, Cl, Sr, Mn, Ti, Zn, Pb, and Ba concentrations between FIs from stage I and those from stage IV (Fig. 2; e.g., 1,000-10,000 ppm Pb in stage I, and 1-10 ppm Pb in stages III-IV).

Elements such as B (and Li to a lesser extent) show similar contents in FIAs from all the stages with values of 1,000-10,000 ppm B. Iron, Sn, and Cu were not detected in most of the FIs. Nevertheless, brine FIAs belonging to stage I yield anomalously high Fe (1-10 wt.% Fe) and high Sn concentrations (200-2,000 ppm Sn). In addition, FIAs from stage I show higher values of Fe and Na/K ratio than most FIs from stages II, III, and IV.

4.2 Chlorite geochemistry

Chlorite is a major gangue mineral in stages II, III, and IV, typically intergrown with quartz, cassiterite and sulfides. Chlorite in veins and their alteration halos has been analyzed from the three stages of mineralization, although most analyses have been performed on vein chlorite.

Most of the studied chlorite aggregates at San Rafael is classified as Fe-chlorite (ripidolite and daphnite), except for several chlorites from Quenamari which correspond to Al-chlorite (diabentite). Furthermore, chlorites in samples

from stage IV at Quenamari are enriched in Mn (1-2.5 wt% MnO) relative to those from stages II and III at San Rafael (~0.3 wt% MnO).

The most abundant trace elements in the analyzed chlorites are Li (200-900 ppm), B (3-50 ppm), Ti (10-1,000 ppm), V (1-100 ppm), Co (1-1,000 ppm), Ni (1-1,000 ppm), Cu (0.01-1,000 ppm), Zn (20-5,000 ppm), Sr (0.1-10 ppm), Sn (10-1,000 ppm), and Pb (1-1,000 ppm). However, it must be noticed that the contents of several elements such as Pb, Cu, Zn, Ni, and Ti vary remarkably across chlorites from different stages. Concentrations of Cu, Zn, and Pb in stage IV chlorite are ~2 orders of magnitude higher than that in stages II and III. Conversely, Ni contents are within one sample systematically lower in stage IV than in stages II and III.

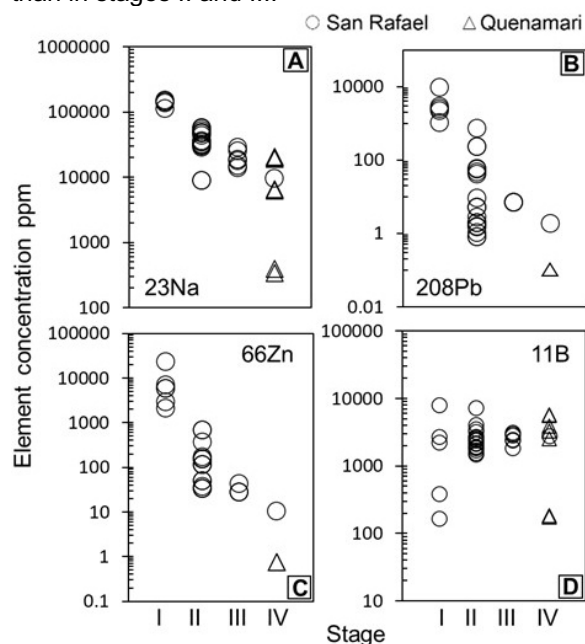


Figure 2. Element concentrations analyzed by LA-ICP-MS in individual quartz-hosted fluid inclusions from stages I, II, III, and IV. Each symbol corresponds to an individual fluid inclusion analysis. A) Sodium. B) Lead. C) Zinc. D) Boron.

5 Discussion

5.1 Fluid evolution

Fluids of magmatic origin were the dominant fluid type during the early stage of mineralization. They are characterized by high Fe concentrations (found in some FIs belonging to stage I, as indicated by LA-ICP-MS analyses and the presence of hibbingite and Fe-pyrosmalite daughter crystals), and relatively low Na/K ratios in comparison to FIs from the later stages. As proposed by some authors (Audétat et al. 1998; Harlaux et al. 2017), fluid mixing between an early, high-temperature, metal-rich magmatic fluid and a low-temperature, low-salinity, and metal-depleted fluid may cause the drop of 2-3 orders of magnitude of element concentrations within the evolution of the early- to

the late-stage FIAs (Figs. 2A-C), in parallel to a constantly decreasing homogenization temperature (Figs. 3B-D) and salinity. The presence of CH₄ in the studied FIAs is indicative of the reduced character of the fluids, which is consistent with the mineral paragenesis of the ore assemblages. Previous stable isotope studies (Wagner et al. 2009; Harlaux et al. 2021a) demonstrated the importance of fluid mixing between magmatic fluids and meteoric waters for ore deposition at San Rafael.

Stage-I FIs show high concentrations of Sn (100-1000 ppm), which highlights the potential of these fluids to precipitate large amounts of cassiterite during the late stage. Boron concentrations in the fluid are constant from early to late stages of mineralization (Figs. 2D and 3A; 1,000-10,000 ppm), that could result from the shift from tourmaline alteration in stage I to chloritization, replacing tourmaline, from stage II onwards (this study; Mlynarczyk 2005). When tourmaline is replaced by chlorite, B is released again into the fluid, which seems to result in elevated and constant B concentrations in the fluid..

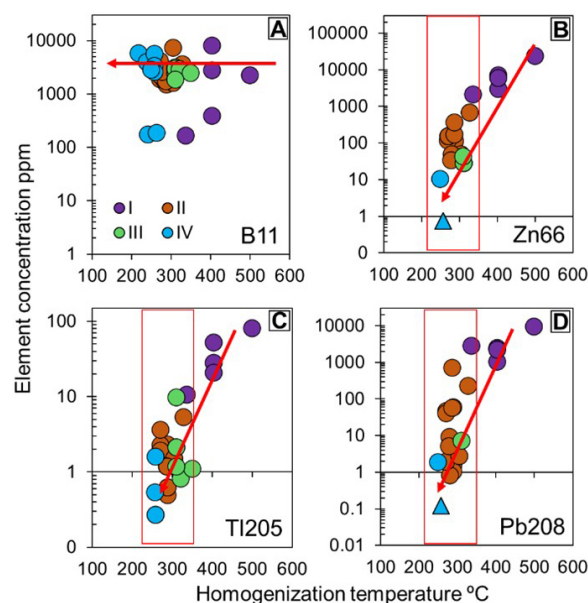


Figure 3. Element concentration in individual fluid inclusions. vs. homogenization temperatures plots of A) Boron, B) Zinc, C) Thallium, and D) Lead. Each spot represents an individual fluid inclusion. Red square represents the interpreted temperature range at which fluid mixing took place. Red arrows represent the general evolutionary trend from early to late stages.

5.2 Chlorite compositions

High Mn content in chlorite from the Quenamari prospect – stage IV – is attributed to the presence of a late well-developed Mn-rich assemblage in the Quenamari prospect (Corthay 2014), which is missing in the San Rafael deposit.

As proposed by Wilkinson et al. (2015), chlorite trace element ratios, such as Ti/Pb, can be used as

vectors for high-temperature centers in porphyry ore deposits. In the present study, chlorite trace element ratios of specific elements (following the methodology of Wilkinson et al. 2015) were compared to FI homogenization temperatures obtained for the same sample (Fig. 4). Results show that the samples with the lowest homogenization temperatures (Fig. 4A) are those yielding the lowest values for the Ni/Cu and Ti/Pb ratios (Figs. 4B-C), and vice versa.

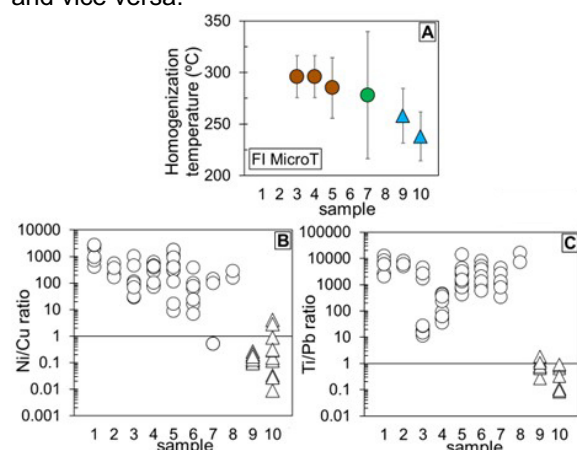


Figure 4. A) Average fluid inclusion homogenization temperatures for samples where chlorite geochemistry was studied. Error bars correspond to standard deviation. B) Ni/Cu and C) Ti/Pb ratios in chlorites from the San Rafael deposit.

6 Conclusions

Fluid inclusion analysis document a distinct decrease in trace element concentrations from early to late stages at San Rafael, consistent with a progressive decrease in temperature and salinity of the fluids. Fluid systematics are interpreted to be related to fluid mixing at 250-350°C of early hypersaline (40-50 wt% NaCl), hot (>400°C), metal-rich (20,000-130,000 ppm Fe, 100-1,000 ppm Sn, 1,000-10,000 ppm Zn, 1,000-10,000 ppm Pb) magmatic fluids, with lower-temperature (~200°C), low-salinity (~1 wt% NaCl), metal-poor meteoric waters. Constant B concentrations in early- to late-stage FIAs is interpreted to result from tourmaline replacement by chlorite, maintaining a constant release of B along the fluid flow path. Mn-bearing chlorite at Quenamari are indicative of the presence of a Mn-rich stage developed in that part of the district, which has not been previously recognized at the San Rafael deposit. The Ti/Pb and Ni/Cu trace element ratios in chlorite at San Rafael are proposed as possible proxies for high-temperature mineralization centers, possibly unexposed in the Quenamari area.

References

Arenas MJ (1980) El distrito minero San Rafael, Puno – Estación en el Perú. *B Soc Geol Perú* 66:1-11.
Audétat A, Günther D, Heinrich CA (1998) Formation of a magmatic-hydrothermal ore deposit: Insights with LA-ICP-

MS analysis of fluid inclusions. *Sciences* 279(5359): 2091-2094.
Clark AH, Farrar E, Kontak DJ, Langridge RJ, Arenas FMJ, France LJ, McBride SL, Woodman PL, Wasteneys HA, Sandeman HA, Archibald DA (1990) Geologic and geochronologic constraints on the metallogenic evolution of the Andes of southeastern Peru. *Econ Geol* 85:1520-1583
Corthay G (2014) The Quenamari prospect, San Rafael tin District, southern Peru: Geology, mineral assemblages, fluid inclusion microthermometry, and stable isotopes. Unpubl. MSc thesis, University of Geneva, Switzerland.
Kontak DJ, Clark AH (2002) Genesis of the giant, bonanza San Rafael lode tin deposit, Peru: origin and significance of pervasive alteration. *Econ Geol* 97:1741-1777.
Harlaux M, Mercadier J, Bonzi WME, Kremer V, Marignac C, Cuney M (2017) Geochemical signature of magmatic-hydrothermal fluids exsolved from the Beauvoir rare-metal granite (Massif Central, France): Insights from LA-ICPMS Analysis of primary fluid inclusions. *Geofluids*:1-25.
Harlaux M, Kouzmanov K, Gialli S, Laurent O, Rielli A, Dini A, Chauvet A, Menzies A, Kalinaj M, Fontboté L (2020) Tourmaline as a Tracer of Late-Magmatic to Hydrothermal Fluid Evolution: The World-Class San Rafael Tin (-Copper) Deposit, Peru. *Econ Geol* 115:1665-1697.
Harlaux M, Kouzmanov K, Gialli S, Clark AH, Laurent O, Corthay G, Prado Flores E, Dini A, Chauvet A, Ulianov A, Chiaradia M, Menzies A, Villón Durand G, Kalinaj M, Fontboté L (2021a) The upper Oligocene San Rafael intrusive complex (Eastern Cordillera, southeast Peru), host of the largest-known high-grade tin deposit. *Lithos* 400-401:106409.
Harlaux M, Kouzmanov K, Gialli S, Marger K, Bouvier AS, Baumgartner LP, Rielli A, Dini A, Chauvet A, Kalinaj M, Fontboté L (2021b) Fluid mixing as primary trigger for cassiterite deposition: Evidence from in situ $\delta^{18}\text{O}$ - $\delta^{11}\text{B}$ analysis of tourmaline from the world-class San Rafael tin deposit, Peru. *Earth Planet Sci Lett* 563:116889.
Harlaux M, Kontak DJ, Clark AH, Kouzmanov K, Holm-Denoma CS, Gialli S, Laurent O, Spinkings R, Chauvet A, Dini A, Kalinaj M, Fontboté L (accepted) Depositing over 1.5 Mt of Sn within 1Ma of initial granitic intrusion in the San Rafael Sn (-Cu) deposit, southeastern Peru. *Econ Geol*.
Lehmann B, Ishihara S, Michel H, Miller J, Rapela CW, Sanchez A, Tistl M, Winkelmann L (1990) The Bolivian tin province and regional tin distribution in the central Andes: A reassessment. *Econ Geol* 85:1044-1058.
Minsur S.A. (2021) Annual Report: March 28, 2022, 71 p., www.minsur.com.
Mlynarczyk MS, Sherlock RL, Williams-Jones AE (2003) San Rafael, Peru: geology and structure of the world's richest tin lode. *Miner Deposita* 38:555-567.
Mlynarczyk MSJ (2005) Constraints on the genesis of lode-style tin mineralization: Evidence from the San Rafael Tin-Copper deposit, Peru. PhD Thesis, Department of Earth and Planetary Sciences, McGill University, Montreal, Canada.
Mlynarczyk MS, Williams-Jones AE (2005) The role of collisional tectonics in the metallogeny of the Central Andean tin belt. *Earth Planet Sci Lett* 240:656-667.
Mlynarczyk MS, Williams-Jones AE (2006) Zoned tourmaline associated with cassiterite: implications for fluid evolution and tin mineralization in the San Rafael Sn-Cu deposit, southeastern Peru. *Can Mineral* 44:347-365.
Palma VV (1981) The San Rafael tin-copper deposit, Puno, SE Peru. Master's Thesis, Queen's University, Kingston, Ontario, United States of America.
Prado Flores E (2015) San Rafael Tin Mine, Peru: Geology, mineralogy, O and H stable isotopes, and fluid inclusions microthermometry of the deep level 3600m. Unpubl. MSc thesis, University of Geneva, Switzerland, 89 p.
Wagner T, Mlynarczyk MS, Williams-Jones AE, Boyce AJ (2009) Stable isotope constraints on ore formation at the San Rafael tin-copper deposit, Southeast Peru. *Econ Geol* 104: 223-248.
Wilkinson JJ, Chang Z, Cooke DR, Baker MJ, Wilkinson CC, Inglis S, Chen H, Gemmel JB (2015) The chlorite proximator: A new tool for detecting porphyry ore deposits. *J Geoch Explor* 152: 10-26.

Multi-phase tungsten mineralisation at the world class Hemerdon deposit, south-west England

Eimear Deady^{1,2}, K. Moore¹, R.K. Shail¹, K.M. Goodenough² and S. Chenery²

¹Camborne School of Mines, University of Exeter, UK

²British Geological Survey, UK

Abstract. Tungsten mineralisation in the form of wolframite is commonly hosted in greisen stockworks associated with peraluminous granites globally. Tungsten mineralisation at the world-class Hemerdon deposit, located in south-west England, has a complicated mineralogical and chemical history, which records repeated fluid-derived alteration, dissolution and (re)precipitation. Limited evidence for the coeval deposition of cassiterite with wolframite has been found at Hemerdon.

1 Introduction

The Variscan granite-related mineralisation at Hemerdon comprises one of the largest tungsten deposits in the world. It has a combined, JORC-compliant, mineral resource estimate of 351.5 Mt at 0.12% WO₃ and 0.03% Sn (Tungsten West, 2022). The Hemerdon Ball Granite is a G2 muscovite granite cupola and dyke (Simons et al. 2016), separate but adjacent to the Dartmoor Granite in Devon, south-west England. The Cornubian Batholith is subclassified into five different peraluminous granites, where G2 represents the muscovite granite. It hosts a greisen-bordered sheeted vein system with ferberite and wolframite (\pm cassiterite) mineralisation approximately 100+ m wide. Mineralisation extends into the metasedimentary host rocks. The deposit was recently exploited (2015–18) at the Drakelands Mine and is in the process of redevelopment by Tungsten West (2020–present).

This study uses combined optical microscopy, cathodoluminescence, SEM, EPMA, fluid inclusion microthermometry, stable and radiogenic isotopes and LA-ICP-MS point and mapping analysis to establish a detailed paragenetic succession for the mineralisation at the Hemerdon deposit. We also determine the concentration of major and trace elements in wolframite. Our aim is to provide new constraints on the physico-chemical evolution of sheeted vein wolframite deposits.

2 Petrography

2.1 Mineral assemblages and paragenetic relationships

Tungsten mineralisation is typically hosted in greisen, or greisen-absent quartz-dominated veins. The metallic mineral assemblages comprise wolframite and/or ferberite (the iron-rich end-member of the wolframite series) + arsenopyrite \pm chalcopyrite, pyrite, native bismuth, cassiterite

(Figure 1). Both wolframite and ferberite are present as primary phases at Hemerdon, while secondary, recrystallised ferberite is common along crystal boundaries, fractures, and occasionally as a replacement (or alteration) phase associated with the pervasive alteration of wolframite (Figure 2a). Accessory phases in the tungsten-bearing veins include, in varying amounts, apatite, fluorite, monazite, tourmaline, rutile, scorodite, cassiterite, native bismuth, xenotime and zircon. The role the accessory phases, in particular the phosphates and fluorides, play in the deposition of wolframite (Wang et al., 2023) will be considered in the ongoing research.

Mineral	Early greisen stage	Vein stage	Supergene stage
Quartz			
Muscovite			
Orthoclase			
Apatite			
Wolframite			
Ferberite			
Scheelite			
Arsenopyrite			
Chalcopyrite			
Pyrite			
Cassiterite			
Bismuth			
Russellite			
Scorodite			
Iron oxide			

Figure 1. Generalised paragenesis at Hemerdon (this study, McAllister 2016, Cameron 1951).

The wolframite-quartz veins are part of a wider ore system that comprises multiple generations of barren and mineralised veins (McAllister, 2016, unpublished). The relationship between these veins is being investigated as part of this project.

2.2 Scanning Electron Microscopy (SEM) analysis of wolframite petrogenesis

SEM-based, back scattered electron microscopy has been used to identify the range of wolframite-ferberite textures that occur throughout the Hemerdon deposit. The mineralisation is dominated by the Fe-rich end member, ferberite, with variable distribution of wolframite. The textures range from heavily altered and porous, with secondary precipitation of ferberite, to unaltered, fresh wolframite (Figure 2A-D). The distribution of the alteration throughout the deposit is currently being assessed as part of this project

to inform mine planning. Limited evidence for the coeval deposition of cassiterite with wolframite has been found at Hemerdon.

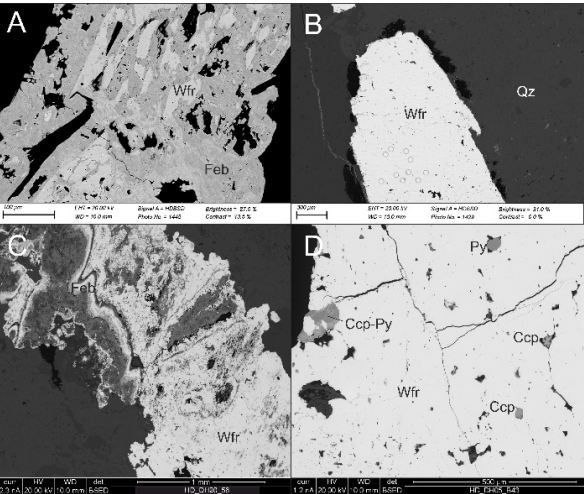


Figure 2. Back scatter electron (BSE) images of A wolframite with ferberite overgrowths; B unaltered wolframite with minor dissolution along crystal boundaries; C dissolution-reprecipitation of wolframite-ferberite; D fresh unaltered wolframite with sulfide

inclusions. Wfr–wolframite, Feb–ferberite, Ccp–chalcopyrite, Py–pyrite (after Warr, 2021).

2.3 LA-ICP-MS major and trace element mapping

The textural variability and ferberite-wolframite relationships indicate that metallogenesis involved a complicated and protracted fluid history. The crystallographic and geochemical variations are indistinguishable under normal SEM BSE analysis conditions. However, variation on the microscale is apparent using LA-ICP-MS element mapping and it indicates that multiple fluids had variable Fe/Mn ratios and trace element budgets. Mapping of individual crystals shows five stages of wolframite precipitation in an otherwise relatively fresh wolframite: 1. an initial Mn-rich, Fe-poor wolframite core with; 2. a subsequent Nb-Ta-rich, Fe-rich wolframite, with elevated Sn, followed by; 3. a Ti-Mn-rich wolframite which is depleted in the other major and trace elements. Stage 4 repeats stage 2, while stage 5 is a later stage of Bi-Mo ±Fe secondary mineralisation (Figure 3).

3 Further work

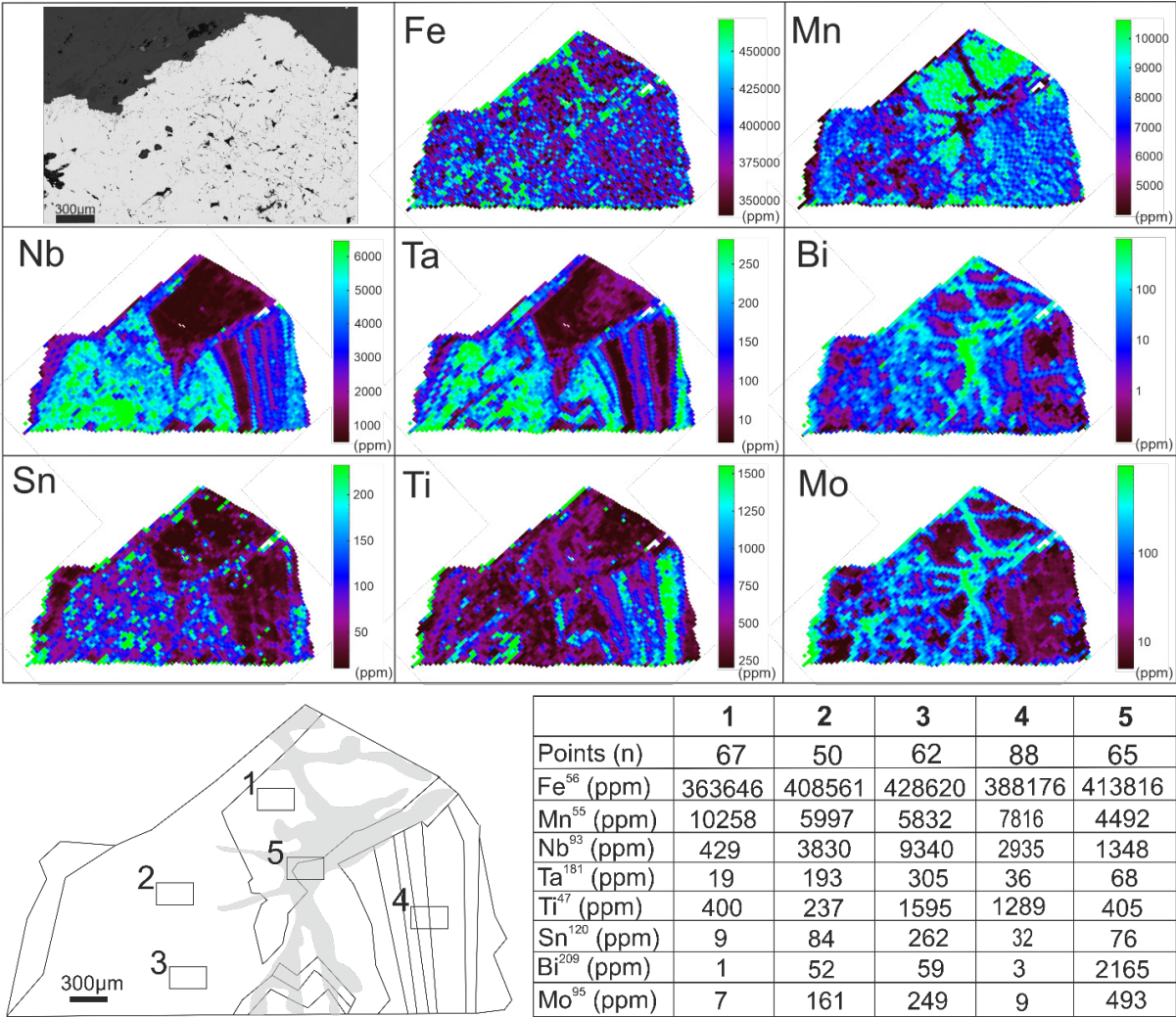


Figure 3. LA-ICP-MS mapping of wolframite from the Hemerdon deposit showing zones described in the text. Average composition data from five areas within the mapped region show the range of compositional variation.

Initial observations indicate a complex, multi-generational fluid history for wolframite-ferberite precipitation at Hemerdon. The tungsten-bearing veins form just one part of the system and so need to be put in the context of the later veins. Cassiterite mineralisation at Hemerdon appears to be hosted in a separate generation of fluids, based on the dearth of veins hosting co-precipitated cassiterite and wolframite, so, the relationship between these fluids and vein sets needs further analysis to interpret the relationship.

Acknowledgements

The authors thank staff at the Hemerdon deposit mine site (then Wolf Minerals, now Tungsten West) for facilitating access and sample collection at Hemerdon and fruitful discussions. John Fletcher (BGS) is thanked for the preparation of exemplary polished thin sections. The BGS Innovations Flexible Fund supported the development of the LA-ICP-MS mapping method.

References

- Cameron J (1951) The geology of Hemerdon wolfram mine, Devon Transactions of the Institute of Mining and Metallurgy 61:1-14
- Simons B, Shail RK, Andersen JC (2016) The petrogenesis of the Early Permian Variscan granites of the Cornubian Batholith: lower plate post-collisional peraluminous magmatism in the Rhenohercynian Zone of SW England Lithos 260:76-94 doi:<https://doi.org/10.1016/j.lithos.2016.05.010>
- Wang X-S, Williams-Jones A, Hu R-Z, Jiang Z-Q, Shang L-B, Bi X-W (2023) Apatite and fluorite control the transport of tungsten in calcium-bearing hydrothermal fluids Geochimica et Cosmochimica Acta 346:1-14 doi:<https://doi.org/10.1016/j.gca.2023.02.001>
- Warr LN (2021) IMA–CNMNC approved mineral symbols Mineralogical Magazine 85:291-320 doi:<https://doi.org/10.1180/mgm.2021.43>

U-Pb columbite-tantalite ages from NW-Amazonian Craton, Colombia

Jose A. Franco^{1,2}, Albrecht Von Quadt³, Amed Bonilla², Alejandro Piraquive^{2,4}, Thomas Cramer^{1,2}, Zeze Amaya²

¹Universidad Nacional de Colombia. Bogotá, Colombia

²Grupo de Estudios en Geología Económica y Mineralogía Aplicada (GEGEMA). Bogotá, Colombia

³Institute of Petrology and Geochemistry ETH. Zurich, Switzerland

⁴Geological Survey of Norway. 7491 Trondheim, Norway

Abstract. At E-Colombian Vichada and Guainía region, Mesoproterozoic rocks of the northwest part of the Amazonian Craton are potential sources of Columbite Group Minerals (CGM), cassiterite, and REE mineralizations. Columbite grains were extracted from colluviums and pegmatitic dykes at San Jose (LOC 5), from colluviums at Barranquilla (LOC 6) and as closely (LOC 2), from colluviums of La Fortuna and El Burro-Venezuela. In pan concentrates, the common mineral assembly is rutile-(Nb,Ta) and REE-minerals. In the latter, metallographic and SEM-EDX analyses revealed columbite-Fe grains containing inclusions of up to 0.2 mm length of ixiolite, rutile-(Nb,Ta), and occasionally tantalite-Mn and microlite. Major and trace elements concentrations obtained through XRF and EPMA reveal matrix variations in the Nb₂O₅, Ta₂O₅, TiO₂, and Fe₂O₃ contents. Sufficient U, Pb, and Th in single columbite crystals permitted conducting LA-ICP-MS U-Pb dating yielding concordant ages at ca. 1549 ± 5 Ma for (LOC 5) and 1531 ± 12 Ma for (LOC 6) and 1472 ± 12 Ma for Venezuelan columbites. The reported ages are coeval with ages of granitoid suites documented in the vicinity of the Orinoco River ranging between ca. 1600-1350 Ma, indicating thus a genetic link between columbite-Fe ores and early Mesoproterozoic magmatism.

1 Introduction

Minerals of the columbite-tantalite group (CT) constitute an isomorphic series (Mn²⁺, Fe²⁺)(Ta,Nb)₂O₆ with end members of Nb and Ta that include elements such as Fe, Mn, and substitutions to a lesser extent by cations such as Ti, Ca, Na, U, Th, Y, and REE. They crystallize mainly in the orthorhombic system and present dimorphism with minerals of the tapiolite series becoming the object of comprehensive studies (e.g. Cerny, 1989; Cerný et al., 2012; Ercit et al., 1995; Möller et al., 1989).

Columbite (Nb) and tantalite (Ta) minerals may present diverse paragenesis in rocks such as miaskites, nepheline syenites, carbonatites, or in (anorogenic) alkaline granites enriched in rare earth elements and their associated pegmatites.

Brazil and Canada are the main producers of niobium mineral concentrates, whereas Australia is the main producer of tantalum. The presence of Nb-rich ores associated with carbonatites in Brazil as is represented by the Araxá, and Six Lakes Carbonatites, the latter located in the vicinity of the Colombian border.

Most of the columbite-tantalite minerals in the world are extracted from weathered material derived from felsic pegmatitic rocks, especially in

Rwanda, Sierra Leone, and Cameroon (Elsner, 2010). Much less common are Nb-rutiles or ilmenorutile (Ti⁴⁺, Nb⁵⁺, Fe³⁺)O₂ with more than 13 wt% Nb₂O₅ reported with columbite in pegmatites of Manitoba, Canada (Cerny et al. 1981).

(CT) are widespread in almost all continents and geological times. Although, the most important deposits seem to be associated with Archean and Paleoproterozoic rocks, Cenozoic columbites have been reported. In South America, columbites are found in Brazil, Argentina, and Bolivia and sporadically but less studied in Venezuela and Colombia, for which a late Mesoproterozoic age has been documented (Melcher et al. 2017)

In this study, we attempt to trace the possible sources for columbite-tantalite deposits in Colombia. For this purpose, we integrate a new comprehensive mineral characterization including BSE imagery, geochemical and isotopic analyses performed on columbite-tantalite crystals mainly collected from colluvial deposits covering Mesoproterozoic rocks in E-Colombia, which are part of the NW-Amazonian Craton. The columbite-tantalite ores are apparently related to enriched zones or pegmatites of anorogenic origin represented mainly by rapakivi granites outcropping locally along the Orinoco, Inírida, Guainía and Cuyari rivers (see

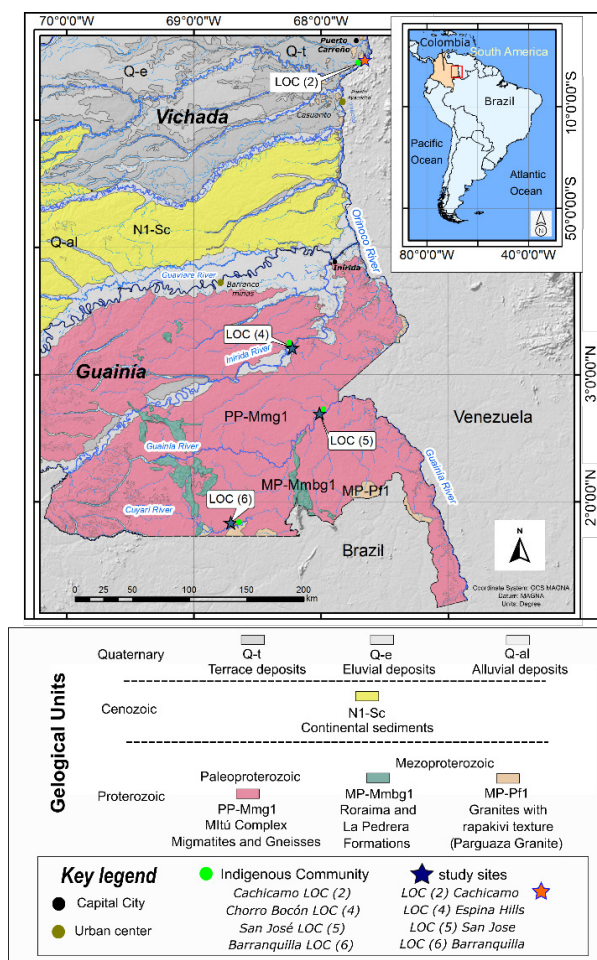


Figure 1).

2 Geological Background

The ca. 1500-1550 Ma Parguaza Rapakivi Batholith, is found outcropping over 90% in Venezuela and some 10% in Colombia, where it intrudes the Amazon Craton Paleoproterozoic migmatitic complexes (Bonilla-Pérez et al., 2013; Gaudette et al., 1978; Gonzalez and Pinto, 1990). The Parguaza granites are well-documented as a primary ore for Sn, Nb, Ta, and REE minerals (Aarden and Davidson, 1977; Mariño-Pardo, 2012, 2013). Most of the batholith is covered by partially laterized Cenozoic sediments in plains and valleys, whereas fresh outcrops correspond to localized exposures in rivers and inselbergs. Alluvial-colluvial deposits in the Venezuelan localities of El Burro, La Fortuna, and Aguamena yield concentrations of cassiterite, rutile (Nb,Ta), columbite-tantalite and REE minerals. In the easternmost part of Colombia, the Parguaza Rapakivi suites occur in tributaries to the Orinoco River

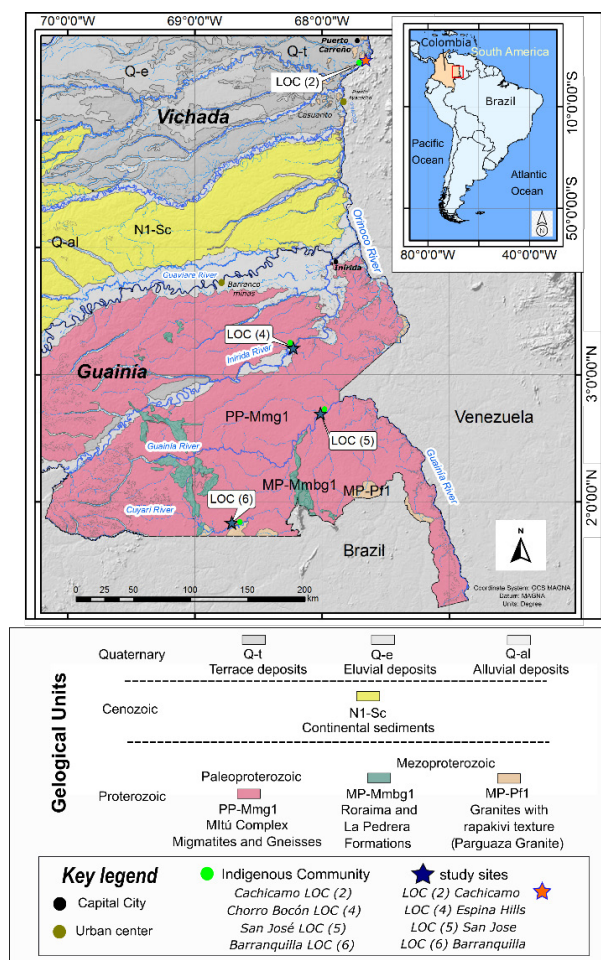


Figure 1, LOC (2)). Similarly, other exposures are identified in the riverbanks of the Inirida River LOC (4), the Guainia River LOC (5), and the Cuyari River LOC (6) (Bonilla Perez et al., 2016; Kroonenberg, 2019).

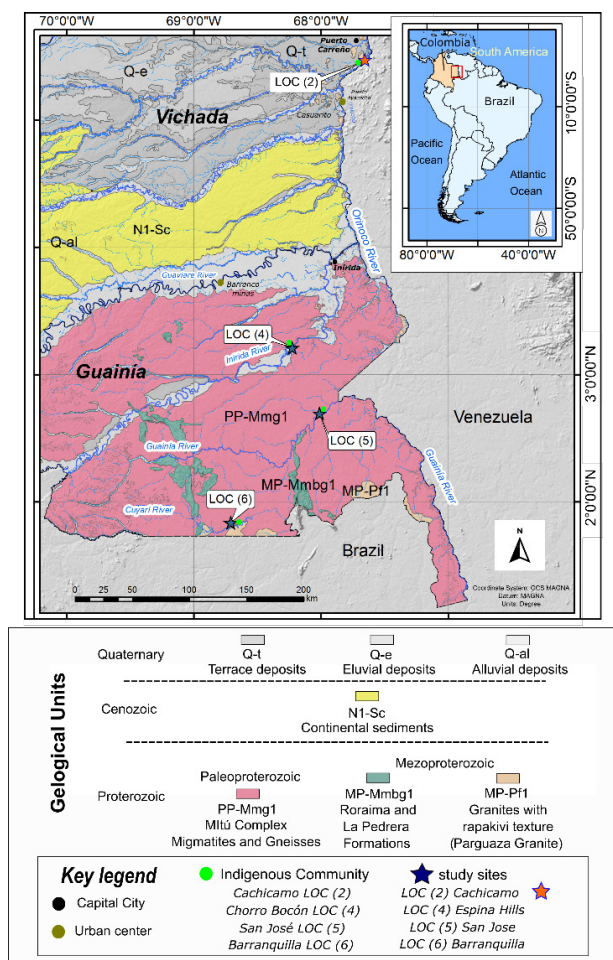


Figure 1. Geological map of E-Colombia showing the Guainía and Vichada departments, the studied locations LOC (5) and (6). For reference and comparison, LOC (2) and LOC (4) samples of rutile-(Nb, Ta) with columbite-Fe inclusions yielded an age of 1342 ± 27 Ma (Franco et al. 2019). Modified from the Geological Map of Colombia (Gómez Tapias et al., 2015).

3 Methodology

From pan concentrates of each locality, 30 up to 0.5 cm long columbite-Fe crystals were handpicked and identified further using a Bruker Tracer III-V pXRF instrument. Fragments of the thirty crystals for LOC (5 and 6) were mounted in epoxy resin pucks. For Venezuelan columbite, we polished a 3 cm crystal long that we analyzed by EPMA and LA-ICP-MS. Remaining fragments were pulverized using an agate mortar and fused at 1200 °C to pearls for XRF analyses employing a PANanalyticalAXios instrument at the Universidad Nacional de Colombia. For EPMA analysis, the polished epoxy pucks were coated with graphite.

EPMA analysis of major elements was performed employing a JEOL JXA-8900 electron microprobe at LMA-CM-UFGM - Universidade Federal de Minas Gerais (UFGM), Brazil. The CGM geochemistry was confirmed by energy-dispersive X-ray spectroscopy (EDS).

BSE images of the columbite crystals allowed choosing the most homogeneous zones, free of inclusions or in very low proportion. LA-ICP-MS

analyses were performed using a Thermo Scientific Element XR, with a single collector, high resolution, magnetic sector ICP-MS and an excimer Argon fluoride laser (193 nm) at the Institute of Geochemistry and Petrology of ETH-Zürich, following the methodology described by Von Quadt et al. (2019) and compared with Melcher et al. (2015, 2017) and Che et al. (2015).

For U-Pb dating, laser ablation of the grains was performed in spots of 40 microns, with a frequency of 5 Hz and an intensity of 7 J/cm^2 . T_X36 columbite-Fe standard and standard glass NIST-610 were used as primary reference materials for correcting laser-induced element fractionation and matrix effects, whereas GJ-1 zircon was analyzed as secondary reference material for monitoring age accuracy and reproducibility. Data over 20% discordant were excluded from the calculation of Concordia ages.

4 Results of characterization and LA-ICP-MS dating

4.1 LOC (5) San Jose - Guainía River

Columbite-Fe found in pegmatitic dykes and colluvial deposits near San Jose occurs together with crystals of rutile-Nb, monazite, xenotime, tourmaline, and magnetite. The pegmatite is hosted in the Paleoproterozoic Mitú Complex rocks and related to rapakivi granite intrusions as the Tabaquen Granite and other unnamed plutons along the Guainía River (Figure 1). The EPMA and ICP-MS analyses reveal an average composition in wt% of up to 52 % Nb_2O_5 , 11 % Ta_2O_5 , 16 % TiO_2 , 9 % Fe_2O_3 , 7 % MnO and 1% WO_3 . Among the minor elements appear up to 600 ppm of Si, W, and Al, up to 405 ppm of Mn, Zr, Cr, Y, and Pb, less than 50 ppm of Cr, P, and Hf, and below 10 ppm of La, Ce, Pr, Nd, Sm, Eu, Gd, Tb, Dy, Ho, Rb, Tm and Lu. The BSE images and-EDS composition show rutile-(Nb, Ta) inclusions and tantalite-Mn (Figure 2 A to B').

The LA-ICP-MS data yield a concordia age of 1549 ± 5 Ma (MSWD= 5; n=50) (Figure 2 C).

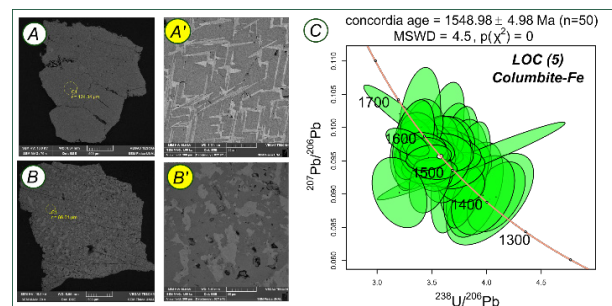


Figure 2. A. Columbite-Fe crystal with exsolutions and inclusion; A'. Zoom of the yellow circle zone showing the texture of columbite-Fe and tantalite-Mn (light gray); B. Columbite-Fe crystal with inclusion; B'. Zoom of the yellow circle zone showing tantalite-Mn (light gray), and C. U-Pb-Concordia diagram for columbite-Fe from San Jose LOC (5)

4.2 LOC (6) Barranquilla – Cuyarí River

The columbite-Fe crystals from Barranquilla are found in colluvial deposits with blocks of pegmatites composed of quartz and muscovite together with beryl and crystals of rutile-Nb, monazite, xenotime, tourmaline, REE-enriched zircons, and garnets near to the Cuyari river (

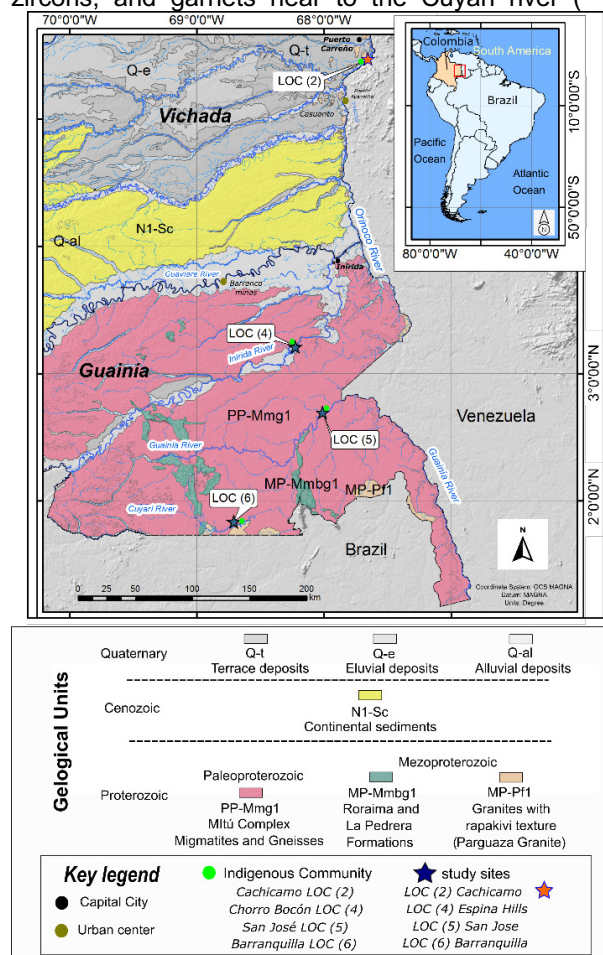


Figure 1). The XRF analyses exhibit an average composition of up to 42 wt% Nb₂O₅, 32 wt% Ta₂O₅, 3 wt% TiO₂, 8 wt% Fe₂O₃, 9 wt% MnO, 2 wt% WO₃ and 1 wt% SiO₂. The minor elements are up to 600 ppm V, Ca, Zr, Hf, Zn, Ba, Nd, and Y. The SEM-EDS images reveal inclusions of tantalite-(Mn) and rutile-(Nb-Ta) (Figure 3 A to C).

The U-Pb LA-ICP-MS data yield a concordia age of 1531 ± 12 Ma (MSWD= 3; n=15) (Figure 3 D).

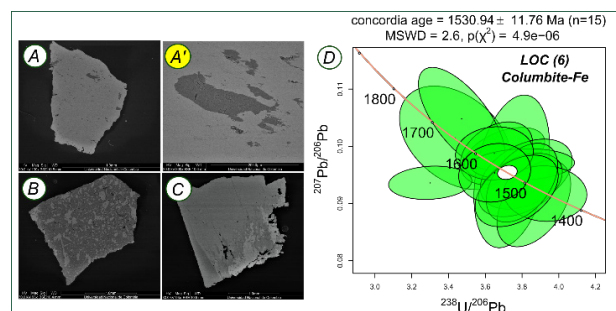


Figure 3. A. Columbite crystal with inclusions and **A'** ampliation showing rutile-(Nb,Ta) inclusion (Dark gray)

columbite-Fe; **B.** Columbite crystal with tantalite-Mn inclusions (Light gray); **C.** Columbite crystal with tantalite-Pb inclusions (Light gray), and **D.** U-Pb concordia diagram of columbite-tantalite from Barranquilla-Cuyarí River LOC (6).

4.3 Columbite-tantalite from Venezuela

Samples of columbite-Fe and tantalite-Mn from Aguamena, El Burro y La Fortuna in Venezuela were found in colluvial deposits over the Parguaza Granite together with crystals of cassiterite, struverite, ilmenorutile, monazite, and tourmaline. The XRF and EPMA analyses exhibit an average composition of up to 35 wt% Nb₂O₅, 34 wt% Ta₂O₅, 4 wt% TiO₂, 11 wt% Fe₂O₃, 9 wt% Mn₂O₃, 3 wt% WO₃, 1 wt% SiO₂ and 0,5 wt% SnO₂. Among the minor elements are up to 600 ppm of Al and Zr, Hf, V, Ca, U, and Yb. The BSE-EDS images show a paragenesis with struverite, tantalite-Mn, cassiterite, and in some Ta-rich grains microlite (Figure 4 A to C').

The U-Pb LA-ICP-MS data yield a concordia age of 1472 ± 6 Ma (MSWD= 9; n=17) (Figure 4 D).

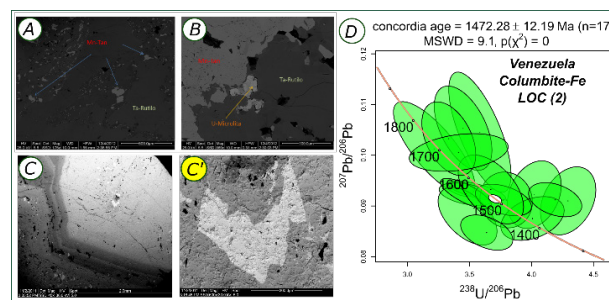


Figure 4. A. Picture of columbite-tantalite with inclusion of U-microlite and struverite; **C.** Rutile-(Nb,Ta) with zonation and inclusions; **C'.** Zoom showing the columbite- tantalite inclusions (with), and **D.** U-Pb concordia diagram of columbite-tantalite crystals from El Burro and La Fortuna in Venezuela.

5 Discussion

5.1 Geochemical constrains.

The new XRF and EPMA data of major and trace elements in the columbites agree with the former data in their general composition and affiliation to the ferro-mangano columbite-tantalite series. Amazonian Craton columbites are enriched in rare earth elements (REE), especially in heavy REE. High radioactivity comparative measurements confirm the high U content up to 1 wt%, especially in the columbites from Venezuela. In general, minerals show a small variability within their matrix, but crystals with less than 10 wt% of TiO₂ and no inclusions provided the best results for LA-ICP-MS dating.

5.2 Age of mineralization and provenance

The columbite U-Pb crystallization ages found for LOC (5) of 1549 ± 5 Ma (MSWD= 5; n=50) overlap within age uncertainties with ages from LOC (6)

columbites of ca. 1531 ± 12 (MSWD=3; n=15) and correspond to previously obtained U-Pb ages from rutile-(Nb,Ta) at LOC (2) (Franco et al., 2021) of 1512 ± 12 Ma. Differently, Venezuelan columbite-tantalite samples exhibit younger U-Pb ages of 1472 ± 6 Ma (MSWD= 6; n=17). In summary, these results interpreted as crystallization ages comprise the time span from 1600 to 1470 Ma, bracketing the crystallization of the Parguaza-rapakivi batholith suites reported for this part of the Amazonian Craton. Besides, columbite concordant ages may indicate at least two generation events prior to the Early Mesoproterozoic major magmatic episode.

On the other hand, U-Pb-in rutile-(Nb,Ta) LA-ICP-MS ages acquired from LOC (5) and LOC (6) of 1377 ± 1 Ma and 1411 ± 5 Ma, respectively (Franco et al., 2019) can be correlated with 1411 Ma ages reported by Melcher et al. (2017) for Colombian CGM samples, based on U-Pb isotopes in wodginite-ixiolite, CGM, rutile, and cassiterite, with a mineralization age ranging from 1453 to 1277 Ma, although without reporting their exact provenances.

6 Conclusion

The acquired and compared ages suggest a major mineralization event for the Colombian columbite formation ranging from ca. 1550 to 1500 Ma and at least another younger mineralization or reworking event between ca. 1411 to 1370 Ma.

7 Acknowledgements

We express our gratitude to the indigenous communities of Cachicamo, San Jose y Barranquilla. Special thanks to the laboratories of the National University of Colombia, UFMG in Brazil, and GEGEMA group in Bogota.

8 References

- Aarden, H., Davidson, M., 1977. Minerales de estaño, niobio, tántalo y titanio en la zona del Cano Aguamena, Estado Bolívar, analizados con microsonda de electrones, in: *Memorias V Congreso Geológico Venezolano*. Caracas, pp. 919–940.
- Bonilla-Pérez, A., Frantz, J.C., Charão-Marques, J., Cramer, T., Franco-Victoria, J.A., Mulocher, E., Amaya-Perea, Z., 2013. Petrografía, Geoquímica y Geocronología del Granito de Parguaza en Colombia. *Bol. Geol.* 35, 83–104. <https://doi.org/10.18273/revbol.v35n1-2016001>
- Bonilla Perez, A., Frantz, J.C., Charão-Marques, J., Cramer, T., Franco Victoria, J.A., Amaya-Perea, Z., 2016. Magmatismo rapakivi en la cuenca media del Río Inírida, Departamento de Guainía, Colombia. *Bol. Geol.* 38, 17–32. <https://doi.org/10.18273/revbol.v38n1-2016001>
- Cerny, P., 1989. Exploration strategy and methods for pegmatite deposits of tantalum, in: Möller, P., Cerny, P., Saupé, F. (Eds.), *Lanthanides, Tantalum and Niobium: Mineralogy, Geochemistry, Characteristics of Primary Ore Deposits, Prospecting, Processing and Applications - Proceedings of a Workshop in Berlin, Nov. 1986*. Springer, Berlin, Heidelberg, New York, London, Paris, Tokyo, pp. 274–302.
- Cerný, P., London, D., Novák, M., 2012. Granitic Pegmatites as Reflections of Their Sources. *Elements* 8, 289–294. <https://doi.org/10.2113/gselements.8.4.289>
- Che, X.D., Wu, F.Y., Wang, R.C., Gerdes, A., Ji, W.Q., Zhao, Z.H., Yang, J.H., Zhu, Z.Y., 2015. In situ U-Pb isotopic dating of columbite-tantalite by LA-ICP-MS. *Ore Geol. Rev.* 65, 979–989. <https://doi.org/10.1016/j.oregeorev.2014.07.008>
- Elsner, H., 2010. Heavy Minerals of Economic Importance. BGR, Hannover.
- Ercit, T.S., Wise, M.A., Cerny, P., 1995. Compositional and structural systematics of the columbite group. *Am. Mineral.* 80, 613–619.
- Franco, J.A., Cramer, T., Bonilla, A., Piraquive, A., Campos, H., 2019. Nb-rutile: A reference mineral for timing of Sn, Nb-Ta, U-Th and REE mineralization at NW part of the Amazonian Craton. 15th Biennial Meeting of the Society for Geology Applied to Mineral Deposits: Life With Ore Deposit on Earth. Glasgow, Scotland Abstract Volumes 3.
- Franco, J.A.; Cramer, T.; Bonilla, A.; Castañeda, A.J.; Poujol, M.; Amaya, Z. 2021. Mineralogía y geocronología de rutilo-(Nb,Ta) relacionado a casiterita y columbita-tantalita provenientes de rocas Mesoproterozoicas del Cratón Amazónico cerca de Cachicamo, Colombia. *Boletín de Geología*, 43(1), 99-126. <https://doi.org/10.18273/revbol.v43n1-2021005>
- Gaudette, H.E., Mendoza, V.S., Hurley, P.M., Fairbairn, H.W., 1978. Geology and age of the Parguaza rapakivi granite, Venezuela. *Geol. Soc. Am. Bull.* 89, 1335–1340. [https://doi.org/10.1130/0016-7606\(1978\)89<1335:GAAOTP>2.0.CO;2](https://doi.org/10.1130/0016-7606(1978)89<1335:GAAOTP>2.0.CO;2)
- Gómez Tapias, J., Montes Ramírez, N.E., Nivia Guevara, Á., Diederix, H., 2015. Mapa Geológico de Colombia, 1:1.000.000, in: *Atlas Geológico de Colombia*. SGC, Bogotá, p. 2 hojas.
- Kroonenberg, S.B., 2019. The Proterozoic Basement of the Western Guiana Shield and the Northern Andes, in: Cedié, F., Shaw, R.P. (Eds.), *Geology and Tectonics of Northwestern South America*. Springer International Publishing, Cham, pp. 115–192. https://doi.org/10.1007/978-3-319-76132-9_3
- Mariño-Pardo, N., 2013. Coltán (Nb y Ta): Ubicación, extracción ilegal y potencial minero en el Municipio Cedeño del Estado Bolívar, Venezuela, *Propuestas. V Simposio Venezolano de Rocas Ígneas y Metamórficas*, Auditorio de Geología, UCV, del 27 al 29/11/2013. UCV, Venezuela.
- Mariño-Pardo, N., 2012. Potencial minero del Bajo Parguaza. *Rev. Commod. Venez.* 2, 44–47.
- Melcher, F., Graupner, T., Gäbler, H.-E., Sitnikova, M., Henjes-Kunst, F., Oberthür, T., Gerdes, A., Dewaele, S., 2015. Tantalum–(niobium–tin) mineralisation in African pegmatites and rare metal granites: Constraints from Ta–Nb oxide mineralogy, geochemistry and U–Pb geochronology. *Ore Geol. Rev.* 64, 667–719. <https://doi.org/10.1016/j.oregeorev.2013.09.003>
- Melcher, F., Graupner, T., Gäbler, H.-E., Sitnikova, M., Oberthür, T., Gerdes, A., Badanina, E., Chudy, T., 2017. Mineralogical and chemical evolution of tantalum–(niobium–tin) mineralisation in pegmatites and granites. Part 2: Worldwide examples (excluding Africa) and an overview of global metallogenetic patterns. *Ore Geol. Rev.* 89, 946–987. <https://doi.org/10.1016/j.oregeorev.2016.03.014>
- von Quadt, A., M. Guillon, O. Laurent, I. Peytcheva, M. Galinski. 2019: U-Pb dating of columbite-bearing ores with a new columbite reference material. – *Rev. Bulg. Geol. Soc.*, 80, 3–“Gesciences 2019”, 94–95.

Rare-earth element mineralization in altered pegmatites from the Djurkovo Pb-Zn deposit, Central Rhodopes

Sylvina Georgieva¹, Rossitsa D. Vassileva¹, Georgi Milenkov¹, Jan Cempírek², Radek Škoda²

¹ Geological Institute, Bulgarian Academy of Sciences, Sofia, Bulgaria

² Dept. of Geological Sciences, Masaryk University, Brno, Czech Republic

Abstract. The Djurkovo polymetallic vein deposit is formed by veins filling open space in various gneisses that compose the high-grade metamorphic complex in the Central Rhodopes. Abundant deformed concordant or crosscutting pegmatites of varying thickness are common in the metamorphic sequence. The studied pegmatite dykes consist mainly of plagioclase, K-feldspar, quartz, and minor micas. The main accessory minerals are allanite- (Ce), titanite, apatite and zircon. Late hydrothermal overprint and alteration of pegmatites led to formation of epidote-group minerals, adularia, albite, sericite, chlorite, carbonate, quartz and leucoxene. The secondary minerals also include rare earth element (REE+Y) and Th, U fluorocarbonate – phosphate – oxide assemblages. This mineral association typically occurs as very fine-grained (< 20 µm) anhedral disseminations, observed along fractures and dissolved zones in allanite and titanite that evidently are the main source for the REEs. This indicates remobilization of REEs followed by formation of new phases during the late-stage hydrothermal activity. Limited mobility of REEs is illustrated by precipitation of the newly-formed minerals within the grains of the altered accessory minerals. The studied pegmatites retain a significant amount of accessory minerals rich in incompatible elements and despite being hydrothermally altered they could be considered as their potential source.

1 Introduction

Rare-earth elements (REEs), along with Y, Th, and U, are generally incompatible in crystal structures of the main rock-forming minerals due to their geochemical properties (large ionic radii, high ionic charge). For this reason, these elements are usually concentrated in the upper continental crust through low-degree partial melting and fractional crystallization processes, and are commonly mobile in magmatic-hydrothermal systems having the ability to complex with F, Cl etc. (Ballouard et al. 2020 and references therein). Being of strategic importance and belonging to the critical materials list, most of these elements are crucial for high technology development. Recent increase of interest in pegmatites as sources of critical elements as well as industrial materials (ceramic feldspar) requires revision and detailed investigation of pegmatite-rich regions (Linnen et al. 2012).

Numerous pegmatite bodies with various size, shape and position are important rock constituents intruded in the metamorphic complex, hosting the main vein and metasomatic polymetallic ore mineralization in the Central Rhodopes, south Bulgaria. The current mining activity in the region facilitates the investigation of these pegmatite bodies with regards to their mineral and geochemical properties and to evaluate their resource potential for critical elements.

This study provides preliminary data about the primary and secondary REE mineralization that occurs in pegmatites from the Djurkovo Pb-Zn deposit.

2 Methodology

Materials used in this study are hydrothermally altered pegmatite samples from the Eastern Apophysis area, level 472 of the Djurkovo Pb-Zn deposit. Prior to EPMA study, the mineral relationships and representative spots in the thin sections were chosen using optical and scanning-electron microscopy.

The chemical composition of the minerals was analysed with a Cameca SX100 electron microprobe (EMP) at the Joint Laboratory of Electron Microscopy and Microanalysis, Department of Geological Sciences, Masaryk University, and Czech Geological Survey, Brno. Wavelength-dispersive mode with an accelerating voltage of 15 kV, a beam current of 4-20 nA and a beam size 2–6 µm were applied. The following standards and X-ray K α and L α lines were used: sanidine (Si, Al, K), albite (Na), olivine (Mg), almandine (Fe), fluorapatite (Ca, P), tephroite (Mn), anatase (Ti), chromite (Cr), columbite (Nb), ScVO₄ (V), SrSO₄ (Sr), topaz (F), vanadinite (Cl), barite (Ba), LaPO₄ (La), CePO₄ (Ce), PrPO₄ (Pr), NdPO₄ (Nd), SmPO₄ (Sm), GdPO₄ (Gd), ThO₂ (Th), U (U).

3 Geological setting

The Djurkovo Pb-Zn deposit is located in the Laki ore region, situated in the northern part of the Central Rhodope metamorphic complex, south Bulgaria. This region hosts numerous hydrothermal Pb-Zn (\pm Ag) ore deposits and occurrences, accumulated in extensional tectonic settings (Marchev et al. 2005). The polymetallic mineralization is connected to several predominantly NNE ore-bearing faults that also crosscut the volcanics of the near Borovitsa caldera to the east. The ore mineralization occurs either as subvertical veins formed by open-space filling in the metamorphic rocks (mostly gneisses) or forms rich replacement ore bodies in the marble layers. The mineralization of the Djurkovo deposit is located in two major NNE-SSW trending ore veins, developed in gneisses and marbles, named Eastern Apophysis and West 2 (Buret and Kouzmanov 2011). Apart from the gneisses and marbles, abundant pegmatite bodies with different size, shape and position are important rock constituents cutting the metamorphic complex. These bodies are often

deformed, boudinaged, folded or cut by later faults (Fig. 1A, B).

Regarding the vein mineralization in the deposit, three main paragenetic stages are outlined (Buret and Kouzmanov 2011): 1) early quartz-pyrite; 2) polymetallic (galena, sphalerite); 3) late carbonate stage. A prograde skarn stage occurred during metasomatic replacement in the marbles due to fluid-rock interaction that generally resulted in formation of diopside (\pm olivine). The related hydrothermal alteration in pegmatites led to formation of adularia, epidote, chlorite, and later carbonatization (Vassileva et al. 2020 and references therein).

According to the $^{40}\text{Ar}/^{39}\text{Ar}$ thermochronology on hydrothermal K-feldspar from the Laki ore district, the age of the economic mineralization in the Djurkovo deposit is constrained between 32–30 Ma (Buret et al. 2013).

4 Results

Petrographic study showed that the quantity of quartz in the studied pegmatite bodies is about 20–25 % of the rock volume, and plagioclases prevail over K-feldspars. The studied pegmatites do not show clear zonal mineral distribution. Myrmekite intergrowth textures are typically observed on the borders between plagioclase and K-feldspar. Quartz forms irregularly distributed medium- to fine-grained anhedral grains, often occupying the interstitial space between plagioclase and K-feldspar. Undulate extinction and lobate grain boundaries are often observed in the quartz. Minor amounts of muscovite and biotite are present. Rare sub- to anhedral grains of garnet (up to 5 mm) with inclusions of K-feldspar, quartz, allanite, calcite, and chlorite occur among quartz and feldspars. The garnet contains dominant almandine (49.6–44.9 mol.%), and high amounts of grossular (28.8–20.9 mol.%), and spessartine (26.1–13.5 mol.%) components. The garnet mainly forms in the peripheral zone of some pegmatite bodies, close to the contact with gneisses, which suggests a metasomatic influence.

The main pegmatite accessory minerals are allanite, apatite, titanite, and zircon (Fig. 1C–F). Allanite typically forms brown, euhedral to subhedral crystals up to 1 mm large among feldspar and/or quartz grains. Frequently, the crystals are replaced or fragmented and intersected by late hydrothermal epidote (*sensu lato*) (see Fig. 1C). The dominant REE₂O₃ in the mineral are Ce₂O₃ (up to 8.5 wt%), La₂O₃ (3.9 wt%) and Nd₂O₃ (3.5 wt%). Thorium contents (up to 3.4 wt% ThO₂) are elevated. Because of the hydrothermal alteration, part of the mineral is transformed to REE-rich clinozoisite with patchy or irregular zonal patterns that can be observed clearly in back-scattered electron (BSE) images. Apart from epidote, late REE fluorocarbonates form in cracks and zones within the allanite grains.

Titanite is developed as euhedral to subhedral crystals (up to 2 mm long) in association with

feldspars. Some of the crystals are deformed and cracked. Weak compositional zoning could be outlined in BSE images. The content of Fe₂O₃ in the mineral is less than 0.97 wt%, whereas Al₂O₃ reaches up to 8.97 wt%. The main trace elements incorporated in the mineral are Nb (\leq 3.23 wt% Nb₂O₅), Y (\leq 1.35 wt% Y₂O₃), Ce (\leq 0.3 wt% Ce₂O₃), Nd (\leq 0.23 wt% Nd₂O₃), and Ta (\leq 0.21 wt% Ta₂O₅). Titanite is partly or entirely replaced by leucoxene (mostly anatase according to Raman spectroscopic data; see Fig. 1E, F). Apatite forms euhedral crystals (up to 600 μm) within the feldspar and quartz matrix. Its content of F reaches up to 3.6 wt%, elevated are also Cl (up to 0.3 wt%) and Y₂O₃ (up to 0.3 wt%). It is chemically homogeneous; no apatite dissolution, alteration, or reaction textures were observed. Zircon occurs as euhedral crystals (up to 200 μm) associated with feldspars. Clear chemical zoning is defined by incorporation of HfO₂ (up to 2.68 wt%) and UO₂ (up to 1.12 wt%).

The pegmatite bodies are overprinted by clearly visible late hydrothermal alteration. The mineral association comprises epidote-group minerals, adularia, albite, sericite, chlorite, carbonates, REE fluorocarbonates, leucoxene, xenotime, thorite, uraninite and quartz. Rare thin veinlets and disseminations of galena, sphalerite and minor chalcopyrite are present. The main alteration assemblage is similar to those in pegmatites from other deposits in the region (e.g., Petrovitsa Pb-Zn deposit, Madan ore region, Georgieva et al. 2022). Epidote-group minerals are the prevalent hydrothermal alteration products; they generally occur as sub- to euhedral prismatic crystals (up to 500 μm) or clusters which, along with carbonate, adularia, and sericite, form nests and veins among feldspars. Their composition generally varies between clinozoisite and Fe³⁺-rich clinozoisite. Sericite, carbonate, adularia and albite replace almost the entire volume of feldspars, forming thin network of veinlets and nests. Monomineralic adularia veins (up to 500 μm thick) with well-shaped subhedral crystals were also observed. Chlorite is developed mainly replacing micas and also as thin veinlets and nests along with aforementioned secondary mineral assemblage.

Late carbonate-dominated rare-element (REE+Y, Th, U) mineral assemblage, typically developed as less than 20 μm large anhedral grains and aggregates, precipitated along the fractures and dissolved zones in allanite and titanite as their alteration product. It is represented by the minerals from the bastnäsitesynchysite series, including parisite and röntgenite intermediate members. Their EMP analyses show that the main REEs are Ce (14.84–25.90 wt% Ce₂O₃), La (7.10–12.23 wt% La₂O₃), Nd (3.76–10.96 wt% Nd₂O₃), Sm (0.35–2.76 wt% Sm₂O₃) and Gd (0.3–2.36 wt% Gd₂O₃). Part of the analyses shows high contents of ThO₂ (up to 25.17 wt%) as well. The contents of CaO strongly varies between 2.98 and 18.74 wt%, whereas F

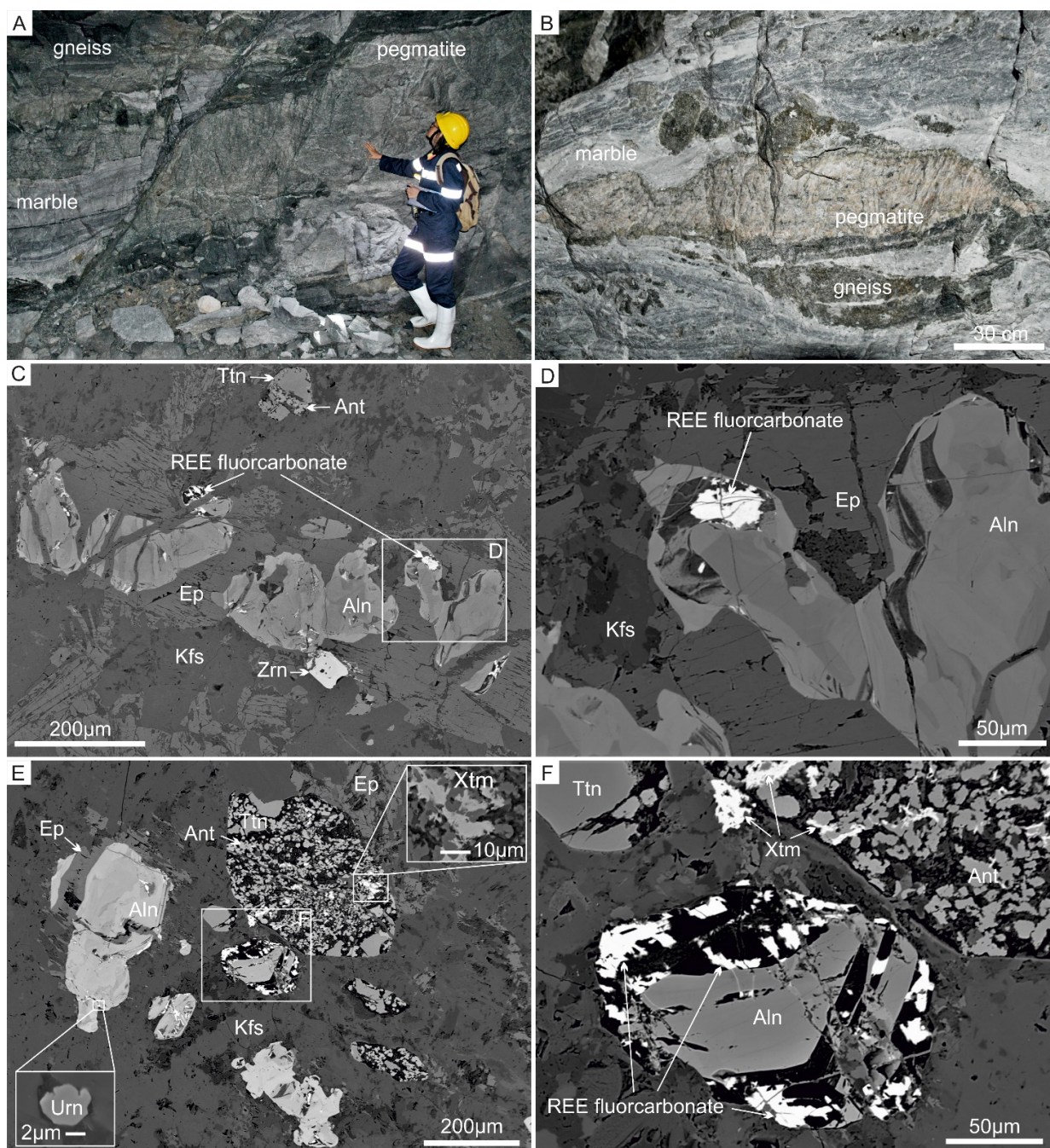


Figure 1. A; B, Macrophotographs of pegmatite outcrop, the Djurkovo mine, level 472; C–F, BSE images of occurrence and mineral relationships of the accessory minerals. Abb.: Kfs – K-feldspar; Ep – epidote; Aln – allanite; Ttn – titanite; Zrn – zircon; Ant – anatase; Xtm – xenotime; Urn – uraninite.

contents are relatively stable (5.57–7.19 wt%). Because of the complex structure and composition of these phases, their natural ability to form intergrowths of several fluorcarbonates (Zeug et al. 2021), and their small size in the studied pegmatites, it was commonly impossible to assign the exact mineral species; some of their chemical compositions correspond to parisite-(Ce) and thorbastnäsite. Xenotime is present as irregular aggregates less than 20 μm in size, associated with leucoxene in the altered titanite. Its Y_2O_3 content reaches up to 41.9 wt%; it is accompanied by HREEs, such as Er (4.46 wt% Er_2O_3), Yb (4.44 wt%

Yb_2O_3), and Dy (4.37 wt% Dy_2O_3). Uranium reaches 0.82 wt% UO_2 . Thorite and uraninite occur as $<5 \mu\text{m}$ large grains enclosed in titanite, allanite, and zircon. According to our observations, both allanite and titanite enclose grains of REE+Th fluorcarbonates and uraninite ($\sim 5 \mu\text{m}$), whereas thorite and xenotime occur along with leucoxene in the altered titanite.

5 Concluding remarks

Deformed, boudinaged and folded pegmatites, often cut and displaced by faults, cross-cut the

metamorphic rocks hosting the Pb-Zn Djurkovo deposit, Central Rhodopes. The bodies are of varying thickness and position (concordant or oblique) towards the metamorphic foliation. Detailed petrographic and EMP study revealed the presence of accessory minerals such as allanite, titanite, apatite and zircon that usually accumulate significant amounts of incompatible elements such as REE+Y, Th and U. Late-stage hydrothermal alteration of the pegmatites led to partial or complete dissolution of the accessory minerals (e.g., allanite, titanite), and extraction and reprecipitation of the incompatible elements (REE+Y, Th, U) as new phases – mainly fluorcarbonates and phosphates. These new minerals precipitated within the altered accessory crystals due to the presumable limited mobility of REE in fluids hampering any long-distance transport of these elements. As a rule, REE fluorcarbonates and uraninite formed mainly within the grains of the altered allanite, whereas xenotime and thorite precipitated within the altered titanite crystals.

The hydrothermal alteration of the REE-bearing accessory minerals (e.g., allanite, titanite, apatite, zircon) from the pegmatites gives a better insight on the trace elements extraction, redistribution and reprecipitation processes in the altered igneous rocks.

Acknowledgements

The study is financially supported by the Bulgarian National Science Fund KP-06-N34/4 project and complements ERA-MIN PEGMAT project KP-06-DO02/2.

References

- Ballouard C, Massuyeau M, Elburg MA, Tappe S, Viljoen F, Brandenburg J-T (2020) The magmatic and magmatic-hydrothermal evolution of felsic igneous rocks as seen through Nb-Ta geochemical fractionation, with implications for the origins of rare-metal mineralizations. *Earth Sci Rev* 203, 103115, ISSN 0012-8252, <https://doi.org/10.1016/j.earscirev.2020.103115>
- Buret Y, Kouzmanov K (2011) Polymetallic mineralization in the Laki mining district Southern Bulgaria: Paragenesis and fluid evolution. In: Abstract Volume 9th Swiss Geoscience Meeting. Zurich, 11–13 November 2011, Symposium 2: Mineralogy, Petrology, Geochemistry, 88–89
- Buret Y, Kouzmanov K, Spikings R, Gerdjikov Y (2013) Timing of polymetallic Pb-Zn mineralisation in the Laki district, southern Bulgaria – constraints from ⁴⁰Ar/³⁹Ar dates. In: Abstract Volume 11 Swiss Geoscience Meeting. Lausanne, 15–16 November 2013, Symposium 2: Mineralogy, Petrology, Geochemistry, 49–50
- Georgieva S, Vassileva R, Milenkov G, Stefanova E (2022) Major and trace element signature of epidote-group minerals in altered pegmatites from the Petrovitsa Pb-Zn deposit of the Madan ore region, Central Rhodopes, Bulgaria: Evidence of allanite/epidote transformation. *Geol Carp* 73(4): 365–380. <https://doi.org/10.31577/GeolCarp.73.4.5>
- Linnen RL, Van Lichtervelde M, Cerný P (2012) Granitic pegmatites as sources of strategic metals. *Elements* 8: 275–280. <https://doi.org/10.2113/gselements.8.4.275>
- Marchev P, Kaiser-Rohrmeier M, Heinrich C, Ovtcharova M, von Quadt A, Raicheva R (2005) Hydrothermal ore deposits related to post-orogenic extensional magmatism and core complex formation: The Rhodope Massif of Bulgaria and Greece. *Ore Geol Rev* 27: 53–89. <https://doi.org/10.1016/j.oregeorev.2005.07.027>
- Vassileva RD, Grozdev V, Peytcheva I, von Quadt A, Salnikova E (2020) Andradite from Pb-Zn Djurkovo deposit, Central Rhodopes: chemical composition and U/Pb dating. *Rev Bulg Geol Soc (Geosciences)* 2020) 81(3): 58–60
- Zeug M, Nasdala L, Ende M et al (2021) The parisite–(Ce) enigma: challenges in the identification of fluorcarbonate minerals. *Miner Petrol* 115: 1–19. <https://doi.org/10.1007/s00710-020-00723-x>

Pegmatite REE-mineral association from the Kroushev Dol base metal deposit (south Bulgaria): mineral replacements and timing of formation

Rossitsa D. Vassileva¹, Sylvína Georgieva¹, Georgi Milenkov¹, Jan Cempírek², Radek Škoda², Elitsa Stefanova¹, Valentin Grozdev¹, Irena Peytcheva¹

¹Geological Institute, Bulgarian Academy of Sciences, Bulgaria

² Department of Geological Sciences, Masaryk University, Brno, Czech Republic

Abstract. The region of the Central Rhodopes, south Bulgaria, is known for large Pb-Zn deposits located in the Madan and Laki districts. The economic sulphide mineralization is hosted by the high-grade rocks of the Rhodope metamorphic complex. Mining operations revealed that pegmatite injections into the host gneisses, amphibolites and marbles represent a substantial part of the wall rocks in depth. Mineral composition of these dykes is represented by K-feldspar, plagioclases, and quartz as major constituents. In the pegmatites from the Kroushev Dol deposit (Madan district), REE-bearing mineralization includes accessory monazite, zircon, apatite, allanite, titanite, and thorite. Primary minerals of REE are monazite (LREE) and zircon (HREE); the REE were consequently redistributed among secondary apatite, allanite, thorite, and titanite. Common mineral breakdowns (e.g. oligoclase to albite; monazite to apatite; allanite to epidote; titanite to anatase) and replacement of the primary pegmatite minerals by the epidote-chlorite-carbonate association were caused by hydrothermal alteration by acid Pb-Zn ore-precipitating fluids. There seems to be no genetic link between the pegmatite emplacement and the economic galena-sphalerite accumulations and the U-Pb geochronometry on monazite, zircon and titanite proved that pegmatite formation (~40 Ma) significantly precedes the origin of the base metal mineralization (~30 Ma).

1 Introduction

The processes of crustal formation and granitic magmatism are responsible for accumulation of incompatible elements, including Th, U and rare-earth elements (REE). Owing to their chemical properties and geochemical behavior, they are seldom incorporated into major rock-forming minerals and preferably tend to form minerals in late stages of magma differentiation. REE-minerals frequently occur in pegmatites, which makes them potential sources for strategic metals and critical elements (e.g. Linnen et al. 2012).

Large pegmatite injections are part of wall rocks within the Pb-Zn deposits in Central Rhodopes, south Bulgaria. The Cenozoic (~30 Ma) base metal vein and metasomatic sulphide mineralization with economic importance is formed by hydrothermal fluid circulation/precipitation as open-space fillings or replacements in the host gneisses, marbles and amphibolites of the Rhodope metamorphic complex (Madan Unit). An ongoing study on the mineral and chemical composition of pegmatites exposed in the underground mine of Kroushev Dol revealed details on the abundance and diversity of REE accessory minerals (Fig. 1). This contribution describes Th- and

U- bearing REE minerals from a selected pegmatite dyke on the 865 m.a.s.l. in the Kroushev Dol deposit, their mineral relationships, replacements, chemical composition, and U-Pb ages.

2 Results

2.1 Pegmatite mineralogy

The pegmatite is placed conformably in the host marble; it was studied in a profile across the body, perpendicular to the contacts. The main mineral composition comprises K-feldspar (Or₈₃₋₉₆), plagioclases (mostly oligoclase, Ab₆₆₋₇₃An₂₆₋₃₁) and quartz. Mineral relationships suggest that the observed albite (Ab₉₁₋₉₈) and adularia are later products. Albitization of primary plagioclase occurs as widespread alteration, preserving relics of oligoclase. Later adularia veinlets cut the matrix including albite (e.g. Fig. 1K), which corresponds to stages of intensive overprint by epidote-chlorite-carbonate alteration. Hydrothermal alteration affects the whole pegmatite volume but it is most intensively developed along the pegmatite contact with the host marbles and metasomatic ore mineralization.

Detailed petrographic study revealed that accessories have zonal distribution across the pegmatite. The inner pegmatite zone is characterized by association of monazite, zircon, allanite, apatite and thorite (Fig. 1 A-L), while in the areas proximal to the lithological contacts large titanite crystals prevail (Fig. 1 M-P).

The REE-minerals often form aggregates and/or accumulations in the pegmatite as seen by the optical and BSE observation. Most of the accessories (allanite, zircon, apatite, titanite; Fig. 1) generally form single well-shaped crystals within the feldspar-quartz matrix, apart from the monazite and thorite grains. They are both observed within the allanite crystals. Monazite appears as large subhedral relics (Fig. 1 A-F), while thorite grains (below 10 µm) mostly form intergrowths with apatite (Fig. 1 G, F), and/or are attached to microfractures in allanite volume (Fig. 1 I). Apatite occurs either as crystals and masses within allanite volume in close association with monazite/thorite (Fig. 1 A-H) or as aggregates (Fig. 1 J) and single crystals often in assemblage with zircon (Fig. 1 G, K). The latter is observed as long prismatic well-shaped crystals with fine oscillatory zoning (Fig. 1 L) and without inherited cores (as seen by CL-microscopy). Most of the

aforementioned REE-minerals are observed as inclusions in allanite crystals (Fig. 1 A-I). The pegmatite periphery, especially along the contacts with marbles is characterized with Ca-rich mineralization and titanite occurrence (Fig. 1 M-P). The euhedral to subhedral crystals are large (more than 200 μm) and replaced on places by fine grained

mineral mixture (leucoxene) dominated by anatase (proved by the X-Ray powder diffraction and Raman spectroscopy). Titanite closely associates with epidote-chlorite-carbonate alteration. Occasionally apatite completes the assemblage.

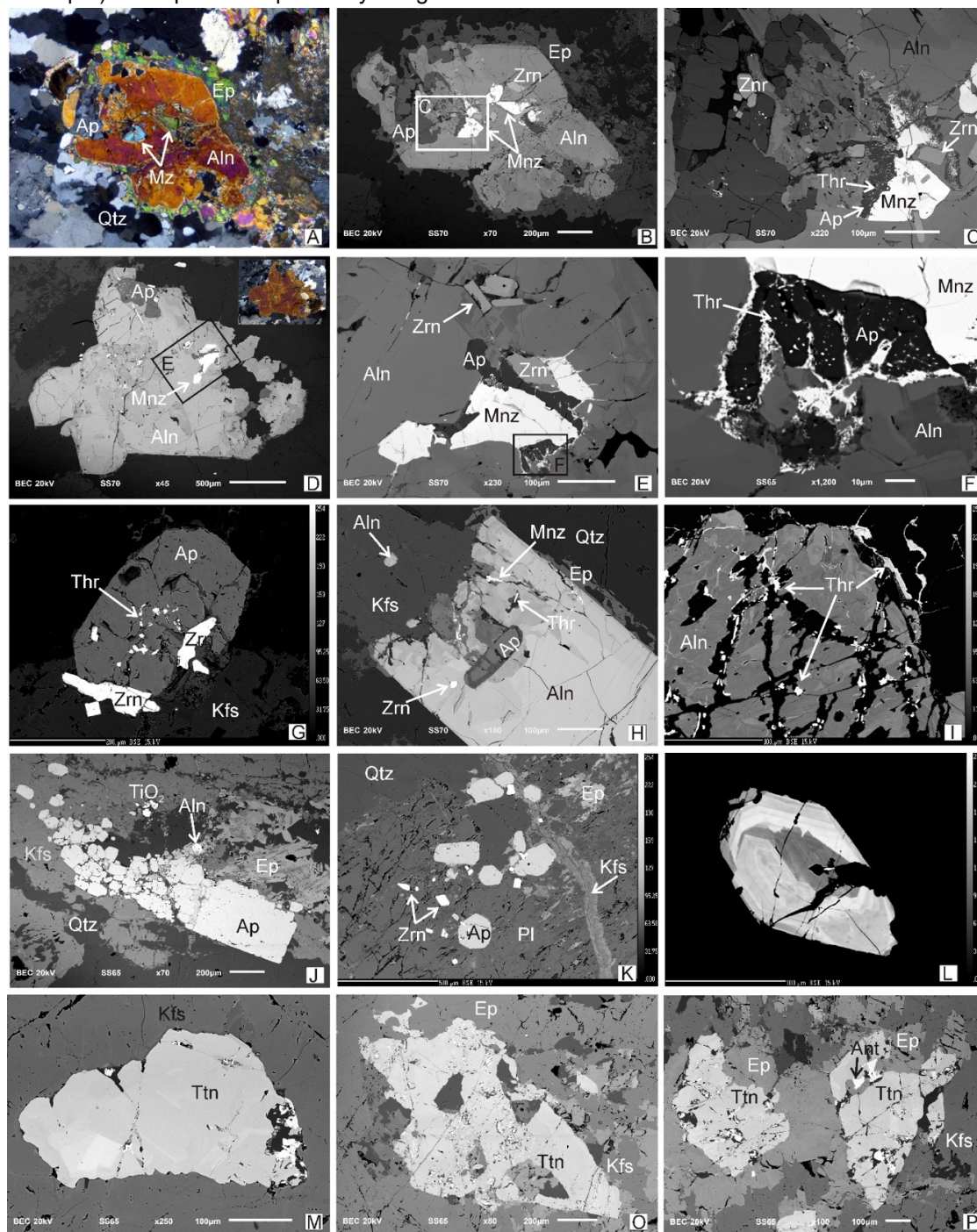


Figure 1. Mineral relationships and textures within the pegmatite-hosted REE association: (A) Epidote-overgrown allanite crystal with inclusions of monazite, zircon, apatite and thorite, PPL; (B) BSE image of crystal from A; (C) close view of the inner parts of allanite crystal, showing zircon and monazite grains and apatite-thorite intergrowths; (D) allanite crystal with apatite and monazite inclusions; (E) monazite relics, close view of (D); (F) thorite-apatite at monazite's expense in allanite crystal; (G) thorite grains and zircon crystals in apatite; (H) zircon and euhedral apatite in allanite; (I) thorite crack-fillings in inhomogeneous allanite; (J) apatite aggregate associating with later epidote; (K) zircon and apatite crystals in altered pegmatite, BSE; (L) oscillatory zoned zircon; (M) titanite in K-feldspar matrix; (O-P) large epidote-associated titanite crystals partly replaced by anatase. Abbreviations refer to: Ap – apatite, Aln – allanite, Ant – anatase, Cc – carbonate, Ep – epidote-clinozoisite, Qtz – quartz; Kfs – K-feldspar, Mnz – monazite, Pl – plagioclase, Thr – thorite, Ttn – titanite, Zr – zircon

2.2 Compositional and geochemical features of REE-minerals

Determination of the chemical composition with electron probe microanalysis (EPMA) and laser ablation in inductively coupled plasma with mass spectrometry (LA-ICP-MS) revealed that the studied minerals concentrate large amounts of critical elements with potential importance. REE, U and Th are initially contained by monazite (LREE) and zircon (Hf, HREE) and consequently redistributed among the other accessory phases – allanite, apatite, thorite, and titanite.

Monazite is classified as monazite-(Ce) with significant La (La_2O_3 14.5-16.54 wt.%) and Nd incorporation (Nd_2O_3 ~9-10 wt.%). Lower, although notable contents of Y, Pr, Sm and Th were detected as major elements. The sum of REE varies between 476425 and 521923 ppm. Uranium content averages 2826 ppm. Chondrite-normalized pattern is characterized by extremely high values for the LREE, well pronounced negative Eu-anomaly and consecutive depletion towards HREE from Gd to Lu.

Apatite is characterized by F-content of ~3 wt.%. Significant Y incorporation (mostly ranging 1000-4000, reaching up to ~7000 ppm) is common for all measured crystals as well as trace amounts of Ga, Ge, and Sr. Certain compositional variations of the mineral depend on the mineral association and the co-existing REE phases and reflect on its geochemical signatures. Apatite crystals in assemblage with thorite and allanite (\pm monazite; Fig. 1A-F) have the highest values for all incorporated elements, compared to zircon-associated apatite single crystals (Fig. 1K) and apatite aggregate with epidote (Fig. 1J). Chondrite-normalized patterns of all apatites show negative Eu-anomaly, $\text{LREE}_{\text{CN}} < \text{HREE}_{\text{CN}}$, due to the concurrent growth with allanite and thorite.

Zircon composition has sufficient content of HREE, especially Yb (up to 2500 ppm) and Hf (0.9-1.78 wt.%). Significant incorporation of Th and U and their variation define the zonal pattern of the crystals. Fluorine amount of ~3500 ppm is steady in all measured compounds. Zr/Hf ratio is mostly ranging 40-42, while REE_{CN} are typical for the igneous rocks with positive Ce- and negative Eu-anomalies and enrichment in HREE.

Allanite to REE-bearing clinozoisite compositions show distinct chemical inhomogeneity (Fig. 1 B, D, H, I), which is defined generally by the variation of $(\text{REE}+\text{Th}+\text{Y})/\text{Ca}$ and to a less extend by $\text{Fe}^{3+}/\text{Al}^{3+}$ ratios. Sufficient Ce- (up to 10 wt. % Ce_2O_3) and La-content (2-5 wt. % La_2O_3) substituting Ca are complemented by ~3 wt. % Nd_2O_3 . Central parts of the crystals (around monazite relics; see Fig. 1 B, D) are enriched in Ce, while La increases towards the rims. Significant minor elements include Pr, Sm, Gd, Th and traces of Ga, Ge, and Y. REE_{CN} -pattern (plot by Milenkov et al 2023) resembles that of monazite but one order of magnitude lowered.

Titanite single crystals (Fig. 1M-P) reveal incorporation of Al, which defines the chemical inhomogeneity observed in BSE regime in some crystals (e.g. Fig. 1M). Characteristic trace element contents of V, Ni, Sn substitute for Ti^{4+} by means of polyvalent

isomorphism. Yttrium, Nb, Zr and LREE, Th, U are present in significant amounts. Chondrite-normalised pattern of REE is characterised by the positive Eu anomaly (see plot by Milenkov et al 2023).

2.3 U-Pb geochronology

In-situ LA-ICP-MS U-Pb geochronology was applied on monazite, zircon and titanite. The monazite grains (Fig. 1B-F) were dated *in-situ* ($n=17$) and yielded lower intercept age of 40.8 ± 2.6 Ma (MSWD=0.35; Fig. 2A). CL-observation on internal texture of zircon crystals revealed oscillatory magmatic growth zones without inherited cores that suggest magmatic origin (e.g. Fig. 1L). The defined zircon age (based on 14 measurements) is 40.0 ± 2.1 Ma (MSWD=0.085; Fig. 2B). Titanite formation is estimated at 38.6 ± 2.1 Ma (MSWD=1.07; $n=20$).

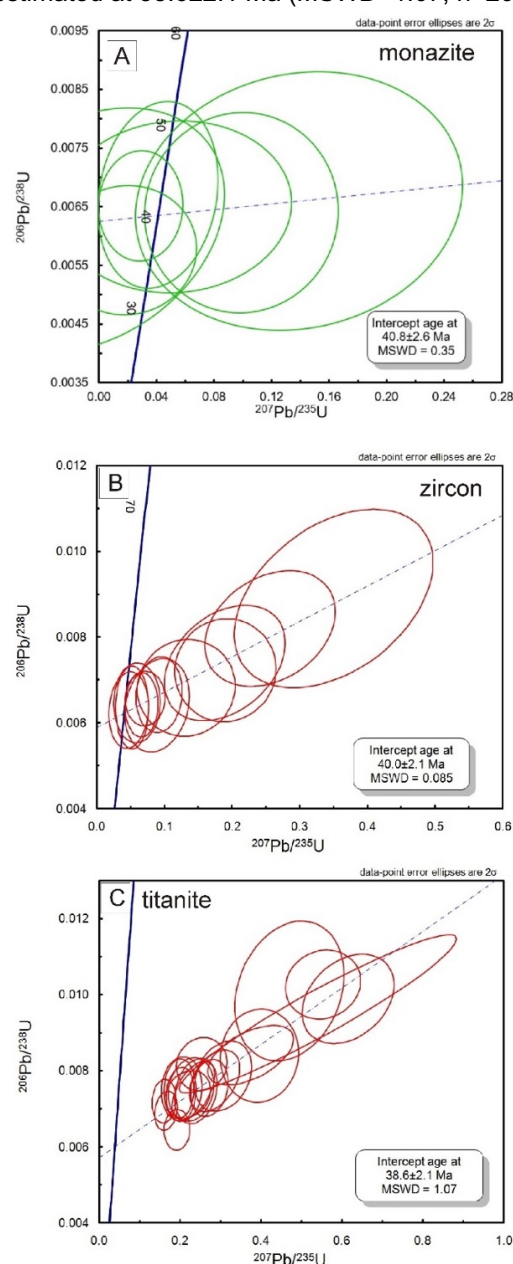


Figure 2. Concordia plots of monazite (A); zircon (B) and titanite (C)

2 Discussion

Mineral replacements

Despite the coexistence of several REE-bearing minerals, their relationships, chemical composition and U-Pb dating suggest continuous process of formation and phase transitions within the early REE-bearing minerals association. Considering their occurrence and morphology, monazite and zircon form in the earlier stages of pegmatite crystallization as proved also by the U-Pb ages. Initially, REE are partitioned between monazite (LREE) and zircon (HREE). The acid leaching of the host rocks (e.g. marbles) or host rock assimilation during pegmatite emplacement led to high initial Ca in the border zone (formation of titanite) and development of late-stage Ca-enriched fluid, which lowered significantly the monazite stability, while zircon remained stable. Dissolution and decomposition of the existing monazite caused redistribution of the incorporated elements. The released LREE (Ce, La) and P are fixed in newly-formed apatite and allanite (Fig. 1A-F). The transition from REE- to Ca-phosphate (monazite to apatite) was facilitated by the high Ca-content (Spear 2010) and strong partitioning of LREE to allanite. Liberated Th contributes to formation of thorite. Limited mobility of LREE from monazite in the fluid phase results in the observed close proximity of allanite. LREE-enrichment in allanite around the monazite grains and its chemical inhomogeneity indicate partial fractionation of La/Ce combined with high Ca content in fluid. On the other hand, apatite is depleted in LREE and shows increased HREE. Yttrium, instead of forming xenotime, is incorporated in apatite. A simplified expression of the monazite alteration suggested by Sato et al. (2014) is: monazite-(Ce) + Ca-rich fluid → allanite + apatite + thorite

After pegmatite solidification, later hydrothermal activity influenced partial replacement of allanite rims (Fig. 1A-B) by epidote-clinozoisite. Transformation within the epidote group minerals (allanite/clinozoisite; Armbruster et al 2006) is common for the studied pegmatites from the Madan Pb-Zn district (Georgieva et al., 2022).

Age of the pegmatite

Timing of the pegmatite emplacement was estimated by U-Pb geochronometry on monazite, zircon and titanite. As suggested by the mineral relationships the initial accessories were monazite and zircon evidenced also by the in-situ U-Pb LA-ICP-MS ages of 40.8 ± 2.6 Ma and 40.0 ± 2.1 Ma, respectively. Despite the slightly older monazite age, the results for both minerals are overlapping in their uncertainties. Pegmatite is injected into the high-grade rocks of the Rhodope metamorphic complex with Jurassic protolith age soon after the tectono-metamorphic regime switched from compressional to extensional. The late Alpine post-collisional history in the region is marked by partial melting and intrusion of granitic bodies at ~42 Ma (e.g. Smilyan pluton) and consequent

migmatization, pegmatite and rhyolite dykes formation (Kaiser-Rohrmeier et al 2013; Ovtcharova et al. 2003; Hantsche et al. 2017; Milenkov et al 2022 and references therein). In the Madan region, these dykes predate the ore mineralization, which precipitated at ~30 Ma (Kaiser-Rohrmeier et al. 2004). The obtained titanite age is similar to the age of the titanites from pegmatites in the nearby Petrovitsa Pb-Zn deposit (Milenkov et al 2022).

Acknowledgements

The study is financially supported by the Bulgarian National Science Fund project KP-06-N34/4. Microprobe analyses at Masaryk University, Brno, were performed in cooperation within the ERA-MIN3 PEGMAT project from Bulgarian (KP-06-DO02/2) and Czech (TH79020002) grants.

References

- Armbruster T, Bonazzi P, Akasaka M, Bermanec V, Chopin C, Gier R, Heuss-Assbichler S, Liebscher A, Menchetti S, Pan Gier'e R, Heuss-Assbichler S, Liebscher A, Menchetti S, Pan Y, Pasero M (2006) Recommended nomenclature of epidote-group minerals. *European Journal of Mineralogy* 18(5):551–567.
- Georgieva S, Vassileva R, Milenkov G, Stefanova E (2022) Major and trace element signature of epidote-group minerals in altered pegmatites from the Petrovitsa Pb–Zn deposit of the Madan ore region, Central Rhodopes, Bulgaria: Evidence of allanite/epidote transformation. *Geologica Carpathica*, 73 (4): 365–380, <https://doi.org/10.31577/GeolCarp.73.4.5>
- Hantsche AL, Kouzmanov K, Dini A, Vassileva R, Guillong M, von Quadt A, (2017) U-Pb age constraints on skarn formation in the Madan Pb-Zn district, Bulgaria: zircon evidence from Tertiary magmatism. 15th Swiss Geoscience Meeting, Abstract volume, 124–125.
- Kaiser-Rohrmeier M, Handler R, von Quadt A, Heinrich C (2004) Hydrothermal Pb-Zn ore formation in the central Rhodopian dome, South Bulgaria: review and new time constraints from Ar-Ar geochronology. *Swiss Bulletin of Mineralogy and Petrology* 84 (1): 37–58.
- Kaiser-Rohrmeier M, von Quadt A, Driesner T, Heinrich, CA, Handler R, Ovtcharova M, Ivanov Z, Petrov P, Sarov ST, Peytcheva I (2013) Post-orogenic extension and hydrothermal ore formation: high-precision geochronology of the central Rhodopian metamorphic core complex (Bulgaria-Greece). *Econ Geol* 108(4):691–718. <https://doi.org/10.2113/econgeo.108.4.691>
- Linnen RL, Lichtervelde MV, Cerni P (2012) Granitic pegmatites as sources of strategic metals. *Elements* 8(4):275–280, DOI: 10.2113/gselements.8.4.275
- Milenkov G, Vassileva R, Georgieva S, Grozdev V, Peytcheva I (2022) Trace-element signatures and U-Pb geochronology of magmatic and hydrothermal titanites from the Petrovitsa Pb-Zn deposit, Madan region, Central Rhodopes (Bulgaria). *Geologica Balcanica* 51(2): 79–91.
- Milenkov G, Vassileva RD, Georgieva S, Kouzmanov K, Cempirek J, Georgieva Y (2023) Comparative study of pegmatites from the Central Rhodopean Pb-Zn deposits (Bulgaria), this volume
- Ovtcharova M, von Quadt A, Frank M, Kaiser-Rohrmeier M (2003) Triggering of hydrothermal ore mineralization in the Central Rhodopean core complex (Bulgaria) - insight from isotope and geochronological studies on Tertiary magmatism and migmatization. In: Eliopoulos D.G. (Ed.) *Mineral exploration and sustainable development*, 1: 367–370.
- Sato K, Minakawa T, Kato T, Maki K, Iwano H, Hirata T, Hayashi S, Suzuki K (2014) Behavior of rare elements in Late Cretaceous pegmatites from Setouchi province, inner zone of southwest Japan. *Journal of Mineralogical and Petrological Sciences* 109: 28–33
- Spear F S (2010) Monazite–allanite phase relations in metapelites. *Chemical Geology* 279: 55–62, doi:10.1016/j.chemgeo.2010.10.004

Comparison of the Beauvoir and Cínovec rare metal granite/greisen systems: Role of muscovitization on Li-Sn-W-Ta hydrothermal remobilization

Matthieu Harlaux, Olivier Blein, Blandine Gourcerol
BRGM – French Geological Survey, 45060 Orléans, France

Abstract. We provide a comparative review of greisenization in the Beauvoir (France) and Cínovec (Czech Republic/Germany) deposits, which are two of the world's best studied examples of peraluminous Li-Sn-Ta-W-mineralized granitic systems. While the Cínovec granite cupola is two-to-eight times less enriched in rare metals than Beauvoir, a Li-Sn-W greisen deposit was formed in the former but not in the latter. At Beauvoir, alteration of igneous lepidolite produced Sn-rich and Li-W-Ta-depleted greisen muscovite. In contrast, igneous and greisen zinnwaldite at Cínovec have similar contents of Li, Sn, W and Ta. Late replacement of zinnwaldite by muscovite in the Cínovec greisen is marked by enrichment in Sn and depletion in Li, W and Ta, similar to greisen muscovite from Beauvoir. We conclude that muscovitization, although associated with secondary Sn enrichment, is not essential for the formation of mineralized greisens, which are primarily controlled by the emplacement depth of magmas and the intensity of pervasive alteration.

1 Introduction

Rare metal granites (RMG) represent the most fractionated members of granitic suites and are characterized by significant enrichment in rare lithophile elements such as Li, Be, Sn, W, Cs, Ta and Nb (Černý et al. 2005; Linnen and Cuney 2005). While the magmatic evolution and the magmatic-hydrothermal transition of RMG systems have been extensively studied (Linnen and Cuney 2005; Ballouard et al. 2016; Breiter et al. 2017; Harlaux et al. 2017; Kaeter et al. 2018; Michaud and Pichavant 2020), the factors controlling metal remobilization and the formation of mineralized alteration zones around granitic plutons are much less understood.

Among metasomatic processes that affect granitic cupolas, greisenization is commonly associated with Sn-W and RMG deposits (Černý et al. 2005). This feldspar-destructive alteration results from high-temperature interactions between granitic rocks and acidic fluids, locally forming Li-Sn-W deposits (Černý et al. 2005; Breiter et al. 2017). Although greisenization has been investigated from mineralogical, geochemical, experimental and modelling standpoints (Halter et al. 1996, 1998; Breiter et al. 2017; Launay et al. 2019, 2023), it is still unclear why some RMG systems develop mineralized greisen deposits while other do not.

In this paper, we provide a comparative review of greisenization at Beauvoir (France) and Cínovec (Czech Republic/Germany), which are two well-studied examples of RMG in Europe (Gourcerol et al. 2019). The greisens in these two localities show major differences in terms of volume of altered rocks and metal enrichment. Comparing the Beauvoir and

Cínovec deposits can provide, therefore, useful insights to better understand what controls the development of mineralized RMG-greisen systems.

2 Geological background

2.1 The Beauvoir RMG

The Beauvoir granite is located within the Echassières granitic complex in the NE part of the French Massif Central which belongs to the Moldanubian zone of the European Variscan belt. The Beauvoir granite was emplaced at ca. 315-310 Ma and is characterized by a strongly peraluminous S-type composition with a disseminated Sn-Li-Ta-Nb-Be mineralization (Cuney et al. 1992; Raimbault et al. 1995). The 900-m-long GPF-1 borehole drilled through the Beauvoir granite revealed a vertical zoning with three granitic units, which are from the upper to the lower (Cuney et al. 1992; Raimbault et al. 1995): (i) B1 unit (-100 to -450 m) corresponding to an albite-lepidolite-rich leucogranite containing globular quartz and rare anhedral perthitic K-feldspar; (ii) B2 unit (-450 to -750 m) consisting of a lepidolite-rich granular granite with idiomorphic quartz and low amounts of K-feldspar; and (iii) B3 unit (-750 to -880 m), which contains euhedral pink-colored K-feldspar and zinnwaldite. The abundance of accessory minerals (topaz, cassiterite, columbite-tantalite, microlite, and Li-Be phosphates) increases upward from the B3 to the B1 units, the latter being the most evolved (Cuney et al. 1992; Raimbault et al. 1995). The uppermost B1 unit exhibits greisen alteration consisting of a quartz-muscovite-topaz assemblage developed along fractures without significant mineralization (Monnier et al. 2020).

2.2 The Cínovec RMG

The Cínovec granite is located within the Krušné hory/Erzgebirge in the NW part of the Bohemian Massif which belongs to the Saxo-Thuringian zone of the European Variscan belt. The granite was emplaced at ca. 325-322 Ma into rhyolites of the Altenberg-Teplice caldera within a large volcanic-plutonic complex and is characterized by a moderately peraluminous A-type composition with enrichment in Li, Rb, Cs, Ta, Sn, W (Štemprok 2016; Breiter et al. 2017). Vertical zonation at Cínovec was documented by the 1600-m-long CS-1 borehole and consists of four major units, which are from top to bottom (Štemprok 2016; Breiter et al. 2017): (i) granite canopy (CnG; down to -260 m) composed of

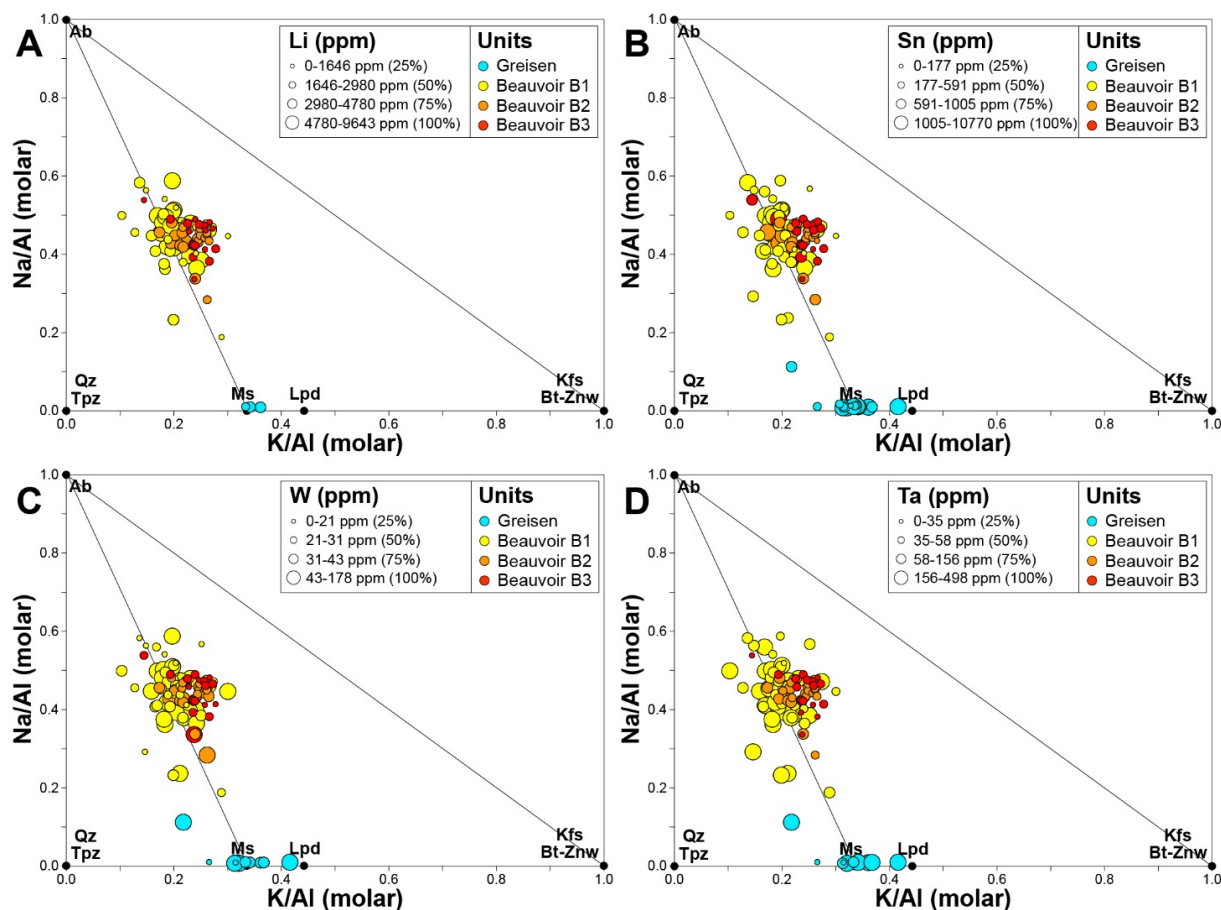


Figure 1. Bubbleplot diagrams of K/Al vs. Na/Al molar ratios for rock samples from Beauvoir illustrating the contents of Li, Sn, W, and Ta in granites and greisens. The bubble diameters correspond to quartile distribution (25%, 50%, 75%, 100%) of element concentrations. The node locations of common silicate minerals identified in these rocks are also plotted (Ab = albite, Bt = biotite, Kfs = K-feldspar, Lpd = lepidolite, Ms = muscovite, Qz = quartz, Tpz = topaz, Znw = zinnwaldite).

an equigranular fine-grained albite-zinnwaldite granite with subhedral albite, globular quartz, and rare K-feldspar; (ii) medium-grained porphyritic mica-free granite (MfG; -260 to -370 m), which contains subhedral quartz and anhedral K-feldspar and albite; (iii) fine- to medium-grained porphyritic albite-zinnwaldite granite (ZiG(m); -370 to -735 m) which shows evidence of commingling; and (iv) a lower suite of biotite granites (BtG; -735 to -1596 m) comprising fine-to-medium-grained porphyritic to coarse-grained equigranular facies with perthitic K-feldspar and subhedral plagioclase. Quartz-zinnwaldite greisens occur in the granite canopy, locally forming massive alteration zones. Disseminated mineralization in the greisen consists of irregularly distributed cassiterite, fluorite, topaz, columbite-tantalite, scheelite, wolframite and REE-F-carbonates (Breiter et al. 2017, 2019).

3 Results

3.1 Whole-rock compositions

Based on a compilation of whole-rock geochemical data from the Beauvoir and Cínovec RMG-greisen systems (Cuney et al. 1992; Raimbault et al. 1995; Dolejš and Štemprok 2001; Monecke et al. 2007;

Štemprok 2016; Breiter et al. 2017; Müller et al. 2018), we compared the enrichment in Li, Sn, W and Ta related to greisenization. Data were plotted in the K/Al vs. Na/Al molar ratio diagram, which is convenient to identify alteration trends and related mineralogical changes (Davies and Whitehead 2010). Compared to the uppermost Beauvoir granite (B1 unit: avg Li = 4575 ppm; Sn = 1077 ppm; Ta = 179 ppm; W = 41 ppm), the quartz-muscovite greisens have moderate enrichment in Sn (avg = 1944 ppm; +81%) but no specific enrichment in Li (avg = 3403 ppm; -26%), Ta (avg = 236 ppm; +32%) and W (avg = 45 ppm; +9%; **Fig. 1**). In contrast, quartz-zinnwaldite greisens at Cínovec are moderately to strongly enriched in Li (avg = 4314 ppm; +292%), Sn (avg = 1126 ppm; +744%), W (avg = 491 ppm; +1884%) and Ta (avg = 78 ppm; +97%) compared to the uppermost granite (CnG unit: avg Li = 1100 ppm; Sn = 133 ppm; W = 25 ppm; Ta = 40 ppm; **Fig. 2**).

3.2 Mica compositions

To further investigate the evolution of Li, Sn, W and Ta contents during greisenization of RMG systems, we also compared the trace element concentrations of igneous and greisen micas from Beauvoir and

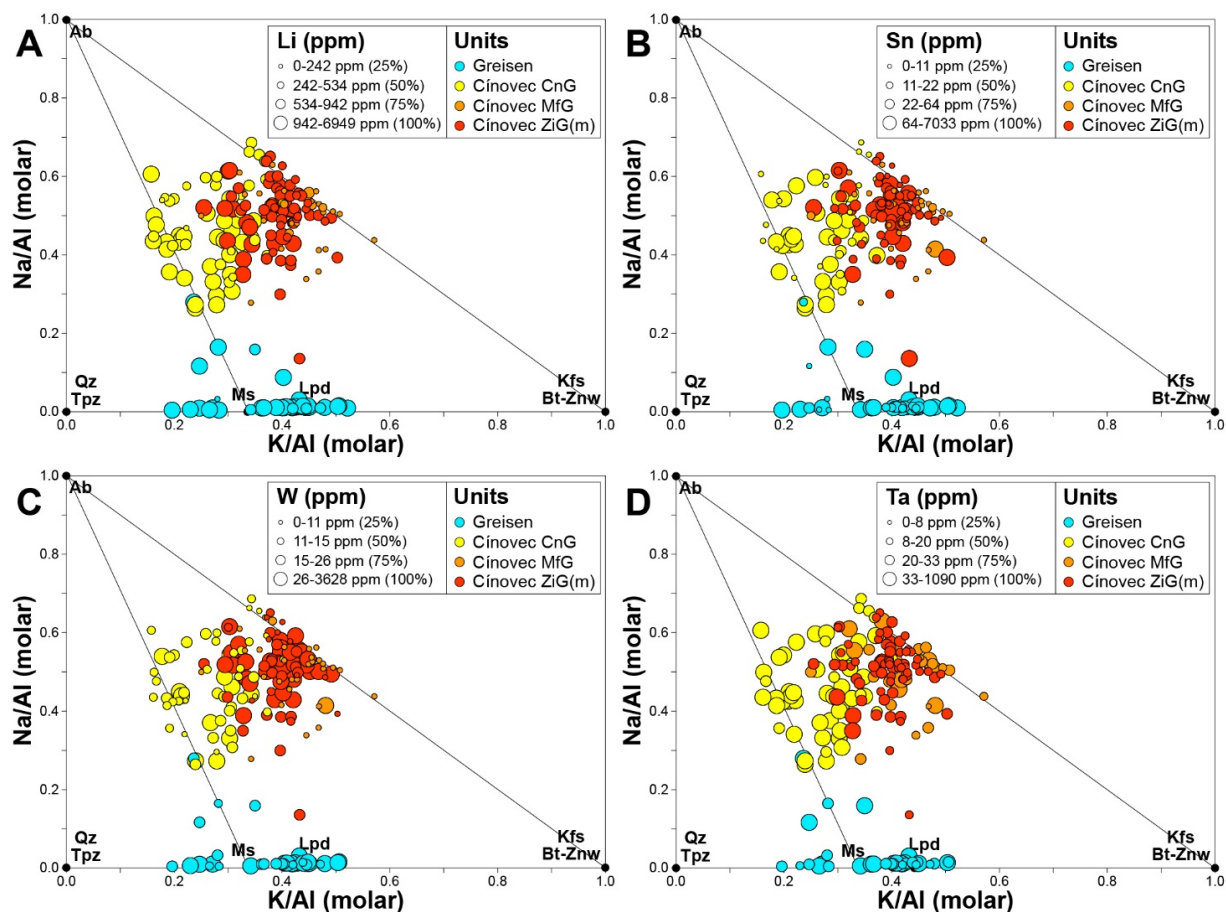


Figure 2. Bubbleplot diagrams of K/Al vs. Na/Al molar ratios for rock samples from Cínovec illustrating the contents of Li, Sn, W, and Ta in granites and greisens. The bubble diameters correspond to quartile distribution (25%, 50%, 75%, 100%) of element concentrations. The node locations of common silicate minerals identified in these rocks are also plotted (Ab = albite, Bt = biotite, Kfs = K-feldspar, Lpd = lepidolite, Ms = muscovite, Qz = quartz, Tpz = topaz, Znw = zinnwaldite).

Cínovec (Breiter et al. 2019; Monnier et al. 2022). At Beauvoir, greisen muscovite is strongly enriched in Sn (avg = 1173 ppm; +677%) but is significantly depleted in Li (avg = 648 ppm; -97%), W (avg = 2 ppm; -99%) and Ta (avg = 29 ppm; -52%) compared to igneous lepidolite from the B1 granite (avg Li = 25,127 ppm; Sn = 151 ppm; W = 246 ppm; Ta = 61 ppm; **Fig. 3A**). In contrast, greisen zinnwaldite from Cínovec has similar contents of Li (avg = 16,568 ppm), Sn (avg = 124 ppm), W (avg = 20 ppm) and Ta (avg = 19 ppm) compared to igneous zinnwaldite from the granite canopy (CnG unit: avg Li = 15,819 ppm; Sn = 122 ppm; W = 35 ppm; Ta = 40 ppm; **Fig. 3B**). However, late muscovite locally replacing zinnwaldite in the Cínovec greisen shows a marked enrichment in Sn (avg = 1287 ppm; +938%) and significant depletions in Li (avg = 3961 ppm; -76%), W (avg = 6 ppm; -70%) and Ta (avg = 17 ppm; -11%) relative to greisen zinnwaldite (**Fig. 3B**).

4 Discussion and conclusions

While the Cínovec RMG cupola is less enriched in rare metals than Beauvoir with two-to-eight times lower average contents of Li (1100 ppm vs. 4575 ppm), Sn (133 ppm vs. 1077 ppm), W (25 ppm vs. 41

ppm) and Ta (40 ppm vs. 179 ppm), it is associated with a highly-mineralized Li-Sn-W greisen deposit. This difference of metal enrichment is recorded by the composition of micas, which are petrogenetic monitors of the evolution of RMG-greisen systems. At Beauvoir, alteration of Li-Sn-W-enriched igneous lepidolite produced Sn-rich and Li-W-Ta-depleted greisen muscovite, thus releasing Li, W and Ta in the hydrothermal fluid (Monnier et al. 2022). At Cínovec, there are no major changes of Li, Sn, W and Ta contents between igneous zinnwaldite and greisen zinnwaldite, the latter being interpreted to have fully re-equilibrated with the greisen-forming fluid (Breiter et al. 2019). Late alteration of zinnwaldite to muscovite in the Cínovec greisen is marked by a strong enrichment in Sn and depletion in Li, W and Ta, similar to greisen muscovite at Beauvoir. Therefore, muscovitization occurring in both RMG cupolas was not essential for the formation of mineralized greisens. Although it is associated with secondary Sn enrichment, muscovite alteration seems more an inhibitor of metal enrichment in greisens. The fact that massive mineralized greisens were formed at Cínovec but not at Beauvoir is likely related to different emplacement depths of magmas and volumes of

fluids released. Greisenization and veining at Cínovec were favored by hypabyssal emplacement (0.5–1.5 km) of the granitic magmas, thus causing widespread hydraulic fracturing and pervasive alteration of significant rock volumes (Štemprok 2016; Breiter et al. 2017). In contrast, the greater emplacement depth of the Beauvoir RMG (ca. 3–4 km) induced mostly fracture-related alteration, which may explain the lack of massive mineralized greisens (Cuney et al. 1992).

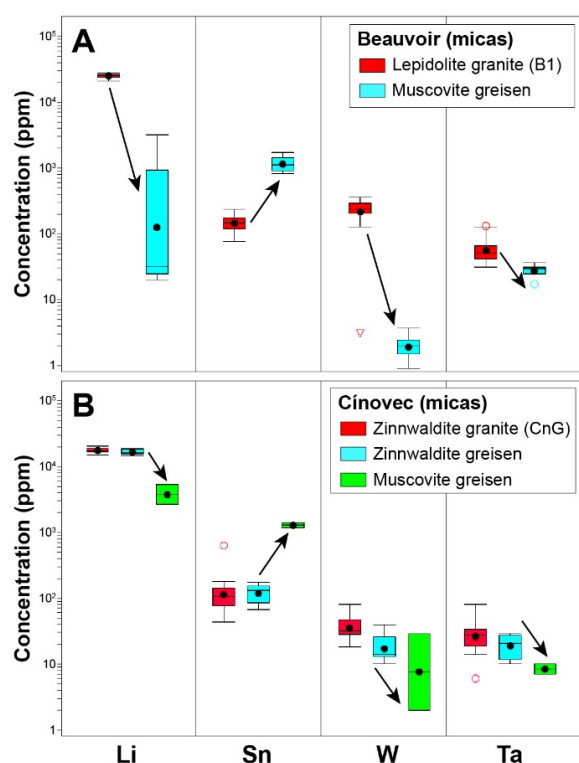


Figure 3. Box plots illustrating the evolution of Li, Sn, W and Ta contents in micas during greisenization of the granitic cupolas at Beauvoir (A) and Cínovec (B).

Acknowledgements

This project is supported by funds from the Horizon Europe research and innovation programme under Grant Agreement number 101057357, EIS – Exploration Information System (<https://eis-he.eu>).

References

- Ballouard C, Poujol M, Boulvais P, Branquet Y, Tartèse R, Vigneress JL (2016) Nb-Ta fractionation in peraluminous granites: A marker of the magmatic-hydrothermal transition. *Geology* 44:231–234.
- Breiter K, Ďurišová J, Hrstka T, Korbelová Z, Vaňková MH, Galiová MV, Kanický V, Rambousek P, Kněsl I, Dobeš P, Dosbaba M (2017) Assessment of magmatic vs. metasomatic processes in rare-metal granites: a case study of the Cínovec/Zinnwald Sn–W–Li deposit, Central Europe. *Lithos* 292:198–217.
- Breiter K, Hložková M, Korbelová Z, Galiová MV (2019) Diversity of lithium mica compositions in mineralized granite–greisen system: Cínovec Li–Sn–W deposit, Erzgebirge. *Ore Geol Rev* 106:12–27.
- Černý P, Blevin PL, Cuney M, London D (2005) Granite-related ore deposits. *Econ Geol* 100th:337–370.
- Cuney M, Marignac C, Weisbrod A (1992) The Beauvoir topaz-lepidolite albite granite (Massif Central, France): The disseminated magmatic Sn–Li–Ta–Nb–Be mineralization. *Econ Geol* 87:1766–1794.
- Davies JF, Whitehead RE (2010) Alkali/alumina molar ratio trends in altered granitoid rocks hosting porphyry and related deposits. *Explor Min Geol* 19:13–22.
- Dolejš D, Štemprok M (2001) Magmatic and hydrothermal evolution of Li–F granites: Cínovec and Krásno intrusions, Krušné hory batholith, Czech Republic. *Bull Czech Geol Surv* 76:77–99.
- Gourcerol B, Gloaguen E, Melleton J, Tuduri J, Galiegue X (2019) Re-assessing the European lithium resource potential – A review of hard-rock resources and metallogeny. *Ore Geol Rev* 109:494–519.
- Halter WE, Williams-Jones AE, Kontak DJ (1996) The role of greisenization in cassiterite precipitation at the East Kemptville tin deposit, Nova Scotia. *Econ Geol* 91:368–385.
- Halter WE, Williams-Jones AE, Kontak DJ (1998) Modeling fluid–rock interaction during greisenization at the East Kemptville tin deposit: implications for mineralization. *Chem Geol* 150:1–17.
- Harlaux M, Mercadier J, Bonzi WME, Kremer V, Marignac C, Cuney M (2017) Geochemical signature of magmatic-hydrothermal fluids exsolved from the Beauvoir rare-metal granite (Massif Central, France): insights from LA-ICP-MS analysis of primary fluid inclusions. *Geofluids* 2017:1–25.
- Kaeter D, Barros R, Menuge JF, Chew DM (2018) The magmatic–hydrothermal transition in rare-element pegmatites from southeast Ireland: LA-ICP-MS chemical mapping of muscovite and columbite–tantalite. *Geochim Cosmochim Acta* 240:98–130.
- Launay G, Sizaret S, Guillou-Frottier L, Fauguerolles C, Champallier R, Gloaguen E (2019) Dynamic permeability related to greisenization reactions in Sn–W ore deposits: Quantitative petrophysical and experimental evidence. *Geofluids* 2019:1–23.
- Launay G, Branquet Y, Sizaret S, Guillou-Frottier L, Gloaguen E (2023) How greisenization could trigger the formation of large vein-and-greisen Sn–W deposits: a numerical investigation applied to the Panasqueira deposit. *Ore Geol Rev* 105299.
- Linnen RL, Cuney M (2005) Granite-related rare-element deposits and experimental constraints on Ta–Nb–W–Sn–Zr–Hf mineralization. *GAC Short Course Notes* 17:45–68.
- Michaud JAS, Pichavant M (2020) Magmatic fractionation and the magmatic-hydrothermal transition in rare metal granites: evidence from Argemela (Central Portugal). *Geochim Cosmochim Acta* 289:130–157.
- Monecke T, Dulski P, Kempe U (2007) Origin of convex tetrads in rare earth element patterns of hydrothermally altered siliceous igneous rocks from the Zinnwald Sn–W deposit, Germany. *Geochim Cosmochim Acta* 71:335–353.
- Monnier L, Salvi S, Jourdan V, Sall S, Bailly L, Melleton J, Béziat D (2020) Contrasting fluid behavior during two styles of greisen alteration leading to distinct wolframite mineralizations: The Echassières district (Massif Central, France). *Ore Geol Rev* 124:103648.
- Monnier L, Salvi S, Melleton J, Lach P, Pochon A, Bailly L, Béziat D, De Parseval P (2022) Mica trace-element signatures: Highlighting superimposed W–Sn mineralizations and fluid sources. *Chem Geol* 600:120866.
- Müller A, Herklotz G, Giegling H (2018) Chemistry of quartz related to the Zinnwald/Cínovec Sn–W–Li greisen-type deposit, Eastern Erzgebirge, Germany. *J Geochem Explor* 190:357–373.
- Raimbault L, Cuney M, Azencott C, Duthou JL, Joron JL (1995) Geochemical evidence for a multistage magmatic genesis of Ta–Sn–Li mineralization in the granite at Beauvoir, French Massif Central. *Econ Geol* 90:548–576.
- Štemprok M (2016) Drill hole CS-1 penetrating the Cínovec/Zinnwald granite cupola (Czech Republic): An A-type granite with important hydrothermal mineralization. *J Geosci* 61:395–423.

Dating and trace-element characterisation of Sn-W skarn-, greisen- and metamorphic vein-type occurrences from East-Greenland

Nynke Keulen, Benjamin Heredia, Sebastian Malkki, Tonny B. Thomsen, Diogo Rosa, David Whitehead
Geological Survey of Denmark and Greenland (GEUS), Øster Voldgade 10, 1350 Copenhagen, Denmark

Abstract. The traceability of Sn- and W-minerals to their deposit type (skarn, greisen or hydrothermal veins) was tested on rock samples and stream sediments from East Greenland. Scheelite and cassiterite grains from nine occurrences were analysed for their host rock mineral assemblage and geochemical fingerprint (trace elements and dates by laser-ablation inductively coupled plasma mass spectrometry). Samples from eight localities were collected from skarn, greisen or metamorphic vein occurrences, while the ninth consists of loose blocks transported by a glacier. The mineralogy of the samples was investigated with automated quantitative mineralogy (AQM) and trace elements of minerals from these outcrops were compared to trace element values for the same deposit types in literature. Furthermore, U/Pb-dating of the scheelite, cassiterite as well as zircon, apatite and rutile formed during the same mineralising events were estimated, to determine the timing of the mineralisation. AQM observations on the thin sections match well with trace element data, while new dates of the minerals reveal a more complex mineralisation history than previously known, with seemingly comprising at least three pulses during the Caledonian orogeny.

1 Introduction

Tin (Sn) and especially tungsten (W) occurrences in East Greenland were extensively studied by the exploration company Nordisk Mineselskab A/S from the late 1960s to early 1980s, sporadically followed up by investigations by GEUS and the Greenlandic Ministry of Mineral Resources (MMR) in the forty years afterwards, latest during the Summer 2022. Most of the occurrences are connected to the Caledonian orogeny in East-Greenland (Figure 1). Mineral occurrences are found in the uppermost Caledonian thrust sheet and in the passively overlying sediments of the Franz Joseph allochthon and are thought to be associated with the intrusion of Silurian and Devonian S-type granites (Higgins et al. 2004). Sn-mineralisation is observed as cassiterite, while W is found in scheelite. Mineralised rocks are found as skarn, greisen or metamorphic vein occurrences, depending on their host rock and the proximity to granites (Hallenstein & Pedersen, 1982).

Literature data reveal that different deposit types, like skarns, greisen, and metamorphic vein-type each have their own set of mineral trace element compositions (e.g., Wang et al. 2022, Sciuba et al. 2020 and many others). A good understanding of these properties can serve in assessing the potential for what deposit types are

expected to be found upstream based on analysed stream sediment or till samples.

2 Geological setting

The occurrences can be divided into three major groups (Hallenstein & Pedersen, 1982, Strachan et al. 2001): 1) Skarn deposits related to the formation of thin granitic sheets in high-grade metamorphic sediments of the Krummedal sequence in the Hagar Bjerg thrust sheet. These are all scheelite occurrences; 2) Greisen deposits related to magmatic fluids and large granitic bodies intruding into the lower Eleonore Bay Supergroup of the Franz Joseph allochthon. Both cassiterite and scheelite occur; 3) In metamorphic quartz-scheelite veins, associated with antimony, arsenic, and copper found in bituminous limestone beds of the upper part of the Eleonore Bay Supergroup. Samples from nine different localities in East Greenland were investigated (Figure 1).

3 Analytical methods

3.1 Automated quantitative mineralogy (AQM)

Thin sections of samples were investigated with AQM to study the mineral assemblage formed during the mineralisation. AQM is a scanning electron microscope technique that combines back-scattered electron imaging with chemical analyses by energy dispersive spectroscopy in a mosaic with a small step-size (Keulen et al. 2020). Each analysis is interpreted as a mineral species and is coloured as a pixel in the false-coloured mineral map. Furthermore, cathodoluminescence (CL) imaging is performed to study growth zonations within scheelite and cassiterite.

3.2 LA-ICP-MS investigations

Laser-ablation inductively coupled plasma mass spectrometry (LA-ICP-MS) analyses were performed with two purposes: 1) to investigate the age constraints of mineralisation of scheelite, cassiterite together with other minerals formed at the same time, and 2) to characterise the deposit type by estimating the characteristic range of trace elements in its minerals. For this second purpose a database of literature data for cassiterite (K. Foltyn), scheelite and tourmaline was built.

To facilitate the matrix-matched cassiterite dating by LA-ICP:MS, a new standard was

developed, following a procedure described elsewhere at this conference (Thomsen et al.).



Figure 1. Map of East Greenland showing known scheelite and cassiterite localities. So far, the mineralisation dates of samples from Blokadedal (red), Margeries Dal (blue), Berserkerbræ (pink) and Kalkdal (green) have been determined. Data on other five occurrences will be shown during the conference.

4 Results

4.1 Field observations

Field observations in Blokadedal show the close association of a S-type granite and its alteration zones with tourmaline, fluorite, Y-La-allanite, yellowish-green mica minerals and quartz veins (Figure 2). Cassiterite is found in the alteration zone (greisen), while the more distal hydrothermal quartz veins host both scheelite and cassiterite.

4.2 Mineralogy

AQM observations confirm the three main settings with skarn, greisen and metamorphic vein occurrences, but also reveal differences in the mineral assemblages from the individual occurrences depending on the composition of the host rock and variations in the metasomatic fluids. The Blokadedal occurrence (Figure 3A) shows that cassiterite is present in three settings; associated with tourmaline, topaz and fluorite; with

Li-bearing muscovite and biotite; or with muscovite and beryl.

The Margeries Dal occurrence (Figure 3B) shows quartz veins intruded in limestone, where scheelite precipitates. A range of different settings exists; scheelite occurs as veins, often coated with quartz or calcite, as dispersed grains in a matrix with quartz, dolomite, calcite, \pm apatite, \pm ankerite. Locally, scheelite is observed within siliciclastic sediments. The veined scheelite shows clear oscillatory zonation (Figure 3B). In the north-western part of the area, stibnite is deposited in quartz veins.

4.3 Dating of the mineralisation

ICP-MS analyses showed that the mineralisation of Sn and W did not occur in a single event but consisted of at least three different pulses likely between 441-378 Ma (Figure 1). This indicates that the mineralisation was triggered by local events, rather than a single regional event and that the timeslot with optimal conditions for melting and fractionation was longer than previously assumed.

4.4 Trace elements in scheelite and cassiterite

Comparison of the trace elements reveals that the scheelite occurrences from the study area compare well to literature trace element data and that the vein-type deposits, which were classified as the most tungsten-rich by Nordisk Mineselskab A/S can easily be distinguished from skarn-type scheelite (Figure 4).

5 Discussion

Formation of scheelite and cassiterite was possible during at least three stages in the history of the area: The first pulse at ca. 445-441 Ma was observed as the dates of cassiterite in Berserkerbræ. This age is not well understood, as it is older than the Caledonian S-type granites. Migmatization was reported in the metasedimentary rocks of the Hagar Bjerg thrust sheets from 446 Ma onwards (Gilotti & McClelland 2008). This might have caused a local fractionated melt, resulting in enrichment in Sn (and W) and the formation of greisen with cassiterite.

Most S-type granites were emplaced near 425 Ma (Kalsbeek et al. 2008). S-type granites are typically the source of Sn and W in occurrences. McClelland and Gilotti (2003) define this period as the first stage of synorogenic extension, thus transporting heat to the Krummedal metasediments, which will likely promote partial melting and fractionation of Sn and W in the magma.

During the main pulse of mineralisation both scheelite and apatite from Kalkdal, as well as cassiterite and rutile from Blokadedal all give the same date (ca. 403 Ma), which is the possible age

of chemically evolved Devonian granites in area (Steenfelt 1982). AQM observations reveal that

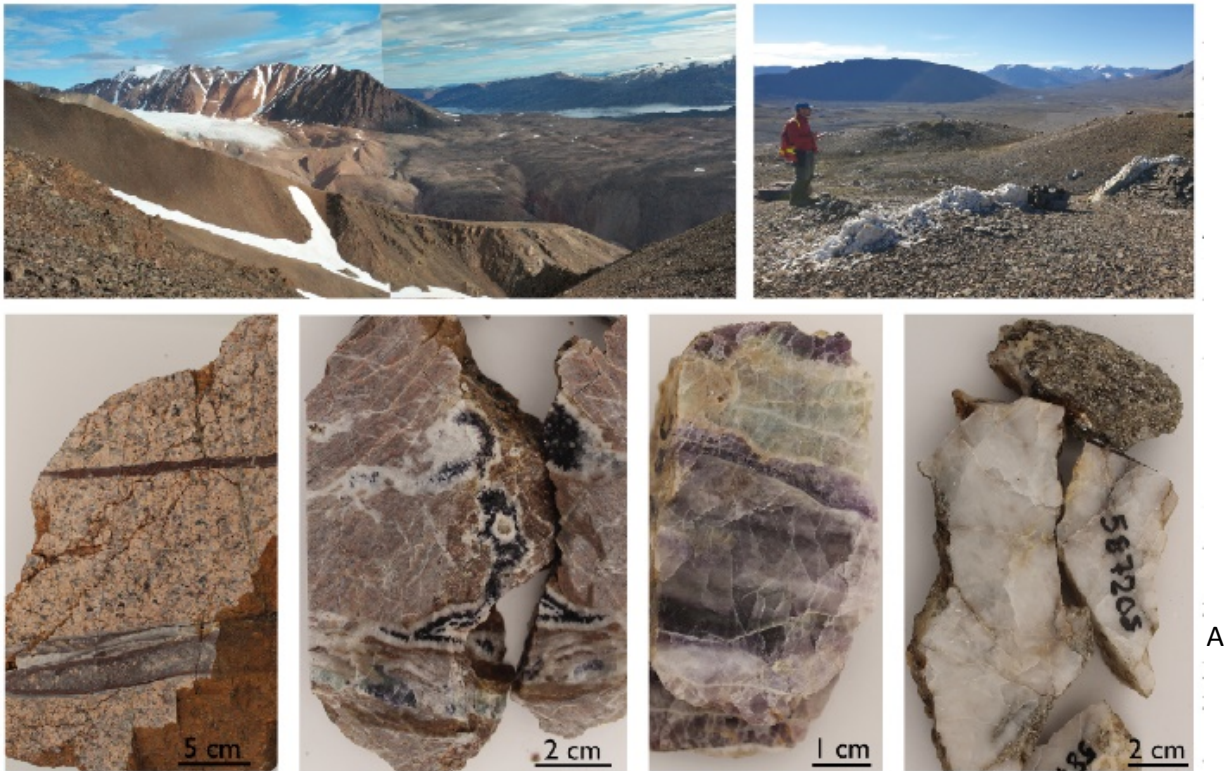
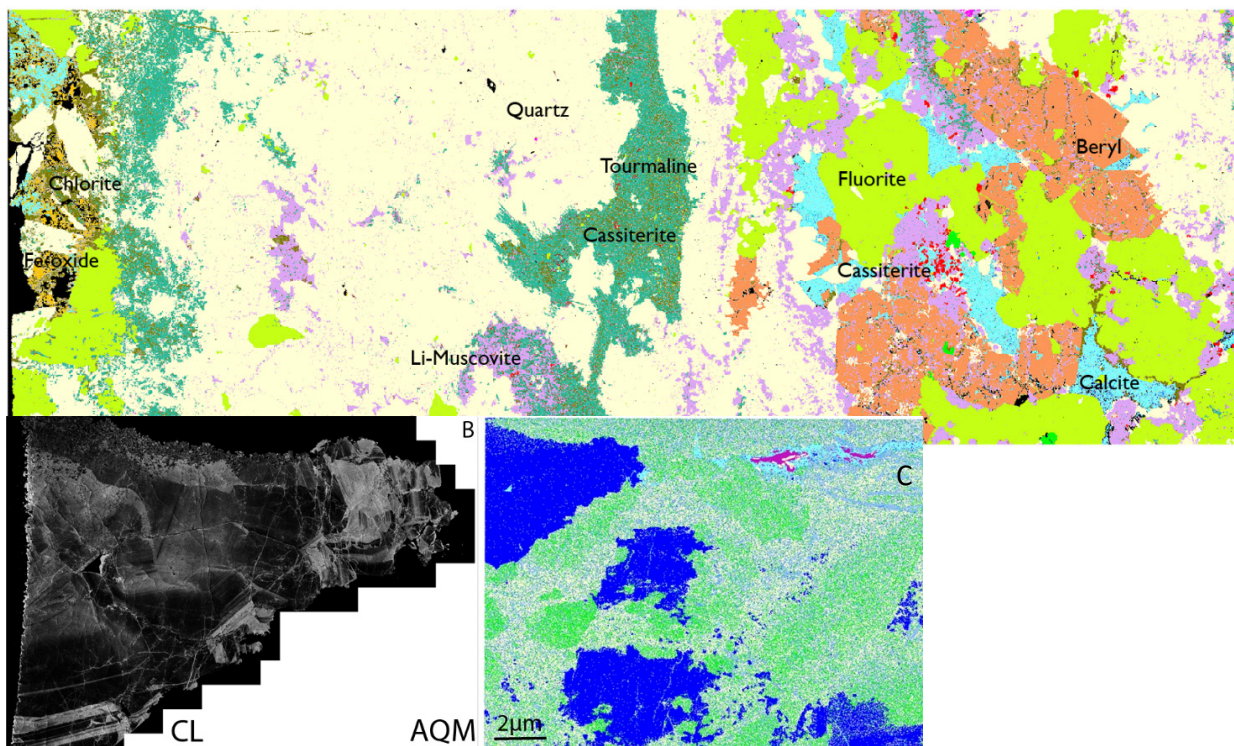


Figure 2 (above). Field observations from Blokadedal. Top row: Blokadedal with tin-bearing granite intrusion (pink, arrow). Sets of quartz-veins crosscut the Eleonore Bay Supergroup rocks. Bottom row: Altered granite samples with siliceous veins, including tourmaline (black), fluorite (green-purple) and brecciated rock. Quartz-veins with yellowish-green mica were previously correlated with enhanced W-Sn concentrations.

Figure 3 (below). **A)** Automated quantitative mineralogy (AQM) map of a cassiterite-bearing sample from Blokadedal. Cassiterite (red) is here associated with tourmaline and muscovite. **B)** AQM map and CL image of scheelite-bearing sample from Margeries Dal. Scheelite (dark blue) occurs as at least two generations of oscillatory hydrothermal veins that crosscut the altered bituminous limestone host-rock.



rutile and apatite grew as part of the mineralisation process and most likely not were present before the mineralisation. Therefore, it is likely that a renewed fractionation occurred, which produced granitic magma enriched in Sn and W. McClelland & Gilotti (2003) associated an age of 404 Ma with late orogenic extension and exhumation, which is a likely explanation for this renewed fractionation.

The last pulse of mineralisation is observed in the Margeries Dal area and is significantly younger (376 Ma). These, as well as other upper Eleonore Bay Supergroup scheelite occurrences, are not spatially associated with a granite, which is in agreement with the trace element signature in tourmaline and scheelite from the same occurrences.

Further integration of absolute dating and trace element compositions on the scheelite and cassiterite occurrences in the area will lead to a better understanding of the different mineralisation styles. Furthermore, the methodologies presented here act as a platform serving to improve our understanding of the geological processes relevant for the formation of cassiterite and scheelite deposits in eastern Greenland.

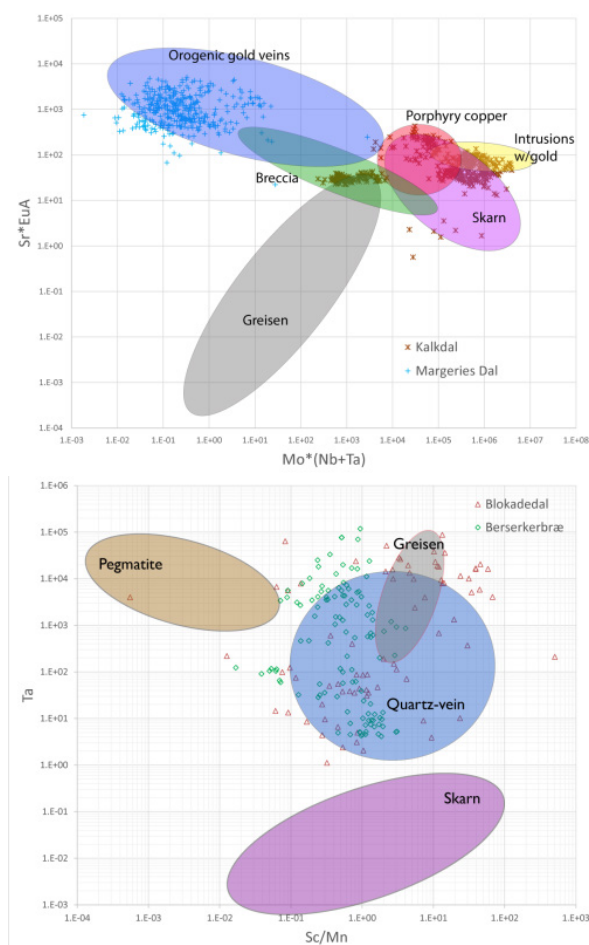


Figure 4. Trace element distribution for scheelite from Kalkdal and Margeries Dal and for cassiterite from Blokadedal and Berserkerbræ, compared to compositions reported in literature for different mineralisation types.

Acknowledgements

The project was financed by GEUS, EIT-RM project MinExTarget #109674 and the Greenlandic Ministry of Mineral Resources, Government of Greenland. Geologists from Nordisk Mineselskab A/S are thanked for collecting samples. M. Alaei and H. Vesturklett are thanked for laboratory assistance. K. Foltyn is thanked for collecting cassiterite trace element data from literature.

References

- Gilotti JA & McClelland WC 2008 Geometry, kinematics, and timing of extensional faulting in the Greenlandic Caledonides – A synthesis. In: Higgins, AK, Gilotti, JA & Smith, MP (eds.). The Greenland Caledonides – evolution of the northeast margin of Laurentia. Geol Soc Am Mem 202:251-271
- Hallenstein C & Pedersen J 1982 Study of Scheelite Mineralization in Central East Greenland. Nordisk Mineselskab A/S, 152pp. GEUS Dodex file report 20688
- Higgins A, Elvevold S, Escher JC, Frederiksen KS, Gilotti JA, Henriksen N, Jepsen HF, Jones KA, Kalsbeek F, Kinny, PD, Leslie AG, Smith MP, Thrane K & Watt GR 2004 The foreland-propagating thrust architecture of the East Greenland Caledonides 72–75 N. J Geol Soc, London, 1661:1009-1026
- Kalsbeek F, Higgins AK, Jepsen HF, Frei R & Nutman AP 2008 Granites and granites in the East Greenland Caledonides. In: Higgins AK, Gilotti JA & Smith MP (eds.). The Greenland Caledonides – evolution of the northeast margin of Laurentia. Geol Soc Am Mem 202: 227-249
- Keulen N, Malkki SN, Graham S 2020 Automated Quantitative Mineralogy Applied to Metamorphic Rocks. Minerals 10:47, 29pp. DOI: 10.3390/min10010047
- McClelland WC, Gilotti JA 2003 Late-stage extensional exhumation of high-pressure granulites in the Greenland Caledonides. Geology 31:259-262
- Sciuba M., Beaudoin G., Grzela D. & Makvandi S. (2020) Trace element composition of scheelite in orogenic gold deposits. Mineral Dep 55:1149-1172
- Steenfelt A. 1982 Uranium and selected trace elements in granites from the Caledonides of East Greenland. Mineral Mag 46:201-210
- Strachan RA, Martin MW, Friderichsen, JD 2001 Evidence for contemporaneous yet contrasting styles of granite magmatism during extensional collapse of the northeast Greenland Caledonides. Tectonics 20:458-473
- Wang C, Zhao K, Chen J & Ma X 2022 Examining fingerprint trace elements in cassiterite: Implications for primary tin deposit exploration. Ore Geol Rev 149: 105082, 13pp

Magmatic silica caps associated with intrusion-related ore deposits

Douglas Kirwin¹, Reimar Seltmann²

¹Consultant Geologist, Bangkok, Thailand

²Natural History Museum, London, UK

Abstract. Magmatic silica caps comprising massive milky to cloudy mottled quartz have been observed in a number of cupolas associated with mineralized felsic intrusions. Furthermore, those silica-enriched zones may transition to an underlying comb quartz UST (Unidirectional Solidification Texture) horizon reflecting magma quench processes due to undercooling and oscillatory crystallization of excess silica during the magmatic to hydrothermal transition. Silica caps normally occur at the cupola contact with the host wall rocks and may vary considerably in terms of lateral extent and thickness from several meters to tens of meters. In many cases, they are well mineralized, particularly in highly evolved porphyry stocks hosting copper-gold-molybdenum mineralization. There are also many barren examples which at a district scale, represent pre-mineral magmatic accumulations, and as such, are vectors for adjacent fertile mineralized stocks. If the fluid pressures greatly exceed the lithostatic pressure once the silica cap has crystallized, then magmatic-hydrothermal breccias with clasts of “silica cap” quartz may form, either as carapace breccias or breccia pipes. Magmatic silica caps are not well documented in the literature, perhaps due to lack of recognition or destruction by overprinting late-magmatic or hydrothermal events.

1 Introduction

One of the first published records of a cupola-related silica cap is by Butler and Vanderwilt (1933) who, while working for the USGS at the Climax molybdenum deposit in Colorado, USA, mapped a 900 feet zone of massive fine-grained quartz in the White Tunnel and commented that it resembled quartzite. Brown (1939) reported on a prominent banded siliceous outcrop approximately 30 meters in diameter associated with a small monzonite plug in the Sedimentary Hills near Tucson, Arizona. The massive quartz was observed to be locally intergrown with coarse feldspar. This occurrence was later studied by Bennett (1957) who also alluded to the banded quartz outcrops. Another excellent example of a silica cap is that which occurs at the Sadisdorf tin deposit in the Erzgebirge district in Germany (Figure 1). Oelsner (1952-in German), referred to a “quarzglocke” located at the apex of a granitic tin-bearing greisen which was illustrated as a crescent-shaped cap in a mine cross section. A very prominent silica cap with underlying UST’s at the Panasqueira tungsten mine in Portugal was described by Kelly and Rye (1979). The UST horizon was mentioned as “zebroid muscovite-quartz layers” (Figure 2). During the late 1970’s, mine geologists working at the AMAX Climax and Henderson molybdenum deposits compiled

extensive data about the silica caps, numerous UST and stockscheider horizons that were present in several of the highly mineralized cupolas.

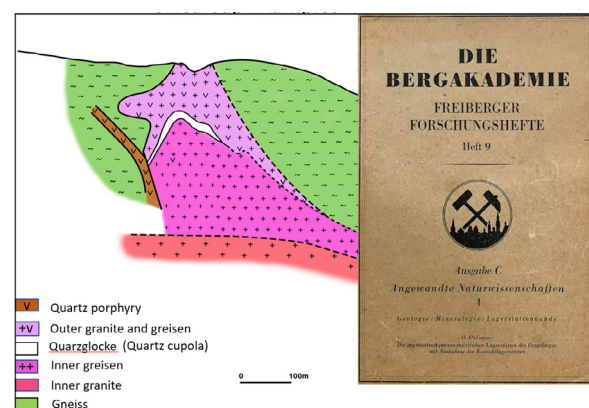


Figure 1. Cross section illustrating the silica cap at the Sadisdorf tin mine, Erzgebirge, Germany. (redrawn from Oelsner, 1952)

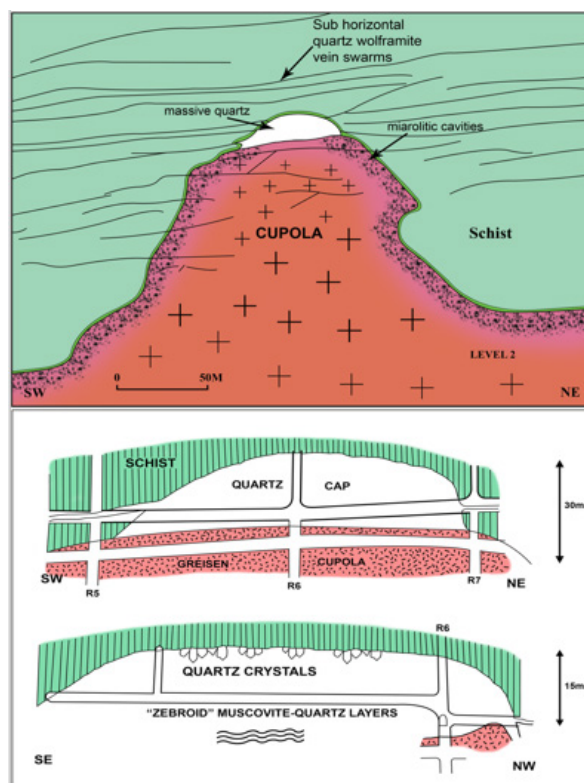


Figure 2. Schematic section illustrating the silica cap at the Panasqueira tungsten mine, Portugal (Kelly and Rye 1979).

A massive silica cap and underlying UST stockscheider zone at the Neo-Proterozoic alkali-

granite cupola at Jabal Umm Al Suqian in Saudi Arabia was studied by Bokhari et al. (1986). This important reference is the first record of very well-preserved cupola textures in Proterozoic intrusions. Another example of a cupola-related massive silica cap is the Max molybdenum deposit in British Columbia, Canada (Lawley 2009). Based on observations from numerous silica cap occurrences throughout Mongolia, Kirwin (2005) described examples from a variety of intrusion-related mineral systems, including the Oyu Tolgoi, Khongor, Tsagaan Survaga, Zun Mod, Bronze Fox porphyry copper-gold deposits, the Tsagaan Chuluut Au deposit, and Umnu Hutul tungsten deposits.

2 Silica caps associated with porphyry copper-gold-molybdenum deposits

During the exploration drilling conducted by Ivanhoe Mines Ltd, in 2002 at the Hugo Dummett deposit at Oyu Tolgoi in Mongolia, a thick zone of massive quartz with high grade gold and copper mineralization was intersected (Figure 3). This was termed the QV90 due to the presence of greater than 90% quartz and considered to be very high density stockwork veining (Khashgerel et al. 2006).

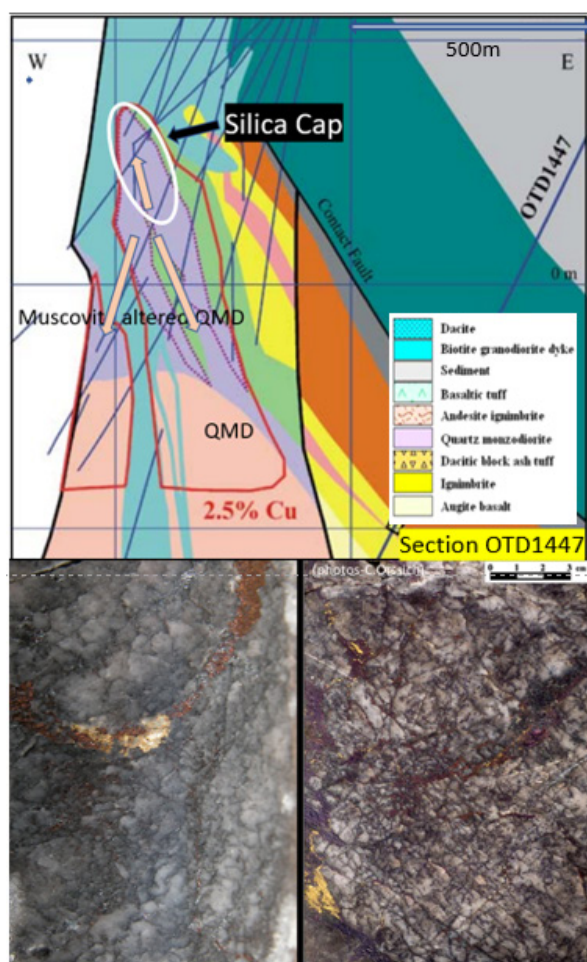


Figure 3. Drill section OTD1447 illustrating the massive high grade silica cap with fracture in fill comprising bornite and chalcopyrite, Oyu Tolgoi.

Closer observation of the QV90 core revealed that the uppermost part was comprised of cloudy and translucent quartz which has a distinctive mottled texture. The bornite and chalcopyrite mineralization was deposited during late-stage shattering of the silica cap. The QV90 zone has a vertical thickness of 10's of meters and occurs in a cupola of a quartz monzonite stock. Similar examples of porphyry-related mineralized silica caps are present at the Golpu deposit in Papua New Guinea, North Parkes and Briggs, Australia, Red Chris mine in British Columbia, Nabor porphyry at Basay in the Philippines, the Provost porphyry in Jamaica and Gajah Tidur at the Grasberg mine in Indonesia. Two interesting occurrences in southwest Arizona are located in the Saginaw and Sedimentary Hills, both of which transition downward into UST layers. The high silica zones in cupolas with underlying UST horizons at the Climax mine in Colorado could be interpreted to be examples associated with porphyry molybdenum mineralization. A much smaller "Climax-type" deposit is located at Mt. Unicorn in north-eastern Victoria, Australia where drilling by Dart Mining intersected a molybdenum-bearing massive silica zone, underlain by UST's and stockwork quartz veining (www.dartmining.com.au). Another molybdenum bearing silica cap occurs at the Lana Corina copper-molybdenum deposit in Chile where drilling recently intersected 85 meters of 0.13% Mo in a massive quartz cupola at the top of a granodiorite stock (www.culpeominerals.com.au).

3 Silica caps associated with intrusion-related gold, tin, uranium, tungsten, REE fluorite mineralization

An intriguing silica cap associated with intrusion-related gold mineralization occurs at Tsagaan Chuluut in northeast Mongolia where a three-meter-thick layer of massive silica transitions into UST's layers with exceptionally large milky quartz crystals which C axis dimensions are greater than one meter. Numerous smaller silica caps outcrop within several square kilometers of extensive alluvial gold mine workings. Another very prominent silica cap 25 meters high and with a diameter of 75 meters known as "The Quartz Blow" is located near the town of Ravenswood in northeast Queensland, Australia. There are several current open pit and underground mines in the district which has produced in excess of 5M ozs Au. The silica cap (and numerous UST occurrences) is barren and represents the early magmatic component of systems which host breccia pipe (Mt Wright gold mine) and sheeted vein style gold mineralization (Nolans gold mine) post the magmatic hydrothermal transition. Other barren examples have been observed at Hada Sumu in the

vicinity of the Bilihe gold mine in Inner Mongolia, China.

Spectacular large silica caps are present at three uranium, fluorite and tin deposits in the Proterozoic Arabian Shield. The largest, located at Jabal Umm Al Suqian comprises at least 50MT of massive milky quartz which transitions into a five-meter-thick UST zone and underlying greisenized fine grained monzonitic stocks with abundant miarolitic cavities (Bokhari et al.1986). Very large individual mega quartz crystals (Figure 4) near the top of the cupola appear to have grown in a suspended silica melt during crystallization with a period of extreme volatile and fluid over pressuring.

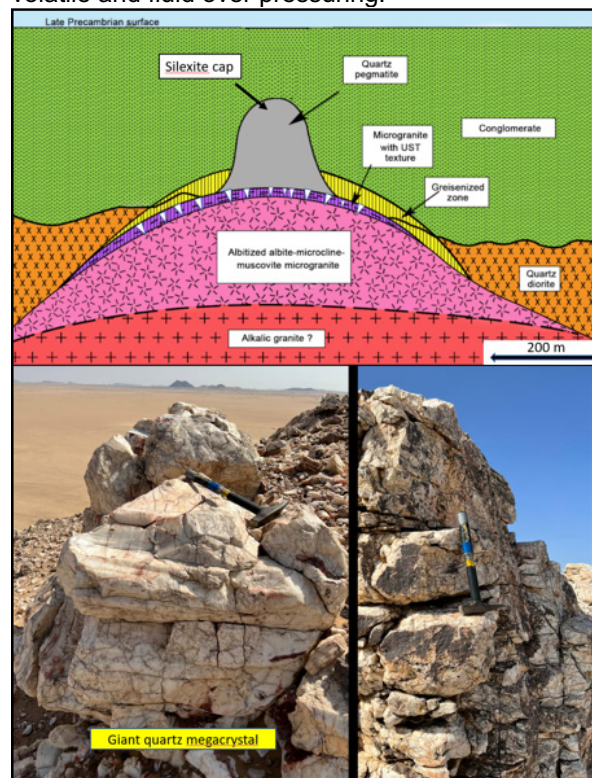


Figure 4. Geological section of the Jabal Umm Al Suqian silica cap and cupola (Bokhari et al.1986) and quartz mega crystal located near the apex of the silica cap.

A similar silica cap overlying a fluorine-rich magmatic pegmatite cupola is present at Jabal Ablah, Numerous euhedral mega quartz crystals may be observed at this locality. The Silsilah tin district in the northern part of the Arabian shield also features several prominent relatively small silica caps with underlying UST and stockscheider zones with large plumose feldspars. The Panasqueira tungsten mine in Portugal has a well-defined silica cap as described by Kelly and Rye (1979). Greisen-related tungsten-topaz deposit in the Torrington district, New South Wales, Australia feature magmatic silica caps (Lishmund 1974). A well-defined silica cap has been documented at the Knöte stock in the Krupna tungsten district in the Czech Republic (Eisenreich and Breiter 1993). The upper most part of the stock is composed of a

coarse grained quartz rock (previously described as quartzite) with accessory molybdenum, fluorite and topaz. The contacts between coarse and fine grained quartz-rich rocks or greisens, are observed to be sharp. The Jabal Hamra silica cap in Saudi Arabia is a crescent-shaped stock 300 meters long by 100 meters wide, that averages over 6000 ppm combined REE (Jackson and Douch 1986).

4 Magmatic silica carapace breccias

Magmatic silica carapace breccias form at the contact of a silica cap and adjacent wall rocks where both rock types are clasts incorporated in a magmatic and or hydrothermal matrix. The breccia morphology reflects that of the host contact. A highly mineralized example occurs at the Maria copper-gold deposit in the Cananea district in Sonora, Mexico. A dome shaped quartz-sulphide breccia measuring 200 by 100 meters and 50 meters thick contains 1.6MT @ 6% Cu and 0.36% Mo (Wodzicki, 1992). Careful examination of the quartz clasts reveals micro-UST's with cloudy and translucent mottled textures. A smaller adjacent cupola has contact breccias with a tourmaline matrix. A detailed description of cupola carapace breccias is that by Klemm et al. (1997) from the Questa molybdenum mine in New Mexico. The Goat Hill breccia is located above and southward of the apex of an aplitic stock, which is considered to be the source for the mineralizing fluids. The association of high-Mo grade with the breccia bodies, and the volume and proximity of the breccias above intrusions, led to the interpretation that the mineralization was the result of direct volatile exsolution from shallow intrusions (Ross et al. 2002).

If continued over-pressuring is sufficient to allow escape of the mineralizing volatiles and fluids from the silica cap into the overlying wall rocks, then a breccia pipe would be initiated. This appears to have occurred at the Didipio gold-copper mine in the Philippines where a high-grade quartz clast breccia pipe (QBx) transitions at depth into a syenite cupola (Hermo et al. 2022). The clasts in the breccia are unmineralized and have wispy micro-UST's, whereas the matrix contains very high copper and gold values. The silica cap formed during pre-mineral magmatic conditions was subsequently shattered during the magmatic to hydrothermal transition and became incorporated as clasts in the breccia ore body. Clasts with massive silica and UST's have been observed in the gold-bearing hydrothermal breccia at Kidston, Australia implying that a similar sequence of events took place there.

5 Conclusions

Silica caps associated with intrusion-related ore deposits are not well described in the literature. This may be due to lack of recognition and poor preservation during destructive processes related to the magmatic to hydrothermal transition. In some

examples they have been interpreted as large veins or silicified alteration zones. Magmatic silica caps occur in a variety of metallogenetic settings, and in particular, very high-grade zones in porphyry copper-gold and molybdenum deposits. There are numerous cases where unmineralized silica caps are present in mineralized districts, implying they formed prior to main-stage mineralization. Both scenarios are favourable exploration vectors for intrusion-related mineral deposits.

In many instances the massive silica displays a distinctive cloudy and translucent mottled texture with thin irregular wispy UST bands. Furthermore, massive silica caps frequently transition into underlying UST bands, most likely due to decreasing oscillating volatile and fluid over pressuring.

Acknowledgements

The authors wish to acknowledge the invaluable assistance provided Mr Nasir Jahdali, Dr Abdullah Nabhan, Mr Ghazi Kattu, Mr Mohammed Jehani and Mr Eid Marudah from the Saudi Geological Survey for arranging field trips to the silica cap localities in the Arabian Shield.

References

- Bennett KC (1975) Geology and origin of the breccias in the Morenci-Metcalf district, Greenlee County, Arizona. MSc. Thesis, Univ of Arizona 181
- Bokhari MM Jackson NI Oweidi K AL (1986) Geology and mineralization of the Jabal Umm Al Suqian albitized apogranite, southern Najd región, Kingdom of Saudi Arabia. *J African Earth Sci* 4 189-198.
- Brown WH (1939) Tucson Mountains, an Arizona basin range. *Bull Geol Soc Am* 50 697-760.
- Butler BS and Vanderwilt JW (1933) The Climax molybdenum deposit, Colorado. U.S.G.S. Bull 846-C, 195-337.
- Eisenreich M and Breiter K (1993). Krupka, deposit of Sn-W-Mo ores in the eastern Krušné Hory Mts. *Bull Czech Geol Surv* 68(3) 15-22 (in Czech).
- Hermo MA Balangue-Tarriela MI Takashi R Gabor-Ratio JA
- Frias S (2022) Mineralization styles and ore forming conditions of the quartz-fragment-rich breccia (QBX) at the Didipio alkalic porphyry Cu-Au deposit, Nueva Vizcaya, Philippines. *Ore Geol Rev* 124 21.
- Jackson NJ and Douch CJ (1986) Jabal Hamra REE-mineralized silicite, Hijaz Region, Kingdom of Saudi Arabia. *J African Earth Sci* 4 269-274.
- Kelly W and Rye R (1979) Geologic, fluid inclusion and stable isotope studies of the tin-tungsten deposits of Panasqueira, Portugal. *Econ Geol* 74 1721-1822.
- Khashgerel B Kavalieris I Hayashi, K (2008) Mineralogy, textures, and whole-rock geochemistry of advanced argillic alteration: Hugo Dummett porphyry Cu-Au deposit, Oyu Tolgoi mineral district, Mongolia. *Miner Depos* 43, 913-932.
- Kirwin DJ (2005) Unidirectional solidification textures associated with intrusion-related Mongolian mineral deposits. In: Seltmann R. Gerel O and Kirwin D. (Eds.) 2005, *Geodynamics and Metallogeny of Mongolia with a Special Emphasis on Copper and Gold Deposits*, IAGOD Guidebook Series 11 63-84.
- Klemm LM Petke T Heinrich CA (2008) Fluid and source magma evolution of the Questa porphyry Mo deposit, New Mexico, USA. *Miner Depos* 43 533-552
- Lawley CM (2009) Age, geochemistry and fluid characteristics of the Max porphyry Mo deposit southeast British Columbia. MSc thesis Univ Alberta 177
- Lishmund SR (1974). The Torrington silicite deposits. *Geol Surv New South Wales. Quarterly Notes* 17: 3-6.
- Oelsner O (1952) Die pegmatitisch-pneumatolytischen Lagerstätten des Erzgebirge mit Ausnahme der kontaktpneumatolytischen Lagerstätten, Freiberg. *Forsch Hft* 41-80 (in German)
- Ross P Jebrak M and Walker BM (2002) Discharge of hydrothermal fluids from a magma chamber and concomitant formation of a stratified breccia zone at the Questa porphyry molybdenum deposit, New Mexico. *Econ Geol* 97 1679-1698
- Wodzicki WA (1992) The Maria deposit, Sonora, Mexico: A telescoped porphyry system. MSc thesis Univ California 49

Fluids involved in W-Be skarns from the Canadian Cordillera: example from the Cantung and Lened deposits, NWT, Canada

Hélène Legros¹, Vanessa Elongo¹, Oscar Laurent^{2,3}, Erin Adlakha⁴, Hendrik Falck⁵, Cyril Chelle-Michou³, Pilar Lecumberri-Sanchez¹

¹Department of Earth and Atmospheric Sciences, University of Alberta, Edmonton, AB T6G 2E3, Canada

²CNRS, Géosciences Environnement Toulouse, Observatoire Midi-Pyrénées, 31400 Toulouse, France

³Institute of Geochemistry and Petrology, ETH Zurich, 8092 Zurich, Switzerland

⁴Department of Geology, Saint Mary's University, 923 Robie St., Halifax, NS B3H 3C3, Canada

⁵Northwest Territories Geological Survey, 5310 44 St., Yellowknife, NWT X1A 1K3, Canada

Abstract. The Lened and Cantung deposits are located in the Tombstone-Tungsten belt of the Canadian Cordillera, the only plutonic belt with world-class tungsten deposits in western North America. This study examines the boron and metal (including tungsten) concentrations of fluid inclusions hosted in several minerals from the Cantung and Lened W-(Be) deposits and discusses (i) the analytical challenges involved during fluid salinity calculations of B-rich fluids and (ii) the relationship between fluid chemistry and ore-forming processes of W-(Be) skarns. High Cs and Li of the fluid suggests a high degree of differentiation of a magmatic fluid source, while Sr and Ba show fluid–rock interaction with the surrounding limestone.

1 Introduction and context

Tungsten and beryllium-rich magmatic-hydrothermal systems are associated with highly differentiated peraluminous granites and are responsible for the precipitation of emerald and tungsten minerals (such as scheelite) in veins and skarns (Meinert et al. 2005).

Recent publications debate the potential mechanisms of tungsten precipitation in hydrothermal deposits, including depressurization of magmatic fluids (Korges et al. 2018), fluid-rock interaction (Lecumberri-Sanchez et al. 2017) and fluid cooling/mixing (Legros et al. 2019).

Also, high boron in these systems, indicated by extensive tourmalinization (Launay 2018) could be part of the decisive factors for enrichment.

The Cantung, and Lened W-(Be) skarn deposits are located at the border between the Northwest Territories and Yukon of Canada (Figure 1). These deposits are part of a large metallogenic belt that contains all major tungsten deposits in western North America (Elongo et al. 2020). Both deposits are associated with Middle to Late Cretaceous age quartz-monzogranites, and are interpreted to be the result of hydrothermal processes involving the local lower Palaeozoic carbonate rocks (Dick and Hodgson 1982). In both deposits, scheelite precipitated throughout the entire history of skarn evolution and subsequent hydrosilicate alteration but scheelite abundance peaked during the biotite-rich facies (Elongo et al. 2020).

This study aims at characterizing both the least-modified magmatic fluid and the chemical signature of the magmatic fluids modified by

interaction with the limestone in the context of skarns, where very little data is currently published.

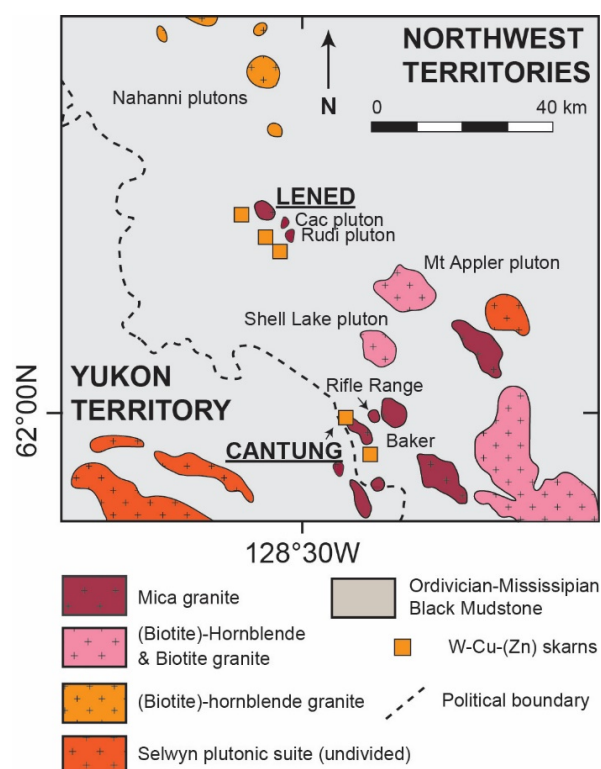


Figure 1. Local geological map showing the Lened and Cantung deposits (Legros et al. 2020, 2022)

2 Methods and results

A precise description of the mineralogical sequence was established prior to the fluid inclusion study for both Cantung and Lened deposits (Elongo et al. 2020)

The aqueous fluid inclusions have high CO₂-CH₄ and boron contents (Legros et al. 2020). At the Lened deposit, boron content is extremely high, as indicated by the presence of sassolite crystals (H₃BO₃) in fluid inclusions (Legros et al. 2022).

2.1 Boron concentration and salinity

In the case of the Lened deposit, the main components of the fluid system are $\text{H}_2\text{O}-\text{CO}_2-\text{NaCl}_{\text{eq}}-\text{H}_3\text{BO}_3$. Two methods currently exist to determine the salinity of fluids in the $\text{H}_2\text{O}-\text{NaCl}_{\text{eq}}-\text{H}_3\text{BO}_3$ system, closest system to our case study. The determination of salinity is especially crucial since it is often used as internal standard to process fluid inclusion trace element data acquired by LA-ICP-MS. The first method uses sassolite melting temperature measured by microthermometry (Peretyazhko et al. 2000) and the second method uses Raman peak intensities corresponding to the H_3BO_3 and H_2O species (Thomas 2002). The calculation of salinity of the Lened fluid inclusions in the $\text{H}_2\text{O}-\text{NaCl}-\text{H}_3\text{BO}_3$ system gives 3.5 to 5 wt. % NaCl_{eq} . Both methods also indicates that the fluid has 3 to 4 wt. % of H_3BO_3 (Legros et al. 2022). In our case, the calculation of salinity is not very precise and using NaCl_{eq} as an internal standard would introduce a lot of uncertainty in the trace element data calculation. Moreover, a recent article suggested that, in a system where H_3BO_3 is almost the most dominant aqueous specie, using B as an internal standard would be more appropriate (Sirbescu et al. 2013). In our case, the boron content of the aqueous liquid phase is estimated to 0.5 wt. %.

2.2 Metal concentration

At Cantung, quartz veins with various mineralogical assemblages hosted in the granitic pluton and the overlying skarn host rocks were sampled. Trace element data of the fluids show relatively high concentrations of Li (40 to 474 ppm), Al (56 to 1003 ppm), As (36 to 490 ppm) and Cs (68 to 296 ppm); and lower concentrations of Rb (3.6 to 77 ppm), Sr (0.4 to 23 ppm), Sb (1 to 32 ppm), Ba (0.6 to 163 ppm), Mg (6.9 to 7.6 ppm) and other metals, such as Be (2.4 to 10.2 ppm), W (2.4 to 27 ppm) and Cu (5.1 to 73 ppm) (Legros et al. 2020, Figure 2).

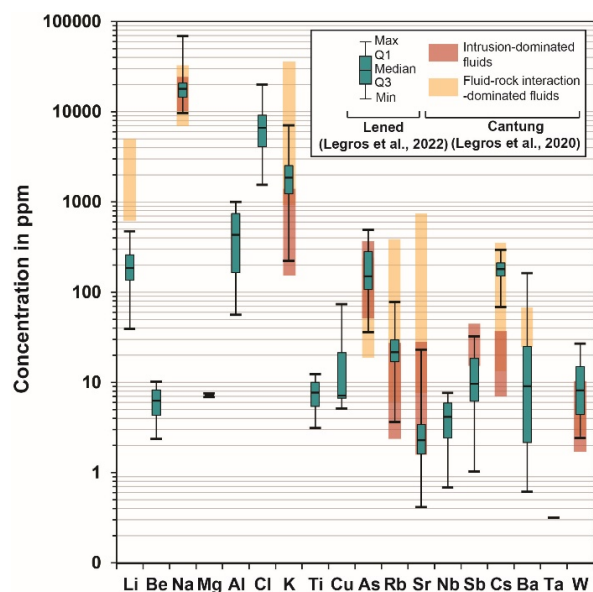


Figure 2. Trace element concentration measured in fluid inclusions from the Lened deposit, compared to the data acquired for the Cantung deposit (Legros et al. 2020, 2022)

At Lened, fluid inclusions in a single quartz vein systematically represented a boron-rich fluid. Using 0.5 wt. % B as an internal standard, the fluid inclusions had relatively high concentrations of Li (40 to 474 ppm), Al (56 to 1003 ppm), As (36 to 490 ppm) and Cs (68 to 296 ppm); and lower concentrations of Rb (3.6 to 77 ppm), Sr (0.4 to 23 ppm), Sb (1 to 32 ppm), Ba (0.6 to 163 ppm), Mg (6.9 to 7.6 ppm) and elements of economic interest, such as Be (2.4 to 10.2 ppm), W (2.4 to 27 ppm) and Cu (5.1 to 73 ppm) (Legros et al. 2022, Figure 2).

3 Discussion and conclusion

The high Cs and Li concentrations suggest a magmatic origin of the metals, while the moderate concentrations in Sr and Ba are indicative of fluid-rock interaction with the surrounding limestone during skarn formation (Figure 3).

High concentrations of B, K, Rb and Cs in the Fls, as well as the high salinity, indicate a high degree of fractionation of the magma, as often observed in these deposits (Korges et al. 2019; Pan et al. 2019).

The presence of sassolite (H_3BO_3) suggests that these fluids were highly acidic (Peretyazhko et al. 2000). The neutralization of the fluid through interaction with the surrounding limestone is the most probable trigger for scheelite precipitation.

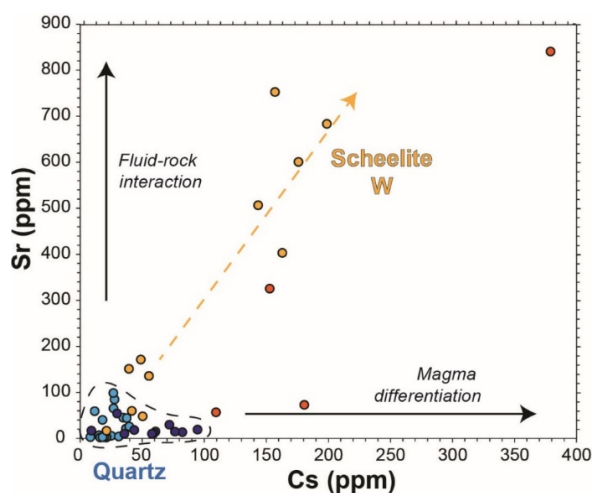


Figure 3. Binary diagram showing the influence of the two principal processes involved in Cantung fluid evolution (modified after Legros et al. 2020)

The presence of such high boron content in the magmatic fluid at Lened indicates a, potentially higher than usual, H_2O concentration in the magma (Peretyazhko 2010). More H_2O in the magma would imply a longer time to crystallize

and potentially a higher concentration in incompatible element when the fluid was exsolved.

Finally, identifying high boron concentration in the fluid as well as the potential occurrence of sassolite is essential to proper salinity calculation of the fluid (Legros et al. 2022).

Acknowledgements

This research was supported by NSERC and the Polar Continental Shelf Project. We would like to thank the executive team at the Cantung mine and the NWT Geological Survey for providing access and helping in the mine and the field. We are also grateful to Marie-Camille Caumon (GeoRessources lab, Nancy, France) for her help with the Raman method, Matthew Steele-McInnis for his help with the microthermometry equipment (University of Alberta, Canada).

References

- Dick LA, Hodgson CJ (1982) The MacTung W-Cu(Zn) contact metasomatic and related deposits of the northeastern Canadian Cordillera. *Econ Geol* 77:845–867. <https://doi.org/10.2113/gsecongeo.77.4.845>
- Elongo V, Lecumberri-Sanchez P, Legros H, et al (2020) Paragenetic constraints on the Cantung, Mactung and Lened tungsten skarn deposits, Canada: implications for grade distribution. *Ore Geol Rev* 125: <https://doi.org/https://doi.org/10.1130/G39601.1>
- Korges M, Weis P, Lüders V, Laurent O (2018) Depressurization and boiling of a single magmatic fluid as a mechanism for tin-tungsten deposit formation. *Geology* 46:75–78. <https://doi.org/https://doi.org/10.1130/G39601.1>
- Korges M, Weis P, Lüders V, Laurent O (2019) Sequential evolution of Sn–Zn–In mineralization at the skarn-hosted Hämmerlein deposit, Erzgebirge, Germany, from fluid inclusions in ore and gangue minerals. *Miner Depos* 1–16
- Launay G (2018) Hydrodynamique des systèmes minéralisés péri-granitiques: étude du gisement à W-Sn-(Cu) de Panasqueira (Portugal)
- Lecumberri-Sanchez P, Vieira R, Heinrich CA, et al (2017) Fluid-rock interaction is decisive for the formation of tungsten deposits. *Geology* 45:579–582. <https://doi.org/https://doi.org/10.1130/G38974.1>
- Legros H, Elongo V, Laurent O, et al (2022) Formation of the Lened W-(Be) Skarn Deposit by Neutralization of a Magmatic Fluid—Evidence from H₃BO₃-Rich Fluids. *Geosciences* 12:236
- Legros H, Lecumberri-Sanchez P, Elongo V, et al (2020) Fluid evolution of the Cantung tungsten skarn, Northwest Territories, Canada: differentiation and fluid-rock interaction. *Ore Geol Rev* 127C:103866. <https://doi.org/10.1016/j.oregeorev.2020.103866>
- Legros H, Richard A, Tarantola A, et al (2019) Multiple fluids involved in granite-related W-Sn deposits from the world-class Jiangxi province (China). *Chem Geol* 508:92–115. <https://doi.org/10.1016/j.chemgeo.2018.11.021>
- Meinert LD, Dipple GM, Nicolescu S (2005) World Skarn Deposits. *One Hundredth Anniv. Vol. 0*
- Pan J-Y, Ni P, Wang R-C (2019) Comparison of fluid processes in coexisting wolframite and quartz from a giant vein-type tungsten deposit, South China: Insights from detailed petrography and LA-ICP-MS analysis of fluid inclusions. *Am Mineral J Earth Planet Mater* 104:1092–1116. <https://doi.org/10.2138/am-2019-6958>
- Peretyazhko IS (2010) Genesis of mineralized cavities (miaroles) in granitic pegmatites and granites. *Petrology* 18:183–208
- Peretyazhko IS, Prokofev VY, Zagorskii VE, Smirnov SZ (2000) Role of Boric Acids in the Formation of Pegmatite and Hydrothermal Minerals: Petrologic Consequences of Sassolite (H₃BO₃) Discovery in Fluid Inclusions. *Petrol C/C Petrol* 8:214–237
- Sirbescu M-LC, Krukowski EG, Schmidt C, et al (2013) Analysis of boron in fluid inclusions by microthermometry, laser ablation ICP-MS, and Raman spectroscopy: Application to the Cryo-Genie Pegmatite, San Diego County, California, USA. *Chem Geol* 342:138–150
- Thomas R (2002) Determination of the H₃BO₃ concentration in fluid and melt inclusions in granite pegmatites by laser Raman microprobe spectroscopy. *Am Mineral* 87:56–68

Metallogeny of tin: From rocks to ore

Bernd Lehmann

Mineral Resources, Technische Universität Clausthal, 38678 Clausthal-Zellerfeld, Germany

Primary tin ore deposits are part of magmatic-hydrothermal systems invariably related to late leucocratic granite phases (tin granites/porphyries, pegmatites) of much larger - and often unexposed - felsic intrusions. Cassiterite (SnO_2) is the only tin mineral of economic significance. Due to its density (7.4 g/cm^3), hardness and chemical stability cassiterite may become dispersed by exogenic processes and then eventually form placer deposits within a few km from their primary source. Alluvial placer deposits were usually the starting point for tin mining, and have provided at least half of all tin mined historically.

The small-volume and late granitic phases in spatial, temporal and chemical relationship to tin ore deposits are highly evolved, i.e. near the low-pressure thermal minimum of the quartz-alkalifeldspar system with very few mafic components and very low Ti, Ca and Mg contents, but enrichment of incompatible trace elements, such as Sn, W, Ta, U, Li, Cs, Rb, Be, F, B. Systematic element distribution patterns in these granitic phases and their associated much larger multiphase granite systems suggest fractional crystallization as the main petrogenetic process controlling magmatic evolution and magmatic tin enrichment. This process can operate in granite melts of any origin, i.e. tin enrichment can be observed in I-, S- or A-type granites and their various tectonomagmatic environments. Oxidation state controls the bulk tin distribution coefficient, with low oxidation state favoring incompatible behavior of divalent tin in felsic systems, also mineralogically expressed by accessory ilmenite ($\text{FeO}\cdot\text{TiO}_2$) as opposed to accessory magnetite ($\text{FeO}\cdot\text{Fe}_2\text{O}_3$) in more oxidized melt systems where Sn^{4+} is dominant. This difference in the accessory mineralogy, and hence metallogenic potential (ilmenite- versus magnetite-series granites), can be easily detected in the field by a hand-held magnetic susceptibility meter.

The hydrothermal system is a continuation of the magmatic evolution trend and necessary consequence of the crystallization of a hydrous melt. The exsolved saline aqueous fluid phase, enriched in boron and/or fluorine plus a wide metal spectrum, can be accommodated and stored by the intergranular space in some crystallized melt portions, or accumulate in larger physical domains, accompanied by focused release of mechanical energy (brecciation, vein formation). The hydrothermal mobility of tin is largely as Sn^{2+} -chloride complexes; the precipitation of tin as cassiterite involves oxidation.

Tin typically characterizes the inner part of km-sized zoned hydrothermal systems with the chemical signature Sn-W-Cu-As-Bi in the inner part (greisen, vein/stockwork/breccia systems, skarn) and a broader halo with vein- or replacement-style Pb-Zn-Ag-Sb-Au-U mineralization. This zoning pattern may also occur telescoped on each other.

A particular feature of many tin systems is greisen alteration, i.e. texturally destructive coarse-grained quartz-muscovite alteration combined with fluorine, boron and lithium metasomatism. Such greisen alteration may affect the igneous rocks (endogreisen) or their country rocks (exogreisen) and is mineralogically expressed by topaz/fluorite, tourmaline and Li-rich mica, and the absence of feldspar. Cassiterite forms stout prismatic crystals at elevated temperature ($400 \pm 100^\circ\text{C}$), and acicular crystals (needle tin) at lower temperature. Tungsten is a common component of hydrothermal tin systems but often occurs spatially separated due to the different solubility control of wolframite ($[\text{Fe},\text{Mn}]\text{O}\cdot\text{WO}_3$) compared to cassiterite, with the formation of scheelite ($\text{CaO}\cdot\text{WO}_3$) in Ca-rich country rocks.

Tin Deposition from Cooling Magmatic Fluids Revealed by Ion Probe Cassiterite Oxygen Isotope Analysis

Yang Li¹, Olivier Bachmann², Xian-Hua Li³

¹School of Earth and Planetary Sciences, Peking University, Beijing, China

²Department of Earth Sciences, ETH Zürich, Zurich, Switzerland

³Institute of Geology and Geophysics, Chinese Academy of Sciences, Beijing, China

Abstract. The formation of tin deposits requires a mechanism to significantly reduce tin-solubility in fluids to deposit cassiterite, but the exact trigger of tin deposition is highly debated, and proposed mechanisms include mixing between magmatic fluids and surface water, cooling of magmatic fluids, and water-rock interaction. Here we push our understanding forward via the newly developed ion probe cassiterite oxygen isotope proxy (Li et al., 2022, 2022b and 2023). Using first-principle-calculation, we first show that the interpretation of cassiterite $\delta^{18}\text{O}$ is temperature insensitive, and an uncertainty of 100°C in temperature estimates only leads to a bias of 0.2 ‰ in calculated fluid- $\delta^{18}\text{O}$. We then developed a matrix-matched reference material-Yongde-CST and reached an analytical precision of <0.3 ‰ using large geometry ion probe. Ore-forming fluids from 9 tin-bearing deposits show a predominately magmatic affinity, with limited to no evidence of fluid mixing and/or water-rock interaction. Critically, cassiterite-quartz $\delta^{18}\text{O}$ thermometry indicates that cooling from pure magmatic fluid is an efficient driver for tin deposition.

1 The conceptual model of magmatic-hydrothermal ore systems

Magmatic-hydrothermal deposits are the primary source of Cu, Mo, Sn, W and other metals. Their formation is ultimately controlled by felsic magmatic reservoirs at depth. Upon extensive cooling and crystallization, metalliferous fluids will exsolve in magmatic reservoirs and then rise to shallow levels. The fluids then will experience cooling, phase separation, mixing with surface water, and variable degrees of water-rock interaction.

Oxygen is the major component of fluids and rocks; hence its isotope composition ($\delta^{18}\text{O}$) is one of the best studied proxies to decipher sources of fluids, and to trace fluid evolution, for which robust and precise analytical approaches are fundamental, and data interpretation without ambiguity is critical.

2 Cassiterite oxygen isotope analysis

A promising avenue to circumvent the aforementioned challenges is targeting cassiterite, the primary ore mineral of tin.

Using first-principle-calculation (Li et al. 2022a), we show that the interpretation of cassiterite- $\delta^{18}\text{O}$ is extremely insensitive to the accuracy of temperature estimates (Fig. 1), which is very different to other minerals such as quartz (Fig. 1). An uncertainty of 100-200 °C in temperature estimates only leads to a bias of 0.2-0.5 ‰ in

calculated fluid- $\delta^{18}\text{O}$ (Fig. 1). This unique feature of cassiterite lifts the requirement of robust temperature-estimates, and we can always obtain fluid- $\delta^{18}\text{O}$ with high confidence even when the temperature is loosely constrained.

Before our study, cassiterite oxygen isotope analysis is only possible via gas source isotope ratio mass spectrometry. As a bulk analytical approach, it is time consuming and does not permit assess $\delta^{18}\text{O}$ zone by zone.

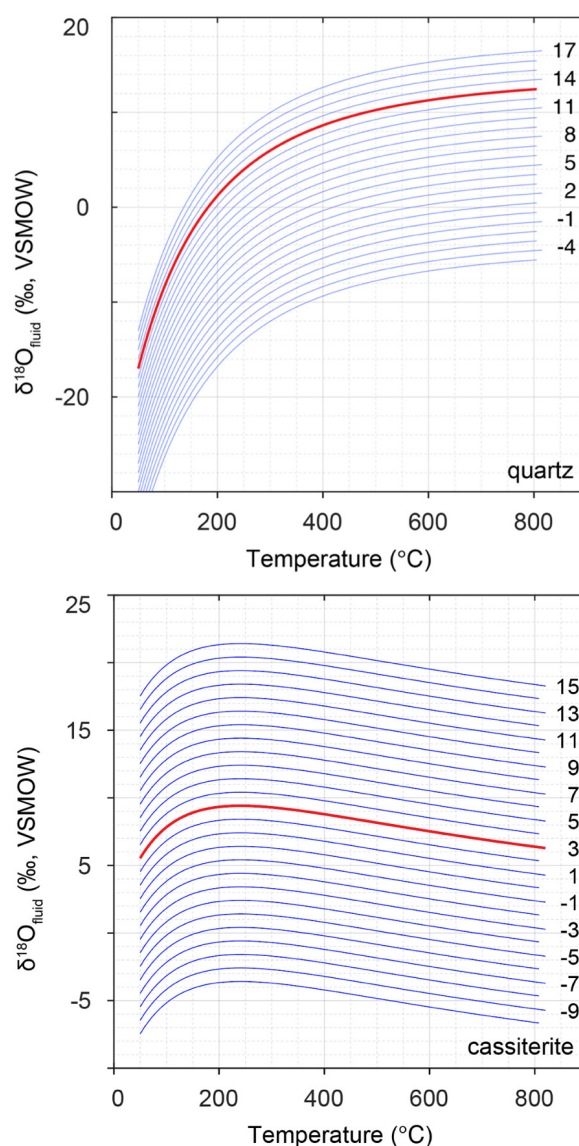


Figure 1. Oxygen isotope fractionation between mineral (top: quartz; bottom: cassiterite) and water as a function of temperature (Li et al. 2022a).

Our experiments show that cassiterite has no detectable crystallographic orientation effect and position effect at current analytical precision (i.e., 0.2-0.3 ‰). We then characterized Yongde-CST, the first matrix matched reference material for SIMS cassiterite oxygen isotope analysis with a recommended $\delta^{18}\text{O}$ of 1.36 ± 0.16 ‰ (Li et al. 2022a), which is freely available and has been distributed to tens of laboratories worldwide already.

3 Coupling cassiterite and quartz oxygen isotopes provides tight constraints on both temperature and $\delta^{18}\text{O}$ of ore-forming fluids

When converting mineral- $\delta^{18}\text{O}$ to fluid- $\delta^{18}\text{O}$, quartz and cassiterite show dramatic differences in response to temperature (Fig. 1). This makes them an idea mineral pair for oxygen isotope thermometry (Li et al. 2022a).

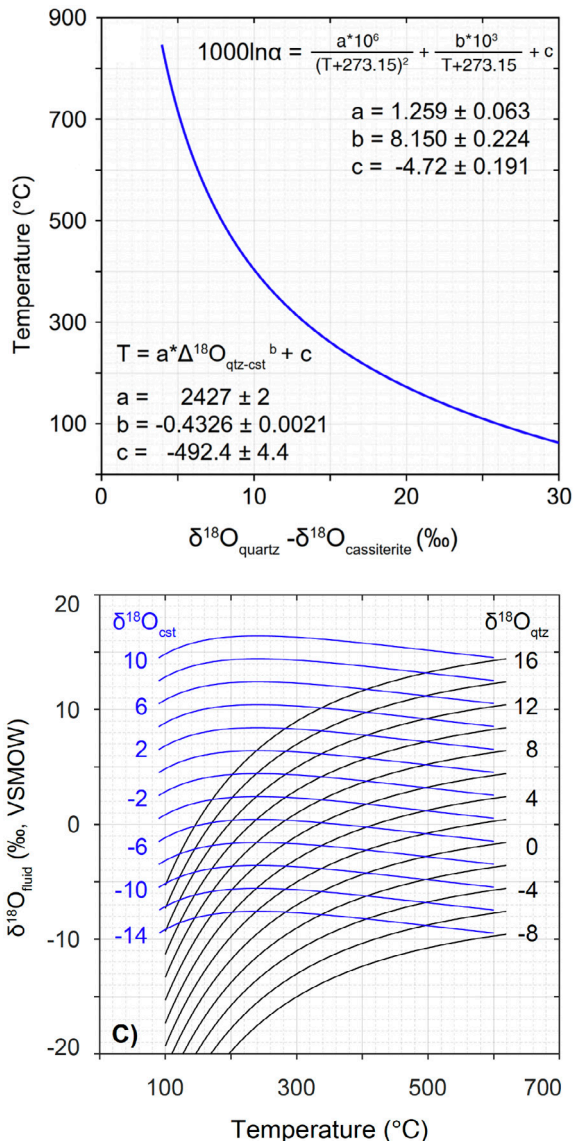


Figure 2. The $\delta^{18}\text{O}_{\text{quartz-cassiterite}}$ shows a strong dependence on temperature, hence using their oxygen

isotope composition in tandem (bottom) could provide tight constraints on temperature and $\delta^{18}\text{O}$ of ore-forming fluids (Li et al. 2022a).

Current SIMS analysis has a precision of 0.2-0.3 ‰, this corresponds to an uncertainty of 10 °C for temperature obtained from quartz-cassiterite oxygen isotope thermometry. This approach also gives fluid- $\delta^{18}\text{O}$ at the same time (Fig. 2).

As a preliminary test to the newly developed SIMS cassiterite oxygen isotope analytical method, we have analyzed cassiterite grains from six deposits with different ages and geological backgrounds (Li et al. 2022a).

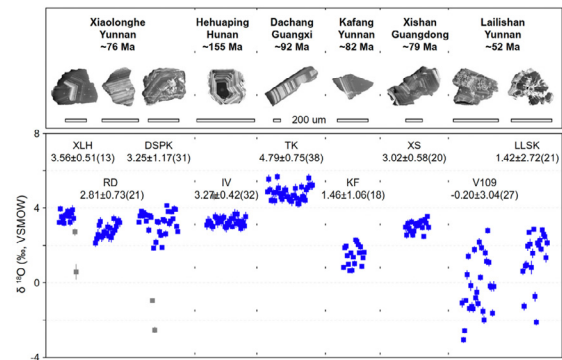


Figure 3. CL images and $\delta^{18}\text{O}$ of cassiterite grains from six deposit (Li et al. 2022a).

Fresh grains have a more clustered distribution in $\delta^{18}\text{O}$ between 2 ‰ and 4 ‰ and peak at 3.3 ‰, corresponding to fluid- $\delta^{18}\text{O}$ of 9.3 ‰ (Fig. 3). Grains with alteration show considerable variations in $\delta^{18}\text{O}$ between -3.1 ‰ and 2.9 ‰ (Fig. 3), both within and among grains (Li et al. 2022a).

The results highlight a magmatic affinity for ore-forming fluids in general, while the inter- and intra-deposit variations is likely jointly controlled by $\delta^{18}\text{O}$ of primary magma, and the degree of fluid mixing and/or water-rock interaction (Li et al. 2022a). This makes cassiterite $\delta^{18}\text{O}$ a promising proxy to investigate these processes.

4 Pulsed tin mineralization inferred from SIMS $\delta^{18}\text{O}$ mapping of a single cassiterite crystal

We further test whether cassiterite chemistry can be used to reveal the dynamics of ore formation. A zoned cassiterite grain from the Piaotang Sn-W deposit, Nanling, China, has been selected for SIMS $\delta^{18}\text{O}$ mapping and XRF elemental mapping (Li et al. 2022b).

Core and rim of the crystal have $\delta^{18}\text{O}$ of -2.1 ‰ and +2.4 ‰, respectively (Fig. 4). The $\delta^{18}\text{O}$ mapping mimics that of Fe-Nb-Ta contents, with high values occurring in the rim (Fig. 4). Low $\delta^{18}\text{O}$ of the first stage requires significant contribution of meteoric water (33 %), but the second (main) stage is dominated by magmatic fluids (>90 %).

In line with the early stage tin-bearing veins being cut by the second, and main stage

mineralization, our results are best explained by a two-stage growth history. This case study demonstrates that cassiterite chemistry is a powerful tool to decode the dynamics of fluid evolution during tin mineralization (Li et al. 2022b).

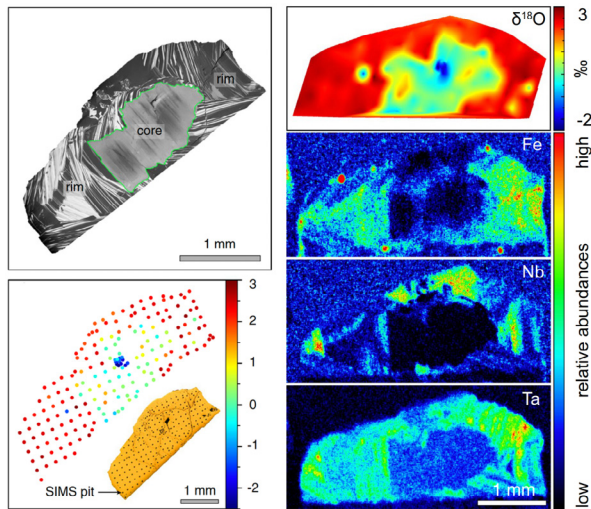


Figure 4. CL, $\delta^{18}\text{O}$ mapping and XRF elemental mapping of a single cassiterite grain from Piaotang (Li et al. 2022b).

5 Cooling, not mixing induced transient tin mineralization (~5,000 years) within a long-lived hydrothermal system (>250,000 years)

Quartz vein-type tin deposit is characterized by simply mineral assemblages and growth history, which is ideal to reconstruct fluid evolution. The euhedral nature and big grain sizes of quartz and cassiterite permit the realisation of high temporal resolution (core to rim analysis using SIMS).

Here we demonstrate the above scenario using paragenetically constrained cassiterite-quartz veins from the Weilasituo Sn deposit, inner Mongolia, China, as an example (Li et al. 2023).

5.1 Gradual Cooling during tin deposition without fluid mixing or water-rock interaction

At Weilasituo, textural evidence suggests that cassiterite precipitation started at the end of stage 1 quartz core (Q1-core) and ceased at the beginning of Q1-rim; hence Q1-core, Q1-mantle and Q1-rim are pre-, syn- and post-ore, respectively (Fig. 5). Q2 and Q3 are post-ore as well (Li et al. 2023).

Q1-core has a $\delta^{18}\text{O}$ of 11.4 ± 0.4 ‰. Q1-mantle shows a rimward increase in $\delta^{18}\text{O}$ from 11.4 ‰ to 13.5 ‰, and co-precipitated cassiterite has a $\delta^{18}\text{O}$ of 3.6 ± 0.4 ‰. Q1-rim has a $\delta^{18}\text{O}$ of 13.7 ± 0.4 ‰ (Fig. 6). $\delta^{18}\text{O}$ of Q2 fluctuate between 12.7 ‰ and 15.3 ‰. $\delta^{18}\text{O}$ values of Q3 gradually decrease from 11.8 ‰ to 9.5 ‰ (Fig. 7).

The rimward increase of $\delta^{18}\text{O}$ for Q1-mantle and consistent $\delta^{18}\text{O}$ values for co-precipitated

cassiterite suggest that Q1-mantle and cassiterite both were precipitated from fluids with a $\delta^{18}\text{O}$ of 8.6 ± 0.4 ‰, with temperatures progressively decreasing from ~ 500 °C to ~ 390 °C ($\Delta T = 110$ °C, Fig. 6). Hence tin mineralisation is triggered by cooling of pure magmatic fluids; mixing with external fluids and/or water-rock interaction are not evidenced (Li et al. 2023).

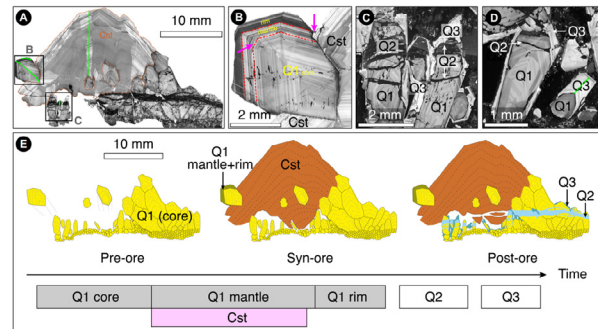


Figure 5. Paragenesis of quartz and cassiterite at Weilasituo, inner Mongolia, China (Li et al. 2023).

The rimward increase of $\delta^{18}\text{O}$ for Q1-mantle and consistent $\delta^{18}\text{O}$ values for co-precipitated cassiterite suggest that Q1-mantle and cassiterite both were precipitated from fluids with a $\delta^{18}\text{O}$ of 8.6 ± 0.4 ‰, with temperatures progressively decreasing from ~ 500 °C to ~ 390 °C ($\Delta T = 110$ °C, Fig. 6). Hence tin mineralisation is triggered by cooling of pure magmatic fluids; mixing with external fluids and/or water-rock interaction are not evidenced (Li et al. 2023).

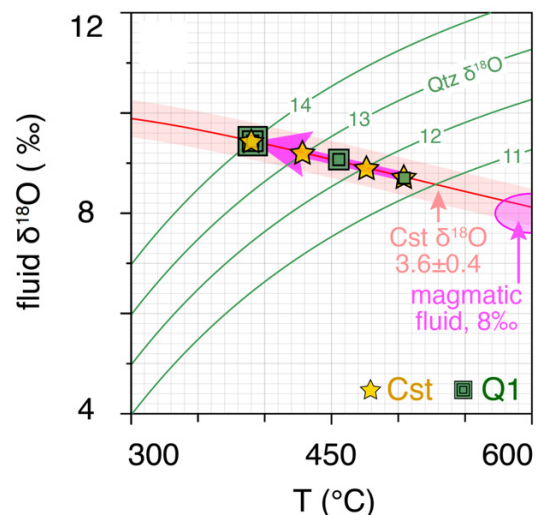


Figure 6. Quartz and cassiterite oxygen isotope thermometry tightly constrains the gradual cooling path during tin deposition at Weilasituo (Li et al. 2023).

After mineralization, as evidenced by the brittle fractures in Q1, Q2 marks the transition from lithostatic to hydrostatic conditions. Minor involvement of meteoric water occurred at this stage (Fig. 7). A further incursion of meteoric water was recorded by Q3 (Li et al. 2023).

5.2 Rapid (~5,000 years) tin mineralization within a long-lived (>250,000 years) system

Co-precipitation between quartz and cassiterite permits the application of quartz-cassiterite oxygen isotope thermometry, and a cooling history with high temporal resolution can be obtained when the euhedral quartz and cassiterite grains are analyzed by ion probe from core to rim. The timescales of this cooling history can be quantified using Al diffusion in quartz chronometry, which yields growth timescales (Fig. 7) of ~50 kyr, 2-10 kyr and 140-240 kyr for the core (pre-ore), mantle (syn-ore) and rim (post-ore) of Q1, respectively (Li et al. 2023).

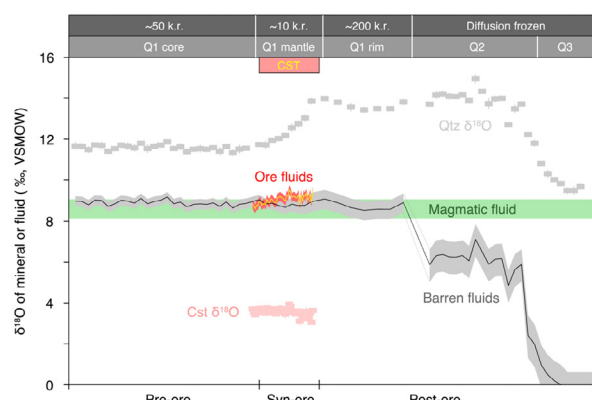


Figure 7. Oxygen isotope evolution of the Weilasituo hydrothermal system indicates pure magmatic fluids during tin mineralization, also shown is the timescales from quartz aluminum diffusion chronometry (Li et al. 2023).

The bulk tin at Weilasituo was deposited within ~5,000 years, within a much longer time window (>250,000) when only gangue minerals were formed. Hence only <5% of the hydrothermal system's lifetime was effective for mineralization (Li et al. 2023). This highlights that effective time needs to be considered in the future when studying ore-forming rates and efficiency.

The above advances highlight the importance of translating texture-controlled information into temporal patterns, which is readily applicable to other magmatic-hydrothermal systems.

Conclusion

Here we present a new proxy (cassiterite-quartz $\delta^{18}\text{O}$) which can decipher the temperature and $\delta^{18}\text{O}$ of ore-forming fluids with high confidence and high temporal resolution. The power and beauty of this new proxy has been demonstrated via a series of case studies, and indicates that tin-bearing fluid exsolution likely is pulsed, with cassiterite precipitation being driven by cooling, while fluid mixing and water-rock interaction are not evidenced in most cases.

Acknowledgements

We thank our colleagues for providing samples and supporting this research in various ways. Results presented here were summarized from our recent publications as listed at the end of this abstract, please check full papers for details. The Yongde-CST reference material is available to the community upon reasonable request. We are also open for collaborative research. We thank Prof. Mathias Burisch for detailed and informative review. We acknowledge support from National Natural Science Foundation of China (grant No. 42022022) and National Key Research and Development Program of China (2018YFA0702600).

References

- Li Y, He S, Zhang R-Q, Bi X-W, Feng L-J, Tang G-Q, Wang W-Z, Huang F, Li X-H (2022a) Cassiterite oxygen isotopes in magmatic-hydrothermal systems: in situ microanalysis, fractionation factor, and applications. *Mineralium Deposita* 57:643-661. doi: 10.1007/s00126-021-01068-x.
- Li Y, Zhang RQ, He S, Chiaradia M, Li XH (2022b) Pulsed exsolution of magmatic ore-forming fluids in tin-tungsten systems: a SIMS cassiterite oxygen isotope record. *Mineralium Deposita* 57:343-352. doi: 10.1007/s00126-022-01093-4.
- Li Y, Pan J-Y, Wu L-G, He S, Bachmann O, Li X-H (2023) Transient tin mineralization from cooling of magmatic fluids in a long-lived system. *Geology* 51:305-309. doi: 10.1130/g50781.1.

In situ LA-ICP-MS U-Pb age of cassiterite from the Auxiliadora Sn-W vein type deposit, northwestern Spain

Iván Losada¹, Iñigo Borrajo², Joaquín E. Ruiz-Mora³, Luis M. Rodríguez-Terente⁴, John M. Hanchar⁵, Fernando Tornos²

¹ University of Salamanca

² Instituto de Geociencias (IGEO, CSIC-UCM)

³ Consultant. A Coruña

⁴ Museum of Geology, University of Oviedo

⁵ Department of Earth Sciences, Memorial University of Newfoundland

Abstract. The Auxiliadora deposit is a small mine located in the town of Noia, Galicia (northwestern Spain). Here, mineralization occurs in several quartz veins which crop out along the coast. This work is focused in the cassiterite mineralization which occurs intergrown with a micaceous selvage along the veins. The obtained U-Pb ages in cassiterite of 285.2 ± 2.4 Ma, corresponds to the last stage of the Hercynian orogenesis and is coeval with that obtained in other deposits in the area.

1 Introduction

Some of the most important Sn and W metallogenic districts in the world are found in the European Variscan belt. One of these districts is the Iberian massif (Spain and Portugal). Here, numerous Sn-W deposits occur in the northwesternmost region of Galicia, associated with the youngest Variscan magmatism at ca. 300 – 285 Ma (Borrajo et al. 2022; Losada et al. 2022). Several high grade mineralization like San Finx (Losada et al. 2022), Santa Comba (Cuenin 1982), Fontao (Nesen 1979) and Penouta (Llorens et al. 2017) stand out, however there are dozens of small deposits that were mostly mined during the Second World War.

The Auxiliadora Sn-W vein type deposit is one of these small deposits, and it is part of a group of Sn-W mineralization located in the municipalities of Noia and Lousame (Ruiz Mora 1982). Among them, the San Finx, located 7 km to the southwest is the most important (figure 1).

In this study we present LA-ICP-MS U-Pb ages on cassiterite from the Auxiliadora deposit. This mineral is chemically and physically resistant, and its U-Pb isotopic composition is increasingly being used as a reliable geochronometer of the Sn mineralization event (e.g., Yuan et al. 2011; Carr et al. 2020).

2 History

The mining history in the area of Noia can be start in various concessions requested in the area of Santa Cristina de Barro (Noia), around the second half of the 19th century, with some prospecting work or mining in any case only testimonial.

At the end of 1937, the "Auxiliadora" concession was requested, covering practically the entire peninsula immediately to Noia with 30 hectares.

During the 1940s, due to the extremely high prices of tungsten and the good tin market, work

was carried out clandestinely throughout the area, without mechanization or hardly technical supervision. In 1945, a hundred of workers produced between 40 and 50 kg per day of cassiterite concentrates. The ore was sent for magnetic separation to the facilities of a mine that dredged the sediments of the ria and that was located a few hundred meters to the north. The mining of the numerous veins outcropping on the coast was completely superficial, being more important than the underground mine, equipped with two shafts of 20 meters each. Another part of the mined deposit was the alluvium or coastal maritime sediments, which supported the bulk of the activity due to its ease of exploitation, and from which cassiterite, wolframite, scheelite and rutile concentrates were obtained. The mine worked during the Second World War and another 5 years in the following decade. The production obtained is difficult to assess, but perhaps it was around 60 t of cassiterite in total and about 20 t of wolframite during the years 1943-1944. Around 1956 the mine was closed.

3 Geological setting

Auxiliadora is located on the Barro peninsula (Figure 1), in the town of Noia. The best outcrops are found at Abruñeiras-Punta da Cruz beach.

The host rock is mainly the Borneiro orthogneiss, from the Malpica Tui high-pressure, low-temperature unit (Llana Fúnez 2020). It is a coarse-grained, heterogeneously deformed rock with a granodioritic composition. In an area of ca 15 km surrounding the mine, syn-late to post-variscan granites crop out.

The deposit is composed of dozens of quartz veins with irregular thickness between 1 mm and 5 cm. The veins trend 090-120/80 NE. They develop a muscovite-rich selvage with cassiterite at the contact with the host rock (Figure 2). The quartz infilling is absent in the narrow zones of the veins where they are composed mainly of muscovite. Other minerals present are wolframite, scheelite, chalcopyrite and pyrite.

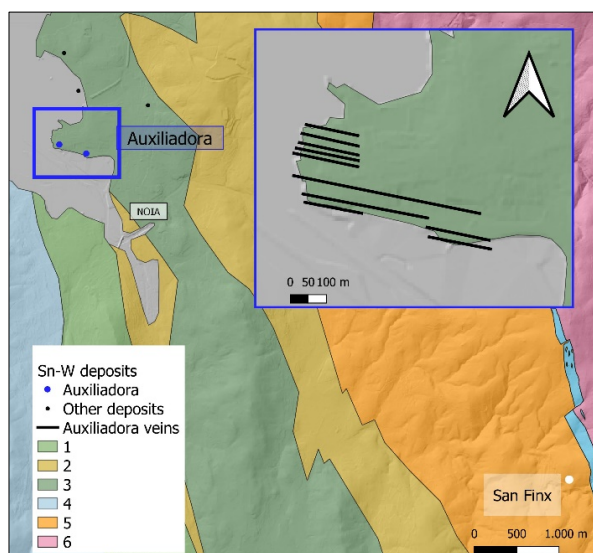


Figure 1 Simplified Geological map of the area near the town of Noia. (1) Malpica Tui unit – Peralcaline ortogneiss (2) Malpica Tui unit – Beo paragneiss (3) Malpica Tui unit – Borneiro ortogneiss (4) early granodiorite (5) schist domain (6) Monte Freito granite. Modified from Llana Fúnez (2000) and Ruiz Mora (1982).

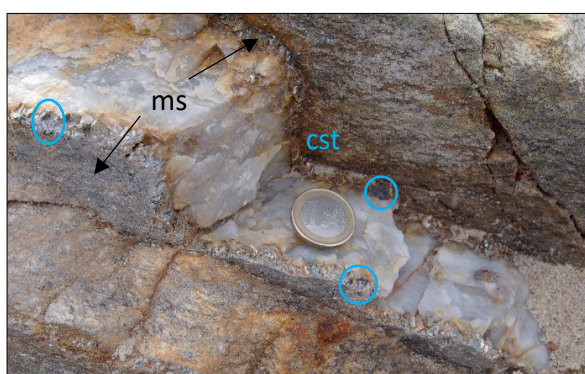


Figure 2. Quartz vein with muscovite (ms) and cassiterite (cst, darkest mineral) on the selvages. Abruñeiras beach.

4 Cassiterite geochemistry

The observed crystals (Figure 3) are formed by combinations of the prism {100} and the tetragonal dipyrramids {111} and to a lesser extent {101}, agreeing with frequent habits in this type of deposits, already described by Murciego et al. (1986).

Cassiterite crystals are black and completely opaque, which may be due to impurities of metallic elements (Fe, Ti, Mn, Nb and Ta). Of the mentioned elements, electron microprobe analyses show significant titanium contents as an outstanding impurity, greater than 1% wt. of TiO_2 , in most of the analyses.



Figure 3 Cassiterite crystal on quartz from the Abruñeiras beach.

One epoxy mount of cassiterite crystals were examined by cathodoluminescence to reveal internal structures and zoning before EPMA and LA-ICPMS analysis at Memorial University of Newfoundland.

Point analyses and quantitative X-ray maps were acquired on a JEOL JXA 8230 electron EPMA with a W filament and five wavelength dispersive spectrometers (WDS). Operation conditions for the point analysis were a electron beam current of 20 nA, a spot diameter of 3 μm , and an accelerating voltage of 15 kV. The count time was 30 seconds, with off-peak (background) count times of 15 seconds. For X-ray map, an accelerating voltage of 15 kV, sample current of 250 nA, and a pixel dwell time of 150 ms were used.

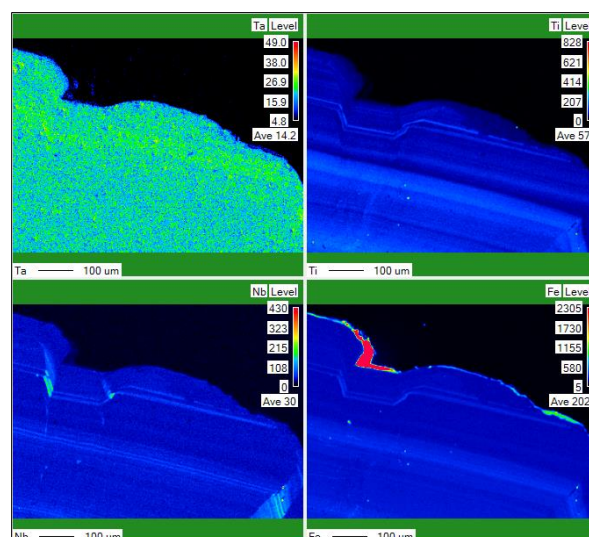


Figure 4. X-ray maps of cassiterite showing Ta, Ti, Nb and Fe distribution.

In Figure 4, the trace elements in a cassiterite crystal are shown. A homogeneous distribution of Ta is observed throughout the section of the crystal, while the distribution of traces of Ti, Nb and Fe are located in certain growth intervals of the cassiterite, being evident by the zoning that can be observed in the images of the mentioned elements.

In view of the represented values, only the Ti impurities are significant, mainly during the initial stages of formation. The elements Nb, Fe and Ti replace Sn in the cassiterite structure. The studied sample displays homogeneous and very low Ta values.

5 Geochronology

5.1 Methods

Large (> 5 mm) grains of cassiterite were easily separated by handpicking and mounted in an epoxy disc. Samples were carefully checked under a binocular microscope and areas free of cracks or inclusions were selected for U-Pb dating by using optical microscopy and BSE images.

LA-ICP-MS U-Pb analysis of cassiterite was performed at the Micro Analysis Facility (MAF) of the Memorial University of Newfoundland, St. John's, Canada by using a Thermo Finnigan Element XR high-resolution. The U-Pb analysis were collected during a single session in November 2022. The spot size diameter was of 110 μm . The conditions were set at an energy density of 4 J/cm² and a pulse frequency of 10 Hz. Yankee cassiterite was used as the primary standard (Carr et al. 2020).

5.2 Results

Seventeen analyses in different grains from Auxiliadora cassiterite sample yielded a lower intercept age in the Tera-Wasserburg diagram of 285.2 ± 2.4 Ma (2 σ , MSWD = 0.25). The initial $^{207}\text{Pb}/^{206}\text{Pb}$ ratios were anchored following the two stages Pb model from Stacey and Kramers (1975). The same analysis gave a ^{207}Pb corrected weighted average $^{206}\text{Pb}/^{238}\text{U}$ age of 285.9 ± 1.2 Ma (MSWD = 0.87). This age is in good agreement with the obtained U-Pb Tera-Wasserburg intercept. Approximated U and Th concentrations range between 662 ppm and 18 ppm for U and 0.47 ppm and 0.03 ppm for Th in the studied sample. Crystal zoning has no effect on the U, Th and Pb concentrations and the U-Pb dating.

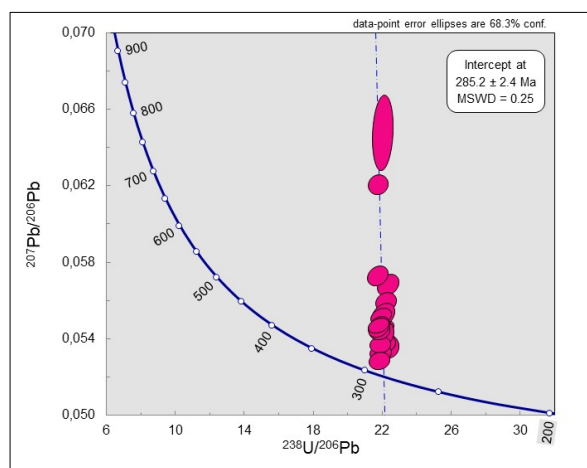


Figure 5. Tera-Wasserburg diagram of Auxiliadora cassiterite.

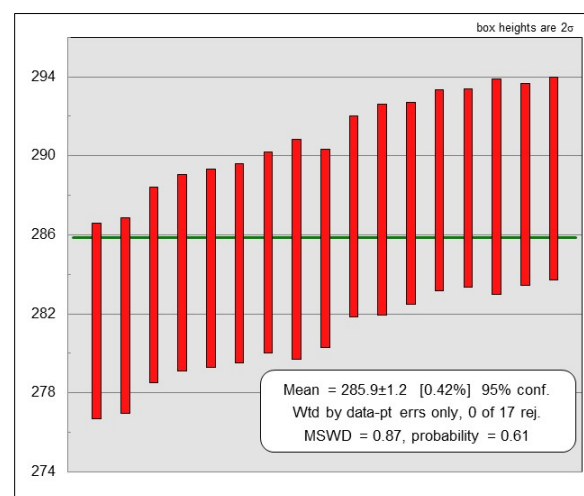


Figure 6. ^{207}Pb corrected weighted average $^{206}\text{Pb}/^{238}\text{U}$ age of Auxiliadora cassiterite.

5 Conclusions

The age obtained on the cassiterite from the Auxiliadora deposit is 285.2 ± 2.4 Ma and is coeval with that obtained on the mica (287.75 ± 1.03 Ma) and apatite (281.7 ± 6.3 Ma) from the San Finx mine, 7 km to the southeast (Losada et al. 2022). This supports a single W-Sn hydrothermal event probably related with the emplacement of post-Variscan granites in the region.

Acknowledgements

This research has been conducted within the iTarg3T (Innovative targeting & processing of W-Sn-Ta-Li ores: towards EU's self-supply) project and has received funding by the EIT Raw Materials of the European Union's Horizon 2020 research and innovation programme under Grant Agreement N° 18036.

Thanks to Xael, Diego and Marcos Chouza, and Cristina M. for their invaluable help in the search and sampling of the veins.

Thanks to Matthieu Harlaux for his constructive comments which improve the manuscript.

References

- Borrajó I, Tornos F, Stein, HJ (2022) Re-Os evidence for diachronous W-Sn mineralization in Iberia (Spain and Portugal). In: *Advances in Magmatic Mineral Systems, Magmatic and Hydrothermal Deposits Related to Felsic Rocks*. 16th SGA Biennial Meeting 1:37-40.
- Carr PA, Zink S, Bennett VC, Norman MD, Amelin Y, Blevin PL (2020) A new method for U-Pb geochronology of cassiterite by ID-TIMS applied to the Mole Granite polymetallic system, eastern Australia. *Chem Geol* 539:119539.
- Cuenin O (1982) *Interpretation des lèbres géologiques dans la mine de Santa-Comba Galice Espagne*. Dissertation, University of Nancy.

- Llana-Fúnez, S. (2000) La estructura de la unidad Malpica Tui (Cordillera Varisca en Iberia). Dissertation, University of Oviedo.
- Llorens-González T, García-Polonio F, Lopez-Moro F, Fernández-Fernández A, Sanz-Contreras J, Moro-Benito M (2017) Tin-tantalum-niobium mineralization in the Penouta deposit (NW Spain): Textural features and mineral chemistry to unravel the genesis and evolution of cassiterite and columbite group minerals in a peraluminous system Tin-tantalum-niobium mineralization. *Ore Geol Rev* 81:79-95.
- Losada I, Borrajo I, Tornos F, Hanchar J (2022) Geochronology of San Finx Sn-W vein type deposit, northwestern Spain. In: *Advances in Magmatic Mineral Systems, Magmatic and Hydrothermal Deposits Related to Felsic Rocks*. 16th SGA Biennial Meeting 1:208–211.
- Murciego A; Martín Pozas JM, García Sánchez A (1986) Parámetros cristalinos de casiteritas de yacimientos españoles. *Boletín de la Sociedad Española de Mineralogía* 9:217-224.
- Nesen G (1979) Une mineralization étain-tungstène liée à un complexe granitique annulaire à endogranite et stockscheider en Galice (mine de Fontao, Espagne). *Comptes Rendus* 288:787-790.
- Ruiz Mora JE (1982) Mineralizaciones estannovolfamíferas en Noia y Lousame. Estudio previo. *Cadernos do Laboratorio Xeolóxico de Laxe* 3:595-624.
- Stacey J, Kramers J (1975) Approximation of terrestrial lead isotope evolution by a two-stage model. *Earth Planet Sci Lett* 26:207–221.
- Yuan S, Peng J, Hao S, Li H, Geng J, Zhang D (2011) In situ LA-MC-ICP-MS and ID-TIMS U–Pb geochronology of cassiterite in the giant Furong tin deposit, Hunan Province, South China: New constraints on the timing of tin–polymetallic mineralization. *Ore Geol Rev* 43:235-242.

U-Pb Zircon Geochronology of the San Rafael Sn(-Cu) Deposit San Rafael (Peru): Sources of Magmas and Magmatic Evolution

Sava Markovic¹, Lorenzo Tavazzani¹, Dawid Szymanowski¹, Kalin Kouzmanov², Cyril Chelle-Michou¹

¹*Institute of Geochemistry and Petrology, Swiss Federal Institute of Technology (ETH Zurich), Zurich 8092, Switzerland*

²*Department of Earth Sciences, University of Geneva, Geneva 1205, Switzerland*

Abstract. The steadily rising demand for Sn metal imposes a need to better understand the factors controlling the distribution and size of granite-related Sn deposits. In this contribution, we employ in situ and high-precision U-Pb zircon geochronology, tools commonly applied to porphyry systems, to study the evolution of the magmatic system associated with the San Rafael Sn(-Cu) deposit in southern Peru. The intrusive complex at San Rafael comprises a suite of roughly coeval, reduced peraluminous (S-type) granitic intrusions, and subordinate lamprophyres. The age-spectra of xenocrystic zircon suggest that the oxidized redbeds of the Middle Triassic Mitu Group may have potentially represented the predominant source for the reduced Sn-mineralizing granitic magmas at San Rafael, a hypothesis that is challenged by the very contrasting oxidation states of the two rock units. Our preliminary dataset of high-precision U-Pb zircon dates for three intrusions suggests that the intrusive complex at San Rafael was constructed over timescales of ~400 kyr, between ~24.41–24.02 Ma.

1 Introduction

Granite-related magmatic-hydrothermal deposits provide a significant share of Sn required to meet the societal needs (e.g., Cerny et al. 2005). The rising demand for Sn necessitates a better understanding of the factors controlling the spatial distribution and sizes of these deposits, which could aid their more efficient discovery. U-Pb zircon geochronology has proven to be a powerful tool for studying the evolution of mineralizing magmatic-hydrothermal systems (e.g., Large et al. 2021). In particular, studies focusing on porphyry Cu-Au(-Mo) deposits showed great success in disentangling fine temporal relationships between different mineralizing intrusions, and even tentatively suggested that the size of these mineralized systems may be gauged during early exploration stages based on the quantified duration of magmatic activity (Chelle-Michou et al. 2017; Chelle-Michou and Rottier 2021). Nonetheless, this approach is yet to be applied to granite-related Sn systems, and this work presents a pioneering study. In this contribution, we present in situ (LA-ICP-MS) and preliminary high-precision (ID-TIMS) zircon U-Pb dates of intrusives from the San Rafael Sn(-Cu) deposit (Peru) with the aim of better understanding the sources and timescales of evolution of Sn mineralizing magmas.

2 Deposit Geology

The granite-related Sn(-Cu) San Rafael deposit of southern Peru represents one of world's largest crustal anomalies of Sn, with over 1 Mt of contained Sn metal at an average grade of ~2% (Harlaux et al., 2020). San Rafael belongs to the northernmost Central Andean Sn-W(-Ag) metallogenic province, and is located in the Cordillera de Carabaya of Eastern Cordillera (Figure 1; e.g., Clark et al. 1983). The Sn ore cassiterite (SnO₂) is mined underground at San Rafael, and provides for ~12% of world's Sn supply (Minsur 2022). The cassiterite is hosted by NW-SE-striking, quartz-cassiterite-sulphide-chlorite veins and associated hydrothermal breccias that extend vertically over 1.2 km, from within the intrusive complex up into the thermally metamorphosed cover (Kontak and Clark 2002).

The stratigraphy of the broader Cordillera de Carabaya is represented by 1) unexposed Precambrian metamorphic rocks, 2) Ordovician–Devonian metaclastics of the San José, Sandia, and Ananea Formations, 3) Late Paleozoic metasandstones and carbonates of the Carboniferous Ambo and Tarma Groups, and Permian Copacabana Group, 4) Middle Triassic sequence of red sandstones and intercalated volcanics of the Mitu Group, and 5) Cretaceous sandstones and carbonates of the Cotacuchco Group (Laubacher 1978; Reitsma 2012).

The precursor magmatism to Sn mineralization at San Rafael comprises a suite of texturally variable, feldspar-biotite-cordierite-bearing, reduced, peraluminous (S-type) granitoids, and subordinate lamprophyres. Six distinct rock types have been mapped at San Rafael, including: 1) a megacrystic granite, 2) a fine-grained granite, 3) a medium-grained granite, 4) a tourmaline-bearing leucogranite, 5) a porphyritic granite, and 6) two lamprophyre dykes (Harlaux et al. 2021). Ubiquitous macroscopic textures of mingling and mixing between highly evolved granitic, and mafic magmas (e.g., mutual co-magmatic enclaves with lobate boundaries, and dismembered dykes) imply roughly coeval crystallization/emplacment of these units, the age of which was quantified by previous U-Pb zircon and monazite geochronology

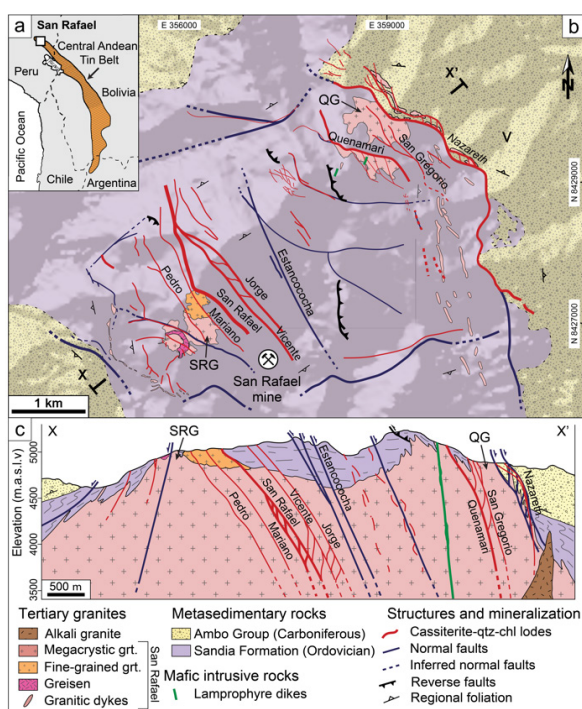


Figure 1. **a** Location of the Sn-Cu deposit San Rafael within the Central Andean tin belt of Eastern Cordillera (southeast Peru; modified after Mlynarczyk et al. 2003). **b** Geological map of the immediate area and **c** longitudinal cross-section of San Rafael (modified after Harlaux et al. 2021). SRG—San Rafael granite, QG—Quenamari granite. to ~24 Ma (Kontak and Clark 2002; Harlaux et al. 2021).

3 Methodology

Zircon crystals were separated from the magmatic rocks, thermally annealed (Mattinson 2005), and embedded in epoxy mounts. Cathodoluminescence (CL) images of the internal texture of zircon were acquired on a JEOL JSM-6390 LA scanning electron microscope (SEM) equipped with a Deben Centaurus panchromatic CL detector.

In situ isotopic U-Pb analyses were carried out using a S155-LR ASI Resolution Excimer laser ablation system coupled with a Thermo Scientific Element-XR sector-field (SF)-ICP-MS at ETH Zurich. Zircon grains showing a relatively homogeneous CL texture and no inheritance based on the results of in situ dating were selected for high-precision geochronology using isotope dilution-thermal ionization mass spectrometry (ID-TIMS). The selected grains were chemically abraded, washed in multiple cycles in HCl and HNO₃, spiked with the ET(2)535 tracer solution, and dissolved. U and Pb were separated from the matrix elements in solution by HCl-based ion-chromatography. Isotopic ratios of U and Pb were measured on a Thermo TRITON Plus TIMS instrument.

4 Results and discussion

4.1 CL images, and age-spectra of xenocrystic zircon

Zircon from different intrusions at San Rafael were classified into bright, intermediate, and dark according to their CL tone, and deformed, oscillatory, sector-zoned, and plane based on their CL texture. Notably, dark oscillatory rims, rich in U (1 000–5 000 ppm, and up to 15 000 ppm) are characteristic for zircon from all samples. Apart from this, no systematic features have been observed in zircon CL texture across different samples. Out of a total of 233 zircon grains dated in situ, 27% contained a xenocrystic component (i.e., core or whole zircon xenocryst), indicating a substantial crustal component in the makeup of San Rafael magmas.

U-Pb analyses of xenocrystic zircon display two major peaks, of Permian/Triassic and Cambrian/Ordovician age, and fewer points plotting within Proterozoic age-range (Figure 2). Our results are largely consistent with those of Harlaux et al. (2021), who identified the same major peaks, but did not observe the Proterozoic zircon population. The age spectra of our analyses reproduce well those obtained for the oxidized, red sandstones of the Middle Triassic Mitu Group (Harlaux et al. 2021), suggesting that this unit statistically represents the most likely predominant protolith for the reduced S-type granitic magmas at San Rafael. The Mitu Group consists of a volcano-sedimentary rift sequence deposited in a phase of Permo-Triassic magmatism in the Eastern Cordillera, in association with the break-up of Pangea (Reitsma 2012; Spikings et al. 2016). Nonetheless, the Mitu Group being a direct source of the reducing granitic magmas of San Rafael is not consistent with the differing oxidation states of the two, and would require an intermediate reduction step to produce the S-type magma compositions. Alternatively, the chemically more suitable (i.e., reduced) protoliths (e.g., finer-grained Proterozoic/Cambrian units) may be underrepresented or missing in the age-spectra due to the equally unlikely absence or extreme partial melting conditions (fluid absent, >925 °C) and complete dissolution of zircon in the source (Mintrone et al. 2020).

4.2 Oligocene magmatic evolution of San Rafael

Preliminary high-precision ²³⁰Th-corrected ²⁰⁶Pb/²³⁸U zircon dates for the megacrystic, medium-grained, and fine-grained granite at San Rafael are presented in Figure 3. The distribution of individual zircon dates from the three units records magmatic crystallization on time-scales of ~400 kyr, from ~24.41–24.02 Ma. The megacrystic and fine-

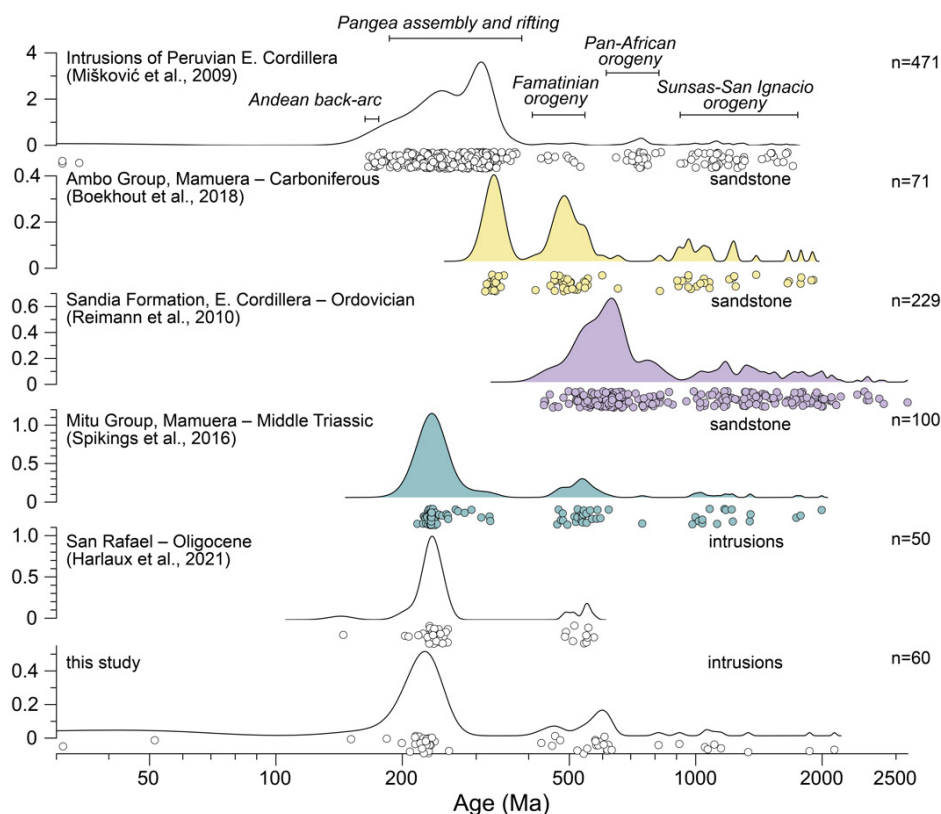


Figure 2. Comparison of U-Pb probability density distributions for xenocrystic zircon from San Rafael, and zircon of proximal sedimentary units and regional intrusions of the Peruvian Eastern Cordillera.

grained granites display a continuous date distribution, whereas the distribution of zircon dates from the medium-grained granite is strongly bimodal. Megacrystic and medium-grained granites record the first phase of magmatic crystallization, which started ~ 24.35 Ma. The youngest interval of the magmatic history is recorded by the younger population of zircon dates from the medium-grained granite, which fall in the range between ~ 24.08 – 24.02 Ma. Zircons from the fine-grained granite, as well as the younger zircons of the megacrystic granite, record crystallization from 24.30 to 24.18 Ma, intermediate between the two age groups of the medium-grained granite.

The spread of our ID-TIMS zircon dates overlaps within uncertainty with the in situ weighted-mean dates of the same units by Harlaux et al. (2021), and is somewhat younger than the single crystal ID-TIMS zircon (24.7 ± 0.2 Ma) and monazite (24.6 ± 0.2 Ma) ages of Kontak and Clark (2002). Our zircon dates of the megacrystic and fine-grained granites are consistent with their coeval emplacement implied from their field relationships. To the contrary, the younger zircon distribution in the medium-grained porphyry granite records magmatic crystallization >100 kyr after the cooling of the previous two units.

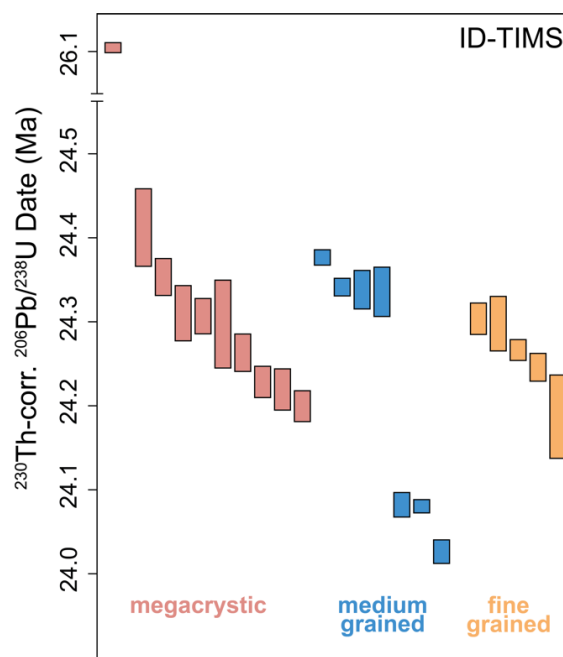


Figure 3. High-precision U-Pb dates of zircon from the megacrystic, medium-grained, and fine-grained granite at San Rafael.

5 Conclusions

This contribution presents preliminary results of in situ and high-precision zircon U-Pb geochronology from intrusions of the Sn(-Cu) magmatic-hydrothermal deposit San Rafael (Peru). Zircons from different intrusions contain a high proportion of xenocrystic components, and appear in bright, intermediate, and dark cathodoluminescence CL tones, and deformed, oscillatory, sector-zoned, and plane textures. The age-spectra of xenocrystic zircon from San Rafael is most akin to that of the regional oxidized redbeds of the Middle Triassic Mitu Group. However, considering the Mitu group as a protolith for the reduced granitic magmas at San Rafael is challenged by the very contrasted oxidation states between the two rock units. The preliminary dataset of high-precision U-Pb zircon dates for different intrusions suggest that the intrusive complex at San Rafael was assembled in several pulses over a timescale of ~400 kyr, between ~24.41–24.06 Ma.

Acknowledgements

The authors acknowledge the generous funding received through the ETH Zurich Research Grant. We also thank the geological team of Minsur S.A. for their logistical support and assistance, and collaborators L. Torró, M. Harlaux, and K. Kouzmanov for field guidance, providing the first samples from San Rafael, and motivating discussions.

References

- Cerny P, Blevin P, L, Cuney M, London D (2005) Granite-related ore deposits. *Society of Economic Geologists* 100:337-370.
- Chelle-Michou C, Rottier B, Caricchi L, Simpson G (2017) Tempo of magma degassing and the genesis of porphyry copper deposits. *Sci Rep-Uk* 7:1-12. doi: ARTN 40566 10.1038/srep40566.
- Chelle-Michou C, Rottier B (2021) Transcrustal Magmatic Controls on the Size of Porphyry Cu Systems: State of Knowledge and Open Questions Tectonomagmatic Influences on Metallogeny and Hydrothermal Ore Deposits: A Tribute to Jeremy P Richards (Volume I). pp 87-100.
- Clark AH, Palma VV, Archibald DA, Farrar E, Arenas F. MJ, Robertson RCR (1983) Occurrence and Age of Tin Mineralization in the Cordillera Oriental, Southern Peru. *Econ Geol* 78:514-520.
- Harlaux M, Kouzmanov K, Gialli S, Clark AH, Laurent O, Corthay G, Flores EP, Dini A, Chauvet A, Ulianov A, Chiaradia M, Menzies A, Durand GV, Kalinaj M, Fontbote L (2021) The upper Oligocene San Rafael intrusive complex (Eastern Cordillera, southeast Peru), host of the largest-known high-grade tin deposit. *Lithos* 400. doi: ARTN 10640910.1016/j.lithos.2021.106409.
- Kontak DJ, Clark AH (2002) Genesis of the giant, bonanza San Rafael Lode tin deposit, Peru: Origin and significance of pervasive alteration. *Econ Geol Bull Soc* 97:1741-1777. doi: Doi 10.2113/97.8.1741.
- Large SJE, Buret Y, Wotzlaw JF, Karakas O, Guillong M, von Quadt A, Heinrich CA (2021) Copper-mineralised porphyries sample the evolution of a large-volume silicic magma reservoir from rapid assembly to solidification. *Earth Planet Sc Lett* 563:1-12. doi: ARTN 11687710.1016/j.epsl.2021.116877.
- Laubacher G (1978) Estudio geológico de la region norte del Lago Titicaca. Instituto Geología y Minería, Peru.
- Mattinson JM (2005) Zircon U-Pb chemical abrasion ("CA-TIMS") method: Combined annealing and multi-step partial dissolution analysis for improved precision and accuracy of zircon ages. *Chem Geol* 220:47-66. doi: 10.1016/j.chemgeo.2005.03.011.
- Minsur (2022) Responsible Minerals Assurance Process—Due Diligence Report.
- Mintrone M, Galli A, Laurent O, Chelle-Michou C, Schmidt MW (2020) Quantifying frozen melt in crustal rocks: A new melt-o-meter based on zircon rim volumes. *Chem Geol* 551:119755.
- Reitsma MJ (2012) Reconstructing the Late Paleozoic: Early Mesozoic plutonic and sedimentary record of south-east Peru: Orphaned back-arcs along the western margin of Gondwana. PhD thesis, University of Geneva, Switzerland, pp 246.
- Spikings R, Reitsma MJ, Boekhout F, Miskovic A, Ulianov A, Chiaradia M, Gerdes A, Schaltegger U (2016) Characterisation of Triassic rifting in Peru and implications for the early disassembly of western Pangaea. *Gondwana Res* 35:124-143. doi: 10.1016/j.gr.2016.02.008.

Critical minerals in Climax-type magmatic-hydrothermal systems

Celestine N. Mercer¹, Mario Guzman¹, Albert H. Hofstra¹, Joshua M. Rosera²

¹U.S. Geological Survey, Denver, CO, USA

²U.S. Geological Survey, Reston, VA, USA

Abstract. Today's global economy is challenged to meet the growing demand for commodities used in existing and emerging advanced technologies. Critical minerals are commodities found in a wide variety of ore deposits that are vital to the economic or national security of individual nations that are vulnerable to supply disruption. The U.S. Geological Survey is striving to advance understanding of critical mineral resources by employing a Mineral Systems approach. Climax-type systems are one of 17 mineral systems currently under investigation. The aim of this work is to inventory and assess knowledge gaps on the abundance of 50 critical minerals in Climax-type systems. Here we synthesize geochemical data from ore concentrates, ore, waste, and minerals together with information on production from, and resources in, ore deposits. The goal of this work is to estimate the amount of critical minerals present in processed mine waste and unmined resources, discuss those that could potentially be recovered in the future, and identify important future areas of research.

1 Distribution of Climax-type magmatic-hydrothermal systems

Climax-type magmatic-hydrothermal systems occur in post-subduction, continental rift settings with thick cratonic crust and are associated with hydrous, fluorine-rich bimodal magmatism (Sinclair, 1995; Ludington and Plumlee, 2009; Rosera et al., 2022). Most well-known Climax-type magmatic-hydrothermal systems are located in western North America, although in recent years several significant Climax-type systems have been recognized in the East Qinling-Dabie orogenic belt of China (Shapinggou, Nannihu-Sandaozhuang, Donggou, Yechangping and Yongping-Shizito; Zeng et al., 2013; Audétat and Li, 2017). The North American systems typically range in age from early Eocene (as old as ~51 Ma, Big Ben, MT) to Pliocene (as young as ~5 Ma, Silver Creek, CO). With few exceptions, these systems are products of bimodal magmatism involving hydrous, fluorine-rich, highly evolved (i.e., rare metal) granites and topaz rhyolites (dominantly A-type or "ferroan"; Frost and Frost, 2011; commonly ~77 wt% SiO₂, >300 ppm Rb, >80 ppm Y+Nb) and contemporaneous hydrous mafic intrusions (trachybasalt to trachyandesitic) that appear to be unique to melting Proterozoic lithosphere during the transition from Laramide shortening to continental extension and subsequent rifting (White et al., 1981; Ludington and Plumlee, 2009; Audétat and Lee, 2017; Rosera et al., 2021).

Exsolution of supercritical magmatic fluids derived from a series of felsic intrusions, perhaps supplemented by fluid components sparged from

mafic intrusions (e.g; Hattori and Keith, 2001; Hofstra et al., 2014b; Audétat and Li, 2017), drive formation of a variety of ore deposits as they ascend, boil, react with country rocks, mix with groundwater, and vent to the surface. The broad spectrum of deposit types results from the considerable thermal and chemical gradients that extend from the deep plutonic root zones to the surface fumarolic portions of the system. The nature of host rocks and preexisting structures do not exert a strong control on root zone and porphyry deposits because focusing is dominated by magma emplacement and hydrofracturing processes, while peripheral and shallow deposits are localized by permeable rocks and dilatant structures.

2 Anatomy, deposits, and commodities from root zone to vapour phase

Climax-type systems contain a wide variety of important ore deposit types, including plutonic root-zone deposits (pegmatite, greisen), porphyry stock and peripheral deposits (porphyry, skarn, polymetallic sulfide vein, distal disseminated), lithocap zone deposits (epithermal, lithocap), and volcanogenic and vapor phase deposits (Fig. 1). Principal commodities include beryllium (Be), fluorite (CaF₂), aluminum (Al), potash (K₂SO₄), copper (Cu), zinc (Zn), yttrium (Y), niobium (Nb), molybdenum (Mo), silver (Ag), tin (Sn), tungsten (W), gold (Au), lead (Pb), and uranium (U). While some of these primary commodities are classified as critical minerals, an assortment of other critical minerals may be found in Climax-type systems in elevated concentrations, including antimony (Sb), arsenic (As), bismuth (Bi), gallium (Ga), germanium (Ge), indium (In), lithium (Li), magnesium (Mg), niobium (Nb), rhenium (Re), and tantalum (Ta). Some of these critical minerals have been historically produced while others are potential byproducts. It should be noted that only rarely do individual systems exhibit all of the possible deposit types and coevolved intrusions are frequently barren (e.g., Audétat, 2019).

Predominant ore minerals in Climax-type systems include alunite, bertrandite, cassiterite, chalcocopyrite, fluorite, galena, molybdenite, scheelite, sphalerite, uraninite, and wolframite. However, a wide variety of minerals occur in the spectrum of deposit types generated by Climax-type systems and many contain critical minerals.

3 Data sources

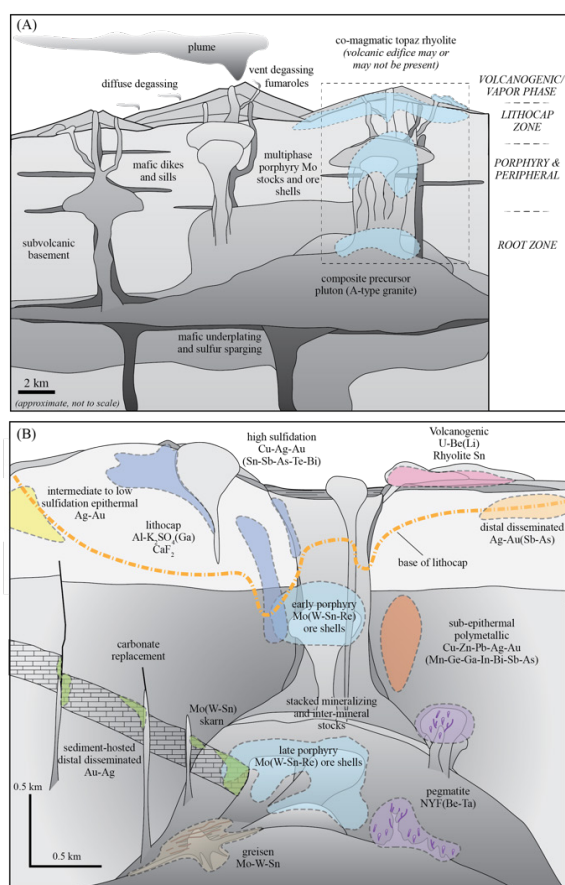


Figure 1. Schematic model for Climax-type magmatic-hydrothermal systems from root zone to vapor phase. (A) Mid- to upper crustal polybaric magma reservoirs, mafic intrusions, multiphase porphyry Mo stocks, and volcanic edifices, which may or may not be present. Climax-type system zones of mineralization are shown in blue, including the root zone, porphyry and peripheral zone, lithocap zone, and vapor phase zone. Horizontal scale is approximate, vertical aspect is exaggerated. Dashed box shows approximate inset shown in part B. Modified after Mercer et al. (2015). (B) Anatomy of Climax-type ore deposits within the magmatic-hydrothermal system. Modified after Launay et al (2021), Richards and Mumin (2013), Sillitoe (2010), and Seedorff and Enaudi (2004). Scale is approximate.

Mineral site information for this report was acquired primarily from the USMIN Mineral Deposit Database, the Keith Long Significant Deposit Database (Long et al., 1998), the Giant Porphyry-Related Camps of the World-A Database (v.2.7; Mutschler et al., 2000), and USGS deposit models (Climax-type porphyry: Ludington and Plumlee, 2009; Volcanogenic U: Breit et al. 2011; Volcanogenic Be: Foley et al., 2012). This was supplemented with site information from the USGS Mineral Resource Data System that were cross referenced using additional authoritative sources. Climax-type mineral sites ranging from occurrences to prospects to well-characterized deposits are documented in this report, but for the purpose of

quantifying critical minerals this work focuses on significant known deposits.

Existing whole rock geochemical data on mineralized and altered rock samples were compiled from several sources including the National Geochemical Database on Ore Deposits: Legacy Data (Granitto et al., 2021), the Global Geochemical Database for Critical Minerals in Archived Mine Samples (Granitto et al., 2020), and additional published data.

166 new whole rock multi-element data were acquired from available mineralized and altered rock samples and ore concentrates compiled in the National Geochemical Database on Ore Deposits: New Data (Granitto et al., in prep.). 57 archived samples with older geochemical analyses were reanalyzed for more modern and complete geochemical profiles, while 79 samples were newly collected from research collections, university collections, and personal collections in an effort to expand the number of deposits for which multi-element geochemical information exists.

Geochemical data were evaluated relative to their abundance in upper crust using box plots, where a box of length equal to the interquartile range is divided at the median of the data. Whiskers extend to the furthest data point within 1.5 times the interquartile range beyond the edge of the box, and outliers beyond the whiskers are represented with circles. Median values of each element were interpreted to be more representative than mean values given the skewed nature of the datasets.

4 Critical mineral enrichments

The deepest root-zone levels of Climax-type systems reside near the top of A-type granitic plutons where fluids and metals are derived from a subjacent magmatic reservoir. This zone lies beneath the porphyry ore zone, and while no two systems are alike, some may mineralize niobium-yttrium-fluorine (NYF) pegmatites or Mo-W-Sn-(Bi) greisen (i.e., muscovite \pm topaz \pm fluorite \pm tourmaline) and vein deposits (Fig. 1). Ore samples from this realm (e.g., Sweet Home, Mt. Antero, CO) have anomalous median concentrations $>100\times$ crustal value of Be, Bi, Cd, In, Re, Sb, and Te (in addition to Cu, Mo, Pb, and Zn).

Extending from the pluton roof lies the porphyry stock Mo(W-Sn) realm and a variety of deposits may develop peripherally away from this zone, including proximal and distal skarn, sub-epithermal polymetallic vein, and distal disseminated deposits (Fig. 1). Climax-type systems are best known for their massive porphyry Mo deposits (e.g., Climax, Henderson, CO; Questa, NM, Fig. 2) with median concentrations $>10\times$ crustal value of Cd, Re, Se, and Te (in addition to primary commodities Mo and W). Porphyry molybdenite (MoS₂) concentrates (Mt Hope, NV; Climax, Henderson, CO) are enriched $>1000\times$ crustal value in Cd, Re, and Te; wolframite (WO₄) concentrates (Climax, CO) $>1000\times$ crustal

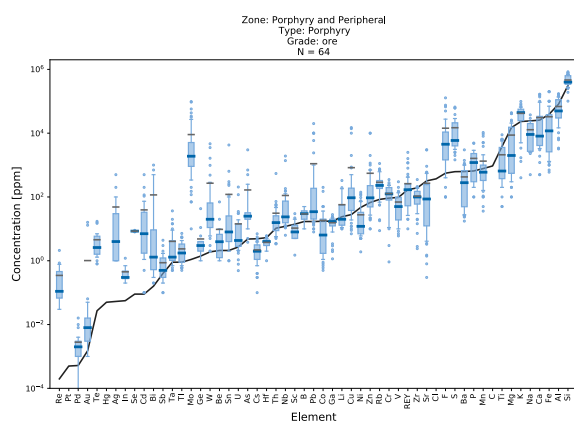


Figure 2. Box plot of elemental abundance in ore samples from porphyry Mo deposits relative to upper crustal abundance (black line). Median shown with bold blue line.

value in Re; monazite ($\text{REE}(\text{PO}_4)$) concentrates (Climax, CO) >1000x crustal value in Bi, Cd, Mo, Nb, Sn, Ta, U, and W; and pyrite (FeS_2) concentrates (Climax, CO) >1000x crustal value in In. Polymetallic vein and replacement ore samples (e.g., Climax, Henderson, Mt. Emmons, Sunnyside, CO; Victorio, NM; Deer Trail, UT, Fig. 3) have anomalous median concentrations >100x crustal value of As, Au, Bi, In, Sb, Se, and Te (in addition to Pb and Zn) and >1000x crustal value of Cd and Re. Above and commonly overprinting the porphyry realm lies the lithocap environment (Fig. 1). This zone is eroded away at most well known Climax-type porphyry Mo deposits but has been identified in porphyry Mo deposit systems in New Mexico, Utah, and Colorado (Hofstra et al., 2014a). Much of the lithocap zone may be barren, but some portions contain significant alunite, from which potash (K_2SO_4) and alumina (Al_2O_3) have been historically produced, kaolinite ($\text{Al}_2\text{Si}_2\text{O}_5(\text{OH})_4$), and fluorite (CaF_2) (e.g., Alunite Ridge, UT) while some areas locally host a variety of intermediate- and high-sulfidation epithermal deposits and polymetallic vein and replacement deposits. This realm is an indicator of Mo and other system-related resources at depth (Mercer et al., 2022). Intermediate- and high-

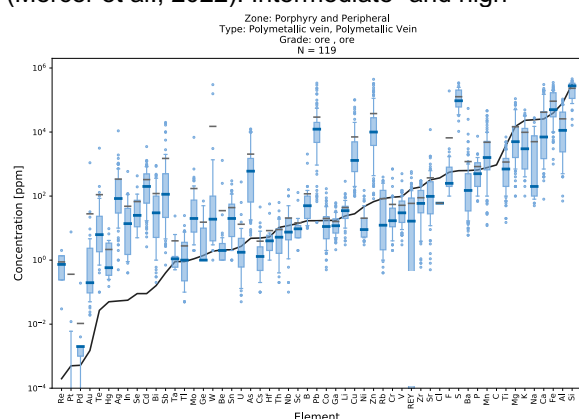


Figure 3. Box plot of elemental abundance in ore samples from polymetallic vein and replacement

deposits relative to upper crustal abundance (black line). Median value shown with bold blue line.

sulfidation epithermal deposits (e.g., Red Mountain, CO) have anomalous median concentrations >100x crustal value in Bi, In, Se, and Sn (in addition to Cu, Pb, and Zn) with >1000x crustal value of As, Cd, Sb, and Te.

At the top of the volcanic pile (e.g., topaz rhyolite flows, domes, tuffs) lies the volcanogenic and vapor phase zone, the shallowest lithological expression of Climax-type systems (Fig. 1). Here mineralization occurs post-eruptively when fluids (e.g., hydrothermal fluids driven by magmatic heat, fluids expelled from devitrification of volcanic glass, meteoric water, volcanic lakes) leach and react with vitric felsic volcanic rocks, remobilizing and concentrating critical elements. Important resources of Be and U form in this realm (Breit and Hall, 2011; Foley et al., 2012). The world's largest volcanogenic Be deposit (Spor Mountain, UT) contains anomalous median concentrations >10x crustal value of Bi, Cd, Li, and Ta (in addition to Pb, Sn, W, and Zn) and >100x crustal value of Be, F, In, and U.

5 Critical mineral estimates based on primary commodity ratios

Median ratios of critical minerals to primary commodities may be used along with existing commodity grade, tonnage, or assessed endowments to estimate potential critical mineral grade, tonnage, or endowment values. Current geochemical and commodity grade/tonnage data on many Climax-type ore deposits are sparse, which presently limits the utility of this approach.

Preliminary calculations for the median porphyry molybdenite ore concentrates returns ratios with Mo including $\text{Cd}/\text{Mo} = 0.0011$, $\text{Re}/\text{Mo} = 0.000012$, $\text{Te}/\text{Mo} = 0.00009$ with notable ratios of $\text{Bi}/\text{Mo} = 0.000097$, $\text{REE}/\text{Mo} = 0.000098$, and $\text{Sn}/\text{Mo} = 0.00006$. Porphyry wolframite ore concentrates yield ratios with W including $\text{Re}/\text{W} = 0.000006$, $\text{Nb}/\text{W} = 0.009$, $\text{REE}/\text{W} = 0.0011$, $\text{Sn}/\text{W} = 0.0014$, and $\text{Ta}/\text{W} = 0.0005$. Porphyry monazite ore returns ratios with REE of $\text{Bi}/\text{REE} = 0.2$, $\text{Nb}/\text{REE} = 5.0$, $\text{Sn}/\text{REE} = 13$, $\text{Ta}/\text{REE} = 0.94$, $\text{U}/\text{REE} = 1.3$, $\text{Cd}/\text{REE} = 0.02$, and $\text{Sc}/\text{REE} = 0.08$. Molybdenite ore ratios suggest potential endowment of the Climax-Sweet Home ore deposit with 144 tonnes Te (298% of 2022 U.S. imports for consumption), 155 tonnes Bi (5% of 2022 U.S. imports for consumption), 157 tonnes REM (1.6% of 2022 U.S. imports for consumption), and 96 tonnes Sn (0.2% of 2022 U.S. imports for consumption).

Initial calculations for median beryllium ore concentrations returns significant ratios with Be of $\text{Ce}/\text{Be} = 1.004$, $\text{Li}/\text{Be} = 2.149$, $\text{Zn}/\text{Be} = 2.819$, $\text{Cs}/\text{Be} = 0.583$, $\text{Nb}/\text{Be} = 0.883$, $\text{Y}/\text{Be} = 0.811$, and $\text{Zr}/\text{Be} = 0.816$. These ratios suggest the potential existence at the Spor Mountain mine of 15,261 tonnes Ce (no consumption data available, but

~3,000% current U.S. stockpile), 32,665 tonnes Li (960% of 2022 U.S. imports for consumption), 42,849 tonnes Zn (6000% of 2022 U.S. imports for consumption), 13,422 tonnes Nb (150% of 2022 U.S. imports for consumption), 12,327 tonnes Y (1500% of 2022 U.S. imports for consumption), and 12,403 tonnes Zr (47% of 2022 U.S. imports for consumption).

6 Conclusions and future areas of research

Climax-type systems are indeed an important past, current, and future source of critical minerals. Despite considerable knowledge and data on Climax-type magmatic hydrothermal systems, there are considerable gaps in existing geochemical datasets on the abundance of critical minerals, especially in whole rock data from root zone, lithocap, volcanogenic and vapour phase deposits. Existing high-spatial resolution, multi-element geochemical analyses of ore and gangue are rare and we highlight this as an area for future research as well.

These data are preliminary or provisional and are subject to revision. They are being provided to meet the need for timely best science. These data have not received final approval by the U.S. Geological Survey (USGS) and are provided on the condition that neither the USGS nor the U.S. Government shall be held liable for any damages resulting from the authorized or unauthorized use of the data.

Acknowledgements

We thank M. Granitto, D. Schmidt and R. Khoury for help compiling literature data and sample processing. We also thank C.M. Mercer for programming expertise.

References

- Audétat A and Li W (2017) The genesis of Climax-type porphyry Mo deposits—Insights from fluid inclusions and melt inclusions. *Ore Geol Rev* 88:436–460.
- Audétat A (2019) The Metal Content of Magmatic-Hydrothermal Fluids and Its Relationship to Mineralization Potential. *Econ Geol* 114:1033–1056.
- Breit GN and Hall SM (2011) Deposit model for volcanogenic uranium deposits. USGS OFR 2011–1255:1–5.
- Foley NK, Hofstra AH, Lindsey DA, Seal RR II, Jaskula B, Piatak NM (2012) Occurrence model for volcanogenic beryllium deposits, Chap. F of Mineral deposit models for resource assessment. USGS SIR 2010–5070–F:1–43.
- Frost CD and Frost BR (2010) On Ferroan (A-type) Granitoids: their Compositional Variability and Modes of Origin. *J Petro* 52:39–53.
- Granitto M, Wang B, Shew NB, Karl SM, Labay KA, Weldon MB, Seitz SS, Hoppe JE (2019) Alaska geochemical database version 3.0 (AGDB3)—including “best value” data compilations for rock, sediment, soil, mineral, and concentrate sample media. USGS Data Series 1117. <https://doi.org/10.3133/ds1117>.
- Granitto M, Emsbo P, Hofstra AH, Orkild-Norton AR, Bennett MM, Azain JS, Koenig AE, Karl NA (2020) Global Geochemical Database for Critical Minerals in Archived Mine Samples: U.S. Geological Survey data release, <https://doi.org/10.5066/P9Z3XL6D>.
- Granitto M, Schmidt DE, Karl NA, Khoury RM (2021) National Geochemical Database on Ore Deposits: Legacy data. USGS Data Release, <https://doi.org/10.5066/P944U7S5>.
- Hattori KXI and Keith J (2001) Contribution of mafic melt to porphyry copper mineralization: evidence from Mount Pinatubo, Philippines, and Bingham Canyon, Utah, USA. *Miner Deposita* 36:799–806.
- Hofstra, A. H., Cosca, M.A., and Rockwell, B.W. (2014a) Advanced argillic lithocaps above Climax-type Mo porphyries? Evidence from porphyry clusters in New Mexico, Utah, and Colorado: SEG Annual Meeting, Keystone, CO, 1 pg.
- Hofstra AH, Landis GP, Rye RO (2014b) Magmatic Steam Alunite Veins: The Epithermal Expression of UST Layers in Porphyry Intrusions? Pan-American Current Research on Fluid Inclusions (PACROFI-XII) 21–22.
- Long KR, DeYoung JH Jr, Ludington SD (1998) Database of Significant Deposits of Gold, Silver, Copper, Lead, and Zinc in the United States. USGS OFR 98-206a-b:33.
- Ludington S and Plumlee GS (2009) Climax-type porphyry molybdenum deposits. USGS OFR 2009–1215:16.
- Launay G, Sizaret S, Lach P, Melleton J, Gloaguen E, Poujol M (2021) Genetic relationship between greisenization and Sn-W mineralizations in vein and greisen deposits: Insights from the Panasqueira deposit (Portugal). *Bul Soc Géolog France* 192:1–29.
- Mercer CN, Hofstra AH, Todorov TI, Roberge J, Burgisser A, Adams DT, Cosca M (2015) Pre-Eruptive Conditions of the Hideaway Park Topaz Rhyolite: Insights into Metal Source and Evolution of Magma Parental to the Henderson Porphyry Molybdenum Deposit, Colorado. *J Petrol* 56:4:645–679.
- Mercer CM, Cosca MA, Hofstra AH, Premo WR, Rye RO, Landis GP (2022) ⁴⁰Ar/³⁹Ar Geochronology of Magmatic-Steam Alunite from Alunite Ridge and Deer Trail Mountain, Marysville Volcanic Field, Utah: Timing and Duration of Miocene Hydrothermal Activity Associated with Concealed Intrusions. *Minerals* 12:1533.
- Mutschler FE, Ludington S, Bookstrom AA (2000) Giant porphyry-related camps of the world – A database, USGS OFR 99-556 Version 2.7, <https://pubs.usgs.gov/of/1999/of99-556/>.
- Richards JP and Mumin AH (2013) Magmatic-hydrothermal processes within an evolving Earth: Iron oxide-copper-gold and porphyry Cu ± Mo ± Au deposits. *Geol* 41:767–770.
- Rosera JM, Gaynor SP, Coleman DS (2021) Spatio-Temporal Shifts in Magmatism and Mineralization in Northern Colorado Beginning in the Late Eocene. *Econ Geol* 116:4:987–1010.
- Rosera JM, Frazer R, Mills R, Jacob K, Gaynor, S, Coleman D, Farmer L (2022) Fluorine-Rich Mafic Lower Crust In The Southern Rocky Mountains: The Role Of Pre-Enrichment In Generating Fluorine Rich Silicic Magmas And Porphyry Mo Deposits. *Am Min* DOI: <https://doi.org/10.2138/am-2022-8503>
- Seedorff E and Einaudi MT (2004) Henderson porphyry molybdenum system, Colorado: I. Sequence and abundance of hydrothermal mineral assemblages, flow paths of evolving fluids, and evolutionary style. *Econ Geol* 99:3–37.
- Sillitoe RH (2010) Porphyry Copper Systems. *Econ Geol* 105:3–41.
- Sinclair WD (1995) Porphyry Mo (Climax-type), Selected British Columbia mineral deposit profiles Volume 1. *Metallics and coal*, Lefebvre DV and Ray GE, eds. British Columbia Ministry of Energy of Employment and Investment Open File 1995–20:105–108.
- White WH, Bookstrom AA, Kamilli RJ, Ganster MW, Smith RP, Ranta DE, Steininger RC (1981) Character and origin of Climax-type molybdenum deposits. *Econ Geol* 75th Anniv Vol:270–316.
- Zeng Q, Liu J, Qin K, Fan H, Chu (2013) Types, characteristics, and time–space distribution of molybdenum deposits in China. *Internat Geol Rev* 55:1311–1358.

Comparative study of pegmatites from the Central Rhodopean Pb-Zn deposits (Bulgaria)

Georgi Milenkov¹, Rossitsa D. Vassileva¹, Sylvina Georgieva¹, Kalin Kouzmanov², Jan Cempírek³, Yana Georgieva⁴

¹Geological Institute, Bulgarian Academy of Sciences, Sofia, Bulgaria

²Department of Earth sciences, University of Geneva, Geneva, Switzerland

³Department of Geological Sciences, Masaryk University, Brno, Czech Republic

⁴Sofia University "St. Kliment Ohridski", Sofia, Bulgaria

Abstract. Pegmatites are one of the main sources of some critical elements required for the 'green transition'. This specific lithology is commonly observed as a host rock for polymetallic mineralization in Pb-Zn deposits from the Central Rhodopes in Bulgaria. The main pegmatite-forming minerals are feldspar, quartz and mica. Allanite, titanite, zircon, monazite and apatite are commonly observed as accessory minerals. Despite no genetic relation between the Pb-Zn mineralization and the pegmatites, the latter are altered by the ore-forming fluids in these deposits. The hydrothermal alteration resulted in redistribution of various components to new minerals phases such as thorite, bastnäsité, parisite, xenotime, REE-bearing clinozoisite and others.

We studied pegmatites from four different deposits located in two districts - Madan (Petrovitsa and Krushev Dol deposits) and Laki (Djurkovo and Govedarnika deposits). Macroscopically, the pegmatites from the different localities do not vary much; however, their geochemical signatures (e.g., feldspars, allanite and titanite compositions) differ significantly. Proximity to the hydrothermal fluid source, structural control, metamorphic grade, and deformation were essential factors that influenced the geochemistry of the pegmatite minerals.

1 Introduction

Pegmatite geochemistry, origin and economic potential have been vastly studied in the past decades. The traditional usage of pegmatites for ceramics shifted towards their importance as a major source for rare and critical elements needed for the "green transition" (Li, Be, Cs, Ta, Nb, U, REE). To properly define pegmatite exploration strategies and evaluate their economic potential, mineralogical and geochemical studies of pegmatites are essential as they allow recognition of their genetic mechanisms and identification of potential ore minerals.

Abundant pegmatite dykes are observed in some of the Pb-Zn deposits in the Central Rhodopes, Southern Bulgaria (Figure 1). New data on the mineralogical and geochemical characteristics, geochronology, and general mineral zonation were recently reported (Georgieva et al. 2022; Milenkov et al. 2022). In this study we compile and compare recent and newly obtained geochemical data of major and accessory minerals of pegmatites from four Pb-Zn deposits, two in the Madan district (Petrovitsa and Krushev Dol) and two in the Laki district (Djurkovo and Govedarnika).

2 Geological setting

The region is part of the Alpine-Balkan-Carpathian-Dinaride province in south-eastern Europe. The studied deposits are currently underground mining operations. Despite their affiliation to two different ore districts (Laki and Madan; Figure 1B), the ore bodies are hosted by the rocks of the Madan lithotectonic unit. The unit belongs to the Middle Allochthone of the Rhodope Metamorphic Complex (Jahn-Awe et al. 2012) and is composed of biotite gneisses, amphibolites and marbles. In both Laki and Madan areas, the Pb-Zn deposition is controlled by NNW- (Madan) or NNE-trending (Laki) transtensional fault systems; the ores are mainly present in quartz-sulphide veins and metasomatic skarn bodies hosted by the high-grade metamorphic rocks.

At ~42 Ma, magmatism related to post-collisional extensional tectonics began locally by the intrusion of the Smilyan granite, shifting towards extension-related rhyolite dykes and ignimbrite deposit emplacement (Smolyan Basin) at ~31 Ma (Kaiser-Rohrmeier et al. 2013). Skarn formation and sulfide mineralization in the Madan ore district was constrained between 31.41 ± 0.39 Ma (U-Pb dating on zircon in pre-ore rhyolite; Hantsche et al. 2017) and 29.95 ± 0.23 Ma (Ar-Ar dating on hydrothermal sericite; Kaiser-Rohrmeier et al. 2004). The origin of the Pb-Zn mineralization is still under debate.

Formation of the studied pegmatite dikes pre-dates timing of the hydrothermal and skarnification processes; ages of pegmatite formation range from 50 to 40 Ma (Milenkov et al. 2022).

3 Local geology

All studied pegmatites in the Madan unit share the same main characteristics. The pegmatites are commonly observed as layer-like bodies concordant to the main metamorphic foliation (Figure 1C, D, E). Most of the studied pegmatites underwent several stages of ductile and brittle deformation, causing their sigmoidal shape with several groups of fractures (Figure 1C and D). Their thickness varies between 0.1 and 5 m. Sometimes pegmatite injections crosscut the other host rocks.

Besides the observed deformation, the pegmatites also underwent later hydrothermal alteration. Its intensity is stronger towards the lithological contacts with other rocks from the metamorphic sequence. The boundary between

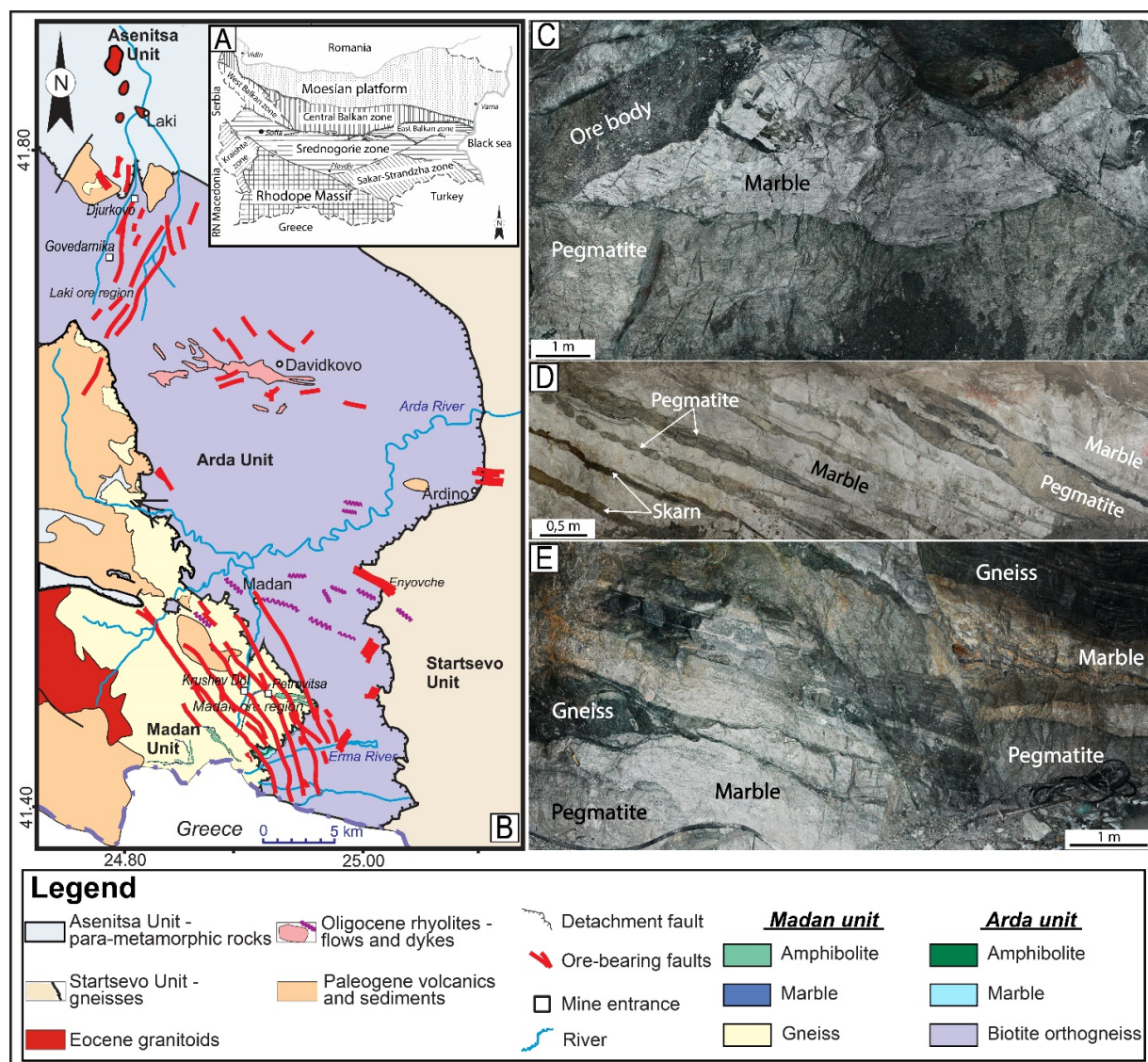


Figure 1. A) Tectonic map of Bulgaria; B) Geological map of the Central Rhodopes and the main ore districts and deposits (Vassileva et al. 2009); Pegmatite outcrops in C) Petrovitsa, D) Govedarnika, and E) Djurkovo deposits.

pegmatites and marbles favours precipitation of anorthite at the expense of the other feldspars. Epidote-chlorite-adularia-(\pm hematite) and sericite-carbonate are other very typical hydrothermal associations.

The primary mineral assemblage consists of K-feldspar, plagioclase, quartz and micas, while titanite, allanite, zircon, apatite and monazite are the main accessories (Milenkov et al. 2022). Alteration minerals such as albite, epidote, chlorite, clinopyroxene, sericite, kaolinite, rutile, adularia and calcite replace the primary pegmatite minerals. Based on the genetic classification of Ivanov (1991), the studied pegmatites belong to the Rare-Element class, corresponding to Niobium-Yttrium-Fluorine (NYF) family according to Černý and Ercit (2005).

4 Results

Feldspars are the most abundant pegmatite-forming minerals, followed by quartz. Based on petrography

study either plagioclase prevail over K-feldspar or vice versa. Mica appears sporadically within the bodies. Feldspar composition is highly variable (Figure 2A). K-feldspar (orthoclase) is typical for all localities, while the Ca-plagioclase (anorthite) is observed only at Petrovitsa. Orthoclase, oligoclase, albite and andesine compositions are the most common feldspars within both Madan and Laki districts.

Allanite-REE-rich clinozoisite and titanite are the most widespread accessory minerals in the pegmatites. Their size highly varies between 5 μ m and 1.5 mm, the shape is subhedral to anhedral. Patchy zonation rarely occurs in titanite but is characteristic for allanite. The sum of REE, Th and Y contents shows that most of the allanites suffered hydrothermal alteration and are partly transformed to REE-rich clinozoisite (Figure 2B). The most preserved allanites come from Krushev Dol, while in Petrovitsa the analyses show mainly clinozoisites. The Govedarnika deposit shows a mixed pattern.

Recently, Milenkov et al. (2022) distinguished magmatic and hydrothermal titanite (with ages of formation ~50 Ma and ~40 Ma, respectively) in the pegmatite from the Petrovitsa deposit. Geochemical (EPMA and LA-ICP-MS) data of titanites from Petrovitsa, Krushev Dol and Govedarnika show variable concentrations of critical elements (Figure 2C). The two titanite generations from Petrovitsa show differences in minor and trace element behavior. Compared to the magmatic type (Titanite 1) with relatively uniformly high contents of all elements, the hydrothermal type (Titanite 2) is depleted in V, Ga, Sr, Hf, Th, and REE, and has generally higher but more variable contents of Y, Nb, Ta and U. The sum of REE is twice higher in the magmatic titanites. Samples from Krushev Dol show the highest concentrations of most of the studied elements. In contrary, most of the lowest contents are present in titanite crystals at Govedarnika. Chondrite-normalized REE patterns from both allanite and titanite are shown in Figure 2D.

The Petrovitsa magmatic titanite (Titanite 1) has a narrow spread of $\Sigma(\text{REE})$ with light rare-earth elements (LREE)-enriched pattern whereas the Petrovitsa Titanite 2 and the analyses from Krushev Dol show the opposite trend - wider $\Sigma(\text{REE})$ spread and flat to heavy rare-earth elements (HREE)-enriched pattern. The pattern of titanites from Govedarnika deposit is flatten but the REE concentrations are very low. Negative Eu anomaly is observed in both titanites from Petrovitsa whereas those from Krushev Dol and Govedarnika show a positive one. The REE_{CN} patterns of allanite from the three studied deposits are strongly LREE-enriched with negative Eu anomaly and minor differences in pattern slope; the highest La_{CN}/Lu_{CN} is present in allanite from Krushev Dol whereas the lowest in allanite from Govedarnika (Figure 2D).

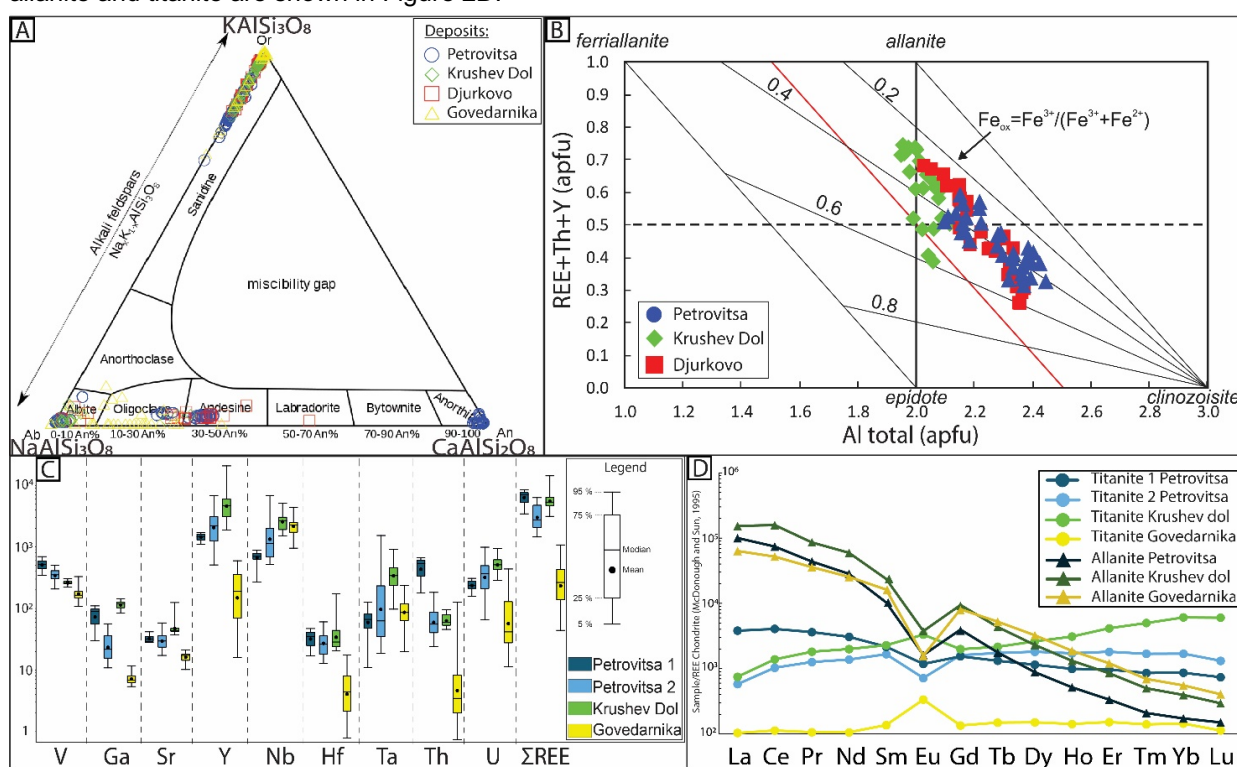


Figure 2. Comparison between the concentrations of studied minerals from different deposits: A) Feldspar compositions in apfu (atoms per formula unit); B) Composition of epidote-group minerals represented on the classification diagram REE+Th+Y vs. Al (Petrik et al. 1995); C) Minor and trace-element concentrations within the titanites in ppm; D) Chondrite-normalized REE patterns.

5 Discussion and conclusions

Macroscopically, the studied pegmatite bodies from the Madan and Laki outcrops do not show significant differences. They are all very similar in terms of size, shape and position relative to host rocks and structures. However, geochemical signatures of their main and accessory minerals vary significantly among the different localities. The differences mainly arise from the influence of the Ca-rich (epidote-forming) alteration.

Titanite from pegmatites in the Petrovitsa deposit occurs in magmatic (Titanite 1) and hydrothermal (Titanite 2) generations distinguished by their Th/U and LREE/HREE ratios, sum of REE, Eu-anomaly, and age of formation (Milenkov et al. 2022). The new titanite data from the Krushev Dol and Govedarnika deposits allow comparison of titanite geochemistry in pegmatites from the three deposits. Almost all the studied titanite crystals from Govedarnika have very low contents of trace elements. In addition, the Th/U ratio below 0.3 and positive Eu anomaly

are indicative of a metamorphic origin for the studied mineral (Scibiorski et al. 2019). In contrast, titanite from Krushev Dol shows very high minor and trace element contents and REE patterns similar to those of Titanite 2. Other features (Th/U ratio, HREE>LREE, positive Eu anomaly) also indicate more hydrothermal influence rather than magmatic (Milenkov et al. 2022), but a possible mixture of both as an overlapping process can be considered as well.

Composition of the epidote-supergroup minerals (allanite-clinozoisite) varies among and within the individual localities. According to the recommended nomenclature of epidote-group minerals by Armbruster et al. (2006), the approved chemical criterion to assign minerals to the allanite subgroup is $\text{REE} + \text{Th} + \text{U} > 0.5 \text{ apfu}$. This condition is fulfilled by most of the analyses from Krushev Dol with minor REE-rich epidote only. Compositions from Petrovitsa mostly represent only REE-rich clinozoisite whereas values from Djurkovo fall both in allanite and REE-rich clinozoisite fields. This indicates the advanced hydrothermal alteration on the pegmatites in Petrovitsa. At all localities, the influx of multiphase hydrothermal events partly or entirely transformed allanite to REE-rich epidote-clinozoisite, causing remobilization of REE in secondary minerals (Georgieva et al. 2022). The interaction between allanite and oxidized fluids caused considerable REE leaching from the mineral. The presumable limited mobility of these elements in fluids prevents their significant transport, therefore they are incorporated in closely crystalized epidote-clinozoisite. Besides allanite and titanite, also thorite, REE-fluorcarbonates, apatite, monazite and zircon from the studied pegmatite localities concentrate REE.

Pegmatite bodies located in the Middle Allochthon of the Rhodopean metamorphic complex show different geochemical characteristics mainly controlled by the hydrothermal alterations overprinting them. The bodies in the Petrovitsa deposit (Madan district) are the most altered, which may support the work of Hantsche et al. (2021) suggesting that the magmatic source for the Pb-Zn mineralization is closest exactly to this deposit. As the pegmatite bodies pre-date formation of the Pb-Zn mineralization, the hydrothermal fluids had a significant influence on them. The other deposit from the Madan district, Krushev Dol, features less alterations in pegmatite, which may indicate lower interaction between fluids and pegmatites and/or more distal magmatic source. The pegmatite bodies located in Govedarnika deposit (Laki district) have experienced high metamorphism and deformation, and it can be assumed that they have been metamorphosed. The major element compositions in minerals from Djurkovo (Laki district) are intermediate between the other studied deposits. Further analysis on this deposit will be obtained in

order to clarify its origin, stages of alteration and deformation.

Acknowledgements

The study is financially supported by the Bulgarian National Science Fund: projects KP-06-N34/4 and KP-06-DO02/2. Part of the EPMA results are financed by the ERA-MIN3 PEGMAT project.

References

- Armbruster T, Bonazzi P, Akasaka M, Bermanec V, Chopin C, Giere R, Heuss-Assbichler S, Liebscher A, Menchetti S, Pan Gier'e R, Heuss-Assbichler S, Liebscher A, Menchetti S, Pan Y, Pasero M (2006) Recommended nomenclature of epidote-group minerals. *European Journal of Mineralogy* 18(5):551–567.
- Černý P, Ercit TS (2005) The classification of granitic pegmatites revisited. *Can. Mineral.* 43: 2005–2026.
- Georgieva S, Vassileva R, Milenkov G, Stefanova E (2022) Major and trace element signature of epidote-group minerals in altered pegmatites from the Petrovitsa Pb-Zn deposit of the Madan ore region, Central Rhodopes, Bulgaria: Evidence of allanite/epidote transformation. *Geologica Carp* 73(4): 365–380.
- Hantsche AL, Kouzmanov K, Dini A, Vassileva R, Guillong M, von Quadt A, (2017) U-Pb age constraints on skarn formation in the Madan Pb-Zn district, Bulgaria: zircon evidence from Tertiary magmatism. 15th Swiss Geoscience Meeting, Abstract volume, 124–125.
- Hantsche AL, Kouzmanov K, Milenkov G, Vassileva RD, Vezzoni S, Dini A, Sheldrake T, Laurent O, Guillong M (2021) Metasomatism and cyclic skarn growth along lithological contacts: physical and geochemical evidence from a distal Pb-Zn skarn. *Lithos* 400–401 (3): 106408.
- Ivanov I (1991) Granite Pegmatites in Bulgaria. Publishing House of the Bulgarian Academy of Sciences, Sofia. (In Bulgarian with English abstract), 204 p.
- Jahn-Awe S, Pleuger J, Frei D, Georgiev N, Froitzheim N, Nagel T (2012) Time constraints for low-angle shear zones in the Central Rhodopes (Bulgaria) and their significance for the exhumation of high-pressure rocks. *International Journal of Earth Sciences* 101, 1971–2004.
- Kaiser-Rohrmeier M, von Quadt A, Driesner T, Heinrich, CA, Handler R, Ovtcharova M, Ivanov Z, Petrov P, Sarov ST, Peytcheva I (2013) Post-orogenic extension and hydrothermal ore formation: high-precision geochronology of the central Rhodopian metamorphic core complex (Bulgaria-Greece). *Econ Geol* 108(4):691–718.
- Kaiser-Rohrmeier M, Handler R, von Quadt A, Heinrich C (2004) Hydrothermal Pb-Zn ore formation in the central Rhodopian dome, South Bulgaria: review and new time constraints from Ar-Ar geochronology. *Swiss Bulletin of Mineralogy and Petrology* 84 (1): 37–58.
- Milenkov G, Vassileva R, Georgieva S, Grozdev V, Peytcheva I (2022) Trace-element signatures and U-Pb geochronology of magmatic and hydrothermal titanites from the Petrovitsa Pb-Zn deposit, Madan region, Central Rhodopes (Bulgaria). *Geologica Balc* 51(2): 79–91.
- Petrík I, Broska I, Lipka J, Šíman P (1995) Granitoid Allanite-(Ce): Substitution Relations, Redox Conditions and REE Distributions (On an Example Of I-Type Granitoids, Western Carpathians, Slovakia). *Geologica Carpathica* 46, 79–94.
- Scibiorski E, Kirkland CL, Kemp AIS, Tohver E, Evans NJ (2019) Trace elements in titanite: A potential tool to constrain polygenetic growth processes and timing. *Chem Geol* 509: 1–19.
- Vassileva RD, Atanassova R, Bonev IK (2009) A review of the morphological varieties of the ore bodies in the Madan Pb-Zn deposits, Central Rhodopes, Bulgaria. *Geochem Mineral Petrol* 47:31–49.

Regional rock geochemistry of granites and elvans in SW England: delineation of composite intrusions and Sn-Li potential

Charles J. Moon^{1,3}, Beth Simons^{2,3}, Nick P. J. Harper⁴, Frederick A. Jackson⁵, Robin K. Shail³ and Chris M. Yeomans⁵

¹*Moon Geology, Rose Cottage, Calstock, Cornwall, UK cjm@moongeology.co.uk*

²*Park an Fenten, St Agnes, Cornwall*

³*Camborne School of Mines, University of Exeter, Penryn, Cornwall*

⁴*Deep Digital Cornwall, Camborne School of Mines, University of Exeter, Penryn, Cornwall*

⁵*Cornish Lithium Ltd, Tremough Innovation Centre, Penryn, Cornwall*

Abstract. Comprehensive major and trace element suites were determined on elvans from SW England. Results were combined with F, B and Cl on previously reported non-mineralised granite samples in a search for vectors to mineralisation. PCA and machine learning confirmed the classification of granites into 5 groups mainly based on trace elements. Lithium enrichment in granites (and potential) is strongly correlated with F, both in G4/5 groups (Li-mica, topaz) as well as, more weakly, in G2 (muscovite) granites, which host greisen Sn-W deposits. There is also correlation of F with W and Ta, in G4/5 although only disseminated Sn-W mineralisation is known. Boron is enriched in G2 and G5 but most strongly in G4. There is no enrichment of background granites in Sn.

The elvans are related to both G1/G2 and G4/G5 granites, based largely on Nb/Zr ratios, although Ni and REE indicate intrusion of some may have been driven by lamprophyres. Several of the G1/G2 ungreisened elvans are strongly enriched in Sn. In contrast some G4/G5 elvans (ongonites) are enriched in Li-Ta-Sn-F and are geochemically similar to aplite/ pegmatites. The chemistry of elvans is proposed to indicate the location of subsurface mineralising processes, and hence potential.

1 Introduction

Granites are known to host and be genetically linked to the formation of tin and lithium deposits in SW England (Alderton 1993). Elvan (quartz-porphry/ rhyolite) dykes (1-10 m thick, up to 2 km long) are closely linked, spatially and temporally to Sn-base metal veins but are slightly younger than comparable granites. The composite nature and detailed systematic geochemistry are less well known for both granites and elvans

This study details an extension of earlier studies of the 75 background granites that established components using XRF/ ICP geochemistry and textures (Simons et al 2016, 2017) by analysing their samples for F, Cl and B as well as collecting and determining trace and major elements for 151 elvan samples. This latter study is the first comprehensive geochemical study of the elvans. It builds on earlier elvan studies notably of Henley 1972 and Antipin et al. 2002.

2 Analytical Methods

The granite samples of Simons et al. were originally analysed by a combination of XRF and 4

acid ICP-MS. These have been further analyzed for F, Cl and B by ion chromatography and ICP-MS by ALS in Ireland and Vancouver. Elvan samples were mainly analysed for majors and trace elements at ALS by a combination of fusion ICP-ES/MS as well as 4 acid and aqua regia ICP-MS; F was determined by fusion ion chromatography.

3 Granites

Early Permian granites were intruded into Devonian and Carboniferous sediments. They were subdivided into 5 groups (G1-G5) based on their textures and major as well as trace element chemistries by Simons et al 2016. These correspond to older (c. 290-282 Ma) and younger granites of the geochronological studies of Chen et al. (1993) and Chesley et al. (1993).

Mineralisation consists of vein Sn-W-Cu, sheeted- vein Sn-W and later crosscutting Pb-Zn-F veins. Sn-Cu veins are often zoned or telescoped. The timing of emplacement of Sn-Cu veins has been much debated but appear slightly later than G2 granites with crosscutting Cu-rich veins younger than Sn veins in the same area. Lithium targets are bulk mineable Li-enriched micas, mainly zinnwaldite, and limited petalite or amblygonite in aplites and pegmatites. Current hard rock Li targets are all in G4/5 granites.

This study shows lithium enrichment in granites is strongly correlated with F both in the G4/5 granites (Li-mica, tourmaline/ topaz) as well as more weakly in G2 (muscovite) granites (Figure 1). The latter are the main host to greisen Sn-W deposits. Enrichment of F in the G4/5 correlates with distinct Ta and weak W enrichment but not Sn. Boron is enriched in G2 and G5 granites but most strongly in the G4 granites, reflecting their mappable tourmaline. Disseminated Sn-W mineralisation is known from G4/5 granites. Chlorine is low in G1-G2 granites as well as greisens but high in G3-G5 granites.

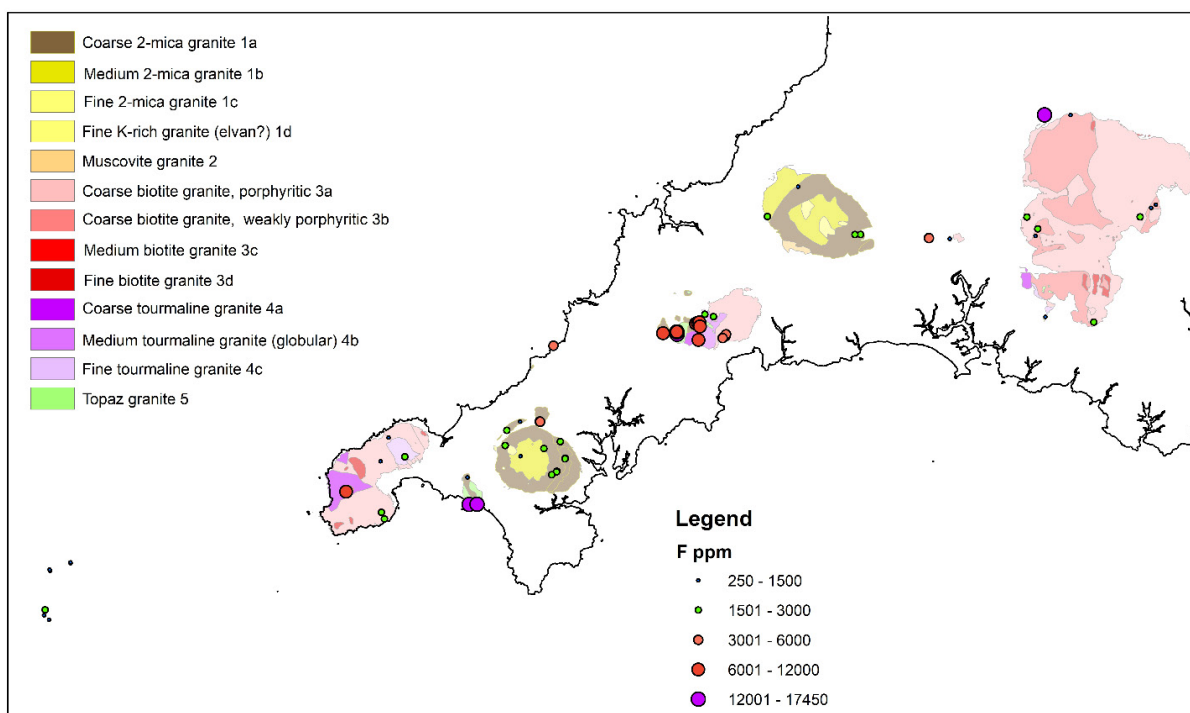


Figure 1. Fluorine in granites, n=75

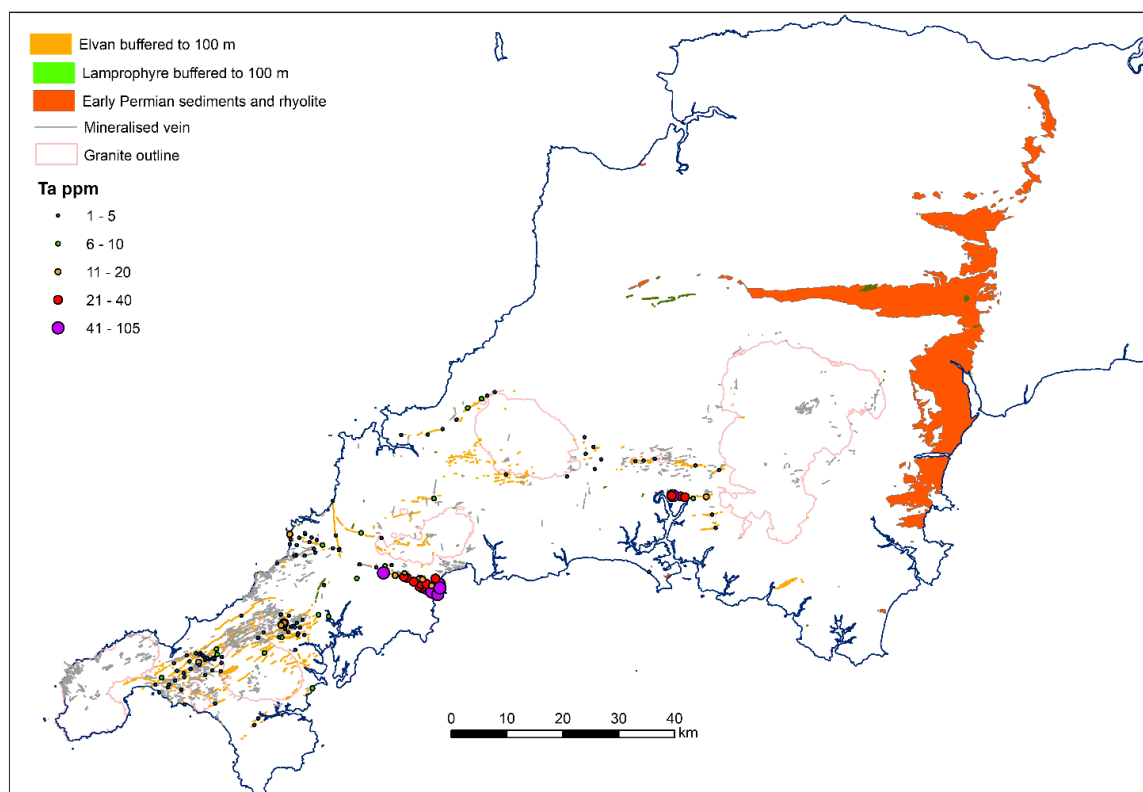


Figure 2. Tantalum in elvans, fusion ICP-MS, n=151.

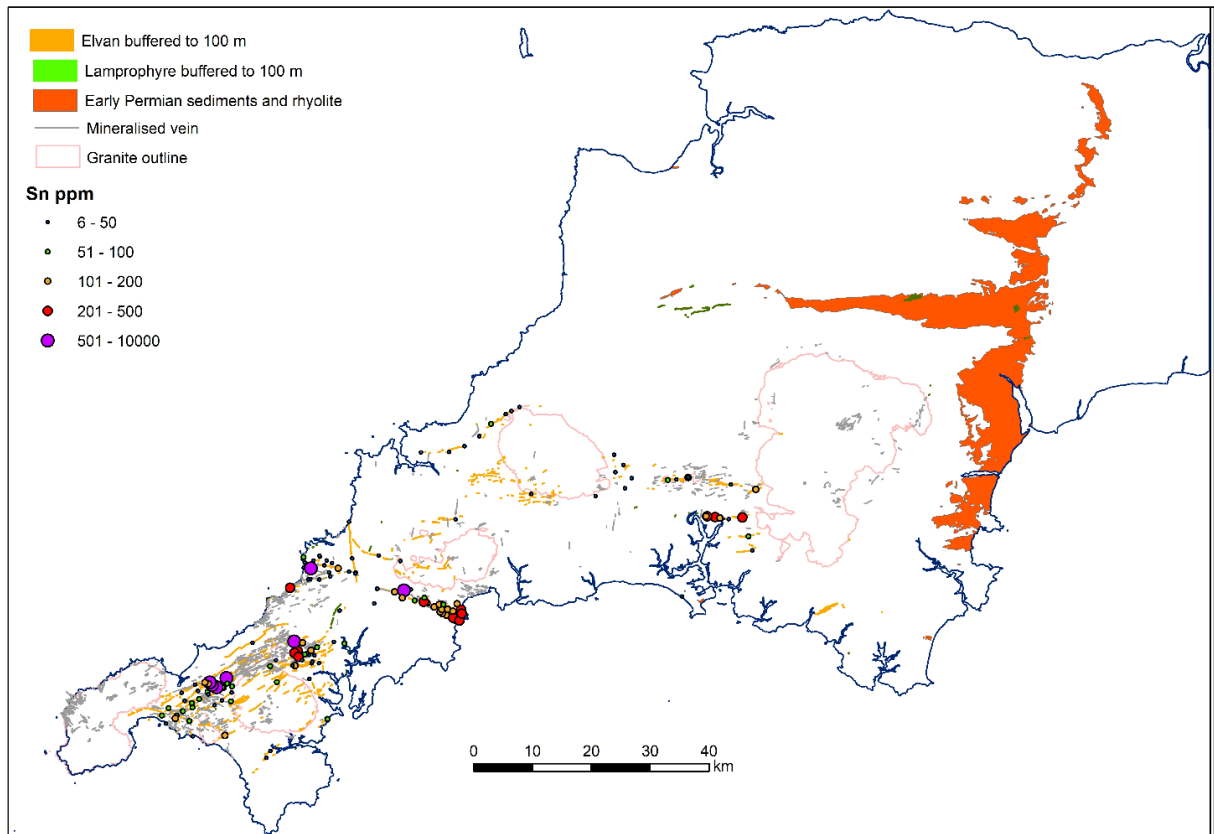


Figure 3. Tin in elvans, fusion ICP-MS. N=151. Top cut at 10000 ppm Sn

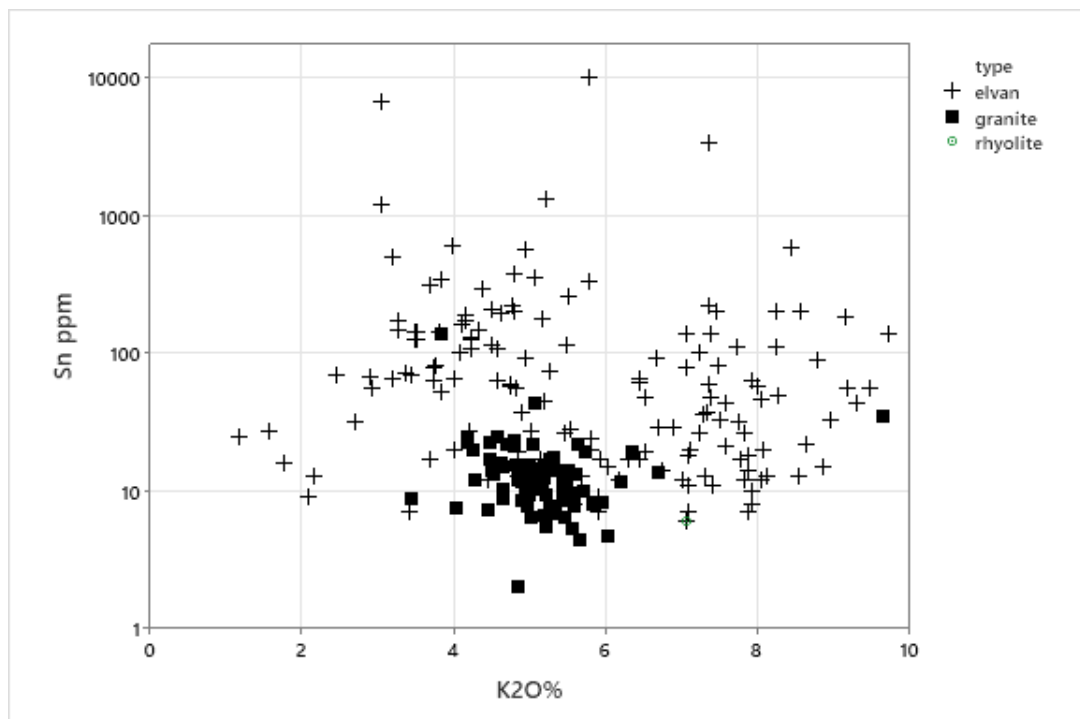


Figure 4. Scattergram Sn ppm vs K₂O%. Note distinct bimodal K₂O distribution.

The granite dataset has been subject to multivariate (Principal Component Analysis/Clustering) and machine learning analysis. This confirms the classification of Simons et al is robust and allows more detailed discrimination of individual samples. Determination of F, B and Cl aids trace element determination in this classification and improves that based on Nb/Zr used by Manning et al. 1996

Multi-element rock geochemistry locates distinct areas of Li enrichment for further work. However, there is no background enrichment in Sn and no obvious vector to Sn-bearing veins.

4 Elvans

The origin of the elvan dykes of Cornwall and Devon has been an enigma with very little work in the last 40 years due to alteration. They are clearly closely related to granite intrusions, cutting all but the latest granites, and even more closely related to mineralization (Goode 1973). The limited published analyses suggest enrichment in K₂O and derivation from G1/G2 granites (Stone 1968; Hall 1970; Henley 1972).

In several areas elvans are spatially related with lamprophyres, notably near St Kew, where lamprophyre fragments are contained in elvans. What is not clear is whether lamprophyres have driven elvan intrusion or used the same structures. Lamprophyric input can be recognized through high MgO, Ni and REE in elvans. Elvans in a number of cases are also intruded in the same locations as high Zr acid intrusives of projected Devonian age. An example is the Kingsand area where intrusive elvans cut red beds and are close to interbedded rhyolite.

Plots of Nb/Zr show affinity with both G1/3, G2 and G4/5 granites of Simons et al 2016. The high Nb elvans are chemically similar to ongonites (high level F-rich intrusives) of the Trans-Baikal and Mongolia (Antipin et al. 2002; Dostal et al. 2015) and are the first reports in the UK. These ongonitic elvans are significantly enriched in Li, F, Ta, (Figure 2) resembling the Meldon Aplite in chemistry, and in Sn. Tin is also particularly enriched in low-Li elvans in the area west of Camborne where some elvans are tourmaline-rich (Figure 3).

Enrichment in K₂O (Figure 4) has been cited as essential. This study reveals it is district specific. Cationic plots after Charoy (1984), indicate sericitization probably occurs as overprints.

Variation in chemistry suggests that within districts, individual elvans were intruded over time but with differing sources. Intrusion is controlled by NW-SE faults indicating these structures tapped magmas or hydrothermal systems at depth and may reveal the location of major hydrothermal activity.

Acknowledgements

Deep Digital Cornwall funded granite F, Cl and B analyses to Moon Geology. Cornish Lithium Ltd funded much of the elvan study and Chris Harker is thanked for support. Sharon Uren at CSM analysed early samples for Ben Thompson and Luke Holroyd in MSc studies of elvans.

References

- Alderton DHM (1993) Mineralization associated with the Cornubian granite batholith In: Patrick RAD, Polya DA (eds) Mineralization in the British Isles. Chapman & Hall, pp.270-354.
- Antipin VS, Halls C, Mitichkin MA, Scott P, Kuznetsov AN (2002) Elvans of Cornwall (*England*) and Southern Siberia as Subvolcanic Counterparts of Subalkalic Rare Metal Granites. *Russian Geology and Geophysics* 43:847-857.
- Charoy B (1984) A Discussion of the Paper by Ball and Basham Petrogenesis of the Bosworgey Granitic Cusp in the SW England Tin Province and Its Implications for Ore Mineral Genesis *Mineral Deposita* 19: 318-319
- Chen Y, Clark AH, Farrar E, Wasteneys HAHP, Hodgson MJ, Bromley AV (1993) Diachronous and independent histories of plutonism and mineralization in the Cornubian Batholith, southwest England. *Journal of the Geological Society, London* 150:1183-1191.
- Chesley JT, Halliday AN, Snee LW, Mezger K, Shepherd TJ, Scrivener RC (1993) Thermochronology of the Cornubian Batholith in southwest England: implication for pluton emplacement and protracted hydrothermal mineralisation. *Geochimica et Cosmochimica Acta* 57:1817-1835.
- Dostal J, Kontak DJ, Gerel O, Gregory Shellnutt J, Fayek M (2015) Cretaceous ongonites (topaz-bearing albite-rich microleucogranites) from Ongon Khairkhan, Central Mongolia: Products of extreme magmatic fractionation and pervasive metasomatic fluid: Rock interaction. *Lithos* 236-237:173-189. doi: 10.1016/j.lithos.2015.08.003.
- Goode AJJ (1973) The mode of intrusion of the Cornish elvans. IGS Report 73/7 Her Majesty's Stationery Office, London, 8pp.
- Hall A (1970) The composition of Cornish quartz-porphyry("elvan") dykes. *Proceedings of the Ussher Society* 2:205-208.
- Henley S (1972) Petrogenesis of Quartz Porphyry Dykes in South-West England. *Nature* 235:95-96.
- Manning DAC, Hill PI, Howe JH (1996) Primary lithological variation in the kaolinized St Austell Granite, Cornwall, England. *Journal of the Geological Society* 153:827-838. doi: 10.1144/gsjgs.153.6.0827.
- Simons B, Shail RK, Andersen JCO (2016) The petrogenesis of the Early Permian Variscan granites of the Cornubian Batholith: Lower plate post-collisional peraluminous magmatism in the Rhenohercynian Zone of SW England. *Lithos* 260:76-94. doi: 10.1016/j.lithos.2016.05.010.
- Simons B, Andersen JCØ, Shail RK, Jenner FE (2017) Fractionation of Li, Be, Ga, Nb, Ta, In, Sn, Sb, W and Bi in the peraluminous Early Permian Variscan granites of the Cornubian Batholith: Precursor processes to magmatic-hydrothermal mineralisation. *Lithos* 278-281:491-512. doi: 10.1016/j.lithos.2017.02.007.
- Stone M (1968) A study of the Praa Sands elvan and its bearing on the origin of elvans. *Proceedings of the Ussher Society* 2:37-43.

Scheelite in the Panasqueira tungsten deposit. An example of host rock control in tungstate composition.

Fernando Noronha¹, Filipe Pinto², Jorge Ferreira³

¹ICT-Porto Pole – Faculdade de Ciências Univ. Porto. Portugal

²Beralt Tin and Wolfram Portugal AS. Panasqueira. Portugal

³LNEG- UCTM-LAB Amieira. Portugal

Abstract Previous studies have shown that in the tungsten deposits of the Iberian Massif, the deposition of wolframite (Fe,Mn)WO₄ is related with modified aquo-carbonic fluids resulting from the fluid-rock interaction. In the case of the Panasqueira deposit, the tungstate exploited is wolframite and the surrounding rocks are schists of Late Ediacaran to Early Cambrian age. The interaction of primary magmatic fluids with the surrounding schists produced modified fluids enriched in Fe and Mn necessary for wolframite deposition. This study focuses the mineral assemblage present in a vein under exploration at level 1, L1D23R6AW30, in the Barroca Grande sector. In this vein, in addition to wolframite, there is also scheelite present, a rare mineral in Panasqueira deposit. It should be noted that unlike all the veins with wolframite, this one, with scheelite, cuts a basic rock, intrusive in the schists. Scheelite is later than wolframite and occurs associated with ferromagnesian chlorites and ferromagnesian carbonates. We consider that there was a lithological control in the deposition of scheelite and that the Ca, necessary for the deposition of scheelite, resulted from the fluid-rock interaction between hydrothermal fluids and the pre-existing basic rock hosting the vein.

1 Introduction

The most important W deposits in the Iberian Peninsula, in terms of W concentrate production, are located in the Central Iberian Zone (CIZ) of the Iberian Massif. This zone forms the spine of the Iberian Variscan unit, and it is characterized by the occurrence of a very thick autochthonous formation the “Schist-Greywacke Complex” (SGC) pre-Ordovician in age (Thadeu 1951).

The Panasqueira W (Sn-Cu) deposit, located in Central Portugal, is the largest quartz-vein type deposit in the Iberian Peninsula. Wolframite is the main ore being cassiterite and chalcopyrite by-products. The production in 2021 was 908 T of wolframite, 78 T of cassiterite and 839 T of chalcopyrite concentrates per month.

This study analyses the mineralogy present in a vein recently explored in level 1 (L1D23R6AW30) in the Barroca Grande sector, where scheelite, a rare mineral in Panasqueira, is found. The occurrence of scheelite, also at level 1, (L1D23R5AW14), was reported in 1978 by Décio Thadeu, in a personal communication to Kelly and Rye (1979, pp. 1758). However, it was not the subject of any description in the works followed. It should be noted that in both cases the veins cut a pre-ore basic rock dyke.

2 Geology and mineralogy

The Panasqueira district is flanked to the Northeast by the Serra da Estrela granite pluton of Variscan age. Country rocks underlying the Panasqueira district consist of folded metasedimentary sequences, regionally metamorphosed to low grade (chlorite-sericite) during the Variscan orogeny. These sequences are mainly composed of a several thousand metre thick lower marine flyschoid series of schist and greywackes from SGC.

The schists are cut by N-S, NE-SW and NNE-SSW faults. Pre-ore and post-ore veins of intrusive basic rocks are quite frequent and cut the SGC. These rocks occur often very weathered and there are few geochemical and petrographic studies that allow the classification of these basic rocks (Thadeu 1951, 1977).

The evidence of acid magmatism only occurs at depth through a greisen dome, that corresponds to the upper part of the Panasqueira granite intrusion found in the deeper levels of the underground mine workings (Kelly and Rye 1979). The results from a recent intensive drilling campaign confirm the shallow underlying batholith composed of several granite facies (Marignac et al. 2020; Breiter et al. 2023).

The Panasqueira deposit consists of a dense swarm of sub-horizontal quartz-veins which host the wolframite mineralization. The ore-bearing veins occupy flat sets of open joints. Individual veins are from 5 to 100 cm thick (averaging 30 cm). They have a dip of about 8-10° SW and frequently exhibit a structure resulting from different phases of infilling related to reopening events.

In a pioneering work Kelly and Rye (1979) described a deposition sequence with different deposition stages separated by periods of fracture and reopening episodes. Wolframite and cassiterite belongs to a first stage of mineralization, the “oxide silicate stage” (OSS), followed by the second main stage “the main sulphide stage” (MSS) (arsenopyrite, pyrite, pyrrhotite, sphalerite, chalcopyrite, stannite), and third stage “pyrrhotite alteration stage” (PAS) (pyrite, marcassite chalcopyrite, galena, Pb-Bi-Ag sulphosalts and siderite). A latter stage characterised by chlorite and a widespread carbonates deposition was also considered (LCS).

However, it should be noted that the mineralogy and mineral deposition sequence of Panasqueira are extremely complex, not only due to its great extension and, the longevity of fluid circulation systems but also to the fact the exploration of the deposit has been active for over a century. So it is practically impossible to present a complete

paragenetic picture in order to represent the entire history of the deposit.

Thus, the paragenetic sequence and mineral assemblage characteristic of each stage, proposed by Kelly and Rye (1979), were complemented by several authors namely Wimmers (1985), studying in detail the sulphides of the MSS stage and Lourenço (2002) defining three different types of mineralization, a W-Sn-Cu main mineralization, a Pb-(Zn) mineralization associated with N-S and NE-SW faults and a Sn-Cu mineralization in late fractures.

More recently, Martins et al. (2020) and Mateus et al. (2020) defined three stages roughly comparable to OSS, MSS and LCS stages of Kelly and Rye (1979) and consider a intermediary stage that marks the transition from MSS to LCS characterized by a magmatic-hydrothermal rejuvenation of the mineralizing system. Cathelineau et al. (2022) also consider OSS, MSS and LCS, but they excluded cassiterite from the OSS and consider a sub-stage characterized by the occurrence of rutile, topaz and cassiterite and a fourth stage, previous to LCS with minerals represented in previous stages, but present in geodes.

The study of the fluids associated with the main stages of mineralization led to the conclusion that the mineralizing fluids contemporary with the wolframite deposition (OSS) were aquo-carbonic ($\text{H}_2\text{O}-\text{CO}_2-\text{CH}_4-\text{N}_2-\text{NaCl}$) and that the fluids associated with MSS were aqueous, with a low volatile phase density and with a progressive enrichment in H_2O and CH_4 content (Kelly and Rye 1979; Bussink et al. 1984; Polya 1989; Noronha et al. 1992; Lourenço 2002 and Cathelineau et al. 2022). Later fluids from LCS were predominantly aqueous and saline of the $\text{H}_2\text{O}-\text{NaCl}$ (CaCl_2) type (Lourenço, 2002).

As for the origin of the fluids, they were considered magmatic by several authors (Kelly and Rye 1979; Bussink et al. 1984; Lecumberri et al. 2017) while other pointed to the fundamental role of modified aquo-carbonic fluids in the genesis of W mineralization (Polya, 1989; Noronha et al. 1992; Cathelineau et al. 2022).

3 Methodology

Samples from the vein and from the basic rock were taken for laboratory work. They were analyzed using optical microscopy, scanning electron microscope with energy dispersive X-ray spectroscopy (SEM-EDS) and MRFx analysis.

Petrographic analysis of polished thin-sections was performed at the Faculty of Sciences of the University of Porto (FCUP), Portugal, using a stereomicroscope Zeiss Stemi SV11 Apo coupled with a Sony Cyber-Shot DSC-S75 digital camera and using a Leica DM LSP polarizing microscope, with transmitted and reflected light, coupled with a Leica camera with LAS EZ software 2.0.0.

SEM-EDS analyses were performed at the Materials Centre of the University of Porto (CEMUP), Portugal, using an FEI Quanta 400 FEG-ESEM/EDAX Genesis X4M instrument. The SEM

was operated at 15 kV in high-vacuum mode, manual aperture, 5 μm beam spot size.

MRFx map analysis were carried out at the UCTM-LAB from LNEG Amieira Porto using Bruker M4 TORNADO® operating at 50kV - 600 μA - 20 μm -40 ms (pixel time),

The abbreviations used to identify the different mineral phases followed the nomenclature proposed in Whitney and Evans (2010).

4 Results and Discussion

The basic rock has a greenish-black appearance and medium to fine granularity. The petrographic study revealed a very metasomatized rock that is currently essentially formed by titanium-altered pyroxene (Ti confirmed by SEM-EDS), olivine (generally serpentinized), hornblende, actinolite, plagioclase, metallic minerals (titanomagnetite, pyrite and sphalerite), chlorite, sphene, minerals from the epidote group, apatite, biotite, leucosene and calcite were also observed. SEM-EDS maps reveal that the whole-rock composition (in Atm%) is Fe (2.84 to 3.07), Al (4.27 to 6.00), Ca (2.67 to 5.40), C (7.67 to 8.97), Mg (1.49 to 2.82), Na (1.69 to 1.96), Ti (0.50 to 0.86), K (0.13 to 0.16) and P (0.12 to 0.35).

The mineralized vein with an average thickness 10cm, (Figure 1A) was observed in the mine under UV-light which allowed the identification of scheelite in the central zone and the apatite in contact with the host basic rock (Figure 1B). Along the vein contacts, with the basic rock, fine selvages (1 cm) of muscovite were observed, both in the hanging wall and in the footwall, associated with apatite, small subhedral crystals of wolframite, and some arsenopyrite. In the center of the vein white quartz crystals, occurs together with some sphalerite, scheelite and abundant chlorite and carbonates.

Figure 2 shows MRFx mapping carried out in one of the collected samples where we find all the minerals observed in the vein and which allows a better visualization of the relationship between them.

Wolframite, occurs in small crystals, associated with muscovite, apatite and arsenopyrite. It is black in color and under the microscope sometimes shows dark red internal reflections. It should be noted that the crystals show variations in composition, but it is not possible to define zones characterized by enrichment in Fe or Mn. SEM-EDS semiquantitative analyzes reveal that it has an average ferberitic composition (16.6 to 18.1 Atm % Fe, 15 to 3.1 Atm % Mn and 22.5 to 24.8% W).

Scheelite occurs in crystals, which can reach 3 cm, surrounded by chlorite and siderite, making it difficult to establish its place in the deposition sequence. However, it predates calcite. SEM-EDS semiquantitative analyzes reveal an average composition of 31.9 to 38.6% Atm% W and 21.2 to 21.7 Atm% Ca. Chlorite occurs in dark green masses infilling the spaces between the quartz crystals which, in turn, are surrounded by a thin layer of latter muscovite. It is latter than wolframite and associated minerals

(muscovite, apatite, arsenopyrite and muscovite) sphalerite and scheelite and before Fe-Mg-Mn carbonates, dolomite and calcite (Figure 2). Under the microscope, chlorite reveals a strong pleochroism between green and yellow and a birefringence in which it exhibits anomalous blue colors. SEM-EDS semiquantitative analyzes reveal that it is a chlorite rich in Fe and Mg (11.6 to 12.6 Atm % of Fe and 6.4 to 6.9 Atm % of Mg).

After the chlorite, a yellowish carbonate in small crystals occurs that are brownish under the microscope (Figure 3). When in masses it integrates fine grains of pyrite, calcite and dolomite. SEM-EDS semiquantitative analyzes reveal that it is a Fe-Mg-Mn carbonate (16.9 to 19.5 Atm % Fe, 9.0 to 10.9 Atm % Mg and 2.5 to 3.2 Atm % of Mn) ("magnesian siderite").

Calcite and dolomite were the last minerals to be deposited in the vein.

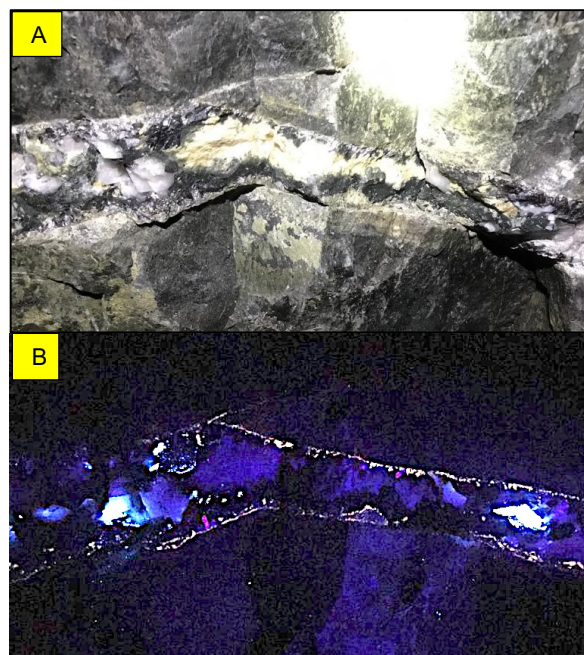


Figure 1. A - Subhorizontal vein mineralized with scheelite and wolframite; B – The same vein illuminated with ultraviolet light with scheelite (white) in the center and apatite (yellow) in the selvages.

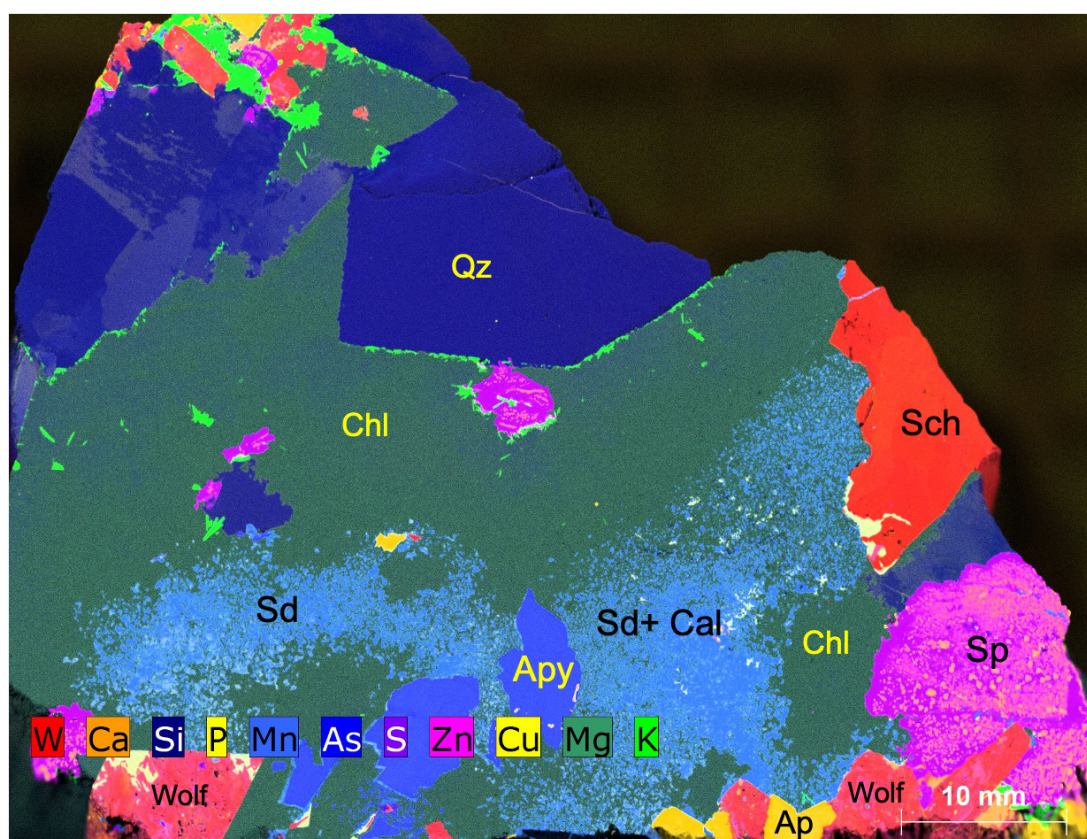


Figure 2- MRFX map from the collected sample. (Qz-quartz; Sch-scheelite; Wolf-wolframite; Chl-chlorite; Sd- "magnesian siderite"; Sp-sphalerite; Apy-arsenopyrite; Ap-apatite; Cal-calcite; Muscovite (light green)). Minerals are represented by colors that do not exactly correspond to the grid proposed for each chemical element but result from the combination of these colors. For example, scheelite (W+Ca) corresponds to a brighter red than wolframite (W+Mn+Fe).

The occurrence of chlorite was first reported by Kelly and Rye (1979). Mateus et al (2020) consider three generations of chlorite: chlorite I, the earliest and occurring at the end of the OSS; chlorite II that occurs at the end of what they consider the "rejuvenation event"; and a chlorite III already associated with a late hydrothermal activity related to the filling of fault zones.

In our study the fine-grained chlorite that occurs in masses in the vein, considering its relationship with wolframite and sphalerite and with "magnesian siderite", corresponds to chlorite II from Mateus et al (2020). The estimated temperatures using the geothermometer of Bourdelle et al. (2013) indicate an event between 200 and 250°C corresponding to Fe, Mg-chlorite crystallization.

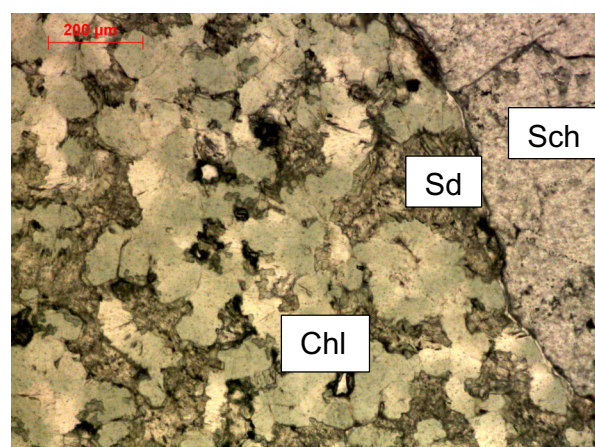


Figure 3- Scheelite (Sch) associated with chlorite (Chl) and "magnesian siderite" (Sd). Polarized light (N//)

Lecumberri et al. (2017) demonstrated quantitatively that the Panasqueira ferberite deposited from a W bearing primary fluid that interacted with the surrounding schists contributed with the iron necessary to precipitate ferberite (FeWO_4). The absence of Ca in the schists does not allow the precipitation of scheelite (CaWO_4) which will only be deposited if the Ca-bearing fluids necessary for its deposition are supplied to the fluids carrying W.

5 Conclusions

We consider that there was a lithological control in the deposition of scheelite in the studied vein and that the Ca necessary resulted from the fluid-rock interaction between a hydrothermal fluid and the pre-existing basic rock hosting the vein.

Since chlorite and siderite are magnesian, we also consider that the basic rock, by interaction with the hydrothermal fluid, was the source of Fe and Mg necessary for the formation of these later minerals.

Acknowledgements

Thanks to Beralt Tin and Wolfram (Portugal, S.A.), for the realization of this work. Thanks to Prof. M.R. Machado Leite for the use of MRFx from UCTM-LAB at LNEG. This work is supported by FCT-IP, projects UIDB/04683/2020 and UIDP/04683/2020. The comments by anonymous reviewers were appreciated.

References

- Bourdelle, F., Parra, T., Chopin, C. and Beyssac, O. (2013) A new chlorite geothermometer for diagenetic to low-grade metamorphic conditions. *Contributions to Mineralogy and Petrology*, 165, 723–735.
- Breiter K, Ďurišová J, Korbellová Z, Galiová V, Hložková M. (2023) Granite Pluton at the Panasqueira Tungsten Deposit, Portugal: Genetic Implications as Revealed from New Geochemical Data. *Minerals*, 13, 163, 1-35.
- Bussink R, Kreulen R & Jong A, (1984). Gas analyses, fluid inclusions and stable isotopes of the Panasqueira tungsten-tin deposits, Portugal. *Bull. Minéral.*, 107:703-713.
- Cathelineau M, Boiron M C, Marignac C, Doura M, Dejean M, Carocci E, Truche L, Pinto F (2020). High pressure and temperatures during the early stages of tungsten deposition at Panasqueira revealed by fluid inclusions in topaz. *Ore Geology Reviews* 126, 10374, pp 17.
- Kelly WC, Rye RO (1979) Geologic, fluid inclusions and stable isotope studies of the tin-tungsten deposits of Panasqueira, Portugal. *Econ. Geol.* 74:1721-1822.
- Lecumberri-Sanchez P, Vieira R, Heinrich CA, Pinto F, Wälle, M (2017) Fluid-rock interaction is decisive for the formation of tungsten deposits. *Geology* 45, 579–582.
- Lourenço A, (2002) Paleofluidos e mineralizações associadas às fases tardias da Orogenia Hercínica. Unpublished Thesis. Porto Univ., pp. 303.
- Marignac C, Cuney M, Cathelineau M, Lecomte A, Carocci E, Pinto F, (2020). The Panasqueira rare metal granite suites and their involvement in the genesis of the world-class Panasqueira W-Sn-Cu vein deposit: a petrographic, mineralogical and geochemical study. *Minerals* 10, 562
- Martins I, Mateus A, Figueiras J, Rodrigues P, Pinto F (2020). Thermal evolution of the W-Sn(-Cu) Panasqueira ore system (Portugal): Insights from pyrite-pyrrhotite and arsenopyrite geothermometers. *Comunicações Geológicas* 107, Especial II, 69-74
- Mateus A, Figueiras J, Martins I, Rodrigues PC, Pinto F (2020). Relative abundance and compositional variation of silicates, oxides and phosphates in the W-Sn-rich lodes of the Panasqueira Mine (Portugal): implications for the ore-forming process. *Minerals* 10, 551.
- Noronha F, Doria A, Dubessy J, Charoy B (1992) Characterization and timing of the different types of fluids present in the barren and ore-veins of the W-Sn deposit of Panasqueira, Central Portugal. *Mineral. Deposita*, 27:72-79.
- Polya D (1989) Chemistry of the main-stage ore-forming fluids of the Panasqueira W-Cu(Ag)-Sn Deposit, Portugal: Implications for models of ore genesis. *Econ. Geol.*, 84: 1134-1152.
- Thadeu D (1951) Geologia do couro mineiro da Panasqueira. *Comun. Serv. Geol. Portg.* 32:5-64
- Thadeu D (1977) Hercynian paragenetic units of the Portuguese part of the Hesperic Massif. *Bol. Soc. Geol. Portg.* 20:247-276.
- Wimmers D (1985) Silver minerals of Panasqueira, Portugal: A new occurrence of Te-bearing canfieldite. *Mineral.Mag.* 49, 745–748.
- Whitney DL, Evans BW (2010) Abbreviations for names of rock-forming minerals. *Am Mineral*, 2010, 95, 185-187.

Ore-forming events at the W-rich Santa Comba deposit, NW Spain

Candela Pita¹, Fernando Tornos¹, Iñigo Borrajo¹, Lluís Boixet³, Elena Crespo²

¹ Geosciences Institute (IGEO, CSIC-UCM), Madrid, Spain.

² Complutense University of Madrid (UCM), Madrid, Spain.

³ Rafaella Resources, Brisbane, Queensland, Australia

Abstract. The NW of the Iberian Peninsula is known to have abundant W-Sn deposits associated with peraluminous Variscan granites. The Santa Comba deposit is one of them but despite being commonly known as a quartz vein swarm with W mineralization it also contains a large disseminated mineralization hosted by a porphyritic intrusion. The mineralization is zoned around and related to an epizonal, zoned intrusive complex that includes several units whose relationships fit the Exogranite-Stockscheider-Endogranite model. Disseminated ore is enriched in wolframite but from a certain depth becomes enriched in scheelite. Our findings show that in Santa Comba there are four events of tungsten mineralization associated with three different ore-forming events with different compositions and ore-trapping mechanisms.

1 Introduction

The Santa Comba mine is located in NW Spain and is one of the largest tungsten deposits of Iberia. Aside from the historically mined vein swarm mineralization, the hosting granite has disseminated W-Sn mineralization. This mineralization is found in the youngest magmatic intrusion (endogranite) of several units that define an epizonal, zoned poly-intrusive complex of late Variscan age.

Although the relationships between the units that comprise this magmatic complex fit the Exogranite-Stockscheider-Endogranite model proposed by Nesen (1979), Santa Comba is a rather unique and poorly studied type of deposit. The disseminated mineralization seems to be related to zones of pervasive high-temperature hydrothermal alteration and stockwork-like systems, sometimes sharing features with porphyry-like deposits.

Mineralogy includes both hubnerite (MnWO_3) and ferberite (FeWO_3); they usually form zoned crystals and are commonly associated with scheelite (CaWO_4). Disseminated scheelite becomes increasingly important with depth but is also present concentrated in veins. The relationship between the two tungsten ores has genetic implications since scheelite and wolframite have different compositions and precipitate under different T-P-X conditions.

In this study, we explore the nature and implications of the tungsten-bearing assemblages to gain a better understanding of the ore-forming events.

2 Geology of Santa Comba

2.1 Geological setting

The Santa Comba mine is about 45 km northwest of Santiago de Compostela, Galicia, Spain. The

deposit is within the Iberian Massif, in the westernmost section of the Variscan Orogen (Martínez Catalán et al. 1990). Here, a Neoproterozoic to Early Paleozoic Terrane (Central Iberian Zone) is overthrust by rocks with oceanic affinities that belong to the Allochthonous Terrain of Galicia-Trás-os-Montes (Fig. 1).

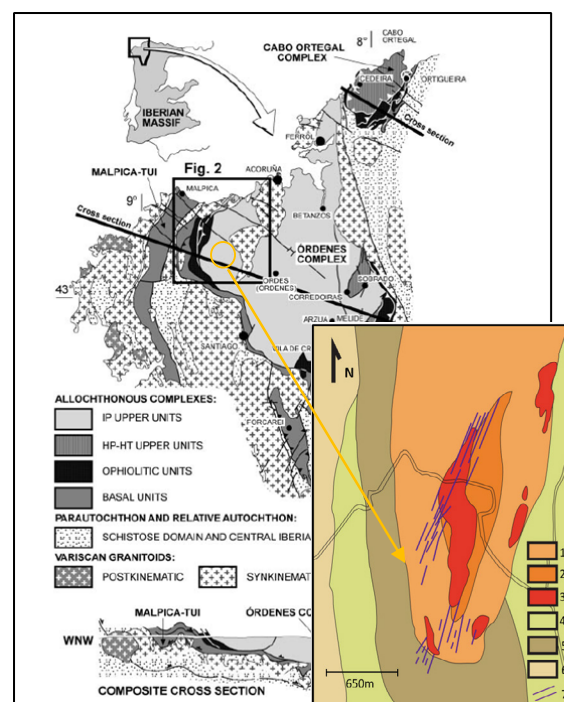


Figure 1. To the left: Map and geological section showing the three Allochthonous Complexes mentioned and their location within the Iberian Massif (modified from Abati et al. 2003). To the right: Geological map of Santa Comba (modified from Borrajo et al. 2022). 1-2: exogranite; 3: endogranite; 4: Ordenes Complex; 5: orthogneisses; 6: schists; 7: quartz veins with Sn-W.

The area includes widespread peraluminous magmatism associated with crustal thickening and later orogenic collapse related to the collision of Gondwana and Laurasia, between 330-285 My ago (Gutiérrez-Alonso et al. 2011). The mineralization and the hosting intrusion are located in a pull-apart structure formed on a major N-S dextral shear zone that bounds the contact between both Terranes.

2.2 Geology of the mineralization

The Santa Comba Plutonic Complex includes four different lithologies, all of them showing a penetrative N-S magmatic foliation. There are two

barren external units. The outer intrusion is a two-mica porphyritic granite with abundant biotite whereas the inner unit is somewhat similar but muscovite is the more prominent mica.

The youngest and most internal unit of the complex is a leucocratic equigranular granite (endogranite) with pervasive hydrothermal alteration. Apart from the absence of biotite, its most distinctive feature is the presence of a "stockscheider" that shapes the contact between the endogranite and the muscovite-rich exogranite. Nesen (1979) described this rock as consisting primarily of large, up to 10 cm long, crystals of perthitic alkaline feldspar that grow inwards to the youngest intrusion. These structures are spatially related to an alternating tourmaline-rich and albite-rich banding and probably limit a cooling carapace of the endogranite.

Due to the presence of abundant tourmaline along large areas of the endogranite, Cuenin (1982) also differentiated between common endogranite (rich in muscovite) and tourmaline-rich endogranite. In general, foliation in the tourmaline-rich facies is more diffuse.

2.3 The hydrothermal alteration of the endogranite

The endogranite shows a pervasive hydrothermal alteration that includes an early albitization of oligoclase followed by a potassic alteration with the growth of K-feldspar + muscovite and a later quartz + muscovite (phyllic) alteration. Quartz is the only residual magmatic phase; early quartz occurs as large (3–4 mm) subhedral grains with evidence of brittle-ductile deformation. Later hydrothermal quartz occurs as significantly smaller anhedral grains intergrown with muscovite. There are also two generations of muscovite. Early muscovite crystals are large and deformed while the younger muscovite grains related to the phyllic alteration are much smaller, replacing K-feldspar or intergrown with quartz.

The endogranite also includes large but scarce pods of greisen alteration of uncertain chronology. It is a coarse-grained rock including muscovite, tourmaline, quartz, and sometimes topaz. This evolution suggests that exsolved fluids accumulated below the carapace were in equilibrium with the host granite leading to potassic alteration; later cooling would drop the pH and form the phyllic alteration.

3 The mineralization

Wolframite, scheelite, and cassiterite occur both disseminated in the leucogranite and in later hydrothermal veins. The disseminated mineralization includes mm-sized, randomly located, anhedral to subhedral grains of wolframite I with less abundant cassiterite. They seem to be related to the most tourmaline-rich facies of the endogranite. Disseminated wolframite has a H/F ratio of ca. 52 and is usually associated with low-Mo

scheelite (scheelite I), which becomes the predominant phase at greater depths. Both wolframite I and scheelite I can be rimmed by a micron-thick layer of wolframite II (Fig. 2).

Crosscutting the endogranite, the exogranite and the host metamorphic rocks there is an N-S trending swam of quartz veins with coarse-grained wolframite II which has a more hubneritic composition, H/F= 63 (Table 1). They are accompanied by cassiterite and only have small selvages of muscovite. Wolframite shows a widespread replacement by late, also Mo-poor, scheelite II along grain edges and cracks (Fig. 2). In the veins, scheelite II is also associated with a late hydrothermal event as large, undeformed anhedral crystals intergrown with quartz, white mica, chlorite, and sulfides (arsenopyrite, pyrite, base metal sulfides), and gold (Fig. 3). These veins are channelized along extensional brittle structures related to late NE-SW shearing.

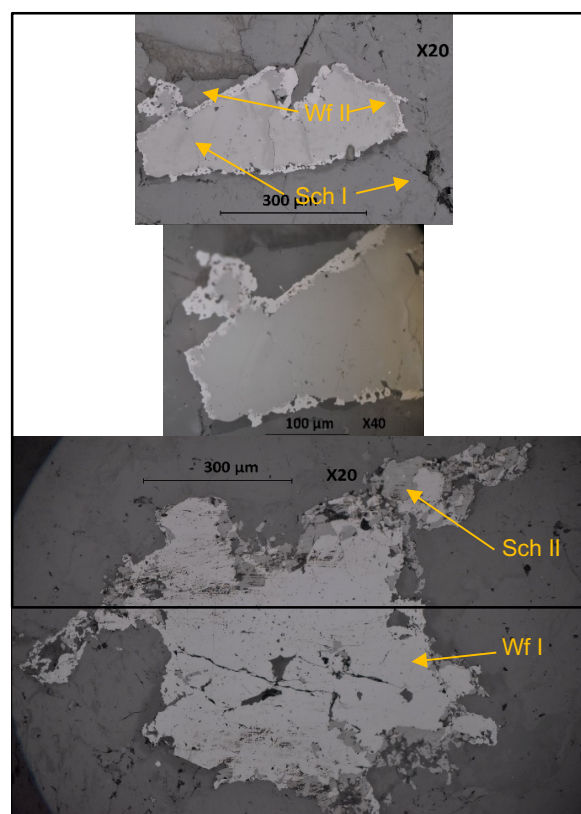


Figure 2. Microphotographs of two different wolframite-scheelite grains in the altered endogranite.

Of major interest is the presence of scheelite I, which is the dominant tungsten-bearing phase at depth in the disseminated ore and is coated by wolframite II or occurs as small inclusions in wolframite I and II. Scheelite I shows signs of deformation such as undulant extinction and fractures and hosts at least two generations of fluid inclusions (Fig. 3).

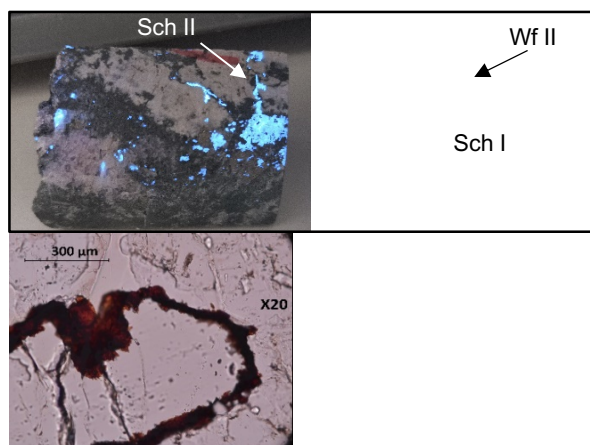


Figure 3. Scheelite-rich mineralization in the disseminated ore. Left: massive scheelite II replacing wolframite I (blue under UV light, sample 10 cm long). Right: Grain of scheelite I with an edge of wolframite II.

The temporal evolution of wolframite with an increase in the hubnerite endmember can be interpreted as related to an increase in the Mn/Fe ratio of the fluid during the later stages of the magmatic-hydrothermal evolution, matching the results of Borrajo et al. (2022). The ferberite/hubnerite ratio in the mineralization is controlled by the Fe/Mn ratio of the fluid, the K_D , and the temperature of precipitation.

	Stg 1		Stg 2	Stg 3
Element	Wf I	Sch I	Wf II	Sch II
FeO	13.34	0.02	8.29	0.17
MnO	11.77	0.00	16.13	0.15
MgO	0.00	0.00	0.00	0.00
CaO	0.02	21.09	0.15	21.27
Na ₂ O	0.00	0.00	0.00	0.00
K ₂ O	0.00	0.00	0.00	0.00
TiO ₂	0.01	0.00	0.00	0.00
NiO	0.00	0.00	0.00	0.02
Nb ₂ O ₅	0.77	0.00	0.02	0.00
MoO ₃	0.07	0.02	0.03	0.05
Ta ₂ O ₅	0.16	0.00	0.00	0.05
PbO	0.00	0.00	0.00	0.00
WO ₃	72.89	77.98	74.01	78.09
SnO ₂	0.02	0.00	0.02	0.00
Total	99.03	99.11	98.64	99.79

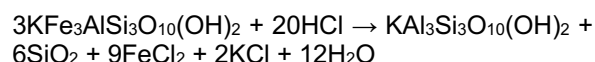
Table 1. Average compositions (wt.%) of the different generations of scheelite (Sch) and wolframite (Wf).

4 Discussion

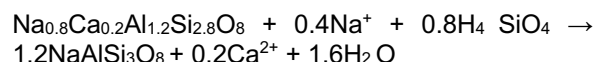
Mineralization at Santa Comba can be grouped into three ore-forming events. Scheelite I and wolframite I would co-precipitate during the First Stage as disseminated mineralization while wolframite II

would represent the Second Stage and scheelite II the Third Stage (Fig 4).

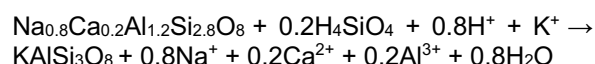
We interpret the First Stage as the precipitation of tungsten during granite replacement due to metasomatic alteration. This is done by the reaction of ascending fluids with an already consolidated carapace. The reactions involved in this process would be similar to the ones described by Pollard and Taylor (1986) but on a much larger scale (Fig. 5). The first hydrothermal fluids reacting with the endogranite cupola would induce the replacement of biotite by muscovite in the endogranite following the reaction



An increase in $a\text{Fe}^{2+}/a\text{H}^{+2}$ due to the destruction of biotite would promote the early precipitation of ferberite. Deeper replacement of magmatic oligoclase by albite following the reaction



And then the replacement of oligoclase by K-feldspar



would increase $a\text{Ca}^{2+}/a\text{H}^{+2}$, promoting the precipitation of scheelite I since, as Wood and Samson (2000) describe, the Ca/Fe ratio of a solution in equilibrium with both scheelite and ferberite decreases strongly with increasing temperature, meaning that the field of stability of scheelite expands with increasing temperature.

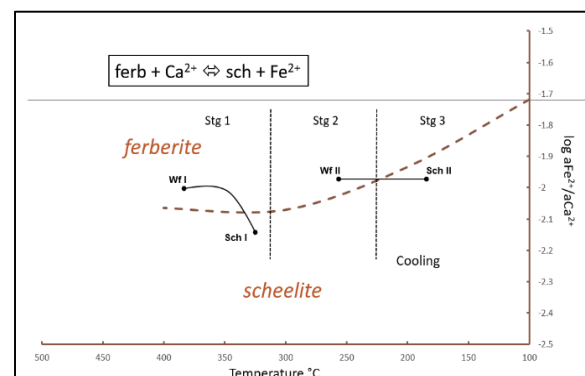


Figure 4. $\log a\text{Fe}^{2+}/a\text{Ca}^{2+}$ against temperature calculated from thermodynamic data of Dick (2019).

During late-hydrothermal stages, the entrance of fluids with increased Mn/Fe and Mn/Ca ratios would stabilize more Mn-rich wolframite II at the expense of scheelite and ferberite. This is consistent with the fact that evolving magmatic-hydrothermal fluids are gradually enriched in Mn due to the early precipitation of Fe-Ca-rich phases, stabilizing Mn-

bearing minerals in the very late assemblages (Burt 1977). Minor wolframite II would precipitate as hubneritic rims in both, wolframite I and scheelite I but become the main ore in the vein system. The Third stage would precipitate at lower temperatures, where scheelite is the dominant tungsten-bearing phase for a wide range of $a\text{Fe}^{2+}/a\text{Ca}^{2+}$ ratios (Fig. 4).

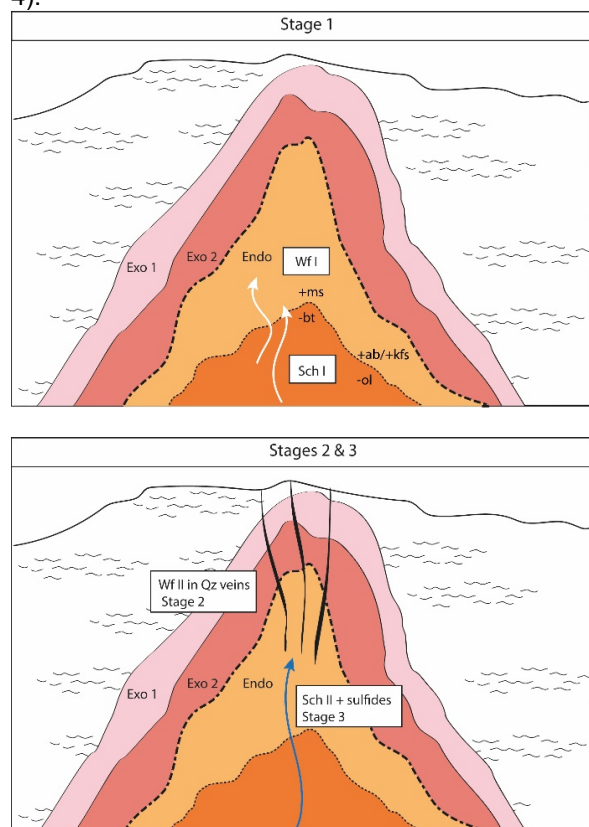


Figure 5. Diagram depicting the evolution of the endogranite during the different mineralization stages.

5 Conclusions

This preliminary study on the mineralogy of the disseminated W-Sn ore at Santa Comba suggests that hydrothermal alteration played a major role in the precipitation of tungsten-bearing minerals. Probably, the ultimate reason for the precipitation of ferberite, hubnerite, or scheelite is the availability and competition between Fe, Mn, and Ca in an evolving system. Limited availability of Fe in peraluminous granitoids, especially if hydrothermally altered, expands dramatically the

stability fields of scheelite and hubnerite. In extreme cases, scheelite can be the early phase to precipitate instead the more common presence of ferberite in other more Fe-rich systems.

Acknowledgments

This study was conducted within the EIS (Exploration Information System) project of Horizon Europe (contract 101057357). This study would not have been possible without a training scholarship granted by Rafaella Resources. We would like to thank César Casquet and Pedro Granda for their support and advice.

References

- Abati J, Arenas R, Martínez-Catalán JR, Díaz-García F (2003) Anticlockwise P-T path of granulites from the Monte Castelo Gabbro (Órdenes Complex, NW Spain): *J Petrol* 44:305-327.
- Borrajó I, Tornos F, Boixet L (2022). Porphyry-like magmatic-hydrothermal W-(Sn) mineralization: Fontao and Santa Comba deposits (northwestern Spain). 22nd Biennial SGA Meeting Abstract volume.
- Burt DM (1977). Mineralogy and petrology of skarn deposits. *Rend Soc It Min e Pet* 33:859–873.
- Cuenin O (1982) Interpretation des lèvres géologiques dans la mine de Santa-Comba Galice Espagne. Dissertation, University of Nancy.
- Dick JM (2019) CHNOSZ: Thermodynamic calculations and diagrams for geochemistry. *Front Earth Sci* 7:108.
- Gutiérrez-Alonso G, Fernández-Suárez J, Jeffries TE, Johnston ST, Pastor-Galán D, Murphy JB, Gonzalo JC (2011) Diachronous. post-orogenic magmatism within a developing orocline in Iberia, European Variscides. *Tectonics*: 30:1-17.
- Martínez-Catalán JR (1990) A non-cylindrical model for the northwest Iberian allochthonous terranes and their equivalents in the Hercynian belt of Western Europe. *Tectonophysics* 179: 253-272.
- Nesen G (1979) Les endogranites a stockscheider de Fontao et Santa Comba, Galice Espagne: un nouveau modele de gisement Sn-W en Galice. In: VI Reunión sobre la geología del NW de la Península Ibérica Oviedo 1979.
- Pollard PJ, Taylor RG (1986) Progressive evolution of alteration and tin mineralization; controls by interstitial permeability and fracture-related tapping of magmatic fluid reservoirs in tin granites. *Econ Geol*; 81: 1795–1800.
- Wood SA, Samson I (2000). The Hydrothermal Geochemistry of Tungsten in Granitoid Environments: I. Relative Solubilities of Ferberite and Scheelite as a Function of T, P, pH, and mNaCl. *Econ Geol*. 95: 143-182.

feldspar Eibenstock granite in Germany. There is a subtle compositional trend from the least altered (i.e., those with mica without clays or zeolites) through kaolinite-dominant to smectite-dominant Lithium-rich Tuff samples toward the field of hydrothermal vein fluorite (Fig. 8b). This suggests sub-solidus metasomatic reactions with fluids enriched in a variety of ligands (e.g., B, F), leading to fractionation between geochemical twin pairs – i.e., non-CHARAC behavior – due to selective molecular complexation (Bau 1996). For example, F-complexes are more stable for Y than Ho and hence would explain the higher Y/Ho in most Lithium-rich Tuff samples relative to CHARAC. Also, Zr/Hf ratios <25 in peraluminous granites are often interpreted to reflect sub-solidus hydrothermal alteration by F-rich, acidic, reduced fluids of magmatic origin (Ballouard et al. 2016).

Finally, the samples 2021-MAC-038 and 2021-MAC-051 stand as outliers in most compositional diagrams (Figs. 6, 8). The sample 2021-MAC-038 has a relatively low LOI value (2 wt.%) and yields the lowest contents of high-field strength elements and ΣREE (Fig. 5). Since the stability of $[\text{REE}(\text{F})_2]^-$ complexes increases from La to Lu, the observed higher $(\text{La}/\text{Sm})_{\text{CN}}$ in this sample may reflect REE leaching by fluids distinctively enriched in F. Further, the anomalously high Zr and Y (up to 714 and 48 ppm, respectively) contents, and super-CHARAC Zr/Hf and Y/Ho ratios (up to 315 and 41, respectively; Fig. 8) in both 2021-MAC-038 and 2021-MAC-051 suggest strong metasomatic enrichment by F-rich fluids under neutral to alkaline pH (see Inguaggiato et al. 2015), in contrast to the acidic alteration conditions constrained for the rest of the Lithium-rich Tuff samples.

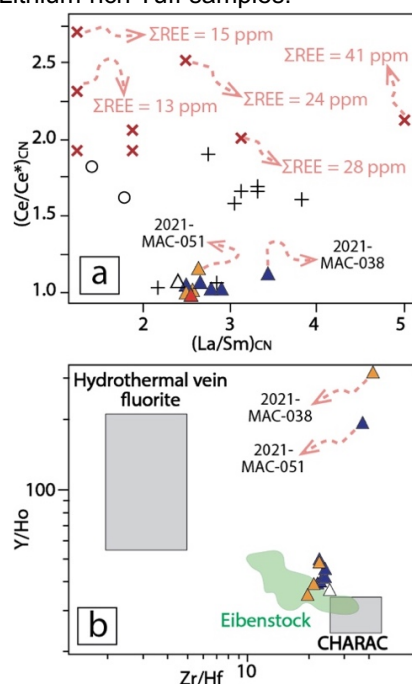


Figure 8. Trace element ratio bivariate plots of Lithium-rich Tuff, ash-flow tuffs, and 'macusanite'. (a) $(\text{La}/\text{Sm})_{\text{CN}}$ vs $(\text{Ce}/\text{Ce}^*)_{\text{CN}}$ plot. (b) Zr/Hf vs Y/Ho plot showing fields

of Eibenstock granite after Bau (1996). Symbols as in Fig. 3.

6 Conclusions

The composition of Lithium-rich Tuff samples from the MVF indicates derivation from a strongly peraluminous rhyolitic magma. Incompatible trace element compositions and CN REY patterns of Lithium-rich Tuff samples are more similar to those of 'macusanite' than to previously reported ash-flow tuffs from the MVF suggesting a higher proportion of 'macusanite'-like glass in the tuff previous to its alteration. Major element compositions reflect alkali and silica leaching during feldspar hydrolysis under acidic conditions and the formation of secondary clays (Ca-Mg-smectite in the most pervasively altered samples, and kaolinite) and zeolites. Incompatible trace element composition indicates post-depositional, metasomatic reactions with hydrothermal fluids enriched in complexing agents such as F.

Acknowledgements

We want to thank the geologists from Macusani Yellowcake for the help and hospitality during sampling tasks. This research work was supported by the Peruvian PROCENCIA-FONDECYT project 1122-2020 E041-2020-01-01.

References

- Bau M (1996) Controls on the fractionation of isovalent trace elements in magmatic and aqueous systems: evidence from Y/Ho, Zr/Hf and lanthanide tetrad effect. *Contrib Mineral Petrol* 123:323–333.
- Ballouard C, Poujol M, Boulvais P, Branquet Y, Tartèse R, Vigneresse JL (2016) Nb-Ta fractionation in peraluminous granites: A marker of the magmatic-hydrothermal transition. *Geology* 44:231–234.
- Cheilletz A, Clark AH, Farrar E, Arroyo Pauca G, Pichavant M, Sandeman HA (1992) Volcano-stratigraphy and $^{40}\text{Ar}/^{39}\text{Ar}$ geochronology of the Macusani ignimbrite field: monitor of the Miocene geodynamic evolution of the Andes of southeast Peru. *Tectonophysics* 205:307–327.
- García D, Fontelles M, Moutte J (1994) Sedimentary fractionations between Al, Ti, and Zr and the genesis of strongly peraluminous granites. *J Geol* 102:411–422.
- Inguaggiato C, Censi P, Zuddas P, Londono JM, Chacon Z, Alzate D, Brusca L, D'Alessandro W (2015) Geochemistry of REE, Zr and Hf in a wide range of pH and water composition: The Nevado del Ruiz volcano-hydrothermal system (Colombia). *Chem Geol* 417:125–133.
- Li V (2016) The uranium mineralization of the Macusani District, southeast Peru: Mineralogy, geochemistry, geochronology and ore-genetic model. Doctoral dissertation, Queen's University, Canada.
- López JC (1996) Geología del cuadrángulo de Nuñoa. Hoja 29-u. Instituto Geológico, Minero y Metalúrgico, pp 1–171.
- López Steinmetz RL, Salvi S (2021) Brine grades in Andean salars: When basin size matters. A review of the Lithium Triangle. *Earth Sci Rev* 217:103615.
- McDonough WF, Sun SS (1995) Composition of the Earth. *Chem Geol* 120:223–253.
- Munthali NW, Johan E, Aono H, Matsue N (2015) Cs^+ and Sr^{2+} adsorption selectivity of zeolites in relation to radioactive decontamination. *J Asian Ceram Soc* 3:245–250.
- Nupen S (2019) Mineral resource estimates for the Falchani Lithium Project in the Puno District of Peru - under the guidelines of national instrument 43-101. The Mineral Corporation, Bryanston, pp 1–72.

Major and trace element composition of the Lithium-rich Tuff from the Macusani Volcanic Field, Puno, Peru

Johan S. Ramírez-Briones¹, Lisard Torró¹, Lorenzo Tavazzani², Loïs Monnier³, Oscar Laurent³, Mariana K. Segovia-More¹, Mercy K. Sanandres-Flores¹, Jean Vallance¹, Cyril Chelle-Michou², Stefano Salvi³, Patrice Baby^{1,3}

¹Geological Engineering Program, Faculty of Sciences and Engineering, Pontifical Catholic University of Peru, Peru

²Department of Earth Sciences, ETH Zürich, Switzerland

³GET-UMR CNRS/IRD/Univ. Paul Sabatier, Toulouse, France

Abstract. A major Li resource has been announced in the Falchani Lithium Project, Macusani Volcanic Field, Puno, Peru. The main Li host is the so-called Lithium-rich Tuff, in which Li values are mostly between 3,000 and 4,000 ppm. Major element compositions of Lithium-rich Tuff samples are consistent with alkali and silica leaching during feldspar hydrolysis and formation of clay (Ca-Mg-smectite in the most pervasively altered samples, and kaolinite) and zeolite minerals during hydrothermal alteration by acidic, reduced fluids rich in complexing agents such as F. The general composition of the Lithium-rich Tuff differs from that of previously reported ash-flow tuffs in the Macusani Volcanic Field. Rather, it approximates the composition of highly evolved peraluminous obsidian glasses known as 'macusanite'.

1 Introduction

The volcanogenic lithium Falchani Lithium Project hosts 60.9 Mt indicated resources grading 2,954 ppm Li and 260.1 Mt inferred resources grading 2,706 ppm Li (<https://americanlithiumcorp.com/falchani-lithium-project>). It is located 750 km to the northeast of the so-called *Lithium Triangle of the Andes* (López Steinmetz and Salvi 2021) (Fig. 1), which contains more than 50% of the global Li resources. The mineralization at Falchani is hosted by pyroclastic horizons of the Macusani Volcanic Field (MVF), chiefly in a unit referred to as Lithium-rich Tuff in which Li attains contents higher than 4,000 ppm (Nupen 2019). These tuffs, deposited in a lacustrine environment (Nupen 2019), are variably altered to clays and zeolites (Segovia-More et al. 2023). In this abstract, we discuss the magmatic provenance and post-depositional alteration of the Lithium-rich Tuff from a geochemical perspective.

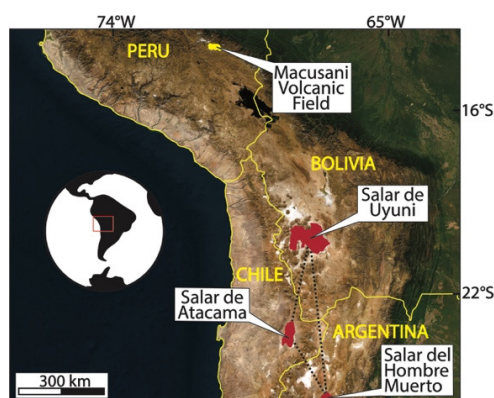


Figure 1. Location of the Macusani Volcanic Field (Peru) and the *Lithium Triangle of the Andes*.

2 Geological setting

The MVF is the northernmost Oligocene-Miocene volcanic field in the NW-trending Macusani Structural Zone (Perez et al. 2016) (formerly known as the Precordillera de Carabaya; Sandeman et al. 1997) of the southern Peruvian Eastern Cordillera. These volcanic fields rest on sialic Paleozoic basement, Triassic syn-rift continental deposits and intra-plate alkaline basalts (Mitu Group) and, to a lesser extent, pre-Oligocene marine siliciclastic rocks (Perez et al. 2016). Tertiary extrusive rocks in the Macusani Structural Zone were grouped by Sandeman et al. (1997) into the Crucero Supergroup, which exhibits two petrologically and temporally distinct suites: i) late Oligocene–early Miocene S-type rhyodacites and rhyolites, high-K calc-alkaline basalts, and shoshonites of the Picotani Group; and ii) mid- to late-Miocene, strongly peraluminous, S-type rhyolites of the Quenamari Group.

The Macusani Formation, the youngest unit of the Quenamari Group of Sandeman et al. (1997), is amply exposed in the MVF. It encompasses 250 to 450-m-thick unwelded, poorly stratified, crystal-rich, rhyolitic pyroclastic flows of ash- and lapilli-sized fragments and unusual accessory mineral phases such as sillimanite, andalusite, muscovite, and tourmaline (Cheilletz et al. 1992). Two volcanic eruptive events were dated by Cheilletz et al. (1992) at 10 ± 1 (Lower member) and 7 ± 1 Ma (Upper member). López (1996) has proposed the subdivision of the Macusani Formation (in full synonymy with 'Quenamari Formation') into 3 members: the Chacacuniza Member (equivalent to the Lower member of Cheilletz et al. 1992), the Sapanuta Member, and the Yapamayo Member. The Lithium-rich Tuff described in the Falchani Lithium Project is stratigraphically correlated with the Sapanuta Member (Nupen 2019).

Noteworthy, the MVF first caught the interest of the geoscientific community in the 1920s due to the discovery of 'macusanite', a rhyolitic glass extremely enriched in incompatible lithophile elements (e.g., up to 3,717 ppm Li) and with an exotic mineralogy including andalusite and sillimanite phenocrysts. It was interpreted as a rare case of extreme fractionation of felsic peraluminous magmas (Pichavant et al. 1987). Its extrusion was coeval with the deposition of the Macusani Formation between ca. 8 and 4 Ma (Cheilletz et al. 1992; Pichavant et al. 1987; Poupeau et al. 1993).

3 Methodology

Twelve Lithium-rich Tuff samples from outcrops and three drill holes in Falchani Lithium Project were analyzed. Major and trace element contents were measured on fused lithium tetraborate beads. Major element compositions were determined by X-ray fluorescence (XRF) using a Bruker-S8 Tiger at PUCP, Peru. Trace elements were analyzed by laser ablation-inductively coupled plasma-mass spectrometry (LA-ICP-MS) using a 193-nm ArF Excimer laser with an ELAN 6100 DRC quadrupole mass spectrometer, at ETH in Zurich, Switzerland.

4 Results

The major composition of Lithium-rich Tuff samples comprises SiO_2 (60.4-73.9 wt.%), Al_2O_3 (14.0-20.1 wt.%), K_2O (1.3-6.8 wt.%), and Na_2O (1.3-4.6 wt.%; Fig. 2). Other elements found in minor amounts (TiO_2 , FeO , MnO , MgO , CaO , and P_2O_5) add to 1.2 wt.%, on average. LOI values are higher in smectite-dominant (8.2-13.5 wt.%) samples than in kaolinite-dominant (2.0-4.4 %) samples (Fig. 2). In the TAS diagram, most samples plot in the rhyolite field (Fig. 3). However, a positive covariance between $\text{K}_2\text{O}+\text{Na}_2\text{O}$ and SiO_2 ($r = 0.8$) is observed, indicating progressive depletion in alkalis and silica toward the samples most pervasively altered to smectite and zeolite. TiO_2 contents remain nearly constant and show positive correlation with Al_2O_3 ($r = 0.8$) reflecting residual enrichment (Fig. 4).

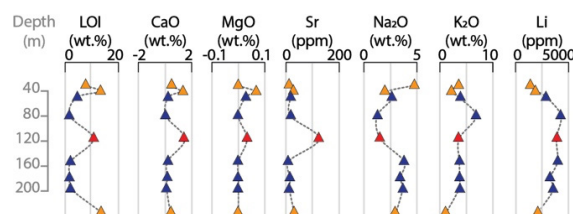


Figure 2. Compositional vertical profiles of Lithium-rich Tuff drill-hole samples. Symbols as in Fig. 3.

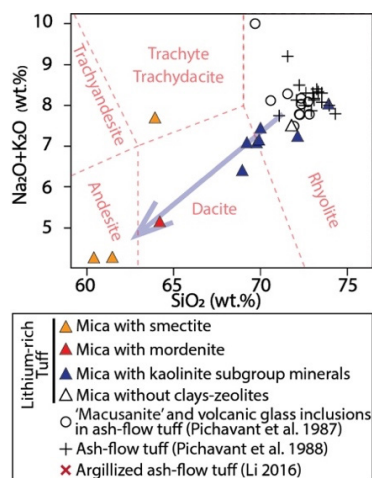


Figure 3. $\text{Na}_2\text{O}+\text{K}_2\text{O}$ vs SiO_2 (TAS) plot of Lithium-rich Tuff samples, ash-flow tuffs, and 'macusanite'. Mineralogical groups of Lithium-rich Tuff after Segovia-More et al. (2023).

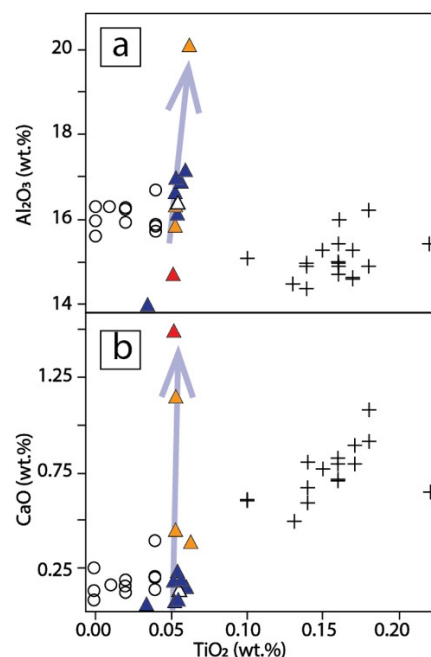


Figure 4. (a) TiO_2 vs Al_2O_3 plot and (b) TiO_2 vs CaO plot of volcanic rocks from the MVF. Symbols as in Fig. 3.

The abundances of most trace elements analyzed are normally <100 ppm. However, the contents of Cs (210-8,993 ppm), Rb (540-2,177 ppm), Sn (175-274 ppm), and Be (54-271 ppm) are conspicuously high. Total rare earth element contents (ΣREE) are in the range of 12.3 to 21.6 ppm, and of Y, in the range of 4.3 to 48.1 ppm. Chondrite-normalized (CN) REY (lanthanides + Y) patterns display negative slopes and systematic strong negative Eu anomalies ($(\text{Eu}/\text{Eu}^*)_{\text{CN}} = 0.1\text{-}0.2$; Fig. 5). Two samples exhibit a differential strong positive anomaly of Y.

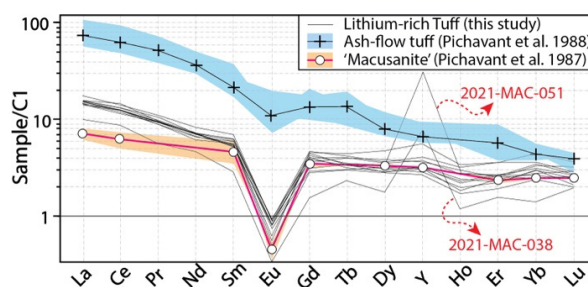


Figure 5. Chondrite-normalized REY patterns (C1 values after McDonough and Sun 1995) of Lithium-rich Tuff samples. Average (line) and upper and lower (shaded colors) values for 'macusanite' and ash-flow tuffs are shown.

5 Discussion

5.1 Magmatic source rocks

All Lithium-rich Tuff samples (except 2021-MAC-038 and 2021-MAC-051), 'macusanite' (data from Pichavant et al. 1987), and ash-flow tuffs (data from Pichavant et al. 1988) from the MVF plot in the field of strongly peraluminous (1.5-3.1 aluminum-saturation index) igneous rocks in the $\text{Zr}-\text{Al}_2\text{O}_3-\text{TiO}_2$ ternary diagram (Fig. 6).

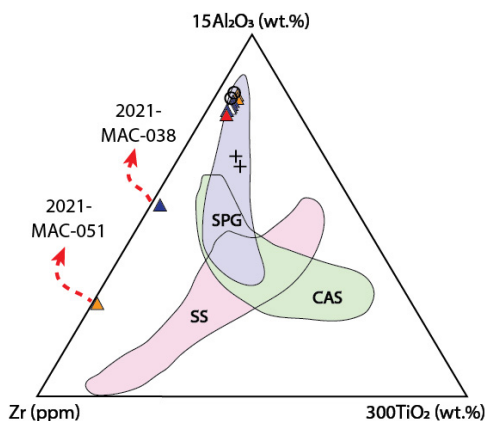


Figure 6. Composition of Lithium-rich Tuff samples, ash-flow tuffs (Pichavant et al. 1988), and 'macusanite' (Pichavant et al. 1987) in the provenance discrimination plot for weathered rocks after García et al. (1994). Symbols as in Fig. 3. Key: SPG: strongly peraluminous granite; CAS: calc-alkaline igneous suites; SS: shales and sandstones.

In general, Lithium-rich Tuff samples are closer in composition to 'macusanite' than to ash-flow tuffs except for enrichment in Be, Cu, Zr, Mo, Cs, and TiO_2 , and a strong depletion in V, Tl, and Pb (Fig. 7). Likewise, Lithium-rich Tuff samples generally show similar CN REY patterns as 'macusanite' except for slightly higher La/Sm values (Fig. 5). In contrast, ash-flow tuffs yield higher ΣREE , $(\text{La}/\text{Sm})_{\text{CN}}$, and $(\text{Sm}/\text{Yb})_{\text{CN}}$, and much lower Eu negative anomalies relative to Lithium-rich Tuff samples.

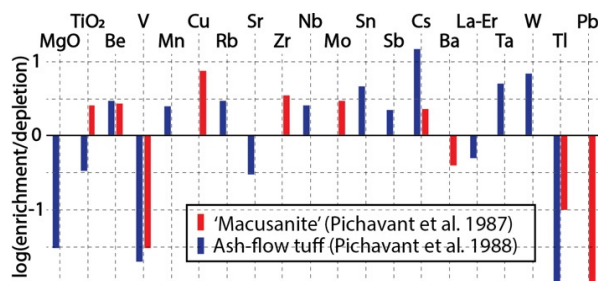


Figure 7. Enrichment/depletion patterns of average values for selected elements in Lithium-rich Tuff samples compared to ash-flow tuffs and 'macusanite'.

The fact that the Lithium-rich Tuff samples are compositionally more akin to 'macusanite' than to previously reported ash-flow tuffs could reflect a major component of highly evolved volcanic glass (equivalent or similar to 'macusanite') in this unit, previous to its alteration. Noteworthy, Torró et al. (2023) have described contrasting compositions for micas (zinnwaldite and lepidolite) hosted in the 'Li-rich tuff' relative to micas in other pyroclastic and intrusive rocks from the MVF, suggesting crystallization from a more evolved rhyolitic magma.

5.2 Geological controls on the composition of the Lithium-rich Tuff

The observed $\text{K}_2\text{O}+\text{Na}_2\text{O}$ and SiO_2 depletion (Fig. 3) and CaO and Al_2O_3 enrichment (Fig. 4) trends in Lithium-rich Tuff samples connect the compositions

of smectite-rich and kaolinite-rich tuffs and are consistent with alkali and silica leaching during feldspar hydrolysis under acidic conditions and clay formation. Higher LOI, CaO, and MgO contents accord well with a predominance of Ca(-Mg)-smectite in the most pervasively altered samples (Fig. 2). Li (2016) also documented widespread argillic alteration in ash-flow tuffs from the eastern sector of the MVF characterized by the crystallization of Ca-smectite and illite, the latter with exceptionally high F contents (7.8-8.7 wt.%). Lower $(\text{Ce}/\text{Ce}^*)_{\text{CN}}$ in Lithium-rich Tuff samples compared to the altered samples analyzed by Li (2016) (Fig. 8a) suggests alteration under more reducing conditions in the former. On the other hand, the strong positive correlation between Sr and Cs ($r = 0.99$) and the distinctively high contents of these two elements in the sample 2021-MAC-053 are consistent with Cs^+ and Sr^{2+} being selectively adsorbed by zeolites such as mordenite (e.g., Munthali et al. 2015).

CHARAC (i.e., CHARGE-and-RADIUS-Controlled; Bau 1996) behavior in geochemical systems means that elements partition is controlled by ion's charges and radii and that isovalent elements with similar radii retain their respective chondritic ratios. In the Y/Ho vs Zr/Hf diagram shown in Figure 8b, most samples plot in a narrow area outside the CHARAC field and display similar compositions as the autometasomatized topaz-zinnwaldite, alkali-feldspar Eibenstock granite in Germany. There is a subtle compositional trend from the least altered (i.e., those with mica without clays or zeolites) through kaolinite-dominant to smectite-dominant Lithium-rich Tuff samples toward the field of hydrothermal vein fluorite (Fig. 8b). This suggests sub-solidus metasomatic reactions with fluids enriched in a variety of ligands (e.g., B, F), leading to fractionation between geochemical twin pairs – i.e., non-CHARAC behavior – due to selective molecular complexation (Bau 1996). For example, F-complexes are more stable for Y than Ho and hence would explain the higher Y/Ho in most Lithium-rich Tuff samples relative to CHARAC. Also, Zr/Hf ratios < 25 in peraluminous granites are often interpreted to reflect sub-solidus hydrothermal alteration by F-rich, acidic, reduced fluids of magmatic origin (Ballouard et al. 2016).

Finally, the samples 2021-MAC-038 and 2021-MAC-051 stand as outliers in most compositional diagrams (Figs. 6, 8). The sample 2021-MAC-038 has a relatively low LOI value (2 wt.%) and yields the lowest contents of high-field strength elements and ΣREE (Fig. 5). Since the stability of $[\text{REE}(\text{F})_2]^-$ complexes increases from La to Lu, the observed higher $(\text{La}/\text{Sm})_{\text{CN}}$ in this sample may reflect REE leaching by fluids distinctively enriched in F. Further, the anomalously high Zr and Y (up to 714 and 48 ppm, respectively) contents, and super-CHARAC Zr/Hf and Y/Ho ratios (up to 315 and 41, respectively; Fig. 8) in both 2021-MAC-038 and 2021-MAC-051 suggest strong metasomatic enrichment by F-rich fluids under neutral to alkaline pH (see Inguaggiato et al. 2015), in contrast to the

acidic alteration conditions constrained for the rest of the Lithium-rich Tuff samples.

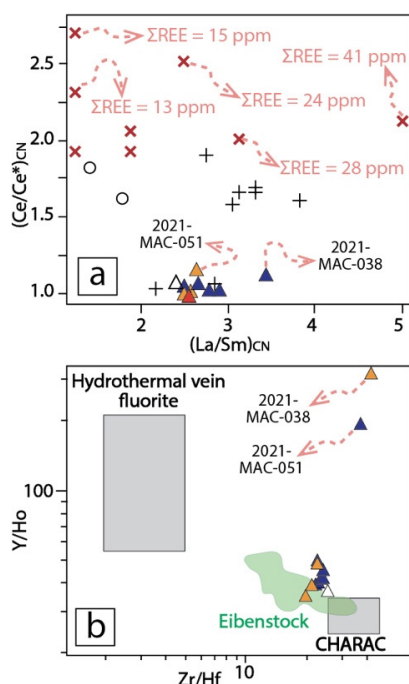


Figure 8. Trace element ratio bivariate plots of Lithium-rich Tuff, ash-flow tuffs, and 'macusanite'. (a) $(La/Sm)_{CN}$ vs $(Ce/Ce^*)_{CN}$ plot. (b) Zr/Hf vs Y/Ho plot showing fields of Eibenstock granite after Bau (1996). Symbols as in Fig. 3.

6 Conclusions

The composition of Lithium-rich Tuff samples from the MVF indicates derivation from a strongly peraluminous rhyolitic magma. Incompatible trace element compositions and CN REY patterns of Lithium-rich Tuff samples are more similar to those of 'macusanite' than to previously reported ash-flow tuffs from the MVF suggesting a higher proportion of 'macusanite'-like glass in the tuff previous to its alteration. Major element compositions reflect alkali and silica leaching during feldspar hydrolysis under acidic conditions and the formation of secondary clays (Ca-Mg-smectite in the most pervasively altered samples, and kaolinite) and zeolites. Incompatible trace element composition indicates post-depositional, metasomatic reactions with hydrothermal fluids enriched in complexing agents such as F.

Acknowledgements

We want to thank the geologists from Macusani Yellowcake for the help and hospitality during sampling tasks. This research work was supported by the Peruvian PROCENCIA-FONDECYT project 1122-2020 E041-2020-01-01.

References

Bau M (1996) Controls on the fractionation of isovalent trace elements in magmatic and aqueous systems: evidence

- from Y/Ho, Zr/Hf and lanthanide tetrad effect. *Contrib Mineral Petrol* 123:323–333.
- Ballouard C, Poujol M, Boulvais P, Branquet Y, Tartèse R, Vigneresse JL (2016) Nb-Ta fractionation in peraluminous granites: A marker of the magmatic-hydrothermal transition. *Geology* 44:231–234.
- Cheilletz A, Clark AH, Farrar E, Arroyo Pauca G, Pichavant M, Sandeman HA (1992) Volcano-stratigraphy and $^{40}Ar/^{39}Ar$ geochronology of the Macusani ignimbrite field: monitor of the Miocene geodynamic evolution of the Andes of southeast Peru. *Tectonophysics* 205:307–327.
- García D, Fontelles M, Moutte J (1994) Sedimentary fractionations between Al, Ti, and Zr and the genesis of strongly peraluminous granites. *J Geol* 102:411–422.
- Inguaggiato C, Censi P, Zuddas P, Londono JM, Chacon Z, Alzate D, Brusca L, D'Alessandro W (2015) Geochemistry of REE, Zr and Hf in a wide range of pH and water composition: The Nevado del Ruiz volcano-hydrothermal system (Colombia). *Chem Geol* 417:125–133.
- Li V (2016) The uranium mineralization of the Macusani District, southeast Peru: Mineralogy, geochemistry, geochronology and ore-genetic model. Doctoral dissertation, Queen's University, Canada.
- López JC (1996) Geología del cuadrángulo de Nuñoa. Hoja 29-u. Instituto Geológico, Minero y Metalúrgico, pp 1–171.
- López Steinmetz RL, Salvi S (2021) Brine grades in Andean salars: When basin size matters. A review of the Lithium Triangle. *Earth Sci Rev* 217:103615.
- McDonough WF, Sun SS (1995) Composition of the Earth. *Chem Geol* 120:223–253.
- Munthali NW, Johan E, Aono H, Matsue N (2015) Cs^+ and Sr^{2+} adsorption selectivity of zeolites in relation to radioactive decontamination. *J Asian Ceram Soc* 3:245–250.
- Nupen S (2019) Mineral resource estimates for the Falchani Lithium Project in the Puno District of Peru - under the guidelines of national instrument 43-101. The Mineral Corporation, Bryanston, pp 1–72.
- Perez ND, Horton BK, Carlotto V (2016) Structural inheritance and selective reactivation in the central Andes: Cenozoic deformation guided by pre-Andean structures in southern Peru. *Tectonophysics* 671:264–280.
- Pichavant M, Valencia Herrera J, Boulmier S, Briqueu L, Joron JL, Juteau M, Marin L, Michard A, Sheppard AMF, Treuil M, Vernet M (1987) The Macusani glasses, SE Peru: evidence of chemical fractionation in peraluminous magmas. In: Mysen BO (ed) *Magmatic processes, physicochemical principles*. *Geochem Soc Special Publ* 1:359–373.
- Pichavant M, Kontak DJ, Briqueu L, Valencia Herrera J, Clark AH (1988) The Miocene-Pliocene Macusani Volcanics, SE Peru - II. Geochemistry and origin of a felsic peraluminous magma. *Contrib Mineral Petrol* 100:325–338.
- Poupeau G, Labrin E, Sabil N, Bigazzi G, Arroyo G, Vatin-Pérignon N (1993) Fission-track dating of 15 macusanite glass pebbles from the Macusani volcanic field (SE Peru). *Nucl Tracks Radiat Meas* 21:499–506.
- Sandeman HA, Clark AH, Farrar E, Arroyo-Pauca G (1997) Lithostratigraphy, petrology and $^{40}Ar-^{39}Ar$ geochronology of the Crucero Supergroup, Puno Department, SE Peru. *J South Am Earth Sci* 10:223–245.
- Segovia-More MK, Torró L, Villanova-de-Benavent C, Ramírez-Briones J, Vallance J, Monnier L, Laurent O, Salvi S, Baby P, Proenza JA, Nieto F (2023). Mineralogy of 'lithium-rich tuffs' from the Macusani Volcanic Field, Puno, Peru. This volume.
- Torró L, Villanova-de-Benavent C, Monnier L, Laurent O, Segovia-More MK, Sanandres-Flores M, Ramírez-Briones J, Vallance J, Salvi S, Baby P, Proenza JA, Nieto F (2023) Lithium-bearing micas in tuffs from the Macusani Volcanic Field, Puno, Peru. This volume.

High-temperature meteoric water incursion in the Beauvoir rare-metal granite: insights from apatite

Océane Rocher¹, Julien Mercadier¹, Antonin Richard¹, Christophe Ballouard¹, Loïs Monnier², Oscar Laurent², Nordine Bouden³, Johan Villeneuve³, Patrick Fullenwarth⁴

¹ Université de Lorraine, CNRS, GeoRessources, Vandœuvre-lès-Nancy, France

² Université de Toulouse, CNRS, IRD, UPS, CNES, Géosciences Environnement Toulouse (GET), Toulouse, France

³ Université de Lorraine, CNRS, Centre de Recherche Pétrographique et Géochimiques, Vandœuvre-lès-Nancy, France

⁴ Imerys Ceramics France - Kaolins de Beauvoir, Echassières, France

Abstract. Magmatic and hydrothermal apatite generations of the Beauvoir rare-metal (Li-Ta-Nb-Sn-Be) granite (Massif Central, France) were investigated through textural observations, in-situ major elements (EPMA) and oxygen isotopic (SIMS) compositions in order to trace the origin(s) of fluids having affected the intrusion as well as their geochemical evolution. Magmatic apatite shows relatively low $\delta^{18}\text{O}$ values ($\sim 4\text{--}8\text{‰}$) corresponding to $\delta^{18}\text{O}_{\text{melt}}$ values of $\sim 5\text{--}10\text{‰}$ at 550°C , i.e., lower than expected for typical peraluminous granitic melts. This could be explained either by percolation into the magma of meteoric water, or by isotopic re-equilibration of magmatic apatite during subsolidus interaction with external fluids at $\sim 450\text{--}400^\circ\text{C}$. Furthermore, cathodoluminescence imaging reveals complex textures for hydrothermal apatite highlighting their partial recrystallisation and chemical modification with the evolution of fluid chemistry. The wide range of $\delta^{18}\text{O}$ values (-9 to $+13\text{‰}$) and Mn contents of hydrothermal apatite suggest a progressive mixing of reduced magmatic and oxidized meteoric fluids during metasomatism. Moreover, an interaction of greisen-related fluids with micaschist country-rocks is evidenced by relatively high $\delta^{18}\text{O}$ values and S concentration in one apatite generation. Our results support protracted oxidized meteoric fluid incursions in the Beauvoir granite, possibly from supra- to sub-solidus conditions, which may have significantly affected metal deposition processes.

1 Introduction

The Beauvoir granite (French Massif Central-FMC) is characterised by disseminated Sn-Li-Ta-Nb-Be mineralisation and represents one of the best examples worldwide of peraluminous high-phosphorus rare-metal granite (PHP-RMG; Cuney et al. 1992). Its mineralogical and geochemical evolution is closely linked to the hydrothermal system active from its crystallisation to its exhumation (Merceron et al. 1992; Cuney et al. 1992; Monnier et al. 2019). Previous fluid inclusion studies have shown the complex fluid circulations that affected the granite, in particular the mixing dynamics of magmatic and external fluids (Aïssa et al. 1987; Monnier et al. 2020), as well as hydrothermal mobility of rare metals during the magmatic-hydrothermal transition (Harlaux et al. 2017). As apatite [$\text{Ca}_5(\text{PO}_4)_3(\text{F,OH,Cl})$] is a common accessory mineral throughout the intrusion and occurs as several generations associated to the major fluid circulation episodes, we use its geochemistry and oxygen isotope composition to

trace the origin of hydrothermal fluids in the Beauvoir granite and their geochemical evolution.

2 Geological setting

The Echassières granitic complex of the northern FMC was emplaced within the internal zone of the European Variscan belt during its late-orogenic Carboniferous evolution. The complex consists of three granitic units that intruded the autochthonous micaschists of the Sioule metamorphic series: (i) the oldest La Bosse granite, concealed at depth and presumed to be at the origin of a quartz-wolframite vein system, the La Bosse stockwork; (ii) the Colettes granite, a cordierite-bearing two-mica granite; and (iii) the Beauvoir granite, an highly-evolved albite-lepidolite-topaz leucogranite hosting disseminated Sn-Li-Ta-Nb-Be mineralisation and characterised by the presence of three distinct magmatic facies (from top to bottom: B1, B2 and B3; Cuney et al. 1992).

The Beauvoir granite was emplaced at ca. 310–315 Ma (Cheilletz et al. 1992; Melleton et al. 2015) and has a complex magmatic-hydrothermal history. The intrusion, as well as the surrounding rocks, have been affected by several fluid circulation episodes, the two majors being (i) a greisenisation episode possibly triggered by the exsolution of magmatic fluids from the melt and having progressively mixed with external fluids and (ii) the late development of sub-vertical quartz veins, fluorite and low-temperature phosphate precipitation, and widespread kaolinisation (Merceron et al. 1992; Monnier et al. 2019). Greisen alteration has been particularly intense at the apical part of the Beauvoir granite but is also encountered at depth, especially at the transition zones between the three facies. It consists in the replacement of igneous minerals, essentially feldspar, by a quartz-muscovite assemblage, which is commonly associated with the precipitation of other secondary minerals, such as apatite and topaz.

3 Material and methods

Eleven samples taken from the historic drillhole GPF1 were studied. They are representative of the different generations of apatite occurring within the Beauvoir intrusion. Here, we focus on magmatic apatite encountered in the B2 and B3 facies, as

well as the distinct hydrothermal apatite generations observed in the B3 facies. The mineralogy and textural relationships were investigated using backscattered electron (BSE) and cathodoluminescence (CL) imaging, and major and minor element compositions were obtained using a Cameca SX100 electron microprobe (EMP) at GeoRessources. Oxygen isotopic composition was measured in the vicinity of EMP spots at the Centre de Recherches Pétrographiques et Géochimiques (CRPG) using a Cameca IMS 1280HR ion microprobe (SIMS). The analytical conditions were similar to those used by Decrée et al. (2020).

4 Results

4.1 Petrography

Although magmatic apatite was only described by Cuney et al. (1992) within the B2 and B3 facies, it seems to be present throughout the entire intrusive complex. Its colour varies from green to blue and it forms anhedral to sub-euhedral grains co-crystallising with magmatic topaz (Fig. 1a). It also commonly contains zircon inclusions, especially in the B2 facies. As expected for peraluminous granites, apatite shows a Mn^{2+} -activated yellow-greenish CL signal (Kempe and Götze 2002). It is characterized by a magmatic oscillatory zonation, evolving from a dark greenish to yellowish colour in the core to a relatively brighter rim, whereas altered areas have the brightest emission (Fig. 1a).

Petrographic observations revealed the existence of three hydrothermal apatite generations in the B3 facies (Fig. 2): (1) early hydrothermal, (2) greisen- and (3) late greisen-related apatite.

Early hydrothermal apatite (1) has been found in association with topaz, quartz and cassiterite within a vein (Fig. 1b). It shows a complex CL texture with dark primary areas replaced by brighter zones.

Greisen alteration is associated with a heterogeneous apatite population (2-3). *Greisen-related apatite* (2) locally forms anhedral crystals co-crystallising with a quartz-muscovite assemblage and is found as replacement of magmatic minerals such as feldspar, lepidolite or amblygonite (Fig. 1c). It has also been observed in greisen veins or greisenised zones as sub-euhedral to euhedral crystals associated with quartz \pm muscovite. Wolframite has been identified in two samples and seems related to greisen alteration and apatite crystallisation. Greisen-related apatite (2) CL signature is characterised by a more greenish colour than magmatic apatite. Finally, a *late greisen-related apatite type* (3) was identified as replacement of other phosphate minerals, potentially the Ca-Be phosphate herderite, in a greisenised area from the B3 facies. It differs from greisen-related apatite (2) by a distinctive orange CL signature (Fig. 1d).

4.2 Major elements content

Magmatic and early hydrothermal (1) apatite are F-rich (3.9– 5.5 wt% and 1.9– 3.7 wt% respectively) and are, thus, fluorapatite, whereas the greisen-related apatite population (2-3) shows heterogeneous F content ranging from 1.0 to 5.2 wt% (i.e., hydroxy- to fluoro-apatite). Mn content strongly vary between apatite generations from less than 0.25 wt% in late greisen-related apatite (3) up to ~4.6 wt% in magmatic apatite.

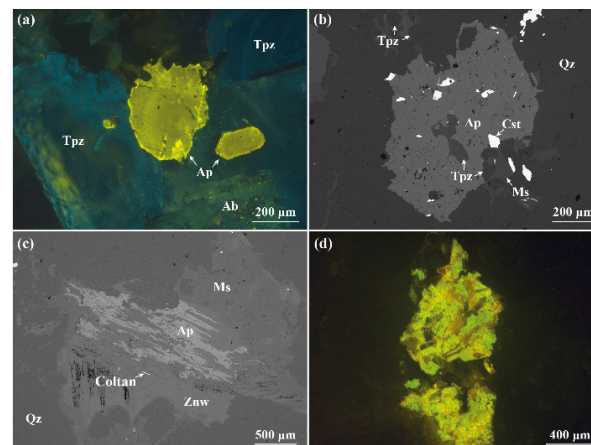


Figure 1. (a) CL image of magmatic apatite in the B2 facies; (b) BSE image of early hydrothermal apatite (1); (c) BSE image of greisen-related hydrothermal apatite (2) replacing igneous zinnwaldite (a Li-Fe-mica); (d) CL image of late greisen-related hydrothermal apatite (3). (Ab: albite, Ap: apatite, Cst: cassiterite, Ms: muscovite, Qz: quartz, Coltan: columbo-tantalite, Tpz: topaz, Znw: zinnwaldite)

4.3 Oxygen isotopic composition

The O isotopic compositions ($\delta^{18}O$) of magmatic apatite from the B2 and B3 facies range from 3.9 to 6.7 ‰ and 6.0 to 8.9 ‰, respectively. Hydrothermal apatite generations of the B3 facies show a wide range of $\delta^{18}O$ values, lying between 4.0 and 7.5 ‰ for early hydrothermal apatite (1), - 8.8 and +12.6 ‰ for greisen-related apatite (2), and -7.5 and +9.2 ‰ for late greisen-related apatite (3).

5 Discussion

5.1 Incursion of meteoric water at the magmatic stage?

Oxygen isotopic composition of the melt can be estimated from $\delta^{18}O$ data obtained for magmatic apatite using the crystal-melt temperature-dependent fractionation factor of Zhao and Zheng (2003) for rhyolitic melt (Fig. 2). $\delta^{18}O_{melt}$ values calculated for a crystallisation temperature of 550°C (Cuney et al. 1992; Pichavant 2022) range from 5.0 to 8.2 ‰ and 6.4 to 10.6 ‰ for the B2 and B3 units, respectively. Such values are significantly lower than the bulk rock $\delta^{18}O$

compositions of other variscan peraluminous granites, typically above 11 ‰ when their magmatic signature is preserved (Fig. 2; Bernard-Griffiths et al. 1985; Turpin et al. 1990; Tartèse and Boulvais 2010; Ballouard et al. 2017). The ^{18}O depletion of the melt could be explained by the exchange and interaction with meteoric water at high temperatures (Taylor 1968). Previous bulk-rock or mineral O isotope studies of the Beauvoir granite have already suggested the percolation into the magma of meteoric water having previously circulated within the host micaschists (Fouillac and Rossi 1991). They observed a decrease in $\delta^{18}\text{O}$ from the deepest B3 to shallowest B1 units, interpreted as reflecting an intensification of the interactions with surface-derived waters at the apical part of the intrusion. The decrease in $\delta^{18}\text{O}$ of magmatic apatite from the B2 to B3 units is also consistent with such phenomenon (Fig. 2).

The incursion of oxidizing meteoric water in the Beauvoir granite at the magmatic stage could have key implications regarding the crystallization kinetics of ore minerals; notably, because the solubility of redox sensitive element-bearing phases such as cassiterite (SnO_2) is expected to decrease drastically in granitic melt with increasing oxygen fugacity ($f\text{O}_2$) (Bhalla et al. 2005; Pichavant 2022).

Such interaction at suprasolidus conditions has however been questioned by Cuney et al. (1992), on the basis of fluid inclusion data, textural observations indicating a possible re-equilibration of igneous minerals and the evidence of disequilibrium in $\delta^{18}\text{O}$ data. They proposed that the interaction of the granite with external fluids occurred at lower temperatures (450 to 400°C), resulting in the isotopic re-equilibration of igneous minerals.

From the in-situ data presented here, it is difficult to favour any of these two hypotheses, yet; as magmatic apatite grains show little alteration on CL images, an isotopic re-equilibration at hydrothermal stage cannot be confirmed. Future study of fluid inclusions trapped into apatite crystals will probably provide key information to explain their relatively low $\delta^{18}\text{O}$ values.

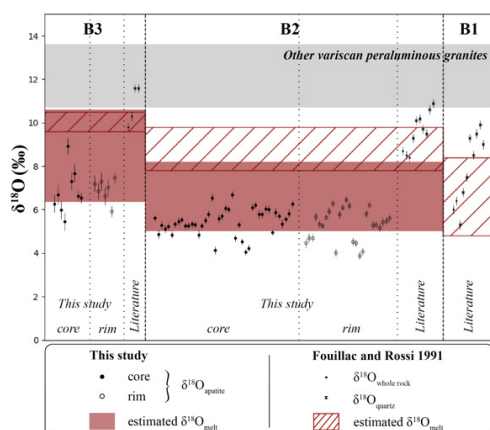


Figure 2. $\delta^{18}\text{O}$ data of magmatic apatite from the B2 and B3 facies (this study), of quartz and whole rock (Fouillac and Rossi 1991) and recalculated $\delta^{18}\text{O}$ of the melts in equilibrium using Zhao and Zheng (2003) fractionation factors and a crystallisation temperature of 550°C (Cuney et al. 1992; Pichavant 2022).

5.2 Sub-solidus evolution of the hydrothermal system

As shown for magmatic apatite, oxygen isotopic composition of the parent fluid can be estimated from $\delta^{18}\text{O}$ data of hydrothermal apatite through correction of the temperature-dependent fractionation (Fig. 3; Zheng 1996). Temperatures used derive from fluid inclusion studies. Early hydrothermal apatite (1) is presumed to have crystallised from magmatic fluids exsolved from the melts. These fluids were observed in fluid inclusions in the B1 facies and are characterised by homogenization temperatures (T_H) ranging from 370 to > 600°C (L1- and L2-fluids described by Aïssa et al. 1987 and Harlaux et al. 2017). Greisenising fluids inferred to be at the origin of hydrothermal apatite (2) resulted from the mixing between magmatic and external fluids and have been trapped into fluid inclusions of various petrographic properties and characterised by a wide range of T_H (400-190°C; Monnier et al. 2020). The petrographic heterogeneity of the greisen-related apatite population (2-3) could reflect the evolution of the magmatic-hydrothermal system over time. The late greisen-related apatite (3) could thus have crystallised from cooler greisenising fluids.

An overall decrease in $\delta^{18}\text{O}_{\text{fluid}}$ values is observed from early hydrothermal apatite (1) (3.4 to 8.0 ‰) to greisen-related (2) and late greisen-related apatite (3) (-13.9 to +12.0 ‰ and -12.6 to +8.6 ‰ respectively; Fig. 4a). This could be explained by the progressive mixing of magmatic fluids with ^{18}O -depleted external fluids which had already been outlined through the study of fluid inclusions (Aïssa et al. 1987). Negative values obtained for greisenising fluids, down to -13.9 ‰ for apatite crystallisation temperature ranging from 200 to 400°C, are characteristic of a meteoric origin.

We also observe a significant decrease in Mn concentrations of apatite, from more than 4.0 wt% for magmatic apatite to < 0.25 wt% for late greisen-related apatite (3). Mn content in apatite is dependent on magma or fluid compositions and $f\text{O}_2$ (Belousova et al. 2002 and references therein). Apatite preferentially incorporates Mn^{2+} over Mn^{3+} and Mn^{4+} as it directly substitutes for Ca^{2+} (Belousova et al. 2002). As previously suggested for other granite-related hydrothermal deposits from the Variscan belt (e.g., Ballouard et al. 2018), the progressive decrease of Mn content in apatite over time could thus be explained by $f\text{O}_2$ increase in the magmatic-hydrothermal system due to the progressive mixing with meteoric water. This is

consistent with the rough correlation between apatite Mn content and $\delta^{18}\text{O}$ values (Fig. 3).

The late greisen-related apatite generation (3) is characterised by the lowest Mn concentrations (< 0.25 wt%; Fig. 3b) and is also relatively enriched in S and Na (up to ~ 1.4 wt% and 1.1 wt% respectively). The strong correlation observed between S and Na content of the Beauvoir granite apatite (not shown) most likely results from the substitution scheme ($\text{SO}_4^{2-} + \text{Na}^+ = \text{PO}_4^{3-} + \text{Ca}^{2+}$; Pan et al. 2002). The enrichment in S could be related to a protracted circulation of the greisenising fluids within the micaschists, also leading to the isotopic equilibration of the fluids with the micaschists, explaining the relatively high $\delta^{18}\text{O}$ values obtained for this apatite type.

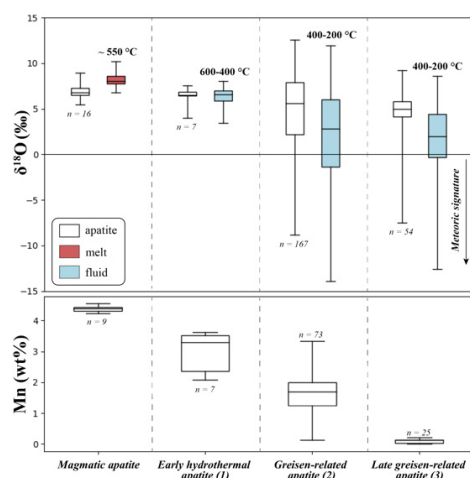


Figure 3. (a) $\delta^{18}\text{O}$ data of apatite generations from the B3 facies and recalculated $\delta^{18}\text{O}$ for the parent melt or fluid using Zhao and Zheng (2003) and Zheng (1996) equations; (b) Mn concentrations of apatite crystals.

6 Conclusion

O isotopic and major elements compositions of the distinct apatite generations identified in the Beauvoir granite suggest an early incursion of meteoric water in the hydrothermal system, possibly at the magmatic stage, as well as the progressive increase in $f\text{O}_2$ leading to an overall decrease in apatite Mn content. Constraining the timing of meteoric fluid incursion in the Beauvoir magmatic-hydrothermal system is crucial, as it might have major implications regarding the crystallisation mechanism of rare metal-bearing minerals in granitic magmas.

Acknowledgements

We would like to acknowledge Imerys, the LabEx RESSOURCES 21 [ANR-10-LABX-21-01] and the CNRS-INSU through its TelluS-SYSTER program for providing financial support to this study.

References

Aïssa M, Weisbrod A, Marignac C (1987) Caractéristiques chimiques et thermodynamiques des circulations hydrothermales du site d'Échassières. *GPF* 2-3:335-350.
 Ballouard C, Poujol M, Boulvais P et al (2017) Magmatic and hydrothermal behavior of uranium in syntectonic leucogranites: The uranium mineralization associated with

the Hercynian Guérande granite (Armorican Massif, France). *Ore Geol Rev* 80:309-331.
 Ballouard C, Poujol M, Mercadier J et al (2018) Uranium metallogenesis of the peraluminous leucogranite from the Pontivy-Rostrenen magmatic complex (French Armorican Variscan belt): the result of long-term oxidized hydrothermal alteration during strike-slip deformation. *Miner Depos* 53:601-628.
 Bhalla P, Holtz F, Linnen RL, Behrens H (2005) Solubility of cassiterite in evolved granitic melts: effect of T, fO_2 , and additional volatiles. *Lithos* 80:387-400.
 Belousova EA, Griffin WL, O'Reilly SY, Fisher NI (2002) Apatite as an indicator mineral for mineral exploration: trace-element compositions and their relationship to host rock type. *J Geochem Explor* 76:45-69.
 Bernard-Griffiths J, Peucat JJ, Sheppard S and Vidal P (1985) Petrogenesis of Hercynian leucogranites from the southern Armorican Massif: contribution of REE and isotopic (Sr, Nd, Pb and O) geochemical data to the study of source rock characteristics and ages. *Earth & Planet Sci Lett* 74:235-250.
 Cheilletz A, Archibald DA, Cuney M, Charoy B (1992) $^{40}\text{Ar}/^{39}\text{Ar}$ ages of the Beauvoir topaz-lepidolite leucogranite and the Chedeville sodolitic pegmatite (North French Massif Central). *Petrologic and geodynamic signification. C R de Acad Sci Serie 2* 315:329-336.
 Cuney M, Marignac C, Weisbrod A (1992) The Beauvoir topaz-lepidolite albite granite (Massif Central, France); the disseminated magmatic Sn-Li-Ta-Nb-Be mineralization. *Econ Geol* 87:1766-1794.
 Decrée S, Cawthorn G, Deloule E et al (2020) Unravelling the processes controlling apatite formation in the Phalaborwa Complex (South Africa) based on combined cathodoluminescence, LA-ICPMS and in-situ O and Sr isotope analyses. *Contr Mineral Petrol* 175:1-31.
 Fouillac A, Rossi P (1991). Near-solidus $\delta^{18}\text{O}$ depletion in a Ta-Nb-bearing albite granite; the Beauvoir Granite, France. *Econ Geol* 86:1704-1720.
 Harlaux M, Mercadier J, Bonzi WME et al (2017) Geochemical signature of magmatic-hydrothermal fluids exsolved from the Beauvoir rare-metal granite (Massif Central, France): Insights from LA-ICPMS analysis of primary fluid inclusions. *Geofluids* 2017.
 Kempe U and Gotze J (2002) Cathodoluminescence (CL) behaviour and crystal chemistry of apatite from rare-metal deposits. *Mineral Mag* 66:151-172.
 Melleton J, Gloaguen E and Frei D (2015) Rare-elements (Li–Be–Ta–Sn–Nb) magmatism in the European Variscan belt, a review. *Proceedings of the 13th Biennial SGA Meeting* 2:24-27.
 Merceron T, Vieillard P, Fouillac AM, Meunier A (1992) Hydrothermal alterations in the Echassières granitic cupola (Massif Central, France). *Contr Mineral Petrol* 112:279-292.
 Monnier L, Salvi S, Melleton J, et al (2019) Multiple generations of wolframite mineralization in the Echassières district (Massif Central, France). *Min* 9:637.
 Monnier L, Salvi S, Jourdan V et al (2020) Contrasting fluid behavior during two styles of greisen alteration leading to distinct wolframite mineralizations: The Echassières district (Massif Central, France). *Ore Geol Rev* 124.
 Pan Y, Fleet ME (2002) Compositions of the apatite-group minerals: substitution mechanisms and controlling factors. *Rev in mineral and geochem* 48:13-49.
 Pichavant M (2022) Experimental crystallization of the Beauvoir granite as a model for the evolution of Variscan rare metal magmas. *J Petrol* 63.
 Tartèse R and Boulvais P (2010) Differentiation of peraluminous leucogranites "en route" to the surface. *Lithos* 114:353-368.
 Taylor HP (1968) The oxygen isotope geochemistry of igneous rocks. *Contr Mineral Petrol* 19:1-71.
 Turpin L, Cuney M, Friedrich M et al (1990) Meta-igneous origin of Hercynian peraluminous granites in NW French Massif Central: implications for crustal history reconstructions. *Contr Mineral Petrol* 104:163-172.
 Zhao ZF and Zheng YF (2003) Calculation of oxygen isotope fractionation in magmatic rocks. *Chem Geol* 193:59-80.
 Zheng YF (1996) Oxygen isotope fractionations involving apatites: Application to paleotemperature determination. *Chem Geol* 127:177-187.

High-resolution mineralogy of Lithium-rich Tuff from the Macusani Volcanic Field, Puno, Peru

Mariana K. Segovia-More¹, Lisard Torró¹, Cristina Villanova-de-Benavent², Johan Ramírez-Briones¹, Jean Vallance¹, Loïs Monnier³, Oscar Laurent³, Stefano Salvi³, Patrice Baby^{1,3}, Joaquín A. Proenza², Fernando Nieto⁴

¹Geological Engineering Program, Faculty of Sciences and Engineering, Pontifical Catholic University of Peru, Peru

²Departament de Mineralogia, Petrologia i Geologia Aplicada, Facultat de Ciències de la Terra, Universitat de Barcelona, Spain

³Géosciences Environnement Toulouse, CNRS/IRD/CNES/Univ. Paul Sabatier, Toulouse, France

⁴Departamento de Mineralogía y Petrología and IACT, Universidad de Granada-CSIC, Spain

Abstract. With Li contents ranging as high as ~2,000 to 4,000 ppm, the so-called Lithium-rich Tuff in the Macusani Volcanic Field hosts the main lithium resource in the recently discovered Falchani Project in south-eastern Peru. These tuffs comprise quartz, plagioclase (albite), K-feldspar (sanidine), trioctahedral micas (zinnwaldite + lepidolite), kaolinite ± halloysite, and dioctahedral smectites, in addition to cristobalite and mordenite in a few samples. The highest Li contents (3,000–4,200 ppm Li) are found in the central portion of the Lithium-rich Tuff sequence, which is characterized by micas + kaolinite subgroup minerals ± mordenite. In the upper and lower domains of the tuff sequence, Li contents reach values of 2,000 ppm and the mineralogy is dominated by micas + dioctahedral smectite ± kaolinite ± halloysite. Lithium is contained mostly in zinnwaldite and lepidolite, and probably also adsorbed onto, or in interlayer positions in clay minerals.

1 Introduction

Lithium is a critical raw material for the development of eco-efficient energy technologies. Examples include Li-ion batteries for electric vehicles, much needed to promote the transition from fossil fuels to renewable energy sources in order to achieve EU's 2025 carbon neutrality goal (IRENA 2019; European Commission 2020). Finding new conventional (e.g., granitic pegmatites, salars) and non-conventional (e.g., volcanogenic, oilfield brines) Li resources is thus essential to cover the ever-growing demand for this metal (Bowell et al. 2020; Jowitt et al. 2021; Graham et al. 2021).

In November 2017, the discovery of a major lithium resource in the Falchani Lithium Project in the central area of the Macusani Volcanic Field, located in the Eastern Cordillera of the Andes (Puno Department) in south-eastern Peru, was announced by Macusani Yellowcake S.A.C., the Peruvian subsidiary of American Lithium Corp. As of 2023, indicated resources amount to 0.39 Mt Li₂O while inferred are 1.52 Mt Li₂O (<https://americanlithiumcorp.com/falchani-lithium-project>). Lithium mineralization occurs in Neogene breccias and tuffs. Out of these, the main lithium resource, and the highest grades – mostly between 2,000 and 4,000 ppm Li – are found in the so-called Lithium-rich Tuff (The Mineral Corporation 2019).

In spite of the economic importance of this tuff, a detailed mineralogical characterization is not available to this day. In this abstract, we present new mineralogical data, with an emphasis on clay

minerals, in order to discuss the mineralogical expression of lithium in the Lithium-rich Tuff and a classification of the Falchani deposit.

2 Geological setting

The unit referred to as Lithium-rich Tuff by companies exploring in south-eastern Peru belongs to the Macusani Volcanic Field (Fig. 1), a sequence of volcanic and volcano-sedimentary units mostly exposed in the Quenamari Meseta plateau, at an altitude of 4,400 m a.s.l., and is part of the Neogene ignimbrite centers of the Central Andes. The Macusani Volcanic Field is located between the Cordillera de Carabaya and the central Andean backthrust belt, and belongs to the Macusani Structural Zone (Perez et al. 2016), previously known as the Precordillera de Carabaya (Sandeman et al. 1997). It relates to tectonic shortening/crustal thickening and contemporaneous lithospheric removal/thinning (Salisbury et al. 2011; Göğüş et al. 2022).

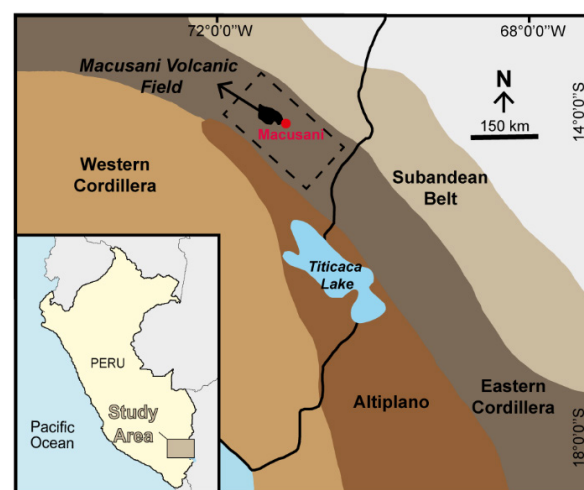


Figure 1. Location of the Macusani Volcanic Field within the geomorphotectonic map of the Central Andes.

Late Oligocene to late Miocene volcano-sedimentary sequences exposed in the Macusani Volcanic Field were grouped by Sandeman et al. (1997) under the Crucero Supergroup and subdivided into the Quenamari and Picotani groups. Rhyolitic ash-flow tuffs of the late Miocene (6.8 – 10.5 Ma) Macusani Formation, in which the studied Lithium-rich Tuff is found, are part of the Quenamari

Group. The Macusani Formation comprises whitish-grey, poorly consolidated, lapilli-crystal tuffs mineralogically consisting of quartz, sanidine, plagioclase, sillimanite, andalusite, muscovite, biotite, and tourmaline (Sandeman et al. 1997). Geochemically, they are characterized by felsic and highly peraluminous signatures, with 71.5–75 wt% SiO₂, high Al₂O₃ (normative corundum >2%), and high alkalis, with an enrichment in lithophile trace elements (e.g., Li, Be, Cs, Nb; Pichavant et al. 1988). López (1996) renamed the Macusani Formation as Quenamari Formation and proposed its subdivision, from bottom to top, into the Chacacuniza, Sapanuta and Yapamayo members. In the Falchani Project, rocks of the Sapanuta Member, including the Lithium-rich Tuff, are widely exposed (The Mineral Corporation 2019).

3 Analytical methods

Thirty-two representative samples of Lithium-rich Tuff were analysed by powder XRD using a Bruker D8 Discover diffractometer in Bragg-Brentano $\theta/2\theta$ geometry of 240 mm radius, at the Centro de Caracterización de Materiales of the Pontifical Catholic University of Peru (CAM-PUCP). Seventeen mica- and clay-rich samples, eleven of which from drill core, were analysed by XRD on oriented mounts using the same equipment and setup as for powdered samples, in air dried, ethylene glycol-saturated (ETG), and heated (at 400 °C to 550 °C) preparations. Three samples were studied using a Quanta 650 FEI scanning electron microscope (SEM) equipped with an EDAX–Octane Pro Energy Dispersive Spectrometry (EDS) microanalysis system at CAM-PUCP. Three more samples were studied by Transmission Electron Microscopy (TEM), using powder specimens deposited onto formvar-covered Cu grids, to determine the mineral composition by Analytical Electron Microscopy (AEM) in the Thalys microscope of the CIC of the University of Granada, calibrated with natural standards.

4 Results

Powder XRD results show that the tuffs are mainly composed of quartz, plagioclase (probably albite), K-feldspar (probably sanidine), and mica (zinnwaldite and lepidolite; see Torró et al. 2023), with variable proportions of clay minerals (kaolinite subgroup minerals and smectites), mordenite, and cristobalite. The tuff samples can be grouped into four categories according to their prevalent mineralogy: i) mica with no zeolite nor clay minerals, ii) mica with kaolinite subgroup minerals (Fig. 2a), iii) mica with smectite (Fig. 2b), and iv) mica with mordenite.

According to oriented-mount XRD data, the clay mineral peaks with $d_{(001)}$ spacing of 12 to 15.1 Å correspond to smectite. The $d_{(001)}$ spacing expands with ETG to 16.6 to 17 Å, and contracts to ~10 Å with oven-dried treatment at 400°C and 550°C.

Moreover, the clay presenting peaks with $d_{(001)}$ spacing of 7.1 to 7.2 Å at $2\theta \sim 12.3^\circ$ for air dried samples corresponds to kaolinite subgroup minerals. ETG and 400° heat treatments have no effect on the diffractogram of this mineral, but the $d_{(001)}$ spacing peak was destroyed by heat treatment at 550°, which is consistent with the aforementioned subgroup.

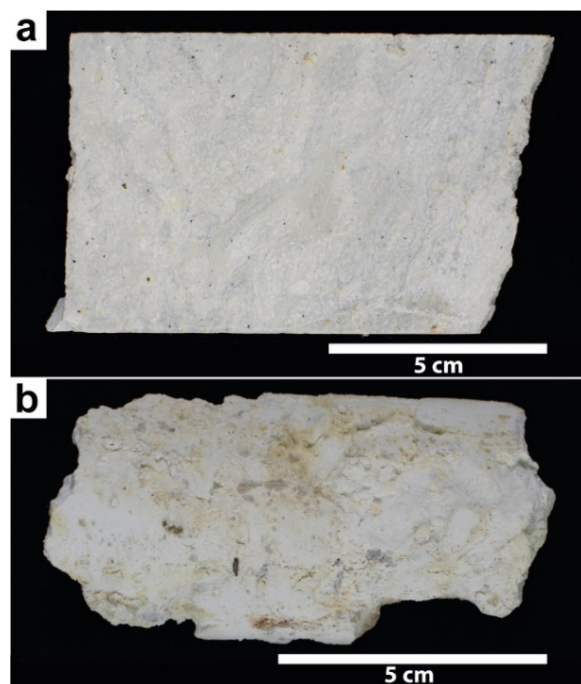


Figure 2. Lithium-rich Tuff samples from the Macusani Volcanic Field. a) 2021-MAC-040: mica (scattered black grains) with kaolinite subgroup minerals. b) 2021-MAC-051: mica with smectite.

In Figure 3, the diffractograms obtained from powder XRD analysis of drill-core samples are ordered according to their relative depth, with their corresponding lithium contents. A vertical mineral

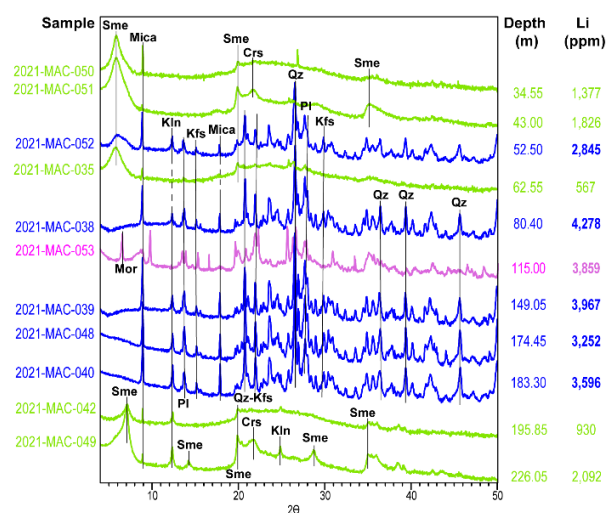


Figure 3. Drill core samples classified according to the prevalent mineralogy (color) and ordered according to their relative depth. Key: plagioclase (Pl), mica (Mica), quartz (Qz), K-feldspar (Kfs), kaolinite (Kln), smectite (Sme), cristobalite (Crs), and mordenite (Mor).

zoning comprising three main domains is observed. The upper domain presents Li contents in the range of 567 to 1,826 ppm and is dominantly composed of smectite and micas. The central domain has the highest Li contents – ranging from 2,845 to 4,278 ppm – and is dominated by micas and kaolinite. Finally, the lower domain presents Li contents between 930 and 2,092 ppm and the mineralogy consists predominantly of smectite, micas \pm kaolinite.

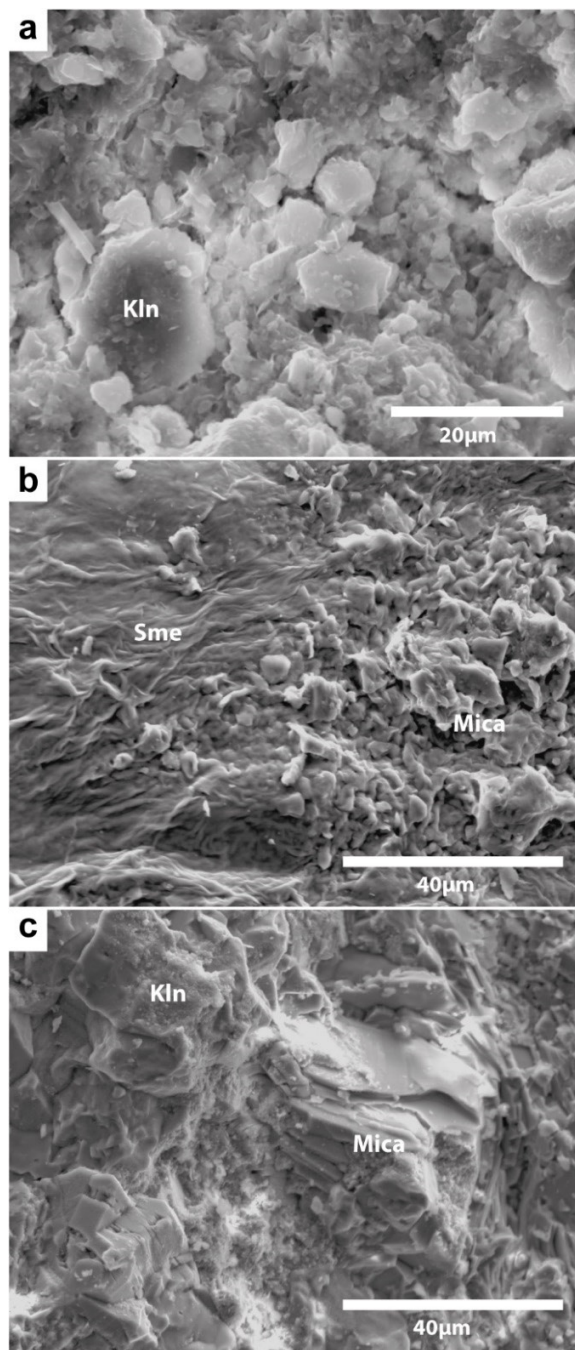


Figure 4. Secondary-electron SEM images of samples from the Lithium-rich Tuff. a) Pseudohexagonal plates of kaolinite with sheet-like masses probably corresponding to mordenite. b) Hybrid morphologies of tightly interwoven flakes characteristic of smectite and areas with scalloped edges of micas. c) Flaky grain of mica and kaolinite aggregates.

Secondary-electron SEM images of samples 2021-MAC-026, 2021-MAC-035, and 2021-MAC-039 show the morphologies of clay minerals, micas, and zeolites. In sample 2021-MAC-026, small plates of variable thicknesses are observed, most probably corresponding to kaolinite subgroup minerals, according to their pseudohexagonal morphology (Fig. 4a). In addition, some grains yield high contents of O and Si in EDS spectra, compatible with the zeolite mordenite. In sample 2021-MAC-035, tightly interwoven and wavy flakes with curved-edges are distinctive of smectite (see Keller et al. 1986), whereas mica grains show scalloped edges (Fig. 4b). SEM-EDS analyses in smectite reveal relatively high contents of Si and Al and minor proportions of Mg, Ca, and Na. Finally, in sample 2021-MAC-039, a flaky grain of mica and kaolinite subgroup minerals are observed (Fig. 4c).

The TEM study shows that the fine fraction of samples 2021-MAC-049 and 2021-MAC-050 is majorly composed of smectite (Fig. 5a) showing dioctahedral characteristics in the electron diffractions (Fig. 5b), and chemical compositions with the octahedral population approaching 2 atoms per formula unit (apfu). Iron and Mg contents are low, with some analyses showing a slight octahedral deficit. Interlayer occupancy is deficient and composed of small quantities of Na, K, and Ca. The fine fraction of sample 2021-MAC-038 contains predominantly mica and kaolinite subgroup minerals. Mica consists mostly of Si, Al, and K, with very scarce Mg and Fe, and its composition can be approximated to that of 'lepidolite'. Assumption of the normal values of Li for this type of mica brings the octahedral occupancy to values in the range of 3 apfu (see also Torró et al. 2023).

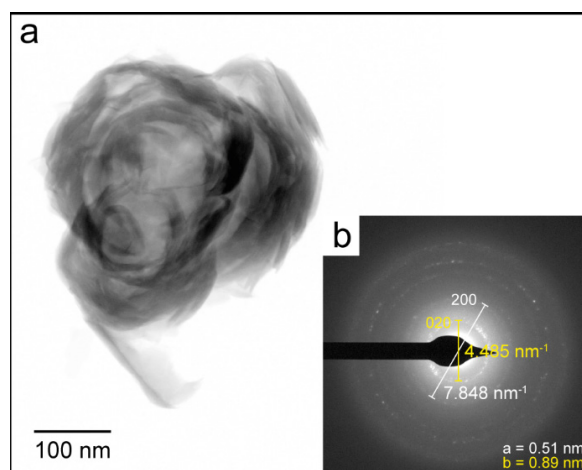


Figure 5. a) TEM image showing a flower-shaped smectite aggregate with curved morphologies. b) Electron diffraction pattern showing the crystal parameters ($a = 5.1$ Å, $b = 8.9$ Å) indicative of dioctahedral smectite.

5 Discussion

A close correlation between lithium mineralization and pyroclastic units would ascribe the Falchani Lithium Project in the Macusani Volcanic Field to the

volcanogenic lithium deposit type. Volcanogenic deposits stand as 'non-conventional' Li resources – in front of 'conventional' LCT pegmatites and hydromorphic ('salar') deposits (Bowell et al. 2020). Enrichment in lithium to economic grades in volcanogenic deposits is considered to result from the interaction of pre-existing volcanic rocks enriched in lithium and atmospheric or hydrothermal fluids in rhyolitic calderas, triggering the deposition of secondary, Li-rich minerals (Benson et al. 2017; Bowell et al. 2020).

Volcanogenic lithium deposits are subdivided into clay, ion-clay, and jadarite subtypes depending on the nature of prevalent lithium-bearing phases (Bowell et al. 2020). From a mineralogical point of view, the best studied volcanogenic lithium deposits are those in the McDermitt Caldera in Nevada (USA). Castor and Henry (2020) concluded that, in the Thacker Pass deposit of the McDermitt Caldera, lithium occurs in hectorite (Li-smectite), in an illitic clay that is chemically similar to tainiolite, and in a mixed-layer smectite-illite clay. These authors reported a vertical mineral zonation consisting of i) illitic clays in the lower sedimentary section (~ 3,000 ppm Li), ii) a transitional zone with mixed smectite-illite (tainiolite?) clays (~ 2,000 ppm Li), and iii) an overlying upper sedimentary section dominated by hectorite (< 2,000 ppm Li).

Based on the XRD, SEM-EDS, and TEM data presented here, the mineralogy of the Lithium-rich Tuff unit in the Macusani Volcanic Field consists of quartz, plagioclase, K-feldspar, trioctahedral micas, mordenite, cristobalite, and clay minerals (kaolinite ± halloysite and dioctahedral smectite). The trioctahedral micas correspond to zinnwaldite and lepidolite and are interpreted as igneous in origin (see textural and compositional details in Torró et al. 2023). No other lithium-bearing minerals have been identified in the studied samples. However, preliminary metallurgical tests on Lithium-rich Tuff from the Falchani Lithium Project reported by The Mineral Corporation (2019) describe Li recovery as high as 90 % by leaching with sulfuric acid at 90–95°C, thus suggesting that Li may also occur adsorbed or in interlayer positions in smectite and/or kaolinite subgroup minerals. Our ongoing mineralogical work on samples from the Falchani Lithium Project will help assess the contribution of relict (i.e., zinnwaldite-lepidolite) and secondary (i.e., smectite, kaolinite subgroup minerals) phases to the bulk lithium resource and refine the classification of the deposit.

Acknowledgements

We wish to thank the geologists from Macusani Yellowcake for their help and hospitality during fieldwork. This research work was financed by the Peruvian PROCENCIA-FONDECYT project 1122-2020 E041-2020-01-01, and logistically supported by the 2021 SGR 00239 project of the Agència de Gestió d'Ajuts Universitaris i de Recerca de Catalunya.

References

- Benson TR, Coble MA, Rytuba JJ, Mahood GA (2017) Lithium enrichment in intracontinental rhyolite magmas leads to Li deposits in caldera basins. *Nat Commun* 8:270.
- Bowell RJ, Lagos L, de los Hoyos CR, Declercq J (2020) Classification and characteristics of natural lithium resources. *Elements* 16:259–264.
- Castor SB, Henry CD (2020) Lithium-rich claystone in the McDermitt Caldera, Nevada, USA: geologic, mineralogical, and geochemical characteristics and possible origin. *Minerals* 10:1-39.
- European Commission (2020) Study on the EU's list of Critical Raw Materials. European Commission, Brussels, Belgium, 158 p.
- Göğüş OH, Sundell K, Uluocak EŞ, Saylor J, Uğurcan Ç (2022) Rapid surface uplift and crustal flow in the Central Andes (southern Peru) controlled by lithospheric drip dynamics. *Sci Rep* 12:5500.
- Graham JD, Rupp JA, Brungard E (2021) Lithium in the green energy transition: the Quest for both sustainability and security. *Sustainability* 13:11274.
- IRENA (2019) Global energy transformation: a roadmap to 2050. Abu Dhabi, 52 p.
- Jowitt SM, McNulty BA (2021) Battery and energy metals: future drivers of the minerals industry? *SEG Discovery* 127:11-18.
- Keller WD, Reynolds RC, Inoue A (1986) Morphology of clay minerals in the smectite-to-illite conversion series by scanning electron microscopy. *Clays Clay Miner* 34:187-197.
- López JC (1996) Geología del cuadrángulo de Nuñoa. Hoja 29-u. Instituto Geológico, Minero y Metalúrgico, 171p
- Perez ND, Horton BK, Carlotto V (2016) Structural inheritance and selective reactivation in the central Andes: Cenozoic deformation guided by pre-Andean structures in southern Peru. *Tectonophysics* 671:264–280
- Pichavant M, Kontak DJ, Briquieu L, Valencia Herrera J, Clark AH (1988) The Miocene-Pliocene Macusani Volcanics, SE Peru - II. Geochemistry and origin of a felsic peraluminous magma. *Contrib Mineral Petrol* 100:325–338.
- Salisbury MJ, Jicha BR, de Silva SL, Singer BS, Jiménez NC, Ort MH (2011) ⁴⁰Ar/³⁹Ar chronostratigraphy of Altiplano-Puna volcanic complex ignimbrites reveals the development of a major magmatic province. *GSA Bulletin* 123:821-840
- Sandeman HA, Clark AH, Farrar E, Arroyo-Pauca G (1997) Lithostratigraphy, petrology and ⁴⁰Ar-³⁹Ar geochronology of the Crucero Supergroup, Puno Department, SE Peru. *J South Am Earth Sci* 10:223–245
- The Mineral Corporation (2019) Mineral Resource Estimates for the Falchani Lithium Project in the Puno District of Peru. Bryanston, pp 1-72.
- Torró L, Villanova-de-Benavent C, Monnier L, Laurent O, Segovia-More MK, Sanandres-Flores M, Ramírez-Briones J, Vallance J, Salvi S, Baby P, Proenza JA, Nieto F (2023) Lithium-bearing micas in the 'lithium-rich tuff' from the Macusani Volcanic Field, Puno, Peru. This volume.

Characteristics of productive and barren Jecheon adakitic intrusions in the Hwanggangri mineralized district, Republic of Korea

Jieun Seo¹, Seon Gyu Choi¹, Gi Eun Shin¹, Young Jae Lee¹

¹T Department of Earth and Environmental Sciences, Korea University, Korea

Abstract. The Hwanggangri mineralized district (HMD) in South Korea contains a variety of mineral deposit types. The Jurassic Jecheon and Songhaksan granodiorite in the Hwanggangri district have similar adakitic geochemical characteristics in major and trace element variation and REE patterns, but they have different petrology and mineralogy. The Jecheon granodiorite is classified as coarse-grained hornblende-biotite granodiorite with observed hornblende, greenish brown colored biotite, and sphene with mafic microgranular enclave (MME) by mingling and mixing. It has oxidized I-type, magnetite-series characteristics with higher magnetic susceptibility values of $3.60\text{--}13.04 \times 10^{-3}$ SI and Mg#. On the other hand, the Songhaksan granodiorite is S-type medium-grained two mica granodiorite having lower magnetic susceptibility values of $0.01\text{--}0.05 \times 10^{-3}$ SI and Mg#. Therefore, the Jecheon (southwest) and Songhaksan (northeast) granodiorites were originated different source material because they have different magnetic susceptibility, mineralogy, and mineral chemistry. In addition, there are two types of MME in Jecheon granodiorite, which were formed in the process of mixing with two veins. The Jecheon granodiorite in the southwest is barren, while the Songhaksan granodiorite in the northwest is a productive igneous rock that formed the Dongmyeong Skarn type W deposit.

1 Introduction

The Hwanggangri mineralized district (HMD) is located on the boundary of the Okcheon metamorphic belt and the Taebaeksan Basin (Fig. 1). The HMD contains a number of Jurassic and Cretaceous intrusive rocks. The HMD contains a variety type of mineral deposits (porphyry, skarn, carbonate replacement, and fissure-filling vein types). W–Mo deposits are one of the major types of metal ores in South Korea, and they are widely distributed and closely related to Jurassic–Cretaceous magmatism (Shimazaki et al, 1987; Park et al. 1988a,b; So et al. 1991; Lee et al. 2022). The W–Mo deposits have variable ratios of the constituent metals because of the variety of fluids derived from different emplacement depths of magmas during the Jurassic and Cretaceous (Choi et al. 2007). The HMD is a representative area of major metals and fluorite mineralization in South Korea, and it stretches from south of the Jecheon intrusion to the northern part of the Weolaksan intrusion. Numerous Mo–W–Cu–Pb–Zn–Au–Ag polymetallic deposits occur in this area, and there are many fluorite deposits among the intrusion bodies (Hwang 2002). Most of the deposits are related Late Cretaceous intrusions and shown the age of mineralization is Late Cretaceous (96.5–76.2

Ma) including Geumseong, Jungbo, Kwangsins, and Geumsil mines, with the exception of the Dongmyeong deposit, which is 176.6 ± 5 Ma (Choi et al. 1993). These deposits are hosted in limestones/dolomitic limestones of the Joseon Supergroup. The Dongmyeong tungsten skarn deposit formed in the contact area between the Joseon Supergroup (Paleozoic limestone) and the Jecheon intrusion (Jurassic granitoids). Uniquely, the Jecheon intrusion related to the Dongmyeong deposit appears to be a single intrusive body, however, the northeastern and southeastern part of body show different geochemical characteristics. In this study, we described the petrology, mineralogy, and geochemistry of Jecheon Jurassic intrusions in the HMD that are associated with barren or productive deposits and described the mixing/mingling features within Jecheon intrusion.

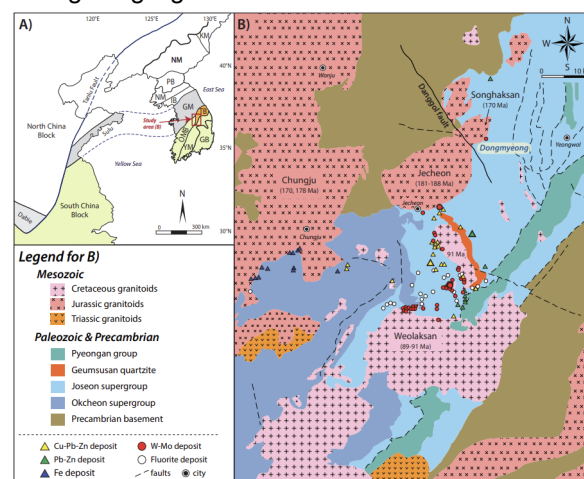


Figure 1. A) Simplified geological map of the Korean Peninsula, B) Geological map of the Hwanggangri mineralized district (HMD), showing the location of various types of deposits (modified from Lee et al. 2022). Abbreviations: KM = Kwanmobong massif, NM = Nangrim massif, PB = Pyeongnam basin, IB = Imjingang belt, GM = Gyeonggi massif, OMB = Okcheon metamorphic belt, TB = Taebaeksan basin, YM = Yeongnam massif, GB = Gyeongsang basin.

2 Geological background

The Korean Peninsula is located on the northeastern Asia plate, and it is made up of three Precambrian massifs (Nangrim, Gyeonggi, and Yeongnam), three Phanerozoic basins (Pyeongnam, Taebaeksan, and Gyeongsang), and two metamorphic belts (Imjingang and

Okcheon) (Fig. 1A). The study area includes the boundary between the Okcheon metamorphic belt and Taebaeksan Basin. The Joseon Supergroup within the Taebaeksan Basin consists mainly of Cambrian–Ordovician sedimentary rocks (Fig. 1B; Chough 2013). The Carboniferous–Lower Triassic clastic sedimentary units of the Pyeongan Supergroup overlie unconformably the Cambrian–Ordovician carbonate sequences of the Joseon Supergroup, and they have been intruded by Mesozoic igneous rocks. Jurassic and Cretaceous igneous intrusive rocks are widespread in both the Okcheon metamorphic belt and the Taebaeksan Basin, and in particular it is the Late Cretaceous (90–70 Ma) igneous rocks that are associated with mineralization (Sagong et al. 2005; Choi et al. 2005). The Mesozoic intrusions show a trimodal age distribution are reported by several researchers (Jwa 1988; Chough et al. 2000), which may be related to the Songrim disturbance in the Triassic (248–210 Ma), the Daebo orogeny in the Jurassic (200–155 Ma), and the Bulguksa of Magmatism in the Cretaceous–Early Tertiary (110–50 Ma).

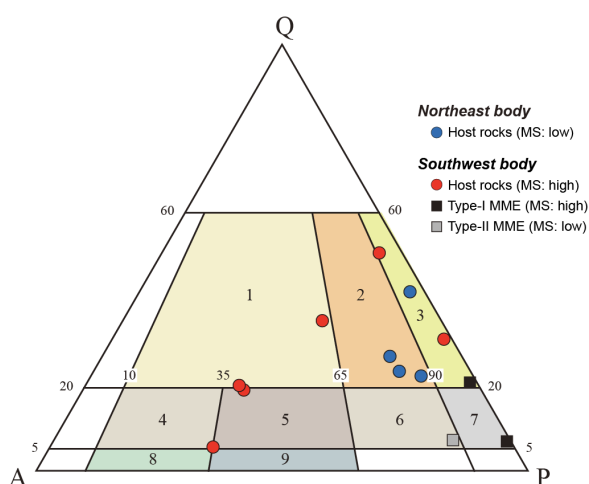


Figure 2. QAP rock classification scheme for the studied plutonic rocks based on the modal composition: 1, granite; 2, granodiorite; 3, tonalite; 4, quartz syenite; 5, quartz monzonite; 6, quartz monzodiorite; 7, diorite; 8, syenite; 9, monzonite (IUGS classification of the igneous rocks).

The Jecheon intrusion appears to be a single intrusive body, but the northeast (Songhaksan granodiorite) and southwest (granotoids) parts are divided by the Danggol Fault (Fig. 1B). The Jecheon intrusion was emplaced at 3.8kbar depth (Cho and Kwon 1994) and consists of megacrysts of K-feldspar, porphyritic texture biotite granite and coarse-grained biotite granodiorite (Jin et al., 1992). It has characteristics of magnetite-series, I-type, and adakitic granitoid (Ishihara et al. 2005). The Jecheon intrusion yields SHRIMP U-Pb ages of 181–188 Ma (Zhai et al. 2016). MME observed within the Jecheon intrusion body have SHRIMP U-Pb ages of 178.9 and 184.2 Ma. MME intruded at a similar period with the Jecheon intrusion. The

ages of the Songhaksan intrusion are reported as SHRIMP U-Pb age of 170 ± 2 Ma (Zhai et al. 2016). The emplacement depth of Jecheon granodiorite estimated by hornblende geobarometry is 3.8kbar and it has been reported to have been emplaced at deeper depths (Cho and Kwon, 1994).

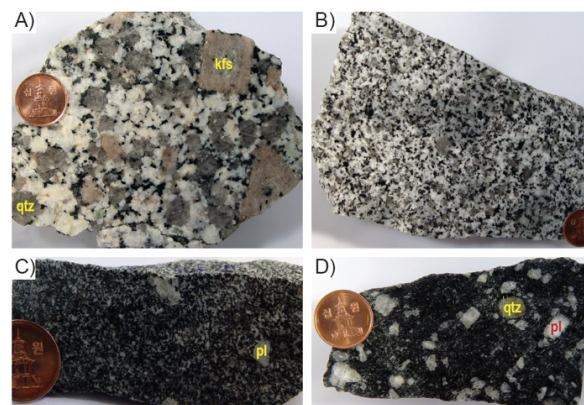


Figure 3. Photographs of hand specimens of Jurassic intrusions in the HMD. A) Southwestern part of Jecheon intrusion, which shown euhedral pinkish K-feldspar megacrysts and mafic minerals, B) Northeastern part of Jecheon intrusion, C) Type-I MME within the southwestern part of Jecheon intrusion, D) Type-II MME within the southwestern part of Jecheon intrusion.

The Jecheon intrusion is composed of granodiorite and micro mafic enclaves (MME), which are interpreted as evidence of mingling and mixing. The Jecheon granotoids show slightly heterogeneous grain size and mineralogy and show a common granodiorite to granite composition (Fig. 2). The mineralogy of the Jecheon granodiorite is dominated by plagioclase, quartz, alkali feldspar and mafic minerals of hornblende and biotite with minor amounts of sphene implying granodiorite formed in an oxidized environment. The Jecheon granodiorites are commonly coarse grained (5 to 10mm) with mega crystals of alkali feldspar (Fig. 3A). Mega crystals of alkali feldspar formed by mingling and mixing. Mafic minerals are observed around these alkali feldspar phenocrysts. Biotite showing greenish brown pleochroism is not altered and it suggests the Jecheon granodiorite formed in an oxidized environment. MME within the Jecheon granodiorite is divided into two types according to the difference in magnetic susceptibility (MS) (Fig. 3C, D). While, the Songhaksan granodiorite has medium grained texture with 2 to 5mm grain size (Fig. 3B). The mineralogy is dominated by quartz, plagioclase, alkali feldspar, mafic minerals and the percentage of alkali feldspar is lower than the Jecheon granodiorite. Plagioclase showing porphyritic texture forms well zoned crystals and most feldspars are strongly altered to sericite. The volume percentage of mafic minerals of 7 to 10% is similar to the Jecheon granodiorite. Biotite showing reddish brown pleochroism suggests that the Songhaksan granodiorite formed in a reduced environment and some biotite is altered to chlorite. Primary muscovite formed in magma and

secondary muscovite by alteration ranging from 1 to 2 %.

3 Methodology

Whole rock major, trace, and rare earth element (REE) concentrations in the intrusions and enclaves were determined using inductively coupled plasma atomic emission spectrometry (FUS-ICP-AES; Termo JarrelAsh ENVIRO II) and inductively coupled plasma mass spectrometry (FUS-ICP/MS; Perkin Elmer Optima 3000) at Activation Laboratories Ltd., Canada. Ferrous iron was determined by a gravimetric method (TITR).

Electron microprobe analyses of the minerals in the Jecheon adakitic intrusions, non-adakitic intrusions, and enclaves were performed using a JEOL JXA-8600 SX microprobe at Korea University, Seoul, South Korea. Accelerating voltage, beam current, probe diameter, and livetime were 15.0 kV, 3.0 nA, 3 μ m, and 100s, respectively.

4 Results

The samples of the southwestern part of Jecheon intrusions (Jecheon granodiorite, MME) and northeastern part of Jecheon intrusions (Songhaksan granodiorites) were shown different magnetic susceptibility (MS). The Jecheon granodiorite have 3.60 to 13.04×10^{-3} SI of high MS. The MS of Songhaksan granodiorite shows low values ranging from 0.01 to 0.05×10^{-3} SI. According to Ishihara et al. (1990), the Jecheon granodiorite is magnetite series with high MS while the Songhaksan granodiorite consists of ilmenite series showing lower than 3×10^{-3} SI. The samples of MME show 0.58 to 1.51 and 3.42 to 15.71×10^{-3} SI divided into two groups and it implies that different magmas occurring mixing and mingling intruded.

The Jecheon granodiorite has low SiO_2 (66.47–70.68 wt. %), and high TiO_2 (0.38–0.53 wt. %), Al_2O_3 (13.47–16.30 wt. %), $\text{Fe}_2\text{O}_3^{\text{tot}}$ (3.03–4.17 wt. %), MgO (1.03–1.58 wt. %), CaO (2.67–4.61 wt. %), and P_2O_5 (0.13–0.17 wt. %). MME is characterized by lowest SiO_2 (50.17–53.74 wt. %) among the studied granitoids and high TiO_2 (0.89–1.21 wt. %), Al_2O_3 (14.90–18.17 wt. %), $\text{Fe}_2\text{O}_3^{\text{tot}}$ (7.80–12.14 wt. %), MgO (3.20–5.99 wt. %), CaO (7.27–8.63 wt. %), and P_2O_5 (0.17–0.22 wt. %) whereas contains low K_2O (2.85–3.57 wt. %) and Na_2O (3.42–3.66 wt. %). It seems that the Jecheon and Songhaksan granodiorites show similar major element distributions.

The Jecheon and Songhaksan granodiorite have similar geochemical characteristics of Rb, Zr, Y, Nb, and V contents. The Jecheon granodiorite and MME

have contents of Ba (291–1189; 200–644 ppm), Sr (316–570; 259–787 ppm), respectively and show wide ranges of Ba and Sr contents compared to the Songhaksan granodiorite contents of Ba (848–1240 ppm) and Sr (503–535 ppm). These chemical properties correspond to adakitic properties. (Fig. 4A,B).

The total contents of rare earth elements of Jecheon granodiorite, MME, and Songhaksan granodiorites are 107.32–176.56 ppm, 163.63–262.36 ppm, and 146.67–189.47 ppm, respectively. These granitoids are mostly enriched in light rare earth elements (LREE) and depleted in high rare earth elements (HREE). The Jecheon granodiorite, MME, and Songhaksan granodiorite have no Eu anomaly and high $(\text{La}/\text{Yb})_N$ values of 21.20–24.20, 6.20–17.59, and 27.66–53.82, respectively (Fig 4C, D,E,F). These features of high $(\text{La}/\text{Yb})_N$ suggest that the Jurassic granitoids are associated with adakite.

Two types of dykes and two types of MME are observed in the Jecheon intrusion, which is the result of the mixing/mingling processes of granodiorite and mafic dykes.

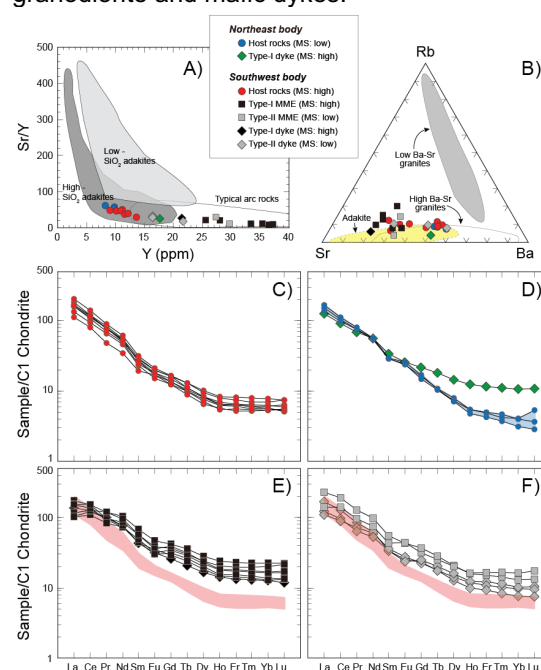


Figure 4. Geochemical characteristics of the Jecheon intrusions. A) Sr/Y versus Y diagram (modified after Defant and Drummond, 1990; Martin et al., 2005; He et al., 2012). B) Rb-Sr-Ba ternary diagram for high and low Ba-Sr granite fields (after Tarney and Jones, 1994). C) Chondrite-normalized rare earth element (REE) patterns for the southwestern part of Jecheon intrusion (granitoids) (Sun and McDonough, 1989). D) the northeastern part of Jecheon intrusion (granitoids and mafic dykes). E) the southwestern part of Jecheon intrusion (MMEs). F) the southwestern part of Jecheon intrusion (mafic dykes).

5 Conclusions

The Jecheon and Songhaksan granodiorites were reported as one granite mass (Ishihara et al., 2000;

Shibata et al., 1983) while Jin et al. (1992) reported that the Jecheon and Songhaksan granodiorites are bounded by a fault. The differences between the Jecheon and Songhaksan granodiorites are as follows. In magnetic susceptibility values, the Jecheon granodiorite is magnetite series with more 3×10^{-3} SI while the Songhaksan granodiorite consists of ilmenite series with relatively lower magnetic susceptibility values. The Jecheon granodiorite is classified as I-type granitoids of coarse-grained hornblende-biotite granodiorite with mega crystal of K-feldspars whereas the Songhaksan granodiorite shows S-type granitoids of medium grained two mica granodiorite with muscovite. The sphene and greenish brown colored biotite implying formed in oxidized environment are observed in the Jecheon granodiorite. On the other hand, the Songhaksan granodiorite has reddish brown pleochroism biotite and it suggests that the Songhaksan granodiorite formed in reduced environment. In this study, it suggests that they were derived from magma that originated from a different source with different magnetic susceptibility values, grain size, and mineralogy.

The Jecheon granodiorite and MME have a wide range of K_2O contents with similar SiO_2 contents and have characteristics of calc-alkaline series to high-K calc-alkaline series due to mingling and mixing, but the Songhaksan granodiorite is high-K calc-alkaline series (Rickwood 1989).

The Jurassic W skarn type Dongmyeong deposit (176.5 Ma) is related to the Songhaksan granodiorite located on the northern side of the Hwanggangri district. The Songhaksan granodiorite is metaluminous to peraluminous S-type granitoids and has less evolved geochemical features of Rb/Sr ratio and Eu/Eu^* values. The Dongmyeong deposit has no greisen alteration and fluorite. The Jecheon granodiorite, MME, Songhaksan granodiorite have high Nb/Ta values of 7.07–12.38, 8.11–15.98, and 11.63–13.80, respectively and have features of less evolution in diagrams for fractionation in peraluminous granites.

The Jecheon hornblende-biotite granodiorite, which shows high magnetic susceptibility values (magnetite series) and greenish pleochroic biotite, is not associated with W deposits. While, the Songhaksan granodiorite with lower magnetic susceptibility values of $0.01\text{--}0.05 \times 10^{-3}$ SI is identified as ilmenite series and S-type granite, is associated with W deposits.

Acknowledgements

This research was supported by Basic Science Research Program through the National Research Foundation of Korea (NRF) funded by the Ministry of Education (NRF-2022R111A1A01071269).

References

- Cho DL, Kwon ST (1994) Hornblende geobarometry of the Mesozoic granitoids in South Korea and the evolution of crustal thickness. *Jour. Geol. Soc. Korea* 30:41-61.
- Cho SG, Park JW, Seo J, Shin JK, Kim NH, Yoo IK, Ahn YH (2007) Hidden Porphyry-Related Ore Potential of the Geumseong Mo Deposit and Its Genetic Environment. *Econ. Environ. Geol.* 40:1-14.
- Choi SG, Ryu IC, Pak SJ, Wee SM, Kim CS, Park ME (2005) Cretaceous epithermal gold-silver mineralization and geodynamic environment, Korea. *Ore geol. Rev.* 26:115-135.
- Choi SH, So CS, Shelton KL, Kim SJ (1993) Mineralogy and geochemistry of the Dongmyeong tungsten mine, Korea. *Journal of Southeast Asian Earth Sciences* 8:349-358.
- Chough SK (2013) *Geology and sedimentology of the Korean peninsula*. Elsevier, London, 363.
- Chough SK, Kwon ST, Ree JH, Choi DK (2000) Tectonic and sedimentary evolution of the Korean peninsula: a review and new review, *Earth-Science Rev.* 52:175-235.
- Defant MJ, Drummond MS (1990) Derivation of some modern arc magmas by melting of young subducted lithosphere. *Nature* 347:662-665.
- He H, Zhaochong Z, Timothy K, Dongyang Z, Tong H (2012) Geochronology and geochemistry of the Chuanwulu complex in the South Tianshan, western Xinjiang, NW China: Implications for petrogenesis and Phanerozoic continental growth. *Lithos* 140-141: 66-85.
- Hwan, J (2002) Geochemistry of groundwater in limestone and granite of Hwanggangri fluorite mineralized area. *J. Korea Earth Sci. Soc.* 23 486-493.
- Ishihara S, Jin MS, Terashima S (2005) Mo-related adakitic granitoids from non-island-arc setting: Jecheon pluton of South Korea. *Resource Geol.* 55:385-396.
- Jin MS, Kim SJ, Shin SC, Choo SH, Chi SJ (1992) Thermal history of the Jecheon granite pluton in the Ogcheon fold belt, South Korea. *Jour. Petrol. Soc. Korea* 1:49-57.
- Jwa YJ (1988) Temporal, spatial and geochemical discriminations of granitoids in South Korea. *Res. Geol.* 48:273-284.
- Lee JH, Seo J, Choi SG, Oh CW, Lee YJ (2022) Different characteristics of barren and W-Mo-productive Cretaceous granites in the Hwanggangri mineralized district, South Korea. *Ore Geology Reviews* 141:104645.
- Lee KS, Chang HW, Park KH (1998) Neoproterozoic bimodal volcanism in the central Ogcheon belt, Korea: age and tectonic implication. *Precambrian Res.* 89:47-57.
- Mutch EJJ, Blundy JD, Tattich BC, Cooper FJ, Brooker RA (2016) An experimental study of amphibole stability in low-pressure granitic magmas and a revised Al-in-Hornblende geobarometer. *Contributions to Mineralogy and Petrology* 171:1-27.
- Park HI, Chang HW, Jin MS (1988a) K-Ar ages of mineral deposits in the Taebag mountain district. *J. the Korean Inst. of Mining Geol.* 21:57-67.
- Park HI, Chang HW, Jin MS (1988b) K-Ar ages of mineral deposits in the Gyeonggi massif. *J. the Korean Inst. of Mining Geol.* 21: 263-275.
- Rickwood PC (1989) Boundary lines within petrologic diagrams which use oxides of major and minor elements. *Lithos* 22:247-263.
- Sagong H, Kwon ST, Ree JH (2005) Mesozoic episodic magmatism in South Korea and its tectonic implication. *Tectonics*, 24:1-18.
- Schmidt MV (1992) Amphibole composition in tonalite as a function of pressure: an experimental calibration of the Al-in-hornblende barometer. *Contributions to Mineralogy and Petrology* 110:304-310.
- Shimazaki H, Shibata K, Uchiumi S, Lee MS, Kaneda H (1987) K-Ar ages of some W-Mo deposits and their bearing on metallogeny of South Korea. *Mining Geol.* 37: 395-401.
- So CS, Shelton KL, Chi SJ, Yun ST (1991) Geochemical studies of the Gyeongchang W-Mo mine, Republic of Korea: Progressive meteoric water inundation of a magmatic hydrothermal system. *Econ. Environ. Geol.* 86: 750-767.
- Tarney J, Jones CE (1994) Trace element geochemistry of orogenic igneous rocks and crustal growth models. *Journal of the Geological Society of London* 151: 855-868.
- Zhai MG, Zhang YB, Zhang XH, Wu FY, Peng P, Li QL, Hou QL, Li TS, Zhao L (2016) Renewed profile of the Mesozoic magmatism in Korean Peninsula: Regional correlation and broader implication for cratonic destruction in the North China craton. *Science China Earth Sciences* 59:2355-2388.

Structural features tied to mineral deposits deformed by shear zones

Stanislav Jacko¹, Roman Farkašovský¹, Julián Kondela¹, Alexander D. Thiessen¹

¹Department of Geosciences, Faculty BERG, Technical University of Košice, Slovakia

Abstract. The argentiferous Strieborna vein of the Rožňava ore field (ROF) is closely connected with Transgemic shear zone (TGSZ) evolution. Spatial geometry of the vein segments is the product of four boudin evolution stages: (1) pre-deformed, (2) initial, (3) boudin forming and (4) boudin differentiation stage controlled by vertical mineralization allocation. During the Cretaceous transpressional events, the vein was segmented into five morphologically individual symmetrical – asymmetric bodies with different mass value of chemical elements. Results of the Strieborna vein sulphosalt spatial analysis confirm their vertical zonation. Sb and Ag contents show a tendency for decreasing concentrations with depth, while Bi contents increase with depth and preserves boudin evolution stages created at different rheological environments. Rheological contrast between the boudin body and the surrounding rocks creates different boudin shapes. The higher the contrast, the higher the asymmetry. The economically most prospective elements are concentrated in the asymmetric boudins tension shadows (low pressure areas).

1 Introduction

Vein-type deposits overprinted by later shearing around the world, are not commonly economically mined. Sparse resources, structural reworking, mineralization heterogeneity and exploration costs moved the shear zone deposits outside of economic interest. However, some visibly sheared and boudinaged gold (Baker et al. 2002; Smith et al. 2013; Martins et al. 2016) or iron deposits (Roache 2004; Rajabzadeh and Rasti 2017) are profitably mined. Structural research and understanding of the shear zones in the economically potential areas may affect the mining exploration. Research may also as increase the quality and quantity of raw materials in the heterogenic structural space. The Strieborna vein represents a significant, and recently one of the most valuable ROF ore vein bodies situated at the TGSZ. The vein occurs within two rheologically different Early Paleozoic rock sequences controlled by a competence contrast, i.e. in between brittle-deformed meta-pyroclastics underlying the vein, and ductile-deformed phyllites forming the vein's hanging wall. The Strieborna vein shows a record of multiple epigenetic hydrothermal processes (Sasvári and Maťo 1998; Hurai et al. 2002). This study focuses on the Strieborna vein boudinage development at rheologically contrasting parent rocks. It aims to identify boudin formation continuity based on the analysis of boudin geometry, the structural pattern of the boudin bodies, and also to check temporal

and spatial evolution of ore phases throughout the vein boudinage deformation.

2 Geological Setting

The Rožňava ore field is located in the Gemic belt (the Gemic Superunit cf. Plašienka 1999; Bezák et al. 2009) of the Western Carpathians (Figure 1). It is the southernmost unit of the Western Carpathians (Andrusov 1968) formed in the south edge of Variscan orogeny. Structurally, the Gemic belt consists of southwardly dipped nappe sheets evolved initially from Variscan fold structures (Rozložník 1976; Grecula et al. 1995). Broadly preserved cleavage sets transposing the basement rocks primary foliation belong partly to Variscan structural remnants (Grecula et al. 1995; Faryad 1995; Lexa et al. 2003), or to the Alpine shortening results (Maluski et al. 1993; Dallmeyer et al. 1994) as they occur in both Late Paleozoic and Mesozoic cover formations (Jacko and Sasvári 1990; Plašienka 1999; Németh 2002). Also, regionally significant shear zones of NE-SW and NW-SE directions cutting either basement or Mesozoic formations belong to the Alpine origin.

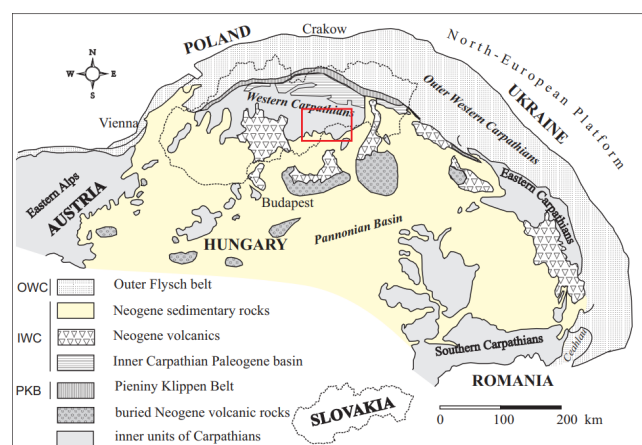


Figure 1. Location of the study area at the Western Carpathians.

Early Paleozoic volcano-sedimentary, a low-grade metamorphic suite of the Gelnica Group itself is divided into three formations (Vlachovo, Bystrý potok, Drnava; Bajanič et al. 1983; Vozárová and Ivanička 1996). Only the last of them is present in the ROF area. During Variscan and Alpine regional metamorphism, the Gelnica Group sequence was metamorphosed under lower greenschist P-T conditions to variously colored phyllites, metasandstone/

metagreywackes, crystalline limestones and metavolcanic rocks (Faryad 1991, 1995; Vozárová 1993).

3 Methodology

The structural analysis of the Strieborna vein was realized at the surface as well as underground. The Strieborna vein itself was systematically surveyed at five underground mining levels. Geological structures were also correlated with controlling audio-frequency magnetotelluric sources at higher spectral band (~1 Hz to 80 kHz) signals. Boudins geometrical classification is based on Ramsay and Huber (1987), Hammer and Passchier (1991), Goscombe and Passchier (2003), Goscombe et al. (2004), Rodrigues et al. (2016) and extended by parameters described by Samanta et al. (2017). We compared surface structural research with the ore vein mineralization distribution and structural pattern of the Strieborna vein ore body.

4 Results and discussion

4.1 Structure and lithology

The Drnava Formation rock sequences (Figure 2) show NE-SW direction and generally moderate SE inclination of the structural planes. They were deformed by the Transgemic shear zone (TGSZ) of the strike same direction in the studied area. The ROF rock suites, including mineralized veins, were incorporated into the TGSZ structural pattern.

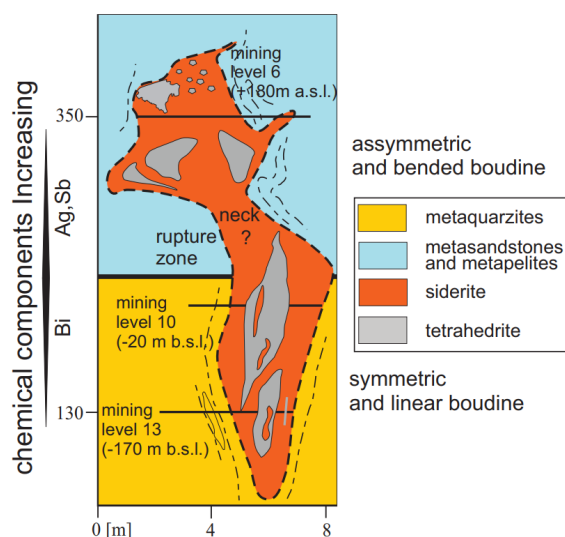


Figure 2. Vertical scheme illustrates dependence between vein boudin morphology and surrounding rocks rheology. Distribution of chemical compositions relates to successive mineralization process of tetrahedrite and sulphosalts as well as boudin formation.

Ore veins of the ROF area were developed within metapsammitic rocks of the Drnava Formation that are irregularly intercalated by dark metapelites with tiny conglomeratic and carbonate layers (Figure 2). All mentioned rocks are

metamorphosed at greenschist facies conditions (Faryad 1991, 1995; Vozárová 1993).

4.2 Cleavage and folds

A typical feature of the Gelnica Group rocks is a steep cleavage set that relates to area shortening. Early Cretaceous tectonometamorphic processes (deformation stage AD1 sensu Németh et al. 1997) formed an asymmetric positive fan structure across the entire length of the Gemeric belt (Lexa et al. 2003). A progressive structural evolution, caused by shear strain, successively transposed Alpine folds into a position parallel to the curved structure of the Gemeric belt. Consequently, fold axes orientation varies between SW–NE and SSW–NNE, depending on their position in the above-mentioned bent structure. An average fold amplitude at the shear zone varies from 0.5 to 2.0 meters. The fold axial cleavage planes are frequently injected by hydrothermal quartz veins. They are well-identified in the adjacent fold limbs, mainly at rheological boundaries between slates and hydrothermal quartz filling.

4.3 Boudins

Nicely preserved Strieborna vein boudins occupy a depth interval between the 6th and 10th mining levels, forming five boudin bodies. Their length varies from several tens to more than 100 m. They originated along two dislocation sets filled by mylonites of meter to decimeter wide thicknesses. Structural data indicate that the process of the Strieborna vein boudinage is closely related to the strike-slip activity of the mentioned fault sets. The Strieborna vein and the Čučma stibnite vein recline at the same NNE–SSV fault structure and they contain the same mineral associations of the quartz–sulphidic phase (Grecula et al. 1995; Sasvári and Maťo 1998; Mikuš et al. 2018). They probably underwent a similar hydrothermal evolution during the final steps of vein formation. The brittle–ductile mylonitic shear zone up to 1 m thick runs near the Strieborna vein at 6th mining level, parallel to foliation in the metapelitic rocks. The dark phyllites enclose lenses of white hydrothermal quartz with variable lengths and visible signs of shear deformation. They are segmented by shear bands, or they form boudins, asymmetric objects, and remnants of isoclinal folds. The minor veins can be also deformed by shear bands or folded.

Based on the kinematics (sensu Goscombe et al. 2004), the minor boudins can be divided into two types: boudins, the origins of which relate to tension deformation (Figure 3), and those that are segmented by shear movement (Figure 4). According to the boudin geometry, they can be divided into three main categories. Asymmetric shear band boudins have boudin blocks separated by shear planes. The boudin blocks are formed mainly by siderite, less by quartz.

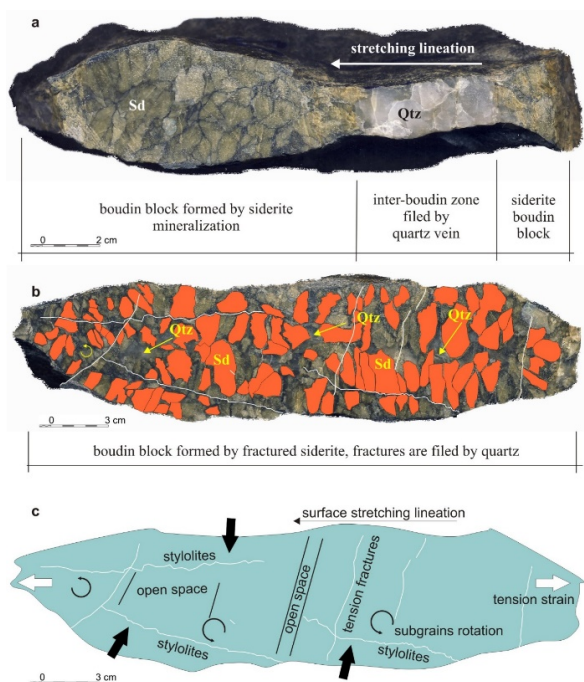


Figure 3. Structural geometry of symmetric torn boudins. a – Position of younger extensional quartz into siderite. b – Cleavage planes and siderite tensile fractures filled by younger hydrothermal quartz. c – Tensile boudin internal structure composed of several structure elements, i.e. responded paleostress marked by stylolites and tension fractures. Boudinal stretching also allowed subgrains rotation into paleostress free boudin segments.

The inter-boudin zone is filled by quartz or by surrounding metapelitic rock. In some cases, the terminal parts of the shear band boudin blocks were dragged in the direction of the boudin separation and form drawn boudins. The boudin blocks of the symmetric torn boudins are always formed by siderite, and inter-boudin zones are filled with quartz. The siderite in the boudin blocks is brittly deformed. Single grains are separated from each other, or they are fractured along their cleavage planes. The open space among the separated parts of the siderite grains is filled with quartz. Various microstructural markers were observed in torn boudins, these were previously unknown in the ROF area. Pressure markers like tapered stylolite teeth and stylolitic joint surfaces indicate a maximal compressive stress oriented perpendicularly to the foliation. The minor siderite veins deformed as a brittle material set in the more ductile metapelites. The foliation planes of the surrounding metapelites are bent around the boudin structures (Figure 4).

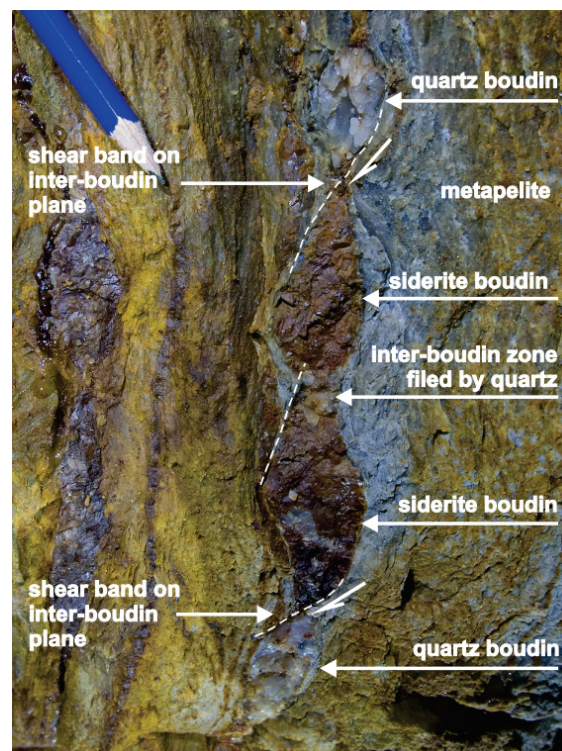


Figure 4. Asymmetric shear bands distribution at an inter-boudin plane filled by brown siderite and light quartz. Lens-like distribution of sideritic and quartzose boudins, divided by shear band inter-boudin planes resulting from shear deformation of relatively much more thickened ductile phyllite surrounding.

3 Conclusion

The Strieborna vein deformations were evidently related to the sinistral brittle–ductile shearing along the Transgemic shear zone (TGSZ). Five boudin bodies, several tens to more than 100 m in length, were present between 6th and 10th mining levels of the vein. They were created at two regional dislocation sets of NNE–SSW and NE–SW directions. Both spatially corresponded to the principal Alpine structures of the Rožňava mining area and show slightly to moderately inclined strike-slip kinematics.

Boudins of sample dimensions provide valuable information about the successive evolution of shear zone deformation, kinematics, and internal geometry as well as the precipitation of individual vein associations.

The oldest demonstrable Strieborna vein boudinage stage was the post-quartz–siderite one, which tied to consecutive deformations. The presence of siderite grains rotated in the direction of the stretching lineation and diagonally oriented stylolitic patterns seem to follow successive deformations of the TGSZ.

The rheological contrast between the boudin body and the surrounding rocks creates different boudin shapes. The higher the contrast, the higher the asymmetry. The economically most

prospective elements are concentrated in the asymmetric boudins tension shadows (low pressure areas).

References

- Andrusov D (1968) Grundriss der Tektonik der Nördlichen Karpaten. Slovak Academy of Sciences, Bratislava, pp 1–188
- Bajaník Š, Hanzel V, Ivanička J, Mello J, Pristaš J, Reichwalder P, Snopko L, Vozár J, Vozárová A (1983) Explanation to geological map of the Slovenské Rudohorie Mts. –eastern part. Dionýz Štúr Geological Institute, Bratislava, pp 1–223 (in Slovak)
- Baker DEL, Seccombe PK, Collins WJ (2002) Structural history and timing of gold mineralization in the northern East Strelley Belt, Pilbara Craton, Western Australia. *Econ Geol* 97: 775–785
- Bezák V, Biely A, Broska I, Bóna J, Buček S, Elečko M, Filo I, Fordinal K, Gazdačko L, Grecula P, Hraško L, Ivanička J, Jacko S sen., Jacko S jun., Janočko J, Kaličiak M, Kobulský J, Kohút M, Konečný V, Kováčik M, Lexa J, Madaras J, Maglay J, Mello J, Nagy Z, Németh Z, Olšovský M, Plašienka D, Polák M, Potfaj M, Pristaš J, Šiman P, Šimon L, Teták F, Vozárová A, Vozár J, Žec B (2009) Explanations to the general geological map of Slovak Republic, scale 1: 500 000. *Geol Surv Slov Rep*, Bratislava, pp 1–534 (in Slovak with English summary)
- Dallmeyer RD, Neubauer F, Fritz H, Mocanu V (1994) Pre-Variscan, Variscan and Alpine tectonothermal evolution within the southern Carpathians, Romania: evidence from 40Ar–39Ar hornblende and muscovite ages. *J Czech Geol Soc* 39: 18–19
- Faryad SW (1991) Metamorphism of the Early Paleozoic sedimentary rocks in the Gemicum. *Miner Slov* 23: 315–324
- Faryad SW (1995) Determination of P–T metamorphism conditions in the Early Paleozoic Gemicum rock sequences. *Miner Slov* 27: 9–19
- Goscombe B, Passchier CW (2003) Asymmetric boudins as shear sense indicators – an assessment from field data. *J Struct Geol* 25: 575–589
- Goscombe B, Passchier CW, Hand M (2004) Boudinage classification: end-member boudin types and modified boudin structures. *J Struct Geol* 26: 739–763
- Grecula P, Abonyi A, Abonyiová M, Antaš J, Bartalský B, Bartalský J, Dianiška I, Drnzik E, Ďuďa R, Gargulák M, Gazdačko L, Hudáček J, Kobulský J, Lörincz L, Macko J, Návesňák D, Németh Z, Novotný L, Radvanec M, Rojkovič I, Rozložník L, Rozložník O, Varček C, Zlocha J (1995) Mineral deposits of the Slovak ore Mountains, Vol. 1., Geocomplex, Bratislava, pp 1–834
- Hanmer, S, Passchier C (1991) Shear-Sense Indicators: A Review. *Geological Survey of Canada Papers* 90-17, pp 1–72
- Hurai V, Harčarová E, Huraiová M, Ozdín D, Prochaska W, Wiegrová V (2002) Origin of siderite veins in the Western Carpathians I. P–T–X– $\delta^{13}\text{C}$ – $\delta^{18}\text{O}$ relations in ore-forming brines of the Rudňany deposits. *Ore Geol Rev* 21: 67–101
- Jacko S, Sasvári T (1990) Some remarks to an emplacement mechanism of the West Carpathian Paleo-Alpine nappes. *Geol Carpath* 41: 179–197
- Lexa O, Schulmann K, Ježek J (2003) Cretaceous collision and indentation in the West Carpathians: view based on structural analysis and numerical modeling. *Tectonics* 22: 1066, DOI: 10.1029/2002TC001472
- Maluski H, Rajlich P, Matte P (1993) 40Ar–39Ar dating of the Inner Carpathian Variscan basement and Alpine mylonitic overprinting. *Tectonophysics* 223: 313–337
- Martins BD, Lobato LM, Rosiere CA, Hagemann SG, Santos JOS, Villanova FLDP, Silva RCCE, Lemos LHD (2016) The Archean BIF-hosted Lamego gold deposit, Rio das Velhas greenstone belt, Quadrilátero Ferrífero: evidence for Cambrian structural modification of an Archean orogenic gold deposit. *Ore Geol Rev* 72: 963–988
- Mikuš T, Kondela J, Jacko S, Milovska S (2018) Garavellite and associated sulphosalts from the Strieborna vein in the Rožňava ore field (Western Carpathians). *Geol Carpath* 69: 221–236
- Németh Z (2002) Variscan suture zone in the Gemicum: contribution to reconstruction of geodynamic evolution and metallogenetic events of Inner Western Carpathians. *Slovak Geol Mag* 8: 247–257
- Németh Z, Gazdačko L, Návesňák D, Kobulský J (1997) Polyphase tectonic evolution of the Gemicum (the Western Carpathians) outlined by review of structural and deformational data. In: Grecula P, Hovorka D, Putiš M (eds) *Geological Evolution of the Western Carpathians*. Geocomplex, Bratislava, pp 215–224
- Plašienka D, Grecula P, Putiš M, Kováč M, Hovorka D (1999) Evolution and structure of the Western Carpathians: an overview. In: Grecula P, Hovorka D, Putiš M (eds) *Geological Evolution of the Western Carpathians*. Geocomplex, Bratislava, pp 1–24
- Rajabzadeh MA, Rasti S (2017) Investigation on mineralogy, geochemistry and fluid inclusions of the Goushti hydrothermal magnetite deposit, Fars Province, SW Iran: a comparison with IOCGs. *Ore Geol Rev* 82: 93–107
- Ramsay JG, Huber MI (1987) *The Techniques of Modern Structural Geology. Volume 2: Folds and Fractures*. Academic Press, London, pp 516–633
- Roache TJ (2004) Shear zone versus fold geometries at the Cannington Ag–Pb–Zn deposit: implications for the genesis of BHT deposits. *J Struct Geol* 26: 1215–1230
- Rodrigues BC, Peternell M, Moura A, Schwindinger M, Pamplona J (2016) P–T path development derived from shearband boudin microstructure. *J Struct Geol* 90: 95–110
- Rozložník L (1976) Relationship of Siderite Metallogenesis and Tectonics of the Spis Ore Mountains and Their Position in Alpides. Faculty BERG, Košice, pp 1–301
- Samanta SK, Majumder DB, Sarkar G (2017) Geometry of torn boudin – an indicator of relative viscosity. *J Struct Geol* 104: 21–30
- Sasvári T, Maťo L (1998) The characteristics of the Rožňava ore district, in relation to the structural–tectonic analysis and mineralization exemplified by the deposition conditions of the Strieborna vein, Mária mine, Rožňava. *Acta Mont Slov* 3: 33–117
- Smith MT, Rhys D, Ross K, Lee C, Gray JN (2013) The long canyon deposit: anatomy of a new off-trend sedimentary rock-hosted gold discovery in northeastern Nevada. *Econ Geol* 108: 1119–1145
- Vozárová A (1993) Variscan metamorphism and crustal evolution of the Gemicum. *Západ Karpaty Sér Mineral Petrogr Geochem Metalogen* 16: 55–117 (in Slovak with English summary)
- Vozárová A, Ivanička J (1996) Geodynamic position of acid volcanism of the Gelnica Group (Early Paleozoic, southern Gemicum; Inner Western Carpathians). *Slovak Geol Mag* 3–4: 245–250

Tourmaline composition records fluid-rock interaction: implications for cassiterite precipitation in the Triassic Chacaltaya district, Bolivia

Lisard Torró¹, Matthieu Harlaux², Angela Castro-Morante¹, Jean Vallance¹, Lorenzo Tavazzani³, Anne-Sophie Bouvier⁴, Thomas Bovay⁴, Cyril Chelle-Michou³, Thierry Sempere⁵, Joan Carles Melgarejo⁶

¹Geological Engineering Program, Pontifical Catholic University of Peru (PUCP), Peru

²BRGM – French Geological Survey, 45060 Orléans, France

³Department of Earth Sciences, ETH Zürich, Switzerland

⁴Institute of Earth Sciences, University of Lausanne, Switzerland

⁵ANDES C&P, Lima, Peru

⁶Departament de Mineralogia, Petrologia i Geologia Aplicada, Universitat de Barcelona, Spain

Abstract. The Triassic Chacaltaya Sn-polymetallic district, located in the Cordillera Real of Bolivia, is spatially and genetically associated with major tourmalinization. We document three petrographic types of tourmaline associated to pre-ore greisens (Tur-1) and syn-ore tourmaline-cemented breccias (Tur-2) and veins (Tur-3). Tourmalines belong to the alkali group and have Fe-rich compositions with overlapping Fe/(Fe+Mg) ratios. Tur-1 is relatively enriched in Zn and Li whereas Tur-3 is relatively enriched in Ca, Sc, V, Cr, Sr, Sn, Y, Cs, Be, and Zr, with Tur-2 showing intermediate compositions between those of Tur-1 and Tur-3. Strong positive Eu anomalies in all tourmaline types indicate dominantly reduced hydrothermal conditions while Tur-1 to Tur-3 record a shift towards HREE-enriched compositions. In situ $\delta^{18}\text{O}$ and $\delta^{11}\text{B}$ analyses of tourmaline indicate a dominant magmatic origin of the hydrothermal fluids. Collectively, these results suggest that cassiterite mineralization at Chacaltaya resulted from the interaction of magmatic fluids derived from a peraluminous S-type granite with the metamorphic host rocks.

1 Introduction

Tourmaline is a useful indicator mineral to trace geologic processes associated with the formation of ore deposits (Slack and Trumbull 2011). It is a common mineral in most ore deposits and associated igneous rocks along the Central Andean tin belt (Kelly and Turneure 1970), which produced ~14% of the historic world tin supply (Lehmann 2021). Previous studies on tourmaline from the Central Andean tin belt have been mainly focused on the late Oligocene San Rafael Sn-Cu deposit (Mlynarczyk and Williams-Jones 2006; Harlaux et al. 2020, 2021). Here we combine petrographic and in situ geochemical analyses of tourmaline from the Triassic Chacaltaya Sn-polymetallic district in the Cordillera Real of Bolivia (Fig. 1) to provide new constraints on the geological processes leading to cassiterite deposition.

2 Geological setting

The Central Andean tin belt stretches over >900 km from southeast Peru across Bolivia to northernmost Argentina (Fig. 1) along the Eastern Cordillera. This belt can be divided into a northern branch trending NW-SE, and a southern branch trending N-S (Fig.

1; Mlynarczyk and Williams-Jones 2005). In the northern branch, Sn-W deposits consist mainly of lodes, veins/breccias, and stratabound bodies, which are spatially associated to granitic plutons of Triassic and late Oligocene ages (Fig. 1). Triassic-age Sn-W-polymetallic deposits occur immediately south and north of the orocline core hinge along the Cordillera Real of northern Bolivia, including the Chacaltaya district, and the Cordillera de Carabaya of southeast Peru, respectively (Lehmann et al. 1990).

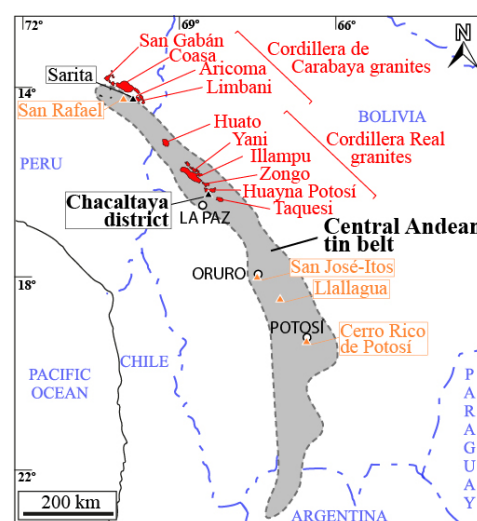


Figure 1. Map of the Central Andes showing the location of the Chacaltaya district in the Central Andean tin belt (grey field). The main Triassic plutons along the Cordillera Real and Cordillera de Carabaya are shown in red. The Triassic Sn deposits are labelled in black color, and late Oligocene-Miocene Sn deposits, in orange color.

The Chacaltaya district is located 20 km north of La Paz and ~5 km south of the Triassic (ca. 240–218 Ma) Huayna-Potosi two-mica granite batholith (Fig. 1). Rocks exposed in this district consist mostly of mid-Silurian dark shales and siltstones interbedded with thin sandstone beds of the Uncía Formation, and the overlying late-Silurian interbedded quartz-arenites and mudstones of the Catavi Formation. The Paleozoic metasedimentary rocks have been intruded by a small stock of cordierite-bearing peraluminous granite, which is

exposed in the central part of the Cerro Chacaltaya massif. Three types of hydrothermal features are distinguished in the Chacaltaya district: greisens, hydraulic breccias, and veins. Greisen occurs in most of the exposed Chacaltaya granitic stock (Lehmann 1985). Hydraulic breccias occur mostly on the eastern side of the Chacaltaya stock and are hosted by quartzites of the Catavi Formation. Finally, discordant veins and concordant-stratabound veins and veinlets are widespread across the Chacaltaya district (Lehmann 1985). The stratabound mineralization is chiefly associated with quartzitic lithologies of the Catavi Formation; a U-Pb LA-ICP-MS date of 218.3 ± 5.5 Ma was determined on cassiterite from the stratabound mineralization (Gemrich et al. 2021).

3 Results

Three petrographic types of tourmaline (referred as Tur-1, 2, and 3) were identified in the Chacaltaya district based on detailed mineralogical and textural observations. Tourmaline in the greisen (Tur-1) occurs as disseminated millimeter- to centimeter-size grains and aggregates intergrown with white mica and quartz, or as pseudomorph after magmatic K-feldspar phenocrysts (Fig. 2A). At the microscopic scale, Tur-1 forms orange, subhedral, elongate to acicular crystals commonly showing a radial texture. Tur-1 crystals are optically homogeneous (Fig. 2B) except for discrete core to rim zoning observed locally in a few grains. Tourmaline in breccias (Tur-2) constitutes the cement of heterolithic rock fragments and mineral clasts (Fig. 2C) and forms a dense aggregate of very fine-grained, acicular crystals that commonly grew perpendicular to the clast borders in triangular and acute-angle spaces (Fig. 2D). Tur-2 crystals are dark green in color and show a discrete core to rim zoning. Isolated Tur-1 clasts up to 1 mm in size are cemented or epitaxially overgrown by Tur-2 within the breccia, thus demonstrating that Tur-1 formed prior to Tur-2. Finally, Tur-3 occurs in quartz veins hosted in the metasedimentary rocks and their alteration haloes (Fig. 2E). Tur-3 is characterized by a dark green color, and appears as subhedral, elongated to acicular crystals, which often form radial aggregates ranging from 30 μm to 2 mm in length intergrown with comb-textured quartz. Both Tur-2 and Tur-3 are locally finely intergrown with cassiterite indicating their co-crystallization from the same hydrothermal fluid (Figs. 2D, F).

Major and minor element analyses of tourmaline were performed at the University of Barcelona using a JEOL JXA-8230 electron microprobe. The three tourmaline types belong dominantly to the alkali group and have mostly Fe-rich compositions, close to the schorl endmember, and partly extending into the compositional fields of foitite and dravite. Tur-1 has mostly schorl to foitite compositions with $\text{Fe}/(\text{Fe} + \text{Mg}) = 0.58$ to 0.94 and $X_{\square}/(X_{\square} + \text{Na} + \text{K}) = 0.19$ to 0.61. Tur-2 is also characterized by schorl to foitite compositions with

$\text{Fe}/(\text{Fe} + \text{Mg}) = 0.54$ to 0.97 and $X_{\square}/(X_{\square} + \text{Na} + \text{K}) = 0.08$ to 0.70. Finally, Tur-3 has dominantly schorl compositions with a few analyses extending into the foitite and dravite compositional fields, with $\text{Fe}/(\text{Fe} + \text{Mg}) = 0.35$ to 0.92 and $X_{\square}/(X_{\square} + \text{Na} + \text{K}) = 0.05$ to 0.71.

Tourmaline trace element analyses were carried out at the ETH Zürich by LA-ICP-MS using the same equipment, instrumental setup, reference materials, measured isotopes, and data reduction process as in Harlaux et al. (2020). Tourmaline contains between 100s and some 1,000s ppm of K, Mn, and Zn, and between 10s to some 100s ppm of Li, Be, P, Sc, V, Cr, Ni, Sr, Sn, and Pb. Compared to major element compositions, trace elements in tourmaline show a wider range of variations. Principal component analysis (PCA) of trace element data shows that Tur-1 is distinguishably enriched in Zn and Li relative to Tur-2 and Tur-3 (Fig. 3A). In contrast, Tur-3 is relatively enriched in Sc, V, Cr, Sr, Sn, Y, Cs, Be, and Zr and depleted in Zn and Li. Tur-2 has trace element compositions intermediate between those of Tur-1 and Tur-3, except for a slight enrichment in U and Th. The contents of rare earth elements (REE) tend to increase from Tur-1 ($[\Sigma\text{REE}]_{\text{avg.}} = 5$ ppm) to Tur-2 ($[\Sigma\text{REE}]_{\text{avg.}} = 14$ ppm) and Tur-3 ($[\Sigma\text{REE}]_{\text{avg.}} = 12$ ppm), principally marked by an enrichment in HREE (Fig. 3B). The UCC-normalized REE diagrams show systematic strong Eu positive anomalies (Fig. 3B).

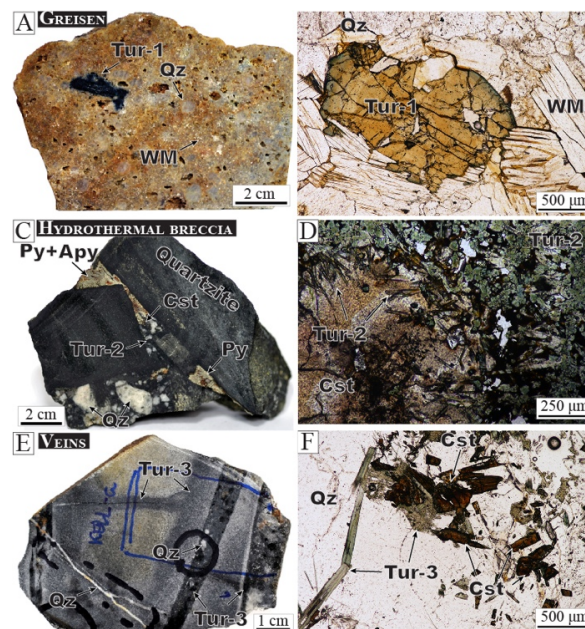


Figure 2. Mineralogical and textural features of tourmaline from the Chacaltaya district. A) Greisen composed of white mica, quartz, and tourmaline (Tur-1). B) Subhedral, millimetric tourmaline (Tur-1) crystal intergrown with secondary white micas and quartz in the greisen. C) Hydraulic breccia composed of angular rock fragments of quartzites (Catavi Formation) within a cement of fine-grained tourmaline (Tur-2), cassiterite, and sulfides. D) Needles of green tourmaline (Tur-2) intergrown with cassiterite composing the cement of the hydraulic breccia. E) Tourmaline (Tur-3)-rich veins and

veinlets crosscutting quartzites of the Catavi Formation. F) Tourmaline (Tur-3) intergrown with cassiterite in a quartz vein. Apy: arsenopyrite; Cst: cassiterite; Py: pyrite; Qz: quartz; Tur: tourmaline; WM: white mica.

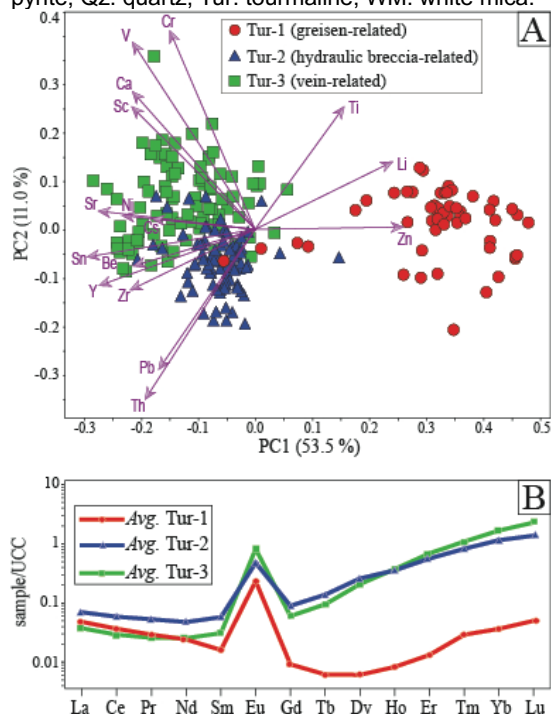


Figure 3. Principal component analysis (PCA) of log-transformed data set of selected minor and trace elements (A) and average UCC-normalized REE contents (B) of tourmaline from the Chacaltaya district. Upper continental crust values (UCC) after Rudnick and Gao (2014).

Oxygen and boron isotope analyses of tourmaline were performed at the SwissSIMS ion probe national facility at the University of Lausanne using the instrumental setup, reference materials, and data reduction process as in Harlaux et al. (2021). Tur-1 has $\delta^{18}\text{O}$ values ranging between 10.9 ‰ and 12.6 ‰, and $\delta^{11}\text{B}$ values between -13.5 ‰ and -10.5 ‰ (Fig. 4A). Tur-2 has $\delta^{18}\text{O}$ in a range between 13.5 ‰ and 17.0 ‰, and $\delta^{11}\text{B}$ in a range between -14.4 ‰ and -12.3 ‰. Finally, Tur-3 yields $\delta^{18}\text{O}$ values comprised between 12.5 ‰ and 14.4 ‰ and $\delta^{11}\text{B}$ in a range between -14.7 ‰ and -9.9 ‰.

4 Discussion

The three petrographic types of tourmaline identified in the Chacaltaya district are of hydrothermal origin. Tourmaline in the greisen (Tur-1) was formed by the replacement of primary igneous minerals during high-temperature interactions between the granitic rocks and B-rich hydrothermal fluids. In contrast, tourmaline in the cassiterite-bearing breccias (Tur-2) and veins (Tur-3) crystallized as open-space filling.

The conspicuous increase of Sn content from Tur-1 to Tur-3 (Fig 3A) may suggest increasing Sn activity in the hydrothermal fluid over time, eventually leading to cassiterite deposition coevally with Tur-2

and Tur-3 formation. High contents of Li (10s to >100 ppm) and Sn (100s to >1000 ppm), as observed in Tur-1, are typical of tourmaline that crystallized from magmatic-hydrothermal fluids (Harlaux et al. 2020; Codeço et al. 2021). In contrast, high contents of Sr, V, and Cr in tourmaline seem to be more likely attributed to crystallization from a fluid of metamorphic origin, or that equilibrated with metamorphic rocks (Sciuba et al. 2021). Following these findings, Tur-3, and to a lesser extent also Tur-2, which are enriched in Sr, V, and Cr relative to Tur-1, probably record interaction of a magmatic-hydrothermal fluid with the surrounding metamorphic rocks and/or mixing with a metamorphic fluid component. On the other hand, the fact that tourmaline from the Chacaltaya district systematically shows strong positive Eu anomalies in all tourmaline types indicate dominantly reduced conditions of the hydrothermal fluids (van Hinsberg 2011; Liu et al. 2017).

Considering crystallization temperatures of 500°C for Tur-1, 450°C for Tur-2, and 400°C for Tur-3, estimated from previous studies (Kelly and Turneaure 1970; Lehmann 1985), we calculated the $\delta^{18}\text{O}$ and $\delta^{11}\text{B}$ composition of water in equilibrium with tourmaline (Fig. 4B) using the O and B isotope fractionation factors of Zheng (1993) and Meyer et al. (2008), respectively. The isotopic compositions of water equilibrated with greisen-hosted Tur-1 fall in a range of $\delta^{18}\text{O}$ and $\delta^{11}\text{B}$ values typical of magmatic fluids derived from a peraluminous S-type granite, thus suggesting a magmatic origin for the greisen-forming fluids. A fluid equilibrated with breccia-hosted Tur-2 and vein-hosted Tur-3 yields $\delta^{11}\text{B}$ values that overlap those of Tur-1 but has $\delta^{18}\text{O}$ values that are mostly higher and fall outside of the typical compositional range for magmatic fluids. Geochemical modelling based on the measured O and B isotopic compositions of tourmaline and using the calculations detailed by Harlaux et al. (2021) is shown in Figure 4C. Rayleigh fractionation driven by tourmaline crystallization from a magmatic fluid at decreasing temperatures from 500 to 450 °C, results in a trend of near-constant $\delta^{18}\text{O}$ and increase in $\delta^{11}\text{B}$ values, which reproduces closely the composition of greisen-related Tur-1 for a fractionation degree of 10 to 70 %. Interaction between the magmatic fluid and the host metasedimentary rocks was modeled for different water/rock ratios (0.1 to 10) at 500 °C by assuming isotopic exchange with muscovite in the host rocks and initial values of $\delta^{18}\text{O} = 14.0$ ‰ and $\delta^{11}\text{B} = -6.0$ ‰ (see Harlaux et al. 2021). Results of the fluid-rock interaction modeling reproduce the measured isotopic compositions of Tur-2 to Tur-3 for moderate water/rock ratios of 0.1-0.5.

5 Conclusions

The textural, chemical, and isotopic characteristics of tourmaline from the Chacaltaya Sn district indicate that the hydrothermal conditions were sustainably reduced during the deposition of pre-

and syn-ore tourmaline. In situ isotope data in tourmaline record interaction of a magmatic-hydrothermal fluid with the metasedimentary host rock or with fluids that equilibrated with the host rock. Therefore, water-rock interaction was probably key to the precipitation of cassiterite in the Chacaltaya district.

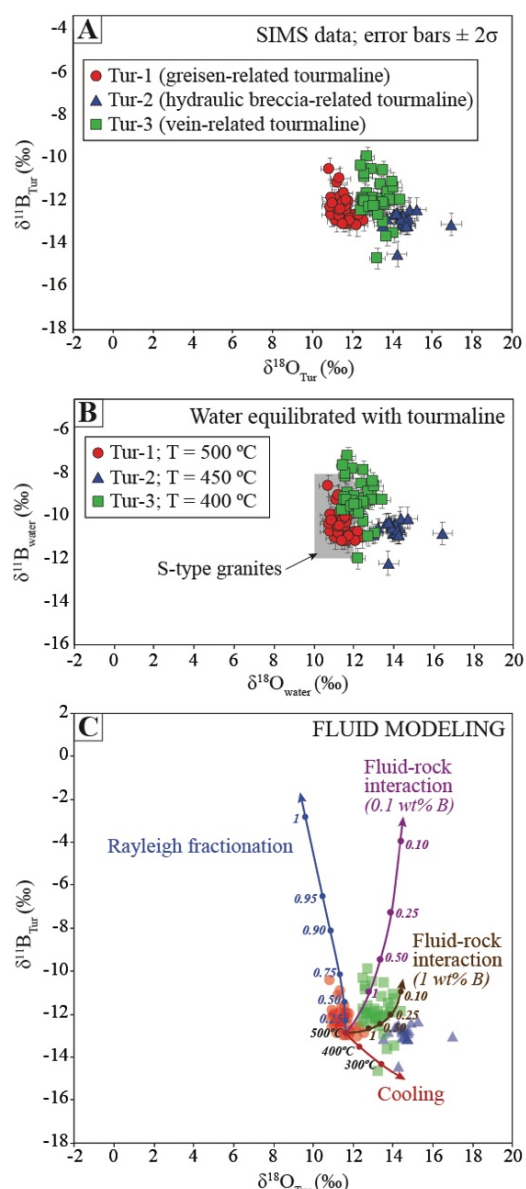


Figure 4. A) Plot of $\delta^{18}\text{O}$ vs. $\delta^{11}\text{B}$ composition of tourmaline from the Chacaltaya district determined by SIMS. B) Calculated $\delta^{18}\text{O}$ vs. $\delta^{11}\text{B}$ composition of water isotopically equilibrated with tourmaline by assuming crystallization temperatures of 500 °C for Tur-1, 450 °C for Tur-2, and 400 °C for Tur-3. The field for peraluminous S-type granites is from Harris et al. (1997) and Trumbull and Slack (2018). C) Modeling of $\delta^{18}\text{O}$ vs. $\delta^{11}\text{B}$ composition of tourmaline calculated for different evolution scenarios.

Acknowledgements

This research work was supported by the Peruvian PROCENCIA-FONDECYT project (grant 1122-

2020 E041-2020-01-01) and the FAI-0009-2021 project granted by PUCP.

References

- Codeço MS, Weis P, Trumbull RB, Van Hinsberg V, Pinto F, Lecumberri-Sanchez P, Schleicher AM (2021) The imprint of hydrothermal fluids on trace-element contents in white mica and tourmaline from the Panasqueira W–Sn–Cu deposit, Portugal. *Miner Deposita* 56:481–508.
- Gemmrich L, Torró L, Melgarejo JC, Laurent O, Vallance J, Chelle-Michou C, Sempere T (2021) Trace element composition and U–Pb ages of cassiterite from the Bolivian tin belt. *Miner Deposita* 56:1491–1520.
- Harlaux M, Kouzmanov K, Gialli S, Laurent O, Rielli A, Dini A, Chauvet A, Menzies A, Kalinaj M, Fontboté L (2020) Tourmaline as a tracer of late-magmatic to hydrothermal fluid evolution: The world-class San Rafael tin (-copper) deposit, Peru. *Econ Geol* 115:1665–1697.
- Harlaux M, Kouzmanov K, Gialli S, Marger K, Bouvier A-S, Baumgartner LP, Rielli A, Dini A, Chauvet A, Kalinaj M, Fontboté L (2021) Fluid mixing as primary trigger for cassiterite deposition: Evidence from in situ $\delta^{18}\text{O}$ – $\delta^{11}\text{B}$ analysis of tourmaline from the world-class San Rafael tin (-copper) deposit, Peru. *Earth Planet Sc Lett* 563:116889.
- Harris C, Faure K, Diamond RE, Scheepers R (1997) Oxygen and hydrogen isotope geochemistry of S- and I-type granitoids: the Cape Granite suite, South Africa. *Chem Geol* 143:95–114.
- Kelly WMC, Turneure FS (1970) Mineralogy, paragenesis and geothermometry of the tin and tungsten deposits of the Eastern Andes, Bolivia. *Econ Geol* 65:609–680.
- Lehmann B (1985) Formation of the strata-bound Kellhuani tin deposits, Bolivia. *Miner Deposita* 20:169–176.
- Lehmann B (2021) Formation of tin ore deposits: A reassessment. *Lithos* 402:105756.
- Lehmann B, Ishihara S, Michel H, Miller J, Rapela C, Sanchez A, Tistl M, Winkelmann L (1990) The Bolivian tin province and regional tin distribution in the Central Andes: a reassessment. *Econ Geol* 85:1044–1058.
- Liu W, Etschmann B, Migdisov A, Boukhalfa H, Testemale D, Müller H, Hazemann J-L, Brugger J (2017) Revisiting the hydrothermal geochemistry of europium (II/III) in light of new in-situ XAS spectroscopy results. *Chem Geol* 459:61–74.
- Meyer C, Wunder B, Meixner A, Romer RL, Heinrich W (2008) Boron-isotope fractionation between tourmaline and fluid: an experimental re-investigation. *Contrib Mineral Petr* 156:259–267.
- Mlynarczyk MSJ, Williams-Jones AE (2005) The role of collisional tectonics in the metallogeny of the Central Andean tin belt. *Earth Planet Sc Lett* 240:656–667.
- Mlynarczyk MSJ, Williams-Jones AE (2006) Zoned tourmaline associated with cassiterite: implications for fluid evolution and tin mineralization in the San Rafael Sn–Cu deposit, southeastern Peru. *Can Mineral* 44:347–365.
- Rudnick RL, Gao S (2014) Composition of the continental crust. In: Holland HD, Turekian KK (Eds) *Treatise on Geochemistry*, 2nd ed. Elsevier, Amsterdam.
- Sciuba M, Beaudoin G, Makvandi S (2021) Chemical composition of tourmaline in orogenic gold deposits. *Miner Deposita* 56:537–560.
- Slack JF, Trumbull RB (2011) Tourmaline as a recorder of ore-forming processes. *Elements* 7:321–326.
- Trumbull RB, Slack JF (2018) Boron isotopes in the continental crust: granites, pegmatites, felsic volcanic rocks, and related ore deposits. In: Marschall HR, Foster GL (Eds) *Boron Isotopes - The Fifth Element, Advances in Isotope Geochemistry: Gewerbestrasse*, Springer-Verlag, p. 249–272.
- van Hinsberg VJ (2011) Preliminary experimental data on trace-element partitioning between tourmaline and silicate melt. *Can Mineral* 49:153–163.
- Zheng Y-F (1993) Calculation of oxygen isotope fractionation in hydroxyl-bearing silicates. *Earth Planet Sc Lett* 120: 247–263.

Lithium-bearing micas in the ‘Lithium-rich Tuff’ from the Macusani Volcanic Field, Puno, Peru

Lisard Torró¹, Cristina Villanova-de-Benavent², Loïs Monnier³, Oscar Laurent³, Mariana K. Segovia-More¹, Mercy K. Sanandres-Flores¹, Johan S. Ramírez-Briones¹, Jean Vallance¹, Stefano Salvi³, Patrice Baby^{1,3}, Joaquín A. Proenza², Fernando Nieto⁴

¹Geological Engineering Program, Faculty of Sciences and Engineering, Pontifical Catholic University of Peru, Peru

²Departament de Mineralogia, Petrologia i Geologia Aplicada, Facultat de Ciències de la Terra, Universitat de Barcelona, Spain

³GET-UMR CNRS/IRD/Univ. Paul Sabatier, Toulouse, France

⁴Departamento de Mineralogía y Petrología and IACT, Universidad de Granada-CSIC, Spain

Abstract. The Falchani Lithium Project has a resource of 0.9 Mt Li hosted in Neogene volcanic tuffs and breccias of the Macusani Volcanic Field. The main host is a newly-defined unit known as ‘Lithium-rich Tuff’ in which Li contents are mostly between 3,000 and 4,000 ppm. Although this tuff is pervasively altered to clays (dioctahedral smectite and kaolinite subgroup minerals) and zeolites, magmatic zinnwaldite and lepidolite crystals are preserved. The composition of the micas in the ‘Lithium-rich Tuff’ is systematically more evolved, i.e., richer in Li and other incompatible lithophile elements, relative to micas in other pyroclastic units and nearby intrusive rocks of the Macusani Volcanic Field.

1 Introduction

In November 2017, Macusani Yellowcake S.A.C., the Peruvian subsidiary of American Lithium Corp., announced the discovery of a major lithium resource in the Falchani Lithium Project, Puno department of south-eastern Peru (Fig. 1). As of February 2023, indicated resources amount to 0.2 Mt Li @ 2,954 ppm Li and inferred resources, to 0.7 Mt Li @ 2,706 ppm Li (<https://americanlithiumcorp.com/falchani-lithium-project>). Lithium resources are hosted by Tertiary rhyolitic tuff, breccia, and ignimbrite of the Macusani Volcanic Field (MVF), chiefly by the so-called ‘Lithium-rich Tuff’ in which Li contents are almost systematically between 3,000 and 4,000 ppm (Nupen 2019).

The general mineralogy of the ‘Lithium-rich Tuff’ is described and discussed in Segovia-More et al. (2023). It comprises relict igneous quartz, feldspar, and micas, and secondary phases such as fine-grained quartz, clays (kaolinite, dioctahedral smectites), and zeolites. In this abstract, we present the first data available on Li-bearing micas from the ‘Lithium-rich Tuff’ and nearby granites, breccias, and ignimbrites from the MVF. Variations in mica compositions are discussed focusing on their contribution to the Li endowment and source magmas.

2 Geological setting

The MVF (Fig. 1) is an ignimbrite basin exposed in the Quenamari Meseta, a plateau at an altitude of 4,400 m.a.s.l. in the Eastern Cordillera of southern Peru (Cheilletz et al. 1992). It is part of the Neogene ignimbrite centers of the Central Andes related to tectonic shortening, crustal thickening, and

contemporaneous lithospheric removal and thinning (Salisbury et al. 2012; Göğüş et al. 2022). The MVF is located between the Cordillera de Carabaya and the Central Andean backthrust belt, and belongs to the Macusani Structural Zone (Perez et al. 2016) previously known as the Precordillera de Carabaya (Sandeman et al. 1997). It is underlain by Triassic syn-rift continental deposits of the Mitu Group, now exposed in the Eastern Cordillera due to tectonic inversion of the Triassic rift during Cenozoic Andean shortening.

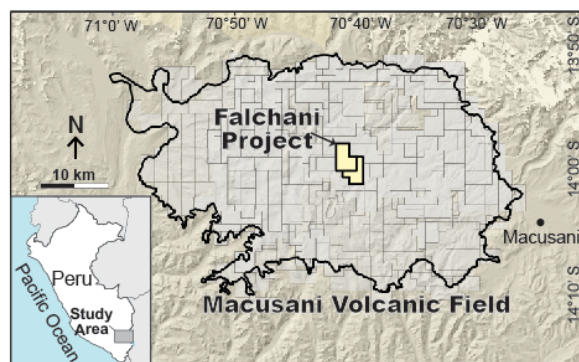


Figure 1. Location of the study area in SE Peru (inset) and of the Falchani Lithium Project concessions in the MVF.

Extrusive and intrusive suites exposed in the Macusani and neighboring volcanic fields represent the youngest igneous events recorded in the Macusani Structural Zone (Clark et al. 1990) and were grouped by Sandeman et al. (1997) into the Crucero Supergroup and the Crucero Intrusive Supersuite, respectively. Volcanic units, including lavas and pyroclastic deposits, were subdivided by these authors into the late Oligocene–early Miocene Picotani Group – comprising medium- to high-K calc-alkaline basalts, shoshonites and S-type rhyodacites and rhyolites – and the mid- to late Miocene Quenamari Group – comprising exclusively silicic peraluminous rocks. In the MVF, volumetrically dominant extrusive rocks belong to the Macusani Formation, the youngest unit of the Quenamari Group. This formation comprises a ~280 to 450 m-thick sequence of strongly peraluminous, rhyolitic, whitish-grey, poorly-consolidated, crystal-rich (~ 45 vol.%), ash-flow tuffs deposited between ca. 10.1 and 6.5 Ma (Cheilletz et al. 1992; Sandeman et al. 1997).

The lithium mineralization in the Falchani project is hosted by rocks of the Macusani Formation. The 'Lithium-rich Tuff' unit has a thickness comprised between 50 and 140 m and is sandwiched between an Upper and a Lower breccia, which are interpreted as deposited in a volcano-sedimentary environment and are also mineralized with average Li contents of ~1,400 and 1,900 ppm, respectively (Nupen 2019). The 'Lithium-rich Tuff' is interpreted to have deposited sub-aerially in an active crater-lake volcano (Nupen 2019).

3 Analytical methods

Point analyses of minerals of the mica group were performed using a CAMECA SXFive electron microprobe (EMPA) at the Centre de Microcaractérisation Raimond Castaing, Toulouse. X-ray (compositional) maps were acquired using a five-channel JEOL JXA-8230 electron microprobe at the Centres Científics i Tecnològics of the University of Barcelona (CCiT-UB). The structural formula of micas was normalized to 11 O, H₂O was determined by assuming (OH+F+Cl) = 2 atoms per formula unit (apfu), and lithium contents were calculated using equations tri1 [SiO₂ > 34 % and MgO < 6 %] and tri2 [SiO₂ > 34 % and MgO > 6 %] of Tischendorf et al. (1997). Raman spectra were obtained on polished thin sections with a HORIBA JobinYvon LabRam HR 800 dispersive spectrometer equipped with an Olympus BXFM optical microscope at the CCiT-UB. Mica grains from a 'lithium-rich tuff' sample were studied by Transmission Electron Microscopy (TEM) to determine the mineral composition by Analytical Electron Microscopy (AEM) in the Thalos microscope of the CIC of the University of Granada, calibrated by natural standards.

3 Results

In the 'Lithium-rich Tuff' unit of the MVF, mica-bearing tuff displays a variety of structures including fine, often contorted, alternating light and dark laminae, as well as nodular, porous, and massive layers. They consist mostly of igneous micas, quartz, and feldspars in a matrix composed of quartz plus clay minerals (see Segovia-More et al. 2023). Mica grains are dark brown to black in color and their size ranges between 0.5 and 5 mm. They commonly disrupt the laminations in the tuff and are enclosed in sag structures. Although these mica grains are largely subhedral with straight outlines, some show embayments filled with clay and quartz. In the powder sample studied by TEM, mica appears without a definite morphology or size, but grains have high-crystallinity electron-diffraction and are larger than the co-existing clay minerals.

Mica grains from the 'Lithium-rich Tuff' are characterized by an octahedral occupancy > 2.8 apfu, which classifies them as tri-octahedral. Two contrasting compositions, labelled as zinnwaldite and lepidolite, were found. Zinnwaldites plot in the field of the siderophyllite-polyolithionite series close to

the siderophyllite end-member (Fig. 2). They yield higher Fe (0.85-1.02 apfu; EPMA data) than Mg (0.26-0.38 apfu) contents, relatively high Ti (0.04-0.09 apfu), and much lower Mn (0.02-0.04 apfu) and Zn (<0.02 apfu). Calculated Li contents are in the range of 0.41 to 0.61 apfu. In the interlayer position, K (0.81-0.90 apfu) is more abundant than Na (0.06-0.10 apfu), whereas the contents of Rb (0.01-0.02 apfu) and of Ca, Cs, and Ba (<0.01 apfu) are much lower. Their F content is of 1.01-1.51 apfu.

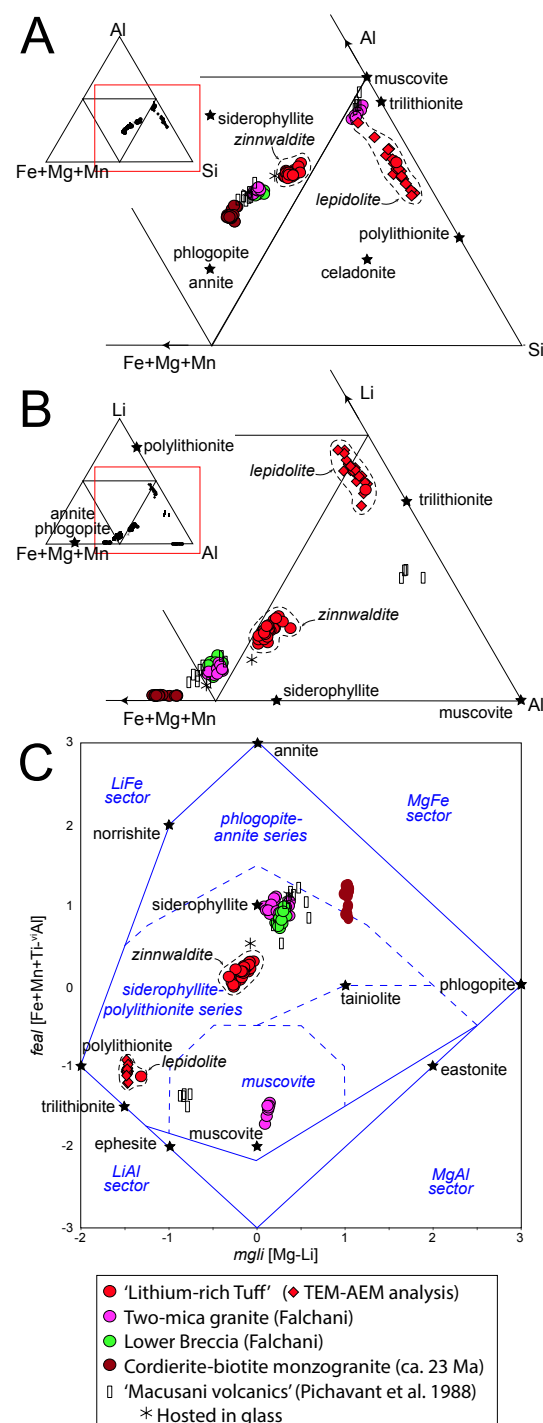


Figure 2. Classification of mica from the MVF in the ternary diagrams after Monier and Robert (1986) (A-B) and the binary diagram after Tischendorf et al. (2007) (C). TEM data were adjusted assuming Li = 1.5 apfu.

Only one EMPA analysis of lepidolite was obtained so far. Its composition plots close to the polyolithionite end-member in the classification scheme of Tischendorf et al. (2007). It has a Li content of 1.35 apfu and much lower contents of Fe (0.13 apfu), Mg (0.04 apfu), Mn (0.02 apfu), Ti (0.01 apfu), and Zn (0.01 apfu). The K content (0.85 apfu) is higher than the Na (0.06 apfu), Rb (0.03 apfu), and Cs (0.01 apfu) contents and F is very high, at 2 apfu. This composition agrees nicely with the analyses obtained on TEM on another sample in which zinnwaldite was absent and lepidolite was the only mica present (Fig. 2).

The X-ray maps in Figure 3 show a subhedral mica grain from the 'Lithium-rich Tuff' that is compositionally zoned with a zinnwaldite core and a lepidolite rim. The latter is richer in F and Rb and poorer in Ti than the zinnwaldite core.

Micro-Raman spectra obtained on the core and the rim of the same grain are shown in Figure 4. Zinnwaldite displays one strong band at 190, two weaker bands at 92 and 687, and a shoulder at 646 cm^{-1} , whereas lepidolite is characterized by four strong bands at 93, 177, 255, and 705 cm^{-1} . The latter, at 705 cm^{-1} , is often observed in the lepidolite series, and in the trilithionite and polyolithionite endmembers (RRUFF).

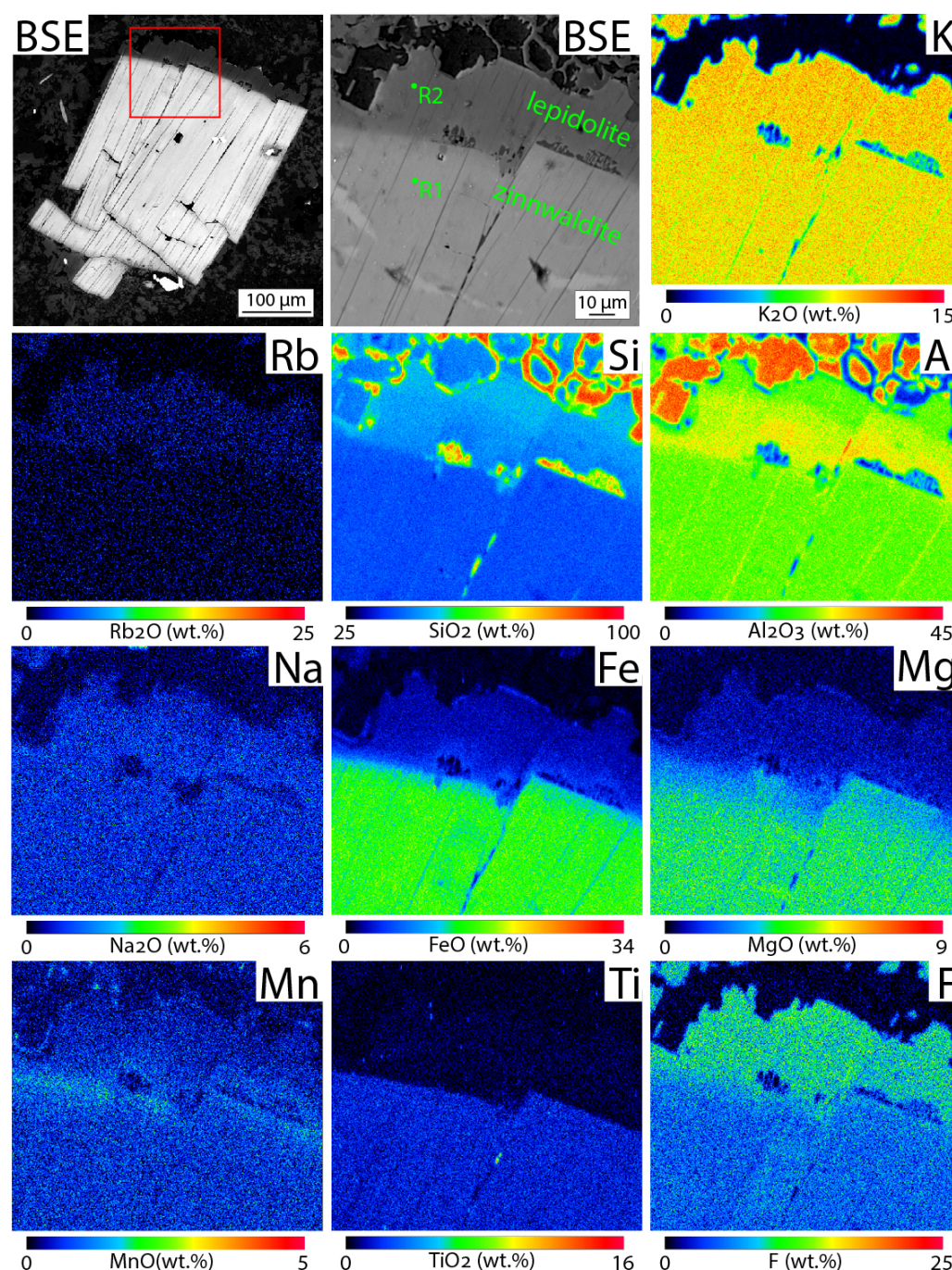


Figure 3. SEM (BSE mode) and quantitative X-ray images of a zoned mica grain from the 'Lithium-rich Tuff' in the Falchani Lithium Project, comprising a zinnwaldite core and a lepidolite rim.

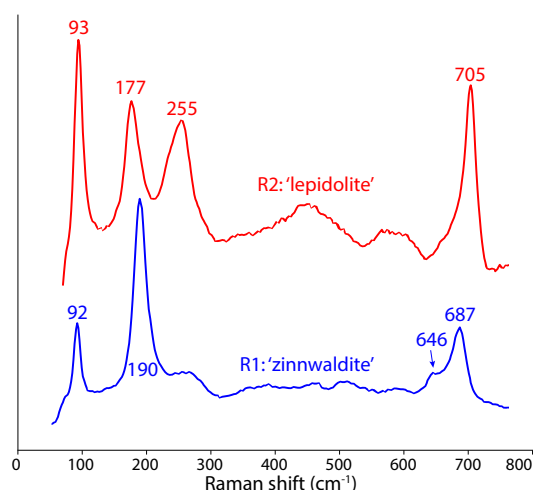


Figure 4. Raman spectra measured in a mica grain from sample 2021-MAC-11, for 20 s (5 accumulations) using a 532 nm laser, a 50x objective and a 50% grating. Location of point analyses (R1 and R2) shown in Fig. 3.

4 Discussion

The correlation between the lithium mineralization and rocks of volcanic origin ascribes the Falchani Lithium Project to the volcanogenic lithium deposit type (Bowell et al. 2020). In volcanogenic lithium deposits, Li enrichment from pre-enriched volcanic or volcanogenic rocks occurs during intense alteration that arises from the circulation of fluids of magmatic and/or meteoric origin in restricted basins such as volcanic calderas (Benson et al. 2017). These authors argue that the large volumes of Li-enriched rhyolites that are needed to form volcanogenic lithium deposits are typically emplaced in intracontinental settings through partial melting or assimilation of thick, felsic crust and, particularly, in strongly evolved melts through fractional crystallization.

The compositions of micas in the 'Lithium-rich Tuff' from the MVF contrast to those of micas in granites and ignimbrites in the area (new data plus published mica analyses in 'Macusani Volcanics' by Pichavant et al. 1988; Fig. 2). In particular, micas from the 'Lithium-rich Tuff' are systematically enriched in Li, Rb, and F relative to micas in the Lower Breccia (Nupen 2019) and nearby two-mica granites. All of them, in turn, are enriched in these elements compared to micas in older (ca 23 Ma; Sandeman et al. 1997), late Oligocene, cordierite-biotite monzogranites found in the southern margin of the MVF (Fig. 2). The marked enrichment in Li and other incompatible elements such as Rb in mica grains preserved in the 'Lithium-rich Tuff' would illustrate crystallization in equilibrium with a highly evolved rhyolitic magma during a particular period of magmatism in the Neogene MVF.

Acknowledgements

We want to thank the geologists from Macusani Yellowcake for the help and hospitality during

sampling tasks and to Drs. Philippe de Parseval and Xavier Llovet for assistance during EMPA data acquisition. This research work was supported by the Peruvian PROCENCIA-FONDECYT project 1122-2020 E041-2020-01-01, and logistically, by the project 2021 SGR 00239 (AGAU).

References

- Benson TR, Coble MA, Rytuba JJ, Mahood GA (2017) Lithium enrichment in intracontinental rhyolite magmas leads to Li deposits in caldera basins. *Nat Commun* 8:270.
- Bowell RJ, Lagos L, de los Hoyos CR, Declercq J (2020) Classification and characteristics of natural lithium resources. *Elements* 16:259–264.
- Cheilletz A, Clark AH, Farrar E, Arroyo Pauca G, Pichavant M, Sandeman HA (1992) Volcano-stratigraphy and $^{40}\text{Ar}/^{39}\text{Ar}$ geochronology of the Macusani ignimbrite field: monitor of the Miocene geodynamic evolution of the Andes of southeast Peru. *Tectonophysics* 205:307–327.
- Clark AH, Farrar E, Kontak DJ, Langridge RJ, Arenas MJ, France LJ, McBride SL, Woodman PL, Wasteneys HA, Sandeman HA, Archibald DA (1990) Geologic and geochronologic constraints on the metallogenetic evolution of the Andes of southeastern Peru. *Econ Geol* 85:1520–1584.
- Göğüş OH, Sundell K, Uluocak EŞ, Saylor J, Çetiner U (2022) Rapid surface uplift and crustal flow in the Central Andes (southern Peru) controlled by lithospheric drip dynamics. *Sci Rep-UK* 12:5500.
- Monier G, Robert JL (1986) Evolution of the miscibility gap between muscovite and biotite solid solutions with increasing lithium content: an experimental study in the system $\text{K}_2\text{O}-\text{Li}_2\text{O}-\text{MgO}-\text{FeO}-\text{Al}_2\text{O}_3-\text{SiO}_2-\text{H}_2\text{O}-\text{HF}$ at 600 °C, 2 kbar $\text{P H}_2\text{O}$: comparison with natural lithium micas. *Mineral Mag* 50:641–651.
- Nupen S (2019) Mineral Resource Estimates for the Falchani Lithium Project in the Puno District of Peru - under the Guidelines of National Instrument 43-101. The Mineral Corporation, Bryanston, pp 1-72.
- Perez ND, Horton BK, Carlotto V (2016) Structural inheritance and selective reactivation in the central Andes: Cenozoic deformation guided by pre-Andean structures in southern Peru. *Tectonophysics* 671:264–280.
- Pichavant M, Kontak DJ, Valencia Herrera J, Clark AH (1988) The Miocene-Pliocene Macusani Volcanics, SE Peru - I. Mineralogy and magmatic evolution of a two-mica aluminosilicate-bearing ignimbrite suite. *Contrib to Mineral Petrol* 100:300–324.
- Salisbury MJ, Jicha BR, de Silva SL, Singer BS, Jiménez NC, Ort MH (2011) $^{40}\text{Ar}/^{39}\text{Ar}$ chronostratigraphy of Altiplano-Puna volcanic complex ignimbrites reveals the development of a major magmatic province. *GSA Bull* 123:821–840.
- Sandeman HA, Clark AH, Farrar E, Arroyo-Pauca G (1997) Lithostratigraphy, petrology and $^{40}\text{Ar}-^{39}\text{Ar}$ geochronology of the Crucero Supergroup, Puno Department, SE Peru. *J South Am Earth Sci* 10:223–245.
- Segovia-More MK, Torró L, Villanova-de-Benavent C, Ramírez-Briones J, Vallance J, Monnier L, Laurent O, Salvi S, Baby P, Proenza JA, Nieto F (2023). High-resolution mineralogy of 'lithium-rich tuff' from the Macusani Volcanic Field, Puno, Peru. This volume.
- Tischendorf G, Gottesmann B, Förster H-J, Trumbull RB (1997) On Li-bearing micas: estimating Li from electron microprobe analyses and an improved diagram for graphical representation. *Mineral Mag* 61:809–834.
- Tischendorf G, Förster H-J, Gottesmann B, Rieder M (2007) True and brittle micas: compositions and solid-solution series. *Mineral Mag* 71:285-320.

Fluid exsolution in the outer zones of the Emmons Pegmatite (Maine, USA)

Laura M. van der Does¹, Niels Hulsbosch¹, Jan Elsen¹, Philippe Muchez¹ and Mona-Liza C. Sirbescu²

¹Department of Earth and Environmental Sciences, KU Leuven, Belgium

²Department of Earth and Atmospheric Sciences, Central Michigan University, MI, USA

Abstract. Pegmatites are an important source of critical and rare metals (e.g., Li, Ta, Sn, Nb). Understanding processes occurring during pegmatite crystallization are therefore key to understanding the mechanisms responsible to concentrating these elements. Several contrasting models for pegmatite formation have been put forward but it is still unclear when, and how fluid exsolution occurs. Here we investigate the timing of fluid exsolution through detailed studies of fluid inclusions (FIs) trapped in tourmaline crystals from the outer zones of the Emmons pegmatite, Maine, USA. Comb-like tourmaline from the border zone and quartz-tourmaline intergrowths (QTIs) from the border and wall zones are further subdivided based on morphology. Trapped FIs can be observed in all tourmaline types, with a consistent H₂O-CO₂-NaCl-(N₂-CH₄) and low to moderate salinity composition. The abundance of FIs sharply increases from the center outwards in the QTIs. This variation may result from the crystallization of the skeletal parts of the QTIs from a boundary layer formed around the central tourmaline. The fluid present during crystallization of the central tourmaline, which contains numerous melt inclusions and only rare primary fluid inclusions was exsolved as highly localized pools, whereas it was more prevalent in the boundary layer during skeletal tourmaline crystallization.

1 Introduction

Granitic pegmatites provide an important source for rare and critical metals, gemstones, and industrial minerals. LCT (Li-Cs-Ta) pegmatites, like the Emmons Pegmatite, are of particular importance as they may host high concentrations of Ta, Nb and Sn among other critical metals (Linnen et al. 2012). Studying the pegmatite-forming processes is important for understanding advanced magma evolution and the concentration of rare metals. Although previous studies indicate that many of these elements become concentrated as a result of magmatic processes, element enrichment in pegmatites at the magmatic-hydrothermal transition and the hydrothermal stage are not yet fully understood (Linnen et al. 2012).

The importance of an aqueous phase for pegmatite formation has been suggested by Jahns & Burnham (1969), inferring that an exsolved aqueous fluid is needed for the formation of pegmatites. Experimental and natural studies indicate that up to three different immiscible fluids can be present, simultaneously, during pegmatite formation, one of which is a low-saline aqueous fluid (Thomas et al. 2000; Veksler and Thomas 2002; Veksler et al. 2002; Veksler 2004).

A contrasting model has been put forward by London (1999, 2009, 2014, 2018) that suggests

that the pegmatites form from a single-phase, hydrous melt. These studies acknowledge that the melt must be water and flux rich at least near the crystal surfaces to enhance the diffusion rates required to grow large crystals (London 2009) and that, ultimately, fluid exsolution occurs at late stages to form miarolitic cavities and replacement units (e.g., London 1986).

Most studies focus on fluid saturation in the transition from granite to pegmatite or between the internal zones of the pegmatite (Sirbescu and Nabelek 2003; Hulsbosch et al. 2016; Hulsbosch and Muchez 2020). This study instead examines, in detail, fluid inclusions (FIs) from the outer zones of the pegmatite, to learn more about the temporal evolution occurring on a much smaller scale.

The main aim, of this study, is to trace when and how fluid saturation happens in the border and wall zone of the internally zoned Emmons pegmatite. This is done through detailed studies of FIs trapped in tourmaline crystals, by petrography, microthermometry and Raman spectroscopy.

The Emmons Pegmatite is a relatively thin (5-10 m) internally zoned, miarolitic dike, located in the Oxford Pegmatite field, Maine, USA (Falster et al. 2019). Samples studied here all originate from the border and wall zone. This pegmatite is highly enriched in B, Li, Cs and Ta and hosts many rare minerals (Falster et al. 2019). The pegmatite is intruded into the metasedimentary rocks belonging to the Sebago Migmatite Domain (Solar and Tomascak 2009) and is thought to have been derived by anatexis of the metamorphic country rock (Falster et al. 2019) as opposed to fractionation from a parental pluton. No significant alteration or contact metamorphism occurred as the dike was intruded into the country rock (García-Serrano et al. 2017)

1.1 Tourmaline textures and morphology types

Two different textures were studied: subhedral prisms of comb-like tourmaline (5-10 cm) (Type 1) nucleating directly on the pegmatite border and quartz-tourmaline intergrowths (QTIs) from the wall zone (up to 30-40 cm in length). The QTIs are divided into three types, based on their morphology (Figure 1): larger, prismatic, central tourmaline (Type 2), less euhedral, second tier tourmaline, extending from Type 2 (Type 3) and skeletal tourmaline surrounding the central and second tier tourmaline (Type 4).

Type 1 tourmaline is the paragenetically earliest, nucleating directly on the border between

host rock and pegmatite. The QTIs occur further inwards in the wall zone and consequently crystallize later in the paragenetic sequence.

Studies on the QTIs by van der Does et al. (*in review*) infer that a boundary layer has an influence on the formation of the QTIs. A boundary layer forms around the first, rapidly growing tourmaline crystal (Type 2) in the QTIs. It will progressively become concentrated in elements incompatible in tourmaline, which includes H₂O and other fluxing elements, such as F and Li. This boundary layer becomes concentrated in components that are incompatible in tourmaline, which includes water. Based on the boundary layer model by van der Does et al. (*in review*), Type 2 tourmaline is the paragenetically earliest, in the QTIs, followed by Type 3 and lastly Type 4.

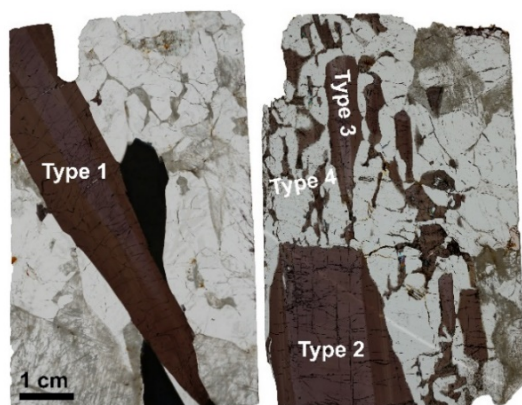


Figure 1. Micrographs of comb-like tourmaline (left) and a quartz-tourmaline intergrowth (right).

2 Methods

Doubly polished wafers were examined using an Olympus BX40 petrographic microscope to identify FI assemblages and types. Selected FI assemblages underwent cooling and heating using a Linkam MDS600 heating-freezing stage, mounted on an Olympus BX51 microscope, at the Department of Earth and Environmental Sciences, KU Leuven to measure phase transition temperatures including CO₂ melting (T_{mCO_2}), clathrate melting (T_{mCL}) and CO₂ homogenization (T_{hCO_2}) of the FI. The eutectic temperature (T_{fm}) and final ice melting (T_{mice}) temperatures were not clear for most FIs. Therefore, only a limited number of temperatures were acquired for these phase transitions. Inclusions were first cooled to -120°C, to ensure they were entirely frozen. Heating rates varied from 10-30°C/min but were reduced to 1°C/min near phase transitions.

The composition of the homogenized carbonic phase was analyzed using a Horiba Jobin-Yvon LabRAM HR evolutions spectrometer coupled to an Olympus BX41 confocal microscope at the Department of Chemistry, KU Leuven. A 532 nm Nd:YAG laser was used to excite the carbonic phase and the scattered light was subsequently measured with a Peltier-cooled Synapse (EM)-CCD detector. Results were processed in LabSpec

6.5.2 software to calculate the molar fractions gaseous species in the carbonic phase.

3 Results

3.1 Fluid inclusion petrography

Fluid inclusions occur in all studied tourmaline types. This study only focusses on primary inclusions, that were recognized as clusters of FIs that occur unrelated to fractures. Generally, Types 1 and 2 have the least abundance of FIs (on average 7-8 analysed FIs per sample) and typically FI assemblages are only composed of 1-3 FIs (Figure 2). The inclusion assemblage is mainly dominated by primary clusters and pseudosecondary trails of melt inclusions (MIs). The amount of FIs increases in Type 3 (on average 10 FIs analysed per sample) and especially in Type 4 (on average 27 FIs analysed per sample). In the latter types, fields are usually composed of many more FIs together (Figure 2). MIs still occur, but the inclusion assemblage is dominated by FIs. The FIs found in Types 1 and 2 tend to be larger in size (\bar{x} = 44 μ m and \bar{x} = 61 μ m, respectively) compared to FIs in Types 3 and 4 (\bar{x} = 34 μ m and \bar{x} = 27 μ m, respectively).

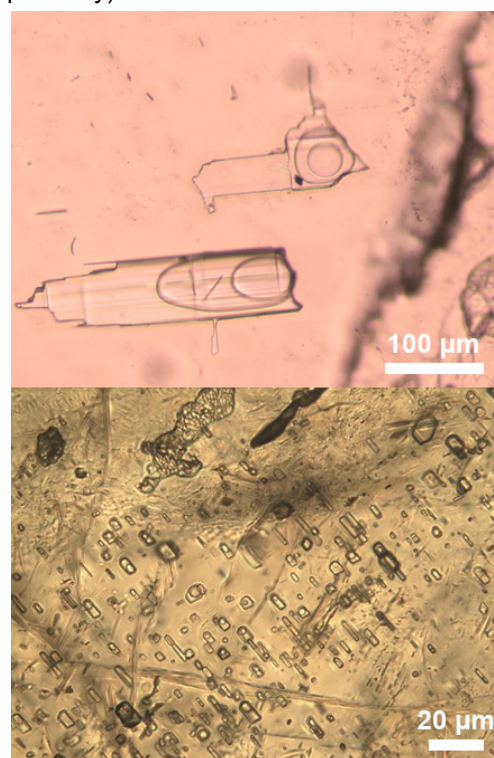


Figure 2. Typical FI fields in Type 2 tourmaline (top) and Type 4 tourmaline (bottom).

3.2 Fluid properties

The temperatures at which the different phase transitions occur are similar for the four tourmaline types (Table 1). T_{mCO_2} varies between -61.1°C and -56.6°C, T_{mCL} between 6.2°C and 9.9°C, and T_{hCO_2} has a large range between 7.9°C and 30.2°C., but

generally $Th_{CO_2} > 20^\circ C$. The largest variations are seen within Types 1 and 2. Type 2 trends to higher Th_{CO_2} , but this appears to be mainly caused by one sample having higher Th_{CO_2} than other FIs in Type 2 tourmaline.

Tfm could not always be clearly observed, so only a few temperatures were acquired (n=10). The acquired Tfm vary between $-21.9^\circ C$ and $-21.3^\circ C$. Tm_{ice} overlap in Types 2, 3 and 4, with temperatures ranging from $-11.5^\circ C$ to $-3.6^\circ C$ (n=43), while Tm_{ice} in Type 1 extend to higher temperatures ($-2.3^\circ C$ to $-0.6^\circ C$, n=3).

Table 1. Ranges, means and number of measurements for selected phase transitions in the different tourmaline types studied.

Tourmaline type	Tm_{CO_2}	Tm_{CL}	Th_{CO_2}
Type 1	$-58.5^\circ C - -57.0^\circ C$ $\bar{x} = -57.7^\circ C$ n = 14	$6.6^\circ C - 9.2^\circ C$ $\bar{x} = 7.8^\circ C$ n = 14	$7.8^\circ C - 28.1^\circ C$ $\bar{x} = 22.2^\circ C$ n = 14
Type 2	$-61.6^\circ C - -56.6^\circ C$ $\bar{x} = -57.7^\circ C$ n = 36	$6.2^\circ C - 9.9^\circ C$ $\bar{x} = 7.7^\circ C$ n = 37	$9.6^\circ C - 30.2^\circ C$ $\bar{x} = 25.6^\circ C$ n = 36
Type 3	$-58.8^\circ C - -56.6^\circ C$ $\bar{x} = -57.6^\circ C$ n = 28	$7.0^\circ C - 9.5^\circ C$ $\bar{x} = 8.0^\circ C$ n = 30	$8.8^\circ C - 28.8^\circ C$ $\bar{x} = 25.5^\circ C$ n = 29
Type 4	$-59.3^\circ C - -56.7^\circ C$ $\bar{x} = -57.5^\circ C$ n = 74	$6.6^\circ C - 9.9^\circ C$ $\bar{x} = 8.1^\circ C$ n = 79	$8.2^\circ C - 29.3^\circ C$ $\bar{x} = 24.6^\circ C$ n = 79

Raman measurements (Figure 3) reveal that the vapor phase is heavily dominated by CO_2 (70-100%, majority >90%). N_2 composes up to 30%, while CH_4 usually makes up less than 5%. The carbonic phases are generally similar between the tourmaline types.

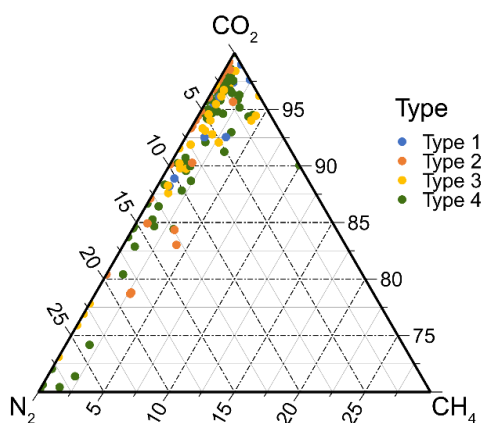


Figure 3. Ternary diagram of the composition of the carbonic phase in the fluid inclusions.

Salinity and density (Table 2) were calculated using the Q2 program from Bakker (1997). Where no Raman data was acquired, the equation from Darling (1991) was used. The salinity falls within the same range for the four tourmaline types, between 0.1 and 8.5 wt% NaCl eq. The densities show a

large range, especially in Types 1 and 4, that overlaps in all tourmaline types.

Table 2. Ranges, means and number of measurements for the density and salinity of FIs in the different tourmaline types.

Tourmaline type	Density (g/cc)	Salinity (wt% NaCl eq.)
Type 1	0.5 – 1 $\bar{x} = 0.8$ n = 14	2.2 – 6.4 $\bar{x} = 5.0$ n = 14
Type 2	0.7 – 1 $\bar{x} = 0.8$ n = 35	0.7 – 8.5 $\bar{x} = 4.8$ n = 37
Type 3	0.6 – 1 $\bar{x} = 0.8$ n = 30	0.1 – 7.0 $\bar{x} = 4.0$ n = 27
Type 4	0.5 – 0.9 $\bar{x} = 0.7$ n = 67	0.4 – 7.4 $\bar{x} = 4.2$ n = 77

4 Discussion

The phase transition temperatures and composition of the fluid do not vary significantly among the different tourmaline types, so it is concluded that this is the same fluid type throughout all tourmaline types. However, the calculated densities show a large variation in this parameter, caused by the large variation of temperature of the phase transitions within each tourmaline type, such as the Th_{CO_2} values. Tfm just below $-21^\circ C$ infers that the fluid is dominantly H_2O -NaCl. The slight negative offset from the eutectic for this system could indicate that some amount of KCl is also present in the system. However, determining Tfm during microthermometric measurements was very difficult, therefore it is uncertain how precise the temperatures were determined. The high proportion of CO_2 in the carbonic phase, and only moderate to low proportions of N_2 and CH_4 indicate the vapor phase is strongly dominated by CO_2 in most FIs. Together, these observations demonstrate a H_2O - CO_2 -NaCl- (N_2 - CH_4) composition of the FIs.

The fluid has a relatively low salinity compared to other FIs found in the outer zones of pegmatites from the Gatumba-Gitarama pegmatite field in Rwanda (e.g. Hulsbosch et al. 2016; Hulsbosch and Muchez 2020). Lower salinity FIs in pegmatites have been reported by Sirbescu and Nabelek (2003), in pegmatites associated with the Harney Peak Granite in South Dakota, USA. They consider the low salinity fluids to represent the first exsolved magmatic fluid.

The presence of primary FIs in the tourmaline from the border and wall zone of the Emmons Pegmatite indicates that water saturation occurred very early in the crystallization of the pegmatite. The lack of significant alterations around the pegmatite (García-Serrano et al. 2017) indicates that no exsolved aqueous fluid was present upon intrusion of the dike. Studies on other pegmatites also found primary FIs in the outer zones, and

made a similar conclusion (e.g. Mulja and Williams-Jones 2018; Hulsbosch and Muchez 2020). The increase in FI abundance from Types 1 and 2 to Types 3 and 4 tourmaline indicates changes in some factors, influencing the trapping potential. The lower abundance in Types 1 and 2 could indicate that the exsolved fluid was only present as localized droplets forming at the crystal-liquid interface during rapid crystallization. The FIs in Types 3 and 4 are less localized in the crystal and FI fields are larger, which could suggest an exsolved fluid was more abundant in their crystallization environment. Experimental studies have shown that a H₂O-undersaturated melt can reach local fluid exsolution in e.g. a melt boundary layer (London and Morgan 2017; Sirbescu et al. 2017). A melt boundary layer is suggested, for the formation of the QTIs by van der Does (*in review*). The increase in FI abundance, and decrease in MI abundance, could therefore be caused by the progressive concentration H₂O, leading to fluid exsolution, in the boundary layer formed around the rapidly crystallizing Type 2 tourmaline. Although less prevalent, MIs continue to be present in Types 3 and 4 tourmaline, indicating that these types also crystallized in the presence of a magma and not solely from a fluid.

5 Conclusion

The fluid, trapped in the tourmaline of the border and wall zone of the Emmons Pegmatite, is a low to moderate saline fluid with an H₂O-CO₂-NaCl-(N₂-CH₄) composition. CO₂ dominates the vapour phase in most FIs. The fluid properties do not vary significantly between the different tourmaline types studied.

The presence of FIs in all tourmaline types studied indicates that fluid exsolution occurs very early in the formation of the Emmons Pegmatites. The fluid exsolution likely occurs as localized droplets on the crystal-melt interface, during the crystallization of Types 1 and 2, but changes to a more pervasive exsolution, constrained in a melt boundary layer, during crystallization of Types 3 and 4.

Acknowledgements

Herman Nijs (KU Leuven) is thanked for preparation of the wafers used in this study. The Raman equipment was acquired via the medium-scale research infrastructure FWO grant Raman-SIM² (number I000718N).

References

Bakker RJ (1997) Clathrates: Computer programs to calculate fluid inclusion V-X properties using clathrate melting temperatures. *Comput Geosci* 23:1–18. [https://doi.org/10.1016/S0098-3004\(96\)00073-8](https://doi.org/10.1016/S0098-3004(96)00073-8)

Darling RS (1991) An extended equation to calculate NaCl contents from final clathrate melting temperatures in H₂O-CO₂-NaCl fluid inclusions: Implications for P-T isochore location. *Geochim Cosmochim Acta* 55:3869–3871. [https://doi.org/10.1016/0016-7037\(91\)90079-K](https://doi.org/10.1016/0016-7037(91)90079-K)

Falster AU, Simmons WB, Webber KL, et al (2019) The Emmons Pegmatite, Greenwood, Oxford County,

Maine. *Rocks Miner* 94:498–519. <https://doi.org/10.1080/00357529.2019.1641021>

García-Serrano J, Roda-Robles E, Villaseca C, Simmons W (2017) Fe-Mn-(Mg) distribution in primary phosphates and silicates, and implications for the internal evolution of the Emmons rare-element pegmatite (Maine, USA). *NGF Abstr Proc* 2:37–40

Hulsbosch N, Boiron MC, Dewaele S, Muchez P (2016) Fluid fractionation of tungsten during granite-pegmatite differentiation and the metal source of peribatholithic W quartz veins: Evidence from the Karagwe-Ankole Belt (Rwanda). *Geochim Cosmochim Acta* 175:299–318. <https://doi.org/10.1016/j.gca.2015.11.020>

Hulsbosch N, Muchez P (2020) Tracing fluid saturation during pegmatite differentiation by studying the fluid inclusion evolution and multiphase cassiterite mineralisation of the Gatumba pegmatite dyke system (NW Rwanda). *Lithos* 354–355:105285. <https://doi.org/10.1016/j.lithos.2019.105285>

Jahns RH, Burnham CW (1969) Experimental Studies of Pegmatite Genesis: I. A model for the Derivation and Crystallization of Granitic Pegmatites. *Econ Geol* 64:843–864. <https://doi.org/10.2113/gsecongeo.64.8.843>

Linnen RL, Van Lichtenvelde M, Černý P (2012) Granitic Pegmatites as Sources of Strategic Metals. *Elements* 8:275–280. <https://doi.org/10.2113/gselements.8.4.275>

London D (1986) Formation of tourmaline-rich gem pockets in miarolitic pegmatites. *Am Mineral* 71:396–405

London D (1999) Melt Boundary-Layers and the Growth of Pegmatitic Textures. *Can Mineral* 37:826–827

London D (2009) The Origin of Primary Textures in Granitic Pegmatites. *Can Mineral* 47:697–724

London D (2014) A petrologic assessment of internal zonation in granitic pegmatites. *Lithos* 184–187:74–104. <https://doi.org/10.1016/j.lithos.2013.10.025>

London D (2018) Ore-forming processes within granitic pegmatites. *Ore Geol Rev* 101:349–383. <https://doi.org/10.1016/j.oregeorev.2018.04.020>

London D, Morgan GB (2017) Experimental Crystallization of the Macusani Obsidian, with Applications to Lithium-rich Granitic Pegmatites. *J Petrol* 58:1005–1030. <https://doi.org/10.1093/PETROLOGY/EGX044>

Mulja T, Williams-Jones AE (2018) The physical and chemical evolution of fluids in rare-element granitic pegmatites associated with the Lacorne pluton, Québec, Canada. *Chem Geol* 493:281–297. <https://doi.org/10.1016/j.chemgeo.2018.06.004>

Sirbescu M-LC, Nabelek PI (2003) Crystallization conditions and evolution of magmatic fluids in the Harney Peak Granite and associated pegmatites, Black Hills, South Dakota - Evidence from fluid inclusions. *Geochim Cosmochim Acta* 67:2443–2465. [https://doi.org/10.1016/S0016-7037\(02\)01408-4](https://doi.org/10.1016/S0016-7037(02)01408-4)

Sirbescu M-LC, Schmidt C, Veksler I V., et al (2017) Experimental Crystallization of Undercooled Felsic Liquids: Generation of Pegmatitic Texture. *J Petrol* 58:539–568. <https://doi.org/10.1093/petrology/egx027>

Solar GS, Tomascak PB (2009) The Sebago Pluton and the Sebago Migmatite Domain, southern Maine: Results from New Studies. 2009 Annu Meet Northeast Sect Geol Soc Am Field Trip:1–24

Thomas R, Webster JD, Heinrich W (2000) Melt inclusions in pegmatite quartz: Complete miscibility between silicate melts and hydrous fluids at low pressure. *Contrib to Mineral Petrol* 139:394–401. <https://doi.org/10.1007/s004100000120>

Veksler I, Thomas R, Schmidt C (2002) Experimental evidence of three coexisting immiscible fluids in synthetic granitic pegmatite. *Am Mineral* 87:775–779. <https://doi.org/10.2138/am-2002-5-621>

Veksler I V. (2004) Liquid immiscibility and its role at the magmatic-hydrothermal transition: a summary of experimental studies. *Chem Geol* 210:7–31. <https://doi.org/10.1016/j.chemgeo.2004.06.002>

Veksler I V., Thomas R (2002) An experimental study of B-, P- and F-rich synthetic granite pegmatite at 0.1 and 0.2 GPa. *Contrib to Mineral Petrol* 143:673–683. <https://doi.org/10.1007/s00410-002-0368-3>

Large-scale HFSE and REE mobility linked to the formation of vein-type U-deposits in the Moldanubian Zone of the Bohemian Massif

Martin Kubeš^{1,2}, Vojtěch Wertich^{1,2}, Jaromír Leichmann¹, Markéta Holá¹, Julien Mercadier³, Michel Cuney³

¹Masaryk University, Brno, Czech Republic

²Czech Geological Survey, Prague, Czech Republic

³Université de Lorraine, Nancy, France

Abstract. Multi-element EMP maps and analyses of major accessory phases and their possible alteration products from ultrapotassic rocks (durbachites), in combination with LA-ICP-MS analyses of hydrothermal U-mineralization, provided constraints on potential U source of vein-type U-deposits in the Moldanubian Zone of the Bohemian Massif. The extensive metal mobilization in durbachites, recorded by EMP imaging, was controlled by self-induced radiation damage (metamictization) and subsequent fluid-driven alteration of U-bearing phases (thorite, allanite, zircon). Unusual trace element signatures of low-T hydrothermal U-mineralization (e.g., extremely high Zr, Nb, Ti, Σ REE) from the vein-type deposits reflect the large-scale HFSE and REE mobility via aqueous solutions. The character of late alteration of primary phases (zircon dissolution vs. resistance of apatite) and mineral assemblages of hydrothermal phases in durbachites (e.g., synchisite, F-rich titanite, monazite) indicates the importance of alkali-, F-, and P-rich fluids in the formation of U-deposits. The infiltration of oxidized, highly alkaline basinal brines likely played a key role in HFSE and REE mobility during the Permian hydrothermal event, as suggested by EMP chemical dating of U-mineralization.

1 Introduction

The Moldanubian Zone of the Variscan Bohemian Massif (Figure 1a, b) usually hosts significant hydrothermal U-deposits associated with shear zones in the high-grade metamorphic basement. The formation of hydrothermal U-deposits in the entire European Variscan belt is assumed to be related to the fluid-driven alteration of Late-Carboniferous peraluminous granites (Cuney 2009). However, within the Bohemian Massif, there is a lack of evidence of genetic and/or spatial link of vein-type U-mineralization to U fertile leucogranites, thus a potential U source remains a matter of debate. Accordingly, the high-grade metamorphic complexes hosting the Moldanubian U-deposits are currently considered as possible U source, related to hydrothermal decomposition of U-bearing accessories.

In the largest Moldanubian U-deposit (the Rožná deposit with total mine production of 23 000 t U), three major mineralization events were previously described (Kříbek et al. 2009): (1) pre-U quartz-sulfide and carbonate-sulfide mineralization, (2) U-mineralization, and (3) post-U quartz-carbonate-sulfide mineralization. As a result of the hydrothermal U-mineralizing event, three different types of U ore have formed in the Rožná deposit: (1) network-disseminated Coff>Urn in cataclasites

of shear zones (2) Urn (\pm Coff) in carbonate veins, and (3) disseminated Coff (\pm Urn) in metasomatites adjacent to shear zones (Kříbek et al. 2009). The aim of this study was to identify the potential U source of the vein-type U-mineralization.

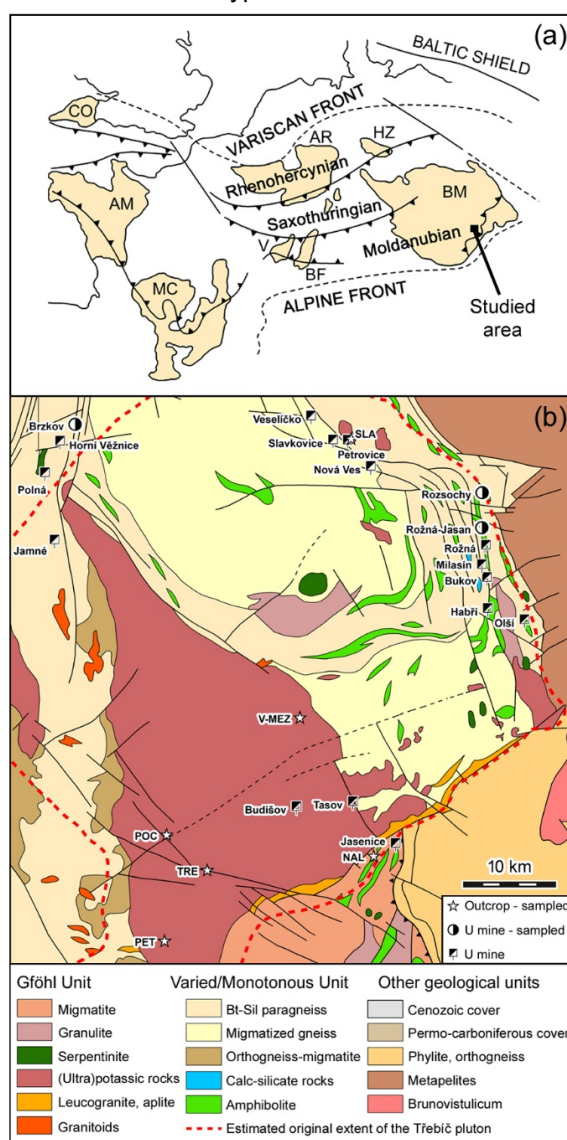


Figure 1. a Location of the Moldanubian U-deposits in the regional frame of western-central Europe. b Detail of sample locations in the Moldanubian Zone. Geological map modified after Kubeš et al. (2022).

Despite similar, low-temperature conditions of the origin of the vein-type U-mineralization in the Moldanubian Zone (150–170 °C; Kříbek et al. 2009), individual deposits are characterized by different chemical composition. They commonly exhibit highly variable rare earth element (REE) patterns and may incorporate a significant amount of high field strength elements (HFSE) in unaltered pristine uraninite (Wertich et al. 2022).

To explain such unusual trace element chemistry of U-deposits in the Moldanubian Zone, we focused on important U-bearing phases in highly alkaline (ultra)potassic rocks that experienced late fluid-driven alteration responsible for extensive HFSE and REE mobilization according to our previous findings (Kubeš et al. 2021). Particularly, element distribution imaging represents a powerful tool for obtaining direct evidence for the mobilization of incompatible elements from minerals during a fluid-driven alteration and could thereby help to determine which regions may correspond to primary sources of U and other metals in geological environment.

2 Methodology

In total, 9 samples of high-grade U ore from the Rožná-Jasan, Rozsochy and Brzkov deposits (3 samples from each locality) (Figure 1b) were gathered from the archives of Moravian Museum and DIAMO s.e. (organization dealing with the remediation of former U mining activities). These particular deposits were selected to decipher the origin of their anomalous trace element chemistry (high Zr, Nb, Ti, Σ REE; Wertich et al. 2022) and, importantly, identify the main source of these metals.

Building upon our previous observations of extreme mobility of HFSE and REE in highly alkaline K-rich syenites (Kubeš et al. 2021), (ultra)potassic plutons of durbachites series were sampled, some of which are spatially associated with U-deposits. The individual samples sites (Figure 1b) included localities within the Třebíč pluton (Pocoucov = POC, Petrůvky = PET, Třebíč = TRE, Velké Meziříčí = V-MEZ) and its smaller satellite bodies near Nové Město na Moravě (Slavkovice = SLA) and Náměšť nad Oslavou (Naloučany = NAL).

Major accessory phases from polished thin sections of durbachite samples were studied using backscattered electron (BSE) imaging and electron microprobe (EMP) imaging and analyses. Polished thin sections of selected ore samples were used for reflected light microscopy and BSE imaging in order to precisely earmark unaltered uraninite domains suitable for laser ablation-inductively coupled plasma-mass spectrometry (LA-ICP-MS) analyses. BSE images together with the chemical composition of main U-bearing phases in durbachites were obtained by EMP Cameca SX 100 at the Department of Geological Sciences, Masaryk University, Brno. Operating conditions for spot analyses were as follows: wavelength-dispersive

mode, an accelerating voltage of 15 kV, a beam current of 6–20 nA, and a beam size of 2–10 μ m for primary accessory phases (zircon, apatite, thorite, uraninite, allanite, Th-rich monazite) and their alteration products (REE-fluorocarbonate, F-rich titanite, Th-poor monazite). X-ray element maps were acquired with an accelerating voltage of 15 kV, step size of 1 μ m using a fully focused electron beam, and dwell time of 0.1 s.

Trace element concentrations of U-mineralization were measured by LA-ICP-MS at the Department of Chemistry, Masaryk University, Brno. The system consisted of Analyte G2 laser ablation device and Agilent 7900 ICP-MS analyser with an octopole reaction cell. The laser operated at a wavelength of 213 nm with a pulse duration ~4 ns. Spot ablations with a 50 μ m spot diameter, repetition rate of 10 Hz, and fluence of 9 J cm⁻² were performed for 60 s. External calibration was performed using the standard reference materials (SRM) NIST 610 and NIST 612. More than 50 isotopes representing both the major components and trace elements of the samples were monitored with a total integration time of 4.5 s.

3 Deciphering potential U source

Within the following sections, based on the chemical composition of low-T hydrothermal vein-type U-mineralization and major primary U-bearing phases and their alteration products in durbachites, this contribution unravels the potential U source of the Moldanubian ore deposits and describes major physicochemical factors controlling large-scale HFSE and REE mobility in hydrothermal fluids.

3.1 Chemistry of U-mineralization

A typical feature of analysed uraninite samples from the studied hydrothermal low-T vein-type U-deposits is their significant HFSE enrichment (e.g., Zr, Nb, Ti) resembling those of granite/pegmatite-hosted U-deposits (Figure 2a, b). Moreover, REE patterns of uraninite significantly differ between individual vein-type deposits (Figure 2c). Uraninite from the Brzkov deposit typically shows LREE-enriched patterns (La_N/Yb_N 3.41–19.65) along with considerably high Σ REE (up to 1.12 wt%). By contrast, uraninite from the Rozsochy deposit has HREE-enriched patterns (La_N/Yb_N 0.01–0.59) similar to uraninite from the Rožná-Jasan deposit with relatively less pronounced HREE enrichment (La_N/Yb_N 0.29–1.48).

Observed anomalous HFSE enrichment along with highly variable REE patterns of uraninite simply rule out a different genetic type and formation temperature of hydrothermal vein-type U-deposits as the major mechanism controlling their unusual trace element signatures, considering the similar mineralogical and textural features of uraninite typical of low-temperature shear zone-hosted U veins (Kříbek et al. 2009).

Contrarily, the uncommon HFSE signatures and conspicuously variable REE patterns (Figure 2) are most likely a result of a combination of the chemistry of mineralizing fluids and element availability in the main source region. From this follows that our observations provide constraints on important physicochemical factors controlling HFSE and REE mobility in ore-forming fluids and major metal sources from which these incompatible elements were leached during fluid-rock interaction.

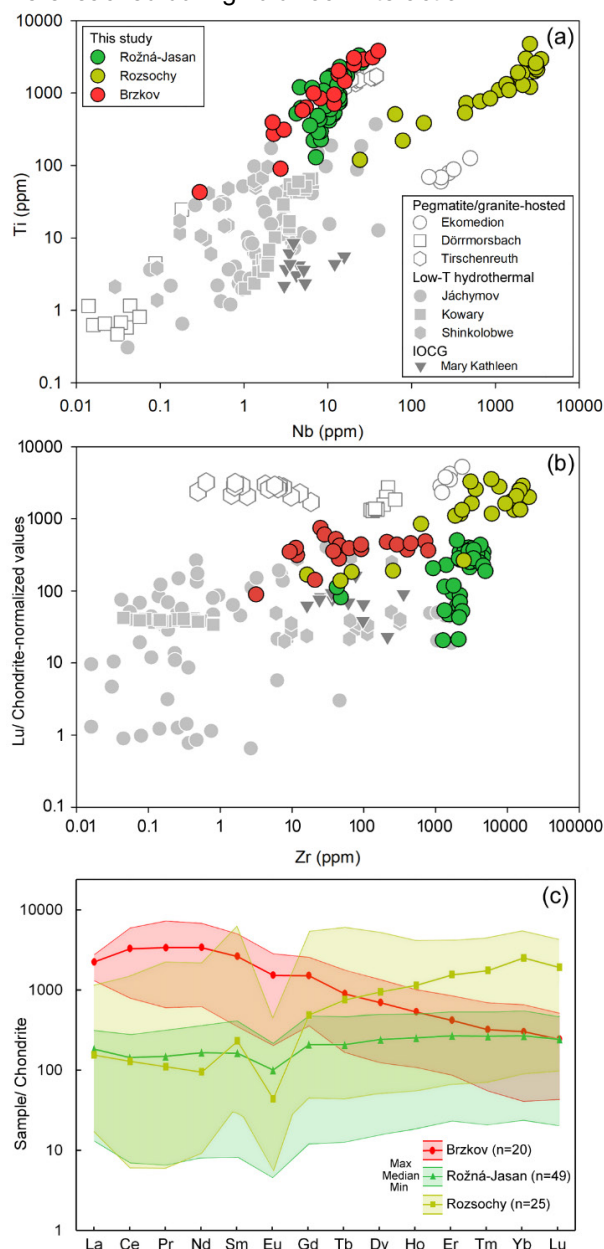


Figure 2. a, b Trace element chemistry of low-T hydrothermal uraninite from the Moldanubian deposits. Chemical composition of uraninite from different deposit types is from Frimmel et al. (2014). c Chondrite-normalized REE patterns of uraninite. Standardized values are from McDonough and Sun (1995).

3.2 Leaching metals from durbachites

Building up on our previous findings, highly alkaline potassic to ultrapotassic rocks of durbachite series experienced extensive post-magmatic hydrothermal alteration responsible for the leaching of HFSE and REE from their initial primary sources (Kubeš et al. 2021, 2022). The massive mobilization of U together with HFSE and REE in durbachites is well-documented by EMP imaging and analyses of their main U-bearing phases (Figure 3). Subsequent to metamictization of major U carrier in durbachites, radiation-damaged thorite experienced pervasive fluid-driven alteration, as evidenced by low BSE intensity, deficient EMP analytical totals, highly variable and low ThO₂ and UO₂ contents typical of altered thorite domains. In addition, rare occurrences of pristine magmatic uraninite, an easily leachable phase during oxidizing fluid circulation (Cuney 2009), observed in some durbachite samples suggest that most uraninite was probably entirely decomposed due to fluid-rock interaction. Apart from the abundant thorite, other refractory U-bearing minerals usually include zircon and allanite, both of which became metamict over a time interval sufficient to release U and other metals from their crystal structure during subsequent fluid-induced alteration, as documented by BSE imaging of extensively altered allanite and EMP maps showing the pervasive dissolution of metamict zircon triggering massive HFSE remobilization (Figure 3). Indeed, the variable REE signatures of Moldanubian vein-type U-deposits suggest the decomposition of two or more sources, at least one HREE- and one LREE-dominated (e.g., zircon vs. allanite). For instance, the extensive metal leaching from radiation-damaged zircon was triggered by interaction with post-magmatic hydrothermal fluids infiltrating through microfractures formed by volume expansion due to zircon metamictization (Kubeš et al. 2021). Accordingly, enhanced HFSE mobility in circulating hydrothermal fluids is reflected by presence of Zr-Th-U-Si phase that typically fills abundant microfractures intimately surrounding metamict zircon (Figure 3). Thus, the extreme HFSE and REE mobilization linked to the extensive dissolution of major U-bearing phases in durbachites provide the most likely explanation for the unusual chemistry of Moldanubian U-deposits.

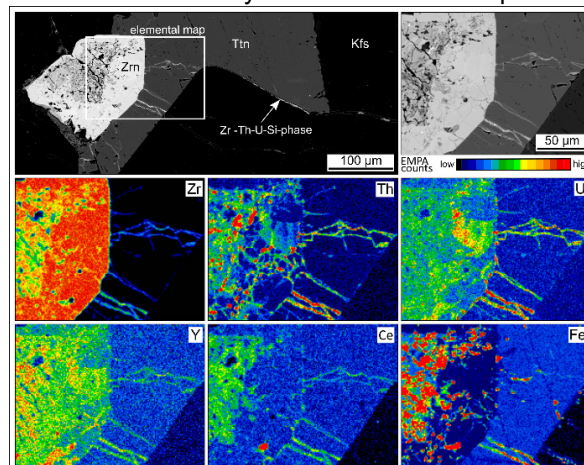


Figure 3. BSE image and EMP maps showing massive fluid-driven HFSE mobilization from altered zircon. Abbreviations: Zrn = zircon, Ttn = titanite, Kfs = K-feldspar.

The character of prevailing hydrothermally-derived accessory minerals in durbachites, such as REE-fluorocarbonates and Th-poor monazite after primary allanite and F-rich titanite after biotite, indicates that transport of incompatible elements was controlled by CO₂-, F-, and P-rich fluids. The replacement of chloritized biotite by hydrothermal F-rich titanite suggests that altered biotite supplied a significant F amount to interacting fluids through extensive chloritization. The key role of fluoride as one of the principal complexing ligands in fluids is further supported by: (1) high F content in hydrothermal Zr-Th-U-Si phase and altered primary thorite and Th-rich monazite (2) enhanced solubility of Th-rich monazite (3) extensive Th mobilization, and (4) presence of secondary fluorite in strongly altered durbachite samples. Furthermore, the pervasive zircon dissolution and resistance of apatite to alteration demonstrate alkaline conditions of the hydrothermal system (pH 8–12). Besides, dissolution of magmatic uraninite in durbachites and subsequent complexation of U in fluids, illustrated in Figure 3, points towards oxidizing conditions of the hydrothermal alteration. Taken together, the large-scale fluid-driven HFSE and REE mobilization, reflected by anomalous trace element signatures of low-T hydrothermal U-mineralization from the Moldanubian deposits (Figure 2a, b), was controlled by highly alkaline, oxidized aqueous solutions containing F- and P-dominated complexing ligands. The EMP chemical dating of U-mineralization revealed main Permian mineralizing event (ca. 270 Ma; Wertich et al. 2022) responsible for the formation of hydrothermal vein-type U-deposits in the Moldanubian zone. The recognition of the Permian age of the Moldanubian U-deposits suggests the importance of oxidized highly alkaline basinal brines, important ore-forming fluids in the entire Variscan belt (Cuney 2009), generated from Permo-Carboniferous sedimentary cover overlaying the crystalline basement hosting many hydrothermal U-deposits (Kříbek et al. 2009). Taking into account a much larger original extent of the highly alkaline (ultra)potassic intrusions, intervening up to the important tectonic boundary between Gföhl and Svatka Units (Leichmann et al. 2017) where most Moldanubian U-deposits are located (Figure 1b), HFSE- and REE-rich durbachites can account for an important source of U and other metals released during the infiltration alkaline brines triggering the pervasive dissolution of main U-bearing phases.

4 Conclusions

The unusual trace element chemistry of the low-T hydrothermal vein-type deposits (high Zr, Nb, Ti, Σ REE) and their close spatial association with

HFSE- and REE-rich durbachite intrusions in the Moldanubian Zone of the Bohemian Massif most likely point towards their mutual genetic relation. We propose that radiation damage of major refractory minerals likely enhanced permeability due to their volume expansion, which facilitated fluid-mineral interaction and thus promoted HFSE and REE leaching from their source. The release of U and other metals from durbachites was documented by EMP distribution maps and analyses of main accessory phases. The large-scale mobility of incompatible elements, reflected by HFSE and REE enrichment typical of some Moldanubian U-deposits, could have been related to the infiltration of oxidized, alkaline basin-derived waters that became mineralizing fluids during the interaction with basement-hosted durbachites (release F and P during alteration) and gave rise to the formation of U-deposits during the Permian hydrothermal event.

Acknowledgements

This research was carried out under the OP VVV project CZ.02.1.01/0.0/0.0/16_026/0008459 (GeoBarr) from the European Regional Development Fund, and was supported also by the Czech Grant Agency (GACR) project GA22-33820S.

References

- Cuney M (2009) The extreme diversity of uranium deposits. *Miner Deposita* 44:3–9.
- Frimmel HE, Schedel S, Brätz H (2014) Uraninite chemistry as forensic tool for provenance analysis. *Appl Geochem* 48:104–121.
- Kříbek B, Žák K, Dobeš P, Leichmann J, Pudilová M, René M, Scharm B, Scharmová M, Hájek A, Holéczy D, Hein UF, Lehmann B (2009) The Rožná uranium deposit (Bohemian Massif, Czech Republic): shear zone-hosted, late Variscan and post-Variscan hydrothermal mineralization. *Miner Deposita* 44:99–128.
- Kubeš M, Leichmann J, Wertich V, Mozola J, Holá M, Kanický V, Škoda R (2021) Metamictization and fluid-driven alteration triggering massive HFSE and REE mobilization from zircon and titanite: Direct evidence from EMPA imaging and LA-ICP-MS analyses. *Chem Geol* 586, 120593.
- Kubeš M, Leichmann J, Buriánek D, Holá M, Navrátil P, Scailliet S, O'Sullivan P (2022) Highly evolved miaskitic syenites deciphering the origin and nature of enriched mantle source of ultrapotassic magmatism in the Variscan orogenic root (Bohemian Massif, Moldanubian Zone). *Lithos* 432, 106890.
- Leichmann J, Gnojek I, Novák M, Sedlák J, Houzar S (2017) Durbachites from the Eastern Moldanubicum (Bohemian Massif): erosional relics of large, flat tabular intrusions of ultrapotassic melts—geophysical and petrological record. *Int J Earth Sci* 106:59–77.
- McDonough W, Sun SS (1995) The composition of the Earth. *Chem Geol* 120:223–253.
- Wertich V, Kubeš M, Leichmann J, Holá M, Haifler J, Mozola J, Hršelová P, Jaroš M (2022) Trace element signatures of uraninite controlled by fluid-rock interactions: A case study from the Eastern Moldanubicum (Bohemian Massif). *J Geochem Explor* 243, 107111.

Preliminary results of U-Pb dating and trace element analysis of cassiterites from the Western Sudetes, SW Poland

Władysław Zygo¹, Krzysztof Foltyn¹, Tonny Bernt Thomsen², Benjamin Dominguez Heredia², Adam Piestrzyński¹

¹Faculty of Geology, Geophysics and Environmental Protection, AGH University of Science and Technology in Kraków, Poland

²Geological Survey of Denmark and Greenland (GEUS), Department for Mapping and Mineral Resources, Copenhagen, Denmark

Abstract. Many tin deposits in Central Europe (e.g. Erzgebirge) are related to the emplacement of granites at the late stages of the Variscan Orogeny. The cassiterite crystals from selected, primary tin occurrences in Western Sudetes (Gierczyn-Przecznica, Czarnów, Piława Górna pegmatite) were investigated using LA-ICP-MS age of the mineralisation and trace elements composition. The results of cassiterite age from Czarnów and Piława Górna are slightly older than available data (dating of zircons, monazites and uraninites). The age of cassiterite from Gierczyn-Przecznica reveals that two distinguished types of cassiterite represent two separate events. The first event at 353 ± 14 and 360 ± 5 Ma can be related to the regional metamorphism event while the second is younger (318 ± 6 Ma) and can be associated with the emplacement of the Karkonosze Granite.

1 Introduction

Cassiterite has been found in many places in Western Sudetes in SW Poland, either in primary rocks or in placers. In the mica-quartz-chlorite schists of the Stara Kamienica Schist Belt, accumulations were significant enough to warrant extraction of tin in the past but despite interest and exploration efforts in the 20th century, mining has not been resumed and the resources are considered subeconomic. Origin of this deposit is not yet fully understood and it is assumed that the tin-polymetallic mineralisation most likely originated from complex interplay of hydrothermal, magmatic and metamorphic processes (Małek and Mikulski 2021), but the details are still a matter of discussion and several genetic models have been suggested (for detailed reference list see Michniewicz et al. 2006 and Mochnacka et al. 2015). The “usual suspect” is hydrothermal activity related to granitic intrusion, either to the Cambrian-Ordovician granitic protolith of the Iżera Gneisses (pre-metamorphic, e.g. Michniewicz et al. 2006) while others to the Variscan Karkonosze Granite (post-metamorphic e.g. Mochnacka et al. 2015). The main aim of this work was to conduct U-Pb dating of cassiterite and study trace elements in them in order to provide new data on geochronology and origin of the mineralisation. Additional cassiterites collected in two other locations in Sudetes (Czarnów and Piława Górna) were also analyzed for comparison.

2 Geological setting

2.1 Gierczyn-Przecznica area

The Karkonosze-Iżera Massif (KIM) is located in the south-central part of the West Sudetes on the NE margin of the Bohemian Massif, at the border of Poland and Czech Republic (Figure 1). The KIM can be subdivided into the Karkonosze Granite intrusion and its metamorphic envelope. Granite bodies crystallized around 312–306.9 Ma (Mikulski et al. 2020). The Iżera Massif part consists of the texturally diversified Iżera Gneisses, which were formed during Late Devonian to Early Carboniferous deformations of Early Palaeozoic porphyritic Iżera and Rumburk granites (Ober-Dziedzic et al. 2005). The Iżera-Kowary Unit contains several W-E extending metasedimentary belts composed of mica schists with minor interbeds of amphibolite, calc-silicate rocks, quartzite and quartz-feldspar schist, all metamorphosed under conditions of upper greenschist and lower amphibolite facies (Żelaźniewicz et al. 2003). The Stara Kamienica Schist Belt dipping toward the north at angles of 37.5 – 57.5° , hosts low-grade cassiterite mineralisation disseminated in the chlorite-mica-quartz schist (in some cases also rich in almandine garnet), locally accompanied by a polymetallic sulphide/sulphosalt association with the dominance of chalcopyrite and pyrrhotite (Michniewicz et al. 2006, Mochnacka et al. 2015 and references therein). The tin-bearing schists are 100–200 m thick and surrounded on both sides by barren schist, distinction between them is based on geochemical data (Sn content $> 0.004\%$) rather than lithological boundaries (Michniewicz et al. 2006).

Two types of cassiterite have been distinguished in the area, “brown” and “colourless”.

2.2 Czarnów

The eastern parts of the Iżera-Kowary Unit (IKU) include the Kowary Gneisses and the Czarnów Schist Formation, composed of mica schists, marbles, erlans, skarns, amphibolites and quartzofeldspathic rocks. Czarnów deposit consists of a steeply dipping (80° toward SE) SW-NE trending, 0.5–3 m thick quartz-ore vein, located at the tectonic contact of schists and calc-silicate rocks (Mochnacka et al. 2015).

The ore mineralisation is composed mostly of massive or coarse-grained euhedral crystals of

arsenopyrite and pyrrhotite that form lens-like bodies within the main quartz vein, or semi-massive impregnations in the country rocks (Mikulski et al. 2020). Minor quantities of pyrite, chalcopyrite, stibnite, cassiterite, magnetite or galena with sphalerite were also noted. Two separate generations of early formed cassiterite crystallized at temperatures of 440–384 °C and 340–300 °C at a pressure of 1.2–1.1 kbar from a fluid with total salinity 24–16 wt.% of NaCl equivalent (Mikulski et al. 2007). Several stages of ore crystallization have been identified, at least the main two of which were genetically associated with contact metasomatic and post-magmatic activity in the KP (Mikulski et al. 2007, Mikulski 2010).

The zircon grains from Czarnów porphyritic granite gave the weighted mean $^{206}\text{Pb}/^{238}\text{U}$ age from 14 analyses of 312.0 ± 2.9 Ma (Mikulski et al. 2020) while a similar Re-Os age (312 ± 3 Ma) has been obtained for Co-bearing arsenopyrite (Mikulski and Stein 2011). High-temperature Fe-Cu-As-Sn mineralisation was fractured, brecciated and overprinted by a younger generation of base metal sulphides, with visible Au and Bi-Ag-Te-Se sulphosalt mineralisation (Mikulski et al. 2020).

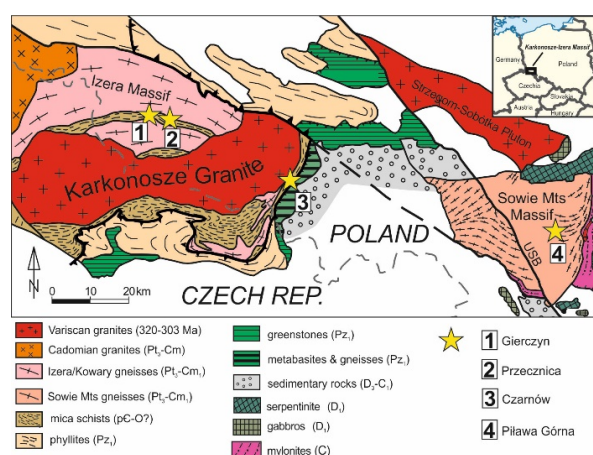


Figure 1. Geological map of Western Sudetes with the location of cassiterites collected for this study

2.3 Piława Górna

One of the major geological units of the Central Sudetes is the triangular Góry Sowie Block (Figure 1). It is composed predominantly of migmatitic para- and orthogneisses, amphibolites, and minor granulites, garnet meta-peridotites, pegmatites and calc-silicate rocks (Żelaźniewicz 1990). The late Proterozoic–Early Cambrian protolith underwent polymetamorphic evolution. An early high-pressure/high-temperature (HP–HT) episode at 400–395 Ma was followed by amphibolite-facies migmatization ca. 385–380 Ma and rapid cooling ca. 370–360 Ma (Kryza and Fanning 2007, Szuszkiewicz et al. 2013). Decompression resulted in local partial melting and formation of pegmatites from anatectic granitic magmas (Szuszkiewicz et al. 2013). The metamorphic suite is cut by granites, aplites, pegmatites, rhyolitic and

lamprophyric dikes as well as by barite and quartz hydrothermal veins.

The pegmatites are composed mainly of microcline, Na-plagioclase, quartz, biotite and muscovite, accompanied by schorl, almandine-spessartine garnet and beryl (Pieczka et al. 2018). Pegmatites show geochemical variability and range from primitive and moderately fractionated pegmatites, enriched in Nb-REE-Be-B and belonging to the NYF (niobium-yttrium-fluorine) pegmatitic family, to rare and much more strongly fractionated pods in the axial parts of the largest dykes that contain Li-Cs-Ta-Be-B mineralisation of the LCT (lithium-caesium-tantalum) type (Pieczka et al. 2018). In both types cassiterite crystals were observed.

3 Samples and methods

3.1 Samples

Cassiterite in samples from Gierczyn and Przeczница (Stara Kamienica Schist Belt) typically occurs as a small (20–200 µm) translucent grains with white/colorless internal reflections (Figure 2 A-B), disseminated in a quartz-mica-chlorite schist. “Spongy” cassiterite with brown internal reflections, sometimes intergrown with the more common translucent cassiterite, are more rare but was also targeted for LA-ICP-MS study (Figure 2 C-D). Due to small sizes, only coarser aggregates were selected for the U-Pb dating and trace elements analysis.

Cassiterite in Czarnów occurs as aggregates of subhedral to euhedral crystals (500–1000 µm in size), often forming intergrowths with arsenopyrite. Internal reflections reveal zonation in some of the cassiterite crystals.

Material from Piława Górna is represented by an approximately 7 mm large cassiterite crystal.

3.2 Methods

Chemical analyses of cassiterite in micro area were carried out using a JEOL JXA-8230 Super Probe electron microprobe at the Laboratory of Critical Elements AGH-KGHM in Kraków.

U-Pb dating of cassiterite as well as trace elements were analysed at the LA-ICP-MS facility at GEUS in Copenhagen employing an Element 2 single-collector magnetic sector field inductively coupled plasma mass spectrometer (SF-ICPMS) that is coupled to an NWR 213 nm Nd:YAG laser ablation system. All data were collected with laser spot diameter of 40 µm (pre-ablation of 50 µm), a laser repetition rate of 10 Hz and laser energy density of between 3.5 and 4.0 J/cm². The GJ1 zircon and NIST612 glass standard were used as a primary non-matrix-matched standards to correct for instrumental Pb-isotope fractionation and calculation of trace elemental compositions.

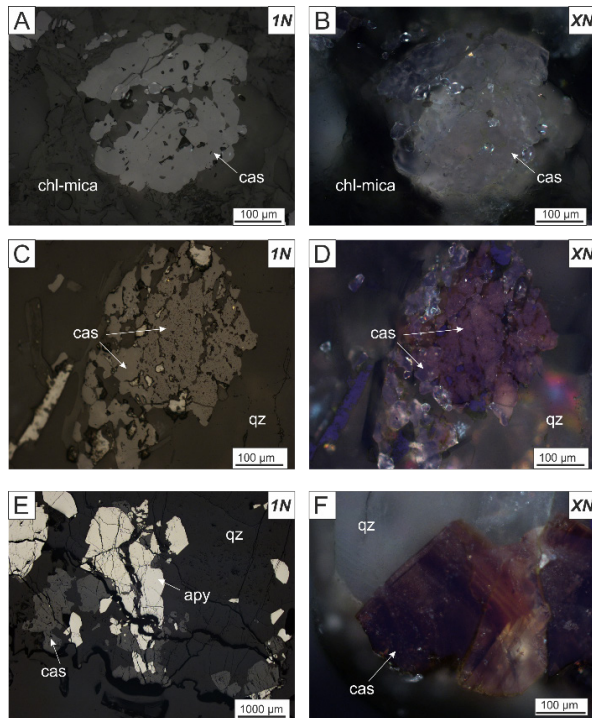


Figure 2. Photomicrographs of cassiterite from Gierczyn-Przecznica and Czarnów. A-B Typical quartz-chlorite mica schist hosted cassiterite with white/colorless internal reflections. C-D Przecznica, example of two intergrown types of cassiterite: one with white/colorless internal reflections and second “spongy” one with brownish internal reflections. E Typical cassiterite-arsenopyrite association from Czarnów. F Oscillatory zoned cassiterite from Czarnów

4 Results

4.1 Trace elements

Investigation of trace elements composition in cassiterites can help to distinguish different tin mineralisation types (Wang et al. 2022 and references therein). Although Wang et al. 2022 study only a few selected types of Sn mineralisation, pegmatite, greisen, skarn and quartz-vein types clearly cluster in different fields. The LA-ICP-MS analyses of cassiterites from Gierczyn-Przecznica, Czarnów and Piława Górna reveal significant differences between them. The cassiterites from Piława Górna are enriched in Ta and Nb, in Czarnów the same trend is observed for W and V. In the Gierczyn-Przecznica area, Hf and Mn are depleted, while these elements are enriched in the other types.

The trace elements composition of cassiterite from Czarnów show significant variations (Figure 3) this can be explained by presence of crystal zonation (Figure 2F).

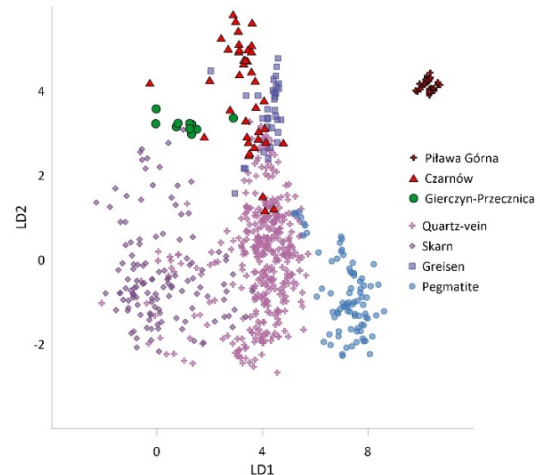


Figure 3. Discrimination diagram for the mineralisation types of cassiterite based on the fingerprint elements after Wang et al. (2022)

4.2 Geochronology

The small grain size made the analyses difficult, and those that were successful, point to 353 ± 14 and 360 ± 5 Ma age of the translucent cassiterite, whereas “spongy” grains yielded younger dates towards 318 ± 6 Ma (Figure 4).

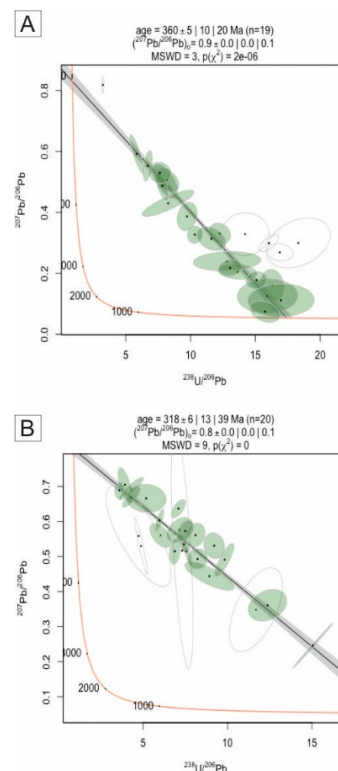


Figure 4. Tera-Wasserburg U-Pb plots for cassiterites from the Gierczyn-Przecznica tin deposit. (A) Plots reveal the cassiterite age at 360 ± 5 Ma; (B) Plots reveal the cassiterite age at 318 ± 6 Ma

Results from Czarnów (332 ± 1 Ma) are older than the Re-Os age (312 ± 3 Ma) (Figure 5B) obtained for Co-bearing arsenopyrite by Mikulski and Stein (2011). Similarly, cassiterite from Piława Górna

(404±1 Ma) gave age slightly older (Figure 5A) than previous geochronological studies (e.g., 377.6–380.7 Ma).

Difference of approximately 6% between established ages and results for Czarnów and Piława Górna presented here might be partially due to non-matrix matched standard used for analyses. However, even assuming that similar differences exist for cassiterite from Gierczyn and Przecznica (there is no geochronological data for comparison), translucent cassiterite still seems to precede the emplacement of the Karkonosze Granite. Devonian/Early Carboniferous ages are coeval with the regional metamorphism which might suggest that the obtained data could in fact represent the resetting of U-Pb ages during metamorphism. Younger, ‘spongy’ cassiterite age is contemporaneous with the emplacement of the Karkonosze Granite.

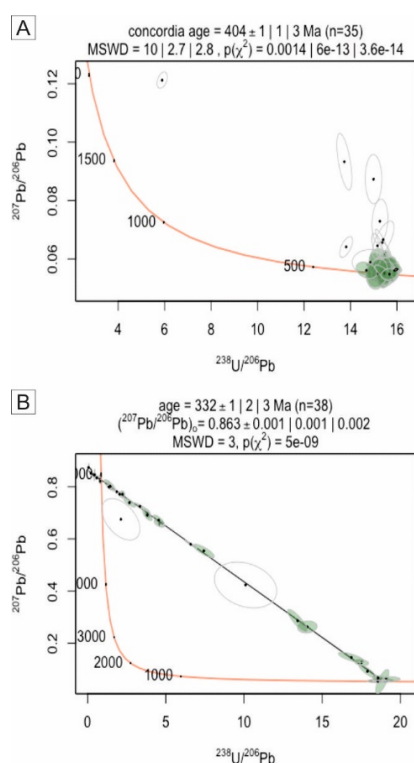


Figure 5. Tera–Wasserburg U–Pb plots for cassiterites from the Piława Górna (A) and Czarnów (B). The cassiterite age for Piława Górna – 404±1 Ma and for Czarnów – 33±1 Ma

Acknowledgements

This activity was carried out under the project “Enhanced Use of Heavy Mineral Chemistry in Exploration Targeting (MinExTarget)” that received funding from the European Institute of Innovation and Technology (EIT), a body of the European Union, under Horizon 2020, the EU Framework Programme for Research and Innovation. This work was partially funded by statutory funds of the Faculty of Geology, Geophysics and

Environmental Protection, AGH University of Science and Technology, Kraków, Poland (No. 16.16.140.315).

References

- Kryza R, Fanning CM (2007) Devonian deep-crustal metamorphism and exhumation in the Variscan Orogen: evidence from SHRIMP zircon ages from the HT-HP granulites and migmatites of the Góry Sowie (Polish Sudetes). *Geodin Acta* 20(3):159-175
- Małek R, Mikulski SZ (2021) A rare indium-bearing mineral (Zn-In-Cu-Fe sulphide) from the Stara Kamienica Schist Belt (Sudetes, SW Poland). *Geological Quarterly*. <http://dx.doi.org/10.7306/gq.1572>
- Michniewicz M, Bobiński W, Siemiątkowski J (2006) The mineralisation in the middle part of the Stara Kamienica Schist Belt (Western Sudetes). *Prace PIG* 185:5-136 (in Polish with English summary)
- Mikulski SZ (2010) The characteristic and genesis of the gold-bearing arsenic polymetallic mineralisation in the Czarnów deposit (Western Sudetes). *Biuletyn PIG* 439:303-320 (in Polish with English summary)
- Mikulski SZ, Kozłowski A, Speczik S (2007) Fluid inclusion study of gold-bearing quartz-sulphide veins and cassiterite from the Czarnów As deposit ore (SW Poland). In: Colin AJ et al. (ed) *Mineral exploration and research: digging deeper*, Proceedings of the 9th SGA Biennial Meeting, Dublin, Ireland. Cambridge Mineral Resources, Navan, pp 805-808
- Mikulski SZ, Stein HJ (2011) Re-Os age for molybdenite from the Variscan Karkonosze massif and its eastern metamorphic cover (SW Poland). In: Barra F et al. (ed) *Let's Talk Ore Deposits*, Proceedings of the 11th SGA Biennial Meeting, Antofagasta, Chile. Ediciones Universidad Católica del Norte, Antofagasta, pp 130–133
- Mikulski SZ, Williams IS, Stein HJ, Wierchowicz J (2020) Zircon U-Pb Dating of Magmatism and Mineralizing Hydrothermal Activity in the Variscan Karkonosze Massif and Its Eastern Metamorphic Cover (SW Poland). *Minerals*. <https://doi.org/10.3390/min10090787>
- Mochacka K, Oberc-Dziedzic T, Mayer W, Pieczka A (2015) Ore mineralisation related to geological evolution of the Karkonosze–Izera Massif (the Sudetes, Poland) - Towards a model. *Ore Geol Rev* 64:215-238
- Oberc-Dziedzic T, Pin C, Kryza R, (2005) Early Palaeozoic crustal melting in an extensional setting: petrological and Sm-Nd evidence from the Izera granite-gneisses, Polish Sudetes. *Int J Earth Sci* 94:354–368
- Pieczka A, Gołębiewska B, Jeleń P, Włodek A, Szełęg E, Szuszkiewicz A (2018) Towards Zn-dominant tourmaline: A case of Zn-rich fluor-elbaite and elbaite from the Julianna system at Piława Górna, Lower Silesia, SW Poland. *Minerals*. <https://doi.org/10.3390/min8040126>
- Speczik S, Wiszniewska J (1984) Some comments about stratiform tin deposits in the Stara Kamienica Chain (southwestern Poland). *Miner Deposita* 19(3):171-175
- Szuszkiewicz A, Szełęg E, Pieczka A, Ilnicki S, Nejbert K, Turniak K, Michałowski P (2013) The Julianna pegmatite vein system at the Piława Górna mine, Góry Sowie Block, SW Poland—preliminary data on geology and descriptive mineralogy. *Geological Quarterly* 57:467-484
- Wang C, Zhao K, Chen J, Ma X (2022) Examining fingerprint trace elements in cassiterite: Implications for primary tin deposit exploration. *Ore Geol Rev* 149:105082
- Żelaźniewicz A (1990) Deformation and metamorphism in the Góry Sowie gneiss complex, Sudetes, SW Poland. *Neues Jahrb Geol Palaontol Abh* 179:129–157
- Żelaźniewicz A, Nowak I, Achramowicz S, Czapliński W, Ciężkowski A, Wojewoda J (2003) The northern part of the Izera-Karkonosze Block: a passive margin of the Saxothuringian terrane. In: Ciężkowski W et al. (ed) *Sudety Zachodnie—od wendy do czwartorzędu WIND*, Wrocław, pp 17-32. (in Polish with English summary)

Genthelvite from the world-class beryllium-polymetallic deposit - Perga, Ukraine

Adam Piestrzyński¹, Barbara Zygo¹, Władysław Zygo¹, Jadwiga Pieczonka¹, Anatoliy Berezovsky²

¹AGH University of Science and Technology, Faculty of Geology, Geophysics and Environmental Protection, Krakow, Poland

² Kryvyi Rih National University, Kryvyi Rih, Ukraine

Abstract. Beryllium deposit Perga is located in the north-west part of Ukraine (Zhytomyr region). Geologically, it is situated within the Perga complex, which is the part of the Sushchano-Perga zone (NW of the Ukrainian Shield). The mineralization is related to rare metal granites (apogranites), in which are responsible for the variety of mineral species and geochemically unusual signature. About 70 minerals are distinguished within the boundaries of the complex. They belong to different classes (silicates and aluminosilicates, oxides, phosphates, sulphides, haloids and native elements).

1 Introduction

The Perga beryllium deposit is a unique phenomenon on a global scale – it is the only object in the world, in which commercial concentrations of beryllium are associated with a very rare mineral – a genthelvite ($\text{Zn}_4\text{Be}_3(\text{SiO}_4)_3\text{S}$). This deposit was discovered in the late 1960's, covers an area of approximately 21 km² and is confined to the Perga granites. Systematic exploration of the Perga deposit has begun in 1950's and continues to present days. In the period of 1960-1977, detailed exploration work was carried out (Metalidi et al. 1977) and based on the results of these works, reserves of beryllium ores were calculated and approved in 1977.

2 Geological settings

2.1 Regional geology

The Perga beryllium deposit is located in the northern part of the Ukrainian shield, within the Sushchano-Perga faults zone, which separates the Korosten and Osnitsk blocks (Figure 1 and 2). The Korosten block is part of the Volyn megablock and includes mostly Palaeoproterozoic rocks. The Osnitsk block belongs to the Osnitsk-Mikashevitsky volcanic belt. The deposit is restricted to the middle part of the Sushchano-Perga zone, which is distinguished as the Perga ore field (Figure 2). Deep fault zones isolate the Volyn megablock from other large tectonic elements of the Ukrainian Shield (Metalidi et al. 1997, Pieczonka et al. 2016). From the north and northwest, the Volyn mega block is separated from the Osnitsk-Mikashevitsky volcanic belt by the Sushchano-Perga faults zone. In the south, it is set apart from the Podole megablock by the Andrushivsky faults zone. In the east, the Zvizdal-Zalesk faults zone splits the Volyn megablock from the Brusilov suture zone (Metalidi et al. 1997). Repeated tectonic activations of the

Volyn megablock led to numerous displacements of the block and its parts in both vertical and horizontal directions. The Sushchano-Perga faults zone is a system of faults striking in north-easterly directions. It has a width of 0.5-15 km and a length of about 200 km. The planes of individual faults in the Sushchano-Perga zone dip north-westward and have dip angles of 50–80°. Dynamo-metamorphism and intrusive magmatism manifested repeatedly within the boundaries of the Sushchano-Perga zone. This zone is an ore control structure and contains deposits and ore occurrences of rare, rare-earth, non-ferrous and noble metals. The Sushchano-Perga zone is composed of various rocks of different ages. Among them, the most widespread are quartzites, disthenic quartzites, greisens, syenites, alkaline syenites, alkaline metasomatites, granites, granite-porphyrries, and subalkaline granites. The main ore mineralization of the Sushchano-Perga zone is associated with granites, which are distinguished under the name Perga granites. The Perga ore field is characterized by extensive development of alkaline metasomatites. The most common metasomatites are quartz-feldspar, albite - K-feldspar, and biotite-K-feldspar metasomatites (Metalidi and Nechaev 1983).

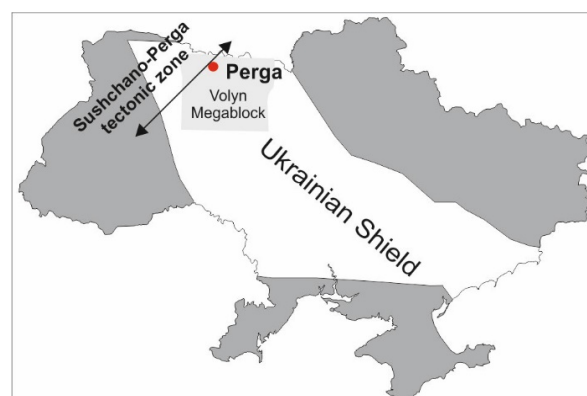


Figure 1. Location of Perga deposits within the Ukrainian Shield (not to scale)

The most productive part of the Perga complex is located between the Plotnitsky and Ubort faults, where metasomatically altered syenites and Perga granites contains Be, Zr-REE and Nb-Ta-F mineralization (Dagelaysky 1997).

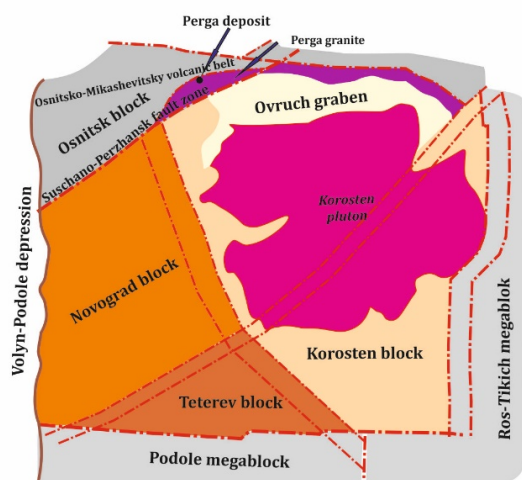


Figure 2. Structural map of Volyn megablock (not to scale).

The Purga ore field is composed of alkali syenites and granites enriched in volatile substances that are subjected to widespread metasomatism. These granites were identified as apogranites (albitized and greisenized granites around the edges of intrusions, commonly enriched in rare metals - including Nb, Ta, Li, Rb, Be, Sn, W, Mo) (Galetsky 1974 vide Dagelaysky 1997).

2.2 Ore mineralization

The rocks that build the Purga complex (Figure 3) are characterized by the occurrence of a diverse set of ore and accessory minerals, among which the following are distinguished: zircon, fluorite, cryolite, weberite, pachenolite, thorite, cassiterite, molybdenite, columbite, bastnaesite, hematite, magnetite, galena, sphalerite, phenakite, genthelvite, and gahnite (Esipchuk et al. 1993). Geochemical research conducted by Metalidi and Nechaev (1983) showed that the presence of: F, Be, Ta, Nb, REE, Zr, Pb, Zn, Li, Rb, Ce, Ga, Tl and Cd is typical for the Purga type of syenite and apogranite metasomatites (Remezova 2016).

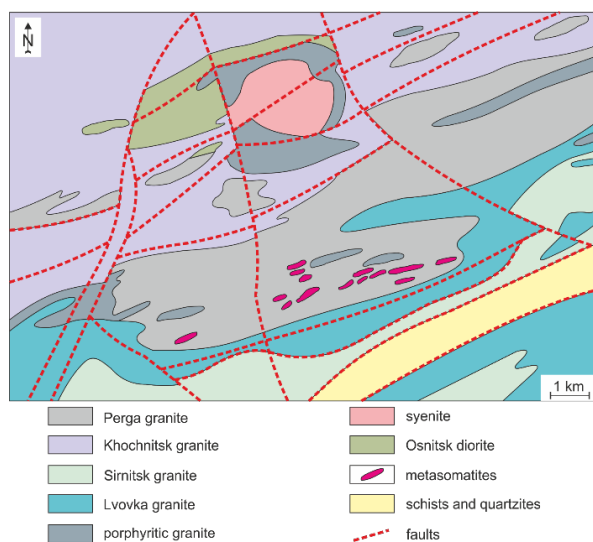


Figure 3. Geological map of the Purga deposit (Metalidi and Nechaev 1983)

Beryllium ores are restricted to mica-quartz-feldspar metasomatites (Figure 4). Within deposit, 8 ore zones up to 3000 metres length and 40 to 80 metres width were identified. In each zones from 1 to 35 ore bodies are distinguished. The distance between ore bodies varies from 5 to 30 metres (Figure 3). The main ore minerals are genthelvite and in restricted areas also phenakite. The genthelvite ore represents 69% of the ore, phenakite ore is just about 2% solely. The four types of genthelvite can be distinguished based on mineral's colour: brown, green, crimson (Figure 5) and light-pink (Figure 6). The genthelvite occurs as crystals and grains ranging in size from 0.01 mm to 5 mm.

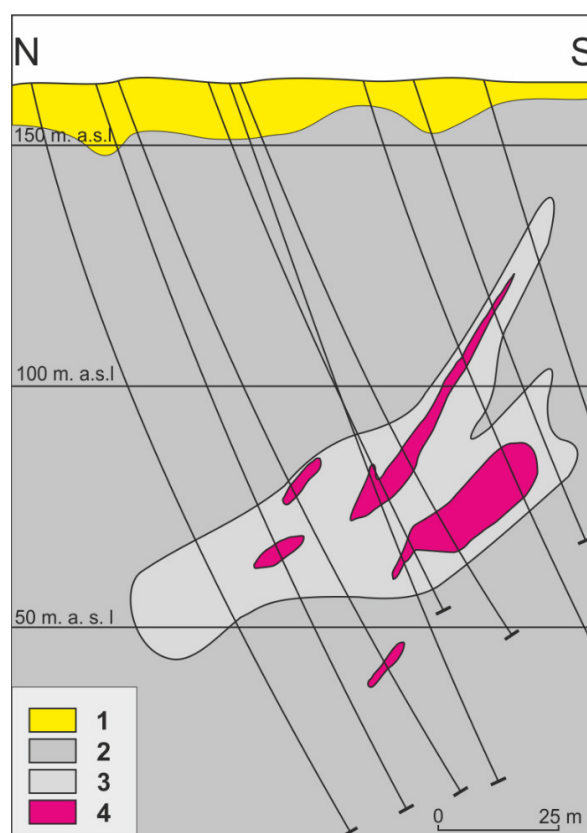


Figure 4. Schematic geological cross section of beryllium ore body. 1 - quaternary sediments, 2 - Purga granite, 3 - ore body, 4 - metasomatites

The first generation of genthelvite occurs in feldspar metasomatites and pure albitites. It is constituted by light yellow or brown crystals and irregular grains ranging in size from 0.1 mm to 1 mm, which have a barely visible zoning (their inner core is lighter than the outer zone). The characteristic elemental impurities include cadmium and titanium.



Figure 5. Crystals of crimson genthelvite in microcline metasomatite, galena crystals are located almost in the centre of the sample. Sample size 15 cm (Phot. by V.V. Levitsky)



Figure 6. Pink variety of genthelvite in quartz-microcline metasomatite

The genthelvite of the second generation occurs in albite-feldspar metasomatites and is represented by tetrahedrons and corroded grains. It is characterized by a pronounced zoning. The core of crystals or grains is light yellow or yellow. The outer zone is brown or light brown. The zones are separated from each other by a white stripe. There is often a multiple alternation of these zones of different colours. The characteristic impurity elements are cadmium, germanium and thorium.

Genthelvite of the third generation is found in feldspar-quartz-mica, feldspar metasomatites and is represented by brown-red and brown grains of irregular shape, as well as fragments of tetrahedron crystals, which have a weakly noticeable zoning.

It should be noted that, according to various studies, eight generations of genthelvite have been identified in the Sushchano-Perga zone (Metalidi and Nechaev 1983).

In the Sushchano-Perga zone, beside Beryllium deposit, 8 placer deposits of Sn-Nb-Ta-Zr were

recognized (Galetskiy et al. 2016) and numerous showings were identified.

3 Methods and samples

The samples from the Perga beryllium deposit in Ukraine were collected in 2015-2018, during the annual student's field work organized by the AGH University of Science and Technology. Selection of the ore specimens were done with the help of local geologists. Due to the fact that beryllium cannot be determined using an electron microprobe, its percentage in genthelvite was calculated from the formula proposed by Dunn (1976):

$$(\text{Mn}, \text{Fe}^{2+}, \text{Zn}, \text{Ca}, \text{Mg}) : \text{Be} = 4/3$$

Reflected and transmitted light microscopy was used to identify and characterize ore and rock forming minerals. Chemical analyses of genthelvite and sulphides were carried out using a JEOL JXA-8230 Super-Probe electron microprobe at the Laboratory of Critical Elements AGH-KGHM in Kraków. The microprobe was operated in the wavelength-dispersion mode at an accelerating voltage of 15kV and probe current of 20 nA. The following standards and spectral lines were used for genthelvite: albite (SiK α , AlK α), rodonite (MnK α), diopside (CaK α , MgK α), sanidine (KK α), willemite (ZnK α), fayalite (FeK α), anhydrite (SK α). Electron microprobe data were corrected using the ZAF procedure and JEOL software.

4 Results

Genthelvite belongs to the helvite group with the general formula $\text{Be}_3\text{M}_4(\text{SiO}_4)_3\text{S}$ (where M = Fe $^{2+}$, Zn or Mn), which also includes helvite (Mn member) and danalite (Fe $^{2+}$ member). Of these, genthelvite is the rarest species. Theoretically, it contains: 54.54% ZnO, 12.58% BeO, 30.19% SiO $_2$ and 5.37% S (Dunn 1976).

Three types of genthelvite were recognized during microscopic and microprobe study. Due to the colour of the crystals, the following types were identified: pink (type 1), green (type 2) and brown (type 3).

In order to determine the chemical composition and the influence of admixtures on genthelvites colour, 75 analyses were performed – 11 for type 1, 28 for type 2 and 36 for type 3 (Table 1, Figure 7 and 8).

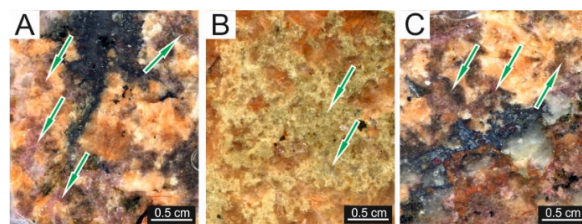


Figure 7. Different types of genthelvite (A - Type 1 – pink, B - Type 2 – green, C - Type 3 - brown).

Table 1. Representative, average composition (in wt. %) of genthelvite from Perga deposit. BeO content was calculated following Dunn (1976).

	T.C.	Type 1 (n = 11)	Type 2 (n = 28)	Type 3 (n = 36)
SiO ₂	30.19	31.63	30.94	31.59
MnO	-	1.15	0.62	1.0
ZnO	54.54	42.44	50.56	36.56
FeO	-	8.55	1.37	14.21
S	5.37	5.71	5.66	5.71
BeO	12.58	12.28	12.17	12.37
S=O	2.68	2.85	2.82	2.85
Total	100.00	98.93	98.56	98.61

T.C. – theoretical composition after Dunn (1976)

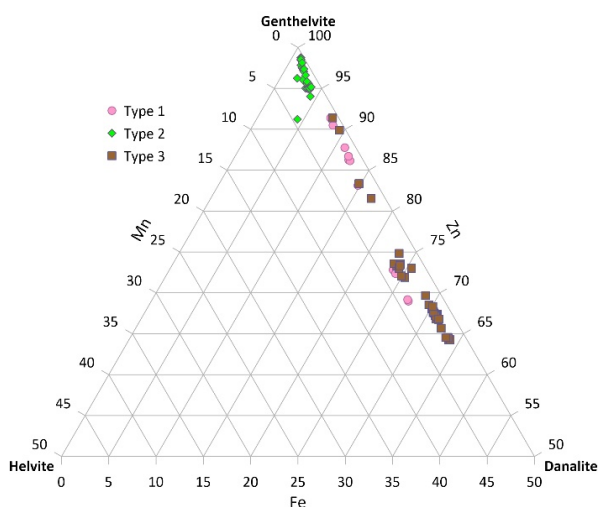


Figure 8. Ternary Fe-Mn-Zn plot of genthelvite from Perga deposit.

5 Conclusion

Quantitative measurements of macroscopically coloured varieties of genthelvite confirmed the differences in their composition.

The pink variety of genthelvite (type 1) comprises 12.28% of BeO, 42.44% of ZnO, 8.55% of FeO and 1.15 % of MnO in average. The type 3 (brown) is characterized by lower content of ZnO (36.56%) and a higher share of BeO (12.37%) and FeO (14.21%). It contains also less ZnO (36.56%) and MnO (1.0%) in comparison with type 1. The average content of the type 2 genthelvite is presented as follows: 12.17% of BeO, 50.56% of ZnO, 1.37% of FeO and 0.62% of MnO.

Of all the varieties studied, ZnO content is sometimes close to the theoretical green variant of genthelvite. The result is aligned with Dunn's (1976) statement that pure genthelvite can vary in colour from colourless to light green. As a result of the performed chemical analyses, it was found that the darker genthelvite, the more Fe and Be as well as less Zn it contains.

Acknowledgements

This work was partially funded by statutory funds of the Faculty of Geology, Geophysics and

Environmental Protection, AGH University of Science and Technology, Kraków, Poland (No. 16.16.140.315). We would like to thank geologists B. Wysocki and M. Masko for their help as well as effort with field works and sample collection.

References

- Dunn PJ (1976) Genthelvite and the helvine group. *Mineralogical Magazine* 40:627-636
- Dagelaysky VB (1997) Ukrainian Shield. In: Rundqvist DV, Gillen C (rd) *Precambrian Ore Deposits of the East European and Siberian Craton*. Elsevier Science B.V., Amsterdam, pp 107-153
- Esipchuk KYe, Sheremet YeM, Sveshnikov KI (1993) Rare metal granites and related rocks of the Ukrainian Shield. *Bulletin of the Geological Society of Finland* 65/ II:131-141
- Metalidi SV, Slysh RA, Bilchenko PB, Lebed NI, Garkusha AP, Liskevich RM (1977) Perga deposit of beryllium / Report on the results of exploration carried out in 1962-1977 in the Olevisk district of the Zhytomyr region of the Ukrainian SSR. Book 1. Text. Kiev, 519 p
- Metalidi SV, Nechaev SV (1983) Sushchano-Perzhanskaia zona (heolohiia, mineralohiia, rudonosnost). *Naukova dumka*, Kyiv, 136 (in Russian)
- Pieczonka J, Piestrzyński A, Paranko I (2016) *Geology of the selected mineral deposits of Ukraine*. WG AGH Krakow, 157p (in Polish)
- Galetskiy LS, Khrushchov DP, Remezova OO, Yaremenko OV, Kravchenko OA (2016) Modern interpretation of the Perga cassiterite-columbite placer deposit geological construction. *Geological Journal* 3:7-20

Assessing REE-phosphate mineral chemistry for ISCG exploration.

Travis Batch^{1,2}, Caroline Tiddy^{1,2}, Adrienne Brotodewo^{1,2}, David Giles^{1,2}

¹ Future Industries Institute, University of South Australia, Mawson Lakes, South Australia, Australia

² MinEx CRC, University of South Australia, Mawson Lakes, South Australia, Australia

Abstract. Challenges related to thick cover sequences that bury rocks prospective for and/or hosting mineralisation make exploration challenging and financially risky. In response geochemical targeting tools based on mineral chemistry are being developed to aid deep exploration. One such tool being developed is based on the mineral chemistry of REE-bearing phosphate minerals (monazite, rhabdophane) to indicate proximity to Cu-Au ore deposits. To develop this tool, examples from known ore deposits must be tested. Here we present the initial results from the Jericho iron sulfide-copper-gold (ISCG) deposit in the Cloncurry District, Queensland, Australia. Metamorphic REE-bearing phosphates can be distinguished from mineralisation-associated hydrothermal REE-bearing phosphates based on Ca concentrations in combination with Th and S concentrations.

1 Introduction

The successful discovery of ore deposits is becoming increasingly difficult as explorers are forced to search within prospective terranes buried beneath thick cover sequences. This challenge is reflected in increased expenditure and declining rates of discovery. Decreasing rates of discovery are impacting global supplies of minerals, especially critical elements such as copper and rare-earth elements (REE), that are essential for the energy transition. To ensure we reach this future, more mineral deposits containing these critical minerals are required. New techniques are being developed for the exploration toolkit to increase the success rate of deposit discovery. Such techniques include the development of geochemical targeting tools that use mineral chemistry to understand proximity to ore deposits.

REE-bearing phosphates (e.g. monazite) are an ideal candidates for such a geochemical targeting tool, as these minerals occur in most geological environments and their chemistry can easily alter in response to changing environmental conditions, including those associated with mineralisation (Forbes et al. 2015; Tiddy et al. 2021). They can also be used as indicator minerals for mineralisation (McClenaghan et al. 2017; Layton-Matthews and McClenaghan 2022). Here, we consider the chemistry of REE-bearing phosphate minerals for iron sulfide-copper-gold (ISCG) exploration.

The Cloncurry District in Queensland, Australia (Figure 1) hosts a spectrum of iron oxide-copper-gold (IOCG) and ISCG deposits. IOCG deposits include Ernest Henry, E1, Starra line and Osborne, and ISCG deposits include Eloise, Kulthor and Jericho. This study focusses on the Jericho ISCG

deposit (14.1 Mt @ 1.46% Cu, 0.29 g/t Au and 1.6 g/t Ag; Demetallica 2022).

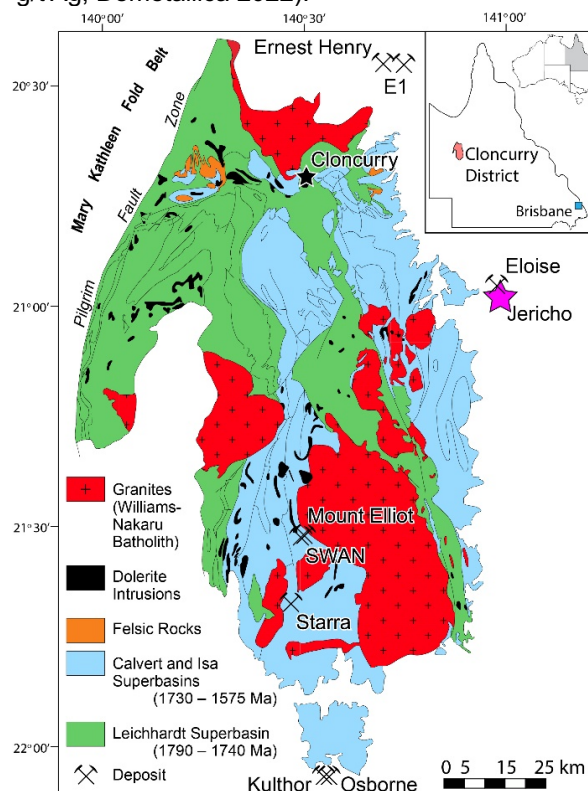


Figure 1. Extent of outcrop in the Cloncurry District in Queensland, Australia. Areas outside of the coloured areas east of the Pilgrim Fault Zone lie beneath sedimentary cover sequences. The location of Jericho is shown by the purple star. Locations of other major IOCG/ISCG deposits are shown. Modified after Betts et al. (2006). Inset: Map of Queensland, Australia showing the location of the Cloncurry District.

Jericho is located to the east of the Cloncurry District, approximately 58 km south-east of the Cloncurry township and about 2.5 km south of the Eloise ISCG deposit. Sulfide mineralisation is hosted in psammite and psammopelite primarily composed of K-feldspar, quartz, biotite, and relict tourmaline. Foliation is defined by the orientation of biotite. Low-grade metamorphic minerals (hornblende, scapolite) indicate the host rock has been metamorphosed and triple junctions at quartz grain boundaries indicate recrystallisation.

Mineralisation is dominated by pyrrhotite and chalcopyrite and occurs as three parallel lodes, aptly named J1, J2 and J3. They all dip steeply to the west, sub-parallel to foliation. Lodes have a strike

length of ~3.5 km and have a maximum width of ~13 m. J1 and J2 are the main mineralised lodes and occur 120 m apart.

2 Methods and Results

2.1 Sample Selection, Preparation and SEM Analysis

Polished thin sections for the J1 lode at Jericho were provided by Demetallica. Petrographic analysis was performed on the thin section before being coated with carbon. REE-bearing phosphates were imaged with a Zeiss Merlin FEG SEM. Operating conditions included a 20 kV accelerating voltage, 3 nA probe current and a working distance of 10 mm. Backscatter electron (BSE) images (Figure 2a) and energy dispersive spectroscopy (EDS) maps (Figure 2b-d) were used to locate REE-bearing phosphates and identify surrounding mineral phases. Apatite was found commonly associated with REE-bearing phosphates, likely indicating some formed from a fluid-apatite reaction, where REEs are leached from apatite and bond with P (Harlov et al. 2002, 2005; Harlov and Förster 2003).

Three textural types of REE-bearing phosphates were found at Jericho. The first are metamorphic, paragenetically late in the host rock, occasionally associated with sulfide minerals, and are large compared to other textural types, generally being 50 – 400 μm in length. The second group are hydrothermal, commonly associated with sulfide minerals, sometimes associated with apatite, and are small, normally 10 – 100 μm with rare grains up to 200 μm in length. A third textural type of phosphate is also hydrothermal, occurs as veins up to 1 mm long and 20 μm in width. These are the least common texture of phosphates.

2.2 Electron Probe Microanalyser (EPMA)

EPMA data was collected at Adelaide Microscopy, University of Adelaide using a Cameca SXFive Electron Microprobe. Light to middle REEs (La – Dy), U, Th, Ca, Al, Si, P, As and S were analysed. Oxygen was calculated from stoichiometric oxides. Combined conditions were used, with a 15 kV accelerating voltage and 20 nA beam current used for La, Ce, Pr, Nd, Sm, Al, Si, P and Th, while a 15 kV accelerating voltage and 100 nA beam current were used for Eu, Gd, Tb, Dy, Y, Ca, U, S and As. Results were filtered to only include analytical totals from 90 – 105 wt.%, Al + Si < 10 wt.%, Ca < 5 wt.% and S < 1 wt.%. This ensured the signal from surrounding mineral phases was limited. Filtered analyses were subsequently normalised to 100 wt.%

Metamorphic REE-bearing phosphates were characterised by higher U and Th concentrations and lower Ca and S concentrations than their hydrothermal counterparts. The Eu anomaly in metamorphic REE-bearing phosphates ($\text{Eu}/\text{Eu}^* = 0.02 - 1.97$) was also much more variable than hydrothermal REE-bearing phosphates ($\text{Eu}/\text{Eu}^* =$

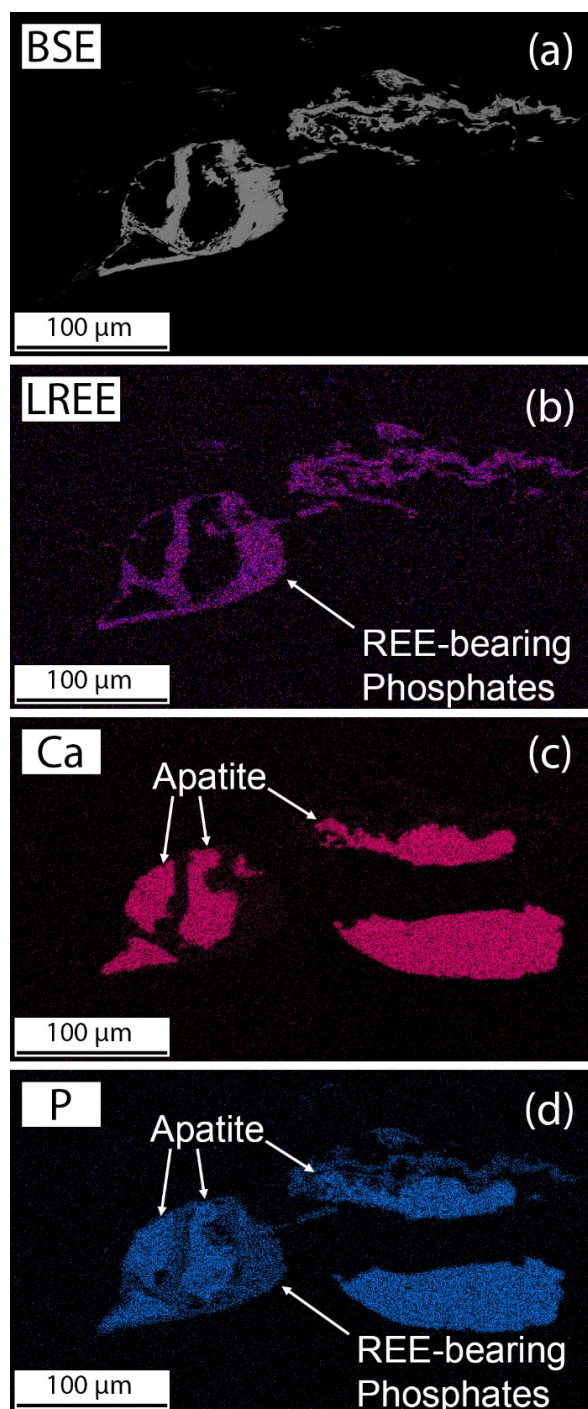


Figure 2. a BSE image and b-d EDS maps of REE-bearing phosphates and nearby mineral phases. Coincident LREE and P peaks show the presence of REE-bearing phosphates. Phosphates are associated with apatite as shown by coincident Ca and P peaks.

0.15 – 0.64). Prior to normalisation, metamorphic REE-bearing phosphates typically have analytical EPMA totals between 97 and 100%, compared to hydrothermal REE-bearing phosphate analytical totals between 90 and 98% (Figure 3).

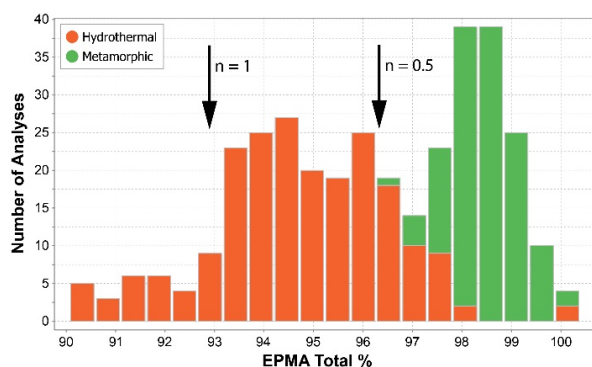


Figure 3. EPMA totals before normalisation. Arrows mark the EPMA total expected when the stoichiometric amount of water for rhabdophane is 0.5 and 1.

3 Discussion

REE-phosphate minerals present at Jericho could be monazite or rhabdophane. Monazite (LREEPO_4) and rhabdophane ($\text{LREEPO}_4 \cdot n \text{H}_2\text{O}$, where $n = 0.5 - 1$; where $n = 1$ in the rhabdophane formula, it can incorporate roughly 7 – 8 wt.% water) are geochemically indistinguishable when analysed by EDS, however the deficit in analytical totals from EPMA analysis can allow broad distinction between the two minerals whereby the water contained within rhabdophane is too light to be analysed by EPMA, and is reflected in low analysis totals. Both minerals are related, as monazite can alter to rhabdophane during low-grade and retrograde alteration in the presence of hydrothermal fluids (Berger et al. 2008; Nagy and Draganits 1999; Nagy et al. 2002).

At Jericho, the metamorphic REE-bearing phosphates with analytical totals between 97 and 100% (Figure 3) are interpreted to be monazite. The smaller hydrothermal grains that are associated with sulfides and the hydrothermal phosphate phase in the veins which yield low analytical totals between 90 and 98 wt.% (Figure 3) are interpreted to be rhabdophane. At Jericho, Ca concentrations can be used to discriminate between metamorphic and hydrothermal REE-bearing phosphates, while S and Th concentrations can mostly discriminate between the two types. Low Th is typical of hydrothermal REE-bearing phosphates (Schandl and Gorton 2004). Compared to metamorphic monazite from the Gawler Carton (Forbes et al. 2015), metamorphic monazite from Jericho has lower concentrations of U, Th and Ca, and higher concentrations of light REEs.

There is also a notable difference between the space groups of monazite and rhabdophane. Monazite is in the monoclinic P21/n space group (Ni et al. 1995) while rhabdophane is in the hexagonal P6₂22 space group (Mooney 1950). With this structural difference, rhabdophane tends towards an apatite stoichiometry rather than a monazite stoichiometry (Poitrasson et al. 2000; Nagy et al. 2002; Figure 4).

The stability fields of monazite and rhabdophane are close at low temperatures (Poitrasson 2005) with fluid activity dictating which mineral is formed (Krenn

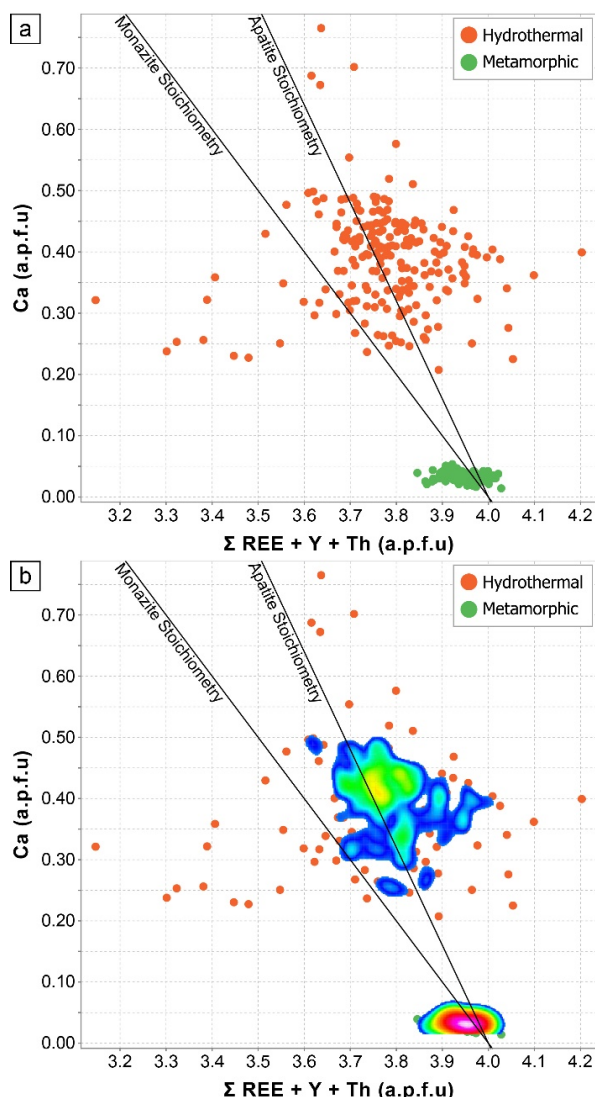


Figure 4. **a** Atomic proportions within REE-bearing phosphates at Jericho, recalculated based on 16 oxygen atoms per formula unit (a.p.f.u). Lines indicate ideal monazite and apatite stoichiometries (from Poitrasson et al. 2000). **b** As indicated by the heat map, most hydrothermal REE-bearing phosphates cluster around the apatite stoichiometry line. Metamorphic REE-bearing phosphates contain < 0.2 wt.% Ca, so all cluster around the bottom of the graph.

and Finger 2007). The mineralising fluid at Jericho may have been the cause of rhabdophane formation considering the close relationship between rhabdophane and apatite (fluid-apatite reactions), and rhabdophane with sulfide minerals. This would indicate that rhabdophane formation is coeval with mineralisation and its chemistry reflects its association with mineralisation. Its presence also indicates mineralisation at Jericho occurred at low temperatures.

4 Conclusion

Initial development of a geochemical targeting tool using REE-bearing phosphate mineral chemistry shows promise for ISCG exploration, being able to

distinguish between different phases associated and unassociated with the mineralising event at Jericho. Ca, S and Th have been shown to be the main discriminators for rhabdophane and metamorphic monazite. Hydrothermal REE-bearing phosphates were found to be rhabdophane based on analytical totals and their tendency towards an apatite stoichiometry, indicating Jericho is a low temperature system. Further development of this exploration tool using REE-bearing phosphates will be achieved by comparing this data to other ISCG deposits in the area (Kulthor and Eloise).

Acknowledgements

The authors would like to acknowledge the contributions of Tony Belperio and Glen Little for providing the samples. Nobuyuki Kawashima from the University of South Australia is thanked for his help with the collection of SEM and EDS data. Benjamin Wade from Adelaide Microscopy is thanked for his help with the collection of EPMA data. This project was kindly supported by MinEx CRC whose activities are funded by the Australian Government's Cooperative Research Centre Programme.

References

- Berger A, Gnos E, Janots E, Fernandez A, Giese J (2008) Formation and composition of rhabdophane, bastnäsite and hydrated thorium minerals during alteration: Implications for geochronology and low-temperature processes. *Chem Geol* 254(3):238–248 <https://doi.org/10.1016/j.chemgeo.2008.03.006>
- Betts P, Giles D, Mark G, Lister G, Goleby B, Aillères L (2006) Synthesis of the Proterozoic evolution of the Mt Isa Inlier. *Aust J Earth Sci* 53(1):187–211. <https://doi.org/10.1080/08120090500434625>
- Demetallica (2022) Jericho mineral resource delivers 62% increase in contained copper. Demetallica ASX Release. <https://openbriefing.com.au/AsxDownload.aspx?pdfUrl=Report%2FComNews%2F20221024%2F02586599.pdf> Accessed 31 October 2022
- Forbes C, Giles D, Freeman H, Sawyer M, Normington V (2015) Glacial dispersion of hydrothermal monazite in the Prominent Hill deposit: An exploration tool. *J Geochem Explor* 156:10–33. <https://doi.org/10.1016/j.gexplo.2015.04.011>
- Harlov D, Förster HJ, Nijland T (2002) Fluid-induced nucleation of (Y + REE)-phosphate minerals within apatite: Nature and experiment. Part I. Chlorapatite. *Am Min* 87(2–3):245–261. <https://doi.org/10.2138/am-2002-2-306>
- Harlov D, Förster HJ (2003) Fluid-induced nucleation of (Y + REE)-phosphate minerals within apatite: Nature and experiment. Part II. Fluorapatite. *Am Min* 88(8–9):1209–1229. <https://doi.org/10.2138/am-2003-8-905>
- Harlov D, Wirth R, Förster HJ (2005) An experimental study of dissolution-reprecipitation in fluorapatite: fluid infiltration and the formation of monazite. *Contrib Miner Petrol* 150(3):268–286. <https://doi.org/10.1007/s00410-005-0017-8>
- Krenn E, Finger F (2007) Formation of monazite and rhabdophane at the expense of allanite during Alpine low temperature retrogression of metapelitic basement rocks from Crete, Greece: Microprobe data and geochronological implications. *Lithos* 95(1):130–147 <https://doi.org/10.1016/j.lithos.2006.07.007>
- Layton-Matthews D, McClenaghan M (2022) Current techniques and applications of mineral chemistry to mineral exploration; examples from glaciated terrain: A review. *Minerals* 12(1):59. <https://doi.org/10.3390/min12010059>
- McClenaghan M, Paulen R, Kjarsgaard I, Fortin R (2017) Rare earth element indicator minerals: An example from the Strange Lake deposit, Quebec and Labrador, eastern Canada. In: McClenaghan M, Layton-Matthews D (ed) Application of indicator mineral methods to bedrock and sediments, Geological Survey of Canada Open File 8345 pp 78–86. <https://doi.org/10.4095/306305>
- Mooney R (1950) X-ray diffraction study of cerous phosphate and related crystals. I. Hexagonal modification. *Acta Crystallographica* 3(5):337–340 <https://doi.org/10.1107/S0365110X50000963>
- Nagy G, Draganits E (1999) Occurrence and mineral-chemistry of monazite and rhabdophane in the Lower and? Middle Austroalpine tectonic units of the southern Sopron Hills (Austria).
- Nagy G, Draganits E, Demény A, Pantó G, Árkai P (2002) Genesis and transformations of monazite, florencite and rhabdophane during medium grade metamorphism: Examples from the Sopron Hills, Eastern Alps. *Chem Geol* 191:25–46. [https://doi.org/10.1016/S0009-2541\(02\)00147-X](https://doi.org/10.1016/S0009-2541(02)00147-X)
- Ni Y, Hughes J, Mariano A (1995) Crystal chemistry of the monazite and xenotime structures. *Am Min* 80(1–2):21–26 <https://doi.org/10.2138/am-1995-1-203>
- Poitras F (2005) Experimental studies of the stability of monazite in aqueous solutions. *Geochimica et Cosmochimica Acta* 69(10):6 <https://doi.org/10.1016/j.gca.2005.03.023>
- Poitras F, Chenery S, Shepherd T (2000) Electron microprobe and LA-ICP-MS study of monazite hydrothermal alteration: Implications for U-Th-Pb geochronology and nuclear ceramics. *Geochimica et Cosmochimica Acta* 64(19):3283–3297. [https://doi.org/10.1016/S0016-7037\(00\)00433-6](https://doi.org/10.1016/S0016-7037(00)00433-6)
- Schandl E, Gorton M (2004) A textural and geochemical guide to the identification of hydrothermal monazite: Criteria of selection of samples for dating epigenetic hydrothermal ore deposits. *Economic Geology* 99(5):1027–1035. <https://doi.org/10.2113/gsecongeo.99.5.1027>
- Schodde R (2017) Challenges of exploring under deep cover. AMIRA International's 11th Biennial Exploration Managers Conference, 28th – 31st March
- Tiddy C, Zivak D, Hill J, Giles D, Hodgkison J, Neumann M, Brotdewo A (2021) Monazite as an exploration tool for iron oxide-copper-gold mineralisation in the Gawler Craton, South Australia. *Minerals* 11(8):809. <https://doi.org/10.3390/min11080809>

Alteration Footprints of Metasomatic Iron and Alkali-Calcic Systems in the Northern Norrbotten, Sweden

Olivier Blein¹, Matthieu Harlaux¹, Louise Corriveau², Edward P. Lynch³, Tero Niiranen⁴, Vladimir Lisitsin⁵, Kathy Ehrig⁶, Jean-François Montreuil⁷, Blandine Gourcerol¹

¹BRGM, 3 avenue Claude-Guillemin, BP 36009 – 45060 Orléans cedex 2 - France

²Geological Survey of Canada, Natural Resources Canada, Québec City, Canada

³Geological Survey of Sweden, P.O. Box 670, SE-75128 Uppsala, Sweden

⁴Geological Survey of Finland GTK, P.O. Box 77, FI-96190 Rovaniemi, Finland

⁵Geological Survey of Queensland, Brisbane, Australia

⁶BHP-Olympic Dam, Adelaide, Australia

⁷MacDonald Mines Exploration, Toronto, Canada

Abstract. Metasomatic iron and alkali-calcic mineral systems include a wide range of deposits with critical and precious metals, notably IOA, IOCG, skarn, albitite-hosted U, iron-rich Co (Au, Bi, Cu), and polymetallic vein deposits. Host systems evolve along diagnostic metasomatic paths with: 1) Na (albitite) and local skarn, 2) high-temperature (HT) Ca-Fe, 3) HT K-Fe, 4) K and K-Ca-Mg (K-skarn), 5) low-temperature (LT) K-Fe and Ca-Mg-Fe-(Si, CO₂), and 6) epithermal alteration. In this contribution, we show that chalcopyrite-rich IOCG-style deposits from the Northern Norrbotten, Sweden, are characterized by early Na alteration overprinted by Ca-Fe and K-Fe alteration with a geochemical footprint distinct from magnetite-rich (Great Bear magmatic zone) or hematite-rich (Olympic Dam) IOCG deposits. The IOCG-style deposits from the Northern Norrbotten have similarities with some found in the Cloncurry district in Australia.

1 Introduction

Metasomatic iron and alkali-calcic (MIAC) mineral systems chemically and texturally transform the entire upper crust across <500 km², precipitating successive metasomatic alteration facies rich in iron, alkali, and alkaline earth (e.g. Na, Ca) elements. Each facies shows distinct geochemical signatures, metal associations, and genetically linked deposits. Alteration footprints are thus key to explore mineral systems at deposit to province scales, and to interpret deposit types (Corriveau et al. 2016, 2022a-c; Day et al. 2016; Montreuil et al. 2016; Blein et al. 2022).

Globally, MIAC systems comprise regional albitite corridors (Na) and local skarn (±W, Fe), followed by HT Ca-Fe alteration and iron oxide-apatite (IOA) deposits, iron-rich Ni and REE deposits, HT Ca-K-Fe and iron-rich Co deposits, and HT K-Fe to LT K-Fe and Ca-Mg-Fe-Si-CO₂, with IOCG and iron-rich to iron-poor deposits (Corriveau et al. 2022a-c). Albitite-hosted deposits, deposits with iron-rich silicates, carbonates or sulfides instead of oxides, and polymetallic vein (e.g. five-element) deposits also occur (Montreuil et al. 2015; Hofstra et al. 2021; Corriveau et al. 2022c).

In this contribution, we characterize the metasomatic footprints of IOCG-style deposits in the Northern Norrbotten province (Sweden), and we show similarities to IOCG deposits from the Cloncurry district, Australia. These results allow for improving metallogenic models and optimizing the

exploration for critical mineral resources in Europe and beyond.

2 Alteration footprints of MIAC

Alteration facies in MIAC systems display highly distinctive molar proportions of Na, Ca, K, Fe, and Mg which can be visualized in diagnostic barcodes as proportions of intense alteration and overprints significantly differ from those in igneous, metamorphic, or sedimentary rocks. Least-altered samples have relatively balanced proportions of these cations. In contrast, metasomatized rocks display barcodes with one or two dominant elements and their distinctive associations serve as proxies for discriminating alteration facies. Plotting Na-Ca-Fe-K-Mg barcodes in the Alteration Index Iron-Oxide Copper-Gold (AIOCG) diagram of Montreuil et al. (2013) provides a visual representation of the evolution of metasomatic paths for MIAC systems. Increasing albitization of a least-altered rock is discriminated from overprints on albitite and the transition from albitite to HT Ca-Fe alteration by the diagnostic proportions of Ca-Fe-K-Mg of the overprinting alteration facies and the decreasing trend of Na from the Na field in the AIOCG diagram (Blein et al. 2022; Corriveau et al. 2022b).

In Figure 1A, strongly altered samples from the magnetite-rich deposits of the Great Bear magmatic zone (GBMZ) in Canada define a prograde metasomatic path (in blue) across the fields of the five main alteration facies (Na, HT Ca-Fe, HT K-Fe, K, and LT K-Fe). This dataset is complemented by the footprint of the hematite-rich Olympic Dam deposit. The footprint of increasing alteration of least-altered rocks (in yellow) is illustrated by the trend from least-altered granite to K-Fe alteration in Figure 1B along which Na-Ca proportions decrease and K-Fe proportions increase. Therefore, IOCG deposits having abundant iron oxides fall within the Fe-rich fields of the AIOCG diagram, while IOA deposits plot within the Fe-rich, Ca-Fe field, and albitite-hosted deposits along a trend between the Na field of the albitite and the field of the alteration overprint(s) (Blein et al. 2022; Corriveau et al. 2022b).

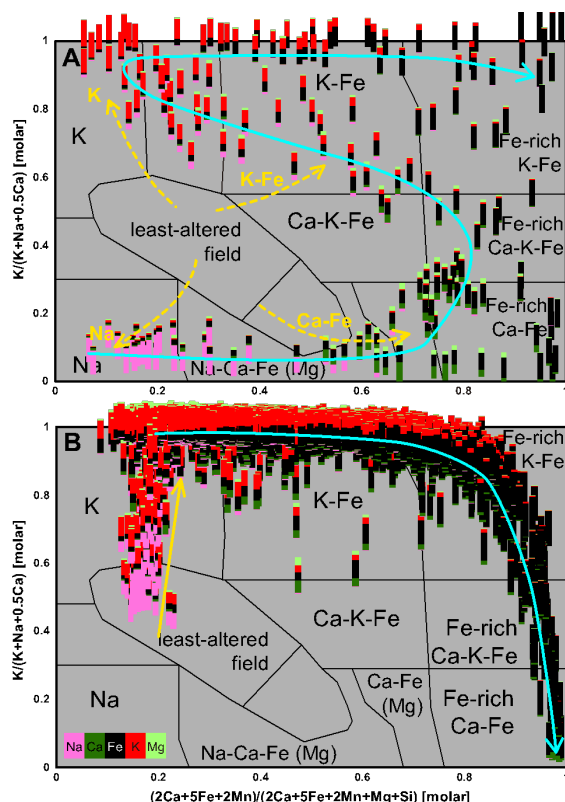


Figure 1. Evolution of metasomatic paths of the GBMZ (A) and Olympic Dam deposit (B), modified from Blein et al. (2022). Data: Corriveau et al. (2015), and BHP Olympic Dam (unpublished data; boreholes RD2366 and RD2382). Blue trend: most intense alteration. Yellow trend: least to most altered trends.

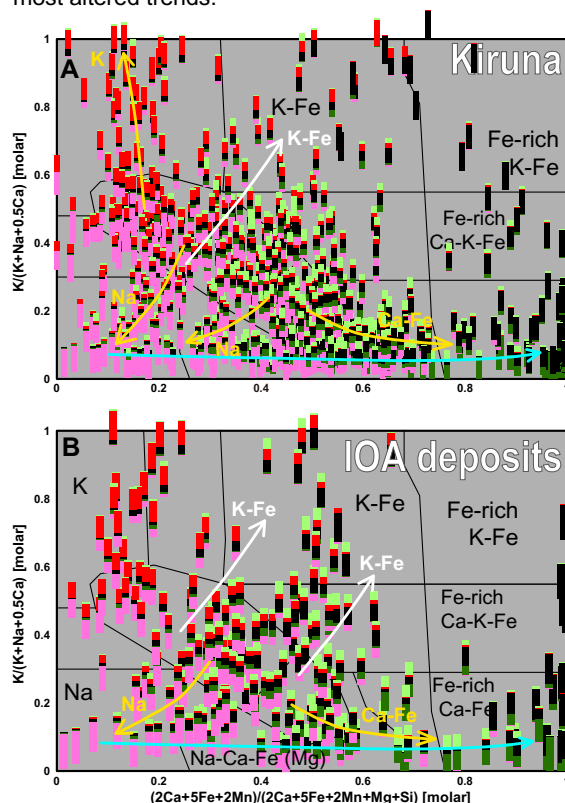


Figure 2. Diagnostic trends of the MIAC system for the Kiruna area (A), and IOA deposits subset (B). Data: Geological Survey of Sweden (SGU) lithogeochemistry database. White trend: overprints on albitite.

3 The Northern Norrbotten district, Sweden

The MIAC systems in the Northern Norrbotten formed in an intracontinental back-arc basin and were associated with comagmatic volcano-plutonic rocks dated at ca. 1.89-1.86 Ga. These processes resulted in the formation of IOA deposits, such as Kiruna and Malmberget, before undergoing crustal shortening and basin inversion (Martinsson et al. 2016; Sarlus et al. 2020; Andersson et al. 2021).

Epigenetic Cu-Au and Au deposits formed subsequently and are hosted within the basin inversion structures; those with iron oxide and iron silicate gangue minerals were assigned to IOCG such as the Nautanen deposit (Andersson et al. 2021; Bauer et al. 2022). The Northern Norrbotten district also includes Paleoproterozoic stratabound sulfide, iron skarn, and BIF deposits (Billström et al. 2010). Deposits assigned to the IOCG also occur in the Pajala-Kolari region (Niiranen et al. 2007).

Lithogeochemical samples collected within 20 km of the main deposits in the Kiruna area define trends from the least-altered field to the Na, K, K-Fe, and Ca-Fe fields (Fig. 2A). Samples close (< 2 km) to IOA deposits define a horizontal path starting from the Na field through the Na-Ca-Fe and Ca-Fe fields, and trends from the least-altered field to Na and Ca-Fe fields (Fig. 2B). The Na to Fe-rich Ca-Fe and Na to K-Fe trends recorded by the Fe-rich with Na barcodes and uneven increase of the normal Ca-Fe-K-Mg proportions of least-altered rocks as Na decreases is typical of albitite overprinted by a Ca-Fe or K-Fe alteration or transitioning to HT Ca-Fe alteration. Skarn (Ca-Mg barcodes), Fe-rich skarn (Ca-Fe-Mg barcodes), and apatite-rich ore (Ca-Fe barcodes) plot along a Na-Ca-Fe to Fe-rich Ca-Fe trend (Fig. 2B, Corriveau et al. 2022b).

Samples within 20 km of the main deposits in the Gallivare area plot essentially along least-altered to Na, least-altered to Ca-K-Fe and K-Fe or K trends, and albitite transitioning to Fe-rich Ca-Fe (Fig. 3A). The Nautanen deposit records a Ca-K-Fe to K-Fe alteration with localized Ca-Fe metasomatism (Fig. 3B) while for the Malmberget deposit the evolution from Na-Ca-Fe to K-Fe and Fe-rich Ca-Fe fields is typical of albitite overprinted by K-Fe alteration and transitioning to HT Ca-Fe alteration (Fig. 3C).

Samples within 20 km of the main deposits in the Pajala-Kolari area plot along least-altered felsic and mafic to Na trends, least-altered to K and K-Fe trends, and albitized mafic to the Fe-rich Ca-Fe trend (Fig. 4A). The Cu-Au deposits assigned to IOCGs fall along these trends with a better-defined path marked by decreasing Na and increasing Ca-Mg or Fe (Fig. 4B). Similar to the Kiruna district, skarn alteration plots along the Ca-Fe and Fe-rich Ca-Fe fields, with Ca-Mg±Fe-rich barcodes.

4 The Cloncurry district, Australia

In the Cloncurry district, 1.85–1.60 Ga supracrustal sequences intruded by several generations of granitoids hosts several magnetite-bearing Cu-Au

deposits, including the Ernest-Henry magnetite-group IOCG deposit (Williams 2010). The IOCG deposits consist of iron oxide breccias among regional, albite-rich Na-(Ca) alteration and proximal HT K-Fe and LT Ca-Mg-Fe alteration synchronous with and hosting most of the Cu-Au mineralization, which typically overprints the earlier Na-(Ca) alteration (Marshall and Oliver 2008; Corriveau et al. 2022a).

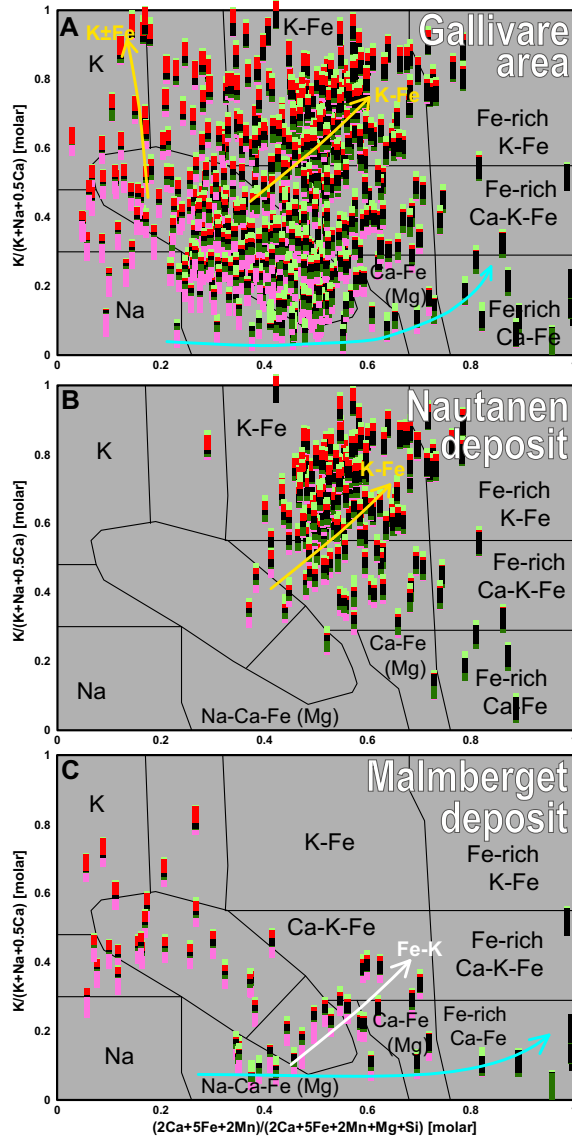


Figure 3. Diagnostic trends of the samples from the Gallivare area (A), Nautanen IOCG (B), and Malmberget IOA deposits (C). Data: SGU lithogeochemistry database.

Samples from the magnetite-rich IOCG Ernest-Henry deposit plot in the K-Fe, Ca-K-Fe, Ca-Fe, and Fe-rich alteration fields with few least-altered samples (Fig. 5A). High Na proportions reaching the Fe-rich fields are expected considering the preserved evidence of multiple overprints on albite in the deposit (Corriveau et al. 2022a, b). Samples from the magnetite-rich Cu-Au skarn of the SWAN deposit define a horizontal Na to Fe-rich Ca-Fe trend (in blue; Fig. 5B). Some samples present a K-Fe alteration superimposed on earlier albite (in white).

Similar to the Northern Norrbotten district, the Cloncurry district is characterized by extensive Na alteration overprinted by Ca-Fe and K-Fe alterations.

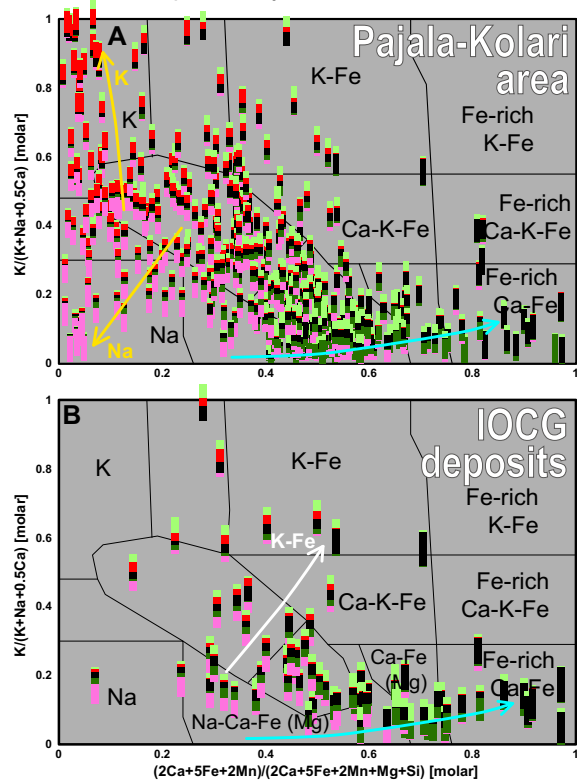


Figure 4. Diagnostic trends of the samples from the Pajala-Kolari area (A), and deposits assigned to the IOCG type (B). Data: SGU lithogeochemistry database and Rasilainen et al. (2007).

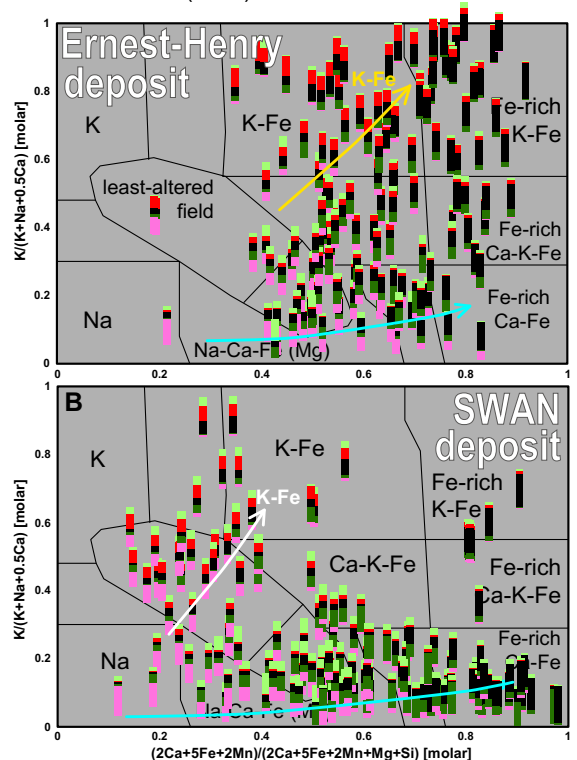


Figure 5. Diagnostic trends of the samples from the Ernest-Henry (A), and SWAN (B) IOCG deposits from the Cloncurry district. Data: Dhnaram et al. (2021).

5 Discussion

In the Pajala-Kolara area, Cu-Au deposits formally assigned to the IOCG class show metasomatic footprints which are distinct from magnetite- and hematite-rich IOCG deposits such as Olympic Dam (Fig. 1B) and Ernest-Henry (Fig. 5A). The alteration footprint is typical of HT Ca-Fe and K-Fe trends overprinting and increasingly replacing regionally albitized and/or scapolitized host rocks as exemplified by IOA deposits of the Kiruna district. In the Pajala-Kolara area, Cu-Au mineralization has HT Ca-Fe \pm weak HT K-Fe alteration overprinting skarn and albitite. According to the ore deposition model and case studies by Corriveau et al. (2022c), additional types of mineralization may occur within these Scandinavian MIAC systems and their known deposits.

Acknowledgments

Financial support from the European Union's Horizon Europe research and innovation program under Grant agreement n°1010557357, EIS – Exploration Information System (<https://eis-he.eu>). Research took place in collaboration with the Targeted Geoscience Initiative program and is Natural Resources Canada contribution 20220593.

References

- Bauer TE, Lynch EP, Sarlus Z, Drejning-Carroll D, Martinsson O, Metzger N, Wanhainen C (2022) Structural controls on iron oxide copper-gold mineralization and related alteration in a Paleoproterozoic supracrustal belt: Insights from the Nautanen deformation zone and surroundings, Northern Sweden. *Econ Geol* 117:327–359
- Billström K, Broman C, Eilu P, Martinsson O, Niiranen T, Ojala J, Wanhainen C, Weihed P (2010) IOCG and related mineral deposits of the Northern Fennoscandian Shield. In: Porter TM (ed) *Hydrothermal Iron Oxide Copper-Gold and related deposits: A global perspective advances in the understanding of IOCG deposits*, v. 4. PGC Publishing, Adelaide, p. 381–414
- Blein O., Corriveau L, Montreuil J-L, Ehrig K, Fabris A, Reid A, Pal D (2022) Geochemical signatures of metasomatic ore systems hosting IOCG, IOA, albite-hosted uranium and affiliated deposits: a tool for process studies and mineral exploration. In: Corriveau L, Potter EG, Mumin AH (eds) *Mineral systems with iron oxide copper-gold (IOCG) and affiliated deposits*. Geol Assoc Canada, Special Paper 52, p. 263–298
- Corriveau L, Lauzière K, Montreuil J-F, Potter EG, Hanes R, Premont S (2015) Dataset of geochemical data from iron oxide alkali altered mineralizing systems of the Great Bear magmatic zone (NWT). *Geol Survey Canada, Open File* 7643, 19 p.
- Corriveau L, Montreuil J-F, Potter EG (2016) Alteration facies linkages among IOCG, IOA and affiliated deposits in the Great Bear magmatic zone, Canada. *Econ Geol* 111:2045–2072
- Corriveau L, Montreuil JF, Potter EG, Ehrig K, Clark JM, Mumin AH, Williams PJ (2022a) Mineral systems with IOCG and affiliated deposits: part 1 – metasomatic footprints of alteration facies. In: Corriveau L, Potter EG, Mumin AH (eds) *Mineral systems with iron oxide copper-gold (IOCG) and affiliated deposits*: Geol Assoc Canada, Special Paper 52, p. 113–158
- Corriveau L, Montreuil JF, Blein O, Ehrig K, Potter EG, Fabris A, Clark JM (2022b) Mineral systems with IOCG and affiliated deposits: part 2 – geochemical footprints. In: Corriveau L, Potter EG, Mumin AH (eds) *Mineral systems with iron oxide copper-gold (IOCG) and affiliated deposits*. Geol Assoc Canada, Special Paper 52, p. 159–204
- Corriveau L, Montreuil J-F, Potter EG, Blein O, de Toni, AF (2022c) Mineral systems with IOCG and affiliated deposits: part 3 – metal pathways and ore deposit model. In: *Mineral systems with iron oxide copper-gold (IOCG) and affiliated deposits*, Corriveau L, Potter EG, Mumin AH (eds) Geol Assoc Canada, Special Paper 52, p. 205–245
- Day WC, Slack JF, Ayuso RA, Seeger CM (2016) Regional geologic and petrologic framework for iron oxide \pm apatite \pm rare earth element and iron oxide copper-gold deposits of the Mesoproterozoic St. Francois Mountains terrane, southeast Missouri, USA. *Econ Geol* 111:1825–1858
- Dhanaram C, Lisitsin V, Gopalakrishnan S, Tang J, Killen D, von Gnielinski F (2021) Eastern Mount Isa Province IOCG data package. *GSQ Technical Notes* 2021/06
- Hofstra A, Lisitsin V, Corriveau L, Paradis S, Peter J, Lauzière K, Lawley C, Gadd M, Pilote J-L, Honsberger I, Bastrakov E, Champion D, Czarnota K, Doublier M, Huston D, Raymond O, VanDerWielen S, Emsbo P, Granitto M, Kreiner D (2021) Deposit classification scheme for the critical minerals mapping initiative global geochemical database. *USGS, Open-File Report* 2021–1042, 60 p
- Marshall LJ, Oliver NHS (2008) Constraints on hydrothermal fluid pathways within Mary Kathleen Group stratigraphy of the Cloncurry iron-oxide-copper-gold district, Australia. *Precamb Res* 163:151–158
- Martinsson O, Billström K, Broman C, Weihed P, Wanhainen C (2016) Metallogeny of the northern Norrbotten ore province, northern Fennoscandian Shield with emphasis on IOCG and apatite-iron ore deposits. *Ore Geol Rev* 78: 447–492
- Montreuil J-F, Corriveau L, Grunsky EC (2013) Compositional data analysis of IOCG systems, Great Bear magmatic zone, Canada: to each alteration types its own geochemical signature. *GEEA* 13: 229–247
- Montreuil J-F, Corriveau L, Potter EG (2015) Formation of albitite-hosted uranium within IOCG systems: The Southern Breccia, Great Bear magmatic zone, Northwest Territories, Canada. *Miner Depos* 50:293–325
- Montreuil J-F, Corriveau L, Potter EG, De Toni AF (2016) On the relation between alteration facies and metal endowment of iron oxide–alkali-altered systems, southern Great Bear magmatic zone (Canada). *Econ Geol* 111:2139–2168
- Niiranen T, Poutiainen M, Mänttari I (2007) Geology, geochemistry, fluid inclusion characteristics, and U–Pb age studies on iron oxide–Cu–Au deposits in the Kolari region, northern Finland. *Ore Geol Rev* 30:75–105
- Rasilainen K, Lahtinen R, Bornhost TJ (2007) The rock geochemical database of Finland manual. *Geologian tutkimuskeskus, Tutkimusraportti* 164 – Geological Survey of Finland, Report of Investigation 164, 38 p
- Sarlus Z, Andersson UB, Martinsson O, Bauer TE, Wanhainen C, Andersson JBH, Whitehouse MJ (2020) Timing and origin of the host rocks to the Malmberget iron oxide-apatite deposit, Sweden. *Precamb Res* 342:105652
- Williams PJ (2010) “Magnetite-group” IOCGs with special reference to Cloncurry and Northern Sweden: settings, alteration, deposit characteristics, fluid sources, and their relationship to apatite-rich iron ores. In: Corriveau L, Mumin AH (eds) *Exploring for iron oxide copper gold deposits: Canada and global analogues*. Geol Assoc Canada, Short Course Notes 20:23–38
- Williams PJ, Barton MD, Fontboté L, deHaller A, Johnson DA, Mark G, Oliver NHS, Marschik R (2005) Iron oxide-copper-gold deposits: Geology, space-time distribution and possible modes of origin. *Econ Geol* 100th, 371–405

Similarities, yet differences: Olympic Dam, Oak Dam West, Wirrda Well, Island Dam and Acropolis IOCG deposits, Olympic Cu-Au Province, South Australia

Kathy Ehrig^{1,2}, Cristiana L. Ciobanu², Nigel J. Cook², Vadim S. Kamenetsky³, Maya Kamenetsky³, Jocelyn McPhie³

¹BHP Olympic Dam, 10 Franklin St., Adelaide, South Australia, 5000, Australia

²School of Chemical Engineering, University of Adelaide, Adelaide, South Australia, 5005, Australia

³School of Natural Sciences, University of Tasmania, Hobart, Tasmania, 7005, Australia

Abstract. The Olympic Cu-Au Province hosts not only one of the world's largest Cu-Au-U deposits, Olympic Dam, but also Prominent Hill and Carrapateena. Additionally, REEs, other critical minerals (e.g. Sb, Bi, C, Co, W, Se, Te) plus F, S, As, Fe, Mo, Pb, Sn, Y, Zn are present at concentrations greater than mean continental crust. Other IOCGs (Fe-oxide Cu-Au) occur within a radius of ~150 km from Olympic Dam, which broadly defines the Olympic Cu-Au Province. These mineralised occurrences include, but are not limited to, Acropolis, Wirrda Well, Island Dam, Oak Dam East, Vulcan, Titan, Emmie Bluff, and the recently discovered Oak Dam West. Like any other global ore deposit type, IOCGs in the Olympic Cu-Au Province display similarities (e.g. hydrothermal magnetite/ hematite, hematite ages, U-Mo-Sn-W enriched hematite, Cu(±Fe) sulfides) and differences (e.g. host lithologies with different ages, nanoprecipitates/inclusions preserved in Fe-oxides, mineralization styles and depths of post-mineral cover). Simple down-drillhole magnetic susceptibility and total Fe concentration profiles reveal some of the complexities of these deposits. However, when coupled with micro- to nanoscale mineralogical characterisation, the macroscale trends can be articulated in terms of systematic transitions from magmatic magnetite to hydrothermal magnetite and finally to multi-generations of hematite.

1 Introduction

Hematite and magnetite are ubiquitous minerals in IOCG deposits, recording repeated cycles of replacement, remobilization and recrystallization from magmatic to hydrothermal conditions. A volume of research has been published focussed on the macro- to nanoscale Fe-oxide mineralogy and overall geochemical trends at Olympic Dam (OD), Wirrda Well (WW), Acropolis (AC), and Island Dam (ID). See detailed references in Ciobanu et al. (2019) and Cook et al. (2022). The present study shows magnetite susceptibility (*k*) values (i.e. proxy for magnetite abundance) and total Fe concentration, measured on 1-5m composite diamond drill core samples, to describe macro-scale magnetite and total Fe concentration at OD, WW, AC, ID and Oak Dam West (OKD). Published micro- to nanoscale mineralogical studies for OD, WW, AC, ID, and OKD are then used to clarify overall characteristics of the Olympic Dam Province IOCG deposits.

2 Geology and Mineralization Summary

Salient geology, sulfide mineralogy and geochronology data, mineralisation styles and geochemically anomalous element groups (see

References section) for OD, WW, AC, ID and OKD are presented in Table 1.

	OD	WW	AC	ID	OKD
post-mineral cover thick (~m)	300-550	340-580	360-770	270-380	650-960
gravity anomaly	yes	yes	yes	yes	yes
magnetic anomaly	yes	yes	yes	yes	no
deposit host	HS	DS	GRV	WG	DS
host age (~Ma)	1590	1850	1590	1750	1850
other lithology	WG, BCF		DS, HS	DS	WG, GRV
mafic/UM dykes	GRV, GDS	TS, GDS		GDS	TS, GRV, GDS
mineral style	diss	diss	vein	skarn, lenses	diss
Cu±Fe sulfides	py-cp-bn-cc	py-cp, trace bn-cc	py-cp, trace bn-cc	py-cp, trace bn-cc	py-cp-bn-cc
anomal. whole-rock geochem	U-W-Sn-Mo	U-W-Sn-Mo	U-W-Sn-Mo	U-W-Sn-Mo	U-W-Sn-Mo
	HFSE, REE	HFSE, REE	HFSE, REE	HFSE, REE	HFSE, REE
	TM	TM	TM	TM	TM
dominant alteration	hydro	hydro	hydro	hydro	hydro
early alteration	alkali-calcic	alkali-calcic	alkali-calcic	alkali-calcic	alkali-calcic

Table 1. Geology, ages and sulfide mineralogy (refer to References section). Abbreviations are Donington Suite granitoids (DS, ~1850Ma), Tournefort Metadolerite Dykes (TS, ~1810Ma), Wallaroo Group metasediments and metavolcanics (WG, ~1750Ma), Hiltaba Suite Granitoids (HS, ~1590Ma), felsic, mafic, ultramafic Gawler Range Volcanics lavas and dykes (GRV, ~1590Ma), bedded clastic facies (BCF, ~1590Ma), Gairdner Dyke Swarm (GDS, ~830Ma), disseminated (diss), transition metals (TM = Zn, Mn, Co, Ni, Cr), hydrolytic alteration (hydro). References for 1) BCF is McPhie et al. 2016, 2) mafic and ultramafic dykes are Huang et al. 2015, 2016 and 3) anomalous whole-rock geochemistry trends, refer to Ehrig et al. 2012, Dmitrijeva et al. 2019a, 2019b, 2022.

3 Macroscale Magnetite-Hematite Variation

Down-hole magnetic susceptibility and Fe concentration profiles for OD (Figs 1A-B), WW (Fig 2A), ID (Fig 2B), AC (Fig 3A) and ODW (Fig 3B). As a rough guide, magnetic susceptibility (*k*) values of 0.1, 10, 100, 1000 x 10⁻³ SI units are approximately 0.025, 0.25, 2.5, 25 vol% magnetite (Clark and

Emerson, 1991). Scaling of k and Fe concentration axis are consistent between graphs for easy visualization of the trends.

k ranges for Olympic Dam sulfide mineralized granitic to hematite breccias are $0.25\text{--}2 \times 10^{-3}$ SI (RD2852A, Fig 2A), very low magnetite content (Verdugo-Ihl et al. 2017). k values $> 5 \times 10^{-3}$ SI are anomalous and typically occur at depth and on the deposit margins (Fig 2B, RD2366), i.e. distal deposit margins with significant Fe-oxide addition (Verdugo-Ihl et al. 2020). RD2366 contains zones of magnetite-bearing hematite breccias below $\sim 700\text{m}$ depth and a few isolated narrow zones from 450–525m.

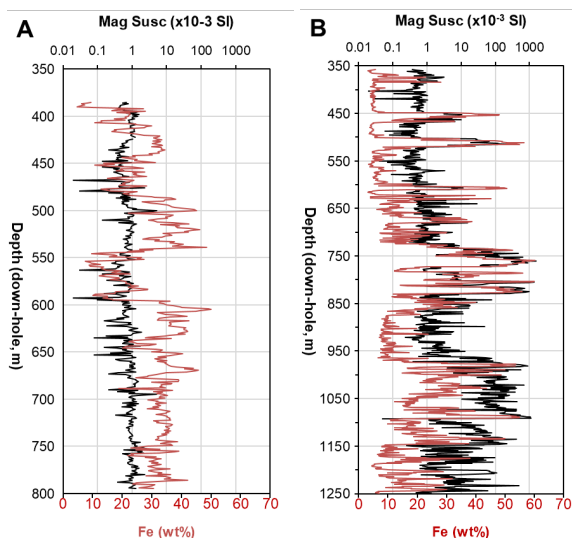


Figure 1. Magnetic susceptibility and Fe drill hole profiles for Olympic Dam A) RD2852A and B) RD2366.

k ranges for Wirrda Well sulfide mineralized granitic to hematite and magnetite-bearing hematite breccias (Fig 2A) are very similar to equivalent Olympic Dam breccias (Fig 1A–1B, respectively). However, significant short-scale variation in the WW Fe concentration reflects relatively narrow thickness, yet high frequency, of the Fe-oxide breccias within granitic breccias. Magnetite-bearing hematite breccias are dominant below 900m depth.

Island Dam Fe-oxides (Fig 2B, relatively low total %Fe) occur in skarn-style altered Fe-oxide bearing Wallaroo Group metasediments (Keyser et al. 2022). Intense hematite alteration of GRV feldspar-phyrlic rhyolites dominates above $\sim 920\text{m}$ depth (Fig 3A) at Acropolis. The mineralisation style changes to magnetite-apatite veins in less intensely altered rhyolites from $\sim 920\text{--}1065\text{m}$ and fine-grained dacite below 1065m depth (Kneta et al. 2017, Courtney-Davies et al. 2019, McPhie et al. 2020, Verdugo-Ihl et al. 2021).

A distinct magnetic anomaly is not present at Oak Dam West (Davidson et al. 2007, Oliveira 2012). This is different to the other IOCG deposits which are typified by spatial coincident gravity and magnetic anomalies. However, very low concentrations of magnetite are present (Fig 3B). Copper-barren ($\sim 680\text{--}1050\text{m}$) and sulfide-bearing ($\sim 1050\text{--}1415\text{m}$) hematite breccias occur in the profile, with altered

Donington granitoids below 1450m (Fig 4A) (BHP 2019). The total REE+Y oxide (TREO) concentration is typically >1000 ppm in hematite breccias (Fig 4B). Felsic GRV dykes intersect the hematite breccias and deformed/altered granites in multiple locations.

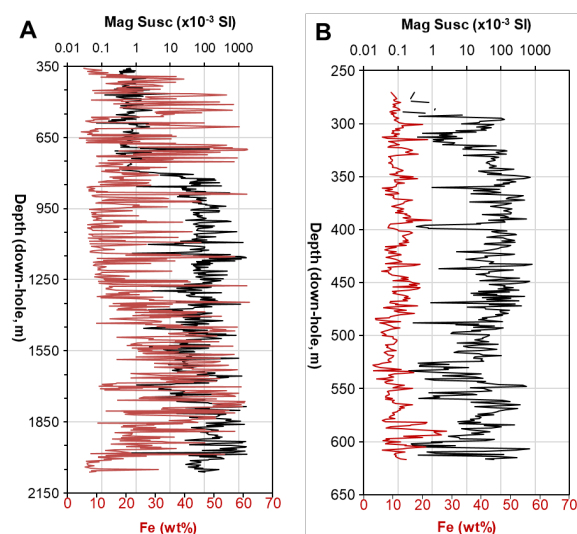


Figure 2. Magnetic susceptibility and Fe drill hole profiles for A) Wirrda Well WRD33 and B) Island Dam IDD4W1.

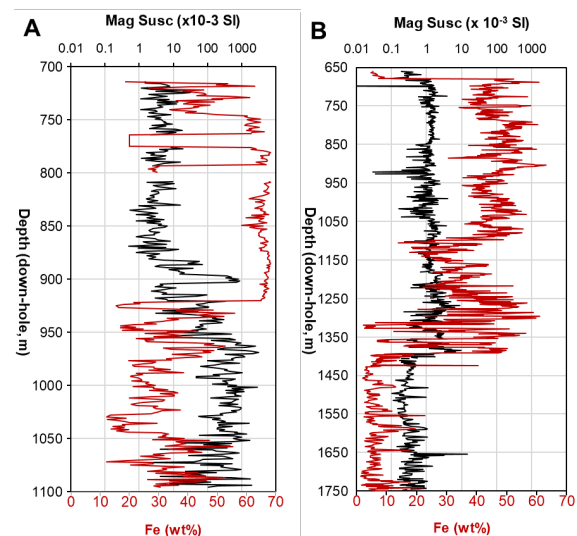


Figure 3. Magnetic susceptibility and Fe drill hole profiles for A) Acropolis ACD1 and B) Oak Dam West AD27W3.

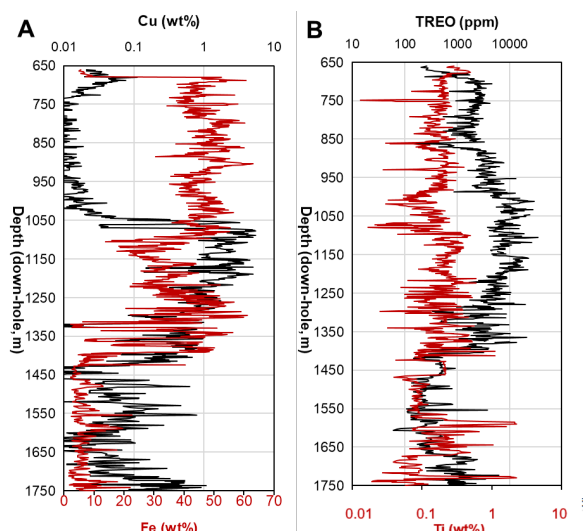


Figure 4. Cu, Fe (A) and TREO, Ti (B) profiles for Oak Dam West AD27W3.

4 Discussion and Implications

Essential attributes from Fe-oxide micro- to nanoscale studies across the Olympic Cu-Au Province are summarised in Table 2.

	OD	WW	AC	ID	OKD
mt of other origin (predating IOCG event)	U-bearing mt, older BIF	older metam. mt, fts incl., Si-Fe nano-defects			?
silician mt <111> Si-Fe nanoscale defects, silicate nano-incl.	act, ep, ser	chl	no	yes (nanoscale work lacking)	?
titanomagnetite: trellis ilm, spinel incl. (herc, ulv, etc.)	preserved magmatic accessory from RDG	no	yes	no	no
hematite	yes	yes	yes	yes	yes
hem trace element signature	U-W-Sn-Mo	U-W-Sn-Mo	U-W-Sn-Mo	U-W-Sn-Mo	U-W-Sn-Mo
	Ti-V		Ti-V	Ti-V	
	Cu-As				

Table 2. Magnetite, hematite and alteration types summarized from previous micro- and nanoscale studies. Abbreviations: magnetite (mt), hematite (hem), banded iron formation (BIF), actinolite (act), epidote (ep), sericite (ser), chlorite (chl), ilmenite (ilm), hercynite (herc), ulvöspinel (ulv), ferrotschermakite (fts), hydrolytic alteration (hydro).

Iron-oxides were precipitated, replaced, or modified more or less continuously from the earliest stages of host rock alteration to the late, fluid-assisted overprinting events recorded throughout the province. Rock-buffered, coupled dissolution reprecipitation (CDRR)-driven reactions document a pervasive early alkali-calcic to late-stage hydrolytic alteration recognized across the Olympic Province

(Krneta et al. 2017; Kontonikas-Charos et al. 2018, 2019).

In contrast to CDRR-driven alteration, fluid-buffered vein-filling at AC assists formation of high-temperature (~600 °C) trellis titanomagnetite (Verdugo-Ihl et al. 2021). At OD, the alkali calcic stage is recorded within silician magnetite (Ciobanu et al. 2019; Verdugo-Ihl et al. 2020).

Alteration of host granites leads to release of Si, Al, Mg, and Ca, elements that assist formation of silician magnetite and associated (calc)-silicate inclusions also at WW and ID (Ciobanu et al. 2022; Keyser et al. 2022). The preservation of ferrotschermakite nanoinclusions within magnetite at WW (Ciobanu et al. 2022) are evidence for a pre-1590 Ma metamorphism of the otherwise altered country rock.

Interconversion between Fe-oxides, a phenomenon common to all deposits discussed here, contributes to enrichment in trace elements. Whilst the U-W-Sn-Mo signature is the most conspicuous (Courtney-Davies et al. 2019; Verdugo-Ihl et al. 2020; Keyser et al. 2022), the presence of up to hundreds of ppm REE and HFSE in iron-oxides is also noteworthy (Cook et al. 2022a, b). The U-Mo-W-Sn signature, although most pronounced in hematite formed during hydrolytic alteration, persists throughout the lifespan of the IOCG mineralizing system as OD (Verdugo-Ihl et al. 2017; Courtney-Davies et al., 2020).

Recognition of iron-oxides from older Fe-rich lithologies, including a ~1760 Ma uranium-bearing magnetite documented at OD (Courtney-Davies et al. 2020) provide new clues to interpret the spatial-temporal links between BIFs and IOCG mineralization in the Olympic Province, with broader implications for analogous terranes elsewhere.

Hematite geochemistry and U-Pb geochronology, explored beyond OD at WW, AC and ID, can resolve the genetic and temporal links among IOCG deposits in the Olympic Cu-Au Province (Courtney-Davies et al. 2019; Keyser et al. 2022). Moreover, and as demonstrated by a study of Andean systems in Northern Chile (Verdugo-Ihl et al., 2022), iron-oxides are a powerful interpretive tool that will find broad application elsewhere.

Acknowledgements

We acknowledge Australian Research Council funding through LP130100438, LP200100156 and IH130200033, co-supported by BHP Olympic Dam, and by the FOX project funded by BHP Olympic Dam and the South Australian Government Mining and Petroleum Services Centre of Excellence.

References

- BHP (2019) Operational Review for the quarter ended 30 September 2019 – Appendix. https://www.bhp.com/-/media/documents/media/reports-and-presentations/2019/191017_bhpoperationreviewforthequarterended30september2019.pdf?la=en
- Ciobanu, CL, Verdugo-Ihl MR, Slattery A, Cook NJ, Ehrig K,

- Courtney-Davies L, Wade BJ (2019) Silician magnetite: Si-Fe-nanoprecipitates and other mineral inclusions in magnetite from the Olympic Dam deposit, South Australia. *Minerals* 9:311
- Ciobanu CL, Verdugo-Ihl MR, Cook NJ, Ehrig K, Slattery A, Courtney-Davies L (2022) Ferro-tschermakite with polysomatic chain-width disorder identified in silician magnetite from Wirrda Well, South Australia: a HAADF STEM study. *Am Mineral* 107:765-777
- Cherry A, Ehrig K, Kamenetsky VS, McPhie J, Kamenetsky M, Crowley J (2018) Precise geochronological constraints on the origin, setting and incorporation of ca. 1.59 Ga surficial facies into the Olympic Dam Breccia Complex, South Australia. *Precamb Res*, 315:162-178
- Clark DH, Emerson DW (1991) Notes on rock magnetization characteristics in applied geophysical studies. *Exploration Geophysics* 22:547-555
- Cook NJ, Ciobanu CL, Verdugo-Ihl MR, Courtney-Davies L, Ehrig K, Li W, Liu W, Xu J (2022a) Trace elements in minerals: where do we stand on the road between the Holy Grail and a can of worms? In: *The Critical Role of Minerals in the Carbon-Neutral Future*, Proc 16th SGA Biennial Meeting, Rotorua, New Zealand
- Cook NJ, Ciobanu CL, Ehrig K, Slattery AD, Gilbert S (2022b) Micron- to atomic-scale investigation in iron oxides. *Front Earth Sci* 10:967189
- Courtney-Davies L, Ciobanu CL, Verdugo-Ihl MR, Dmitrijeva M, Cook NJ, Ehrig K, Wade B (2019) Hematite geochemistry and geochronology resolve genetic and temporal links among iron-oxide copper gold systems, Olympic Dam district, South Australia. *Precamb Res* 334:105480
- Courtney-Davies L, Ciobanu CL, Verdugo-Ihl MR, Cook NJ, Ehrig K, Wade B, Zhu Z, Kamenetsky VS (2020a) ~1760 Ma magnetite-bearing protoliths in the Olympic Dam deposit, South Australia: Implications for ore genesis and regional metallogeny. *Ore Geol Rev* 118:103337
- Courtney-Davies L, Ciobanu CL, Tapster SR, Cook NJ, Ehrig K, Crowley JL, Verdugo-Ihl M, Wade BP, Condon DJ (2020b) Opening the magmatic-hydrothermal window: High precision U-Pb geochronology of the Mesoproterozoic Olympic Dam Cu-U-Au-Ag deposit, South Australia. *Econ Geol* 115:1855-1870
- Davidson GJ, Paterson H, Meffre S, Berry RF (2007) Characteristics and Origin of the Oak Dam East Breccia-Hosted, Iron Oxide Cu-U-(Au) Deposit: Olympic Dam Region, Gawler Craton, South Australia. *Econ Geol* 102:1471-1498
- Dmitrijeva M, Ehrig K, Ciobanu CL, Cook NJ, Verdugo-Ihl M, Metcalfe AV (2019a) Defining IOCG signatures through compositional data analysis: A case study of lithogeochemical zoning from the Olympic Dam deposit, South Australia. *Ore Geol Rev* 105:86-101
- Dmitrijeva M, Ciobanu CL, Ehrig K, Cook NJ, Metcalfe A, Verdugo-Ihl M, McPhie J (2019b) Mineralization-alteration footprints in the Olympic Dam IOCG district, South Australia: The Acropolis prospect. *J Geochem Explor* 205:106333
- Dmitrijeva M, Ciobanu CL, Ehrig K, Cook NJ, Verdugo-Ihl M, Metcalfe A, Kamenetsky VS, McPhie J (2022) Geochemical data analysis of iron-oxide copper gold mineralization, Wirrda Well prospect, South Australia. *Econ Geol* 117:853-874
- Ehrig K, McPhie J, Kamenetsky VS (2012) Geology and mineralogical zonation of the Olympic Dam iron oxide Cu-U-Au-Ag Deposit, South Australia. In: Hedenquist JW, Harris M, Camus F (eds) *Geology and Genesis of Major Copper Deposits and Districts of the World - A tribute to Richard H Sillitoe*, SEG Spec Publ 16:237-268
- Huang Q, Kamenetsky VS, McPhie J, Ehrig K, Meffre S, Maas R, Thompson J, Kamenetsky M, Chambefort I, Apukhtina O, Hu Y (2015) Neoproterozoic (ca. 820–830 Ma) mafic dykes at Olympic Dam, South Australia: Links with the Gairdner Large Igneous Province. *Precamb Res* 271:160–172.
- Huang Q, Kamenetsky VS, Ehrig K, McPhie J, Kamenetsky M, Cross K, Meffre S, Agangi A, Chambefort I, Dreen N G, Maas R, Apukhtina O (2016) Olivine-phyric basalt at the Olympic Dam iron oxide Cu-U-Au-Ag deposit: insights into the mantle source and petrogenesis of the Gawler Silicic Large Igneous Province, South Australia. *Precamb Res*, 281:185-199
- Keyser W, Ciobanu CL, Ehrig K, Dmitrijeva M, Wade BP, Courtney-Davies L, Cook NJ (2022) Skarn-style alteration in Proterozoic metasedimentary protoliths hosting IOCG mineralization: the Island Dam Prospect, South Australia. *Miner Deposita* 57:1227-1250
- Kontonikas-Charos A, Ciobanu CL, Cook NJ, Ehrig K, Krneta S, Kamenetsky VS (2018) Rare earth element geochemistry of feldspars: Examples from Fe-oxide Cu-Au systems in the Olympic Cu-Au Province, South Australia. *Mineral Petrol* 112:145-172
- Kontonikas-Charos A, Ehrig K, Cook NJ, Ciobanu CL (2019) Crystal chemistry of titanite from the Roxby Downs Granite, South Australia: Insights into petrogenesis, subsolidus evolution and hydrothermal alteration. *Contrib Mineral Petrol*, 174:59
- Krneta, S, Cook, NJ, Ciobanu, CL, Ehrig, K and Kontonikas-Charos, A (2017) The Wirrda Well and Acropolis prospects, Gawler Craton, South Australia: Insights into evolving fluid conditions through apatite chemistry. *J Geochem Explor* 181:276-291
- McPhie J, Orth K, Kamenetsky V, Kamenetsky M and Ehrig K (2016) Characteristics, origin and significance of Mesoproterozoic bedded clastic facies at the Olympic Dam Cu-U-Au-Ag deposit, South Australia. *Precamb Res* 276: 85-100
- McPhie J, Ehrig K, Kamenetsky M, Crowley J, Kamenetsky VS (2020) Geology of the Acropolis prospect, South Australia, constrained by high-precision CA-IDTIMS ages. *Austr J Earth Sci* 67:699-716
- Oliveira T (2021) Oak Dam Update: South Australian Exploration and Mining Conference, 26 November 2021, Adelaide
- Verdugo-Ihl M, Ciobanu CL, Cook NJ, Ehrig K, Courtney-Davies L, Gilbert S (2017) Textures and U-W-Sn-Mo signatures in hematite from the Olympic Dam Cu-U-Au-Ag deposit, South Australia: defining the archetype for IOCG deposits. *Ore Geol Rev* 91:173-195
- Verdugo-Ihl MR, Ciobanu CL, Slattery A, Cook NJ, Ehrig K, Courtney-Davies L (2019) Copper-arsenic nanoparticles in hematite: Fingerprinting fluid-mineral interaction. *Minerals* 9: 388.
- Verdugo-Ihl M, Ciobanu CL, Cook NJ, Ehrig K, Courtney-Davies L (2020) Defining early stages of IOCG systems: evidence from iron-oxides in the outer shell of the Olympic Dam deposit, South Australia. *Miner Deposita* 55:429-452
- Verdugo-Ihl, MR, Ciobanu CL, Cook NJ, Ehrig K, Slattery A, Courtney-Davies L, Dmitrijeva M (2021) Nanomineralogy of hydrothermal magnetite from Acropolis, South Australia: Genetic implications for iron-oxide copper gold mineralization: *Am Mineral* 106:1273-1293
- Verdugo-Ihl MR, Ciobanu CL, Courtney-Davies L, Cook NJ, Slattery A, Ehrig K, Tornos F, Hanchar JM (2022) U-Pb geochronology and mineralogy of hematite from Mantoverde and Carmen de Cobre, Northern Chile: Constraints on Andean IOCG mineralization. *Econ Geol* 117:943-960

Apatite and REE in iron oxide-apatite (IOA) deposits

Daniel E. Harlov¹

¹*Deutsche GeoForschungsZentrum GFZ, Telegrafenberg, Potsdam 14473, Germany*

Iron oxide-apatite (IOA) deposits world-wide are commonly exploited for their iron ore. However, their potential as REE ore deposits has neither been explored nor exploited. Over the last 20 or more years a number of studies have been made specifically focussing on the presence of REE in IOA deposits (Harlov et al. 2002, 2016; Taghipour et al. 2015; Jonsson et al. 2016; Normandeau et al. 2018; Maraszewska et al. 2023; Yin et al. 2023).

The primary host for REE in IOA deposits is fluorapatite, which, when metasomatically altered, results in the formation of monazite, xenotime, allanite, REE-carbonates, and REE-fluorides as secondary REE-bearing minerals (cf. Harlov 2015). Metasomatic alteration of the fluorapatite occurs by a coupled dissolution-reprecipitation process (Putnis 2002, 2009) such that the REE are liberated to form the above minerals either as inclusions in or rim grains associated with the fluorapatite.

In a number of IOA deposits, dating of monazite inclusions in fluorapatite or monazite associated with fluorapatite, using EPMA, LA-ICP-MS, and/or SHRIMP, have demonstrated that the monazite formed right after or even during the genesis and mineralization of the IOA ore body. Examples include Pea Ridge, SE Missouri, USA (Harlov et al. 2016; Neymark et al. 2016), Chogart, Bafq region, central Iran (Torab and Lehmann 2007; Stosch et al. 2011), or Heiyingshan, Beishan Metallogenic Belt, NW China (Yin et al. 2023).

Additional remobilization of REE due to further fluid infiltration, coupled with tectonic reworking, results in the remobilization of these REE-bearing minerals such that they become intergrown with magnetite, hematite, and silicate minerals in the IOA ore deposit or are redeposited in surrounding country rock that is in direct contact with the IOA ore deposit.

The REE content in IOA deposits world-wide is extremely variable ranging from IOA deposits that are quite enriched in REE, such as Pea Ridge, SE Missouri, USA (Harlov et al. 2016), to the IOA ore bodies of the middle to lower Yangtze River metallogenic belt (MLYRMB), east central China, which are relatively depleted in REE (Hu et al. 2020).

This broad variability in the REE content among different IOA ore bodies appears to be linked to the mechanism(s) involved behind their formation and the sources of Fe, P, Ca, REE, F, etc exploited during this formation. IOA deposits are associated with sub-volcanic intrusions and volcanic terranes in general. These volcanic terranes in turn are generally associated with subduction zone environments in the case of IOA deposits dating from the late Proterozoic to the late Cenozoic. However, the genesis and evolution of IOA deposits

is still somewhat controversial fluctuating between an igneous vs. a metasomatic origin.

Recently Hu et al. (2020), building on the work of Knipping et al. (2015a,b) and others, has proposed a dual magmatic-metasomatic origin, which takes into account the close physical and temporal relationship in the MLYRMB between IOA deposits, associated subvolcanic diorite porphyry intrusions, and local iron skarns in what was originally a subduction zone environment during the collision between the Yangtze craton and the North China craton at around 130-132 Ma.

In such a scenario, genesis of the diorite porphyry intrusions began as a complex melting event in the enriched mantle wedge above the subducting oceanic plate associated with the collision. These melts then rose and ponded at the crust-mantle boundary from which a diorite porphyry diapir differentiated and ascended due to its buoyancy. The mechanisms associated with this genesis would suggest that the diorite porphyry diapir would have had an NaCl-H₂O component derived ultimately from fluids/melts originating from the subducting oceanic plate.

While presumed to be a one phase melt at the crust-mantle boundary, as this diapir rises upwards into the crust, and lower pressures, it is assumed that there would be a separation of the melt into a diorite porphyry magma and a NaCl-rich fluid or perhaps NaCl-melt of sorts with an H₂O component. This NaCl-rich fluid is then presumed to act as a scavenger for Fe, P, Ca, and F from the diorite porphyry melt, along with various trace elements such as the REE, since all of these elements can complex as chlorides. The affinity of REE as both chloride and fluoride complexes at high temperatures and pressures (800 °C, 1000 MPa) is well known from the NaCl-, KCl-, and NaF-bearing solubility experiments of Tropper et al. (2011, 2013) and Mair et al. (2017).

Due to their lower density, these NaCl-rich fluids would rise to the top of the diapir. Upon being emplaced into the upper crust a kilometer or two below the surface as part of a volcanic system, the high temperature (900–1000 °C) NaCl-rich fluid at the top of the magma chamber would then be injected into the fractured country rock by the interaction between the diapir and deep-seated meteoric waters. This injected NaCl-rich fluid, along with the various elements inherent to it as chlorides, is the progenitor of the IOA deposit with the Fe, P, Ca, F, etc. crystallizing out as magnetite and fluorapatite plus minor amounts of silicate minerals such as pyroxenes and amphiboles. The NaCl would have been removed from the IOA deposit via deep seated circulating meteoric waters causing the

surrounding country rocks to be albitized in the form of a contact aureole. Further migration and dilution of these cooling NaCl-rich fluids further up along the fractured rock column and their chemical interaction with the surrounding rocks would then have resulted in the formation of associated iron skarns.

Evidence for NaCl-rich fluids/salt melts associated with IOA deposits has been documented in NaCl melt inclusions from both fluorapatite and pyroxene in a variety of IOA deposits including El Laco in Chile (Broman et al. 1999) and IOA deposits of the MLYRMB, central eastern China (Li et al. 2015). In addition, many IOA deposits such as those in the MLYRMB (Hu et al. 2020), Great Bear magmatic zone, Slave Craton, north-western Canada (Normandeau et al. 2018), and Bafq, central Iran (Taghipour et al. 2015) are characterized by albitization of the country rock surrounding the IOA deposit.

If this scenario regarding IOA deposit formation is correct, then the REE content of an IOA deposit is dependent first on the magma source of the original one phase melt, originating in the mantle wedge and ponding at the crust mantle boundary, and secondly on the ability of Cl to scavenge REE from the melt as chloride complexes and subsequently incorporate them into the NaCl-rich fluid/melt during phase separation from the diorite porphyry melt. Assuming that the mechanism behind the phase separation of melts and scavenging of elements from the melt by an NaCl-dominated fluid are basically the same for all IOA deposits, the high variability in REE content seen between different IOA ore deposits, which appears to be independent of their age, would suggest that the source area of the IOA deposit is responsible for this variability in REE content. That is for REE-poor IOA deposits, the source of the melts responsible for the deposit was poor in REE whereas for REE-rich deposits, the source was rich in REE. It is also possible in such a scenario that during its migration upwards from the crust mantle-boundary the melt might have encountered REE-enriched regions or deposits such as carbonatites or been relatively more efficient at scavenging REE's from the lower crust as it passed through due to the particular nature of its whole rock and fluid chemistry.

In order to confirm this hypothesis, experiments at 900 – 1000 °C and 200 – 1000 MPa involving simple Fe-, P-, Ca-, and F-bearing granitoid melts with an NaCl-H₂O melt component that were seeded with one or two REE, such as Ce and Y, as proxies would need to be performed in order to see if, along with Fe, P, Ca, and F, the REE would be naturally partitioned into a separate NaCl-H₂O melt allowing for magnetite and fluorapatite to crystallize out separate from the granitoid melt in the capsule as the capsule is slowly cooled from 900 – 1000 °C to 500 – 600 °C over a period of days.

References

- Broman C, Nyström JO, Henriquez F, Elfman, M (1999) Fluid inclusions in magnetite-fluorapatite ore from a cooling magmatic system at El Laco, Chile; *Geol Fören Stockholm Förhand* 121:253–267
- Harlov DE, Andersson UB, Förster H-J, Nyström JO, Dulski P, Broman, C (2002) Apatite–monazite relations in the Kirunavaara magnetite–apatite ore, northern Sweden *Chem Geol* 191:47–72
- Harlov DE, Meighan CJ, Kerr ID, Samson IM (2016) Mineralogy, chemistry, and fluid-aided evolution of the Pea Ridge Fe oxide-(Y + REE) deposit, southeast Missouri, USA. *Econ Geol* 111:1963–1984
- Harlov DE (2015) Apatite: a fingerprint for metasomatic processes. *Elements* 11:171–176
- Hu H, Li J-W, Harlov DE, Lentz DE, McFarlane RM, Yang, Y-H (2020) A genetic link between iron oxide-apatite and iron skarn mineralization in the Jinniu volcanic basin, Daye district, eastern China: evidence from magnetite geochemistry and multi-mineral U-Pb geochronology. *Geol Soc Am Bull*, <https://doi.org/10.1130/B35180.1>
- Jonsson E, Harlov DE, Majka J, Högdahl K, Persson-Nilsson K (2016) Fluorapatite-monazite-allanite relations in the Grängesberg apatite-iron oxide ore district, Bergslagen, Sweden. *Am Mineral* 101:1769–1782
- Knipping JL, Bilenker LD, Simon AC, Reich M, Barra F, Deditius AP, Lundstrom C, Bindeman I, Munizaga R (2015a) Giant Kiruna-type deposits form by efficient flotation of magmatic magnetite suspensions. *Geology* 43: 591–594
- Knipping JL, Bilenker LD, Simon AC, Reich M, Barra F, Deditius AP, Wälle M, Heinrich CA, Holtz F, Munizaga R (2015b) Trace elements in magnetite from massive iron oxide-apatite deposits indicate a combined formation by igneous and magmatic-hydrothermal processes. *Geochim Cosmochim Acta* 171:15–38
- Li W, Audétat A, Zhang J (2015) The role of evaporates in the formation of magnetite-apatite deposits along the Middle and Lower Yangtze River, China: evidence from LA-ICP-MS analysis of fluid inclusions. *Ore Geol Rev* 67:264–278
- Mair P, Tropper P, Harlov DE, Manning CE (2017) The solubility of CePO₄ monazite and YPO₄ xenotime in KCl-H₂O fluids at 800 °C and 1.0 GPa: implications for REE transport in high-grade crustal fluids. *Am Mineral* 102: 2457–2466
- Maraszewska M, Majka J, Harlov DE, Manecki M, Schneider DA, Broska I, Myhre P-I (2023) Multi-stage metamorphic and metasomatic imprints on apatite-monazite-xenotime assemblages in a set of small iron oxide-apatite (IOA) ore bodies, Prins Karls Forland, Svalbard. *Ore Geol Rev* 155: 105344
- Neymark L A, Holm-Denoma CS, Pietruszka A, Aleinikoff JN, Fanning, C. M., Pillers, R. M., Moscati, R. J. (2016) High spatial resolution U-Pb geochronology and Pb isotope geochemistry of magnetite-apatite ore from the Pea Ridge iron oxide-apatite deposit, St. Francois Mountains, southeast Missouri, USA. *Econ Geol* 111:1915–1933
- Normandeau PX, Harlov DE, Corriveau L, Paquette J, McMartin I (2018) Characterization of fluorapatite within iron oxide alkali-calcic alteration systems of the Great Bear magmatic zone: a potential metasomatic process record. *Can Mineral* 56:167–187
- Putnis A (2002) Mineral replacement reactions: from macroscopic observations to microscopic mechanisms. *Mineral Mag* 66:689–708
- Putnis A, (2009) Mineral replacement reactions: thermodynamics and kinetics of water-rock interaction; *Rev Mineral Geochem* 70:87–124
- Stosch H-G, Romer RL, Daliran F, Rhede D (2011) Uranium–lead ages of apatite from iron oxide ores of the Bafq District, East-Central Iran. *Mineral Dep* 46:9–21

- Taghipour S, Kananian A, Harlov D, Oberhänsli R (2015) Kiruna-type iron oxide-apatite deposits, Bafq district, central Iran: fluid-aided genesis of fluorapatite-monazite-xenotime assemblages. *Can Mineral* 53:479-496
- Torab F, Lehmann B (2007) Magnetite-apatite deposits of the Bafq district, central Iran: apatite geochemistry and monazite geochronology. *Mineral Mag* 71:347-363
- Tropper P, Manning CE, Harlov DE (2011) Solubility of CePO_4 monazite and YPO_4 xenotime in H_2O and $\text{H}_2\text{O}-\text{NaCl}$ at 800 °C and 1 GPa: implications for REE and Y transport during high-grade metamorphism. *Chem Geol* 282:58-66
- Tropper P, Manning CE, Harlov DE (2013) Experimental determination of CePO_4 and YPO_4 solubilities in $\text{H}_2\text{O}-\text{NaF}$ at 800 °C and 1 GPa: implications for rare earth element transport in high-grade metamorphic fluids. *Geofluids* 13: 372-380.
- Yin Y, Li J-W, Harlov D, Pan Z-J, Hu H (2023) Timing of fluid-induced alteration of fluorapatite in iron oxide-apatite deposits: Insights from monazite U-Pb geochronology of the Heiyingshan IOA deposit, Beishan Metallogenic Belt, Northwest China; *Ore Geology Reviews* (submitted).

Fe-O isotope systematics and magnetite chemistry of the Malmberget iron-oxide apatite deposit, Sweden

Jens S Henriksson^{1,2}, Valentin R Troll¹, Ellen Kooijman³, Ilya Bindeman⁴

¹Exploration Department, Luossavaara Kiirunavaara Aktiebolag, Sweden

²Department of Earth Sciences, Uppsala University, Sweden

³Department of Geosciences, Swedish Museum of Natural History, Stockholm, Sweden

⁴Department of Earth Sciences, University of Oregon, Eugene, USA

Abstract. Fe-O isotopes from drill core samples and whole rock chemistry from massive magnetite in LKAB's geochemical database have been used to unravel the origin, affinity, and stratigraphic position of the ore bodies in the Malmberget iron-oxide apatite deposit. Fe-O isotopes suggest a magmatic to magmatic-hydrothermal origin of the Malmberget deposit. Seven distinct magnetite populations have been identified using a novel Fe/V versus V/Ti magnetite discrimination diagram. Six of the magnetite populations form distinct spatio-geochemical clusters, whereas the massive magnetite data from the Fabian-Kapten ore body are scattered. Aggregated, this can be explained by a system where separate events form chemically distinct sill-type apatite-iron oxide intrusions within the volcano-sedimentary package, and repeated eruptions form a chemically scattered ore package on top.

1 Introduction

The Malmberget iron-oxide apatite (IOA) deposit, located in northern Sweden (67°14'N, 20°41'E), is the second largest underground iron mine in the world. Current annual production amounts to 19 Mt at 39.4 Fe wt.%, with total mineral resources, excluding reserves, estimated to 981 Mt at 53.8 Fe wt.%. The formation of giant-sized IOA deposits remains ambiguous and is surrounded by intense scientific debate (c.f. Geijer 1910; Parák 1975; Hildebrand 1986; Hitzman et al. 1992; Jonsson et al. 2013; Dare et al. 2015; Knipping et al. 2015; Bilenker et al. 2016; Tornos et al. 2016; Simon et al. 2018; Troll et al. 2019). Recent stable isotope thermometry studies on global IOA deposits predominately suggest a high-temperature (high-T) origin (>800 °C), where the chemically inert and refractory massive magnetite buffers the system with regards to post-depositional reequilibration of the Fe-O composition and low-T hydrothermal features are attributed to a progressively cooling magmatic system (e.g. Jonsson et al. 2013; Bilenker et al. 2016; Troll et al. 2019). Aside from two poorly constrained oxygen isotope values (Lund 2014), no Fe-O isotope data have previously been reported for the Malmberget deposit.

The trace element composition of magnetite chemistry has previously been used to classify magnetite from different ore-forming environments (e.g. Dupuis and Beaudoin 2011; Dare et al. 2014; Nadoll et al. 2014), but also to identify deposit-scale chemical differences (Ovalle et al. 2018). Wen et al. 2017 questioned the applicability of these discriminatory diagrams for genetic interpretation, especially for reequilibrated magnetite.

In this contribution, we use Fe-O isotopes and whole rock geochemical data from massive magnetite to: (1) Investigate the Fe-O isotopes of the Malmberget magnetite to constrain the ore-source and compare the Fe-O isotope signatures to those of global IOA ore deposits; and (2) characterise magnetite chemistry to identify affinities and discrepancies between the geometrically complex ore bodies in the Malmberget deposit.

1.1 Geological background

The Malmberget area occupies the southernmost part of the Paleoproterozoic northern Norrbotten ore province and comprises over twenty historically defined ore bodies that are hosted in a package of mafic to felsic metavolcanics (Figure 1). Age constraints from U-Pb dating of oscillatory zoned zircons from the metavolcanic host rocks yield magmatic ages between 1.89 and 1.87 Ga and metamorphic ages between 1.80 and 1.77 Ga, where the later age coincides with the emplacement of the minimum melt Lina-type granite-pegmatite suite (Sarlus et al. 2018; Sarlus et al. 2020). Further U-Pb dating of zircons from the Kiirunavaara ore constrains IOA deposit formation in the region between 1.88 and 1.87 Ga (Westhues et al. 2016).

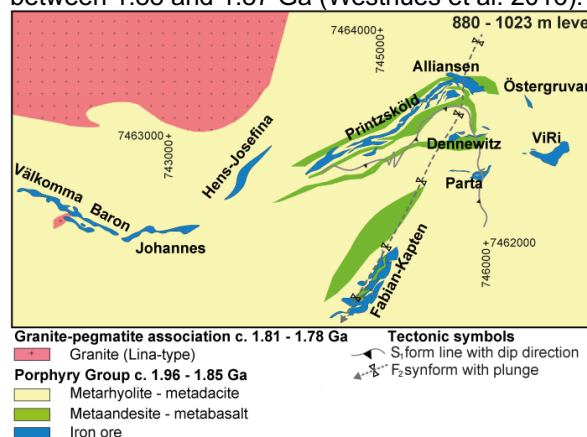


Figure 1. Simplified geological map of the Malmberget IOA deposit at the 880-1023 m level below surface.

The geology of the Malmberget area is characterised by multiple events of alteration, deformation and metamorphism that have overprinted primary textures and features of both host rock and ore, as well as transpositioned the originally continuous, bedding parallel ore-bearing volcano-sedimentary package (Geijer 1930;

Martinsson et al. 2016; Bauer et al. 2018). Consequently, the affinity and stratigraphic position of the individual ore bodies is complex and remains unclear. Lund (2013) suggested that the Malmberget ore is hosted in three different stratigraphic positions, where Fabian-Kapten (FA-KA) and Vitåfors-Ridderstolpe (ViRi) ore bodies sit at the lowest position, Printzsköld-Alliansen (PR-AL) at the middle position, and the Vålkomma (VA), Baron (BA), Johannes (JH) and Hens-Josefina (HN-JS), collectively referred to as the Western Field (WF), at the highest position. On the contrary, Bauer et al. (2018) interpreted at least two stratigraphic positions of the ore from structural data, suggesting that the stratigraphically lower ore position forms a ca. 5 km semi-continuous ore zone, from the WF through PR-AL to Östergruvan (ÖG), Dennewitz (DE), Parta (PA) and ViRi in the east. The stratigraphically upper ore position comprises the FA-KA ore body and is situated in the hinge of the Malmberget synform. Work on the Malmberget stratigraphy (Allen 2022) interprets at least five stratigraphic positions for the ore, from the lowest position to the highest position: WF, PR-AL, DE, PA, and FA-KA.

2 Methodology

For Fe-O isotope analysis, we collected massive magnetite samples along two drill cores transecting the FA-KA ($n=5$) and the ViRi ($n=1$) ore bodies at depths of -1550 m and -1220 m, respectively. The magnetite samples were crushed, magnetically separated, and inspected to ensure purity at Uppsala University.

Oxygen isotopes were analysed at the University of Oregon following the procedures of Bindeman et al. (2022), using a MAT 253 gas isotope ratio mass spectrometer with a fluorination line attached, in dual inlet mode, and using BrF_5 as a reagent. An in-house Gore Mountain garnet standard ($+6.52\text{‰}$) was used for calibration before and after sample analysis. Oxygen isotope values are reported relative to SMOW.

Iron isotope analysis was conducted at the Vegacenter at the Swedish Museum of Natural History in Stockholm. Digestion and purification of the crystals was achieved in HF , HNO_3 and 10 M HCl acid following the procedures of Borrok et al. (2007) and Millet et al. (2012). Before analysis, each sample was diluted with 0.3 M HNO_3 to a concentration of 2–3 ppm. The instrument used for Fe isotope analyses was a Nu Plasma II HR-MC-ICP-MS in pseudo-high-resolution mode. All values were corrected for mass bias and are reported relative to IRMM-014 from Isotopic Reference Materials and Measurements (Brand et al. 2014).

Literature magnetite Fe-O isotopes from global IOA ore deposits, combined with Fe-O isotopes from volcanic, igneous, low-T hydrothermal and hydrothermal replacement magnetite have been used to establish reference fields for the Fe-O data.

Whole rock assays from 63 480 drill core samples have been queried for massive magnetite from LKAB's geochemical database using the following parameters: $\text{Fe} > 65.00 \text{ wt.}\%$, magnetite/hematite > 10.00 , and $\text{P}_2\text{O}_5 < 0.25 \text{ wt.}\%$, with a total of 1964 samples fitting the established criteria. All samples have been analysed by ALS Laboratories or MSALABS for ferrous iron by titration and for whole rock chemistry using a lithium metaborate/tetraborate fusion with XRF finish.

Clusters were identified in geochemical plots of the massive magnetite were evaluated based on their spatio-geochemical relationships.

3 Fe-O isotopes

The Malmberget magnetite samples plot within the range of common igneous magnetite ($1\text{‰} < \delta^{18}\text{O} < 4\text{‰}$ and $0.05\text{‰} < \delta^{56}\text{Fe} < 0.9\text{‰}$), despite the observed equilibrated textures in (Geijer 1930), reflecting the original, magmatic origin of the Malmberget deposit (Figure 2). In addition, all the Malmberget samples plot within the field of the Kiruna deposit established in Troll et al. (2019) and emphasise the similarities of the two deposits.

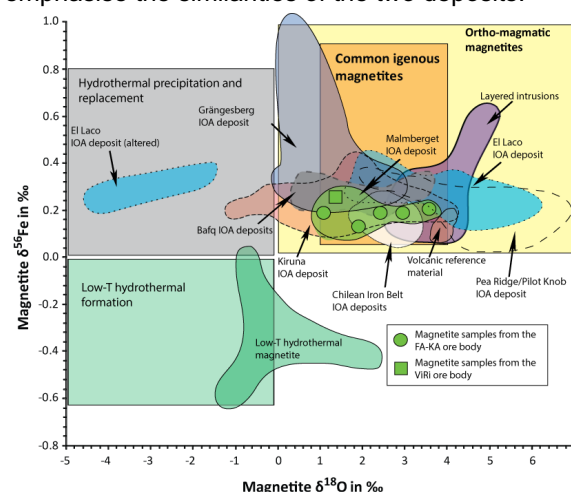


Figure 2. Discriminatory diagram for magnetite based on $\delta^{18}\text{O}$ -values and $\delta^{56}\text{Fe}$ -values. The coloured fields correspond to the distribution of values reported in Troll et al. (2019) and Xie et al. (2021).

Equilibrium calculations (Table 1) have been conducted to evaluate the potential magnetite source(s). Potential sources include basaltic to dacitic magmas (900°C) and magmatically derived high-T fluids (800°C). For $\delta^{18}\text{O}$ -values, three samples are in equilibrium with a basaltic source, five samples with an andesitic source, five samples with a dacitic source, and all six samples with a high-T fluid source. All samples have $\delta^{56}\text{Fe}$ -values in equilibrium with a magma source, whereas all samples except ViRi-01 are in equilibrium with a high-T fluid source. Thus, uniform equilibrium for the FA-KA magnetite is exclusively attained with a high-T fluid source, whereas the ViRi magnetite is in equilibrium with a dacitic to andesitic magma.

Table 1. Results for the magnetite-magma (900°C) and magnetite-magmatic fluid (800°C) equilibrium calculation.

Sample	$\delta^{18}\text{O}$	2σ	$\delta^{56}\text{Fe}$	2σ	$\delta^{18}\text{O}$ Basalt	$\delta^{18}\text{O}$ Andesite	$\delta^{18}\text{O}$ Dacite	$\delta^{18}\text{O}$ Fluid	$\delta^{56}\text{Fe}$ Magma	$\delta^{56}\text{Fe}$ Fluid	Formation Temp.
FA-001	2.0	± 0.2	0.16	0.07	5.4	6.0	6.3	7.2	0.13	-0.08	$\geq 800^\circ\text{C}$
FA-003	1.1	± 0.2	0.18	0.07	4.5	5.1	5.4	6.3	0.15	-0.06	$\geq 800^\circ\text{C}$
FA-004	3.7	± 0.2	0.19	0.07	7.1	7.7	8.0	8.9	0.16	-0.05	$\geq 800^\circ\text{C}$
FA-005	2.5	± 0.2	0.18	0.07	5.9	6.5	6.8	7.7	0.15	-0.06	$\geq 800^\circ\text{C}$
FA-006	3.2	± 0.2	0.18	0.08	6.6	7.2	7.5	8.4	0.15	-0.06	$\geq 800^\circ\text{C}$
ViRi-01	1.7	± 0.2	0.25	0.07	5.1	5.7	6.0	6.9	0.22	0.01	$> 800^\circ\text{C}$

Bold=in equilibrium. **Oxygen:** 1000ln α mt - (basalt) or (andesite) or (dacite) or (magmatic water 800°C) = (-3.4 ‰), (-4.0‰), (-4.3‰), (-5.2‰); range of basalts, arc andesites/dacites +5.7‰ to +8.0‰ (Taylor 1968; Bindeman et al. 2022); range of high-T magmatic fluids 5-10 ‰ (Zheng 1991; Hoefs 1997). **Iron:** 1000ln α mt - (magma) or (magmatic water 800°C) = (0.03 ‰), (0.24 ‰); range for arc andesites/dacites +0.00 to +0.12 ‰ (Heimann et al. 2008); range for high-T magmatic fluids 0.00 to -0.35 ‰ (Heimann et al. 2008; Severmann and Anbar 2009).

The observed magnetite-source dissimilarity between the ViRi and FA-KA ore bodies supports the interpretation of Bauer et al. (2018) and Allen (2022), where ViRi sits in a structurally lower position, more proximal to the magmatic centre of the ore-forming system.

4 Whole rock magnetite geochemistry

The massive magnetite, queried from LKAB's geochemical database, has been colour-coded by ore body and plotted on Ti+V vs Al+Mn, Fe vs V/Ti and Fe/V vs V/Ti magnetite discrimination diagrams (Figures 3a-f; Dupuis and Beaudoin 2011; Wen et al. 2017; this study).

In all three geochemical plots (Figure 3a,c,e), the FA-KA ore is comparatively scattered to the massive magnetite from the other ore bodies. The scattering of the FA-KA data agrees with the chemically distinct sub-units described for FA-KA in Lund (2013).

The massive magnetite from PR-AL has V/Ti ratios >1 , which is indicative of hydrothermal magnetite (Dupuis and Beaudoin 2011). The hydrothermal character of PR-AL is possibly related to the D₁ shear-zone described in Bauer et al. (2018), where the shear-zone acted as a conduit for the hydrothermal fluids that may have remobilised the mobile elements (i.e. vanadium).

In the Ti+V vs Al+Mn plots (Figures 3a,b) four spatio-geochemical clusters have been identified: FA-KA, PR-AL, WF, and DE-PA-PR-ViRi-ÖG. Spatio-geochemical clusters cannot be identified in the Fe vs V/Ti plot (Figures 3c,d), however, the plots clearly display the reequilibration trend from magmatic magnetite to hydrothermal magnetite (Wen et al. 2017).

In Figures 3e,f we present a novel discriminatory diagram for magnetite. The diagram is a modification of the diagram in Wen et al (2017). Fe wt.% has been substituted for Fe/V to circumvent the increase in iron and vanadium contents coupled to iron and mobile trace element purification of magnetite by hydrothermal fluid induced reequilibration by magnetite-magnetite dissolution and reprecipitation (Wen et al. 2017). Five distinct spatio-geochemical clusters have been identified for the main ore bodies using the discriminatory diagram: FA-KA, PR-AL, WF, WF-HW, DE, and PA-ViRi-ÖG. Two additional clusters have been identified, one in the PR hanging wall (HW) and one in the WF hanging wall. The

identified clusters agree with the stratigraphic interpretation of Allen (2022), and highlight the affinity of the isolated PA, ViRi and ÖG ore bodies in the eastern part of the deposit.

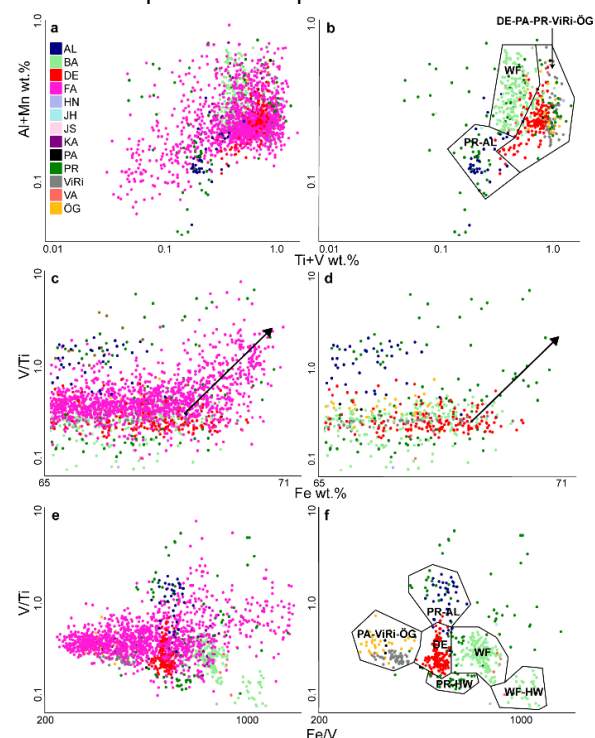


Figure 3. Magnetite chemistry plots (Dupuis and Beaudoin 2011; Wen et al. 2017). **a** Ti+V vs Al+Mn for all ore bodies and **b** for all ore bodies excluding FA-KA. **c** Fe vs V/Ti for all ore bodies and **d** for all ore bodies excluding FA-KA. The black arrow shows the trend of magnetite-magnetite reequilibration. **e** Fe/V vs V/Ti for all ore bodies and **f** for all ore bodies excluding FA-KA. The fields in **b** and **f** outlines the identified spatio-geochemical clusters.

5 Conclusion

Combined, our data suggest that the Malmberget IOA deposit is primarily of magmatic to magmatic-hydrothermal origin and that the main ore bodies of the structurally complex deposit originally belonged to at least five spatio-geochemically distinct ores. All ore bodies, except FA-KA, are characterised by tightly clustered geochemical data. This discrepancy is likely related to the stratigraphic position of the ore bodies. We propose an ore-forming scenario for the Malmberget IOA deposit where coupled intrusive-extrusive events emplace chemically distinct sill-type

ore intrusions at different stratigraphic positions in the volcano-sedimentary package and simultaneously deposit the FA-KA ore at surface.

Acknowledgements

We thank Vetenskapsrådet (grant number 2020-03789) for funding this project.

References

- Allen R (2022) Defining host-rocks stratigraphy and structure in order to explore for new ore lenses: Malmberget. LKAB Internal Report.
- Bauer T, Andersson JBH, Sarlus Z, Lund C, Kearney T (2018) Structural Controls on the Setting, Shape, and Hydrothermal Alteration of the Malmberget Iron Oxide-Apatite Deposit, Northern Sweden. *Economic Geology* 133:377–395.
- Bindeman IN, Ionov DA, Tollan PME, Golovin AV (2022) Oxygen isotope ($\delta^{18}\text{O}$, $\Delta^{17}\text{O}$) insights into continental mantle evolution since the Archean. *Nature Communications* 13:3779.
- Bilenker LD, Simon AC, Reich M, Lundstrom CC, Gajos N, Bindeman I, Barra F, Munizaga, R (2016) Fe–O stable isotope pairs elucidate a high-temperature origin of Chilean iron oxide-apatite deposits. *Geochimica et Cosmochimica Acta* 177:94–104.
- Brand WA, Coplen TB, Vogl J, Rosner M, Prohaska T (2014) Assessment of international reference materials for isotope-ratio analysis (IUPAC Technical Report). *Pure and Applied Chemistry* 86:425–467.
- Borrok DM, Wanty RB, Ridley WI, Wolf R, Lamothe PJ, Adams M (2007) Separation of copper, iron, and zinc from complex aqueous solutions for isotopic measurement. *Chemical Geology* 242:400–414.
- Dare SAS, Barnes S, Beaudoin G (2015) Did the massive magnetite “lava flows” of El Lago (Chile) form by magmatic or hydrothermal processes? New constraints from magnetite composition by LA-ICP-MS. *Mineralium Deposita* 50:607–617.
- Geijer P (1910) Igneous rocks and iron ores of Kiirunavaara, Luossavaara and Tuollavaara. Scientific and Practical Researches in Lapland arranged by the Luossavaara-Kiirunavaara Aktiebolag. *Geology of the Kiruna district 2*, Stockholm: 278 p.
- Geijer P (1930) Gällivare malmfält: geologisk beskrivning. *Sveriges Geologiska Undersökning C* 22: 115 p
- Hildebrand R.S (1986) Kiruna-type deposits; their origin and relationship to intermediate subvolcanic plutons in the Great Bear magmatic zone, Northwest Canada. *Economic Geology* 81:640–659.
- Hitzman MW, Oreskes N, Einaudi MT (1992) Geological characteristics and tectonic setting of Proterozoic iron oxide (Cu–U–Au–REE) deposits. *Precambrian Research* 58:241–287.
- Heimann A, Beard BL, Johnson CM (2008) The role of volatile exsolution and sub-solidus fluid/rock interactions in producing high $^{56}\text{Fe}/^{54}\text{Fe}$ ratios in siliceous igneous rocks. *Geochimica et Cosmochimica Acta* 72:4379–4396.
- Hoefs J (1997) *Stable isotope geochemistry*. Springer, Berlin, 286 p
- Jonsson E, Troll VR, Högdahl K, Harris C, Weis F, Nilsson KP, Skelton A (2013) Magmatic origin of giant ‘Kiruna-type’ apatite-iron-oxide ores in Central Sweden. *Scientific Reports* 3:1644–1644.
- Knipping JL, Bilenker LD, Simon AC, Reich M, Barra F, Deditius AP, Lundstrom C, Bindeman I, Munizaga R (2015) Giant Kiruna-type deposits form by efficient flotation of magmatic magnetite suspensions. *Geology* 43:591–594.
- Lund C (2013) Mineralogical, chemical and textural characterisation of the Malmberget iron ore deposit for a geometallurgical model. Ph.D. thesis, Luleå University of technology, 190 p
- Lund J (2014) A lithogeochemical study of Northern Sweden and the Kiruna and Malmberget iron-apatite ore deposits. M.Sc. thesis, Uppsala University, 99 p
- Martinsson O, Billström K, Broman C, Weihed P, Wanhainen C (2016) Metallogeny of the Northern Norrbotten Ore Province, northern Fennoscandian Shield with emphasis on IOCG and apatite-iron ore deposits. *Ore Geology Reviews* 78:447–492.
- Millet MA, Baker JA, Payne CE (2012) Ultra-precise stable Fe isotope measurements by high resolution multiple-collector inductively coupled plasma mass spectrometry with a Fe-57-Fe-58 double spike. *Chemical Geology* 304: 18–25.
- Ovalle JT, La Cruz NL, Reich M, Barra F, Simon A, Konecke BA, Rodriguez-Mustafa MA, Deditius AP, Childress TM, Morata D (2018) Formation of massive iron deposits linked to explosive volcanic eruptions. *Scientific Reports* 8.
- Parák T (1975) Kiruna iron ores are not “intrusive-magmatic ores of the Kiruna Type. *Economic Geology* 70:1242–1258.
- Simon AC, Knipping J, Reich M, Barra F, Deditius AP, Bilenker, L, Childress T (2018) Kiruna-Type Iron Oxide-Apatite (IOA) and Iron Oxide Copper-Gold (IOCG) Deposits Form by a Combination of Igneous and Magmatic-Hydrothermal Processes: Evidence from the Chilean Iron Belt. In: Arribas AM, Mauck JL (2018) *Metals, Minerals, and Society*. Society of Economic Geologist, Special Publication 21, p. 89–114.
- Sarlus Z, Andersson UB, Martinsson O, Bauer TE, Wanhainen C, Andersson JBH, Whitehouse MJ (2020) Timing and origin of the host rocks to the Malmberget iron oxide-apatite deposit, Sweden. *Precambrian Research* 342:105652.
- Sarlus Z, Martinsson O, Bauer TE, Wanhainen C, Andersson JBH, Nordin R (2018) Character and tectonic setting of plutonic rocks in the Gällivare area, northern Norrbotten, Sweden. *GFF* 141:1–20.
- Severmann S, Anbar AD (2009) Reconstructing paleoredox conditions through a multitracer approach: the key to the past is the present. *Elements* 5:359–364.
- Taylor HP (1968) The oxygen isotope geochemistry of igneous rocks. *Contributions to Mineralogy and Petrology* 19:1–71.
- Tornos F, Velasco F, Hanchar JM (2016) Iron-rich melts, magmatic magnetite, and superheated hydrothermal systems: The El Lago deposit, Chile. *Geology* 44:427–430.
- Troll VR, Weis FA, Jonsson E, Andersson UB, Majidi SA, Högdahl K, Harris C, Millet M, Chinnasamy SS, Kooijman E, Nilsson KP (2019) Global Fe–O isotope correlation reveals magmatic origin of Kiruna-type apatite-iron-oxide ores. *Nature Communications* 10:1712–1712.
- Wen G, Li JW, Hofstra AH, Koenig, AE, Lowers HA, Adams D (2017) Hydrothermal reequilibration of igneous magnetite in altered granitic plutons and its implications for magnetite classification schemes: Insights from the Handan-Xingtai iron district, North China craton. *Geochimica et Cosmochimica Acta* 213:255–270.
- Westhues A, Hanchar JM, Whitehouse MJ, Martinsson O (2016) New constraints on the timing of host-rock emplacement, hydrothermal alteration, and iron oxide-apatite mineralization in the Kiruna district, Norrbotten, Sweden. *Economic Geology* 111:1595–1618.
- Xie QH, Zhang ZC, Campos E, Deng J, Cheng Z, Fei X, Ke S (2021) Constraints of Fe–O isotopes on the origin of magnetite in the El Lago Kiruna-type iron deposit, Chile. *Ore Geology Reviews* 130:103967.
- Zheng Y (1991) Calculation of oxygen isotope fractionation in metal oxides. *Chemical Geology* 55:2299–2307.

Variations in Trace Element Chemistry of Pyrite from the Starra IOCG deposit, Queensland, Australia as proxy for Cu-Au mineralization

Max Hohl¹, Jeffrey A. Steadman¹, Jonathan Cloutier¹, Shaun L.L. Barker², David R. Cooke¹

¹CODES (Centre for Ore Deposit and Earth Sciences), University of Tasmania, Hobart TAS 7001, Australia

²Mineral Deposit Research Unit, Department of Earth and Ocean Sciences, University of British Columbia, Vancouver, Canada BC V6T1Z4

Abstract. Iron oxide copper-gold (IOCG) systems are globally significant ore deposits that host essential and critical minerals. Copper-Au mineralization at the Starra IOCG deposit is hosted in magnetite-hematite-rich ironstone lodes, which are emplaced along the Starra shear. Pyrite is a key mineral to assess fluid conditions due to its presence in all rock types and hydrothermal assemblages at Starra. Imaging analysis via LA-ICPMS of pyrite reveals diverse internal chemical zonation with Co, As, Ni and Se as the main non-stoichiometric elements. Cobalt concentrations reach a maximum of 6 wt.%. Gold is predominantly deported together with Te and Bi as micro-inclusions in pyrite. The presence of a high temperature, high salinity magmatic-hydrothermal fluid, likely of a mafic source is inferred from Co/Ni ratios ~100, which locally exceed 1,000. Changes in Ni/Se ratio within a single pyrite grain indicate fluctuating redox and/or temperature conditions. Starra's setting along a major shear zone allowing for efficient fluid movement together with an effective chemical trap such as the abundant magnetite-hematite ironstone lodes could have served as major driver in mineralization and especially in Au enrichment.

1 Introduction

Iron oxide copper-gold (IOCG) deposits are a loosely defined group of hydrothermal ore deposits. Since its inception in the early 1990s (e.g., Hitzman et al. 1992), multiple studies have attempted to constrain their paragenetic and geological context (e.g., Williams et al. 2005; Groves et al. 2010). Various criteria like structural setting, relationship to intrusive units, predominant ore mineralogy, and alteration paragenesis have been employed to achieve an agreed definition of a typical IOCG deposit, but it has remained elusive. Common mineral assemblages and spatial association in the Andes between IOCG and iron oxide-apatite (IOA) deposits have provoked ongoing debate about a genetic relationship between both deposit types (e.g., Sillitoe 2003; Knipping et al. 2015; Reich et al. 2016; Tornos et al. 2021). Proposed fluid sources range from purely magmatic (e.g., Rotherham, 1997) to oxidized evaporitic brines (e.g., Barton, 1996) as well as mixtures of both fluid types (e.g., Haynes et al. 1995).

Pyrite chemistry as a proxy for fluid evolution is an established tool in IOCG systems (Rusk et al. 2010; Steadman et al. 2021; del Real et al. 2020). Pyrite occurs in most IOCG systems, where it ranges from being an accessory phase at hematite-dominant IOCG deposits like Olympic Dam (Haynes

et al. 1995) to significantly higher abundance in more magnetite-rich members of the IOCG clan, such as Ernest Henry (Williams et al. 2005, Rusk et al. 2010).

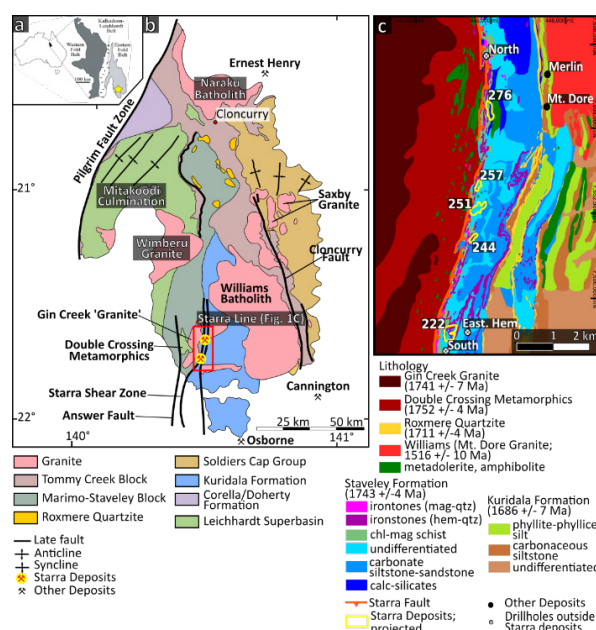


Figure 1. a Location of the Mt. Isa Inlier in Northwest Queensland. b Geological map of the Easter Fold Belt with the Starra deposits located in the southern part. c Main lithological units in the Starra area

The Starra IOCG system is in the southern part of the Cloncurry district, within the Eastern Succession of the Mt. Isa Inlier in northwest Queensland, Australia. Mineralization occurs at five physically separate deposits in association with unique magnetite-hematite ironstone lodes along the Starra shear (Fig. 1). An early model for Starra included a syngenetic origin for the ironstones and a sedimentary-exhalative process for Cu-Au mineralization (Davidson, 1989). Subsequent studies suggested a hydrothermal origin for both ironstones and mineralization (Rotherham, 1997) or an involvement of metamorphic derived fluids (Duncan et al. 2014). Among IOCG deposits Starra is considered a relatively Au-rich deposit relative to its Cu content, with a pre-mining resource of 37.4 Mt @ 1.2% Cu and 1.6 g/t Au (Groves et al. 2010).

The main iron oxide in the ironstones ranges between hematite and magnetite dominant. Chalcopyrite is the most abundant Cu-mineral at Starra, followed by bornite and chalcocite. Gold occurs as

Au-Bi tellurides, free gold, and electrum. Gangue minerals in the ironstones are mainly albite, quartz, calcite, and chlorite. Mushketovite, magnetite after hematite, occurs in the magnetite ironstones containing inclusions of scheelite (CaWO_3 , Fig. 2a).

Metasiltstones of the Staveley Formation in the Starra footwall are strongly hydrothermal altered with mineral assemblages consisting of actinolite, magnetite, biotite and pyrite formed during Ca-Fe-K alteration overprinting earlier albite (Fig. 2b).

In this study, we present trace elemental maps of two pyrite grains using quantitative wavelength dispersive X-ray spectrometry (WDS) and laser ablation-inductively coupled plasma mass spectrometry (LA-ICPMS). The pyrites are from Starra 222 mineralized ironstone and barren footwall. Principal component analysis (PCA) was used to extract covariation of elements across both pyrite grains. Results from the PCA were used for k-nearest neighbor (k-NN) classification to identify chemical comparable zones in both pyrites.

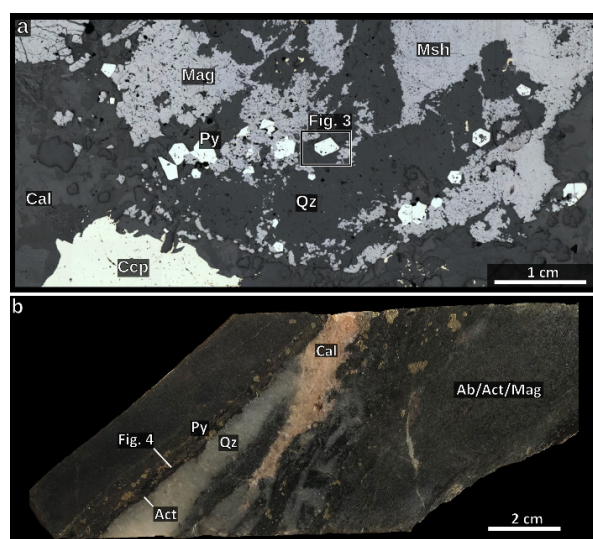


Figure 2. **a** Reflected light photomicrograph of mineralized magnetite-rich ironstone containing mushketovite and pyrite from Starra 222. **b** Strongly altered footwall sample crosscut by calcite – quartz vein

2 Methods

2.1 Laser ICPMS

All trace element images were acquired at CODES, University of Tasmania. The laser systems consisted of a RESOLUTION Laser ablation platform with Coherent COMPex Pro 193 laser and Lauren Technic S-155 ablation cell, which was connected to an Agilent 7700 ICPMS, equipped with an extraction lens. For measurement of chalcophile and siderophile elements in sulfides, both STDGL2b2 and STDGL3 were used as standard material. Reference material was analyzed by using a 51 μm round beam ablating at 10 Hz.

2.2 Microprobe

Mineralogy, textural and paragenetic relations were assessed by both reflected light and scanning electron microscopy. Back-scattered electron (BSE) imaging was performed using a Hitachi SU-70 field emission (FE) scanning electron microscope (SEM) housed at the Central Science laboratory (CSL), University of Tasmania (UTAS). Quantitative WDS element maps (S $K\alpha$, Fe $K\alpha$, Ni $K\alpha$, Co $K\alpha$, As $K\alpha$) were acquired using a JEOL JXA-8530F Plus field emission electron probe microanalyzer (EPMA) at CSL, UTAS. The electron beam was operated at an accelerating voltage of 15 kV, a beam current of 150 nA and a beam diameter of 0.5 μm . Dwell time for each step was 100 ms with a step size of 1 μm .

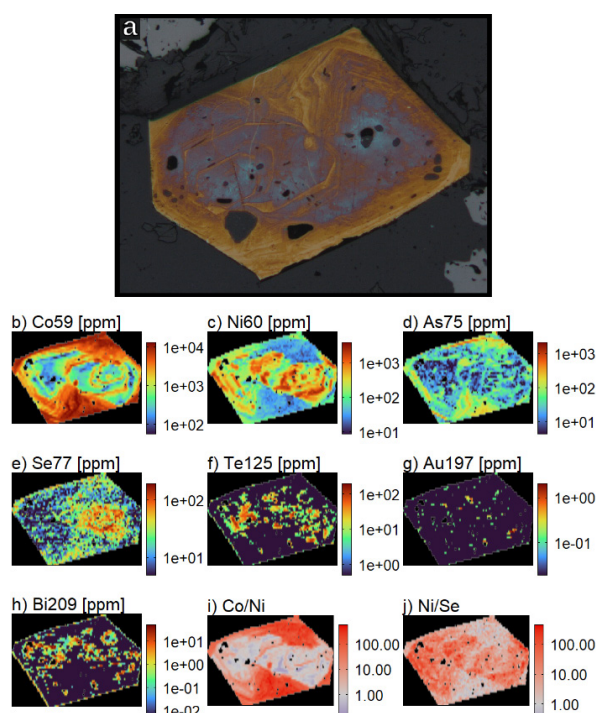


Figure 3. **a** Reflected light photomicrograph of etched pyrite from the magnetite ironstone. **b-J** Laser ICPMS trace element images of the pyrite shown in **a**

3 Results

3.1 Trace elements composition of pyrite

Concentrations of Co, Ni, As and Se can vary over multiple order of magnitudes within a single pyrite grain (Fig. 2). Cobalt, As and Ni concentration can locally exceed 1 wt. %. Arsenic concentration of > 100 ppm are commonly associated with high Co concentration, whereas high Se of > 100 ppm are correlated with elevated Ni concentrations. Gold occurs as micro inclusions together with Te and Bi, unrelated to As concentrations.

3.2 Multivariate Analysis

Combining both pyrite laser images resulted in 9443 sweeps of the spectrometer. The first principal component (PC) reflects the largest variance within the data set and is defined by correlated variations

in Co, As and \pm Se. The second PC is defined by covarying Ni and Se. To a lesser degree Au, Bi and Te variations are covered by the second PC suggesting a mild affinity of gold deportment associated with elevated Ni and Se concentration.

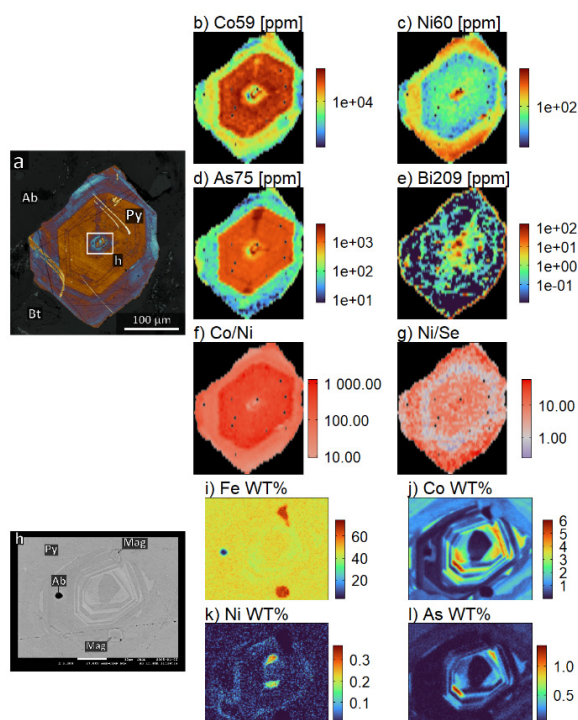


Figure 4. a Reflected light photomicrograph and b-g corresponding LA-ICPMS trace element images. h Backscattered electron (BSE) photograph and WDS images i-l of the pyrite core reveals chemical micron scale zonation, with Co concentration reaching locally up to 6 wt. %

Eigenvalues from the first five PCs, explaining ~88.2 % of the data, are used for a k-NN clustering algorithm, from which three clusters were extracted (Fig. 5). Cluster3 high Co and As concentration, cluster 2 reflects elevated Ni and Se concentration and cluster 3 low concentration of non-stoichiometric elements in pyrite such as Co, Ni, As, Te, Ti, Zn, Cu and Pb. Pyrite from the mineralized ironstone has a core that is represented by cluster 2 and a rim classified as cluster 3. The pyrite associated with early Ca-Fe-K alteration contains all three clusters, with cluster 1 defining the core and 3 defining the rim.

4 Discussion

4.1 Trace Element Systematics

High Co/Ni ratios in pyrite ($\text{Co/Ni} > 50$) are thought to be characteristic of high temperature magmatic-hydrothermal fluids likely sourced from a mafic magma (Reich et al. 2016). Both Co and Ni are enriched in mafic magmas compared to more evolved melts; however, Co distribution coefficient between the melt and the fluid is higher, which results in a higher Co/Ni concentration in the

hydrothermal fluid (Liu et al. 2011, 2012). In pyrite a Co/Ni ratio > 50 and a Co/As ratio > 1 can also be associated with hypersaline brines (Keith et al. 2022), which were likely present at Starra during mineralization (Williams et al. 2001). High Co/Ni ratios in pyrite are common in IOCG systems globally (e.g., Rusk et al. 2010; del Real et al. 2020; Steadman et al. 2021) as well as in IOA systems (Reich et al. 2016). This may indicate a potential mafic affinity of the fluids involved in different IOCG systems, as suggested for some of the Andean systems (Sillitoe 2003; Reich et al. 2016; Real et al. 2020).

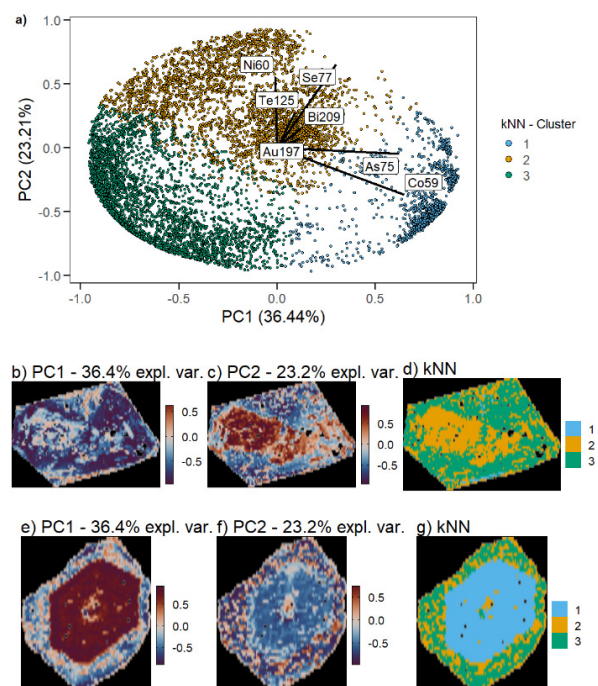


Figure 5. Principal component (PC) analysis of the combined pyrite trace element data. a The first two PC separate 3 distinct cluster determined by k-nearest neighbor analysis. b-g Eigen Values of PC1 and 2 for both pyrite grains and their corresponding cluster

4.2 Fluid mixing and mineralization

The first PC (based on $\text{Co} \pm \text{As}$) represents changes in fluid type and source (Reich et al. 2016), the second PC, based on positive correlation between Ni and Se, reflects changes in fluid temperature and/or redox state (Huston et al. 1995, del Real et al. 2020). The three clusters defined by kNN represent major changes in the pyrite chemistry, which are interpreted to be the result of fluids from different sources. Cluster 1 only occurs in pyrite associated with early, high-temperature Ca-Fe-K alteration stage (Fig. 5g), which likely reflects highly saline and a mafic affinity of the fluid present during this stage. Gold-Te-Bi inclusions are associated with cluster 2, relatively low Co/Ni and high Ni/Se ratio implying gold deportment under relative oxidizing conditions. The rim of the pyrite associated with mineralization formed likely under more reduced

condition compared to the core based on Ni/Se ratio (Fig. 3i-j). A pulse of reduced fluid following more oxidized conditions is also suggested by the occurrence of musketovite in the ironstone assemblage, which coincides with chalcopyrite formation. The difference between Cu and Au deportment suggests that at least two distinct fluids contributed to the mineralization at Starra. It is likely that the regional structures, such as the Starra Shear, functioned as fluid conduits for basinal brines, that led ultimately to Au enrichment of the Starra deposits, explaining their relative Au-rich nature compared IOCG deposits globally (Groves et al. 2010).

5 Conclusions

Trace element analysis of pyrite has revealed highly variable chemical clusters, reflecting a complex, multistage fluid evolution leading to Cu-Au mineralization. Changes in fluid conditions such as temperature and/or fO_2 are a major process controlling the mineralization at Starra. In the magnetite ironstones Cu mineralization coincides with the formation of musketovite. Pyrite rims formed during this stage have high Co/Ni (~100) and low Ni/Se (~1) ratios suggesting a reduced, highly saline fluid, with a mafic affinity. Gold inclusion in pyrite are associated with a more oxidized, lower salinity fluid. Starra's emplacement along ironstone horizons and regional structures, which likely represented major conduits for basinal derived fluids, are inferred to be crucial in making Starra an Au-rich member within the IOCG deposit spectrum.

Acknowledgements

The Geological Survey of Queensland is thanked for providing funding and Chinova Resources for assistance during field work. CODES Analytical Laboratories and Central Science Laboratories, both at UTAS, are thanked for laboratory assistance.

References

- Barton MD, Johnson DA (1996) Evaporitic-source model for igneous-related Fe oxide-(REE-Cu-Au-U) mineralization. *Geology* 24:259–262
- Bastrakov EN, Skirrow RG, Davidson GJ (2007) Fluid evolution and origins of iron oxide cu-au prospects in the Olympic Dam district, Gawler craton, South Australia. *Economic Geology* 102:1415–1440
- Davidson GJ (1989) Starra and trough tank: iron-formation-hosted gold-copper deposits of North-West Queensland, Australia. PhD thesis, University of Tasmania
- Duncan RJ, Hitzman MW, Nelson EP, Togtokhbayer O (2014) Structural and lithological controls on iron oxide copper-gold deposits of the southern Selwyn-Mount Dore corridor, Eastern fold belt, Queensland, Australia. *Economic Geology* 109:419–456
- del Real, I., Thompson, J.F.H., Simon, A.C., and Reich, M., 2020, Geochemical and isotopic signature of pyrite as a proxy for fluid source and evolution in the Candelaria-Punta del Cobre iron oxide copper-gold district, Chile: *Economic Geology*, v. 115, p. 1493–1517.
- Groves DI, Bierlein FP, Meinert LD, Hitzman MW (2010) Iron oxide copper-gold (IOCG) deposits through Earth history: Implications for origin, lithospheric setting, and distinction from other epigenetic iron oxide deposits. *Economic Geology* 105:641–654
- Haynes DW, Cross KC, Bills RT, Reed MH (1995) Olympic Dam ore genesis; a fluid-mixing model. *Economic Geology* 90:281–307
- Hitzman MW, Oreskes N, Einaudi MT (1992) Geological characteristics and tectonic setting of Proterozoic iron oxide (Cu-U-Au-REE) deposits. *Precambrian research* 58:241–287
- Hu, X., Chen, H., Beaudoin, G., and Zhang, Y., 2020, Textural and compositional evolution of iron oxides at Mina Justa (Peru): Implications for musketovite and formation of IOCG deposits: *American Mineralogist: Journal of Earth and Planetary Materials*, v. 105, p. 397–408.
- Huston D, Sie S, Suter G (1995) Selenium and its importance to the study of ore genesis: the theoretical basis and its application to volcanic-hosted massive sulfide deposits using PIXE analysis. *Nuclear Instruments and Methods in Physics Research Section B: Beam Interactions with Materials and Atoms* 104:476–480
- Keith, M., Haase, K. M., Chivas, A. R., and Klemm, R., 2022, Phase separation and fluid mixing revealed by trace element signatures in pyrite from porphyry systems: *Geochimica et Cosmochimica Acta*.
- Knippling JL, Bilenker LD, Simon AC, et al (2015) Trace elements in magnetite from massive iron oxide-apatite deposits indicate a combined formation by igneous and magmatic-hydrothermal processes. *Geochimica et Cosmochimica Acta* 171:15–38
- Liu W, Borg SJ, Testemale D, et al (2011) Speciation and thermodynamic properties for cobalt chloride complexes in hydrothermal fluids at 35–440 °C and 600 bar: An in-situ XAS study. *Geochimica et Cosmochimica Acta* 75:1227–1248
- Liu W, Migdisov A, Williams-Jones A (2012) The stability of aqueous nickel (II) chloride complexes in hydrothermal solutions: Results of UV-visible spectroscopic experiments. *Geochimica et Cosmochimica Acta* 94:276–290
- Reich M, Simon AC, Deditius A, et al (2016) Trace element signature of pyrite from the Los Colorados iron oxide-apatite (IOA) deposit, Chile: A missing link between Andean IOA and iron oxide copper-gold systems? *Economic Geology* 111:743–761
- Rotherham JF (1997) Origin and fluid chemistry of the Starra ironstones and high grade Au-Cu mineralisation, Cloncurry district, Mount Isa inlier, Australia. PhD thesis, James Cook University of North Queensland
- Rusk B, Oliver N, Cleverley J, et al (2010) Physical and chemical characteristics of the Ernest Henry iron oxide copper gold deposit, Australia; implications for IOCG genesis. PGC Publishing
- Sillitoe RH (2003) Iron oxide-copper-gold deposits: an Andean view. *Mineralium Deposita* 38:787–812
- Steadman JA, Large RR, Olin PH, et al (2021) Pyrite trace element behavior in magmatic-hydrothermal environments: An LA-ICPMS imaging study. *Ore Geology Reviews* 103878
- Tornos F, Hanchar JM, Munizaga R, et al (2021) The role of the subducting slab and melt crystallization in the formation of magnetite-(apatite) systems, Coastal Cordillera of Chile. *Mineralium Deposita* 56:253–278
- Williams, P. J., Dong, G., Ryan, C. G., Pollard, P. J., Rotherham, J. F., Mernagh, T. P., and Chapman, L. H., 2001, Geochemistry of hypersaline fluid inclusions from the Starra (Fe oxide)-Au-Cu deposit, Cloncurry district, Queensland: *Economic Geology*, v. 96, p. 875–883.
- Williams PJ, Barton MD, Johnson DA, et al (2005) Iron oxide copper-gold deposits: Geology, space-time distribution, and possible modes of origin. *Economic Geology* 371–405

Hydrothermal origin of bladed titanomagnetite during early alteration stages at the Starra IOCG deposits, Queensland, Australia

Max Hohl¹, Jeffrey A. Steadman¹, Jonathan Cloutier¹, Karsten Goemann²

¹CODES (Centre for Ore Deposit and Earth Sciences), University of Tasmania, Hobart TAS 7001, Australia

²Central Science Laboratory, University of Tasmania, Hobart, TAS 7001, Australia

Abstract. The Starra iron oxide copper-gold (IOCG) deposits are located in the Cloncurry district, Queensland, Australia. Mineralization at Starra is hosted by extensive hematite and magnetite lodes, locally referred to as ironstones. The origin of both ironstones and Cu-Au mineralization in the Cloncurry district remains debated. Improving our understanding of fluid conditions during early IOCG formation is critical for future exploration success in the district.

In this study we present a sample from the Starra footwall containing titanomagnetite hosted by a calcite vein. The calcite vein crosscuts unaltered metasedimentary host rocks and is associated with early alteration stages. The titanomagnetites texture resembles specular hematite and contains exsolution of ilmenite and rutile. Near its tip the titanomagnetite breaks down into a mixture of titanite, anhydrite, and calcite. Based on the titanomagnetites texture, associated mineralogy and

the stratigraphic position of the calcite vein a hydrothermal origin of the mineral assemblage is inferred. The bladed texture of the titanomagnetite implies rapid growth, which promotes the incorporation of trace elements into the magnetite lattice. The high Ti concentration of the magnetite implies the presence of a highly saline and/or high temperature fluid, which can mobilize significant Ti concentrations, during early alteration stages at Starra.

Acknowledgements

The Geological Survey of Queensland is thanked for providing funding and Chinova Resources for assistance during field work. CODES Analytical Laboratories at UTAS are thanked for laboratory assistance.

A geological update on the Viscaria Cu-Fe deposit, Kiruna district, Northern Sweden.

Marcello Imaña¹, Ross Armstrong^{1,2}, Daniel Sandoval^{1,2}, Maciej Jeż^{1,3}, Elvis Nkioh¹, Maximilian Krockert¹

¹Copperstone Resources AB

²Uppsala University, Sweden

³Polish Academy of Sciences, Poland

Abstract. The Viscaria Cu-Fe ore deposit is located adjacent to the Fe-oxide-apatite-REE Kiruna mining operation in the Proterozoic domain of Northern Sweden. Despite common geological features existing between Viscaria and the epigenetic Kirunavaara ores, an initially conceived syngenetic hypothesis for Viscaria ore formation has remained unquestioned. This contribution brings a re-evaluation through a holistic interpretation of both historical and new stratigraphic, geochemical, and geophysical data. Primary lithological and structural constraints are outlined as key controls for fluid flow and metal deportment, thus impacting the exploration outlook for undiscovered Cu deposits in the district.

The Viscaria deposit consists of stratabound, massive and semi-massive magnetite with varied proportions of Fe and Cu sulphides and carbonate. Mineralization extends laterally within a well-preserved low metamorphic volcano-sedimentary stratigraphy, showing preference to horizons of enhanced permeability within areas of contrasting redox compositions. High temperature coarse grained calc-silicate-sulphides assemblages occur in dissolution and upward escape channel breccias and vein networks to pervasive replacement of pre-existing Fe-enriched lithologies, indicating that the ore fluid was underpressured. A mineral and textural zonation indicates that stratigraphically upper parts of the stratigraphy receive higher proportion of volatile and finer grained components indicating that vertical temperature gradients appeared prior to major tectonic tilting.

1 Introduction

The Viscaria Cu deposit was subject to continuous open pit and underground mining between 1985 and 1995, yielding a production of 12.54 Mt of ore at 2.3% Cu. The updated total resources (mined and remaining) in the deposit contains over 1 Mt metal Cu, as well as a significant amount of magnetite and minor accompanying metals such as Co, Ag, Zn, REEs and Au. The Viscaria system is of particular interest not only for its proximal location to the stratigraphically-higher Kirunavaara Fe-apatite ore deposit (>2000 Mt @ 62% Fe) but also due to the spatial and temporal relationship that is commonly observed between Fe and Cu-Fe deposits in mining districts across the world: e.g., the Malmberget-Nautanen district (Sweden), Punta del Cobre district (Chile), Carajas district (Brazil), the Coastal Cu Belt (Peru), and the Eastern Gawler Craton (Australia). The subaqueous nature of the Viscaria greenstones and the close connection of parts of the Cu mineralization with carbonaceous shales has led to the traditional acceptance of VMS-type ore genesis for Viscaria. In addition to Viscaria, several other Cu deposits exist in the district (Fig.1), emplaced at similar but also different stratigraphic positions,

ranging from stratabound replacements to discordant hydrothermal breccias and shear-hosted orebodies: e.g., Rakkurijarvi, (Smith et al. 2007), Pahtohavare (Martinsson 1997), and Kiskamavaara (Martinsson 2011).

Despite the Proterozoic age of the host formation, deformation and metamorphism have only had a limited effect and a penetrative fabric is widely missing in the area, except for very localized shear zones. The volcano-sedimentary sequence is well-preserved and tilted 90 degrees, with a distinct geophysical signature that can be traced for several kilometers. Therefore, tectonic tilting and a subsequent lack of major intrusion emplacement in the area has left an unusually thick and continuous succession of altered stratigraphy exposed that represents a transition from 2.1 to 1.88 Ga volcanic activity. Despite the Viscaria ore being hosted in the westward, older parts of the sequence, its emplacement style and links to common structural and paragenetic features with the overlying Kiruna ores possibly point toward a similar age of emplacement.

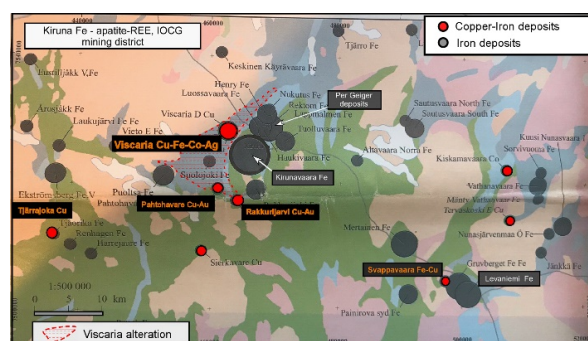


Figure 1. Map showing the location of the Kiruna deposit within the Kiruna mining district

2 District architecture, alteration footprint and metal deposition

2.1 District architecture

Good preservation and a lower intensity of regional metamorphism is characteristic of the Viscaria-Kiruna area (Andersson et al 2021). The area is mostly buried by moraine cover which has enabled the utilization of regional and district scale geophysical datasets to investigate the structural configuration. The Viscaria-Kiruna deposits coincide within a NW-SE trending gravity lineament that is interpreted to represent reactivated basement structures originated as part of a failed regional rift

during the Rhyacian period. Magnetic and airborne electromagnetic information have outlined local reactivated structures that link Viscaria and Per Geijer ores. Figure 2.

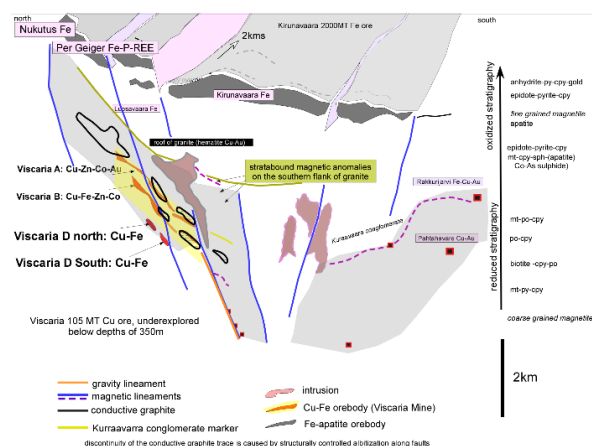


Figure 2. Schematic section originated from airborne and ground geophysical data tilted 90 degrees from Viscaria Kiruna area.

2.2 Alteration footprint

The near-surface extent of hydrothermal alteration in Viscaria exceeds an area of 20 km², affecting several kilometers of the stratigraphic sequence. A part of the alteration in the district is represented by Fe-enriched facies, followed by enrichments in Na, K and Mg represented by albite, biotite and tremolite-actinolite alterations respectively. The extent of these alterations is much larger than areas where sulphur reduction and Cu-sulphide precipitation has occurred.

Alteration is pervasively constrained within permeable lithologies, and the composition varies drastically from west to east, from deeper to shallower levels of the stratigraphy being affected with Mg, K and Na enrichment accordingly. Favorable structural lineaments transect the stratigraphy from west to east without producing major dislocations. Fluid flow carried out along these structures has affected the composition of adjacent rock sequences; this effect is more-clearly observed in areas where pervasive albitization has bleached and obliterated the strong conductivity signature of black shales, representing areas of a consequently reduced conductivity signature and truncation of magnetic anomalies. Proximal alteration linked to sulphide precipitation is represented by amphibole and epidote formation accompanied by lower temperature barren talc, silica and carbonate deposition.

2.3 Depositional pathways

These structures can be extrapolated into the northeastern parts of the district where they transect upper volcanic rhyodacitic sequences host of the Kiruna and Per Geijer ores (Figure 2). At this level,

limited overprinting sulphide mineralization has a more oxidized character than observed in Viscaria. Coherent sills of gabbroic composition occur within the Viscaria stratigraphy and are vein-mineralized in proximity to main ENE WSW structures.

3 Discussion and Conclusions

The Viscaria Kiruna stratigraphy depicts the incursion and pervasive interaction and mixing with variably saline brines resulting in a clear stratigraphic differentiation of the alteration composition. The oxide and sulphide paragenesis is represented by early magnetite replacement of hematite, magnetite pyrite, cobaltite-Ag, magnetite-pyrrhotite-chalcopyrite and late pyrite-chalcopyrite-anhydrite veins. The relative abundance of these paragenesis is dictated by the redox potential encountered at different levels of the stratigraphy. Higher in the stratigraphy, the Per Geijer ores are typical of the more oxidised, hydrous, lower temperature assemblages that occur above magnetite in IOCG deposits (Hitzmann et al., 1992). Thus, they give a vector that indicates that the upper parts of the system occur to the northeast and east (Redwood 2022).

Although there is an impressive Fe enrichment and magnetite formation towards the stratigraphy hosting the Kirunavaara Fe ores, these ores lack the exceptional Cu and sulphide enrichment observed in the lower Viscaria level. Oxidized sulphur (anhydrite) carbonates and apatite are all common component depicting devolatilization and accumulation of these component towards the upper parts of stratigraphy. The overall magmatic hydrothermal flux is suspected to have happened before the major compression that has originated the present days tilted geology of the volcanic and sedimentary Viscaria-Kirunavaara succession. Thus, continuous epigenetic fluid flux is highly influenced by the redox behaviour of early alteration assemblages and the organic carbon.

Acknowledgements

Copperstone Resources AB is acknowledged for allowing to present this contribution. District geology and drillcore discussions with Dr. Stewart Redwood and Dr. William X. Chavez during their visits to the Viscaria site are greatly appreciated.

References

- Andersson JBH, Bauer TE, Martinsson O (2021) Structural Evolution of the Central Kiruna Area, Northern Norrbotten, Sweden: Implications on the Geologic Setting Generating Iron Oxide-Apatite and Epigenetic Iron and Copper Sulfides. *Economic Geology* 116:1981–2009. <https://doi.org/10.5382/ECONGEO.4844>
- Martinsson O (1997) Tectonic Setting and Metallogeny of the Kiruna Greenstones. Luleå University of Technology
- Martinsson O (2011) Kiskamavaara a shear zone hosted IOCG-style of Cu-Co-Au deposit in Northern Norrbotten, Sweden. In: The 11th Biennial Meeting of The SGA, Antofagasta, Chile. pp 393–414

Redwood SD (2022) Review of the exploration, geology and deposit model of the Viscaria copper project, Norrbotten County, Sweden

Smith M, Coppard J, Herrington R, Stein H (2007) The Geology of the Rakkurijarvi Cu-(Au) Prospect, Norrbotten: A New Iron Oxide-Copper-Gold Deposit in Northern

Sweden. *Economic Geology* 102:393–414.
<https://doi.org/10.2113/gsecongeo.102.3.393>

The Formation of the Pilot Knob Iron Ore Cluster in Southeast Missouri, USA: Implication for the Exploration for Iron Oxide Apatite Deposits

Marek Locmelis¹, Bolorchimeg Nanzad Tunnell², Brandon Sullivan³, Cheryl Seeger⁴, Sarah Dare⁵, Marilena Moroni⁶, Ryan Mathur⁷

¹Department of Geosciences and Geological and Petroleum Engineering, Missouri University of Science and Technology, Rolla, Missouri, USA

²Department of Geology and Hydrogeology, Mongolian University of Science and Technology, Ulaanbaatar, Mongolia

³Doe Run Company, Viburnum, Missouri, USA

⁴Missouri Department of Natural Resources, Missouri Geological Survey, USA

⁵Département de Sciences Appliquées, Université du Québec à Chicoutimi, Canada

⁶Department of Earth Sciences, University of Milan, Italy

⁷Juniata College, Huntingdon, Pennsylvania, USA

Abstract. The St. Francois Mountains Terrane in southeast Missouri, USA, contains 7 major Iron Oxide Apatite (IOA) and Iron Oxide Copper Gold (IOCG) deposits as well as numerous smaller iron ore deposits. These deposits were mined for iron ore from the 1800s until 2001. Although there are currently no iron ore mining activities in Missouri, there is renewed interest in these deposits because of their 'critical mineral' potential, most notably cobalt and the rare earth elements. Here we present the findings of an ongoing study that examines the potential of the St. Francois Mountains Terrane to host undiscovered IOA and IOCG deposits. The focus is on the Pilot Knob Ore cluster that comprises the subsurface Pilot Knob Magnetite IOA deposit, and the outcropping Pilot Knob Hematite, Shepherd Mountain, and Cedar Hill deposits. New data is presented for hematite from the Cedar Hill deposit and integrated with data from the other deposits in the Pilot Knob Ore Cluster. We argue that all deposits are part of the same magmatic to hydrothermal plumbing system and that studies of other outcropping small-scale deposits in southeast Missouri may lead to the discovery of subsurface IOA ore bodies.

1 Introduction

The St. Francois Mountains Terrane in southeast Missouri, USA, contains 7 major Iron Oxide Apatite (IOA) and Iron Oxide Copper Gold (IOCG) deposits. Additionally, the region hosts more than twenty smaller deposits, including steeply dipping vein-type deposits and low-temperature hydrothermal hematite replacement ore deposits that occur within early-to-middle Mesoproterozoic plutonic, volcanic and volcanoclastic sedimentary rocks. These deposits were mined for iron ore from the 1800s until 2001. Although there are currently no iron ore mining activities in Missouri, there is renewed interest in these deposits because of their 'critical mineral' potential, most notably cobalt and the rare earth elements. Here we present the findings of an ongoing study that examines the potential of the St. Francois Mountains Terrane to host undiscovered IOA and IOCG deposits.

2 Geologic Overview

Iron ore deposits in southeast Missouri are hosted in 1.3 to 1.5 Ga granites and rhyolites of the St.

Francois Mountains Terrane (Fig. 1). The terrane is characterized by extensive caldera-forming volcanism and cogenetic subvolcanic and plutonic rocks, mostly rhyolitic in composition with minor intermediate to mafic rocks. Iron ore deposits in the region have been suggested to be genetically associated with early Mesoproterozoic ring intrusions (1.50–1.44 Ga) with a structurally controlled emplacement of iron ore along caldera-related ring structures (Tunnell et al. 2021 and references therein).

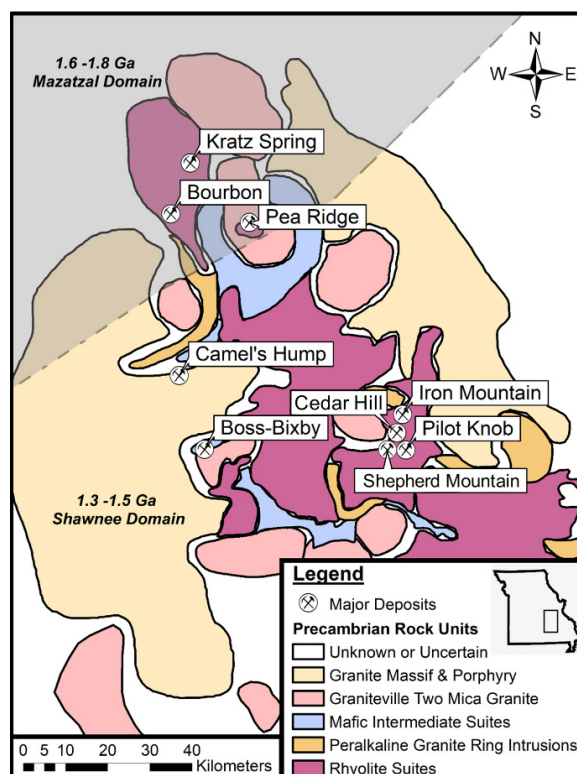


Figure 1. Geologic map that shows the location of the Pilot Knob Ore Cluster in the St. Francois Mountains Terrane modified from Day et al. (2016) and Sullivan et al. (2023). The inset shows the location of the map within the US State of Missouri.

2.1 The Pilot Knob Ore Cluster

The Pilot Knob Ore Cluster is located near the town of Pilot Knob in Iron County, Missouri. The cluster comprises four iron ore deposits that were previously mined, i.e., (i) the Pilot Knob Magnetite subsurface IOA deposit, and the outcropping (ii) Pilot Knob Hematite deposit that is located 240 m stratigraphically above the IOA ore body, (iii) the vein-type Shepherd Mountain magnetite-dominated deposit, and (iv) the vein-type Cedar Hill hematite-dominated deposit. The four deposits occur within less than 2 km of one another.

3 Methodology

New data is presented for the vein-type Cedar Hill deposit. Because the ore veins are fully mined out, sampling was restricted to tailing piles. Representative samples were prepared as polished thin sections and reflection mounts. The major and minor element chemistry of hematite was determined using a JEOL JXA-8200 electron microprobe in the Department of Earth Sciences, University of Milan, Italy. Major elements were determined with an accuracy of better than 3% and an external precision of better than 3 % (2-sigma). Minor elements were determined with an accuracy of better than 5% and an external precision of better than 4% (2-sigma). The trace element composition of iron oxide minerals was determined via laser ablation ICP-MS analysis at LabMaTer at the Université of Québec at Chicoutimi, Canada, using a Resonetics M-50 193 nm laser unit connected to an Agilent 7900 ICP-MS. Most trace elements were determined with a precision of better than 8% and an external precision of better than 6% (2-sigma). The iron isotope chemistry of hematite concentrates was conducted using a Neptune multi-collector ICP-MS at Pennsylvania State University, USA, following hematite dissolution in aqua regia and iron purification using BioRad MP-1 anion exchange resin. Errors were within the range of 0.1‰ (2-sigma) of the standards.

4 Results

Iron ore mineralization at Cedar Hill occurred in two approximately parallel veins that were emplaced into a pinkish to greyish tuff breccia that is interlayered with flow-banded rhyolites, imbricated breccias and conglomerates, massive rhyolite ash-flow tuffs, and banded rhyolite tuffs. The fully mined-out veins were 0.3-1.2 m in width and outcropped for a distance of about 30 m in a northwest-southeast direction (Crane, 1912). Petrographic studies of representative samples from tailing piles show that the mineralization is dominated by laminated fine-grained hematite (Fig. 2A-B) with locally rounded hematite grains with colloform textures (Fig. 2C). In some samples, coarse crosscutting specular hematite fills open spaces within the host volcanic breccia (Fig. 2D).

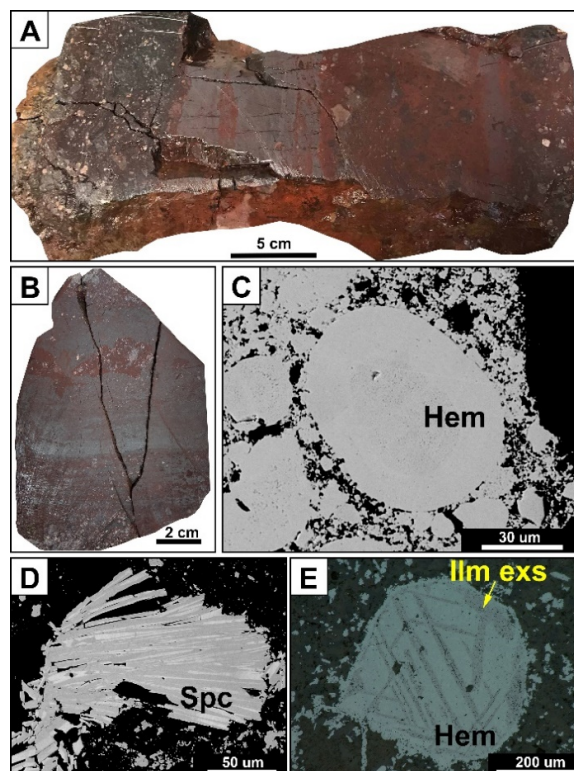


Figure 2. (A-B) Hand samples showing the laminated hematite ore within tuff breccia at Cedar Hill. (C-D) Back-scattered electron images showing rounded hematite (Hem) with colloform texture and specularite (Spc). (E) Hematite with ilmenite exsolutions in reflected light from the Cedar Hill deposit.

Locally, hematite grains contain ilmenite exsolutions (Fig. 2E), similar to hematite observed in brecciated ores from the Pilot Knob Hematite deposit. The major, minor and trace element chemistry of hematite from the Cedar Hill deposit is notably similar to the composition of hematite from other iron ore deposits in the Pilot Knob cluster, i.e., the Pilot Knob hematite deposit (Fig. 3A) and the Shepherd Mountain and Pilot Knob Magnetite IOA deposits (Fig. 3B). The $\delta^{56}\text{Fe}$ values of hematite from Cedar Hill range from -0.13‰ to -0.41‰. These values are similar to the $\delta^{56}\text{Fe}$ values observed for iron oxide minerals from Shepherd Mountain ($\delta^{56}\text{Fe}$ = -0.07‰ to -0.55‰), slightly lower than ratios of brecciated hematite reported for the Pilot Knob Hematite deposit ($\delta^{56}\text{Fe}$ = -0.19‰ to 0.01‰), and notably lower when compared to iron oxides from the bedded hematite and magnetite zones from the two Pilot Knob deposits ($\delta^{56}\text{Fe}$ = 0.06‰ to 0.30‰; Fig. 4).

5 On the formation of the Cedar Hill Deposit

The presence of hematite with ilmenite exsolutions is interpreted to reflect a magmatic origin wherein ilmenite exsolved from Ti-rich magmatic magnetite along its crystallographic planes prior to eruption. The magnetite was subsequently replaced by hematite during more oxidizing conditions, resulting in hematite with ilmenite lamellae, similar to the

observations made for the brecciated hematite with ilmenite lamellae from the Pilot Knob Hematite deposit (Tunnell et al. 2021). Later hydrothermal fluids infiltrating the brecciated tuff precipitated fine-grained hematite and specular hematite ('specularite') within the host breccia tuff. The narrow range of $\delta^{56}\text{Fe}$ values of hematite from Cedar Hill (-0.13‰ ~ -0.41‰) likely reflect precipitation from hydrothermal fluid(s) as opposed to a sedimentary origin that commonly results in more variable $\delta^{56}\text{Fe}$ signatures (Dauphas et al., 2007). A hydrothermal origin, rather than a sedimentary origin, is also in agreement with the vein-type emplacement style of the Cedar Hill ore veins. Similar to the observations made for the Shepherd Mountain deposit (Tunnell et al. 2022), the slightly lighter $\delta^{56}\text{Fe}$ values of Cedar Hill hematite when compared to brecciated hematite from the Pilot Knob Hematite deposit, likely reflect the higher stratigraphic emplacement level of the Cedar Hill deposit and associated Fe isotope fractional upon ascend/cooling, as well as mixing with meteoric waters.

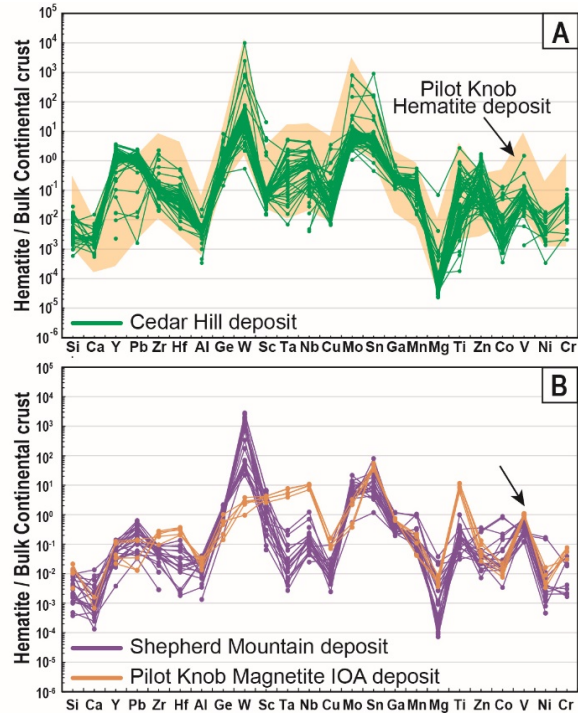


Figure 3. (A) Composition of hematite from the Cedar Hill and the Pilot Knob Hematite deposits. (B) Composition of hematite from the Shepherd Mountain and the Pilot Knob Magnetite IOA deposits. The order of elements is based on increasing compatibility into magnetite (Dare et al. 2014). All data are normalized against the composition of the bulk continental crust after Rudnick and Gao (2003).

6 New insights into the formation of the Pilot Knob Ore Cluster

Recent studies have shown that the Pilot Knob Magnetite IOA deposit and the outcropping Pilot

Knob Hematite and Shepherd Mountain deposits are genetically related (Tunnell et al. 2021, 2022). Magmatic-hydrothermal fluid(s) exsolved from a deep-seated magma chamber migrated upwards and formed the subsurface Pilot Knob Magnetite IOA deposit. Further upward migration of hydrothermal fluids along local fault systems resulted in the formation of the hematite-dominated replacement ore in the Pilot Knob Hematite deposit and the magnetite-dominated vein-type Shepherd Mountain deposit.

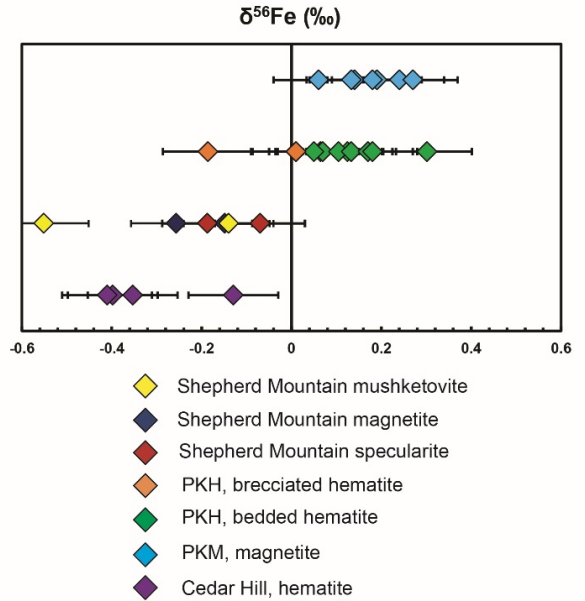


Figure 4. The $\delta^{56}\text{Fe}$ iron isotopic compositions of hematite from the Pilot Knob Ore cluster. Magnetite data are included for comparison. With data from Childress et al. 2016, Tunnell et al. 2021 (Pilot Knob), (Pilot Knob), and Tunnell et al. 2022 (Shepherd Mountain).

Several lines of evidence suggest that the Cedar Hill deposit is also genetically related to the other deposits in the Pilot Knob ore cluster. In addition to the spatial proximity and the vein-type emplacement style similar to the Shepherd Mountain deposit, the chemistry of hematite is notably similar to hematite from the other deposits in the ore cluster (Fig. 3). Moreover, there are distinct similarities in the $\delta^{56}\text{Fe}$ iron isotopic values for iron oxide minerals from the two vein-type deposits in the system, i.e., Cedar Hill and Shepherd Mountain (Fig. 4). It is noted that these values are notably lower when compared to the Pilot Knob Hematite deposit replacement ore, as well as the underlying IOA deposit, likely reflecting the higher stratigraphic emplacement level of the vein-type deposits as discussed above.

Because of the similarities, it is argued that all four iron ore deposits in the Pilot Knob area belong to the same magmatic-hydrothermal plumbing system. In this scenario, the fluids that were exsolved from the Pilot Knob Magnetite IOA ore body and migrated upwards along local faults not only formed the Pilot Knob hematite and Shepherd

Mountain deposits, but also the iron ore veins at Cedar Hill (Fig. 5).

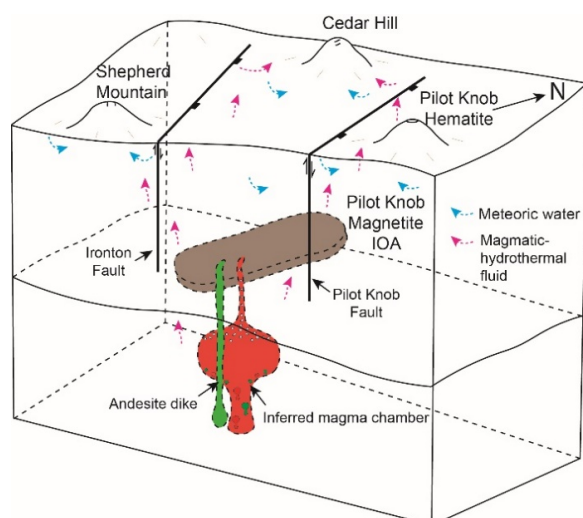


Figure 5. Proposed model for the formation of the Pilot Knob Ore Cluster integrating observations from this study and Tunnell et al. (2021, 2022). Not to scale.

7 Implications for the Exploration for IOA and IOCG Deposits

The model for the formation of the Pilot Knob ore cluster illustrated in Figure 5 suggests that the Pilot Knob Hematite, Shepherd Mountain, and Cedar Hill deposits are the outcropping hydrothermal expressions of the deeper magmatic-hydrothermal ore-forming processes that formed the sub-surface Pilot Knob Magnetite IOA deposit. It is noted that more than 20 other prospects exist in the St. Francois Mountains terrane that were discovered, but never scientifically studied. Prominent examples include Ketcherside Gap, Cuthbertson Mountain, and College Hill all of which occur along the edge of caldera ring structures (Day et al. 2016). We argue that understanding the magmatic-hydrothermal plumbing system that was feeding the near-surface-near prospects might lead to the discovery of subsurface IOA ore bodies. It is noted that this hypothesis appears to be supported by the presence of large subsurface magnetic susceptibility anomalies that were discovered during aeromagnetic surveys (e.g., McCafferty et al. 2016; 2019). Our future research will integrate geophysical models with field studies and petrological, mineralogical, and geochemical studies to guide conceptual exploration targeting for subsurface IOA ore bodies in Southeast Missouri.

Acknowledgements

M. L. acknowledges support through the National Science Foundation (NSF) CAREER award

#1944552 "Investigating the source, transport and deposition of economically important metals in the lower continental crust". Audrey Lavoie at LabMaTer of the UQAC is thanked for carrying out the LA-ICP-MS analysis. We further thank Mr. Andrea Risplendente, University of Milan, for assistance during the microprobe analyses. Lisa Lori from the Doe Run Company and Patrick Scheel from the Missouri Department of Natural Resources are thanked for help during fieldwork.

References

- Crane GW (1912) The iron ores of Missouri. Missouri Bureau of Geology and Mines. 10:434.
- Childress TM, Simon AC, Day WC, Lundstrom CC, Bindeman IN (2016) Iron and Oxygen Isotope Signatures of the Pea Ridge and Pilot Knob Magnetite-Apatite Deposits, Southeast Missouri, USA. *Econ Geol* 111:2033-2044. <https://doi.org/10.2113/econgeo.111.8.2033>.
- Dare SA, Barnes SJ, Beaudoin G, Méric J, Boutroy E, Potvin-Doucet C (2014) Trace elements in magnetite as petrogenetic indicators. *Miner Deposita* 49:785-796. <https://doi.org/10.1007/s00126-014-0529-0>.
- Dauphas N, Cates NL, Mojzsis SJ, Busigny V (2007) Identification of chemical sedimentary protoliths using iron isotopes in the >3750 Ma Nuvvuagittuq supracrustal belt, Canada. *Earth Planet Sci Lett* 254:358-376. <https://doi.org/10.1016/j.epsl.2006.11.042>.
- Day WC, Slack JF, Ayuso RA, Seeger CM (2016) Regional Geologic and Petrologic Framework for Iron Oxide ± Apatite ± Rare Earth Element and Iron Oxide Copper-Gold Deposits of the Mesoproterozoic St. Francois Mountains Terrane, Southeast Missouri, USA. *Econ Geol* 111:1825-1858. <https://doi.org/10.2113/econgeo.111.8.1825>.
- McCafferty AE, Phillips JD, Driscoll RL (2016) Magnetic and Gravity Gradiometry Framework for Mesoproterozoic Iron Oxide-Apatite and Iron Oxide-Copper-Gold Deposits, Southeast Missouri. *Econ Geol* 111:1859-1882. <https://doi.org/10.2113/econgeo.111.8.1859>.
- McCafferty AE, Phillips JD, Hofstra AH, Day WC (2019) Crustal architecture beneath the southern Midcontinent (USA) and controls on Mesoproterozoic iron-oxide mineralization from 3D geophysical models. *Ore Geol Rev* 111:102966. <https://doi.org/10.1016/j.oregeorev.2019.102966>.
- Rudnick RL, Gao S (2003) Composition of the continental crust. *Treatise on Geochemistry* 3:659-723.
- Sullivan B, Locmelis M, Tunnell BN, Seeger C, Moroni M, Dare S, Mathur R, Schott T (2023) Genesis of the 1.45 Ga Kratz Spring Iron Oxide Apatite Deposit Complex in Southeast Missouri, USA: Constraints from Oxide Mineral Chemistry. *Econ Geol* in press.
- Tunnell BN, Locmelis M, Seeger C, Mathur R, Dunkl I, Sullivan B, Lori L (2021) The Pilot Knob Iron Ore Deposits in Southeast Missouri: A High-To-Low Temperature Magmatic-Hydrothermal Continuum. *Ore Geol Rev* 131:103973. <https://doi.org/10.1016/j.oregeorev.2020.103973>.
- Tunnell BN, Locmelis M, Seeger C, Moroni M, Dare S, Mathur R, Sullivan B (2022) The Shepherd Mountain iron ore deposit in Southeast Missouri, USA – An extension of the Pilot Knob magmatic-hydrothermal ore system: Evidence from iron oxide chemistry. *Ore Geol Rev* 141:104633. <https://doi.org/10.1016/j.oregeorev.2021.104633>.

Assessing silicate-liquid immiscibility using trace element in titanomagnetite and ilmenite in the Raftsund intrusion, Lofoten-Vesteraalen AMCG suite, Northern Norway

Nolwenn Coint, Eduardo Mansur, Jakob K. Keiding

¹Geological Survey of Norway (NGU), Leiv Eirikssons vei 39, 7040 Trondheim, Norway

²Geological Survey of Denmark (GEUS), Øster Voldgade 10, 1350 Copenhagen, Denmark

Abstract. Magmatic processes responsible for the formation of Fe-Ti-P-rich rocks and nelsonites remain contentious. Fractional crystallization coupled with crystal sorting, magma mixing, and silicate-liquid immiscibility are the three processes considered. The two first processes are relatively well understood and testable, whereas the third one remains difficult to assess, especially in intrusive systems where melt compositions are rarely preserved. This study uses trace element in titanomagnetite and ilmenite to test these processes in the Raftsund intrusion, Northern Norway, where the role of silicate-liquid immiscibility has already been demonstrated. The Raftsund intrusion, composed mainly of monzonite and syenite, contains Fe-Ti-P-rich rocks and nelsonite occurrences. Ilmenite and titanomagnetite from the occurrences show enrichments in elements that behave compatibly and incompatibly in fractionating monzodioritic systems (e.g. Sc, V, Mn, Zn, Zr, Hf), compared to the same mineral in the host monzonite and syenite. The trace element behaviour in Fe-Ti oxides, combined with field observation and textural evidence of the presence of two separate melts, suggests that silicate-liquid immiscibility played an important role in the formation of the Fe-Ti-P-rich rocks in the Raftsund intrusion.

1 Geological setting

The Raftsund intrusion, a 75 by 35 km large monzonitic to syenitic batholith, was emplaced at 1800 Ma as part of the Lofoten-Vesteraalen Anorthosite-Mangerite-Charnockite-Granite (AMCG) suite.

While such suites are usually characterized by the presence of massif anorthosite, the Lofoten-Vesteraalen AMCG one is composed of large volumes of monzonite and syenite, whereas gabbro and anorthosite are subordinate.

The two main anorthosite intrusions, Eidsfjord and Flakstadøen, show evidence of polybaric crystallization from 9 to 4 kbar, whereas monzonites and syenites crystallized at 4 kbar (Markl and Frost, 1998). Temperature estimates using the QUILF equilibria reach 925 °C for the monzonite, oxygen fugacity was -0.6 below the FMQ buffer, while the silica activity was around 1.

The Raftsund intrusion is the most voluminous monzonitic intrusion of the AMCG suite and contains occurrences of Fe-Ti-P-rich rocks and nelsonite.

2 Raftsund intrusion

2.1 Type II monzonite

The Raftsund intrusion can be subdivided in three units based on textural observation. In this study we focus on the medium-grained equigranular type-II unit.

This unit can be further subdivided into an inverted pigeonite-augite syenite (Pgt-Aug syenite), cropping out in the north and a fayalite-augite monzonite (Fay-Aug monzonite) in the south. The contact between the two has not been observed in the field but seem to occur gradually in a zone where orthopyroxene and augite characterize the mineral assemblage instead of inverted pigeonite or fayalite. Evidence of mingling between type II and type III monzonite is preserved in the centre of the intrusion.

The Pgt-Aug syenite is composed of subhedral ternary feldspars, inverted pigeonite and augite (Mg#:51-57). Biotite and hornblende are late phases. Accessory minerals consist of titanomagnetite, ilmenite, apatite and zircon.

The Fay-Aug monzonite is characterized by subhedral ternary feldspar and Fe-rich mineral clusters composed of subhedral fayalite (Fo17-8.3), augite (Mg#:38-18), ilmenite and rare titanomagnetite. Apatite, locally abundant zircon, and allanite are accessory phases.

2.2 Associated Fe-Ti-P-rich rocks occurrences

Fe-Ti-P-rich rocks, associated with the Pgt-Aug syenite occur as scattered lenses which can reach up to 120 x 50 m. They consist of inverted pigeonite of subhedral Fe-rich olivine (Fo22-29), augite (Augite M#: 29-65), surrounded by interstitial titanomagnetite and ilmenite containing abundant apatite inclusions. Hornblende and biotite are minor interstitial phases. Resorbed ternary feldspar are abundant close to the contact between the host-syenite but are absent in the center of the largest Fe-Ti-P-rich rock lenses. Thin μm -scale plagioclase rims are locally preserved at the contact between resorbed ternary feldspar and the Fe-rich minerals. The contact between the Fe-Ti-P-rich rocks is sharp but curved attesting to the syn-magmatic nature of the mineralizations.

Fe-Ti-P-rich rocks from the Fay-Aug monzonite are limited to the mingling zone between the type II and type III monzonite. Centimeter-thick Fe-Ti-P-rich-rocks presenting a similar mineral assemblage as

the Fe-rich clusters in the host monzonite occur at the border of the type-III monzonite enclaves.

Nelsonite bodies are located towards the southwestern part of the intrusion and are hosted by the Fay-Aug monzonite. The sole location visited for this study, is a 15 by 20 m-lage massive nelsonite lenses. The contact between the nelsonite and the surrounding monzodiorite and monzonite can be sharp and lobate or gradational like in a mingling zone (Fig. 1). The nelsonite consists of titanomagnetite, ilmenite, subhedral apatite, mm-size resorbed zircon crystals and subordinate Fe-rich silicates (Fig. 1).

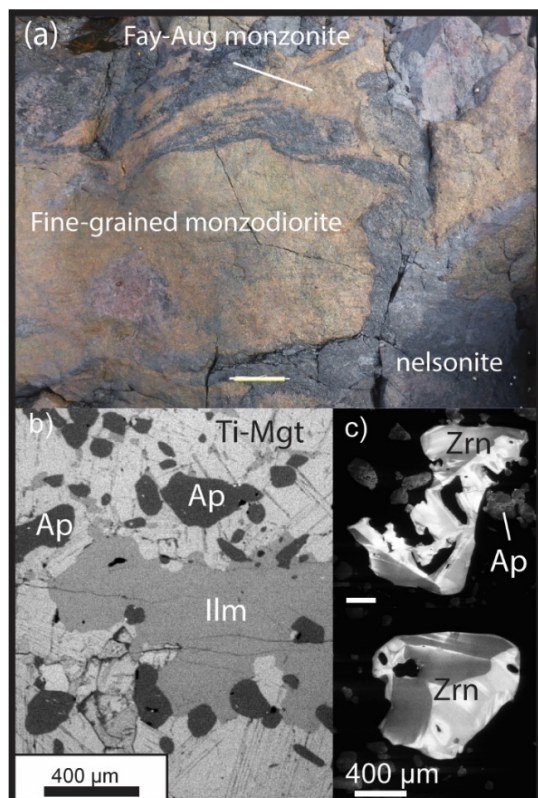


Figure 1. Nelsonite occurrence in the Fay-Aug monzonite. a. Contact between the nelsonite and the surrounding monzonite and monzodiorite. b. Mineral assemblage of the nelsonite. c. Resorbed zircon crystals.

3 Geochemistry

3.1 Whole-rock data

Whole-rock geochemistry indicate that Fe-Ti-P-rich rocks associated with the Pgt-Aug syenite have composition reaching up to 50 wt.% $\text{Fe}_2\text{O}_3^{\text{tot}}$, 9 wt.% TiO_2 and 6 wt.% P_2O_5 . They are enriched in compatible elements such as Sc, V, Co but also in incompatible elements such as REE and to a lesser extend HFSE, compared to the host syenite.

Centimetre-thick Fe-Ti-P-rich rocks in the Fay-Aug monzonite are difficult to analyse because of their reduced size, but based on their mineral assemblages (abundant apatite and zircon), they

clearly are enriched in REE and HFSE compared to the host monzonite.

The nelsonite, which contains only 3 wt% SiO_2 but in contrast >70 wt% $\text{Fe}_2\text{O}_3^{\text{tot}}$, 15 wt% TiO_2 and 2.8 wt% P_2O_5 is characterized by similar but more pronounced enrichments relative to the Fe-Ti-P-rich rocks.

These elements are predicted to concentrate in an Fe-rich melt formed by silicate liquid-immiscibility (e.g. Charlier and Grove, 2012; Veksler and Charlier, 2015) but can, however, often not be observed in whole-rock data because whole-rock compositions in cumulates are affected by extensive accumulation and thus rarely represent melt compositions. An alternative method to test silicate-liquid immiscibility is to analyze the minerals which composition is controlled by the chemistry of the conjugate immiscible melts.

3.2 Trace element record of Ilmenite and titanomagnetite

Titanomagnetite and ilmenite from the Fe-Ti-P-rich rocks associated with Pgt-Aug syenite are enriched in Mg, Al, Sc, Zn and Mn and V compared to the one in the host syenite (Fig. 2). In addition, ilmenite is enriched in Hf and Zr, elements more compatible in the latter mineral than in titanomagnetite.

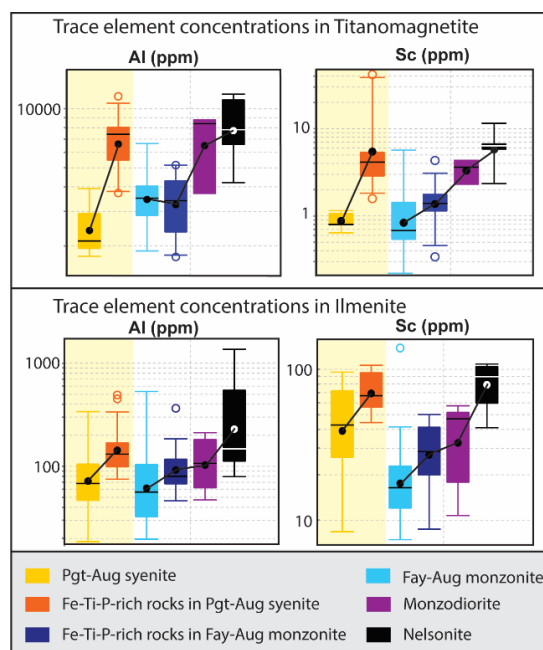


Figure 2. Variations of trace element concentration in titanomagnetite and ilmenite from the various investigated units.

Such enrichments in the Fe-Ti oxides from the Fe-Ti-P-rich rocks associated with the syenite and the nelsonite support that neither fractional crystallization nor magma mixing can explain the mineral record. Instead, they favour silicate-liquid immiscibility where they would result from the

crystallization of an Fe-rich melt enriched in numerous elements such as Mg. Furthermore, high concentrations of Sc and Al in both Fe-Ti oxide phases are consistent with crystallization from a melt enriched in Sc, despite the crystallization of augite, but where feldspar was not stable.

It is worth noticing however that Fe-Ti oxides from the Fe-Ti-P-rich rocks associated with the Fay-Aug monzonite do not record such enrichments. In this unit, Fe-rich mineral clusters, found scattered in the monzonite are thought to result from silicate-liquid immiscibility (Coint et al., 2020). The centimetre-thick veins are therefore best explained by the simple ponding of Fe-rich droplets at the contact with the type III monzonite.

The trace element record of Fe-Ti oxides from the nelsonite, showing enrichments in Al, Sc but also Mg and Mn, similar to the ones observed in Fe-Ti-P-rich rocks, indicate that silicate-liquid immiscibility is also involved in the formation of nelsonite in the Raftsund intrusion. The lack of lower temperature hydrous minerals precludes an important influence of hydrothermal fluids.

The transition between an Fe-rich melt presumably containing at least 30 wt.% SiO₂ and the formation of the nelsonite remains unclear. Segregation between the Fe-silicates and Fe-Ti-oxides, apatite and zircon upon fractional crystallization is a likely explanation, however it is not supported by experiments, often performs on systems of different compositions.

4 Conclusions

Fe-Ti-P-rich rocks associated with monzonites and syenites from the Raftsund are best explained as the product of silicate-liquid immiscibility, as summarized in figure 3. These results indicate that the process can influence thoroughly the evolution of dry and hot magmas of intermediate to felsic composition.

The process can be assessed by looking for evidence of textural disequilibrium between the minerals in the monzonite or syenite, and associated Fe-Ti-P-rich rocks and/or nelsonite.

The trace element record of minerals such as ilmenite and titanomagnetite can be used as an important tool to identify and unravel magmatic processes including ore formation. Specifically, in this case, Fe-Ti oxides trace element record attest to the important role of liquid-immiscibility in the genesis of nelsonite.

The transition between Fe-Ti-P-rich rocks and a nelsonite, however, remains poorly understood and require further experiments with appropriate composition and intrinsic variables.

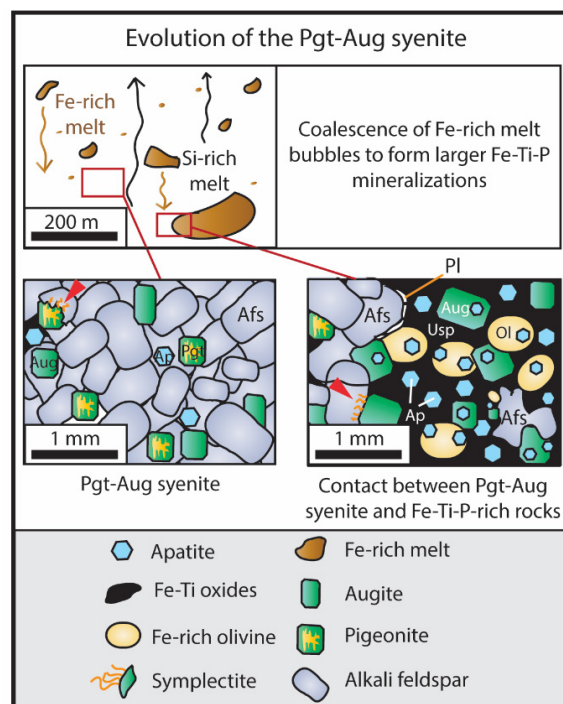


Figure 3. Petrogenesis of Fe-Ti-P-rich rocks associated with the Pgt-Aug syenite (from Coint et al., 2020)

Acknowledgements

The authors are grateful for the assistance of the lab at the Geological Survey of Norway, where most analyses were conducted and to Kristian Drivenes (NTNU, Trondheim, Norway) and Jessica Langlade (IFREMER, Brest, France) who helped with the microprobe analysis.

The Research Council of Norway is acknowledged for the support to the Norwegian Laboratory for Mineral and Materials Characterisation, MiMaC, project number 269842/F50.

References

- Charlier, B and Grove TL (2012). "Experiments on liquid immiscibility along tholeiitic liquid lines of descent." *Contributions to Mineralogy and Petrology* **164**: 27–44. doi:10.1007/s00410-012-0723-y
- Coint, N, Keiding JK and Ihlen PM (2020) Evidence for Silicate-Liquid Immiscibility in Monzonites and Petrogenesis of Associated Fe-Ti-P-rich rocks: Example from the Raftsund Intrusion, Lofoten, Northern Norway. *Journal of Petrology* **61**(4) <https://doi.org/10.1093/petrology/egaa045>
- Markl, G, Frost, RB, and Bucher K (1998). The origin of anorthosites and related rocks from the Lofoten Islands, Northern Norway: I. Field relations and estimation of intrinsic variables. *Journal of Petrology* **39**(8): 1425-1452.
- Veksler, IV and Charlier B (2015). Silicate Liquid Immiscibility in Layered Intrusions. *Layered intrusions*. Charlier B, Namur O, Latypov R and Tegner C, Springer Geology (eds.), Layered Intrusions: 229-258. https://doi.org/10.1007/978-94-017-9652-1_5

Genesis of iron ore deposit at Ga-Nchabeleng area.

Julia M. Maponya¹, Humbulani R. Mundalamo¹, Jason S. Ogola¹

¹Department of Earth Sciences, University of Venda, South Africa.

Abstract. The study area falls within the Sekhukhune District Municipality in Limpopo province. It is situated near the contact between the Bushveld Igneous Complex and the Transvaal Group sedimentary rocks. The aim of the study was to establish the mode of occurrence and origin of iron ore deposits at Ga-Nchabeleng area. The outcrops of the iron ore cover mainly the four hills with the host rocks forming mainly contacts between the iron ore. The geological mapping was conducted along traverses drawn across the general strike of the lithology. Iron ore and host rock samples were collected at an exposed area within and around four hills. Ore sampling was done following the trend of the ore deposits. Collected rock and iron samples were physically and geochemically characterised and X-ray fluorescence spectrometry method was used for selected samples for geochemical characterisation.

1 Introduction

Iron ore is a rock from which metallic iron can be extracted from. Iron is the most common element in the world and makes up close to 5% of the Earth's crust. Iron ore that contains a high quality of hematite or magnetite are known as "natural ore" and they can be entered directly into blast furnaces that produce iron. It has been argued that iron ore is the most important commodity in the global economy except for perhaps oil (www.softschools.com/facts/rocks/iron_ore_facts/2986/). Iron ore is an important commodity because it is the primary source of iron, the metal most used by man. The most common gangue minerals in iron ores are quartz, feldspar, calcite, dolomite, clays, and carbonaceous matters. Ore deposits are natural concentrations of different metals in a wide range of geological settings, such as sedimentary, metamorphic, hydrothermal, and magmatic formations. The exploration of new deposits, and knowledge about their formation is crucial to today's society.

The Rustenburg Layered Suite which represents the Bushveld Igneous Complex in this region, consists of several igneous rock types varying from dunite and pyroxenite to norite, gabbro, anorthosite (Johnson et al 2009). The Ga-Nchabeleng area is characterised with hills of iron ore separated with granitic rocks in between. Consequently, the study focused on the characterisation of the host rocks samples to understand the mode and origin of the iron ore within the study area. This paper focuses on the genesis of the iron ore deposit at Ga-Nchabeleng area. To achieve more certainty about the formation of the Ga-Nchabeleng iron ore deposit, natural samples from the area were investigated as a case study with various petrological and geochemical methods. It lies in the south-eastern part of the Limpopo province, bordering on the Capricorn and Second Mopani

Districts in the north, Mpumalanga province on Nkangala and Ehlanzeni Districts in the south a and east, and the Waterberg District in the west.

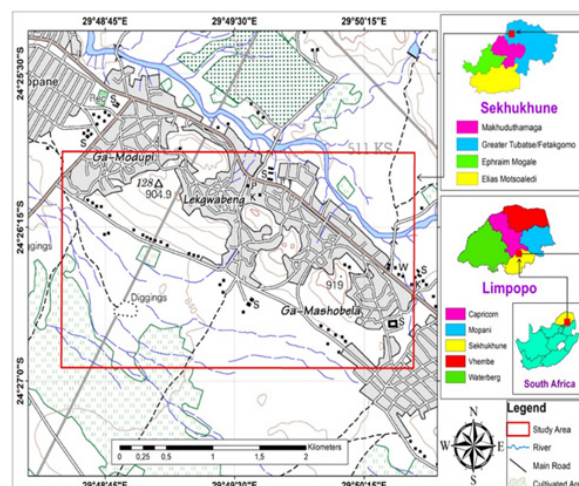


Figure 1. Location of the study area ArcGIS (2019).

2 Methodology

Fieldwork involved the collection of geological data in the study area. During fieldwork, geological field mapping, ore and rock sampling was carried out. The information required include identification of types of rocks, their location altitudes, and their structural features. The equipment which were used during fieldwork included; tape measure which was used to measure the thickness and the length of the outcrops, geological and sledgehammer were used for collection of specimens, hand lens was used as a magnifier for mineralogical identification in the fields, sample bags, clino-ruler, GPS was used to take coordinates of the sampling points, base map, map tube, clip board, permanent marker, crayons, tracing paper, field book and pens.

2.1 Geological field mapping.

The main objective of carrying out geological field mapping was to come up with a detailed geological map and to identify lithologies that host iron ore deposit. The study area was demarcated into an area of 1.8 km by 2.4 km. The demarcated area was divided into four traverses of 600 m each cutting across the lithologies in Figure 2. The GPS was used in the field for location purposes in the field in relation to the base-map and compass was used to show direction. The compass was also used to measure attitudes of lithologies while the GPS was used to record the location of outcrops. The geological and sledgehammer were used to break the fresh sample from the outcrop. Then rock samples were numbered according to the traverse,

position which they are found at, using permanent marker.

During the geological field mapping, the description of texture and mineralogy of the rock specimens was done with an aid of a hand lens and recorded in a notebook. The contact between the rock outcrop and geological structures were recorded in a notebook and photographed for later referencing when compiling a geological map of the study area.

2.2 Sampling

A total of 58 samples of rock specimen and ore were collected during the field mapping for rock identification, petrographic study, and geochemical analysis. About 2 kg of fresh specimens and ore samples were collected for laboratory work. The rock specimen was collected for further laboratory analysis using petrographic study and whole-rock microscopy. Data collected from the geological field mapping was used to compile a geological map of the area as well as a cross-section.

The study area was divided into four hills, the hills were identified based on the availability of iron ore. The sampling points of each hill are represented on Figure 3 a to d. A permanent marker was used to mark the samples during sampling, and the sample was then stored in a sample bag. The samples were also collected from contacts of host rocks and veins filled with magnetite.

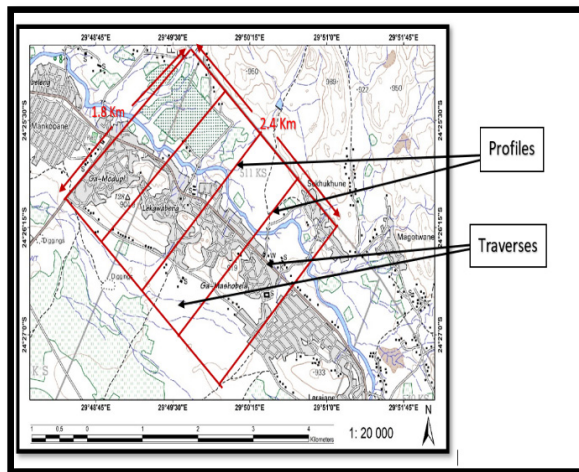


Figure 2. Map indicating the traverses that were mapped in the study area Google Earth (2019).

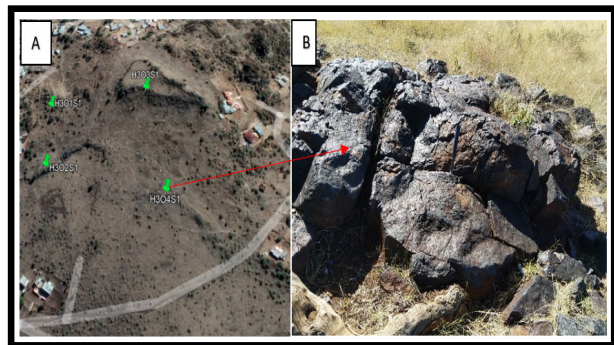
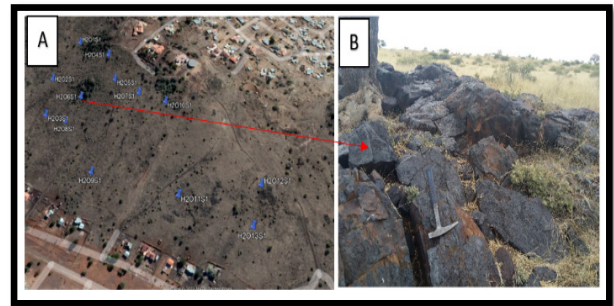
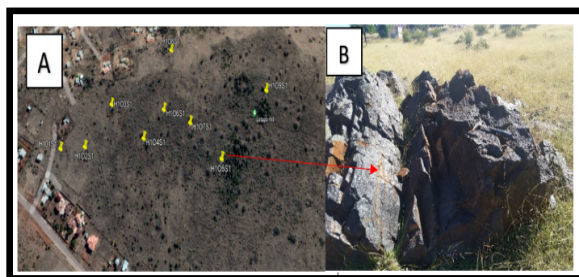


Figure 3. a Sampling points of iron ore: A-Hill 1; and B-Outcrop in Hill 1. b Sampling points of iron ore: A-Hill 2; and B-Outcrop in Hill 2. c Sampling points of iron ore: A-Hill 3; and B-Outcrop in Hill 3. d Sampling points of iron ore: A-Hill 4; and B-Outcrop in Hill 4.

2.3 Laboratory work

Laboratory work involved rock identification, petrographic studies, and X-ray florescence. This was done to gain information on the physical and chemical characteristics of iron ore and rock samples collected from the study area. Thirteen samples were dried for 12 hours in the Vacutec drying oven at 330°C to release any moisture before milling to avoid the jamming of the milling pots. Samples were milled using the Restch RS 200 milling machine on manual operation mode for 5 minutes to particle size of about 75 μm . Milling pots were cleaned using quartz to prevent contamination before analysis, the pots were cleaned to ensure that quartz will not affect the SiO₂ content of the sample during analysis.

The samples were pelletized by adding the sample into a pallet cup and using boric acid powder as a binding agent and acetone to prevent cross

contamination of samples. Pulverized sample powder was then pressed with about 3 grams of boric acid. The pellet cup was placed on the manual hydraulic press and a force of 30 tons was applied for 30 seconds. Once the pellet is ready was removed from the die-set and placed in a container with label indicating sample number and then ready for X-Ray Fluorescence spectrometry analysis.

3 Findings of the Current study

On the current study, the mode of occurrence and genesis of Ga-Nchabeleng iron ore deposit has been studied. The geological processes that are responsible for ore mineralization and genesis of the Ga-Nchabeleng iron ore deposits has been studied. The distribution of the iron ore at Ga-Nchabeleng area revealed the stock-work - stringers - finger-like structures wherein geologic structures such as veins acted as conduits. Several lithologies were identified that included varieties of gabbronorite and an iron ore magnetite. Mineralization occurred along micro-fractures which resulted in ore stockworks. The bulk chemical composition of magnetite samples revealed the occurrence of the following major oxides: SiO₂, Al₂O₃, Fe₂O₃, MgO, CaO and Na₂O as well as minor oxides of TiO₂, MnO, K₂O and P₂O₅ in Figure 4. The Ga-Nchabeleng iron ore was dominated by the presence of TiO₂, Al₂O₃ and Fe₂O₃ with average of 24.16%, 7.69% and 52.36% respectively. TiO₂, Fe₂O₃ and SiO₂ were the most abundant oxides at Ga-Nchabeleng area this enrichment can be corroborated by the prevalence of quartz minerals and hematite in the iron noted in petrographic study of iron ore. Hill three was the one with high content iron oxides, and this concludes that it was the one with rich magnetite at 55.56%.

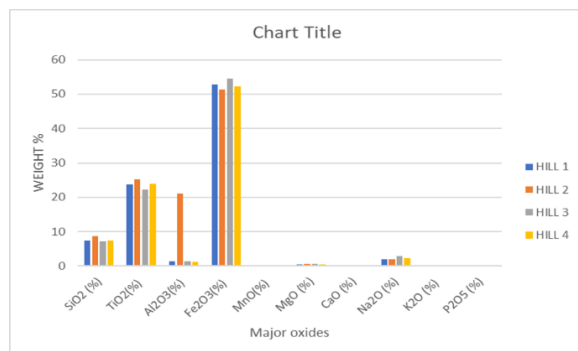


Figure 5. Major oxides average of 4 hills.

4 Genetic Model of Ga-Nchabeleng iron ore deposit.

Genesis of ore deposits is very complex, and researchers tend to change the origin of the source material so that it can match the depositional environment of the deposits (Mundalamo 2019). Iron forms under different conditions which may range from magmatic to metamorphic. The Ga-Nchabeleng iron ore deposit is an example of ore

that was formed during the magmatic eruption. A genetic model is there to show an order of information describing how a mineral deposit was formed. It also describes different attributes and factors which contributed to the formation even though their relationship is not known. There are aspects which are required for a genetic model; it must be clear and open to allow new types of deposits in the future and the model must be appropriate to the rock and the environment being investigated (Mundalamo 2019).

Mode of occurrence can be used as the first aspect when trying to identify a genetic model. The genetic concepts are used to help in knowing how the ore was formed based on site-specific concepts. The Ga-Nchabeleng iron ore deposit is of epigenetic in nature because the orebodies were localized along the fault planes and around the igneous rocks namely gabbronorite. Geological structures also help in the formation of ore deposits because they give direction of ore occurrence. Fractures in the area suggest that faults acted as a way for magma to erupt on the ground that finally resulted in the localized iron ore deposit. There was a direct crystallization of Fe-rich melt separated from a parent silica magma. The ore occurred as veins and disseminated orebodies which suggest that mineralization took place along microfractures which resulted in stockworks. The Ga-Nchabeleng orebody was formed during magmatic segregation which involved the separation of an immiscible Fe-P-rich melt from a silicate melt with the subsequent intrusion and crystallization of an Fe-rich ore body at upper crustal level. The ore contains a very pure magnetite, containing more than 50% iron. The mineralized solution originated from magma as shown in Figure 5.

This was supported by the fact ore mineralogy, ore microscopy, and the geochemical results of the area. The iron ore composed entirely of magnetite and less content of hematite. It also had a high amount of vanadium and titanium oxide which is evidence of magmatic origin.

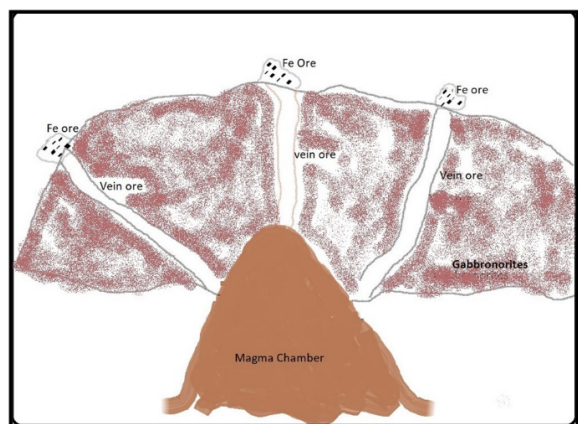


Figure 5. Genetic model of the Ga-Nchabeleng Iron ore deposit.

5 Conclusions

A detailed geological map of Ga-Nchabeleng area was produced and the following rock is associated with Iron ore; Dark and light Gabbronorite. These rocks strike to the north-west. These rocks are not associated with any other rock type in their occurrence and some are far away from the magnetite ore. Iron ore at Ga-Nchabeleng area was formed during magmatic eruption and crystallization of magma. This is further corroborated by the presence of rocks associated with magma such as Gabbronorite.

The rock is associated with rock forming minerals and have high content of iron oxide. The study concluded that the iron ore is hosted by intermediate to felsic igneous rocks which were found to be gabbronorite and the magnetite ore formed stringers zones that were randomly oriented veins associated with fractional crystallization of the layered complexes.

Acknowledgements

DSI-NRF CIMERA for funding the project and all other guidance. University of Pretoria for the analysis of samples for the geochemical results. My supervisors for support and patience throughout the project.

References

- Jonsson, E., Troll, V.R., Högdahl, K., Harris, C., Weis, F., Nilsson, K.P. and Skelton, A., (2013): Magmatic origin of giant 'Kiruna-type' apatite-iron-oxide ores in Central Sweden. *Scientific reports*, 3, p.1644
- Google earth V 6.2.2.6613. (2019). Digital Globe 2012. <http://www.earth.google.com> [April 30, 2019].

Insights into IOA and IOCG deposit genesis from comparative isotopic analysis of Fe and Cu isotope compositions in magnetite and ores

Ryan Mathur¹, Michael Di Maio², Linda Godfrey², Adam C. Simon³, Chris Empro³, Vladamir Lisitsin⁴, Courtney Dhnaram⁴, Ioan Sanislav⁵, Irene del Real⁶

¹ Geology Department, Juniata College, Huntingdon PA U.S.A.

² Department of Earth and Planetary Sciences, Rutgers University, U.S.A.

³ Department of Earth & Environmental Sciences, University of Michigan, Michigan, U.S.A.

⁴ Geological Survey of Queensland, Brisbane, Australia

⁵ Earth and Environmental Science, James Cook University, Townsville Australia

⁶ Department of Geology, Universidad Austral de Chile, Chile

Abstract.

Transition metal isotope compositions of ores from IOA and IOCG deposits compared to each other as well as other deposit types provides insight into mechanisms of ore deposit formation. In this contribution, we provide new Fe isotope data from classic IOAs in Bafq, Iran, several Fe-oxide apatite deposits in New Jersey and compare them to data in the literature. Clearly, IOAs have tighter ranges of values than IOCGs and higher mean values which could indicate magmatic /orthomagmatic versus hydrothermal processes that operated in each deposit type respectively. New copper isotope data from chalcopyrite in IOCGs from Candelaria, Ernst Henry, Jericho, and Mina Justa show an identical range to porphyry copper deposits and have a lower mean value to porphyry copper sulfides Figure 2. Sed Ex copper deposits and VMS have larger ranges and higher means values as well. Potential interpretations for these distinct differences in copper isotope compositions could range from ligand transport mechanism to different copper sources. Constraining sources for the ores can difficult given overlapping values of crustal and mantle sources (figure 2). The comparative analysis presented show the importance of metal isotope analysis and how direct information can be obtained to metal transport and ore genesis through study of the isotopes of the metal commodities.

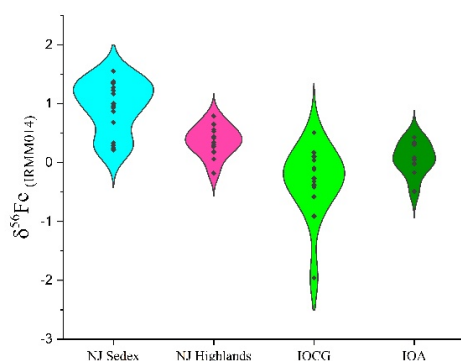


Figure 1- Fe isotope data presented here and from the literature from magnetite.

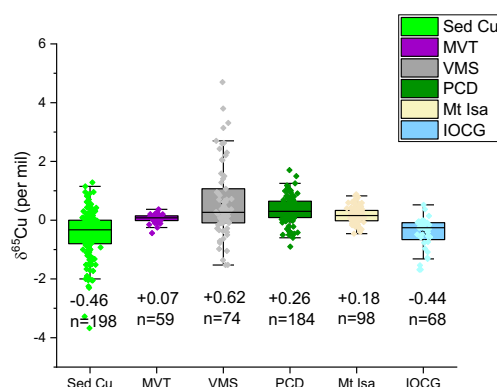


Figure 2- Copper isotope comparison of chalcopyrite from major ore deposit types, data presented here and taken from the literature. Data reported relative to NIST 976.

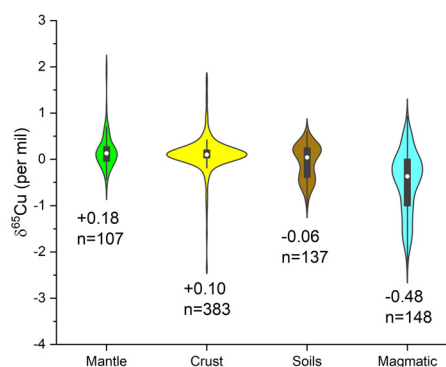


Figure 3- Summary of copper isotope data of geological materials, data taken from the literature. Data reported relative to NIST 976.

Controls on iron oxide-Cu-Au mineralisation: dogma versus data

Tobias U. Schlegel, Weihua Liu, Helen B. McFarlane, Renee Birchall, and James R. Austin
CSIRO Mineral Resources, Australia

Abstract. The shear zone hosted Starra-276 IOCG deposit shows high Au/Cu ratios combined with high Cu ore grades. Zoning in gold, copper and Cu sulphides corresponds to a transition from hematite-quartz-carbonate ironstones and breccias to magnetite (\pm hematite)-quartz-chlorite-muscovite-carbonate altered rocks. Systematically collected, SEM-based modal mineralogy, structural information from measurements of the anisotropy of magnetic susceptibility in combination with thermodynamic alteration calculations enable a consistent model for IOCG ore formation in which hydrolytic alteration and in particular the fluid-rock ratios during alteration exert control on the zoning of principal alteration minerals and the distribution of gold, copper and Cu sulphides in the deposit. Hematite-quartz \pm carbonate \pm barite ironstones and breccias form simultaneously with the precipitation of gold and native copper via acidic fluid-neutralisation in hydrothermal alteration regimes characterised by increasing fluid-rock ratios because intense hydrolytic alteration produces new porosity. Copper sulphides precipitate in areas of lower fluid-rock ratio showing aluminosilicate-stable hydrothermally altered rocks. The zonation in Au-Cu-chalcocite-bornite-chalcopyrite-pyrite is the result of a low-T, very acidic, SO₄-bearing ore fluid. Our alteration models involving Fe-Na-K-Cl-rich and CO₂-H₂S-bearing brines failed to reproduce ore mineral assemblages.

1 Introduction

Iron oxide-copper-gold (IOCG) deposits are characterised by a system-scale alteration mineral zoning with some deposits showing distinct, yet unexplained, gross (or partial) zoning of economic elements and minerals from centre to margin Au-Cu-chalcocite-bornite-chalcopyrite-pyrite (e.g., at Olympic Dam, Ehlig et al. 2012) consistent with the transition from hematite-quartz \pm carbonate \pm barite breccias and ironstones to hematite/magnetite-aluminosilicate bearing breccias and ironstones. Although Cu-Au mineralisation has been interpreted to result from hydrothermal brecciation and genetically-related infill and veining, ore bodies typically form by host rock replacement and show spatial relations to faults, shear zones, unconformities, and breccias which led to the widely accepted, but weakly defined, interpretation that IOCG deposits are structurally controlled. The structures typically extend beyond the footprint of the deposit and are largely barren; thus, it is unlikely that they control the exact location of high-grade Cu-Au mineralization. The structures are thought to primarily act as fluid pathways allowing ore fluids to migrate from their source regions towards target areas where mineralisation is caused by alteration-related infill into rock pores, the breccia matrix, and by replacement of pyrite. Regardless of their

importance for fluid flow and mineralisation, structures and neighbouring rocks represent locations of extreme contrasts in fluid-rock ratio (f/r). Importantly, the f/r exerts primary control on mineral stability at any given conditions during alteration and mineralisation (e.g., T, P, oxidation and sulfidation state, fluid conditions, Reed 1997). The Cloncurry METAL project characterised 1590 samples from 23 deposits and prospects across the Cloncurry district in Australia and resulted in a published integrated, geoscience dataset with data from 10 analytical techniques (Austin et al. 2021).

In this contribution, we focus on the Starra-276 shear zone hosted IOCG deposit and use modal mineralogy, structural data, and thermodynamic modelling to decipher the cause for the zoning in alteration, ore minerals (Figures 1 and 2) and explore the basis for high-grade Cu mineralisation (Figure 3). We test if the mineral zoning can be obtained by hydrothermal alteration reactions between host rocks and previously proposed ore-fluid compositions and conditions between 550°C and 200°C determined from fluid inclusions (Baker et al. 2008, Schlegel et al. 2018). Previous alteration studies conducted at Starra focused on mineral paragenesis, structural controls and described general relations among zones of alteration minerals (e.g. McFarlane et al. 2020), but insufficiently explained why the Starra-276 deposit shows many aspects of a quality IOCG deposit including high Au/Cu ratio paired with high Cu grades in ores. Together, several deposits along the Starra and related shear zones produced 11.4Mt @ 2.1% Cu and 3.2g/t Au between 1992 and 2002 (McGeough and Faulkner 2017).

2 Methodology

The mineralogy in samples from the Starra-276 deposit was determined using a scanning electron microscope (SEM), coupled with 3 EDAX energy dispersive X-ray spectroscopy (EDS) detectors and a backscatter electron (BSE) detector combined with a Tescan Integrated Mineral Analyser (TIMA) at the CSIRO in Perth, Australia. Standard electron beam alignment, focusing, and calibration of the detectors were conducted before each analytical run of up to 22 samples. The anisotropy of magnetic susceptibility (AMS) was determined from the same samples. The AMS defines an ellipsoid of the magnetic susceptibility of a rock. The technique reflects the grain shape of magnetite or the crystallographic-preferred orientation and alignment of Fe-bearing minerals, thus defining the magnetic fabric, allowing the calculation of a dominant

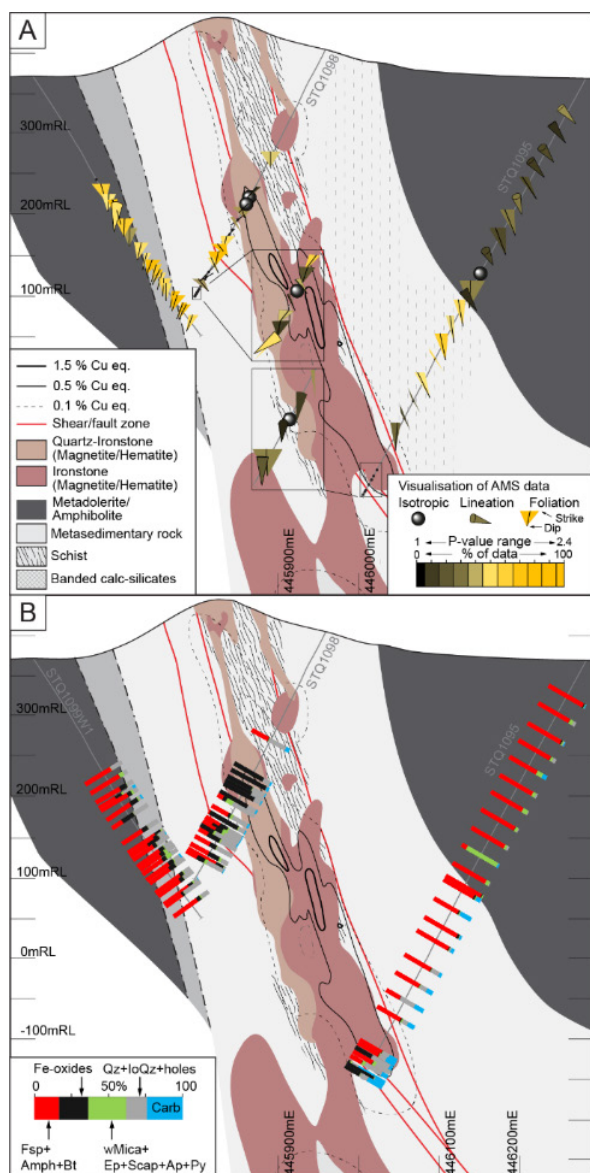


Figure 3. E–W trending cross-section across the Starra-276 deposit showing (A) AMS data and (B) the alteration zoning illustrated in 100% stacked bar mini-illustrations for each sample in relation to the Cu grades and simplified lithologies derived from company data.

intensively quartz–hematite \pm carbonate (siderite, dolomite, calcite) altered, and aluminosilicate depleted, originally magnetite ironstones (Figure 1, Columns N–R). Chalcocite, covellite, and bornite formed at the transition between quartz–hematite–siderite ironstones and magnetite (\pm hematite)–quartz–chlorite–muscovite–carbonate ironstones (Figure 1, Columns E–W) whereas chalcopyrite is hosted in ironstones and magnetite–pyrite schists showing abundant chlorite and white mica which partially (or completely) replace feldspar, biotite, and amphibole bearing host rocks and early alteration minerals (Figure 1, Columns S–X). The zoning suggests that economic mineralisation was associated with H^+ – CO_2 (hydrolytic) alteration. The high-grade ore zone is surrounded by sheared rocks affected by Fe(\pm K)–S alteration (magnetite–hematite–biotite–apatite–quartz–pyrite), which overprinted

broad zones of Na–Ca altered host rocks (albite–actinolite–scapolite; Figure 1, Columns Y–AB). The dominant type of feldspar in the medial to distal alteration halo around the ore zone is albite but the type of feldspar is irrelevant because mineralisation-related hydrolytic alteration was feldspar-destructive (Figure 2B).

4 Thermodynamic calculations and interpretations

Hydrothermal alteration at Starra was modelled by reacting two fluid types A and B to a mineral assemblage, aiming to reproduce the ore mineral compositions at the Starra-276 deposit (Figure 1, Columns G–AA). Fluid A is a low salinity and at low-T very acidic, SO_4 -bearing fluid containing 1000 ppm Cu (ore fluid A in Schlegel et al., 2018). Fluid B is a Fe–Na–K–Cl-rich, CO_2 , H_2S , and Cu-bearing brine (fluid B with 100 ppm Cu and added CO_2 , see Schlegel et al. 2018). The brine approximates the composition of one fluid inclusion for which Cl, K, Fe, Cu concentrations are available. In absence of more relevant compositional fluid inclusion data from Starra, thermodynamic models explored hydrothermal alteration conditions between 550 °C

/2.5 kbar and 125 °C/ P_{sat} representing the range of homogenisation temperatures of fluid inclusions from Starra (Baker et al., 2008). Both fluids reacted to a rock showing a mineral composition characteristic of the medial alteration footprint at the Starra-276 deposit (Figure 1). Alteration models at 200 °C involving fluid A reproduce the quartz–hematite–chlorite–muscovite ironstones and result in high Cu grades from chalcocite (~2.5 vol.%) at f/r between 25 and 60 (Figure 3A). Bornite (~1.2 vol.%) and chalcopyrite (~1.5 vol.%) form in quartz–magnetite/hematite–chlorite–muscovite ironstones and in magnetite/hematite–chlorite altered host rocks at f/r between about 3 and 12. The calculated mineral composition is consistent with the mineral abundance in the marginal ore zone. Cuprite formed at 125 °C in quartz–hematite–chlorite–muscovite ironstones, thus in rocks like sample STA205 (Figure 1). Addition of CO_2 to fluid A results is quartz–hematite–siderite–muscovite ironstones with chalcocite (~2 vol.%), bornite (~0.3 vol.%) and chalcopyrite (~0.6 vol.%) between f/r of 5 and 40. All models with fluid A resulted in IOCG-characteristic chalcocite–bornite–chalcopyrite–pyrite zoning (Figure 3A) and thus indicate that the mineral sequence develops due to a systematic decrease in fluid-rock ratio from the ore-fluid feeder zone to significantly more rock-dominant parts of the developing ore body and its alteration footprint (Figures 2 and 3A). Importantly, alteration models between 400 °C and 250 °C result in significant reduction of the rock volume (Figure 3B).

As a result, reactions between ore fluid A and the host rocks likely foster fluid-flow by enhancing the permeability of the shear zone due to increasingly connected rock-pores and may even by local

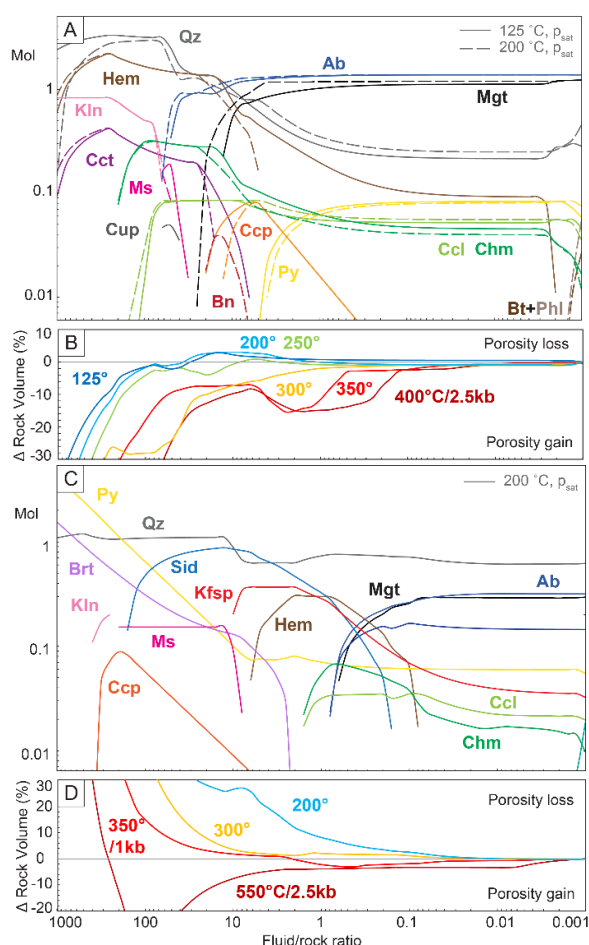


Figure 3. Static closed system models of alteration reactions between albite-magnetite schists and (A, B) the low salinity, ore fluid A, and (C, D) a Fe-Na-K-Cl-rich, CO_2 -bearing brine B at variable T and P. Vertical concentration lines are not. Abscissa shows decreasing f/r ratios from left to right. (A, C) Alteration minerals in moles/kg of initial fluid. (B, D) Change of the rock volume. Mineral abb. Whitney and Evans (2010).

collapse brecciation. Alteration models between fluid B and the host rock at 500 °C/2.5 kbar and high f/r result quartz-magnetite-barite ironstones. Mineral assemblages including feldspars, diopside, and biotite/phlogopite form at low f/r. Cooling and decompression to about 200 °C/ P_{sat} result in increasing amounts of pyrite, hematite, quartz, muscovite, and chalcopyrite at high f/r and in siderite, K-feldspar, chlorite-bearing rocks at low f/r (Figure 3C). Any of the models resulted in a composition like the quartz-hematite-siderite-chlorite-muscovite ironstone with sulphides as they occur in the ore zone (Figure 1), or in the characteristic Cu sulphide zoning. In addition, all but one model resulted in a large increase in rock volume at any f/r between about 0.1 and about 100 (Figure 3D). The alteration mineral assemblages would successfully clog ore-fluid flow in the Starra shear zone, or in any geologically reasonable structure, and thus inhibit economic Cu-Au mineralisation. For these reasons, the saline Fe-Na-K-Cl ($\pm\text{CO}_2$) rich fluid B alone is an implausible ore fluid. In contrast, fluid-rock reactions involving

fluid B likely produce mineral assemblages like the ones observed in IOCG prospects containing subeconomic Cu grades.

5 Conclusions

The Au-Cu-cuprite-chalcocite-bornite-chalcopyrite-pyrite mineral zoning in IOCG deposits is controlled by changes in f/r ratio active during mineralisation and associated hydrolytic alteration. Gold-bearing, but Cu-barren quartz-hematite ($\pm\text{siderite}\pm\text{barite}$) ironstones and breccias develop where ore fluids enter the mineralising system. At the transition to chlorite-muscovite-feldspar bearing ironstones and breccias, which host the Cu ores, alteration reactions occur at lower f/r and Cu sulphides precipitate due to acidic-fluid neutralisation. Economic mineralisation involves at least one Cu-Au charged ore fluid A containing S as sulphate. The reactions of ore fluid A with the rocks previously modified by Na-Ca \pm Fe alteration foster ore-fluid infiltrations by changes in the porosity-permeability patterns within and adjacent to faults, shears, breccias, and unconformities. These structures exert control on regional to more local fluid flow but not necessarily on the location of economic mineralisation itself.

References

- Austin JR, Stromberg J, Birchall R, et al (2021) The Cloncurry METAL Geodatabase mk1: A scale-integrated relational geodatabase for the Cloncurry District, Northwest Queensland. Part I: Cloncurry METAL Report 2018/21. CSIRO, Australia, 50p.
- Baker T, Mustard R, Fu B, Williams PJ, et al (2008) Mixed messages in iron oxide-Cu-Au systems of the Cloncurry district, Australia: insights from PIXE analysis of halogens and copper in fluid inclusions, *Min Dep* 43:599–608.
- Ehrig K, McPhie J, and Kamenetsky V (2012): Geology and mineralogical zonation of the Olympic Dam iron oxide Cu-U-Au-Ag deposit, South Australia, *Econ Geol Spec Pub* 19:237–267.
- McFarlane HB, Austin JR, Schlegel TU, et al (2021) Starra 276: Redox Gradients and Structural controls: Integrated petrophysical, structural and mineralogical analysis: Part V: Cloncurry METAL Report 2018/2021 CSIRO, Australia, 58p.
- McGeough MA, and Faulkner IL (2017) Selwyn mineral field, In Phillips GN (ed) *Australian Ore Deposits*, AusIMM, Melbourne, 864p.
- Reed ME (1997) Hydrothermal alteration and its relationship to ore fluid composition, In Barnes HL, (ed) *Geochemistry of hydrothermal ore deposits*, 3rd edn, Wiley New York, pp 303–365.
- Rochette P, Jackson M, and Aubourg C (1992) Rock magnetism and the interpretation of anisotropy of magnetic susceptibility, *Rev of Geophys* 30:20–226.
- Schlegel TU, Wagner T, Wälle M, Heinrich CA (2018) Hematite breccia-hosted iron oxide copper-gold deposits require magmatic fluid components exposed to atmospheric oxidation: evidence from Prominent Hill, Gawler craton, *Econ Geol* 113:597–644.
- Shvarov, YV (2008) HCh: New potentialities for the thermodynamic simulation of geochemical systems offered by windows, *Geochemistry International* 46: 834–839.

Characterization of the Kiskamavaara IOCG-(Co) deposit, northern Norrbotten, Sweden.

Iris van der Werf¹, Joel B. H. Andersson¹, Tobias E. Bauer¹ Thomas Kearney²

¹ Division of Geosciences, Luleå University of Technology, 97187 Luleå Sweden.

² Talga Group AB, Kungsgatan 5B, 972 35 Luleå

Abstract. This study presents new insights into the structural geometry and the distribution of cobalt in the Kiskamavaara IOCG-(Co) deposit which is located in the northern Norrbotten ore province in Sweden. The aim of the study is to determine the structural controls and cobalt distribution in the ore body along with establishing the correlation between Co-Cu mineralization in deposit scale by drill core logging, geophysical map interpretation, 3D modelling, and geochemical analyses. The results show that the host rock is composed of rhyolites/dacites, andesites and basalts that belong to the Porphyry group. Most mineralization styles form the matrix of hydrothermal breccias of several generations and form three clusters that are situated at junctions between a first order shear zone and associated second order structures. Geochemical analyses show a weak correlation between cobalt and copper, especially at the mineralization margins, either indicating an evolving mineralization system, a multi-stage mineralization event or different mobilization behaviors during overprinting alteration events. Kiskamavaara as a case study has the potential to increase the understanding of the origin and evolution of cobalt in IOCG systems within Norrbotten and perhaps beyond.

1 Introduction

The Kiskamavaara ore deposit is classified as an iron oxide-copper-gold (IOCG) deposit and is located in northern Norrbotten, Sweden (Martinsson et al. 2011). The deposit is situated in the Karesuando–Arjeplog deformation zone (Fig. 1; KADZ; Bergman et al. 2001). However, recently Bauer and Andersson (2021) argue for a SSE deflection of the crustal shear zone into the Nautanen deformation zone (NDZ), which also hosts the Nautanen IOCG- and the Aitik porphyry Cu-Au-Ag deposits.

The Kiskamavaara deposit was discovered by the Swedish Geological Survey (SGU) during a drilling campaign between 1972-1980 (Persson 1980). The Fe, Cu and Au mineralization is hosted within three elongated lenses that are also enriched in Co (Persson 1980). Due to the increasing importance of cobalt as a battery metal in recent years, SGU classified the Kiskamavaara deposit as a deposit of 'national interest' (SGU 2018). The deposit constitutes a mineralized zone that is approximately 900 m in length. The total resource is estimated at 3.2 Mt at 0.06% Co and 0.37% Cu (Persson 1981; Persson 1982).

Despite the general interest in northern Norrbotten ore deposits, only few studies have

focused on the Kiskamavaara deposit itself (Martinsson, 2011; Metzger, 2019). Instead, several studies investigated the regional geology and structure (e.g., Bergman et al. 2001; Weihed et al. 2005; Martinsson et al. 2016; Bauer and Andersson 2021), thus providing a robust regional framework for further deposit- to grain-scale studies.

This study aims to understand the structural and geochemical controls on the Kiskamavaara IOCG-(Co) deposit with a focus on Co-Cu distribution at the deposit scale. Establishing a more detailed framework on Cu-Co distribution and associated structural and geochemical controls on the Kiskamavaara deposit has the potential to increase the understanding of the origin and evolution of cobalt in IOCG deposits.

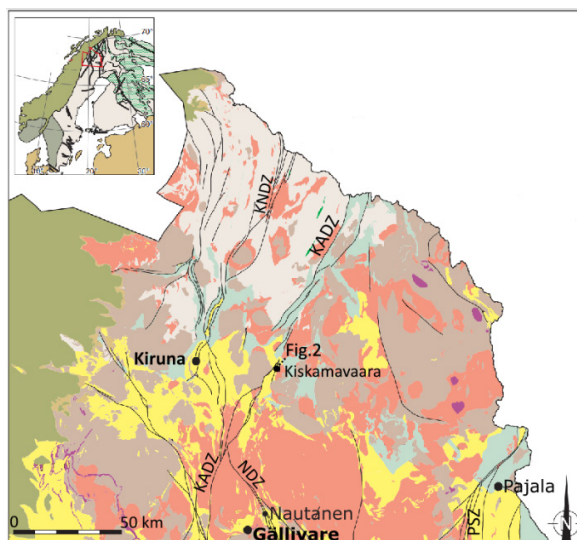


Figure 1: Simplified geological map of northern Norrbotten area (modified after Bergman, 2018). Green= Allochthonous rock, Mustard= Sedimentary cover rock, Purple= Gabbro, metagabbro, diabase, Orange= intrusive rocks (c. 1.8 Ga), Brown= Intrusive rocks (c. 1.89-1.84), Yellow= Svecofennian supracrustal rock, Turquoise= Karelian rock, Grey= Archean rock, NDZ= Nautanen deformation zone, black line= ductile shear zone, KADZ= Karesuando–Arjeplog deformation zone, PSZ= Pajala shear zone, KNDZ= Kiruna-Naimakka deformation zone.

2 Geological background of the northern Norrbotten area

Northern Norrbotten is part of the Fennoscandian shield. The basement rocks consist of Archean (3.2-2.7 Ga) tonalite-trondhjemite-granodioritic gneisses (Martinsson et al., 2018; Bergman et al. 2001). Between 2.44 and 2.01 Ga intracontinental rifting caused mafic volcanism and the deposition of

deposited during the Svecokarelian orogeny (ca 1.9–1.8 Ga). These rocks are strongly influenced by crustal reworking, magmatic intrusion events and metamorphism widespread in the northern parts of the Fennoscandian shield. In northern Norrbotten, deformation processes are associated to multistage magmatic and metamorphic events that are linked to early approximately N-S convergent continental margin processes and subsequent E-W crustal shortening, which caused a complex structural-metamorphic pattern (Bergman et al. 2001).

3 Geological characteristics of the Kiskamavaara deposit.

The primary lithologies in the Kiskamavaara area are intermediate porphyritic reddish-grey volcanoclastic rocks, tuffs and quartzite. Intense K-feldspar alteration affected the overall bedrock whereas scapolite-biotite alteration is limited to tuffites (Martinsson 2011). Carbonate-albite alteration is present in more distal parts of the deposit (Persson 1980; Martinsson 2011). Additionally, two intrusions are present in the Kiskamavaara area. An Orosirian granodiorite southwest of the deposit, and a metadiabase intruding the mineralization in the southern part of the deposit (Martinsson 2011).

The mineralization in Kiskamavaara comprises of magnetite, chalcopyrite, and Co-bearing pyrite (Ekström 1978). Central parts of the ore lenses consist largely of pyrite infill as the breccia matrix and decreases in intensity to disseminated pyrite-chalcopyrite-magnetite within the matrix at the lens margins (Martinsson 2011).

The deposit is flanked by two steep WNW-dipping shear zones with reverse oblique dextral components (Metzger 2019). Sets of brittle-ductile faults offset the shear zones with both dextral and sinistral sense-of-shears. Additionally, double plunging non-cylindrical folds with fold axes trending sub-parallel to the shear zones are present in the area (Bauer and Andersson 2021).

4 Results and discussion

4.1 Geological structures

Geophysical aeromagnetic data provided by Talga Group AB, shows a set of magnetic-high lineaments interpreted as fault/shear structures based on results in previous studies, e.g., Lynch et al. (2018) and Bauer et al. (2022). The magnetic anomalies indicate a set of NE-SW trending first order ore proximal structures of which one deflects into a E-W trend (Fig. 2). Between the NE-SW trending structures, four N-S trending second order structures connecting both first order structures are indicated on the aeromagnetic map (Fig. 2). Most of the lineaments show dextral offsets along later NW-SE structures or sinistral offset along E-W to NE-SW directions.

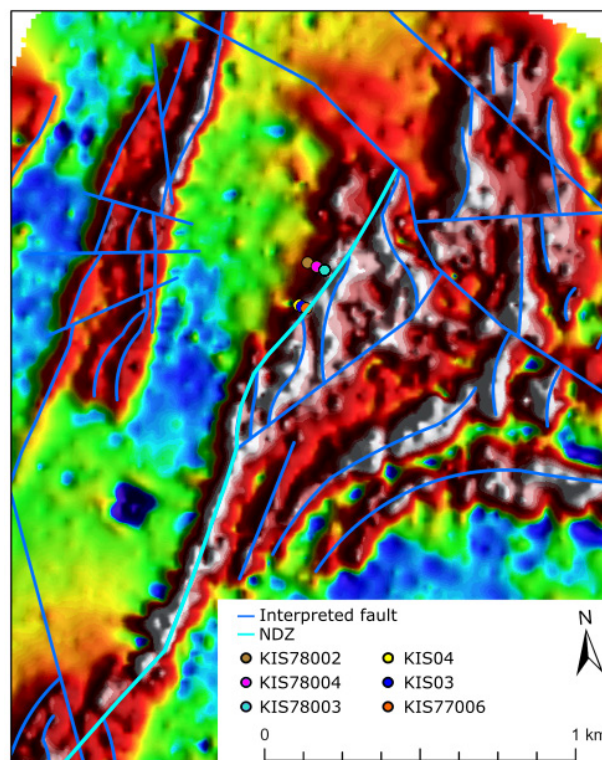


Figure 5: Structural interpretation of the Kiskamavaara deposit on top of EM geophysical map. The drill core locations correspond with the drill cores in Figure 4. NDZ = Nautanen deformation zone.

4.2 Geochemical analyses

Chemical analyses of four drill cores in the central part of the deposit indicate the rocks are sub-alkaline with basaltic, andesitic, rhyolitic/dacitic and minor trachytic compositions (Pearce 1996; Fig.3). The trachytes exhibit a similar composition to the rhyolite/dacite group albeit being slightly more alkaline. Therefore, the rhyolite/dacite and trachyte will be regarded as one group.

Furthermore, the rock samples display low concentrations of Ti and Zr, indicating that the porphyritic rocks in the central part of the Kiskamavaara deposit belong to the Porphyrite group (Bergman et al. 2001). Plotting Cu vs Co shows a cluster without a clear trend, indicating a low correlation between the occurrence and distribution of both metals in the deposit (Fig. 3).

We suggest the low correlation between Co and Cu mirrors either an evolving mineralization system or a multiphase mineralization/remobilization event(s). In either case further evaluation of the mineralization is needed for concluding remarks.

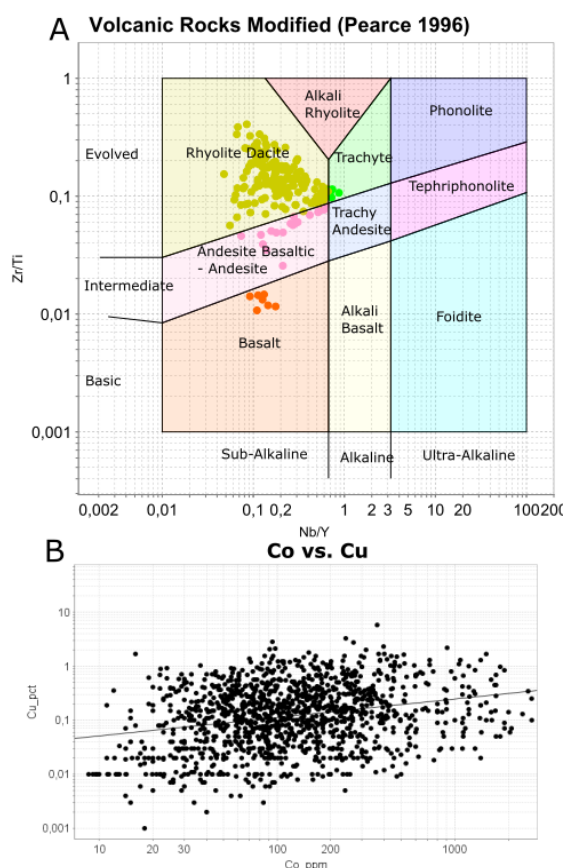


Figure 6: A: The rock classification model after Pearce (1996) shows that four rock types are present in the Kiskamavaara area. B: Co vs. Cu plot with regression line shows a weakly correlated cluster of datapoints between both elements.

4.3 Co-Cu Mineralization geometry

Geochemical analyses of drill cores obtained by SGU and Talga Group AB, combined with structural interpretations based on aeromagnetic maps indicate that the junctions between first and second order structures were the most favorable trap sites in the system. The second-order structures were only drilled near the ore proximal first order structure. Since the mineralization is located around the fault junctions the mineralization may extend along the second order structures and is not yet constrained in that direction. Such an interpretation would be largely in line with the structural configuration of the Nautanen deposit (Bauer et al. 2022).

The Kiskamavaara mineralization Consists of three separate clusters along the first order structure. Of the three clusters, the middle cluster exhibits the highest Co-Cu concentrations with an enrichment factor of 108.8 Co and 953.3 Cu compared to the average upper continental crust in up to 2 meter intervals (Fig.4). The mineralization clusters show a zoning pattern of central mainly Co-bearing pyrite, grading into decreasing Co concentrations but increasing Cu concentrations. Towards the cluster margins Cu decreases again and only some Co remains. Presence of cobalt without copper in the furthest margins of the

mineralization possibly indicates either primary Co-Cu deposition with a changing mineralization character or that cobalt was transported further than copper during remobilization. However, further investigations are necessary to fully comprehend the metal evolution in the deposit.

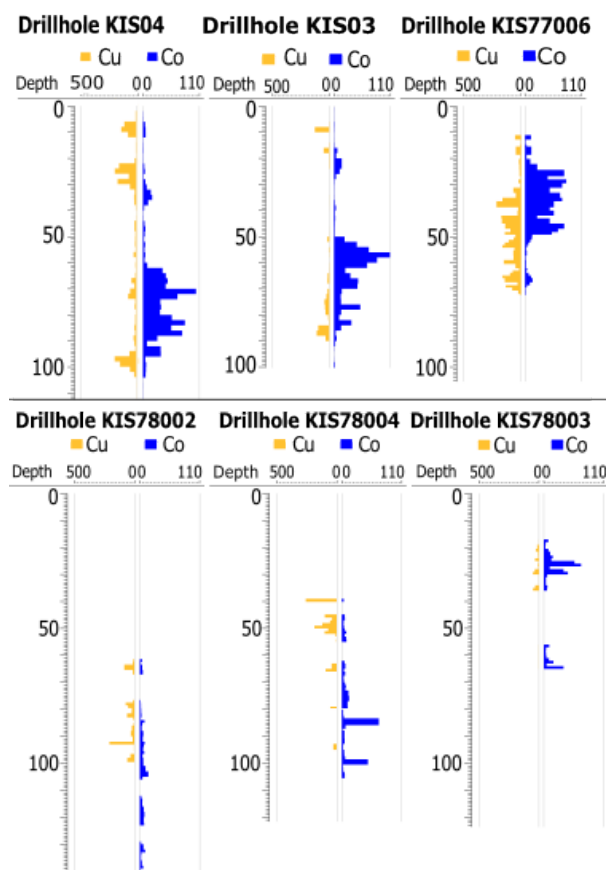


Figure 7: Schematic overview of drill cores showing the Co-Cu distribution normalized to the average upper continental crust within the center of the mineralization (top panel) and the mineralization margin (bottom panel). Drill core locations in Figure 2.

5 Conclusions

The Kiskamavaara deposit is a structurally controlled IOCG-(Co) deposit, characterized by the occurrence of three Co-Cu mineralization clusters with the highest mineralization grades concentrated in the central part decreasing outwards. The zonation pattern of the mineralization shows a wider distribution of cobalt compared to copper into the mineralization margins, which either indicates an evolving mineralisation character, a multiphase mineralization event or different behaviors during later remobilization. The centers of the mineralization clusters are primarily situated at the junction of the main NNW-SSE shear zone and second-order brittle-ductile NW-SE structures. Cobalt bearing pyrite is the main ore mineral in the Kiskamavaara deposit and frequently accompanied by chalcopyrite.

Whole rock geochemical analysis indicates that the central part of the Kiskamavaara deposit is composed of three rock types: basalts, rhyolites/dacites and andesites (Pierce 1996). Both the Ti and Zr content in the porphyritic rocks are low, which indicates that they belong to the Kiruna porphyrite group.

Acknowledgements

This project was funded from the European Union's Horizon Europe research and innovation program under Grant agreement n°1010557357, EIS – Exploration Information System.

References

- Bauer TE, & Andersson J, (2021) Structural controls on Cu-Au mineralization in the Svappavaara area, northern Sweden—the northern continuation of the IOCG-hosting Nautanen deformation zone. In *Paleoproterozoic deformation in the Kiruna-Gällivare area in northern Norrbotten, Sweden: Setting, character, age, and control of iron oxide-apatite deposits*. Doctoral thesis, Luleå University of Technology.
- Bauer TE, Lynch EP, Sarlus Z, Drejning-Carroll D, Martinsson O, Metzger N, & Wanhainen C, (2022) Structural Controls on Iron Oxide Copper-Gold Mineralization and Related Alteration in a Paleoproterozoic Supracrustal Belt: Insights from the Nautanen Deformation Zone and Surroundings, Northern Sweden. *Economic Geology*, 117(2), 327–359. <https://doi.org/10.5382/econgeo.4862>
- Bergman S, (2018) Geology of the Northern Norrbotten ore province, northern Sweden. *SGU Rapport och meddelanden*
- Bergman S, Kübler L, & Martinsson O, (2001) Description of regional geological and geophysical maps of northern Norrbotten County (east of the Caledonian orogen).
- Ekström T, (1978). Koboltförande pyrit i två profiler från Kiskamavaara. *Sveriges geologiska undersökning Brap 78001*.
- Gaal, G, & Gorbatshev R, (1987) An Outline of the Precambrian Evolution of the Baltic Shield. In *Precambrian Research* (Vol. 35). [https://doi.org/10.1016/0301-9268\(87\)90044-1](https://doi.org/10.1016/0301-9268(87)90044-1)
- Lynch, EP., Bauer, TE., Jörnberger, J., Smarlus, Z., Morris, G., & Persson, PO. (2018). Petrological and structural character of c. 1.88 Ga meta-volcanosedimentary rocks hosting iron oxide-copper-gold and related mineralisation in the Nautanen–Aitik area, northern Sweden. *SGU Rapport och meddelanden*, 141, 107–150.
- Martinsson O, (1997) Tectonic setting and metallogeny of the Kiruna greenstones. Doctoral thesis, Luleå University of Technology.
- Martinsson O, (2011) Kiskamavaara a shear zone hosted IOCG-style of Cu-Co-Au deposit in Northern Norrbotten, Sweden. Biennial SGA meeting, Antofagasta, Chile, Abstract, 470-472.
- Martinsson O, Billström K, Broman C, Weihed P & Wanhainen C, (2016) Metallogeny of the Northern Norrbotten Ore Province, northern Fennoscandian Shield with emphasis on IOCG and apatite-iron ore deposits. *Ore Geology Reviews*, 78, 447-492. <https://doi.org/10.1016/j.oregeorev.2016.02.011>
- Martinsson O, Bergman S, Persson PO & Hellström, FA, (2018) Age and character of late-Svecokarelian monzonitic intrusions in north-eastern Norrbotten, northern Sweden. In: Bergman, S.: *Geology of the Northern Norrbotten ore province, northern Sweden*. Rapport och Meddelanden 141, Sveriges geologiska undersökning. pp 381–399.
- Metzger N, (2019) Structural controls on the shear zone hosted, IOCG-style Kiskamavaara Cu-Co-Au mineralization. MSc-thesis, Luleå University of Technology.
- Pearce JA (1996) Pearce 1996 volcanic model. In Wyman, D.A., Ed., *Trace Element Geochemistry of Volcanic Rocks: Applications for Massive Sulphide Exploration: Geological Association of Canada, Short Course Notes*, 12, 79–113.
- Persson G (1980) Kiskamavaara koppar-koboltfyndighet Geologisk beskrivning och kvantitativ beräkning av koppar-koboltinnehållet del 1, Sveriges geologiska undersökning Brap 80524.
- Persson G (1981) Kobolt-kopparfyndigheten vid Kiskamavaara. Del 1 tonnage och haltberäkning, del 2 borrhprotokoll och analysintyg, Sveriges geologiska undersökning Brap 81552.
- Persson G (1982) Kiskamavaara tonnageberäkning på koppar och kobolt, Sveriges geologiska undersökning Brap 82509.
- SGU (2018) Nautanen och Kiskamavaara blir riksintressen, <https://www.sgu.se/arkiv/arkiv-nyheter/2018/juli/nautanen-och-kiskamavaara-blir-riksintressen/>
- Weihed P, Arndt N, Billström K, Duchesne JC, Eilu P, Martinsson O, Papunen H, & Lahtinen R, (2005) 8: Precambrian geodynamics and ore formation: The Fennoscandian Shield. <https://doi.org/10.1016/j.oregeorev.2005.07.008>



17th Biennial SGA Meeting
ETH Zurich, Switzerland
August 28 – September 1